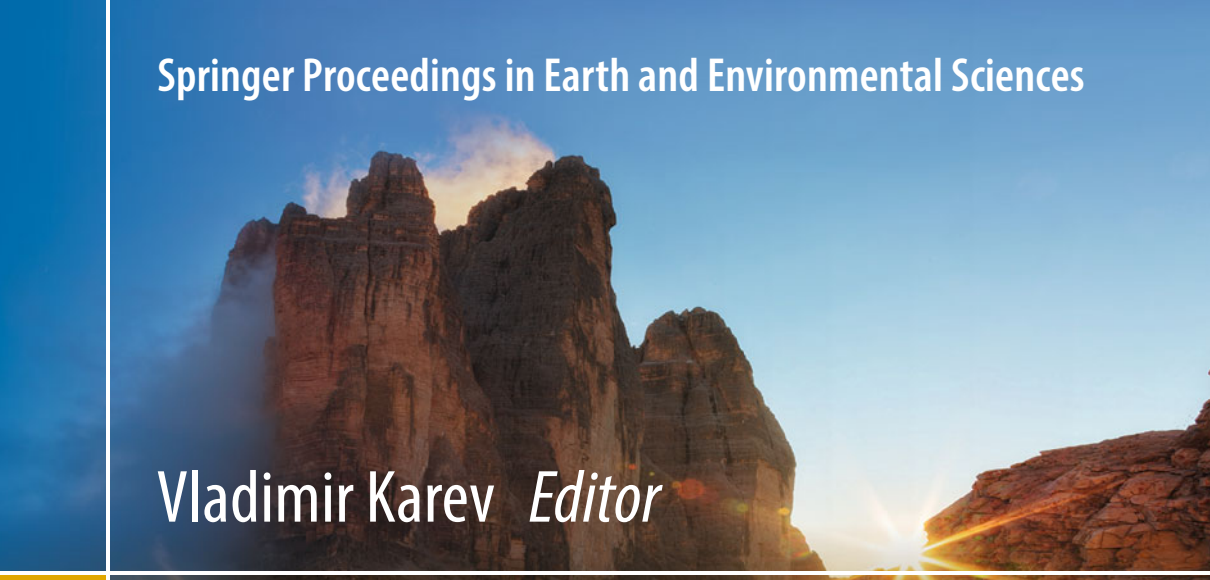
Springer Proceedings in Earth and Environmental Sciences



Vladimir Karev *Editor*

Proceedings of the 9th International Conference on Physical and Mathematical Modelling of Earth and Environmental Processes

Springer

Springer Proceedings in Earth and Environmental Sciences

Series Editors

Natalia S. Bezaeva, The Moscow Area, Russia

Heloisa Helena Gomes Coe, Niterói, Rio de Janeiro, Brazil

Muhammad Farrakh Nawaz, Institute of Environmental Studies, University of Karachi, Karachi, Pakistan

The series Springer Proceedings in Earth and Environmental Sciences publishes proceedings from scholarly meetings and workshops on all topics related to Environmental and Earth Sciences and related sciences. This series constitutes a comprehensive up-to-date source of reference on a field or subfield of relevance in Earth and Environmental Sciences. In addition to an overall evaluation of the interest, scientific quality, and timeliness of each proposal at the hands of the publisher, individual contributions are all refereed to the high quality standards of leading journals in the field. Thus, this series provides the research community with well-edited, authoritative reports on developments in the most exciting areas of environmental sciences, earth sciences and related fields.

Vladimir Karev
Editor

Proceedings of the 9th International Conference on Physical and Mathematical Modelling of Earth and Environmental Processes

Springer

Editor
Vladimir Karev
Fontanars dels Alforins, Valencia, Spain

ISSN 2524-342X ISSN 2524-3438 (electronic)
Springer Proceedings in Earth and Environmental Sciences
ISBN 978-3-031-54588-7 ISBN 978-3-031-54589-4 (eBook)
https://doi.org/10.1007/978-3-031-54589-4

© The Editor(s) (if applicable) and The Author(s), under exclusive license to Springer Nature Switzerland AG 2024

This work is subject to copyright. All rights are solely and exclusively licensed by the Publisher, whether the whole or part of the material is concerned, specifically the rights of translation, reprinting, reuse of illustrations, recitation, broadcasting, reproduction on microfilms or in any other physical way, and transmission or information storage and retrieval, electronic adaptation, computer software, or by similar or dissimilar methodology now known or hereafter developed.
The use of general descriptive names, registered names, trademarks, service marks, etc. in this publication does not imply, even in the absence of a specific statement, that such names are exempt from the relevant protective laws and regulations and therefore free for general use.
The publisher, the authors and the editors are safe to assume that the advice and information in this book are believed to be true and accurate at the date of publication. Neither the publisher nor the authors or the editors give a warranty, expressed or implied, with respect to the material contained herein or for any errors or omissions that may have been made. The publisher remains neutral with regard to jurisdictional claims in published maps and institutional affiliations.

This Springer imprint is published by the registered company Springer Nature Switzerland AG
The registered company address is: Gewerbestrasse 11, 6330 Cham, Switzerland

Paper in this product is recyclable.

Contents

Development of the Structure of a Unified Hydrobiological and Hydrochemical Database for the Information and Analytical System "Lake Onego and Its Cathment" 1
V. N. Baklagin

Analysis of Current Fields and Beryllium-7 Concentration in the Shore Area of the Southern Coast of Crimea in the Summer of 2016 According to the Modeling Results 11
Natalia Evstigneeva and Olga Dymova

Digital Examination of Pore Space Characteristics and Structural Properties of a Gas Condensate Field Reservoir on the Basis of μCT Images 23
V. V. Khimulia

Identification of the Location and Possible Release Time of the Pollution Source Based on the Method of Adjoint Equations 35
V. S. Kochergin and S. V. Kochergin

Effect of UV Radiation and Ozone on the Viability of Biofilms and Resting Forms of *Pseudomonas Aeruginosa* Bacteria 43
M. A. Kotov, N. G. Solovyev, A. N. Shemyakin, M. Y. Yakimov, O. V. Kalmantaeva, M. A. Makarova, and O. Y. Manzenyuk

Features Distribution of Platinoids in Oil and Gas Fields of the Orenburg Region 63
G. A. Ponomareva

Dynamics of Near-Surface Air Temperatures in the Lower Don Basin for the Period 1966–2020 69
A. Parfenova, V. Kulygin, A. Ioshpa, and A. Evlanova

Noble Metals of the Gaysky Copper-Zinc Massive Sulphide Deposit of Orenburg Region 79
G. A. Ponomareva

Cryomicrophotography in a Cold Room at the Faculty of Geography of Moscow State University Named After M.V. Lomonosov 87
D. M. Frolov, G. A. Rzhanitsyn, A. V. Koshurnikov, V. E. Gagarin, and P. A. Krilovets

Wave Variation of the Magnitude of Rock Salt Mass Transfer Coefficient Under Hydrodynamic Influence of Solution Along the Height of Underground Excavations of UGS 93
V. P. Malyukov

On Stability of Inverse Problem Solution for Rock Mass Stress State Reconstruction Based on Natural Fractures Analysis 99
E. V. Novikova and N. V. Dubinya

Cox-Munk Model Limitations in Describing the Reflection of Sunlight on the Sea Surface 115
I. P. Shumeyko, A. Yu. Abramovich, and V. M. Burdyugov

Neural Network for Seismic Waves Phase Picking Based on Wavelet Scattering 123
I. A. Abzalilov, N. A. Baryshnikov, and S. B. Turuntaev

Regularities of Spatio-Temporal Distribution of Energy Parameters of Induced Seismicity in the Development of Mineral Deposits by Field Observations and Mathematical Modeling Data 133
Larisa Nazarova, Nelly Miroshnichenko, and Leonid Nazarov

Stress Trajectories and Crack Propagation in Elastic Plate Under Combined Mechanical and Thermal Loading 145
Alexander N. Galybin

Parameterization of a Two-Component Gaussian Mixture for Description of the Sea Surface 157
A. S. Zapevalov and A. S. Knyazkov

Evolution of Small-Scale Turbulence in a Stratified Shear Flow, Affected by Interplay of the Kinetic and Potential Turbulent Energies 165
D. Gladskikh, L. Ostrovsky, I. Soustova, and Y. Troitskaya

The Flow a Drop of Water Around a Thin Thread in Zero Gravity and Under Normal Gravity Conditions 175
A. I. Fedyushkin, A. A. Gnevushev, A. S. Zaharov, and A. N. Rozhkov

Study of Sand Production in Vertical and Horizontal Boreholes on a True Triaxial Loading Unit 183
Yu. F. Kovalenko, V. I. Karev, S. O. Barkov, and K. B. Ustinov

Experience of Ultrasonic Technology Application in the Samotlor Field Wells (Western Syberia) 191
M. S. Mullakaev, Y. A. Saltykov, A. A. Saltykov, and R. M. Mullakaev

Investigation of Spontaneous Movement of Ice Cover in Natural Reservoirs 197
T. O. Chaplina

Thermoacoustic Technology for High-Viscous Oil Production 207
M. S. Mullakaev, R. M. Mullakaev, D. G. Sarvarov, and A. A. Ruhman

Zoning of the Water Area by Ocean Surface Temperature Using Cluster Analysis 213
Eugene P. Istomin, Yaroslav A. Petrov, and Irma A. Martyn

Seasonal and Long-Term Variability of Ice Conditions in the Western Arctic 223
Yaroslav A. Petrov, Eugene P. Istomin, and Irma A. Martyn

Model for Forecasting the Hydrometeorological Situation as a Component of the Development of the Transport and Logistics System of the Arctic Region 235
Artem Yu. Sidorenko, Yaroslav A. Petrov, and Evgeniy P. Istomin

Pore-Scale Computational Study of Permeability and Pore Space Geometry in Gas Condensate Reservoir Rocks 243
V. V. Khimulia and V. I. Karev

Changes in the Composition and Properties of Basaltic Andesites Under Sulfuric Acid Leaching Conditions 257
I. E. Bolshakov and M. A. Nikulina

Some Problems of Well Stability in Reservoirs of Underground Gas Storages 269
V. Karev, Yu. Kovalenko, and K. Ustinov

Physical and Numerical Modeling of Nonelastic Deformations During an Impact of Spherical Indenter on Ice Disc 275
Epifanov Viktor Pavlovich, Guseva Evgeniya Kirillovna, and Shigaev Nikita Olegovich

On the Possibility of Managing Dew Point Height in Mountain Areas to Reduce the Risks of Natural Emergencies 283
A. V. Kholoptsev, D. V. Sedov, and R. G. Shubkin

Studying the Features of Measuring Rock Deformations During Tests at the High Pressure High Temperature Triaxial Apparatus 295
S. O. Barkov

Physical Modeling of Sand Production in Vertical and Horizontal Wells of Underground Gas Storage Facilities Using a True Triaxial Loading Setup 303
N. I. Shevtsov

Structure of Technogenic Landscapes of the Blyavinsky Copper-Crusted Deposit 309
Vadim Petrishchev, Galina Ponomareva, and Inna Kudelina

Kurtmaly Gold Placer: Geology, Geochemical Features of the Metal, Relationship with Indigenous Sources (Southern Urals, Russia) 315
A. V. Snachev

Experimental Study of the Distribution of Hydrocarbons Over the Water Surface 325
V. P. Pakhnenko

Simulation of Falling Rocks Using Two-Fluid Model 337
N. S. Orlova and M. S. Bezuglov

Long-Shore Sediment Movements in the Area of a Small Port Facility (South-West of Sakhalin) 345
V. V. Afanas'ev, I. O. Leont'ev, and A. V. Uba

Dynamic Processes at the Boundary of the Earth's Liquid Core 355
S. I. Peregudin and S. E. Kholodova

Coastal Protection System on the Barrier Form of the Lagoon (North-East of Sakhalin) 365
V. V. Afanas'ev, I. O. Leont'ev, and A. V. Uba

Hydrocarbon Composition of Kazantip Cape Coastal Sediments (Azov Sea, Crimea) 379
O. V. Soloveva and E. A. Tikhonova

Experimental Studies of Submerged Jets of Various Liquids 389
T. O. Chaplina and V. P. Pakhnenko

Origin of Solar System Comets in the Light of Galactocentric Paradigm 399
Azariy Barenbaum

Studies of Mass Transfer of Gas Salt Clathrates. Determination of Mass Transfer Coefficient Value During Construction of Underground Excavation-Capacity in Rock Salt at Agcm 431
V. P. Malyukov

On the Parameterization of Aerodynamic Roughness in Numerical Modeling of the Land Water Bodies 437
D. Gladskikh, E. Mortikov, and R. Ahtamyanov

Waves at the Ice-Liquid Border from Localized Sources 447
V. V. Bulatov

Persistent Organic Pollutants in Waterfowls of the Southern Primorye 455
Maksim A. Belanov, Maksim M. Donets, Mikhail Yu. Shchelkanov, Dmitry V. Pankratov, and Vasiliy Yu. Tsygankov

Calculation of Multifrequency Impulse Effects on Inhomogeneous Media Using the Lebesgue Integral 463
I. Kh. Enikeev

Energy Spectra of Sea Level Fluctuations During Propagation Long Waves in Branched Bays 471
A. Yu. Belokon and D. I. Lazorenko

Vegetation of Marshes of Coastal-Marine Wetlands (Carbon Landfill in Salmon Bay, Southern Sakhalin) 485
I. O. Rozhkova-Timina

Experimental Study of the Influence of Impermeable Inclusions on the Stress–Strain State of Cement in Sedimentary Rock Under the Influence of Filtration Flow 493
Iudochkin Nikita, Tairova Aliya, and Belyakov George

On the Possibility of Using the Lithosphere Relief to Estimate the Velocity at the Horizontal Upper Boundary of an Intensive Vortex in the Mantle Under the Eastern Part of the Mediterranean Sea 507
S. Yu. Kasyanov

Effect of Bottom Geometry on Surface Waves in a Vertical Circular Cylinder 517
S. V. Nesterov and V. A. Kalinichenko

Wind Wave Regime in the Alupka Area 527
V. V. Fomin, A. A. Polozok, and I. N. Fomina

Zoning and Modeling of the Underground Hydrosphere of the Orenburg Region 537
I. V. Kudelina, T. V. Leontyeva, and M. V. Fatyunina

On the Possibility of Using Lithospheric Topography to Estimate the Velocity at the Horizontal Upper Boundary of an Intense Vortex in the Mantle Beneath the Sea of Japan Region 549
S. Yu. Kasyanov

Development of the Concept of a Modern Approach to Well Construction 559
R. R. Galliamov and R. A. Ismakov

The Black Sea Northern Part Spatial Zoning in Terms of the Mixing Processes Intensity Based on the Data Processing Results of 87, 92, 102 and 110 Voyages of the R/V "Professor Vodyanitsky" 569
D. A. Kazakov, A. S. Samodurov, and O. I. Pavlenko

New Image Particle Method for Kinetic Simulation of Wakes in Plasma with Weak and Strong Coupling 583
Maxim Glebovich Ponomarev

On the Possible Influence of an Intense Vortex in the Mantle Beneath the Sea of Japan Region on the Formation of Lithospheric Relief and Sea of Japan Water Circulation 593
S. Yu. Kasyanov

Development of a Thermometric Well on a Site Without Natural Cover of the Moscow State University Meteorological Observatory 615
V. E. Gagarin, A. V. Koshurnikov, G. A. Rzhanitsyn, and D. M. Frolov

The Potential of Sustainability, Evolution and Adaptation of Coastal Geosystems in the Conditions of Climatic and Man-Made Changes (The Example of Sakhalin) 621
V. V. Afanas'ev

Assessment of Investment Scenarios for Russia's Energy Transition to Carbon Neutrality Using the Monte Carlo Method 629
K. V. Pokazeev, K. S. Degtyarev, D. A. Solovyev, and M. Y. Berezkin

Distribution of Spatial Long Waves to the Channel with the Deformable Basis 641
S. I. Peregudin and S. E. Kholodova

Marine Carbonate System Parameters Variability in the Kara Sea in 2019 and 2021 647
N. K. Alekseeva, I. V. Shved, A. D. Tarasenko, T. N. Eremeiko, A. E. Novikhin, I. A. Gangnus, A. V. Vesman, N. A. Lis, E. A. Chernyavskaya, and M. S. Makhotin

Chlorinated Organic Compounds in Mollusks Soft Tissue from Vostok Bay (The Sea of Japan) 655
Aleksandra D. Borovkova, Maksim M. Donets, and Vasiliy Y. Tsygankov

Hydrography Tapering and Stream Order Computing for GIS-Based Mapping 661
D. A. Ignatenko, N. A. Razvalov, O. P. Yakimova, I. E. Sidorina, and A. V. Kochetova

Modelling of Stress–Strain State of Artificially Improved Foundation During Construction of a Residential Complex in a Megacity 673
Dmitriy Neguritsa, German Alekseev, Evgeny Medvedev, Konstantin Slobodin, and Ivan Tereshin

Theoretical Calculations of Plasmon Spectra for a Rectangle with a Two-Dimensional Electron Gas 687
Denis V. Fateev, Olga V. Polischuk, and Konstantin V. Mashinsky

Features of the Algorithm for Calculating Induced Currents by an Electromagnetic Wave in a Rectangle with a Two-Dimensional Electron Gas 693
Denis V. Fateev, Olga V. Polischuk, and Konstantin V. Mashinsky

Development of the Structure of a Unified Hydrobiological and Hydrochemical Database for the Information and Analytical System "Lake Onego and Its Cathment"



V. N. Baklagin

Abstract The work is devoted to the creation of the structure of the database of hydrobiological and hydrochemical characteristics of Lake Onego, obtained as a result of field observations for the period 1960–2022. This database will be used as a full-scale basis for the information and analytical system "Lake Onego and its catchment", which is being actively developed within the framework of the Russian Science Foundation project No. 22-17-00193. This is a necessary tool for the calibration and verification of Lake Onego ecosystem models. The paper presents an algorithm and methodology for the formation of a single network of sampling stations, for the possibility of integrating the results of hydrobiological and hydrochemical measurements. The technique takes into account the spatial and temporal heterogeneity of the available data.

Keywords Database · Lake Onego · Information and analytical system

The intensification of the use of large lakes—important sources for the development of the regional economy (for water supply, sanitation, bio resources, water transport, energy, tourism, and aquaculture) should be accompanied by the improvement of systems for monitoring the state of lakes, systems for managing their resources. These systems should provide management decision-making with information to correct existing and justify future economic projects. Decision support systems are based on mathematical models, the calibration and verification of which is carried out according to observational data obtained both on the Agency on Hydrometeorology and Environmental Monitoring network and according to experiments performed by academic organizations.

V. N. Baklagin (✉)
Northern Water Problems Institute Karelian Research Centre Russian Academy of Sciences, Petrozavodsk, Republic Karelia, Russia
e-mail: slava.baklagin@mail.ru

© The Author(s), under exclusive license to Springer Nature Switzerland AG 2024

V. Karev (ed.), *Proceedings of the 9th International Conference on Physical and Mathematical Modelling of Earth and Environmental Processes*, Springer Proceedings in Earth and Environmental Sciences, https://doi.org/10.1007/978-3-031-54589-4_1

The Agency on Hydrometeorology and Environmental Monitoring ensures the monitoring of the state and pollution of the environment, the assessment of changes occurring in it, as well as forecasting the development of the environment. However, the existing system of state monitoring of water bodies is insufficient both in terms of the composition of controlled substances and in terms of the location of observation points, and in terms of sampling frequency [1]. In addition, there was not enough observational data on the state of lake ecosystems obtained by academic organizations.

Now, there is extensive experience in creating databases of hydrometeorological observations both here and abroad. The WMO (World Meteorological Organization) International Data Center (www.hydrolare.net) has created a database of hydrometeorological observations. This database contains data on long-term observations at lake stations and posts, including monthly average data on the water level, water surface temperature (SST), maximum ice thickness per year, and other characteristics of the ice cover. This database contains data on 420 lakes and 170 reservoirs in Russia and the countries of the former USSR.

There is a base of hydrometeorological data of Russian Hydro Meteorological Data Research Institute in Obninsk. At the Institute of Lake Science of the Russian Academy of Sciences, the information system «Lakes of Russia» is being developed, which contains information about various parameters (location, morphometric and hydrological characteristics, as well as indicators water quality) of more than 300 lakes in Russia (http://www.limno.org.ru/win/rlake.php). A database was created for the Great American Lakes (GAL) in the USA and Canada based on NOAA (http://www.lre.usace.army.mil/Portals/). Using this database, a modern system for forecasting seasonal fluctuations in water levels, currents, temperature, ice, and bottom sediments of the Great American Lakes—"Great Lakes Coastal Forecasting System—GLCFS" has been developed. It is used to ensure the tasks of water transport and energy. There is also the Great Lakes Advanced Hydrological Prediction System (AHPS), which is a semi-automated system that combines observational data with mathematical models. With the help of this system, the water level and other hydrological characteristics of Great American Lakes are predicted. The Northern Water Problems Institute Karelian Research Centre Russian Academy of Sciences has developed a database and GIS "Lakes of Karelia", which includes data on long-term observations of the chemical-biological, morphometric and hydrological characteristics of lakes [2].

In addition, within the framework of the RSF project No. 14-17-00740, a database was created that made it possible to structure and summarize information on the long-term dynamics of the hydrological characteristics of the largest lakes in Russia [3]. The database contains information about Onego and Ladoga lakes, as well as climatic characteristics in the watersheds of these lakes for a period of more than 100 years. The database has functionality implemented in the C# programming language, which includes several blocks. A block for calculating regression coefficients and other statistical characteristics (determination coefficient, standard error of regression, etc.), integrated into the structure of the database on the hydrological characteristics of lakes, which allows the user to perform data analysis without using

third-party tools. Visualization of the given sections of the lake basin. A block for calculating various bathymetric indicators (area at a selected depth, volumes of parts of the basin of the lake under consideration, and others) necessary for modeling thermohydrodynamic processes in the lake. The results of the analysis by the tools included in the developed information system can be used to modeling thermohydrodynamics and lake ecosystems, lake models and Lake Ecosystem models in text, binary and XML formats.

Also, within the framework of the RSF project No. 14-17-00740; an information system [4] was developed for working with data. In the information system, it is possible to obtain the calculated characteristics necessary for performing research. For example, to calculate heat fluxes through the surface of lakes, average monthly solar radiation, etc.

However, the created databases do not allow providing the developed information and analytical systems with full data and solving the tasks set—using them for calibration and verification of the created ecosystem models [5]. Difficulties in creating a unified database for the complex of hydrological, chemical and biological parameters of Lake Onego are due to the failure to comply with the basic principles of organizing and conducting observations to solve problems related to assessing the state and changes in lake ecosystems: according to hydrophysical, hydrochemical, hydrological, hydrobiological indicators, as well as in bottom sediments; consistency of the timing of their implementation with the characteristic phases of the hydrological regime of water bodies; determination of chemical and biological parameters of water by comparable methods.

In this regard, the purpose of this work is to form a method and structure of a common unified database of chemical and biological observations of Lake Onego in order to use it as a natural basis for calibrating and verifying ecosystem models.

For the purposes of integration of field and model data, the information and analytical system (IAS) “Lake Onego and its catchment” is being actively developed within the framework of the RSF project No. 22-17-00193 [5]. The IAS functionality provides spatio-temporal visualization of both direct modeling results and field measurement data linked to the electronic basis of Lake Onego, as well as products of their individual and joint analysis of various levels of generalization (statistics, integration, statistical analysis, etc.). An important function of the IAS is the possibility of automated comparison of natural and calculated data (hydrological, hydrochemical characteristics) used in the project of the mathematical model of the ecosystem of Lake Onego [6, 7].

To create a single database within the framework of the developed information-analytical system “Lake Onego and its catchment”, both data from long-term observations of the chemical-biological, morphometric and hydrological characteristics of Lake Onego, obtained on the Agency on Hydrometeorology and Environmental Monitoring network from 1984 to 2022, as well as data collected by the Northern Water Problems Institute of Karelian Research Centre of the Russian Academy of Sciences starting from the second half of the twentieth century.

Long-term data were used, which are presented in the database and publications: chlorophyll-a [8, 9], benthos [10], phytoplankton [11], zooplankton [12] and primary

production for the period 1960–2022, and by chemical indicators using comparable methods for the period 1992–2022 [13–15]. The functional blocks of the database and information system were used, created within the framework of the RSF project No. 14-17-00740, described in the work [4].

After 1991, data collection was dictated by the conditions for carrying out various kinds of private research tasks on state assignments, projects and grants, carried out by various research teams, which, unfortunately, did not have a comprehensive (interdisciplinary) and systematic character. In addition, different equipment for sample analysis was used in different periods of time, some methods for determining a number of parameters, for example, nutrients, primary production of phytoplankton, etc., changed, which led to the problem of comparability of results. The implementation of unrelated programs influenced the formation of networks of stations on the lake. Therefore, within the framework of this work, the task was set, which consisted in the generalization and unification of data for the possibility of integrating field data in an information-analytical system "Lake Onego and its catchment".

Works on the generalization of existing databases were carried out in the following points: formation of a single network of stations with their geographical reference; bringing data to a single format of dimensions; search and correction of errors; definition of data arrays, according to comparable methods; software implementation of the database manager system and its placement on the server of the Northern Water Problems Institute of Karelian Research Center of the Russian Academy of Sciences.

One of the most important and complex tasks is the formation of a unified network of stations. To solve this problem, the following operations were carried out, which required both manual and automated actions:

- A reliable (reference) station group has been identified based on peer review.
- An algorithm has been developed to classify the rest of the stations and records found in the databases of hydrobiological and hydrochemical observations based on the updated list of stations.

Figure 1 shows a block diagram that implements the algorithm for generating a single list of stations and updating the geodata of hydrobiological and hydrochemical data base records in a single database. The result of the algorithm (implemented as an application in the python programming language) made it possible to obtain a single list of stations (412 names—shown in Fig. 2) that have a geographic reference on the ground, as well as relational links with records of measurements in the databases developed by the Northern Water Problems Institute.

On the ground, the stations were grouped according to the limnic regions of Lake Onego, according to the description presented in Ref. [15] to enable comparison of the modeling results with the data of field observations within a separate region of Lake Onego. Figure 2 shows the location of sampling stations on Lake Onego for 1960–2022 (a fragment of a web application that implements the information and analytical system "Lake Onego and its catchment" is given).

Identification and elimination of gross errors in the values of hydrobiological and hydrochemical characteristics was carried out according to the "three sigma" criterion described in Sergeev [16]. Found records that did not meet the criterion

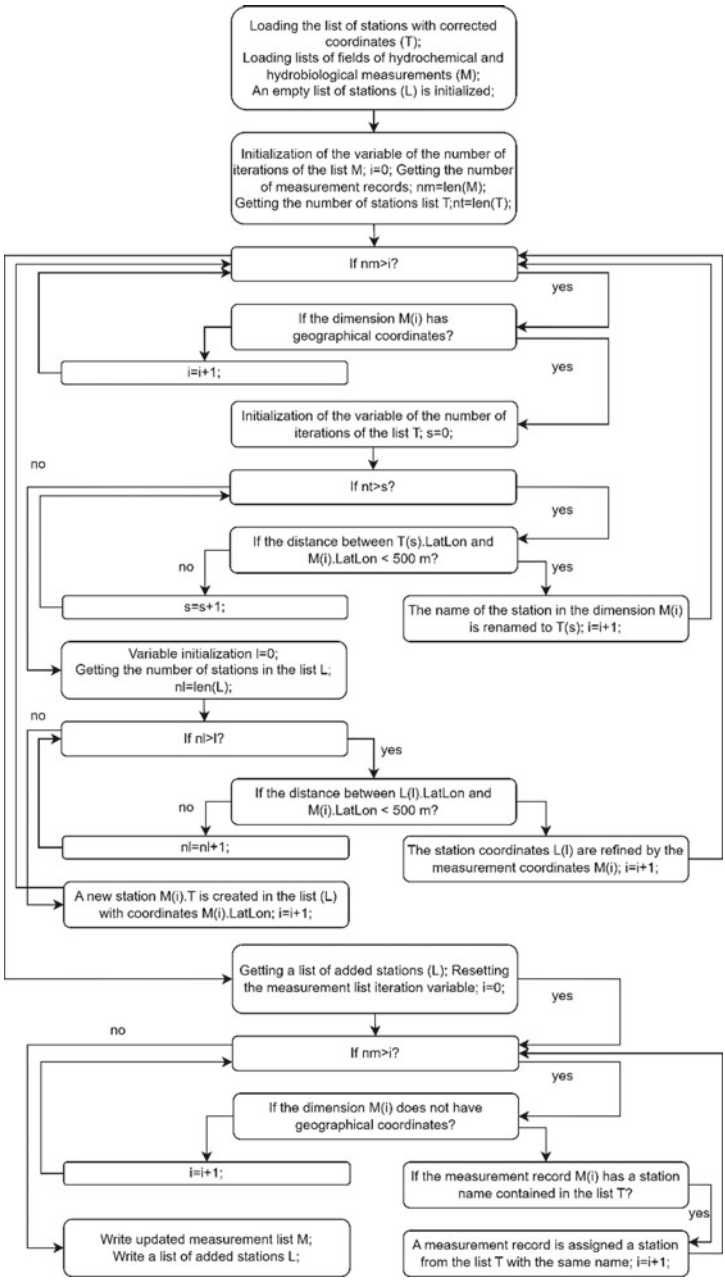


Fig. 1 Block diagram that implements the algorithm for generating a single list of stations and updating the geodata of records in hydrobiological and hydrochemical databases

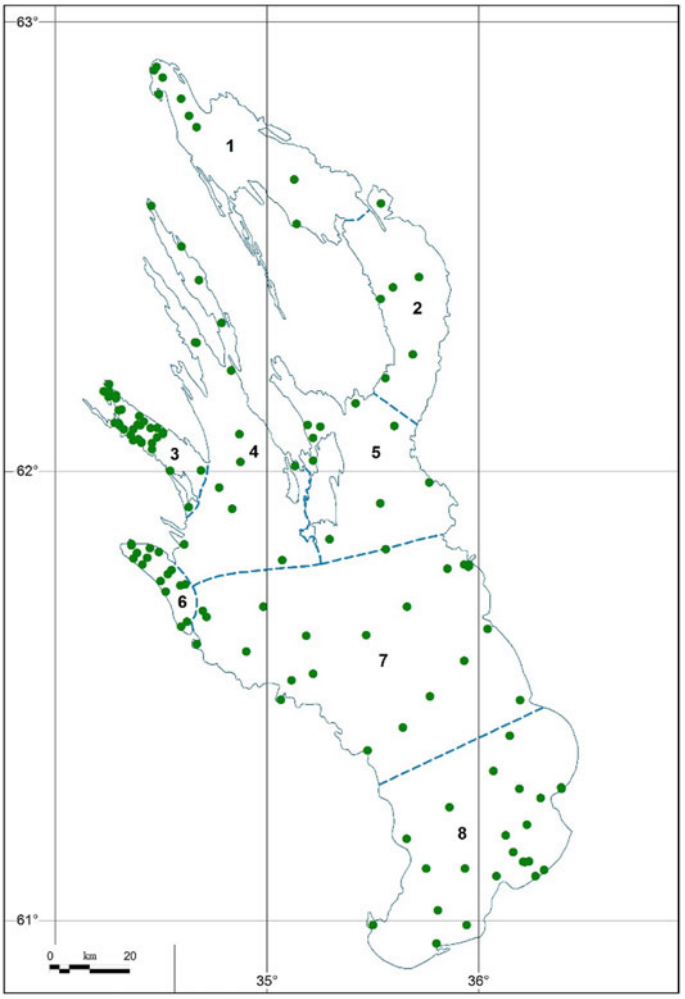


Fig. 2 Location of sampling stations on Lake Onego for 1960–2022: 1—Poveneckij bay, 2—Zaonezhskij bay, 3—Kondopozhskaya bay, 4—Bol'shoe Onego, 5—Maloe Onego, 6—Petrozavodskaya bay, 7—Central'noe Onego, 8—Yuzhnoe Onego

of "three sigma" were submitted for peer review by experts in the relevant field for adequacy. According to the "three sigma" criterion, it is considered that with a probability of $P = 0.9973$ and a significance of $\alpha = 0.0027$, the occurrence of even one random error greater than an unlikely event and it can be considered a gross error if:

$$x_i > 3S_x,$$

where S_x is the estimate of the standard deviation of the measurements.

The values of S_x are calculated without taking into account the extreme values of x_i.

The three sigma method used the following procedure:

1. The doubtful value of the measured value was revealed—the largest or the smallest.
2. The arithmetic mean value of the sample was calculated without taking into account the doubtful value of the measured value.
3. The S_x values of the sample were determined without taking into account the doubtful value of the measured value.
4. The difference between the arithmetic mean and the doubtful value of the measured value was calculated and a comparison was made.

If the inequality is true:

$$|x_i - \overline{x}| > 3S_x,$$

that doubtful value was subjected to peer review, otherwise, the value was left in the series.

Extremely high and low, experts for adequacy further analyzed values of the parameters. For example, despite the very high detected values of chlorophyll-a concentration (57.99 mg/l) in the area of the Kondopoga Bay on August 22, 2007 station K27 (62.179167°N, 34.252222°E) (Fig. 3), experts confirmed (proved) the reliability of these data in scientific works [9, 17, 18].

As a result of processing the measurements, the results were structured in the form of relational (two-dimensional) tables for each of the sections. To convert data into SQL format, a software module has been developed built into the web application that implements the information and analytical system, which allows you to generate SQL tables from CSV files (field observation data, as a rule, consist of files represented by office formats.doc,.xls,.csv), this makes it possible to carry out operational and technological updating of the database, due to this, the generalization and reduction to a single format of the accumulated field measurements and the results of expeditionary research, as well as the integration of data into a single database.

In addition, an important and necessary functionality of the information and analytical system "Lake Onego and its catchment" is the ability to compare simulation results with field data. In this regard, the problem of processing field data unevenly distributed in space was solved in order to compare these data with the results of modeling on a model grid (with a horizontal step of 1 km). The solution of this problem was carried out by applying the interpolation method—the method of inverse weighted distances (IWR). The essence of this method lies in the fact that the points that are closer to those at which the characteristics are evaluated (in this case, hydrophysical, hydrobiological, hydrochemical)—reference points, have a greater influence than remote points. The value of the characteristic at the desired point (node of the model grid) will be most similar to the property values at nearby control

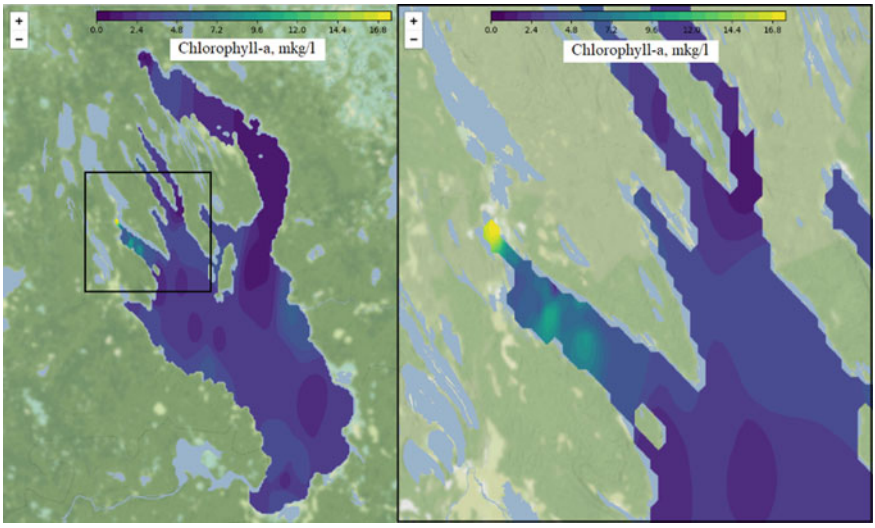


Fig. 3 Distribution of chlorophyll-a concentration (mg/l) on the surface of Lake Onego for the period 1992–2020 (averaged values for August) according to field observations [8, 9] (a fragment of a web application that implements the information and analytical system "Lake Onego and its catchment" is presented)

points, and less similar to the values at remote control points. The share of "participation" of the value of the characteristic in the reference point in the calculation of the desired value is expressed as a weighting factor ω. The weighting coefficients are calculated as inversely proportional to the distance to the power of p. The value of the characteristic in the node of the model grid is calculated by the formula:

$$Z(x_0, y_0) = \sum_{i=1}^{N} \omega_i \cdot Z(x_i, y_i),$$

where $Z(x_i, y_i)$ is the value of the characteristic at the i-th reference point; ω_i is the weight coefficient of the i-th reference point; N is the number of reference points.

The above calculation algorithm is implemented in the python programming language and embedded in the developed information and analytical system. Further work is aimed at solving the problems associated with the development of a methodology for checking the adequacy of model calculations in the conditions of a limited spatio-temporal series of available field data, since standard statistical methods cannot be applied due to the small volume of reference values.

Thus, the structure of a unified database of hydrochemical and hydrological parameters of Lake Onego has been developed, which will allow monitoring the state of the Lake Onego ecosystem, but also being a natural basis for calibrating and verifying mathematical models of the lake ecosystem.

Acknowledgements The work was supported by the RSF project No. 22-17-00193.

References

1. *Rumyantsev V.A., Filatov N.N. & Kondratiev S.A.*, 2021. Current state and improvement of the monitoring system of Lake Ladoga/Current state and problems of anthropogenic transformation of the ecosystem of Lake Ladoga in a changing climate. M: RAS: 540–558 (in Russian).
2. Lakes of Karelia, 2013. Handbook/ed. *N.N. Filatov & V.I. Kukharev*. Petrozavodsk: Karelian Scientific Center of the Russian Academy of Sciences: 463 (in Russian).
3. *Filatov N.N., Baklagin V.N., Bogdanova M.S. & Balagansky A.F.*, 2018. Hydrological characteristics of lakes in Russia/Certificate of state registration of the database No. 2018621718 dated 02.11.2018 (in Russian).
4. Diagnosis and forecast of thermohydrodynamics and ecosystems of the great lakes of Russia, 2020/ed. *N. N. Filatov*. Petrozavodsk: Karelian Scientific Center of the Russian Academy of Sciences: 255 (in Russian).
5. *Filatov N.N., Baklagin V.N., Isaev A.V., Kondratiev S.A. & Savchuk O.P.*, 2022. Developing a "lake-catchment" information analysis system as a method for basic research and a tool for decision-making (Lake Onego case Study). *Transactions of Karelian Research Center of Russian Academy of Science: Limnology and Oceanology*. 6: 161–172. https://doi.org/10.17076/lim1683 (in Russian).
6. *Isaev A., Vladimirova O., Eremina T., Ryabchenko V. & Savchuk* O., 2020. Accounting for Dissolved Organic Nutrients in an SPBEM-2 Model: Validation and Verification. *Water*. 12: 1307. https://doi.org/10.3390/w12051307.
7. *Savchuk O. P., Isaev A. V. & Filatov N. N.* 2020. Three-dimensional hindcast of nitrogen and phosphorus biogeochemical dynamics in Lake Onego Ecosystem, 1985–2015. Part II: seasonal dynamics and spatial features; integral fluxes. *Fundamental and applied hydrophysics*. 15(2): 98–109. https://doi.org/10.48612/fpg/9mg5-run6-4zr8.
8. *Sabylina A.V., Tekanova E.V. & Kalinkina N.M.*, 2018. Chlorophyll-a in the water of Lake Onego/Certificate of state registration of the database No. 2018621068 dated 06/13/2018 (in Russian).
9. *Kalinkina N. M. & Tekanova E. V.*, 2022. The Dependence of Chlorophyll a Concentration on Total Phosphorus in Water Bodies with Increasing Water Color. *Inland Water Biology*, 15(5): 539–542. https://doi.org/10.1134/S1995082922050108.
10. *Polyakova T. N.*, 2012. Macrozoobenthos of Lake Onego/Certificate of state registration of the database No. 2012620882 dated 08.31.2012.
11. *Chekryzheva T.A.*, 2018 Resource potential of the food base of Lake Onego: phytoplankton of Lake Onego/Certificate of state registration of the database No. 2018621090 dated 07/16/2018 (in Russian).
12. *Syarki M. T. & Kulikova T. P.*, 2012. Zooplankton of Lake Onego/Certificate of state registration of the database No. 2012621150 dated 9.11.2012 (in Russian).
13. *Galakhina N., Zobkov M. & Zobkova M.*, 2022. Current chemistry of Lake Onego and its spatial and temporal changes for the last three decades with special reference to nutrient concentrations. *Environmental Nanotechnology, Monitoring & Management*. 17: 100619. https://doi.org/10.1016/j.enmm.2021.100619.
14. *Zobkov M., Zobkova M., Galakhina N., Efremova T., Efremenko N. & Kulik N.*, 2022. Data on the chemical composition of Lake Onego water in 2019-2021. *Data in Brief*. 42: 108079. https://doi.org/10.1016/j.dib.2022.108079.
15. The largest lakes-reservoirs of the North-West of the European territory of Russia: the current state and changes in ecosystems under climatic and anthropogenic impacts, 2015/ed. *N.N. Filatov*. Petrozavodsk: Karelian Scientific Center of the Russian Academy of Sciences: 375.

16. *Sergeev A. G.*, 2005. Metrology: Textbook.—M.: Logos: 272.
17. *Kalinkina N.M., Tekanova E.V., Efremova T.V., Palshin N.I., Nazarova L.E., Baklagin V.N., Zdorovennov R.E. & Smirnova V.S*, 2021. Response of Lake Onego Ecosystem in the Spring–Summer Period to Anomaly High Air Temperature in Winter 2019/2020. *Izvestiya Rossiiskoi Akademii Nauk. Seriya Geograficheskaya.* 85(6): 888–899 (In Russian). https://doi.org/10.31857/S2587556621060078.
18. *Tekanova E. V., Kalinkina N. M., Zdorovennov R. E. & Makarova E. M.*, 2018. Results of the study of Lake Onego Ecosystem in the period of summer stratification based on measured data from a 2017 expedition//*Transactions of Karelian Research Center of Russian Academy of Science: Limnology and Oceanology*. 9: 44–53. https://doi.org/10.17076/lim753.

Analysis of Current Fields and Beryllium-7 Concentration in the Shore Area of the Southern Coast of Crimea in the Summer of 2016 According to the Modeling Results



Natalia Evstigneeva and Olga Dymova

Abstract Based on the hydrodynamic model of the MHI, adapted to the conditions of the Black Sea coastal area with open boundaries, a numerical experiment was carried out to reconstruct the fields of currents and beryllium concentration with the assimilation of hydrological data and satellite sea surface temperature in the summer of 2016. We used a high spatial resolution (horizontal grid ~500 × 500 m). A higher spatial resolution allowed to reconstruct a submesoscale structure of the current fields in the upper and deep layers and to obtain quantitative and qualitative characteristics of the eddies and currents more accurately compared to calculations on a ~1.6 km grid. An increased radionuclide content was reproduced in the field of beryllium-7 concentration in the coastal zone of Yalta and in the Feodosiya Bay, associated in the first case with atmospheric precipitation, and in the second case with submesoscale dynamics. Reduced values were detected at the periphery of the Rim Current and near Cape Sarych. At the same time, it was possible to reconstruct the decrease in beryllium content near the southern tip of the Crimea, recorded by in-situ measurements, only with the help of the model with a resolution of ~500 m. The decrease in the concentration of beryllium-7 was associated with the formation of coastal upwelling, not reproduced by the model with a resolution of ~1.6 km.

Keywords Black Sea · Numerical modeling · High spatial resolution · Assimilation of observational data · Submesoscale eddies · Beryllium-7

N. Evstigneeva (✉) · O. Dymova
Marine Hydrophysical Institute RAS, Sevastopol, Russian Federation
e-mail: naevstigneeva@yandex.ru

© The Author(s), under exclusive license to Springer Nature Switzerland AG 2024

V. Karev (ed.), *Proceedings of the 9th International Conference on Physical and Mathematical Modelling of Earth and Environmental Processes*, Springer Proceedings in Earth and Environmental Sciences, https://doi.org/10.1007/978-3-031-54589-4_2

1 Introduction

Radioactive isotopes, such as beryllium-7 (^{7}Be), are informative tracers of the processes that determine the supply and transport of substances in the active layer of seas and oceans on various time scales. Since numerical modeling makes it possible to reconstruct and analyze the evolution of the radionuclide concentration field, the models of their transfer are of great interest and are used, in particular, to assess the state and predict changes in the ecosystem [1]. A necessary condition for the correct simulation of the radionuclide field evolution is the exact reconstruction of hydrodynamic fields close to observed.

A number of investigations for the Black Sea have been carried out on the numerical assessment of the transport of various impurities in the coastal zone, including the influence of fast submesoscale eddies. A three-dimensional model of beryllium-7 transport in the marine environment with a resolution of 5 km was proposed in Kremenchutskii et al. [2]. Validation of the calculation results was carried out according to the data from the stationary oceanographic platform in the urban-type settlement Katsiveli (Southern Coast of Crimea). Using the results of field observations, it was shown that the model allowed to correctly reproduce the evolution of the field of ^{7}Be concentration in the surface water layer.

Preliminary estimates of the transfer of passive impurities in 2016 and comparison with measurement data in the upper layer were made in Dymova and Demyshev [3] on the basis of the model developed at the Marine Hydrophysical Institute (MHI) for carrying out calculations with a spatial resolution of ~1.6 km. The analysis showed that the modeling errors exceeded the measurement error for stations close to the shore, while for deep-sea stations a good agreement was observed (less measurement error). This result makes it necessary to increase the model resolution on the shelf.

Eddy structures of different scales, regularly recorded on satellite radar images, make a significant contribution to the circulation of the coastal zone and are an effective mechanism for the transfer of various kinds of impurities of natural and anthropogenic origin. The studies [4–7], done to date on modeling, forecasting and observation of hydrophysical fields with high spatial resolution, contain new results on meso- and submesoscale features of the Black Sea circulation.

Calculations of the distribution of pollutants in the coastal zone of the Adler-Sochi region were presented in Diansky et al. [4], based on the INMOM hydrodynamic model, implemented in two versions (with a uniform spatial resolution of ~4 km and uneven, with a step reduction of up to 50 m). It was shown that the version of the model with a higher spatial resolution reproduced the eddy circulation more adequately.

Hydrophysical fields were calculated with a high spatial resolution (horizontal grid ~350 × 350 m and 38 vertical horizons) in the period from 1 to 31 October 2006 in Demyshev and Evstigneeva [5], based on the hydrodynamic model of MHI in the coastal region of the South Coast of Crimea (between 44.25 and 44.72° N and 33.95 and 34.55° E) with open boundaries. The fields of currents, level, temperature and salinity on the northwestern shelf of the Black Sea were reconstructed with a

spatial resolution of 500 m in the autumn period of 2007, also based on the MHI model, in Demyshev and Evstigneeva [6]. Due to the finer grid step in Demyshev and Evstigneeva [5, 6], it was possible to reconstruct the meso- and submesoscale structure of hydrophysical fields in the upper and deep layers and obtain quantitative and qualitative characteristics of eddies and jets more accurately compared to previous calculations.

Data on the evolution of the dynamic and thermohaline structure of submesoscale cyclonic eddies, attached to the Batumi anticyclone, were obtained in Bogdanov et al. [7], on the basis of the results of numerical modeling using the NEMO model for 2008–2009 and the algorithm for automatic identification of eddies.

Our study is a continuation of the development of a three-dimensional model of beryllium-7 transport in the waters of the Black Sea, developed earlier in Kremenchutskii et al. [2] and Dymova and Demyshev [3], in order to more correctly describe the spatial and temporal variability of the radionuclide concentration in the coastal zone. The reconstruction of the current fields and the beryllium-7 concentration in the area of the Crimean shelf was performed with ultra-high spatial resolution (horizontal grid ~500 × 500 m) and assimilation into the model of available observational data (in-situ temperature and salinity measurements, satellite sea surface temperature), based on the experience of previous works [5, 6, 8]. The expediency of using a finer grid step, when reconstructing the meso- and submesoscale features of the coastal circulation and radionuclide distribution, was shown by comparing with fields, obtained with a coarser grid step (~1.6 km).

2 Parameters of the Numerical Model and Description of Experiments

We used a z-coordinate three–dimensional nonlinear model of the Black Sea [9], based on the complete equations of ocean thermohydrodynamics in the Boussinesq approximation, hydrostatics and incompressibility of seawater in the form of Gromeka-Lamb, which was developed at the MHI. The model was supplemented with a block for calculating passive impurity transfer and assimilation of observational data. Wind friction stresses, heat, moisture and matter (radionuclide) fluxes from the atmosphere were set as boundary conditions on the free surface. Friction on the bottom was not taken into account; conditions for the absence of normal momentum, heat and matter fluxes on the solid boundary were set. The choice of conditions on open boundaries was determined by the type of experiment: for the entire basin or a limited area of the sea. The basin bathymetry was constructed with the help of the depths array by EMODnet (EMODnet Digital Bathymetry (DTM 2020)-Tile D3. https://emodnet.ec.europa.eu/geonetwork). The fields of sea surface height, temperature, salinity, radionuclide concentration and horizontal velocity were set at the initial time. Finite-difference discretization of the model equations, initial and boundary conditions was carried out on the C grid.

To set the fields of tangential wind friction stress, heat fluxes, short-wave radiation, precipitation and evaporation, we used ERA5 atmospheric reanalysis data with a resolution of (1/4)° (Copernicus Climate Change Service, Climate Data Store, (2023): ERA5 hourly data on single levels from 1940 to present doi: https://doi.org/10.24381/cds.adbb2d47). To assimilate the sea surface temperature (SST), satellite data from the Copernicus Marine Research Center (Black Sea product—High Resolution and Ultra High Resolution L3S Sea Surface Temperature https://doi.org/10.48670/moi-00158) were used.

The boundary conditions describing the total (dry plus wet deposition) flux of beryllium-7 from the atmosphere were constructed using a one-dimensional model [10]. The model also took into account the deposition of the radionuclide on particulate matter. The particulate matter concentration fields were calculated using the uplink brightness data measured by the MODIS satellites and the regional algorithm [11].

Two numerical experiments on modeling the circulation and transport of beryllium-7 were carried out in the work for the period June–July 2016: for the Crimean section of the shelf and for the entire basin. The choice of the interval was due to the fact that 87th cruise of the R/V "Professor Vodyanitsky" was held at that time in the area of the Southern Coast of Crimea [12] and direct measurements were carried out not only of hydrological characteristics, but also of the concentration of $^{7}\mathrm{Be}$.

Experiment 1 was carried out for the area, located between 33.37–36.46°E and 43.99–45.15°E and covering a section of the shelf from Cape Chersonesus to the tip of the Kerch Peninsula. The spatial resolution was 0.00696° in longitude and 0.005° in latitude (~560 m). We used 27 vertical z-horizons with depths 2.5, 5, 10, 15, 20, 25, 30, 40, 50, 62.5, 75, 87.5, 100, 112.5, 150, 200, then every 100 m to 500, then after 200 m to 1700, 2100 m.

Dirichlet conditions were implemented for the equations of motion on the open part of the lateral boundaries (velocity components were specified, using a model with a coarser resolution for each calculated moment of time). From the analysis of the influence of various types of boundary conditions (Dirichlet conditions, free flow and mixed type) for temperature and salinity at the liquid boundary on the formation of thermohaline fields, those conditions were selected that provided a more accurate reproduction of temperature and salinity near open boundaries. For the border sections, where water flowed into the region, temperature and salinity were set (Dirichlet conditions); for the border sections, where water flowed out of the region, Orlansky conditions were set to determine T and S on the open border [13]. The discretization of those conditions was carried out using a central explicit numerical scheme [14] to calculate the disturbance transfer rate.

The coefficients of turbulent viscosity and horizontal diffusion were chosen $\nu^H = 5{\cdot}10^5$ cm^2/s, $\kappa^H = 3{\cdot}10^5$cm^2/s. The coefficients of turbulent momentum exchange and vertical diffusion were calculated in accordance with the Pakanovski-Philander approximation [15].

To assimilate the hydrological survey data, a four-dimensional analysis procedure was used [8], based on the method of sequential optimal interpolation. Covariance functions of thermohaline fields were approximated by an exponential type function $\exp\left(-\lambda\left[(x - x\prime)^2 + (y - y\prime)^2\right]\right)$, where λ was a dimensional parameter (equal to $0.023 \cdot (\Delta x)^{-2}$) corresponding to value of the correlation function of 0.1. The data of the hydrological survey of the 87th cruise of the R/V "Professor Vodyanitsky" were taken from the Bank of Oceanographic Data of the MHI.

The stations from the area under consideration were grouped by days and assimilation was carried out once a day: July 6–6 stations, July 8–3 stations, July 9–2 stations, July 10–6 stations, July 11–8 stations, July 12–4 stations, July 14–9 stations, July 15–5 stations, July 16–7 stations.

Experiment 2 was carried out for the entire Black Sea on a grid with a resolution of 0.020° and 0.015° in longitude and latitude, respectively (~1.6 km), the vertical resolution was similar to experiment 1. The open boundaries in the calculation were river mouths and straits where Dirichlet conditions were set. Vertical turbulent exchange was parametrized by the Mellor-Yamada closure model, horizontal diffusion and viscosity were defined with the help of the biharmonic Laplace operator with constant coefficients equal to 10^{16} cm^4/s. Satellite surface temperature was assimilated once a day. Assimilation of contact temperature and salinity profiles was carried out similarly to experiment 1. Due to the peculiarities of the implementation of the four-dimensional analysis procedure, the data were assimilated if at least two measurement stations on a specific date were located at a distance of less than 20 km from the model grid node.

When performing calculations, all initial and boundary fields were interpolated to the corresponding grid. The total time of integration of the model equations in experiment 1 was 26 days (06/26/2016–07/21/2016), in experiment 2—one year (01.01.2016–12.31.2016). The output data of both models were daily three-dimensional fields of thermohydrodynamic characteristics and beryllium-7 concentrations. The analysis was carried out for the area bounded by 33.37–36.46° E and 43.99–45.15° N.

3 Analysis of Current Fields, Reconstructed with Ultra-High Resolution

The initial field of currents was mainly characterized by westward flows with a maximum velocity 44 cm/s at the upper horizons; an anticyclonic eddy was observed in the 10–30 m layer in the Yalta Bay (between 34 and 34.4°E), anticyclonic eddy formations below 30 m—between 34.2 and 35.2° E. Figure 1 illustrates the fields of surface currents for 29th of June, 4th, 11 and 16th of July, 2016.

The Rim Current jet was observed along the Crimean coast, the maximum velocity could reach 50 cm/s at the upper horizons. During the considered summer period

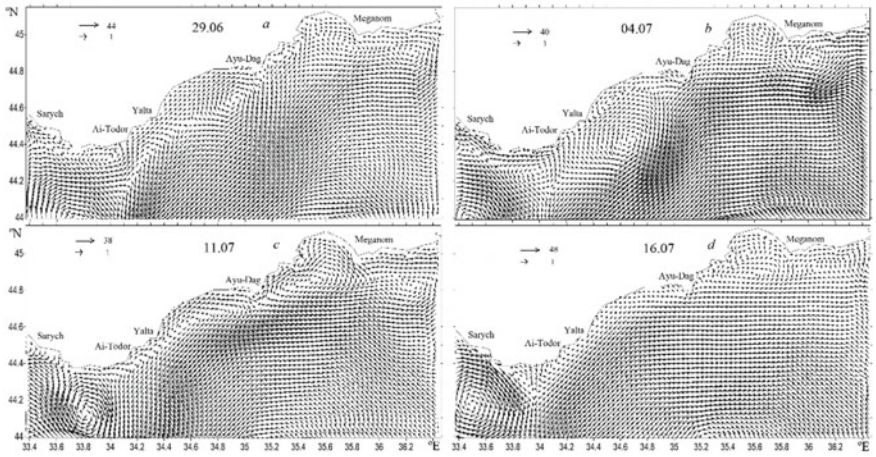


Fig. 1 Fields of currents (cm/s), calculated in experiment 1, at the depth of 3 m on 29th of June 29 (**a**), 4th of July (**b**), 11 of July (**c**) and 16th of July (**d**), 2016

meso- and submesoscale eddies were formed and developed in the upper layer between the coastline and the Rim Current.

An anticyclonic eddy with a radius of about 20 km was generated and moved along the direction of the movement of the Rim Current in the upper 30-m layer between Yalta and Cape Ayu-Dag from 27th of June to 15th of July (for example, Fig. 1a, b and c). An anticyclonic vorticity in the field of currents was observed in the Yalta Bay (between 34 and 34.4° E) (Fig. 1a) from 26th of June to 30th of June, a cyclonic eddy—near Cape Ai-Todor.

Chains of eddies of different scales and signs of vorticity were formed during the entire calculation period between Cape Ayu-Dag and Cape Meganom, when the Rim Current flowed around the uneven coastline (for example, Fig. 1). An anticyclonic eddy with a radius of about 20 km was observed from 9 to 18th of July between 33.4 and 33.9 ºE in the upper 30-m layer.

Changes with depth in the fields of currents were also analyzed. The fields of currents at the depth of 3, 10, 30 and 100 m on 27th of June and 12ve of July, 2016 are presented on Fig. 2.

An intense jet of Rim Current along the Crimean coast was noted at all horizons. Anticyclonic and cyclonic eddies were reconstructed in the upper 10-m layer west of Yalta on 27th of June, an anticyclonic vorticity was formed below 10 m between the Rim Current and the shore. An anticyclonic eddy between Cape Sarych and Cape Ai-Todor was obtained on 12th of July in the upper 30-m layer. Anticyclonic eddies were generated along the coast between Yalta and Cape Meganom.

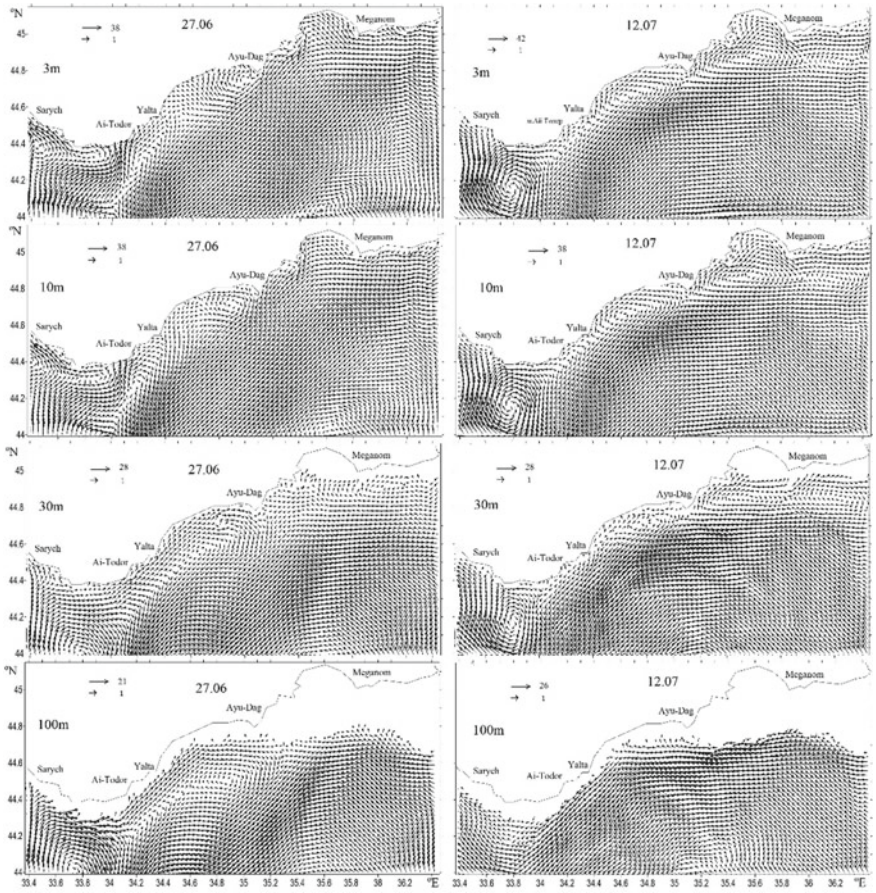


Fig. 2 Fields of currents (cm/s), calculated in experiment 1, at the depth of 3, 10, 30 and 100 m on 27th of June and 12th of July, 2016 (every fifth arrow was shown)

4 Comparison of the Results of Two Experiments (With a Resolution of ~500 m and ~1.6 km)

Fields of currents. Some qualitative differences were detected in the structure of the fields, when analyzing the fields of currents, calculated in two experiments. A number of eddy formations in the experiment with a lower resolution were absent or were less pronounced. It was possible to reproduce the circulation along the coast on the upper horizons in more detail in the experiment with a higher resolution. As an illustration, we present the fields on 29th of June, 2016.

Figure 3a and b show the fields of currents, calculated by the model with a resolution of ~500 m at 3 and 30 m levels (every sixth arrow is shown); Fig. 3c and d—the fields of currents, calculated by the model with a resolution of ~1.6 km at the depth

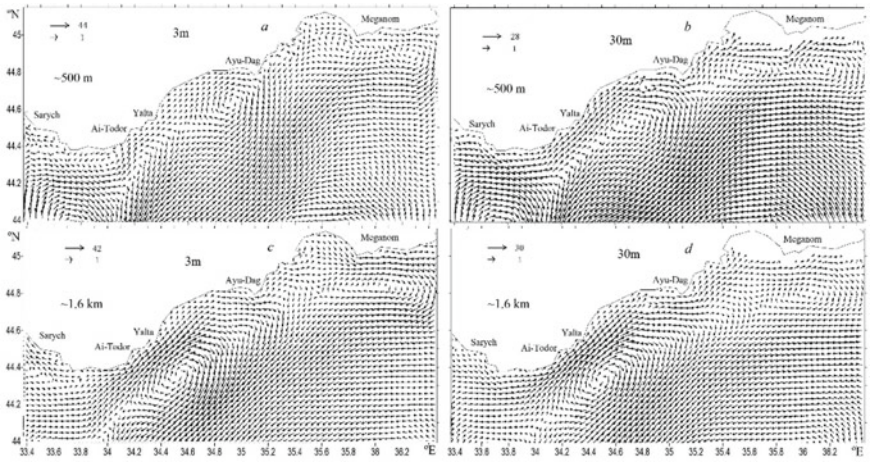


Fig. 3 Fields of currents (cm/s), calculated in experiments 1 and 2, at the depth of at 3 and 30 m on 29th of June, 2016

of 3 and 30 m horizons (the second arrow is shown). A qualitative agreement was obtained when comparing the fields of currents, presented on Fig. 3, however, due to a finer grid step, it was possible to specify the structure of the fields. An anticyclonic eddy formation in the Yalta Bay, a cyclonic eddy near Cape Ai-Todor and two anticyclonic eddies near Cape Meganom were reconstructed on the upper horizon (Fig. 3a). An anticyclonic eddy formation between 33.4 and 34º E was more clearly observed (Fig. 3c) at the deep horizon (30 m).

The field of beryllium-7 concentration. A comparison of the fields of concentration, based on the results of two calculations, showed that both models provided qualitatively similar data: increased concentrations of $^{7}\mathrm{Be}$, due to the advective transport of Rim Current, were observed in the southeastern part of the polygon. The values of concentration were lower at the periphery of the Rim Current, and the greatest differences were observed in the coastal zone. Figure 4 shows the fields of beryllium-7 concentration on 19th of July, 2016. The elevated concentrations of $^{7}\mathrm{Be}$ in the area of urban-type settlement Gurzuf and Partenit, were apparently associated with atmospheric precipitation (Fig. 4c), while in the Feodosiya Bay, the concentration field was formed by submesoscale processes (Fig. 3a). Significant differences in the coastal zone were found in the area of Cape Sarych. According to the data of experiment 1 (Fig. 4b), the concentration here was approximately 1.5 times lower than in experiment 2 (Fig. 4a).

Comparison of the simulation results with observational data showed that both experiments gave similar values of concentration in the seaward part that fell within the measurement error themselves, and experiment 1 gave more accurate data near the shore. As can be seen from the Fig. 5, the $^{7}\mathrm{Be}$ concentration, reconstructed in experiment 1, lied within the measurement error for the station, performed on 19th of July, 2016 at the point (33.55° E, 44.43° N), while it exceeded both data observations

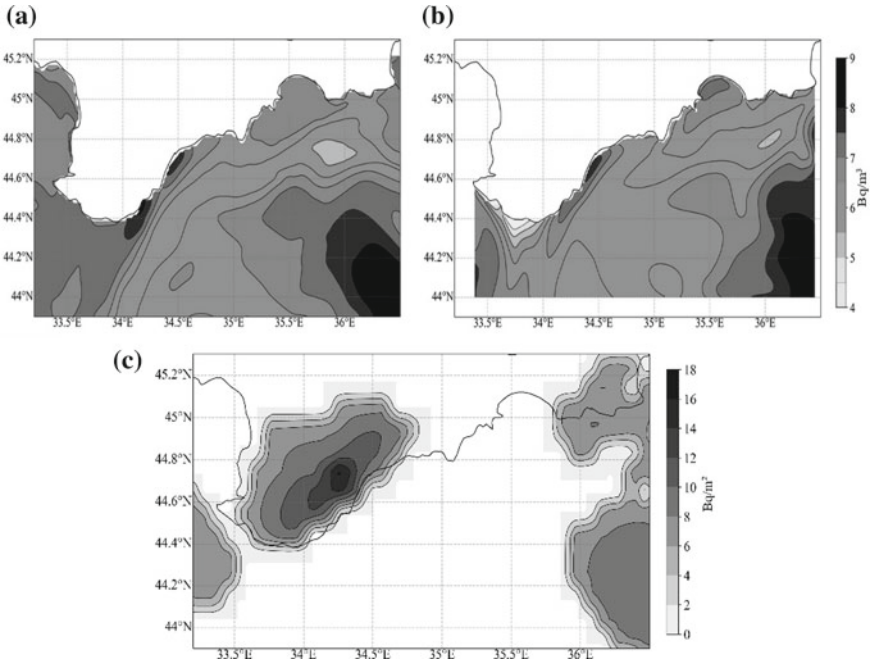


Fig. 4 Field of ^{7}Be concentration at the depth of 3 m according to the results of experiment 2 (**a**), experiment 1 (**b**) and the field of the ^{7}Be flux from the atmosphere (**c**) on 19th of July, 2016

as well as ultra-high resolution data in experiment 2. The features of the field of beryllium concentration, reproduced in experiment 2, were presumably related to the upwelling zone: its decrease was detected in the fields of model temperature on 19th and 20th of July, 2016. It was not possible to confirm that assumption with satellite images of the sea surface temperature due to cloudiness. However, the wind situation those days (north-northeast wind with a velocity of more than 10 cm/s (see data http://dvs.net.ru/mp/data/vel/jpg/wind/wind_nomads_20160719 12.jpg)) and the region were consistent with the conditions of upwelling formation typical for the Crimea South Coast [16]. The model with ultra-high spatial resolution made it possible to reconstruct not only fast submesoscale coastal eddies, but also to identify the beginning of upwelling through the radionuclide concentration field, the active phase of which was instrumentally recorded on 21–24 of July, 2016 at the Black Sea sub-satellite polygon of MHI in the urban-type settlement of Katsiveli [16].

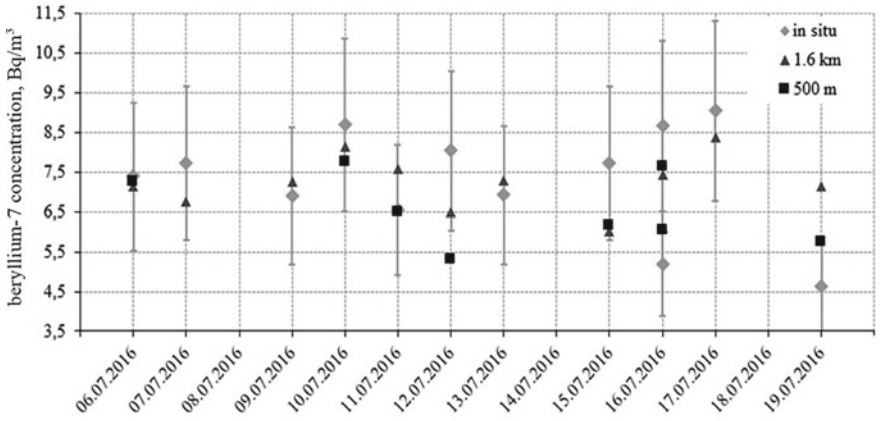


Fig. 5 Comparison of the $^{7}\mathrm{Be}$ concentration by the data of 87th cruise of the R/V "Professor Vodyanitsky" and by the simulation data. Measurement error interval is 25%

5 Conclusion

The fields of current velocity, temperature, salinity and concentration of beryllium-7, continuous in time and space, were reconstructed in the Crimean section of the shelf with high spatial resolution (horizontal grid ~500 × 500 m and 27 vertical horizons) by using hydrodynamic model and contact observation data temperature and salinity during the 87th cruise of the R/V "Professor Vodyanitsky", as well as data on satellite temperature of the sea surface.

The jet of the Rim Current along the Crimean coast was observed during the considered summer period. The following features of circulation were obtained between the coastline and the Rim Current. Anticyclonic eddy with a radius of about 20 km was generated and moved in the direction of the Rim Current in the upper 30-m layer between the city of Yalta and Cape Ayu-Dag. Anticyclonic eddy between 33.37 and 33.9º E was clearly manifested in the upper 30-m layer from 9 to 18th of July. Anticyclonic and cyclonic eddies of small scales in the upper layer near Cape Ayu-Dag and Cape Meganom could be generated during the Rim Current flow around the coastline and inhomogeneities of the bottom topography.

Increased content of the radionuclide was reproduced in the coastal zone of the city of Yalta and in the Feodosiya Bay in the field of beryllium-7 concentration. Moreover, in the first case, the increase in concentration was associated with atmospheric precipitation, and in the second case, with submesoscale dynamics. Decreased values were achieved on the periphery of the Rim Current and near Cape Sarych.

Comparison of the results on grid of ~500 m and ~1.6 km, as expected, showed that the elements of the eddy motion were not reconstructed accurately enough in the coastal zone at coarser resolution. Anticyclonic eddy between 33.4 and 34 ºE in the water layer of 30–100 m in experiment 2 was not always reproduced or was reproduced weakly. Differences were revealed in the field of concentration: the decrease

in concentration near Cape Sarych and the increase in the Feodosiya Bay were not reproduced in the calculation with resolution of ~1.6 km. At the same time, comparison with the data of direct measurements of concentration confirmed the correctness of the data, obtained with resolution of ~500 m. The work demonstrates the expediency of using model with ultra-high spatial resolution to analyze the distribution of impurities in the coastal zone and reconstruct such complex and fast submesoscale processes as small eddies and coastal upwellings.

Acknowledgements The analysis of the fields of currents and concentrations of beryllium-7 in the zone of the Southern coast of Crimea with spatial resolution of ~500 m was carried out with the support of the grant of the RSF 22-77-10056. The calculation of the hydrophysical fields of the Black Sea with spatial resolution of ~1.6 km for the Crimean section of the shelf was carried out within the framework of the state assignment on topic No. FNNN-2021-0003 (code "Operational Oceanology").

References

1. Kadko D, Olson D (1996) Beryllium-7 as a tracer of surface water subduction and mixed-layer history. Deep Sea res. Part I: Oceanogr. Res. Pap. Vol. 2 (43): 89–116. https://doi.org/10.1016/0967-0637(96)00011-8
2. Kremenchutskii DA, Dymova OA, Batrakov GF et al. (2018) Numerical simulation of the intra-annual evolution of beryllium-7 (^{7}Be) in the surface layer of the Black Sea. Environmental Science and Pollution Research. 11(25): 11120–11127. https://doi.org/10.1007/s11356-018-1269-y
3. Dymova OA, Demyshev SG (2018) Computing complex for modeling the Black Sea. IOP Conference Series: Earth and Environmental Science. 211 (1): 012082. https://doi.org/10.1088/1755-1315/211/1/012082
4. Diansky NA, Fomin VV, Zhokhova N.V. et al. (2013) Simulations of currents and pollution transport in the coastal waters of Big Sochi. Izv. Atmos. Ocean. Phys. 49: 611–621. https://doi.org/10.1134/S0001433813060042
5. Demyshev SG, Evstigneeva NA (2016) Modeling meso- and submesoscale circulation along the eastern Crimean coast using numerical calculations. Izv. Atmos. Ocean. Phys. 52: 560–569. https://doi.org/10.1134/S0001433816050042
6. Demyshev SG, Evstigneeva NA (2018) Simulations of Hydrophysical Fields with High Spatial Resolution over the Northwestern Shelf of the Black Sea. Oceanology. 58: 164–174 https://doi.org/10.1134/S0001437018020029
7. Bogdanov AA, Mizyuk AI, Kubryakov AA (2022) Evolution of sub-mesoscale cyclones on the Batumi anticyclone periphery based on the numerical simulation data. Physical Oceanography. 29(6): 550–566. https://doi.org/10.22449/1573-160X-2022-6-550-566
8. Demyshev SG, Evstigneeva NA, Alekseev DV et al. (2021) Analysis of the dynamic and energy characteristics of water circulation near the western Crimea coast and in the Sevastopol region based on the observational data assimilation in the numerical model of the Black Sea dynamics. Physical Oceanography. 28(1): 20–36. https://doi.org/10.22449/0233-7584-2021-1-23-40
9. Demyshev SG (2012) A numerical model of online forecasting Black Sea currents. Izv. Atmos. Ocean. Phys. 48: 120–132. https://doi.org/10.1134/S0001433812010021
10. Kremenchutskii DA, Konovalov SK (2022) Beryllium-7 (7Be) and its variability in the near-surface atmosphere of Crimea, the Black Sea region. Atmospheric Pollution Research. 13(5): 101406. https://doi.org/10.1007/s11356-018-3157-x

11. Kremenchutsky DA, Kubryakov AA, Zavyalov PO et al. (2014) Determination of the concentration of suspended matter in the Black Sea according to the MODIS satellite//Ecological Safety of Coastal and Shelf Zones of Sea. 29: 5–9. (in Russian)
12. Artamonov YuV, Skripaleva EA, Alekseev DV et al. (2018) Hydrological research in the northern part of the Black Sea in 2016 (87th, 89th and 91st cruises of R/V Professor Vodyanitsky). Phys. Oceanogr. 25(3): 229–234. https://doi.org/10.22449/1573-160X-2018-3-229-234
13. Orlanski I (1976) A simple boundary condition for unbounded hyperbolic flows. J. Comput. Phys. 21(3): 251–269
14. Kantha L, Blumberg A, Mellor G (1990) Computing phase speeds at open boundaries. J. Hydraulic Engineering. 116: 592–597
15. Pacanowski RC, Philander SGH (1981) Parameterization of vertical mixing in numerical models of tropical oceans. J. Phys. Oceanogr. V. 11(11):1443–1451
16. Simonova YuV, Stanichny SV, Lemeshko EM (2019) Characteristics of upwelling in the area of the southern coast of Crimea on the basis of a comprehensive analysis of contact and remote observations. Materials of the 17th All-Russian Open conference “Modern problems of remote sensing of the Earth from space”. Institute of Space Research of the Russian Academy of Sciences. 335. (in Russian)

Digital Examination of Pore Space Characteristics and Structural Properties of a Gas Condensate Field Reservoir on the Basis of μCT Images



V. V. Khimulia

Abstract The paper presents the results of digital studies of pore space and rock matrix properties of gas reservoirs using ProCon X-Ray CT-MINI high-resolution scanner of the Institute for Problems in Mechanics RAS. The studies included analysis of heterogeneities, cavernosity, initial fracture formation, spatial distribution of matrix granules, digital pore size distribution, granulometry of the rock matrix, and computer modeling of filtration processes. The results of modeling of filtration flows and porosity calculation showed good agreement with experimental data, which indicates the correctness of the applied methodology. It was determined that the rocks are practically isotropic in terms of filtration properties. The granulometric composition of the rocks was determined and the homogeneity of the matrix and pore space was shown. The non-destructive methods described in this work allow to simplify the data acquisition on core material characteristics. Application of the obtained results in combination with geomechanical tests of rocks is intended to expand the existing approaches to complex analysis of core material of gas and gas condensate reservoirs, as well as to complement and clarify the mathematical and operational models of the studied objects. The obtained pore and granule size distributions are important data for filling the reservoir model and can be used to solve the problems of sand manifestation, loss of well stability, as well as reduction of permeability during technical works on wells.

Keywords Permeability anisotropy · Porosity · Reservoir filtration properties · Pore space structure · Navier–Stokes numerical modeling · Digital granulometry · Computed tomography (CT) · GeoDict software · Pore size distribution · Gas reservoir properties

V. V. Khimulia (✉)
Ishlinsky Institute for Problems in Mechanics RAS, Moscow, Russia
e-mail: valery.khim@gmail.com

© The Author(s), under exclusive license to Springer Nature Switzerland AG 2024

V. Karev (ed.), *Proceedings of the 9th International Conference on Physical and Mathematical Modelling of Earth and Environmental Processes*, Springer Proceedings in Earth and Environmental Sciences, https://doi.org/10.1007/978-3-031-54589-4_3

1 Introduction

In the present day, the Russian Arctic shelf hosts over 20 discovered fields, most of which are categorized as unique and substantial based on current classifications. These fields hold immense promise for expanding the nation's resource reserves. Nonetheless, the development of the Arctic region is currently at a notably low level. This is primarily attributed to the considerable complexities associated with field development and operation in the challenging offshore conditions, as well as the elevated economic costs associated with traditional development methods. This challenge is particularly pronounced when it comes to gas and gas condensate reservoirs in the Russian Arctic shelf. These reservoirs consist of loosely cemented, highly permeable sandstones with relatively low strength characteristics. Effectively developing and exploiting such reservoirs necessitates comprehensive and multifaceted preliminary investigations of core materials. This is essential for creating precise geomechanical and hydrodynamic models and for preventing adverse processes in wells, such as sand clogging, stability issues, and reductions in permeability in the bottomhole zones.

Understanding the physical properties of reservoir rocks is crucial for developing reservoir models, forecasting well performance, and devising innovative strategies to enhance well productivity. To establish accurate hydrodynamic and geological reservoir models, in-depth and comprehensive studies are imperative, including laboratory core analysis. The main reservoir characteristics that have a major influence on reservoir processes are porosity, permeability, matrix structure and rock pore space. This is because the flow of fluids through the pore spaces within the reservoir is a fundamental process [1]. Historically, the assessment of rock permeability and porosity involved laboratory tests or well logging procedures, or it was indirectly inferred through correlations with other rock attributes [2]. However, a relatively novel and promising approach to studying rock properties in the laboratory is the numerical simulation of filtration processes using structures acquired via microcomputed X-ray tomography (μCT).

X-ray computed tomography stands as a significant non-destructive technique for examining the internal structure of rocks, serving as a valuable complement to direct laboratory investigations. This method involves reconstructing the spatial distribution of the linear attenuation coefficient of X-rays through computer processing of acquired projections during the radiation scan. The outcome of a CT investigation is presented in the form of a series of grayscale images, forming a three-dimensional representation of X-ray absorption within the examined specimen [3]. Specialized software is then employed to determine attributes like linear dimensions, quantity, sphericity, and anisotropy of elements within the specimen [4]. To facilitate quantitative material analysis and the utilization of tomography results for numerical process modeling, image segmentation becomes necessary [5]. Segmentation is a technique that involves analyzing images and transitioning from X-ray absorption to the spatial distribution of the specimen's constituent components within the specimen space. Segmentation can be binary (two-phase) or multiphase. In the industry, pore imaging

experiments coupled with modeling serve as valuable tools for predicting geological and physical properties [6], such as porosity and permeability [7]. These calculations are carried out on a segmented image, primarily focused on the macropore space. This space comprises pores with well-defined boundaries that can be effectively segmented into fluid and solid grains on a voxel basis [8]. When the rock grains are impermeable and the pore openings are considerably larger than the image resolution, achieving an accurate segmentation becomes crucial to obtain a realistic assessment of flow through the rock [9].

Recent research, combined with extensive experience in developing complex hydrocarbon fields, has highlighted the substantial influence of reservoir property heterogeneity and anisotropy on mass transfer processes within reservoirs. Considering the anisotropy of filtration properties is essential for addressing production optimization challenges and improving recovery rates. Reservoir models that disregard permeability anisotropy often result in overestimation or underestimation of key reservoir characteristics, potentially causing significant economic setbacks for the industry. Additionally, data regarding reservoir permeability anisotropy can be invaluable when determining the optimal field development approach [10]. Furthermore, factors such as bedding, layering, shear, and compaction can hinder fluid flow [11]. It's widely acknowledged that varying degrees of reservoir structure heterogeneity and filtration property distribution exist in most fields [12]. The permeability anisotropy within rocks has a noticeable impact on fluid flow within reservoirs, extending from injection wells to production wells. This effect becomes particularly pronounced in the later stages of field development and can result in a lower reservoir coverage factor, especially for facilities equipped with horizontal wells [13].

This work presents the results of rock structure digital studies carried out on the base of ProCon X-Ray CT-MINI high-resolution scanner of the Institute for Problems in Mechanics RAS. Digital studies of filtration and capacitance properties, fractional composition of the rock matrix are described. The studies included analysis of heterogeneities, cavernosity, initial fracture formation, spatial distribution of matrix granules, digital pore size distribution, granulometry of the rock matrix, and computer modeling of filtration processes. The methods for processing tomography images within the GeoDict software are outlined, followed by numerical simulations of filtration flows through the structures obtained. Filtration fields are computed utilizing both the Navier–Stokes and Stokes-only solvers from the FlowDict module within the GeoDict package. Subsequently, the modeling results are juxtaposed with those from physical experiments conducted on the examined rock specimens. Conclusions were made about the characteristics of rock pore space, the degree of anisotropy of filtration properties was defined, and the granulometric composition of rocks was determined.

2 Research Methodology

The core material under study was a reservoir from a gas condensate field on the Arctic shelf of Russia. The studied rocks were highly porous friable sandstones with low strength and cementation. Cube-shaped specimens with 40 mm facets were made from the cores. Computed tomography images were taken at two scales: full-scale imaging of the specimens to obtain a complete picture of the internal structure, and high-resolution imaging of individual geomaterial parts for digital analysis.

The computed tomography procedure and image acquisition of the specimens were conducted using the ProCon X-Ray CT-MINI high-resolution micro-CT scanner, as shown in Fig. 1 [14]. This device boasts dimensions of 1300 × 850 × 600 mm and features a sturdy base composed of a monolithic granite slab. This design choice ensures the practical elimination of temperature-induced drift and precise alignment of X-ray optical and other system components within the device, guaranteeing measurement accuracy and stability throughout the entire working range.

The scanner incorporates a vertical core placement scheme for research purposes, accommodating specimens with a maximum height of 200 mm and a maximum diameter of 200 mm. The device can handle loaded specimens weighing up to 5 kg. To facilitate precise measurements, a precision positioning system (manipulator) is integrated into the design, allowing for a distance of 335 mm from the tube to the object. Moreover, the detector can move perpendicularly to the main system axis within a range of +/−25 mm. The manipulator enables a 360-degree rotation of the specimen around its axis, achieving an angular position reproducibility accuracy of 1.5 angular seconds. The microfocus X-ray tube, characterized by high resolution and closed-loop operation, offers an adjustable output voltage range from 20 to 90 kV and an adjustable current range from 10 to 160 μA. The tube's maximum output power reaches 8 W, with the smallest focal spot size measuring 5 μm. The X-ray

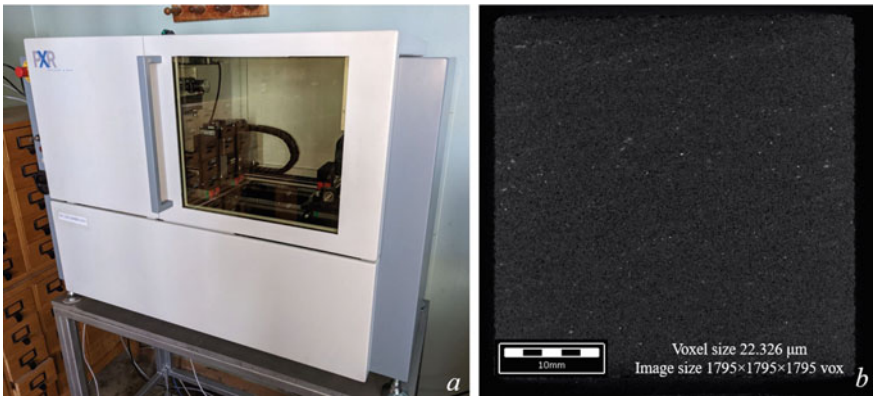


Fig. 1 **a**—ProCon X-Ray CT-MINI scanner; **b**—Side projection of one of the specimens after reconstruction (gray and white—material, black—air)

detector boasts high sensitivity and low noise, featuring a pixel count of 2940 × 2304 and a pixel size of 49.5 μm. The active (sensitive) area of the detector spans 146 × 114 mm.

The scans were reconstructed using VGSTUDIO software, while 3D image processing was carried out using Geodict Math2Market GmbH software [15]. GeoDict is a comprehensive solution for multiscale 3D image processing, material modeling, visualization, material property determination, material development through modeling, and process optimization. In addition to its fundamental image processing capabilities, GeoDict provides various techniques for image segmentation. Moreover, GeoDict offers diverse solution methods for modeling fluid flow, conductivity, and mechanics in porous media for both single-phase and two-phase scenarios.

Filtration fields were determined through the utilization of the FlowDict module from the GeoDict package. This module predicts effective material properties, such as flow velocity, flow permeability, and flow resistivity, by emulating flow experiments and subsequently analyzing the simulation outcomes. FlowDict forecasts the mean flow velocity under specified pressure conditions [16] and computes the permeability of a porous structure by employing Darcy's law. This versatile module is proficient in computing incompressible, stationary Newtonian flows, employing various approximations derived from the Navier–Stokes equations. Researchers worldwide actively employ FlowDict for modeling flows in diverse materials [17–20].

For numerical filtration simulations in this study, we harnessed the LIR solver [21]. LIR stands out as the latest and exceptionally swift iterative finite volume method. This solver calculates not only permeability but also velocity and pressure fields within extensive three-dimensional images. The rate of convergence is contingent upon the intricacy and heterogeneity of the pore space. Nonetheless, it's important to note that this approach faces certain limitations, including the simulation of exceptionally rapid flows characterized by high Reynolds numbers, leading to turbulence and boundary layer complexities. Additionally, simulating slip conditions at the boundary proves to be a challenging task. Nevertheless, it's essential to recognize that these limitations are applicable to all methods relying on voxel grids.

The selected termination criterion for the flow simulations is the error bound, which possesses the ability to detect convergence oscillations and prevent premature termination of the process at local minima or maxima [22]. Specifically, the termination threshold was set to 0.1 for the LIR solver, causing it to stop once the relative difference in comparison to the prediction falls below 0.1. Multigrid was also employed in the calculations. The core concept behind Multigrid involves utilizing multiple coarser adaptive grids to accelerate convergence while demanding only minimal additional memory [23]. To assess the geometric and statistical homogeneity of the pore space across all specimens, porometric analysis and pore geometry visualization were conducted using MatDict [24] and PoroDict modules based on segmented images.

3 Experimental and Simulation Results

Large-scale images allow to cover a large amount of material for analysis, but reduce the available imaging resolution. Scanning parameters for cube specimens were next: source voltage was 90 kV, amperage was 89 μA, exposition time was 0.28 s, number of averages was 3, rotation step was 0.125 degree and the voxel size was 22.326 μm. Figure 1b shows the lateral projection of one of the specimens after reconstruction. For all specimens, the initial structure of the interior space was homogeneous. Caverns and fracturing are absent. Impurities of denser material as well as traces of metals are found throughout the volume. The total volume of impurities is not more than 1%. There are no clear areas of layering, but traces of fluid movement in the reservoir in the form of directional impurities are recognizable. The angle of their inclination varies from 0 to 18 degrees.

After determining the homogeneity of the internal structure of the specimens on the full-scale images, high-resolution images were taken. They allow to clearly distinguish the grain and pore boundaries, which makes statistical quantitative analysis and modeling possible. All high-resolution imaging was performed with the next parameters: source voltage was 90 kV, amperage was 89 μA, exposition time was 0.2 s, number of averages was 15, rotation step was 0.125 degree and the voxel size was 4.957 μm. After scanning and reconstruction, the detailed work with images was carried out in the GeoDict software. The Non Local Means (NLM) filter was used to smooth the image and simplify the segmentation procedure. Figure 2a shows the projection obtained in high resolution after reconstruction, and Fig. 2b shows the same region after processing. Segmentation was performed using the Global Tresholding method to refine the grain boundaries. Figure 2c shows the result of segmentation of the same image.

Further digital research was carried out on the basis of the established structures. A representative elementary volume (REV) was analyzed for the specimens, which will be discussed further. Overall, open, closed and dead-end porosity was estimated for all specimens using PoroDict. On average, the porosity of the described series of specimens varied between 29–34%. The number of closed pores is not more

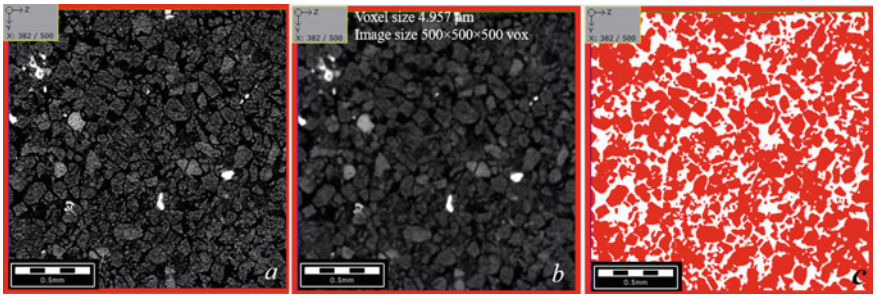


Fig. 2 **a**—Slice of high-resolution 3D image after reconstruction; **b**—Same slice after NLM filtering; **c**—Same slice after segmentation (red—matrix material, white—pores)

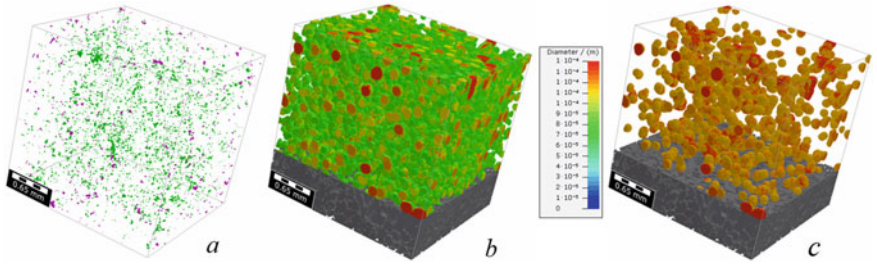


Fig. 3 **a**—Distribution of closed (green) and dead-end (purple) pores over the volume of the presented specimen; **b**—Distribution of granules with a diameter of more than 75 μm; **c**—Distribution of granules with a diameter of more than 110 μm

than 0.05%, which indicates a high cohesion of the pore space. For the specimen described in the example, the open porosity was 33.8982%, the closed porosity was 0.0476056%, and the dead-end porosity was 0.0105248%. In Fig. 3a shows the distribution of closed (green) and dead-end (purple) pores over the volume of the presented specimen. It can be seen that their distribution is uniform, there is no clearly distinguished direction. The result of the closed porosity assessment indicates the absence of caverns or closed pores of large size.

Porometry and granulometry analyses were conducted employing the PoroDict and MatDict modules to undertake a quantitative examination of the rock matrix's and pore space structure. These modules facilitated the acquisition of statistical distributions for pores and rock granules based on their characteristic sizes. In Fig. 4, we present the resultant diagrams illustrating the relationship between the volume fraction of each size category and the diameter of pores/granules, using one of the specimens as an example. The graphs show that the size distribution of matrix grains is uniform. Large silty (large sized aleurite 0.1–0.05 mm) particles predominate in the matrix composition. Their content for the described specimen is 55.4%. The content of fine sandy fractions (powdery 0.25–0.1 mm) is 24%. The pore size distribution has two expressed maxima at 20–30 μm and 35–45 μm. For pores larger than 50 μm, an increase in size is accompanied by a uniform decrease in number.

To analyze the spatial distribution of granules in the rock matrix, Fig. 3b and c presents a visualization of granules with sizes greater than 75 μm and 110 μm,

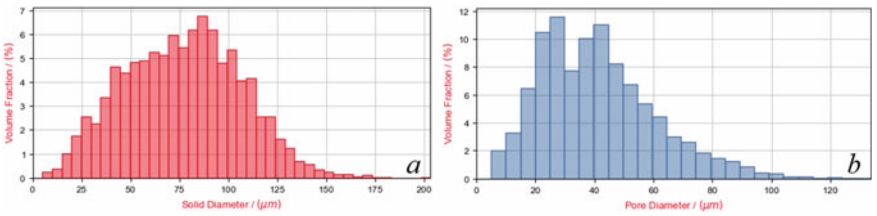


Fig. 4 **a**—Result of granulometry analysis; **b**—Result of porometry analysis

respectively. The color scale shows the size of the granules. It can be observed that the granules are uniformly distributed over the volume. There are no areas of compaction. Large granules (over 120 μm) are found in the whole volume of the specimen.

To assess the filtration properties and their anisotropy, we conducted a filtration flow modeling process. Before this, we measured the rock permeability using laboratory techniques. For all specimens the air permeability was measured using the TILTS facility of the Institute for Problems in Mechanics [25]. For this purpose, a cubic specimen was covered with an impermeable film on four faces. Air was passed through two open faces along one of the specimen axes [26]. The pressure drop did not exceed 0.1 bar. To simulate the filtration flow within the resulting structure using the FlowDict module, we employed two filtration models: Stokes and Navier–Stokes [27]. To replicate the conditions of laboratory permeability measurements, we selected the following flow parameters: fluid—air, pressure drop of 0.1 bar, temperature at 20 °C, boundary conditions in the filtration direction—periodic with an implicit region of 10 voxels, and in the tangential direction—symmetric. In the linear Stokes model, a pressure drop of 100 Pa was employed to ensure laminar conditions were met.

Figure 5 shows the flow velocity fields along the bedding for both models. For both models, a uniform distribution of main flows over the specimen volume is observed. The filtration channels are wide, and the change in size is smooth along the entire structure. The Table 1 presents the results of laboratory permeability measurements for the studied interval along the two directions in the rock, as well as the calculated permeability values for both models.

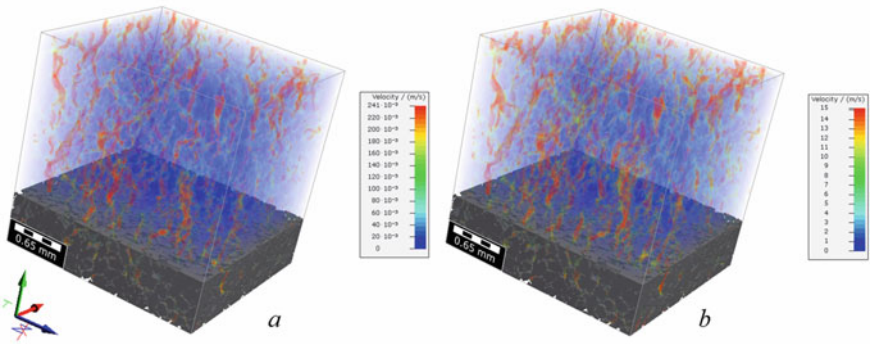


Fig. 5 **a**—Velocity field by Stokes model; **b**—Velocity field by Navier–Stokes model

Table 1 Results of measurements and simulation of filtration flow

Filtration model/Measurement	Permeability across the bedding, D	Permeability along the bedding, D	
Laboratory value	5.200	5.500	
Stokes	6.883	7.489	7.019
Navier–Stokes	5.455	5.820	5.516

As can be seen from the table, the permeability calculated by both models is in good agreement with the laboratory data. The permeability along the core axis for both models also remains lower than in the layering directions, which indicates a weak degree of transversal anisotropy. At the same time, the values obtained within the Navier–Stokes model correlate more closely with the laboratory data due to the greater complexity of the model and its applicability to higher velocity flows. The Renolds number for the simulation within the Stokes model did not exceed 0.030759 for the characteristic pore size. For the Navier–Stokes model, the pressure drop was higher, so the Reynolds number was of the order of 2. Gurley value for this specimen was 0.854677 s.

An important step in digital research is the identification of a representative elementary volume (REV)—the smallest volume beyond which domain properties do not change. To estimate it, a characteristic parameter, such as porosity, permeability or others, is calculated on the original 3D digital model. A certain number of subsamples with a decreasing number of cells are then cut from the original model and similar parameters are estimated for comparison with the original model. The size at which the parameter value becomes stable is considered the smallest representative volume [28]. When calculating REV, the porosity was estimated in process of all-round decrease of linear dimensions of the structure. Figure 6 shows the result of REV calculation for the specimen described in this article. On the vertical axis is plotted the normalized porosity (related to the value for the maximum size cube). On the horizontal axis is the linear size of the corresponding cube for which the porosity calculations were performed.

Through visual inspection, it becomes evident that images with a linear size of 250 voxels adequately capture the porosity of the entire specimen volume. This observation underscores the high level of homogeneity within the rock's pore space, a conclusion further supported by the porometry analysis. Thus, the 500 voxel edge cubic structures used for analysis and modeling are representative.

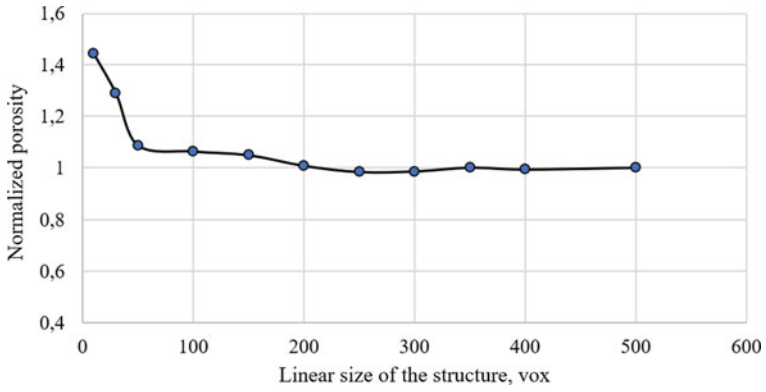


Fig. 6 Normalized porosity as a function of image size

The data obtained in this work are the first stage of the planned comprehensive studies of the rocks of this deposit. The results obtained from the numerical analysis agree well with traditional laboratory tests of similar rocks from Arctic gas fields [29]. The results of studying the pore space and filtration processes in these rocks allow us to conclude that these rocks are practically isotropic in terms of filtration properties, which will greatly simplify the hydrodynamic model of the field. The quantitative material assessment findings can be complemented by exploring related parameters like sorting, rounding, and packing characteristics, as well as mineral composition. The digital analysis methodology of CT images presented in this study streamlines the acquisition of core material characteristics, serving as a valuable addition to laboratory and in-situ investigations of reservoir properties.

4 Conclusion

This work presents the results of rock structure digital studies carried out on the base of ProCon X-Ray CT-MINI high-resolution scanner of the Institute for Problems in Mechanics RAS. Digital studies of filtration and capacitive properties, fractional composition of the rock matrix are described. The studies included analysis of heterogeneities, cavernosity, initial fracture formation, spatial distribution of matrix granules, digital pore size distribution, granulometry of the rock matrix, and computer modeling of filtration processes. Filtration fields are computed utilizing both the Navier–Stokes and Stokes-only solvers from the FlowDict module within the GeoDict package. Subsequently, the modeling results are juxtaposed with those from physical experiments conducted on the examined rock specimens. The methodology of digital analysis of CT images using GeoDict package is described. The results of modeling of filtration flows and porosity calculation showed good agreement with experimental data, which indicates the correctness of the applied methodology. It was determined that the rocks are practically isotropic in terms of filtration properties. The granulometric composition of the rocks was determined and the homogeneity of the matrix and pore space was shown. The result of the closed porosity assessment indicates the absence of caverns or closed pores of large size. The obtained pore and granule size distributions are important data for filling the reservoir model and can be used to solve the problems of sand manifestation, loss of well stability, as well as reduction of permeability during technical works on wells.

Acknowledgements The research was supported by the Russian Science Foundation grant № 23-77-01037, https://rscf.ru/project/23-77-01037/.

References

1. Ganat T. A. A. O. Fundamentals of reservoir rock properties. Cham, Switzerland: Springer, 2020. https://doi.org/10.1007/978-3-030-28140-3.
2. Ivanov M.K. et al. Petrophysical Methods for Study of Core Material // M.: Publishing house of Moscow State University. 2008. P. 112. (in Russian).
3. Lichun J., Mian C. 3D imaging of fractures in carbonate rocks using X-ray computed tomography technology // Carbonates and Evaporites. 2014. V. 29. I. 2. pp. 147–153. https://doi.org/10.1007/s13146-013-0179-9.
4. Diaz M. et al. Surface roughness characterization of open and closed rock joints in deep cores using X-ray computed tomography // International Journal of Rock Mechanics and Mining Sciences. 2017. V. 98. pp. 10–19. https://doi.org/10.1016/j.ijrmms.2017.07.001.
5. Gerke K.M., Korost D.V., Karsanina M.V., Korost S.R., Vasiliev R.V., Lavrukhin E.V., Gafurova D.R. Modern approaches to pore space scale digital modeling of core structure and multiphase flow // Georesources. 2021. 23(2). pp. 197–213. https://doi.org/10.18599/grs.2021.2.20.
6. Menke H.P. et al. Using Nano-XRM and High-Contrast Imaging to Inform Micro-Porosity Permeability During Stokes–Brinkman Single and Two-Phase Flow Simulations on Micro-CT Images // Frontiers in Water. 2022. V. 4. P. 935035. https://doi.org/10.3389/frwa.2022.935035.
7. Blunt M.J. Multiphase Flow in Permeable Media: A Pore-scale Perspective // Cambridge: Cambridge University Press. 2017. https://doi.org/10.1017/9781316145098.
8. Mostaghimi P., Blunt M.J., Bijeljic B. Computations of absolute permeability on micro-CT images // Math. Geosci. 2013. V. 45. Pp. 103–125. https://doi.org/10.1007/s11004-012-9431-4.
9. Alyafei N., Raeini A.Q., Paluszny A., Blunt M.J. A sensitivity study of the effect of image resolution on predicted petrophysical properties // Transp. Porous Media. 2015. V. 110. 157–169. https://doi.org/10.1007/s11242-015-0563-0.
10. Krivoshchekov S., Kochnev A., Kozyrev N., Ozhgibesov E. Factoring Permeability Anisotropy in Complex Carbonate Reservoirs in Selecting an Optimum Field Development Strategy // Energies. 2022. 15 (23). 8866. https://doi.org/10.3390/en15238866.
11. Vajdova V., Baud P., Wong T. Permeability evolution during localized deformation in Bentheim sandstone // J. Geophys. Res. 2004. 109. B10406. https://doi.org/10.1029/2003JB002942.
12. Aliev Z.S., Kotlyarova E.M. Approximate method of UGS creation and operation in heterogeneous formations using horizontal wells. Envir. Responsib. of Oil and Gas Ind. 2017. 46–55 (in Russian).
13. Maksimov V.M., Dmitriev N.M., Antonievich Yu.S. Effects of tensor nature of relative phase permeabilities at mutual gas displacement by water in anisotropic reservoirs // Georesour., Geoenerg., Geopolit. 2010. 1 (1), 25 (in Russian).
14. CT-MINI by ProCon X-Ray GmbH available at https://procon-x-ray.de/en/ct-mini.
15. GeoDict – The Digital Material Laboratory: (digital source) URL: https://www.math2market.de/ (Date of request: 23.09.2023).
16. Kling T. et al. Simulating stress-dependent fluid flow in a fractured core sample using real-time X-ray CT data // Solid Earth. 2016. V. 7. 1109–1124. https://doi.org/10.5194/se-7-1109-2016.
17. Herdtle T., Xue Y., Bolton J. S. Numerical modelling of the acoustics of low density fibrous media having a distribution of fiber sizes. Publications of the Ray W. Herrick Laboratories. 2017. Paper 167.
18. Balucan R. et al. Coal permeability stimulation by NaClO oxidation // The APPEA Journal. 2019. V. 59. №. 2. P. 846–850. https://doi.org/10.1071/AJ18142.
19. Soltani P. et al. Experimental and computational analysis of sound absorption behavior in needled nonwovens // Journal of Sound and Vibration. 2018. V. 426. P. 1-18. https://doi.org/10.1016/j.jsv.2018.04.007.
20. Steel K.M. et al. Identification of preferential pathways in the pore microstructure of metallurgical coke and links to anisotropic strength properties // Fuel. 2021. V. 296. P. 120688. https://doi.org/10.1016/j.fuel.2021.120688.
21. Linden S. et al. The LIR space partitioning system applied to the Stokes equations // Graphical Models. 2015. V. 82. pp. 58–66. https://doi.org/10.1016/j.gmod.2015.06.003.

22. Pan Z., Liang Y., Tang M. et al. Simulation of performance of fibrous filter media composed of cellulose and synthetic fibers // Cellulose. 2016. 26, 7051–7065. https://doi.org/10.1007/s10570-019-02605-8.
23. Saxena et al. References and benchmarks for pore-scale flow simulated using micro-CT images of porous media and digital rocks // Advances in Water Resources. 2017. 109. pp. 211–235. https://doi.org/10.1016/j.advwatres.2017.09.007.
24. Rief S., Hilden J., Planas B. MATDICT User Guide. GeoDict release 2022. December 8, 2021. https://doi.org/10.30423/userguide.geodict2022-matdict.
25. Karev V., Kovalenko Y., Ustinov K. Advances in Oil and Gas Exploration and Production. Switzerland: Springer International Publishing. 2020. 166 p. https://doi.org/10.1007/978-3-030-26608-0.
26. Karev V., Kovalenko Y. Triaxial loading system as a tool for solving geotechnical problems of oil and gas production. True triaxial testing of rocks. 2013. Leiden: CRC Press/Balkema: 301–310.
27. Hilden J., Cheng L., Linden S., Planas B. FlowDict User Guide GeoDict release 2022. Published: November 9, 2021. https://doi.org/10.30423/userguide.geodict2022-flowdict.
28. Pelissou C., Baccou J., Monerie Y., Perales F. Determination of the size of the representative volume element for random quasi-brittle composites // Int. J. Solids and Struct. 2009. 46 (14–15), 2842–2855. https://doi.org/10.1016/j.ijsolstr.2009.03.015.
29. Pyatakhin M. V., Shulepin S. A., & Gaidash Y. M. Experimental studies of reservoir rock fracture in the bottomhole zone of wells. Territory Neftegaz, 2020. (9-10), 30–37. (in Russian).

Identification of the Location and Possible Release Time of the Pollution Source Based on the Method of Adjoint Equations

V. S. Kochergin and S. V. Kochergin

Abstract The aim of the article is to construct procedure for determining the location of the pollution release from the measurement information on contaminants in water body. Besides that, the problem of determining the possible moment of contamination entering the sea at a known source location of the source is decided. The parameters of an instantaneous point source in the passive impurity transport model for the Azov Sea are defined.

Keywords Adjoint equations · Concentration field · Identification of pollution source · Azov Sea

1 Introduction

Intensive anthropogenic impact on the ecosystem of the Azov Sea call for development of environmental observation systems that assume brisk and effective estimation of the situation in domains to anthropogenic effects, chiefly in zones of active navigation and the building of different objects. This areas include the Kerch Strait, the Taganrog Bay, the waters of ports, raid parking places. The study of such tusks is realizable with the help of mathematical modeling [1, 2] and methods for solving inverse problems [3–5], when, according to measurement data due to their assimilation, the identification of model parameters necessary for more accurate prediction of pollution concentration fields in the sea occurs. Variational procedures of data assimilation and approach of conjugate equations are intensively work out and applied to solve oceanological tusks [6–8]. An extensive review on this topic is presented in Shutyaev [9]. The algorithms for assimilation of measurement data are based on finding of the cost function minimum that characterizes forecast discrepancies. The model of passive impurity transfer imposes its limitations on the variations of the model parameters. In Kochergin and Kochergin [10], a procedure for finding the

V. S. Kochergin (✉) · S. V. Kochergin
Marine Hydrophysical Institute RAS, Kapitanskaya Str. 2, 299011 Sevastopol, Russia
e-mail: vskocher@gmail.com

© The Author(s), under exclusive license to Springer Nature Switzerland AG 2024

V. Karev (ed.), *Proceedings of the 9th International Conference on Physical and Mathematical Modelling of Earth and Environmental Processes*, Springer Proceedings in Earth and Environmental Sciences, https://doi.org/10.1007/978-3-031-54589-4_4

force of the source is discussed. In it work, the conjugate formalizm [11] is exploited to locate of the source of pollution and determine the time interval in which such pollution could occur.

2 Method of Adjoint Equations

Let the model of passive impurity transfer in σ-coordinates have the form:

$$\frac{\partial DC}{\partial t} + \frac{\partial DUC}{\partial x} + \frac{\partial DVC}{\partial y} + \frac{\partial WC}{\partial \sigma} = \frac{\partial}{\partial x} A_H \frac{\partial DC}{\partial x} + \frac{\partial}{\partial y} A_H \frac{\partial DC}{\partial y} + \frac{\partial}{\partial \sigma} \frac{K}{D} \frac{\partial C}{\partial \sigma} \tag{1}$$

with the add conditions on boundaries:

$$\Gamma : \frac{\partial C}{\partial n} = 0, \tag{2}$$

$$\begin{aligned} \sigma = 0 : \frac{\partial C}{\partial \sigma} = 0 \\ \sigma = 1 : \frac{\partial C}{\partial \sigma} = 0 \end{aligned} \tag{3}$$

and initial data:

$$C(x, y, \sigma, 0) = C_0(x, y, \sigma), \tag{4}$$

where x_0, y_0—location of the source; D—the value of dynamical depth; C—the value admixture concentration; U, V, W—velocities; A_H and K—coefficients of turbulent diffusion; n—normal to the boundary, M—the domain of the model solving; Γ—the boundary of the domain M; t—time; $M_t = M \times [0, T]$.

From Eqs. (1)–(4) with the help of equation in σ—coordinates:

$$\frac{\partial D}{\partial t} + \frac{\partial DU}{\partial x} + \frac{\partial DV}{\partial y} + \frac{\partial W}{\partial \sigma} = 0, \tag{5}$$

and the following conjugate problem:

$$-\frac{\partial DC^*}{\partial t} - \frac{\partial DUC^*}{\partial x} - \frac{\partial DVC^*}{\partial y} - \frac{\partial WC^*}{\partial \sigma} - D\frac{\partial}{\partial x} A_H \frac{\partial C^*}{\partial x} - D\frac{\partial}{\partial y} A_H \frac{\partial C^*}{\partial y} - \frac{\partial}{\partial \sigma} \frac{K}{D} \frac{\partial C^*}{\partial \sigma} = 0, \tag{6}$$

$$\Gamma : \frac{\partial C^*}{\partial n} = 0; \sigma = -1 : \frac{\partial C^*}{\partial \sigma} = 0; \sigma = 0 : \frac{\partial C^*}{\partial \sigma} = 0, \tag{7}$$

$$t = T : C^* = h, \tag{8}$$

we obtain following equation:

$$\int_M ChdM = \int_M C^* C_0 dM\,, \tag{9}$$

where:

$$h = \begin{cases} \frac{1}{mes(\Omega)} - in\Omega \\ 0 - outside\Omega \end{cases}. \tag{10}$$

At the left part of the (9), we have the average mean $\overline{C}_T$ in Ω at the last time moment T:

$$\overline{C}_T = \int_M C^* C_0 dM\,. \tag{11}$$

With the help of solution of the conjugate problem (6)–(8), the equality (11) can be exploited to evaluate the means of an admixture in a given cellule. Numerical experiments from Dymova and Kochergin [8], Kochergin and Kochergin [10] demonstrate sufficiently well preciseness of calculating the means of concentration field by the initial data. In Eqs. (9) and (11) C^* it is practically a function of the influence of the initial data. Due to its structure, you can investigate the effect of the initial data on the solution of the transport model. Then we get:

$$\int_S C^* \cdot Q \cdot dM = \int_S g \cdot C \cdot ds \tag{12}$$

where S is the surface aria of the domain M, $g = \delta(x - x_n) \cdot \delta(y - y_n) \cdot \delta(t - T)$, $n = 1, \ldots, N$, N is the total quantity of data measurement at a final time$T$. From (12) we obtain:

$$C_n^*(0, x_0, y_0, 0) Q_S = C(x_n, y_n, 0, T), n = 1, \ldots, N \tag{13}$$

Formula (12) agrees with the formula of the algorithm of Kochergin [12] calculation means of the concentration from different initial data and [9] through the source force and the outcome of the conjugate problem. If the problem of finding the coordinates of the ejection point is solved, it is necessary to solve the conjugate problems (6)–(8) and determine the area where the areas of significant values are. To determine the time interval in which a pollution release may have occurred, it is necessary to solve a number of related tasks at different time intervals. Such a problem can be solved provided that the coordinates of the source are known. This may be the coordinates of the roadstead of ships or the main routes of intensive shipping. Knowing the time

interval of a possible release of pollution, taking into account a priori information (a list of ships located in the area), it is possible to determine the source of pollution itself.

3 Results of Numerical Experiments

Calculations were done with the help of model [1] for the domain of the Azov Sea. To apply the determination procedure, a numerical experiment was carried out to install a model velocities with input parameter of a constant east wind stress near 10 m/s. Also coefficients of the model was calculated. This dynamic fields are input parameters during to solving transfer model for a time period of 4 days. Figure 1 shows the calculation result when specifying a single instantaneous source on the sea surface.

The location of such a source is also represented by a black dot in the figure below. Information about the concentration values is received at the end time from 5 measurement points located on the periphery of the contamination spot. The result of solving of the adjoint equations and location of the source of pollution is represented in Fig. 2.The result of integrating five conjugate problems (6)–(8) is displayed in this figure. The grey area respective to these adjoint tasks is highlighted in the figure. From Fig. 2 we can see that that the true placement of the source belongs to the region. It should be noted that the area of the shaded area significantly depends on the parameters of the problem being solved—these are the coefficients of model, and velocities, the location of measurement points, as well as the integration time of the problem.

When solving the second problem, in order to determine the possible time interval at which the ejection occurred at a known point shown in Figs. 2 and 3, it is necessary

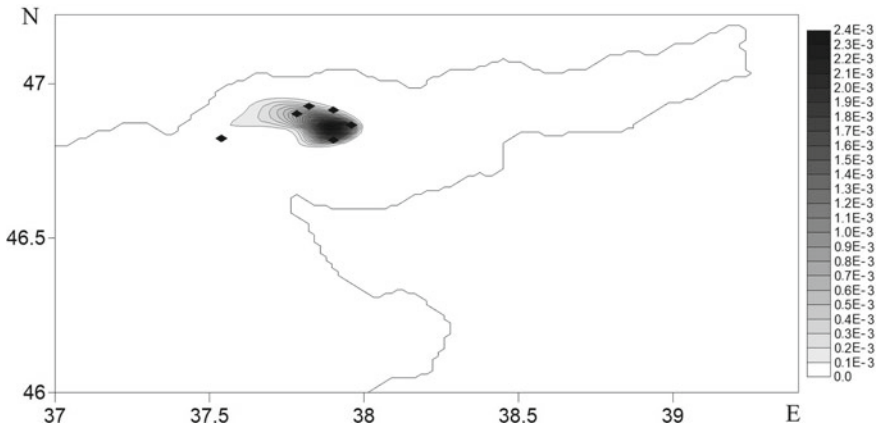


Fig. 1 Location of the source and measurements of concentration

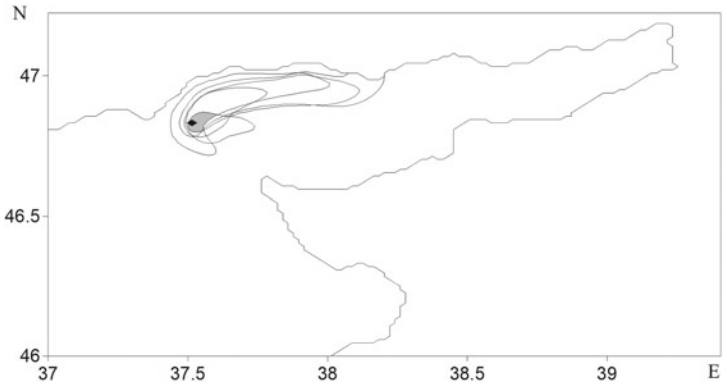


Fig. 2 Solution of related problems, area and locationof the pollution source

to solve a series of problems for different measurement points and setting different time intervals for integrating the model. For example, Fig. 3 present the measurement point near the maximum concentration value, as well as solutions to related problems for a period of 4 days (bold line), 2.5 days dotted line and a thin solid line indicates the influence function for a period of 5.5 days of model integration. For shorter or longer periods of the model time, the concentration in the source of contamination does not significantly affect the concentration values at the selected measurement point. I.e., the coordinates of the source do not fall inside the corresponding influence function. Thus, the release could occur in this source during the specified three-day period of time.

Note that the area of the shaded area in Fig. 2 is significantly smaller than the area of the area depicted by a solid bold line in Fig. 3, which corresponds to the solution of the conjugate problem, provided that the measurement point is selected in the

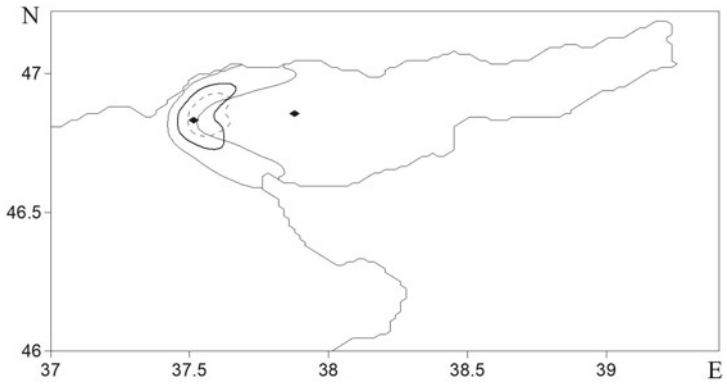


Fig. 3 Location of an instantaneous point source, measurement point and solutions of adjoint problems for different time intervals

region of maximum values. It should also be noted that, for example, it is difficult to determine the area of maximum concentration from images from space, the pollution boundary is determined quite accurately. On the other hand, the most precise value of the true value of the force of the pollution source is calculated when points of measurements are located in the region of the biggest values of the admixture field.

4 Conclusions

In general, the conducted numerical experiments demonstrated the stable operation of the algorithm for searching for the parameters of the pollution source in relation to the model of passive impurity transfer in the AZOV Sea. The results of the work can be successfully applied in the study of the influence of anthropogenic sources of pollution on the waters of the Azov Sea.

Acknowledgements The work was carried out within the framework of the state task on the topic FNNN-2021-0005 "Complex interdisciplinary studies of oceanological processes that determine the functioning and evolution of ecosystems of the coastal zones of the Black and Azov Seas" (code "Coastal research").

References

1. Marchuk G.I., Sarkisyan A.S.: Mathematical modeling of ocean circulation, Moscow, Nauka, (1988).
2. Ivanov V.A., Fomin V.V.: Mathematical modeling of dynamic processes in the sea-land zone. ECOSI-Gidrophisika, Sevastopol (2008).
3. Marchuk G.I., Penenko V.V. Application of optimization methods to the problem of mathematical simulation of atmospheric processes and environment // Modelling and Optimization of Complex Systems / Ed. G.I. Marchuk. Proc. of the IFIP-TC7 Working conf. NewYork: Springer, 1978. P. 240–252.
4. Kochergin V.S., Kochergin S.V.: Modeling of admixture propagation in the Sea of Azov based on solving related problems. Ecological safety of coastal and shelf zones and comprehensive use of shelf resources 4, 15–18 (2016).
5. Penenko V.V.: Estimation of parameters of discrete models of atmospheric and ocean dynamics. Meteorology and hydrology 7, 77–90 (1979).
6. Agoshkov V.I., Parmuzin E.I., Shutyaev V.P.: Assimilation of observational data in the problem of Black Sea circulation and sensitivity analysis of its solution 6(49), 643–654 (2013).
7. Zalesny V.B., Agoshkov V.I., Shutyaev V.P., Le Dime F., Ivchenko V.O.: Problems of numerical modeling of ocean hydrodynamics with variational assimilation of observational data. Izv. RAS. Physics of the atmosphere and ocean 4(52), 488–500 (2016).
8. O. A. Dymova, V. S. Kochergin, S. V. Kochergin Identification of the location of a possible source of pollution in the water area of the Heraclea Peninsula based on the method of adjoint equations. Ecological bulletin of the scientific centers of the Black Sea economic cooperation 3, 72–77 (2018). https://doi.org/10.31429/vestnik-15-3-72-77.
9. Shutyaev V. P. Izvestiya, Atmospheric and Oceanic Physics volume 55, pages17–31 (2019). https://doi.org/10.1134/S0001433819010080.

10. Kochergin V.S., Kochergin S.V. Identification of a Pollution Source Power in the Kazantip Bay Applying the Variation Algorithm In: Physical oceanography, no. 2, pp. 79–88 (2015).
11. Marchuk G.I.: Mathematical modeling in the environmental problem. Nauka, Moskva, (1982).
12. Kochergin V.S.: Determining of the concentration field with use the data measurements based on solving of adjoint problems. Ecological safety of coastal and shelf zones and comprehensive use of shelf resources 25(2), 377–381 (2011).

Effect of UV Radiation and Ozone on the Viability of Biofilms and Resting Forms of *Pseudomonas Aeruginosa* Bacteria



M. A. Kotov, N. G. Solovyev, A. N. Shemyakin, M. Y. Yakimov, O. V. Kalmantaeva, M. A. Makarova, and O. Y. Manzenyuk

Abstract This article contains the results of bactericidal treatment of Pseudomonas aeruginosa. Using a specially designed irradiator with a concentrator of diffusely scattering material, biofilms and dormant forms of these bacteria were exposed to UV radiation, ozone, and their combination. Numerical estimates of the radiation density directly on the processed samples are presented. The ratio of living and dead cells was determined using confocal laser scanning microscopy. The results of the work showed a good experimental effectiveness of the complex effect on the super-resistant forms of Pseudomonas aeruginosa.

Keywords Mercury lamp · UV · Ozone · Germicidal irradiator · Biofilms · *Pseudomonas aeruginosa* · Confocal laser scanning microscope

1 Introducion

The bactericidal effect of ultraviolet (UV) radiation on biological objects (cells, bacteria, viruses, etc.) is well known and has been studied since the beginning of the last century [1]. If we consider a single cell of such objects as an elementary structural unit of a living organism, then we can say that UV radiation can lead to irreversible damage in the cell due to photochemical reactions. As a rule, this is primarily understood as a violation of the structures of bacterial and viral DNA and RNA, as well as proteins and their other components [2, 3]. It can be said that the universal nature of the action of UV radiation on microorganisms leads to the

M. A. Kotov (✉) · N. G. Solovyev · A. N. Shemyakin · M. Y. Yakimov
Ishlinsky Institute for Problems in Mechanics RAS, Moscow, Russia
e-mail: kotov@ipmnet.ru

O. V. Kalmantaeva · M. A. Makarova · O. Y. Manzenyuk
FBIS State Research Center for Applied Biotechnology and Microbiology, Obolensk, Russia

© The Author(s), under exclusive license to Springer Nature Switzerland AG 2024

V. Karev (ed.), *Proceedings of the 9th International Conference on Physical and Mathematical Modelling of Earth and Environmental Processes*, Springer Proceedings in Earth and Environmental Sciences, https://doi.org/10.1007/978-3-031-54589-4_5

induction of lethal mutations and the death of almost the entire (99.9%) microbial population [4].

Ozone gas (O_3) is a very strong oxidizing agent, it is able to destroy almost all known living microorganisms and their forms [5–8]. In fact, with sufficient processing time, its detrimental effect on any kind of bacteria is known, with the exception of the most resistant to aggressive environments, for example, Deinococcus radiodurans [9, 10]. Ozone interacts with the bacterial cell wall by oxidizing its constituent lipids and lipoproteins, which have a large number of chemical bonds between atoms. As a result, there is an active formation of new chemical angular configurations and compounds that are incompatible with cell viability. When ozone interacts with proteins, it sequentially penetrates through the cell membrane, reacts with the contents of the cytoplasm, destroys extrachromosomal genetic elements—plasmids, and prevents further cell division [11, 12].

In difficult conditions of aggressive environments, some types of viruses and microorganisms on the surfaces of carriers can combine into special structures, biofilms, which allows them to maintain their viability and more effectively resist external influences. A biofilm is an organized collection of microorganisms living in a self-produced matrix of extracellular polymeric substances (EPS) that is attached to a biotic or abiotic surface. Biofilm formation is a complex and dynamic process in which organized microbial communities are encased in an EPS matrix that groups microbial cells together. EPS are primarily composed of polysaccharides, proteins, lipids, and nucleic acids (RNA and extracellular ecosystem DNA eDNA) that form a highly hydrated polar mixture that contributes to the overall framework and three-dimensional structure of the biofilm. This survival organization provides bacteria with numerous benefits, including protection from external threats. Therefore, biofilm-forming bacteria numerically and metabolically predominate in almost all ecosystems, and also participate in the development of chronic bacterial infections of the human body [13, 14].

Biofilms are a constantly renewing community of microbes fixed on a biogenic or abiogenic substrate and surrounded by a polymer matrix. Such structures can be formed quite quickly, including on the surfaces of various medical devices and devices (medical equipment, surgical instruments, implants and catheters, elements of external and internal prosthetics, etc.). This is the reason for the interest of scientists in the problems of biofilm formation and the issues of their inactivation, which has been growing in recent years [15, 16].

Pseudomonas aeruginosa is a gram-negative, facultative (opportunistic) human pathogen that rarely causes infectious diseases in healthy people, but is often associated with nosocomial (nosocomial) infections. *P. aeruginosa* causes pulmonary infections in 16% of cases, urinary tract infections in 12% of cases, surgical wound and burn infections in 8%, generalized blood infections in 8% of cases, and generalized blood infections in 10% [17–19].

To date, the situation with the treatment of infections caused by *P. aeruginosa* has worsened with the emergence of strains with multiple resistance to antibacterial drugs: in some cases, this nosocomial infection cannot be treated with modern antibiotics due to the resistance of the bacteria to these drugs. For example, in the United

States in 2013, in absolute terms, more than 51,000 hospital infections caused by *P. aeruginosa* were registered, of which 13% of cases were due to multidrug-resistant strains, and lethality from infection was 440 cases per year [20]. A possible reason for the underestimation of the clinical significance of this infection could be the theoretical premise that prevailed until the 1970s of the last century. Then it was believed that bacteria, and in particular Pseudomonas, live in the environment in the form of single organisms (planktonic lifestyle). Since the 1990s, the main attention of researchers has been focused on studying the mechanisms of survival of pathogenic microorganisms in the external environment in the form of biofilms and the phenomenon of multidrug resistance to a wide range of antibacterial drugs [21].

This work is devoted to the study of the possibility of growth inhibition and inactivation of *P. aeruginosa* biofilms resistant to irradiation with commercial UV lamps using separate or combined exposure to UV radiation and ozone. For this, a special generator with a low-pressure mercury lamp was designed, which made it possible to irradiate the samples under study at wavelengths of 254 and 185 nm. At 185 nm radiation in the air medium in which the experiments were carried out, ozone was formed, the effect of which on the test sample could be both combined with UV irradiation and isolated from it using a special plug.

The biofilm-forming strain *P. aeruginosa* ATCC9027, which is pathogenic for humans, served as the object of the study. It is able to produce the pigment pyocyanin, which is considered the main pathogenicity of *P. aeruginosa* in acute and chronic infections—it damages epithelial cells, suppresses lymphocyte proliferation and inactivates the alpha protease inhibitor, which leads to tissue damage. In addition, pyocyanin inhibits the production of prostacyclin by pulmonary endothelial cells and limits the growth of T-lymphocytes due to the release of interleukin. Also, this strain contains genes encoding rhamnolipid proteins, which perform the function of protection against the immune system of the carrier (human). In practice, the methods of inactivation considered in this work can be a successful alternative to traditional biocides—antibiotics, especially considering the high resistance of *P. aeruginosa* to the latter [22, 23].

2 Experimental Setup

To conduct these studies, a special irradiator was designed (Fig. 1). The source was a low-pressure mercury lamp with a power consumption of 5 W, emitting in the UV range at the transitions of mercury atoms at 253.7 and 185 nm. The position of the lamp could be adjusted in height in the range of 5–10 cm from the plane of the base, where the test samples were placed. For the experiments presented in this paper, the distance between the lower boundary of the mercury lamp and the plane of the medium with the irradiated samples was 64 mm. A special PTFE concentrator was built to homogenize the radiation. It was located above the lamp, had a high diffuse scattering coefficient, and increased the concentration of irradiation directly on the placed sample. A special glass slide with 8 wells made of a biocompatible plastic

material [24] containing the studied bacteria was used as a sample. The working cavity during the experiments, depending on the task of the study, could be limited by a desiccator. On the one hand, this made it possible to create the required conditions for the irradiation medium through the gas pumping/inlet system, and on the other hand, it limited the influence of external factors (third-party irradiation, motion of media, dissipation of gas particles) on the course of irradiation and on the results obtained.

The experiments were carried out in a laminar box with the air flow turned on and off, which made it possible to cut off the effect of ozone formed under 185 nm radiation on the irradiated medium. To place the medium with irradiated microorganisms, we used a μ-Slide 8 Well slide with an ibidi polymer cover slip, which contained 8 individual cells with a square section of 1 cm^2 each [24]. The cells of the irradiated sample were placed in a medium containing a strain of *Pseudomonas aeruginosa.* Using confocal microscopy, the processed bacterial samples were monitored during preparation (growth phase), before and after the experiment.

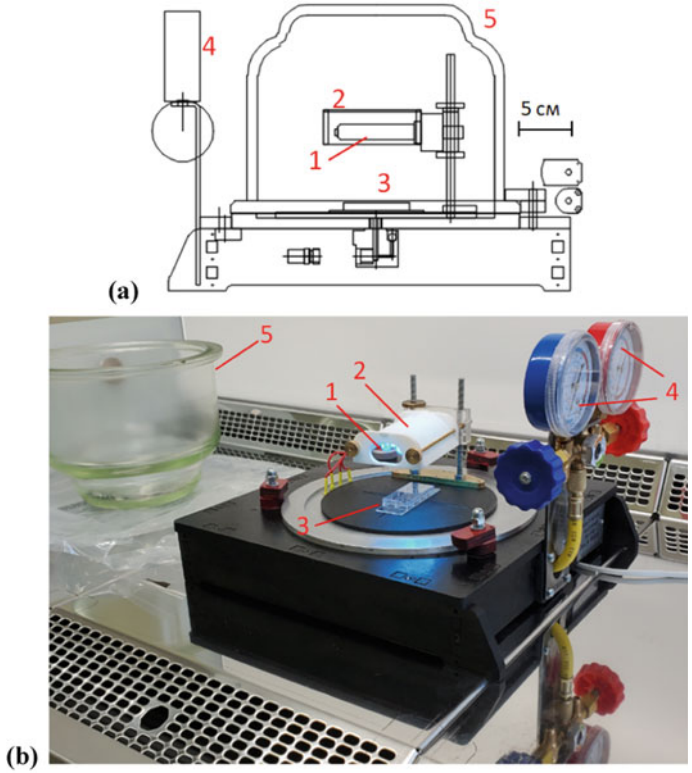


Fig. 1 Construction scheme (**a**) and photo of the irradiator placed in a laminar box (**b**): 1 low pressure mercury lamp; 2 radiation concentrator; 3 irradiated sample (cells with microorganisms); 4 gas pumping/supply system; 5—desiccator

3 About the Intensity of UV Radiation

The papers [25–29] discuss aspects that affect the emission spectrum of mercury lamps in the UV region and its intensity. In particular, Schalk et al. [29], Ref. [30] contain data on the dependence of the energy levels and radiative transitions of the mercury atom on the type of lamp and its power consumption. It is shown that the ratio between the 185 and 253.7 nm lines averages approximately 1:5 in the case of low mercury vapor pressure, when reabsorption is low. If we talk about the radiation of these resonant transitions of the mercury atom, then the radiating surface of the lamp absorbs all the received radiation, since the absorption cross section of resonant radiation by mercury atoms is large. However, most of the atoms excited during absorption almost immediately re-emit a quantum in an arbitrary direction. Some of the re-emitted quanta leave the volume of the mercury lamp, the rest of the quanta are reabsorbed and re-emitted later or die in non-emission energy transitions.

For a small mercury lamp, which was used in the experiments, the condition of low reabsorption is practically fulfilled. In Ref. [30], the efficiency of lamps was approximately calculated and the absorption spectra of various materials from which lamp tubes were made were given, and the values of radiation fluxes at 253.7 nm were also given. It follows from Schalk et al. [29], Ref. [30] that if a mercury lamp with a power consumption of 5 W emits 0.9–1 W in the 253.7 nm line, then a good estimate for 185 nm (taking into account the transmission of the material of the lamp walls) will be from 5 to 10% of radiation level at 253.7 nm, that is, from 0.045 to 0.09 W. Or if we talk about the density of radiation that comes from the surface of the lamp used in the experiment (1 in Fig. 1), then taking into account the fact that the total length of its cylindrical discharge part is about 9 cm, it turns out to be about 100 mW/cm at 253.7 nm and 5 to 10 mW/cm at 185 nm.

4 Numerical Simulation of Radiation Concentration

To estimate the density of radiation incident on the sample, calculations were made of the propagation of radiation in a diffusely reflecting concentrator and without it (Fig. 2). The ray tracing method was used in the Comsol software environment [30]. The simulation was carried out both in the presence of a concentrator and in its absence. A geometric two-cylinder model was set as a lamp. The dimensions of all model elements of the setup and their mutual arrangements coincide with the data of real experiments given in Sect. 2.

The initial and boundary conditions were as follows. The lamp radiation was described by a set of Lambert sources uniformly located on the outer surfaces of the lamp cylinders. The probabilistic distribution of the beam direction vector was given by the law of cosines over the angle of the hemisphere, i.e. the probability of beam propagation in a given direction within the solid angle $d\omega$ was determined by the expression $cos\theta d\omega$, where θ is the angle between the beam direction and the normal

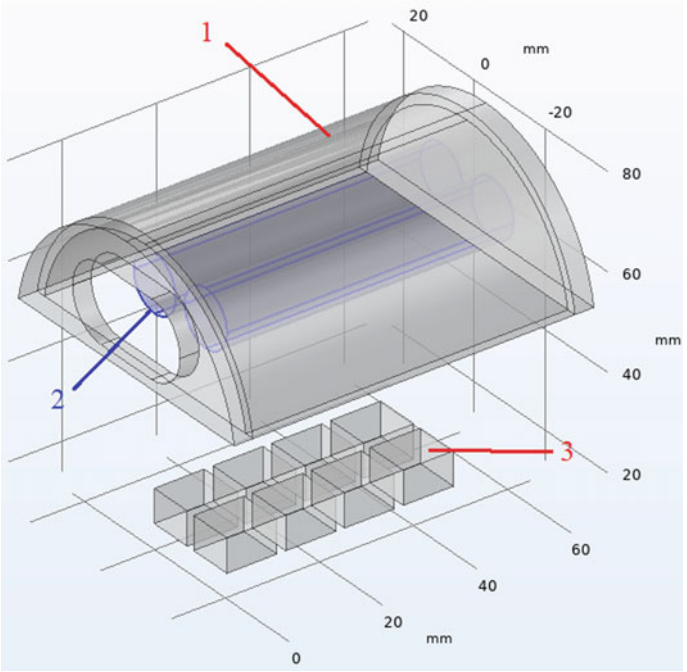


Fig. 2 Computational area: 1 radiation concentrator made of PTFE; 2—irradiator (mercury lamp); 3 irradiated cells

to the plane. Diffuse reflection from the walls of the lamp and the concentrator was described in a similar way.

The radiation density distribution on the source surface was assumed to be uniform. To do this, the lamp radiation was described by a set of Ns diffuse sources located on the surface of the lamp cylinders, with rays propagating outward. These sources radiated with a probability distribution based on Lambert's law. Each source emitted Nr rays sampled from a hemisphere in wave vector space with a probability density based on the law of cosines. The total number of beams of the lamp model was $N_s \times N_r = 10^8$. More detailed information about the calculation method used is presented in Kotov et al. [31, 32].

Consider the radiation of a mercury lamp from the experiment. Let us assume that, taking into account what was stated in Sect. 3, the power of its radiation at a wavelength of 253.7 nm for the numerical case is 1 W (100%). Those the total radiation power of the set of sources N_s is $E = 1$ W (100%). The radiation flux enters the receiving zone of the sample—four square zones in the upper plane of the cell, in which the processed microorganisms were located (Sect. 2). The model is located under the middle of the lamp at a distance of 45 mm from its walls, which corresponds to the real case. The upper planes of its eight cells absorb all the radiation that enters them (Fig. 2a). The average value of the radiation density on the surface of the receiving areas turned out to be $E_{ave} = 369 \cdot 10^{-2}$ mW/cm^2 (0.369%/cm^2).

The geometry of the computational domain in the presence of a concentrator that diffusely scatters radiation is shown in Fig. 2. On its entire inner surface, the diffuse reflection condition was set: reflection from the surface in a random direction, subject to a probability distribution based on the Lambert cosine law. The reflection coefficient $R = 0.87$, its value was chosen in accordance with the data presented for PTFE in Clark [33], Kotov [34]. The absorbed fraction of the incoming radiation was 1 *R*.

The unstructured tetrahedral computational grid consisted of 118419 elements, of which 98462 elements were located at the boundaries of the computational regions. For the rays reflected from the surface of the concentrator and falling on the surface of the cylinders of the lamp, the reflection coefficient 1—*k* was set. As in the case with a concentrator, the diffuse reflection condition was set on the lamp surface with the absorbed fraction *k* of the incoming radiation. The beam propagation time was 1 ns (the maximum possible distance of one beam was slightly less than 30 cm), $k = 0.5$. The average value of the radiation density on the area of the sample turned out to be $E_{ave_c} = 686 \cdot 10^{-2}$ mW/cm^2 (0.686%/cm^2). So, in the calculation with the presence of a diffusely reflecting concentrator, the radiation flux to the receiving areas increased by 1.86 times (from 369 to 686×10^{-2} mW/cm^2).

Taking into account the information in Sect. 3, we can say that in the experiment without the use of a desiccator and with the organization of air blowing in the laminar box to cut off the effect of ozone in the space between the mercury lamp and the samples, the average value of the radiation density at 253.7 nm per cell of the irradiated samples reached $686\ 10^{-2}$ mW/cm^2. In total, 54.89 mW (5.489% of the power of all outgoing radiation) comes to the area of all eight cells of the cup. Without using a concentrator, the value was 29.52 mW (2.952%).

The intensity distribution of the incoming radiation is shown in Fig. 3. An increase in the intensity of the radiation density in the central cells (up to $793\ 10^{-2}$ mW/cm^2) is observed, which is associated with the relative position of the mercury lamp and the radiation concentrator (Fig. 2, positions 1 and 2). In the case of 185 nm, it is necessary to take into account the absorption of such radiation in the air, as well as the generation of ozone. We will evaluate these aspects in the next section.

5 Influence of Radiation Below 200 nm

According to Sect. 3, the value of the total radiation power at a wavelength of 185 nm for the lamp used in the experiment can reach 0.1 W directly at the outer wall of its discharge channel, i.e. at the edge of the lamp. Under such irradiation, O_2 oxygen molecules in the air dissociate into two atoms, which is described by the 175–200 nm Schumann–Runge bands [35], from which O_3 ozone molecules are then formed. In Lunin et al. [36], estimates are given for the rate of ozone formation. An experiment was set up to irradiate an air mixture (80% N_2 + 20% O_2) at 185 nm, pumped through a volume, the pressure in which was maintained at a level of 1 atm. The rate of ozone

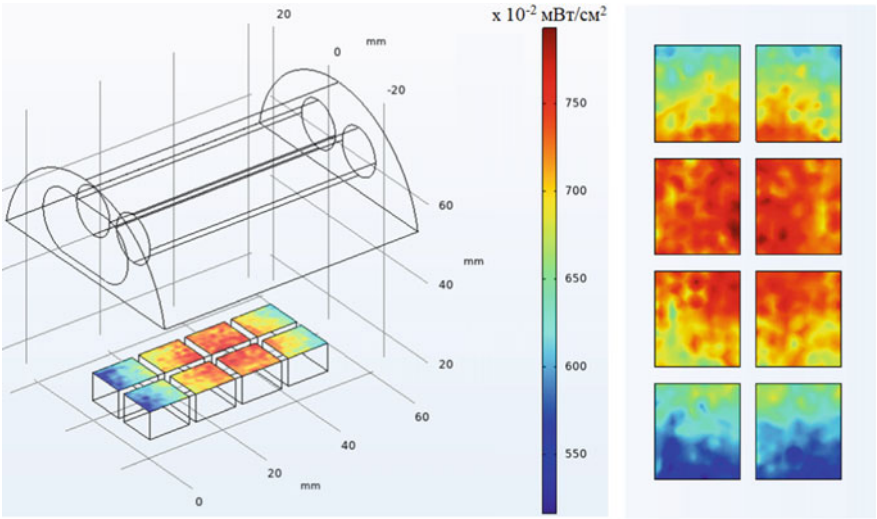


Fig. 3 Two-dimensional distribution of the calculated radiation density at $\lambda = 253.7$ nm in the experiment without use of desiccator. The average value is $686 \cdot 10^{-2}$ mW/cm^2

formation was about 13 cm^3/min per 1 m^3 of the mixture, which can serve as a rough estimate when the air is irradiated with a low-pressure mercury lamp, however:

- This speed is rather determined by the characteristics of the used radiation source, in particular, by the intensity at 185 nm, because other things being equal, the rate of ozone formation is proportional to the radiation incident on oxygen.
- In practice, more often they deal with a non-monochromatic radiation source. For example, a low-pressure mercury lamp, as in our case, emits a line at 253.7 nm, which is absorbed by ozone and causes its decomposition (Hartley bands [36]).
- And then it is also necessary to take into account the thickness of the layer of the irradiated air mixture, because the concentration of ozone in a particular area will depend on its distance from the radiation source.

In Lunin et al. [36], stationary concentrations of ozone in oxygen are calculated for different layer thicknesses and different intensity ratios of 253.7 and 185 nm. In the case of the experiment considered in this paper, this ratio is up to 10 times (Sect. 3), which is equivalent to the formation of an ozone concentration of up to 1% in oxygen at lengths up to 10 cm from the radiation source (Fig. 4). If we consider a dry air mixture (80% N_2 + 20% O_2), then due to the high degree of inertness of molecular nitrogen to this UV radiation, we can estimate an ozone concentration of 0.25%. However, in the case of room air, it is necessary to take into account the influence of impurities that it contains, namely, to take into account the absorption of UV radiation by carbon dioxide and water vapor.

Carbon dioxide in room air has a volume fraction of about 0.03%. The relative air humidity at the time of the experiments was no less than 50%, which corresponds to

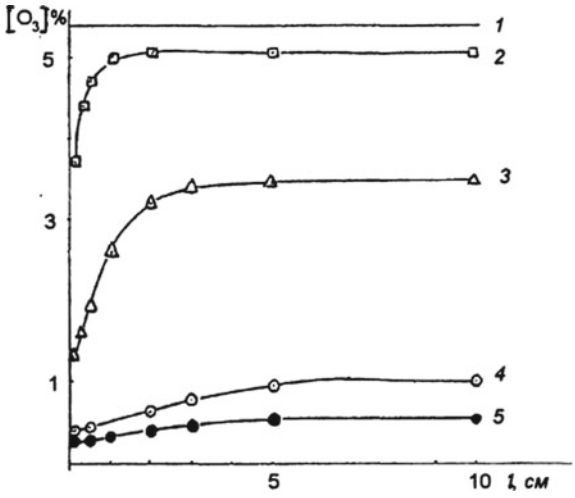


Fig. 4 Dependence [36] of ozone concentrations on the thickness of the absorbing oxygen layer at different intensity ratios of the 253.7 and 185 nm lines: 1 0; 2–0.1; 3–1; 4–10; 5–20

an approximate water content of 8.8 g/m^3 at room temperature or a volume fraction of 0.00088%. If we consider the receiving areas of all cells as one area equal to 9.4 × 10.7 × 8 pieces = 804.64 mm^2, then the volume of air between the planes of the cells and the mercury lamp is more than 40 cm^3 (at a distance from the lamp of 5 cm) and in this volume contains more than 12 mm^3 of carbon dioxide and more than 0.4 mm^3 of water. The works [37–40] give data on the absorption of UV radiation by water vapor, which can be quite significant, especially in the region of electronic transitions corresponding to radiation wavelengths in the range of 106–198 nm, which directly affects the absorption of 185 nm oxygen and the level of concentration ozone in the air.

6 Exposure Modes

Since, due to the information given above, the correct assessment of the concentration of ozone formed during irradiation in the air seems to be rather problematic (as well as the assessment of the effect of this concentration on the irradiated samples of cell bioforms), the following operating modes of the installation were chosen to separate the influence factors:

1. **UF + O_3** desiccator removed, laminar airflow turned off (Fig. 1b). The surface of the samples placed in the cells is subjected to a complex effect of UV radiation at 253.7 nm and ozone molecules generated by radiation at 185 nm, which descend and also interact directly with the surface of the samples under study. The effect of 185 nm radiation on the sample surface can be neglected due to its low intensity (Sect. 5).

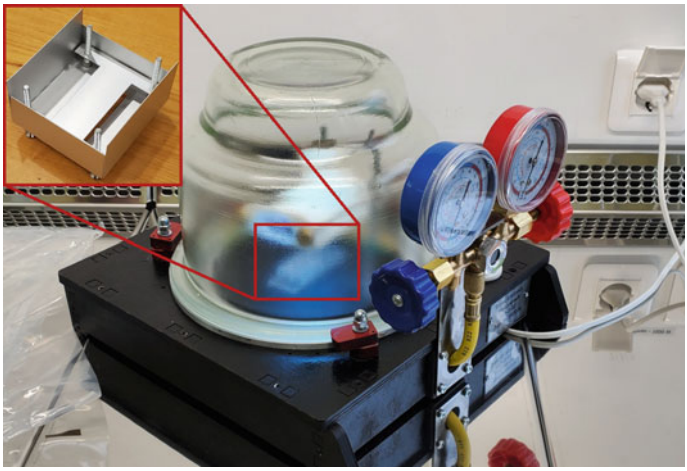


Fig. 5 O_3 operating mode of the irradiator placed in a laminar flow hood

2. **UF**—desiccator removed, laminar airflow turned on (Fig. 1b). The surface of the samples placed in the cells is exposed to UV radiation at 253.7 nm. Ozone molecules are carried away by the gas flow in the laminar and do not affect the surface of the samples.
3. **O_3**—the design of the irradiator is covered with a desiccator, a metal plug is placed above the cells (Fig. 5), which reflects and absorbs the UV radiation of the lamp, thus preventing it from affecting the surface of the samples. Molecules of ozone formed under the action of 185 nm radiation interact directly with the surface of the samples under study.
4. **OFF** (no exposure)—samples are in a closed air environment at room temperature. This mode is used to create control lots and determine the degree of degradation of samples over time.

7 Materials and Methods

In this work, studies were carried out with a strain of the pathogen *P. aeruginosa*, which is included in the international collection of bacteria (American Type Culture Collection, ATCC [41]) under the number ATCC 9027 with a standardized biological and genetic portrait. The subject of the study was the dormant form (PF/Dormant Form, DF) of *P. aeruginosa* ATCC9027. The starvation shock was 8 weeks (56 days). This aspect is important for the verification and reliability of the results, since the experiments carried out with the metabolic forms of pathogenic strains obtained from patients are of great applied medical importance.

Bacterial biofilms were grown in the same slides with 8 wells [24], in which they were then processed (Fig. 1). The study of exposure to UV irradiation (UF mode)

was carried out on the vegetative form obtained within 24 h from the original cell (Sect. 8.1) and biofilms formed within 24 and 48 h (Sect. 8.2). Control cells for these experiments were not irradiated (OFF mode). Resting forms of *P. aeruginosa* were also treated (Sect. 8.3). This is not a biofilm, but also a fairly stress-resistant form of bacteria, from which antibiotic-resistant bacteria are formed. Unlike the vegetative form, which is in a state of growth and reproduction, viable and viable, the dormant form of *P. aeruginosa* is viable, but not viable (no growth and reproduction), it has a sharply reduced metabolism and energy (hypobiosis, anabiosis). More detailed information on various forms of *P. aeruginosa* can be found in [17, 42]. Thus, in the presented work, the following modes of action on *P. aeruginosa* were implemented:

- vegetative (single) bacteria **OFF**, **UF**;
- biofilms **OFF**, **UF**;
- stress resistant bacteria (resting forms) **OFF**, **UF**, **UF + O_3, O_3**.

To visualize DNA of living/dead cells using laser scanning confocal microscopy, a combination of fluorescent dyes TOTO-1 (1 μM, Ref. [43]) and SYTO 60 (1 μM, Ref. [44]) was used as the optimal staining method [45]. To do this, TOTO-1 was added to the biofilms at a dilution of 1:1500, 100 μl per well. The staining (incubation) time was 15 min, this is the time of the dye action on the cell structures. SYTO 60 was then added with the same conditions and incubation period. After that, the samples were washed twice, followed by fixation with a solution of 2.5% glutaraldehyde in cacodylate buffer (0.05 M sodium cacodylate solution, pH 7.0–7.5).

Microscopic observations and imaging were performed with an OLYMPUS FV3000 laser scanning confocal microscope using a UPLXAPO60XO 60X oil immersion objective. To visualize the samples, lasers with wavelengths of 488 nm (for TOTO-1 dye) and 640 nm (SYTO 60 dye) were used. Before scanning, a separate check was carried out for each dye, then a binary color was visualized. For statistical significance, five random fields were recorded for each test sample, which were selected in such a way that dead and living cells could be counted. To determine their quantitative ratio, confocal images were analyzed using the ImageJ program [46].

Confocal laser scanning microscopy makes it possible to study the effect of antimicrobial agents on a biofilm over time and in its different layers. Thus, in biofilms exposed to antimicrobial agents, the method shows the effectiveness of the drug against the metabolically active outer layers and metabolically weakened inner layers, and thus the destruction of the biofilm, which depends on time [47]. Using this method, it is possible to observe the architecture of a *P. aeruginosa* biofilm formed within 24 h (Fig. 6).

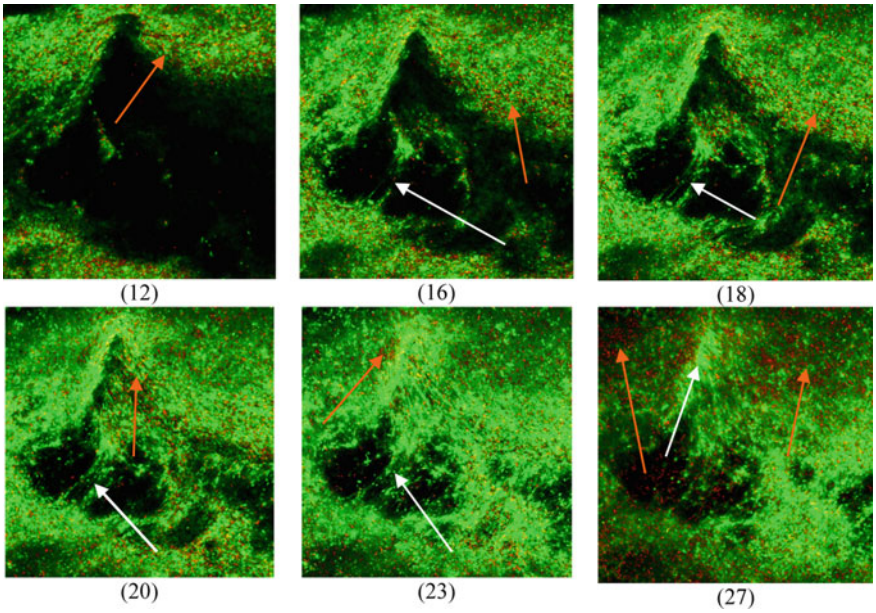


Fig. 6 Serial optical sections (12–27) of a *P. aeruginosa* biofilm formed within 24 h. In the inner layers of the biofilm, eDNA strands (white arrows) and living cells (orange arrows) are observed

8 Results

8.1 Vegetative Form

The maximum bactericidal concentration of pathogenic microorganisms in control experiments was more than 107–108 CFU/ml (Table 1). Here, CFU/ml are colony-forming units per milliliter, a value that characterizes the ability of microorganisms to form colonies on a dense nutrient medium.

Taking into account the data in Sect. 4, it is possible to estimate the irradiation dose at a wavelength of 253.7 nm received by microorganisms for different times. Its average value for 3 min was 1.23 J/cm^2; however, at this dose, continuous cell growth continued to be observed; this effect was not effective (Table 1, symbol #).

Table 1 Dependence of the viability of vegetative (single) *P. aeruginosa* cells on the time of UV irradiation

Microorganism	Viability (concentration), CFU/ml, mean value (**OFF**)	After exposure time in **UF** mode:		
		3 min	8 min	16 min
P. aeruginosa	5×10^7	#	12	0

Table 2 Live/dead ratio of *P. aeruginosa* biofilms, 24 h of formation

Data	Control (**OFF**)			**UF**, 8 min		
	Total	Dead cells	%	Total	Dead cells	%
Field 1	11912	462	4	330	281	85
Field 2	11472	687	6	524	481	92
Field 3	12625	1158	9	325	304	94
Field 4	1769	86	5	331	311	94
Field 5	2880	118	4	140	108	77
Mean	8132	502	**6**	330	297	**88**

Table 3 Live/dead ratio of *P. aeruginosa* biofilms, 48 h of formation

Data	Control (**OFF**)			**UF**, 8 min		
	Total	Dead cells	%	Total	Dead cells	%
Field 1	509	93	18	1286	939	73
Field 2	449	30	7	701	529	75
Field 3	616	78	13	414	161	39
Field 4	1583	113	7	464	324	70
Field 5	903	49	5	454	273	60
Mean	812	73	**10**	664	445	**63**

In the case of 16 min, the irradiation dose was 6.6 J/cm^2, which was an excessive indicator, since no colony-forming units were observed after such exposure. Thus, the time of bactericidal UV irradiation (UF mode) was at least 8 min at an initial viable cell concentration of more than 10^7 CFU/ml.

The data obtained in the experiments are presented in Tables 2, 3 and 4 and in Figs. 7, 8 and 9. Experiments have shown that UV irradiation for 8 min (**UF** mode) has a bactericidal effect on suspensions of planktonic cultures of *Pseudomonas aeruginosa.* The average value of the radiation dose at a wavelength of 253.7 nm, according to the data in Sect. 4, is 3.3 J/cm^2.

8.2 Biofilms

When determining the quantitative ratio of live/dead cells in biofilms (24 h of formation), it was found that exposure to UV led to an increase in the percentage of dead cells in the biofilm by 15 times compared to the control wells (Table 2)—6% in the control batch (**OFF** mode) and 88% in wells after UV exposure (**UF** mode).

The control biofilm from Table 2 (Fig. 7a) is dominated by living cells (red). After exposure to UV for 8 min, their number significantly decreases (Fig. 7b), and dead cells predominate (green color).

Table 4 Live/dead ratio of *P. aeruginosa* RF, 48 h of formation

Data	Control (**OFF**)			**UF**, 8 min			**UF + O3**, 8 min			**O3**, 8 min		
	Total	Dead cells	%	Total	Dead cells	%	Total	Dead cells	%	Total	Dead cells	%
Field 1	1778	928	52	1347	643	48	1231	1147	93	1404	977	70
Field 2	2154	1307	61	1094	498	46	1323	1105	84	3682	2917	79
Field 3	464	396	85	688	320	47	1555	1330	86	155	92	59
Field 4	1016	794	78	678	363	54	742	519	70	225	142	63
Field 5	835	408	49	1609	697	43	1673	1116	67	337	219	65
Mean	1249	767	**65**	1083	504	**48**	1305	1043	**80**	1160	869	**67**

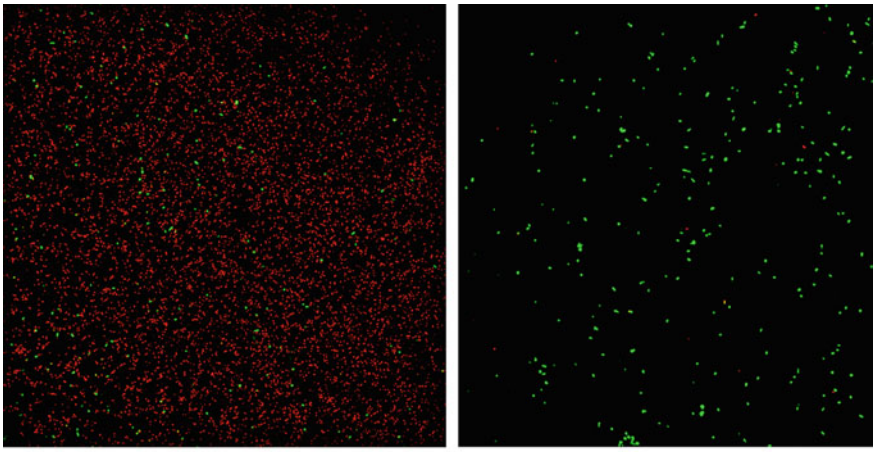


Fig. 7 Representative images of the spatial organization of *P. aeruginosa* biofilms (24 h): **a** control cells; **b**—after 8 min **UF** exposure

At 48 h of biofilm formation, the number of dead cells after UV irradiation increased 6 times compared to the control wells (10% in the control lot and 63% in the wells after UV exposure, Table 3).

In the biofilm control (48 h), a predominant number of live *P. aeruginosa* cells was found (Fig. 8a). UV exposure (Fig. 8b) resulted in an increase in the number of dead cells (green).

Thus, as a result of the data obtained, it can be concluded that *P. aeruginosa* biofilms formed within 24 h are more sensitive to the bactericidal action of UV within 8 min compared to biofilms formed within 48 h. This can be judged from Tables 2 and 3, where the percentage of dead biofilm cells 24 h after UV exposure is 88%, and the percentage of dead biofilm cells 48 h after UV exposure is 63%. Also in Fig. 8b, more living cells can be observed (red) compared to Fig. 7b.

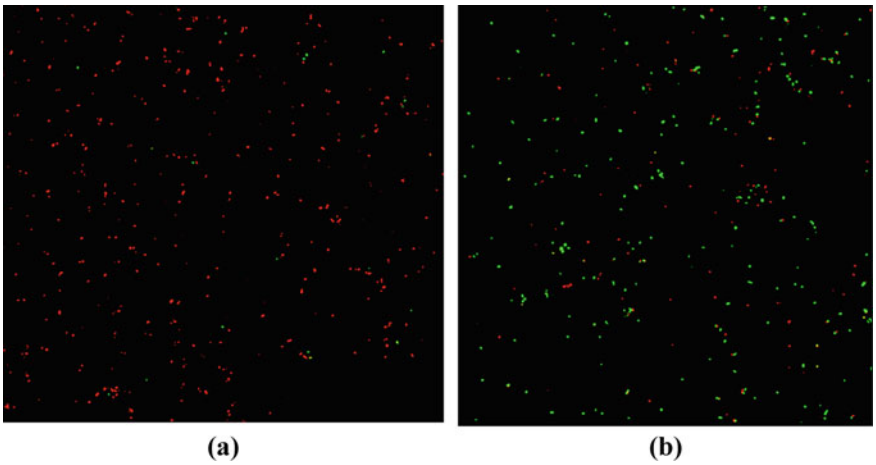


Fig. 8 Representative images of the spatial organization of *P. aeruginosa* biofilms (48 h): **a** control cells; **b**—after 8 min **UF** exposure

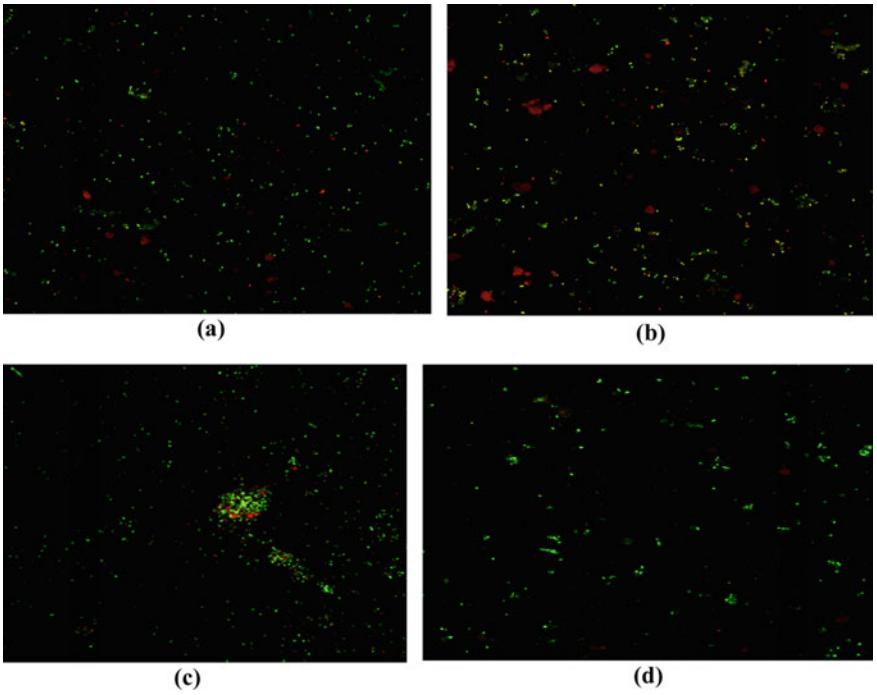


Fig. 9 Representative images of the spatial organization of *P. aeruginosa* RF (48 h): **a** control cells (**OFF**); **b** after **UF**; **c** after $\mathbf{O_3}$; **d** after $\mathbf{UF + O_3}$

8.3 Resting (Dormant) Forms

The study of the survival of pathogenic bacteria in the presence of lethal doses of antibiotics led to the discovery and comprehensive study of persister cells (P) as a phenotype responsible for the development and spread of antibiotic resistance, but not capable of long-term survival. With prolonged incubation (1 month) under non-growth conditions, Ps mature into ametabolic resting forms (RF), which can be responsible for both persistence (the ability of infections to linger in the host body for a long period of time, years or more) and pathogen survival in the environment [48, 49].

Resting forms (RF) of bacteria retained their viability during long-term storage (after 2 months of storage, the titer of viable cells was $\approx 10^7$ CFU/mL) under provocative conditions (lack of food sources, temperature 20 °C, limited oxygen supply). They also possessed thermal resistance and acquired the distinctive features of ultrastructural organization characteristic of the IF of non-spore-forming bacteria (compacted nucleoid, thickened cell walls) [50].

The complex treatment with UV radiation and ozone had a fairly effective bactericidal effect on *P. aeruginosa* PF—80% (Table 4) with the required achievable effect of 99%. UV irradiation alone produced a modest effect on *P. aeruginosa* PF (48%, Table 4), comparable to control samples that were not exposed to UV irradiation (65%, Table 4). The number of dead cells in the control samples can be explained by the decrease in viable cells under provocative conditions (lack of food sources).

In the control of RFs, much fewer living cells were found (Fig. 9a, red color) than in the case of biofilms (Figs. 7a and 8a). On Fig. 9c and d structural associations of living and dead cells are visible, allowing living cells to survive the bactericidal effect. However, as the results show, this does not reduce the overall high bactericidal effectiveness of the complex treatment.

9 Conclusions

If we consider the method of UV treatment of biological objects, then we can say that in the case of *P. aeruginosa* biofilms formed for 24 h, its bactericidal efficiency is at a high level, and an irradiation dose of 3.3 J/cm^2 at 253.7 nm is sufficient to destroy the vast majority living cells (88%). In the case of a longer period of biofilm formation (48 h), the effectiveness of such a dose is reduced by about a quarter (up to 63%). If we talk about concentrated exposure to ozone, which can potentially be effective, for example, in the practice of treating medical premises, then it is also necessary to take into account household procedures that must be carried out after such treatment (ventilation of the room, etc.). In the case of UV irradiation, there are no such problems, and recent studies show that even portable devices with comparable radiation doses can be effective and used for mobile treatment and disinfection of object surfaces, incl. against various variants of coronavirus [51].

In the case of dormant forms of *P. aeruginosa*, the bactericidal action of ozone alone or only UV irradiation is not sufficient for effective treatment and indicates either the need to correct the spectral composition of UV irradiation in relation to stress-resistant forms of bacteria towards shorter wavelengths while maintaining the total dose of irradiation, or the need for a complex multifactorial impact. In the presented study, the efficiency of simultaneous treatment with UV radiation and ozone was at a high level and reached 80% in relation to dead cells to living ones.

The results of this work are of particular interest for several reasons. First, the design of a disinfectant capable of operating in three modes is presented: UV irradiation, exposure to ozone and their combination. Secondly, such a disinfectant uses a special concentrator, which makes it possible to improve the effectiveness of the bactericidal effect due to diffuse scattering of UV radiation and an increase in its dose directly on the treated samples. The paper also contains numerical estimates of the density of the radiation incident on the samples, which confirm this effect. Thirdly, in contrast to the studies presented in epidemiological sources, this work used a genetically characterized strain of *P. aeruginosa* ATCC 9027 from the international collection of microorganisms, which carries genetically characterized markers of virulence and pathogenicity for humans, and, therefore, can serve as a model for testing new generations of effective antibacterial compositions. Fourth, for the first time, experimental studies of various treatment modes were carried out both on *P. aeruginosa* biofilms and on its dormant forms.

The general conclusion of the work is the following. In the case of super-resistant forms of the causative agent of *Pseudomonas aeruginosa* infection, the most effective results of treatment are shown by a complex effect, both in relation to the purulent-septic infections themselves, and in case of their complications. It makes sense to place special emphasis in further research on increasing the effectiveness of bactericidal radiation, its biological safety when used in surgical practice, as well as on the search for potentially effective physical and biological combinations, such as the combination of UV irradiation with the addition of an enzyme, bacteriophage, and neuroleptic hormone. If we talk about increasing the dose of UV radiation, it makes sense to consider a more powerful source of radiation [52, 53].

Acknowledgements This work was supported by the Russian Science Foundation (project no. 23-25-00459). The use of the state collection of pathogenic microorganisms "Obolensk" to obtain strains of the *P. aeruginosa* pathogen and their dormant forms was carried out within the framework of the industry program of Rospotrebnadzor.

References

1. Rentschler H. C., Nagy R., Mouromseff G. Bactericidal effect of ultraviolet radiation //journal of bacteriology. 1941. 41. 6. 745-774.
2. Kowalski W. Ultraviolet germicidal irradiation handbook: UVGI for air and surface disinfection. Springer science & business media, 2010.

3. Reed, G. The history of ultraviolet germicidal irradiation for air disinfection. Pubic Health Rep. 2010, 125, 15–27.
4. Miller J. H. Experiments in molecular genetics 1972 Cold Spring Harbor, N //NY: Cold Spring Harbor Laboratory.
5. Sunnen G. V. Ozone in medicine: overview and future directions //J Adv Med. 1988. 1. 3. 159–174.
6. Bocci V. A. Scientific and medical aspects of ozone therapy. State of the art //Archives of medical research. 2006. 37. 4. 425–435.
7. Nogales C. G. et al. Ozone therapy in medicine and dentistry //J Contemp Dent Pract. 2008. 9. 4. 75–84.
8. Moore G., Griffith C., Peters A. Bactericidal properties of ozone and its potential application as a terminal disinfectant //Journal of food protection. 2000. 63. 8. 1100–1106.
9. Cox M. M., Battista J. R. Deinococcus radiodurans—the consummate survivor //Nature Reviews Microbiology. 2005. 3. 11. 882–892.
10. Slade D., Radman M. Oxidative stress resistance in Deinococcus radiodurans //Microbiology and molecular biology reviews. 2011. 75. 1. 133–191.
11. Scott D. B. M. N., Lesher E. C. Effect of ozone on survival and permeability of Escherichia coli //Journal of bacteriology. 1963. 85. 3. 567–576.
12. Hunt N. K., Mariñas B. J. Kinetics of Escherichia coli inactivation with ozone //Water Research. 1997. 31. 6. 1355–1362.
13. Lewis K. I. M. Riddle of biofilm resistance //Antimicrobial agents and chemotherapy. 2001. 45. 4. 999–1007.
14. Watnick P., Kolter R. Biofilm, city of microbes //Journal of bacteriology. 2000. 182. 10. 2675–2679.
15. Flemming H. C., Wingender J. The biofilm matrix //Nature reviews microbiology. 2010. 8. 9. 623–633.
16. Tolker-Nielsen T. Biofilm development //Microbial Biofilms. 2015. 51–66.
17. Moradali M. F., Ghods S., Rehm B. H. A. Pseudomonas aeruginosa lifestyle: a paradigm for adaptation, survival, and persistence //Frontiers in cellular and infection microbiology. 2017. 7. 39.
18. Soh E. Y. C. et al. Disruption of the Pseudomonas aeruginosa Tat system perturbs PQS-dependent quorum sensing and biofilm maturation through lack of the Rieske cytochrome bc 1 sub-unit //PLoS Pathogens. 2021. 17. 8. e1009425.
19. World Health Organization et al. Antibacterial agents in clinical development: an analysis of the antibacterial clinical development pipeline, including tuberculosis. World Health Organization, 2017. WHO/EMP/IAU/2017.11.
20. Hampton T. Report reveals scope of US antibiotic resistance threat //Jama. 2013. 310. 16. 1661–1663.
21. Manzenyuk, O. Y., Firstova, V. V., Mukhina, T. N., & Shemyakin, I. G. (2018). Molecular Regulation of Pseudomonas Aeruginosa Biofilms. Annals of the Russian academy of medical sciences, 73(4), 244–251.
22. Yakovlev, S.V. (2007). Ustoichivost Pseudomonas aeruginosa k karbapenemam: uroki issledovania MYSTIC. Farmateka, 8(9), 56–62. (in Russian).
23. Goossens H. Susceptibility of multi-drug-resistant Pseudomonas aeruginosa in intensive care units: results from the European MYSTIC study group //Clinical microbiology and infection. 2003. 9. 9. 980–983.
24. https://ibidi.com/chambered-coverslips/13--slide-8-well-ibitreat.html.
25. Waymouth J. F. Electrical discharge lamps. Cambridge, MA: MIT Press, 1971. 70–102.
26. Voronov A., Arnold E., Roth E. Long life technology of high power Amalgam lamps // Proceedings of the Second International Conference on Ultraviolet Technologies, Vienna, Austria, International Ultraviolet Association, Ayr, ON, Canada. 2003.
27. Vasilyev A. I. et al. Influence of starting mode on service life of low pressure powerful amalgam lamp electrodes //Light & Engineering. 2009. 17. 4.Vasilyak, L.M.
28. Heering W. UV sources–basics, properties and applications //IUVA news. 2004. 6. 4. 7–13.

29. Schalk S. et al. UV-lamps for disinfection and advanced oxidation-lamp types, technologies and applications //IUVA news. 2006. 8. 1. 32–37.
30. The Ray Optics Module User's Guide-COMSOL Documentation. https://doc.comsol.com/5.4/doc/com.comsol.help.roptics/RayOpticsModuleUsersGuide.pdf.
31. Kotov M. A. et al. Increase in illumination of 253.7 nm in a cylindrical PTFE cavity //Processes in GeoMedia—Volume V. Cham: Springer International Publishing, 2022. 117–130.
32. Kotov M. A. et al. Symmetrization and amplification of germicidal radiation flux produced by a mercury amalgam UV lamp in cylindrical cavity with diffusely reflective walls //Symmetry. 2022. 14. 1. 125.
33. Clark R. W. Methods and apparatus for diffuse reflective UV cavity air treatment: заяв. пат. 13464431 США. 2012.
34. Kotov M. A. On the Determination of Diffuse Reflectance of PTFE //Advanced Hydrodynamics Problems in Earth Sciences. Cham: Springer Nature Switzerland, 2023. 123–130.
35. Dohan J. M., Masschelein W. J. The photochemical generation of ozone: Present state–of–the–art. 1987.
36. Lunin V.V., Popovich M.P., Tkachenko S.N. Physical chemistry of ozone. Moscow State University Publishing House //Moscow. 1998. 480 p.
37. Watanabe K., Zelikoff M. Absorption coefficients of water vapor in the vacuum ultraviolet // JOSA. 1953. 43. 9. 753–755.
38. Thompson B. A., Harteck P., Reeves Jr R. R. Ultraviolet absorption coefficients of CO_2, CO, O_2, H_2O, N_2O, NH_3, NO, SO_2, and CH_4 between 1850 and 4000 a //Journal of Geophysical Research. 1963. 68. 24. 6431–6436.
39. Makogon, M. M., Ponomarev, Y. N., & Tikhomirov, B. A. (2013). The problem of water vapor absorption in the UV spectral range. Atmospheric and Oceanic Optics, 26(1), 45–49.
40. Patterson E. M., Gillespie J. B. Simplified ultraviolet and visible wavelength atmospheric propagation model //Applied optics. 1989. 28. 3. P. 425–429.
41. https://www.atcc.org/.
42. Lazareva, A. V., Chebotar, I. V., Kryzhanovskaya, O. A., Tchebotar, V. I., & Mayansky, N. A. (2015). Pseudomonas aeruginosa: pathogenicity, pathogenesis and diseases.
43. https://www.thermofisher.com/order/catalog/product/T3600.
44. https://www.thermofisher.com/order/catalog/product/S11342.
45. Okshevsky M., Meyer R. L. Evaluation of fluorescent stains for visualizing extracellular DNA in biofilms //Journal of Microbiological Methods. 2014. 105. 102–104.
46. Nichele L. et al. Quantitative evaluation of ImageJ thresholding algorithms for microbial cell counting //OSA Continuum. 2020. 3. 6. 1417–1427.
47. Rudilla H. et al. New and old tools to evaluate new antimicrobial peptides //AIMS microbiology. 2018. 4. 3. 522.
48. Levin-Reisman I. et al. Antibiotic tolerance facilitates the evolution of resistance //Science. 2017. 355. 6327. 826–830.
49. Mulyukin A. L. i dr. Strukturnoe i fiziologicheskoe raznoobrazie cistopodobnyh pokoyashchihsya kletok bakterij roda Pseudomonas //Mikrobiologiya. 2008. 77. 4. 512–523. (in Russian).
50. Manzenyuk O.YU. i dr. Stressoustojchivye pokoyashchiesya formy bakterij: biologicheskie i ul'trastrukturnye svojstva Moraxella catarrhalis, Kocuria rhizophila//Byulleten' eksperimental'noj biologii i mediciny, 2023. (in Russian).
51. Masyakin D. N. i dr. Obezzarazhivanie poverhnostej, kontaminirovannyh koronavirusom SARS-CoV-2, ul'trafioletovym izlucheniem rtutnoj lampy nizkogo davleniya //Problemy osobo opasnyh infekcij. 2023 2 134–139. (in Russian).

52. Kotov M. A. i dr. Baktericidnoe dejstvie korotkovolnovogo UF, generiruemogo plazmoj, podderzhivaemoj lazernym izlucheniem //Lazery v nauke, tekhnike, medicine. 2020. 159–163. (in Russian).
53. Kotov M. A. i dr. Baktericidnaya effektivnost' uf, generiruemogo lazerno-plazmennym istochnikom //Lazery v nauke, tekhnike, medicine: Sbornik nauchnyh trudov. Tom 32/pod red. VA Petrova-M.: MNTORES im. AS Popova, 2022g.–216 s. Sbornik nauchnyh trudov podgotovlen po materialam dokladov, postupivshih na XXXII Mezhdunarodnuyu konferenciyu. 2022. 140. (in Russian).

Features Distribution of Platinoids in Oil and Gas Fields of the Orenburg Region



G. A. Ponomareva

Abstract The purpose of present research is to study the features of the distribution of platinum and palladium in association with gold and silver in the Orenburg part of the Volga-Ural oil and gas province. Oil samples were taken and analyzed from carbonate and terrigenous collectors of fields of different structural-tectonic elements of the first order. To identify features distribution of noble metals, schemes of isoconcentrates of ones are constructed, the analysis of which makes it possible to establish that the distribution of platinoids in oil fields of the platform Orenburg region obeys different-scale spatial patterns of their localization in the structures of the platform cover—structural-tectonic zones and oil and gas geological areas. Two zones have been identified, sharply differing in the concentration of platinum in oils. The results obtained indicate the influence of geological and structural elements on the spatial distribution of platinoids in oils and may be used for predictive estimate of the territory on the presence for noble metals under the performance of geological-structural worcks, metallogenic studies and for stratigraphic correlation of oil-saturated beds.

Keywords Oil · Platinoids · Noble metals · Distribution patterns · Zones

1 Introduction

The study of the metal content of oils is of great theoretical and applied importance. On the one hand, the elucidation of the genesis of platinoids in oil and gas fluids can help clarify a number of points in the geological history of the Urals associated with poorly studied processes of hydrocarbon generation. At the same time, many cases of detecting in oils above the Clarke concentrations of noble metals make it possible in the foreseeable future to hope for the possibility of their profitable extraction. In addition, noble and non-ferrous metals traditionally determine the prospects for the

G. A. Ponomareva (✉)
Orenburg State University, 13 Pobeda Ave., Orenburg 460018, Russia
e-mail: galy.ponomareva@mail.ru

© The Author(s), under exclusive license to Springer Nature Switzerland AG 2024

V. Karev (ed.), *Proceedings of the 9th International Conference on Physical and Mathematical Modelling of Earth and Environmental Processes*, Springer Proceedings in Earth and Environmental Sciences, https://doi.org/10.1007/978-3-031-54589-4_6

metal-bearing of the carbonaceous formations of the Ural metallogenic province, which occupy the fold region of the same name in the Eastern Orenburg region.

The main purpose of present research is to study the features distribution of platinum and palladium with gold and silver in oil and gas fields in the platform part of Orenburg region, which will allow to solve a number of theoretical and practical problems, in particular, determination the causes of the occurrence of element concentrations, migration, behavior in various geological conditions, and to model processes occurring in the bowels of the Earth, to find answers to questions related to the genesis of various geological objects.

2 Materials and Methods

To solve the set tasks, 39 oil samples from 22 fields were analyzed. In total, more than 200 analyzes were performed using a unified technique [7–9]. Oil samples were taken by a reservoir tester from carbonate and terrigenous reservoirs of various, but strictly controlled, stratigraphic and structural-tectonic affiliation.

Determination of noble metals was carried out by atomic absorption spectrometry with an electrothermal atomizer on an MGA-915 spectrometer in the laboratory of physical research methods of the Department of Geology of Orenburg State University using an additional own patented method of decomposition of the carbon part of the analyzed samples (Patent RF 2409810). Data on the noble metals content in hydrocarbon fields of the first-order structural-tectonic zones of the platform part of Orenburg region are presented in the Table 1. The numerator shows the ranges of the metal content, the denominator—the average metal content.

3 Results and Discussion

The Table 1 shows, that the Buzuluk depression (23 samples) and the East Orenburg arch uplift (9 samples)—the main areas of hydrocarbon production, covering about 90% of the oil and gas area of the Orenburg region are the most studied in this regard. Noble metal specialization of oil and gas fields in all zones, as a rule, are palladium-platinum, with an average Pt/Pd ratio of ~2.2. The distribution of Pt and Pd in oils has an ultramafic character.

The identification of regional regularities in the distribution of Pt and Pd, Au and Ag in oil is based on the schemes of structural-tectonic zoning and oil-and-gas-bearing of the platform part of the Orenburg region [2, 8]. To determine the features distribution of platinoids, schemes of isoconcentrates of metals were constructed using geostatic Kryging algorithms that reduce the influence of the sampling network features, combined with the structural-tectonic basis (Fig. 1).

Table 1 Average contents of Pt, Pd, Au, Ag in oil of fields of various structural-tectonic zones in the Orenburg part of the Volga-Ural oil and gas province, mg/t

Structural tectonic zones	Number of samples	Pt	Pd	Au	Ag	Pt/Pd
BDNR	13	1–102 26	1–29 8	1–33 14	6–90 30	3,25
BDSD	10	2–78 21	1–51 9	0,3–153 21	0,1–21 3,1	2,33
EOAU	9	1–30 8	1–17 6	0,4–9 3,1	0,1–30 10	1,33
SIA	4	9–11 10	6–18 14	0,3–16 11	1–46 26	0,71
SSTA	3	9–18 13	8–10 9	3–9 6	8–17 12	1,44
Average for all zones	39	0,4–102 18	0,6–51 8	0,3–153 13	0,1–68 17	2,2

Note EOAU—East Orenburg arch uplift, SSTA—The southern slope of the Tatar arch, SIA—Sol-Iletsk arch, BDNR—Buzuluk depression: northern region, BDSD—Buzuluk depression: southern dive

The analysis of the presented schemes shows that in the history of the distribution of Au and Pt there is more common (Fig. 1a and b) than in the other tow metals—Ag and Pd (Fig. 1c and d).

It is possible that relatively simple aureole of Pd and Ag arose due to a long and uniform diffusional redistribution of these elements in oils, which was interrupted by a certain process that affected a narrow and very long meridional zone crossing not only the Orenburg region, but also adjacent territories.

The borders of the zone are recognized by extremely sharp gradients of Pt and Au concentrations, which form a step-like decrease in the geochemical field of these elements in an easterly direction. Thus, the content of platinum and gold in the oils of numerous fields of the Buzuluk depression is more than 3 times higher than in the fields of the East Orenburg arch uplift, the Sol-Iletsk arch and the Caspian syneclise (Fig. 1a and b). The described zone has clear angular outlines characteristic of linear tectonic structures, which is also confirmed by a generalized analysis of seismic data. At the same time, in plan, the eastern border of the zone coincides with the line of pinching out of the Riphean-Vendian deposits, which are absent in most part of the Buzuluk depression [1, 8–11]. In any case, the above facts, according to the author, deserve additional study.

Geochemical interpretation of quantitative data on the distribution of noble metals in the oils of the fields of the edge-platform part of the Orenburg region makes it possible to distinguish the following platinum-containing oil-bearing zones:

– the western zone, which unites most of the Buzuluk depression and the southern slope of the Tatar arch;
– the eastern zone, which includes the East Orenburg arched uplift, the Sol-Iletsk arch and the northern edge of the Caspian syneclise.

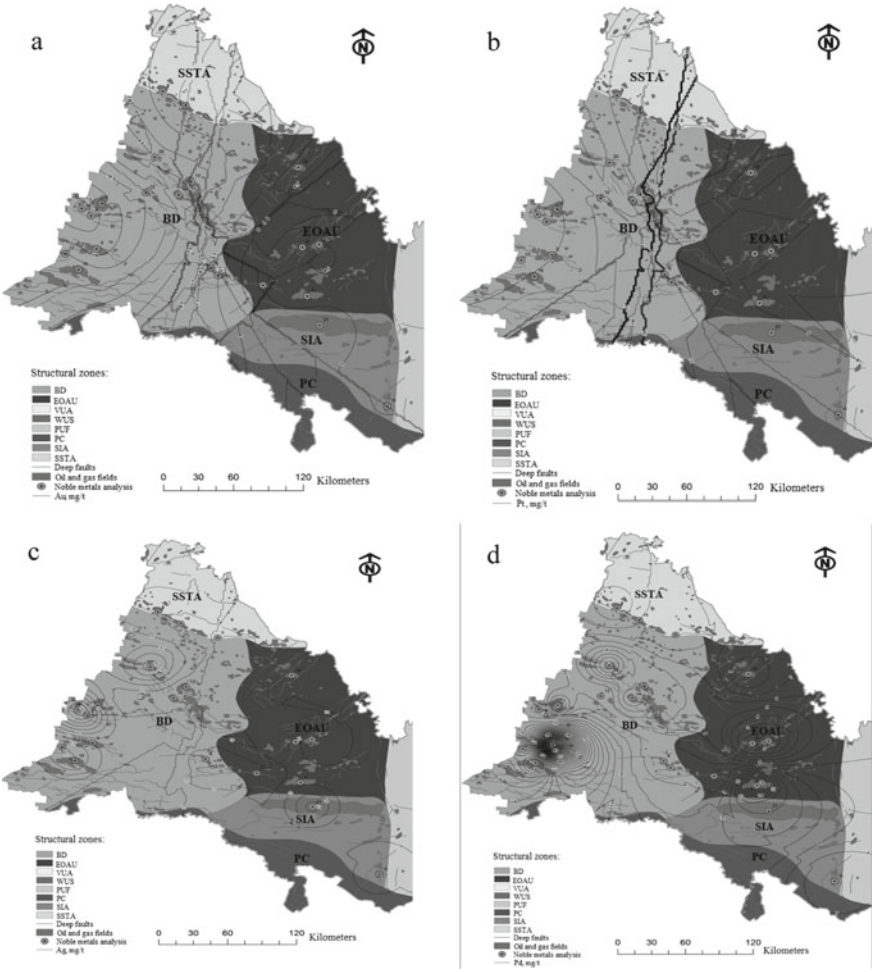


Fig. 1 Schemes of distribution of precious metals in oils of the Orenburg region. Structural zones: BD—uzuluk depression, EOAU—East Orenburg arch uplift, VUA—Volga-Ural anteclise, WUS—Western Ural structures, PUF—Pre-Ural foredeep, PC—Pre-Caspian syneclise, SIA—Sol-Iletsk arch, SSTA—The southern slope of the Tatar arch

In the western platinum-containing zone, heightened contents of Pd, as well as Au and Ag are found (South-Buzuluk and Mukhano-Erokhovsky oil and gas geological regions) [8, 11].

It should also be noted that the Buzuluk depression is possibly complicated by structural elements of a lower order. The study of the distribution of elements over the entire area reveals concentric zones that mark individual basins existing within a given structure and differing in the nature of sedimentation. Examples of such depressions with increased metal concentrations are known within the Red Sea rift

and are well covered in the literature (Atlantis 1, Atlantis 2, and others, which differ in the density of brines and the concentration of metals in them).

Increased noble metals concentrations, as a rule, spatially coincide with the outcrops of ultrabasic rocks of the peridotite-pyroxenite-gabbronorite formation in the crystalline basement, the existence of which has been proven by deep drilling with opening the basement in the areas (Rostashinskaya, wells 171, 172; Tananykskaya, well 166, Tverdilovskaya, well 14, etc.), which is reflected on the geological map of the crystalline basement of the southeast of the East European platform and in publications [1].

Analysis of samples of these ultramafic rocks for the content of Pt, Pd, Au, Ag showed the presence of metals in rather high concentrations with the palladium-platinum specialization of this complex of the East European platform Pt > Pd > Au > Ag [8].

In addition, the features of igneous rocks of the crystalline basement include their oil-and-gas-bearing, established in a number of exploration areas within the Buzuluk depression.

So, according to Yakimenko [12], the oil and gas content of the basement was confirmed at the Davydovskaya area—well 50; Sorochinskiy ledge; Olkhovskaya area—well 778; Rostashinskaya area—well 171 and other, from which an oil inflow was obtained with a flow rate of 1.8 m^3/day, etc [12].

The fact that many hydrocarbon fields of the Orenburg region contain helium, on average, about 0.05%, can serve as an argument in favor of the presence of deep-seated substances in oil [5]. Thus, the hypothesis about the direct role of the mantle component in the noble metal specialization of hydrocarbon fluids cannot be ruled out.

4 Conclusions

The data obtained confirm the conclusion [4, 6] about the ultramafic geochemical-mineragenic specialization of oil, about the relationship between the formation and geochemical features of hydrocarbon fluids "with the structure of oil and gas provinces, the age of their basements, of the thickness of the consolidated crust and sedimentary cover, of the type and degree of manifestation of magmatism, that is with the nature of geodynamic development and evolution of the lithosphere" [6].

Zoloev [3] proposed a model for the joint formation of oil and gas hydrocarbons, as well as a number of solid minerals, such as sulfides, etc., as a result of degassing occurring in deep faults, with gabbro playing the main role—hyperbasite complexes and alpine-type ophiolites [3].

Thus, the distribution of platinoids in the oil fields of the Orenburg part of the Volga-Ural oil and gas province obeys different-scale spatial patterns of their localization in the structures of the platform cover—structural-tectonic zones and oil and gas geological regions. Two zones (western and eastern) have been identified, sharply differing in the concentration of platinum in oils. The results obtained indicate the

influence of geological-structural elements on the spatial distribution of platinoids in oils. Isoconcentrates repeat the borders of structural tectonic elements and oil and gas geological areas, often forming steps at their borders.

References

1. Galimov AG, Makarova SP. The absolute age of crystalline rocks of the Precambrian south-eastern part of the Volga-Ural anteclise. Geology and operation of oil and gas fields in the Orenburg region: scientific. Works. ONAKO, OrenburgNIPIneft. Orenburg: Orenburg book publishing house, 2001;342–54.
2. Geological structure and oil-and-gas-bearing capacity of the Orenburg region. Ed. by AS Panteleev and NF Kozlov. Orenburg: Orenburg. Book publishing house; 1997.
3. Zoloev KK. Predictive and mineragenic zoning in the format of cluster analysis. Lithosphere. 2009; 6:3–16.
4. Ivanov KS, Fedorov YuN., Erokhin YuV. et al. Oil is a product of the ultramafic mantle of the Earth. Proceedings of the III international. Conf. Ekaterinburg "Ultramafic-mafic complexes of folded regions and associated deposits". Institute of Geology and Geophysics, Ural Branch of the Russian Academy of Sciences, 2009, pp. 200–202.
5. Kontorovich A.E., Korzhubaev A.G., Eder L.V. Raw materials base and prospects for the development of the helium industry in Russia and the world. Mineral Resources of Russia. Economics and Management. 2006; 2:17–24.
6. Marakushev AA, Pisotskii BI, Paneyakh NA, Gottikh RP. Geochemical specific character of oil and origins of its filds. Reports of the Academy of Sciences. 2004;398(6):795–799.
7. Ponomareva G.A., Ponomarev A.A. Distribution patterns of platinoid in halogen rock masses in the Southern Urals. Mining Journal. M.: 2021, No. 12, pp. 10–14. https://doi.org/10.17580/gzh.2021.12.02.
8. Ponomareva G.A. Spatial patterns of platinoid distribution in hydrocarbon deposits of the Orenburg region. Geology, geoecology and resource potential of the Urals and adjacent territories. M.: "Pero", 2022, pp. 156–160.
9. Ponomareva G.A., Petrishhev V.P. The material composition of bitumen of the Orenburg Urals. Proceedings of Voronezh State University. Series: Geology, 2023, No. 1, pp. 80–88. https://doi.org/10.17308/geology/1609-0691/2023/1/80-88.
10. Ponomarev A.A., Nesterenko M.Yu., Ponomareva G.A. Development of a software and hardware complex for monitoring parameters of hydraulic fracturing during the exploitation of oil and gas fields by microseismic methods. Modern science: actual problems, 2021, № 3, pp. 139–143. https://doi.org/10.37882/2223-2966.2021.03.26.
11. Sokolov AG. Identification and tracking of tectonic faults based on seismic data and forecasting of near-fault traps in the platform Orenburg region. Orenburg: OSU; 2010.
12. Yakimenko Yu.N. On the prospects of oil and gas potential of the Dodevonian deposits of the Orenburg region. Environmental Protection in the Oil and gas industry, 2008, No. 9, pp. 31–35.

Dynamics of Near-Surface Air Temperatures in the Lower Don Basin for the Period 1966–2020



A. Parfenova, V. Kulygin, A. Ioshpa, and A. Evlanova

Abstract Significant changes in dynamics of meteorological parameters are observed throughout Russian Federation and there is no exception for the he basin of the Lower Don—an important economic and transport hub of the South of Russia. One of the most crucial consequences of these changes is the modern low-flows period. This paper presents the results of the analysis of the dynamics of air temperature for the period 1966–2020. The research is based on long-term data obtained from of Federal Service for Hydrometeorology and Environmental Monitoring (RosHydroMet). A statistically significant increase in air temperature after 1998 was revealed. Using the model of stepwise changes, periods characterizing the observed changes were identified.

Keywords Climate change · Lower Don · Air temperature

1 Introduction

Significant changes in dynamics of meteorological parameters are observed throughout Russian Federation. The object of this research is the basin of the Lower Don—one of the key regions of the south of the Russian Federation, in which a low-runoff period has been observed since 2007. Gladkov et al. [1] noted that recently number of low-flows episodes has been increased, which resulted in the decrease in the patency (navigability) of the river. In his research Vovk [2] pointed that such state of the river has a negative impact on navigation. Among the consequences of the current situation, the deterioration of the state of the Azov Sea ecosystem, as well as damage to various sectors of the economy, stands out.

A. Parfenova (✉) · A. Ioshpa · A. Evlanova
Southern Federal University, Rostov-on-Don, Rostov Region, Russia
e-mail: annparfenowa@mail.ru

A. Parfenova · V. Kulygin
Federal Research Center Southern Scientific Center of the Russian Academy of Sciences, Rostov-On-Don, Rostov Region, Russia

© The Author(s), under exclusive license to Springer Nature Switzerland AG 2024

V. Karev (ed.), *Proceedings of the 9th International Conference on Physical and Mathematical Modelling of Earth and Environmental Processes*, Springer Proceedings in Earth and Environmental Sciences, https://doi.org/10.1007/978-3-031-54589-4_7

The Lower Don basin plays an important role for the Sea of Azov: river runoff directly affects the hydrological and hydrochemical regime of the Sea. A reduction in Don runoff leads to an increase in salinity in the Sea of Azov and a decrease in freshwater marine animal species and the distribution of typically marine ones [3–5].

The research of hydrometeorological processes in the Lower Don region, causing changes in its water reserves, is an urgent and important issue, which becomes especially significant in connection with the expected (according to some estimates) shortage of fresh water in the world [6].

Many scientific organizations have been involved in fundamental research of the Lower Don basin over the years: the Institute of Geography of the Russian Academy of Sciences, Lomonosov Moscow State University, the Institute of Water Problems of the Russian Academy of Sciences, the Federal Research Center Southern Scientific Center of the Russian Academy of Sciences (SSC RAS), Southern Federal University (SFU), "All-Russian Research Institute of Fisheries agriculture and oceanography" ("AzNIIRH") and others. All research works of these organizations were mainly aimed at studying issues related to the transformation of water reserves and the ecological state in its catchment area [7, 8]. However, it is necessary to take into account the dynamics of heat and moisture transfer processes immediately above the Lower Don basin, especially when studying the water balance and obtaining estimates of possible changes in the ecological state of the water area in the future.

The main reason for the current low-flows period is a climate change. The WMO notes that the average global temperature in 2022 was 1.15 °C higher than in the period 1850–1900 [9]. Linear trend coefficients of temperature range from 0.18 °C/10 years (for the Earth as a whole) to 0.34 °C/10 years (for the Northern Hemisphere), and on the territory of the Russian Federation the positive trend of air temperature is 0.45 °C/10 years. The south of the European territory of Russia (ETR) is also characterized by warming: 0.74 °C/10 years [10, 11]. All these factors actualize the thorough research of changes in near-surface air temperature within the Lower Don basin.

2 Materials and Methods

The sources of long-term series of near-surface air temperature were datasets from 24 weather stations from the archives of the Russian Research Institute of Hydrometeorological Information—the World Data Center (RRIHMI-WDC) [12] for the period 1966–2020. The location of each weather station is presented in Fig. 1. To characterize the basin of the Lower Don, 8 stations located on the territory of the basin were considered first of all. Single gaps in monthly values were filled on the basis of data from the nearest weather stations.

Linear regression analysis was used to determine trends in changes in meteorological parameters, as well as to reveal dependencies between annual data series. In this research work method of paired (simple) linear regression based on the correlation between the dependent and independent variable was applied. This method describes



Fig. 1 Location of weather stations in the Lower Don basin. *Note* Stations located in the Lower Don basin are colored in red, stations outside the basin are colored in yellow

systems in which, among all the factors influencing on resultant variable (effective sign), one most important factor is identified, which mainly determines the variation of resultant variable.

As a measure of the intensity of changes in meteorological parameters, the linear trend coefficient was used (constructed from the angle of the regression line), its significance was determined by statistical testing of the hypothesis of its equality to zero using the Student's t-test with a significance level of 5%.

To construct grid temperature areas, geostatistical interpolation methods (ordinary kriging) were used. The cell size of the grid area is chosen to be 30 km. Grid areas reflecting average monthly values were constructed for each month of each year of the period under consideration.

To clarify the dynamics of changes in the linear trend, a stepwise change model was used. This model is a set of stationary models for parts of a time series, and is characterized by the invariance over time of the mean value and standard deviation

for each part of the series [13]:

$$\begin{aligned} E_1(t_1) &= \text{const1}, \ \sigma 1(t1) = \text{const1}, \\ E_2(t_2) &= \text{const2}, \ \sigma 2(t2) = \text{const2}, \end{aligned} \tag{1}$$

here E1, σ1—the mean value and standard deviation of the first part of the time series when t_1 changes from 1 to t_n, E2, σ2—the mean value and standard deviation of the second part of the time series when t_2 changes from t_{n+1} to n; n—time series volume.

The moment of stepwise changes (t_n) was determined by minimizing the value of the sums of squared deviations of two parts of the time series from the model values during the iterative expanding window procedure:

$$\sigma_1^2(n_1 - 1) + \sigma_2^2(n_2 - 1) \rightarrow \min, \tag{2}$$

here ${\sigma_1}^2$ and ${\sigma_2}^2$—variances, n_1 и n_2—volumes of each resulting time series.

At each step of the expanding window procedure, n_1 increases by one, n_2 decreases, and the approximation error is calculated by Eq. (2). The initial value for n_1 (the minimum volume of the first part of the time series) was chosen to be 5 years.

The verification was carried out by means of the Fisher's criterion (for estimation of the homogeneity of variances), and the Student's t-test (for estimation of their variability). The level of statistical significance was chosen equal to 5%.

The algorithm for allocating periods was made recursive, i.e. after the initial division of the time series into two periods, the same procedure was applied to each of them to search for subperiods. To construct grid areas of the studied meteorological parameters, the geostatistical interpolation method—kriging—was used.

Kriging is a method that calculates interpolated values based on a linear combination of values at nearby data points. It is based on a statistical model that takes into account the changing uncertainty and spatial correlation of a set of points. The basic idea of kriging is that when moving through space, data (for example, meteorological data) has both a certain spatial trend (for example, a mean value) and a certain spatially correlated randomness (closer points have more similar values) [14].

All kriging methods are based on the linear regression estimation formula [15]:

$$V * (x) - m(x) = \Sigma wi(x)ni - 1, \tag{3}$$

here $wi(x)$-the weights assigned to the data $V(xi)$, which in turn are realizations of the spatial variable V. The values $m(x)$ and $m(xi)$ are the mathematical expectations of the spatial variables $V(x)$ and $V(xi)$. The number of data n used for estimation, as well as their weights, can vary depending on the estimation point x.

In present research ordinary kriging was used, that means a local interpolation with the weighting of data points in accordance with distance. This method is used to interpolate point measurements in physical space.

The model of ordinary kriging is described as follows:

$$m(x) = m = \text{const}, \tag{4}$$

here $m(x)$—mathematical expectation of spatial (random) variables $V(x)$ and $V(xi)$ from formula (3).

For this research, the size of the grid area cells was chosen equal to 30 km. Grid areas were constructed for each month of each year of the period under consideration. Calculations were performed in the Jupiter Notebook environment using Python.

3 Results

To reveal the presence of monotonous changes (linear trend) of meteorological parameters at weather stations located within the Lower Don basin, the corresponding linear regression dependences on the year number were constructed.

The obtained parameters of linear regressions for average annual and monthly temperatures indicate warming within the Lower Don basin (Table 1).

As for temperature changes per month, the strongest increase (0,8 °C/10 years) is observed at the Bogoroditskoye-Fenino, Valuyki and Remontnoe weather stations during the winter period (January and February), a weak significant increase—during the summer-autumn period (0,3 °C/10 years). Over the year, for almost the entire territory of the basin, the warming trend is significant at the level of 5%, with the exception of April, May, November and December. Also, insignificant coefficients of temperature growth are observed in January and February at the Rostov-on-Don weather station and in October at the Rostov-on-Don and Remontnoe weather stations. Over a century-long period, the magnitude of warming in the Rostov region, which is almost completely located within the Lower Don basin, is less: the linear trend coefficient for the period 1900–2020 averages 0.3 °C/10 years [7, 8], increasing especially strongly

Table 1 Coefficients of the linear trend of air temperature per month and year in the Lower Don basin for 1966–2020, °C/10 years

Stations	Year	Jan	Feb	Mar	Apr	May	June	July	Aug	Sept	Oct	Nov	Dec
Bogoroditskoe-Fenino	0,4	0,8	0,8	0,6	0,2	0,1	0,3	0,4	0,4	0,4	0,4	0,2	0,5
Kharkiv	0,4	0,7	0,6	0,6	0,2	0,2	0,4	0,5	0,5	0,5	0,3	0,2	0,4
Valuyki	0,5	0,8	0,8	0,6	0,1	0,2	0,4	0,5	0,5	0,4	0,4	0,2	0,5
Chertkovo	0,4	0,7	0,7	0,6	0,1	0,1	0,4	0,4	0,5	0,3	0,4	0,1	0,4
Tsimlyansk	0,4	0,7	0,7	0,7	0,1	0,2	0,5	0,5	0,6	0,4	0,5	0,0	0,2
Rostov-on-Don	0,3	0,5	0,5	0,5	-0,1	0,0	0,3	0,3	0,5	0,3	0,3	-0,1	0,1
Gigant	0,4	0,7	0,7	0,6	-0,1	0,1	0,5	0,4	0,6	0,4	0,4	-0,1	0,2
Remontnoe	0,4	0,7	0,8	0,7	-0,1	0,1	0,5	0,4	0,5	0,3	0,4	-0,1	0,2
Average meaning among stations	0,4	0,7	0,7	0,6	0,1	0,1	0,4	0,4	0,5	0,4	0,4	0,1	0,3

Notes Statistically significant positive coefficients are highlighted with an orange fill

during the cold period (0.69 °C/10 years) [9]. One of the reasons for the increase of near-surface air temperature is the fluctuation of blocking processes after 1988 [16].

To analyze the spatial nature of changes in meteorological parameters for each month of each year for the period 1966–2020, grid areas were created by means of interpolation. Then regressions were built in each cell of the grid area, the linear coefficient of which was displayed on the cartographic diagram.

The regional coefficients of the trend of changes in near-surface air temperature are shown in Fig. 2. Warming is observed throughout the basin, except for a couple of months. In January and February, the maximum growth rates of the average annual temperature were observed (in the range of 0.75–0.1 °C/10 years), the warming was most revealed in the north and south of the basin. In April, May, November and December, no significant changes in near-surface temperature were detected during the research period.

To explore in detail the nature of observed changes during 1966–2020, the time period of research was divided into periods based on a stepwise change model. To examine in detail the nature of observed changes during 1966–2020, the time period under study was divided into periods based on a step change model. As for the temperature at all weather stations where it was possible to determine a change in

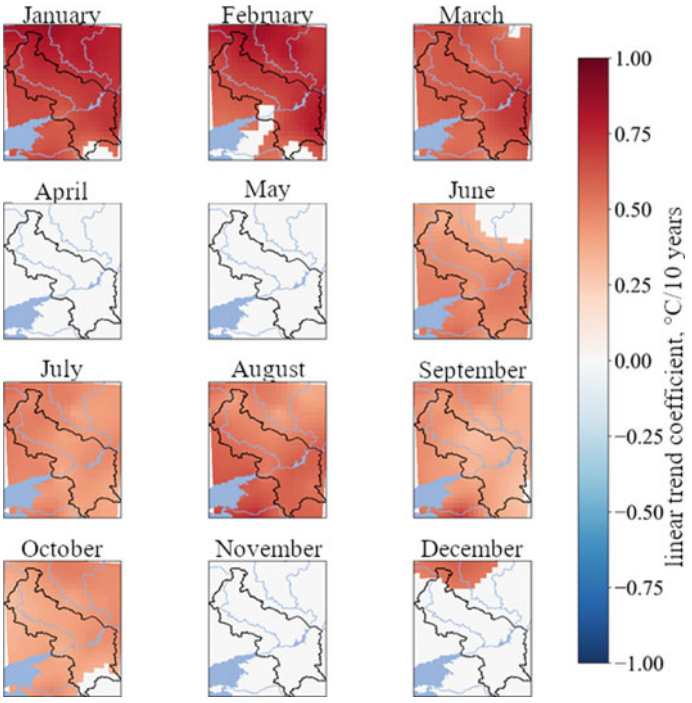


Fig. 2 Trend coefficients of near-surface air temperature in the Lower Don basin per month, °C/10 years

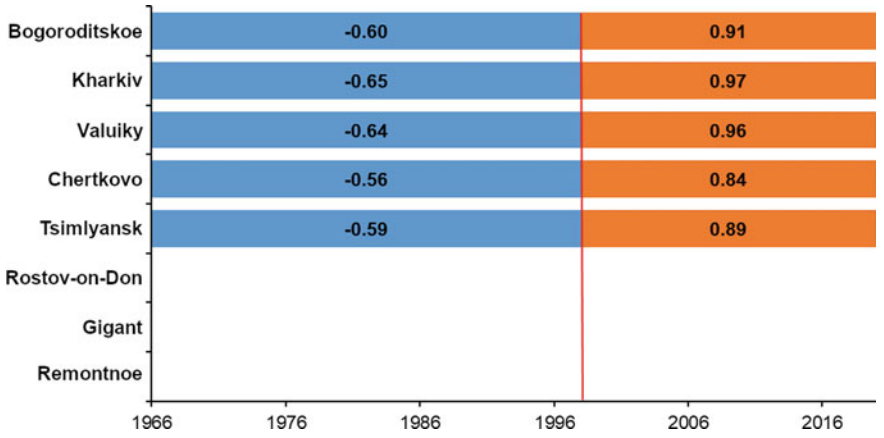


Fig. 3 Change of the near-surface air temperature regime in the Lower Don basin for 1966–2020, °C/period

regime, 2 identical time periods clearly appeared: 1966–1998 and 1999–2020. The exceptions are the weather stations Rostov-on-Don, Gigant, and Remontnoe (Fig. 3).

The results of division into periods according to stepwise model were compared with division into 30-year periods, which are recommended by the WMO for calculating climate norms. To make more clear the obtained average annual values which were displayed according overmentioned two different scales, they were combined in one diagram (Fig. 4). Figure 4 shows weather stations which are demonstrated data from the north-west (Bogoroditskoye-Fenino) and south-east (Remontnoe) of the Lower Don basin. Each chart shows two time bars: the upper part shows data according to division into periods within the stepwise change model, the lower part—according to division into 30-year periods.

4 Discussion

Comparison of the average temperature values of both scales demonstrated that the obtained values are, for the most part, identical and sufficiently reflect the observed changes. For a given meteorological parameter, the model of stepwise changes allows not only to track the growth trend, but also to detect the initial point of the changes (1998). However, the periods found by means of the stepwise change model reflect more realistic dynamics of the meteorological parameter under consideration. This indicates the dependence of statistical indicators of a small data sample (up to 100) on their volume. For this reason, it is better to specify the boundaries of the periods based on the available data, taking into account their homogeneity.

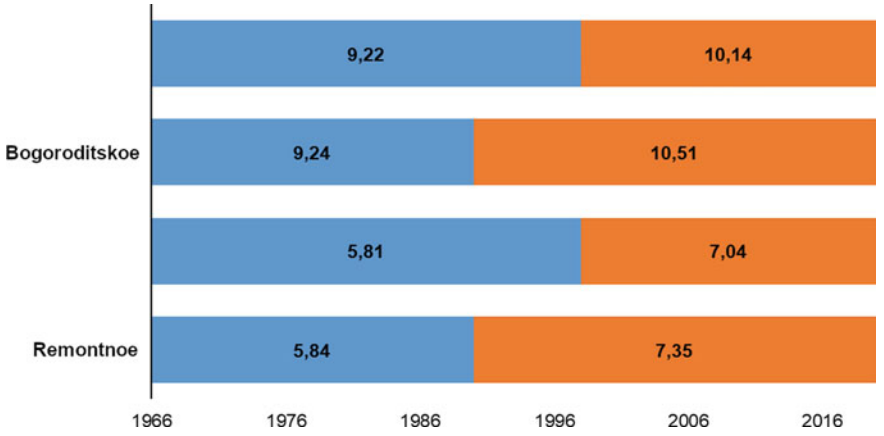


Fig. 4 Comparison of average values that obtained Bogoroditskoye-Fenino and Remontnoe weather stations and displayed according two different scales: the upper part shows data according to division into periods within the stepwise change model, the lower part—according to division into 30-year periods

5 Conclusion

In given research paper, the trends in changes of near-surface air temperatures in the Lower Don basin for the period 1966–2020 were analyzed. Based on the analysis of the calculated linear trend coefficients of the average annual and average monthly values of the near-surface air temperature, a statistically significant increase in the magnitude of this meteorological parameter was revealed. One of the main reasons for such change is considered the alteration of large-scale atmospheric circulation regimes in the early 1970s. A particularly significant increase is observed in the winter period (January and February). This can negatively affect the river flow: at high temperatures there are no conditions for snow formation and freezing of the necessary soil layer to further creation of sufficient water flow level in the spring (flood). Only in April, May, November and December no statistically significant changes in the near-surface air temperature regime was detected. Maps, designed on near-surface air temperature data, confirmed the presence of changes in this meteorological parameter, especially in the north of the basin. Due to the model of stepwise changes, the initial points of alternation of meteorological parameter's state were determined, therefore the entire time interval under consideration was divided into two subperiods: 1966–1998 and 1999–2020 respectively).

A comparison of the average temperature values within the identified (by means of the model of stepwise changes) periods and within the 30-year periods recommended by the WMO for calculating climate norms showed that the obtained values of the two scales are, for the most part, identical and sufficiently reflect the observed fluctuations. However, the periods revealed using the stepwise change model reflect more realistic dynamics of meteorological parameters.

References

1. Gladkov G. L., Nadezhinskaya N. I., Yarve P. A. Riverbed regime and navigable conditions on the Lower Don // Transport business of Russia, 2018. No. 5. pp. 124–130.
2. Vovk V. N. Liquidation of limiting sites on inland waterways // Transport of the Russian Federation, 2015. No. 1(56). pp. 3–6.
3. Matishov G. G. Ecological and socio-economic consequences of reconstruction of hydraulic structures on the Lower Don // Science of the South of Russia, 2016. Vol. 12, No. 4. pp. 41–49.
4. Afanasyev D. F., Mirzoyan Z. A., Martynyuk M. L. Early summer zooplankton of the Sea of Azov during the period of salinity// Biology of inland waters, 2019. № 2–2. pp. 51–60.
5. Stepanyan O. V. Distribution of macroalgae and sea grasses of the Sea of Azov, Kerch Strait and Taman Bay // Oceanology, 2009. Vol. 49, No. 3. pp. 393–399.
6. Collins M., Tett S.F.B., Copper C. The internal climate variability of HadCM3, a version of the Hadley Centre coupled model without flux adjustments // Clim. Dyn.–2001, V. 17. P. 61–81.
7. Matishov G.G., Kovaleva G.V. "Blooming" of water in reservoirs of the south of Russia and disruptions in water supply (on the example of Volgodonsk) // Bulletin of the Southern Scientific Center of the Russian Academy of Sciences. 2010. T. 6. No. 1. P. 71–79.
8. Gelfan A. N., Frolova N. L., Magritsky D. V. et al. The influence of climate change on the annual and maximum flow of rivers in Russia: assessment and forecast // Fundamental and Applied Climatology. 2021. T. 7. No. 1. P. 36–79.
9. WMO annual report highlights continuous advance of climate change / WMO. 2023. https://public.wmo.int/en/media/press-release/wmo-annual-report-highlights-continuous-advance-of-climate-change. Accessed on 2023/04/30.
10. Report on climate features in the Russian Federation for 2021, 2022. Moscow, 2022. 104 p.
11. Gudko V., Usatov A., Ioshpa A., Denisenko Y., Shevtsova V., Azarin K. Agro-climatic conditions of the southern federal district of Russia in the context of climate change// Theoretical and Applied Climatology. 2021. V. 145. № 3-4. P. 989–1006.
12. Bulygina O. N. et al. Description of the data array of the average monthly air temperature at the stations of Russia // Certificate of state registration of the database. 2014. № 2014621485.
13. Lobanov V. A. Textbook on regional climatology. St. Petersburg: RGGMU, 2020. 170 p.
14. Goovaerts P. et al. AM-29-Kriging Interpolation. https://gistbok.ucgis.org/bok-topics/kriging-interpolation Accessed on 2023/04/30.
15. Elementary introduction to geostatistics / Kanevsky M. F., Demyanov V. V., Savelyeva E. A. et al. // Problems of the environment and natural resources. M.: VINITI, 1999. No. 11. 136 p.
16. Kononova N. K. Changes in the atmospheric circulation of the Northern Hemisphere in the 20th–21st centuries and their consequences for the climate // Fundamental and Applied Climatology, 2015. Vol. 1, pp. 133–162.

Noble Metals of the Gaysky Copper-Zinc Massive Sulphide Deposit of Orenburg Region



G. A. Ponomareva

Abstract The article provides data on the quantitative content of noble metals (platinum, palladium, gold and silver) and their distribution in the ores and minerals of the Gaysky copper-zinc massive sulphide deposit. The Gaysky field is unique in terms of reserves and has been mined since the middle of the last century. Platinum, palladium, gold and silver were determined in samples from the Gaysky deposit by atomic absorption spectrometry using our own patented method for the simultaneous determination of noble metals, which increases the accuracy of the determination. The quantitative contents of all the indicated noble metals in the ores and minerals of the Gaysky deposit have been determined. Higher concentrations of platinum, palladium, gold, and silver are found in chalcopyrite, and the lowest in pyrite. Based on average values, the content of noble metals in the studied samples is distributed as follows: Ag > Au > Pd > Pt. The significant volumes of mining and processing of massive sulphide ores in the Orenburg region and the entire Urals as a whole make the problem of studying the noble metals of these ores extremely urgent and promising. Taking into account the presence in the region of waste dumps, tailings of concentration plants, as well as with a decrease the copper content in the original ores, these objects can serve as additional sources of raw materials for many metals in the future.

Keywords Noble metals · Platinoids · Gaysky copper-zinc massive sulphide deposit · Dumps

G. A. Ponomareva (✉)
Orenburg State University, 13 Pobeda Ave., Orenburg 460018, Russia
e-mail: galy.ponomareva@mail.ru

© The Author(s), under exclusive license to Springer Nature Switzerland AG 2024

V. Karev (ed.), *Proceedings of the 9th International Conference on Physical and Mathematical Modelling of Earth and Environmental Processes*, Springer Proceedings in Earth and Environmental Sciences, https://doi.org/10.1007/978-3-031-54589-4_8

1 Introduction

In the Orenburg region, all industrial-scale copper deposits are of the massive sulphide type. Currently, 9 such deposits and more than 100 ore occurrences are known. Deposits differ in copper reserves. The unique Gaysky field is one of the super-large ones.

The massive sulphide deposits of the Southern Urals are well studied. The Middle Devonian volcanic rocks of the island-arc basalt-rhyolite formation are host rocks for massive sulphide ores. The host rocks have undergone changes to the greenschist metamorphic facies. Ores most often gravitate towards the upper part of a felsic effusive member, which is overlain by andesite-basalt or low-thickness sedimentary rocks and then an andesite-basaltic member. The recumbent side of massive sulphide ores is confined to felsic lavas and tuffs, where an aureole of hydrothermal-metasomatic transformations of rocks is intensely manifested, expressed in sericitization, silicification, pyritization, chloritization, schistosis and brecciation [1, 2, 8 and others].

Sulphide ores are composed mainly of pyrite, the content of which reaches 95%, chalcopyrite, sphalerite. Table 1 shows the minerals of various ores of the Gaysky deposit [1, 12 and others].

Ores of massive sulphide deposits, as a rule, are complex, they contain valuable associated elements: gold, silver, selenium, cadmium, bismuth, tellurium and others [1, 2, 8, 12]. Of noble metals, in addition to gold and silver, the sulphide ores of the Ural region also contain platinoids, in particular platinum and palladium [1–5, 10, 13].

The content and distribution of noble metals: gold, platinum, palladium and silver in the sulphide ores of the Gaysky deposit, the individual features of their concentration in different mineral-geochemical zones of the deposit, are given in the works of Vikentieva et al. [2], Lazarenkov and Talovina [6] and Lazarenkov et al. [7].

Table 1 Mineral composition of ores of the Gaysky deposit

Mineral	Ore	Non-metallic
The main	Pyrite, chalcopyrite, sphalerite, fahl ore, bornite	Quartz, sericite, chlorite, calcite, barite
Secondary	Galena, chalcocite, marcasite	Dolomite, gypsum, rectorite
Rare, accessory	Gold, silver, argentite, altaite, hessite, krennerite, germanite, mousonite, stannoidite, betechinite, silver sulfotelluride, tellurium bismuthite, digenite, magnetite, ilmenite, arsenopyrite	Fluorite, apatite, prehnite, pumpellite

According to the work [2], the average Au content in ores reaches 1.15 ppm, Ag–14 ppm. The deposit produces about 2 tons of gold per year in copper and zinc concentrates. The total extraction in copper and zinc concentrates is 55% Au, 65% Ag. The highest Au content is in copper concentrate (4–7 ppm), and Ag—in zinc concentrate (80–100 ppm). The total amount of platinoids recovered in the refinery during the processing of Gaysky gold concentrates reaches 80–120 kg per year. Concentrations of noble metals in the ores of the Gaysky deposit are below the sensitivity limit of assay analysis. However, in some ore minerals, ultra-heavy concentrates, 80% by volume of high-grade gold with an admixture of galena and tellurides, and other technological products, significant concentrations of these metals are observed [1, 6, 7]. The content and distribution of platinum, palladium, gold and silver in the ores of the Gaysky deposit according to literature data are presented in Table 2.

At the Orenburg State University at the Department of Geology, many years of research are being conducted on the distribution patterns of platinoids together with gold and silver in the deposits of the platform and folded parts of the Orenburg region. The purpose of this work is to study the quantitative content and distribution of platinoids in association with gold and silver in ores and minerals of the Gaysky copper-zinc massive sulphide deposit. The object of research is the associations of noble metals (platinum, palladium, gold and silver) in ores and minerals. The subject of research is the distribution of noble metals in ores and minerals of the Gaysky deposit.

Table 2 Content of noble metals in various samples of the Gaysky deposit, ppm

Sample	Rh	Pt	Pd	Au	Ag	Literature
Chalcopyrite	0.05	0.04	0.2	5.3	H.a	Lazarenkov et al. [7]
Bornite	0.05	0.17	2.7	1.7	H.a	
Fahl ore	H.a	0.05	0.12	8.6	H.a	
Native Au	H.a	30	40	820000	H.a	
Pyrite	H.a	0.02	0.02	0.9	H.a	
Ultra heavy concentrates	H.a	0.15	1.8	H.a	H.a	Vikentiev et al. [2]
Native Au	H.a	1800	2100	847100	161800	
Galena	H.a	H.a	H.a	300	130	
Bornite	H.a	H.a	H.a	150	400	
Pyrite, sphalerite, chalcopyrite	H.a	H.a	H.a	<10	<10	

2 Materials and Methods

By morphology, the ore bodies of the Gaysky deposit are of various sizes stratum-plate-lenticular deposits of solid massive sulphide and veinlets of disseminated ores, which are consistent with the host rocks and are characterized by sharp contacts from the side of the hanging side and gradual from the side of the recumbent. They form a plate-like submeridian ore zone with a thickness of about 300 m (up to 600–800 m). The deposit was opened by three careers and a deep mine [1, 8 and others]. The presence of platinum metals in the massive sulphide ores of the Urals is mentioned in the works [4, 13]. Studies of copper massive sulphide ores of the Urals, carried out by the author [13], showed that the platinum content in them varies from 0 to 0.1 mg/t. Systematic studies in this direction, initiated by Zoloev et al. in the late 1980-s, culminated in the identification in 1992 of a new type of platinum-bearing ore formations—Gaysky [3]. Later studies in the ores of the Ural massive sulphide deposits established industrially interesting noble metal mineralization [2, 5–8]. The original author's data on the content of noble metals in the massive sulphide ores of the eastern Orenburg region are given in the works [10]. As a result of the work carried out, the metallogenic zoning of the geological and structural zones of the Southern Urals and individual deposits was revealed [10, 11]. The data obtained prompted the author to conduct a deeper study of the content of platinoids in the ores of copper massive sulphide deposits. The choice of the Gaysky deposit is due to a number of reasons: the deposit is super-large in terms of reserves, it is currently being developed, enough knowledge has been accumulated about the geological conditions of placement, geological structure, formation conditions, has been developed from about the middle of the last century, therefore, dumps and waste of the mining processing plant have been accumulated, which in the future can serve as sources of valuable raw materials [9].

Geochemical samples were formed from ore samples from the Gaysky deposit taken in careers, in mine workings, as well as from well core samples. Determination of noble metals in individual minerals was carried out from monomineral samples or by selecting a certain mineral species under a binocular microscope.

In the samples from the above samples, the content of Au, Ag, Pt, Pd was determined, since these metals are industrially significant.

After standard procedures of grinding, mixing and decreasing, the mass of the samples for analysis was 50–30 g. The weight of the weighed portion of the samples was 10 g (with a particle size of not more than 0.07 mm) according to the method of quantitative chemical analysis.

The instrumental determination of metals was performed by atomic absorption spectrometry with an electrothermal atomizer on an MGA-915 device from Lumex (St. Petersburg). The samples were subjected to preliminary chemical preparation according to the method developed at VSEGEI using our own patented method of preliminary additional oxidation of carbon-containing components of the samples (RF Patent 2409810, 2011). In final solutions or finely dispersed systems, the concentrations of noble metals were measured, taking into account the conditions for their

Table 3 Content of noble metals in ores and individual minerals of the Gaysky copper-zinc massive sulphide deposit (average values are given), ppm

№п/п	Sample	Depth, m	Au	Ag	Pt	Pd	Σ БМ
Ores							
1	Ore (chalcopyrite, pyrite) (3)*	695	0,240	2,880	<0,002	–	3,120
Minerals							
1	Chalcopyrite (2)	695	1,995	4,345	0,011	0,047	6,398
2	Pyrite (2)	695	0,163	0,355	0,005	0,013	0,536
3	Bornite (3)	670	1,365	3,019	0,016	0,022	4,427
4	Native Cu (2)	695	0,025	0,192	0,020	0,007	244

Note *—The number of samples is indicated in brackets
Analyzes were performed by G.A. Ponomareva at the Laboratory of Physical Research Methods of the Geological Department of Orenburg State University

determination, the operating manual for the spectrometer, and the chemical composition of the samples. The author's data on the content of noble metals in the samples of the Gaysky copper-zink massive sulphide deposit are shown in Table 3.

3 Results and Discussion

The results obtained by the author in the determination of noble metals indicate their presence both in ores and in individual minerals of the Gaysky deposit. Gold and silver are characterized by an uneven distribution (from 0.025 ppm and 0.192 ppm in native copper to almost 2 ppm and 4.345 ppm in chalcopyrite, respectively). Platinum and palladium are distributed relatively more evenly in all samples. Moreover, palladium prevails. In the samples of chalcopyrite-pyrite ore, the contents of all noble metals are 3.120 ppm.

The quantitative content of platinoids in the samples of ores and minerals is close. Platinum and palladium contents in ores is lower, below the detection limits of the method. Analysis of the results of Table 3 shows that the maximum content of platinum, palladium, gold and silver is observed in chalcopyrite, the amount of noble metals in it is 6.398 ppm, the amount of platinoids is 0.058 ppm. Perhaps this is explained to the large isomorphic capacity of chalcopyrite. Least of all noble metals from sulfides is in pyrite, the sum of noble metals in it is 0.536 ppm, and the sum of platinoids is 0.018 ppm. In bornite, the content of all metals is lower than in chalcopyrite, but higher than in pyrite. The amount of noble metals in bornite is 4.427 ppm, the amount of platinoids is 0.052 ppm. In native copper, the content of almost all metals is lower than in pyrite. In spite of the different contents of noble metals in the given samples, some general patterns of their distribution are also observed. So in pyrite, bornite and chalcopyrite, native copper and ores, the

maximum amounts of silver are observed, then, in absolute amounts, gold, palladium and, finally, the minimum amounts are found for platinum. Based on average values, the content of noble metals in the studied samples is distributed as follows: Ag > Au > Pd > Pt.

According to the data presented, the palladium content is higher than the platinum content in the studied minerals, which is consistent with the author's earlier data when studying the distribution of platinoids in the massive sulphide deposits in the Eastern Orenburg region. The results of these studies also made it possible to establish differences in the distribution of noble metals in ores of the Ural type deposits (platinum-palladium specialization, with Pt/Pd < 1), Baymak and Dombarovsky types (palladium-platinum specialization, with Pt/Pd > 1), while in from west to east, there is a regular increase in the platinum content in massive sulphide ores with a simultaneous decrease in the palladium content [10, 11].

Analysis of paired correlations between noble metals in the samples of the Gaysky deposit using the proprietary package of the "Statistics" program showed the following. In sulphides of the Gaysky deposit, platinum exhibits high correlation coefficients with $Pd_{0.87}$, $Ag_{0.77}$, $Au_{0.77}$, and palladium has significant positive correlation coefficients also with $Ag_{0.50}$, $Au_{0.50}$. As you can see, all noble metals show a direct relationship, perhaps their distribution in the minerals of the Gaysky copper-zinc massive sulphide deposit depends on each other.

4 Conclusions

Sulphide minerals are well-known concentrators of gold and silver, and possibly also platinum and palladium. Among the studied minerals of the Gaysky deposit, chalcopyrite is the most enriched in these metals, and bornite is less. Pyrite contains minimal concentrations of all precious metals. However, it was noted above that pyrite is the most important mineral in massive sulphide ores, therefore, the bulk of noble metals is concentrated in it. From this point of view, pyrite can be considered as an additional source of rare elements. The above data are of particular relevance during the development of copper massive sulphide deposits in the Urals and the Orenburg region in particular. Huge dumps of worked out pits, pyrite waste from mining processing plants are of certain interest in this regard and can serve as raw materials for obtaining a number of valuable components.

The results obtained with the use of our own patented method for the simultaneous determination of platinum, palladium, gold and silver in carbonaceous rocks make it possible to expand the prospects of copper massive sulphide deposits for noble metals.

Despite the low concentrations of platinum metals in the copper massive sulphide ores of the Gaysky deposit, the large reserves of these ores, the significant volumes of their extraction and processing make the whole problem of studying the platinum content of these ores extremely urgent and promising.

The revealed quantitative contents, ratios of platinoids, correlations of noble metals in individual minerals of ores, in the ores themselves make it possible to predict the presence of rare elements in dumps of mined quarries, pyrite waste from massive sulphide deposits. These facts oblige to a more thorough study of the already exhausted massive sulphide deposits of the Orenburg region and the entire Ural region, which can serve as additional sources of raw materials for many metals.

References

1. Gaysky MPP; geology of Gaysky and Podolsky copper-zinc massive sulphide deposits in the Urals. Yekaterinburg: IGiG Uro RAN; 2004. 148 p.
2. Vikentiev VI, Moloshag VP, Yudovskaya MA. Forms of occurrence and conditions of concentration of noble metals in massive sulphide ores of the Urals. Geology of ore deposits. M.: 2006;48(2): 91–125.
3. Dobrovolskaya MG, Distler VV. Platinum metals in ores of copper massive sulphide deposits of the Southern Urals. Ores and metals. 1994; 4:56–64.
4. Zvyagintsev OE. Geochemistry of platinum. Leningrad: ONTI – Chem-theoretic; 1936. 96 p.
5. Zoloev KK, Volchenko YuA, Koroteev VA, Malakhov IA, Mardirosyan AN, Khrypov VN. Platinum-metal mineralization in the geological complexes of the Urals. Yekaterinburg: 2001. 199 p.
6. Lazarenkov VG, Talovina IV. Geochemistry of platinum group elements. SPb: Galart; 2001. 266 p.
7. Lazarenkov VG, Talovina IV, Beloglazov IN, Volodin VI. Platinum metals in supergene nickel deposits and prospects for their industrial extraction. Nedra; 2006. 188 p.
8. Copper massive sulphide deposits of the Urals. Formation conditions. Yekaterinburg: Ural Branch of the Russian Academy of Sciences; 1992. 252 p.
9. Petrishchev VP, Artamonova SV, Dubrovskaya SA, Ryakhov RV, Noreika SYu. Landscape and geoecological foundations of formation of technological systems of copper-planted deposits. Orenburg: OGU; 2019. 156 p.
10. Ponomareva GA, Pankratiev PV. To the question of platinoids content in massive sulphide ores Gay deposit. Geology minerals and geology problems of Bushkortostan, Urals and adjacent territories. Proceedings of the VIII All-Russian Scientific and Practical Conference. Ufa. 2010: pp. 124–127
11. Ponomareva GA, Loschinin VP. Gold occurences in the Paleozoic Blak shale formations of the eastern Orenburg region and theire genesis. Bulletin the Orenburg State University. 2013;5(124): 144–148.
12. Pshenichny GN. Gaysky copper massive sulphide deposit in the South Urals. M.: Nauka; 1975. 187 p.
13. Yushko-Zakharova E.O. Platinum content of ore deposits. M: Nedra; 1975. 248 p.

Cryomicrophotography in a Cold Room at the Faculty of Geography of Moscow State University Named After M.V. Lomonosov

D. M. Frolov, G. A. Rzhanitsyn, A. V. Koshurnikov, V. E. Gagarin, and P. A. Krilovets

Abstract At the Faculty of Geography of Moscow State University named after M.V. Lomonosov, a cold room was equipped to study the properties of snow, ice and frozen soil for the needs of the educational process and scientific research at the Department of Cryolithology and Glaciology and the Laboratory of Snow Avalanches and Mudflows of the Faculty of Geography. In particular, the cold laboratory is equipped for optical photography under a microscope and in polarized light.

Keywords Cold laboratory · Optical microscopy · Photographs in polarized light

1 Introduction

Since snow cover, ice and frozen ground are important indicators of climate change and play an important role in the surface energy balance [1], surface-atmosphere interaction [2] and hydrological processes [3], the Lomonosov Moscow State University Faculty of Geography studies their properties in a cold laboratory. Microphotography of snowflakes makes it possible to study the structure and shape of precipitating atmospheric crystals depending on weather conditions and to demonstrate in the educational process and draw some conclusions about the mechanism of their nucleation and growth. This is done for the needs of the educational process and scientific research at the Department of Cryolithology and Glaciology and the Laboratory of Snow Avalanches and Mudflows of the Faculty of Geography.

D. M. Frolov (✉) · G. A. Rzhanitsyn · A. V. Koshurnikov · V. E. Gagarin · P. A. Krilovets
Faculty of Geography of Moscow State University Named After M.V. Lomonosov, St. Leninskiye Gory, 1, Moscow 119331, Russia
e-mail: frolov@geogr.msu.ru

© The Author(s), under exclusive license to Springer Nature Switzerland AG 2024

V. Karev (ed.), *Proceedings of the 9th International Conference on Physical and Mathematical Modelling of Earth and Environmental Processes*, Springer Proceedings in Earth and Environmental Sciences, https://doi.org/10.1007/978-3-031-54589-4_9

2 Materials and Methods

The cold laboratory at the Faculty of Geography of MSU was created in the 60s of the last century for the needs of the faculty related to the study and modeling of thermal and mechanical processes in snow, ice and frozen ground applicable both in the educational process and in the course of research work. At the beginning of the new millennium the cold laboratory was overhauled with replacement of insulation, refrigeration machines and control and measuring equipment with modern brands. During the overhaul, the insulation was replaced with polyurethane foam panels instead of peat, a refrigeration machine from the German company Bitzer was installed and control measuring equipment was installed, which allows setting the temperature in the cold laboratory in the range from 0 to −20 °C with an accuracy of one degree.

For research work, the cold laboratory is equipped with instruments for optical microscope and polarized light photography, including LoMo and Carl Zeiss microscopes and AxioVision digital imaging system.

To microphotograph snowflakes in a cold room, the following steps were performed: snowflake samples were collected at a certain ambient temperature into boxes with cooled oil to prevent further evaporation of snowflakes, in case snowflakes were falling at the moment. It was also possible to use previously collected snowflake samples. The snowflakes were photographed and their shape was compared with the results of similar work that was done earlier and described in [4–6]. Also in the cold room, ice samples were photographed on a table illuminated with polarized light and through a second polaroid located on a tripod in order to determine the size and orientation of individual crystals in the ice.

The appearance of the setups for microphotography snowflakes in a cold room and for photographing ice samples in polarized light on a table illuminated with polarized light and through a second polaroid is shown in Fig. 1.



Fig. 1 External view of the installation for microphotography of snowflakes and for photographing ice samples in polarized light on a table illuminated with polarized light and through a second polaroid located on a tripod

3 Results and Discussion

Examples of microphotographs of snowflakes obtained by the authors and their primary classification are shown in Fig. 2.

Thus, by obtaining the corresponding images of snowflakes in a cold laboratory based on the results of cryomicroscopy (several hundreds of them were obtained during several winter periods), it was possible to make an initial classification and to make some correspondence with the works [4–6].

Indeed, according to the results of these studies, it can be stated that at colder temperatures of surface air, needles were formed, and at warmer temperatures, dendrites, etc., which is consistent. However, the theories of snow crystal formation mainly consider the temperature of nucleation and growth of crystals in the atmosphere, while in this work the temperature of surface air at the time of deposition was measured.

Also, the photographing of ice samples in polarized light on a table illuminated with polarized light and through a second polaroid located on a tripod in a cold laboratory allowed us to obtain images of ice in polarized light with clearly visible outlines of individual crystals. Such analysis is necessary when studying formation ice, for example [7, 8].

Thus, the opportunities provided at the Faculty of Geography in cold laboratory to prepare and examine and photograph ice, snow, and frozen soil samples are an important part of the research and educational process at the faculty, but also present ample opportunities for similar research to scientists and students in other faculty and organizations.

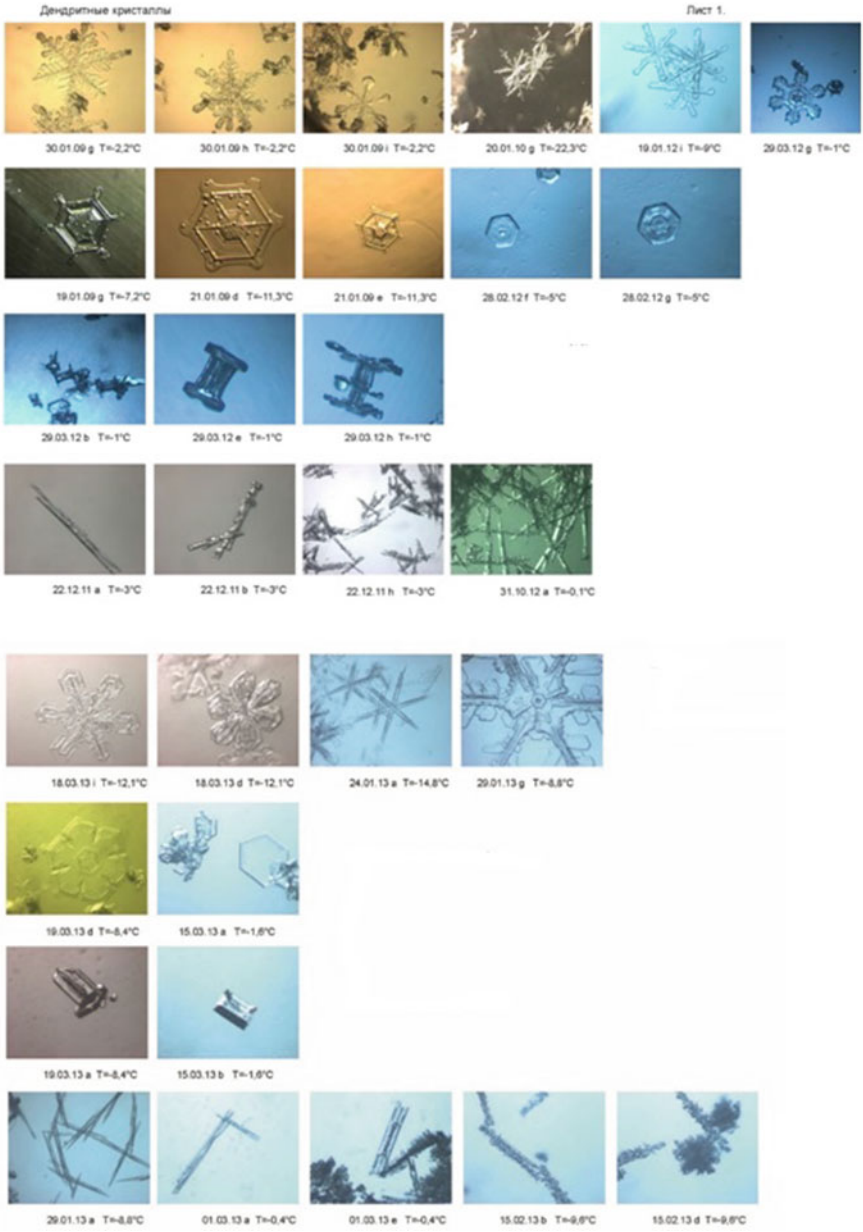


Fig. 2 Examples of snowflake microphotographs obtained by the authors and initial classification of selected snowflake samples

Acknowledgements The work was carried out in accordance with the state budget theme "Evolution of the cryosphere under climate change and anthropogenic impact" (121051100164-0), "Danger and risk of natural processes and phenomena" (121051300175-4). The authors declare no conflict of interest.

References

1. Flanner M.G., Shell K.M., Barlage M., Perovich D.K., Tschudi M.A. Radiative forcing and albedo feedback from the Northern Hemisphere cryosphere between 1979 and 2008. Nat. Geosci. 2011, 4, 151–155.
2. You Q., Wu T., Shen L., Pepin N., Zhang L., Jiang Z., Wu Z., Kang S., AghaKouchak A. Review of snow cover variation over the Tibetan Plateau and its influence on the broad climate system. Earth Sci. Rev. 2020, 201, 103043.
3. Beniston M., Farinotti D., Stoffel M., Andreassen L.M., Coppola E., Eckert N., Fantini A., Giacona F., Hauck C., Huss M., et al. The European mountain cryosphere: A review of its current state, trends, and future challenges. Cryosphere 2018, 12, 759–794.
4. Libbrecht K.G. Snowflake Stamps. www.its.caltech.edu.
5. Furukawa Y. Snow and Ice Crystal Growth, Handbook of Crystal Growth (Second Edition), Elsevier, 2015, pp. 1061–1112, ISBN 9780444563699, https://doi.org/10.1016/B978-0-444-56369-9.00025-3.
6. Photos of snowflakes, snow crystals http://www.snowcrystals.com/.
7. Solomatin V.I. Physics and geography of underground glaciation. Novosibirsk. Geo. 2013. 266 c.
8. Leibman M.O., Rogov V.V., Vasiliev A.A., Ingolfson O. Study of formation ice of the Yugra Peninsula by crystallographic methods. Cryosphere of the Earth 4, 2 (2000), 31–40.

Wave Variation of the Magnitude of Rock Salt Mass Transfer Coefficient Under Hydrodynamic Influence of Solution Along the Height of Underground Excavations of UGS

V. P. Malyukov

Abstract Experimental studies on samples of the mass transfer coefficient of the vertical surface of rock salt (core) under hydrodynamic influence (HDI) of the solution at the height of the underground excavation-capacity (UEC) at the Kaliningrad underground gas storage facility (UGS), located in the Kaliningrad region of the Russian Federation, and at the Gomel UGS, located in the Gomel region of the Republic of Belarus have been carried out. The wave distribution of the mass transfer coefficient value at rock salt reservoirs by the excavation height (from the roof to the bottom) is obtained.

Keywords Rock salt · Physical modeling · Hydrodynamic effect of solution · Wave variation of mass transfer coefficient value

Experimental determination of the mass transfer coefficient of rock salt was performed on samples from the construction interval of underground excavations-capacities of the Kaliningrad UGS (Romanovskaya area). The necessity of UGS construction on the territory of Kaliningrad oblast is conditioned by its remoteness from the Unified Gas Supply System of the Russian Federation. Establishment of UGS facilities will make it possible to ensure regulation of seasonal and peak supply loads in the region in an autonomous mode in case of negative situations with regard to gas supply through the gas pipeline.

The mass transfer coefficient of rock salt is the main indicator of the process, which predetermines the technological characteristics of the construction of underground excavation-capacity when the mud is fed through the borehole.

The salt deposits of the Romanovskaya area are composed of almost monomineral rock with thin anhydrite interlayers up to 1–2 mm thick [1].

V. P. Malyukov (✉)
Peoples' Friendship University of Russia, Moscow, Russia
e-mail: v.malyukov@mail.ru

© The Author(s), under exclusive license to Springer Nature Switzerland AG 2024

V. Karev (ed.), *Proceedings of the 9th International Conference on Physical and Mathematical Modelling of Earth and Environmental Processes*, Springer Proceedings in Earth and Environmental Sciences, https://doi.org/10.1007/978-3-031-54589-4_10

Construction of UGS facilities is carried out in several stages. At the first stage, a UGS facility with an active volume of 261 mln m^3 is being created. The first stage of the storage facility consists of five underground reservoirs with a geometric volume of 400 thousand m^3 each. In order to reduce the time of UGS commissioning it was decided to build and commission two tanks out of five with the volume of 230 thousand m^3, and further increase their volume up to 400 thousand m^3 to be realized in the process of UGS operation by cyclically filling of the tank with fresh water [2, 3].

The growth rate and the final value of solution concentration at the end of the first and subsequent stage of UGS construction depends on the solution supply capacity, surface size and mass transfer coefficient of rock salt under the hydrodynamic action of the solution [4, 5].

The average value of the mass transfer coefficient of the vertical surface of rock salt for the entire interval of the underground excavation-capacity for well 1P was $\overline{K} = 0.01545 \cdot 10^{-5}$ m/s, and for well 2P—$\overline{K} = 0.01622 \cdot 10^{-5}$ m/s. The values of mass transfer coefficient of vertical surface of rock salt from the core of Romanovskaya area are presented in Table 1.

The analysis of geological sections has shown that the optimal intervals of rock salt with the thickness of 120 m for the location of excavations of underground natural gas storage for well 1P is the depth of 902–1022 m, and for well 2P—the depth of 898–1018 m.

For both wells, the change in the value of the mass transfer coefficient by depth of the excavation-capacity interval alternates in a "wave-like" manner. At wells 1P and 2P in the interval of excavation embedment there are 5 such "waves" of 24–25 m in size.

The wave-like change of the mass transfer coefficient value is an alternation of decrease and increase of the mass transfer coefficient value along the UEC height.

The deviation of the maximum from the minimum value of the mass transfer coefficient of rock salt for different intervals along the height of underground excavation for well 1P amounted to 34%, and for well 2P amounted to 28%.

In some samples in the process of dissolution of rock salt the release of hydrocarbon gas from the interlayers and at the contact of salt crystals was noted. The volume of released gas is insignificant [6].

Despite the rather large distance between the wells (about 1 km), homogeneous points (points of growth or points of decrease in the mass transfer coefficient value) are located at approximately the same depth intervals and have close values of the mass transfer coefficient value.

Experimental determination of the mass transfer coefficient of rock salt was carried out on samples from the interval of underground excavations-capacities of Gomel UGS (Alexandrovskaya area). The analysis of geological sections of wells 1P and 2P allowed to choose the optimal intervals of rock salt of the required thickness for the location of underground natural gas storage excavations. The roof of the rock salt layer promising for construction of underground workings-capacities is accepted at the depth of 1185 m, the bottom - at the depth of 1328 m (according to the materials of exploration well 1P).

Table 1 Values of mass transfer coefficient of vertical surface of rock salt from the core of Romanovskaya area

№ of wells	№ of samples	Depth of selection, m	Sample height, m	Duration, s	Temperature, °C	Sample weight, g	Weight loss, g	Mass transfer coefficient K 10^{-5} m/s
1P	1	902	12,6	1800	20	1050,8	23,0	0,01841
	2	911	10,8	–	–	948,0	17,0	0,01588
	3	915	8,6	–	–	750,3	21,2	0,01458
	4	920	11,8	–	–	928,6	18,4	0,01545
	5	927	12,8	–	–	1165,0	19,8	0,01565
	6	930	13,0	–	–	1202,8	24,2	0,01645
	7	933	13,0	–	–	1029,1	18,0	0,01423
	8	940	8,5	–	–	650,0	18,1	0,01581
	9	947	12,5	–	–	1009,2	19,2	0,01589
	10	953	19,6	–	–	1838,4	17,8	0,01576
	11	964	14,5	–	–	1328,0	23,2	0,01574
	12	988	13,7	–	–	1221,9	19,6	0,01616
	13	996	12,9	–	–	1123,4	27,4	0,01441
	14	1001	12,2	–	–	1121,1	19,5	0,01518
	15	1004	15,8	–	–	1462,6	18,3	0,01489
	16	1011	16,9	–	–	1607,1	21,5	0,01471
	17	1014	11,8	–	–	1134,5	19,2	0,01371
	18	1022	11,4	–	–	1057,6	21,1	0,01,512
2P	19	893	12,7	–	–	847,8	14,3	0,0152
	20	903	13,6	–	–	973,3	18,2	0,01847
	21	911	14,1	–	–	1226,3	26,3	0,0168
	22	922	9,1	–	–	769,7	23,5	0,01717
	23	940	10,2	–	–	877,6	21,0	0,01638
	24	956	14,3	–	–	1280,9	19,6	0,01666
	25	965	11,6	–	–	1022,9	24,4	0,01631
	26	978	10,1	–	–	848,5	35,5	0,01595
	27	983,1	5,9	–	–	447,2	20,0	0,01611
	28	983,2	7,2	–	–	572,8	22,6	0,01675
	29	990	11,6	–	–	1018,0	17,4	0,01541
	30	1005	11,7	–	–	1099,5	21,0	0,01703
	31	1018	14,5	–	–	1274,7	21,4	0,01356

Table 2 Values of mass transfer coefficient of vertical surface of rock salt from the core of Alexandrovskaya area

№ of wells	№ of samples	Depth of selection, m	Sample height, m	Duration, s	Temperature, °C	Sample weight, g	Weight loss, g	Mass transfer coefficient K 10^{-5} m/s
1P	1	1093	7,9	1800	20	704,2	191,5	2,040
	2	1128	8,1	–	–	693,6	147,6	1,551
	3	1161	13,9	–	–	1153,9	214,5	1,346
	4	1172	11,2	–	–	911,8	195,8	1,526
	5	1187	8,8	–	–	701,9	151,2	1,505
	6	1202	16,9	–	–	1412,3	337,0	1,786
	7	1212	16,8	–	–	1507,1	309,1	1,581
	8	1226	10,7	–	–	959,4	205,4	1,616
	9	1230	11,9	–	–	1009,2	230,5	1,672
	10	1236	6,7	–	–	582,2	114,8	1,421
	11	1244	16,6	–	–	1517,8	299,5	1,523
	12	1255	14,1	–	–	1244,3	289,0	1,789
	13	1266	14,7	–	–	1340,3	235,7	1,324
	14	1275	12,9	–	–	1065,6	237,6	1,553
	15	1296	17,1	–	–	1484,7	340,1	1,74
	16	1305	12,6	–	–	1048,5	239,6	1,669
	17	1285	11,4	–	–	957,2	246,7	1,884
	18	1294	11,4	–	–	1015,5	239,6	1,794
	19	1298	17,3	–	–	1651,5	373,5	1,814
	20	1313	12,1	–	–	1090,0	251,6	1,75
2P	21	1320	13,6	–	–	1266,2	294,1	1,821
	22	1332	9,7	–	–	890,9	228,5	1,972
	23	1337	11,1	–	–	1054,2	251,6	1,875
	24	1349	17,5	–	–	1561,5	323,4	1,574
	25	1353	12,3	–	–	1143,2	232,7	1,559
	26	1368	13,0	–	–	1157,8	246,1	1,596
	27	1375	12,9	–	–	1087,6	250,6	1,698
	28	1386	17,3	–	–	1537,2	422,9	2,173
	29	1398	7,1	–	–	637,3	181,9	2,181
	30	1333	11,4	–	–	1045,3	269,3	1,973

Values of mass transfer coefficient of vertical surface of rock salt from the core of Alexandrovskaya area for wells 1P and 2P are presented in Table 2.

The average value of the mass transfer coefficient for well 1P was $\overline{K} = 0{,}0163 \cdot 10^{-5}$ m/s, and for well 2P (interval 1295–1400 m)—$\overline{K} = 0{,}0183 \cdot 10^{-5}$ m/s.

The deviation of the maximum value from the minimum value for the mass transfer coefficient of rock salt of different intervals at the height of the underground excavation-capacity at well 1P is 54%, and at well 2P—40%.

For both wells, the change in the value of the mass transfer coefficient by depth alternates "wave-like". The interval for both wells, including decrease and increase of the mass transfer coefficient is 49 m (wavelength) on average.

On separate samples in the process of mass removal of rock salt gas release from interlayers (hydrocarbon gas), from cracks and at the contact of crystals (hydrogen sulfide was released from one sample) was noted. The volume of released gas is insignificant. For the first time the release of two different gases from rock salt in the interval of underground excavation in the process of mass transfer was noted.

The wave distribution of the value of the mass transfer coefficient of the rock salt mass transfer coefficient was obtained for the height of the interval of underground excavations of the Kaliningrad and Gomel UGS [7–9].

As a result of the conducted researches the wave distribution of changes in the value of mass transfer coefficient for rock salt reservoir deposits in the interval of UGS construction was determined. Characteristic for the considered rock salt deposits change of the mass transfer coefficient value—the wave length (one decrease and increase of the mass transfer coefficient value along the height of the UEC) was determined. The wave length for Romanovskaya area is 24–25 m, for Alexandrovskaya area—49 m.

References

1. Ediashvili N.A., Butkovsky Yu.M., Sokhransky V.B., Panov V.D. Kaliningrad saline basin as a natural environment for the location of underground gas storage // Mining Journal. 2010, № 3, pp. 35–37.
2. Kazaryan V.A., Tsibulskiy P.G. Tank construction technology of Kaliningrad underground gas storage // Mining Journal. 2010, № 3, pp. 48–51.
3. Khloptsov V.G. Underground natural gas storages in rock salt deposits. Gas Industry. 2015, № 9, pp. 28–31.
4. Malyukov V.P., Ghazaryan V.A. Investigation of mass transfer during construction of underground storages in rock salt. Science and technology in gas industry. № 1 (29), 2007, pp. 64–71.
5. Smirnov V.I., Kazaryan V.A., Pozdnyakov A.G., Igoshin A.I., Maljukov V.P. Method for experimental determination of rock salt dissolution rate coefficient used in Podzemgasprom, Ltd. SMRI, Fall Mitting 2002, Bad Ischi, Austria, pp. 287–298.
6. Malyukov V.P. Construction of underground tanks for storage of gas and oil products in rock salt with significant gas content. Izdvo: Transport and storage of oil products and hydrocarbon raw materials, No. 2, 2012, pp. 43 – 50.
7. Malyukov V.P. Mass transfer and boundary layer detachment at influence of water solution on rock salt. Processes in geosphere. Moscow: LLC "Kvaternion" Moscow, 2020. № 4 (26).

8. Malyukov V.P., Ghazaryan V.A. Physico-technical processes in the construction of underground rock salt storages. International Conference. UGS: reliability and efficiency. October 11–13, 2006. OOO VNIIGAZ, OAO Gazprom. MOSCOW, 2007, VOL. 2, pp. 32–49.
9. Malyukov V.P. Local mass transfer during creation and operation of underground excavation in rock salt. Processes in Geomedia. 2022. № 1 (31). pp. 1482–1490.

On Stability of Inverse Problem Solution for Rock Mass Stress State Reconstruction Based on Natural Fractures Analysis



E. V. Novikova and N. V. Dubinya

Abstract The paper is devoted to the issue of stability of the solution of the inverse problem of estimating stress state of the rock mass based on data on natural fractures. Within the framework of the used method of estimating stress state of the geologic medium, it is assumed that geophysical methods allow estimating the stress state of individual fractures in the medium. The task of using information on the stress state of a set of fractures in a rock mass to reconstruct the parameters determining the stress state of the entire rock mass is posed. Previously, a method for solving this kind of problems was developed, and it was demonstrated that the inverse problem is ill-posed. In this paper, a synthetic fracture model is used to analyze how sensitive the solution of the inverse problem is to the noise of initial data. It is demonstrated that artificial degradation of the quality of information on the state of natural fractures in a rock mass leads to nonlinear increase in the distance between the true stress state and its estimation obtained by solving the inverse problem. The results of the work are used to determine the requirements for the analysis of natural fractures for the possibility to use its results to assess the stress state of rock masses.

Keywords Geomechanics · Fractures · Critically stressed fractures · Ill-posed problems

E. V. Novikova
Sadovsky Institute of Geospheres Dynamics of the Russian Academy of Sciences, Moscow, Russia

E. V. Novikova · N. V. Dubinya (✉)
Schmidt Institute of Physics of the Earth of the Russian Academy of Sciences, Moscow, Russia
e-mail: helenvn97@gmail.com

Moscow Institute of Physics and Technology (National Research University), Dolgoprudny, Russia

© The Author(s), under exclusive license to Springer Nature Switzerland AG 2024

V. Karev (ed.), *Proceedings of the 9th International Conference on Physical and Mathematical Modelling of Earth and Environmental Processes*, Springer Proceedings in Earth and Environmental Sciences, https://doi.org/10.1007/978-3-031-54589-4_11

1 Introduction

Analysis of the stress state of geological media remains among important problems of rock and soil mechanics. Estimation of in-situ stresses is necessary for solving many issues related, in particular, to the development of mineral deposits. Wellbore studies provide valuable information on the stress state of rocks composing the upper layers of the Earth's crust: according to recent observations [1], about 15% of the data on the directions of action of the main stresses, available in the World Stress Map database, are obtained from interpretation of geophysical well surveys. There are various methods for reconstructing stress profiles from geophysical well surveys, laboratory experiments, and seismic data [2, 3]. The most commonly used stress reconstruction methods include analysis of wellbore breakouts and drilling-induced tensile fractures [4], as well as direct methods for measuring minimum horizontal stress during hydraulic fracturing and injection tests [5]. The paper [3] presents a review of the current state of these methods, and emphasizes that there may be situations in which the standard methods of assessing the stress state of rocks based on logging data analysis are inapplicable, and therefore there is a demand for the development of alternative methods of such assessment.

This paper is devoted to the development of one of such methods—a method for estimating current stresses in a rock mass based on analysis of natural fractures. This approach was firstly proposed in paper [6], the authors of which used information on the natural fractures in rocks of the near-wellbore zone to estimate the values of the principal horizontal stresses. This approach is based on field observations of natural shear fractures in the vicinity of wells developing hydrocarbon fields [7, 8]. It was found that hydraulic conductivity of natural shear fractures is related to the relationship between normal and tangential stresses acting on their planes. In Barton et al. [7], the concept of critically stressed fractures was formulated: such fractures are defined as those with normal stresses σ_n and tangential stresses τ_n acting on their planes, satisfying the criterion $\tau_n \geq \mu\sigma_n$, where μ is the friction coefficient of the rock. This observation has been confirmed by additional studies in different regions and at different scales [9–14], but has been found to be exceptionally affected by the critical effect of temperature on the hydraulic conductivity of natural shear fractures [15] and complex history of stress state change [16]. Nevertheless, in most cases, the above condition can be used as a criterion for the hydraulic conductivity of natural fractures [10], which made it possible to formulate the inverse problem of estimating the stress state of the geological medium based on the analysis of the hydraulic conductivity of natural shear fractures [6, 17].

Within the framework of the mentioned approach, hydraulic conductivity of natural fractures in rocks of the well surrounding rock mass is analyzed on the basis of well logging data, which can include consideration of local extremes of the temperature field caused by fluid flow along the fracture [6], or joint analysis of dynamic mechanical properties and electrical resistance of the host rock [17]. Based on the expression of geophysical indicators of hydraulic conductivity, natural fractures are classified on the basis of conductivity. Further, a set of parameters defining

the stress state of the rock mass is introduced. Studies [6, 17] were performed under the assumption that one of the axes of the natural stress tensor is vertical. In reservoir geomechanics, such an assumption is conditioned by the fact that the free surface of the Earth's crust can be assumed free from external loads that are much smaller than tectonic forces and gravity [4]. In such a case, vertical stress acting in the rock mass (in this paper we will consider effective stresses that take possibility of fluid saturation into account) is governed by the weight of overlying rocks and can be estimated relatively easily. Under this assumption, three of the six independent components of the stress tensor remain significant, often associated [3] with the magnitudes of the minimum and maximum horizontal stresses and the direction of one of them. The principal stresses directions were not considered in Ito et al. [6], Dubinya and Ezhov [17]: in these works, either two relations between principal horizontal stresses and vertical stress [6] or two principal horizontal strains corresponding to additional compression of the medium due to the presence of horizontally oriented tectonic forces [17] were used as parameters determining the stress state. In Dubinya and Ezhov [17], it was found that the problem of estimating even two stress state parameters based on the analysis of natural fracturing is incorrect because it may have a domain of equivalent solutions. Moreover, the results of Dubinya and Tikhotskiy [18], whose authors considered the problem of estimating the stress state from synthetic data, demonstrate that the solution of the inverse problem is unstable when artificial noise is introduced into the initial data on the hydraulic conductivity of natural fractures. At the same time, it was proved that the domain of equivalent solutions of the inverse problem of horizontal stress estimation from natural fracture data contains the "true" solution, which provides a perfect agreement between hydraulically conductive and critically stressed fractures, if the inverse problem is correctly formulated.

Recent results in the field of critically stressed fracture analysis [19] demonstrate that the usage of the hypothesis of verticality of one of the principal axes of the in-situ stress tensor is not necessary. The problem can be considered in the general form of estimation of six independent parameters characterizing stress state of a rock mass, as was successfully demonstrated in a study of field data [20], whose authors extended the algorithm for solving the inverse problem used in Ito et al. [6], Dubinya and Ezhov [17], Dubinya and Tikhotskiy [18] to the case of reconstruction of all components of the stress tensor without assumptions on its shape. Nevertheless, the question of how much the increase in the number of unknown parameters affects the stability of the inverse problem solution and its sensitivity to errors in the interpretation of natural fracture data remains open.

This paper is devoted to the solution of this question. Following the algorithm for formulating and solving the inverse problem for estimating stress state of a rock mass based on the analysis of natural fractures [18], we construct a synthetic fracture model for an arbitrary stress tensor. The analytical solution for critically stressed fractures [19] is used to classify the fractures corresponding to a given stress state. Next, a search for this classification is performed according to the approach of Zhang et al. [20] based on an artificially noised initial fracture classification. The comparison of the initial stress state corresponding to the "clean" data and the solutions of the

inverse problem using the noisy data allows us to draw conclusions about how much the accuracy of stress reconstruction significantly decreases when departing from the hypothesis of verticality of one of the principal axes of the natural stress tensor.

2 Inverse Problem

Next, we briefly present the algorithm for formulating and solving the inverse problem of estimating stress state parameters, which is described in detail in Dubinya and Tikhotskiy [18]. It should be noted that when solving this problem, the best match between the classifications of natural fractures based on hydraulic conductivity and critical stress is sought. In the mentioned paper, several different definitions of such correspondence were proposed—for the purposes of the current study it was decided to limit ourselves to one of them, which is the most suitable for the case of exhaustive information on the properties of natural fractures.

The algorithm proposed in Ito et al. [6] and supplemented in Dubinya and Tikhotskiy [18], Zhang et al. [20] for solving inverse problem of estimating stress state of the medium on the basis of natural fracture analysis consists of four steps.

1. A certain rock mass is considered. As a rule, well studies characterize fractures only in the rocks of the near-wellbore zone, so the position of the fracture in space is determined by just one coordinate—the coordinate along the wellbore or depth. The depth interval under consideration, where natural fracture information is present, is divided into many intervals, each of which contains one fracture.
2. Each selected depth interval is characterized by a certain anomaly index, reflecting the degree of anomalousness in logging data obtained in this interval. It is possible to introduce the concept of geophysical indicator—a certain property of the rock in the vicinity of the observed fracture, characterizing its ability to conduct fluid. As mentioned above, such an indicator can be temperature [6] or a combination of mechanical and electrical properties of the rock [17]. To determine the degree of anomaly, the measured and average value of the geophysical indicator can be considered:

$$p_j = y(z_i)/y_{mean}(z_j), \tag{1}$$

   where $y(z)$ is the profile of geophysical indicator y along the well trajectory as a function of the coordinate along the well z (depth, if the well is vertical); z_j is the coordinate of the j-th fracture; $y_{mean}(z_j)$ is the indicator y value in the vicinity of the j-th fracture, averaged in a certain sliding window.
3. Simplifying assumptions about the form of the stress tensor are introduced. It is assumed that principal stress directions do not change over the depth interval under consideration, and the relations between the principal stress values remain constant. A finite set of parameters characterizing the stress state and the ranges of variation of these parameters are determined as described below. The set of

parameters characterizing the stress state will be further denoted as σ, and the stress tensor $\boldsymbol{\sigma}$ calculated from it will have components σ_{km} ($k, m = 1, 2, 3$). For each crack located at a known depth, with a known spatial orientation, the normal σ_n and shear τ_n stresses can be calculated for each combination of parameters that define the stress state σ:

$$\mathbf{t} = \sigma \cdot \mathbf{n}, \quad \sigma_n = (\sigma \cdot \mathbf{n}) \cdot \mathbf{n}, \quad \tau_n = \sqrt{\mathbf{t} \cdot \mathbf{t} - \sigma_n^2}, \tag{2}$$

where $\boldsymbol{t}$ is the stress vector acting on the fracture plane, σ is the stress tensor on its depth, $\boldsymbol{n}$ is the unit normal vector to the fracture plane. In this case, for each admissible combination of parameters characterizing the stress state of the medium σ, a stress state index $m_j(\sigma)$ can be introduced for each j-th crack as:

$$m_j(\sigma) = \tau_n / \sigma_n. \tag{3}$$

4. If the hypothesis that there is a relationship between the ratio of shear and normal stresses on the fracture plane and the degree of its hydraulic conductivity is true, then there should be a correspondence between the anomaly index p_j and the criticality index $m_j(\sigma)$. An optimization problem is considered: it is necessary to find such a set of stress state parameters σ, at which the best match between critically stressed and hydraulically conductive fractures was observed. In Ito et al. [6], Dubinya and Tikhotskiy [18] and Zhang et al. [20], the objective function R was defined as the angle between the N-dimensional (N is the number of considered fractures) vectors $\boldsymbol{P}$ and $\boldsymbol{M}(\sigma)$, with $P_j = p_j – p_a$, $M_j(\sigma) = m_j(\sigma) – m_a(\sigma)$, $j = 1 \ldots N$ respectively. Here, the parameters p_a and $m_a(\sigma)$ refer to the indicators (1) and (3) averaged over the whole ensemble of considered fractures. The measure of correspondence between the classifications for hydraulic conductivity (1) and stress state (3) is defined as the angle between these vectors

$$R(\sigma) = \frac{\mathbf{P} \cdot \mathbf{M}(\sigma)}{|\mathbf{P}| \cdot |\mathbf{M}(\sigma)|}. \tag{4}$$

The maximum of the objective function R is searched for all possible combinations of parameters σ defining stress state. The combination of the stress state parameters corresponding to the maximum R is taken as the solution of the inverse problem, which completes the stepwise algorithm of its solution.

As mentioned above, the situation when the combination of parameters σ includes more than two parameters is of considerable interest, and all components of the stress tensor may be different from zero in the coordinate system associated with gravity direction. In this paper, following the approaches implemented in studies [19, 20], the stress state is defined by five independent parameters: three Euler angles θ_1, θ_2 and θ_3, the ratio between the magnitudes of the maximum and minimum principal stresses $N_\sigma = \sigma_1/\sigma_3$, and the Lode-Nadai coefficient $\varphi_\sigma = (\sigma_2 – \sigma_3)/(\sigma_1 – \sigma_3)$. Here σ_1 is the maximum principal stress (compressive stresses are considered positive), σ_2

is the intermediate principal stress, and σ_3 is the minimum principal stress. It should be noted that the linearity of expressions (2) and (3) leads to the fact that during the solution of the inverse problem all principal stress magnitudes can be determined with accuracy to the real multiplier—within the framework of this work we normalize to the minimum principal stress σ_3, which is assumed to be unit.

The use of Euler angles in Dubinya [19] and Zhang et al. [20] was due to the need to analyze the rotations of the principal axes of stress tensor without changing principal stress magnitudes. The following definition of the stress tensor $\boldsymbol{\sigma}$ was proposed: we introduce an initial stress tensor $\boldsymbol{\sigma}_0$ having the same principal stresses as of tensor $\boldsymbol{\sigma}$ directed in a special way. The maximum principal stress σ_1 of the initial stress tensor σ_0 is assumed to act vertically; the intermediate principal stress σ_2 acts in the North–South direction, and the minimum principal stress σ_3 acts in the East–West direction. A coordinate system associated with the same directions is used within the work. Then, three consecutive rotations of the stress tensor are performed: initially, the first and second principal axes are rotated clockwise around the initial direction σ_3 by an angle θ_1; next, the first and third principal axes of the stress tensor are rotated by an angle θ_2 around the current direction of the maximum principal stress direction σ_1; finally, the first and second principal axes of the stress tensor are rotated again around the current direction of the minimum principal stress direction. The variation of Euler angles in the range $[0; \pi]$ allows the stress tensor to be defined with given principal stress magnitudes and arbitrary principal axes [19, 20].

The question of the ranges of variation of the stress state parameters σ deserves a separate attention, which is beyond the scope of this paper. While the range of possible values of the Lode-Nadai coefficient φ_σ remains $[0; 1]$ by definition, the ratio between the maximum and minimum principal stress magnitudes N_σ can in general take any real values higher than one. The maximum value of this parameter is determined by the strength properties of the rock and can be determined, for example, from the Mohr–Coulomb criterion [2]. Within the framework of this methodological study, it was decided not to consider the influence of the strength of the medium on the maximum value of N_σ—this will be done in further studies—and to limit it to the value of 5, consistent with the ideas about the stress state of the upper layers of the Earth's crust and characteristic stresses at the depths of mineral deposits.

Thus, if for a certain set of natural fractures the anomaly indices of rock properties characterizing the hydraulic conductivity of fractures (1) can be determined on the basis of certain geophysical studies, the problem of searching for such a set of parameters characterizing the stress state of the array σ, at which the objective function (4) reaches its maximum, can be set and solved. Then, we set the task of creating a synthetic model of fractures, which can be used to test whether this approach is able to recover the predetermined parameters of the stress state from 'clear' data—for the case in which there is a linear relationship between the degree of expression of the anomaly index p_j and the stress state index $m_j(\sigma)$. Further, the synthetic data are noised, which corresponds to the presence of a confidence interval within which we can speak of a linear relationship between the two indices. The case of nonlinear relationship between the indices is of separate interest, but such a study can be considered as the next stage of this work.

3 Synthetic Model

To analyze the stability of the solution to the inverse problem using the algorithm described in the previous section, we decided to create a synthetic model of fractures. First of all, the assumption of a linear dependence of vertical stress on depth was introduced, which agrees well with the characteristic fluctuations of the density determining its value against the background of its typical values. In this case, if the ratio between the maximum and minimum principal stresses N_σ and the Lode-Nadai coefficient φ_σ remain constant over the depth interval under consideration, the dependence on depth disappears, since all components of the stress tensor appear linearly proportional to it, and expressions (2) and (3) are linear with respect to stress. Thus, without limiting generality for the case of constant N_σ and φ_σ, we can proceed to the case where all cracks are at the same depth.

The next assumption relates to the spatial orientations of the cracks. In Dubinya and Tikhotskiy [18], a synthetic model of fractures was created from the assumption that the normals to natural cracks should obey a Fisher distribution with expectation at the point of maximum ratio of tangent and normal stress. Although this variant is more appropriate for geological conditions, in this paper it is the mathematical analysis of the stability of the solution of the uncorrected inverse problem that is of interest. In this regard, it was decided to create a synthetic model of fractures whose normals are uniformly distributed throughout the solid angle. A fracture model containing $N = 325$ cracks was created: the lower hemisphere was divided by a grid with a step of 10 degrees, each node of the grid was taken as a pole to a separate crack. Then a certain "true" stress state σ^* was selected, characterized by the parameters: $\theta_1{}^* = 45^\circ$, $\theta_2{}^* = 32^\circ$, $\theta_3{}^* = 24^\circ$, $\varphi_\sigma{}^* = 0.41$, $N_\sigma{}^* = 2.2$. If the relationship between the anomaly index and the stress state index is linear, the hydraulic conductivity should be determined by expression (3) for the parameters σ^*. Thus, the anomaly index was calculated for each fracture as:

$$p_j^* = m_j(\sigma^*). \tag{5}$$

Figure 1a shows an equal-area Lambert projection of the lower hemisphere, where the value of the calculated index $p_j{}^*$ corresponding to the "true" stress state σ^* is marked in colour. The region between the fractures is filled according to the results of building an auxiliary fracture model with a smaller step size, which does not take part in further analysis.

The noisy model, in which each value of the anomaly index calculated by expression (5) is modified, is of considerable interest for analysis. A parameter L is introduced, which characterises the degree to which the original data are noisy. Instead of the anomaly index $p_j{}^*$ determined by expression (5), the noisy index is used $p_j{}^L$:

$$p_j^L = p_j^*(1 + Lq), \tag{6}$$

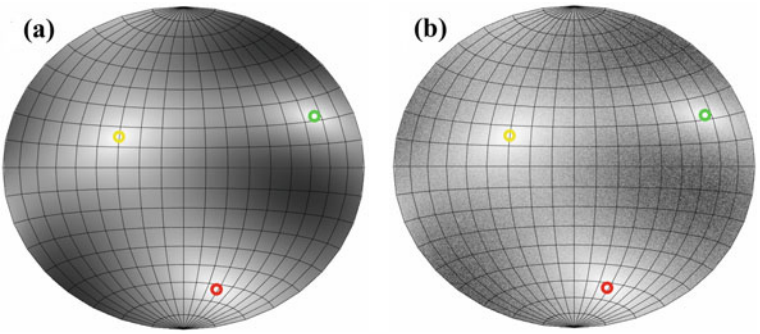


Fig. 1 **a** Anomaly index distribution along the projection of the lower unit hemisphere for the "true" stress state; **b** anomaly index for the noisy model. The red dot shows the direction of maximum principal stress, yellow is for intermediate principal stress, green is for minimum principal stress

where the value q is uniformly distributed on the interval $[-1; 1]$. An example of one realisation of the corresponding p_j^L index distribution for a noise level of 0.3 is shown in Fig. 1b.

The algorithm described above for estimating the stress state parameters was applied to the set of realisations of the noisy fracture models. The main purpose of the study was to analyse the stability of the solution of the inverse problem with respect to the noise of the original data, so two parameters were considered: the maximum obtained value of the objective function $R_{\max}$ and the difference between the obtained solution of the inverse problem and the "true" stress state parameters D. Firstly, such an error was determined in the five-dimensional space of parameters defining the stress state:

$$D = \frac{1}{5}\sqrt{\left(\varphi_\sigma^c - \varphi_\sigma^*\right)^2 + \left(N_\sigma^c - N_\sigma^*\right)^2 + \sum_{n=1}^{3}\left(\sin\theta_n^c - \sin\theta_n^*\right)^2}, \tag{7}$$

where the upper index c corresponds to the set of parameters defining the stress state at which the maximum of the objective function $R_{\max}$ is achieved. The main result of the study is the dependence of these two parameters on the noise level L. The possibility of separate consideration of the error in determining the values of the principal stresses D' was also considered:

$$D' = \frac{1}{2}\sqrt{\left(\varphi_\sigma^c - \varphi_\sigma^*\right)^2 + \left(N_\sigma^c - N_\sigma^*\right)^2} \tag{8}$$

and errors in determining their directions D_1, D_2 and D_3, equal to the angles between the estimated and true directions of the maximum, intermediate and minimum principal stresses, respectively.

4 Results

In the course of solving the inverse problem of reconstructing stress state parameters based on the analysis of natural fractures, a series of Monte Carlo simulations were performed: five parameters—three Euler angles, the ratio between the maximum and minimum principal stresses, and the Lode-Nadai coefficient—were randomly selected from the intervals of permitted values. For each realisation, the objective function between the corresponding fractures classification according to expression (4) and the original classification corresponding to the original stress state parameters according to expression (5) was determined. Then, among all realisations, the one for which the maximum value of the objective function $R(\sigma)$ was achieved was selected. Expressions (7) and (8) were used to calculate the error in the determination of the stress state parameters. In order to be able to speak about statistical regularities of the influence of noise of the initial data on the accuracy of the inverse problem solution, several Monte Carlo simulations were performed for each noise level L from 0.0 to 0.3 (with the maximum ratio of tangential stress to normal stress being 0.4. for the selected "true" stress state).

Figure 2 shows the dependence of the maximum value of the objective function $R_{\max}$ on the noise level L obtained after a series of simulations. First of all, it should be noted that even the noise level $L = 0.0$ does not make it possible to determine the combination of the stress state parameters accurately, to ensure a perfect match between the classifications based on hydraulic conductivity and stress state. This is due to the use of the Monte Carlo method to solve the inverse problem: there is no guarantee that the combination σ^* will be selected among the randomly determined five parameters. This problem can be solved by applying other methods for solving the inverse problem, which can be the subject of further research. Further, it can be seen that as the noise increases, the value of the maximum obtained objective function decreases, which is consistent with the general ideas about the nature of the effect of the deterioration of the initial data on the quality of the solution of the inverse problem. At the same time, the maximum and minimum values of the objective function shown by the dotted lines for five realisations corresponding to the same noise level L but different values of the random variable q diverge as the noise level increases. This indicates that even relatively strong noise of the initial data can lead to the fact that the solution of the inverse problem provides a sufficiently high correlation between the hydraulic conductivity of the fractures and the ratio of tangential and normal stresses acting on their planes. The solid line shows trend determined from the average magnitude of the objective function obtained from five realisations.

Figure 3 shows a similar dependence of the error D in determining the solution of the inverse problem calculated by expression (7) on the noise level. As in the previous case, even zero noise level does not provide zero difference between the obtained solution of the inverse problem and the "true" set of stress state parameters σ^*. It can be seen that the increase in the noise level also leads to an increase in both average error obtained for different values of the random parameter q and the spread

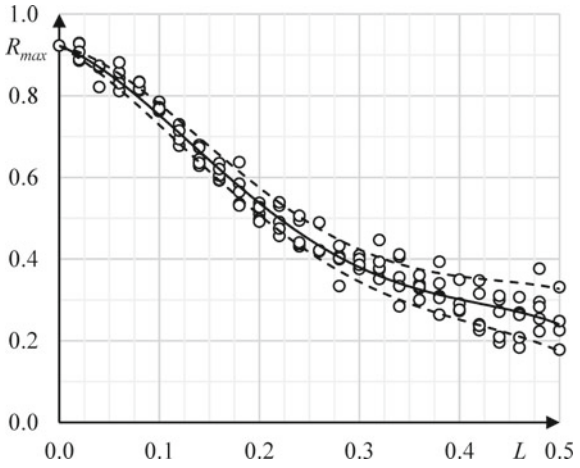


Fig. 2 Effect of input data noise on the maximum value of the objective function among multiple realisations

of these errors: there is a possibility that even a strong noise in the initial data will lead to the fact that the realisation with stress state parameters close to the "true" ones will be accepted as a solution of the inverse problem; on the contrary, there is a possibility that even a slight noise in the initial data will lead to an increase in the error in determining the stress state parameters.

Despite the fact that Fig. 3 allows us to estimate to some extent the accuracy of the solution of the inverse problem as a whole, the question of the relative accuracy of determining individual parameters—the directions of principal stresses and their magnitudes—remains open. For such an analysis, the errors in determining the principal stress directions D_1, D_2, D_3 (corresponding to the maximum, intermediate and minimum principal stresses) and the value D', which determines the error in determining the type of stress ellipsoid according to expression (8), are presented in Fig. 4

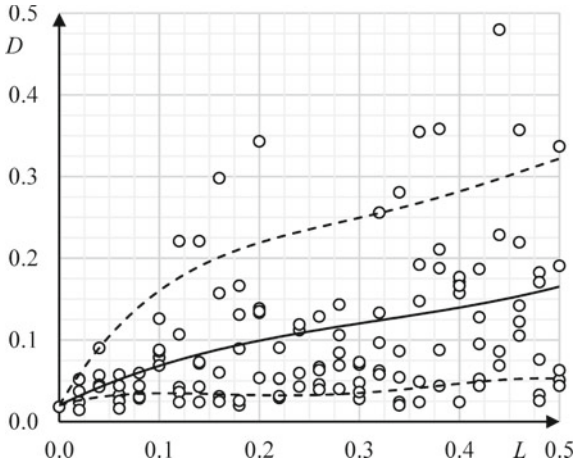


Fig. 3 Effect of source data noise on the overall error in the reconstruction of stress state parameters

in a manner similar to Fig. 3, the captions in the figures indicate which error is being considered. The differences in the accuracy of the determination of the principal stress directions are of interest: there is a tendency for the direction of the minimum principal stress to be determined somewhat more consistently compared to the intermediate and maximum principal stresses. This effect was previously observed in Dubinya [19]: a peculiarity of the distribution of the ratio between the tangential and normal stresses over a unit sphere is that this ratio reaches a maximum in a symmetric region close to the direction of the minimum principal stress. This effect can be particularly observed in Fig. 1a, where areas of increased ratio of tangential stress to normal stress corresponding to a darker fill tone are observed. In the case when the Lode-Nadai coefficient is close to zero or unity, this region acquires a central symmetry, which practically deprives the possibility of independent estimation of the directions of intermediate and maximum principal stresses, whereas the direction of the minimum principal stress is determined quite accurately even with significant noise of the initial data. The unconditional advantages of the described method for assessing the state of the medium include the fact that the directions of principal stresses are reconstructed with a sufficiently high degree of accuracy as the characteristic error is 10–20°, which is comparable to the accuracy of such classical methods for assessing the directions of the axis of maximum horizontal compression as analyses of wellbore breakouts and drilling induced tensile fractures [2, 4, 5].

5 Discussion

The results presented above correspond to one of the simplest cases that arise when attempting to reconstruct the stress state of a medium from natural fractures analysis. It was noted above that one of the main provisions used in the construction of a synthetic model of natural fractures was a linear relationship between the hydraulic conductivity of a natural fracture and the ratio between shear and normal stresses acting on its surface. The noise introduced in the study was set a priori to be uniform, which implies that this linear relationship may be broken for individual fractures, but the overall linear trend is preserved. At the same time, it can be said [6, 17] that such dependence may be nonlinear. It can be expected that the violation of the linear dependence will lead to a change in the results of the study similar to the one carried out. Nevertheless, there are reasons to assume that the main highlighted trends, namely, non-linear growth of the error and drop in the maximum magnitude of the objective function, as well as a more stable reconstruction of the direction of the minimum principal stress, will persist, which is consistent with the recent results of the hydraulic conductivity study of natural fractures [19] and stress state reconstruction based on borehole fracture studies [20].

It is also worth noting that the relationship between the hydraulic conductivity of a natural fracture and the stress state can be redefined within the concept of critically stressed fractures. According to the original studies [7], a natural shear fracture can

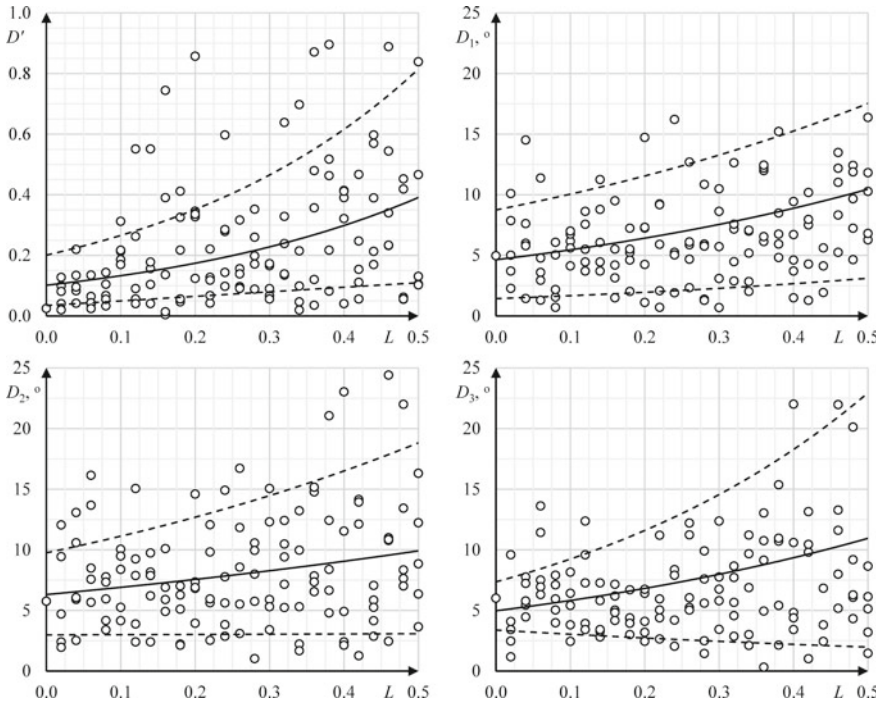


Fig. 4 Effect of source data noise on error in reconstruction of individual stress state parameters

be expected to be hydraulically conductive if and only if the condition is fulfilled:

$$\tau_n \geq \mu\sigma_n, \tag{9}$$

where μ defines the friction coefficient of the medium. Using this expression, the difficulties with the nonlinearity of the relationship between the hydraulic conductivity of the fracture and the relationship between the stresses acting on its surface disappear. As shown in Dubinya and Tikhotskiy [18], this approach makes it possible to replace indices (1) and (3) by binary indices, leading to the possibility of alternative definitions of the objective function used in various studies [6, 17]. Nevertheless, it was shown in Dubinya and Tikhotskiy [18] that the use of continuous indices (1) and (3) provides the best solution to the inverse problem, which led to the definition of these indices within this methodological study.

At the same time, reference to criterion (9) opens up additional possibilities for assessing the state of the geological environment. The friction coefficient μ can be considered as an additional parameter varying in the range [0; 1], which can supplement the set of reconstructed parameters σ. In this case, the range of equivalent solutions of the inverse problem may increase (preliminary calculations show that there is a positive correlation between the reconstructed friction coefficient and the ratio between the maximum and minimum principal stresses). Nevertheless, it becomes

possible to determine current stress state of the rock and a certain mechanical property at the same time.

On the other hand, a reduction in the number of parameters characterising the stress state parameter of the rock mass can be realised if the assumption is made that one of the axes of the stress tensor is vertical. In this case, some of the Euler angles can be equated to 0 or $\pi/2$—depending on the realised tectonic regime—and there will be only three parameters that need reconstruction. Although this assumption is often accepted in the geomechanics of mineral deposits, it can be significantly violated in zones with peculiarities of geological structure—in particular, this assumption is inadmissible when analysing subduction zones or vicinities of large faults. The study shows that this assumption is not critical for successful reconstruction of all components of an arbitrary stress tensor without any assumptions about its form. Failure to use the hypothesis of subverticality of one of the principal axes of the stress tensor only results in an increase in the calculation time, which can be overcome by using alternative methods for solving the inverse problem.

An additional question is raised by the assumption that the stress state parameters are taken constant for the rock mass under consideration. Such an assumption may be unjustified in the case when the rock mass under consideration is significantly heterogeneous at the macrolevel. In this case, it is necessary to consider the inverse problem separately for separate regions of the rock massif characterised by sufficiently unchanged mechanical properties. Such areas can be identified on the basis of petrophysical and geomechanical analyses of different-scale geophysical data, but the issue of their identification remains beyond the scope of this work.

6 Conclusions

This paper presents an analysis of the solution of the inverse problem of reconstruction of parameters characterising the stress state of a rock mass based on natural fractures analysis. Despite the fact that there are examples of successful application of this approach for stress reconstruction at specific geological objects in the literature [6, 17, 20], there is a limited number of studies devoted to the consideration of the peculiarities of the solution of this ill-posed inverse problem. In such studies, significant assumptions are made about the type of the stress state of the medium, and it is assumed that one of the principal axes of the stress tensor is vertical [18]. The results obtained in this study demonstrate that such an assumption is not critical for successful estimation of current stresses.

When reconstructing stresses based on natural fractures analysis, the question often arises as to how much an error in the interpretation of natural fractures information affects the results of the inverse problem. The study carried out in this work shows that a slight artificial noise in the original fracture data does not lead to a sharp deterioration in the accuracy of the inverse problem solution. It is interesting to note that the direction of the minimum principal stress is the most accurately reconstructed parameter; the directions of the intermediate and maximum principal

stresses are reconstructed even less accurately than the relationships between the magnitudes of the principal stresses. This feature can be explained by trends in the development of natural fractures, previously noted in the course of theoretical analytical study [19].

There are prospects for the development of the described method of assessing the stress state of the geological environment based on natural fractures analysis. Promising directions include: substantiation of the functional dependence between the hydraulic conductivity of the fracture and the ratio between the shear and normal stresses; application of alternative methods for solving the inverse problem; joint reconstruction of the parameters determining the stress state of the medium and its mechanical properties. Certainly, the described method has a number of limitations, in particular, it can be applied only to the study of media with developed natural fractures. Nevertheless, if properly developed, this approach can complement the standard methods of assessing the stress state of rocks composing the upper layers of the Earth's crust on the basis of multi-scale geophysical studies.

Acknowledgements The research was performed as part of the State assignment of Schmidt Institute of Physics of the Earth RAS. The authors are grateful to Dr. I. Bayuk for her suggestions on the main subject of the study.

References

1. Heidbach O., Rajabi M., Reiter K., Ziegler M., WSM Team. World Stress Map Database Release 2016 // GFZ Data Services. 2016.
2. Ljunggren C., Chang Y., Janson T., Christiansson R. An overview of rock stress measurement methods // International Journal of Rock Mechanics and Mining Sciences. 2003. V. 40. №7. P. 975–989.
3. Dubinya N.V. An Overview of Wellbore Methods of Investigating Stress State of the Upper Layers of the Earth's Crust // Izvestiya, Physics of the Solid Earth. 2019. V. 55. №2. P. 311–326.
4. Zoback M.D., Barton C.A., Brudy M., Castillo D.A., Finkbeiner T., Grollimund B.R., Moos D.B., Peska P., Ward C.D., Wiprut D.J. Determination of stress orientation and magnitude in deep wells // International Journal of Rock Mechanics and Mining Sciences. 2003. V. 40. №7. P. 1,049–1,076.
5. Gaarenstroom L., Tromp R.A.J., de Jong M.C., Brandenburg A.M. Overpressures in the Central North Sea: implications for trap integrity and drilling safety // Geological Society, London, Petroleum Geology Conference Series. 1993. V. 4. №1. P. 1305–1313.
6. Ito T., Fujii R., Evans K.F., Hayashi K. Estimation of Stress Profile with Depth from Analysis of Temperature and Fracture Orientation Logs in a 3.6 km Deep Well at Soultz, France // Proceedings of SPE/ISRM Rock Mechanics Conference, Irving, 20–23 October 2002. 2002. SPE Conference Paper 78185-MS.
7. Barton C.A., Zoback M.D., Moos D. Fluid flow along potentially active faults in crystalline rocks // Geology. 1995. V. 23. №8. P. 683–686.
8. Townend J., Zoback M.D. How faulting keeps the crust strong // Geology. 2000. V. 28. №5. P. 399–402.
9. Hickman S., Barton C.A., Zoback M., Morin R., Sass J., Benoit R. In-situ Stress and Fracture Permeability in a Fault-hosted Geothermal Reservoir at Dixie Valley, Nevada // Geothermal Resources Council Transactions. 1997. V. 21. P. 181–189.

10. Ito T., Zoback M.D. Fracture permeability and in situ stress to 7 km depth in the KTB scientific drillhole // Geophysical Research Letters. 2000. V. 27. №7. P. 1045–1048.
11. Rogers S. Critical stress-related permeability in fractured rocks. Fracture and in situ stress characterization of hydrocarbon reservoirs // Geological Society, London, Special Publications. 2002. V. 209. P. 7–16.
12. Ligtenberg J.H. Detection of fluid migration pathways in seismic data: implications for fault seal analysis // Basin Research. 2005. V. 17. P. 141–153.
13. Massiot C., Nicol A., McNamara D.D., Townend J. Evidence for tectonic, lithologic, and thermal controls on fracture system geometries in an andesitic high-temperature geothermal field // Journal of Geophysical Research: Solid Earth. 2017. V. 122. №8. P. 6853–6874.
14. Mattila J., Follin S. Does In Situ State of Stress Affect Fracture Flow in Crystalline Settings? // Journal of Geophysical Research: Solid Earth. 2019. V. 124. №5. P. 5241–5253.
15. Fisher Q.J., Knipe R.J. Fault sealing processes in siliciclastic sediments // Geological Society, London, Special Publications. 1998. V. 147. №1. P. 117–134.
16. Sathar S., Reeves H.J., Cuss R.J., Harrington J.F. The role of stress history on the flow of fluids through fractures // Mineralogical Magazine. 2012. V. 76. №8. P. 3165–3177.
17. Dubinya N.V., Ezhov K.A. In-situ horizontal stress estimation based on the geometrical properties of fractures in well vicinity // Geophysical Research. 2017. V. 18. №2. P. 5–26.
18. Dubinya N.V., Tikhotskiy S.A. Method for the inverse problem solution for reconstruction of stress-strain state of rock mass based on natural fractures data // Izvestiya, Physics of Solid Earth. 2022. V. 58. №4. P. 113–134.
19. Dubinya N.V. Spatial orientations of hydraulically conductive shear natural fractures for an arbitrary stress state: An analytical study of governing geomechanical factors // Journal of Petroleum Science and Engineering. 2022. V. 212. P. 110288.
20. Zhang S., Ma X., Zoback M. Determination of the crustal friction and state of stress in deep boreholes using hydrologic indicators // Rock Mechanics Bulletin. 2023. V. 2. №1. P. 100024.

Cox-Munk Model Limitations in Describing the Reflection of Sunlight on the Sea Surface



I. P. Shumeyko, A. Yu. Abramovich, and V. M. Burdyugov

Abstract Light scattering on the sea surface is determined by the level of its roughness, which depends on the statistical characteristics of local slopes. The main model in the problems of sunlight scattering at the ocean–atmosphere boundary is the Cox-Munk (CM) model, which describes the dependence on wind speed of the two-dimensional distribution of slopes and statistical moments. The CM model is based on the decomposition of the two-dimensional probability density of local slope of the surface using the Gram–Charlier series. The coefficients of the series are determined by the statistical moments of the orthogonal components of the slope. Statistical moments are known only up to and including the fourth order, therefore truncated Gram–Charlier series are used. This leads to the appearance of negative values of the probability density function at the tails of the statistical distribution. The acceptance region for the slopes of the CM model, within which it is positive, is determined. It is shown that the boundaries of this region strongly depend on the wind speed. To solve the problems of remote sensing, the boundaries of the region of permissible slope ξ were recalculated into slope angles α using the equation $\alpha = arctg\ \xi$. It has been established that the CM model is valid for light winds at surface angles α of up to ~10°, and for winds of 14 m/s up to ~25°.

Keywords Sunlight · Sun glitter · Sea surface · Slope · Cox-Munk model · Statistical moments · Gram–Charlier series

I. P. Shumeyko (✉) · A. Yu. Abramovich
Sevastopol State University, Sevastopol, Russian Federation
e-mail: shumeyko-irina-74@yandex.ru

V. M. Burdyugov
Marine Hydrophysical Institute RAS, Sevastopol, Russian Federation

© The Author(s), under exclusive license to Springer Nature Switzerland AG 2024

V. Karev (ed.), *Proceedings of the 9th International Conference on Physical and Mathematical Modelling of Earth and Environmental Processes*, Springer Proceedings in Earth and Environmental Sciences, https://doi.org/10.1007/978-3-031-54589-4_12

1 Introduction

The quantity of the information about the processes occurring in the ocean and the lower layer of the atmosphere is provided by the sounding data coming from spacecraft. The interaction of electromagnetic waves with the sea surface is determined by its roughness, one of the main characteristics of which are slopes [1, 2]. Currently, the main model describing slope distributions in problems of light scattering by the sea surface is the Cox-Munk (CM) model [3], the coefficients of which are determined from photographs of sun glitter obtained from an airplane. The CM model was created on the basis of truncated Gram–Charlier series, which represent the decomposition of the desired function by the orthogonal Chebyshev-Hermite polynomials [4].

With passive sensing in the optical range, the signal recorded on the satellite is determined by several basic physical mechanisms. This mechanisms are reflection by the sea surface of direct solar radiation, also scattered by the atmosphere of solar radiation, reflection by the sea surface in arbitrary directions of direct solar radiation, then scattered by the atmosphere towards the satellite [5]. To analyze optical images, it is necessary to know the boundaries of the regions where one or another mechanism dominates, first of all, it is necessary to know the boundaries of the sun glitter region [6].

The use of truncated Gram–Charlier series leads to distortions at the tails of the distribution, where the probability density function can take negative values [7–9]. The purpose of this work is to specify the boundaries of the region within which the CM model correctly describes the distribution of the slope of the sea surface.

2 CM Model

Various kinds of nonlinear mechanisms in sea waves lead to deviations in the distribution of sea surface slopes from the Gaussian distribution, which must be taken into account when analyzing light reflection. In the problems of light reflection by the sea surface, it is customary to distinguish two components of the slope: longitudinal, oriented in the direction of the wind and transverse. Denote these components by the indices u (upwind) and c (crosswind). In situations where expressions match both components, there is no index.

The main model describing the two-dimensional probability density function of sea surface slopes in light scattering problems is the CM model, which has the form

$$P(\xi_u,\xi_c)=\frac{1}{2\pi\sigma_u\sigma_c}\exp\left(-\frac{\tilde{\xi}_u^2+\tilde{\xi}_c^2}{2}\right)\left\{1-\frac{C_{21}}{2}H_2\left(\frac{\xi_c}{\sigma_c}\right)H_1\left(\frac{\xi_u}{\sigma_u}\right)-\frac{C_{03}}{6}H_3\left(\frac{\xi_u}{\sigma_u}\right)+\right.$$
$$\left.+\frac{C_{04}}{24}H_4\left(\frac{\xi_c}{\sigma_c}\right)+\frac{C_{40}}{24}H_4\left(\frac{\xi_c}{\sigma_c}\right)+\frac{C_{22}}{4}H_2\left(\frac{\xi_c}{\sigma_c}\right)H_2\left(\frac{\xi_u}{\sigma_u}\right)\right\}, \quad (1)$$

where σ_u and σ_c are the RMS values of the longitudinal and transverse components of the slope, the coefficients C_{ij} determine the deviation from the normal distribution, the first index refers to the crosswind component of the slope, the second to the upwind, H_n is orthogonal Chebyshev-Hermite polynomials of order n. The CM model uses polynomials H_n up to the fourth order $H_0 = 1, H_1 = x, H_2 = x^2 - 1, H_3 = x^3 - 3x$, $H_4 = x^4 - 6x^2 + 3$. The coefficients C_{ij} of the CM model, calculated from photographs of sun glitter, have the following values

$$C_{21} = 0.01 - 0.0086\ U \pm 0.03, \tag{2}$$

$$C_{03} = 0.04 - 0.033\ U \pm 0.12, \tag{3}$$

$$C_{40} = 0.40 \pm 0.23, \tag{4}$$

$$C_{22} = 0.12 \pm 0.06, \tag{5}$$

$$C_{04} = 0.23 \pm 0.41, \tag{6}$$

where U is the wind speed at an altitude of 10 m, $\pm\,\delta\ C_{ij}$ standard deviations. Photos of sun glitter, from which the coefficients were calculated, were obtained for wind speeds of less than 14.5 m/s.

The CM model contains Chebyshev-Hermite polynomials, and the use of a truncated Gram–Charlier series can lead to the probability density function becoming negative [7, 10]. Consider the distributions of the upwind and crosswind components of the slope, which correspond to the cross-sections of the two-dimensional probability density function $P_u(\xi_u) = P(\xi_u, \xi_c = 0)$ and $P_c(\xi_c) = P(\xi_u = 0, \xi_c)$. Calculated at characteristic values of the skewness (C_{03}) and the excess kurtosis (C_{04}) of the cross-section $P_u(\xi_u)$ are shown in Fig. 1.

Next, we will consider a random variable x, the variance of which is equal to one. This is equivalent to the introduction of normalization $\zeta_u = \xi_u/\sigma_u$ and/or $\zeta_c = \xi_c/\sigma_c$. To determine the boundaries of the range of values x of a random quasi-Gaussian quantity in which the probability density function is positive, it is advisable to represent this function in the form Kwon [10]

$$P(x) = N(x)\ f(x) \tag{7}$$

where $N(x)$ is the standard normal distribution; $f(x)$ is a polynomial of degree n. For the upwind and crosswind components of the slope, we will get two polynomials respectively

$$f_u(\zeta_u) = 1 + \frac{C_{40}}{8} + \frac{C_{21}}{2}H_1(\zeta_u) - \frac{C_{22}}{4}H_2(\zeta_u) - \frac{C_{03}}{6}H_3(\zeta_u) + \frac{C_{04}}{24}H_4(\zeta_u) \tag{8}$$

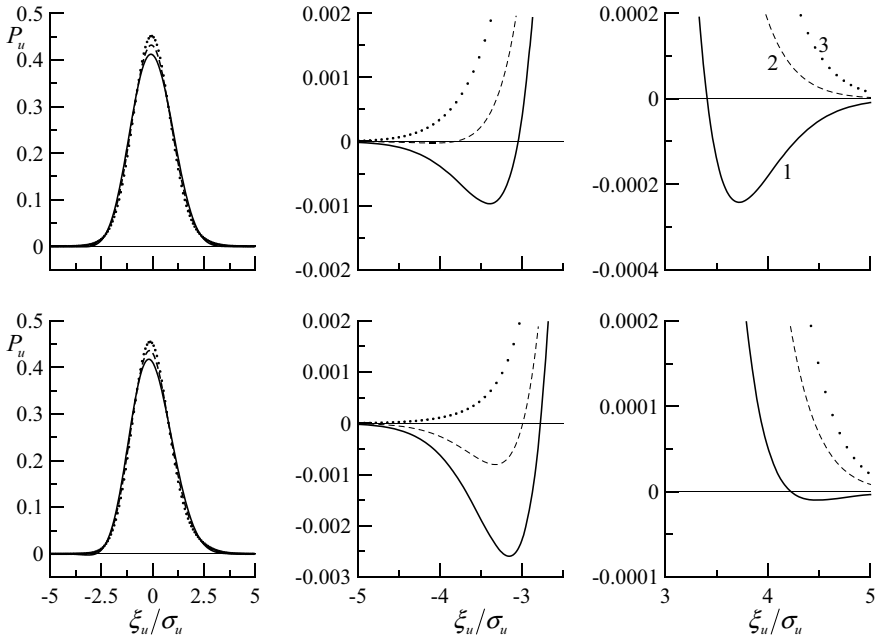


Fig. 1 Dependences of cross sections $P_u(\xi_u/\sigma_u)$ on coefficients C_{03} and C_{04}. Curves 1–3 correspond to values C_{04} equal to -0.4, 0 and 0.4. The upper fragments are obtained at $C_{03} = -0.1$, the lower fragments are obtained at $C_{03} = -0.3$

$$f_c(\zeta_c) = 1 + \frac{C_{04}}{8} - \frac{C_{22}}{4}H_2(\zeta_c) + \frac{C_{40}}{24}H_4(\zeta_c) \tag{9}$$

It is assumed that the distribution of the crosswind component of the slope is symmetrical with respect to the wind direction. Therefore, the polynomial $f_c(x)$ is an even function.

The degree of a polynomial $f(x)$ is determined by the degree of the oldest of the Chebyshev-Hermite polynomials. In the CM model, the degree of the senior polynomial is four. To find the boundary of the region inside which $P(x) > 0$, it is necessary to find the roots of the polynomial $f(x)$.

3 The Boundary of the Region of Negative Values $P(x)$

Distortions on the tails of the distributions of the slope components occur in the region where the condition $\xi > 2.5\sigma$ is fulfilled [3]. In this area, the contribution to Eqs. (8) and (9) terms proportional to the mixed coefficients C_{21} and C_{22} is small. The main parameters defining the roots of the polynomial $f(x)$ for upwind component of the slope are the coefficients C_{03} and C_{04}, for crosswind component a parameter

is the coefficient C_{40}. A sufficient and necessary condition for the existence of real roots of a polynomial $f_c(\zeta_c)$ is the fulfillment of the inequality $C_{40} < 0$. The roots of a polynomial $f_u(\zeta_u)$ can also exist at $C_{04} > 0$, if the absolute value C_{03} is large enough.

Let's introduce the notation, ζ is a boundary of the region of negative values $P(x)$. The dependencies $\zeta_u = \zeta_u(C_{04})$ are shown in Fig. 2. Inthe calculations, the coefficient C_{03} varied within the limits in which it changes at sea.

The boundaries ζ_c of the region of negative values of the probability density function of the transverse component of the slope are shown in Fig. 3. Since the polynomial (9) is an even function, its roots in the region of negative and positive slope values are equal in modulus. Note that the roots of the polynomial (9) practically coincide with the roots of the polynomial (8) obtained under the condition $C_{03} = 0$ (curve 1 in Fig. 2).

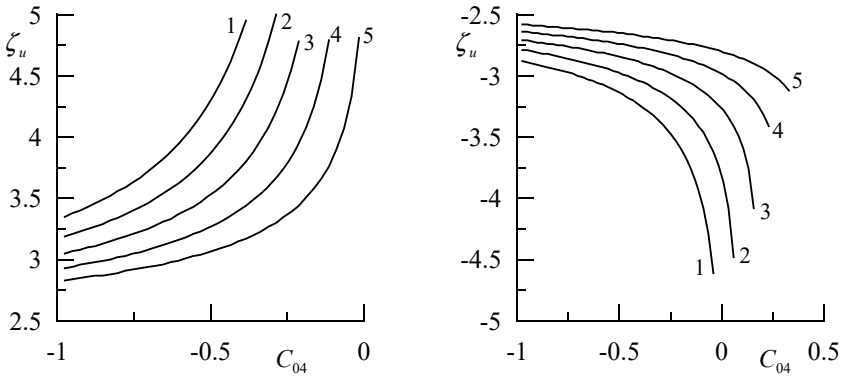


Fig. 2 Boundaries ζ_u of the region of negative values P_u. Curves 1–5 correspond to a change C_{03} from 0 to −0.4 instep of 0.1

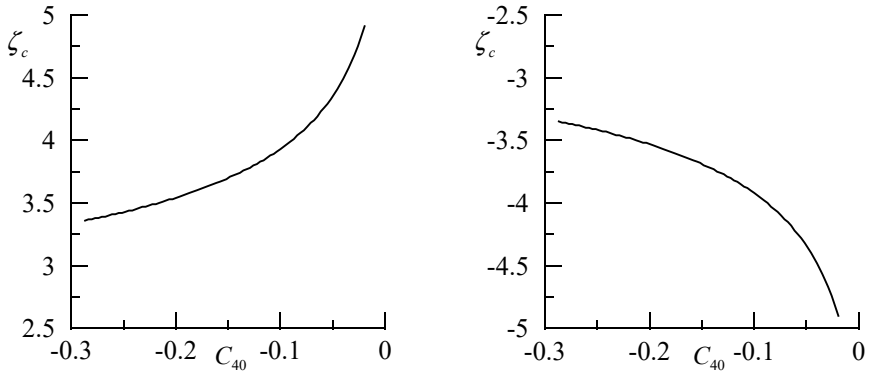


Fig. 3 Boundaries ζ_c of the region of negative values P_c

4 Critical Angles of the Sea Surface Slope

In the problems of scattering sunlight on the sea surface, along with slopes ξ, which are the first spatial derivative of surface elevations, it is necessary to know the angles of inclination α. The slope ξ and angle α are interconnected by a nonlinear relationship $\alpha = arctg\,\xi$. Since the slope are small, numerical equality is usually assumed $\alpha \approx \xi$, where the dimension of the angle is a radian. When analyzing optical images of the sea surface, the bidirectional reflectance distribution function is widely used, the arguments of this function are the angles of incidence and reflection of sunlight [6]. The critical slope angles for the CM model hereafter mean the angles corresponding to the slopes ζ_u and ζ_c.

The level of roughness of the sea surface increases with increasing wind speed [11, 12]. To move from the dimensionless roots of the polynomials (8) and (9) to the slope angles, we first use the relations obtained for the CM model, which relate the variance of the slopes and the wind speed U.

$$\sigma_u^2 = 0.000 + 0.00316\,U \pm 0.004, \tag{10}$$

$$\sigma_c^2 = 0.003 + 0.00192\,U \pm 0.002. \tag{11}$$

Then we convert the slope into an angle.

According to the slope measurements carried out using different types of equipment, it was found that the coefficient C_{03} depends on the wind speed, the coefficients C_{04} and C_{40} do not depend on the wind speed [3, 13]. Since the scattering of electromagnetic waves by the sea surface is determined by the level of its roughness, the lack of connection between the wind speed and the coefficients C_{04} and C_{40} is one of the factors that do not allow unambiguously restoring the speed of the wind according to remote sensing data from the satellite. The angles of incidence and reflection in remote sensing are usually in degrees, so it is also advisable to express the values of critical angles in degrees.

The dependences on the wind speed of the critical angles α_u and α_c, calculated for several characteristic values C_{04} and C_{40} are shown in Fig. 4. The lowest critical values of the angles α_u and α_c are at low winds, where they are approximately equal to 10°. It should be noted that the range of wind speeds 1–4 m/s is characterized by the sharpest change in the dispersion of the slope components and its modulus [12]. With a weak wind, slicks of natural origin appear, in which short waves, which make the main contribution to the variance of slopes, are suppressed [14, 15]. This circumstance was not taken into account in the CM model, and it can be expected that the permissible values for a weak wind will be below 10°.

Thus, the CM model cannot describe the distribution of sea surface slopes, which corresponds to the entire range of sensing angles. It is necessary to build an alternative model that is free from the described disadvantages of the CM model. One of the possible solutions to this problem is the use of a two-component Gaussian mixture,

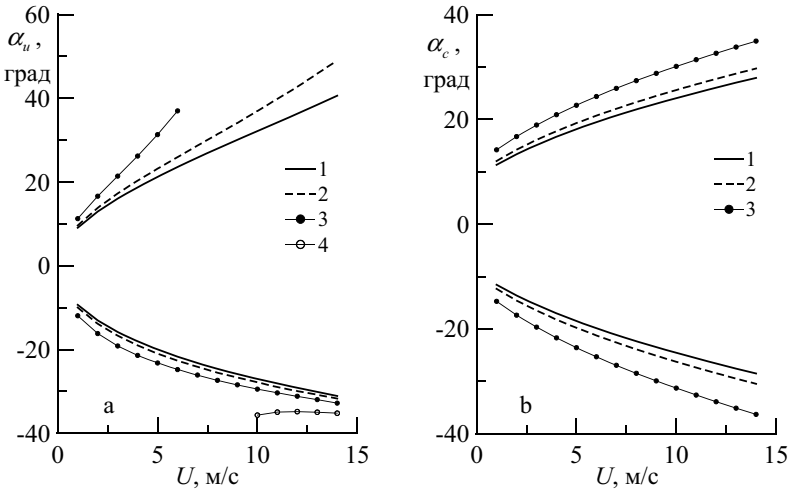


Fig. 4 Dependences on wind speed U of the critical slope angles of the sea surface for the CM model: a is dependence $\alpha_u = \alpha_u(U)$, curves 1–4 correspond to a coefficient C_{04} varying from $\overline{C_{04}} - 3\ \delta C_{04}$ to $\overline{C_{04}}$ with a step δC_{04}; b is dependence $\alpha_c = \alpha_c(U)$, curves 1–3 correspond to a coefficient varying from $\overline{C_{40}} - 3\ \delta C_{40}$ to $\overline{C_{40}} - \delta C_{40}$ with a step δC_{40}

the unknown parameters of which are also calculated from known statistical moments [16, 17].

5 Conclusion

In the analysis and interpretation of optical images obtained during sounding from spacecraft, the CM model describing the distributions of sea surface slopes is widely used. The CM model contains polynomial multipliers, which leads to distortions on the tails of the distribution, which manifest themselves as negative values of the probability density function.

The critical values of the CM model defining the boundaries of the region within which it is positive are determined. These boundaries strongly depend on the wind speed. To solve remote sensing problems, the critical slope values were recalculated into slope angles α. It is shown that with a weak wind, the CM model is valid at surface slope angle up to about 10°, with a wind of 14 m/s up to about 25°.

Acknowledgements This work was carried out as part of a state assignment on the topic No. FNNN-2021-0004 “Fundamental studies of oceanological processes that determine the state and evolution of the marine environment under the influence of natural and anthropogenic factors, based on observation and modeling methods”.

References

1. Bolshakov A. N., Burdyugov V.M., Gradsky S.A., Kudryavtsev V.N. (1988) Determination of the spectrum of energy-carrying surface waves from the image of a sun glitter // Earth Exploration from Space. (5): 11–18.
2. Zapevalov A.S., Lebedev N.E. (2014) Simulation of the sea surface statistical characteristics at the remote sensing in the optical range // *Atmospheric and Oceanic Optics.* (1): 28–33.
3. Cox C., Munk W. (1954) Measurements of the roughness of the sea surface from photographs of the sun glitter // J. Optical. Soc. America. 44(11): 838–850.
4. Kendall M.J., Stewart A. (1958) The advanced theory of statistics. Vol. I. Distribution theory. London: Butler & Tanner Ltd. 675 p.
5. Lebedev N.E. (2013) Determination of wind speed and degree of contamination of the sea surface by radiation measured by satellite optical scanners in the area of sun glint // Ekologicheskaya bezopasnost' pribrezhnoi i shel'fovoi zon i kompleksnoe ispol'zovanie resursov shel'fa. (27): 49–54.
6. Lebedev N.E., Pustovoitenko V.V., Pokazeev K.V., Melnikova ON. (2014) Simulation of the sea surface bidirectional reflectance distribution function // Sovremennye problemy distantsionnogo zondirovaniya Zemli iz kosmosa. 11(3): 310–320.
7. Blinnikov S., Moessner R. (1998) Expansions for nearly Gaussian distributions // Astron. Astrophys. Suppl. Ser. 130: 193–205.
8. Burdyugov V.M. (2022) Modeling of the shape of the reflected radio pulse of an altimeter using a truncated distribution of sea surface elevations // Processes in Geomedia. 3(33): 1724–1729.
9. Zapevalov A.S., Bol'shakov A.N., Smolov V.E. (2011) Simulating of the probability density of sea surface elevations using the Gram–Charlier series // Oceanology. 51(3): 406–413. https://doi.org/10.1134/S0001437011030222.
10. Kwon O.K. (2020) Analytic expressions for the positive definite and unimodal regions of Gram-Charlier series // Communications in Statistics-Theory and Methods. https://doi.org/10.1080/03610926.2020.1833219.
11. Apel, J.R. (1994) An improved model of the ocean surface wave vector spectrum and its effects on radar backscatter. J. Geophys. Res. 99(C8) 16269–16291.
12. Zapevalov A.S. (2002) Statistical characteristics of the moduli of slopes of the sea surface // Physical Oceanography. 12(1): 24–31. https://doi.org/10.1023/A:1014672614293
13. Bréon F.M., Henriot N. (2006) Spaceborne observations of ocean glint reflectance and modeling of wave slope distributions // J. Geoph. Res. 111(C6): C06005.
14. Shumeyko I.P., Abramovich A.Y., Burdyugov V.M. (2022) Changes in sea surface roughness in light wind // Springer Geology. (IV): 357–365. https://doi.org/10.1007/978-3-030-76328-2_37.
15. Monin A.S., Krasitsky V.P. (1985) Phenomena on the ocean surface // L.: Hydrometeoizdat. 375 p.
16. Zapevalov A.S. Knyazkov A.S. (2022) Statistical Description of the Sea Surface by Two-Component Gaussian Mixture. Physical Oceanography, 29(4): 395–403. https://doi.org/10.22449/1573-160X-2022-4-395-403.
17. Tatarskii V.I. (2003) Multi-Gaussian representation of the Cox–Munk distribution for slopes of wind-driven waves // J. of Atmospheric and Oceanic Technology. 20: 1697–1705. https://doi.org/10.1175/1520-0426(2003)020<1697:MROTCD>2.0.CO;2.

Neural Network for Seismic Waves Phase Picking Based on Wavelet Scattering



I. A. Abzalilov, N. A. Baryshnikov, and S. B. Turuntaev

Abstract Recent advances in usage of convolutional neural networks (CNNs) and attention-based models (Transformer) to solve the problem of seismic wave phase picking have generated significant interest in the topic of creating and developing deep learning models for analyzing seismic data. One of the promising directions of development in this area is usage of new approaches to extracting features from the analyzed signal, allowing to preserve its information content and at the same time simplify the process of training the model. This paper compares three methods for extracting features from a signal based on its time–frequency representation (short-time Fourier transform (STFT) on linear and mel scales, as well as the less commonly used wavelet splitting (Wavelet Scattering)) and evaluates their impact on the quality of classification seismic signal plots using the California seismic data set as an example. To do this, three similar deep learning models were created and trained using the encoder from the Transformer architecture. It is shown that Wavelet Scattering is slightly superior to STFT in the normal and mel scales in terms of the Accuracy metric. This makes this decomposition more promising in terms of the quality of seismic signal feature extraction.

Keywords Seismic · Detection · Phase picking · Machine learning

1 Introduction

The task of identifying the first arrivals of ***p*** and ***s*** waves of a seismic signal is of great importance for studying the sources of seismic events. Knowledge about arrival times for different stations afford to determine the time of the event, its coordinates, as well as the physical mechanism of the source. To date, a large number of methods

I. A. Abzalilov (✉) · N. A. Baryshnikov · S. B. Turuntaev
RAS Institute of Geosphere Dynamics, Moscow, Russian Federation
e-mail: geospheres@idg.chph.ras.ru; info@mipt.ru

I. A. Abzalilov
Moscow Institute of Physics and Technology, Dolgoprudny, Russia

© The Author(s), under exclusive license to Springer Nature Switzerland AG 2024

V. Karev (ed.), *Proceedings of the 9th International Conference on Physical and Mathematical Modelling of Earth and Environmental Processes*, Springer Proceedings in Earth and Environmental Sciences, https://doi.org/10.1007/978-3-031-54589-4_13

for identifying first arrivals have been proposed, which are actively used to solve this problem. The classic ones include the "energy" approach—the STA/LTA method [1] and the later widespread method based on the Akaike information criterion [2]. The disadvantages of these methods are the large amount of manual work required to set them up correctly, as well as the need to make this adjustment for each new study area. Modern methods using machine learning algorithms and neural networks allow us to get closer to solving these problems. Methods based on neural networks have become the most actively developed in the last decade. Similar to other areas of science and technology, the application of new neural network models to seismic signal processing was in the nature of borrowing the most advanced architectures. Currently, convolutional [3], recurrent neural networks [4] and models based on the attention mechanism are widely used [4, 5]. The task of identifying the first arrivals of a seismic signal most often comes down to the task of classification—the only difference is whether the entire event record or just a section of it is fed to the model input. Accordingly, if the output of the neural network in the first case is the distribution of the probability of the arrival of a p or s wave, and in the second—the probability of the signal segment belonging to one of the classes (p, s waves and noise). At the moment, the task of identifying first arrivals is most effectively (relative to standard methods) solved using convolutional neural networks or neural networks based on Transformer-type architectures. Due to the large number of trainable parameters, such models are quite difficult to train and have low generalization ability. It is assumed that these problems can be solved by using new approaches to extracting features from a signal, preserving its information content, but at the same time allowing to reduce the number of trained parameters. From this point of view, it is promising to replace trained convolutional layers with a fixed transformation of the signal into its time–frequency representation. The purpose of this work was to study the possibility of time–frequency representation of Wavelet Scattering (WS) [6] as a method of extracting features from a signal in a neural network model. Standard methods of representing a signal in the form of a spectrogram STFT and mel were considered as reference methods for representing a signal spectrograms (mel is a logarithmically frequency-dependent value based on the psycho-physiological perception of sound by a person) [7].

2 Wavelet Scattering Transform

The Wavelet Scattering Transform (WS) [6] procedure generates a time–frequency representation of the signal based on wavelet decomposition, somewhat similar to the result of the windowed Fourier transform. At the same time, WS has the necessary properties of resistance to distortions of the original signal, time shifts, and better preservation of information during decomposition. The WS algorithm is a sequential application of wavelet filters based on the basic Morlet wavelet with a frequency shift, which is similar to the discrete wavelet transform algorithm. The operations of taking the modulus, convolution with a Gaussian filter and averaging are applied

to the already filtered signal—this is how the first level of decomposition is formed. This operation is repeated further at the second level of decomposition until the entire frequency range is covered, and excess coefficients are discarded. Thus, each level of decomposition can be represented using the formulas:

$$S_0 = f * \phi_J$$

$$S_1 = \left\{ \left| f * \psi_{1,k} \right| * \phi_J \right\}_k$$

$$S_2 = \left\{ \left| \left| f * \psi_{1,k} \right| * \psi_{2,n} \right| * \phi_J \right\}_{k,n}$$

Here f is the original signal, ϕ_J is a filter with a window size of 2^J, * is the convolution operation, k and n are the frequency range coefficients for each level. From the point of view of neural networks, WS is analogous to convolutional layers and pooling operations. But, if in the convolutional layer the filters undergo a training procedure, then in the case of using WS they are represented by a set of wavelets, which removes the uncertainty associated with the need to train filters. The Kymatio [8] library was used as a specific implementation of WS in this work.

3 Training Data

To train the models presented in the work, we used a cleaned and labeled data set of local seismic events collected from a fairly dense seismic network of stations in southern California. The authors of the dataset included 4.5 million waveform segments labeled into three classes (***p***, ***s*** waves and noise), suitable for training machine learning models [5, 9]. To evaluate the effectiveness of frequency-waveform representations of a signal, we limited ourselves to 1 million waveforms for model training and validation. Each dataset sample includes a 4-s segment of a waveform (400 points) with a corresponding class label. The sample represented in the original data set is uniform, which was also maintained in the subsample used in the work. Preprocessing of standard seismic data for neural network training involves detrending, filtering, and labeling the data. In the case of using a spectrogram, to remove a trend from a signal, it is necessary to subtract the smoothed value of the time series, while for WS it comes down to removing the first level of decomposition. For the used data, such preprocessing is not required, but this feature of WS can simplify working with the original signal.

4 Model Architecture

The task of identifying the first arrivals in the formulation used is the task of classification of a seismic signal segments: they are classified pointwise by the model, after which the middle of the window with the highest probability for each class is considered the first arrival of the corresponding wave. The neural model used in this work is based on the Transformer architecture [10]. This architecture was originally proposed to solve the problem of machine translation, but the encoder of the original model allows you to effectively extract features from the time–frequency representation of a signal in the same way as extracting features from a vectorized representation of text. Features extracted using several encoder layers make it possible to classify seismic signals with sufficiently high accuracy [5, 9]. The model consists of a Positional Encoding layer, several Transformer Encoder layers (8 in this work) and three fully connected layers with the ReLU activation function. The total number of trained parameters is 220 thousand. The Dropout parameter for all model components is set to 0.1. The dimension of the input data is, where the first component is the channel number of the original recording, the remaining ones are the dimension of the representation along the time and frequency components, respectively. The general diagram of the model is presented in Fig. 1.

5 Model Training and Evaluation

The Adam optimizer was used to train the model with a learning rate of 0.001. The error function is the standard cross-entropy for classification problems:

$$Loss(p) = -\frac{1}{N} \sum_{n,n_class} p_{class}(x) \cdot \log(1 - p_{class}(x))$$

The batch size is 2500. The work with the models was carried out on the NVIDIA Tesla V100 graphics accelerator. To fully train one model, 50 epochs were enough. One epoch took about 5 min. The criterion for completing training was the absence of a decrease in the value of the error function over 5 epochs. The first stage of the work was the selection of optimal WS decomposition parameters. According to Andreux et al. [8], in the implementation of this algorithm in the Kymatio package, the main expansion parameters are $\boldsymbol{J}$ (2^J is the size of the averaging window) and $\boldsymbol{Q}$ (the number of wavelets per octave). The first of them is responsible for the dimension of the time component of the transformation, the second—for the dimension of the frequency component. To select the optimal set of parameters, 13 models with different parameters $\boldsymbol{J}, \boldsymbol{Q}$ were trained. The comparison was made using the Accuracy quality metric, which in the simplest case of binary classification can be represented as:

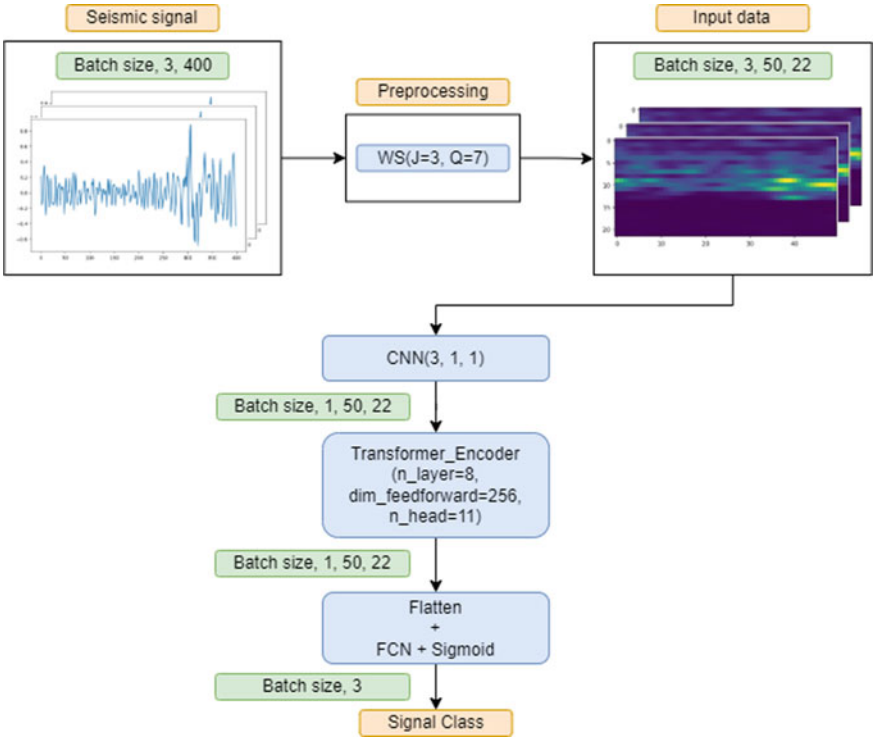


Fig. 1 Schematic diagram of the used neural network. The model takes as input a time–frequency representation of the seismic signal; it includes a convolutional layer, 8 layers of transformer architecture encoders and fully connected layers for the final classification

$$Accuracy = \frac{True\ Positive + True\ Negative}{True\ Positive + False\ Positive + True\ Negative + False\ Negative}$$

where True Positive and True Negative are the proportion of correctly classified objects of both classes, False Positive and False Negative are the proportion of false positive and false negative responses, respectively. This quality metric is easily generalized to the case of classification into a larger number of classes. As already mentioned, the decomposition parameters directly affect the dimension of the input data; accordingly, the number of trained model parameters changes. Based on the results of training the models, $\boldsymbol{J} = 3, \boldsymbol{Q} = 7$ were chosen as the optimal parameters. The complete results of training the models, as well as the dimensions of the input data, are shown in Table 1.

After the optimal WS parameters were found, two additional models were trained, taking a spectrogram and a mel-spectrogram as input, respectively, which have a similar input data dimension. The models were trained in the same way as described above. An example of input data for each of the three signal decompositions is presented in Fig. 2.

Table 1 Model training results for various WS inputs. The name of the model corresponds to the expansion parameters $\boldsymbol{J}$, $\boldsymbol{Q}$

J	Q	Input data dimension	Accuracy
3	5	[3, 50, 18]	0.9654
3	6	[3, 50, 20]	0.9666
3	7	[3, 50, 22]	0.9687
3	8	[3, 50, 23]	0.9675
4	3	[3, 25, 22]	0.9654
4	4	[3, 25, 28]	0.9661
4	5	[3, 25, 38]	0.9643
4	6	[3, 25, 39]	0.9682
4	7	[3, 25, 45]	0.9674
5	3	[3, 13, 35]	0.9648
5	4	[3, 13, 45]	0.9672
5	5	[3, 13, 55]	0.9658
5	6	[3, 13, 64]	0.9681

The result of applying the model to phase picking is presented in the Fig. 3. The highest probability value corresponds to the first arrivals of waves.

6 Results

The results of model training with input data based on various time–frequency decompositions of the seismic signal are presented in Table 2. Models were also compared using the Accuracy metric. The best result was demonstrated by the Wavelet Scattering decomposition. An additional criterion for classification quality was the probability of the class selected by the model, which expresses the degree of confidence in the correctness of the answer. When comparing the average probabilities of the predicted class, a larger value corresponded to the representation of the signal in the form of a mel spectrogram.

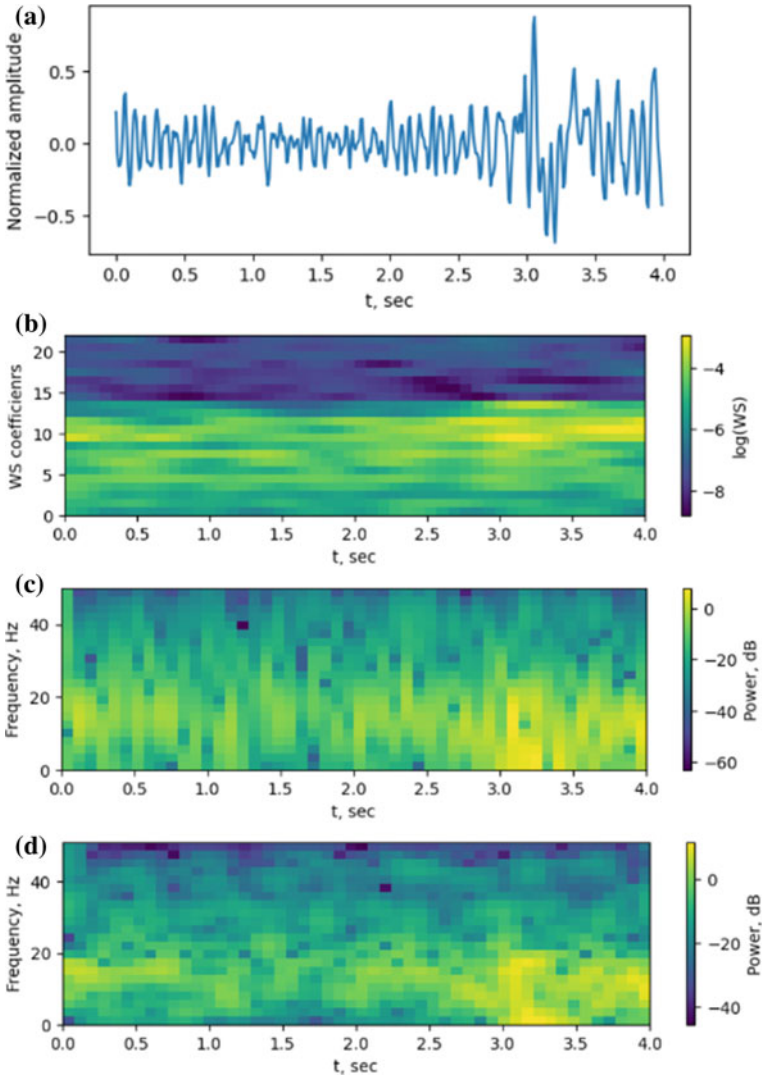


Fig. 2 An example of different time–frequency representations of the original signal (**a**): **b** Wavelet Scattering **c** Spectrogram **d** Mel-spectrogram

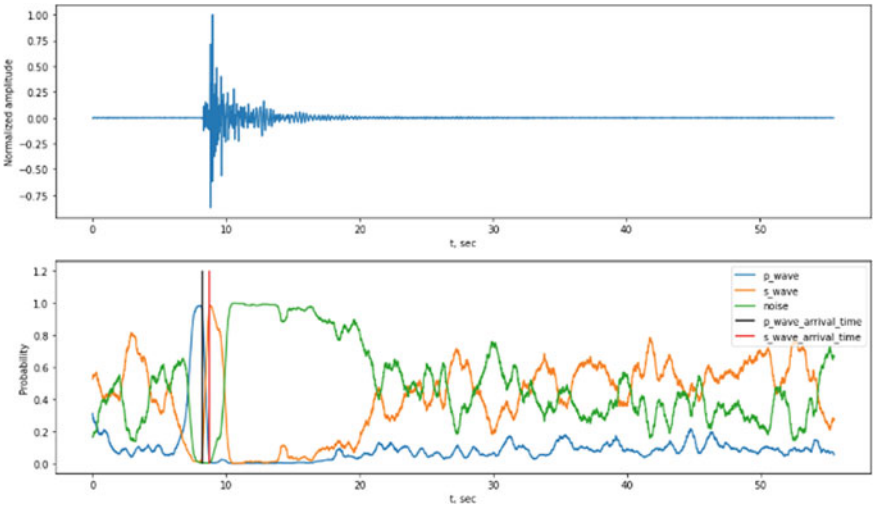


Fig. 3 An example of applying of the neural network model to ***p*** and ***s*** waves phase picking

Table 2 Assessment of the quality of seismic signal classification for various time–frequency representations

	Spectrogram	Mel-spectrogram	Wavelet scattering
Accuracy	0.9603	0.9663	0.9687
Probability	0.9634	0.9704	0.9657

7 Conclusion

The main goal of this work was to conduct a comparative study of various time–frequency representations as applied to the problem of classifying seismic signals using a deep neural network. It is shown that the Wavelet Scattering representation demonstrates greater accuracy than the standard version of the spectrogram, and for the case of the mel spectrogram it gives a result comparable to it. Thus, for the data used in this work, Wavelet Scattering does not provide a clear advantage. At the same time, for higher-frequency events associated with microseismic monitoring, the listed advantages of this signal representation over standard spectrogram options allow us to count on better quality of training of machine learning models, coupled with simplification of preprocessing of source records. All this requires additional research into the effectiveness of using Wavelet Scattering for microseismic data analysis.

Acknowledgements The work was carried out within the framework of the state assignment of the Ministry of Science and Higher Education of the Russian Federation (topic No. 122032900167-1).

Literature

1. Withers M. et al. A comparison of select trigger algorithms for automated global seismic phase and event detection // Bull. Seismol. Soc. Am. 1998. Vol. 88, № 1. P. 95–106.
2. Küperkoch L. et al. Automated determination of P-phase arrival times at regional and local distances using higher order statistics // Geophys. J. Int. 2010. Vol. 181, № 2. P. 1159–1170.
3. Zhu W., Beroza G.C. PhaseNet: A deep-neural-network-based seismic arrival-time picking method // Geophys. J. Int. 2019. Vol. 216, № 1. P. 261–273.
4. Mousavi S.M. et al. Earthquake transformer—an attentive deep-learning model for simultaneous earthquake detection and phase picking // Nat. Commun. Springer US, 2020. Vol. 11, № 1.
5. Stepnov A., Chernykh V., Konovalov A. The seismo-performer: A novel machine learning approach for general and efficient seismic phase recognition from local earthquakes in real time // Sensors. 2021. Vol. 21, № 18.
6. Andén J., Mallat S. Deep scattering spectrum // IEEE Trans. Signal Process. 2014. Vol. 62, № 16. P. 4114–4128.
7. Umesh S., Cohen L., Nelson D. Fitting the Mel scale // ICASSP, IEEE Int. Conf. Acoust. Speech Signal Process. - Proc. 1999. Vol. 1, № April. P. 217–220.
8. Andreux M. et al. Kymatio: Scattering transforms in python // J. Mach. Learn. Res. 2020. Vol. 21. P. 1–6.
9. Ross Z.E. et al. arXiv: 1805. 01075v2 [physics. geo-ph] 11 Jan 2019. Vol. 108. P. 2894–2901.
10. Vaswani A. et al. Attention is all you need // Adv. Neural Inf. Process. Syst. 2017. Vol. 2017-Decem, № Nips. P. 5999–6009.

Regularities of Spatio-Temporal Distribution of Energy Parameters of Induced Seismicity in the Development of Mineral Deposits by Field Observations and Mathematical Modeling Data

Larisa Nazarova, Nelly Miroshnichenko, and Leonid Nazarov

Abstract The concept has been substantiated and a statistical analysis procedure has been developed to identify regularities of spatiotemporal distribution of parameters of deterministic and random processes occurring in the geomechanical space of geotechnical objects at the industrial development stage. The approach consists in long time series creation describing: (1) the evolution of stress fields *S* (obtained by calculation using a verified 3D geomechanical model); (2) the number *N* and total energy *W* of seismic events caused by mining operations in various spatial blocks of the object under study. Next, the correlation coefficients between these series were calculated and statistically significant relationships *N*-*S* and *W*-*S* were revealed, which can be used for predictive estimates of the integral parameters of the seismic process. When implementing the approach, based on the induced seismicity database of the Tashtagol ore mine (Kemerovo region, Russia) and the original 3D geomechanical model (implemented by FEM), it was established that: with increasing mining depth, the centers of seismic energy release in blocks migrate towards the goaf and located, as a rule, in the ore body; at almost all mining levels, there are pairs of spatial blocks in which the total energy *W* and the number *N* of seismic events have a strong correlation with the average value of the maximum shear stress.

Keywords Induced seismicity · Rock mass · Ore deposit · 3D geomechanical model · Stress field · Mining · Regression · Seismic event energy · Long time series

L. Nazarova (✉) · N. Miroshnichenko · L. Nazarov
Chinakal Institute of Mining, Siberian Branch of the Russian Academy of Sciences, 54 Krasny Prospekt, 630091 Novosibirsk, Russia
e-mail: larisa.a.nazarova@mail.ru

© The Author(s), under exclusive license to Springer Nature Switzerland AG 2024

V. Karev (ed.), *Proceedings of the 9th International Conference on Physical and Mathematical Modelling of Earth and Environmental Processes*, Springer Proceedings in Earth and Environmental Sciences, https://doi.org/10.1007/978-3-031-54589-4_14

1 Introduction

Injection of liquefied gas into underground storage facilities [1, 2], burial of liquid and gaseous industrial waste in natural formations and worked-out space [3], development and operation of geothermal deposits [4], fluctuations in water levels in natural [5] and artificial [6] reservoirs, the extraction of hydrocarbons and solid minerals is not a complete list of processes that cause a redistribution of stresses in the geomedium and, as a consequence, an increase in the number and energy of seismic events [7, 8].

The main attention of modern quantitative seismology is focused on the analysis of earthquake seismograms in order to determine focal parameters and identify statistical spatiotemporal dependencies between parameters characterizing the seismic process [9]. The study of the role of the stress state in the evolution of seismicity in geomedium comes down, as a rule, to either assessing the principal stresses based by the mechanisms of earthquake foci and constructing Mohr's circles [10], or to establishing a statistical relation between the levels of stress and seismicity [11], which sometimes makes it possible to implement elements of the forecast [12]. This state of affairs, in our opinion, is due to the complexity of developing and verifying detailed geomechanical models that make it possible to describe the stress field of large-scale geological objects with a lack of information about the structure and properties of the latter.

The presence of a quantitative relationship between stresses and acoustic emission (AE) parameters has been proven in experiments with small-scale objects—rock samples, when the dependence of the AE count, AE count rate and total energy on the loading parameter (for example, axial stress) is close to functional [13–15]. The application of similar dependencies for mesoscale objects (mineral deposits) faces obvious difficulties due to the heterogeneity of stress fields. One of the ways to overcome such difficulties is the use of a concentration strength criterion [16], which allows, based on AE data, to localize the most probable failure zones that are associated with foci of possible dynamic events [17].

The geological structure, physical properties of rocks and the natural stress field components are determined at the stages of field exploration and design of a colliery or ore mine; changes in the configuration of the mined-out space are displayed on mining plans, so development a geomechanical model of such objects does not present technical difficulties [18, 19]. All mining enterprises are equipped with microseismic monitoring systems [20, 21], which monitor the current state and generate catalogs of dynamic events. A complex of such deterministic and stochastic information is used in this article to identify the relationship between geomechanical and seismic fields through regression analysis of long time series of microseismic emission parameters and stress fields in various parts of a medium-scale geotechnical object an operating ore mine.

2 Geomechanical Model of Geotechnical Object and Stress Fields

The Tashtagol iron-ore deposit (TD), discovered in 1931, is located in the middle part of Gornaya Shoria, 220 km southeast of Novokuznetsk (Kemerovo region, Russia). There are 14 known steeply dipping ore bodies at TD that have irregular contours in plan. The dimensions of the ore bodies along the strike are 300–760 m, along the dip 500–1000 m with an average thickness of 40–70 m [22]. The ore deposit is dissected by two submeridional faults (Fig. 1). The largest ore body is located in the northwestern part of TD, discovered at a depth of + 220 m (700 m from the surface). Industrial exploitation of TD began in 1940, the mining method is a horizon one (level height 70 m) with induced caving; since the early 2000s, in some areas the mined-out space has been filled with hardening mixtures [23]. To date, mining operations have reached absolute depths of 800–850 m.

In 1978, the Tashtagol seismic station was put into operation. We had data on induced seismicity from 1991 to 2020 in the standard format $\{D_n, \overrightarrow{R}_n, E_n\}$, where n is the event number, D_n—date and time, $\overrightarrow{R}_n = (X_n, Y_n, Z_n)$ are the local coordinates of the hypocenter, E_n—energy. The database contained about 40,000 records.

The natural stress field, determined by seismotectonic information and instrumental measurement data [24], corresponds to the overthrust type: $\sigma_H = 2.5\sigma_V$, $\sigma_h = 1.3\sigma_V$ and σ_V are maximum, minimum horizontal and vertical stress components (Fig. 1). The stress component σ_H is oriented in the northwest–southeast direction.

The TD geomechanical model [18] was implemented using FEM (hexahedral elements) by the original code [25]. A small fragment of the mesh is shown in Fig. 1. Calculation domain—parallelepiped $G = \{0 \le x \le L_x, 0 \le y \le L_y, 0 \le z \le L_z\}$, the dimensions of which are $L_x = 2500$ m, $L_y = 4000$ m and $L_z = 800$ m along the axes of the Cartesian coordinate system (x, y, z) are selected so that all mineable

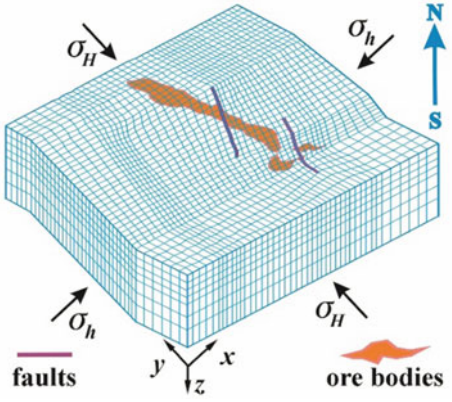


Fig. 1 Structural diagram of Tashtagol iron-ore deposit, fragment of a FEM mesh and orientation of horizontal stress components σ_H and σ_h in a natural field

areas are located inside G at a distance of at least 500 m from ∂G, and the vertical edges are orthogonal to the directions of σ_H and σ_h.

For each mined-out space configuration $m = 1, 2, \ldots, M$ (corresponding to 1991, 1992, …, 2020, $M = 30$), constructed on the basis of mining development plans, a system of equations of the linear elasticity theory

$$\sigma_{ij,j} + \rho g \delta_{iz} = 0,$$

$$\sigma_{ij} = \lambda(\varepsilon_{xx} + \varepsilon_{yy} + \varepsilon_{zz})\delta_{ij} + 2\mu\varepsilon_{ij},$$

$$\varepsilon_{ij} = 0.5(u_{i,j} + u_{j,i})$$

was solved, where σ_{ij} and ε_{ij} are the components of the stress and strain tensors, u_i—displacements; g—acceleration due to gravity; ρ—density; δ_{ij}—bivalent mixed tensor; λ, μ—Lame parameters. The following boundary conditions were formulated at ∂G (Fig. 1):

$$\sigma_{xx}(0, y, z) = \sigma_{xx}(L_x, y, z) = q_x \sigma_V(z),$$

$$\sigma_{xy}(0, y, z) = \sigma_{xy}(L_x, y, z) = 0, \sigma_{xz}(0, y, z) = \sigma_{xz}(L_x, y, z) = 0;$$

$$\sigma_{yy}(x, 0, z) = \sigma_{yy}(x, L_y, z) = q_y \sigma_V(z),$$

$$\sigma_{xy}(x, 0, z) = \sigma_{xy}(x, L_y, z) = 0, \sigma_{yz}(x, 0, z) = \sigma_{yz}(x, L_y, z) = 0;$$

$$\sigma_{zz}(x, y, 0) = \sigma_V(0), u_z(x, y, L_z) = 0,$$

$$\sigma_{xz}(x, y, 0) = \sigma_{xz}(x, y, L_z) = 0, \sigma_{yz}(x, y, 0) = \sigma_{yz}(x, y, L_z) = 0,$$

where $q_x = 2.5$ and $q_y = 1.3$ are the lateral thrust coefficients, $\sigma_V(z) = \rho g(H + z)$ is the vertical (lithostatic) stress in the intact rock mass, $H = 500$ m is the distance from the top face of G to the daylight surface.

The stress fields $\sigma_{ij}(m)$ were calculated at each mining stage m. Figure 2 shows isolines of the σ_{yy} component (along the strike of the ore body) at various stages of mining at the horizon $z = -210$ m. They illustrate the process of evolution of the stress field in the course of mining. We note an increase in areas of tension, as well as the "migration" of stress concentration zones as mining progresses deeper and a corresponding change in the mined-out space configuration.

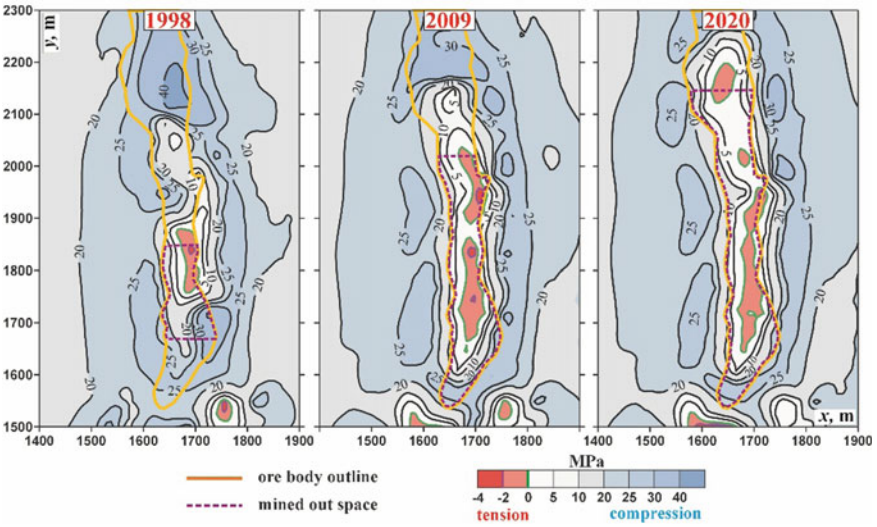


Fig. 2 Distribution of the stress tensor component σ_{yy} (MPa) at the level $z = -210$ m for various stages of mining ($m = 8, 19, 30$)

3 Qualitative Analysis of Induced Seismicity at Tashtagol Deposit

In Table 1 presents the number of weak ($E_n < 10$ kJ, classes from 0 to 3), moderate and strong ($E_n \geq 10$ kJ, fourth class and higher) for five-year periods, as well as their total energy. It can be seen that with increasing mining depth, the number of weak events and their total energy steadily increase. For moderate and strong events in 2000–2010 this pattern is disrupted due to changes in mining technology, which led to a temporary decrease in the number of events with an energy greater than 10 kJ.

Table 1 Number and total energy of seismic events

Class of event	1991–1995	1996–2000	2001–2005	2006–2010	2011–2015	2016–2020
	Lower mining horizon, m					
	−140	−210	−280	−280	−350	−350
	Number of seismic events					
0–3	1319	1774	6188	5920	8428	13324
4–8	208	208	191	210	550	693
	Total energy, MJ					
0–3	0.482	0.808	1.534	1.555	1.611	2.068
4–8	454	993	567	890	318	495

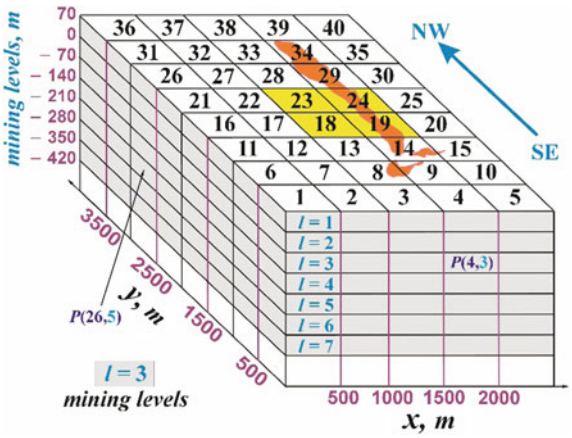


Fig. 3 Separation the computational domain into parallelepipeds for spatio-temporal analysis of induced seismicity parameters

Let's divide the upper part of the calculation domain G into identical spatial blocks $P(k, l)$—parallelepipeds $500 \times 500 \times 70$ m (vertical size is equal to the level height), $l = 1, \ldots, 7$—number of the mining horizon, $k = 1, \ldots, 40$ (Fig. 3).

Using a seismic database, we calculate the number N in each block $P(k, l)$, as well as the total energy W of weak, moderate and strong seismic events

$$N(k, l, m) = \sum\nolimits_{n \in C_{klm}} 1, \; W(k, l, m) = \sum\nolimits_{n \in C_{klm}} E_n,$$

where $C_{klm} = \{n | (X_n, Y_n, Z_n) \in P(k, l) \& 0 < D_n - 1990 - m \leq 1\}$, then find the energy in the vertical column $W_s(k, m) = W_s(k, 1, m) + \cdots + W_s(k, 7, m)$ and coordinates of the seismic energy release center (ERC)

$$\overrightarrow{R}(k, l, m) = \sum\nolimits_{n \in C_{klm}} E_n \overrightarrow{R}_n / W(k, l, m).$$

Note that the block sizes are chosen so that in the zone of influence of mining operations the value of $N(k, l, m)$ for weak events exceeds 30.

Figure 4 shows selected calculation results illustrating the main qualitative patterns of the spatial distribution of the energy of seismic events during cleanup operations:

– with rare exceptions, ERC (green circles show the projection of ERC in vertical column onto the upper edge of the study area G) in blocks $P(19, l)$ and $P(24, 1)$ (where mineral extraction is carried out) is located in the ore body;
– with increasing mining depth, the energy of seismic events in blocks $P(19, l)$ and $P(24, 1)$ increases, while in blocks adjacent to them decreases.

We can offer the following explanation for the identified regularities. Strains increase in the vicinity of the mined-out space, the elastic characteristics of the ore are much greater than those of the country rocks, therefore, it is in the rock ore that

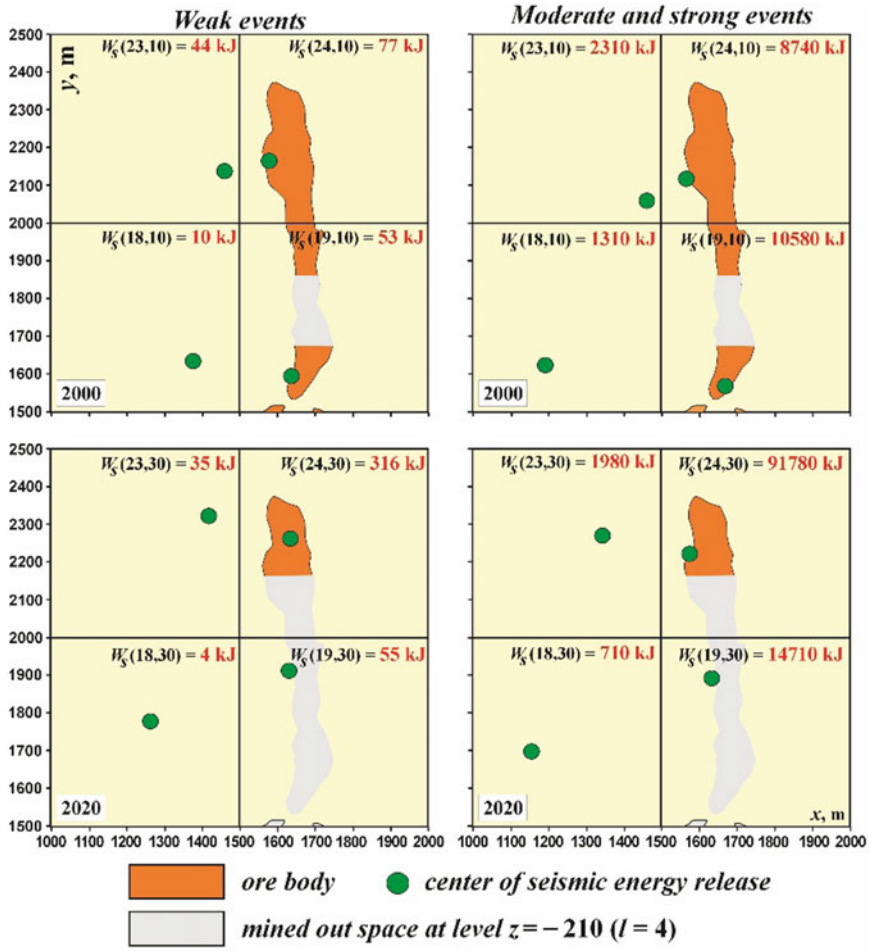


Fig. 4 Spatial energy distribution of weak, moderate and strong events and centers of seismic energy release (level $z = -210$m)

there is a higher concentration of elastic energy, which can be released in the form of dynamic events. With the transition of mining to deeper horizons, this trend is intensifying.

4 Correlation Analysis of Induced Seismicity and Stress Field Parameters

Between 1991 and 2020 at TD, no more than 120 moderate and strong dynamic events occurred per year, i.e. on average less than one event per block. With such a volume of information, it is impossible to conduct a statistical analysis, so we will consider only weak events (class 0–3).

For a joint quantitative analysis of stresses and seismicity, we introduce a generalized quantitative characteristic of the block stress state

$$\tau(k,l,m) = \frac{1}{V} \iiint_{P(k,l)} \tau_{\max}(m) dV, \quad (1) \tag{1}$$

where $\tau_{\max}(m)$ is the maximum shear stress calculated from $\sigma_{ij}(m)$ at each stage of mining m, V is the volume of the block $P(k,l)$. Thus, time series of deterministic $\tau(k,l,m)$ and random $N(k,l,m)$, $W(k,l,m)$ values are formed in each block, and we have the opportunity to calculate the correlation coefficients

$$\xi_N(k,l,p,q) = \frac{\sum_{m=1}^{M}\left[N(k,l,m) - \overline{N}(k,l)\right]\left[\tau(p,q,m) - \overline{\tau}(p,q)\right]}{M\sigma_N(k,l)\sigma_\tau(p,q)},$$

$$\xi_W(k,l,p,q) = \frac{\sum_{m=1}^{M}\left[W(k,l,m) - \overline{W}(k,l)\right]\left[\tau(p,q,m) - \overline{\tau}(p,q)\right]}{M\sigma_W(k,l)\sigma_\tau(p,q)},$$

where $\sigma_N^2(k,l) = \sum_{m=1}^{M}\left[N(k,l,m) - \overline{N}(k,l)\right]^2/M$, $\overline{N}(k,l) = \sum_{m=1}^{M} N(k,l,m)/M$,

$$\sigma_W^2(k,l) = \sum_{m=1}^{M}\left[W(k,l,m) - \overline{W}(k,l)\right]^2/M, \overline{W}(k,l) = \sum_{m=1}^{M} W(k,l,m)/M,$$

$$\sigma_\tau^2(p,q) = \sum_{m=1}^{M}[\tau(p,q,m) - \overline{\tau}(p,q)]^2/M, \overline{\tau}(p,q) = \sum_{m=1}^{M} \tau(p,q,m)/M.$$

The number of coefficients ξ_N and ξ_W exceeds 39000; we will select only those that satisfy three conditions:

- absolute value greater than 0.7 (there is a strong dependence of seismicity parameters on stress);
- Student's t-test was performed at a significance level of 0.05;
- Fisher's F test was performed at a significance level of 0.05.

The analysis showed that statistically significant correlation coefficients occur for pairs of blocks located in the zone of influence of mining operations. Table 2 shows

Table 2 Selected values of correlation coefficients

ξ_W	ξ_N
$\xi_W(19, 4, 19, 4) = 0.70$	$\xi_N(19, 2, 18, 2) = -0.70$
$\xi_W(19, 4, 18, 4) = -0.76$	$\xi_N(19, 6, 18, 6) = 0.70$
$\xi_W(23, 4, 24, 4) = -0.72$	$\xi_N(23, 4, 24, 4) = -0.83$
$\xi_W(23, 5, 23, 5) = 0.72$	$\xi_N(23, 3, 23, 3) = 0.76$
$\xi_W(23, 6, 23, 6) = 0.84$	$\xi_N(23, 3, 23, 4) = -0.74$
$\xi_W(23, 6, 24, 6) = 0.88$	$\xi_N(24, 4, 23, 4) = 0.83$
$\xi_W(24, 5, 23, 5) = 0.75$	$\xi_N(24, 6, 23, 6) = 0.78$
$\xi_W(24, 5, 23, 6) = 0.74$	$\xi_N(24, 4, 24, 4) = 0.70$

some values of ξ_N and ξ_W; it should be noted that for the pair $\{P(23, 4), P(24, 4)\}$ both correlation coefficients are greater than 0.7 in absolute value.

Now let's write down the simple linear regression equations

$$W_{kl}(\tau) = \xi_W(k, l, p, q)\frac{\sigma_W(k, l)}{\sigma_\tau(p, q)}[\tau - \overline{\tau}(p, q)] + \overline{W}(k, l), (2) \quad (2)$$

$$N_{kl}(\tau) = \xi_N(k, l, p, q)\frac{\sigma_N(k, l)}{\sigma_\tau(p, q)}[\tau - \overline{\tau}(p, q)] + \overline{N}(k, l), (3) \quad (3)$$

which describe the dependence of the total energy W_{kl} and the number N_{kl} of events in the block $P(k, l)$ on the average maximum shear stress τ in the block $P(p, q)$. Figure 5 shows regression lines for some pairs of blocks.

The resulting regression relationships can be used to predict the parameters of weak seismicity in blocks that satisfy the three conditions listed above. In accordance with the mining development plan, the stress field $\sigma_{ij}(m)$ in the object at $m > M$ is calculated using the geomechanical model, then $\tau(m)$ is found in the block $P(p, q)$ using (1), and finally using (2) and (3) in block $P(k, l)$ the expected number of weak dynamic events and their total seismic energy are estimated.

5 Conclusions

An approach is substantiated for identifying quantitative dependencies between the parameters of the spatio-temporal distribution of parameters characterizing the evolution of stochastic and deterministic physical fields in geological environments caused by the action of factors of various nature. The approach was tested using data on induced seismicity and geomechanical fields in the geomechanical space of the Tashtagol ore mine. Determined that:

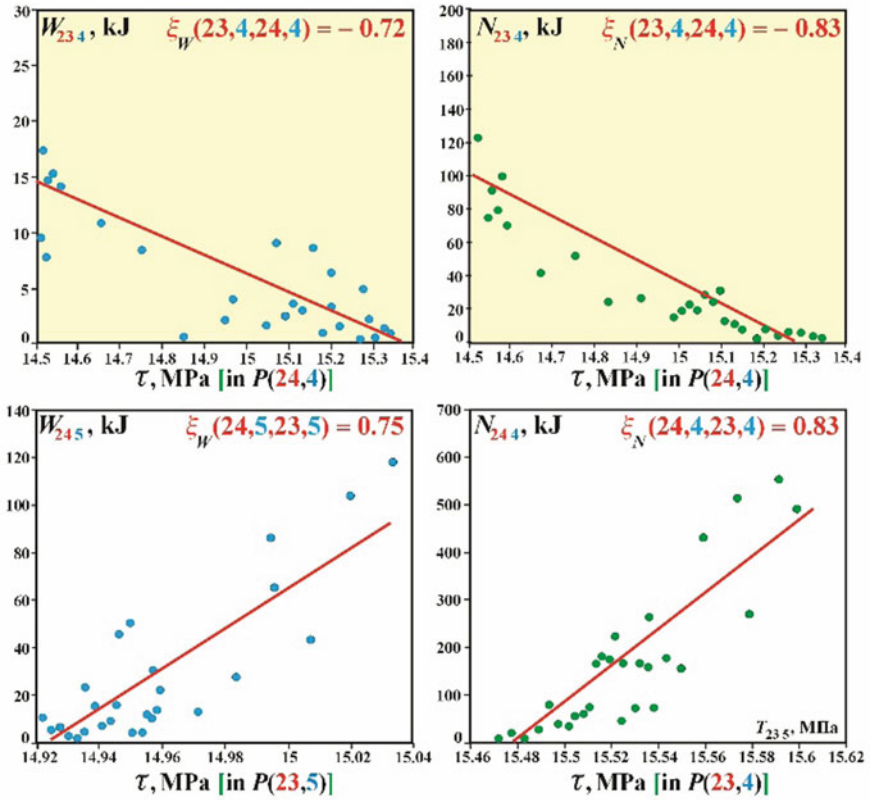


Fig. 5 Selected $W - \tau$ and $N - \tau$ regression lines for blocks with high correlation coefficients

- with increasing mining depth, the foci of moderate and strong seismic events, as well as the center of seismic energy release, move closer to the mined-out space and are concentrated mainly in the ore body, as a more energy-saturated object compared to the country rocks;
- there are spatial blocks in which the number and energy of weak seismic events has a statistically significant strong correlation with the average value of the maximum shear stress;
- these correlation dependencies are suitable for predictive assessments of seismicity parameters through forward calculations of stress fields using verified geomechanical models and long-term mining development plans.

Further research will develop in the following directions:

- verification of the proposed procedure through retrospective analysis using time series of various lengths;
- extension of the proposed approach to other geotechnical objects of various scales, which are characterized by a high level of induced seismicity;

– study of the influence of the geometric dimensions of the block on the stability of correlations between stresses and seismicity parameters.

Acknowledgements The work was carried out within the framework of a Research Project State Registration Number 124020700085-5.

References

1. Tupysev, M.K.: Technogenic stresses dynamics control in rock formations, including cap rocks, during development and operation of underground gas storage facilities. Actual Problems of Oil and Gas 2(25) (2019). https://doi.org/10.29222/ipng.2078-5712.2019-25.art12.
2. Li J., Zhao G., Qi Z. et al.: Stress sensitivity of formation during multi-cycle gas injection and production in an underground gas storage rebuilt from gas reservoirs. Petroleum Exploration and Development 48(4), 968–977 (2021). https://doi.org/10.1016/S1876-3804(21)60081-2.
3. Park, J., Griffiths, L., Dautriat, J. et al.: Induced-seismicity geomechanics for controlled CO2 storage in the North Sea (IGCCS), International J. of Greenhouse Gas Control 115, 103614 (2022). https://doi.org/10.1016/j.ijggc.2022.103614.
4. Grunthal, G.: Induced seismicity related to geothermal projects versus natural tectonic earthquakes and other types of induced seismic events in Central Europe. Geothermics 52, 22–35 (2014). https://doi.org/10.1016/j.geothermics.2013.09.009.
5. Talwani, P.: On the nature of reservoir-induced seismicity. Pure and Applied Geophysics 150, 473–492 (1997). https://doi.org/10.1007/s000240050089.
6. Herath, P., Attanayake, J., Gahalaut, K.: A reservoir induced earthquake swarm in the Central Highlands of Sri Lanka. Scientific Reports 12, 18251 (2022). https://doi.org/10.1038/s41598-022-22791-z.
7. Guha, S.K.: Mining induced seismicity. In: Induced Earthquakes. Springer, Dordrecht, 159–215 (2000). https://doi.org/10.1007/978-94-015-9452-3_5.
8. Feng,X.-T., Liu, J., Chen, B. et al.: Monitoring, warning, and control of rockburst in deep metal mines. Engineering 3(4), 538–545 (2017). https://doi.org/10.1016/J.ENG.2017.04.013.
9. Ammon, C.J., Velasco, A.A., Lay, T., Wallace, T.C.: Foundations of modern global seismology. 2nd Edition. Academic Press (2020). https://doi.org/10.1016/C2017-0-03756-4.
10. Perez-Lopez, R., Ramos, A., Giner-Robles, J.L.: Stress and strain analysis and induced seismicity in geological gas storage (Yela, Spain). J. of Structural Geology 161, 104662 (2022). https://doi.org/10.1016/j.jsg.2022.104662.
11. Bourne, S.J., Oates, S.J. van Elk, J.: The exponential rise of induced seismicity with increasing stress levels in the Groningen gas field and its implications for controlling seismic risk. Geophysical J. International 213, 1693–1700 (2018). https://doi.org/10.1093/gji/ggy084.
12. Smith, J.D., Heimisson, E.R., Bourne, S.J., Avouac, J.-P.: Stress-based forecasting of induced seismicity with instantaneous earthquake failure functions: Applications to the Groningen gas reservoir. Earth and Planetary Science Letters 594, 117697 (2022). https://doi.org/10.1016/j.epsl.2022.117697.
13. Hardy Jr., H.R.: Acoustic emission microseismic activity. V. 1. Principles, techniques and geotechnical applications. CRC Press, London (2003).
14. Rodriguez, P., Celestino, T.B.: Application of acoustic emission monitoring and signal analysis to the qualitative and quantitative characterization of the fracturing process in rocks. Engineering Fracture Mechanics 210, 54–69 (2019). https://doi.org/10.1016/j.engfracmech.2018.06.027.
15. Muralidhara, S., Raghu Prasad, B.K., Eskandari, H., Karihaloo, B.L.: Fracture process zone size and true fracture energy of concrete using acoustic emission. Construction and Building Materials 24(4), 479–486 (2010). https://doi.org/10.1016/j.conbuildmat.2009.10.014.

16. Zhurkov, S.N., Kuksenko, V.S., Petrov, V.A.: Principles of the kinetic approach of fracture prediction. Theoretical and Applied Fracture Mechanics 1(3), 271–274 (1984). https://doi.org/10.1016/0167-8442(84)90007-7.
17. Zavyalov, A.D. From the kinetic theory of strength and fracture concentration criterion to the seismogenic fracture density and earthquake forecasting. Physics of the Solid State 47, 1034–1041 (2005). https://doi.org/10.1134/1.1946852.
18. Nazarova, L.A., Nazarov, L.A., Leont'ev, A.V.: Three-dimensional geomechanical model of the Tashtagol iron-ore deposit. J. of Mining Science 34, 209–216 (1998). https://doi.org/10.1007/BF02803457.
19. Rahman, MJ, Fawad, M., Mondol, N.H.: 3D field-scale geomechanical modeling of potential CO_2 storage site Smeaheia, Offshore Norway. Energies 15(4), 1407 (2022). https://doi.org/10.3390/en15041407.
20. Leake, M.R., Conrad, W.J., Westman, E.C. et al.: Microseismic monitoring and analysis of induced seismicity source mechanisms in a retreating room and pillar coal mine in the Eastern United States. Underground Space 2(2), 115–124 2017. https://doi.org/10.1016/j.undsp.2017.05.002.
21. Zhou, Z., Huang, Y., Zhao, C.: Distribution law of mine ground pressure via a microseismic sensor system. Minerals 13, 649 (2023). https://doi.org/10.3390/min13050649.
22. Shpeikher, E.D., Salikhov, V.A.: Mineral deposits and their exploration: Textbook. SibGIU, Novokuznetsk (2003). [in Russian].
23. Anushenkov, A.N.: Production of stowing works. Using the example of the Tashtagol underground mine. Sib. Federal University, Krasnoyarsk (2016). [in Russian].
24. Nazarova, L.A.: Estimating the stress and strain fields of the Earth's crust on the basis of seismotectonic data. J. of Mining Science 35, 26–35 (1999). https://doi.org/10.1007/BF02562442.
25. Nazarova, L.A., Nazarov, L.A.: Dilatancy and the formation and evolution of disintegration zones in the vicinity of heterogeneities in a rock mass. J. of Mining Science 45(5), 411–419 (2009). https://doi.org/10.1007/s10913-009-0052-3.

Stress Trajectories and Crack Propagation in Elastic Plate Under Combined Mechanical and Thermal Loading



Alexander N. Galybin

Abstract This study is focused on the problem of principal stress trajectory field determination in elastic plates subjected to mechanical and thermal loading. It is believed that analysis of the stress trajectories can form a basis for investigation of inverse problems for both temperature and thermal stress fields identification by observation of fracture patterns distribution near locally overheated zones. Thus study assumes that fracturing may appear due to initiation of additional tensile stresses caused by temperature impact. We consider three simple cases in order to illustrate how non-uniform temperature field affects stress trajectories in elastic plane. In addition the problem of crack initiation and propagation near locally heated zones is considered.

Keywords Elasticity · Thermal stress · Stress trajectories · Fracture pattern · Crack growth

1 Introduction

There are many real-world situations where thermal stresses can damage solids materials and different structures. Example are found in different areas of engineering and natural sciences, e.g. local overheating in blast furnace castings, heating of earth's crust by plumes in the mantle, laser treatment of biological tissues and many other.

In this study we aim to employ the concept of stress trajectories of the principal stresses in order to reveal what kind of fracture patterns can be expected near locally overheated zones. The later in accordance with some fracture criteria mentioned in [1] can correlate with the trajectory field of major (and positive) principal stress.

The concept of stress trajectories is well known from photoelasticity [2]. In geomechanics it has been applied for reconstruction of the in-situ stresses acting in the

A. N. Galybin (✉)
Schmidt Institute of Physics of the Earth (IPE RAS), Moscow, Russia
e-mail: a.n.galybin@gmail.com

© The Author(s), under exclusive license to Springer Nature Switzerland AG 2024

V. Karev (ed.), *Proceedings of the 9th International Conference on Physical and Mathematical Modelling of Earth and Environmental Processes*, Springer Proceedings in Earth and Environmental Sciences, https://doi.org/10.1007/978-3-031-54589-4_15

earth's crust by many authors, for detail see [3–5], or for steady-state hydraulic problems [6]. For thermo-elastic problems, to the best of our knowledge, this technique has not been applied yet.

We also intend to investigate crack initiation and propagation near locally heated zones, which requires the analysis of fracture characteristics. For the purpose of this paper the results for the stress intensity factors summarized in well-known handbook by Murakami [7] will be applied.

The paper is structured as follows. Firstly, the problem formulation for thermo-elasticity in complex coordinates is introduced. Then the solution for the stress trajectories will be obtained for three cases of temperature distribution and finally crack propagation problem is considered.

2 Problem Formulation

The Kolosov-Muskhelishvili formulas for the stress and displacement components in a Cartesian coordinate system Oxy are as follows [8]:

$$P \equiv \frac{\sigma_{yy}+\sigma_{xx}}{2} = \frac{\sigma_1+\sigma_2}{2} = \Phi(\mathrm{z}) + \bar{\Phi}(\mathrm{z}),$$

$$D \equiv \frac{\sigma_{yy}-\sigma_{xx}}{2} + i\sigma_{xy} = \frac{\sigma_1-\sigma_2}{2} e^{i(\pi-2\vartheta)} = \bar{z}\Phi'(z) + \Psi(z), \tag{1}$$

$$2GW \equiv 2G\left(u_x + iu_y\right) = \kappa\phi(z) - z\overline{\Phi(z)} - \overline{\psi(z)}.$$

Here $\sigma_{xx}, \sigma_{yy}, \sigma_{xy}$ are stress components, σ1 and σ2 are major and minor principal stresses respectively ($\sigma_1 \geq \sigma_2$), P is mean stress, D is complex stress deviator, $W = u_x + iu_y$ is complex displacement vectors with the components u_x, u_y along the x and y axes respectively, ϑ is principal direction (the angle between the major principal stress and the x-axis, G is shear modulus, $\kappa = (3–4\ \nu)$ for the plain strain conditions and $\kappa = (3-\nu)/(1+\nu)$ for the plane stress conditions, ν is Poisson's ratio, $\Phi(z) = \phi\prime(z)$, $\Psi(z) = \psi\prime(z)$ are complex potentials (holomorphic functions of a complex variable $\mathrm{z} = x + iy$).

Let us consider an elastic plate biaxially loaded at infinity by normal stresses $\sigma_{xx} = S_h$, $\sigma_{yy} = S_H$, $\sigma_{xy} = 0$ then the stress functions take the following simple form

$$P^0 = \frac{S_H + S_h}{2}, D^0 = \frac{S_H - S_h}{2}, \tag{2}$$

Without loss of generality we further assume that $S_H \geq S_h$.

Let us also consider the case when the plate is locally heated by a constant temperature T_0 over a circle of radius R and is equal to zero outside the circle. Such stationary temperature distribution can be presented as

$$T(r) = T_0 H(R - r), \tag{3a}$$

where $H(r)$ is the Heaviside step function.

Let us also consider non-stationary temperature distribution

$$T(r) = \frac{T_0 R^2}{R^2 + r^2}, \tag{3b}$$

For hollow cylinder the stationary polar symmetric temperature distribution is defined as follows [9]

$$T(r) = T_0 \frac{lnb - lnr}{lnb - lna}, \tag{3c}$$

where a and b are inner and outer radii of the cylinder.

Following [9] one can introduce a pair of complex variables $z, \overline{z}$ instead of Cartesian or polar coordinates. Then a function of two variables (x,y) can be viewed as a function of variables $(z, \overline{z})$ as follows $f(x, y) = f\left(\frac{z+\overline{z}}{2}, \frac{z-\overline{z}}{2i}\right) = \widehat{f}(z, \overline{z})$. We will further omit the cap symbol and keep the same notations as for functions in Cartesian coordinates, i.e. use $f(x, y) = f(z, \overline{z})$. For the differential operators one has [9]

$$2\frac{\partial f}{\partial z} = \frac{\partial f}{\partial x} - i\frac{\partial f}{\partial y}, 2\frac{\partial f}{\partial \overline{z}} = \frac{\partial f}{\partial x} + i\frac{\partial f}{\partial y}, 4\frac{\partial^2 f}{\partial z \partial \overline{z}} = \frac{\partial^2 f}{\partial^2 x} + \frac{\partial^2 f}{\partial y^2}. \tag{4}$$

The later formulas allow one to present formulas (1) for thermal stresses based on solutions in [2] for the plane strain conditions as follows

$$P^t(\mathrm{z}, \overline{\mathrm{z}}) = -\frac{4\alpha E T(\mathrm{z}, \overline{\mathrm{z}})}{1 + \kappa} \tag{5}$$

$$D^t(\mathrm{z}, \overline{\mathrm{z}}) = -2G\frac{\partial \overline{W}^t(\mathrm{z}, \overline{\mathrm{z}})}{\partial z} \tag{6}$$

$$2GW^t(\mathrm{z}, \overline{\mathrm{z}}) = \frac{2\alpha E}{1 + \kappa} \int T(\mathrm{z}, \overline{\mathrm{z}}) dz, \tag{7}$$

where α is the coefficient of thermal expansion and superscript t hereafter stands for thermal stresses.

3 Stress Trajectory Fields

Case 3a

For the temperature distribution given by (3a) the mean stresses are found from (5) straight forward

$$P^t(\mathrm{z},\overline{\mathrm{z}}) = -\frac{4\alpha \mathrm{E}T_0}{1+\kappa} H\left(R^2 - \mathrm{z}\overline{\mathrm{z}}\right) \tag{8}$$

In order to find the displacement vector and the complex stress deviator function we recall that the temperature is independent of the polar angle and satisfies the Laplace equation. Thus, the circumferential component of the displacement vector is zero for the whole plane while the radial component $u_r\,(r)$ is found by integration of the ordinary differential equation

$$\frac{\partial u_r(r)}{\partial r} + \frac{u_r(r)}{r} = \alpha\beta T(r), \tag{9}$$

which follows from the Laplace equation and, $\beta = (1 + \nu)$ for the plain stress conditions and $\beta = (1 + \nu)/(1-\nu)$ for the plane stress conditions. Solution of (5) with the temperature distribution (3a) has the form

$$u_r(r) = \frac{\alpha\beta T_0}{2}\left(rH(R-r) + \frac{1}{r}H(r-R)\right), \tag{10}$$

Bearing in mind that $W(r,\theta) = e^{i\theta}u_r\,(r)$ one obtains (for plane strain conditions)

$$2GW^t(\mathrm{z},\overline{\mathrm{z}}) = \frac{2\alpha E T_0}{1+\kappa}\left(zH\left(R^2 - \mathrm{z}\overline{\mathrm{z}}\right) + \frac{1}{\overline{\mathrm{z}}}H\left(\mathrm{z}\overline{\mathrm{z}} - R^2\right)\right), \tag{11}$$

Complex conjugation of (11) followed by differentiation with respect to z leads in accordance to (6) to the following expression for the stress deviator

$$D^t(\mathrm{z},\overline{\mathrm{z}}) = \frac{2\alpha E T_0}{1+\kappa}\frac{1}{z^2}H\left(\mathrm{z}\overline{\mathrm{z}} - R^2\right), \tag{12}$$

It is worth noting that for the temperature distribution (3a) the argument of D^t is equal to -2 θ, which means that the principal directions outside the heated area coincide with the coordinates lines of the polar system as evident from the second formula in (1). It is also evident that the maximum shear stresses, $\tau_{max} = (\sigma_1 - \sigma_2)/2$, caused by temperature defined by formula (3a) are equal to zero within the heated circle. This, taking into account formulas (8) and (2), results in the following expressions for the total principal stresses acting inside the circle.

$$\sigma_1 = S_H - \frac{4\alpha \mathrm{E} T_0}{1+\kappa}, \sigma_2 = S_h - \frac{4\alpha \mathrm{E} T_0}{1+\kappa}, 0 <]z] < R \tag{13}$$

As soon as the principal stresses are constant the stress trajectory field is homogeneous and presented by the coordinate lines of the Cartesian coordinate system within the heated circle. Moreover these remains compressive inside the circle provided that the remote stresses were compressive.

It follows from (8) that outside of the heated area $\sigma_2 = -\sigma_1$, which manifests that for thermal loading the major principal stress (circumferential stress) is tensile while the minor one (radial stress) is compressive everywhere in the plate outside the heated circle.

By summing (2) and (12) one finds the total stress deviator as follows

$$\mathrm{D}^{\mathrm{t}}(\mathrm{z}, \overline{\mathrm{z}}) = \mathrm{D}^0 + \mathrm{D}^{\mathrm{t}}(\mathrm{z}, \overline{\mathrm{z}}) = \frac{S_H - S_h}{2} + \frac{2\alpha E T_0}{1+\kappa} \frac{1}{z^2},]z] > R \tag{14}$$

In order to analyze the field of stress trajectories outside the circle it is convenient to introduce the following dimensionless parameter

$$B = \frac{S_H - S_h}{4\alpha E T_0}(1+\kappa) \geq 0 \tag{15}$$

Then

$$\arg(\mathrm{D}^{\mathrm{t}}(\mathrm{z}, \overline{\mathrm{z}})) = arg(B + z^{-2}),]z] > R \tag{16}$$

The analytical solutions above have been obtained for the case of plane strain. In order to consider the plane stress conditions it is sufficient to put $\kappa = 0$ in Eqs. (5)–(9) and (11)–(15).

Therefor one of the families of stress trajectories has the following principal directions

$$\vartheta = -\frac{1}{2} arg(B + z^{-2}),]z] > R \tag{17}$$

If $B = 0$ (no remote loading) then ϑ=θ and this family present circumferential stresses that are major principal stresses for thermal loading. If z tends to infinity then arg(D) tends to zero, which means that at infinity this family also coincides with the directions of S_H. Thus, we can conclude that Eq. (17) determines the principal direction of the major principal stress.

The stress trajectories are obtained by integrating the following ordinary differential equation

$$\frac{\mathrm{dz}}{\mathrm{ds}} = exp(i\vartheta(\mathrm{z}, \overline{\mathrm{z}})) \tag{18}$$

Here s is the arc length along a trajectory and the principal direction is specified by (17) outside the circle or by the straight lines parallel to the y-axis inside the circle. Solutions of this equation are found numerically by Euler's method.

Examples of stress trajectory fields are shown in Fig. 1 for different parameters B. The figure shows quarter of the plane as the trajectory field is symmetrical with respect to the coordinate axis, The stress distribution inside the contour (shown by cyan color) is homogeneous and does not depend upon the parameter B. It is evident that for small values of B that indicate essential temperature influence as compare to the difference of the remote stresses the trajectories tend to the polar coordinate net, see Fig. 1a, b. For relatively large B the trajectories are close to the coordinate lines of the Cartesian system, see Fig. 1e, f. For the intermediate values of $B = 0.25$, 0.5 neither of the mentioned above patterns are pronounced though with the growing distance from the heated area one can observe that the trajectories become more coaxial with the remote stresses.

Cases 3b and 3c

These cases can be easily solved using Eqs. (6) and (7), which leads to the following expressions for the complex deviators due to temperature

$$D^t(\mathrm{z},\overline{\mathrm{z}}) = \frac{2\alpha E T_0}{1+\kappa}\left(\frac{\mathrm{z}\overline{\mathrm{z}}}{\mathrm{z}\overline{\mathrm{z}}+R^2} - \ln(\mathrm{z}\overline{\mathrm{z}}+R^2)\right)\frac{R^2}{z^2},\ 0 \le |z| < \infty) \tag{19}$$

in case (3b) and

$$D^t(\mathrm{z},\overline{\mathrm{z}}) = \frac{\alpha E T_0}{1+\kappa}\frac{\overline{\mathrm{z}}}{z},\ a \le |z| \le b \tag{20}$$

in case (3c).

It is evident that the arguments of these functions are the same as in case (3a). Therefore the stress trajectories will be the same as illustrated in Fig. 1.

4 Crack Growth

The fracture pattern presented in Fig. 1 can be considered as possible crack paths in accordance with one of the criteria of crack growth discussed in [1]. Calculations conducted in [10] confirm this criterion for hydraulic fracture paths near injection wells at least at initial stage of the crack growth. In this study we assume that a mode I crack can appear at a locus where the major principal stress reaches its maximum and is positive For the temperature distribution in case (3a) this occurs on the right from the point with the coordinates (R,0) where $R = 1$ and σ_1 has the following distribution along the x-axis

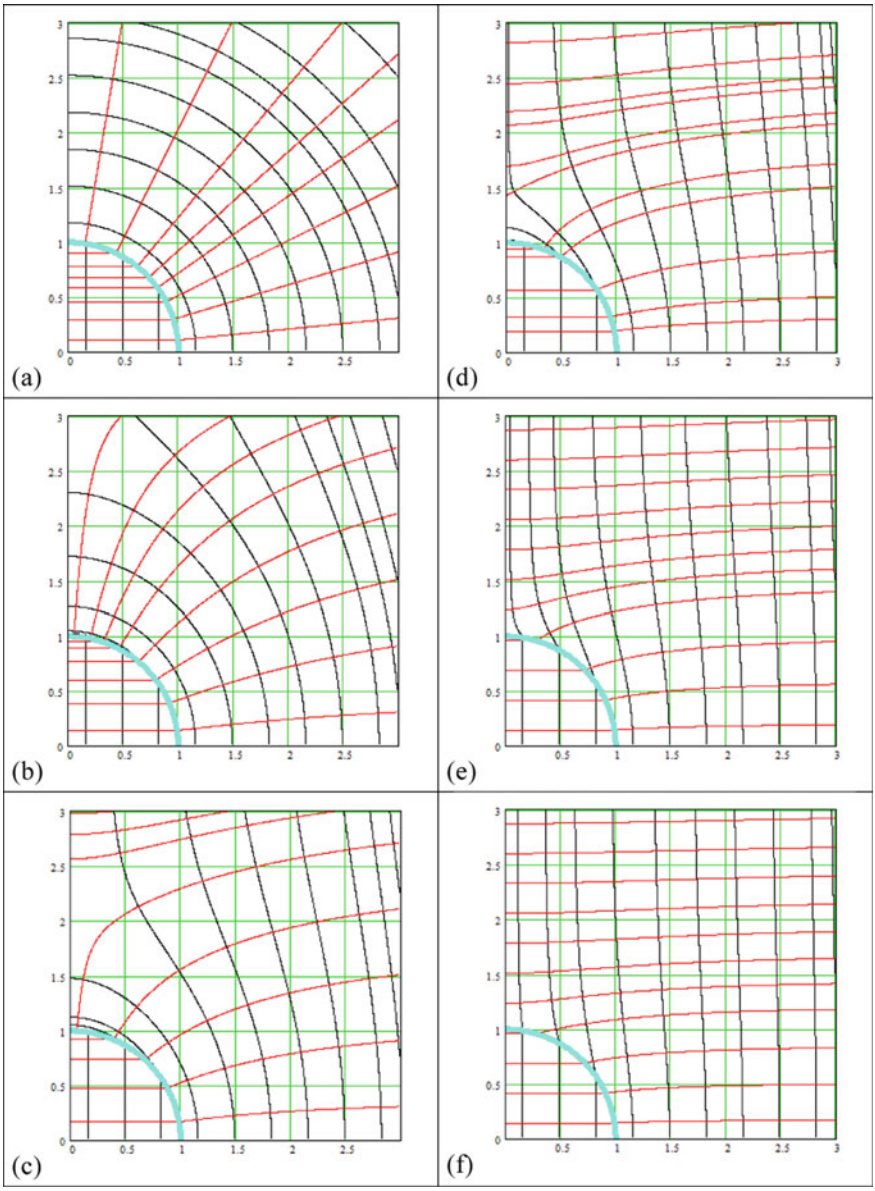


Fig. 1 Stress trajectories in the quarter of a plate with overheated area bounded by a circumference shown by cyan color for different parameters B: **a** B = 0.01, **b** B = 0.1, **c** B = 0.25, **d** B = 0.5, **e** B = 1.0, **f** B = 2.0

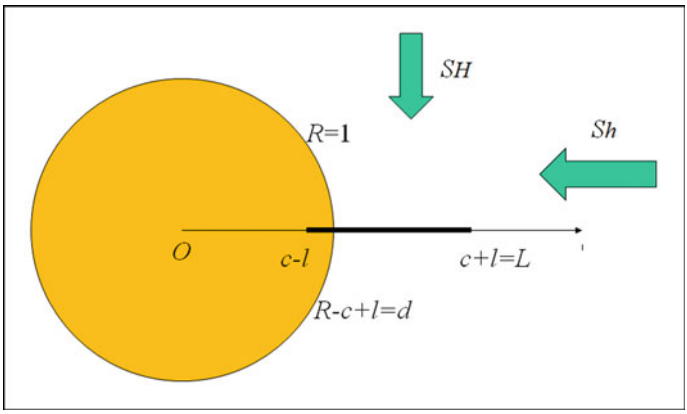


Fig. 2 Fracture near heated zone

$$\sigma_1 = S_H + \frac{2\alpha E T_0}{1+\kappa}\frac{1}{x^2}, x > R \tag{21}$$

Note that the remote load can be negative and therefore for crack appearance the temperature should be substantial co compensate compression.

Let a rectangular crack of the half-length l emerge on an interval $(c\text{-}l, c + l)$ such that $c - l < 1 < c + l$ (where $c > 1$ is the crack center) as illustrated in Fig. 2, then its growth can be determined in accordance with the Irwin criteria [11]

$$K_I{}^{\pm} = K_{Ic}, \tag{22}$$

Here K_{Ic} is the fracture toughness while the mode I stress intensity factor, SIF, in the left-hand side of (22) can be calculated as follows [7]

$$K_I{}^{\pm} = \frac{1}{\sqrt{\pi l}}\int_{-l}^{l}\sqrt{\frac{l \pm t}{l \mp t}}p(t)dt, \tag{23}$$

Here indices $\pm$ mark right/left crack ends respectively and the load $p(t)$ is superposition of thermal and remote loads. The former is positive outside the circle while the latter can be as positive as negative depending on a particular mechanical situation considered. Note that contribution of remote loading into SIF is $K_I{}^0 = S_H\sqrt{\pi l}$, which indicates that for $S_H > 0$ the fracture toughness will be attained at a certain crack length and then the right crack end will propagate to infinity regardless of acting thermal stresses.

The case when $S_H < 0$ is more interesting. One can accept that the crack initiates on the interval (1,L), where $\sigma_1 > 0$ and L is the root of $\sigma_1 = 0$ found from Eq. (20)

$$L = \sqrt{-\frac{2\alpha \mathrm{E} T_0}{S_H(1+\kappa)}}, c - l = 1, c + l = L, \tag{24}$$

In this case the load acting on the crack surfaces can be written as

$$p(t) = S_H + \frac{2\alpha \mathrm{E} T_0}{1+\kappa} \frac{1}{(t+c)^2}, \tag{25}$$

which being substituted into (20) followed by evaluation of the integrals results in

$$K_I{}^{\pm} = \left(S_H + \frac{2\alpha \mathrm{E} T_0}{1+\kappa} \frac{1}{c \pm l} \frac{1}{\sqrt{c^2 - l^2}} \right) \sqrt{\pi l}, \tag{26}$$

By replacing $c - l = 1, c + l = L$ it becomes evident from (25) that $K_I{}^{+} < K_I{}^{-}$, which indicates that the crack will grow in both directions. However, its left end can be arrested due to high compressive stresses acting within the heated zone. These are considerably greater than those acting near the right crack end.

One can estimate how far the crack can penetrated inside the heated circle as follows. Let us assume that it penetrated inside at the distance $d = 1\text{-}(c\text{-}l) > 0$. If $d <$ < 1 one can still use expression in (25) but needs to introduce corrections associated with the discontinuity of the circumferential thermal stresses. Firstly, the thermal term from (13) should be imposed at near the left end of the crack. Secondly, in order to compensate already taken into account the second term into the right-hand side of (25) should be subtracted. The latter, for simplicity, can be taken into account as a mean stress over the interval (c-l, 1). This leads to the following load

$$\Delta p(t) = -\frac{2\alpha \mathrm{E} T_0}{1+\kappa} \frac{3-2d}{1-d} H(1-c-t), \tag{27}$$

Substitution of (26) into (22) followed by evaluation of the integrals results in the following

$$\Delta K_I{}^{\pm} = -\frac{2\alpha \mathrm{E} T_0}{1+\kappa} \frac{3-2d}{1-d} F^{\pm}\left(\frac{d}{l}\right) \sqrt{\pi l}, F^{\pm}\left(\frac{d}{l}\right) = \frac{1}{\pi} cos^{-1}\left(1 - \frac{d}{l}\right) \mp \frac{1}{\pi} \sqrt{1 - \left(1 - \frac{d}{l}\right)^2} \tag{28}$$

Functions $F^{\pm}\left(\frac{d}{l}\right)$ determine corrections for SIFs at both ends that depend on the relative depth of penetration (parameter d/l), they are shown in Fig. 3 where the horizontal axis is d/l. It is evident that correction for the left end (solid red curve) is much more pronounced that for the right end (blue dashed curve). Therefore, one can expect that the crack does not penetrate far into the heated area but grow mostly in opposite direction. The position of the right end of the crack can be found from the Irwin criterion assuming that $c - l = 1$, which results in the following equation on l

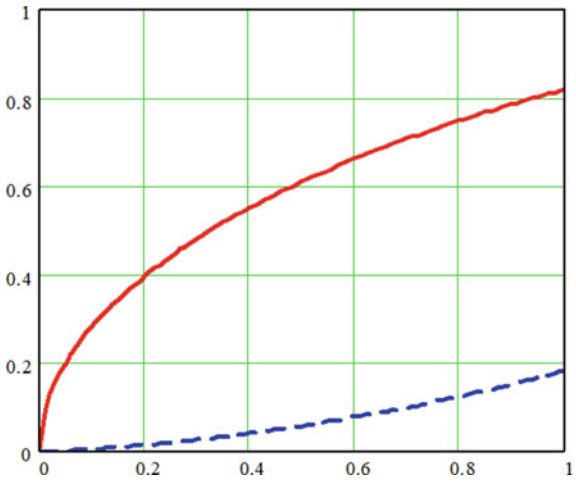


Fig. 3 Functions $F^{+}(d/l)$ (red solid curve) and $F^{-}(d/l)$ (blue dashed curve) in (27)

$$\left(S_H + \frac{2\alpha \mathrm{E} T_0}{1+\kappa}\frac{1}{\sqrt{(c+l)^3}}\right)\sqrt{\pi l} = K_{Ic}. \tag{29}$$

In order to estimate the longest crack caused by heating one can accept that the fracture toughness is small and therefore the term in parenthesis in (28) should vanish. This leads to the following simple estimate for the crack length

$$\sqrt{L_{max}^3} = -\frac{2\alpha \mathrm{E} T_0}{(1+\kappa)S_H} \tag{30}$$

It follows from (23) and (29) that the maximum coordinate of the right crack end is greater than the initial one as follows

$$L_{\max} = L^{4/3}, \quad L > 1 \tag{31}$$

The later relationship demonstrate that the real crack length can be routinely estimated from the condition $\sigma_1 > 0$ by using formula (20).

5 Conclusive Remarks

In this study we have analyzed the trajectories of the principal stresses in an elastic plate biaxially loaded at infinity and subjected to heating by polar symmetric temperature. Three cases have been considered including constant temperature kept in the circle, stationary temperature non-uniformly distributed over the entire plate and the

case of a washer with a given temperature kept on the inner radius and the zero temperature on the outer radius. In all cases the stress trajectory fields were similar. They reflect both types of loading. Namely, for the first considered case the stress families coincide with the coordinate lines of the Cartesian coordinate system inside the circle and in remote areas. Between them they are strongly affected by the thermal stresses. If the later dominate then trajectories are close to the coordinate lines of the polar coordinate system.

Since the trajectories of the principal stresses can be viewed as possible patterns of fractures near locally heated areas one can use this information for analyzing the back problems of temperature and thermo stress identification in practice.

The problem of single fracture propagation near locally heated zone have been analyzed with the aim to estimate possible crack length. It has bee found that for the case of heated circle the crack is located co-axial to the minor principal stress at infinity and its length can be roughly estimated from the condition of positiveness of the major principal stresses acting on the crack surfaces before its appearance.

References

1. Parton, V. Z., Morozov, E. M.1985. Mechanics of elastoplastic fracture. Moscow. Nauka. 504 p
2. Kuske A., Robertson G. 1974. Photoelastic Stress Analysis. London: John Wiley & Sons. 534 p.
3. Jian-Cheng Lee and Angelier J. 1994. Paleostress trajectory maps based on the results of local determinations: the "LISSAGE" program. Computers & Geosciences V. 20, No. 2, pp. 161-191
4. Galybin, A.N. and Sh.A. Mukhamediev, 2004. Determination of elastic stresses from discrete data on stress orientations. Int.ernational Journal of Solids and Structures. Vol. 41 (18–19): pp. 5125–5142.
5. Haderka, P and A.N. Galybin, 2011. The stress trajectories method for plane plastic problems. Int Journal of Solids and Structures, Vol. 48 (3-4): pp. 450-462.
6. Irša, J. and A.N. Galybin, 2010. Stress Trajectories Element Method for stress determination from discrete data on principal directions. Engineering Analysis with Boundary Elements, Vol. 34 (5): pp. 423-432
7. Murakami Y., Hasebe M.T. 1986. Stress Intensity Factors Handbook. Pergamon
8. Muskhelishvili, N.I. 1963.Some basic problems of the mathematical theory of elasticity. P. Noordhoff, Groningen, the Netherlands.
9. Timoshenko S.P., Goodier J.N. Theory of elasticity. McCraw-Hill, Singapore, 1970
10. Andreev, A. A., Galybin A. N. and O. Y. Izvekov. 2015. Application of complex SIE method for the prediction of hydrofracture path. Engineering Analysis with Boundary Elements. Vol. 50 : pp. 133-140
11. Irwin G. 1957. Analysis of stresses and strains near the end of a crack traversing a plate, Journal of Applied Mechanics 24, 361–364.

Parameterization of a Two-Component Gaussian Mixture for Description of the Sea Surface



A. S. Zapevalov and A. S. Knyazkov

Abstract A new approach is proposed for calculating the parameters of a two-component Gaussian mixture for modeling the distribution of sea surface elevations. Unknown distribution parameters are calculated from known statistical moments of a random variable. A two-component Gaussian mixture has five parameters and for their calculation it is necessary to know the statistical moments up to and including the fifth order. In oceanological research, only the first four statistical moments are determined, respectively, only four equations can be used. One of the distribution parameters remains free. This leads to some uncertainty in the constructed distributions. A new approach is proposed. Based on wave measurements carried out in the field, it is shown that there is a linear relationship between the third μ_3 and fifth μ_5 statistical moments of sea surface elevation. The linear regression equation between these parameters is obtained. The correlation coefficient between μ_3 and μ_5 is 0.92. This allows you to use the equation for the fifth statistical moment, setting it based on information about μ_3. With this calculation procedure, the uncertainty of the parameters of the distribution of elevations of the sea surface is excluded.

Keywords Remote sensing · Altimetry · Sea surface · Brown model · Distribution of surface elevations

1 Introduction

Two types of models are used for statistical description of weakly nonlinear sea waves. The first type includes dynamic models based on hydrodynamic equations and Stokes expansion [1–4]. Approximations of the probability density function of sea surface elevations constructed within the framework of these models are usually one-parameter. In such approximations, there is always a functional relationship between skewness and excess kurtosis, which does not agree with the data of wave

A. S. Zapevalov (✉) · A. S. Knyazkov
Marine Hydrophysical Institute RAS, Sevastopol, Russian Federation
e-mail: sevzepter@mail.ru

© The Author(s), under exclusive license to Springer Nature Switzerland AG 2024

V. Karev (ed.), *Proceedings of the 9th International Conference on Physical and Mathematical Modelling of Earth and Environmental Processes*, Springer Proceedings in Earth and Environmental Sciences, https://doi.org/10.1007/978-3-031-54589-4_16

measurements [5], the values of skewness and excess kurtosis are always positive, which also does not correspond to the results of studies of sea waves [6–8].

The second type is formed by models developed within the framework of the statistical theory of random weakly nonlinear processes [9]. In most cases, the probability density function of sea surface elevations is approximated by truncated Gram–Charlier series or Edgeworth series, which are the decomposition of the modeled function by orthogonal Chebyshev-Hermite polynomials [10–12]. The low order of series truncation, due to the lack of information about cumulants older than the fourth order, leads to distortions at the tails of the distribution, which manifest themselves as local maxima or negative values [13–15]. As a consequence, these models allow us to correctly approximate the probability density function only in a limited range of variation of a random variable.

Recently, to approximate the probability density function of sea surface elevations, it was proposed to use a two-component Gaussian mixture, which is always positive [16]. Gaussian mixtures form a large class of functions that are widely used in various fields of science and practice [17–19]. They have not yet found wide application in oceanology due to the complex procedure for calculating their parameters [20].

In this paper, a new approach is proposed to simplify the procedure for calculating the parameters of a two-component Gaussian mixture.

2 Two-Component Gaussian Mixture

A two-component Gaussian mixture of a random variable is the sum of two Gaussians that have different weights [19]

$$P(\xi) = \alpha_1 N_1(\xi, \sigma_1, m_1) + \alpha_2 N_2(\xi, \sigma_2, m_2) =$$

$$= \frac{\alpha_1}{\sqrt{2\pi}\sigma_1} \exp\left(-\frac{(\xi - m_1)^2}{2\sigma_1^2}\right) + \frac{\alpha_2}{\sqrt{2\pi}\sigma_2} \exp\left(-\frac{(\xi - m_2)^2}{2\sigma_2^2}\right), \quad (1)$$

where α_i is a weighting factor, $\alpha_i \in (0, 1)$, m_i is a mathematical expectation, σ_i^2 is a variance. The index i indicates that this parameter is a parameter of the i-th component ($i = 1,\ 2$).The weighting coefficients in Eq. (1) satisfy the condition

$$\alpha_1 + \alpha_2 = 1. \quad (2)$$

To build model (1), taking into account condition (2), it is necessary to find five parameters. These parameters are m_1, m_2, σ_1^2, σ_2^2 and α_1. They can be calculated from the condition for statistical moments, which follows from Eq. (1)

$$\mu_j = \alpha_1 \mu_{i,1} + \alpha_2 \mu_{i,2}, \quad (3)$$

where $\mu_j = \int \xi^j P(\xi)\, d\xi$ is the statistical moment of order j, $\mu_{j,i} = \int \xi^j P_i(\xi)\, d\xi$ are statistical moments of the components of the Gaussian mixture, the first index shows the order of the moment, the second index shows the number of the component.

Thus, in order to find five unknown parameters, it is necessary to solve a system consisting of five equations. It has the following form

$$\alpha_1 m_1 + (1 - \alpha_1) m_2 = \mu_1 = 0, \tag{4}$$

$$\alpha_1 \left(m_1^2 + \sigma_1^2\right) + (1 - \alpha_1)\left(m_2^2 + \sigma_2^2\right) = \mu_2, \tag{5}$$

$$\alpha_1 \left(m_1^3 + 3m_1\sigma_1^2\right) + (1 - \alpha_1)\left(m_2^3 + 3m_2\sigma_2^2\right) = \mu_3, \tag{6}$$

$$\alpha_1 \left(m_1^4 + 6m_1^2\sigma_1^2 + 3\sigma_1^4\right) + (1 - \alpha_1)\left(m_2^4 + 6m_2^2\sigma_2^2 + 3\sigma_2^4\right) = \mu_4, \tag{7}$$

$$\alpha_1 \left(m_1^5 + 10m_1^3\sigma_1^2 + 15m_1\sigma_1^4\right) + (1 - \alpha_1)\left(m_2^5 + 10m_2^3\sigma_2^2 + 15m_2\sigma_2^4\right) = \mu_5. \tag{8}$$

Equality $\mu_1 = 0$ follows from the condition that the average value of a random variable ξ coincides with the level of the undisturbed sea surface. The first four statistical moments have a generally accepted interpretation, μ_2 is a variance, μ_3 is a skewness, $\mu_4 - 3$ is an excess kurtosis. The fifth statistical moment is practically not studied during oceanological research, which makes it impossible to use it when calculating the parameters of a two-component Gaussian mixture.

Therefore, the first four statistical moments are used to calculate the model parameters, while the fifth parameter remains free [12, 20]. The weight coefficient α_1 is chosen as a free parameter, which varies to satisfy the conditions of unimodality and minimization of function inflection. Within the framework of this approach, in addition to computational difficulties, problems arise with the ambiguity of the solutions obtained.

3 The Fifth Statistical Moment

To solve the problem of closing the system of Eqs. (4)–(8) for calculating the parameters of a two-component Gaussian mixture, it is necessary to determine the fifth statistical moment. The statistical moments of the Gaussian distribution are given as

$$\left.\begin{array}{l} \mu_{2j} = \frac{(2j)!}{2^n j!}\mu_2^j, \\ \mu_{2j+1} = 0, \quad j \geq 1, \end{array}\right\}. \tag{9}$$

Deviations of the measured values μ_j from the values corresponding to Eq. (9) are an indicator of the nonlinearity of the wave field. According to field measurements,

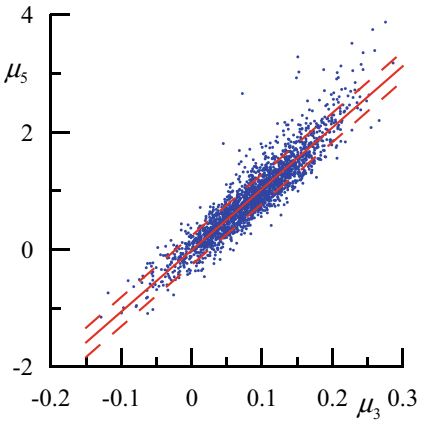


Fig. 1 The relationship of the fifth μ_5 and third μ_3 statistical moments. Points are measurement data, a solid line is regression (10), dashed lines are standard deviations from regression

statistical moments μ_3 and μ_4 are not related to each other [5]. At the same time, earlier in laboratory experiments it was shown that statistical moments (except μ_4) depend on the steepness of the waves [21]. These results suggest that there is a relationship between μ_3 and μ_5.

Studies of the variability of the senior statistical moments of sea surface elevations, having an order of magnitude higher than the second, were carried out on the basis of field measurement data. The data were obtained on a stationary oceanographic platform of the Marine Hydrophysical Institute of the Russian Academy of Sciences, which is located at the northern part of Black Sea. The features of wave research on a stationary oceanographic platform and the wind regime in its vicinity are described in Zapevalov and Garmashov [5], Toloknov and Korovushkin [22] and Solov'ev and Ivanov [23]. The depth in the place where it is located is about 30 m. This depth corresponds to the condition "deep water" for the characteristic Black Seawaves.

The measurement data are presented in Fig. 1, indicate a high correlation between the third and fifth statistical moments. A data array including 2224 estimates of statistical moments was used. Statistical moments were calculated from wave recordings lasting 20 min. The correlation coefficient between μ_3 and μ_5 is 0.93. The presence of high correlation allows us to construct a linear regression equation, which has the form

$$\mu_5 = 10.47\,\mu_3 - 0.015. \tag{10}$$

The standard deviation from regression is 0.25.

Let's consider how qualitatively a probability density function as two-component Gaussian mixture, the parameters of which are calculated by first four equations from Eqs. (4)–(8) with a free fifth parameter reproduces the fifth statistical moment. Let's denote the statistical moments calculated by the model as $\mu_j^{(M)}$. Within the framework of this approach, the accuracy of reproducing statistical moments $\mu_3^{(M)}$

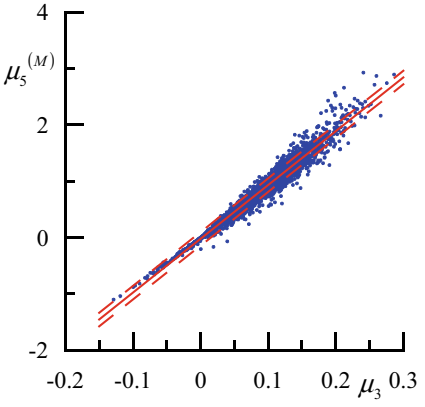


Fig. 2 Dependencies $\mu_5^{(M)} = \mu_5^{(M)}(\mu_3)$. Points are calculated values $\mu_5^{(M)}$, a solid line is regression (11), dashed lines are standard deviations from regression

and $\mu_4^{(M)}$ can be achieved and better 10^{-3} [20]. Taking into account the errors of wave measurements, such accuracy means that $\mu_3^{(M)} = \mu_3$ and $\mu_4^{(M)} = \mu_4$.

Similarly to how the relationship between μ_3 and μ_5 was investigated, let's consider the relationship μ_3 with the model parameter $\mu_5^{(M)}$. There is a high correlation between $\mu_5^{(M)}$ and μ_3. The correlation coefficient is 0.98. A linear regression equation has the form

$$\mu_5^{(M)} = 9.56\,\mu_3 - 0.023. \tag{11}$$

The dependencies $\mu_5^{(M)}$ on μ_3 are shown in Fig. 2.

Comparing how does the calculated and measured fifth statistical moment change it can be noted that the scatter of $\mu_5^{(M)}$ (when μ_3 is fixed) is smaller than the scatter of μ_5. The standard deviation of individual values $\mu_5^{(M)}$ from regression (11) is 0.12. The coefficient at μ_3 in regression (11) is less than in regression (10).

Figure 3 shows the relationship between the measured and calculated fifth statistical moment. The standard deviation $\mu_5^{(M)}$ from μ_5 is equal to 0.25. The correlation coefficient is 0.93. This means that the procedure for calculating parameters, model (1) quite well reproduces the fifth statistical moment of sea surface elevations.

In the data analysis presented here, no selection was carried out according to the conditions of wave measurements. Therefore, these statistical estimates can be considered as average for an ensemble of situations.

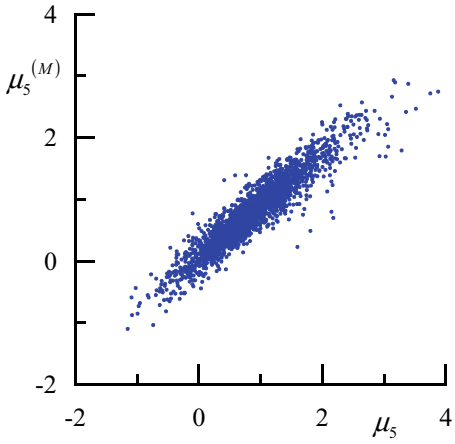


Fig. 3 Dependence $\mu_5^{(M)} = \mu_5^{(M)}(\mu_5)$

4 Conclusion

Sea waves are a weakly nonlinear process. In the framework of the statistical theory of such processes, unknown distribution parameters are calculated from known statistical moments of a random variable. Constructing the distribution of sea surface elevations in the form of a two-component Gaussian mixture, the problem lies in the fact that this model has five parameters and for their calculation it is necessary to know statistical moments up to and including the fifth order. In oceanological research, only the first four statistical moments are determined, respectively, only four equations can be used. One of the parameters of the two-component Gaussian mixture remains free. This leads to some uncertainty in the constructed distributions.

A new approach is proposed for calculating the parameters of a two-component Gaussian mixture when modeling the distribution of sea surface elevations. Based on wave measurements carried out in the Black Sea, it is shown that there is a linear relationship between the third μ_3 and fifth μ_5 statistical moments. The linear regression equation between these parameters is obtained. The correlation coefficient between and is 0.92. High correlation makes it possible to use Eq. (8) for the fifth statistical moment by setting the term in its right part based on the information about μ_3, i.e. using the regression Eq. (10). After substituting μ_5 into Eq. (8), the system of Eqs. (4)–(8) becomes closed. With such a procedure for calculating the distribution parameters, the uncertainty of the distribution parameters of the sea surface elevations is excluded.

It is also shown that the procedure for calculating the parameters of a two-component Gaussian mixture with a free parameter allows us to obtain a distribution of surface elevations, in which the fifth statistical moment corresponds to the measurement data.

Acknowledgements This work was carried out as part of a state assignment on the topic FNNN-2021-0004 “Fundamental studies of oceanological processes which determine the state

and evolution of the marine environment influenced by natural and anthropogenic factors, based on observation and modeling methods".

References

1. Stokes, G.G. (1849) On the theory of oscillatory waves // Trans. Cambridge Philos. Soc. 8: 197–229.
2. Huang N.E., Long S.R., Tung C.C., Yuan Y., Bliven L.F. (1983) A non-Gaussian joint statistical model for surface elevation of nonlinear random wave fields // J. Geophys. Res. 88: 7597–7606.
3. Hou Y., Song G., Zhao X., Song J., Zheng, Q. (2006) Statistical distribution of nonlinear random water wave surface elevation // Chinese Journal Oceanology and Limnology. 24(1): 1–5. https://doi.org/10.1007/BF02842767.
4. Tayfun M.A., Alkhalidi M.A. (2016) Distribution of surface elevations in nonlinear seas // Offshore Technology Conference Asia. https://doi.org/10.4043/26436-ms.
5. Zapevalov A.S., Garmashov A.V. (2021) Skewness and kurtosis of the surface wave in the coastal zone of the Black Sea // Physical Oceanography. 28(4): 414–425. https://doi.org/10.22449/1573-160X-2021-4-414-425.
6. Guedes Soares C., Cherneva Z., Antão E.M. (2004) Steepness and asymmetry of the largest waves in storm sea states // Ocean Engineering. 31: 1147–1167.
7. Jha, A.K., Winterstein S.R. (2000) Nonlinear Random Ocean Waves: Prediction and Comparison with Data. Proceedings of ETCE/OMAE2000 Joint Conference, February 14–17, 2000, New Orleans, paper no. ETCE/OMAE2000–6125, ISBN: 0791819957.
8. Zapevalov A.S., Garmashov A.V. (2022) The appearance of negative values of the skewness of sea-surface waves // Izvestiya, Atmospheric and Oceanic Physics, 58(3) 263–269. https://doi.org/10.1134/s0001433822030136.
9. Kendall M.J., Stewart A. (1958) The Advanced Theory of Statistics. Vol. I. Distribution theory. London: Butler & Tanner Ltd. 675 p.
10. Shumeyko I., Burdyugov V., Abramovich A. (2023) Simulation of sea surface elevations by the Edgeworth distribution // E3S Web of Conferences. 389. 02024. https://doi.org/10.1051/e3sconf/202338902024.
11. Burdygov V.M. (2023) The Features of Simulation of Radar Altimeter Return Waveform Using Hermite Polynomials // Springer Proceedings in Earth and Environmental Sciences. 73–82. https://doi.org/10.1007/978-3-031-25962-3_7.
12. Zapevalov A.S., Ratner Yu.B. (2003) Analytic model of the probability density of slopes of the sea surface // Physical Oceanography. 13(1): 1–13. https://doi.org/10.1023/A:1022444703787.
13. Blinnikov S., Moessner R. (1998) Expansions for nearly Gaussian distributions // Astron. Astrophys. Suppl. Ser. 130: 193–205.
14. Kwon O.K. (2020): Analytic expressions for the positive definite and unimodal regions of Gram-Charlier series, Communications in Statistics-Theory and Methods. https://doi.org/10.1080/03610926.2020.1833219.
15. Lin W., Zhang J.E. (2021). The valid regions of Gram–Charlier densities with high-order cumulants // Journal of Computational and Applied Mathematics 407(2): 113945. https://doi.org/10.1016/j.cam.2021.113945.
16. Gao, Z., Sun, Z., & Liang, S. (2020). Probability density function for wave elevation based on Gaussian mixture models. Ocean Engineering, 213, 107815. https://doi.org/10.1016/j.oceaneng.2020.107815.
17. Zhuravlev, Yu.I., Isaev, I.V. (1979) Construction of recognition algorithms, which are correct for a preset control sample. Zhurnal Vychislitel'noi Matematiki i Matematicheskoi Fiziki. 19(3): 726–738.

18. Carreira-Perpiñán M.A. (2000) Mode-finding for mixture of Gaussian distributions // IEEE Trans. on Pattern Analys. and Mach. Intell. 22(11): 1318–1323.
19. Aprausheva N.N., Sorokin S.V. (2013) Exact equation of the boundary of unimodal and bimodal domains of a two-component Gaussian mixture // Pattern Recognition and Image Analysis. 23(3): 341–347. https://doi.org/10.1134/S1054661813030024.
20. Zapevalov, A.S., Knyazkov, A.S. (2022) Statistical description of the sea surface by two-component Gaussian mixture // Physical Oceanography. 29(4): 395–403. https://doi.org/10.22449/1573-160X-2022-4-395-403.
21. Huang N.E., Long S.R. (1980) An experimental investigation of the surface elevation probability distribution and statistics of wind-generated waves // J. Fluid Mech. 101(1): 179–200.
22. Toloknov Yu.N., Korovushkin A.I. (2010) System of collecting hydrometeorological information // Environmental control systems. (10): 50–53.
23. Solov'ev Yu.P., Ivanov V.A. (2007) Preliminary results of measurements of atmospheric turbulence over the sea // Physical Oceanography. Iss. 3: 154–172.

Evolution of Small-Scale Turbulence in a Stratified Shear Flow, Affected by Interplay of the Kinetic and Potential Turbulent Energies



D. Gladskikh, L. Ostrovsky, I. Soustova, and Y. Troitskaya

Abstract As known, the most energy-dense turbulence in the ocean occurs in its upper layer and it actively interacts with mesoscale motions. We study the evolution of a turbulent layer in stratified ocean using the theory of unsteady turbulent flows in a stratified fluid. The theory starts from a kinetic equation for turbulence parameters and results in the set of equations involving the mutual transformation of the kinetic and potential energies of turbulence that is shown to significantly affect the overall dynamics of energy exchange between small-scale turbulence and mesoscale motions and the formation of the upper mixed layer. Notably, the transformation between kinetic and potential energies eliminates the restriction on the existence of turbulence at large Richardson numbers. The results are applied to the analysis of in situ data for turbulence evolution under the action of shear flows and internal waves, obtained in different areas.

Keywords Turbulence · Ocean · Upper mixed layer · Gradient Richardson number

D. Gladskikh (✉) · L. Ostrovsky · I. Soustova · Y. Troitskaya
Institute of Applied Physics, Russian Academy of Sciences, Division of Geophysical Research, Nizhny Novgorod, Russian Federation
e-mail: daria.gladskikh@gmail.com

D. Gladskikh
M.V. Lomonosov Moscow State University, Research Computing Center, Moscow, Russian Federation

Moscow Center for Fundamental and Applied Mathematics, Moscow, Russian Federation

L. Ostrovsky
Department of Applied Mathematics, University of Colorado, Boulder, CO, USA

© The Author(s), under exclusive license to Springer Nature Switzerland AG 2024

V. Karev (ed.), *Proceedings of the 9th International Conference on Physical and Mathematical Modelling of Earth and Environmental Processes*, Springer Proceedings in Earth and Environmental Sciences, https://doi.org/10.1007/978-3-031-54589-4_17

1 Introduction

It is now known that small-scale turbulence in the ocean (as well as, for example, lakes and reservoirs) requires consideration both when developing global models and when modeling and forecasting regional climate. Small-scale and mesoscale processes interact effectively with each other. The physical basics of these processes have been described in the 1960–1980s [1] using the semi-empirical closing hypotheses for turbulent viscosity and thermal conductivity. Similar equations were used in more specific models of the formation of the upper turbulent layer [2]. In particular, it was shown that velocity shear and non-breaking internal waves can support and enhance small-scale turbulence and induce the formation of intermitted turbulence ("spots") ubiquitous in the ocean [3], even at large values of Richardson number, exceeding both the critical value $Ri = 1/4$ [4, 5] and, according to a less demanding condition: $Ri < Pr_T$ [6], the Prandtl number.

However, in the last decades, we observed fast progress in the development of sensitive measurement tools, as well as effective numerical methods that, in turn, stimulated strong progress in studies of the dynamics of UML. Special attention is paid to the areas of the World Ocean in which the UML dynamics is especially important for climate [7, 8]. They include the equatorial areas (within a few degrees of longitude), where the upper-layer turbulence is anomalously strong and, as a result, very strongly affects the climate, since the most intensive heat absorption occurs at the equator. In particular, the upper equatorial ocean can be a natural "laboratory" for studies of the effects of stratification and shear flows (such as the South equatorial current (SEC) and the equatorial undercurrent (EUC)) on the observed intensification of turbulence in the center of the thermocline. The continental shelves represent another critically important zone affecting the global climate, and the effect of intensive internal waves on turbulent mixing in shelf areas is being actively discussed (e.g., Nash et al. [9]). The progress in long-time measurements with a high spatial resolution using underwater platforms and towed gliders [10, 11] has resulted, among others, in a better understanding of the interaction between internal waves and turbulence. It was shown, in particular, that the rate of internal waves' attenuation correlated well with the rate of turbulent mixing in pycnocline [12].

The theoretical description of stratified turbulence and the corresponding numerical simulation methods, along with the classical semi-empirical schemes such as RANS, used large-eddy simulation (LES) and the direct numerical simulation (DNS). The separation is based on the degree of detail in the resolution of turbulent pulsations and their energy spectrum. Over the past 20 years, new approaches based on spectral theories were developed [13, 14] to describe the features of stratified turbulent flows. These models can in some respects be an alternative to the traditional RANS models; they potentially allow one to more consistently describe non-stationary processes of turbulent-wave interaction than the RANS models.

In this work, we study the evolution of a turbulent layer in a stably stratified fluid under the action of shear flows using a non-stationary model of turbulence dynamics developed in Ostrovsky and Troitskaya [15]. This model starts from a

kinetic equation for turbulence parameters and results in the set of equations involving a mutual transformation of the kinetic and potential energies of turbulence that, as shown below, can significantly affect the overall dynamics of energy exchange between turbulence and internal waves and the formation of UML. Besides, this approach allows an account for some important but usually neglected effects such as the dependence of vertical anisotropy of turbulence on stratification. Notably, the transformation between kinetic and potential energies removes the restriction on the existing of turbulence at large Richardson numbers. The general approach is applied here to the analysis of in situ data for turbulence evolution under the action of shear flows, obtained in different areas of the World Ocean.

2 General Equations

The system [15] for a turbulent flow in stratified fluid includes the equations for the mean values of velocity $\langle \mathbf{u} \rangle$, density $\langle \rho \rangle$, turbulent kinetic energy $k = 3V^2/2$, and variance of density pulsations $\langle \rho'^2 \rangle$:

$$\frac{\partial \langle u_i \rangle}{\partial t} + \langle u_j \rangle \frac{\partial \langle u_i \rangle}{\partial x_j} + \frac{1}{\rho_0}\frac{\partial \langle p \rangle}{\partial x_i} + g_i \frac{\langle \rho \rangle - \rho_0}{\rho_0} = \frac{\partial}{\partial x_j}\left(L\sqrt{k}\left(\frac{\partial \langle u_i \rangle}{\partial x_j} + \frac{\partial \langle u_j \rangle}{\partial x_i} \right) \right),$$

$$\frac{\partial \langle \rho \rangle}{\partial t} + \langle u_i \rangle \frac{\partial \langle \rho \rangle}{\partial x_i} = 2\frac{\partial}{\partial x_i} L\sqrt{k}\left(\frac{\partial \langle \rho \rangle}{\partial x_i} + \frac{3}{2k\rho_0}\left(g_i \langle \rho'^2 \rangle + \mathbf{g}\beta_i \right) \right),$$

$$\frac{\partial k}{\partial t} + \langle u_i \rangle \frac{\partial k}{\partial x_i} - L\sqrt{k}\left(\frac{\partial \langle u_i \rangle}{\partial x_j} + \frac{\partial \langle u_j \rangle}{\partial x_i} \right)^2 - \frac{\mathbf{g}}{\rho_0} L\sqrt{k} \times$$

$$\times \left(\frac{\partial \langle \rho \rangle}{\partial z} + \frac{3\mathbf{g}}{2k\rho_0}\left(\langle \rho'^2 \rangle + \beta_z \right) \right) + \frac{Ck^{3/2}}{L} = \frac{5}{3}\frac{\partial}{\partial x_i}\left(L\sqrt{k}\frac{\partial k}{\partial x_i} \right),$$

$$\frac{\partial \langle \rho'^2 \rangle}{\partial t} + \langle u_i \rangle \frac{\partial \langle \rho'^2 \rangle}{\partial x_i} - 2\frac{\partial \langle \rho \rangle}{\partial x_i} L\sqrt{k}\left(\frac{\partial \langle \rho \rangle}{\partial x_i} + \left(g_i \langle \rho'^2 \rangle - \mathbf{g}\beta_i \right)\frac{3}{2k\rho_0} \right) +$$

$$+ \frac{Dk^{1/2}}{L}\langle \rho'^2 \rangle = \frac{\partial}{\partial x_i} L\sqrt{k}\frac{\partial \langle \rho'^2 \rangle}{\partial x_i}. \tag{1}$$

Here L is the linear scale of turbulence, $\mathbf{g}$ is the gravity acceleration, β_i are the components of the vector which characterizes the effect of pressure fluctuations due to random displacements of a particle in a stratified fluid.

In an incompressible fluid considered here, $\nabla \cdot \mathbf{u} = 0$. This system includes mutual transformation between kinetic and potential energies of turbulent pulsations. Here turbulence can be maintained by mean velocity shear (including that generated by internal waves) at any values of *Ri*. In particular, there is no turbulence "breakdown"

phenomenon, in which, in certain phases of the wave, the velocity shear cannot maintain a nonzero level of turbulent energy.

3 Local Turbulence Dynamics

For a better understanding of the process, we consider the local interaction between average kinetic energy k and average potential energy $\Pi = \frac{\langle \rho'^2 \rangle g^2}{2N^2\rho_0^2}$ with given buoyancy frequency N and current velocity shear S. At first, we consider a spatially homogeneous process when these values are constant and the terms with spatial derivatives in (1) are absent. The resulting equations are

$$\begin{aligned} \frac{dk}{dt} &= S^2 L\sqrt{k} - N^2 L\sqrt{k}\left(1 - \frac{3\Pi}{k}(1-R)\right) - \frac{Ck^{\frac{3}{2}}}{L}, \\ \frac{d\Pi}{dt} &= N^2 L\sqrt{k}\left(1 - \frac{3\Pi}{k}(1-R)\right) - \frac{Dk^{\frac{1}{2}}\Pi}{L}, \end{aligned} \tag{2}$$

where L is the turbulence length scale (equal to 1/3 m in this study), R is the anisotropy parameter (equal to 0.5 in this study), C and D are the empirical constants (equal to 0.05 in this study).

As an example, we used some data from the paper [8] that provided dataset for three cruises made in 2006–2009 in different areas of the World Ocean: North Atlantic (cruise D3406, June–July 2006, and cruise D321, July–August 2007) and Southern Ocean (cruise JC29, November–December 2008). These experiments were aimed at studying turbulent mixing in the presence of a stratified shear flow associated with mesoscale motions such as eddies and fronts.

Figure 1 shows evolution to a stationary state of kinetic and potential energies (m^2/sec^2), obtained by solving the system (2), with a given velocity shear and Brunt-Väisälä frequency from Forryan et al. [8].

As mentioned, here we apply the theory to the data of three cruises described in [8]. First, we digitized red curves in Fig. 2 of that paper (as mentioned, there is a large dispersion of real data, but we naturally use mean profiles). Digitization was carried out using *GetData Graph Digitizer* software. Then, using the given profiles of S and N^2, we calculated the Richardson number as shown in Fig. 2.

Note that for water density of 1000 kg/m^3, static pressure in dbar coincides with depth in meters so that in our calculations we use the depth, neglecting at that point small differences in density.

As seen from Fig. 1, Richardson number exceeds 0.25 within all range of the available data, and its maximum lies in the range of 10–23.

Then, using the interpolation of digitized data for S and N^2 from Forryan et al. [8], we solved Eqs. (2) with the initial conditions $k(0, z) = k_0 \exp(-0.1z)$ and $\Pi(0, z) = \Pi_0 \exp(-0.01z)$, z is a given parameter in the local model. The values k_0

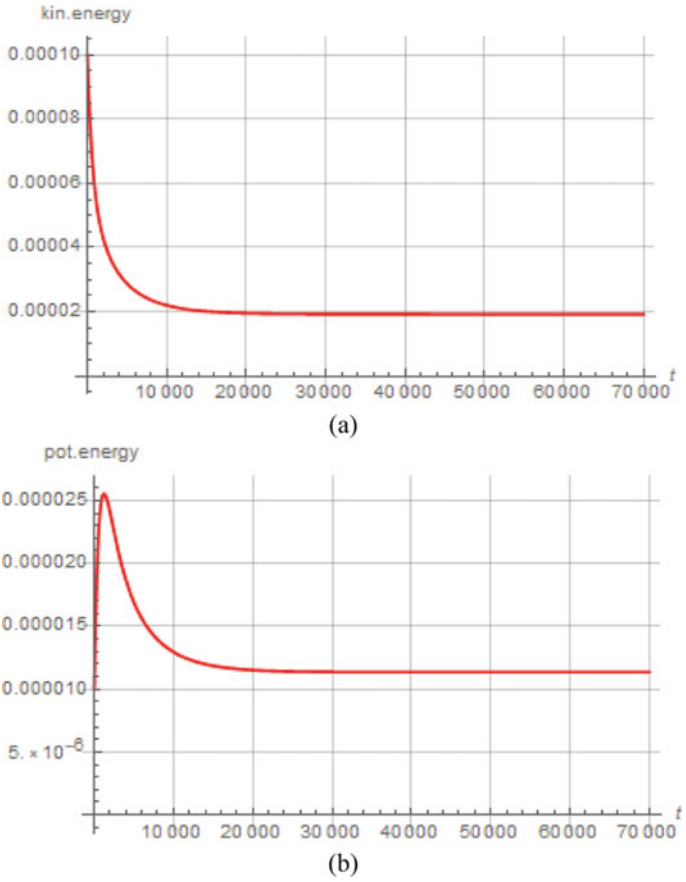


Fig. 1 Evolution to a stationary state of kinetic (**a**) and potential (**b**) energies (m^2/sec^2), obtained by solving the local system on the left, with a given $S^2 = 0.002137 * 0.002137$ sec^{-2} and $N^2 = 0.0000101$ s^{-2} from Forryan et al. [8]

and P_0 varied from 10^{-6} to 10^{-5} m^2/s^2 with slight changes in transient processes but with the same asymptotic values of k and Π at large times.

Since the work [8] presents the profiles of turbulent kinetic energy dissipation rate, it was necessary to make a comparison with them. We also digitized them using *GetData Graph Digitizer* software.

Note that in Eqs. (1) and (2) Kolmogorov's hypotheses for the dissipation rate of turbulent energy ε is used; namely:

$$\varepsilon = \frac{Ck^{3/2}}{L}. \tag{3}$$

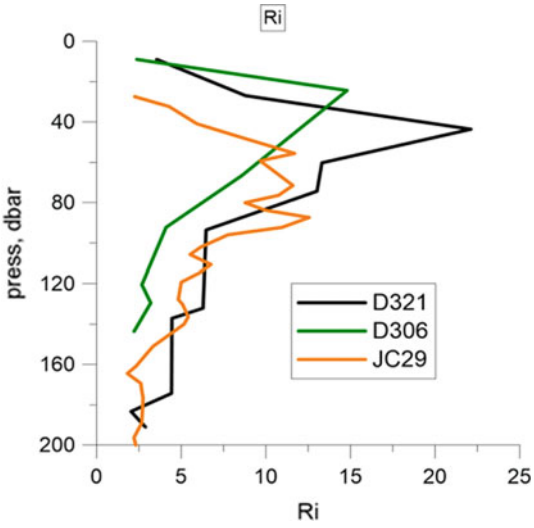


Fig. 2 Profiles of Richardson number for three cruises calculated from Fig. 2 of Forryan et al. [8]

Thus, we made calculations using system (2) for each station, substituting the given S and N^2 for the selected points. Next, for each point, dissipation was calculated using formula (3), and the calculated dissipation rate profiles were compared with those given in the work [8]. Results are presented on the Figs. 3, 4 and 5.

Here the difference between calculations and measurements is mainly within a half-order. Considering the large spread of experimental data, this is a rather good agreement. Thus, model (1), namely its local case (2) in general correctly reproduces

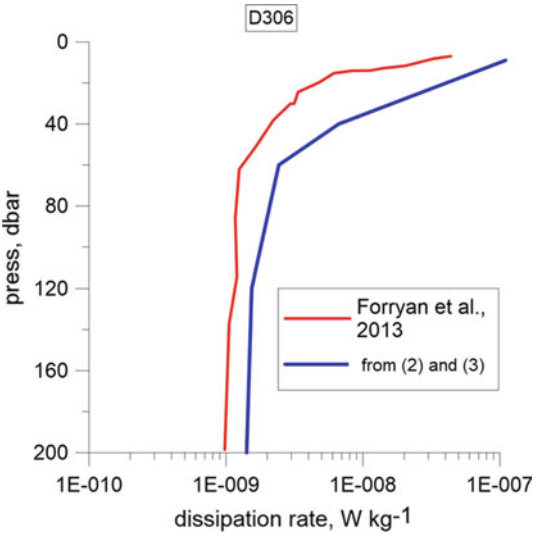


Fig. 3 Profiles of turbulent kinetic energy dissipation rate for D306

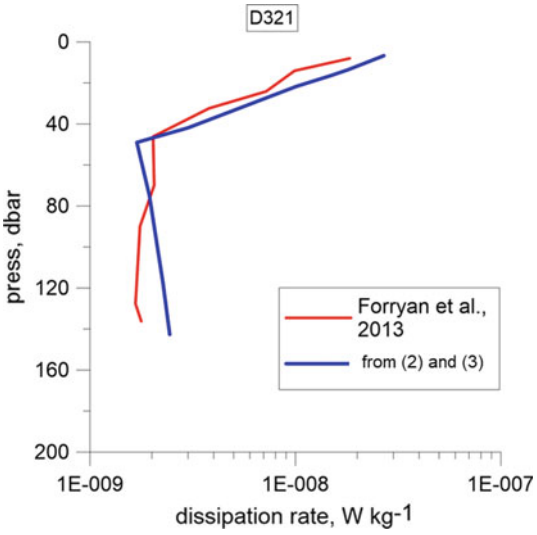


Fig. 4 Profiles of turbulent kinetic energy dissipation rate for D321

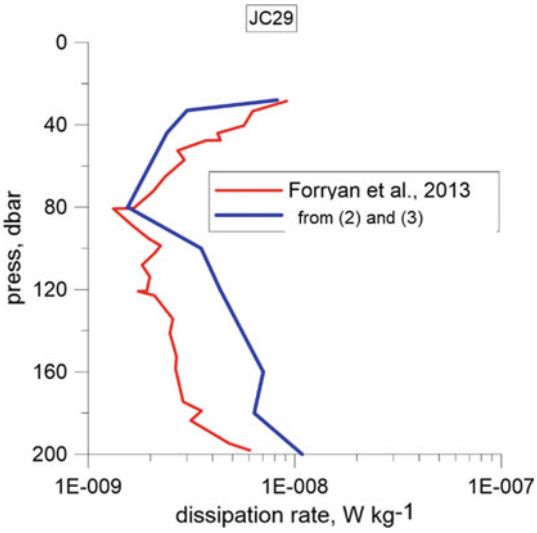


Fig. 5 Profiles of turbulent kinetic energy dissipation rate for JC209

the features of the vertical distribution of the rate of dissipation of kinetic energy in the World Ocean.

4 Conclusions

In this study we used the theory of unsteady turbulent flows in a stratified fluid to describe the turbulent layer in stratified ocean. The results are applied to the analysis of in situ data for turbulence evolution, obtained in different areas of the World Ocean. Although the initial source of turbulence is generally the shear instability, it can be supported and amplified by stable currents at larger Richardson numbers. Moreover, the potential energy of turbulence related to mixing by density fluctuations in a stratified fluid allows the existence of turbulence at any Richardson number. It is confirmed by the data on turbulent energy dissipation rate in the upper ocean. In the future, it is planned to study the application of the full (non-local) model to describe the evolution of turbulence in the World Ocean.

Acknowledgements The work was financially supported by the Russian Scientific Foundation (project № 23-27-00002).

References

1. Monin, A.S.; Ozmidov, R.V. Okeanskaya Turbulentnost'; (Ocean Turbulence); Gidrometeoizdat: Leningrad, Russia, 1981.
2. Ostrovsky, L. A., Soustova, I. A. Upper mixed layer of the ocean as a sink of internal wave energy. Okeanologia 1979, 19, 973–981.
3. Strang, E.J.; Fernando, H.J. Vertical mixing and transports through a stratified shear layer. J. Phys. Oceanogr. 2001, 31, 2026–2048.
4. Miles, J.W. On the stability of heterogeneous shear flows. J. Fluid Mech. 1961, 10, 496–508.
5. Howard, L.N. Note on a paper of John W. Miles. J. Fluid Mech. 1961, 10, 509–512.
6. Monin, A.S.; Yaglom, A.M., Statisticheskaya gidromekhanika. Chast' 1; (Statistical Hydromechanics. Part 1), Golitsyn, G.S., Ed.; Nauka: Moscow, Russia, 1965.
7. Moum, J. N., Hughes, K. G., Shroyer, E. L., Smyth, W. D., Cherian, D., Warner, S. J., et al. Deep cycle turbulence in Atlantic and Pacific cold tongues. Geophysical Research Letters, 2022, 49, e2021GL097345.
8. Forryan, A.; Martin, A.P.; Srokosz, M.A.; Popova, E.E.; Painter, S.C.; Renner AH, H. A new observationally motivated Richardson number based mixing parametrization for oceanic mesoscale flow. J. Geophys. Res. Oceans 2013, 118, 1405–1419.
9. Nash, J., H. Peters, S. Kelly, J. L. Pelegrí, M. Emelianov, and M. Gasser, 2012: Turbulence and high-frequency variability in a deep gravity current outflow. Geophys. Res. Lett., 39, L18611.
10. J.E. Hopkins, G.R. Stephenson, J.M. Green, M.E. Inall, M.R. Palmer Storms modify baroclinic energy fluxes in a seasonally stratified shelf sea: Inertial-tidal interaction. J. Geophys. Res.: Oceans, 119 (10) (2014), pp. 6863–6883.
11. Vlasenko, V., Stashchuk, N., Inall, M. E., and Hopkins, J. E. (2014), Tidal energy conversion in a global hot spot: On the 3-D dynamics of baroclinic tides at the Celtic Sea shelf break, J. Geophys. Res. Oceans, 119, 3249–3265.
12. M. Inall, D. Aleynik, T. Boyd, M. Palmer, J. Sharples. Internal tide coherence and decay over a wide shelf sea. Geophys. Res. Lett., 38 (23) (2011).
13. Sukoriansky, S.; Galperin, B.; Perov, V. Application of a new spectral theory of stably stratified turbulence to atmospheric boundary layer over sea ice. Bound. -Layer Meteorol. 2005, 117, 231–257.

14. Galperin, B.; Sukoriansky, S. QNSE theory of the anisotropic energy spectra of atmospheric and oceanic turbulence. Phys. Rev. Fluids 2020, 5, 063803.
15. Ostrovsky, L.A.; Troitskaya, Y.I. Model of turbulent transfer and the dynamics of turbulence in a stratified shear flux. Izv. Akad. Nauk SSSR, Fiz. Atmos. Okeana 1987, 3, 101–104.

The Flow a Drop of Water Around a Thin Thread in Zero Gravity and Under Normal Gravity Conditions



A. I. Fedyushkin, A. A. Gnevushev, A. S. Zaharov, and A. N. Rozhkov

Abstract The paper presents the results of the research on the dynamics of flows a drop around a thin thread in zero gravity and under normal gravity of the Earth. The characteristic modes of droplet flow around thin thread: repulsion, retention and flow with fragmentation and coalescence of secondary parts of the droplet are shown.

Keywords Numerical simulation · Navier–Stokes equations · Two-phase liquid system · Flow drop · Thin thread

1 Introduction

The study the flow of drop around think thread has both fundamental scientific significances for the investigation of the laws of multiphase hydrodynamics and applied significance in various physical processes. The fragmentation of liquid droplets in collisions with an obstacle is a defining element of modern technologies (coating, inkjet printing, cooling of surfaces, fuel injection into engines, the supply of medicines to the focus of the disease), as well as a determining factor in the penetration of liquid droplets through protective masks, in relation with the protection of people from infectious diseases transmitted by airborne droplets. A lot of papers devoted to the study of droplet dynamics, for example, [1–10]. Detailed

A. I. Fedyushkin (✉) · A. A. Gnevushev · A. S. Zaharov · A. N. Rozhkov
Ishlinsky Institute for Problems in Mechanics RAS, 101(1) Prospect Vernadskogo, Moscow 119526, Russia
e-mail: fai@ipmnet.ru

A. A. Gnevushev
e-mail: gnevushev-98@mail.ru

A. S. Zaharov
e-mail: zakharovartemm@yandex.ru

A. N. Rozhkov
e-mail: rozhkov@ipmnet.ru

© The Author(s), under exclusive license to Springer Nature Switzerland AG 2024

V. Karev (ed.), *Proceedings of the 9th International Conference on Physical and Mathematical Modelling of Earth and Environmental Processes*, Springer Proceedings in Earth and Environmental Sciences, https://doi.org/10.1007/978-3-031-54589-4_18

reviews of works devoted to the study of hydrodynamics during impact and spreading of droplets can be found in Rozhkov et al. [2], Rozhkov [6], Yarin and Weiss [9], Yarin et al. [10].

2 Setting Problem and Mathematical Model

The scheme of the drop motion model is shown in Fig. 1 (H is the height, R is the radius of the cylindrical calculated area, z is the axis of symmetry, $\boldsymbol{g}$ is the acceleration vector of gravity). The centers of the drop and the cylindrical horizontal thread are located on the z axis. At the initial moment, the distance between the surface of the drop and the surface of the thread is equal to the radius of the thread ($d_t/2$), and the drop begins to move down with speed v_i. The problem is characterized by dimensionless Reynolds numbers $Re = \rho v_i d_i/\mu$ and the Weber number $We_i = \rho v_i^2 d_i/\sigma$, where ρ is the density, v_i is the drop rate, d_i is the drop diameter, μ is the viscosity, and σ is the surface tension coefficient.

Numerical simulation is based on the numerical solution of two-dimensional axisymmetric Navier–Stokes equations for two immiscible liquids [11].

$$\frac{\partial(\rho\mathbf{u})}{\partial t} + \nabla\cdot(\rho\mathbf{u}\mathbf{u}) = -\nabla p + \nabla\cdot\left[\mu\left(\nabla\mathbf{u} + \nabla\mathbf{u}^T\right)\right] + \rho\mathbf{g} + \mathbf{F}. \tag{1}$$

For two-phase air–liquid system the only one momentum equation is solved in all calculation domain, and the resulting velocity field is shared among the phases. The momentum Eq. (1) is dependent on the function of the volume fractions ε ($0 \le \varepsilon \le 1$) of liquid phase through the properties: density $\rho = \varepsilon\rho_{air} + (1-\varepsilon)\rho_{\text{liquid}}$ and viscosity

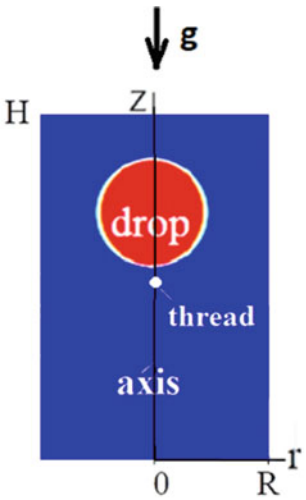


Fig. 1 Schema of model (part of the calculated area near the droplet and thread)

$\mu = \varepsilon\mu_{\text{air}} + (1-\varepsilon)\mu_{\text{liquid}}$, where the values with the index 'air' refer to air, and with the index 'liquid' refer to liquid. The volume fraction of liquid ε was determined from the solution of the transfer equation: $\frac{\partial \rho\varepsilon}{\partial t} + \nabla \cdot (\rho\varepsilon \mathbf{u}) = 0$.

For the two-dimensional case of a two-phase incompressible air–liquid system the Navier–Stokes Eqs. (3) in a cylindrical coordinate system for an axisymmetric approximation without considering the circumferential velocity can be written as follows:

$$\frac{\partial u_1}{\partial x_1} + \frac{u_1}{x_1} + \frac{\partial u_2}{\partial x_2} = 0, \tag{2}$$

$$\frac{\partial(\rho u_1)}{\partial t} + u_1\frac{\partial(\rho u_1)}{\partial x_1} + u_2\frac{\partial(\rho u_1)}{\partial x_2} = -\frac{\partial p}{\partial x_1} + \frac{1}{x_1}\frac{\partial}{\partial x_1}\left(x_1\mu\frac{\partial u_1}{\partial x_1}\right) + \frac{\partial}{\partial x_2}\left(\mu\frac{\partial u_2}{\partial x_2}\right) - \mu\frac{u_1}{x_1^2} + F_1, \tag{3}$$

$$\frac{\partial(\rho u_2)}{\partial t} + u_1\frac{\partial(\rho u_2)}{\partial x_1} + u_2\frac{\partial(\rho u_2)}{\partial x_2} = -\frac{\partial p}{\partial x_2} + \frac{1}{x_1}\frac{\partial}{\partial x_1}\left(x_1\mu\frac{\partial u_2}{\partial x_1}\right) + \frac{\partial}{\partial x_2}\left(\mu\frac{\partial u_2}{\partial x_2}\right) - \rho g + F_2, \tag{4}$$

where t is the time, $x_1 \equiv r$, $x_2 \equiv z$ are the radial and axial coordinates, u_1, u_2 are the radial and axial components of the velocity vector $\boldsymbol{u}(u_1, u_2)$, p is the pressure, ρ is the density, μ is the dynamic viscosity coefficient, and F_1, F_2 are the radial and axial components of external force $\boldsymbol{F}(F_1, F_2)$, acting only in very narrow zone along the air–liquid interface, g is axial component of the gravity acceleration vector $\boldsymbol{g}$.

To describe the fluid flow of a two-phase air–liquid system in the approximation of axial symmetry, a model based on 2D system of Navier–Stokes Eqs. (2–4) was used, which made it possible to determine the velocities for liquid and air. Density and viscosity were determined through the function of the volume fraction of the liquid ε as $\rho = \varepsilon\rho_{\text{air}} + (1-\varepsilon)\rho_{\text{liquid}}$, $\mu = \varepsilon\mu_{\text{air}} + (1-\varepsilon)\mu_{\text{liquid}}$. The function of the volume fraction of the liquid ε was determined from the solution of the transfer equation: $\frac{\partial \varepsilon}{\partial t} + u_1\frac{\partial \varepsilon}{\partial x_1} + u_2\frac{\partial \varepsilon}{\partial x_2} = 0$.

The following boundary conditions were determinate: at the remote external boundaries—flow symmetry conditions, on a solid wall, there were boundary conditions no slip with a wetting angle of $\theta = 90°$, boundary conditions at the air–liquid interface were determined from the equilibrium condition of surface tension forces and pressure forces [11]:

$$(p_1 - p_2 + \gamma \mathrm{k})n_i = (\tau_{1ij} - \tau_{2ij})n_j \tag{5}$$

where γ is the surface tension coefficient assumed to be constant; p_1, p_2 are the liquid and air pressures; $\mathrm{k} = 1/\zeta_1 + 1/\zeta_2$ is the surface curvature, where ζ_1, ζ_2 are the radii of curvature of the air–liquid interface; $\boldsymbol{n}$ is the unit normal vector at the interface directed from the liquid into the air; $\tau_{\alpha\mathrm{ij}}$ is the viscous stress tensor

and phase index α denotes: $\alpha = 1$—liquid, $\alpha = 2$—air. Condition (5) is written for a constant the surface tension coefficient γ. In the case of variability of surface tension (for example, these are cases of heat- or concentration-capillary convection) necessary additionally to consider the changing of the surface tension force along the interface (l) and append the term $\frac{\partial \gamma}{\partial l}$ to the right side of the tangential projection of expression (5).

The changing of the air–liquid interface was performed using the volume of fluid method (VOF). The interface was defined using an implicit VOF method with Euler iterations. To increase the accuracy of calculating the location of the interface, a piecewise linear geo-reconstruction approach was used. The interphase boundary was determined from the solution of the system of Eqs. (2−6) considering surface forces by the method of continuous surface forces (CSF) [12]. The CSF method allows the condition (7) at the interface to be considered through an additional local bulk force $\boldsymbol{F}$ in the right part of the momentum transfer Eq. (5−6). The force $\boldsymbol{F}$ acts only in a very narrow zone enclosed along an interface line of width Δh (Fig. 2). For every point l_s of interface lines l, at Δh striving to zero, the force $\boldsymbol{F}$ can be written, for example, as $\mathbf{F}(l_s) = \gamma k(l_s)\mathbf{n}(l_s)$ that was shown by Brackbill et al. [12], where $k(l_s)$ is the interface curvature at a point l_s, and $\mathbf{n}(l_s)$ is the normal to the site at the interface point l_s (Fig. 2).

The CSF method makes it possible to eliminate the singularity in the case of turning the radius of curvature of the interface to zero and improve the accuracy of calculations when calculating forces at the interface in the form $\mathbf{F} = 2\gamma\rho k\nabla\varepsilon/(\rho_{\text{air}} + \rho_{\text{liquid}})$ [12]. For numerically solve the Navier–Stokes equations the conservative control volume method [13] was used with an adaptive grid. To verify this VOF-CSF mathematical model and determine the accuracy of reproducing changes in the shape of the interface between two liquids, the simulation results were compared with spreading experiments [1, 2, 5] and droplet coalescence [4].

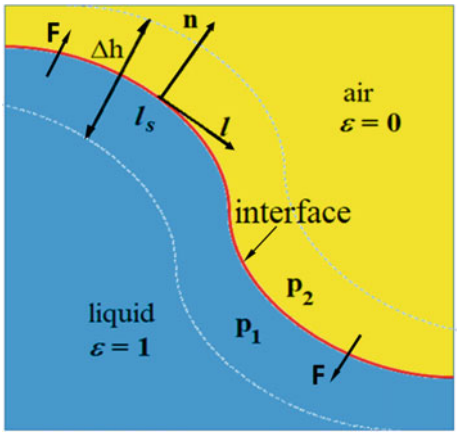


Fig. 2 The scheme of numerical CSF method for definition of interface [12]

3 Results of Numerical Simulation

The results of modeling the flows around a thread ($d_t = 0.2$ mm) by a drop of water ($d_i = 4$ mm) with initial velocities $v_i = 0.1$ m/s and $v_i = 1$ m/s for conditions of weightlessness and normal gravity of the Earth are shown in Figs. 3, 4, 5 and 6.

In Fig. 3 is shown a change in the shape of a drop ($v_i = 0.1$ m/s) flowing around a thread for weightlessness conditions ($g = 0$ m/s^2) (pictures are shown for the time range from $t_0 = 0$ to $t_1 = 73$ ms at regular intervals). The drop impacts the thread, pushes off from the thread and moves in the opposite direction slowing down, and its shape deforms and oscillations for a long time until it takes a spherical shape.

The pictures of changing the shape of the drop ($v_i = 0.1$ m/s) flows around the thread for the normal acceleration of the Earth's gravity (g = 9.81 m /s2) for the time range from $t_0 = 0$ to $t_1 = 60$ ms (at regular intervals) are shown in Fig. 4. The drop is

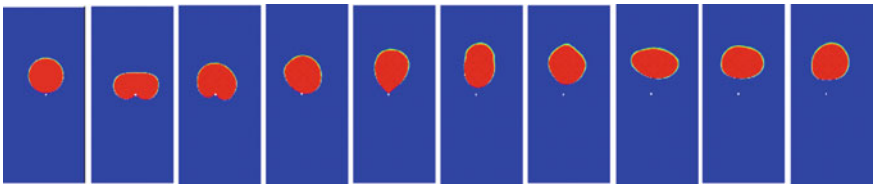


Fig. 3 The changing in the shape of the drop flowing around the thread in zero gravity ($g = 0$ m/s^2, $v_i = 0.1$ m/s, $d_i = 4$ mm, $d_t = 0.2$ mm, the drop patterns are shown at the same time intervals in the range from $t_0 = 0$ to $t_1 = 73$ ms)

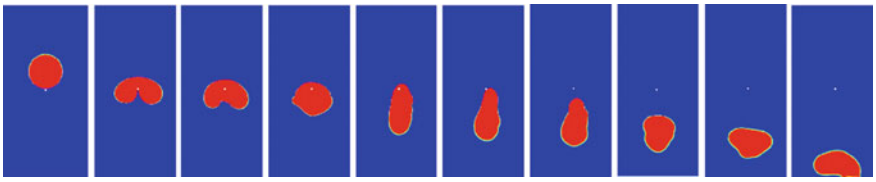


Fig. 4 The changing in the shape of the drop flowing around the thread in normal gravity conditions ($g = 9.81$ m/s^2, $v_i = 0.1$ m/s, $d_i = 4$ mm, $d_t = 0.2$ mm, the drop patterns are shown at the same time intervals in the range from $t_0 = 0$ to $t_1 = 60$ ms)

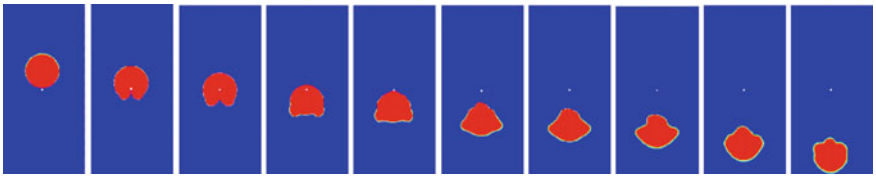


Fig. 5 The changing in the shape of the drop flowing around the thread in zero gravity ($g = 0$ m/s^2, $v_i = 1$ m/s, $d_i = 4$ mm, $d_t = 0.2$ mm, the drop patterns are shown at the same time intervals in the range from $t_0 = 0$ to $t_1 = 11$ ms)

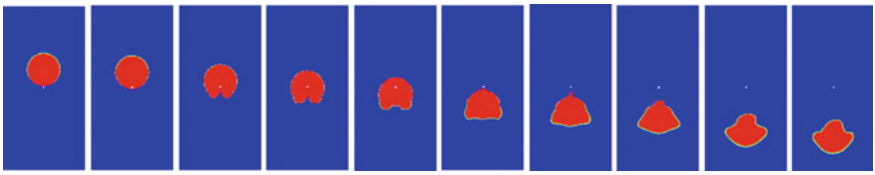


Fig. 6 The changing in the shape of the drop flowing around the thread in normal gravity conditions ($g = 9.81$ m/s^2, $v_i = 1$ m/s, $d_i = 4$ mm, $d_t = 0.2$ mm, the drop patterns are shown at the same time intervals in the range from $t_0 = 0$ to $t_1 = 8.5$ ms)

cut by a thread, passes through the thread, then merging into a single drop, the shape of which is deformed and oscillates in time.

At a high initial velocity of the drop ($v_i = 1$ m/s), the drop flows around the thread in zero gravity and on the Ground almost identically (only in zero gravity, the flow process is slower), this can be seen in Figs. 5 and 6.

4 Conclusions

It is shown that the magnitude of the Earth's gravity at high falling speeds ($v_i > 1$ m/s) practically does not affect the flow mode around a thin thread and can significantly affect at low falling speeds ($v_i < 1$ m/s).

In weightlessness, a thread with a diameter of $d_t = 0.2$ mm can delay the penetration of a drop of water with a diameter of $d_t = 4$ mm, moving at a speed of $v_i = 0.1$ m/ s, due to the forces of the surface tension of the drop.

Acknowledgements This work has been supported by the grants the Russian Science Foundation, RSF No 23-19-00451.

References

1. Rozhkov A, Prunet-Foch B, Vignes-Adler M (2004) Dynamics of a Liquid Lamella Resulting from the Impact of a Water Drop on a Small Target. Proc R Society London Ser A 460(2049):2681–2704
2. Rozhkov A., Prunet-Foch B., Fedyushkin A., Vignes-Adler M. (2023) Fragmentation of water drops in collision with a small obstacle. Atomization and Sprays. Vol. 33, no. 10, pp. 1–15
3. Rozhkov A, Prunet-Foch B, Vignes-Adler M (2010) Impact of drops of surfactant solutions on small targets. Proc R Soc A 466:2897–2916. First published online 14 April 2010. https://doi.org/10.1098/rspa.2010.0015
4. Fedyushkin AI, Rozhkov AN (2020) A coalescence of the droplets. IOP Conf Ser: Mater Sci Eng 927(012055):1–6
5. Fedyushkin AI, Rozhkov AN (2021) Criterion of drop fragmentation at a collision with a solid target (numerical simulation and experiment). J Phys Conf Ser 2057(012129):1–5

6. Rozhkov AN (2005) Dynamics and breakup of viscoelastic liquids (a review). Fluid Dyn 40(6):835–853
7. Villermaux E, Bossa B (2011) Drop fragmentation on impact. J Fluid Mech 668:412–435
8. Vernay C, Ramos L, Ligoure C (2015) Free radially expanding liquid sheet in air: time-and space-resolved measurement of the thickness field. J Fluid Mech 764:428–444
9. Yarin AL, Weiss DA (1995) Impact of drops on solid surfaces: self-similar capillary waves and splashing as a new type of kinematic discontinuity. J Fluid Mech 283:141–173
10. Yarin AL, Roisman IV, Tropea C (2017) Collision phenomena in liquids and solids. Cambridge University Press, UK, Cambridge
11. Landau LD, Lifshitz EM (1987) Fluid mechanics, vol 6, 2nd edn. Pergamon Press, Oxford
12. Brackbill J, Kothe D, Zemach C (1992) A continuum method for modeling surface tension. J Comput Phys 100(2):335–354
13. Patankar SV (1980) Numerical heat transfer and fluid flow. Hemisphere, p 214

Study of Sand Production in Vertical and Horizontal Boreholes on a True Triaxial Loading Unit



Yu. F. Kovalenko, V. I. Karev, S. O. Barkov, and K. B. Ustinov

Abstract This article presents the results of a series of experiments on physical modeling of the process of bottom-hole pressure draw down to the destruction of reservoir rocks in order to study sand production in vertical and horizontal boreholes at one of the West Siberian gas fields. Tests of specimens according to the hollow cylinder program were carried out on the facility Triaxial Independent Load Test System of the Institute for Problems in Mechanics of the Russian Academy of Sciences. The paper presents the stress–strain curves of the specimens under study, as well as the dependence of the mass of sand production on compressive stresses. The values of stresses at which the sand began to be removed were determined and the patterns of fractured holes were analyzed. The results obtained indicate the presence of strength anisotropy of reservoir rocks from one of the West Siberian gas fields. It is shown that for the case of a horizontal borehole, sand production from the holes began at much lower values of compressive stresses, and the mass of the outflow sand was much greater.

Keywords Sand production · True triaxial loading · Stress–strain state · Hollow cylinder test · Stress–strain curves

During the development of oil and gas fields, drilling of wells changes the natural stress–strain state of rocks in their vicinity. The stress field becomes non-uniform and shear stresses appear. In the process of well operation, in order to maintain their flow rate, it becomes necessary to additionally reduce the pressure at the bottom-hole zone. This process causes increase of stresses in the bottom-hole zone, which may lead to significant deformations of rocks, up to its destruction, which is often accompanied by sand production [1]. During the operation and completion of wells, the productive formations of which are represented by unconsolidated rocks, there is often observed sand production. Sand outflow of the reservoir is a serious problem.

Yu. F. Kovalenko · V. I. Karev · S. O. Barkov (✉) · K. B. Ustinov
Ishlinsky Institute for Problems in Mechanics RAS, Moscow, Russia
e-mail: sviatoy97@gmail.com

© The Author(s), under exclusive license to Springer Nature Switzerland AG 2024

V. Karev (ed.), *Proceedings of the 9th International Conference on Physical and Mathematical Modelling of Earth and Environmental Processes*, Springer Proceedings in Earth and Environmental Sciences, https://doi.org/10.1007/978-3-031-54589-4_19

This phenomenon has a negative impact on the productivity and integrity of the well structure and leads to rapid wear and subsequent destruction of equipment [2, 3]. Too much sand outflow is weakening the rock skeleton and can eventually cause it to fail [4]. Sand production is one of the main causes of cavern formation and casing collapse, which is a serious accident.

This problem became especially urgent with the development of thermal methods of extraction of high-viscosity oils [5, 6]. These methods are based on reducing oil viscosity, which increases its fluidity. In this case, unconsolidated reservoirs lose the cementing binding agent—viscous oil. During planned and emergency shutdowns, when heat transfer agent injection is interrupted, the reverse flow of heat transfer agent enters the injection wells and causes mechanical impurities to be carried out, which causes formation of sand plugs in wells and prevents normal injection of heat transfer agent. Any problems associated with sand production are costly and time-consuming to fix.

The study of the causes and mechanisms of sand eruption plays an important role in solving the problems of predicting and preventing this phenomenon [7]. At the moment, there is no unified point of view about the causes of occurrence of sand production. In scientific articles, which are devoted to the study of the technology of fixing unconsolidated sandstones in the bottom-hole formation zone of oil and gas wells by chemical method [8], it was shown that the destruction of unconsolidated sandstones has a selective nature. The destruction is caused by the formation of high-permeability channels along the cracks, evolved in the productive formation both vertically and along the planes of bedding. The main causes and factors of sand production include: unconsolidated reservoir, viscosity of formation fluid, velocity of fluid particles in the formation, stresses in the bottom-hole formation zone, contamination of the bottom-hole formation zone, exceeding the maximum allowable pressure drawdown at the bottom-hole, water breakthrough, formation depletion, abnormal distribution of vertical and horizontal stresses in the formation.

At the same time, the main cause of intensive sand production into the borehole is considered to be the destruction of the bottom-hole formation zone, associated with the occurrence of stresses in the rock, exceeding its ultimate strength [9].

1 Testing Facility and Specimen Preparation

A series of experiments to simulate the process of pressure reduction at the bottom-hole zone up to the destruction of reservoir rocks in the vicinity of the borehole was carried out on a Triaxial Independent Load Test System (TILTS) assembled in the Institute for Problems in Mechanics RAS, presented in Fig. 1a. The development of this system was carried out at the Institute for Problems in Mechanics of the Russian Academy of Sciences (IPMech RAS) [10]. TILTS is intended for studying elastic-strength, rheological and filtration properties of rocks. It allows loading cubic rock specimens with faces of 40 or 50 mm independently along each of the three axes. This makes it possible to experimentally recreate the stress–strain state of any

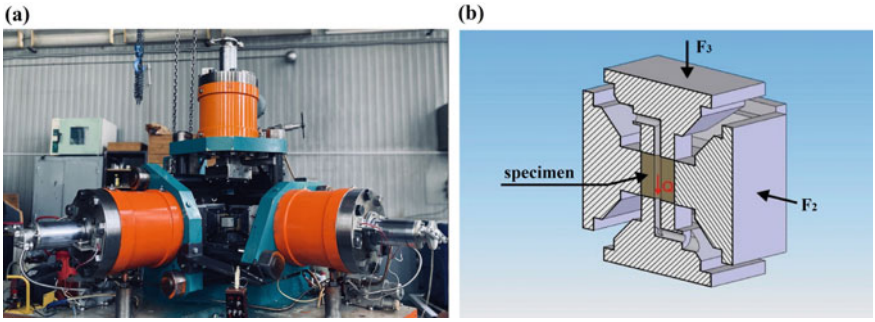


Fig. 1 **a**—Triaxial Independent Load Test System (TILTS), **b**—schematic representation of TILTS pressure plates during the experiments according to the scheme "hollow cylinder"

type occurring in the formation during various technological operations on well. Also TILTS allows studying influence of stress–strain state on rock filtration properties by continuous permeability measurement during the test, for this purpose two pressure plates with holes through which air is blown were specially made (Fig. 1b).

The object of the study are rocks from one of the West Siberian gas fields, from which cubic specimens with an edge of 40 mm were made. The studied rocks are slightly cemented sandstones. In each specimen a hole of a diameter of 10 mm was drilled in the centre of one of the faces in the normal direction, while the remaining four faces of the specimen were covered with an impermeable thin polymer film. A total of six specimens were tested, in half of which the hole was drilled perpendicular to the bedding, and in the rest—along the bedding. The first case qualitatively corresponds to the orientation of a vertical borehole in the formation, and the second to the horizontal one. The orientation of the applied stresses relative to the holes remained unchanged.

2 Methods

As noted earlier, TILTS allows direct simulation of the pressure reduction process at the bottom-hole which is commonly referred to as "hollow cylinder testing". When testing the specimen, air is blown through the perforations in the upper and lower pressure plate, coinciding with the pre-drilled hole in the specimen, at a pressure of about 0.1 MPa. Through the hole in the lower plate, a special tube is used to convey the sand to the electronic scales connected to the computer. Compressive stresses applied to the specimen faces gradually increase over the course of the experiment. Throughout the test deformations in the three directions are recorded and the mass of sand production is measured to within 0.001 g. The test continues until the specimen fractures.

The specimens are loaded by biaxial or triaxial compression programs. The biaxial compression program is shown in Fig. 2. During this program, at the first stage the

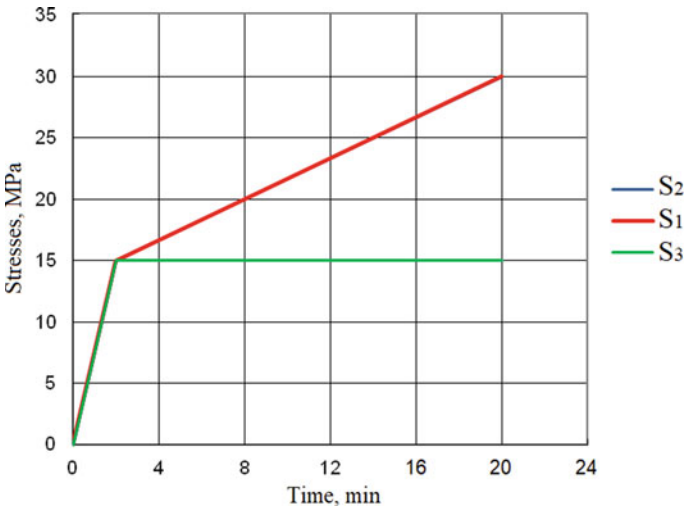


Fig. 2 Biaxial compression program

specimens are loaded uniformly along the three axes at a constant rate to a stress of 15 MPa. In the second stage the loading program changes: the stress acting along the hole (axis 3) is kept constant while the other two stresses continue to increase uniformly. The loading of the specimen at this stage is staggered. At each step, the stress increases uniformly by 1 MPa, followed by a time delay until the sand production ceases.

Hollow cylinder tests allow the direct simulation of reservoir rock fracture processes in the vicinity of the borehole when the pressure at the bottom-hole is reduced. However, due to the scale effect, these experiments do not allow us to quantitatively determine the values of stresses leading to rock failure in the vicinity of the boreholes, but they make it possible to see a qualitative picture of the deformation processes and determine the volume and characteristics of rock particles carried out.

The TILTS has significant advantages over other facilities used to conduct experiments according to the described methodology. The purpose of the classic hollow cylinder testing is to determine the stress at which the sand begins to escape from the hole. The magnitude of this stress is identified with the stress at which the failure of the rock on the walls of the hole begins. Karman-type machines do not allow determining the radial displacement of a cylindrical specimen during such classical experiments. The TILTS makes it possible to measure all three strain components along the three axes of a cubic specimen throughout the test. This provides important additional information. In particular, it turns out that the actual failure of the walls of the hole in the specimen may begin at stresses lower than the stresses corresponding to the beginning of sand production from the specimen [9]. Thus, testing rock specimens on the TILTS allows us to determine the moment of the beginning of failure of the hole walls with greater accuracy and reliability than in the classical experiments.

3 Results and Discussion

Tests according to the hollow cylinder testing were carried out for specimens with different hole orientations relative to their axes. In specimens M5.5 and M7.4 holes were drilled perpendicular to the bedding, which qualitatively corresponds to the orientation of the vertical borehole. In specimens M6.5 and M9.4 holes were drilled along the bedding, which qualitatively corresponds to the orientation of the horizontal borehole.

The test results of specimens M7.4 and M9.4 (Fig. 3) and their photos after the testing (Fig. 4) are presented below.

Specimens M5.5 and M6.5 were selected from another well. Experiments with these specimens were also carried out, but by the loading program "triaxial compression". The test results of these specimens are shown in Fig. 5 and their photos after the experiment presented in Fig. 6.

The results show that the failure of the hole in specimens M7.4 and M5.5 occurred symmetrically along the entire contour of the hole. This is consistent with the fact that the hole was drilled perpendicular to the bedding, in which the strength properties of rocks are isotropic. In the specimen M7.4 the sand production started at a pressure

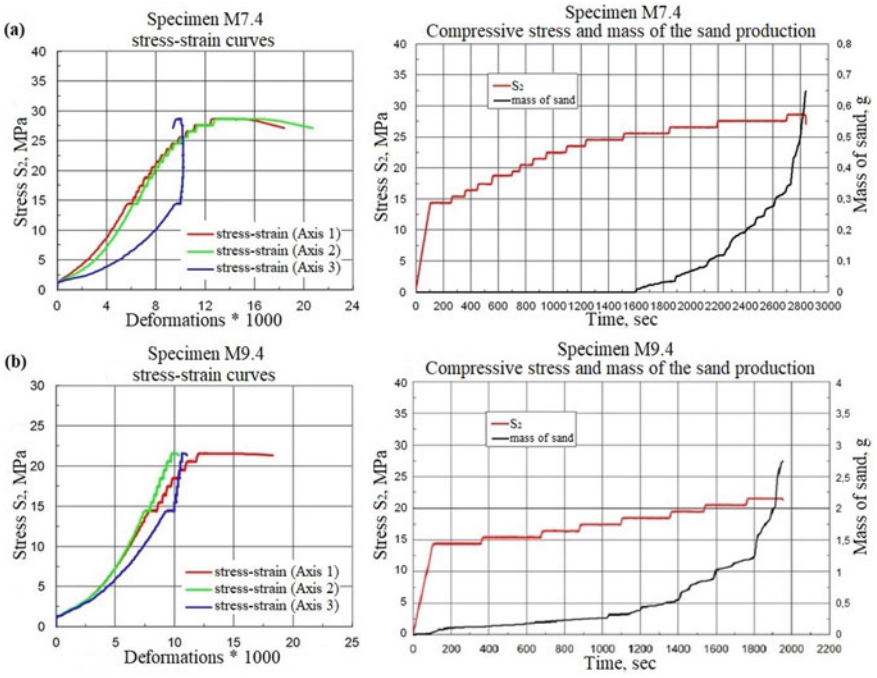


Fig. 3 Stress–strain curves and changes in the mass of sand production during the experiment for specimens M7.4 (**a**) and M9.4 (**b**)

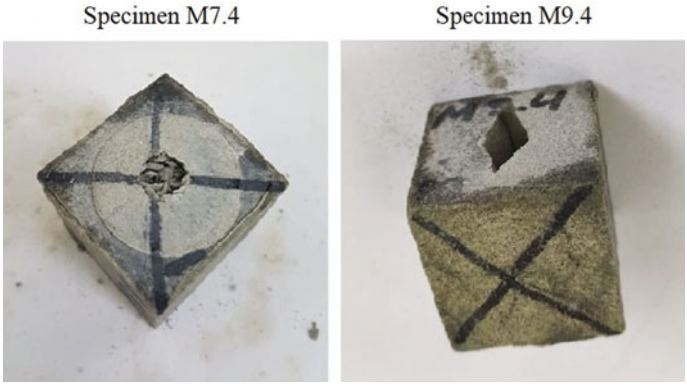


Fig. 4 Photos of specimens M7.4 and M9.4 after the testing

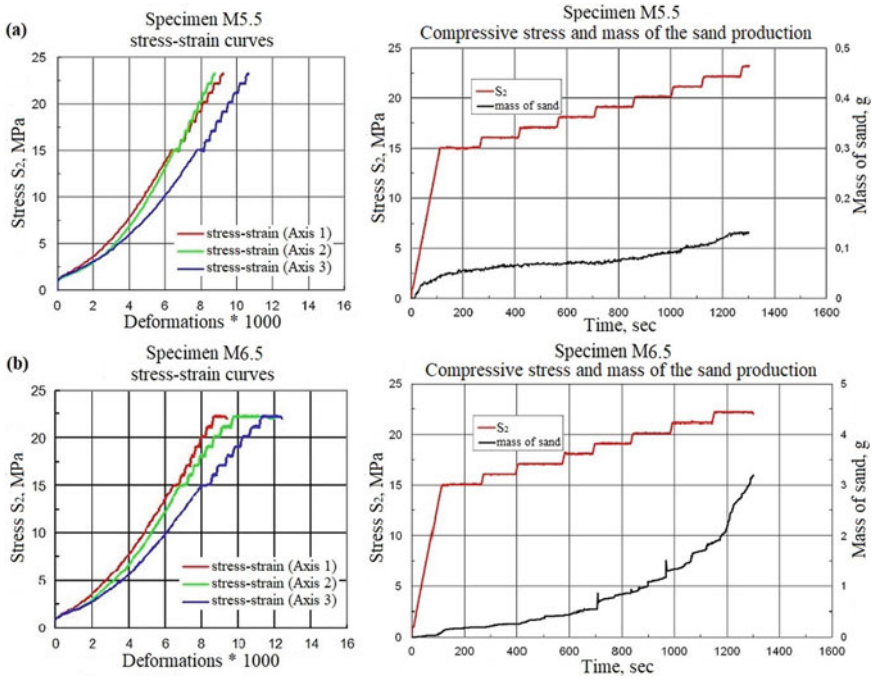


Fig. 5 Stress–strain curves and changes in the mass of sand production during the experiment for specimens M5.5 (**a**) and M6.5 (**b**)

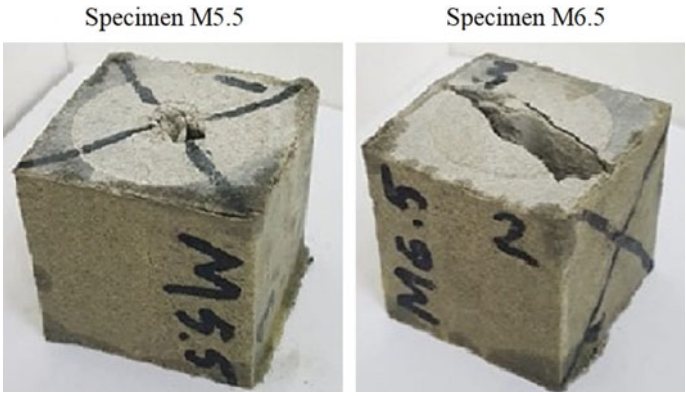


Fig. 6 Photos of specimens M5.5 and M6.5 after the testing

of more than 25 MPa, and the mass of sand was 0.65 g. In the specimen M5.5 the sand production started at a pressure of 2.5 MPa and the mass of sand was 0.13 g.

In specimens M9.4 and M6.5 the hole failure began at the points corresponding to the upper and lower points of the contour of horizontal borehole in the formation, and then continued in the same direction, forming a typical pattern of failure for such boreholes [9, 11]. In the specimen M9.4 the sand production started at 2.9 MPa, and the mass of sand was almost 3 g. In the specimen M6.5 the sand production started at a compression of 3.1 MPa and its mass was a little more than 3 g.

4 Conclusion

As a result of a series of experiments, the strength anisotropy of reservoir rocks from one of the West Siberian gas fields was determined, which can be observed from the failure pattern of the specimens. Tests of specimens according to the hollow cylinder testing were carried out on the unique facility Triaxial Independent Load Test System of the Institute for Problems in Mechanics of the Russian Academy of Sciences. The anisotropy of strength properties is confirmed by the test results of all specimens in which holes were drilled orthogonal to the bedding and those in which holes were drilled along the bedding. It was shown that for the holes drilled in the specimens along the bedding, which corresponds to the case of a horizontal borehole, the sand production from the holes began at much lower values of compressive stresses, and mass of the sand production was much greater.

Acknowledgements This work was financially supported by the Russian Science Foundation Project No. 22-11-00273.

References

1. Karev V.I., Kovalenko Yu.F., Sidorin Y.V., Ustinov K.B. Geomechanical modeling of processes in the bottom-hole zone // *Monitoring. Science and Technology*. 2016. 3. pp. 85–91.
2. Aksenova N.A. Technology and technical means of well completion with unstable reservoirs: monograph // N.A. Aksenova, V.P. Ovchinnikov, A.E. Anashkina. - Tyumen: TIU, 2018. 134 p.
3. Salahi A., Dehghan A.N., Sheikhzakariaee S.J., Davarpanah A. Sand production control mechanisms during oil well production and construction // *Petroleum Research*, Vol. 6, Issue 4, 2021, pp. 361–367.
4. Poroshin M.A., Tananykhin D.S., Grigoriev M.B. Analysis of laboratory methods for studying the process of sand eruption in the development of oil fields // *Eurasian Scientific Journal*. 2. 12. 2020.
5. Jie X., Jingen D., Yi Ch., Lixin J., Yao X., Wei L. Analysis of Casing Instability and Factors Influencing it in Thermal Production Oil Wells // *Chemistry and Technology of Fuels and Oils.* 57. 2021. https://doi.org/10.1007/s10553-021-01310-2.
6. Shemelina O.N., Constructing a heavy oil well // *Petroleum & Petrochemical Engineering Journa*l. 6. 1–6. 2022. https://doi.org/10.23880/ppej-16000300.
7. Bai J., Zhou Y., Wu H., Zhao S., Shang B., Fang T. Experimental study on type and accuracy optimization of sand control in sand-producing heavy oil well. *SPE Eastern Europe Subsurface Conference.* 2021. https://doi.org/10.2118/208563-MS.
8. Tananykhin D.S. PhD thesis: Substantiation of the technology of strengthening weakly cemented sandstones in the bottomhole zone of oil and gas wells by chemical method. St. Petersburg. 2013. 142 p.
9. Kovalenko Y.F., Ustinov K.B., Karev V.I. Geomechanical analysis of formation of dumps on the walls of boreholes // *Mechanics of Solids.* 6. 2022. pp. 148–163.
10. Karev V., Kovalenko Yu., Ustinov K. Geomechanics of Oil and Gas Wells. 2020. *Springer Nature Switzerland AG.* 166 p.
11. Ustinov K.B., Karev V.I., Kovalenko Yu.F., Barkov S.O., Khimulia V.V., Shevtsov N.I. Experimental study of the effect of anisotropy on the orientation of breakouts in wells // *Mechanics of Solids.* Vol. 58, Issue 3, 2023. P. 685–696.

Experience of Ultrasonic Technology Application in the Samotlor Field Wells (Western Syberia)



M. S. Mullakaev, Y. A. Saltykov, A. A. Saltykov, and R. M. Mullakaev

Abstract Presents the results of the pilot-field tests of the ultrasonic technology and equipment, carried out at 68 oil wells of the Samotlor field. The paper analyzes the mechanisms of acoustic impact on the bottom hole formation zone, which is caused by the complexity and diversity of the processes in it as well as shows that the acoustic impact is complex. The analysis of the PFT results of wells with the peculiarities of the geological-physical characteristics of the treated formations was carried out, which allowed to formulate an algorithm of wells-candidate selection for ultrasonic treatment. Proved the high efficiency of the application of the ultrasonic cleaning technology of the bottom hole formation zone, which supplements the existing methods of oil production and can be offered by oil service companies as one of the promising methods for oil production enhancement.

Keywords Oil well · Bottom hole formation zone · Oil production rate · Oil recovery factor · Ultrasound · Acoustic impact mechanisms · Geological-physical characteristics of a formation · Criteria for wells-candidates selection · Ultrasonic equipment and technology · Pilot-field test

The development of the raw material base of the oil industry in Russia depends not onle on the increase of the volume of proven oil reserves, but also on the development of new methods that are applied to enhance oil recovery factor (EOR). A large number of idle wells, an increase in the shape of deposits with heavy and viscous oils, and a decrease in well flow rates indicate a low efficiency of oil extraction technologies [1, 2].

According to Mullakaev [3–5], the method of acoustic stimulation, in particular in the ultrasonic range, is one of the most promising among the wave methods used

M. S. Mullakaev (✉) · R. M. Mullakaev
National University of Oil and Gas "Gubkin University", Moscow, Russia
e-mail: mullakaev@mail.ru

Y. A. Saltykov · A. A. Saltykov
LLC "Ilmasonik-Nauka-Service", Moscow, Russia

© The Author(s), under exclusive license to Springer Nature Switzerland AG 2024

V. Karev (ed.), *Proceedings of the 9th International Conference on Physical and Mathematical Modelling of Earth and Environmental Processes*, Springer Proceedings in Earth and Environmental Sciences, https://doi.org/10.1007/978-3-031-54589-4_20

Table 1 The results of pilot testing of ultrasonic technology

Formation	Number of wells	Success, %,	Average oil production rate, tons/day		Production rate increase, %
			Before UST	After UST	
AV_1^{1-2}	12	92	3,04	6,65	219
$AV_1^{(3)}$	9	100	2,48	3,9	157
$AV_{2\text{-}3}$	23	74	3,47	2,5	72
$AV_{4\text{-}5}$	10	70	3,74	4,1	110
$AV_1^{(3)}$, $AV_1^{(1-2)}$	3	100	1,67	5,3	317
$AV_1^{(3)}$, AV_{2-3}	3	100	1,63	2,8	172
BV_8	3	0	4,2	–1,8	–42
BV_{10}	3	100	1,2	3,1	258
YuV_1	2	100		–	Wells (FPM)
Total	68	80	3,23	4,4	136

to increase wells flow rates. At the same time, the efficiency of the method can be significantly improved through the development of high-performance equipment, proper selection of wells-candidates and mathematical modeling of the physical processes accompanying the acoustic effect.

Ultrasonic treatment results. 68 oil wells of the bottomhole zone of a formation in the Samotlor field were subjected to ultrasonic treatment during 2010–2012.

Table 1 presents the results of pilot testing of ultrasonic well treatment technology with account of the geological-physical characteristics of the formations.

1 Analysis of Formations' Geological-Physical Characteristics and Efficiency of Wells' Ultrasonic Treatment

$\mathbf{AV_1^{1-2}}$ *Formation*

The effective thicknesses of this formation over the area of the Samotlor field is fairly stable, although they vary generally from 0 to 30.4 m. In AV_1^{1-2} formation section there identified two significantly different types of structures with different geological and field characteristics: clay collectors of the "ryabchik" type that occupy most of AV_1^{1-2} formation area (about 80–85%), which filtration processes are of a very complex and not fully understood character.

Ultrasonic treatments of this formation are the most successful. The average flow-rate increase is 6.7 tons/day. Out of 12 ultrasound treatments, only one has a doubtful success of 0.4 tons/day. The success of the ultrasound treatments is primarily

explained by the fact that "ryabchik" formation is characterized by the interlaying of oil-bearing interlayers with impermeable clay layers. Due to the fact that the ultrasonic technology has a very high selectivity, only oil-saturated interlayers were treated.

$\mathbf{AV}_1^3$ *and* $\mathbf{AV}_{2-3}$ *Formations*

These formations belong to thick paleo-Delta sediments and in many respects have a similar structure. The formation is characterized by the lowest average sandiness factor among the AV_{1-5} formations, that makes 0.45 with a rather high dissection of 7.23. Both formations are characterized by a general tendency of effective thicknesses decrease from the southeast to the northwest direction.

Weakly clayish formations that make up 79% of its oil-saturated volume, with an average oil-saturated thickness of 4.4 m predominate in AV_1^3 formation. The share of heavily clay-bearing collectors is 21% with an average oil-saturated thickness of 1.3 m. The zones of raised effective thicknesses are timed to separate channels of north-western striking, in which weakly clayish collectors are found. The length of the channels is up to 10 km with a width of 1–2 km. The maximum thicknesses of such channels are recorded in the north-west of the Priobsky area. The areas between the individual channels are represented by a section with a thin alternation of reservoirs.

AV_{2-3} formation was subjected to the greatest number of operations. 23 wells were treated. The success rate was 74%, the average increase made 2.544 tons/day. Six wells showed the negative results.

Two formations AV_1^3 and $AV_1^{(1-2)}$ in three wells and two more formations AV_1^3 и AV_{2-3}. In also three wells were opened by perforation All six wells were uccessfully treated and the effect made 4 tons/day in the average.

$\mathbf{AV}_{4-5}$ *Formation*

This formation is characterized by an almost monolithic structure, impermeable intrerlayers in its section are represented mostly by compacted carbonized sandstones. In the north and north-western directions there occurs a gradual claying of the section, starting from the top and bottom of the formation. As a result, the middle part of the formation remains weakly dissected, above which the section is represented by frequent re-stratification of reservoir interlayers and impermeable differences. The effective thickness of the formationr in its southern part reaches 68 m. AV_{4-5} formation is characterized by a very high degree of lateral connectivity of reservoirs, lithologic filtration screens are practically absent. At the same time, the presence of often encountered interlayers of compacted carbonized sandstones to a certain extent complicates the vertical migration of fluids, as a result of which, in a vast water–oil zone of the reservoir, the development of reserves occurred without noticeable coning for quite a long time.

Here UST demonstrates pretty good results. Out of 10 treated wells with a success rate of 70%, an average increase made 4.1 tons per day. At the same time, was again performed at three wells were subjected to repeated deoptimization due to the lack of the required equipment. In well No 3788 ESP-25 was lowered instead of ESP-50, in well. No 13549—ESP-15 instead of ESP-25 and in well. No 353999—ESP-35

instead of ESP-50. In all three wells, the dynamic level increased by 100 m or more as compared with the level before the treatment. Excluding these wells, the efficiency makes 6 tons/day.

BV_8 *Formation*

In general, the formation is characterized by effective thicknesses of about 2 … 8 m (2/3 of cases), oil saturation—2 … 4 m (60% of cases). Within the license area, the effective thicknesses of sandstones quite regularly decreases from the east to the west up to full clay alteration at the western boundary of the area. in the east of the field, the sandy geological body can be called massive, in the western part oft he field, sandy bodies lie like separate lenses with a small effective thickness, the total thickness of the formation in the western direction also decreases. Separate lithological deposits of complex configuration are located in the Mykhpaysky area, where the effective oil saturated thickness are not more than 3 m with an average thickness of 1.8 m.

Three ultrasonic treatment operations performed here gave a negative result. Although the number of operations performed does not give grounds to draw definite conclusions, but in our opinion, the main reason is the water percentage increase in the produced fluid. In well No 6155 water increased from 33 to 97%, although the liquid flow rate increased from 6 to 44 m^3. In well No 10896 water cut increased from 52 to 61%, while the coefficient of productivity increased from 0.117 to 0.141. In well No 3804 the water cut increased from 46 to 96%. Thus, the wrong selection of wells was made. The water "funnel" was pulled to them and the flow-rate an increase in provoked its breakthrough.

BV_{10} *Formation*

BV_{10} formation in the sandy facies looks like an extensive semi-lens, surrounded by impermeable rocks in the south-east, south and west. The effective thicknesses within the limits of this sand body reach 13.8 m, but the prevailing values are 2 … 4 m (34% of cases) and 4 … 8 m (31% of cases). The thicknesses of less than 2 m make 23.5%. Almost the same distribution is typical for oil-saturated thicknesses. Approximately 95% of the formation structure is represented by interlaying of sandstones with impermeable rocks, while most often the reservoirs run to the upper part of the formation section. In local areas, individual interlayers merge with each other, creating sections with high degree of sandiness. Permeable interlayers in the upper part of the formation are relatively mature, below they acquire a distinct lenticular form of occurrence.

In the BV_{10} formation, 2 operations were carried out with a success rate of 100% and an effect of 3,1 t/day. The injection wells of BV_{10} and YuV_1 formations were subjected to three US treatments Success rate was 100%. The increase of injectivity was from 300 to 500%.

Pilot tests proved the correctness of the requirements for candidate wells selected for ultrasonic treatment.

Criteria for wells selection to be subjected to ultrasonic treatment. The analysis, obtained as a result of ultrasonic technology pilot using test, was conducted with the

aim of establishing a correlation relationship between the specific daily increase and geological-technological parameters, as well as an assessment of the closeness of this relationship over the period of current operation after UST [5]. The average daily oil increment per well, obtained after 6 months of a well operation after US treatment was used as performance indicators of the efficiency. The geological-technological parameters of the wells were chosen as factors affecting the efficiency, namely, formation pressure, effective and total reservoirformation thickness, permeability, porosity, dissection, number of interlayers by interval perforations, cumulative oil production, cumulative liquid production, sandiness coefficient, coefficient of productivity before the treatment, water cut before UST, etc.

The results of the factor analysis indicate that the daily increase of oil after UST primarily depends on formation pressure maintenance. Treatments were most effective if the ratio of the current formation pressure and the initial one was within the limits of 0.75 … 0.9. The maximum increase of oil flow rates is achieved by reducing the current formation pressure by no more than 15% of the initial one, and the maximum increase is not more than 25%.

The second most important correlation relationship [5] was obtained between the average daily oil increment and well water cut indicators. The effectiveness of treatments became lower if the water content of the candidate wells exceeded 80%. As a rule, the less is the number of interlayers and the more homogeneous is the structure of a formation, the higher is the treatment efficiency. In case when the formation thickness does not exceed 3 … 4 m, the probability of successful treatment is sharply reduced.

Based on the analysis of the literature data [6] and the results of ultrasonic technology pilot tests, the criteria which the formation oil characteristics and the geophysical characteristics of a candidate well should meet for testing ultrasonic equipment and technologies were identified. Thus pilot tests provided an opportunity to formulate a candidate well selection algoritm [7–12].

2 Conclusions

1. After analyzing the experience of UST, the following conclusions can be made:
   - the success of the operations performed was 80%;
   - the number of unsuccessful operations—13, of which, for objective reasons—10;
   - the average increase of oil production rate by wells—4.23 tons/day;
   - the UST of AV_1^{1-1} "ryabchik" formation was the most succesful one due to the advantages of ultrasonic technology in the selectivity of the impact. Prior to UST, chemical treatments were mainly used, where the acid passed along the most permeable washed areas, so part of the interlayers were not included in the work.

- the required condition for conducting high-quality UST is the work on depression, for the removal of reaction products (dispersed clogging products) from the formation into the well, and best of all, to the surface.

2. Among the schemes used to create a depression on a formation in combination with the UST:
   - swabbing is the simplest and least expensive of all the methods used.
   - the most efficient method of creating a depression on a formation is to use a jet pump in combination with UST. Although this method is more expensive in time and cost, however, the average duration of the effect of a well treatment is almost two or more times higher than other methods.
3. Pilot tests proved the importance of proper wells selection for increasing the effectiveness and success of UST based on the well requirements set forth, the well selection algorithm and the availability of experienced specialists.

References

1. *Kuznetzov, O.L., Efimova, S.F.*, Use of ultrasound in oil industry, Moscow: Nedra, 1983, 192 p.
2. *Vakhitov, G.G., Simkin E.M.*, Use of physical fields for oil recovery from reservoirs. *Moscow: Nedra*, 1985, 231 p.
3. *Mullakaev, M.S.*, Ultrasonic intensification of oil production, oil refining, and purification of oil-contaminated water and soil, Sc.D. Dissertation, *Moscow: Moscow State University of Environmental Engineering*, 2011, 391 p.
4. *Mullakaev, M.S.*, Ultrasonic Enhancement of Oil Production and Refining, *Moscow: VNIIOENG,* 2014, 168 p.
5. *Mullakaev M.S.* Ultrasonic intensification of the processes of enhanced oil recovery, processing of crude oil and oil sludge, purification of oil-contaminated water. M.: HELRI, 2018. 376 p.
6. *Apasov, G.T, Apasov, T.K., Saltikov, Yu. A., Apasov, R.T, Abramova, A.V.*, 2012.The factors affecting the efficiency of the effect of ultrasound on the near-wellbore area of formations in the Samotlor oil field. *Sci. FEC* 6, 17–20.
7. *Abramov, V.O., Mullakaev, M.S, Abramova, A.V., Esipov, I.B., Mason, T.J.*, 2013. Ultrasonic technology for enhanced oil recovery from failing oil wells and the equipment for its implemention. *Ultrason. Sonochem.* 20: 1289–1295.
8. *Mullakaev, M.S., Abramov, V.O., Abramova, A.V.,* 2015. Development of ultrasonic equipment and technology for well stimulation and enhanced oil recovery. *J. Pet. Sci. Eng.* 125: 201–208.
9. *Mullakaev, M.S., Abramov, V.O., Abramova, A.V.,* 2017. Ultrasonic automated oil well complex and technology for increasing the productivity of marginal wells. *J. Pet. Sci. Eng.* 159: 1–7.
10. *Mullakaev M.S., Abramov V.O., Abramova A.V.,* 2017. Ultrasonic piezoceramic module and technology for stimulating low-productivity wells. *J. Pet. Sci. Eng.* 158: 529–534.
11. *Abramov, V.O., Mullakaev, M.S., Bayazitov, V.M., Timashev, E.O., and Kuleshov, S.P., Prokoptsev, V.O.*, 2013. Experience in the application of ultrasonic irradiation for restoring the productivity of oil wells in Western Siberia and Samara Region, *Oilfield Eng.*, No. 6, pp. 26–31.
12. *Mullakaev M.S., Saltykov, Yu.A., Saltykov A.A., Mullakaev R.M.*, 2019. Analysis of ultrasonic technology pilot field tests at the Samotlor field wells. *Geology, geophysics and development oil and gas fields.* 7: 71–85.

Investigation of Spontaneous Movement of Ice Cover in Natural Reservoirs

T. O. Chaplina

Abstract The purpose of this work is an experimental study of the formation of vortex streams due to melting and rotation of ice markers, their influence on the transfer of temperature and substances in the environment. This problem is relevant due to the priority of research in the field of Arctic and Antarctic exploration. In addition, a better understanding of the mechanism of formation of convective currents arising in the process of ice melting may be in demand when ensuring the extraction of minerals on the continental shelf.

Keywords Ice · Vortices · Waves · Convection · Multiphase systems · Melting · Admixture · Temperature · Substance and temperature transfer · Laboratory experiment

1 Introduction

One of the rarest natural phenomena that can be seen in winter time is rotating ice circles on water. An ice circle formed on the water surface always has a perfectly round shape, as if drawn out with a circlet on the ice. Ice circles are found on rivers and lakes. But to a greater extent they appear on rivers where there is a slow flow.

The rotational motion of ice floating on calm water, originally documented in the late nineteenth century, has once again piqued the interest of researchers in the laboratory and the field. Despite considerable research, the mechanisms behind the development of convective vortex flows due to ice melting remain elusive. A number of hypotheses proposed have not been substantiated in experiments, mostly due to the intricate nature of theoretical explanations and practical difficulties in carrying out experiments. This problem is relevant due to the priority of research in the field of Arctic and Antarctic exploration. In addition, a better understanding of the

T. O. Chaplina (✉)
Ishlinsky Institute for Problems in Mechanics RAS, Moscow, Russia
e-mail: tanya75.06@mail.ru

© The Author(s), under exclusive license to Springer Nature Switzerland AG 2024

V. Karev (ed.), *Proceedings of the 9th International Conference on Physical and Mathematical Modelling of Earth and Environmental Processes*, Springer Proceedings in Earth and Environmental Sciences, https://doi.org/10.1007/978-3-031-54589-4_21

mechanism of formation of convective currents arising in the process of ice melting may be in demand when ensuring the extraction of minerals on the continental shelf.

The process of ice disc rotation remains inadequately researched. It has been observed that when an ice block is placed on the surface of water, a significant downward spiral current is created beneath the interface of the ice and water. Subglacial hydrological measurements of currents and thermal structure of water in the ring area reveal the presence of an anticyclonic vortex in the geostrophic region beneath the ring. This vortex brings warmer deep water to the lower surface of the ice, resulting in the melting of ice from below. However, the question of why the ice melts from below the ring remains unresolved.

During laboratory studies on the melting process of ice markers, the initial state of the ice-water system is characterized by zero total integral spirality of the medium and zero density of spirality at all local points of the experimental basin. The resulting downward spiral flow is recognized to have non-zero spirality, leading to an issue of generating spirality of hydrodynamic flows in systems lacking external sources of spirality, such as injected swirling jets.

2 Natural Phenomenon in the Form of Ice Circles on the Water

Phenomena involving the rotation of ice disks of differing sizes, ranging from one to hundreds of meters, have been observed on frozen freshwater bodies (see Fig. 1).

According to data from various sources, the angular data transfer rates of such ice discs are in the range of degrees per second (Table 1).

On average, ice circles have a diameter of 5–10 m. In this case, the circle formed on the ice thickness starts to slowly rotate around its axis on the surface of the water body. As a result of rotation, the edges of the ice floe are ground against the surrounding ice, and it takes the shape of a perfectly flat circle. The rotation of the ice floe is due to the eddy currents occurring on the river. Such circles are also often called “dancing ice floes”.

The study of the formation of convective flows arising during the melting of ice is presented in many works [3–14].

The reason for the formation of ice circles on the water is not fully understood to date. Scientists have several versions about the origin of ice circles. According to one version, a round ice floe is formed as a result of the release of methane gas from under the ground. According to another version, the circle is formed due to the passage of wide atmospheric showers in the atmosphere, when space particles brake against the earth’s atmosphere, while releasing a large amount of energy.

But despite the large number of works, the processes of the formation of convective vortex flows formed as a result of ice melting were not fully studied, several formulated hypotheses did not receive confirmation in experiments due to the intricacy of the theoretical description and methodological complexities.

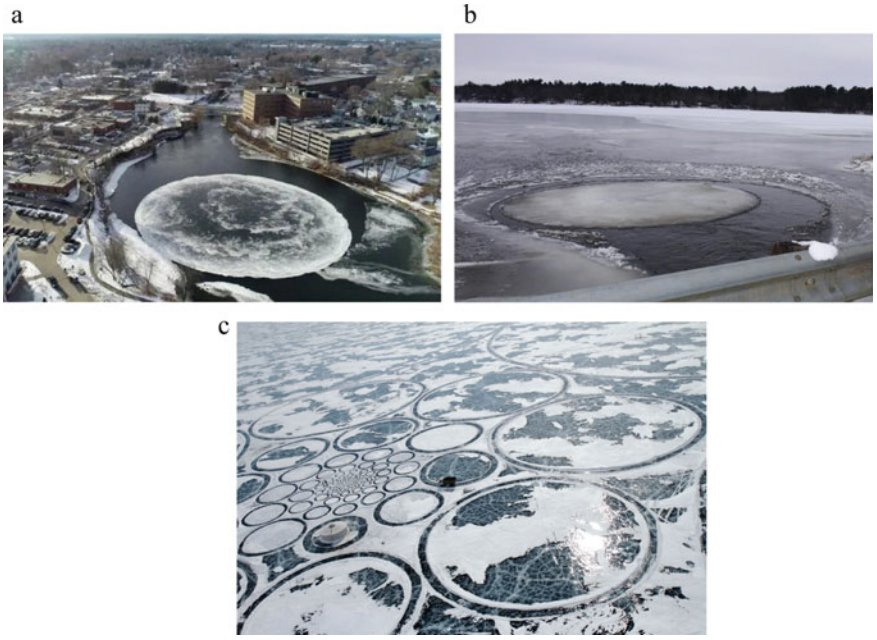


Fig. 1 **a** Large spinning ice disk forms on Presumpscot River in southern Maine [1], **b** The rotating ice disk, Minnesota [2], **c** Ice rings on Lake Baikal

Table 1 Data on observed moving ice circles

Diameter, m	*w*, deg/s	Location	Year	References
2	0,57	Rancho Nuevo Creek, USA	1983	[3]
3	1,4	River Otter, UK	2009	[4]
8	1,4	Mianus River, USA	1895	[5]
49	0,66	Pite River, Noway	1987	[6]
55	1,3	Nidelva River, Norway	1971	[7]

3 Laboratory Studies of the Rotation of Ice Markers on Various Surfaces

In laboratory studies of the process of melting ice markers, the original state of the ice water system is characterized by both zero full integral spirality of the medium and local zero density of spirality at all points of the experimental basin. The descending spiral flow is deliberately possesses unnecessary spilation, which leads to the problem of generating spiralism of hydrodynamic flows in systems without external sources of spirality (in the form of injected twisted streams, etc.).

The exploration of liquid flows caused by positioning an ice marker on a still surface is reliant on numerous factors, including ice and water composition and mineralisation, temperature and salinity, the ice marker's shape and size, the roughness of its surface, and any present underwater or surface flows. When conducting an experiment in laboratory conditions, it is feasible to eliminate or reduce the impact of most inadequately controlled elements and explore a simplified task, thereby reducing its thermodynamic part into the issue of open convection under the smooth surface of the section. The experiments were carried out in vessels of various sizes and shapes.

Ice pieces of different forms, such as circle, rectangle, square, star, and pentagon, were employed as ice markers. Markers made of ice and frozen references were placed on the surfaces of both fresh and salt water (35‰). Experiments were conducted at room temperature (20 °C) for both water and air. Video cameras were mounted on tripods to capture movements.

In order to study the movement of ice outside the vortex flow, it was decided to conduct a series of experiments with the placement of the object on a solid substrate. The assumption that the ice will simply melt and not carry out any movement turned out to be incorrect (Fig. 2).

Experiments were conducted on the study of the movement of the marker on various solid horizontal surface, namely: on aluminum, ceramic, mirror surface and on polystyrene.

It should be noted that when the underlying material experiences similar heat intensities, an increase in the thermal conductivity of the substrate material significantly accelerates all processes. In comparison to other materials used, the thermal conductivity of aluminum is two orders of magnitude higher (Fig. 3).

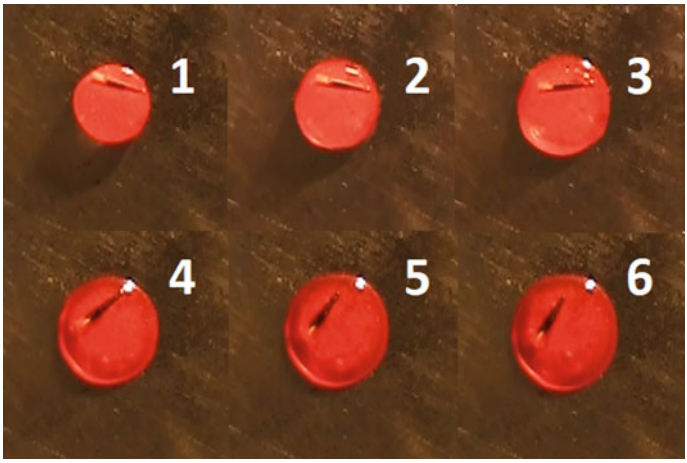


Fig. 2 Rotation of ice around its own axis on the aluminum surface: (1) 10 s; (2) 30 s; (3) 60 s; (4) 90 s; (5) 125 s; (6) 190 s

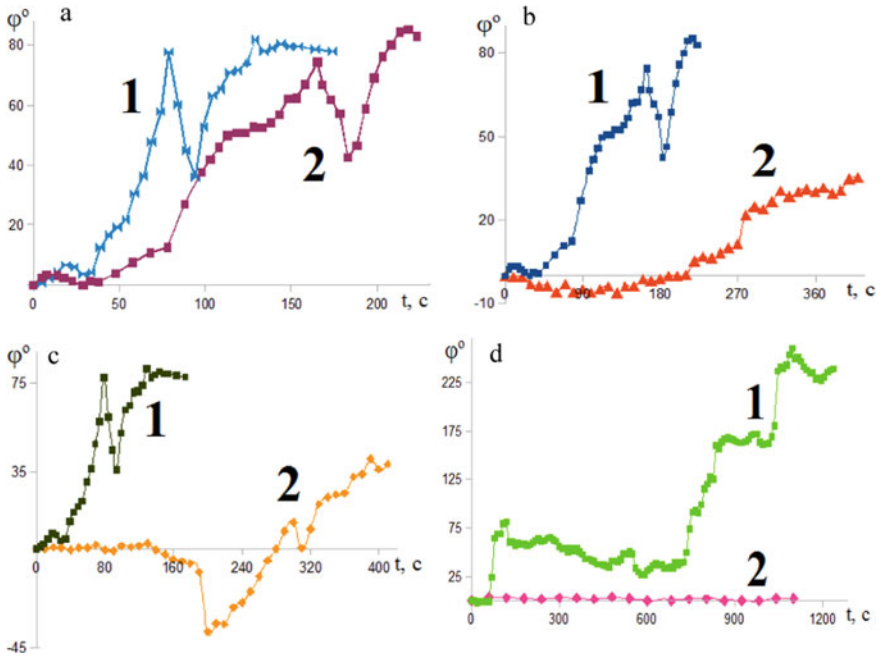


Fig. 3 Graph of the dependence of the angle of rotation of the marker around its own axis from time to time: **a** ice 1 cm, 1—on the aluminum surface, 2—on a ceramic surface; **b** a marker on a ceramic surface, 1—ice 1 cm, 2—ice 2 cm; **c** a marker on the aluminum surface 1—ice 1 cm, 2—ice 2 cm; **d** 1—ice 2 cm on a mirror surface, 2—ice 1 cm on polystyrene

4 Self-Rotation of Ice on the Water's Surface

During the research, the dynamics of ice melting was also clarified—changes in the mass of an ice marker placed on the surface of water at a temperature of 20 °C over time (Fig. 4).

The exponential mass loss of the ice block exhibited similar coefficients in all the graphs shown in Fig. 4, using non-dimensionalization. The interpolation errors in the coefficients, constructed in the exponent form $m = m_0 \exp(-am_0 t)$, were within 1% and decreased with a higher initial mass.

During the experiments, we recorded the rotation of ice blocks of varying sizes on the surface of a still liquid (see Fig. 5). We observed a decrease in the rotation frequency of the ice block as the thickness of the underlying water layer decreased. Specifically, in our experiments with a liquid depth of 3 cm, the ice block's rotation came to a virtual halt (see Fig. 6).

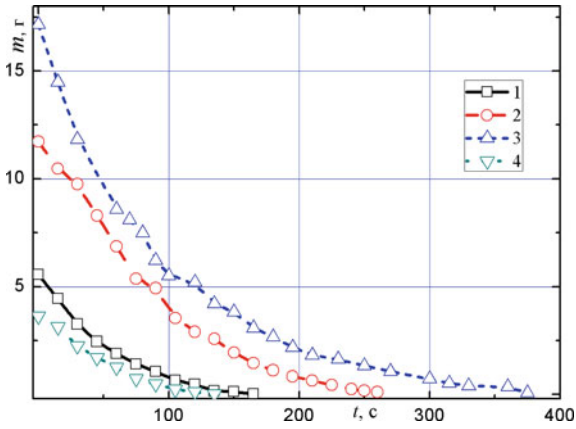


Fig. 4 Change in the mass of the ice block: 1–4 initial masses 18, 12, 6, 2 gramm

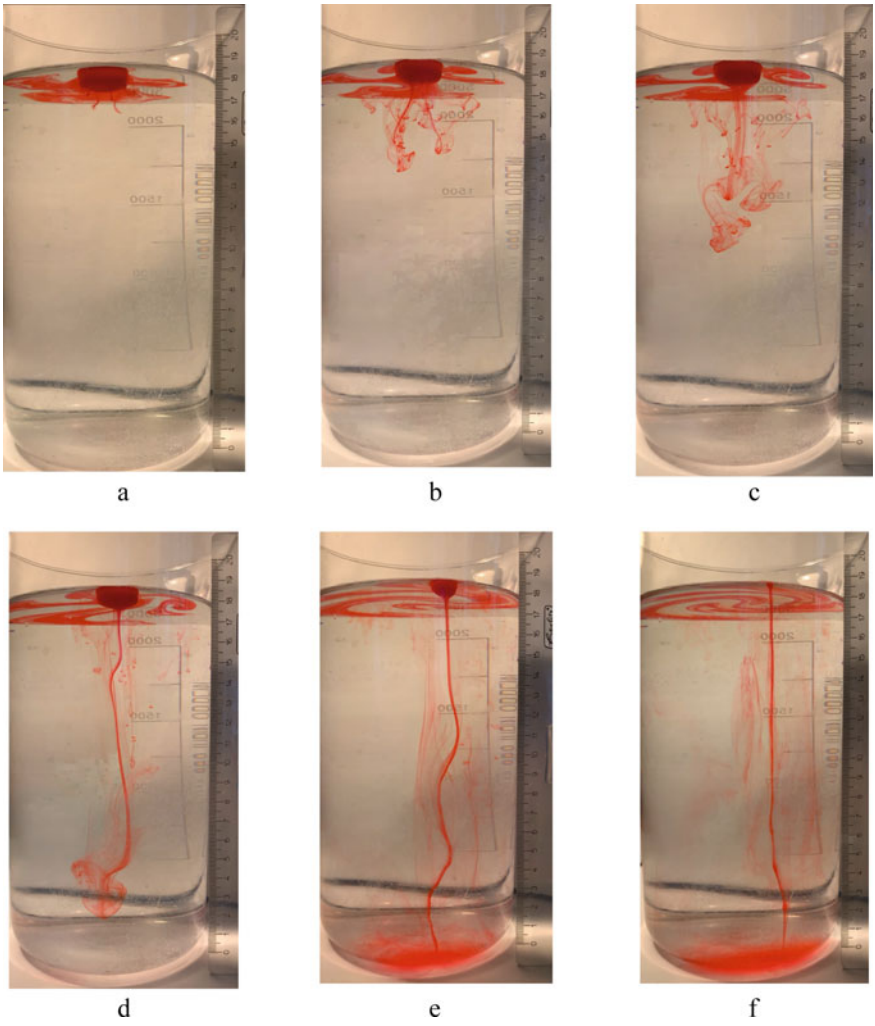


Fig. 5 A 2 cm disc of ice spinning on the surface of the water **a**–**f**: 8, 20, 30, 60, 180, 300 s, S = 0%, T = 20 °C

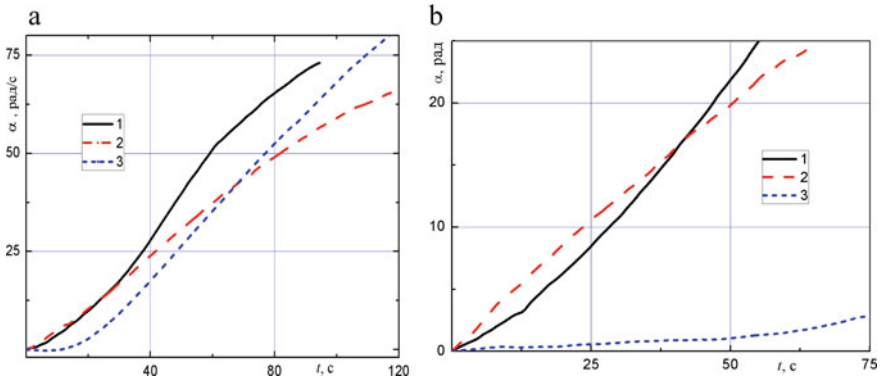


Fig. 6 Dependence of ice block angular position on time: **a** water depth 5 cm, horizontal dimensions of ice blocks 1–13 mm, 2–20 mm, 3–25 mm; **b** ice block 20 mm in size, liquid layer height 1–10 cm, 2–5 cm, 3–3 cm

5 Conclusion

The authors conducted laboratory experiments confirming the phenomenon of spontaneous rotation of melting ice both on a solid substrate and on the water surface. It was found that the rotation rate increases with the temperature of the water body. Using the underpainting technique, the fact of vortex flow occurrence directly under the ice block in experiments on placing the ice block on the free surface of a resting liquid was established. The fixed vortex current generates ice rotation. The parameters of the resulting rotation are measured, and the critical value of the depth of the resting liquid layer necessary for the onset of the ice block rotation is established. The mutual influence of two markers simultaneously placed in the unit on each other is revealed.

It is necessary to use an integrated approach combining experimental and theoretical study of the process of formation of convective eddy currents during ice melting.

Acknowledgements This work was supported by the Russian Science Foundation, project No. 24-27-00029.

References

1. https://abcnews.go.com/US/video/large-spinning-ice-disk-forms-presumpscot-river-southern-82326681
2. https://strangesounds.org/2015/12/rotating-ice-circle-brainerd-minnesota.html
3. Bates J. M., Scientific American 72, 85 (1895)
4. B. Nordell and G. Westerstrom, Weather 52, 17 (1993)
5. Carstens T., La Houille Blanche 7, 642 (1971)

6. Kouraev A.V., Zakharova E.A., Remy F., Kostianoy A.G., Shimaraev M.N., Hall N.M.J., and Suknev A.Ya. Giant Ice Rings on Lakes Baikal and Hovsgol: Inventory, Associated Water Structure and Potential Formation Mechanism // Limnology and Oceanography. 2016**. Vol. 61. P. 1001–1014. https://doi.org/10.1002/lno.10268
7. Dorbolo S., Adami N., Dubois C. and others. (2016) Rotation of Melting Ice Disks Due to Melt Fluid Flow, Phys. Rev., E 93, 033112. https://doi.org/10.1103/Physreve.93.033112
8. Keitzl T., Mellado J. P., Notz D. (2016) Impact of Thermally Driven Thottom Melting of E, j . of PHYS. Oceanogr., 46, 1171
9. Shenn-yu Chao, Ping-Tung Shaw. Fission of Heton-Like Vortices Under Sea Ice Journal of Oceanography, Vol. 55, pp. 65 to 78. 1999
10. Granin N.G. // Science from first -hand. 2009. No. 3. S. 22–23., Granin N.G., Vyushta A // IV Vereshchaginskaya Baikal Conference. September 26-October 1, 2005. P. 52–53
11. Heard W.B. Steady-state convection with melting at a boundary // Physics of Fluids, 1977, V. 20, No. 12, pp. 1993–1999., Granin N.G., Vyushta A
12. Nguyen A.T., Menemenlis D., Kwok R. Improved modeling of the Arctic halocline with a subgrid-scale brine rejection parameterization//Journal of Geophysical Researches, 2009, Granin N.G., Vyushta A, 114(C11), C11014 (https://doi.org/10.1029/2008JC005121)
13. Nguyen A.T., Menemenlis D., Kwok R. Arctic ice–ocean simulation with optimized model parameters: approach and assessment // Journal of Geophysical Researches, 2011,116(C4), C04025 (https://doi.org/10.1029/2010JC006573)
14. Chaplina T.O., Glebova O.A. Investigation of vortex flows formed when ice melting in multi-component liquids // PMMEEP 2022: Physical and Mathematical Modeling of Earth and Environment Processes—2022, 2023, Granin N.G., Vyushta A, P. 625–632. https://doi.org/10.1007/978-3-031-25962-3_62

Thermoacoustic Technology for High-Viscous Oil Production



M. S. Mullakaev, R. M. Mullakaev, D. G. Sarvarov, and A. A. Ruhman

Abstract The work is devoted to one of the most pressing problems of the oil and gas complex—oil production in the fields with hard-to-recover reserves. A thermoacoustic well complex and a combined technology for stimulating the production of high-viscosity and heavy oil have been developed. Pilot tests of the complex and combined technology have been carried out at the fields of the Samara region, which prove their high efficiency. The developed technology and complex will significantly intensify the production of heavy and high-viscosity oil, reduce capital and operating costs, thereby reducing the cost of the oil produced.

Keywords Heavy and high-viscosity oil · Bottomhole zone of a well · Oil flow rate · Thermoacoustic treatment · Ultrasound · Thermoacoustic well complex · Combined technology · Pilot testing

Nowadays a lot of attention is paid to the development and integration of deposits with high-viscosity oil into the industrial development. Moreover, only 10 … 30% of the fields with oil reserves of more than 10 centipoise viscosity have been developed in our country. One of the effective methods of influencing the bottomhole zone of a well (BZW) turned out to be acoustic impact (AI), in particular, in the ultrasonic (US) range [1–3].

The pattern of acoustic exposure on the bottomhole zone of a well (BZW). Analysis of literature sources data, laboratory experiments and model calculations

M. S. Mullakaev (✉) · R. M. Mullakaev
National University of Oil and Gas "Gubkin University", Moscow, Russia
e-mail: mullakaev@mail.ru

D. G. Sarvarov
LLC "Energo", Ekaterinburg, Russia

A. A. Ruhman
LLC "Ultrasonic Generators", Moscow, Russia

© The Author(s), under exclusive license to Springer Nature Switzerland AG 2024

V. Karev (ed.), *Proceedings of the 9th International Conference on Physical and Mathematical Modelling of Earth and Environmental Processes*, Springer Proceedings in Earth and Environmental Sciences, https://doi.org/10.1007/978-3-031-54589-4_22

revealed the following main mechanisms responsible for improving oil filtration in porous media during acoustic impact on the bottomhole zone of a well:

- nonlinear acoustic effects in pores (cavitation, acoustic flows, sound pressure) reduce the effect of capillary forces due to the destruction of surface films and increase the fluid filtration rate [4, 5];
- non-linear acoustic effects can destroy both primary (layered-package associates) and secondary supramolecular formations (micelles) bound by weak van der Waals bonds and, as a result, significantly reduce fluid viscosity [1–5];
- the surface tension, density and viscosity of the fluid decrease due to ultrasonic heating [6–8];
- relative permeability of phases increases [7, 9];
- there occurs a peristaltic movement of the fluid due to the mechanical vibration of the pore walls, through which the fluid is "compressed" into neighboring pores [10];
- microemulsification of oil begins in the presence of natural or introduced surface-active substances (surfactants), the surfactant solubility increases and its adsorption decreases [9, 11];
- oil droplets merge due to Bjerknes forces [16];
- rock permeability and porosity increase due to pore deformation; perforation channels and reservoir pores are cleaned from asphalt-resin-paraffin paraffin (ARPS) deposits and other inclusions and the skin effect decreases [6];
- the occurrence of interporous convection causes a change of the thermal conductivity of the media saturated by fluids, a decrease of the skin effect and, as a result, an increase of a well productivity [6].

Thermoacoustic well complex KSTA-2. KSTA-2 thermoacoustic well complex has been designed for combined treatment of the bottomhole zone of a well (BZW) with high-viscous oil by applying a combined method: ultrasonic (US) and induction heating and their combinations. The block diagram of the KSTA-2 complex is shown in Fig. 1. Technical characteristics of the KSTA-2 complex are given in Table 1.

The KSTA-2 complex includes the following: the automated workstation (AWS), industrial computer (PC); ultrasonic module (ultrasonic generator, downhole thermoacoustic devices PSTA-42 and PSTA-102); geophysical digital module (geophysical recorder, geophysical downhole device); matching device; geophysical power cable on the reel; a set of operational documentation (OD) and technological documentation (TD) on the modes and parameters of the bottomhole zone of a well (BZW) treatment; spare parts and accessories (SPA-O) kit.

1 Pilot Tests of the Technology and the Complex

Criteria for selecting a candidate well. The method is most effective in terrigenous reservoirs with a porosity of 12…30% and a permeability of more than 20 mD with a decrease in productivity by more than 30% over the past six months or a year.

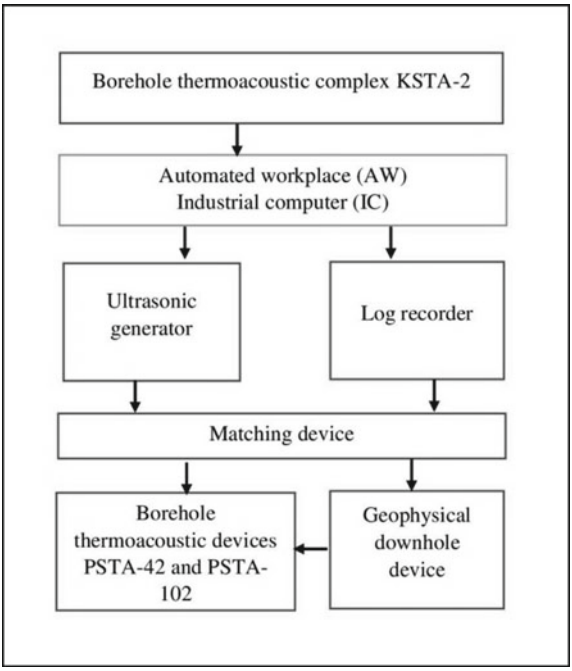


Fig. 1 Block diagram of the complex

Table 1 Technical characteristics of the KSTA-2 complex

Maximum depth of a well treatment, m	Up to 5000
Device power under acoustic impact, kW	2
Operational frequency of the device, kHz	19,0 ±0,5
Maximum power of the device during heating, kW	5
Working temperature of the device, ºC, no more than	120
Range of the measured temperature in a well, ºC	from −40 to +120
Power supply	220/380 V, 50/60 Hz
Power consumed from the network, kW	No more than 10
Overall dimensions, mm, no more – control station – device PSTA-42 – device PSTA-102	880 × 490 × 1060 Ø 42 × 3480 Ø 102 × 3480

Efficiency decreases with the deterioration of reservoir properties and an increase in oil viscosity during a short-term use. It is also necessary to evaluate the development map and the possible influences of neighboring (offset) wells. Well selection criteria are given in [12–16].

Table 2 Results of MSUM-102 module testing

Well	Reservoir	Pump	$Q_ж$, m^3/day	Y_w, %	$Q_н$, t/day	μ, cP	$P_{bottomhole}$, atm
31	C1bb	HB44	23,1	8	9,7	4555	41,8

где $Q_ж$—fluid flow rate, m^3/day; $Q_н$—oil flow rate, m^3/day; Y_w—water cut, %; μ—dynamic viscosity, cP; $P_{bottomhole}$—bottomhole pressure, atm

Registration of well operation parameters before treatment using a geophysical module: (а) descent of the geophysical device and emitter into the treatment interval; (б) binding by a geophysical device; (в) registration of geophysical parameters in the static mode; (г) assessment of well operation parameters in the dynamic mode (creation and registration of depression and flow rate, registration of the inflow profile); (д) evaluation of working intervals, coordination of treatment intervals.

Ultrasonic processing of BZW: (а) planning of operational parameters (UST power and time, frequency of switching on, etc.) of the PSTA-42 and PSTA-102 modules based on the analysis of geophysical surveys and the well operational mode; (б) processing of the specified intervals with the required intensity and time according to the pilot test plan; (в) recording of the flow rate, measurement of depression during periodic shutdowns of US emitters using a geophysical module.

Registration of well operational parameters after UST using a geophysical module: (а) assessment of well operation parameters in dynamic mode (creation and registration of drawdown and flow rate); (б) registration of the inflow profile.

Work with PSTA-102 emitter. The device is lowered by the tubing into the BZW treatment interval, the power line is laid outside the tubing. Depending on the BZW treatment mode, PSTA-102 device can supply power to the emitter through an autonomous (removable) coil with a geophysical cable or an ESP power cable. The inflow is stimulated by means of a jet pump or pumping equipment for production (sucker-rod pumping unit—SRPU or electrical submersible pump—ESP). Downhole parameters are controlled in the same way as in the case of BZW treatment during development.

The results of pilot field tests. The PSTA-102 module was pilot tested at the well. No 31 of the Mordovoozerskoye field in the "Nafta-Ulyanovskneft" (JSC "Ulyanovskneft"—RussNeft) OGPD (oil and gas production department). Prior to UST of the well, viscous oil was produced by the following technology application: flushing by hot oil using a well dewaxing unit (WDU) once every 3 days and injection of a solvent in the volume of 20 m^3 once a month.

The PSMS-102 downhole device was run down by a liner under the NV44 pump into the perforation interval on a permanent basis. The power was supplied through the 3 × 10 flat armored submersible cable (submersible cable for the ESP). The BZW was treated in a periodic mode: during 3 h, once in 3 days. Electricity consumption was 10 kW/h. The results are presented in Table. 2.

Thus, UST using made it possible to abandon hot oil flushing and solvent injection while maintaining the oil flow rate.

References

1. *Mullakaev M.S. Ultrasonic intensification of oil production and processing. Moscow: JSC "VNIIOENG", 2014. 168 p.*
2. *Mullakaev M.S. Ultrasonic intensification of the processes of enhanced oil recovery, processing of crude oil and oil sludge, purification of oil-contaminated water. Moscow: HELRI, 2018. 376 p.*
3. *Mullakaev M.S. Ultrasonic intensification of oil production and refining, purification of oil-contaminated waters and oil sludge processing. Moscow: NII IEP, 2019–412 p.*
4. *Dyblenko V.P. Wave methods of influencing oil reservoirs with hard-to-recover reserves. Review and classification. - M.: JSC "VNIIOENG", 2008. 80 p.*
5. *Nikolaevskiy, V.N*., 1989. Mechanism of vibration for oil recovery from reservoirs and dominant frequencies. *Trans. USSR Acad. Sci*. 307: 570–575.
6. *Fairbanks H.V., Chen W.J.,* 1971. Ultrasonic acceleration of liquid flow through porous media. *Chem. Engineering Progress. Symposium Series*. 67: 108–116.
7. *Mikhailov, D.N., Nikolaevskiy D.N.,* 2000. Dynamics of flow through porous media with unsteady phase permeabilities. *Fluid Dyn.* 35.
8. *Aarts A.C.T.,* 1999. Enhancement of liquid flow through a porous medium by ultrasonic radiation. *SPE J.* 5: 321.
9. *B Abismaïl, J.P. Canselier, A.M. Wilhelm, H. Delmas, C. Gourdon*, 1999. Emulsification by ultrasound: drop size distribution and stability. *Ultrason. Sonochem.* 6: 75–83.
10. *V.F.K. Bjerknes*. Fields of force. New York: *Columbia University Press*, 1906.
11. *Mettin, R., Akhatov, I., Parlitz, U., Ohl, C.D., Lauterborn, W.,* 1997. Bjerknes forces between small cavitation bubbles in a strong acoustic field. *Phys. Rev. E*. 56: 2924–2931.
12. *Mullakaev M.S., Abramov V.O., Prachkin V.G.,* 2015. Development of combined technology and the complex for intensification of oil production by means of ultrasound treatment. *Chem. & Pet. Eng.* 51: 237–242.
13. *Abramov, V.O., Mullakaev, M.S, Abramova, A.V., Esipov, I.B., Mason, T.J*., 2013. Ultrasonic technology for enhanced oil recovery from failing oil wells and the equipment for its implemention. *Ultrason. Sonochem*. 20: 1289–1295.
14. *Mullakaev, M.S., Abramov, V.O., Abramova, A.V.,* 2015. Development of ultrasonic equipment and technology for well stimulation and enhanced oil recovery. *J. Pet. Sci. Eng.* 125: 201–208.
15. *Mullakaev, M.S., Abramov, V.O., Abramova, A.V.,* 2017. Ultrasonic automated oil well complex and technology for increasing the productivity of marginal wells. *J. Pet. Sci. Eng*. 159: 1–7.
16. *Mullakaev M.S., Abramov V.O., Abramova A.V*., 2017. Ultrasonic piezoceramic module and technology for stimulating low-productivity wells. *J. Pet. Sci. Eng.* 158: 529–534.

Zoning of the Water Area by Ocean Surface Temperature Using Cluster Analysis



Eugene P. Istomin, Yaroslav A. Petrov, and Irma A. Martyn

Abstract In the work, the ocean temperature field is zoned for the selected research area. Zoning is performed by the cluster analysis method, called the "without a teacher" classification, the Ward method, the Euclidean metric, and the k-means method. The conclusion is made about the best partitioning variant, and a map with the boundaries of the obtained classes is constructed using the Surfer geoinformation system. Based on the results of the work, the optimal division of the temperature field into three classes is obtained, and the physical conclusions of the clustering result are explained. The map shows the boundaries of the areas of the water area that differ in hydrological characteristics. The cluster analysis results are analyzed from a physical point of view, and the correspondence of the division into classes of the influence of the system of currents, ocean fronts, and water circulation is revealed. The work aims to apply modern data mining technologies for hydrometeorological research in practice, which, in the future, will allow the correct study of a group of hydrometeorological parameters similar in the physical mechanism of formation or influencing factors. The application of the data mining algorithm is shown on the example of zoning the ocean surface temperature in the eastern Pacific Ocean for zoning coastal waters by the type of factors affecting them.

Keywords Data mining · Cluster analysis · Ocean surface temperature · Geoinformation systems

E. P. Istomin · Y. A. Petrov (✉) · I. A. Martyn
Russian State Hydrometeorological University, Saint-Petersburg, Russia
e-mail: yaroslav.petrov025@gmail.com

E. P. Istomin
e-mail: biom@bk.ru

© The Author(s), under exclusive license to Springer Nature Switzerland AG 2024

V. Karev (ed.), *Proceedings of the 9th International Conference on Physical and Mathematical Modelling of Earth and Environmental Processes*, Springer Proceedings in Earth and Environmental Sciences, https://doi.org/10.1007/978-3-031-54589-4_23

1 Introduction

Hydrometeorological data, including oceanographic data for the period of instrumental observations, contain much hidden information about climatic fluctuations [2, 9, 13]. The work aims to classify the Pacific Ocean surface temperature field off the coast of California based on the cluster analysis method, highlighting the groups (districts) closest in structure [5]. The classification is used to zone the ocean surface temperature at 25 points of the Pacific Ocean with a daily resolution from the Columbia University website for the 1981–2020 period [9].

Thus, as information accumulates, a more detailed understanding of the physical processes caused by climate change develops. At present, fluctuations in the ocean–atmosphere system are revealed with a periodicity of 2–3, 3–7, 10–11, 16–18, 20–24, 26–30, and 50–70 years [16, 18]. Climatic shifts in the regions of the oceans are revealed, which indicates changes in atmospheric circulation, and the position and intensity of the main centers of atmospheric action. Climatic indices constructed based on the spatial and temporal variability of the distribution of surface pressure and temperature of the sea surface of water are used to study climatic fluctuations in certain ocean parts [4].

Currently, the use of various data mining methods in natural sciences is being introduced; however, these methods have not yet become very widespread in hydrometeorology, especially in oceanographic research [12]. Cluster analysis technologies are widely used in hydrology [16] and geophysics [18], which makes it possible to divide the territory into districts depending on the task statement. In oceanography, cluster analysis methods are most widely used in determining water masses [4, 19].

2 Materials and Methods

Cluster analysis is one of the most modern data mining technologies, which allows one to find new knowledge in databases. Cluster analysis aims to find and identify independent groups (clusters) and their characteristics in various independent parameters [5].

The source of the initial data on the sea surface temperature at 25 points of the Pacific Ocean was taken from the Columbia University database (Fig. 1) [1].

The temperature field is zoned by the hierarchical Ward method, the Euclidean metric, and the k-means method. Based on the hierarchical classification method, a dendrogram is calculated and visually divided into several classes at the initial stage in the STATISTICA program. For each partition option, the average temperature value in the class is calculated, the average value is compared according to the Student's criterion at a significance level of 5%, and the classes are combined if some averages are equal. Thus, we obtain the optimal partition.

For clustering by the k-means method, we calculate information about interclass and intra-class distances for the classes obtained in the previous method in

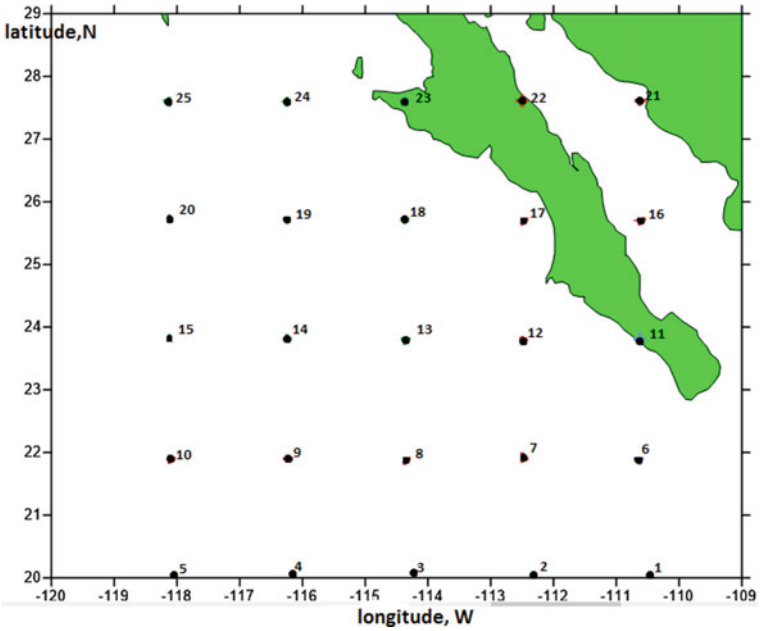


Fig. 1 Location of points on the map. *Source* Compiled by the authors

the STATISTICA package and calculate the optimality criterion (1), (2):

$$J_1 = X/Y, \tag{1}$$

$$J_2 = Y - X, \tag{2}$$

where:

Y—the average inter-class distance;
X—the average intra-class distance.

Based on the results of the obtained optimal division into classes using GIS Surfer, we build a map by drawing class boundaries [12, 16].

3 Results

The results of classification by the hierarchical Ward method and the Euclidean metric are shown in Fig. 2 in the form of a dendrogram.

According to the dendrogram, the division into two and three classes is selected. The optimal partitioning is checked according to the Student's criterion; the results

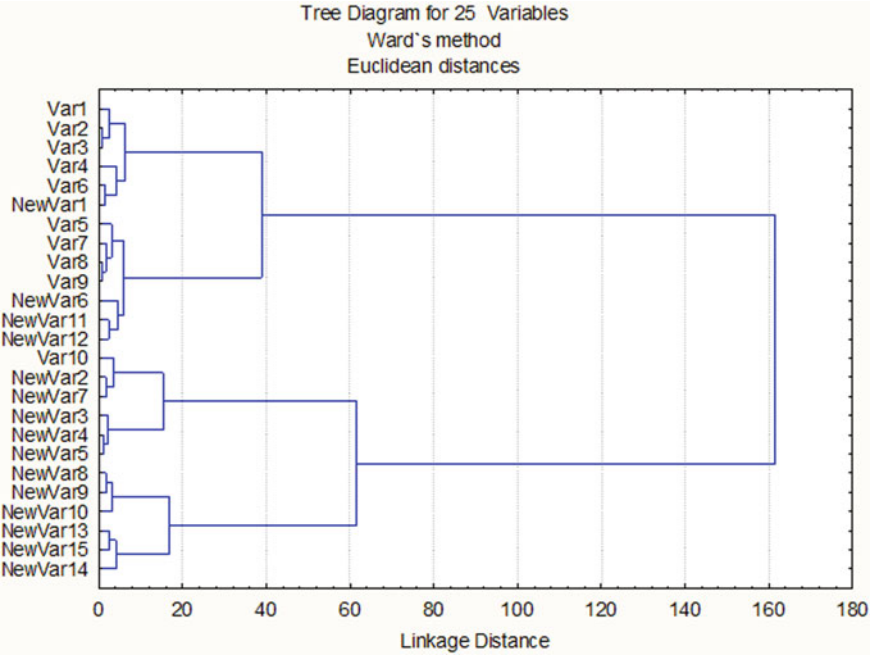


Fig. 2 Dendrogram of field zoning by water temperature. *Source* Compiled by the authors

of the empirical and critical values of the Student's criterion at a significance level of 5% are presented in Table 1.

The results of calculations by the *k*-means method for splitting into two classes are presented in Tables 2–4.

The average intra-class distance is 0.897. The optimality criterion for splitting into two classes $J_1 = 0.246$, $J_2 = 2.749$.

The results of calculations by the k-means method for splitting into three classes are presented in Tables 5–8.

The average distance between clusters is 2.3.

The average intra-class distance is 0.601. The optimality criterion for splitting into two classes is as follows: $J_1 = 0.256$, $J_2 = 1.749$.

The optimal division into three classes is chosen according to the optimality criterion. The boundaries of the cluster districts are plotted on the map (Fig. 3).

Table 1 Empirical and critical values of the Student's criterion at a significance level of 5% for the division into two and three classes

	t^*	t crit	Conclusion
$t1$	39.16	1.96	Significant
$t2$	29.45	1.96	Significant
$t3$	40.65	1.96	Significant

Source Compiled by the authors

Table 2 Inter-class distance when divided into two classes

Euclidean distances between clusters (Spreadsheet 1). Distances below the diagonal. Squared distances above the diagonal		
	No. 1	No. 2
No. 1	0.000000	13.29115
No. 2	3.645703	0.00000

Source Compiled by the authors

Table 3 Intra-class distance in the first class

Members of Cluster 1 (Spreadsheet 1). Distances from the corresponding cluster center. The cluster contains 9 variables	
Point no	Distance
13	1.162188
14	1.363382
15	1.312197
18	0.188579
19	0.256396
20	0.278043
23	1.199543
24	1.647416
25	0.940304

Source Compiled by the authors

In most water areas, the location of the first class is noted, the second class is located in the southern part of the study area and near the California peninsula, and the third class is located at the tip of the peninsula.

4 Discussion

When classifying by the Ward method and the Euclidean metric, we chose a division into two and three classes, calculated the averages in each class, and checked the equality of averages according to the Student's criterion (the Student's criterion for two classes was as follows: $t1 = 39.16$; $t2 = 29.45$). Therefore, it was concluded that classes should not be combined. For three classes, the Student's criterion was as follows: $t3 = 40.65$; $t1 = 39.16$; $t2 = 29.45$. The conclusion is that the classes should not be combined. The division into two classes is the best choice since the difference between $t1$ and $t2$ for three classes is not very large.

By the k-means method, a division was made into two and three classes. For the two classes, the optimality criterion was $J1 = 0.246$ and $J2 = 2.749$; for the three classes, the optimality criterion was $J1 = 0.256$ and $J2 = 1.749$. According to the

Table 4 Intra-class distance in the second class

Members of Cluster 2 (Spreadsheet 1). Distances from the corresponding cluster center. The cluster contains 16 variables	
Point no	Distance
1	1.487976
2	1.225769
3	1.210432
4	0.608328
5	0.284310
6	1.052624
7	0.406792
8	0.492313
9	0.541057
10	1.223945
11	0.875379
12	1.447766
16	0.389350
17	1.465250
21	0.723210
22	0.427343

Source Compiled by the authors

Table 5 Inter-class distance when divided into three classes

Euclidean distances between clusters (Spreadsheet 1). Distances below the diagonal. Squared distances above the diagonal			
	No. 1	No. 2	No. 3
No. 1	0.000000	9.096368	2.84433
No. 2	3.016019	0.000000	22.06017
No. 3	1.686515	4.696825	0.00000

Source Compiled by the authors

optimality criterion, the division into three classes was selected. The map shows the location of all three classes (Fig. 3), which allows concluding about three factors influencing this area and, thus, the division of the water area into three parts differing from each other in terms of the TPO. The TPO is the smallest in the north of the region, and in the south, the area with the warmest temperature stands out. This is due to the fact that the further north, the lower the water temperature as it is farther from the equator, and besides, there is a cold current lowering the water temperature relative to the average temperature of the water area [1-3, 12, 19, 11].

Previously, no cluster analysis study has been carried out for this area; according to the results of the analysis in other water areas, the use of cluster analysis gives

Table 6 Intra-class distance in the first class

Members of Cluster 1 (Spreadsheet 1). Distances from the corresponding cluster center. The cluster contains 10 variables	
Point no	Distance
5	0.566279
7	0.342964
8	0.293388
9	0.247807
10	0.608906
12	0.840164
16	0.714756
17	0.868395
21	0.452161
22	0.497994

Source Compiled by the authors

Table 7 Intra-class distance in the second class

Members of Cluster 2 (Spreadsheet 1). Distances from the corresponding cluster center. The cluster contains 9 variables	
Point no	Distance
13	1.162188
14	1.363382
15	1.312197
18	0.188579
19	0.256396
20	0.278043
23	1.199543
24	1.647416
25	0.940304

Source Compiled by the authors

Table 8 Intra-class distance in the third class

Members of Cluster 3 (Spreadsheet 1). Distances from the corresponding cluster center. The cluster contains 6 variables	
Point no	Distance
1	0.446243
2	0.207386
3	0.237350
4	0.542940
6	0.205182
11	0.352606

Source Compiled by the authors

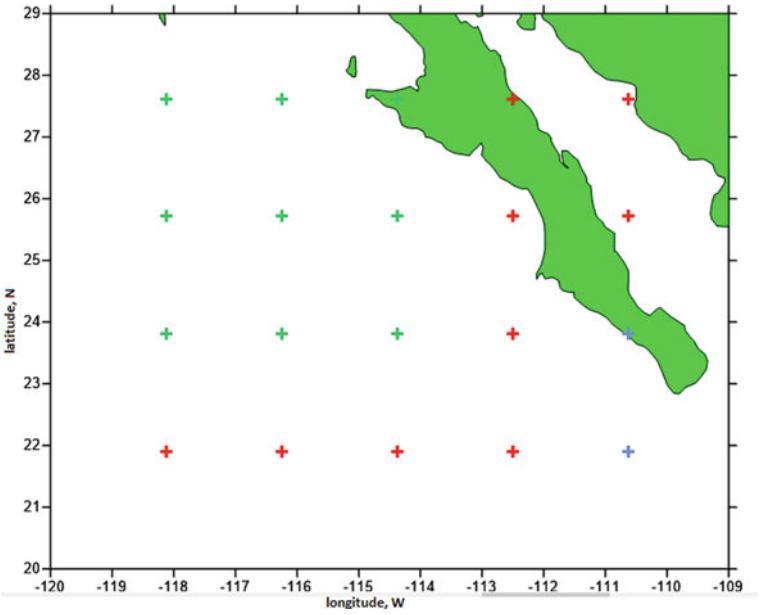


Fig. 3 Location of the boundary of the ocean surface temperature classes. *Source* Compiled by the authors

good results of zoning by ocean surface temperature, which allows further research to analyze various thermal parameters for particular areas of the water area to increase the accuracy of calculations or improve the quality of information [6-8, 10, 14, 15, 17, 20, 21].

5 Conclusion

The use of cluster analysis makes it possible (1) to identify aggregates (groups) of parameters similar in structure that characterize the climate system and (2) to determine the variability of the content of groups in different periods and the relationship between climatic parameters.

The application of the method for zoning the temperature field of the Pacific Ocean off the coast of California allows us to distinguish three different hydrological regions. Zoning is consistent with the location of climatic fronts, the main systems of currents, and water circulation.

The method makes it possible to reduce calculations with a large amount of information, highlighting compact groups with similar characteristics, which will significantly reduce information processing time.

The practical significance of the research lies in the further possibility of using the data obtained for each class to predict or study the formation or nature of the development of a process or phenomenon, which can increase the accuracy of calculations or forecasting by conducting analysis and calculations in similar groups, which, in turn, is also a prospect for further research.

It makes sense to implement the considered method into geographic information systems and management decision support systems.

Acknowledgements The work was carried out at the Russian State Hydrometeorological University within the framework of the State Assignment of the Ministry of Science and Higher Education of the Russian Federation (Project No. FSZU-2020-0009).

References

1. Aoki T, Matsuo J, Yamada I (2003) Cluster species and cluster size dependence of damage formation by cluster ion impact. Nuclear Instruments and Methods in Physics Research Section B: Beam Interactions with Materials and Atoms 206:861–865
2. Barseghyan AA, Kupriyanov MS et al (2004) Methods and Models of Data Analysis. OLAP and DATA Mining. BHV-Petersburg, Saint-Petersburg
3. Chen Ming-Xing, Yan XH (2008) A new magic titanium-doped gold cluster and orientation dependent cluster-cluster interaction. Journal of Chemical Physics 17:174305
4. Climate Data Library (nd) Database of Columbia University. http://iridl.ldeo.columbia.edu/
5. Dmitrieva EV, Rostov ID (2004) Development and Implementation of Oceanographic Databases for the Northern Part Pacific Ocean. Dalnauka, Vladivostok
6. Ergina EI, Zhuk VO (2019) Spatiotemporal variability of the climate and dangerous hydrometeorological phenomena on the Crimean Peninsula. Russian Meteorology and Hydrology 7:494–500
7. Gill A (1986) Dynamics of atmosphere and ocean. Mir 1:130–190
8. Ichikawa K, Imawaki S, Ishii H (1995) Comparison of surface velocities determined from altimeter and drifting buoy data. Oceanography 51:729–740
9. Istomin E, Martyn I, Petrov Y et al (2020) Study of intra-day dynamics of currents in the area of the navigable strait of Baltiysk to adjust the movement of water transport. IOP Conference Series: Materials Science and Engineering 817(1):012013
10. Klemp JB, Rotunno R, Skamarock WC (1994) On the dynamics of gravity current in a strait. J Fluid Mechanics 269:169–198
11. Martyn I, Petrov Y, Stepanov S et al (2020) Climatic changes in the abundance of anchovy in the southeast Pacific Ocean. E3S Web of Conferences 222:05004
12. Martyn I, Petrov Y, Stepanov S et al (2020) Features of the spatial and temporal distribution of chlorophyll "A" and its relation to the water surface temperature by manifestations in the earth remote sensing data. E3S Web of Conferences 222:05005
13. Martyn I, Petrov Y, Stepanov S et al (2020) Spatial-temporal variability of ice cover of the Bering Sea. IOP Conference Series: Earth and Environmental Science 539(1):012198
14. Omstedt A, Elken J, Lehmann A, et al (2014) Progress in physical oceanography of the Baltic Sea during the 2003–2014 period. Progress in Oceanography 128:139–171
15. Perevedentsev YP, Shantalinskii KM, Gur'yanov VV et al (2019) Hydrometeorological hazards in the Volga Federal District. Russian Meteorology and Hydrology 12:802–809
16. Petrov Y, Istomin E, Stepanov S et al (2020) Development of a conceptual GIS model to support management decision making. IOP Conference Series: Earth and Environmental Science 574(1):012062

17. Shin HS, Oh BS (2020) Water transport according to temperature and current in PEM water electrolyzer. International Journal of Hydrogen Energy 1:56–63
18. Sidorenko A, Stepanov S, Petrov Y et al (2020) Application of a remote sensing data processing method for assessment ice cohesion in the Arctic navigation. IOP Conference Series: Earth and Environmental Science 539(1):012128
19. Tatarnikova T, Stepanov S, Petrov Y et al (2020) A conceptual model for geodata processing for sustainable forest management. IOP Conference Series: Earth and Environmental Science 507(1):012029
20. Ullgren JE, Emidio A, Gammelsrod T et al (2016) Observations of strong ocean current event offshore Pemba, Northern Mozambique. Operational Oceanography 9:55–66
21. Zhigalov IA, Lunchin VA (2005) Interannual variability of bottom water temperature on the west Kamchatka shelf, Russian Meteorology and Hydrology 10:55–61

Seasonal and Long-Term Variability of Ice Conditions in the Western Arctic



Yaroslav A. Petrov, Eugene P. Istomin, and Irma A. Martyn

Abstract Currently, various projects are implemented in the Russian Arctic sector, a large number of new projects are planned, and offshore developments are underway. The Northern Sea Route passes in the Arctic sector. To ensure safety and more efficient use of natural resources, one should study the climatic conditions of this region since they play an important role in the economic component and ensure environmental safety. For the analysis of climatic conditions, mathematical statistics and remote sensing methods play the most important role. The assessment of the variability of hydrometeorological characteristics and the possibility of their prediction is an integral part of the effective socio-economic use of the Arctic. The paper presents studies for the seas of the eastern sector of the Arctic: the Pechora, Barents, and Kara seas. The paper aims to study the long-term variability of the sea ice area of the seas of the Western Arctic using the methods of mathematical statistics: (1) trend research, (2) correlation of sea ice coverage, and (3) the method of auto-forecasting the ice extent of each sea with the calculated optimal lead time. As a result, we calculated the nonlinear trends characterizing the negative trend of the ice area for all seas. We also identified a significant message from the Barents and Kara Seas, for the Kara and Pechora Seas. We compiled auto-forecast models with a lead time of 1 year, for the Barents Sea with a lead time of 13 years. We can see a possibility of a touristic sea ice extent in these seas.

Keywords Sea ice · Arctic climate · Data analysis

1 Introduction

The state program "Development of shipbuilding and equipment for the development of offshore fields in 2013–2030 years" was approved by the decree of the RF Government dated 24 December 2012 No. 2514-R (as amended on April 15, 2014 No. 304,

Y. A. Petrov (✉) · E. P. Istomin · I. A. Martyn
Russian State Hydrometeorological University, Saint-Petersburg, Russia
e-mail: yaroslav.petrov025@gmail.com

© The Author(s), under exclusive license to Springer Nature Switzerland AG 2024

V. Karev (ed.), *Proceedings of the 9th International Conference on Physical and Mathematical Modelling of Earth and Environmental Processes*, Springer Proceedings in Earth and Environmental Sciences, https://doi.org/10.1007/978-3-031-54589-4_24

dated March 31, 2017 No. 374 and from March 30, 2018 No. 360). The program aimed to implement public policies to improve the level of technological development of the Russian shipbuilding industry, its competitiveness in the domestic and global markets, and determine the development of the industry until 2030 [6].

For the branches of marine economic activity in the Arctic, an important role is played by considering natural, including climatic, conditions. The climate changes in the Arctic and Subarctic over the past 30–50 years are among the most pronounced on the planet. It includes the variability of the characteristics of the ice cover, water and air temperature, etc. Their assessment and accounting are essential when planning the development and creation of objects of various economic activities [1]. Therefore, the study of climate fluctuations in this region plays an important role in the socio-economic development of the region. The paper aims to establish the characteristic features of the long-term dynamics of the ice cover in the Arctic region, as the most significant hydrometeorological parameter affecting the development of the region's infrastructure [2].

2 Materials and Methods

The paper aims to study the climatic variability of the ice cover of the Western Arctic. The tasks of the work included the collection of numerical data on the area of ice in the seas of the Western Arctic for the period 1981–2020 and the analysis of the obtained data array by methods of mathematical statistics and map analysis of the Arctic and Antarctic Research Institute [AARI]. The source of long-term ice concentration data is the Columbia University database. We selected the average monthly data in November 1981–May 2020 for the entire water area of the Pechora Sea. We used the data on ice conditions from the official website of the AARI [4].

We used statistical and probabilistic methods of data analysis: (1) spectral analysis to assess the prevailing periods of fluctuations in the series, (2) trend analysis, and (3) correlation analysis to assess the degree and nature of the relationship between the variability of ice conditions in adjacent and remote areas of the Arctic.

In addition, we used correlation indicators to assess the density and direction of communication. The correlation coefficient r characterizing the tightness of the linear dependence is calculated by the formula:

$$r = \frac{\sum_{i=1}^{N} [(x_{1i} - \overline{x_i})(x_{2i} - \overline{x}_i)]}{N\sigma_1\sigma_2} \quad (1)$$

where x_{1i} and x_{2i} are the values f the first and second variables, respectively; x_1 and x_2 are the average values of the first and second variables, respectively; σ_1 and σ_2-

standard deviations of the first and second variables respectively; N is the length of the rows of the first and second variables.

Correlation coefficients for several variables (more than two) in all combinations with each other, the set of obtained correlation coefficients is written in the form of a matrix.

To assess the relationship, the correlation coefficients are checked for significance according to the student's criterion, its sample value is calculated by the formula:

$$t* = \frac{|r|}{\sigma_r}, \sigma_r = \frac{1 - r^2}{\sqrt{N - 2}} \tag{2}$$

where σ_r is the mean square error of calculating the correlation coefficient.

Next, we determined the critical value $t_{crit}(\alpha, \nu)$, where the significance level a is taken to be 5%, and the number of degrees of freedom $\nu = N - 2$, where the N - row length.

Compared t* with t_{crit}. If $t* > t_{crit}$ the null hypothesis is rejected, the correlation coefficient is significant, i.e., there is a statistically significant forward (or backward, depending on the sign) between the two variables communication. If $t* < t_{crit}$, there is no reason to reject null hypothesis, i.e., the correlation coefficient is insignificant, i.e., between two variables statistically significant linear no connection.

For most time analysis methods series, one of the main requirements for a series is its stationarity, i.e., invariability of its basic statistical characteristics over time. In particular, this fact concerns its average value and variance. Therefore, at the first stage of the analysis of the time series, its stationarity is assessed, and if it is not detected, the row is converted to a stationary form.

The trend reflects the studied characteristic of a long-period oscillation with a period significantly exceeding the sample length in the temporal variability.

The linear trend equation is:

$$y = a_1 t + a_0 + \varepsilon \tag{3}$$

and nonlinear (quadratic) trend is:

$$y = a_2 t^2 + a_1 t + a_0 + \varepsilon \tag{4}$$

where t is time.

Auto-prediction of any lead time is performed based on a paired linear regression model, which in this case called autoregression of the 1st order. It is formulated in general:

$$x_{i+k} = a_1 x_i + a_0 + \varepsilon \tag{5}$$

where k is the forecast lead time.

3 Results

Currently, various large-scale production and infrastructure projects are being successfully implemented and planned in the Arctic (Fig. 1). In the area of the Kola Peninsula, it is planned to develop the Murmansk transport hub and build an oil terminal. In the area of Arkhangelsk, it is planned to build a deep-water seaport area and develop a shipbuilding cluster. In the Nenets Autonomous District, it is planned to build a deep-water seaport of Indiga, its structure will also include oil and coal terminals and a terminal for the shipment of liquefied gas [6]. As a result, many projects are being implemented in the Far North region, which can be further developed. However, (1) their development, (2) the possibility of implementation, and (3) the cost will depend on climatic conditions [3, 5].

Figure 2–4 show the long-term variability of the weighted average amount of ice on average for the year in the Pechora and Kara Seas based on data from Columbia University for the period November 1981–May 2020.

To identify the relationship and its nature, a correlation analysis was carried out between the ice extent of the studied seas. Table 1 shows the results in the correlation matrix.

Figure 5 shows the interannual dynamics of the parameters of the ice cover in the Arctic, submitted by the AARI from 2008 to 2020. *Source* Compiled by the authors

Figure 6–8 show an automatic forecast of ice coverage for the Pechora, Kara, and Barents Seas.

4 Discussion

In the series of ice cover of the Pechora, Kara, and Barents Seas obtained in 1981–2020, according to the results of the assessment of the nonlinear trend, each of them is significant according to the student's criterion at a significance level of 5% (Figs. 2, 3 and 4). In the Kara and Barents Seas, there is a negative trend of changing the ice area, for the Pechora Sea, a positive trend is observed until the 2000s, after which it is replaced by a negative one. The trend value is -30.4 km^2/year for the Pechora Sea, the ice area is reduced by 74.4 km^2/year for the Kara Sea, and by 81.7 km^2/year for the Barents Sea. The trend makes the greatest contribution to the description of the Barents Sea dispersion, which is about 21%. Thus, there is a decrease in the area of sea ice for the Western Arctic, the lowest rate of decline is observed in the Pechora Sea, the highest—in the Barents Sea. This trend may correspond to the opinion of some climatologists about global warming, which will lead to a reduction in the area of sea ice [2].

To identify the relationship and its nature, we conducted a correlation analysis between the length of the ice of the studied seas. Table 1 shows the results in the correlation matrix. Hence, there is a statistical relationship between the ice conditions of the seas under consideration, there is a highly significant relationship between the



Fig. 1 Map of the location of socially significant infrastructure facilities in the Arctic. [6] Source

Barents and Kara seas, the correlation coefficient is 0.76, which is possible as a result of more open interaction with each other. The relationship between the ice cover of the Pechora Sea and the Barents and Kara Seas is low (r above 0.4) due to the isolation of the Pechora Sea, which has its ice features.

To study the variability of sea ice types, we analyzed the AARI ice maps for the available period 2008–2020 (Fig. 5). For the Barents Sea, which is strongly influenced by the warm Gulf Stream and the ice is concentrated here only in the southern and northern regions of young and annual ice, the largest area of distribution is allocated in 2010 and 2011, in 2020 the area occupied by ice is very small, in the north, there

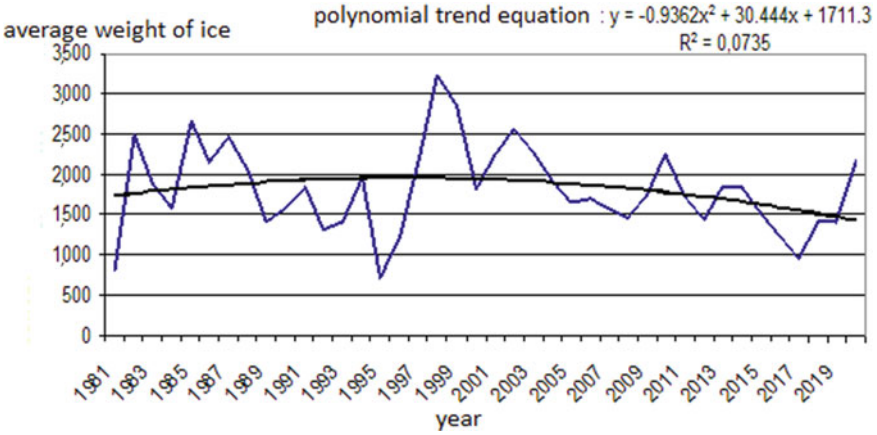


Fig. 2 Long-term changes in the ice coverage of the Pechora Sea on average per year for the period 1981–2020. *Source* Compiled by the authors

Table 1 Correlation matrix between the values of ice extent on average per year in the Pechora, Barents, and Kara seas

	Barents sea	Kara sea	Pechora sea
Barents sea	1		
Kara sea	0.76	1	
Pechora sea	0.47	0.46	1

Source Compiled by the authors

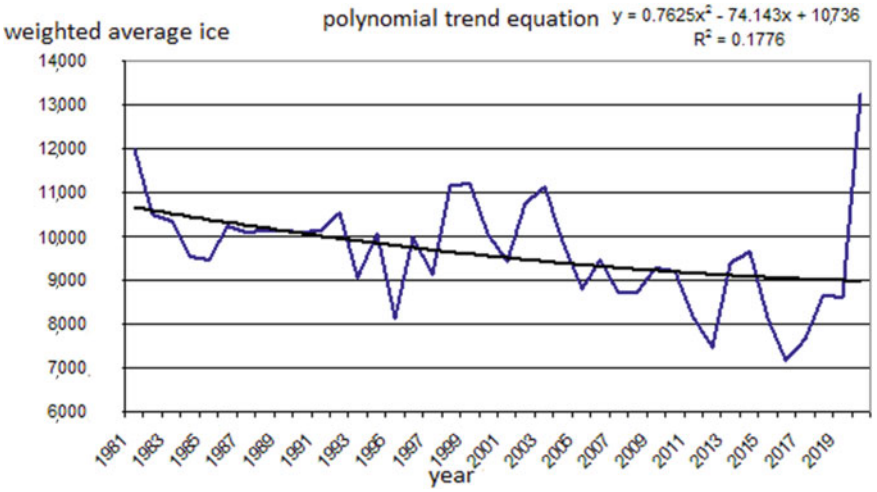


Fig. 3 Long-term changes in the ice coverage of the Kara Sea on average per year for the period 1981–2020. *Source* Compiled by the authors

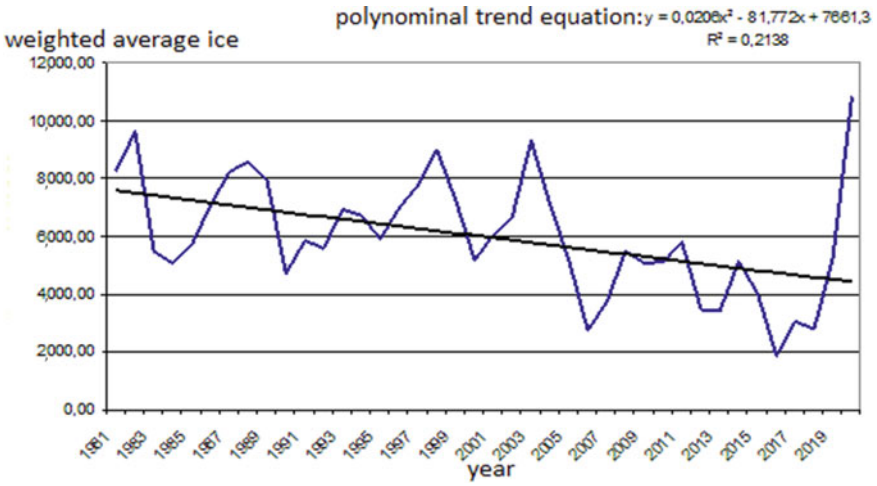


Fig. 4 Long-term changes in the ice coverage of the Barents Sea on average per year for the period 1981–2020. *Source* Compiled by the authors

are nilotic types of ice. In the Kara Sea, there is a diverse change of ice types by year, in 2009, 2012, 2016, and 2019, the sea is almost completely covered with young ice, in the south, there is nilas, in the north, there is annual ice. In 2009, half of the sea is free of ice, in the remaining years, the Kara Sea is mostly covered with young and annual ice, while, as noted above, the types of ice from year to year are highly variable in the area occupied by the sea. The Pechora Sea is characterized by the types of ice—nilas and young ice. These types of ice are almost always found in the Pechora Sea, but recently, the sea is almost free of ice and only a narrow strip along the coast is occupied by nilas and young ice.

Due to the highly variable ice situation in the water area of the selected seas, one should predict the variability of the ice area. Using regression methods, forecast models were compiled for each of the seas, for the Kara Sea, the optimal forecast lead time was 1 year, as for the Pechora Sea. Based on the obtained forecast models, new series were calculated (Figs. 6 and 7) and the forecast model was evaluated, which showed that the regression coefficients are significant according to the student's criterion, the model is adequate to the initial data, the determination coefficient exceeds 0.7 and the model error does not exceed the standard error, which indicates that the models can be used for calculation. A model with an optimal lead time of 13 years was built for the Barents Sea (Fig. 8), the evaluation of the model showed that it can also be used in the future. For each of the models, the graphs calculated from the model repeat the actual graphs. This fact also indicates a fairly good quality of the forecast models.

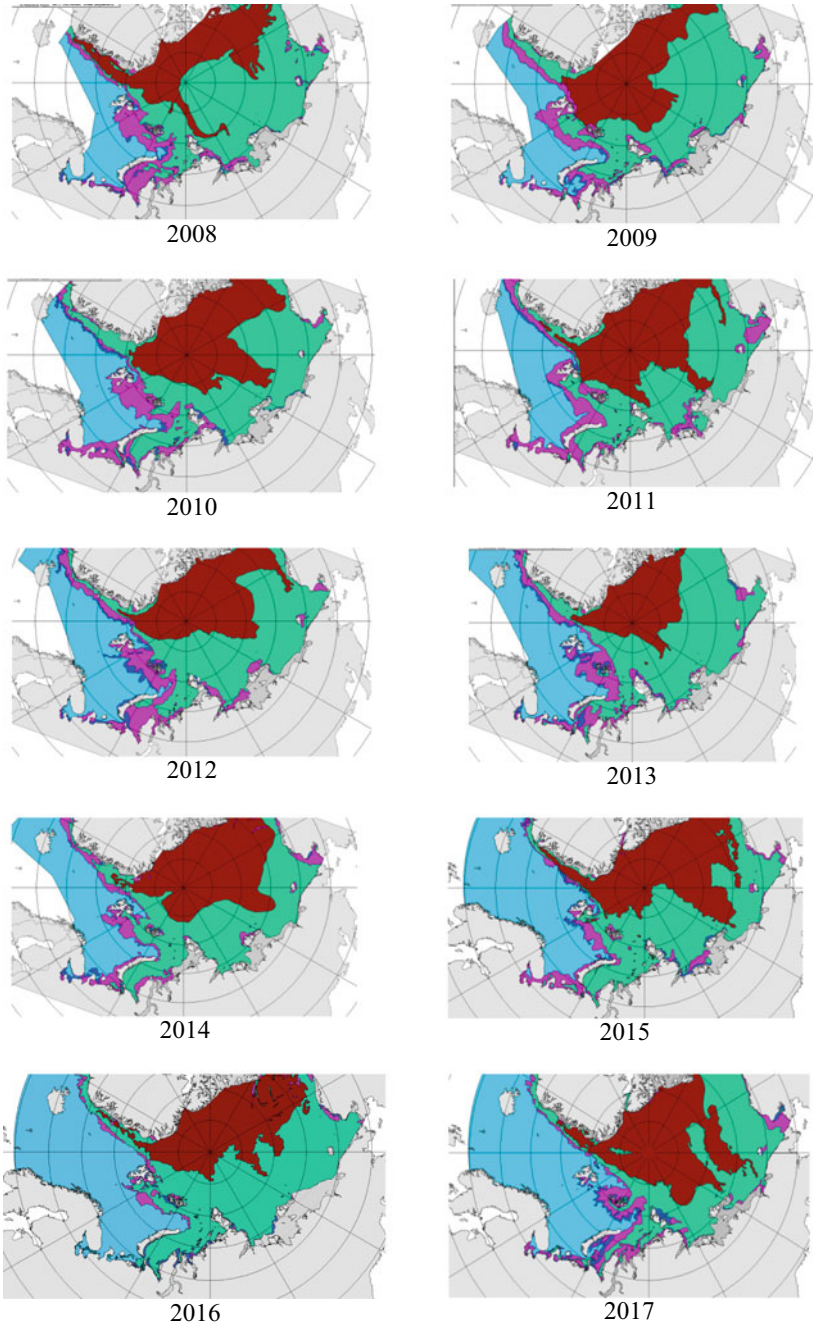
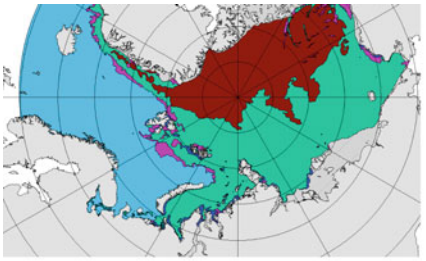


Fig. 5 Interannual dynamics of the parameters of the ice cover of the Arctic seas. Annual data for January 2008–2020 according to AARI. *Source* Compiled by the authors



2018



2019



2020

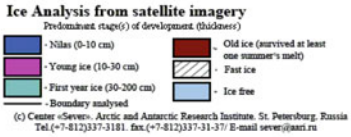


Fig. 5 (continued)

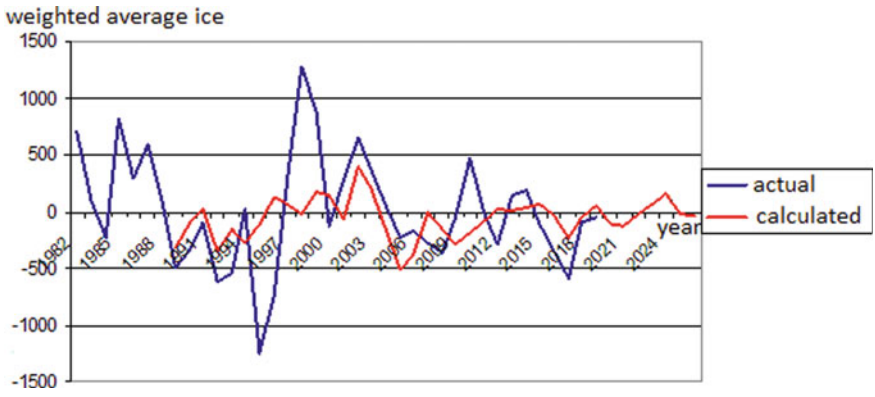


Fig. 6 Actual and calculated according to the auto-forecast model with a lead time of 1 year of the weighted average amount of ice in the Pechora Sea. *Source* Compiled by the authors

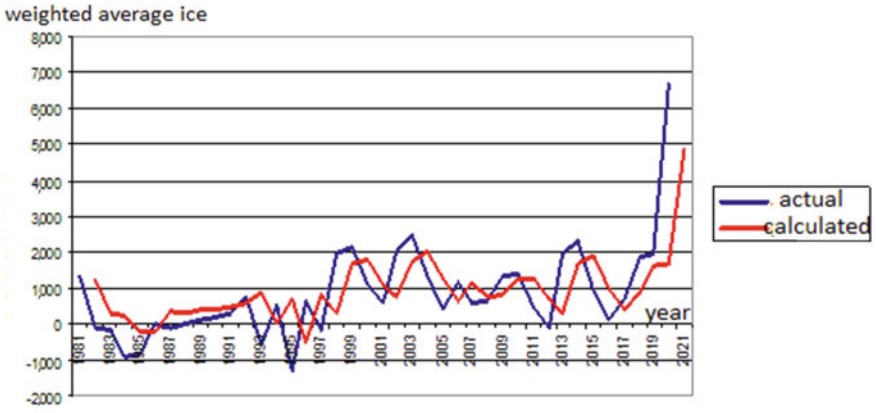


Fig. 7 Actual and calculated according to the auto-forecast model with a lead time of 1 year of the weighted average amount of ice in the Kara Sea. *Source* Compiled by the authors

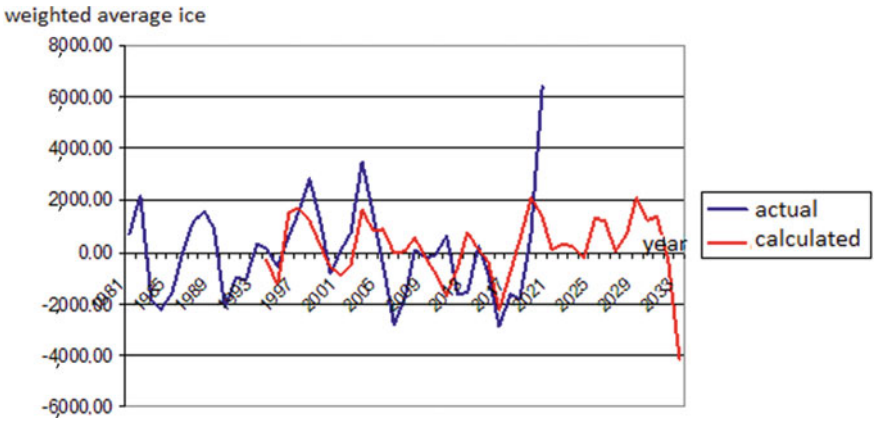


Fig. 8 Actual and calculated according to the auto-forecast model with a lead time of 1 year of the weighted average amount of ice in the Barents Sea. *Source* Compiled by the authors

5 Conclusion

During the period under study, there is a tendency to an increase in the amount of ice until the early 2000s. After that, we can see a decrease in the ice coverage of the seas under consideration, which may be a consequence of global warming [2].

To identify the relationship and its nature, we conducted a correlation analysis between the ice extent of the studied seas. The results are presented in the correlation matrix in Table 1. There is a statistical relationship between the ice conditions of the seas under consideration, a highly significant relationship is noted between the Barents and Kara seas, which is possible as a result of more open interaction with

each other. The relationship between the ice cover of the Pechora Sea and the Barents and Kara Seas is not high (r above 0.4) due to the isolation of the Pechora Sea, which has its ice features.

There are significant changes in the area of various types of ice, which is the main obstacle to navigation in this region. In the Barents and Pechora seas, there are types of ice nilas and young ice to date, there is a tendency to reduce the area of their distribution, and the Kara Sea is covered with types of ice nilas, young and annual ice, while to date there is a tendency to increase the area of annual ice. Heavy old ice is found not only in the high latitudes of the Northern Sea Route but also in low latitudes. The ice cover in the Arctic sector is decreasing in the Barents and Pechora Seas, while in the Kara Sea, on the contrary, the area occupied by heavy ice is increasing. This situation will require taking measures to ensure the safety of navigation in the Arctic. It is possible to increase the duration of icebreaking assistance on the routes of the Northern Sea Route in the Kara Sea area.

In this case, the forecast of ice cover values becomes a necessary part of climate research. Figures 6, 7 and 8 show an automatic forecast of ice coverage for the Pechora, Kara, and Barents Seas. For the Pechora and Kara Seas, a forecast model with a lead time of 1 year was chosen, which gives the best result. For the Barents Sea, a good quality forecast with a lead time of 13 years was obtained [4].

Based on the analysis of long-term climatic changes in the ice coverage of the seas of the western Arctic, we can conclude that the region is currently experiencing a decrease in the total amount of ice. At the same time, part of the old ice of the total area is increasing, which requires the adoption of new safety measures in the field of navigation and economic activities on the shelf. A possible forecast of changes in the amount of ice in the seas of the western Arctic is presented. To obtain more accurate forecast models, the use of other hydrometeorological parameters is required.

References

1. Doronin YP (2007) Oceanography of the Shelf Zone. Russian State Hydrometeorological University, Leningrad
2. Drozdov VV (2019) On the issue of long-term climatic changes in the support zones of the socio-economic development of the Russian Arctic to improve shipping and industrial potential. Scientific Research in the Arctic 2(34):64–79
3. Istomin E, Sidorenko A, Stepanov S et al (2020) Application of Kalman-Bucy filter for vessel traffic control systems in the northern sea route. IOP Conference Series: Materials Science and Engineering 817(1):012012
4. Martyn I, Petrov Y, Stepanov S et al (2020) Spatial-temporal variability of ice cover of the Bering sea conditions. IOP Conference Series: Earth and Environmental Science 539(1):012198
5. Sidorenko A, Stepanov S, Petrov Y et al (2020) Application of a remote sensing data processing method for assessment ice cohesion in the Arctic navigation. IOP Conference Series: Earth and Environmental Science 539(1):012128
6. Vorobiev VN, Drozdov VV, Mitko VB et al (2015) Environmental and hydrometeorological problems of the development of industrial development of oil and gas resources on the shelf of the seas of the Russian Arctic and the ways of their solution. Ecology and Industry of Russia 19(2):50–55

Model for Forecasting the Hydrometeorological Situation as a Component of the Development of the Transport and Logistics System of the Arctic Region

Artem Yu. Sidorenko, Yaroslav A. Petrov, and Evgeniy P. Istomin

Abstract The research touches upon aspects influencing the provision of the transport and logistics system of the Arctic territory of the Russian Federation. This research describes the main geographical and political, as well as economic and strategic components, depending on the logistics highways. The research also identifies the fundamental sea routes connecting the borders of the Eurasian mainland. We revealed an explicit dependence of the predictive assessment of the hydrometeorological situation in relation to transport logistics based on the analysis. Moreover, we highlighted the primary factors influencing the navigation along the Northern Sea Route. It was revealed that ice conditions are the main criterion that impedes the development of ship navigation as a component of the logistics system. Achievements of the set tasks of this study are based on proceeding from the formulation of the main properties and functions of the future model. It is customary to modify and further use the recursive Kalman - Bucy filtering algorithm as a basic mathematical apparatus. In addition, we described the basics of the linear filter and gave the designations of the modified coefficients and their justification. The results of approbation are presented in a visualized form on the graph. A comparative function expresses the predictive assessment in relation to a priori data, reflecting the relevance of the method under study, with a view to applying it in Arctic logistics. Recommendations are given for further improvement of the considered method.

Keywords Kalman – Bucy · The Northern Sea Route · Arctic region · The Optimal filters · Sea ice concentration · Water transport logistics · Hydrometeorological situation · Geodata · Recursion

A. Yu. Sidorenko · Y. A. Petrov (✉) · E. P. Istomin
Russian State Hydrometeorological University, St. Petersburg, Russia
e-mail: yaroslav.petrov025@gmail.com

© The Author(s), under exclusive license to Springer Nature Switzerland AG 2024

V. Karev (ed.), *Proceedings of the 9th International Conference on Physical and Mathematical Modelling of Earth and Environmental Processes*, Springer Proceedings in Earth and Environmental Sciences, https://doi.org/10.1007/978-3-031-54589-4_25

1 Introduction

The territory of the Arctic is one of the richest and most promising regions of the Earth in terms of natural resources and energy reserves. When considering the geopolitical situation, it is crucial to emphasize how transport logistics, navigation and access to resources and the mainland are carried out in the Arctic zones of the Russian Federation and the international space. The lack of major airports is due to extreme climatic conditions and specific geographic locations. Thus, one of the main transport and logistics crossings is waterways. One should also note that the region is actively developing northern tourism, fishing, research activities and other areas of a socio-economic nature, which also require involvement in the logistics component.

Today, two leading water transport arteries connect the Western European and East Asian parts of the mainland. These are the Northern Sea Route [NSR] and the "Southern Sea Turbidity" (passing through the Suez). The arteries of the NSR are located along with the entire territory of the Russian part of the Arctic.

The social and economic development of the Arctic, as the leading region of the planet in the future (in terms of the potential of the world's energy and natural resources), cannot be considered without transport and logistics arteries.

The unique hydrometeorological situation [UHS] of the region, which combines several multiparametric criteria, is the most important condition for the development of Arctic space as a whole. The logistics system of the Arctic is highly dependent on UHS criteria, in particular, if it concerns the impact on shipping along the NSR and the nearest waters.

According to the fundamental factors one can trace the clear dependence of logistics in the polar regions:

- UHS;
- provision of reliable nautical charts based on navigation and hydrographic data;
- provision with communication systems and other means of navigation;
- the ecological situation on the routes;
- the factor of ice conditions on the vessel's route requires separate consideration;
- human factor;
- rescue preparedness;
- infrastructure on the route (the main element of the infrastructure is the nuclear icebreaker fleet).

The main part of the Arctic, particularly the water space, is covered with ice, making this criterion the main obstacle to transport logistics. One should add that the criterion for UHS—ice contains several parameters, such as concentration, thickness, convergence, drift, species, cohesion and others.

Today, there are many methods for processing hydrometeorological data at the output, representing or integrating into separate information systems [IS] [2; 10], in turn, contributing to the facilitation of the logistics of the Arctic sector. Despite the availability of various methods of processing information and IS, the need for improvement, or the development of new models for the development of logistics

routes [7], is still an urgent task, which is confirmed by the relatively low workload of navigation along the NSR.

As noted earlier, the primary criterion that has the greatest impact on water transport logistics is the ice situation on the route, in particular, if we consider the seasonal autumn–spring period (according to the source [10], this particular period is the least busy, from the point of view of navigation along the NSR).

Thanks to the fractal analysis of a number of ice parameters, one should pay the closest attention to the prognostic assessment of the sea ice concentration. Accordingly, it becomes necessary to solve the following tasks:

- Determine the source of a priori data;
- Identify the way to provide the logistics system with predictive data;
- Indicate the system algorithm to obtain a forecast;
- Determine the way to present the results.

Based on a number of sources [4; 5; 12], one can understand the forecast of UHS data as a certain component of the parameters (estimates) of the future state of the system (wind speed, pressure, water environment) obtained as a result of analytical processing. At the same time, the resulting data of the system should have the smallest error, at least satisfying the average statistical data, the basic laws of forecasting, at best-surpassing modern methods of predictive estimates.

2 Materials and Methods

Consequently, the research aims to synthesize a separate algorithm, which in its essence carries a predictive model that contributes to providing the logistics system of navigation in the Arctic with up-to-date geodata.

In tasks of this kind of model, one should provide the following functionality:

- Fetching geodata from external sources. Moreover, such data must correspond to the fundamental properties of the stationarity of the time series;
- The ability to process data for the short and long term;
- The result describes the comparative characteristics between the original data and the resulting forecast.

In order to synthesize a forecasting model of states with complete certainty of the initial values, we analyzed and considered the fundamental foundations of predictive models, as well as a number of algorithms that allow solving the necessary problem [11]. The most effective methods include the following algorithms: models of mathematical statistics, least squares and maximum likelihood methods [1]. As a consequence, it is necessary to use an environment in which one or more of the listed algorithms is used as a basis.

According to these features, we decided to use the algorithm used in the optimal filters as a future forecasting model. One of these techniques is the Kalman–Bucy recursive filtering algorithm.

The Kalman-Bucy filter [13] is a universal technique, the task of which is to build an algorithm that transforms the input signals. An important feature of the linear filter is that when receiving newly received apriori values, the filter updates the current state of the system and then predicts the future state.

Prediction of the future state of the system [9] can be described by different equations of the type.

$$x_t = \Phi(t, t-1)x_{t-1}, \tag{1}$$

where $\Phi(t, t-1)$ is the transition matrix characterizing the structure x_t. In this case, the observations must satisfy the relation.

$$z_t = P_t x_t + \varepsilon_t, \tag{2}$$

where P_t is the matrix of restrictions on observations; ε_t is the observation error.

The solution to Eqs. (1) and (2) will be the well-known relations defining the Kalman – Bucy filter [3]. After transforming these ratios in accordance with the formulation of the forecasting problem, we get:

$$x_{t+1} = x_t + W_t(z_t - P_t x_t), \tag{3}$$

$$W_t = K_t P_t^T \left(P_t K_t P_t^T + R_t\right)^{-1}$$

$$K_{t+1} = K_t - W_t P_t K_t, \tag{4}$$

where x_{t+1}- predicted at a point in time $t+1$ according to the results of observations available at this time, the estimation x (conditional mathematical expectation x); x_t- predicted at a point in time t score x; K_t- vector component covariance matrix x_t; K_{t+1}- vector component covariance matrix x_{t+1}; W_t- filter transfer matrix; z_t- observation results $y(t)$ at the moment t; R_t- measurement error covariance matrix ε_t.

To implement the mathematical apparatus of forecasting, we used a priori estimates of mathematical expectations—the coefficients a_{ij}, their covariance matrix, control results $y(t)$ measurement error covariance matrix. After making calculations, we get the following model:

$$y(t) = a_0 + a_1 t + a_2 t^2, \tag{5}$$

Simplifying the task, we turn to the properties of the filter based on recurrent information processing. This fact endows the model with adaptive properties, which in turn allow the use of simpler models $y(t)$, in particular, a model of the form:

$$y(t) = A \cdot F(t), \tag{6}$$

At the initial moments of the analysis of the object's state, there is no information about the properties of changing its parameters, and the input data for the Kalman–Bucy filter are a priori estimates of the mathematical expectations of the coefficients a_{ij} and their covariance matrix. Therefore, when using model (5), it is necessary to obtain estimates of the mathematical expectations of the coefficients a_{ij} and their covariance matrix. Since in the further process, one can observe a change in the parameter according to the results of its periodic measurements. It is possible to plot the dependence of the change in this parameter over time and make its extrapolation.

According to the conditions necessary for the operation of the Kalman-Bucy filter and relations (3), the covariance matrix K_t has the dimension 3×3. To build this matrix, one should approximate the dependence of the parameter in time three times to obtain estimates of the coefficients a_{ij}.

Therefore, the time dependence of the parameter can be approximated in the following way:

- Make an approximation due to the model (5) for the first four points of control, then for the second, third, fourth and fifth points of control;
- Calculate the mathematical expectations of the coefficients a_{ij} for each of the three segments;
- Construct the covariance matrix K_t based on the obtained results.

Directly for solving the stated research tasks, since the Kalman-Bucy filter was developed for continuous systems [6], the hybrid Kalman filter will be used as an algorithm to extrapolate the state of the forecast equation system of the Kalman-Bucy filter with continuous time (formula 1). In this case, the correction is performed similarly to the discrete previously modified Kalman filter.

$$P = (F + C)^2 + Q, \tag{7}$$

For research purposes, the matrices were modified by bringing them to the difference coefficients. Let us denote the values of the structural coefficients of the modified filter algorithm:

- S_0—initial state of the filter, in fact - the initial state of the analyzed system;
- C—is the prediction error coefficient, which will be further recalculated;
- X—extrapolated state of the system;
- P—estimation of the variances of the calculated state error and covariance, showing the identified relationships between the system state parameters;
- F—is the coefficient of system evolution;
- Q—coefficient of random influence on the system;
- H—is the measurement factor connecting the true state vector and the vector of the measurements made;
- R—is the measurement noise figure.

After analyzing the two presented modifications, we can conclude that the main difference lies in the extrapolation of the system's state, namely, the use of Bucy's algorithm with continuous time as an equation.

The structure of the algorithm has been changed in terms of assigning coefficients to matrix notation, which makes it possible to implement the algorithm in the form of a Kalman-Bucy digital filter model and test it using previously obtained and processed geodata.

We implemented the filter on a computer using the high-level object-oriented programming language C Sharp (C #) in the MS Visual Studio Community 2019 environment.

3 Results

We used data from an external source to experiment with the synthesized model. As the parameter under study, based on the discussion in the third section, we will use data on sea ice concentration for 10 years, from October 2009 to December 2020. The data were sampled using the resources of the International Climate Research Institute and Society of Columbia University. We obtained multiparametric information from a polygon with the following coordinates: E81.5° E, N74.5° N (water area of the Kara Sea).

The predictive model (Fig. 1) shows a positive result based on the obtained results. The modified Kalman-Bucy filter algorithm justifies the set goals and objectives for solving short-term predictive estimates and interpreting a long-term forecast.

One can present the obtained data in discrete form. Then, integrating into an automated cartographic system [ACS], display the predicted data (by geo-positioning the point under study) on a coordinate grid. The resulting values will be a kind of

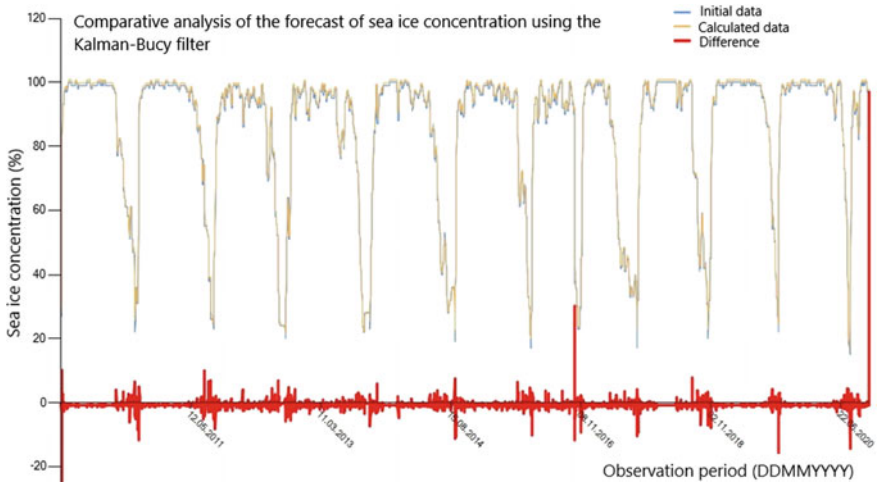


Fig. 1 Comparative assessment of the predicted criterion - "Sea ice concentration" using the modified Kalman-Bucy algorithm. *Source* Compiled by the authors

decision support system contributing to the facilitation of transport logistics in the Arctic sector.

4 Discussion

Analyzing the above results, it is worth noting that the convergence of the predicted result obtained in comparison with the a priori data requires more extensive consideration. In particular, if we talk about the observation periods, one should divide each time interval into certain units and conduct thorough research.

Undoubtedly, if we consider a similar experiment [9] with a description of the unmodified Kalman-Bucy filter, then this model has clear advantages, in particular, smoothing the linearity property of the filter.

Nevertheless, there are a number of other approaches [8] that use recursive-filtering algorithms in their mathematical structure. Accordingly, it is necessary to carry out an additional, more detailed analysis, using more geospatial data of hydrometeorological parameters, as well as to transpose the obtained data for a longer study period, about 50 years.

The next step is to compare all considered long-term and short-term forecasting systems. After such an in-depth analysis, one can argue that this model makes sense to apply in Arctic logistics.

5 Conclusion

The experiment of using the modified recursive filtering algorithm as one of the methods for determining the predictive assessment of the future state of the system as a tool for facilitating logistics operations in the Arctic is justified and relevant. Despite the overall positive result, the graph shows a number of deviations between the predictive estimation and the prior values. The nature of the deviations caused depends on the following factors: the absence of a true coefficient of external control action (since the data are natural processes, describing and reducing stochastic measurements to a discrete form is an extremely difficult task and requires a separate study; gaps (zero values) in a certain period of measurement (feature remote sensing data collection of the Arctic sector); the influence of the linear filter carrier on the error coefficient (gives the filter the property of being limited, therefore, too limited conditions are necessary to obtain the smallest root mean square error).

Nevertheless, the results are encouraging and require further research, with possible additional modifications, in particular, the introduction of a universal coefficient of external control action.

References

1. Istomin E, Petrov YO, Stepanov Syu et al (2020) About the methodology of geo-risk management in forestry. IOP Conference Series: Earth and Environmental Science 507(1):012006
2. Istomin E, Sidorenko AYu, Stepanov Syu et al (2020) Application of Kalman-Bucy filter for vessel traffic control systems in the northern sea route. IOP Conference Series: Materials Science and Engineering 817(1):012012
3. Kalman RE, Koepcke RW (1959) Proc. Western Joint Computer Conference: The Role of Digital Computers in the Dynamic Optimization of Chemical Reactors. The University of Sheffield, Sheffield
4. Lukin YuF (ed) (2017) Arctic Encyclopedia: In 2 vol. An Enlarged and Revised Edition of the "Northern Encyclopedia." Paulsen, Moscow
5. Makosko AA (2013) Hydrometeorological support of navigation along the routes of the Northern Sea Route. Arctic: Ecology and Economy 3(11):40–49
6. Martyn IA, Petrov YO, Stepanov Sy et al (2020) Spatial-temporal variability of ice cover of the Bering Sea. IOP Conference Series: Earth and Environmental Science 539:e012198
7. Petrov YO, Istomin E, Stepanov S et al (2020) Development of a conceptual GIS model to support management decision-making. IOP Conference Series: Earth and Environmental Science 574:e012062
8. Sidorenko AYu (2021) Models and methods of geoinformation navigation control in the Arctic region of Russia. Dissertation, Russian State Hydrometeorological University
9. Sidorenko AYu, Novikov VV, Istomin EP et al (2014) Forecasting the hydrometeorological situation in the western sector of the Northern Sea Route using the linear Kalman-Bucy filter. Information Technologies and Systems: Management, Economics, Transport, Law 3(14):35
10. Sidorenko AYu, Stepanov SYu, Petrov YO, Martyn IA (2020) Application of a remote sensing data processing method for assessment ice cohesion in the Arctic navigation. IOP Conference Series: Earth and Environmental Science 539:e012128
11. Tatarnikova T, Stepanov SYu, Petrov YO et al (2020) A conceptual model for geodata processing for sustainable forest management. IOP Conference Series: Earth and Environmental Science 507:e01029
12. Tolmacheva NI, Timofeeva AG (2017) Tutorial: Measuring Instruments for Hydrometeorological Purposes. IPK Rosgidrometa, Moscow
13. Vasiliev BV (1970) Forecasting the Reliability and Efficiency of Electronic Devices. Soviet radio, Moscows

Pore-Scale Computational Study of Permeability and Pore Space Geometry in Gas Condensate Reservoir Rocks



V. V. Khimulia and V. I. Karev

Abstract This paper presents the results of quantitative and qualitative studies of pore space and filtration properties of rocks of gas condensate fields based on computed tomography images. The research was carried out using ProCon X-Ray CT-MINI high-resolution scanner of the Institute for Problems in Mechanics RAS. The approach for digitally analyzing CT images using the GeoDict package is described in detail. 3D structures of the studied rocks with separation of matrix and pore space were obtained on the basis of CT images. The main filtration-capacitance properties of the rock—porosity and permeability—were determined. The digitally obtained values are in good agreement with laboratory permeability measurements, which indicates the correctness of the applied approach. It is shown that the filtration properties of the rock are close to isotropic with weak transversal anisotropy. For detailed analysis of pore space and reasons of anisotropy appearance, geodesic tortuosity measurements and analysis of percolation paths were carried out. The local porosity point distribution along the directions in the specimen was obtained, and the connectivity of the pore space was evaluated. It is shown that the causes of permeability anisotropy are a combination of pore space features, such as different channel tortuosity along the directions in the rock, different width of percolation paths, local porosity variation along specimen slices, and non-uniform distribution of pore space connectivity. The data necessary for filling the hydrodynamic model of the field, as well as for a better understanding of the fundamentals of the relationship between the filtration process and the structure of the pore space in rocks were obtained. The conducted digital studies are an irreplaceable tool for studying the internal structure of rocks, as well as they complement and expand significantly the range of results obtained by laboratory methods. Their application in conjunction with classical rock testing can help solve important problems in the oil and gas production industry, such as permeability drop in the vicinity of wells, loss of wellbore stability, sand production and operational accidents.

V. V. Khimulia (✉) · V. I. Karev
Ishlinsky Institute for Problems in Mechanics RAS, Moscow, Russia
e-mail: valery.khim@gmail.com

© The Author(s), under exclusive license to Springer Nature Switzerland AG 2024

V. Karev (ed.), *Proceedings of the 9th International Conference on Physical and Mathematical Modelling of Earth and Environmental Processes*, Springer Proceedings in Earth and Environmental Sciences, https://doi.org/10.1007/978-3-031-54589-4_26

Keywords Permeability anisotropy · Porosity · Reservoir filtration properties · Percolation paths · Geodesic tortuosity · Pore space structure · Computed tomography (CT) · GeoDict software · Gas reservoir properties

1 Introduction

The Arctic shelf is a huge treasure trove of hydrocarbons: oil and gas deposits already explored account for a quarter of the world's reserves. The northern shelf of Russia contains up to 25% of the country's oil reserves and up to 70% of its total explored gas reserves. However, the development of the Arctic region is currently facing significant challenges. These challenges primarily stem from the complexities associated with field development and operations in the demanding Arctic offshore conditions, and elevated economic costs. This difficulty is particularly prominent in the case of gas and gas condensate reservoirs found in the Russian Arctic shelf. These reservoirs are often weakly cemented, highly permeable sandstones with relatively low strength properties. Successfully developing and exploiting such reservoirs necessitates thorough and multifaceted preliminary investigations of core materials. These investigations are vital for creating adequate geomechanical and hydrodynamic models necessary for mitigating undesirable processes in wells, including sand production, loss of wellbore stability, and reductions in permeability in the bottomhole zones.

Comprehending the physical properties of reservoir rocks plays a pivotal role in the development of reservoir models and the innovation of strategies to enhance well productivity. To construct adequate hydrodynamic and geological reservoir models, extensive and thorough studies are essential, including laboratory core analysis. The primary reservoir characteristics that significantly impact reservoir processes include porosity, permeability, matrix structure, and rock pore space [1]. Traditionally, the assessment of rock permeability and porosity have been based on laboratory tests, well logging data, or indirectly through correlations with other rock characteristics [2]. There is a relatively recent and promising approach to studying rock properties in the laboratory—the numerical simulation of filtration processes using structures obtained through microcomputed X-ray tomography (μCT).

X-ray computed tomography (CT) represents a significant non-destructive technique for inspecting the internal structure of rocks, providing a valuable complement to direct laboratory investigations. This method entails reconstructing the spatial distribution of X-ray linear attenuation coefficients through computer processing of acquired projections during the radiation scan. The result of a CT examination is presented as a series of grayscale images collectively forming a three-dimensional depiction of X-ray absorption within the examined specimen [3]. Specialized software is subsequently employed to determine attributes such as linear dimensions, quantity, sphericity, and anisotropy of elements within the specimen [4]. To enable quantitative material analysis and the utilization of tomography results for numerical process modeling, image segmentation becomes imperative [5]. Segmentation is a technique involving the analysis of images and the transition from X-ray absorption to

the spatial distribution of the specimen's constituent components within the specimen space. Segmentation can take the form of binary (two-phase) or multiphase segmentation. In the industry, pore imaging experiments combined with modeling serve as valuable tools for determining geological and physical properties [6], including porosity and permeability [7]. The calculations are conducted on a segmented image, primarily focusing on the macropore space. This space comprises pores with well-defined boundaries that can be effectively segmented into fluid and solid grains on a voxel basis [8].

Recent research combined with extensive experience in developing complex hydrocarbon fields has underscored the significant influence of reservoir property heterogeneity and anisotropy on mass transfer processes within reservoirs. Considering the anisotropy of filtration properties is crucial for addressing challenges in production optimization and enhancing recovery rates. Reservoir models that disregard permeability anisotropy often lead to either overestimation or underestimation of critical reservoir characteristics potentially causing substantial economic setbacks for the industry. Moreover, information about reservoir permeability anisotropy proves invaluable when determining the most suitable field development approach [9]. Furthermore, factors like bedding, layering, shear, and compaction can impede fluid flow [10]. It's widely acknowledged that various degrees of reservoir structure heterogeneity and filtration property distribution are present in most fields [11]. The permeability anisotropy within rocks significantly affects fluid flow within reservoirs, spanning from injection wells to production wells. This impact becomes particularly pronounced in the later stages of field development and can lead to a reduced reservoir coverage factor, especially for facilities equipped with horizontal wells [12].

One of the significant advantages of methods based on tomography data is the possibility of detailed analysis of pore space, including its connectivity, tortuosity of filtration paths, pore volume distribution, etc. Structural analysis of pore space allows quantitative assessment of the causes of anisotropy of filtration properties, which is a tremendous advantage compared to other methods of materials research.

This work presents the results of rock structure digital studies carried out on the base of ProCon X-Ray CT-MINI high-resolution scanner of the Institute for Problems in Mechanics RAS. 3D structures of rocks under study were created on the basis of tomography images. Numerical and quantitative analysis of pore distribution in the rock was carried out, pore space connectivity and pore distribution in rock slices were investigated. Images of percolation paths were obtained and the tortuosity of filtration paths in the rock was estimated. Numerical modeling of the filtration process was carried out, permeability values of rocks in three directions were obtained. The data necessary for filling the hydrodynamic model of the field, as well as for a better understanding of the relationship between the filtration process and the structure of the pore space in rocks were obtained. It is shown that the data obtained by modeling on high-resolution images correlate closely with laboratory measured permeability values.

2 Research Methodology

The core material under investigation was obtained from a gas condensate field located on the Arctic shelf of Russia. The rocks under study were sandstone, which has high porosity and low strength. A series of high-resolution tomographic images were taken to obtain a clear picture of the internal structure. Specimens were randomly shaped pieces of the core with dimensions of 5–20 mm to get maximize resolution. The orientation of the axes in the specimens corresponded to the rock layering axes.

The procedure for computed tomography and image acquisition of the specimens was carried out using the ProCon X-Ray CT-MINI high-resolution micro-CT scanner of the Institute for Problems in Mechanics RAS [13]. This device boasts dimensions of 1300 × 850 × 600 mm and incorporates a robust base constructed from a single monolithic granite slab. This design choice effectively eliminates temperature-induced drift and ensures precise alignment of X-ray optical components and other system elements within the device, guaranteeing measurement accuracy and stability across the entire operational range.

The scanner employs a vertical core placement scheme for research purposes, accommodating specimens with a maximum height of 200 mm and a maximum diameter of 200 mm. The device is capable of handling loaded specimens weighing up to 5 kg. To enable precise measurements, a precision positioning system (manipulator) is integrated into the design allowing for a distance of 335 mm from the tube to the object. Furthermore, the detector can move perpendicular to the main system axis within a range of ±25 mm. The manipulator enables a 360-degree rotation of the specimen around its axis, achieving angular position reproducibility accuracy of 1.5 angular seconds. The microfocus X-ray tube, known for its high resolution and closed-loop operation, offers an adjustable output voltage range from 20 to 90 kV and an adjustable current range from 10 μA to 160 μA. The tube's maximum output power reaches 8 W, with the smallest focal spot size measuring 5 μm. The X-ray detector characterized by high sensitivity and minimal noise features a pixel count of 2940 × 2304 and a pixel size of 49.5 μm. The active (sensitive) area of the detector spans 146 × 114 mm.

The scans were reconstructed using VGSTUDIO software, while 3D image processing was carried out using Geodict Math2Market GmbH software [14]. GeoDict is an all-encompassing platform designed for multifaceted 3D image processing, material modeling, visualization, material property assessment, material development via modeling, and process optimization. Beyond its core image processing functionalities, GeoDict offers a range of techniques for image segmentation. Furthermore, GeoDict provides a wide array of solution methods for modeling fluid flow, conductivity, and mechanical behavior within porous media, accommodating both single-phase and two-phase scenarios.

Filtration fields were determined using the FlowDict module from the GeoDict package [15]. This module predicts effective material properties, including flow velocity, flow permeability, and flow resistivity, by simulating flow experiments

and subsequently analyzing the simulation results. FlowDict predicts the mean flow velocity under specific pressure conditions [16] and calculates the permeability of a porous structure by applying Darcy's law. This versatile module is proficient in computing incompressible, stationary Newtonian flows, employing various approximations derived from the Navier–Stokes equations. FlowDict is widely utilized by researchers worldwide for modeling flows in a variety of materials [17–20]. In this study, LIR solver was employed for numerical filtration simulations [21]. LIR is distinguished as the most recent and remarkably fast iterative finite volume method. This solver computes not only permeability but also velocity and pressure fields within extensive three-dimensional images. The convergence rate depends on the complexity and heterogeneity of the pore space. The chosen termination criterion for the flow simulations is the error bound, which possesses the capability to detect convergence oscillations and prevent premature termination of the process at local minima or maxima [22]. Specifically, the termination threshold was established at 0.1 for the LIR solver, causing it to halt once the relative difference in comparison to the prediction becomes less than 0.1. Additionally, Multigrid was utilized in the calculations, a technique that revolves around employing multiple coarser adaptive grids to expedite convergence while requiring minimal additional memory [23].

To evaluate the geometric and statistical homogeneity of the pore space across all specimens, porometric analysis and visualized pore geometry using MatDict [24] and the PoroDict modules were conducted, both of which are based on segmented images.

3 Experimental and Simulation Results

High-resolution computed tomography images were taken of all five specimens. These images offer clear differentiation between grain and pore boundaries, enabling statistical quantitative analysis and modeling. All high-resolution imaging was conducted with the following parameters: a source voltage of 90 kV, an amperage of 89 μA, an exposure time of 0.2 s, 15 averages for each projection, a rotation step of 0.125 degrees, and a voxel size of 4.957 μm. Following scanning and reconstruction, in-depth image processing was carried out using GeoDict software.

To enhance image quality and streamline the segmentation process, the Non-Local Means (NLM) filter was applied. Figure 1a displays the high-resolution projection obtained after reconstruction. For segmentation purposes, the Global Thresholding method was employed to refine the grain boundaries, as illustrated in Fig. 1b.

Further digital research was carried out on the basis of the established structures. A porosity-based representative elementary volume (REV) analysis was performed. It showed that for these rocks, a representative volume starts with a linear cubic structure size of more than 200 voxels. The structures used for the analysis had linear sizes of 500 voxels. Open porosity was estimated for all specimens using PoroDict module. On average, the porosity of the described series of specimens varied between 29 and 34%. Further results of the study will be presented using a typical specimen with

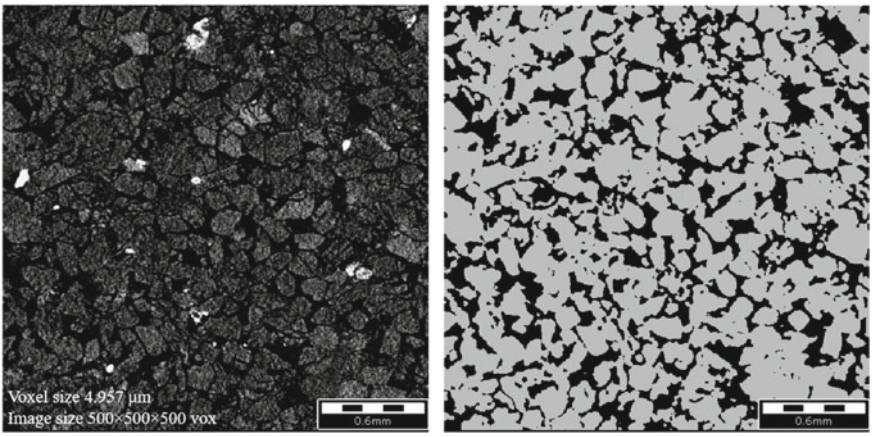


Fig. 1. **a**—slice of high-resolution 3D image after reconstruction; **b**—same slice after segmentation (grey—matrix material, black—pores)

porosity of 33.9%. Figure 2a shows the full 3D structure of the described specimen after processing and segmentation. Figure 2b shows the rock matrix obtained after segmentation. Figure 2c shows the pore space structure of the specimen.

Laboratory measurements of rock permeability were performed to determine the filtration properties of the specimen and to compare with the results obtained by digital method. For all specimens, permeability measurements were conducted using the TILTS facility of the Institute for Problems in Mechanics RAS [25]. For this purpose, cubic specimens with 40 mm edge were made from core material. During permeability measurement specimens were covered with an impermeable film along four edges parallel to the permeability measurement axis. Then air was

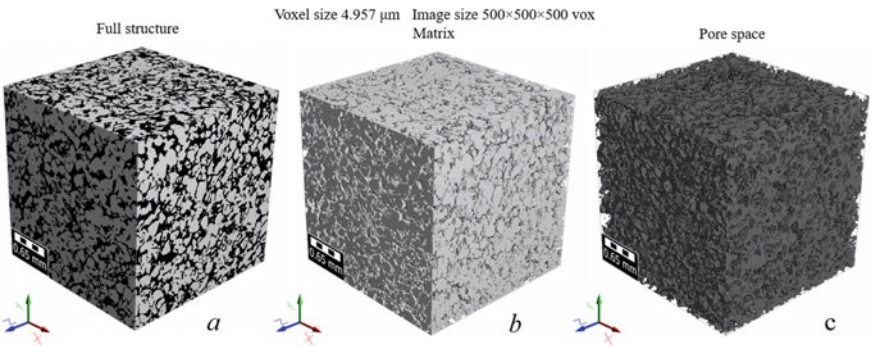


Fig. 2 **a**—full 3D structure of the described specimen after processing and segmentation (grey—matrix material, black—pores); **b**—rock matrix obtained after segmentation; c—pore space structure of the specimen

passed through two open faces under a small pressure drop (0.01 MPa) and its flow rate was measured [26]. The results of permeability measurements along and across the bedding for the tested rock are presented in Table 1, column 3. As it can be seen from the table, the rock has high permeability. It differs insignificantly in the directions along and across the bedding, which indicates a weak degree of transversal anisotropy of the rock in terms of filtration properties.

To evaluate the filtration properties and their anisotropy, a filtration flow modeling procedure was conducted. To simulate the filtration flow within the resulting structure, the Navier–Stokes filtration model was employed using the FlowDict module [15]. To simulate the conditions of laboratory permeability measurements, the following flow parameters were set: fluid is air, a pressure drop of 0.01 MPa, a temperature of 20 s°C, and boundary conditions in the filtration direction set to periodic with an implicit region of 10 voxels (inlet and outlet regions before and after the computed region to homogenize the flow. Additionally, in the tangential direction of structure, symmetric boundary conditions were applied. The results of the simulation on the example of the described specimen are presented in Table 1, column 4. As evidently from the table, the computed permeability closely aligns with the laboratory data. Furthermore, the permeability along the core axis consistently remains lower than in the layering directions. The difference between the values obtained by laboratory and numerical method is not more than 5%, which is a very good result for numerical modeling and confirms the correctness of the chosen model and the created methodology.

The pore space was digitally analyzed using MatDict and PoroDict for a more detailed study of the pore space and the causes of anisotropy.

Geodesic tortuosity values were measured for each direction in the specimen. The mean geodesic tortuosity quantifies the length of paths through the transport phase [27]. To compute it from 3D image data, all shortest paths beginning at the inflow plane were calculated. Tortuosity is defined as the average over all shortest path lengths divided by the thickness of the material [28]. The results of this analysis are presented in column 5 of Table 1. Comparison of the results on three axes shows that the values differ insignificantly. This is evidence of high connectivity of the

Table 1 Results of measurements and digital analysis

Direction in rock	Specimen axis	Laboratory value of permeability, D	Calculated permeability, D	Mean geodesic tortuosity	Minimal pore volume fraction	Mean number of connected pores in direction
Across the bedding (X)	X	5.200	5.455	1.05922	0.088	1060.26
Along the bedding (Y–Z)	Y	5.500	5.820	1.05640	0.118	1075.78
	Z		5.516	1.05651	0.110	1077.24

pore space on all axes. It can be seen that the value of tortuosity perpendicular to the bedding plane has a higher value. As a consequence, the permeability along this direction is lower than in other directions. At the same time, the tortuosity in both directions along the bedding differs insignificantly, despite the difference in permeability values. However, the trend of correlation remains: higher tortuosity corresponds to lower permeability. Thus, it is confirmed that tortuosity can be used in comparative assessment of rock filtration properties. The accuracy of this assessment will depend on the range of permeability values being compared. At the same time, the tortuosity parameter takes into account only the length of the filtration path in the direction, but does not take into account the width and size of particles able to pass along this path. Therefore, hydrodynamic models based only on this parameter may not reflect the actual values of permeability.

The PoroDict module was applied to estimate characteristic pore sizes. The results of the analysis showed that the pore space includes pores with sizes ranging from 10 μm to 140 μm. The highest number of pores have sizes of 20–30 μm and 35–45 μm. At the same time, pores larger than 50 μm account for 30% or more of the total volume. However, despite the large pore widths, filtration fluxes are known to be estimated by the smallest pore size through which a particle must pass during movement. To study them, calculations of percolation pathways were performed. To compute percolation paths, the MatDict method identifies the maximum diameters of spherical particles capable of traversing through the medium. Moreover, it calculates and presents the shortest paths taken by the largest particles. A visualization of 100 random percolation paths is presented in Fig. 3 for two directions in the rock: perpendicular to the bedding (X-axis, Fig. 3a) and along the bedding (Y-axis, Fig. 3b).

For each path, the maximum diameter of a particle capable of traveling along is calculated. In the direction perpendicular to the bedding, the maximum path widths ranged from 18 to 28 μm. In the direction along the bedding, the paths were slightly wider: from 20 to 30.5 μm. Such insignificant differences in the sizes of particles able to pass along the calculated paths define to the differences of permeability values

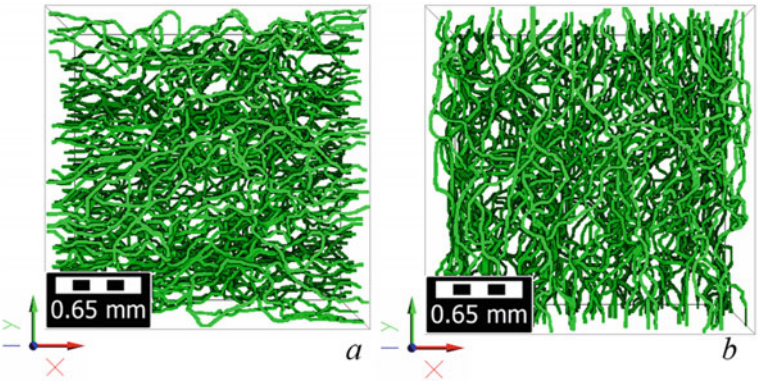


Fig. 3 **a**—Percolation paths perpendicular to bedding; **b**—percolation paths along the bedding

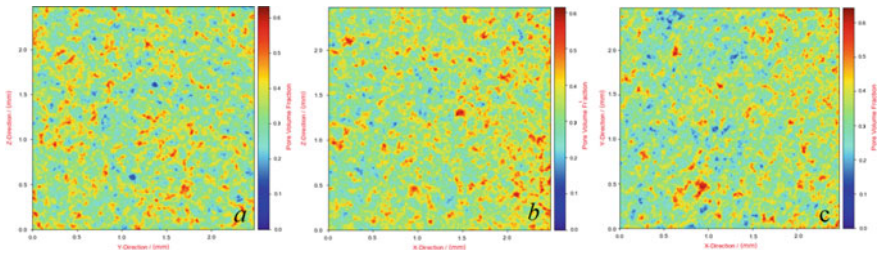


Fig. 4 Distribution of pore volume fraction along the X-direction (**a**), Y-direction (**b**) and Z-direction (**c**)

along different directions and confirm the weak degree of permeability anisotropy. For the structure with a linear size of 2.479 mm (500 voxels), the average percolation path lengths for the X and Y axes were 4.424 and 4.474 mm, respectively. Thus, the path lengths differ slightly along the axes (by 1.1%), with the calculated paths being slightly shorter along the X axis.

To integrally evaluate the pore distribution along each axis of the specimen, 2D Density maps were made. Such distributions are created based on the calculation of the distribution of Pore Volume Fraction in a plane normal to the chosen direction. Each pixel of the plots is calculated by averaging the respective porosity in the direction of interest. Figure 4 shows the integral porosity distributions along each axis of the specimen. The axes of each graph show the specimen lengths in mm along the directions perpendicular to the one under consideration. The color indicates the average porosity values of all pixels along the selected specimen direction.

As it can be seen from these maps, the porosity distribution along each direction is generally uniform. The low porosity (blue) and high porosity (red) regions are homogeneously distributed. On average, the porosity distribution along each axis corresponds to an overall bulk porosity value of 0.33. That is, the filtration process along each axis takes place throughout the entire volume of the specimen, without the strong dominance of isolated highly permeable paths. Meanwhile, it can be seen from Fig. 4b that along the Y direction of the specimen, the highest porosity is slightly concentrated in the right part of the specimen (end of the X axis). This may be the reason for the increased permeability along this direction. Moreover, this occurrence was not seen when analyzing the percolation paths due to their randomness of calculation. The minimum values of pore volume fraction (porosity) in each direction are presented in column 6 of Table 1. Described method allows to evaluate the contribution of porosity to the distribution of filtration fluxes in the presence of a pore space connectedness. However, for an accurate conclusion about the contribution of the local porosity distribution to the filtration properties of the rock, it is necessary to evaluate the connectivity of the pore space in each direction. Even for highly porous rocks, the permeability may differ significantly depending on the number of pore connections.

To analyze the connectivity of the pore space, the Identify Pores methods along with Connected Components of the GeoDict package were applied. The Identify

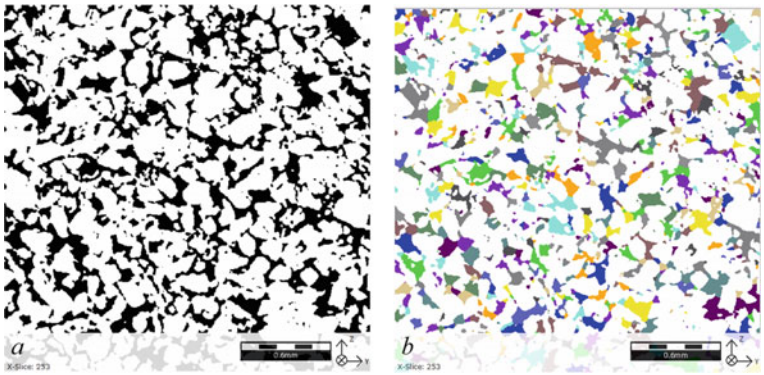


Fig. 5 **a**—slice of the described 3D specimen structure (white is rock matrix, black are pores); the same slice after pore space separation into pores (color shows different pores, white is rock matrix)

Pores method allows, based on additional segmentation, to identify individual pores in the pore space, estimate their size, volume and contact surfaces. The Connected Components method analyzes the voxel-to-voxel relations of the pores or solid material and computes the components that build up the pore fraction. Through this method it is possible to find and count the number of connected components in the 3D structure. A connected component consists of all voxels that are in contact with each other, and which belong to the same phase. Results of the method include the mean number of components per 2D slice in each spatial direction.

Figure 5 shows the result of pore space separation into individual pores. On the left picture is presented a slice of the described structure before the algorithm was applied, on the right one is presented the result of pore separation.

The newly obtained structure was used to apply the Connected Components method, which resulted the distributions of connected pores along each direction in the specimen. Figure 6 shows plots of the number of connected pores for each slice of the structure along the three selected directions.

The plots show that the number of connected components in layers along the bedding axes (Y, Z) is almost identical. The number of connected pores is distributed almost uniformly along planes in three directions with a small deviation from the average value. For the X axis, a more pronounced increase in the number of bound pores is observed along the growth of the layer number. This is due to the previously indicated compaction of the high porosity distribution in the growth region of the X-axis seen in Fig. 4b and the discreet localization of low porosity at the beginning of the X-axis (Fig. 4c). These plots demonstrate well the relationship of the quantitative porosity distribution with the connectivity of the pore space. In this case, the most understandable value when analyzing the influence of this parameter on the filtration properties of the rock will be the average value of connected pores along the selected direction. Table 1, column 7 shows the average values of the number of connected components for each axis of the specimen. It can be observed that the direction perpendicular to the bedding (X) corresponds to a lower value of average connectivity,

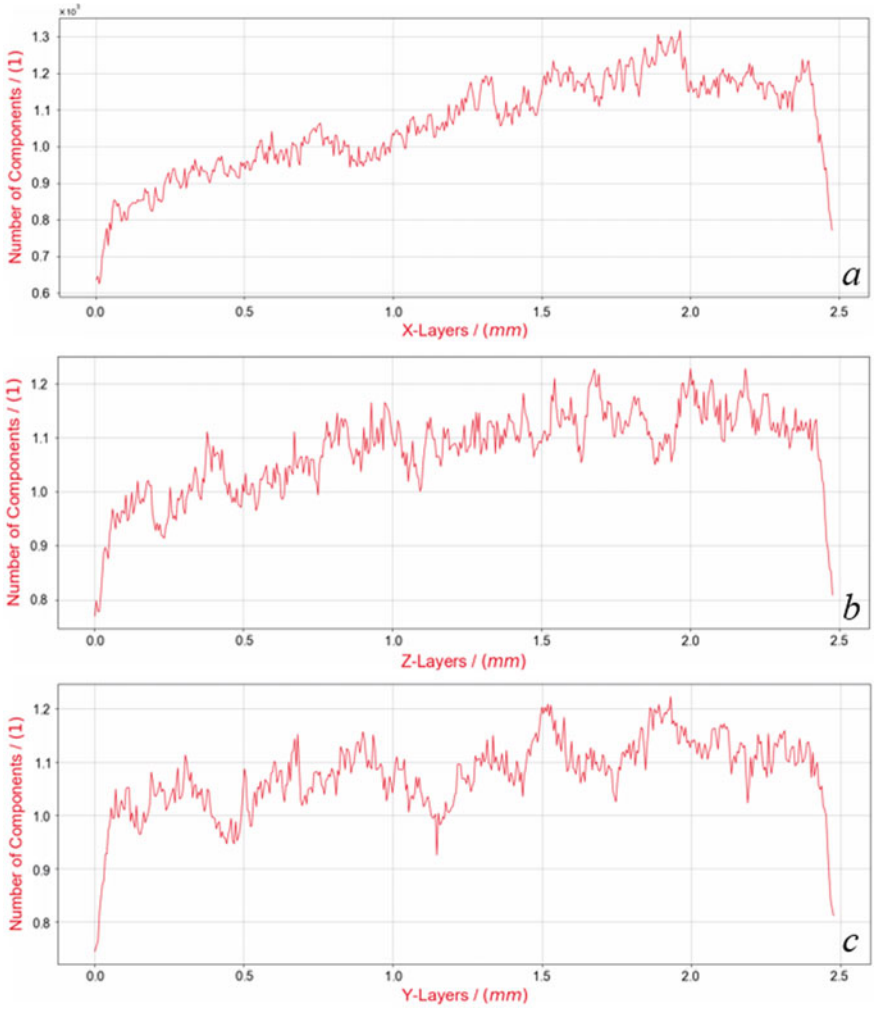


Fig. 6 Number of connected pores for each layer along the X direction (**a**), Z-direction (**b**) and Y-direction (**c**)

while for the Y and Z axes the values are higher and almost equal to each other. This is also a quantitative assessment of the cause of permeability anisotropy in the rock.

The data acquired in this study represent the initial phase of our planned comprehensive examination of the rocks in this deposit. These rocks of the studied interval have a weak degree of transversal isotropy and are practically isotropic in filtration properties. The anisotropy is caused by a local increase in average porosity and pore connectivity along the bedding direction, as well as by the resulting decrease in channel tortuosity and a slight increase in channel width in this direction. The results

obtained through numerical analysis demonstrate well agreement with traditional laboratory tests conducted on similar rocks from Arctic gas fields [29].

The studies described can be extended and refined by additional quantitative evaluation of the material: grain and pore sorting, roundness, packing characteristics and mineral composition. The digital analysis applied to CT images, as demonstrated in this study, proves to be a valuable addition to both laboratory-based and in-situ investigations of reservoir properties.

4 Conclusion

Thus the paper presents the results of digital studies conducted on the pore space and filtration properties of Arctic gas condensate field reservoir rocks. These studies are based on computed tomography (CT) images obtained using the ProCon X-Ray CT-MINI high-resolution scanner of the Institute for Problems in Mechanics RAS. The paper provides a detailed description of the methodology used to digitally analyze CT images using the GeoDict package. Through this analysis, 3D structures of the rocks under investigation were created with a clear separation between the matrix and pore space based on the CT images. The primary filtration-related properties of the rock, namely porosity and permeability, were determined. The digitally obtained values are close to the results of laboratory permeability measurements confirming the accuracy of the applied approach. The study reveals that the filtration properties of the rock are nearly isotropic, there is only weak transverse anisotropy. To delve deeper into the analysis of the pore space and understand the reasons for the observed anisotropy, the study also conducted geodesic tortuosity measurements and analyzed percolation paths. It included evaluating the local distribution of porosity within the specimen and assessing the connectivity of the pore space. The study concludes that the causes of permeability anisotropy are a combination of pore space characteristics, such as varying channel tortuosity along different directions within the rock, differences in percolation path widths, local porosity fluctuations across specimen slices, and non-uniform distribution of pore space connectivity.

The data obtained from this study are essential for developing the hydrodynamic model of the gas field. They also provide a deeper understanding of the relationship between the filtration process and the structure of pore space in rocks. The digital investigations conducted in this study are an important tool for examining the internal structure of rocks and significantly complement and expand the range of results obtained through traditional laboratory methods. The combined application of these digital techniques with classical rock testing can help address critical challenges in the gas production industry, including issues like permeability reduction near wells, wellbore stability problems, sand production, and other operational incidents.

Acknowledgements The Research Was Supported by the Russian Science Foundation Grant № 23–77-01,037, https://rscf.ru/project/23-77-01037/

References

1. Ganat T. A. A. O. Fundamentals of reservoir rock properties. – Cham, Switzerland: Springer, 2020. https://doi.org/10.1007/978-3-030-28140-3.
2. Ivanov M.K. et al. Petrophysical Methods for Study of Core Material // M.: Publishing house of Moscow State University. 2008. P. 112. (in Russian).
3. Lichun J., Mian C. 3D imaging of fractures in carbonate rocks using X-ray computed tomography technology // Carbonates and Evaporites. 2014. V. 29. I. 2. pp. 147–153. https://doi.org/10.1007/s13146-013-0179-9
4. Diaz M. et al. Surface roughness characterization of open and closed rock joints in deep cores using X-ray computed tomography // International Journal of Rock Mechanics and Mining Sciences. 2017. V. 98. pp. 10-19. https://doi.org/10.1016/j.ijrmms.2017.07.001
5. Gerke K.M., Korost D.V., Karsanina M.V., Korost S.R., Vasiliev R.V., Lavrukhin E.V., Gafurova D.R. Modern approaches to pore space scale digital modeling of core structure and multiphase flow // Georesources. 2021. 23(2). pp. 197–213. https://doi.org/10.18599/grs.2021.2.20
6. Menke H.P. et al. Using Nano-XRM and High-Contrast Imaging to Inform Micro-Porosity Permeability During Stokes–Brinkman Single and Two-Phase Flow Simulations on Micro-CT Images // Frontiers in Water. 2022. V. 4. P. 935035. doi: https://doi.org/10.3389/frwa.2022.935035.
7. Blunt M.J. Multiphase Flow in Permeable Media: A Pore-scale Perspective // Cambridge: Cambridge University Press. 2017. doi: https://doi.org/10.1017/9781316145098
8. Mostaghimi P., Blunt M.J., Bijeljic B. Computations of absolute permeability on micro-CT images // Math. Geosci. 2013. V. 45. pp. 103–125. doi: https://doi.org/10.1007/s11004-012-9431-4
9. Krivoshchekov S., Kochnev A., Kozyrev N., Ozhgibesov E. Factoring Permeability Anisotropy in Complex Carbonate Reservoirs in Selecting an Optimum Field Development Strategy // Energies. 2022. 15 (23). 8866. https://doi.org/10.3390/en15238866
10. Vajdova V., Baud P., Wong T. Permeability evolution during localized deformation in Bentheim sandstone // J. Geophys. Res. 2004. 109. B10406, https://doi.org/10.1029/2003JB002942
11. Aliev Z.S., Kotlyarova E.M. Approximate method of UGS creation and operation in heterogeneous formations using horizontal wells. Envir. Responsib. of Oil and Gas Ind. 2017. 46–55 (in Russian).
12. Maksimov V.M., Dmitriev N.M., Antonievich Yu.S. Effects of tensor nature of relative phase permeabilities at mutual gas displacement by water in anisotropic reservoirs // Georesour., Geoenerg., Geopolit. 2010. 1 (1), 25 (in Russian).
13. CT-MINI by ProCon X-Ray GmbH available at https://procon-x-ray.de/en/ct-mini.
14. GeoDict – The Digital Material Laboratory: [digital source] URL: https://www.math2market.de/ (Date of request: 23.09.2023).
15. Hilden J., Cheng L., Linden S., Planas B. FlowDict User Guide GeoDict release 2022. Published: November 9, 2021. https://doi.org/10.30423/userguide.geodict2022-flowdict.
16. Kling T. et al. Simulating stress-dependent fluid flow in a fractured core sample using real-time X-ray CT data // Solid Earth. 2016. V. 7. 1109–1124. https://doi.org/10.5194/se-7-1109-2016
17. Herdtle T., Xue Y., Bolton J. S. Numerical modelling of the acoustics of low density fibrous media having a distribution of fiber sizes. Publications of the Ray W. Herrick Laboratories. 2017. Paper 167.
18. Balucan R. et al. Coal permeability stimulation by NaClO oxidation // The APPEA Journal. 2019. V. 59. №. 2. P. 846-850. https://doi.org/10.1071/AJ18142
19. Soltani P. et al. Experimental and computational analysis of sound absorption behavior in needled nonwovens // Journal of Sound and Vibration. 2018. V. 426. P. 1-18. https://doi.org/10.1016/j.jsv.2018.04.007
20. Steel K.M. et al. Identification of preferential pathways in the pore microstructure of metallurgical coke and links to anisotropic strength properties // Fuel. 2021. V. 296. P. 120688. https://doi.org/10.1016/j.fuel.2021.120688

21. Linden S. et al. The LIR space partitioning system applied to the Stokes equations // Graphical Models. 2015. V. 82. pp. 58-66. https://doi.org/10.1016/j.gmod.2015.06.003
22. Pan Z., Liang Y., Tang M. et al. Simulation of performance of fibrous filter media composed of cellulose and synthetic fibers // Cellulose. 2016. 26, 7051–7065. https://doi.org/10.1007/s10570-019-02605-8
23. Saxena et al. References and benchmarks for pore-scale flow simulated using micro-CT images of porous media and digital rocks // Advances in Water Resources. 2017. 109. pp. 211-235. https://doi.org/10.1016/j.advwatres.2017.09.007
24. Rief S., Hilden J., Planas B. MATDICT User Guide. GeoDict release 2022. December 8, 2021. https://doi.org/10.30423/userguide.geodict2022-matdict
25. Karev V., Kovalenko Y., Ustinov K. Advances in Oil and Gas Exploration and Production. Switzerland: Springer International Publishing. 2020. 166 p. https://doi.org/10.1007/978-3-030-26608-0
26. Karev V., Kovalenko Y. Triaxial loading system as a tool for solving geotechnical problems of oil and gas production. True triaxial testing of rocks. 2013. Leiden: CRC Press/Balkema: 301–310.
27. Holzer L., Marmet P., Fingerle M., Wiegmann A., Neumann M., & Schmidt V. Tortuosity and microstructure effects in porous media: classical theories, empirical data and modern methods. Springer Series in Materials Science. 2023. https://doi.org/10.1007/978-3-031-30477-4
28. Stenzel O., Pecho O., Holzer L., Neumann M., & Schmidt V. Predicting effective conductivities based on geometric microstructure characteristics // AIChE Journal. 2016. 62(5). pp. 1834-1843. https://doi.org/10.1002/aic.15160
29. Pyatakhin M. V., Shulepin S. A., & Gaidash Y. M. Experimental studies of reservoir rock fracture in the bottomhole zone of wells. Territory Neftegaz, 2020. (9-10), 30-37. (in Russian)

Changes in the Composition and Properties of Basaltic Andesites Under Sulfuric Acid Leaching Conditions



I. E. Bolshakov and M. A. Nikulina

Abstract The paper examines the main patterns of composition changes and properties of basaltic andesites under conditions of sulfuric acid leaching on the example of samples of the South Kambalny Central Thermal Field both in natural conditions and as a result of laboratory experiments, during which the samples were exposed to a concentrated solution of sulfuric acid. It was found that the general tendencies of property changes coincide for natural and laboratory modified samples - there was a decrease in strength and deformation characteristics, as well as a decrease in mass, magnetic susceptibility, and density. A number of correlation dependences of changes in properties on the time of laboratory treatment of rocks, reaction temperature and the amount of reacted acid were established.

Keywords Thermal field · Basaltic andesites · Hydrothermal alteration · Sulfuric acid leaching

1 Introduction

In today's world, due to the constant increase of interest in alternative energy sources, the issue of exploitation of geothermal deposits is becoming more and more frequent. Hydrothermal systems contain huge industrial reserves of steam and high-temperature waters, which serve as a basis for the development of geothermal power plants, greenhouses, and heat supply systems. Geothermal power plants are most often located in areas with widely developed surface discharges of thermal waters and steam, thus, the hydrothermally altered rocks serve as the basis for the stations and related structures [3, 4, 6, 12]. In addition, it is known that hydrothermal metamorphism can contribute to the activation of dangerous geological processes [2, 5, 8–11, 13, 14]. That is why it is so necessary to study the influence on the composition and properties of the processes of hydrothermal transformation of rocks, to try

I. E. Bolshakov (✉) · M. A. Nikulina
Faculty of Geology, Lomonosov Moscow State University, Moscow, Russia
e-mail: bolshakov.ilya.210@yandex.ru

© The Author(s), under exclusive license to Springer Nature Switzerland AG 2024

V. Karev (ed.), *Proceedings of the 9th International Conference on Physical and Mathematical Modelling of Earth and Environmental Processes*, Springer Proceedings in Earth and Environmental Sciences, https://doi.org/10.1007/978-3-031-54589-4_27

to model natural processes in laboratory conditions, to reproduce them experimentally. The object of research of this work is basaltic andesites of the South Kambalny Central Thermal Field. The aim of the work is to study the features of changes in the composition and properties of basaltic andesites of the studied field in the conditions of sulfuric acid leaching. To achieve the goal, we set the tasks related to the study of naturally altered samples; conducting experiments simulating natural conditions of sulfuric acid leaching, determining the influence of the process of sulfuric acid leaching on the change in the properties of rocks, analyzing the results obtained.

2 Research Methodology

2.1 Sampling Scheme

In the course of field work in the area of the Pauzhetskaya hydrothermal system at the South Kambalny Central Thermal Field [1] in 2022, 4 samples of basaltic andesites with different degrees of opalization were taken: unaltered, slightly altered, moderately altered, and opalite. The samples were taken in the northern part of the field, which had already cooled down, from three shallow excavations up to 80 cm deep. The sampling site was located approximately 50 m from the warmed part of the field.

3 Laboratory Tests

A total of 54 cylindrical samples were made from the samples. The following indicators of physical and physical–mechanical properties of soils were determined for all samples: density of solid component (ρ_s) using the device of V.Ya. Kalachev's, the velocity of propagation of longitudinal (V_p) and transverse (V_s) waves in air-dry and water-saturated state, magnetic susceptibility (χ_{cp}), air-dry soil density (ρ), dynamic modulus of elasticity (E_{dyn}) and Poisson's ratio (μ), uniaxial compressive strength in dry (R_c) and water-saturated (R_{ws}) states, tensile strength in dry and water-saturated states (R_p), softening coefficient (K_{sof}), water absorption (W_a, %), total (n) and open porosity (n_o, %). All determinations were carried out according to standard methods [7]. In parallel with the determination of properties, the features of void space were studied using Yamato TDM-1000 microtomograph, all samples were described in thin sections using "Olympus BX-41" optical microscope, mineral composition was determined by X-ray diffraction analysis (Ultima-IV device). To investigate the properties of samples altered in laboratory conditions, a series of experiments approximating the conditions of sulfuric acid leaching on the isolated thermal field was performed. On the samples of unaltered basaltic andesite 16 laboratory experiments were carried out: the samples were thermally treated in 10% sulfuric acid solution

at temperatures of 20°C, 50°C, 100°C, 170°C during 1, 3, 7 and 14 days. The same characteristics were determined for the laboratory transformed samples as for the natural samples, and the amount of acid reacted during the reaction was calculated.

4 Petrographic Characterization

In samples transformed in natural conditions, with increasing degree of alteration there is observed development of fracturing, fracture configuration becomes more complicated, new mineral formation is characteristic (opal, cristobalite), many grains become "damaged"—replaced by other minerals, at the final stage (opalite) of alteration all substance of the main mass is completely represented by opal and a small amount of sulfur, rock becomes highly porous (Fig. 1). Similar changes occur at the micro level for laboratory-modified samples thermally treated for 14 days at different temperatures. The changes that occurred in the samples as a result of thermal treatment in the model solution could be observed at the macroscopic level and are generally consistent with those that can be observed under natural conditions. The rock becomes more fractured, partly crumbling, the grains are more replaced by opal with increasing degree of treatment. All samples were photographed before and after exposure to the acid solution (Fig. 2). Macroscopically it is noticeable that in the process of sulfuric-acid leaching at first more contrasting minerals become phenocrysts, which in unaltered rocks are transparent and therefore practically do not stand out against the background of the main mass, and as the intensity of leaching increases, they are colored white due to mineral transformations in crystals. Following the phenocrysts, the main mass of the rock becomes lighter in color.

The changes that occurred in the samples as a result of thermal treatment in the model solution could be observed at the macroscopic level, and in general they correspond to those that can be observed in natural conditions. The rock becomes more fractured, partly crumbling, the grains are more replaced by opal with increasing degree of treatment. All samples were photographed before and after exposure to the acid solution (Fig. 2). Macroscopically it is noticeable that in the process of sulfuric-acid leaching at first more contrasting minerals become phenocrysts, which in unaltered rocks are transparent and therefore practically do not stand out against the background of the main mass, and as the intensity of leaching increases, they are colored white due to mineral transformations in crystals. Following the phenocrysts, the bulk of the rock becomes lighter in color as well.

For a more detailed understanding of the sequence and results of mineralogical transformations during the experimental opalization process, a series of slides (Fig. 3) were prepared from a sample of unaltered basaltic andesite, as well as samples treated at 20, 50 and 170 degrees. At the same time, thin sections were prepared from plate-shaped samples, which were subjected to absolutely identical treatment as cylinders at the corresponding temperatures for 9 days.

On the basis of the information obtained by means of the study of thin sections in transmitted light, it can be stated that the mechanism of opalization occurring in the

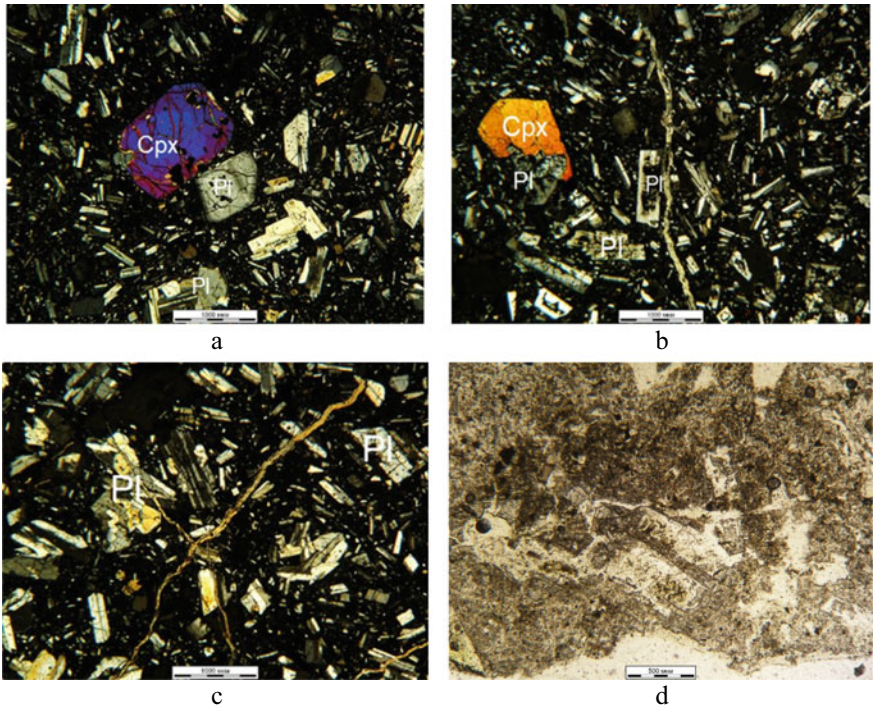


Fig. 1 Changes in the structure of naturally transformed andesibasalts: a) unaltered b) slightly altered c) moderately altered d) opalite; Pl—plagioclase, Cpx—clinopycroxene

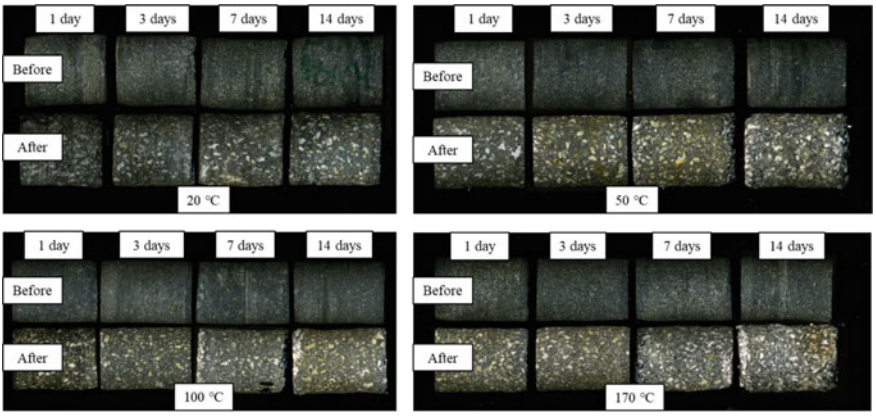


Fig. 2 General view of adesibasalts from the South Kambalny Central Thermal Field before and after interaction with sulfuric acid solution

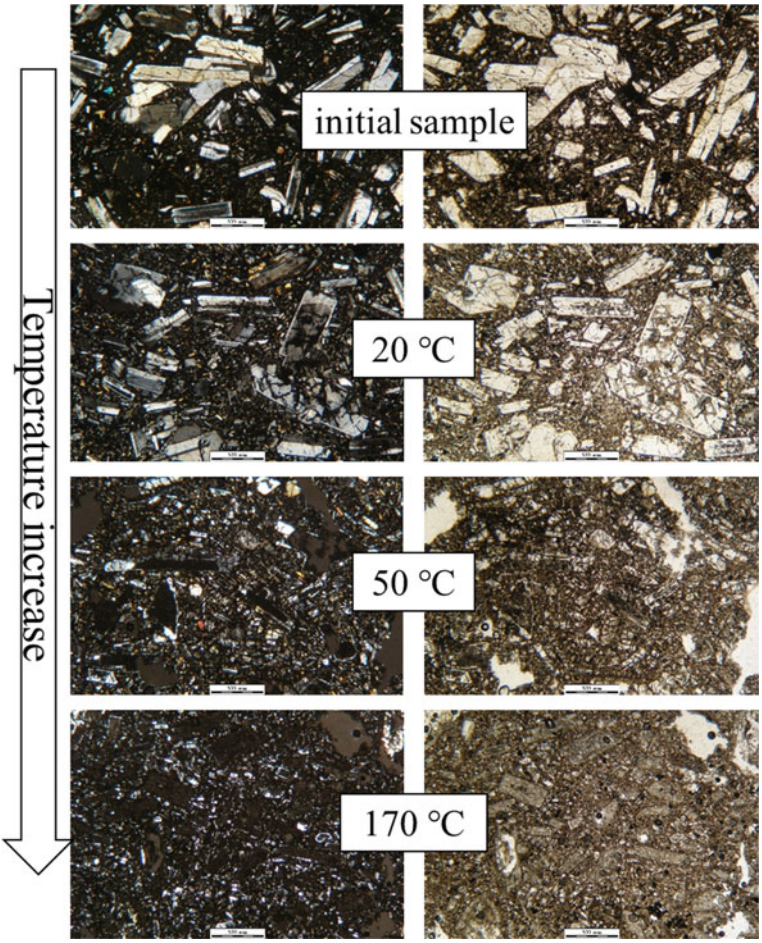


Fig. 3 Samples of andesibasalts subjected to various degrees of experimental opalization under the microscope in one (right) and two (left) nicols

described samples is almost completely identical to the mechanism observed in real thermal fields characterized by the discharge of ultra-acidic thermal waters. Thus, in the beginning the central parts of large phenocrysts and volcanic glass of the main mass are subjected to sulfuric acid leaching, and further opalization develops along the peripheral parts of large phenocrysts and microlites, which have more acidic composition.

In addition, it should be noted that due to the limited exposure time and volume of the interacting solution (due to the experiment in a closed system), opalization does not develop uniformly throughout the entire volume of the sample, but according to the basic principles of diffusion interaction of solids and liquids. That is, in the peripheral part the changes are much more significant than inside the samples. Thus,

the thin sections shown in Figure were prepared precisely from the peripheral parts of the opalized plates. To evaluate the rate of diffusion layer advancement to the central parts of the samples, as well as to determine the effect of the experiment on the structure of the samples, the method of computed tomography was applied. All samples were taken before and after exposure to the sulfuric acid solution, which allowed us to evaluate the extent to which the samples were subjected to opalization. Thus, Fig. 4 shows the results of imaging of the sample that interacted with sulfuric acid solution for 14 days at a temperature of 50 degrees Celsius.

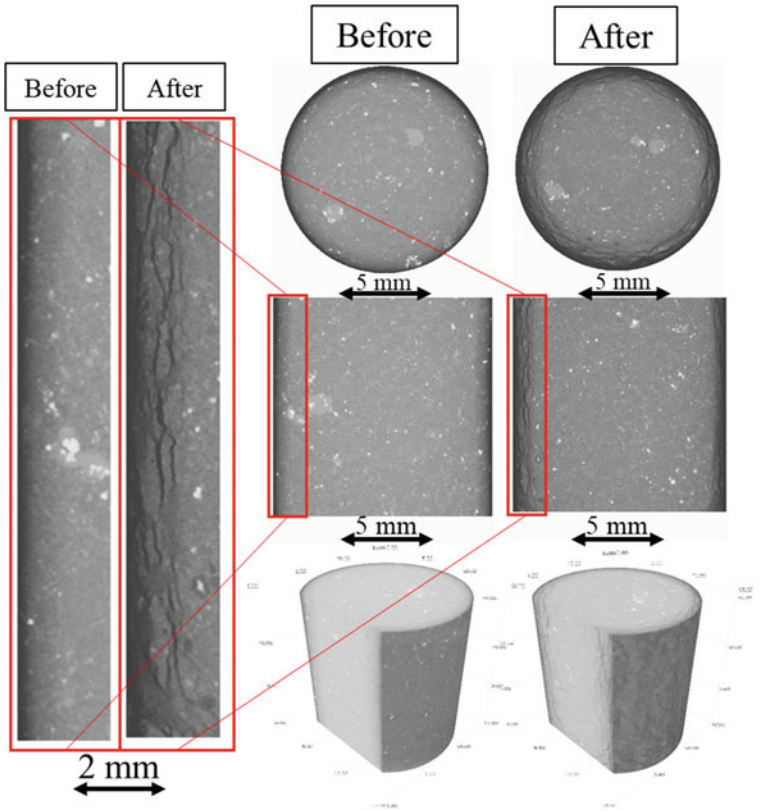


Fig. 4 Tomograms of a sample of andesibasalt subjected to acid leaching at 50 degrees Celsius for 14 days

5 Changes in Physical and Physical–mechanical Properties of Andesibasalts

Samples of naturally transformed basaltic andesites differ in their properties depending on the degree of alteration (from unaltered basaltic andesites to sulfur opalites) (Fig. 5). With increasing degree of change increases, the density value decreases. The unaltered samples have the highest density (2.64 g/cm^3), opalites have the lowest (1.35 g/cm^3). The longitudinal and transverse wave velocities generally decreased with increasing degree of transformation ($V_p = 4.68 - 3.58 - 2.56 - 1.10$ km/s), ($V_s = 2.10 - 1.86 - 1.26 - 0.61$ km/s). Dynamic modulus of elasticity, compressive and tensile strength limits in dry and water-saturated state, magnetic susceptibility also decreased, but porosity increased. According to the softening coefficient, unaltered ($K_{sof} = 0.71$), moderately altered basaltic andesites ($K_{sof} = 0.62$) and opalites ($K_{sof} = 0.24$) are softened, slightly altered basaltic andesites are not softened ($K_{sof} = 0.98$).

For the samples subjected to sulfuric acid leaching in laboratory conditions, in addition to the data on changes in structure, a number of indicators were obtained that demonstrate the process of changing the properties of samples as the process of opalization proceeds (Fig. 6). Thus, for all samples before and after exposure to acid solution the whole standard set of rock properties was determined. Consequently, the only parameter that for all cylinders was determined only once was uniaxial compressive strength, however, 4 control samples that were not subjected to experimental opalization were destroyed unchanged and showed sufficiently close values, so for

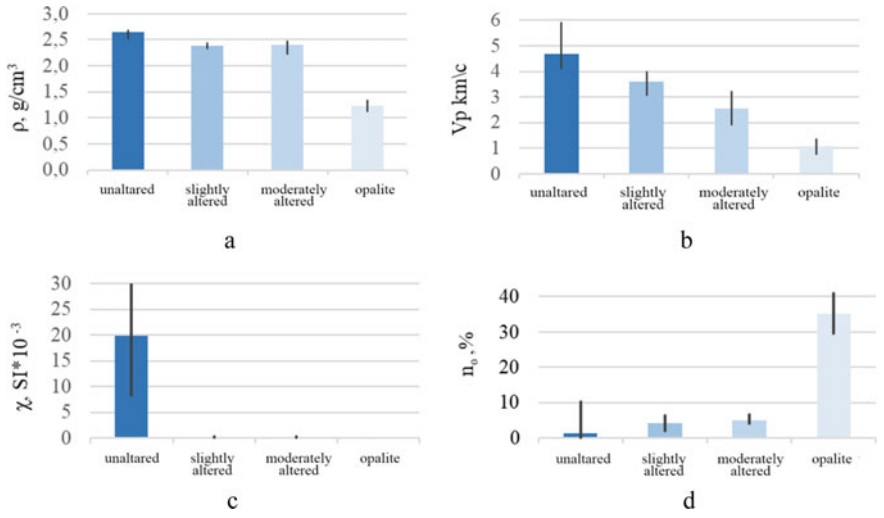


Fig. 5 Variation of andesibasalts property indices (bottom axis signature - sample number; black vertical line - scatter between maximum and minimum values; histograms are plotted by average values): **a** density, **b** longitudinal wave velocity, **c** magnetic susceptibility, **d** open porosity

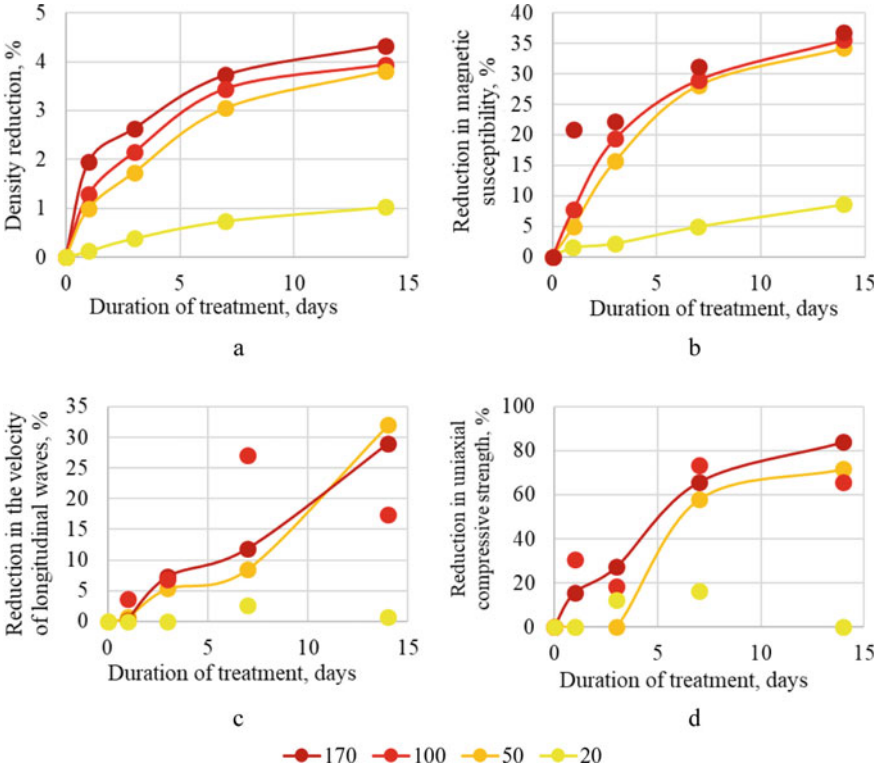


Fig. 6 Change of properties depending on duration and temperature of opalization

all other samples this value was taken as the initial value of uniaxial compressive strength.

From the graphs shown in Fig. 6 graphs clearly show that changes in rock properties correlate well with the duration of treatment. The most distinct dependencies were obtained for the indicators of density reduction and reduction in magnetic susceptibility, measured in percent and defined as the ratio of the difference of the indicator before and after the reaction to the initial value (density reduction = ($\rho_{nonchanged}$-$\rho_{changed}$)/$\rho_{nonchanged}$). From these two graphs, it can be seen that the rate of change of properties decreases with time, which is mainly due to the growth of the diffuse layer that slows down the reaction. On the other hand, it is clearly seen that the rate of change of properties depends on temperature. For example, for the same time interval at 20 °C, the amount of density decrease is smaller by about 3.5 times than that at 50 °C. At the same time, the difference for the temperature branches of 50 °C, 100 °C and 170 °C is not so large, which can be explained by the nonlinear temperature dependence of the chemical reaction rate described by the Arrhenius equation. The decreases in longitudinal wave velocity and uniaxial compressive strength, which were calculated in a similar manner, are somewhat more chaotic, especially in the

region of greatest change. This is most likely due to the fact that, unlike the previous two indices, these properties are much less controlled by regular chemical transformations and are much more dependent on changes in the structure of the samples. As it was shown earlier, at the highest stages of transformation in the samples, fracture systems begin to appear, caused by the inhomogeneous structure of the rock and peculiarities of the opalization process of large phenocrysts. In this connection, the change of strength and deformation properties depending on the time of processing does not form a sufficiently correct regularity, but a trend similar to the first two graphs can be seen in general features. Probably, the value of open porosity, determined through the density in water-saturated state, changes in a similar way. This conclusion can be based from the trend of the twenty-degree curve and the first three points for the remaining curves. Unfortunately, due to the partial destruction of the samples not plotted on the graph, it was not possible to reliably determine the value of their open porosity at the corners of the ends.

In order to level the disadvantages of experiments in a closed system, the hydrogen indices of the initial sulfuric acid solution and all solutions formed as a result of the reaction were measured using the "Expert-001" device and the "ESC-10601/7" electrode. The measurements were carried out after calibration of the device on standard buffer solutions. These measurements, taking into account the known volumes of the sample and the solution in the reaction allowed to determine the amount of reacted sulfuric acid.

Based on the obtained data, a series of graphs reflecting the dependence of the change in the properties of the samples on the amount of reacted acid were drawn up (Fig. 7). From them it is clearly seen that in the observed area of change there is a direct correlation of the change in physical, physical–mechanical and magnetic properties with the amount of reacted acid.

As well as depending on the duration of treatment, depending on the amount of reacted sulfuric acid related to the volume of the sample, the decrease in density and magnetic susceptibility demonstrate a very regular relationship, which is probably explained mainly by the direct chemical nature of the change in these parameters when the mineral composition changes. The coefficients of determination on the observed area for the revealed linear dependence are 0.96 and 0.93 for the density decrease and magnetic susceptibility decrease, respectively. At the same time, the graphs for the decrease in strength and deformation characteristics (Fig. 7) have a slightly larger scatter (coefficient of determination is 0.75 and 0.84 for the decrease of longitudinal wave velocities and uniaxial compression strength, respectively), which is explained only by the indirect dependence of physical and mechanical properties on changes in chemical and mineral compositions. The physical–mechanical properties are much more influenced by the fracturing indicated by mineral transformations, which initially develops in the diffuse layer but later affects the central parts of the tested cylinders.

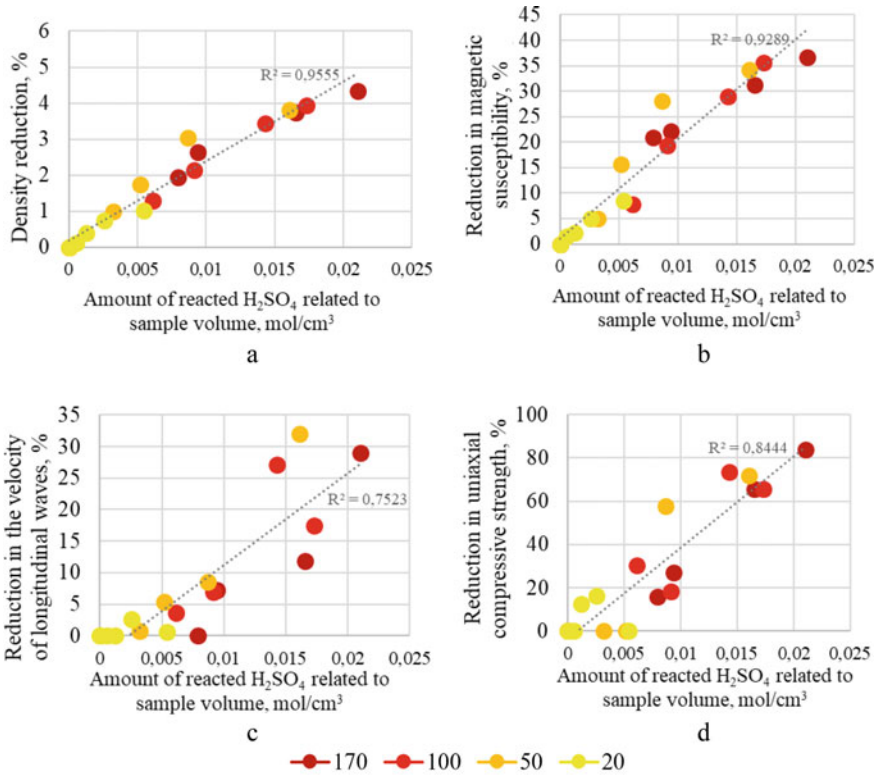


Fig. 7 Variation of andesibasalts properties depending on the amount of reacted H_2SO_4 relative to the sample volume

6 Conclusion

Thus, as a result of the study, the character of changes in the composition and properties of basaltic andesites under conditions of sulfuric acid leaching was evaluated. General tendencies of properties change coincide both for samples modified in situ and for laboratory modified samples. With increasing degree of alteration there is formation of new minerals, decrease in the amount of ore components, development of hollowness, appearance of largely amorphous matter at the final stages. The change of properties in the conditions of laboratory experiment correlates with the time of treatment and with the amount of reacted acid—the longer the duration and temperature of treatment, the greater is the decrease in the values of properties, in particular mass, density, magnetic susceptibility. The dependence of the decrease of the corresponding characteristics on the duration of the experiment has a logarithmic character, on the amount of reacted acid is almost linear. In the perspective of further studies it is planned to bring the experiment to a greater extent closer to natural

conditions, to try to correlate the obtained qualitative and quantitative data with the natural massif and to quantitatively assess the rate of the process.

References

1. Belousov V.I., Sugrobov V.M., Sugrobova N.G. Geological structure and hydrogeological features of the Pauzhetskaya hydrothermal system. Sb. "Hydrothermal systems and thermal fields of Kamchatka". Vladivostok. 1976. pp. 23–57.
2. Della Seta, M., Esposito, C., Marmoni, G.M., Martino, S., Paciello, A., Perinelli, C., Sottili G.: Geological Constraints for aConceptual Evolutionary Model of the Slope Deformations Affecting Mt. Nuovo at Ischia (Italy), Italian Journal of EngineeringGeology and Environment, 2 (2015), p. 15–28.
3. Flynn, T., Goff, F., Van Eeckhout, E., Goff, S., Ballinger, J., Suyama, J.: Catastrophic Landslide at Zunil I Geothermal Field,Guatemala, January 5, 1991, Geothermal Resources Council Transactions, 15, 1991, p. 425-433.
4. Frolova J.V., Chernov M.S., Rychagov S.N., Zerkal O.V. The Impact of Hydrothermal Activity on the Geological Environment, Kamchatka Peninsula // Proceedings World Geothermal Congress 2020, Reykjavik, Iceland, 2021, 10 p.
5. Frolova J.V., Gvozdeva I.P., Chernov M.S., Kuznetsov N.P. Engineering-geological aspects of hydrothermal transformations of tuffaceous rocks of the Valley of Geysers (Kamchatka Peninsula) // Engineering Geology. No. 6. 2015. p. 30-42.
6. Frolova J.V., Ladygin V.M., Rychagov S.N. Engineering-geological features of hydrothermal-metasomatic rocks of Kamchatka and the Kuril Islands // Engineering Geology. No. 1. 2011 P.48–62.
7. Frolova J.V. Rocky soils and methods of their laboratory study: textbook / Yu.V. Frolova - Moscow: Book House University, 2015. - 220 pp.
8. Huang, S., Tian, T. Study of Environmental Impact in Geothermal Development and Utilization. Proceedings of the 7th AsianGeothermal Symposium, 2006, p. 35–44.
9. Marmoni, G.M., Martino, S., Heap, M.J., Reuschlé, T.: Gravitational Slope-Deformation of a Resurgent Caldera: New Insights fromthe Mechanical Behaviour of Mt. Nuovo Tuffs (Ischia Island, Italy), Journal of Volcanology and Geothermal Research, 345. 2017. P. 1–20.
10. Pioquinto, W. P. C., Caranto, J.A. Mitigating the Impact of Landslide Hazards in PNOC-EDC Geothermal Fields, Proceedings,World Geothermal Congress 2005, Antalya, Turkey, 2005.
11. Suemnicht, G.A., Sorey, M.L., Moore, J.N., Sullivan, R.: The Shallow Hydrothermal System of Long Valley Caldera, California.Proceedings, Thirty-Second Workshop on Geothermal Reservoir Engineering Stanford University, Stanford, California, 2007.
12. Voight, B.: Causes of Landslides: Conventional Factors and Special Considerations for Geothermal Sites and Volcanic Regions.Geothermal Resources Council Transactions, 16, 1992, p. 529–533.
13. Wijaya, P.K., Zangel, C., Straka, W., Ottner, F. Geological Aspects of Landslides in Volcanic Rocks in a Geothermal area (KamojangIndonesia). Proceedings, 3th World Landslide Forum, Beijing, 2014.
14. Zerkal O.V., Gvozdeva I.P., Frolova Yu.V., Development of landslide processes in the valley of the river. Geysernaya (Kamchatka) // Abstracts of the III All-Russian Scientific Conference “Geodynamic processes and natural disasters”, Yuzhno-Sakhalinsk, 2019, p. 138–138.

Some Problems of Well Stability in Reservoirs of Underground Gas Storages



V. Karev, Yu. Kovalenko, and K. Ustinov

Abstract Issues related to the influence of the stress state on the stability of wells in underground gas storages (UGS) are considered. It is demonstrated that the main factor influencing the redistribution of the stress state in the vicinity of wells is the change in reservoir pressure in the pumping-injection cycles, with the most dangerous phase being the maximum pumping. The influence of unequal components of the initial stress state is also considered.

Keywords Well stability · Underground gas storages · Stress state · Anisotropy · Fracture

1 Introduction

Preserving the integrity of wells and preventing sand production are among the key problems in the operation of underground gas storage facilities. Previously [1], the authors put forward a hypothesis that a key role in the processes of destruction of wells and sand production is played by changes in pressure in the reservoir as a whole, since it is this that has a decisive influence on the magnitude of stresses acting in the vicinity of wells. This differs from the point of view of many researchers who associate these negative processes with a change in the stress state in the bottomhole zone of the formation caused by draw-downs and increase in wellbore pressure [2, 3]. This work continues the research of the authors [1], with emphasis on the influence of such factors as the unequal composition of the initial stress state and the strength anisotropy of reservoir rocks.

V. Karev · Yu. Kovalenko · K. Ustinov (✉)
Institute for Problems in Mechanics RAS, Moscow, Russia
e-mail: ustinov@ipmnet.ru

© The Author(s), under exclusive license to Springer Nature Switzerland AG 2024

V. Karev (ed.), *Proceedings of the 9th International Conference on Physical and Mathematical Modelling of Earth and Environmental Processes*, Springer Proceedings in Earth and Environmental Sciences, https://doi.org/10.1007/978-3-031-54589-4_28

2 Stress State in the Vicinity of a Horizontal Wellbore

Consider the stress state around a horizontal well located in a horizontal layer. The initial stress state of the massif is generally determined by six values—six components of the stress tensor, or three principal stresses and three angles (for example, Euler angles), which determine the directions of the principal stresses relative to the vertical and the sides of the horizon. For reservoirs of oil and gas fields, in the absence of active tectonics, the presence of "traps" of impenetrable plastic rocks, which actually determine the formation of fluid deposits, should lead to relaxation of tangential stresses in the massif, which suggests that the initial stress state is close to volumetric compression [4, 5]. Nevertheless, at present, the prevailing approach is based on the speculative assumption that the initial stress state is unequal with one of the main stresses acting in the vertical direction. So, assume that the initial stress state is determined by the principal stresses $\sigma_1 = \sigma_2 = q_1, \sigma_3 = q_3,$, the last of which acting in the vertical direction (axes 1 and 2 are oriented in the horizontal plane). Accordingly, for the initial effective stresses acting in the soil skeleton of the formation, one has

$$s_{ij}^0 = \sigma_{ij}^0 + (1 - \delta) p_0 \delta_{ij} \tag{1}$$

where δ is proportion of contact areas relative to the entire grain surface of the soil skeleton [4], p_0 is the initial pore pressure. Equation (1) are often written in terms of Biot's coefficient α, the relation of the two being $\alpha + \delta = 1$. Hereafter, compressive stresses are considered as negative, pressure is positive. A radial effective stress acts on the contour of a well with an open bottom $s_{rr}^0 = -p_0\delta$. The circumferential stresses on the contour of the well under consideration are determined from the solution of the Kirsh problem [6], see also e.g. [7, 8]. For effective stresses in the notation used, the solution is written in the form

$$s_{\theta\theta}^0 = s_1 + s_3 - s_{rr}^0 + 2(s_1 - s_3)\cos 2\theta \tag{2}$$

Here θ is the angle measured from the vertical. Expressing effective stresses in terms of total stresses, we obtain

$$s_{\theta\theta}^0 = q_1 + q_3 - p_0(2 - \delta) + 2(q_1 - q_3)\cos 2\theta \tag{3}$$

Stresses $s_{\theta\theta}^0$, s_{xx}^0, s_{rr}^0 are the principle ones. Stress $s_{\theta\theta}^0$, maximal in its absolute value, has extremes at points $\theta = \pi n/2$ corresponding to the side and top/bottom points of the horizontal wellbore.

In the case of an arbitrary well orientation relative to the principle axes of the stress tensor of the initial field, i.e. if all six components s_{ij}^0 are present, stresses on the well contour are determined from the superposition of solutions of plane and antiplane problems [9, 10].

Deformation anisotropy makes situation more complicated: circumferential stresses, even under an equal-component initial stress state, in the general case do not remain constant along the wellbore contour [11, 12].

Strength anisotropy leads to appearing a dependence of the critical stress on the angle along the wellbore contour. Therefore the critical point would correspond in this case to the point where the difference between the acting stress and the strength is minimal.

The change of the pore pressure in the reservoir during the pumping-injection process results in changing of the stress state of the formation. The nature of the change in boundary conditions is determined by its geometry. On the lateral (vertical) surfaces, due to the large extent of the formation in its plane, the boundary conditions correspond to the constancy of normal (horizontal) displacements $\Delta u_1 = \Delta u_2 = 0$. Contrary to that, on horizontal surfaces, vertical stresses remain constant $\Delta\sigma_3 = 0$. Substituting these boundary conditions into the system of equations of theory of elasticity and neglecting with the influence of the gradient of pore pressure during the injection-pumping process [1] (because working draw-downs and increases in pressure do not exceeding 0.5–1 MPa during UGSs processing), we obtain for changes in the effective stresses in the formation and radial stresses on the well contour from changes in formation pressure Δp_{lay} ($\Delta p_{lay} < 0$ for pore pressure lower than the initial one, $p_{lay} < p_0$, $\Delta p_{lay} > 0$ for pore pressure higher than the initial one, $p_{lay} > p_0$)

$$\Delta s_1 = \Delta s_2 = \frac{\nu}{1-\nu}(1-\delta)\Delta p_{lay}, \quad \Delta s_3 = (1-\delta)\,\Delta p_{lay}, \quad \Delta s_{rr} = -\Delta p_{lay}\delta \quad (4)$$

Here ν is Poisson's ratio. More accurate solution can be obtained by considering the layer as a flattened inclusion [13], the correction, however, will be of the order of the square of the ratio of the thickness of the layer to its length.

Changes in circumferential stresses on the well contour are recorded similarly to (2) with the initial stresses replaced by their increments

$$\Delta s_{\theta\theta} = \Delta s_1 + \Delta s_3 - \Delta s_{rr} + 2(\Delta s_1 - \Delta s_3)\cos 2\theta \quad (5)$$

Substitution (4) into (5) yields

$$\Delta s_{\theta\theta} = \left(1 + \frac{\nu}{1-\nu}(1-\delta)\right)\Delta p_{lay} - 2\frac{1-2\nu}{1-\nu}(1-\delta)\,\Delta p_{lay}\cos 2\theta \quad (6)$$

Note that the change in stress in pumping/injection cycles is described by a fairly simple formula (6), since it does not depend on the initial stress state.

Total effective stresses (3) и (6) will be

$$\begin{aligned} s_{\theta\theta} &= q_1 + q_3 + p_0(2-\delta) - 2(q_3 - q_1)\cos 2\theta + \\ &\left(1 + \frac{\nu}{1-\nu}(1-\delta)\right)\Delta p_{lay} - 2\frac{1-2\nu}{1-\nu}(1-\delta)\,\Delta p_{lay}\cos 2\theta \end{aligned} \quad (7)$$

3 Numerical Results

Distributions of circumferential stresses normalized to the value of vertical stress are presented for a number of cases on Fig. 1, where $q_3 = -1$, $q_1 = 0.7q_3$, $p_0 = 0.44$, $\nu = 0.2$, $\delta = 0.2$. Value Δp_{lay} are accepted as 0, 0.25 и -0.25 for the initial pressure, the maximal injection and the maximal pumping, respectively. It can be seen from the above plots that a decrease in reservoir pressure during gas extraction significantly increases the hoop stresses acting on the contour of a horizontal wellbore $s_{\theta\theta}$, that reaches its maximum at the side point corresponding to $\theta = \pi/2$.

In the absence of strength anisotropy, fracture should be feared at points of the contour with maximum stresses in absolute value (6). In the presence of strength anisotropy, both due to the presence of planes of weakness associated with bedding, and of an atypical type, peculiar to highly porous weak rocks [14, 15], the beginning of destruction should be feared at points of the contour where the operating stresses exceed the tensile strength, depending on the angle θ.

Thus, the study carried out on the basis of geomechanical analysis has shown that as a result of changes in reservoir pressure, the initial stress state in the reservoir, even in the case of initially uniform compression, becomes unequal. The consequence of

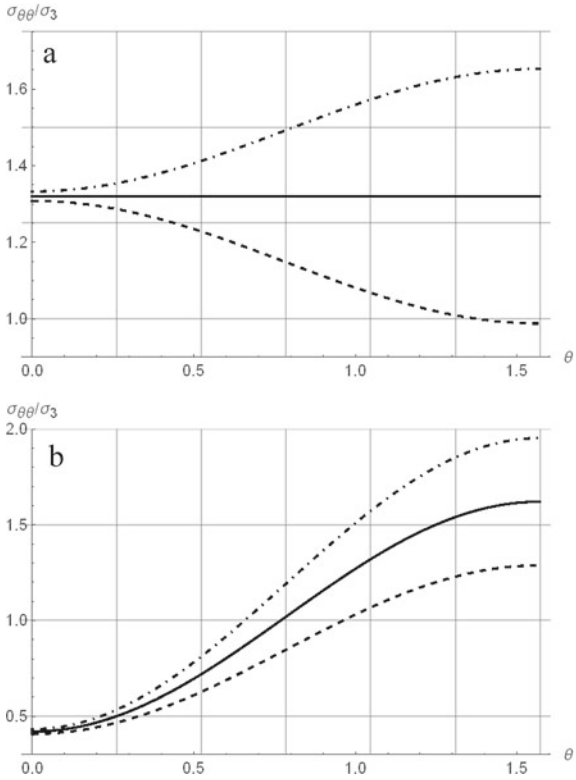


Fig. 1 Dependences of circumferential stresses along the contour of a horizontal well, normalized to the value of the vertical stress, on the angle measured from the vertical; a) due to equal-component initial stress state of the massif, b) with a lateral thrust coefficient of 0.7; solid lines corresponds to initial pressure; dotted lines corresponds to maximum injection condition; dash-dotted lines corresponds to maximum pumping condition

this is a significant increase in stresses acting in the vicinity of the well, which can lead to the destruction of its walls and the sand production into the well.

Based on the calculations performed, programs were drawn up for loading specimens of rock from the reservoirs of a number of UGSs, according to which, using the TILTS installation [16], physical modeling of the deformation processes occurring in the bottomhole zone of underground gas storage reservoirs when cyclic changes in reservoir pressure during gas injection/pumping was carried out. As a result, for specific fields, the maximum permissible draw-downs at the bottom of wells not leading to rock fracture were determined.

4 Summary

Issues related to the influence of stress state on the stability and integrity of wellbores of UGS as well as on sand production into the wellbores are considered. It has been demonstrated that the key factor affecting redistribution of the stresses on the wellbore contour is the change in the pore pressure due to cycles of injection/pumping. It is shown that the most potentially dangerous phase corresponds to the maximal pumping. The influences of unequal components of the initial stress state and strength anisotropy are also considered.

Acknowledgements The study has been carried out with the financial support from RSF, Project № 22-11-00273.

References

1. Karev V.I., Korolev D.S., Kovalenko Yu.F., Ustinov K.B. Geomechanical and physical modeling of deformation processes in the reservoirs of an underground gas storage facility during cyclic changes in reservoir pressure // Gas industry. 2020. Special issue No. 4 (808). pp. 46–52. (in Russian).
2. Pyatakhin M.V. Geomechanical problems during well operation. – M., Gazprom VNIIGAZ, 2012, 266 p. (in Russian).
3. Morita N. Field and Laboratory Verification of Sand-Production Prediction Models. SPE Drilling & Completion, December, 1994. pp. 227- 235.
4. Zheltov Yu.P., Khristianovich S.A. About the hydraulic fracturing of the oil–bearing formation // Izv. USSR. Academy of Sciences. 1955. No. 5. pp. 3 – 41. (in Russian).
5. Karev V., Kovalenko Y., Ustinov K. Geomechanics of Oil and Gas Wells. Springer. 2020. 184 p.
6. E. G. Kirsch, Die Theorie der Elastizitat und die Bedurfnisse der Festigkeitslehre. Zeitschrift des VereinesDeutscher Ingenieure. 42 (29). 1898. pp.797–807.
7. Timoshenko, S.P., Goodier J.N. Theory of elasticity, Tokyo : McGraw-Hill Kogakusha Ltd. 1970. 567 p.
8. Jaeger J.C., Cook N.G.W., Zimmerman R.W. Fundamentals of rock mechanics. Malden, Mass., Oxford: Blackwell, MyLibrary. 2007. 475 p.

9. Y. Hiramatsu, Y. Oka, Analysis of stress around a circular shaft or drift excavated in ground in a three dimensional stress state. Journal of Mining and Metallurgy Institute of Japan 78.1962. pp. 93–98.
10. Y. Hiramatsu, Y. Oka, Determination of the stress in rock unaffected by boreholes or drifts from measured strains or deformations. International Journal of Rock Mechanics and Mining Sciences & Geomechanics Abstracts. 5 (4). 1968. pp. 337–353.
11. Lekhnitsky S.G. Anisotropic Body Elasticity Theory. Moscow. Nauka. 1977. p. 415.
12. Zhuravlev A.B., Ustinov K.B. On values characterizing the degree of elastic anisotropy of transversely isotropic rocks; role of shear modulus. Mechanics of Solids. 2019. V. 54. No. 6. pp. 958-967.
13. T. Mura. Micromechanics of defects in solids. Martinus Nijhoff Publishers. The Hague-Boston. 1982.
14. Yu.F. Kovalenko, K.B. Ustinov, and V.I. Karev. Geomechanical Analysis of the Wellbore Wall Breakouts Formation. Mech. Sol. 2022. V. 57. No. 6. pp.1403-1415.
15. K.B. Ustinov, V.I. Karev, Yu.F. Kovalenko, S.O. Barkov, V.V. Khimulia, and N.I. Shevtsov. Experimental Study of the Effect of Anisotropy on the Orientation of Breakouts in Wells. Mech. Sol. 2023. V. 58 No.3. pp. 685-696.
16. Karev V.I., Kovalenko Yu.F. Triaxial loading system as a tool for solving geotechnical problems of oil and gas production. True Triaxial Testing of Rocks. Leiden, CRC Press, Balkema. 2013. pp. 301–310.

Physical and Numerical Modeling of Nonelastic Deformations During an Impact of Spherical Indenter on Ice Disc

Epifanov Viktor Pavlovich, Guseva Evgeniya Kirillovna, and Shigaev Nikita Olegovich

Abstract Investigation of the changes in ice structure and characteristics under straining has many applications for the problems in the Arctic region, especially during low-speed interactions. This work introduces a complex approach based on the physical and numerical modeling of such deformation processes. The impact of a spherical indenter on an ice disc placed on a massive rigid support with the ability to slip on its surface is studied. As a result of the conducted experiment, instantaneous acceleration of the indenter is obtained. Moreover, local surface and volume deformations of the disc are defined. Numerical simulations are performed in two- and three-dimensional cases. The models' parameters influence on the solutions is identified; a comparison with the experiment is conducted. The applied grid-characteristic method provides an opportunity to accurately reconstruct occurring wave phenomena during the impact. Considered rheological models take into account the formation of the hydrostatic core and the elastoplastic zone. Finally, computations manage to reproduce unique secondary structures observed in experiments.

Keywords Ice deformations · Physical and numerical modeling · Hydrostatic core · Elastoplasticity · Grid-characteristic method

The first solution of a rigid indentation problem into an elastic half-space was obtained by Herz in [1]. It is still commonly used for the evaluation of axial stresses during a direct strike. The next fundamental investigations of ice mechanical behavior

E. V. Pavlovich · G. E. Kirillovna (✉) · S. N. Olegovich
Ishlinsky Institute for Problems in Mechanics of the Russian Academy of Sciences, Moscow, Russia
e-mail: guseva.ek@phystech.edu

S. N. Olegovich
e-mail: shigaev.no@phystech.edu

G. E. Kirillovna · S. N. Olegovich
Moscow Institute of Physics and Technology, Dolgoprudny, Moscow Region, Russia

© The Author(s), under exclusive license to Springer Nature Switzerland AG 2024

V. Karev (ed.), *Proceedings of the 9th International Conference on Physical and Mathematical Modelling of Earth and Environmental Processes*, Springer Proceedings in Earth and Environmental Sciences, https://doi.org/10.1007/978-3-031-54589-4_29

and its residual deformations in the process of contact destruction are featured in several works [2, 3]. Elastoplastic areas and hydrostatic core were found to be formed near the contact surface [4]. In these regions, phase transition, recrystallization, and brittle ice failure take place. However, the mechanisms that cause such structural changes are still understudied, despite their theoretical significance for application tasks. The problem of interactions between the floating ice and engineering structures serves as a good example, especially in cases where the initial velocities are around 0.3–3 m/s.

This work proposes a fundamentally new, complex approach for the physical and numerical modeling of the low-speed impact of a spherical indenter on an ice disc placed on a rigid support with the ability to slip on its surface. The experimental setting is dedicated to the determination of instantaneous values of the indenter's acceleration, velocity, and depth of immersion. It also includes the registration of surface and volume deformations of the ice caused by the collision [5]. The processes of elastic wave generation and their influence on ice rheological characteristics are investigated. The obtained results form the basis for computer simulations of deformation processes using different rheological models for the disc. The significant changes in the local ice structure and wave phenomena during the impact are the central focus of the calculations. The suggested approach may help to get a deeper understanding of the important natural and anthropogeneous processes in the Arctic region.

1 Experiment

The general schematic course of the experiment is presented in Fig. 1. A metal spherical indenter 2 made of hard steel has a diameter of 0.076 m and a mass of 1.76 kg. Inside it, a piezoelectric accelerometer was rigidly held. The indenter was hung on carrier 6 and trigger 1 with an inextensible string. Ice sample 3 was placed on a metal disc 4. The second accelerometer was set on the ice bottom surface along the impact axis. The whole setup, including a massive plate 5, was installed inside a SF-45 Series thermostat. A smooth release of the ball was conducted using an electromagnetic release device. Signals from the accelerometers were registered on a digital oscilloscope (DS1102E). Additional signal processing was conducted on a personal computer; the results are shown in Fig. 1. The blue line stands for the dependence of axial force (kN) on time (ms) obtained based on the oscillograph patterns of the impact. The magenta graph is the stationary wave, the relationship between the amplitude of the periodical curve (V) and time (ms).

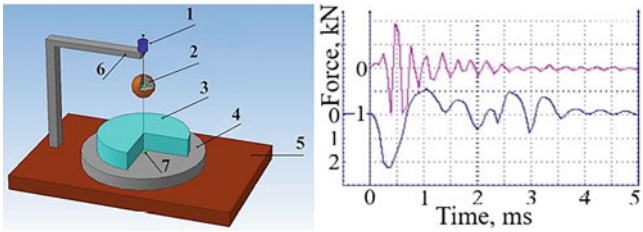


Fig. 1 Design of an experiment and oscillograph patterns (blue curve from the indenter, magenta curve from the bottom surface of the ice along the impact axis). 1: trigger, 2: spherical indenter with piezoelectric accelerometer, 3: ice sample, 4: metal disc, 5: massive metal plate, 6: carrier, 7: second piezoelectric accelerometer

2 Numerical Modeling

2.1 Two-Dimensional Setting

In order to save time and computational resources, the plane problem was initially solved. It provides a great opportunity for the evaluation of the influence of the considered models' parameters on the results in comparison to the experiment and the determination of the predominant mechanisms of the impact.

The instantaneous indenter's velocity and depth of immersion were calculated based on successive integrations of its acceleration. The considered ice rheology model took into account the formation of the hydrostatic core [6], and the elasto-plastic zone with the von Mises flow rule [7]. Both of these regions were realized as concentric hemispheres, with the center at the contact point between the ball's bottom pole and a linear dependence between their radii a and r. For the rest of the disc, the isotropic linear elasticity model [8] was applied. Moreover, the same model was utilized for the core and was compared to its variation with correction, which consists of zeroing out positive principal stresses.

The equations were solved using the grid-characteristic method [9] on structured curvilinear grids with a monotonized explicit third-order scheme [10]. The ice disc, with a diameter of 286 mm and a height of 70 mm, was put on the stand with the ability to slip. In its central area, for 100 mm, the spatial step was set to 0.2 mm; at the borders, it was 1 mm. A time step of 10 ns was calculated based on the fulfillment of the Courant condition (for robustness of calculations). The initial impact velocity was equal to 0.56 m/s. The ball was divided into five parts: a central square and symmetric sectors. The indenter's grids complied with the disc's grids and were moved using Lagrange correction. Between the ice and ball's parts, full adhesion contact conditions were applied; on the ball-ice contact area, a slippage condition was set. On the bottom and lateral sides of the stand, absorbing boundaries were placed; other borders were considered to be free.

In the disc, elastic velocities were equal to 3600 m/s, and 1942 m/s, and density was equal to 917 kg/m^3, maximum shear stress was set to 0.3 MPa. For the core's

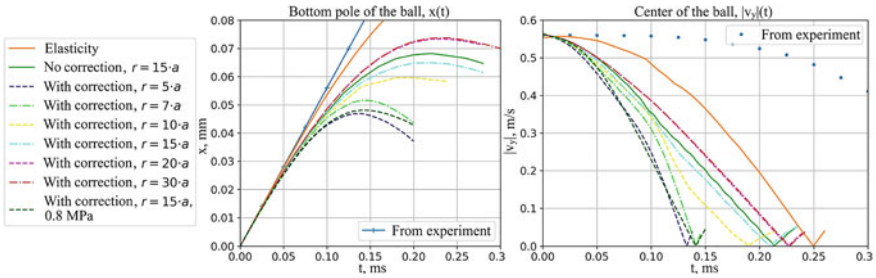


Fig. 2 Instantaneous values of the indenter's coordinate and velocity for different relations between r and a. For comparison, the curve with a changed maximum shear stress of 0.8 MPa is included

parameter evaluation, the initial ice shear modulus was decreased by a factor of 100; the final set was equivalent to 2344 m/s, 194 m/s and 917 kg/m^3. Supplementary calculations were conducted with these values typical of snow and water. However, in these cases, the results proved to be similar. For the ball and the stand, elastic velocities and density were equal to 5700 m/s, 3100 m/s and 7800 kg/m^3.

Figure 2 demonstrates the obtained graphs of the instantaneous values of the indenter's coordinate and velocity for different relations between *r* and *a*. The lines were compared to estimations from the experiment and the simulations in the case of the use of the elasticity model for the ice. Overall, the results appeared to better correspond with the elasticity model curve than with the experiment: the coordinate amplitude is generally lower and the velocities are displaced along the time axis to the left. In order to investigate such a difference, the influence of the model's parameters on the results was studied.

Firstly, for both variants of the model with and without stress correction, the curves appear to be close (solid green and cyan curves in Fig. 2). Secondly, the increase in the ration *r/a* leads to a rise in the depth of the ball's immersion and a movement of the velocity to the right. However, this tendency is limited, and the curves start to coincide (the red and magenta curves). The yield criterion appears to be fulfilled only in areas with heavy stress gradients. Therefore, the plastic flow is localized near the core, and the expansion of the elastoplastic zone does not result in significant changes.

The best agreement with the experiment might be achieved with a decrease in the maximum shear stress. This assumption is supported by the rise of the coordinate amplitude and movement of the velocity to the right when this parameter increases from 0.8 MPa (dark-green curve) to 0.3 MPa (cyan curve).

The incongruity of the two-dimensional simulations with the experiment seems to be caused by the specifically tree-dimensional nature of the expansive process occurring during the impact. Moreover, the evolution of ice structure and texture and their influence are not taken into account. For the same reason, it is too early to make any predictions about the correct model's parameters. Thus, instead of approximating the experimental curves with calculated solutions, let's consider evaluated stress

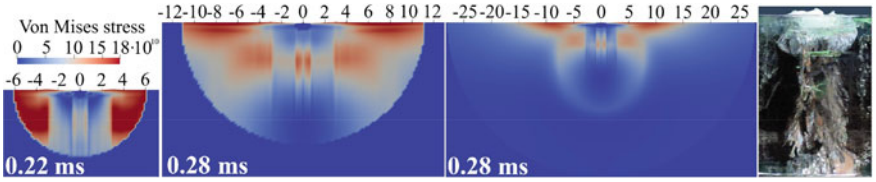


Fig. 3 Calculated von Mises stress in the close time points for the following radiuses of the elastoplastic zones (from left to right): $r = 10a$ (0.22 ms), $r = 15a$ (0.28 ms), $r = 30a$ (0.28 ms). Coordinates are presented in millimeters. On the right—photograph of the columnar textures in the ice formed during the indentation of a plane circle indenter

patterns. They should represent some bulk effects dominating the process even in the plane problem setting.

Figure 3 demonstrates the second invariant of the stress tensor deviator (von Mises stress, Pa^2) in the elastoplastic zone in the case of the model with zeroing of positive principal stresses in the core. In fact, during the impact, a columnar texture is formed. The same phenomenon occurs with the use of other parameters of the core and without stress correction. However, the main factor is the presence of the core and its interactions with the elastoplastic zone. The calculated stress patterns correlate with the columnar structures that can be seen in the photograph in Fig. 3, taken from [11].

Naturally, the question of why such textures are formed arises. They seem to appear due to the influence of the impact disturbance front on ice. The textures assemble as periodic disturbances overlap in the elastoplastic medium. Resembling structures were observed previously [12], after the convergence of the front created with a parabolic pressure stamp in the ice contained inside a de Laval nozzle under hydrostatic compression. A similar mechanism takes place during an impact on the ice disc by the spherical indenter. As a result, the contact area, together with the adjacent ice layer, starts to generate periodic pulses (graph in Fig. 1). Several results of the investigation of the surface and volume deformations caused by the impact are considered in the next section.

Three-dimensional setting. The simulations were conducted with the grid-characteristic method on an unstructured tetrahedral grid with a typical element size of 3.5 mm using the first–second order scheme, [12]. As an example, an ice disc of 300 mm in diameter and 60 mm in height is considered. Its elastic parameters were set to 2908 m/s, 1432 m/s and 910 kg/m^3. In the ball and the stand, they equaled 6015 m/s, 3215 m/s, 7850 kg/m^3. The time step was equal to 0.208 μs. As opposed to the two-dimensional setting, the grids did not move, the contact area stayed the same, and the initial striking velocity was set to 2.5 m/s. For the simulation of the ice, the isotropic linear elasticity model was applied, and the Tsai-Wu, Tsai-Hill, and Drucker-Prager failure criteria were checked. Any cell in which the criterion is satisfied was considered to be permanently destroyed. The elastoplastic model with zero maximum shear stress, [7], was used for the simulation of the failure.

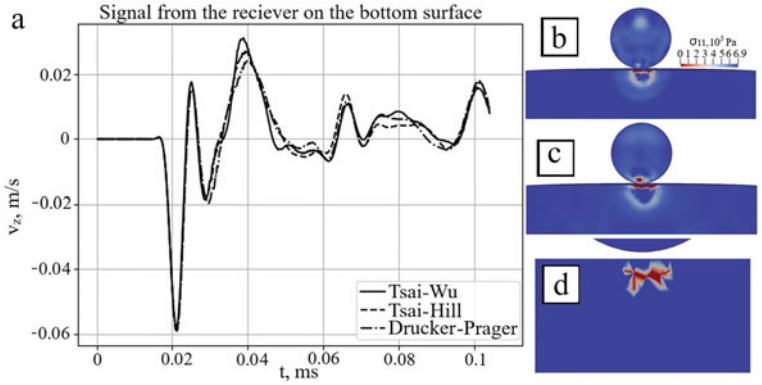


Fig. 4 Three-dimensional calculation results. a) Dependence of vertical projection of the velocity over time on the bottom ice surface along the impact axis. b)-c) Wave propagation in the middle and at the end of the simulation, slice in ZY plane around the ice-ball contact area. d) Destructed area at the end of the simulation

Simulation results are presented in Fig. 4. Both compressive and tensile strengths along the principal directions were set to 2.7 MPa; the limit along the tangential directions was equal to 1 MPa. All graphical information was obtained using arithmetic averaging of values in cells within a square 8×8 mm^2 receiver. In Fig. 4a, the curves of the vertical projection of the velocity over time are depicted.

The model, with all considered failure criteria, managed to reconstruct a compressional plane wave that transitions through the medium without changes. The orientation of the first three high-amplitude peaks qualitatively coincides with the magenta line in Fig. 1. Moreover, a small positive perturbance can be noticed at approximately 0.017 ms. It can indicate the presence of high-frequency oscillations that are almost fully observed by the ice. Another notable fact is the similarities between all curves, which can be used for validation of the results. To be specific, for the other parts in Fig. 1, the Tsai-Wu failure criterion is applied.

Slices 4b-4c show the patterns of the wave propagation (the value of the first principal stress is depicted), and slice 4d demonstrates the destructed area. Due to the asymmetry of the gris, the results also turn out to be asymmetrical. Nonetheless, the core in the zone of impact is clearly visible. Thus, the approach of determining the core's shape using different criteria is very promising.

The graph in Fig. 5 was calculated by integrating the vertical velocity projection obtained from the receiver placed on the upper boundary of the ice, 30 mm apart from the impact axis. The resulting curve can be divided into several sections that signify the occurring wave propagation. At the earlier stages, an almost symmetrical hill forms from approximately 0.007 ms until 0.017 ms. It can be interpreted as the propagation of the elastic wave. Next, from about 0.017 ms until 0.027 ms, the elasticity section continues. At around 0.027 ms, the line has a break that indicates the presence of nonelastic processes. Thus, the conclusion that the destructed area starts to form can be drawn. At approximately 0.06 ms, the curve contains additional

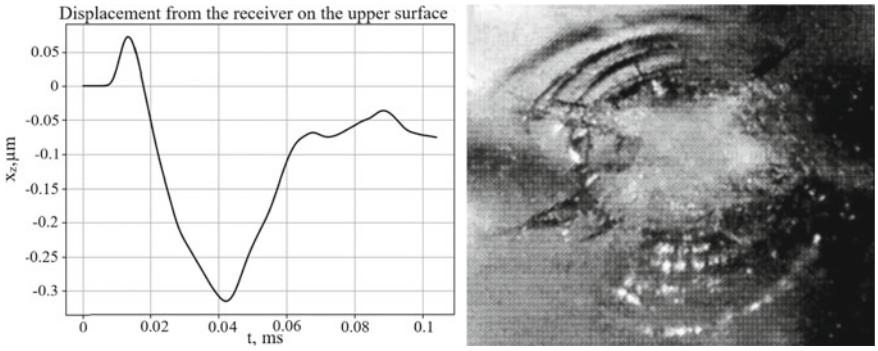


Fig. 5 The calculated dependence of the ice particles displacement on the upper surface, 30 mm apart from the impact axis, and the photograph [11] of the upper surface of the disc after unloading

oscillations related to the effects of waves' overlapping and interference. From this moment in time, the conduct of further analysis is difficult.

Similar phenomena can be seen during the experiments. This fact is confirmed in Fig. 5 with the photograph of the upper boundary of ice. The illustration shows the wave propagation inside the ice and the further destruction. As a result, the simulation managed to qualitatively reproduce such a complex process.

In conclusion, the introduced comprehensive approach proved to have great potential for further investigation of wave and rheological mechanisms during the low-speed impact on an ice disc by a spherical indenter.

Acknowlegements This work was carried out with the financial support of the Russian Science Foundation, project no. 23–21-00384.

References

1. *Herz H.* Über die Beruhrung fester elastichen Korper // Journ. für die reine und angewandte Mathematik. 1882. V. 92. P. 156–171.
2. *Barrette P., Pond J., Jordaan* I. Ice damage and layer formation in small-scale indentation experiments // Ice in the Environment: Proceedings of the 16th International Association for Hydraulic Engineering and Research (IAHR) International Symposium on Ice. 2002. P. 246–253.
3. *Browne T., Taylor R., Jordaan I*., Gürtner A. Small-scale ice indentation tests with variable structural compliance // Cold Regions Science and Technology. 2013. V. 88. P. 2–9.
4. *Ince S.T., Kumar A., Paik J., KInce S.T., Kumar A., Paik J.K.* A new constitutive equation on ice materials // Ships Offshore Struct. 2017a. V. 12, No. 5. P. 610 – 623.
5. *Epifanov V. P*. Ice destruction from impact interactions. Akademiia Nauk SSSR Doklady. 1985. V. 284, No. 3. P. 599–603.
6. *Studman J., Moore M.A., Jones S.E*. On the correlation of indentation experiments // J. Phys. D: Appl. Phys. 1977. V. 10. P. 949–956.
7. *Bruhns O.T.* The Prandtl-Reuss equations revisited // Z. Angew. Math. Mech. 2014. V. 94, №. 3. P. 187–202.

8. *Novatskii V*. Theory of Elasticity. Mir, Moscow, 1975. 872 p. [in Russian]
9. *Petrov I.B*. Grid-characteristic methods. 55 years of developing and solving complex dynamic problems // Computational Mathematics and Information Technologies. 2023. V. 6, № 1. P. 6–21.
10. *Kholodov A.S., Kholodov Ya.A*. Monotonicity criteria for difference schemes designed for hyperbolic equations // Comput. Math. Math. Phys. 2006. V. 46, No 9. P. 1560–1588.
11. *Epifanov V.P.* Contact fracture behavior of ice // Ice and Snow. 2020. V. 60, No 2. P. 274–284. [in Russian]
12. *Vassilevski Y.V., Beklemysheva K.A., Grigoriev G.K., Kazakov A.O., Kulberg N.S., Petrov I.B., Salamatova V., Vasyukov A.V*. Transcranial ultrasound of cerebral vessels in silico: proof of concept // Russian Journal of Numerical Analysis and Mathematical Modelling. 2016. V. 31. P. 317–328.

On the Possibility of Managing Dew Point Height in Mountain Areas to Reduce the Risks of Natural Emergencies



A. V. Kholoptsev, D. V. Sedov, and R. G. Shubkin

Abstract Using the Fire Dinamic Simulator (FDS) mathematical model, it is shown that the risks of natural emergencies in mountainous areas can be reduced by promptly influencing the height of the dew point above the windward slopes of the mountains. This problem is proposed to be solved by thermal impact on the surface layer of the troposphere above the foot of the slope from the side of the earth's surface.

Keywords Troposphere · Dew point height · Forced convection · Air temperature · Relative air humidity · Precipitation · Natural emergencies

1 Introduction

Natural emergencies in mountainous areas (droughts, landscape fires, avalanches, mudflows, landslides, etc.) annually cause irreparable damage to ecosystems, leading to major damage and human casualties. A fairly new and promising way to solve this problem is targeted operational management of rainfall zones. The intensity of rainfall in mountainous areas, as a rule, is excessive on the side of windward mountain slopes (this leads to avalanches, mudflows, landslides) and very low on the side of leeward mountain slopes (this leads to drought and an increased likelihood of landscape fires).

The most important parameter of the state of the troposphere, which has a significant impact on the intensity of rainfall in a particular area of a mountainous region, is the dew point height (hereinafter referred to as DPH). This parameter determines the position of the lower boundary of the clouds. The lower the DPH value in a certain

A. V. Kholoptsev · D. V. Sedov (✉) · R. G. Shubkin
Federal State Budgetary Educational Institution of Higher Education, Siberian Fire and Rescue Academy of the State Fire Service of the Ministry of Emergency Situations of Russia, Zheleznogorsk, St. Severnaya, 1, 662972 Krasnoyarsk Territory, Russian Federation
e-mail: sedov_irk@list.ru

© The Author(s), under exclusive license to Springer Nature Switzerland AG 2024

V. Karev (ed.), *Proceedings of the 9th International Conference on Physical and Mathematical Modelling of Earth and Environmental Processes*, Springer Proceedings in Earth and Environmental Sciences, https://doi.org/10.1007/978-3-031-54589-4_30

area, the greater the likelihood of precipitation occurring there. Therefore, identifying factors that make it possible to quickly manage changes in DPH is a pressing issue in hydrometeorology and safety in emergency situations.

It is advisable to look for such factors among processes that, firstly, occur in the surface layer of the troposphere and, secondly, are capable of causing vertical movement of air masses. Such processes include, first of all, the process of heat transfer and the process of momentum transfer [1]. A change in the average temperature of the surface layer of the troposphere leads to a change in the vertical distribution of relative air humidity, which, in turn, causes corresponding changes in DPH. As a rule, an increase in the average temperature of the specified layer leads to an increase in DPH [2, 3]. The most important source of thermal energy for the surface layer of the troposphere is, as is known, the surface of the earth [2, 4]. Thus, by influencing the temperature value of a certain area of the earth's surface, it is possible to thereby influence the difference in average temperatures Δ in the lower and upper boundaries of the surface layer of the troposphere.

2 The Hypothesis

The search for factors that make it possible to influence the DPH is most appropriate among the processes occurring in the surface layer of the troposphere and causing vertical air movement. One of these processes is a change in the average temperature of the surface layer of the troposphere on a certain area of the earth's surface. This process leads to a change in the vertical distribution of relative air humidity in a given area, which, in turn, causes corresponding changes in the DPH. An increase in the average temperature of the surface layer of the troposphere causes thermal convection, which leads to an increase in air temperature in the considered area of the earth's surface [2, 3, 5]. As stated earlier, the most important source of thermal energy for the surface layer of the troposphere is the earth's surface [2, 4]. This leads to a logical assumption that if you change the temperature of a selected area of the earth's surface, this will lead to a change in the difference in average temperature values between the lower and upper boundaries of the surface layer of the troposphere (hereinafter—Δ). The larger the size of the area over which changes in DPH occur, relative to the size of the area of the earth's surface over which Δ changes, the more effective the control of these changes.

Based on the above, we can put forward a hypothesis: the effect of thermal interaction between an area of the earth's surface and the surface layer of the troposphere can be used as a tool for controlling DPH.

However, this hypothesis is not trivial. The fact is that variations in the value of Δ and changes in the value of DPH can be caused not only by the influence of thermal factors, but also by the influence of dynamic factors.

The most noticeable dynamic factor that influences the characteristics under consideration is forced convection, which appears above the earth's surface as a result of wind [6]. This factor leads to the vertical movement of air from the surface layer of the troposphere, which affects the vertical distribution of its temperature and relative humidity and can lead to a change in DPH. If we exclude all possible equal

conditions, then the intensity of this process will be higher, the more dissected the terrain is and the greater the value of the average wind speed V directly above a given area. Therefore, the strongest decrease in DPH is observed on the windward side of mountain slopes, where wind speed is higher.

The higher V above such a slope, the lower the DPH above it and the greater the intensity of precipitation. At the same time, on leeward slopes the intensity of precipitation will be lower, and the risks of droughts and wildfires will be higher. Therefore, V is an important indicator of the intensity of forced convection, but it is almost impossible to control changes in this parameter.

The ability of a change in Δ over the windward slope to lead to a corresponding change in DPH is beyond doubt. At the same time, it is not so obvious that the thermal impact on the troposphere from a small section of the windward slope in the presence of forced convection can lead to a change in DPH over its entire surface.

The change in DPH is a multifactorial process, since this process depends on the values of Δ, V, as well as on time t and on the distance X between the mountain top and the point where the measurement is taken.

Responses in the values of temperature and relative humidity over the mountain slope under study, which arise as a result of the simultaneous influence of thermal factors and forced convection, can be identified by solving complete nonlinear thermohydrodynamic equations [6, 7]. Their solution will make it possible to determine not only the type of dependence of DPH on the values of Δ, V, t, X, but also the intervals of values of Δ and V in which the put forward hypothesis can be considered adequate.

However, solving these equations is only possible using numerical methods, which significantly complicates both testing the hypothesis and determining the intervals of its adequacy. Because of this, the conditions under which changing Δ over a local portion of a windward mountain slope allows one to control DPH over that entire slope are not well understood.

3 The Purpose

The purpose of this article is to determine the temperature and velocity characteristics of the surface layer of the troposphere, at which the thermal impact on it from a local area at the foot of the windward slope of the mountain will lead to an increase in the dew point height (DPH) over the entire windward slope.

4 Research Methodology and Factual Material

To achieve this goal, the dependences of the DPH over the windward slope of the mountain on the values of Δ, V, t and X during forced convection were studied. It was assumed that the height of the top of the slope above its foot is 1200 m, and the steepness of the slope is 31°, which is close to the parameters of the southern

slope of the Main Range of the Crimean Mountains in the Ai-Rayon Petrinskaya Yayla region (in the leeward territories of this area, droughts and disappearance of reservoirs have been observed for many years, steppe and forest fires).

When determining the response of DPH to changes in Δ and V, a mathematical modeling method was used using the Fire Dinamic Simulator V.6 software product (hereinafter referred to as FDS). This software product allows for the numerical solution of complete nonlinear thermohydrodynamic (Navier–Stokes) equations for low-speed temperature-dependent flows [8, vol. 1, 2]. The work [8, vol. 3] presents an overview of the results of FDS validation, which were carried out for various types of boundary and initial conditions. FDS can also be used to model the movement of air flows over terrain that has complex terrain and uneven temperature distribution [9, 10]. FDS can take into account changes in the concentration of any impurities, as well as changes in the speed, temperature and relative humidity of air above the earth's surface. In this case, the characteristics of the earth's surface (temperature and topography) are also taken into account. With FDS, changes in DPH at any slope location and during forced convection are calculated in three-dimensional (field) format using the finite difference numerical method [11–13].

We investigated the situation when the impact of thermal factors on the surface layer of the troposphere is carried out from a site located at the foot of a mountain slope. This site has the shape of a strip, which is oriented parallel to the top of the mountain range. The width of this strip is 70 m, and its closest border is located at a distance of 1950 m from the top of the mountain range. The thickness of the surface layer of the troposphere is 100 m [6].

During the modeling, it was assumed that the considered changes in DPH, caused by the action of thermal or dynamic factors, can be described in a linear approximation by the Duhamel integral [14]. Therefore, we considered the case when the time dependences of the factors influencing the DPH at the boundaries of the computational domain were described by the Heaviside function [15]. At the same time, at the initial moment of time $t = 0$, the value of Δ above the slope section increased from 0 to the value under consideration, and at any heights above the slope the wind speed changed sharply from 0 to V (that is, at $t = 0$, the values of Δ and V are considered constant).

It is also accepted that at $t = 0$ above the mountain slope, the vertical profiles of the temperature field (T) and relative air humidity field (F) do not depend on time t [16] and correspond to the values characteristic of the southern slope of the Main Range of the Crimean Mountains in the summer months at provided that the air masses over this area are stable and neutral (Table 1).

The dependences of the DPH value on the values of Δ, V, X and t were considered for the following cases: the values of Δ (°C) are in the range from 0 to 35; V values (m/s) range from 7.5 to 15; X (m) values are in the range (0…1200) ctg$S$. Estimated moments of time were determined by the formula (c):

$$t_i = 960 \cdot i / V, \tag{1}$$

where $i = 0, 1, 2, \ldots, 12$—serial number of the moment of time;

Table 1 Dependences of temperature (T, °C) and relative air humidity (F, %) on the height (h, m) above the foot of the slope

h, м	*T*, °C	*F*, %	*h*, м	*T*, °C	*F*, %	*h*, м	*T*, °C	*F*, %
0	29.9	70.2	700	25.5	84.3	1400	20.9	102.3
100	29.4	71.8	800	24.8	86.6	1500	20.3	105.3
200	28.7	73.8	900	24.2	89.0	1600	19.6	108.3
300	28.1	75.7	1000	23.5	91.5	1700	19.0	111.5
400	27.4	77.8	1100	22.9	94.1	1800	18.3	114.8
500	26.8	79.9	1200	22.2	96.7	1900	17.7	118.1
600	26.1	82.1	1300	21.6	99.5	2000	17.1	121.2

V—average wind speed interacting with the terrain, m/s.

DPH values were calculated for certain sections of the uphill slope of the mountain. The distances from the top of the mountain to these sections of the uphill slope of the mountain (m) were determined by the formula:

$$X_k = k \cdot 1200 \cdot \mathrm{ctg}S/20, \tag{2}$$

where $k = 0, 1, \ldots, 20$—serial number of the section;

S—angle of inclination of the mountain slope surface on the windward side (steepness), °.

5 Research Results and Discussion

In accordance with the described methodology and using the FDS software product, the possibility of operational impact on DPH by increasing the temperature of a local section of the windward slope was assessed. The factors that, in the presence of forced convection, cause changes in the average temperature of the surface layer of the troposphere were studied.

At $\Delta = 0$, changes in DPH over the windward mountain slope are driven by forced convection alone. The air carried by the wind rises along the slope to the top of the mountain and cools. Since above the foot of the slope the wind speed $V(z, t)$ is described by the Heaviside function, transient processes occur in the temperature fields $T(X, z, t)$ and relative humidity $F(X, z, t)$ above the slope.

At the moment $t = 0$, the wind speed at all heights changes sharply from 0 to V, and the isolines of air temperature T and relative humidity F are located horizontally. Over time, the interaction of the wind with the slope leads to the appearance of deviations of these contours, which are a consequence of the movement of air up the slope. The minimum absolute heights of the indicated isolines approach the slope over time. The change in circuit configurations stops when $j > 4$, which indicates the completion of transient processes. In the regime established after this, sections

of the T and F isolines corresponding to the minimum absolute heights are located directly on the surface of the slope.

The functions DPH(X_k, t_j) for the process under study are presented in Fig. 1. As can be seen from this figure, at different wind speeds V, the DPH(X_k) functions, which are marked along the mountain slope (on the windward side), have a similar shape. This means that during the transient process, the choice of speed has no significant effect on either the minimum DPH values or the corresponding k and j values.

In the steady state, the values of DPH(X_k) are also practically independent of the wind speed V, which is confirmed by Fig. 2. As can be seen from Fig. 2, in steady state, when the wind speed V doubles (from 7.5 to 15 m/s), the minimum DPH values (at $k = 3$–4) increase by only 25 m (or 3.13%), in this case, the corresponding numbers of cross sections k are reduced by 10%. From Figs. 1 and 2 it follows that at $\Delta = 0$ and different values of V the dependences DPH(X_k, t_j) are similar.

In the same way, the dependences DPH(X_k, t_j) were studied for the case $\Delta > 0$ (the air is heated on the slope at its foot). In Fig. 3 shows the results obtained for the case of $\Delta = 6.4$ °C at different wind speeds V. As can be seen from this figure, at the indicated values of V, the rise of heated air masses occurs near the surface of the mountain slope. Moreover, the more time t passes, the thinner becomes the thickness of the layer in which the heating effect is felt. In steady state, the height of this layer is about 50 m. It is also clear from the figure that the positions of the minimum values of the functions DPH(X_k, t_j) do not significantly depend on V.

The degree of influence of air heating on a slope section on the DPH value can be traced by analyzing the increase in DPH when air is heated on a slope compared to DPH without heating:

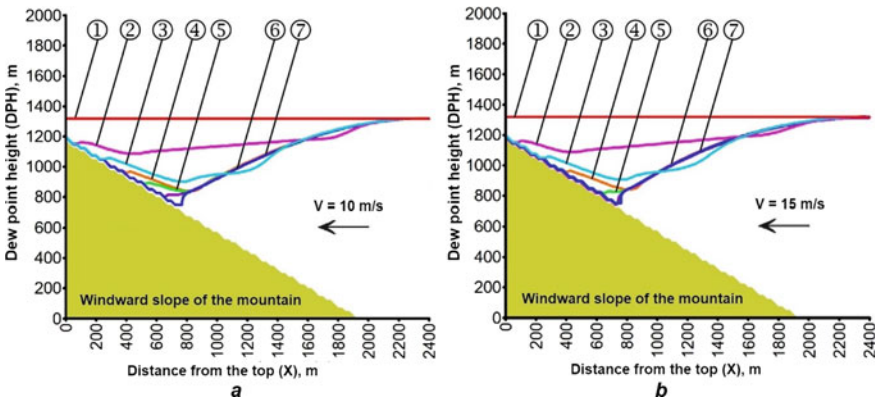


Fig. 1 Dependences of dew point height DPH(X_k, t_j) at $\Delta = 0$ °C and different V: *a*—at $V =$ 10 m/s: curve 1—$t = 0$ c; curve 2—$t = 60$ c; curve 3—$t = 120$ c; curve 4—$t = 180$ c; curve 5—$t =$ 240 c; curve 6—$t = 360$ c; curve 7—$t = 720$ c; *b*—at $V = 15$ m/s: curve 1—$t = 0$ c; curve 2—$t =$ 40 c; curve 3—$t = 80$ c; curve 4—$t = 120$ c; curve 5—$t = 200$ c; curve 6—$t = 280$ c; curve 7—$t =$ 480 c

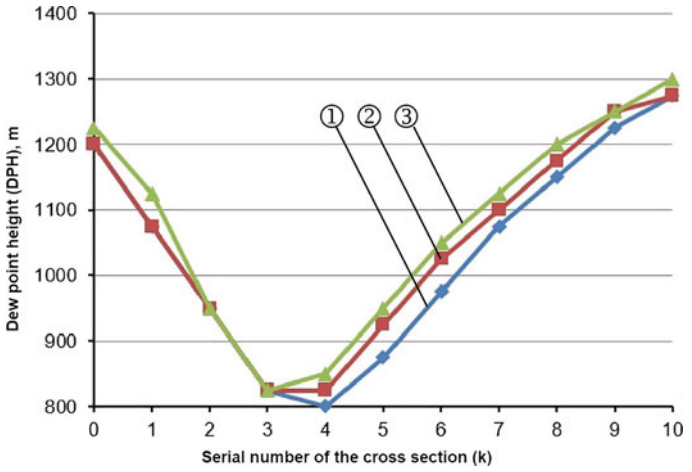


Fig. 2 Dependences of dew point height DPH(k) in steady state (at $j = 12$) at $\Delta = 0$ and different V: Curve 1—7,5 m/s; Curve 2—10 m/s; Curve 3—15 m/s

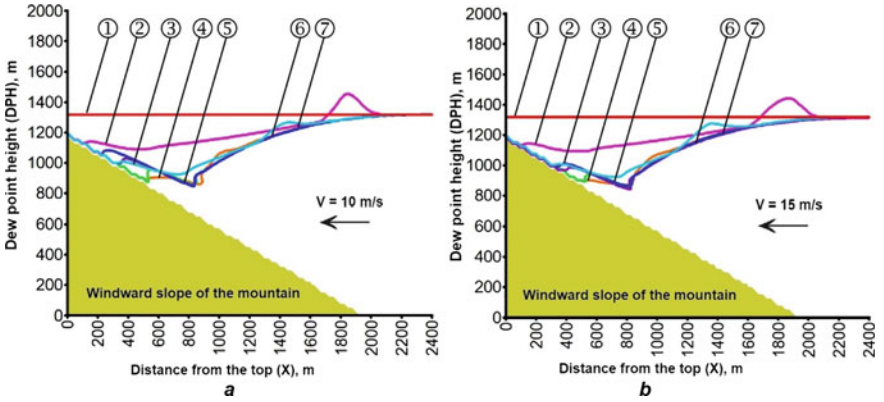


Fig. 3 Dependences of dew point height DPH(X_k, t_j) at $\Delta = 6{,}4$ °C and different V: a—at $V =$ 10 m/s: curve 1—$t = 0$ c; curve 2—$t = 60$ c; curve 3—$t = 120$ c; curve 4—$t = 180$ c; curve 5—$t =$ 240 c; curve 6—$t = 360$ c; curve 7—$t = 720$ c; b—at $V = 15$ m/s: curve 1—$t = 0$ c; curve 2—$t =$ 40 c; curve 3—$t = 80$ c; curve 4—$t = 120$ c; curve 5—$t = 200$ c; curve 6—$t = 280$ c; curve 7—$t =$ 480 c

$$\lambda(\Delta) = BTP(\Delta) - BTP(0). \tag{3}$$

$\lambda(\Delta)$ can take different values when the temperature difference at the opposite boundaries of the surface layer Δ, the wind speed V and the distance from the top of the slope X_k change. In Fig. Figure 4 shows the functions $\lambda(\Delta, k)$ for the steady state (j = 12) and various values of wind speed V for the case when the value $\Delta = 6.4$ °C. As can be seen from this figure, the curves $\lambda(\Delta, k)$ are similar: their maxima and

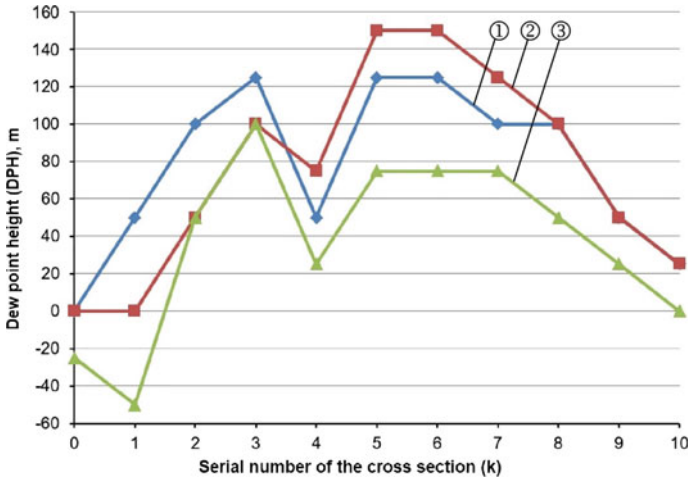


Fig. 4 Dependences $\lambda(\Delta)$ from X_k in steady state (at $j = 12$) at $\Delta = 6.4°C$ and different V: curve 1—7,5 m/s; curve 2—10 m/s; curve 3—15 m/s

minima are located in such a way that they practically do not depend on the wind speed V, although their corresponding values differ.

Analyzing the data presented in Figs. 3 and 4, we can conclude that with thermal impact on air masses from a relatively small area of the earth's surface located at the foot of a mountain slope (on the windward side), DPH values increase over almost the entire surface of this slope. The revealed effect indicates confirmation of our hypothesis. That is, DPH values along the entire mountainside can be monitored from one local area.

It should be noted that the obtained conclusion is not valid for all values of Δ, which is confirmed by Fig. 5, in which, for the case $V = 10$ m/s, the dependences of the DPH(X_k, t) are compared for different Δ. As can be seen from Fig. 5, the dependences DPH(X_k, t) have some similarity only in the steady state (at $t > 180$ s). But at the beginning of the transition process the similarity is not observed. Similarly, it was established that the similarity of the indicated dependences in the steady state occurs only in the case when Δ belongs to the interval 0–10 °C.

Figure 6 shows dependences (3) for λ (Δ, k) in steady state (at $j = 12$) at wind speed $V = 10$ m/s. As can be seen from Fig. 6, the changes in DPH $\lambda(\Delta)$ also have some similarity, which is manifested in the same location of the first maxima (at $k = 3$). At $\Delta > 1$ °C, the positions of the second maxima of the same dependences (at $k = 5$–7) also practically coincide. For $k < 3$, there is no similarity between the considered dependencies.

Comparison of Figs. 3, 4, 5 and 6 allows us to say that the functions DPH(Δ, k) and DPH(V, k) in transient mode and in steady state are similar to each other. This means that a decrease in the DPH value with a slight increase in wind speed V can be compensated by changing the value of Δ. This also indicates the validity of our hypothesis.

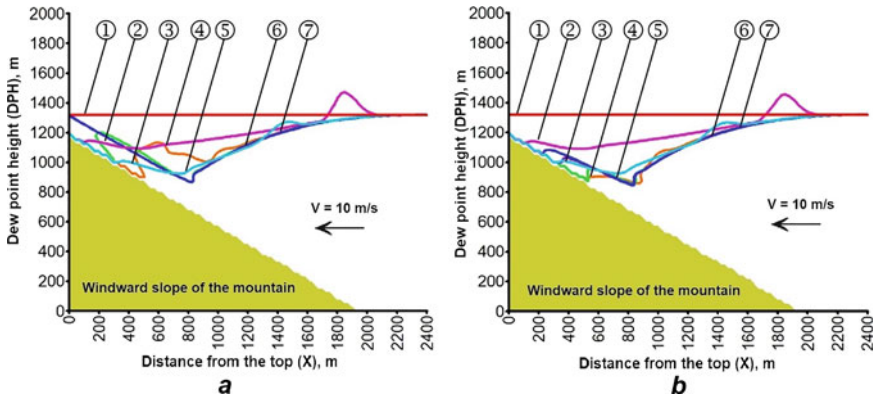


Fig. 5 Dependences of dew point height DPH(X_k, t_j) at $V = 10$ m/s and different Δ: *a*—at $\Delta =$ 31 °C: curve 1—$t = 0$ c; curve 2—$t = 60$ c; curve 3—$t = 120$ c; curve 4—$t = 180$ c; curve 5—$t =$ 240 c; curve 6—$t = 360$ c; curve 7—$t = 720$ c; *b*—at $\Delta = 6{,}4$ °C: curve 1—$t = 0$ c; curve 2—$t =$ 60 c; curve 3—$t = 120$ c; curve 4—$t = 180$ c; curve 5—$t = 240$ c; curve 6—$t = 360$ c; curve 7—$t = 720$ c

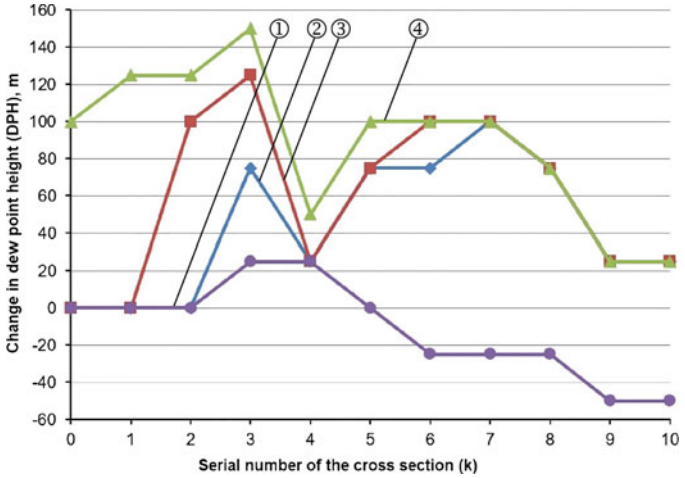


Fig. 6 Dependences $\lambda(\Delta, X_k)$ in steady state (at $j = 12$) at $V = 10$ m/s and different Δ: curve 1—0,2°C; curve 2—1,5°C; curve 3—6,4°C; curve 4—31,0°C

In addition, from these figures it follows that a change in the value of Δ leads to a proportional change in the value of DPH. In this case, the value of DPH(Δ) is close to linear. Similar features appear for other values of Δ and V taken from the corresponding intervals.

The results obtained indicate that heating of the surface layer of the troposphere from a small area of the mountain slope (on the windward side, at the foot of the mountain) leads to a significant increase in DPH on almost the entire mountain slope.

This thermal effect on the surface layer of the troposphere can be used to control the intensity of precipitation in mountainous areas.

A decrease in precipitation intensity on the windward slope of the mountain will lead to an increase in the flux of water vapor penetrating behind the mountain top. This, in turn, will lead to an increase in the intensity of precipitation on the leeward slope of the mountain. It follows that the considered thermal effect on the surface layer of the troposphere can lead to an increase in the intensity of precipitation on the leeward slope of the mountain. Therefore, the described impact on the surface layer of the troposphere can be used to reduce the risk of natural emergencies in mountainous areas.

6 Conclusions

Thus, as a result of our numerical studies, it was established that the thermal effect on the surface layer of the troposphere from a local area at the foot of a mountain slope (on the windward side) under conditions of forced convection can be used to increase DPH over the entire surface of this slope. Taking into account the relationship between the DPH value and the intensity of precipitation, the results obtained indicate the possibility of purposefully reducing the risks of natural emergencies arising from excessive or insufficient moisture of mountain slopes.

Literature

1. Laykhman D.L. Physics of the atmospheric boundary layer. L.: Hydrometeorological Publishing House, 1970. 342 p. (In Russian)
2. Khrgian A.Kh. Atmospheric physics. 3rd ed. L.: Hydrometeorological Publishing House, 1969. 646 p. (In Russian)
3. Matveev L.T. Fundamentals of general meteorology. Atmospheric physics. L.: Gidrometeoizdat, 1965. 752 p. (In Russian)
4. Byzova N.L., Ivanov V.N., Garger E.K. Turbulence in the atmospheric boundary layer. L.: Hydrometeorological Publishing House, 1989. 263 p. (In Russian)
5. Salby M.L. Fundamentals of atmospheric physics. Elsevier: Academic press, 1996. 649 p.
6. Monin A.S. Theoretical foundations of geophysical hydrodynamics. L.: Gidrometeoizdat, 1988. 424 p. (In Russian)
7. Landau L.D., Lifshits E.M. Course of theoretical physics. T. 6. Hydrodynamics. M.: Science. 1988. 736 p. (In Russian)
8. McGrattan K., Hostikka S., McDermott R., Floyd J., Weinschenk C., Over-holt K. Fire Dynamics Simulator, Technical Reference Guide. National Institute of Standards and Technology, Gaithersburg, Maryland, USA, and VTT Technical Research Center of Finland, Espoo, Finland, sixth edition, July 2013. Vol.1: Mathematical Model; Vol. 2: Verification Guide; Vol. 3: Validation Guide; Vol. 4: Configuration Management Plan.
9. Mouilleau Y., Champassith A. CFD simulations of atmospheric gas dispersion using the Fire Dynamics Simulator (FDS). Journal of Loss Prevention in the Process Industries. Published by Elsevier, 2009. No. 22, pp. 316–323.

10. Mniszewski K. The Use of FDS for Estimation of Flammable Gas/Vapor Concentrations. In Proceedings of the 3rd Technical Symposium on Computer Applications in Fire Protection Engineering, Society for Fire Protection Engineers, Bethesda, Maryland, September 2001. pp. 143–155.
11. Deardorff J.W. Stratocumulus-capped mixed layers derived from a three-dimensional model. Boundary - Layer. Meteorol, 1980. No. 18, pp. 495-527.
12. Pope S.B. Turbulent Flows. Cambridge University Press, 2000. No. 9, pp. 21–85.
13. Toro E.F. Riemann Solvers and Numerical Methods for Fluid Dynamics: A Practical Introduction. 2nd edition. Springer, 1999. 763 p.
14. Miroshnik I.V., Nikiforov V.O., Fradkov A.L. Nonlinear and adaptive control of complex dynamic systems. St. Petersburg: Nauka, 2000. 549 p. (In Russian)
15. Volkov I.K., Kanatnikov A.N. Integral transformations and operational calculus / Ed. B.C. Zarubina, A.P. Krischenko. 2nd ed. M.: Publishing house of MSTU im. N. E. Bauman, 2002. 228 p. (In Russian)
16. Poling B.E., Prausnitz J.M., O'Connell J.P. The Properties of Gases and Liquids. McGraw-Hill. 5th edition. New York, 2000. 803 p.

Studying the Features of Measuring Rock Deformations During Tests at the High Pressure High Temperature Triaxial Apparatus



S. O. Barkov

Abstract This paper presents the results of a series of experiments on studying the effect of the sealing membrane type and the mounting technique of LVDT sensors on the accuracy of cylindrical specimen deformation measurement during tests at the high pressure high temperature (HPHT) triaxial apparatus GT1.3.9. The paper presents the stress–strain curves of the testing specimen obtained within the framework of triaxial tests with sealing membranes made of different materials. The most optimal type of sealing membrane and mounting techniques of LVDT sensors are determined. A method of determining the membrane deformation when measuring the circumferential deformation of the specimen during the tests on the HPHT triaxial apparatus GT1.3.9 is proposed.

Keywords Rocks compression · HPHT triaxial apparatus · Triaxial tests · LVDT sensors mounting · Membrane effect · Membrane deformation

1 Introduction

The mechanical properties of reservoir rocks are used as input data for geomechanical modelling and subsequent simulations of various well operations, risk assessment of sand production, drilling safety and wellbore stability. And the quality of these calculations directly depends on the accuracy of determining the mechanical properties of rocks. The elastic and strength characteristics of rocks are of great importance. The most accurate determination of these characteristics is possible during laboratory studies of core material. The main methods of determining the strength characteristics of rocks include uniaxial tension and compression tests of specimens. However, in natural conditions rocks are in a three-dimensional stress field, so the most complete understanding of their properties and failure mechanism in laboratory settings can be

S. O. Barkov (✉)
Ishlinsky Institute for Problems in Mechanics RAS, Moscow, Russia
e-mail: barkov.sviat@yandex.ru

© The Author(s), under exclusive license to Springer Nature Switzerland AG 2024

V. Karev (ed.), *Proceedings of the 9th International Conference on Physical and Mathematical Modelling of Earth and Environmental Processes*, Springer Proceedings in Earth and Environmental Sciences, https://doi.org/10.1007/978-3-031-54589-4_31

obtained by triaxial tests in the total stresses [1, 2]. This method consists in measuring the destructive force loading applied to the faces of a rock specimen under the lateral compression by hydrostatic pressure.

Triaxial tests are realised mainly by means of triaxial axisymmetric compression apparatuses based on the Karman scheme [3, 4]. The main advantage of these facilities is the possibility to create reservoir conditions, including pore pressure, in specimens during tests. To carry out such tests, cylindrical rock specimens are placed in a sealing membrane. Sensors for measuring specimen deformations during loading are mounted on the surface of the confining material. It should be noted that the use of a sealing membrane affects the accuracy of measuring the deformations of the rock specimen and, consequently, its elastic and strength characteristics, therefore, additional research is required [5, 6]. Most of these studies are focused on determining the deviatoric loading correction that needs to be taken into account as a result of specimen strengthening by the membrane. This effect is indeed observed in tests on low-strength, weakly cemented rocks. The effect of the membrane on the strength properties of high-strength, highly cemented rocks is not significant. However, when measuring small circumferential deformations of specimens, the deformation of the membrane itself has a significant influence on the accuracy of measurements, which must be taken into account.

Triaxial tests are often realised on more technically difficult facilities of true triaxial loading, which allow loading cubic specimens of rocks independently along each of the axes [7, 8]. However, triaxial tests on such facilities are carried out in the effective stress, as it is difficult to create formation conditions in the tested specimens because of the difficult construction of the facility's loading system.

The geomechanics laboratory of IPMech RAS uses both types of facilities to determine the elastic and strength characteristics of rocks: a true triaxial loading facility—the unique Triaxial Independent Load Test System (TILTS) [9, 10], and a facility for triaxial axisymmetric compression according to the Karman scheme—high pressure high temperature (HPHT) triaxial apparatus GT1.3.9. In this paper, the effect of different types of sealing membranes and sensor mounting techniques on the accuracy of specimen deformation measurement when tested on the HPHT triaxial apparatus GT1.3.9 is studied.

2 Testing Equipment

A series of experiments to study the effect of membrane type and sensor mounting technique on the accuracy of specimen deformation measurement was carried out on the HPHT triaxial apparatus GT1.3.9 designed and constructed by the Russian company "Geotech". This facility allows loading cylindrical specimens with diameters of 25, 30 and 42 mm and heights of 50, 60 and 84 mm. The maximum vertical load is 500 kN and is applied independently of the confining hydrostatic pressure, which is created in the test chamber by silicone oil using a pressure generator (electromechanically driven piston pump) and can attain up to 70 MPa. The vertical

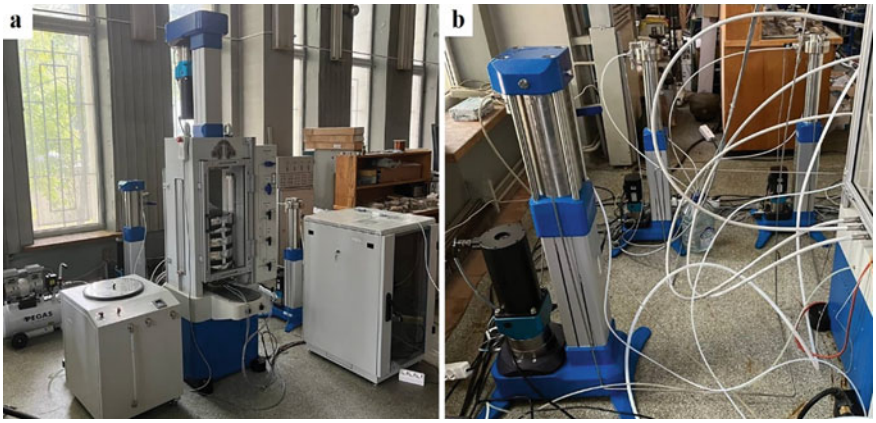


Fig. 1 **a**—HPHT triaxial apparatus GT1.3.9, **b**—system of GT1.3.9 pressure generators

loading device is a load frame with electromechanical actuator. A heating element is integrated into the chamber case, allowing temperature control in the range from +25 to +110 °C. To create pore pressure in the specimen and to carry out filtration tests, two other pressure generators with a maximum pressure of 40 MPa filled with water are additionally used. These generators are connected to the upper and lower stamp of the loading block and, respectively, allow to create fluid pressure at the top and bottom of the specimen. Flowmeters are installed at the output of the pressure generators to determine the volume of fluid entering or leaving the pressure generator. Photo of the HPHT triaxial apparatus GT1.3.9 is presented in Fig. 1.

The specimen is surrounded by an impermeable membrane to ensure sealing and prevent fracture products entering the chamber. The specimen is surrounded by an impermeable membrane to ensure sealing and prevent fracture products entering the chamber. Local longitudinal and circumferential deformations of the specimen during the test are measured using LVDT sensors. In order to correctly measure the longitudinal deformation, the average of two sensors mounted on the lateral surface of the specimen opposite each other is calculated. The use of two sensors is necessary to account for longitudinal bending, which can occur as a result of non-axial load application or the slightest curvature of the specimen faces. To measure the circumferential deformation of the specimen, the LVDT sensor is mounted on a roller chain that is mounted to the middle of the specimen. The chain is constructed with a magnetic fastener to prevent the chain from being damaged if the specimen is severely deformed. The sensors are mounted on the surface of the membrane, which necessitates additional studies of the effect of the membrane material on the accuracy of specimen strain measurement. Photo of concrete specimen in different membranes with mounted sensors is presented in Fig. 2.

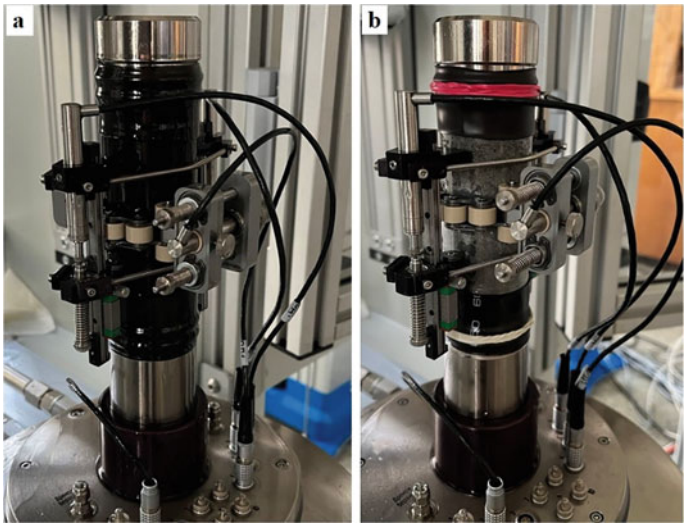


Fig. 2 a—concrete specimen with mounted LVDT sensors in polyolefin membrane (shrink tube), b—concrete specimen with mounted LVDT sensors in polyurethane membrane

3 Specimen Preparation and Experimental Methodology

The effect of the sealing membrane material and LVDT sensors mounting technique on the accuracy of specimen deformation measurements was carried out as part of the triaxial testing methodology elaboration at HPHT triaxial apparatus GT1.3.9. The tests were carried out on a cylindrical specimen made of concrete with a diameter of 42 mm and a height of 84 mm. The surfaces of the concrete specimen were pre-treated using special stonecutting equipment to ensure the quality of surfaces meeting the GOST (State Standard System) requirements.

The program of specimen loading under triaxial testing in one of the experiments is presented in Fig. 3, where $\sigma_1 = \sigma_3 + \Delta\sigma$—total vertical stress, $\sigma_3 = \sigma_2$—confining pressure, $\Delta\sigma$—deviatoric stress. The deviatoric load was applied at confining pressure of 2, 10 and 20 MPa, at the same time, in order to save the specimen and its properties, the loading was carried out before the plastic deformation phase. Triaxial tests were performed both without and in polyolefin (shrink tube), latex and polyurethane membranes. A roller chain construction with and without magnetic fastening was used to measure the circumferential deformation of the specimen. Axial sensors were mounted using conventional (flat) or sharp mounts.

The uniform triaxial compression ($\sigma_1 = \sigma_2 = \sigma_3$) of a brass specimen having a diameter of 30 mm and a height of 60 mm with and without a membrane up to 70 MPa was also carried out. This experiment was carried out to calculate the deformation of the polyolefin membrane during triaxial compression. A photo of the brass specimen with and without the polyolefin membrane is presented in Fig. 4.

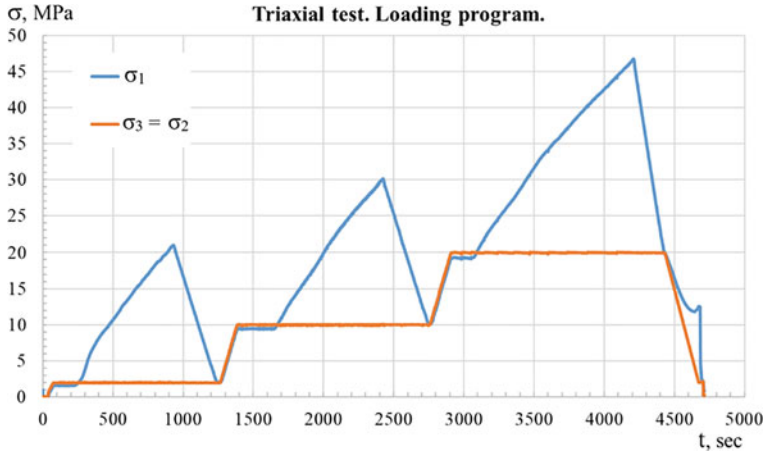


Fig. 3 Triaxial test program in one of the concrete specimen experiments

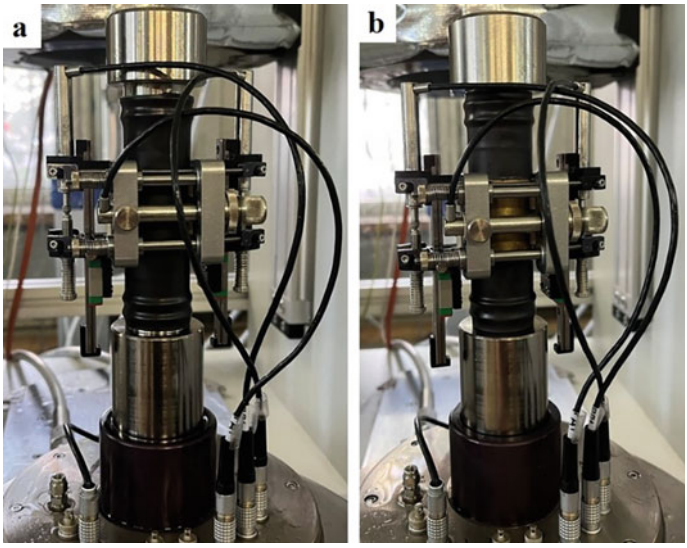


Fig. 4 **a**—brass specimen with mounted LVDT sensors in polyolefin membrane (shrink tube), **b**—brass specimen with mounted LVDT sensors without membrane

4 Results and Discussion

In Fig. 5a the specimen stress–strain curves are presented for the triaxial compression ($\sigma_1 = \sigma_2 = \sigma_3$) stage up to 2 MPa, and Fig. 5b—for the stage of increasing deviatoric load and decreasing it ($\sigma_1 > \sigma_2 = \sigma_3$) at 10 MPa compression. The results show that the membrane has the greatest effect on the accuracy of measuring the circumferential

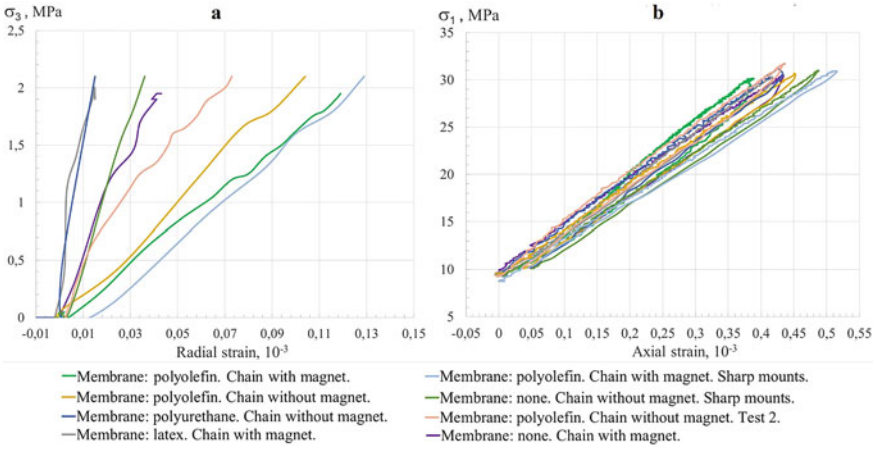


Fig. 5 a—the specimen stress–strain curves for the triaxial compression stage up to 2 MPa, b—the specimen stress–strain curves for the stage of increasing deviatoric load and decreasing it at 10 MPa compression

deformation of the specimen, and the use of a chain construction without magnetic fastening allows to reduce this effect. The thicker membrane, the more significant is its effect on the measured specimen deformation.

The most accurate measurement of the circumferential deformation of the specimen is realized when testing without a membrane. Thus, in case of testing without filtration of high-strength rocks, it is more effective not to use a membrane, otherwise the best option is a polyolefin membrane, because in polyurethane and latex membranes under load there is a violation of sealing. It should be noted that rubber membranes are often used in such facilities [5, 6], but the thickness of such membranes is more than 1 mm, which significantly exceeds the thickness of polyolefin membranes (less than 0.5 mm) and makes a more significant contribution to the measurement of deformations. In addition, the manufacture of rubber membranes requires a large financial cost. When thick-walled membranes are used, it is necessary to carry out additional studies aimed at calculating the deformations of the membrane under load.

The most accurate measurement of axial deformation is provided by sharp sensor mounts, which prevent slippage on the specimen surface. The use of sharp mounts increases the accuracy of specimen axial deformation measurement by 10–15%, which is especially noticeable when testing high-strength rocks. At the same time, filtration tests are impossible with the use of sharp mounts due to the violation of membrane sealing. It should be noted that experiments conducted on weakly cemented low-strength rocks did not demonstrate a significant difference in axial deformations of the specimen measured using sharp and conventional mounts for sensors. In this case, even conventional mounts provide reliable fixation of sensors to the specimen surface.

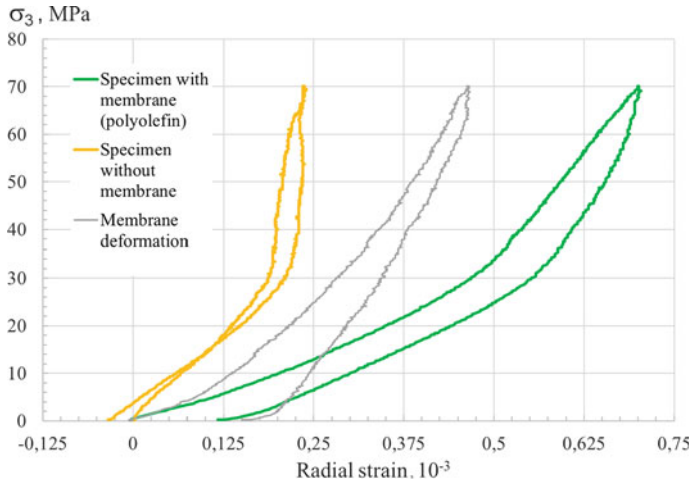


Fig. 6 Stress–strain curves of a brass specimen under triaxial compression with and without a polyolefin membrane and the estimated membrane deformation

In Fig. 6, the stress–strain curves for the brass specimen with and without the polyolefin membrane and the estimated membrane deformation are shown. The membrane deformation was obtained by subtracting the radial deformation of specimen with membrane and the radial deformation of specimen without membrane. With this result, it is possible to make a correction to the radial deformation of the specimen when it is tested in the polyolefin membrane. It is important to note that this membrane is characterized by residual deformation.

5 Conclusion

According to the obtained results, for the most accurate determination of specimen deformations, tests of highly cemented high-strength rocks should be carried out without a sealing membrane using sharp sensor mounts. However, for low stresses that do not result in significant deformation and possible subsequent specimen failure, a chain without magnetic fasteners should be used to more accurately measure circumferential deformation. For low-strength, weakly cemented rock, as well as for filtration tests, a polyolefin sealing membrane, conventional sensor mounts, and chain with magnetic fasteners should be used. For filtration tests that do not result in significant deformation of the specimen, a chain without magnetic fasteners should be used. To determine the deformation of the membrane during the test, identical tests with and without the membrane should be carried out on a specimen made of a high-strength material that will not change its elastic and strength characteristics under high stresses. In the following studies on a brass specimen it is planned to carry out triaxial tests at confining pressure of 2, 10 and 20 MPa in the membrane

and without it, which will allow to consider the deformation of the membrane when testing rocks at the HPHT triaxial apparatus GT1.3.9.

The work was performed within the framework of the state assignment, registration number 123021700046-4.

References

1. Lodus E. V., Pak A. K., Kuznetsov N. N. Analysis of strength characteristics of rocky rocks under triaxial axisymmetric compression // Mining information and analytical bulletin (scientific and technical journal). 2014. V. 6, P. 233-242 (in Russian).
2. Braun P., Delage P., Ghabezloo S. et. al. Inducing Tensile Failure of Claystone Through Thermal Pressurization in a Novel Triaxial Device // Rock Mechanics and Rock Engineering. 2022. V. 55, P. 3881–3899. https://doi.org/10.1007/s00603-022-02838-3.
3. Petrakov D., Kupavykh K., Kupavykh A. Experimental study of elastic-plastic properties of oil reservoir rocks with account of saturation. // Construction of Oil and Gas Wells on Land and Sea. 2020. V. 3 (327), P. 33–38. https://doi.org/10.33285/0130-3872-2020-3(327)-33-38.
4. Liu X., Wang G., Song L. *et al.* Study on the influence of fracture dip angle on mechanical and acoustic emission characteristics of deep granite // Natural Hazards. 2023. V. 118, P. 95–116. https://doi.org/10.1007/s11069-023-05994-z.
5. Raghunandan M.E., Sharma J.S., Pradhan B. A review on the effect of rubber membrane in triaxial tests // Arab J Geosci. 2015. Vol. 8, P. 3195–3206.
6. Alhani I.J., Noor M.J.M., Albadri W.M. Membrane penetration effects on shear strength and volume change of soil during triaxial test // AIP Conf. Proc. 5 October 2018; 2020 (1): 020008.
7. Heping Xie, Jun Lu, Cunbao Li, Minghui Li, Mingzhong Gao. Experimental study on the mechanical and failure behaviors of deep rock subjected to true triaxial stress: A review // International Journal of Mining Science and Technology. 2022. V. 32, I. 5, P. 915–950. https://doi.org/10.1016/j.ijmst.2022.05.006.
8. Zheng Z, Cai Z, Su G, et al. A new fractional-order model for time-dependent damage of rock under true triaxial stresses // International Journal of Damage Mechanics. 2023. V. 32 (1), P. 50-72. doi:https://doi.org/10.1177/10567895221124325.
9. Karev V., Kovalenko Y., Ustinov K. Geomechanics of oil and gas wells. Advances in oil and gas exploration and production. Springer International Publishing Cham: Switzerland, 2020. 166 p.
10. Karev V.I., Kilmov D.M., Kovalenko Y.F. *et al.* Experimental Study of Rock Creep under True Triaxial Loading // Mech. Solids. 2019. V. 54, P. 1151–1156. https://doi.org/10.3103/S0025654419080041.

Physical Modeling of Sand Production in Vertical and Horizontal Wells of Underground Gas Storage Facilities Using a True Triaxial Loading Setup



N. I. Shevtsov

Abstract Underground gas storage (UGS) wells are operated in a cyclic mode—bottom hole pressure increase for gas pumping alternate with bottom hole pressure decrease for gas extraction. This can lead to partial destruction of the bottomhole zone of the formation, which is accompanied by sand production. It leads to clogging of filter channels, a decrease in flow rate and wear of underground and surface equipment. The unique facility Triaxial Independent Loading Test System (TILTS) of the Institute for Problems in Mechanics RAS allows to directly simulate the process of pressure reduction at the bottomhole by the so-called scheme "hollow cylinder" on cubic specimens with a 40 mm edge, which made of core material of reservoir. This paper presents the results of an experiments series conducted on the specimens made of core material of the Udmurt UGS. The results of modeling on these specimens on the "hollow cylinder" scheme obtained on the TILTS unit allow us to conclude about the presence of strength anisotropy of reservoir rocks of this UGSF. Modeling of the creation of pressure drawdown in differently oriented wells showed that the destruction of the well walls and sand production in horizontal wells occurs at lower drawdown values and to a greater extent than in vertical wells.

Keywords Underground gas storage · True triaxial loading · Physical modeling using a hollow-cylinder scheme

1 Introduction

Development of oil and gas fields with large number of wells drilling changes the natural stress state of rocks in their vicinity. Stress fields become highly unequal and shear stresses appear. During well operating cycle, its flow rate gradually drops.

N. I. Shevtsov (✉)
Ishlinsky Institute for Problems in Mechanics RAS, Moscow, Russia
e-mail: Red3991@ya.ru

© The Author(s), under exclusive license to Springer Nature Switzerland AG 2024

V. Karev (ed.), *Proceedings of the 9th International Conference on Physical and Mathematical Modelling of Earth and Environmental Processes*, Springer Proceedings in Earth and Environmental Sciences, https://doi.org/10.1007/978-3-031-54589-4_32

In order to maintain the flow rate at the initial level, the downhole pressure additionally reduced, which causes an increase in bottomhole formation zone stresses. Underground gas storage (UGS) wells are operated in a cyclic mode—pressure drawdown for gas pumping alternate with gas injection cycles, during which bottomhole pressure increases. All this can lead to partial destruction of the bottomhole formation and is often accompanied by sand production [1, 2], which leads to filtration channels clogging and flow rate reduction, wear of drilling equipment [3, 4]. The production of too much sand weakens the soil skeleton and can eventually cause the destruction of the rock composing the bottomhole zone [5].

2 Research Methodology

The unique facility Triaxial Independent Loading Test System (TILTS), created at the Ishlinsky Institute for Problems in Mechanics of the Russian Academy of Sciences [6], allows to directly simulate the process of pressure reduction at the bottomhole formation zone. This experiment scheme called «hollow cylinder». For this purpose a cubic specimens with a 40 mm edge made of core material was used. The TILTS experimental setup (Fig. 1) consists of a loading unit with unique kinematics of the pressing elements—overlapping loading plates allow stresses to be transferred to the entire surface of the specimens without obstructing each other. To reduce friction, thin fluoroplastic spacers were inserted between each specimen face and the loading plates. Center holes with a diameter of 10 mm were cut in the spacers covering the surfaces with holes. Hydraulic cylinders creating pressure allow stresses up to 200 MPa in each direction. The measurement system measures forces and strains in real time along each of the three axes, as well as permeability along one axis. The control and data acquisition are performed by an analog–digital complex with data output to a PC. Due to the scale effect, the «hollow cylinder» experiments do not allow quantifying the pressure draw-dawn values leading to rock fracture in the vicinity of the wells, but they provide to evaluate a qualitative picture of deformation processes and determine the volume and characteristics of the removed from specimens rock particles.

A hole with a diameter of 10 mm was drilled in the center of the specimen's face in the direction of one of the axes for testing according to the «hollow cylinder» scheme (Fig. 1). During the experiment, air at a pressure of about 0.1 MPa was blown through a channel in the tip of the upper active pressure plate coinciding with the hole in the specimen. To discharge the gas that passed through the channel in the specimen, the tip of the lower pressure plate also has a hole coinciding with the channel in the specimen. Through this hole through a special tube, the removed sand was transported to the electronic scales connected to the computer. During the experiment, comprehensive uniform compressive stresses were applied to the specimen ends, which increased continuously with time. The deformations of the specimen in three directions were recorded and the weight of the removed sand of the specimen by the air flow was measured. The accuracy of the electronic scale is 0.001 g and the

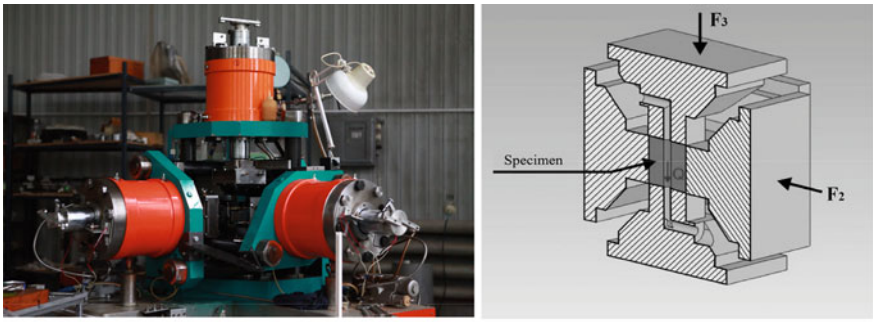


Fig. 1 The unique experimental setup Triaxial Independent Loading Test System TILTS. Photo (**a**) and schematic of pressure plates in «hollow cylinder» tests (**b**)

recording was done every 2 s. The testing of the specimen was continued until the specimen destruction. The loading of the specimen was of a stepwise nature. At each step the stresses along all three axes were uniformly increased by 1 MPa, followed by a time exposure until sand production ceased. CT scanning of the specimens before and after TILTS tests were also performed. A high-resolution X-ray CT scanner ProCon X-Ray CT-MINI was used for computed tomography. The device has a rigid base (monolithic granite slab) for practical exclusion of the influence of temperature drift and precise installation of X-ray optical and other system components inside the device, which provides accuracy and stability of measurements in the whole range of working space. The high-resolution, microfocus and closed-loop X-ray tube has an adjustable output voltage range of 20 kV to 90 kV and an adjustable current range of 10 μA to 160 μA. The maximum output power of the tube is 8 W. The high-sensitivity, low-noise X-ray detector has a pixel number of 2940 × 2304 and a pixel size of 49.5 μm. The size of the active (sensitive) area is 146 × 114 mm. The scans were reconstructed using VGSTUDIO software, while 3D image processing was carried out using Geodict Math2Market GmbH software [7].

3 Experimental and Simulation Results

This paper presents the results of a series of experiments conducted on specimens made from Udmurt UGS core material. Three specimens were tested, all three were made from one piece of core. In specimens V1 and V3 the hole was drilled along the core axis (qualitatively corresponds to a vertical well), in specimen V2—along the bedding (qualitatively corresponds to a horizontal well). A preliminary analysis of the rock was performed using computed tomography. The studied rock was homogeneous, without macrocracks and caverns. Transverse and longitudinal sections showed predominantly uniform distribution of rock density, with small inclusions

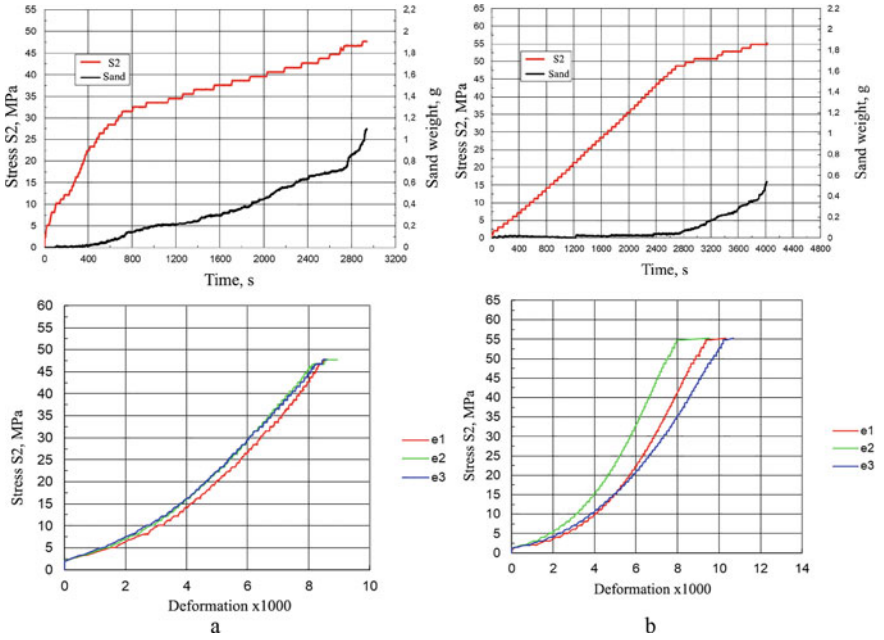


Fig. 2 Dependence of the transported sand mass on compressive stresses and deformation curves for specimens V2 (**a**) and V3 (**b**)

of denser heterogeneities. There was also pronounced layering with minor traces of denser material left by fluid transported through the formation.

From the graphs shown in Fig. 2, it can be seen that sand production in the modeling of a horizontal well (specimen V2, hole in the specimen along the bedding) began at a stress of about 20 MPa, and the failure of the specimen occurred at 47 MPa. In the modeling of a vertical well (specimen V3), sand production began at stress values of about 43 MPa, and failure occurred only after reaching 55 MPa. During the testing of specimen V2, the total mass of produced sand was about 1.1 g, while for specimen V3 this value is about 0.5 g.

Figure 3a and b shows photos of the specimens after the tests. It is easy to see that the fracture of the hole in specimen V2 began at the points corresponding to the upper and lower points of the contour of the horizontal well in the formation, and then continued in the same direction, forming a breakouts typical for wells [8]. Fracture of specimen V3 occurred symmetrically along the entire contour of the hole with three symmetrically located breakouts, which is also visible on tomographic images (Fig. 3c and d). This is consistent with the fact that the hole was drilled perpendicular to the beddings, in which the strength properties of the rock are isotropic.

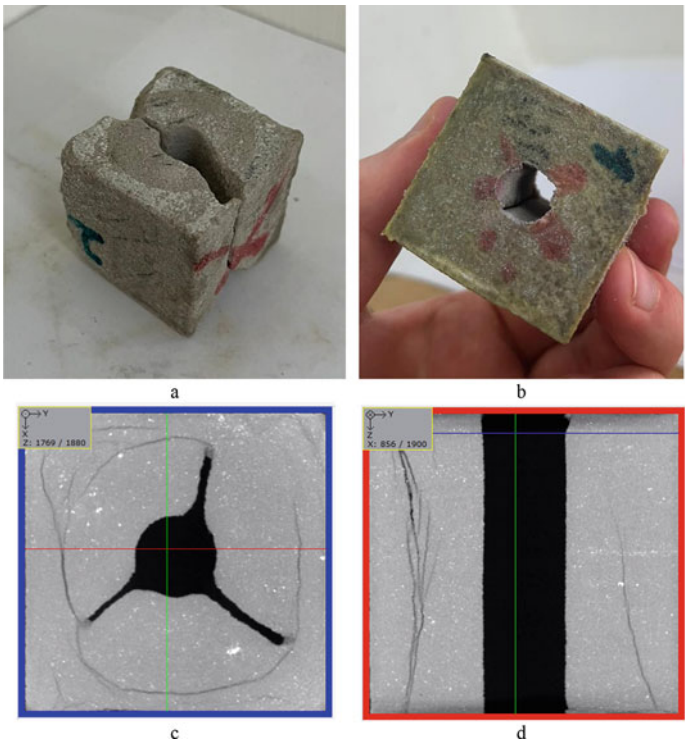


Fig. 3 Photographs of specimens V2 (**a**) and V3 (**b**) after testing. Tomographic images of specimen V3 after the test in two projections (**c**, **d**)

4 Conclusion

The results of modeling of the Udmurt UGS specimens on the «hollow cylinder» scheme obtained on the TILTS unit allow us to conclude that there is strength anisotropy of the reservoir rocks of this UGS. Modeling of pressure draw-down creation in horizontally directed wells showed earlier wall failure and production of more sand compared to similar modeling for vertically directed wells. The shapes of breakouts in the modeling of horizontal and vertical wells differed, which also indicates anisotropy of strength properties of the studied UGS.

Acknowledgements The present work was supported by the Ministry of Science and Higher Education within the framework of the Russian State Assignment under contract No. 123021700046-4.

References:

1. Karev V. I., Kovalenko Yu. F., Sidorin Yu. V., Ustinov K. B. Geomechanical modeling of processes in the bottom-hole zone of a well // Monitoring. Science and Technology. 2016. № 3. с. 85–91. (in Russian)
2. Mirzajanzadeh A. H. Fundamentals of gas production technology.—Moscow: Nedra, 2003. - 880 с. (in Russian)
3. Aksenova N. A. Technology and technical means of well completion with unstable reservoirs: a monograph / N. A. Aksenova, V. P. Ovchinnikov, A. E. Anashkina.—Tyumen: TIU, 2018. —134 с. (in Russian)
4. Arman Salahi, Ali NaghiDehghan, Seyed Jamal Sheikhzakariaee, Afshin Davarpanah, Sand production control mechanisms during oil well production and construction, Petroleum Research, Volume 6, Issue 4, 2021, Pages 361-367
5. Poroshin M.A., Tananykhin D.S., Grigoriev M.B. Fanalysis of laboratory methods for studying the process of sanding during the development of oil fields // Bulletin of Eurasian Science. 2020. (in Russian)
6. Karev V.I., Kovalenko Yu.F. Triaxial loading system as a tool for solving geotechnical problems of oil and gas production. In the collection: True Triaxial Testing of Rocks Сер. "Geomechanics Research Series" Leiden, 2013. С. 301–310.
7. GeoDict – The Digital Material Laboratory: [digital source] URL: https://www.math2market.de/ (Date of request: 23.09.2023).
8. Kovalenko Yu. F., Ustinov K. B., Karev V. I. Geomechanical analysis of the formation of breakouts on well walls // in Proceedings of the Russian Academy of Sciences. Mechanics of Solid State, 2022. (in Russian)

Structure of Technogenic Landscapes of the Blyavinsky Copper-Crusted Deposit



Vadim Petrishchev, Galina Ponomareva, and Inna Kudelina

Abstract The morphological structure of landscapes of technogenic origin was determined by the example of the quarry-dump complex of the Blyavinsky copper-crusted deposit. The choice of the object is due to almost half a century of conservation of the deposit, during which the processes of formation of the morphological structure of the technogeosystem of the deposit were manifested. Among the key tasks, the following stood out: assessment of the degree of manifestation of natural factors of landscape differentiation and identification of the role of processes associated with mining production; analysis of the correlation of the elements of the dump complex with the elements of the quarry complex using data from the classification of satellite information and a combination of channels of different frequency ranges, data from geochemical analysis of soils, subsurface and quarry waters, information obtained on the basis of georadar survey; —identification of the features of the morphological structure of landscapes of technogenic origin associated with the extraction of copper ores.

Keywords Morphological structure of the landscape · Technogenic geosystem · Copper-crusted deposit · Remote sensing data · Georadar survey · Geochemical analysis of technogenic waters

1 Introduction

The subsoil of the Southern Urals is distinguished by a wide variety and significant mineral reserves, which allows it to be classified as a region of the Russian Federation, with a high share of mining industries and a positive balance of mineral exports. In

V. Petrishchev (✉) · G. Ponomareva · I. Kudelina
Orenburg State University, 460018 Orenburg, Russia
e-mail: wadpetr@mail.ru

V. Petrishchev
Orenburg Federal Research Center, Ural Branch of the Russian Academy of Sciense, 460000 Orenburg, Russia

© The Author(s), under exclusive license to Springer Nature Switzerland AG 2024

V. Karev (ed.), *Proceedings of the 9th International Conference on Physical and Mathematical Modelling of Earth and Environmental Processes*, Springer Proceedings in Earth and Environmental Sciences, https://doi.org/10.1007/978-3-031-54589-4_33

this regard, one of the urgent environmental problems of the Orenburg region is the problem of ecological optimization of subsurface use. The consequences of long-term mining of various minerals in the Orenburg region are currently manifested in the form of complex quarry-dump technogenic landscape complexes. Their study is of interest, both from the point of view of geochemical conditionality of the structure of technogeosystems, and assessment of the possibilities of reclamation and detection of abnormal concentrations of rare chemical elements.

2 Materials and Methods

The analysis of the morphological structure of landscape geosystems of technogenic origin is one of the directions of the study of technogeosystems, which will allow to identify and prove the key directions of their restorative dynamics. Of course, the morphological features of technogeosystems formed during the development of various types of ore mineral raw materials can be very different due to different landscape-geochemical ordination [1–3]. The study of technogeosystems of copper-crusted deposits both at the global level and in the Southern Urals has been carried out for a long time and concerns both aspects of the transformation of individual natural components and the study of inter-component interactions, as well as the study of morphological boundaries and the structure of landscapes as a whole [4–8].

To analyze the structure of the technogenic landscape of the Blyavinsky deposit, a Landsat 8 satellite image (dated 11.07.2011) was used, coinciding in time with the time of sampling of soil and water at the quarry dump complex of the deposit. To compare the remote sensing data, the classification capabilities were used, which was carried out in the Q-GIS program. At the same time, in order to add the downloaded image to the coordinate system, each of the channels used was saved in GeoTIFF format in the Global Mapper program. For classification, a mosaic of two combinations of channels was built: Red (4)/Blue (2) and SWIR3 (7)—Green (3)—Coastal/Aerosol (1). The first combination is an index of iron oxide content, and the second one distinguishes classes with exposed rocks [9, 10]. A raster calculator in Q-GIS was used to make mosaics of images. Further data processing was carried out by combining all polygons for each class. Visual identification of the placement of classes was carried out using orthophotoplans and topographic maps. The analytical part of the work was the comparison of the obtained classifications with the sampling indicators, which were output both through digital values at the sampling points and by constructing cartograms. The quarry-dump complexes of the small Blyavinsky deposit, when visually analyzing satellite information, show less sharpness in the severity of the boundaries of the technogenic landscape compared to the enclosing natural geosystems.

3 Results

The Blyavinskoye copper ore deposit is located 7.5 km northeast of the city of Mednogorsk, Orenburg region. The deposit is a steeply falling lenticular body with a capacity of up to 150 m, traced to a depth of 700 m. The pyrite lens lies between quartz albitophyres in the recumbent side and diabases and spilites in the roof. The deposit has developed a powerful (up to 300 m) weathering crust and an oxidation zone, stacked from top to bottom by zones: oxidized ores with a capacity of up to 40 m with a jarosite-destinesite subzone with a capacity of up to 12 m, a leaching zone with a capacity of up to 4 m and a zone of secondary sulfate-sulfide enrichment at depths of 50–300 m. Alumite and gypsum veins are characteristic of the host rocks of the lower oxidation zone. The deposit is overlain by Cretaceous glauconite sandstones with phosphorites and Paleogene trepels. The active interaction of sulfuric acid waters of the oxidation zone and phosphorites led to the formation of a zone of iron sulfophosphates—the so-called destinesite subzone. Ore mining at the deposit was stopped in the late 1970s, but hydrometallurgical extraction of copper was carried out up to the end of the 1980s.

Another method that was used in the study of technogenic geosystems of the Blyavinsky deposit was georadar profiling, which was carried out using the Loza—M georadar. The total length of the georadar survey routes was 1200 m. At the same time, only the upper second tier of the Western dump of the deposit was subject to profiling.

One of the most striking factors of differentiation of technogenic geosystems of the Blyavinsky deposit is the tiered (or level) organization of dump complexes. For the combination of channels 7-3-1, the slopes of the northern/southern exposure, parts of the lower and upper levels of the dump, elements of quasi-natural geosystems that play a host role in relation to the technogenic geosystem, fragments of hydromorphic geosystems of sub-basement watercourses are clearly distinguished.

A comparison of the degree of mosaic and contour of two dumps—the western and southern Blyavinsky deposits, show that a key role in the formation of the complexity of the morphological structure of the dump complexes is played by both natural, physical and geographical factors—a large height and a greater number of hypsometric levels, and lithogenic heterogeneity, determined primarily by correlation with the productive thickness of the quarry.

When analyzing the existing classes of spatial differentiation of the 4/2 channel combination, lithomorphic ediments of dump complexes are distinguished first of all—the foothills of the slopes of both the lower and upper levels of dump complexes, areas of storage of overburden rocks correlating with the upper levels of the quarry, large accumulations of substandard “poor” ores near the quarry.

During georadar profiling, the main goal was to identify the features of the occurrence of rocks belonging to the upper tier of the dump. The occurrence of loose rocks along the periphery of the dump was revealed. They were recorded both by georadar profiling and based on the classification of 4/2 iron oxides. On the contrary, a denser thickness of dump rocks is recorded in the central part. However, it was not without

anomalous inclusions, which filled a small depression in the central part of the dump and marked on the profile in the form of a deep crack.

4 Discussion

Comparison of the sampling data with the classification carried out by a combination of channels 7-3-1 and 4/2 shows the following results.

There is a fairly high correlation between classes within the dumps and in the walls of the quarry. This connection is most clearly recorded between the western side of the quarry and the extreme western slope of the Western Dump. Since it is noted that the upper ledge of the quarry and the first level of the Western dump belong to the same class, it is obvious that overburden rocks are located on this tier. This relationship is confirmed by comparing the classification by channels 7-3-1 and by combination 4/2, which confirms the high content of iron oxides on the upper ledge of the western side of the quarry and on the first tier of the Western dump of the Blyavinsky deposit.

When classifying the mosaic of channels 4/2, it is found that the second (upper) tier of the Western Dump belongs to the same class, completely all the tiers of the Southern Dump and deeper horizons of the quarry. Obviously, this is due to the formation of these parts of the dump complex from substandard "poor" ores. This relationship is clearly recorded by the selected soil samples and a high concentration of iron—250–300 mg/g in the dumps and 667 mg/l in the water samples of the stream coming out in the quarry.

Georadar profiling has shown that loose, strongly fractured soils and blocks of dense dump rocks separated by deep cracks are clearly differentiated. The heterogeneity of the dump thickness is fixed by fragments of hollows filled with loose sediments.

The use of complex data—remote sensing data, georadar profiling and geochemical analysis of soils and man-made waters—allows us to identify the features of the formation of the tiered structure of quarry-dump complexes of technogeosystems formed as a result of mining activities. At the same time, the selection of combinations of satellite images makes it possible to analyze the morphological structure of the technogenic landscapes of the deposit. Landscape-genetic layering and exposure asymmetry are among the most pronounced factors of landscape differentiation of technogenic geosystems of the Blyavinsky deposit, identified on the basis of surface classification when constructing combinations of satellite channels.

Less striking features of the boundaries of the technogeosystem of the dumps of the Blyavinskoye field with adjacent steppe landscapes are defined as more than half a century of completion dates of the field development, the development of defluction and erosion processes, especially on the slopes of the southern exposure with self-fouling of the slopes, as well as weak manifestations of reclamation measures on the southern dump.

The western dump of the Blyavinsky deposit as a whole is an extensive urban landfill of the city of Mednogorsk with a fairly extensive successional overgrowth of ruderal vegetation. At the same time, it is noted that the quarry lake of the Blyavinsky deposit has increased rapidly over the past 20 years due to atmospheric precipitation and groundwater.

One of the obvious reasons for the formation of such landscape-geochemical gradients, in our opinion, is natural leaching by precipitation, as well as phytoleaching with gradual accumulation within the sub-basement links of the catena. They form a kind of ring anomaly around the technogeosystem of the deposit and due to the flow into the system of local watercourses and drainage into the horizons of technogenic groundwater determine a relatively low impact on the soils of adjacent arable and pasture lands. It should also be noted that there is a certain closeness and isolation from the surrounding local basins of the formed system of watercourses of the Blyavinsky technogeosystem, which once again emphasizes the already established structure of intra and inter-component interactions of the technogenic landscape.

The type of technogeosystem of the Blyavinsky deposit, due to the unequal course of recovery processes on the western and southern dumps, has both destructive and regenerating features. For the quarry of the deposit, there is an active overgrowth of the slopes of the sides at all levels, which is confirmed by positive NDVI trends. The western and southern dumps are characterized by asymmetry of overgrowth trends with maximum values along the northern slopes. It is determined by the increased insolation of the southern slopes, the outputs of man-made waters during self-leaching, the sharp tiered differentiation of overburden clay rocks and substandard "poor" ores.

5 Conclusions

Thus, a new type of mining and industrial geosystems is being formed in the Orenburg Region, associated with ore deposits where non-ferrous metal ores have been or are being mined. Reclamation measures within the established technogenic landscape complexes are associated with the need for a comprehensive transformation of all key components—the lithogenic base, including overburden deposits and "poor" ores with heavy elements exceeding the background natural values, technogenically metamorphosed groundwater and formed sub-basement reservoirs, developed specific complexes of technogenic soils.

Acknowledgements The article was prepared with the support of the Russian National Science Foundation grant No. 23-27-10,006 "Analysis of the formation of technogenic geosystems as a result of the development of ore deposits in the Orenburg region in order to rationalize reclamation measures".

References

1. A.I. Perelman, V.N. Levin. Landscape Geochemistry and the Problems of Genesis, Exploration, and Ecology of Uranium Deposits. Geology of Ore Deposits. **41** (1999)
2. L. Willies. The Industrial Landscape of Rio Tinto, Huelva, Spain. **12**. (1989)
3. E. LeClerc, Y.Wiersma, Assessing post-industrial land cover change at the Pine Point Mine, NWT, Canada using multi-temporal Landsat analysis and landscape metrics. Environmental Monitoring and Assessment. **189**. (2017)
4. M. Opekunova, V. Somov,E. Papyan. Soil Contamination in the Impact Zone of Mining Enterprises in the Bashkir Transural Region. Eurasian Soil Science. **50**. (2017)
5. I.Gorokhova, T. Borisochkina, E. Shishkonakova. Assessment of the State of Urban Ecosystems on the Basis of Remote Sensing Data. Eurasian Soil Science. **46**. (2013)
6. A. Kutliahmetov. Bioconservation Of Technogenic Metals By Birch On Industrial Waste Dumps In Bashkortostan. (2020)
7. I.Zenkov, B.Nefedov, Y.Yuronen, E.Kiryushina, V.Vokin,. Technologies of waste dump terrain formation for forest recultivation. Ecology and Industry of Russia. **19**. (2015)
8. A. Mammedov, S. Musaev, Y.Poshivaylo, G.Fedotov. GI support of geological exploration of non-ferrous metal ore deposits. InterCarto. InterGIS. **26**. (2020)
9. T.Adamovich, G.Kantor, T.Ashikhmina, V.Savinykh. The analysis of seasonal and long-term dynamics of the vegetative NDVI index in the territory of the State Nature Reserve "Nurgush". Theoretical and Applied Ecology. **18**. (2018)
10. Y.Murthy, K.Mallick. Interpretation of Landsat MSS data in an iron-ore-bearing zone in Goa, India.. Geophysical Prospecting. **32**. (1984)

Kurtmaly Gold Placer: Geology, Geochemical Features of the Metal, Relationship with Indigenous Sources (Southern Urals, Russia)

A. V. Snachev

Abstract The article briefly outlines the geological structure of the Aktash ore field (East and West Aktash bedrock occurrences and the Kurtmaly placer). It is shown that the East Aktash ore occurrence belongs to the gold-quartz-sulfide formation. The richest mineralization is localized either along the contacts of the gabbro-diorite dike or in it itself. In terms of chemical composition, gold is of medium fineness (821–859) and is most often found in the composition of quartz-sulfide or quartz-carbonate mineral associations. The content reaches tens and even hundreds of grams per ton. Ore bodies of the West Aktash ore occurrence are represented by quartz metasomatites with sulfides and stockwork-type quartz veinlets. Abnormally high gold contents were found in zones of silicification development. The gold is high-fineness (880–998), its typomorphic feature is a consistently high bismuth content (0.1–0.3%), which is characteristic of quartz veins of the gold-quartz formation of the Southern Urals. The Kurtmaly placer, located in the valley of the Aktash creek, contains gold particles of both medium roundness and completely unrounded. Their chemical composition is noticeably different from the gold from nearby ore occurrences; it is low-grade (550–600) gold. The primary sources for the placer could be zones of quartz-sulfide mineralization, brown iron ores of the Kurtmaly deposit, as well as carbonaceous shales of the Avzyan and Zigazin-Komarovo Formations. In conclusion, the article substantiates the high prospects of the Aktash ore field for both primary and placer gold.

Keywords Southern Urals · Gold · Aktash ore field · West Aktash ore occurrence · East Aktash ore occurrence · Kurtmaly placer

The Aktash ore field is located in the Riphean deposits of the Bashkir meganticlinorium (Southern Urals) and is represented by the East Aktash and West Aktash gold ore occurrences, as well as the Kurtmaly placer (Fig. 1). The main structural element

A. V. Snachev (✉)
Institute of Geology, Ufa Federal Research Centre of the RAS, Ufa, Russian Federation
e-mail: savant@rambler.ru

© The Author(s), under exclusive license to Springer Nature Switzerland AG 2024

V. Karev (ed.), *Proceedings of the 9th International Conference on Physical and Mathematical Modelling of Earth and Environmental Processes*, Springer Proceedings in Earth and Environmental Sciences, https://doi.org/10.1007/978-3-031-54589-4_34

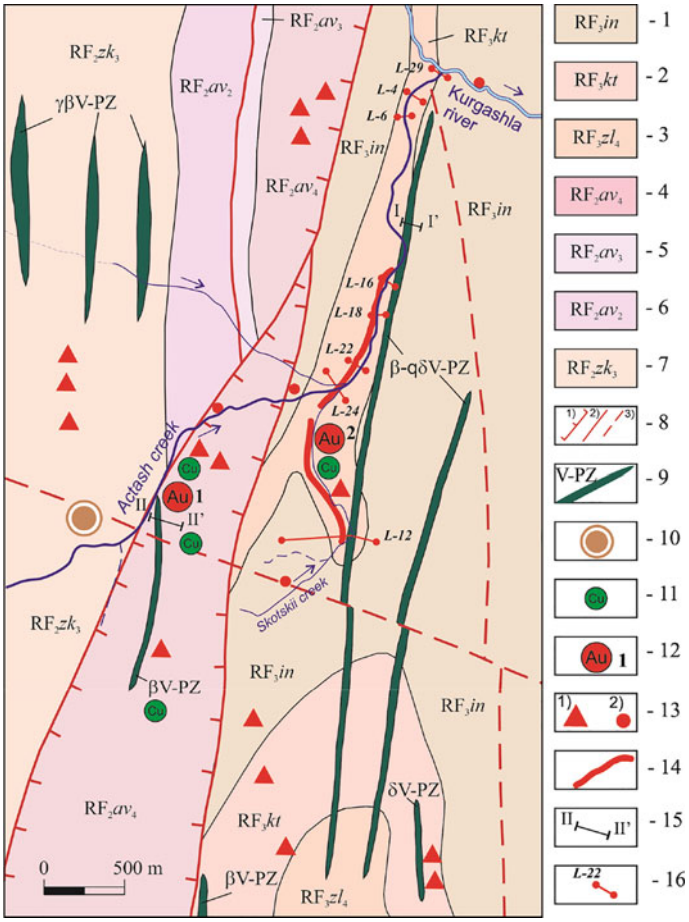


Fig. 1 Geological map of the Aktash ore field (according to T.M. Bikshanov, with modifications by the author)

of the ore field is a large anticlinal fold, the eastern wing of which is crossed by the Karatash thrust, intruded by gabbro-dolerite dikes.

Legend: 1—Inzer Formation (quartz and quartzite-like sandstones, interbedded shales and siltstones), 2—Katav Formation (limestones, marl interlayers), 3—Zilmerdak Formation, Bederyshi Subformation (sericite-chlorite-quartz shales, clayey-sericite-quartz shales), 4–5—Avzyan Formation: 4—Kutkur subformation (sericite-clayey, sericite-quartz shales), 5—Ushakovo Subformation (dolomite, limestone, shale interlayers), 6—Maloinzer Subformation (carbonaceous-clayey, clayey shales, interlayers siltstones), 7—Zigazino-Komarovo Formation, Tukan Subformation (interlayering of sericite-quartz, carbonaceous shales, siltstones), 8—tectonic disturbances (1—thrusts, berg strokes directed towards the fall of the fault plane; 2—other faults; 3—supposed), 9—intrusive rocks of the V-PZ complex (diabases;

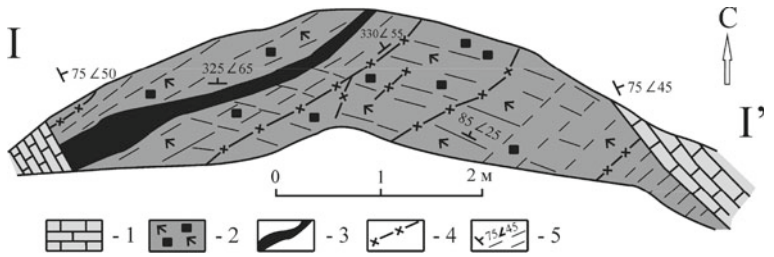


Fig. 2 Section of the East Aktash ore occurrence along line I-I'. Legend: 1—limestones of the Katav Formation, 2—gabbro-diorites with pyrite inclusions, 3—quartz vein, 4—quartz veinlets, 5—bedding elements

gabbro-diabases, quartz diorites), 10—Kurtmaly deposit of brown iron ores, 11—copper ore occurrences, 12—Aktash gold ore occurrence (1—western, 2—eastern), 13—increased gold contents (1—primary, 2—schlich), 14—contour of the Kurtmaly placer, 15—lines of wells and pits, 16—lines of geological sections.

Structural control is clearly demonstrated in the placement of gold mineralization at the **East Aktash** ore occurrence (Fig. 1). It belongs to the gold-beresitic type and is confined to a series of gabbro-diorite dikes cutting through the Upper Riphean limestones of the Katav Formation [8]. Quartz-sulfide mineralization with industrial gold contents is established either in the endo- and exocontacts of the dikes themselves, or in areas where they are crossed by latitudinal faults (Fig. 2). It was formed in the second (late) stage of mineral formation, when the bulk of quartz and sulfide minerals (pyrite and, less commonly, chalcopyrite) were formed. The early stage that preceded it was characterized by the uniform development of fine-crystalline dissemination of pyrite and sericite in the rocks of the dike complex.

Several generations of quartz are known at the ore occurrence [[1, 2, 10]], including: early (quartz-I), developed in limestones at the contact with gabbro-diorites and forming thin veinlets; intermediate (quartz-II), also represented by thin pyrite-ankerite-quartz veinlets in gabbro-diorites, and late (quartz-III), composing fairly large (up to 1.5 m) ladder veins made of milky white quartz.

Native gold is most often observed in beresitized gabbro-diorites (cutting limestones of the Katav Formation) as part of a quartz-sulfide mineral association, where its content in individual samples reaches tens of grams per ton (Table 1). The form of native gold segregations is the most diverse: at the contact of pyrite grains with quartz, the lamellar (cracked) form of gold grains predominates; in pyrite—lump-like and isometric-crystalline segregations; in quartz there is predominantly film gold. The size of gold particles does not exceed 1 mm. In terms of chemical composition, gold is of medium fineness (821–859), its characteristic feature is high silver content (14–17%). Other impurities are represented by copper (0.02–0.1%), bismuth (0.07–0.03%), tellurium (0.06–0.01%); the silver-gold ratio is 0.16–0.21 [8].

In one of the samples, the presence of mercury (0.23%) and arsenic (0.03%) was detected. The mineralization belongs to the gold-quartz-sulfide formation and,

Table 1 Content of trace elements in gold of various types of the Aktash ore field, % [8]

	East-Aktash	West-Aktash	Kurtmaly placer
Number of samples	11	13	8
Au	84.22 81.89–86	93.24 86.6–100	77.5 74.3–83.7
Ag	15.19 13.78–17.4	6.79 0.21–12.56	22.04 15.5–25.4
Hg	0.23	0.11	0.2 0.15–0.3
Se	–	0.05	0.04
Cu	0.045 0.02–0.1	0.06 0.01–0.11	0.04 0.03–0.06
Bi	0.15 0.07–0.3	0.17 0.07–0.31	0.09 0.07–0.12
Te	0.08 0.06–0.1	0.05 0.02–0.08	0.06 0.04–0.07
As	0.03	0.03	0.07 0.03–0.1
Total	99.59 98.65–100.68	99.74 99.17–100.6	99.7 98.7–100.8
Ag/Au	0.18 0.161–0.212	0.08 0.002–0.15	0.29 0.19–0.34
Gold fineness	845.5 821–859	934.6 873–998	777.4 747–842

Note The numerator is the average content; the denominator is the limits of fluctuations. Analyzes were performed in the IGEM mineralography laboratory on a "CAMEBAX" microprobe analyzer (analyst A.I. Tsepin)

based on its chemical composition, can be attributed to the crustal type, formed in near-surface conditions.

The **West Aktash** ore occurrence is located 1.0 km west of the East Aktash, in the development zone of the Karatash thrust and belongs to the gold-jasperoid formation type (Fig. 3). It lies in terrigenous-carbonate deposits of the Avzyan formation.

According to morphological characteristics, the ore occurrence is a small-sized stockwork zone elongated in the submeridional direction, in which 2–3 ore bodies can be identified. Ore bodies are represented by quartz metasomatic rocks with sulfides and quartz veinlets with abnormally high gold contents. In the eluvial deposits of quartz apocarbonate metasomatites, several of its signs were found, irregular and lumpy in shape with a low flatness coefficient, semi-rounded, uneven, rough surfaces.

Gold belongs to the small (0.2 mm) and medium (1.2 mm) size classes, has a golden-yellow color and high fineness (880–998) [8]. The silver content (Table 1) in gold grains varies from 0.2 to 12% (gold predominates with 0.2–1.1% Ag). The distribution of silver in gold grains is uniform, the silver-gold ratio is low and ranges from 0.002 to 0.14, not exceeding 0.1 in most definitions. In addition to silver, the

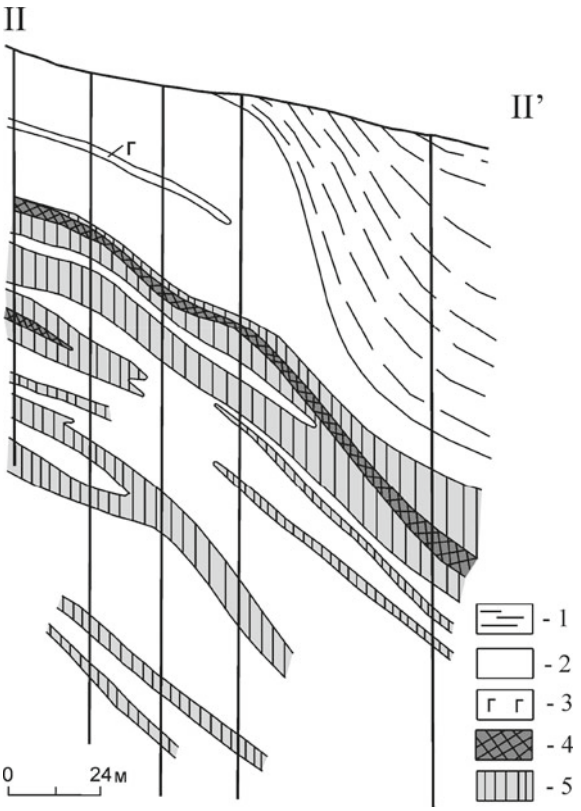


Fig. 3 Schematic geological section of the West Aktash ore occurrence along line II–II′. Legend: 1—carbonaceous-clayey shales, 2—clayey and carbonate-clayey shales with sandstone interlayers, 3—gabbro-diabase, 4—barite, 5—apocarbonate quartz metasomatites (jasperoids)

presence of low contents of copper, mercury, tellurium and arsenic was established. A typomorphic feature of gold is the consistently high content of bismuth impurities (0.1–0.31%). A similar composition of gold is often found in quartz veins of gold-quartz or gold-sulfide-quartz formations, widely represented in the Urals.

The **Kurtmaly placer** is part of the Bainazarovo placer field and is located in the valley of the Aktash Creek, right tributary of the Kurgashla River (right tributary of the Belaya River) [3]. In orographic terms, degree of dissection and morphological features, the work area belongs to the mid-mountain and low-mountain types of relief. From the west, the boundary of the watershed of the Aktash Creek is the Yurmatau ridge (absolute elevation marks 700–750 m), from the south—the mount of Aktash (545.5 m), and from the east, from the valley of the Belaya river it is separated by an unnamed ridge (582–597 m).

The geomorphological appearance of the valley indicates its favorable location for placers. Gold was discovered in the alluvial formations of the Aktash Creek, draining a complex of gabbro-dolerite dikes, brown ironstones of the Kurtmaly deposit, as well as carbonaceous shales of the Zigazino-Komarovo and Avzyan formations (Fig. 1). According to Masalova, the placer was mined by miners using open and underground

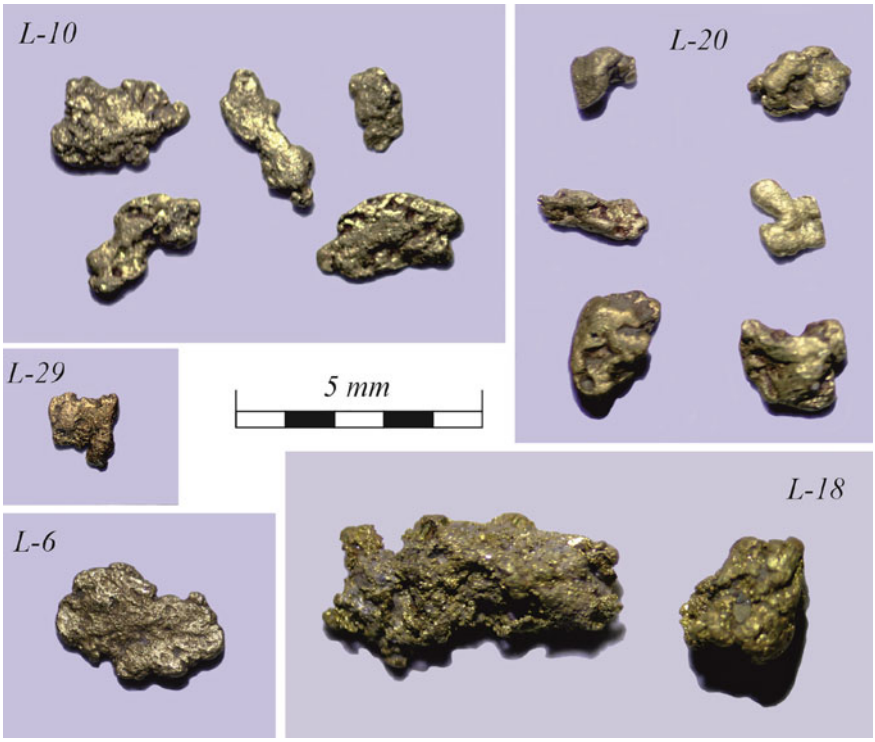


Fig. 4 Photos of large native gold from the Kurtmaly placer. *Note* See the profile numbers in Fig. 1

workings using the muscular method. From 1885 to 1900, 53.2 kg of gold was mined, in 1908—11.2 kg and in 1936—0.6 kg of gold with an average content of 0.7 to 4.3 g/m^3 per layer. The length of the development contour is 750 m, the width is 30–40 m, the thickness of the loose sediments containing the placer is about 5 m. The highest values of the content of the useful component are confined to the near-rout part of the section, represented by sand-boulder-pebble material, slightly clayey. The raft rocks are deposits of the Inzer and Katav formations of the Upper Riphean. The average gold content in pit holes is 125 mg/m^3 per rock mass with a thickness of 3.0 to 3.5 m; in individual penetrations, metal concentrations reach values of up to 1221 mg/m^3. Gold grains are found both smooth and flattened with medium roundness, and completely unrounded with a rough surface (Fig. 4). Their color ranges from golden-yellow to red-yellow, their sizes reach 6 mm, but most of them are fine gold (0.1–0.2 mm).

The chemical composition of some placer gold is fundamentally different from gold of the formation types described above. They are characterized by low fineness (550–600), refinement on the surface with high-grade gold, as well as intergrowths of several grains (Fig. 5). The silver content in gold particles is stable and in most determinations is 20–25%; silver-gold ratio—0.2–0.36 (Table 2). Among other impurities,

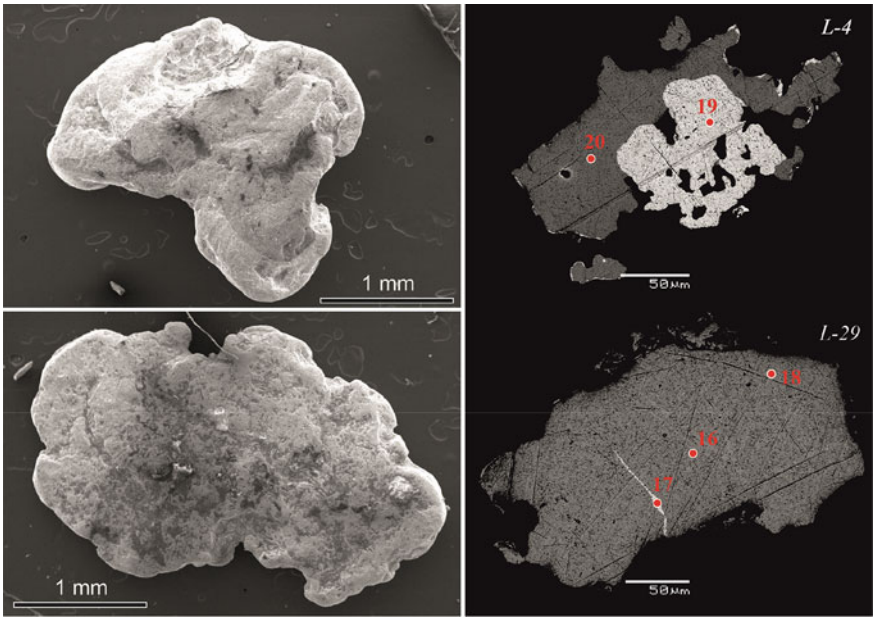


Fig. 5 Photos and sampling points for native gold from the Kurtmaly placer. *Note* the images were taken in back-scattered electrons on a scanning electron microscope, see the profile numbers in Fig. 1

some samples contain low levels of tellurium (0.04–0.07%), arsenic (0.1%), copper (0.04%), selenium (0.04%) and mercury (0.15–0.3%) (Table 1).

The reduced fineness value and the composition of trace elements indicate that part of the metal belongs to the gold-sulfide formation type, which was not noted in the Western and Eastern Aktash deposits. Judging by the shape of the gold particles, the metal was transported a short distance from the supposed root source. They could be zones of quartz-sulfide mineralization and brown iron ores of the Kurtmaly deposit, as well as carbonaceous shales of the Avzyan and Zigazino-Komarovsky formations. The latter contain high contents of silver and gold [10, 12]. In addition, independent silver minerals were discovered within the Uluelga-Kudashman zone (located to the north) [4].

We find confirmation of this when studying concentrates washed from alluvium of the Aktash, Skotskii Creek and their tributaries in the zone of development of deposits of the Katav and Zagizino-Komarovo Formations, where increased concentrations of pyrite, often unoxidized and weakly oxidized, were found. Pyrite is represented by cubic crystals, often with characteristic shading on the faces. The following are widely present in all concentrates: ilmenite, rutile, anatase, sphene, leucoxene; as well as single signs of zircon, monazite, and cinnabar. The latter are typical minerals for siliceous-carbonaceous sediments of the Zigazino-Komarovo formation of the Bashkir meganticlinorium [[4, 5, 7, 9]].

Table 2 Results of microprobe analysis of gold particles from the Kurtmaly placer (wt.%)

Profile No	Note (Analysis No.)	Ag	Au	Total	Ag/Au	Gold fineness
L-4	Au (№19)	0.91	99.30	100.21	0.01	984
	Au–Ag (№20)	22.74	79.10	101.83	0.29	656
L-6	Center	3.79	93.56	97.34	0.04	931
	Rim	0.65	99.33	99.97	0.01	988
L-12	Center	7.00	92.83	100.22	0.08	879
	Rim	7.72	90.99	99.11	0.08	866
L-16	Center	23.62	76.18	99.80	0.31	610
	Rim	22.48	75.89	98.37	0.30	606
L-18	Center	25.20	73.70	98.90	0.34	619
	Rim	26.38	73.93	100.31	0.36	623
L-22	Center	18.21	81.64	99.85	0.22	585
	Rim	17.21	81.16	98.37	0.21	581
L-24-1	Center	12.33	86.21	98.53	0.14	558
	Rim	11.59	85.97	97.57	0.13	555
L-24-2	Center	11.41	88.80	100.21	0.13	552
	Rim	10.67	88.04	98.71	0.12	550
L-29	Center (№16)	12.33	88.06	100.40	0.14	796
	Vein (№17)	0.34	100.38	100.72	0.00	994
	Center (№18)	10.64	90.39	101.03	0.12	823

Note The analysis was performed in the laboratory of "Physical Methods for the Study of Minerals" of Moscow State University on a CAMEBAX SX50 microprobe from CAMESA using standards (analyst I.A. Bryzgalov). The accuracy of the research method is within ±0.01%, analysis conditions: accelerating voltage 20 kV, probe current 30 nA

The data presented show that the Aktash ore field may turn out to be very promising for the discovery of the most important industrial gold deposits in the Urals. Within its boundaries there is gold of three discrete fineness groups, differing in the content of impurity elements, the size and shape of gold particles, and the formational affiliation of the primary sources of the metal. All gold deposits, in their chemical composition and temperature regime of formation, fall within the scope of gold analyzes of the actual gold ore formations of the Urals (Fig. 6).

The prospects of the East Aktash ore occurrence are not limited to its near-surface horizons that have been explored to date. Along the strike of the gold-bearing dike body, a rare system of exploration ditches and pits was passed, which exposed a stockwork zone of gold-quartz-sulfide mineralization to a depth of only a few meters. Obviously, the depth of distribution of mineralization, by analogy with similar objects, will be commensurate with the length of the stockwork and is limited by the exocontact of the gabbroic intrusion assumed at the depth. If the gabbro-dolerites of the East Aktash ore occurrence are considered as a manifestation of the vein facies of

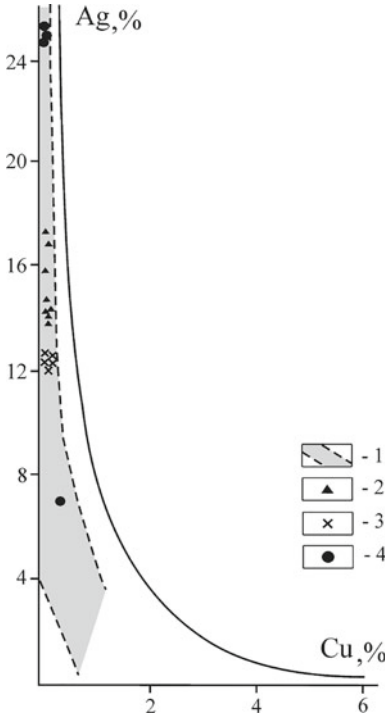


Fig. 6 The ratio of silver and copper content in gold of various formation types of the Aktash ore field. Note: 1—gold analysis field for gold deposits of the Urals formation [Murzin, Malyugin, 1983], 2–4—composition of gold deposits: 2—East Aktash ore occurrence, 3—West Aktash ore occurrence, 4—alluvial deposits of the Aktash Creek and its tributaries. The solid line divides the field of compositions of gold grains with and without decomposition structures of gold-silver-copper solid solutions

a producing intrusion of a gabbroic formation hidden at depth, then the question of intrusive magmatism and metallogeny of the Riphean age becomes of utmost importance.

Within the West Aktash ore occurrence, especially in its northern part, there is an anomalous concentration of gold indicator elements—Ba, Cu, Zn, Mo, Ag. Mineralization points with gold contents of up to 2 g/t are also known here. The study of ore occurrences using single drill holes did not give positive results; the tested intervals of quartz-sulfide mineralization turned out to be non-gold-bearing. However, in quartz metasomatites exposed by pits on the northern flank of the ore occurrence, signs of large gold were discovered, and in the host rocks, anomalous concentrations of one or two orders of magnitude higher than the clarke values were established. The Aktash latitudinal deep structure passes through the northern flank of the ore occurrence—the most important tectonic element of the area, represented on the surface by a zone of increased rock fracturing and fragments of sublatitudinal faults with a high degree of hydrothermal changes in sedimentary deposits.

All this does not exclude the possibility of discovering in this part an ore occurrence that was not exposed by erosion of gold mineralization in quartz metasomatites.

Acknowledgements The work was carried out within the framework of the state order on the Topic no. FMRS-2022–0011.

References

1. Ahmedova RR, Michurin SV, Shiyanova EO, Sergeeva ND, Sharipova AA (2023) Crystal-chemical, mineralogical and geochemical features of dolomites of the Avzyanskaya suite of the Middle Riphean (Southern Urals). Vestnik Voronezhskogo gosudarstvennogo universiteta. Seriya: Geologiya—Proceedings of Voronezh State University. Series: Geology, no. 3, pp. 40–56 DOI: https://doi.org/10.17308/geology/1609-0691/2023/3/40-56
2. Bobokhov AS, Bobokhova RB, Gorozhanin VM, Michurin SV (1993) Thermal-gas-geochemical and isotopic search criteria for pyrite and gold-sulfide mineralization (using the example of deposits in Bashkortostan). Ufa: UFRC RAS, 23 p.
3. Kazakov PV, Salikhov DN (2006) Minerals of the Republic of Bashkortostan (placer gold). Part 2. Ufa: Gilem. 288 p.
4. Kovalev SG, Vysotsky IV, Michurin SV, Kovalev SS (2013) Geology, mineralogy and metallogenic specialization of carbonaceous strata in Uluelga-Kudashmanovskaya zone (west slope of Southern Ural). Lithosphere (Russia), No. 3, p. 67-88.
5. Kovalev SG, Timofeeva EA, Pindyurina EO (2009) Monazite mineralization of the western slope of the Southern Urals. Geological collection No. 8: Information materials of the Institute of Geology UFRC RAS. Ufa: DesignPolygraphService, p. 138–144.
6. Murzin VV, Malyugin AA (1983) New data on the unstability of natural solid solutions of the system Ag-Au-Cu at 350 °C. Doklady Akademy Nauk SSSR 269(3). p. 723-724.
7. Palenova EE, Novoselov KA, Belogub EV, Blinov IA, Grigorieva SD (2018) Mineralogy of alluvial sediments of Avzyan gold region (the Southern Urals). Litosfera, 18(3), 459-474. DOI: https://doi.org/10.24930/1681-9004-2018-18-3-459-474.
8. Rykus MV, Snachev VI (1999) Gold of the western slope of the Southern Urals. Ufa: UFRC RAS, 170 p.
9. Savelyev DE, Musabirov II, Davletshin AR (2017) On the mineralogy of carbonaceous sediments of the Zigazino-Komarovsky formation on Mount Yalangas (Southern Urals). Geological collection No. 13: Information materials of the Institute of Geology UFRC RAS. Ufa: DesignPolygraphService, p. 130–139.
10. Sharipova AA, Michurin SV, Krupenin MT, Garaeva AA, Kanipova ZA (2017) Quartz Reef from Gold Occurrences in Riphean Deposits of the Avzyan Ore Region (South Urals): Mineralogical and Thermocriometric Features. Bulletin of Perm University. Geology, Vol. 16, No. 3. p. 216-232 DOI: https://doi.org/10.17072/psu.geol.16.3.216.
11. Snachev AV, Puchkov VN (2010) First findings of palladium-gold-REE ore mineralization in precambrian carbonaceous shales on the western slope of the Southern urals. Doklady Earth Sciences. Vol. 433. Part 1. pp. 866-869. DOI: https://doi.org/10.1134/S1028334X10070044.
12. Snachev AV, Snachev VI, Ardislamov FR (2015) Forecast Reserves of Gold in Komarovskian Carbon Sediments of Beloretsky Metamorphic Complex (The South Urals). Georesursy [Georesources]. No. 4(63) Vol.1. p. 99–104. DOI: https://doi.org/10.18599/grs.63.4.16

Experimental Study of the Distribution of Hydrocarbons Over the Water Surface



V. P. Pakhnenko

Abstract The process of oil spill response from the water surface is usually to collect the maximum amount of spilled oil in a cost-effective and environmentally friendly manner. In this paper we have conducted and described experimental studies of oil product spreading on the water surface in two principal cases, when the spill on one side is limited by a wall (for example, the spill comes from one side of the river in natural conditions) and when the spill is axisymmetric and the oil slick spreads over the surface in an unrestricted manner. The obtained experimental data were compared with the axisymmetric spreading theory.

Keywords Oil products · Emergency oil spills · Theoretical model · Experimental work

1 Introduction

In today's reality, the state of the hydrosphere is rapidly deteriorating. This situation is caused by the following factors: use of ocean waters for industrial and domestic purposes, fishing, excessive abuse of plastics, oil extraction, catching fish, which every year depletes its reserves in the ocean. The development of technological progress makes the issues of environmental safety even more urgent. Human activity inevitably leads to man-made disasters that cause huge negative changes in the environment.

At present, the great danger is posed by spills of oil and its refined products, the volume of emergency discharges of which is continuously growing and reaches critical values in man-made disasters (accidents at oil fields, ruptures of pipelines). Environmental disasters related to accidents of large-capacity tankers (Aegean Captain, Atlantic Empress, Prestige, Exxon Valdez and others), which were accompanied by

V. P. Pakhnenko (✉)
A.Yu. Ishlinsky Institute for Problems in Mechanics, Prospect Vernadskogo 101-1, Moscow 119526, Russia
e-mail: pvpmos@gmail.com

© The Author(s), under exclusive license to Springer Nature Switzerland AG 2024

V. Karev (ed.), *Proceedings of the 9th International Conference on Physical and Mathematical Modelling of Earth and Environmental Processes*, Springer Proceedings in Earth and Environmental Sciences, https://doi.org/10.1007/978-3-031-54589-4_35

large-scale oil spills and significant consequences for the ecosystems of large areas of the world ocean, have occurred many times in history. In turn, the consequence of such serious accidents was a tightening of modern requirements for ensuring the safety of marine oil transportation.

The most significant and destructive impact on ecosystems is caused by oil spills in the water area located directly near the coastline—the consequences affect not only organisms living in the water, but also the flora and fauna of the coastal zone. Elimination of consequences of accidents in such areas requires much more time (decades) and efforts, and, consequently, large financial investments.

In order to reduce possible negative consequences, special attention should be paid to the study of methods of localization and liquidation of oil product spills and development of an additional set of measures for collection and utilization of hydrocarbons that got into the external environment. As well as experimental and theoretical study of the processes of hydrocarbon spreading dynamics on the water surface, so that the subsequent measures to eliminate hydrocarbons were more effective.

In this paper we have conducted and described experimental studies of spreading of oil products on the water surface in two principal cases, when the spill on one side is limited by a wall (for example, the spill comes from one side of the river in full-scale conditions) and when the spill is axisymmetric and the oil slick spreads over the surface in an unrestricted manner.

In most natural situations, oil spills occur on a two-dimensional surface (open water spaces of bays, lakes, seas, etc.), but special conditions are possible (canals, rivers, narrow aquariums, etc.) when the spill surface can be considered one-dimensional [1]. This fact leads to the need for separate models for one-dimensional and two-dimensional spreading.

Evaporation of oil products or their individual components, leading to a significant change in the physical and chemical properties of the spilled substance [2, 3], requires complication of the mathematical model in the direction of taking into account the reduction in the mass of the spilled substance and the spatial and temporal dependence of its thermodynamic parameters.

The mathematical model in the presence of water flows requires additional complication, since it is necessary to take into account the visco-advective transport of the oil slick by the near-surface water flow [4, 5].

In this paper, a simplified mathematical model is presented to investigate the main dynamic parameters of the spreading process. In this model, the chemical composition and all thermodynamic parameters of the medium are assumed to be constant values, the mass of the spreading slick is assumed to be unchanged, and all media are homogeneous and isotropic.

Since the characteristic velocities of matter transport accompanying the oil spill process are much lower than the speed of sound in any medium, all media are considered incompressible in any propagation model. A comparison with experimental results describing the dynamics of motor oil and crude oil spills is also presented. To obtain these results, a large number of experiments were performed in laboratory conditions for different oils and crude oils with different initial parameters of the

experiment (type of oil product, viscosity, different temperatures of oil products and water surface, different water salinity).

2 Model of Axisymmetric Oil Spreading

A series of experiments were conducted with different types of organic and mineral oils and directly with crude oil. Water of different temperatures, both fresh and with different salinity values to simulate marine and oceanic conditions was used as a base fluid.

The study of the dynamics of immiscible admixture spreading over the water surface was carried out in a rectangular container with a length of 50 cm, width of 40 cm and depth of 15 cm. To avoid glare from the water surface and hydrocarbon staining, the liquid surface was illuminated from above by several spaced light sources placed near the container on the sides and directly above it.

The experimental method involved applying various amounts of Volga M8B-SAE 20 API motor oil ($\rho_0 = 883.7\text{kg/m}^3$, $\upsilon_0 = 3.34 \bullet 10^{-4}\text{m}^2/\text{s}$, , at various ranges of water temperature and salinity) and crude oil from the Mamontovskoye field ($\rho_0 = 878\text{kg/m}^3$, $\upsilon_0 = 2.15 \bullet 10^{-5}\text{m}^2/\text{s}$, , at different ranges of water temperature and salinity) to the surface of a known volume of water and further monitoring of its propagation over the liquid surface. The course of the experiments was recorded using a digital video camera in automatic mode for 4 h, shooting at a rate of 120 frames per minute, and the obtained sequences of frame arrays were processed by various software and analyzed. The position of the oil slick was recorded using the photometry method of processed images obtained from the original frames by batch processing methods (Fig. 1).

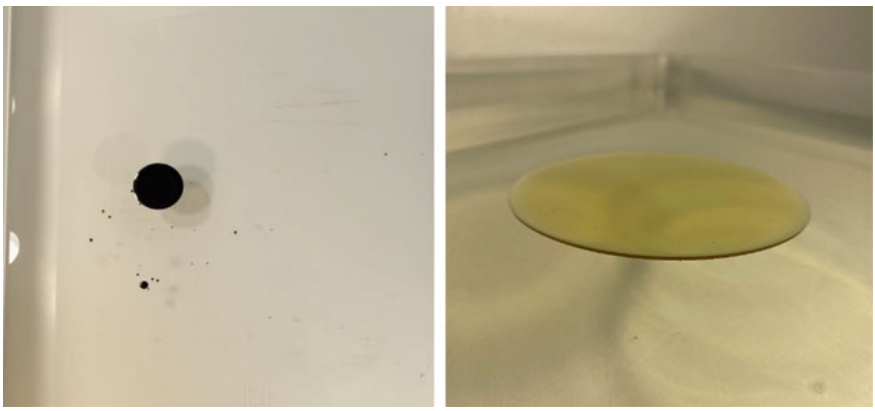


Fig. 1 Clear shots from experiments with motor oil and oil and oil (small volume of oil products) for the case of axisymmetric spreading

The variable parameters of the experiments were oil product volume, water temperature and salinity. In each series of experiments, two of the above parameters were recorded, and the time dependence of the pollution slick spreading area was measured for different values of the remaining parameter.

To eliminate random errors, the experimental data were further processed using the modified shift algorithm (MSA) [7], which showed stable performance in extracting a useful signal from the noise background up to a signal-to-noise ratio of −15 dB.

Only the most characteristic experimental dependencies from many measurement results are summarized below.

In Fig. 2a, the red dots show the experimental dependence of the spill area of Volga M8B-SAE 20 API motor oil on time. The data are normalized by their maximum value, the black dots are the result of processing the set of red dots by the MSA algorithm. All subsequent experimental data presented here were also subjected to MSA algorithm processing.

As can be seen, the behavior of the curve $\overline{S}(t)$ in Fig. 2a corresponds well to the dependence (12) illustrated in Fig. 2b.

According to (12), the deviation from the equilibrium position $F = F_*$ is described by two decreasing exponents $\exp(-a^2t + \mu t)$ and $\exp(-a^2t - \mu t)$. At initial time instants, the contribution from the term containing $\exp(-a^2t - \mu t)$ decreases most rapidly. At subsequent time instants, when the main contribution to the deviation is from the term containing $\exp(-a^2t + \mu t)$, the rate of decrease of the deviation decreases compared to the initial time instants. This fact is reflected in the behavior of the curve in Fig. 2b.

The oscillatory regime described by relation (11) was also observed experimentally, and its processed data are presented in Fig. 3 a.

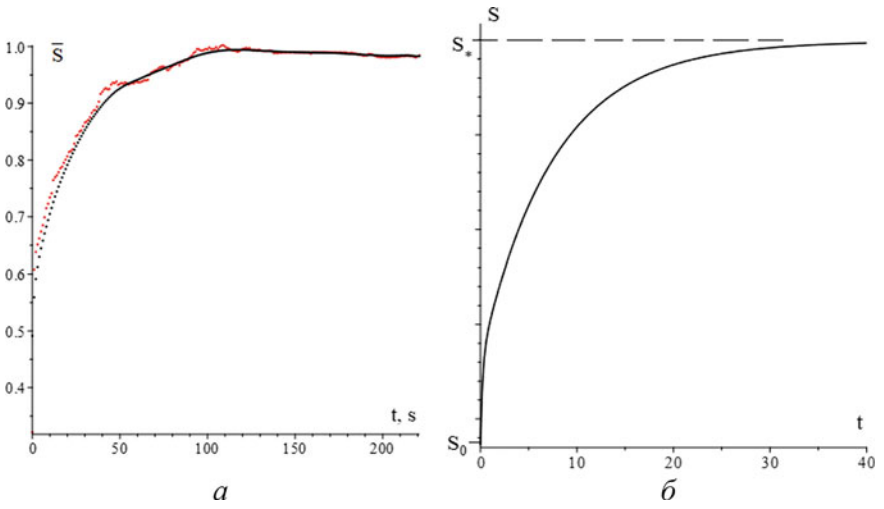


Fig. 2 a—Experimental (red) and processed (black) spreading data of Volga M8B-SAE 20 API machine oil, b—Analytical result (calculated on the basis of (12), $S = F^{1/2}$)

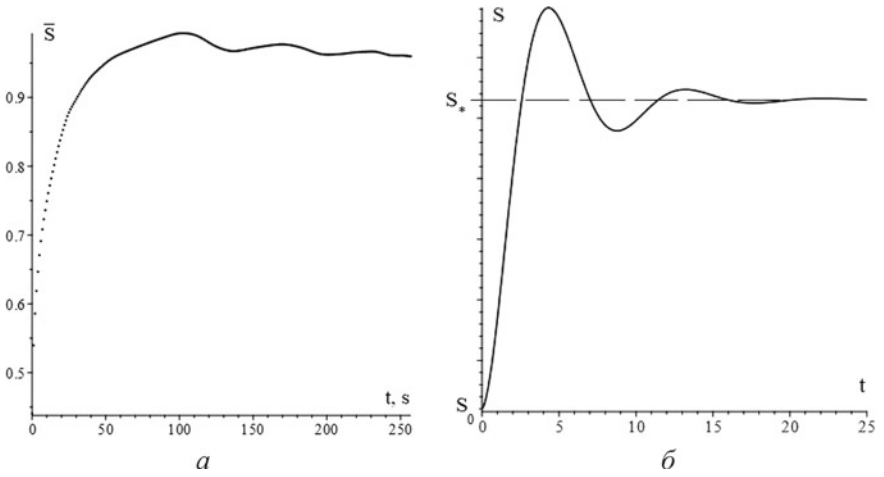


Fig. 3 **a**—Processed Volga M8B-SAE machine oil spreading data, b—Analytical result (Calculated on the basis of (11), $S = F^{1/2}$)

It can be seen that the spill area grows with time, starting from a certain value S_0, reaches the value S_*, overshoots it by inertia, after which a return force occurs, the acceleration $\ddot{F}$ changes sign (becomes negative), the spill area starts to decrease, reaches the value S_*, overshoots it by inertia, after which a return force occurs, the acceleration $\ddot{F}$ changes sign (becomes positive), the spill area starts to increase, reaches the value of S_*, overshoots it by inertia, the acceleration $\ddot{F}$ changes sign (becomes negative), etc. д. The amplitude of the oscillation gradually decreases due to energy transfer from the oil slick to the water (term $a^2\dot{F}$ in Eq. (8)). Eventually, the oil slick acquires its stationary size.

The difference in the behavior of the confined spill region in Figs. 2 and 3 is explained by the fact that in the case of solution (12) the rate of transition of kinetic energy of oil fuel to kinetic energy of water (due to the shape resistance phenomenon) is significantly greater than the rate of transition to surface energy at the interface of the contacting media, in contrast to the case of solution (11), where an inverse correlation of these rates is observed.

Crude oil exhibits a different behavior associated with unrestricted hydrocarbon spillage, the experimental data for which are shown in Fig. 4 a. Since the size of the laboratory setup does not allow tracking the spill over a large area the comparison with the theoretical results (12, 13) is made only for small time intervals from the onset of the process (since oil spreads at a smaller initial volume, over a much larger area compared to oil). The calculations presented in Fig. 4 b, performed in accordance with relations (12, 13), show a good qualitative match between experiment and theory.

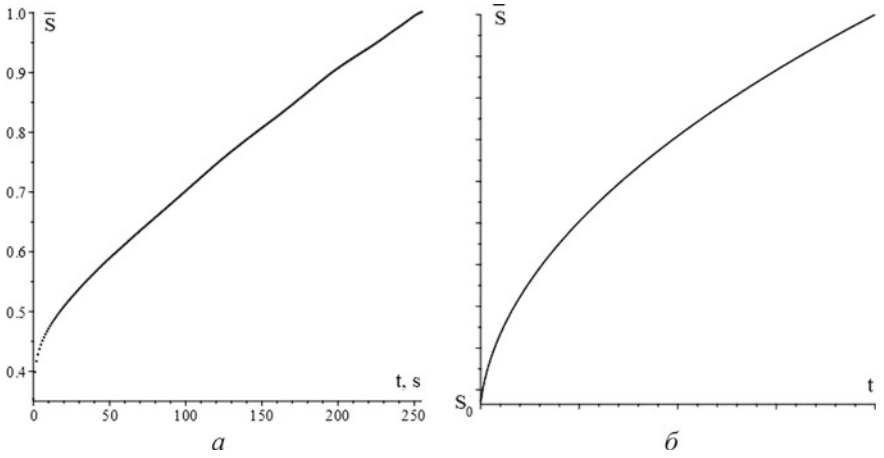


Fig. 4 a—Processed experimental data of crude oil spreading b—Analytical result (12, 13) for crude oil at initial moments of time

3 Experimental Study of One-Dimensional Spreading

Experiments on one-dimensional oil spreading were carried out in containers of different sizes, and different liquid parameters (their volume, height at which the spill occurs and temperature) were chosen.

First, experiments were conducted with an oil slick spreading along a single wall with no sides to limit the spreading of the slick (Fig. 5), the size of the first container being 29.1 × 29.1x29.1 × 10 cm. (The height of the water in this series of experiments was constant and equal to 5 cm). In this experiment at the initial moment of time the stain was limited by the container wall and an additional semicircular wall to prevent premature spreading, after the beginning of the experiment the semicircular wall was removed and the process of spreading of the stain was recorded on a video camera, the data from which served as a material for obtaining data on the experiment.

The change of the spot surface area S from the time t of spreading at different initial volumes of oil ($V = 5$, 10and15 mL) was calculated in Fig. 6. It is worth noting that from a certain point the spot area starts to decrease. This is due to the fact that over time the spreading oil adheres to the wall in an increasingly concentrated layer, which increases the density of the oil slick, but reduces the area of its distribution.

Next, the variation of the spot height with time (how much the spot moves away from the container wall H as much as possible) at different initial oil volumes was examined in detail (Fig. 7). The experiments showed that at 5 and 10 mL the change in H was almost identical and the volume did not have much effect. However, when the oil volume was increased to 15 mL, the height of the spot increased greatly.

It is also worth noting that the change in spot width L was strictly dependent on the initial oil volume. At the same time, the larger the volume was, the greater was the spreading speed along the wall (Fig. 8).

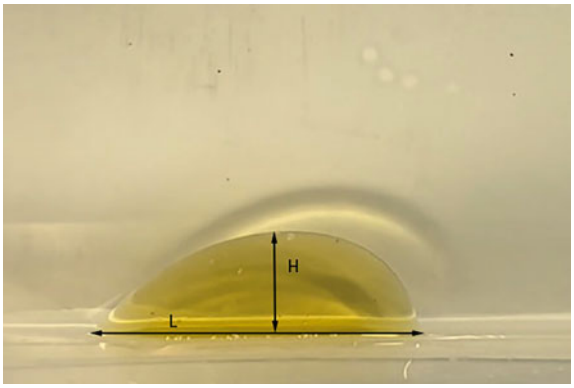


Fig. 5 Oil slick in fresh water at T = 20°C slick height H and slick width L

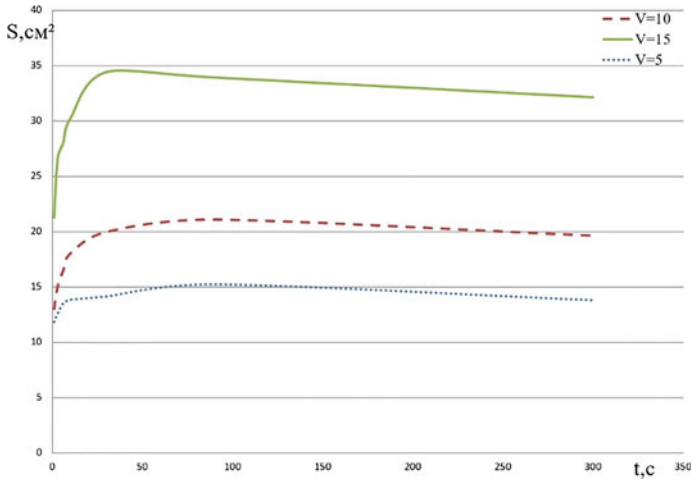


Fig. 6 Graph of dependence of change of spot area S on time t in fresh water

Further experiments were carried out in containers of a different volume 10 × 6 × 10 cm (The height of water in this series of experiments was constant and equal to 7 cm). In this case, the methodology of experiments was slightly changed and at the initial moment of time the oil slick was fixed by a straight wall, which was raised to initiate the spreading process (Fig. 9).

As for the first case, the experiments were performed at temperature $T = 20°C$ in fresh water for different volumes of oil (= 20, 30 and 40 mL). The change of spot surface area S from time t was calculated (Fig. 10).

As in the previous experiments, from a certain point the oil starts to collect into a more concentrated spot sticking unevenly to the walls of the container rather than continuing to spread equally over the water surface.

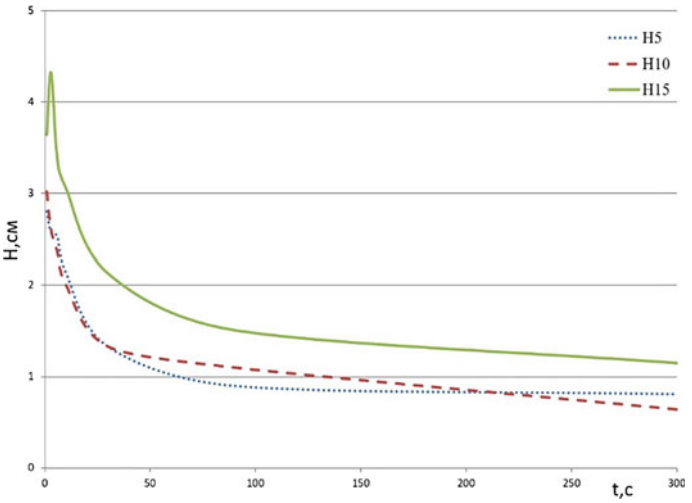


Fig. 7 Graph of dependence of change of spot height H on time t in fresh water

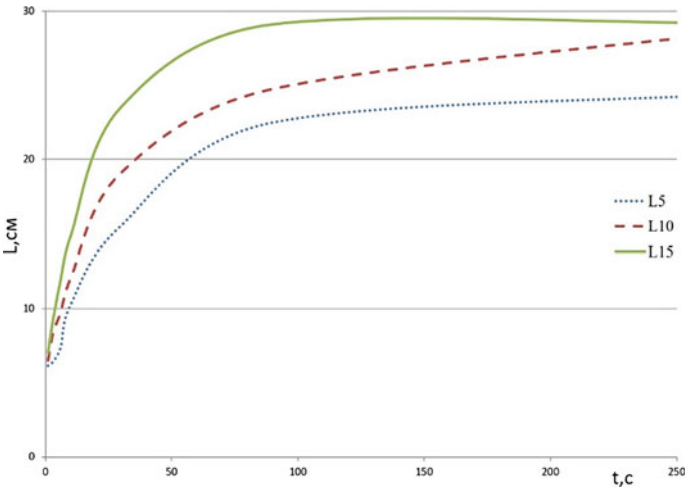


Fig. 8 Graph of dependence of change of spot width L on time t in fresh water

Similar experiments were conducted in 3 × 2 × 30 cm and 5 × 7 × 50 cm containers. For them too, the changes in the surface area of the slick S cm^2 from time t s were calculated. The experiments were carried out with oil volume $V = 5$, 10 and 15 mL). For the smaller volume container, unusual results were obtained (Fig. 11). The oil spread to a certain value of the spill area in a short period of time, then there was a fairly smooth and uniform spreading along the walls, after which the area of the spilled spot remained almost unchanged. For 5 and 10 mL volumes this is most



Fig. 9 Oil slick spreading process

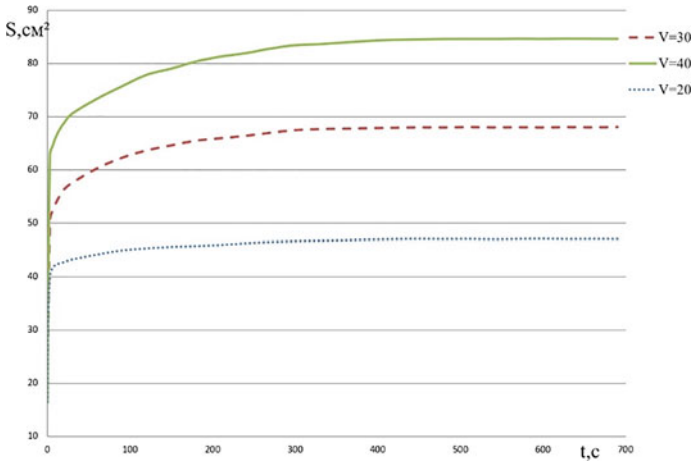


Fig. 10 Graph of dependence of change of spot area S on time t in fresh water

clearly expressed (Fig. 11). The very beginning of the oil spreading dynamics was similar to all previous experiments in larger containers and to the spreading described below. But afterwards, one can see how the growth is linear and this characterizes the moment when the oil spreads exclusively along the walls of the container (without changing the height of the spot H along the free surface of the water). This occurs abruptly up to a certain point in time, after which the spreading stops. At 15 mL, the oil spreads almost immediately to the maximum value of the oil slick area and no such linear growth is observed (Fig. 11).

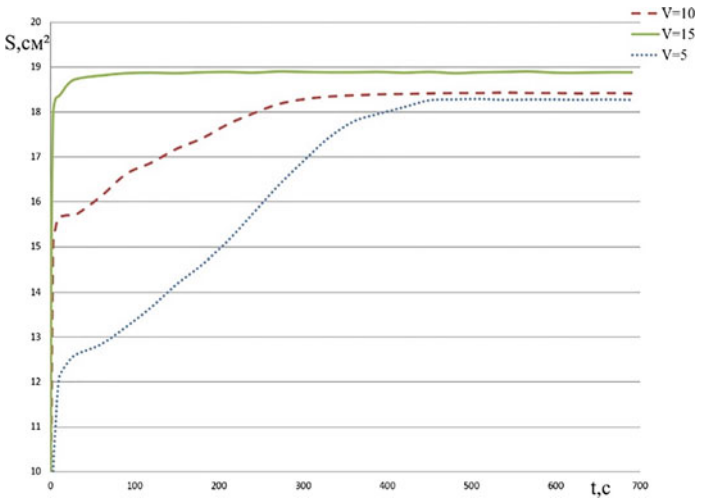


Fig. 11 Graph of dependence of change of spot area S on time t in fresh water

For a container with a volume of 5 × 7 × 50 cm, the results in quite similar to previous experiments, indicating that the ratio of the volume of oil to the volume of the body of water in which it spreads affects the dynamics of the spill (Fig. 12).

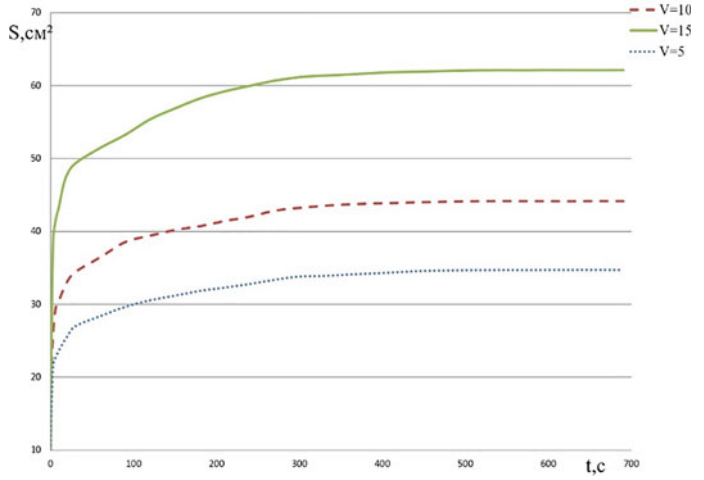


Fig. 12 Graph of dependence of change of spot area S on time t in fresh water

4 Conclusion

A series of experiments with different initial parameters were performed and a large amount of experimental data on the dynamics of oil product spreading on the water surface was obtained.

The constructed theoretical model of spreading in the form of approximate Eq. (11), general for both limited and unlimited area of oil products spill, allowed to obtain explicit analytical solutions for any moment of time of the process.

The workability of the obtained unified equation of oil product spill dynamics is confirmed by comparison with experimental results, which revealed the same modes for different types of oleins as in the theoretical description.

Experimental results for one-dimensional spreading showed that the ratio of the oil volume and the volume of the water body in which it spreads affect the spill dynamics. The effect of sticking and accumulation of the oil slick into a slick with higher density but lower volume was found. As expected, it was obtained that with a larger volume of oil the speed of its spreading over the water surface is higher and the slick spreads over a larger area.

Acknowledgements The work was carried out under the State Assignment 123021700046-4 (FFGN-2023-0006).

References

1. Hoult D.P., Suchon W. The spread of the oil in a channel. Fluid Mechanics Laboratory, Department of Mechanics Engineering, Massachusetts Institute of Technology. 1970, 25 pp.
2. Fingas M.F. Studies on the evaporation of crude oil and petroleum products: I. The relationships between evaporation rate and time// Journal of Hazardous Materials, 1997, V. 56, pp. 227 – 236.
3. Reunhart R., Rose R. Evaporation of crude oil at sea//Water Resources, 1982, V. 16, pp. 1319–1325.
4. DiPietro N.D., Huh C., Cox R.G. The hydrodynamics of the spreading of one liquid on the surface of another//Journal of Fluid Mechanics. 1978. V. 84. Part 3, pp. 529–549.
5. Matsuzaki Y., Ogasawara T., Sakai S., Izumiyama K., Kanada S. Numerical simulation of current-induced deformation and movements of the oil slick under the ice cover//Proceeding of the 18th IAHR International Symposium on Ice, 2006, pp. 219 – 226.
6. Kistovich A.V., Chaplina T.O., Pakhnenko V.P. Spreading of Technical Oils and Crude Oil on the Water Surface, Doklady Earth Sciences, 2023, V. 508, № 2, pp. 290-296.
7. Solodkii D.M., Kistovich A.V. Modified shift algorithm for processing measured data// Measurement Techniques, 2015, V.57, No. 11, pp. 1287-1292. doi: https://doi.org/10.1007/s11018-015-0622-5.

Simulation of Falling Rocks Using Two-Fluid Model

N. S. Orlova and M. S. Bezuglov

Abstract Rockfalls are considered to be very dangerous slope processes that can lead to serious consequences. These processes occur in mountain territories. Investigation of rockfalls motion to estimate affected area and hazard effects is very important. Mathematical and computer modeling methods allow to estimate the influence of the slope parameters (such as the slope angle, the slope height, the slope shape, the volume of the falling rock mass, etc.) on the runout after rockfalls. We present the 3D modeling results of the gravel motion along the slope ending with a horizontal accumulation area in this paper. We obtained the modeling results using the two-fluid model. The base of the two-fluid model is the continuum approach, and the flow motion is represented as the motion of two interacting continua (gas and solid particles). In this model, the continuity equation and the momentum equation are solved for the two phases (the gas phase and the solid phase). We used a free open source software OpenFOAM, in which the two-fluid model was implemented. We compared the obtained results of calculations with experimental data. The calculation results are in good agreement with the experiments. The results of 3D modeling describe the motion of the gravel mass along the slope and the horizontal accumulation area from the experiments qualitatively. There is a small quantitative difference between the results of calculations of the runout of the gravel mass after rockfalls and the experimental data. We concluded, that the two-fluid model can be used to simulate the falling rock.

Keywords Rockfall · Angle of a slope · Height of a slope · Falling gravel · Mathematical modeling · Two-fluid model · Continuum approach

N. S. Orlova (✉) · M. S. Bezuglov
Federal State Budgetary Educational University of Higher Education North Ossetian State University named after Kosta Levanovich Khetagurov, Vladikavkaz, Russia
e-mail: norlova.umi.vnc@gmail.com

© The Author(s), under exclusive license to Springer Nature Switzerland AG 2024

V. Karev (ed.), *Proceedings of the 9th International Conference on Physical and Mathematical Modelling of Earth and Environmental Processes*, Springer Proceedings in Earth and Environmental Sciences, https://doi.org/10.1007/978-3-031-54589-4_36

1 Introduction

Rockfalls are considered to be very dangerous slope processes that can lead to serious consequences. These processes occur in mountain territories. Investigation of rockfalls motion to estimate affected area and hazard effects is very important. Mathematical and computer modeling methods allow to estimate the influence of the slope parameters (such as the slope angle, the slope height, the slope shape, the volume of the falling rock mass, etc.) on the runout after rockfalls. There are many approaches to simulate rockfalls. The main approach is a discrete approach. This approach assumes a description of the motion of individual particles interacting with each other. So this method is more physical to simulate falling rocks, but it requires the use of sufficiently powerful computing resources. There are a lot of the papers [1–7] that present the results of rockfalls modelling using discrete approach.

There is also another approach to simulate slope processes. This is a continuum approach [8–12], which is used mainly to describe debris flows [9, 10]. The models, based on the continuum approach, describe the motion of a falling flow as the motion of a continuous medium [8]. In some cases, it is possible to simulate falling rocks using the continuum approach. The paper [12] presents the results of falling rocks modeling using a model based on the continuum approach. This model takes into account fluidization, that can occur when rocks move along the slope [13]. The obtained results of calculation satisfactorily describe the experimental data and the results of calculation using a model based on the discrete approach. And the results of calculation using the model based on the continuum approach were obtained four times faster than the results of calculations using a model based on the discrete approach. So we should note, that the implementation of models based on the continuum approach do not require the use of powerful computing resources. This fact is very significant when it is necessary to simulate real rockfalls.

We present the 3D modeling results of the gravel motion along the slope ending with a horizontal accumulation area in this paper. We obtained the modeling results using the two-fluid model. The base of the two-fluid model is the continuum approach, and the flow motion is represented as the motion of two interacting continua (gas and solid particles). In this model, the continuity equation and the momentum equation are solved for the two phases (the gas phase and the solid phase) [8]. We used a free open source software OpenFOAM, in which the two-fluid model was implemented [14]. We compared the obtained results of calculations with experimental data from the paper [15].

2 Two-Fluid Model

We used the free open source software for solving the problems of continuum mechanics OpenFOAM to simulate the falling rock [12, 14]. OpenFOAM provides a wide range of tools for solving systems of partial differential equations using the

finite volume method. We used the twoPhaseEulerFoam solver to describe the motion of granular flows along the slope ending with a horizontal accumulation area. Two-fluid (two-phase) model was implemented in the twoPhaseEulerFoam solver. This model is based on a continuum (Eulerian) approach [8], in which the flow motion is represented as the motion of two interacting continua (gas and solid particles). The two-fluid model contains the continuity equation (Eq. (1)) and the momentum equation (Eq. (2)) for the gas phase. Similar equations are used for the solid phase (Eqs. (3) and (4)).

$$\frac{\partial}{\partial t}\left(\alpha_g \rho_g\right) + \nabla \cdot \left(\alpha_g \rho_g \overline{U_g}\right) = 0; \tag{1}$$

$$\frac{\partial}{\partial t}\left(\alpha_g \rho_g \overline{U_g}\right) + \nabla \cdot \left(\alpha_g \rho_g \overline{U_g U_g}\right) = \nabla \cdot \left(\alpha_g \overline{\overline{\tau_g}}\right) - \alpha_g \nabla P + \alpha_g \rho_g \overline{g} - K_{drag} \overline{U_r}; \tag{2}$$

$$\frac{\partial}{\partial t}\left(\alpha_s \rho_s\right) + \nabla \cdot \left(\alpha_s \rho_s \overline{U_s}\right) = 0; \tag{3}$$

$$\frac{\partial}{\partial t}\left(\alpha_s \rho_s \overline{U_s}\right) + \nabla \cdot \left(\alpha_s \rho_s \overline{U_s U_s}\right) = \nabla \cdot \left(\alpha_s \overline{\overline{\tau_s}}\right) - \alpha_s \nabla P - \nabla P_s + \alpha_s \rho_s \overline{g} + K_{drag} \overline{U_r}. \tag{4}$$

α_s and α_g are the volume fraction of the solid phase and the volume fraction of the gas phase, respectively ($\alpha_s + \alpha_g = 1$). ρ_s and ρ_g are the density of the solid phase and the density of the gas phase, respectively. $\overline{U_s}$ is the velocity of the solid phase, and $\overline{U_g}$ is the velocity of the gas phase. $\overline{\overline{\tau_s}}$ is the solid phase stress tensor, and $\overline{\overline{\tau_g}}$ is the gas phase stress tensor. P is the gas phase pressure, and P_s is the solid phase pressure. $\overline{g}$ is the gravitational acceleration. K_{drag} is the drag coefficient between the solid phase and the gas phase. $\overline{U_r}$ is the relative velocity of the phases ($\overline{U_r} = \overline{U_g} - \overline{U_s}$). A more detailed description of the equations is given in the papers [8, 12].

In this study we considered that the solid phase is incompressible ($\rho_s = const$) and the gas phase is compressible. To calculate the density of the gas phase, the equation of state for an ideal gas was used (the gas temperature is constant and equal to 293 K).

The kinetic theory of granular gas was used in the two-fluid model to simulate interaction between particles. Granular temperature θ is introduced as the average energy of fluctuations of particles velocity. In this regard, the following equation is introduced into the model [8]:

$$\frac{3}{2}\frac{\partial(\rho_s \alpha_s \theta)}{\partial t} + \frac{3}{2}\nabla \cdot \left[\rho_s \alpha_s \theta \overline{U_s}\right] = \left(-P_s \overline{\overline{I}} + \overline{\overline{\tau_s}}\right) : \nabla \overline{U_s} - \nabla \cdot (k_\theta \nabla \theta) - \gamma_{\text{inelas}} + \gamma_{\text{vis}} + \gamma_{\text{rel}}. \tag{5}$$

k_θ is the transfer coefficient of the energy of fluctuations (the granular energy conductivity term). γ_{inelas} is the dissipation of granular energy due to inelastic particle–particle collisions. γ_{vis} is the additional dissipation term, namely that due to viscosity damping. γ_{rel} is the term that takes into account the slip between particles and the gas phase. The terms description is given in detail in the papers [8, 12].

3 Calculation Conditions

3D modeling of the falling gravel mass was performed in this study. We compared the results of calculations with experimental data from the paper [15]. The experiments were performed in laboratory conditions and consisted in releasing a dry mass of gravel on a slope ending with a horizontal accumulation area (wood sheets).The experiments were described in details in the papers [15, 16].

We built the computational area in accordance with the laboratory equipment dimensions (Fig. 1). We used the following dimensions of the computational area: the height 4.5 m; the width 2.4 m; the height of the slope 2.5 m; the length of the horizontal part of the area 4 m. There was the mass of gravel in the form of a triangular prism with a volume of 0.02 m^3 and 0.04 m^3. This mass was located at the height of the slope 1 m (the fall height) at the initial moment of time (Fig. 1). The slope angle was equal to 45 degrees. The mass of gravel was represented as a complex of spherical solid particles. The approximate value of the particle diameter was calculated on the base of the experimental data from the paper [15]. We used the value of the particle diameter 0.02 m in computations.

We used the following initial conditions [12]:

$\overline{U_s} = 0$ m/s; $\overline{U_g} = 0$ m/s; $\rho_g = 1.2$ kg/m^3; $P = 101.325$ кPa; $\alpha_s = 0.6$; $\theta = 0$ m^2/s^2.

It should be noted that we used the average density of gravel 1550 kg/m^3.

The boundary conditions on the walls are presented below (wall).

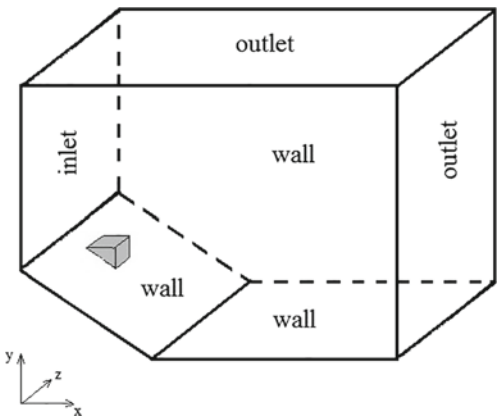


Fig. 1 The computational area

$$\overline{U_s} = 0; \overline{U_g} = 0; \frac{\partial P}{\partial n} = 0; \frac{\partial \alpha_s}{\partial n} = 0; \frac{\partial \theta}{\partial n} = 0.$$

The boundary conditions on the input left border (inlet):

$$\overline{U_s} = 0; \overline{U_g} = 0; \frac{\partial P}{\partial n} = 0; \alpha_s = 0; \frac{\partial \theta}{\partial n} = 0.$$

The boundary conditions on free borders (outlet).

$$\frac{\partial \overline{U_s}}{\partial n} = 0; \frac{\partial \overline{U_g}}{\partial n} = 0; \frac{\partial P}{\partial n} = 0; \frac{\partial \alpha_s}{\partial n} = 0; \frac{\partial \theta}{\partial n} = 0.$$

The time step was equal to 0.0001 s. The average time of the falling was 0.55–0.6 s. The computations were carried out on processor with a frequency of 4.2 GHz. The approximate time of the computation for one case was 2 h.

4 Analysis of the Modeling Results

We obtained the results of modeling using the two-fluid model for different values of the volume of the gravel mass (0.02 m^3 and 0.04 m^3). We presented snapshots of distribution of the solid phase volume fraction ("alpha.particles" in Fig. 2) at the different moment of time. The volume of the gravel mass V is 0.02 m^3.

To calculate the runout of the gravel mass after rockfall we used the method, which is described in details in the paper [12]. We presented a brief description of the method below. The computational area was divided into several longitudinal sections (constructed in the direction of the z axis) along the horizontal part. We built curves of the distribution of the solid phase volume fraction (α_s) along the x axis in each section. The distribution of the solid phase volume fraction along the x axis at z = 1.2 m (the middle of the computational area width) is presented in Fig. 3. It should be noted that the distribution curves constructed in other longitudinal sections at different values of z (near the middle of the computational area width) differ slightly from the curve presented in Fig. 3.

In this work, the boundary that separates the continuous part of the material (gravel) from the part in which the material is loose was determined using the value $\alpha_s = 0.05$ (in accordance with the method from the study [12]). From Fig. 3 we see that the solid phase volume fraction takes on the value of 0.05 at x = 0.71 m. Using this method, we calculated the runout of the gravel mass after rockfall for the case when the volume of the gravel mass V was equal to 0.04 m^3. In this case the runout of the gravel mass was 0.82 m.

We compared the calculated runout of the gravel mass after rockfall with the experimental data for two cases of the volume of the gravel mass (V = 0.02 m^3 and V = 0.04 m^3) [15]. Table 1 shows the results of comparison.

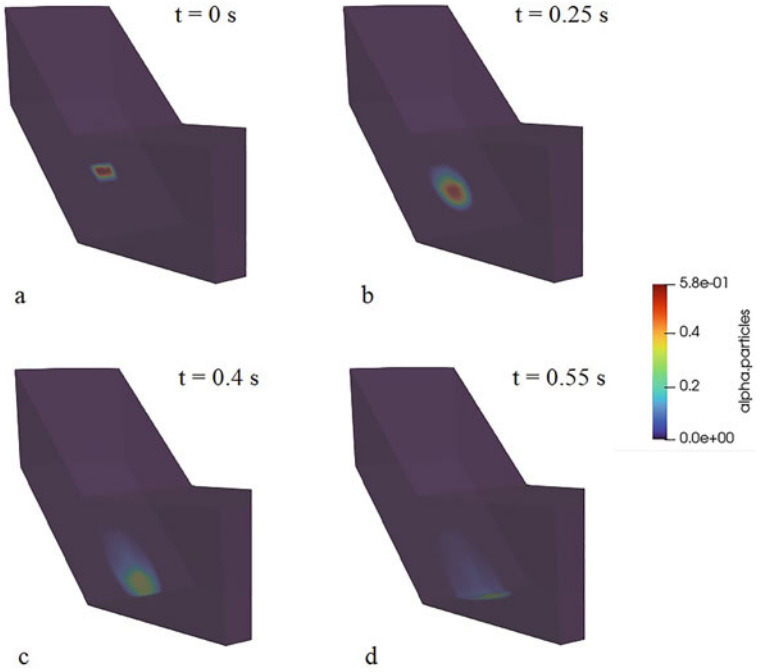


Fig. 2 Snapshots of the solid phase volume fraction distribution at the different moment of time

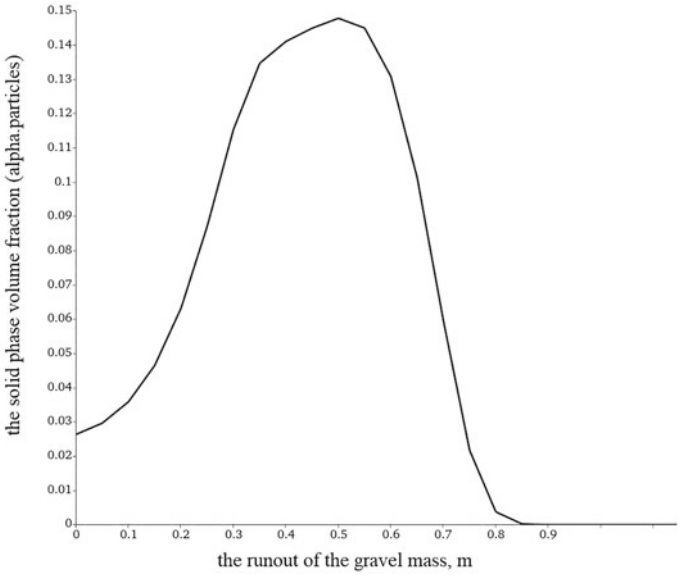


Fig. 3 The solid phase volume fraction distribution after rockfall along the horizontal part of the computational area

Table 1 Comparison the calculated runout of the gravel mass with the experimental data

The volume of the gravel mass, m^3	The runout of the gravel mass after rockfall along the horizontal part, m	
	Calculated	Experimental
0.02	0.71	0.73
0.04	0.82	0.84

The calculation results and the experiments are in good agreement. The 3D modeling results describe the motion of the gravel mass along the slope and the horizontal accumulation area from the experiments qualitatively [15]. In the second case (when the volume of the gravel mass $V = 0.04$ m^3) the value of the runout of the gravel mass after rockfall is greater than the corresponding value of the runout in the first case (when $V = 0.02$ m^3). It should be noted that we used spherical particles in the calculations. In fact, the gravel particles had irregular shape.

We plan to perform additional computational experiments (3D modeling) of the falling rocks using the two-fluid model in the future. These results will be important to determine the runout after rockfall at the different slope height and slope angle and also the slope shape.

5 Conclusions

In general, the calculation results using the two-fluid model and the experiments are in good agreement. The 3D modeling results describe the motion of the gravel mass along the slope and the horizontal accumulation area from the experiments qualitatively. In the second case (when the volume of the gravel mass $V = 0.04$ m^3) the value of the runout of the gravel mass after rockfall is greater than the corresponding value of the runout in the first case (when $V = 0.02$ m^3). There is a small quantitative difference between the results of calculations and the experimental data. So we concluded, that the two-fluid model can be used to simulate the falling rock.

Acknowledgements This study was funded by Russian Science Foundation, project number 23-27-00264, https://rscf.ru/en/project/23-27-00264/.

References

1. Chernomorec, S., Mihajlov, V.: Numerical modeling of catastrophic mudflows, rockfalls and landslides using a three-dimensional discrete model. Georisk. (1), 16–27 (2012).
2. Dorren L.: A review of rockfall mechanics and modeling approaches. Progress in Physical Geography. 27(1), 69–87 (2003).

3. Rammer, W., Brauner, M., Dorren, L., Berger, F., Lexer, M.: Evaluation of a 3-D rockfall module within a forest patch model. Natural Hazards and Earth system Sciences (10), 669–711 (2010).
4. Hungr, O.: A model for the runout analysis of rapid flow slides, debris flows and avalanches. Canadian Geotechnical Journal 32(4), 610–623 (1995).
5. Albaba, A., Schwarz, M., Wendeler, C., Loup, B., Dorren, L.: Numerical modeling using an elastoplastic-adhesive discrete element code for simulating hillslope debris flows and calibration against field experiments. Natural Hazards and Earth system Sciences. 19 (11), 2339–2358 (2019).
6. Mollon, G., Richefeu, V., Villard, P., Daudon, D. Discrete modelling of rock avalanches: sensitivity to block and slope geometries. Granular Matter. (17), 645–666 (2015).
7. Orlova, N., Volik, M.V.: Study of Falling Rocks Using Discrete Element Method. Processes in GeoMedia. Springer Geology. (1), 75–82 (2020).
8. Gidaspow, D.: Multiphase flow and fluidization: Continuum and kinetic theory descriptions. Boston: Academic Press Inc. 211 (1994).
9. Mitchell, A., Zubrycky, S., McDougall, S., Aaron, J., Jacquemart, M., Hübl, J., Kaitna, R., Graf, C.: Variable hydrograph inputs for a numerical debris-flow runout model. Natural Hazards and Earth System Sciences. (22), 1627–1654 (2022).
10. Wei, F., Kaiheng, H., Lopez J., Peng C.: Method and its application of the momentum model for debris flow risk zoning. Chinese Science Bulletin 48(6), 594–598 (2003).
11. Hungr, O., McDougall, S.: Two numerical models for landslide dynamic analysis. Computers & Geosciences. 35(5), 978–992 (2009).
12. Orlova, N., Kamenetskii, E.: Verification of rock falls model using the continuum approach. Sustainable Development of Mountain Territories. 10(1), 7–13 (2018).
13. Okura, Y., Kitahara, H., Sammori, T.: Fluidization in dry landslides. Engineering Geology. 56, 347–360 (2000).
14. The open source CFD toolbox. Available at: https://openfoam.com (accessed 1.09.2023)
15. Manzella, I., Labiouse, V.: Empirical and analytical analyses of laboratory granular flows to investigate rock avalanche propagation. Landslides. (10), 23–36 (2013).
16. Manzella, I., Labiouse, V.: Flow experiments with gravel and blocks at small scale to investigate parameters and mechanisms involved in rock avalanches. Engineering Geology Journal. 109, 146–158 (2009).

Long-Shore Sediment Movements in the Area of a Small Port Facility (South-West of Sakhalin)



V. V. Afanas'ev, I. O. Leont'ev, and A. V. Uba

Abstract The problem of sedimentation of port harbors in the region is very relevant, but there is no understanding of how and why this occurs. This paper presents the results of calculations of longshore sediment flows in the area of the port of Shakhtersk, located on the western coast of Sakhalin in the Tatar Strait. Analysis of repeated bathymetric surveys of the harbour and approach channels has quantitatively confirmed the validity of a methodology that has previously been used on the shores of north-east Sakhalin, Terpeniya Bay and Aniva Bay for coastal protection purposes.

Keywords Sakhalin Island · Coast dynamics · Sediment flows · Mathematical modeling · Repeated depth measurements

1 Introduction

The study area is a complexly constructed section of a basement marine terrace with an erosion-denudation incision filled with estuarine-lagoon sediments of a shallow lagoon of Upper Pleistocene age. The lower boundary of the sedimentary strata was established by us in the height interval of −0.4 to +1.2 m in the height system BS 77.

К сложно построенной морской террасе непосредственно примыкают барьерные формы закрытых лагун оз. Тауро и оз. Проточное. Локация района исследований показана на рисунке 1.

The complexly constructed marine terrace is directly adjacent to the barrier forms of the closed lagoons of Lake Tauro and Lake Protochnoye. The location of the study area is shown in Fig. 1.

V. V. Afanas'ev (✉) · A. V. Uba
Sakhalin State University, Yuzhno-Sakhalinsk, Russia
e-mail: vvasand@mail.ru

I. O. Leont'ev
Shirshov Institute of Oceanology of the Russian Academy of Sciences, Moscow, Russia

© The Author(s), under exclusive license to Springer Nature Switzerland AG 2024

V. Karev (ed.), *Proceedings of the 9th International Conference on Physical and Mathematical Modelling of Earth and Environmental Processes*, Springer Proceedings in Earth and Environmental Sciences, https://doi.org/10.1007/978-3-031-54589-4_37

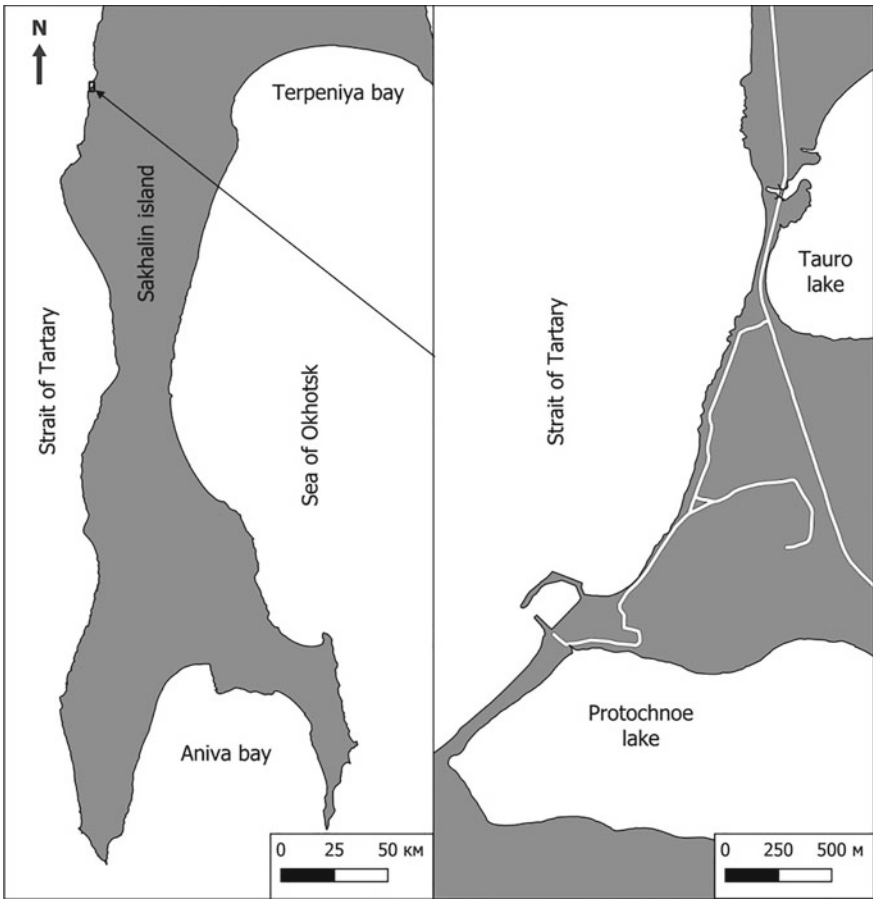


Fig. 1 Location of the study area

Barrier forms are fairly stable, but in the early 1940s the barrier form, Protochnoe Lake, probably began to break up, as evidenced by its geological section, in which technogenic soils are observed approximately one meter below the present position of the rear beach edge. This situation is usually attributed to the formation of new morpholithodynamic cells as a result of the reorganization of the sediment migration system during the construction of port facilities. At present the beach sediment supply here is sufficient to provide full wave extinguishment. The coastal scarp of the accumulative form is stable. To the south of the barrier form, the coastal scarp is actively eroding, ensuring saturation of the south-north sediment flow (Fig. 2). Some intensification of the scouring processes in the southern part of the Lake Protochnoye embankment is associated with the redistribution of sediment during the construction of the bypass pipe.



Fig. 2 Landslide—landslide with the volume of more than 2000 m^3 in 300 m to the south from the embankment of the Protochnoe Lake

Недонасыщенность потока наносов с севера на юг не позволяет формироваться широким пляжам с северной стороны порта, что является причиной активного размыва берегового уступа, особенно там, где он сложен слабо консолидированными породами (рисунок 3).

The undersaturation of sediment flow from north to south does not allow the formation of wide beaches on the northern side of the harbor, which causes active erosion of the coastal scarp, especially where it is composed of weakly consolidated rocks (Fig. 3).

2 Methods and Results

The calculations are based on the methodology described in [Leont'ev, 2001, 2014]. Testing of the methodology on the shores of north-eastern Sakhalin, Terpeniya Bay and Aniva Bay has shown very high convergence between the calculated values of longshore sediment transport and the results of field measurements (Odoptu-Sea Shore Protection…2019, Leont'ev et al., 2019; Afanas'ev et al. 2019; Leont'ev, Afanas'ev 2016].

A shore with a relatively gentle underwater slope (average slope within the 10-m isobath is about 0.01) and a narrow beach leaning against an abrasion cliff. A generalized bottom profile is shown in the bottom graph (Fig. 4). The characteristic average sand size was assumed to be 0.35–0.50 mm. The shoreline is oriented approximately from SSW to NNE.

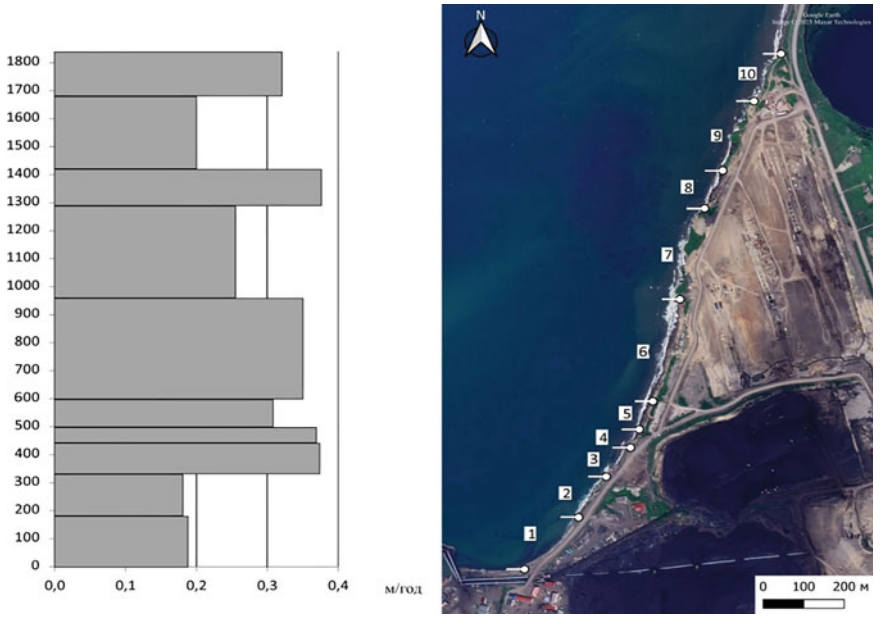


Fig. 3 Mean annual scour rates of a complexly constructed bank scarp

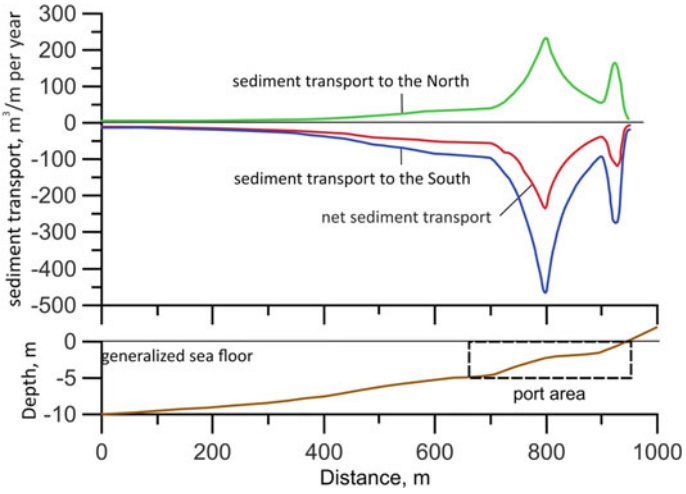


Fig. 4 Distributions of longshore sediment fluxes along the bank profile shown in the bottom graph

The annual duration of waves of different mean heights $\overline{H}$, periods $\overline{T}$ and directions are shown in Table 1.

Here Θ is the angle of wave approach relative to the coastal normal. Positive values correspond to a southward wave approach, which generates northward sediment flows, while southward flows are considered negative.

Table 1 Wind-wave mode

Rumb	W, m/s	$\overline{H}$, m	$\overline{T}$, s	t_w, h
SW, $\Theta = 75°$	2	0.1	1.2	113.9
	3	0.1	1.8	302.2
	5	0.4	2.9	232.2
	9	1.0	4.9	83.2
	13	1.9	6.5	13.2
	17	2.9	7.9	1.3
W, $\Theta = 30°$	2	0.1	1.2	74.5
	3	0.1	1.8	219.0
	5	0.3	2.8	232.2
	9	0.9	4.4	127.0
	13	1.5	5.7	52.6
	17	2.2	6.7	13.2
NW, $\Theta = -15°$	2	0.1	1.2	61.3
	3	0.1	1.8	201.5
	5	0.3	2.8	306.6
	9	0.9	4.6	205.8
	13	1.6	5.9	61.3
	17	2.4	7.1	13.2
NNW, $\Theta = -37.5°$	2	0.1	1.2	59.1
	3	0.1	1.8	177.4
	5	0.4	2.9	229.9
	9	1.0	4.8	148.9
	13	1.8	6.3	46.0
	17	2.7	7.5	10.9
S, $\Theta = -60°$	2	0.1	1.1	56.9
	3	0.1	1.5	153.3
	5	0.2	2.2	153.3
	9	0.5	3.1	92.0
	13	0.7	3.6	30.7
	17	0.9	3.9	8.8

Table 2 Integral longshore sediment fluxes (thousand cubic meters per year)

Flow to the north	Flow to the south	Resulting flow
37.3	−82.2	−44.9

Table 2 gives an idea of integral material flows. In the north direction 37 thousand cubic meters of sand is moved per year, and in the south direction—82 thousand m^3. The resulting flow is southward and is about 45 thousand cubic meters per year.

As can be seen in Fig. 5, the sediment flow is concentrated in the coastal strip with depths of less than 5 m. Two peaks are distinguished, one confined to the underwater ridge (800 m mark) and the other to the calm edge. The first peak is associated with the breaking of relatively large waves, whereas the peak near the edge is more due to the contribution of relatively small waves.

The port fencing structures extend to a depth of about 5 m (Fig. 5).

Consequently, they intercept a significant proportion of the longshore sediment flows. It is estimated that in the initial period after the construction of the port, the breakwaters could have accumulated sand at a rate of 59,000 m^3/year on the north side and 30,000 m^3/year on the south side. This should have resulted in downward scour, which can be traced in the coastal contour on both sides of the port.

The overflow of the Protochnoye Lake lagoon immediately after the construction of the port in 1925–1933 began to erode and active backfilling of waste rock was probably associated with the restoration of the barrier form. At present, the overflow of the closed lagoon of Protochnoye Lake is actively fed by debris from the shore escarpment located to the south of the site.



Fig. 5 Hydrotechnical facilities of Shakhtersk port

The analysis of the sediment flow processes in the port harbor and approach channel can significantly add to the understanding of the dynamics of the sediment flows and its parameters. The bathymetric maps were digitized in QGIS into point vector format. Then, digital elevation models of the underwater relief with a cell size of 0.2 m were constructed using the obtained points by triangulation method. Then, the difference models were obtained by the subtraction method and the areas and volumes were calculated. Gaussian smoothing with a window of 21*21 cells was applied to visualize the models. Figure 6 shows the overlapping areas of the multi-temporal measurements that we have at our disposal. The diagram of sediment volume changes within the calculated areas in Fig. 7 visualizes the quantitative parameters of the underwater deformation plans.

It is evident that the sediment load in the entrance channel is mainly due to the attenuation of sediment flow from the south during the autumn period (Fig. 8). In the northeastern part of the harbor, sediment accumulation undoubtedly occurs as part of the north–south sediment flow infiltrates through the trestle. A significant part of this flow moves along the northern breakwater while forming sediment accumulation zones here. Thus, the interception of 9.5 thousand m^3 of sediment from longshore flows within the morpholithodynamic system during approximately one third of the period of active dynamics and the active destruction of the shore to the north of the port facilities confirms the correctness of the calculations.

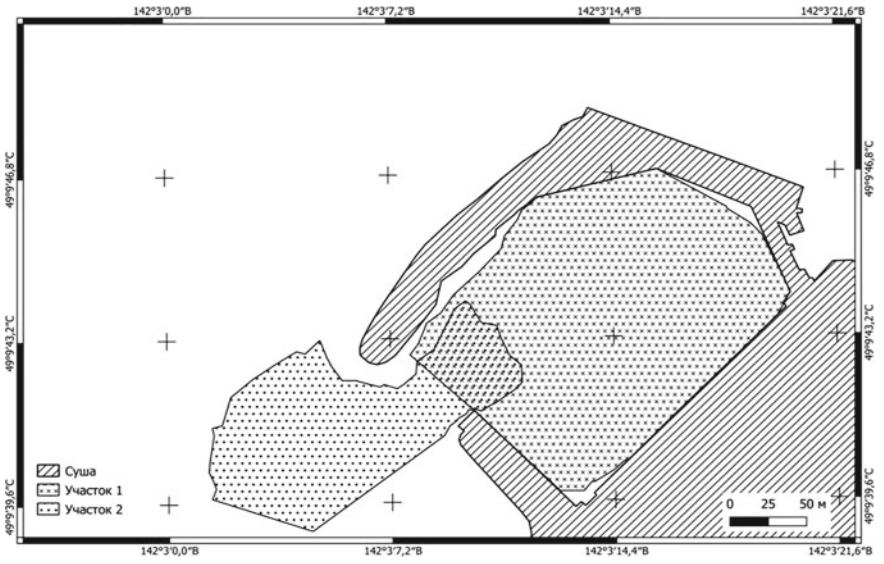


Fig. 6 Areas of calculation of underwater relief deformations

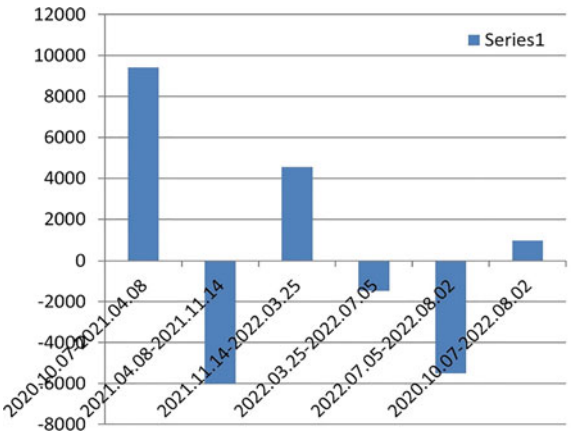


Fig. 7 Chart of drifting and dredging in the Shakhtersk port water area

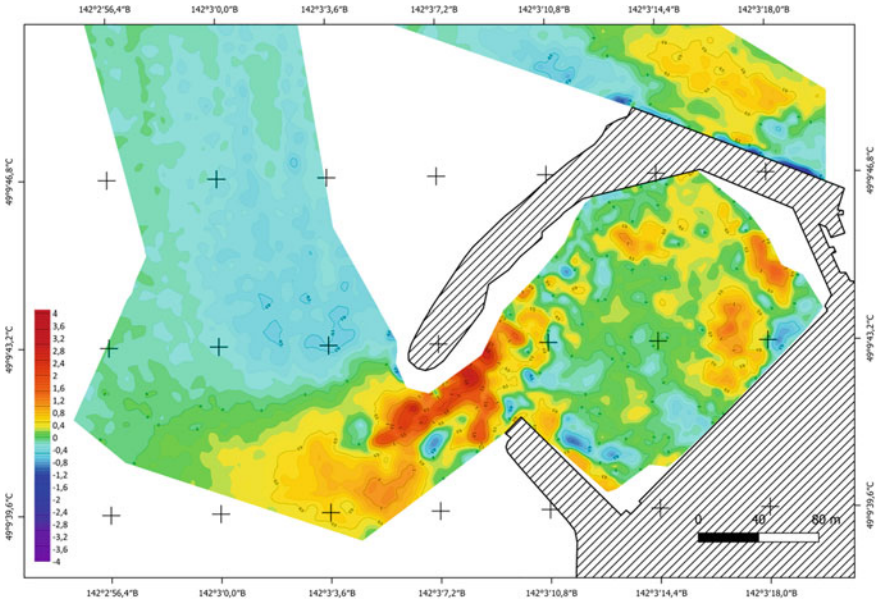


Fig. 8 Underwater landform deformations from 07.10.2020 to 04.08.2021

3 Conclusion

Thus, it has been established that 37,000 m^3 of sediment can move in the northern direction and 82,000 m^3 in the southern direction per year. The resulting flow is directed southwards and amounts to about 45,000 m^3 per year. The northward flow of sediment is ensured by the hydrodynamic situation, mainly during the warm period.

The main part of the northward sediment load flows directly into the harbour water area. The southward flow of sediment is ensured by the stiff swell of late autumn/early winter. A study of the volume of sediment intercepted by port hydraulic structures generally confirms the calculated data. In addition, analysis of the measurement plans shows that part of the sediment flow from the north through the piled ramp at the base of the western breakwater enters directly into the harbour, while some of it bypasses the hydraulic structures during periods of severe storms and reaches the area of the approach channel. Assessing the results of the study as a whole, it should be noted that the coastal zone in the area of the studied site is under the conditions of the established lithodynamic regime of development.

References

1. Leont'ev I.O. Coastal dynamics: waves, flows, sediment flows. M.: GEOS, 2001. 272 p.
2. Leont'ev I.O. Morphodynamic processes in the coastal zone of the sea. Saarbrücken: LAP LAMBERT Academic Publishing, 2014. 251 p.
3. Odoptu Sea coastal reinforcement. Report on morpholithodynamic surveys. Dal'morberegotechnika, 2019, 140 p.
4. Afanas'ev V.V., Leont'ev I.O., Uba A.V. Analysis of the dynamics of the lagoon accumulative barrier form (Sakhalin Island) on the basis of mathematical modeling and maps of relief deformations for a multi-year period // Geosystems of transition zones. - 2019. - V. 3. - №. 1. - pp. 137–143.
5. Leont'ev I.O., Afanas'ev V.V., Uba A.V. Rhythmic structures of the coastal contour in the Gulf of Terpeniya of Sakhalin Island // Oceanology. - 2019. - V. 59. - №. 3. - pp. 497–505.
6. Leont'ev I.O., Afanas'ev V.V. Dynamics of the lagoonal shore of northeastern Sakhalin on the example of the system of Nyisky Bay and Plastun Spit // Oceanology. - 2016. - V. 56. - №. 4. - pp. 618–626.

Dynamic Processes at the Boundary of the Earth's Liquid Core



S. I. Peregudin and S. E. Kholodova

Abstract The investigation of the dynamics of the Earth's magnetic field due to three-dimensional large-scale motion of the inviscid, incompressible, and ideally conducting inhomogeneous rotating fluid, concentrated in liquid Earth's core. The proposed mathematical model of investigated physical process is a closed system of equations consisting of the equations of hydrodynamics taking into account the Earth's rotation, the Lorentz force and the corresponding equations of magnetic dynamics with the required boundary conditions. The analysis of a mathematical model suitable for calculating three-dimensional movements with high temporal scale and spatial horizontal scale, comparable with radius of the Earth. The main idea of the analysis consists in constructing a scheme of successive approximations, in which the geostrophic approximation is the first step. This method of analysis allows, not limited to heuristic reasonings, to deduce the General geostrophic equations, describing the motion of both homogeneous and heterogeneous electrically conducting rotating fluid. An analytical solution to the system of nonlinear equations modeling the geostrophic motion in a spherical layer of ideal conductive inhomogeneous rotating fluid. Structure analysis presents the fields of the MHD variables allows us to conclude the existence of strong changes in a thin layer adjacent to the boundary with the mantle.

Keywords Inhomogeneous rotating fluid · Electrically conducting rotating fluid · Equations · Magnetohydrodynamics · Analytical solution · Electrically conducting ideal rotating liquid · Wave motion · Earth's magnetic field

The Earth's core has a significant influence on many geophysical phenomena and processes that occur and have occurred in the Earth. For example, according to

S. I. Peregudin (✉)
St. Petersburg State University, St. Petersburg, Russia
e-mail: s.peregudin@spbu.ru

S. E. Kholodova
ITMO University, St. Petersburg, Russia

© The Author(s), under exclusive license to Springer Nature Switzerland AG 2024

V. Karev (ed.), *Proceedings of the 9th International Conference on Physical and Mathematical Modelling of Earth and Environmental Processes*, Springer Proceedings in Earth and Environmental Sciences, https://doi.org/10.1007/978-3-031-54589-4_38

generally recognised ideas, the Earth's magnetic field is excited by motion in the liquid part of the Earth's core, but the details of this process are still unclear [1–8].

The study of the dynamics of the Earth's deep interior is the most important and at the same time the most difficult problem, which is solved, first of all, by geophysical methods using seismic and gravitational methods. It is difficult to penetrate directly into the Earth's interior; therefore, theoretical studies are of great importance.

The aim of the paper is to study wave three-dimensional large-scale motions of a non-viscous, incompressible inhomogeneous perfectly conducting rotating fluid centred in a spherical region. The presented studies can be used in astrophysics and geophysics, in particular, in the study of processes occurring in the liquid core of the Earth and in the interior of stars.

The results of the study are not limited only to the application to geophysics, they can also be useful in considering the process of self-excitation of magnetohydrodynamic dynamo in relatively large masses of liquid metal and in technical devices, for example, in technological processes using pressure chambers of fast neutron reactor, blast furnaces, reactors for titanium production and others.

In problems on the generation of magnetic fields, questions often arise as to what kind of motion should be generated and under what conditions magnetic fields can exist for sufficiently large time intervals, i.e., we are interested in the nature of the processes under consideration.

For space objects, the damping time of the magnetic field is very long. If we assume that the liquid core of the Earth consists of molten iron, the damping time of the magnetic field is 15,000 years according to some estimates and years according to others. The damping time of the magnetic field in sunspots is at least 300 years, and that of the Sun's magnetic field is 10^{10} years.

In the studies under consideration, a large time value means a time much shorter than the magnetic field decay time, but at the same time large enough for several generations to notice this decay.

The above estimates are, of course, very tentative. Perhaps, in fact, they are of even higher orders, because, while during the existence of man, the attenuation of the magnetic field has not been clearly manifested, although a decrease in its intensity up to a certain value has been observed, but then, necessarily, followed by its increase. Therefore, if the statement about damping of the magnetic field in relation to the Earth conditions is possible, then, most likely, the order of the considered time is much larger than those given above from the known sources, or still the processes of interest to us represent steady oscillations.

In [9], the role of stratification in the basic dynamics of the studied magnetohydrodynamic processes was studied. The analysis of the obtained solution allowed us to establish the existence of a steady-state mode of oscillations at large values of time, which confirms the important role of stratification of the Earth's liquid core density, which determines in a number of cases its basic dynamics as an important factor in the planet's evolution.

The motion of the presented fluid directly in the thin layer adjacent to the mantle makes a significant contribution to the dynamics of the magnetic field. The paper [10]

analysed and made a corresponding conclusion for perturbations of magnetohydrodynamic fields with a relatively small horizontal scale, much smaller than the Earth radius, developing near some point with spherical coordinates θ_0, ϕ_0. Of particular interest are global perturbations of magnetohydrodynamic quantities with the longest wavelength possible in the spherical layer of the core, taking into account thermodynamic changes at the boundary with the mantle, to which the studies presented in this paper are devoted.

Thus, we will study wave motions at the outer boundary of a thin spherical layer of inhomogeneous fluid.

The motion of a non-viscous perfectly conducting incompressible inhomogeneous fluid in a system rotating with angular velocity ω, in magnetic hydrodynamics in Euler variables is described by a system of equations [1–10]

$$div\, v = 0, \qquad \frac{\partial v}{\partial t} + (v \cdot \nabla)v = -\frac{\nabla p}{\rho} - 2\omega \times v - gz + \frac{1}{\mu\rho}\, rot\, b \times b,$$
$$\frac{\partial b}{\partial t} = rot\,(v \times b), \qquad div\, b = 0,$$

where b—vector of magnetic induction, v—velocity of the fluid in the coordinate system rotating with angular velocity ω, p—pressure, ρ—density, g—magnitude of acceleration of gravity. It is assumed that magnetic permeability μ is constant.

An important property of the magnetic induction equation is that in the case of an infinitely conducting fluid, the flux of the field b through any material surface in the fluid is conserved. This means that the field b changes as if the magnetic lines of force of this field were "frozen" in the moving substance. In bodies of cosmic dimensions the flow of force lines turns out to be very slow and one can consider that the force lines are practically "frozen" in the substance [9–20].

Thus, we will assume that the liquid has very good electrical conductivity, so that the magnetic Reynolds number is large $R_m = \frac{LU}{\tilde{\lambda}} >> 1$, where L, U—hacharacteristic size and velocity, $\tilde{\lambda}$—magnetic diffusion coefficient. The case $R_m >> 1$ is realised in the liquid core of the Earth, is often found in astrophysics and in some techno-logical processes.

If density is considered as a variable, then in addition to the equation of motion, the equation of continuity and Maxwell's equations it is necessary to involve the equation of internal energy balance [3–9]

$$\rho \frac{dE}{dt} = -p\rho \frac{d}{dt}\left(\frac{1}{\rho}\right) + k\Delta T + \chi + \rho Q + \tilde{\lambda}(rot\, b)^2. \tag{1}$$

Due to the fact that the considered fluid is perfectly conducting, the last summand in the right part of Eq. (1) will be absent $\left(\tilde{\lambda} = 0\right)$. In Eq. (1) E—internal energy per unit mass, T—temperature, k—heat conduction coefficient, Q—rate of heat inflow from external sources per unit mass, χ—heat inflow due to viscous dissipation. In the following we will assume that $\chi = 0$.

If the effects of compressibility are negligible, the equation of state is applicable

$$p = \rho_0(1 - \alpha(T - T_0)),$$

where ρ_0 and T_0—average density of the liquid and average temperature, $\alpha = -\frac{1}{p}\left(\frac{\partial\rho}{\partial T}\right)\Big|_{p=const}$ — coefficient of thermal expansion. For incompressible fluid instead of Eq. (1) we will use the heat transfer equation in the following form [3]:

$$\frac{dT}{dt} = \frac{k}{\rho c_p}\Delta T + \frac{Q}{c_p}, \tag{2}$$

where c_p—is the specific heat capacity at constant pressure. Then the temperature in Eq. (2) can be expressed through density

$$\frac{d\rho}{dt} = \kappa\Delta\rho - \frac{\alpha\rho_0}{c_p}Q, \qquad \kappa = \frac{k}{\rho\, c_p}, \tag{3}$$

where κ— thermal diffusivity coefficient.

When considering large-scale motions, the horizontal scale of which is comparable to the Earth radius, the basic equations of quasigeostrophic motion undergo a number of some changes. The reduction of the problem geometry to a plane geometry is no longer a natural approximation. The horizontal variability of the basic density field cannot be neglected either. Thus, to adequately describe motion of such scales it is necessary to consider the basic equations of magnetic hydrodynamics taking into account the corresponding relations between scales. We will assume that the vertical scale of density is large compared to the vertical scale of motion.

Let us represent the dimensional variables marked with asterisks through dimensionless variables as follows:

$$\begin{gathered} r_* = r_0\left(1 + \frac{D}{r_0}z\right), \qquad v_{\lambda_*} = Uv_\lambda, \qquad v_{\theta_*} = Uv_\theta, \qquad b_{\lambda_*} = Ub_\lambda, \qquad b_{\theta_*} = Ub_\theta, \\ v_{r_*} = \frac{D}{r_0}Uv_r = Wv_r, \qquad b_{r_*} = \frac{D}{r_0}Bb_r = Vb_r, \qquad t_* = \frac{r_0}{U}t, \end{gathered} \tag{4}$$

where r_0—radius of the spherical layer, D—vertical scale of motion. As a horizontal scale of motion, we will use the radius r_0, since the horizontal scale has the order of $O(r_0)$, U—scale of horizontal velocity, W—scale of vertical velocity, B—scale of horizontal components of the magnetic field, V—scale of vertical component of the magnetic field. The advection time is chosen as the time scale $\frac{r_0}{U}$.

We choose the scales for the density and pressure fields taking into account that at small Rossby numbers the horizontal component of the pressure gradient is equal in order of magnitude to the Coriolis force, and the assumption of equality in order of magnitude of the buoyancy forces and the vertical pressure gradient, which follows from satisfying the hydrostatic approximation of large-scale motions with a high degree of accuracy.

Thus, the magnetic pressure is comparable to $B^2\mu^{-1}$, and the inertial forces in the equation of motion are equivalent to the kinetic pressure of order ρU^2. The ratio of kinetic and magnetic pressures is of the order of A^2, where A is the Alfvén number [9–20], defined by the formula $A = U\sqrt{\mu\rho}B^{-1}$. The ratio of specific kinetic energy of matter $\rho v^2 2^{-1}$ and magnetic energy $B^2(2\mu)^{-1}$ is also equal to A^2. If the magnetic field is "frozen" into the substance, a large value A means that the magnetic field has little effect on the motion. A small value A means that the motion is mainly determined by the induction of the magnetic field. If $A \approx 1$, then the motion and the field have more or less equal influence on each other and there is an approximately equal distribution of energy between them. The Alfvén number is also called the Alfvén Mach number, which characterises the ratio of the fluid flow velocity to the Alfvén velocity: $M_A = U(U_A)^{-1}$, $U_A = B\left(\sqrt{\mu\rho}\right)^{-1}$. So, let us assume that the kinetic and magnetic pressures are of the same order: $\rho U^2 \sim B\mu^{-1}$, that is, assuming for the Alfvenov Mach number $M_A = U\sqrt{\mu\rho}B^{-1} = O(1)$, and representing the desired functions as a power series over the small Rossby number for the principal terms of the corresponding expansions, the equations of motion are written as follows:

$$
\begin{aligned}
&v_\theta \cos\theta = -\frac{1}{\sin\theta}\frac{\partial p}{\partial \lambda}, \quad v_\lambda \cos\theta = \frac{\partial p}{\partial \theta}, \quad \rho = -\frac{\partial p}{\partial z}, \quad \frac{\partial v_z}{\partial z} + \frac{1}{\sin\theta}\frac{\partial}{\partial\theta}(v_\theta \sin\theta) + \\
&+\frac{1}{\sin\theta}\frac{\partial v_\lambda}{\partial\lambda} = 0, \quad \frac{\partial\rho}{\partial t} + \frac{v_\lambda}{\sin\theta}\frac{\partial\rho}{\partial\lambda} + v_\theta\frac{\partial\rho}{\partial\theta} + v_z\frac{\partial\rho}{\partial z} = \nu\frac{\partial^2\rho}{\partial z^2}, \quad \frac{\partial b_z}{\partial z} + \frac{\partial b_\theta}{\partial\theta} + b_\theta\, ctg\,\theta + \\
&+\frac{1}{\sin\theta}\frac{\partial b_\lambda}{\partial\lambda} = 0, \quad \frac{\partial b_z}{\partial t} = b_\theta\frac{\partial v_z}{\partial\theta} + \frac{b_\lambda}{\sin\theta}\frac{\partial v_z}{\partial\lambda} + b_z\frac{\partial v_z}{\partial z} - v_\theta\frac{\partial b_z}{\partial\theta} - \frac{v_\lambda}{\sin\theta}\frac{\partial b_z}{\partial\lambda} - v_z\frac{\partial b_z}{\partial z}, \qquad (5)\\
&\frac{\partial b_\theta}{\partial t} = b_\theta\frac{\partial v_\theta}{\partial\theta} + \frac{b_\lambda}{\sin\theta}\frac{\partial v_\theta}{\partial\lambda} + b_z\frac{\partial v_\theta}{\partial z} - v_\theta\frac{\partial b_\theta}{\partial\theta} - \frac{v_\lambda}{\sin\theta}\frac{\partial b_\theta}{\partial\lambda} - v_z\frac{\partial b_\theta}{\partial z},\\
&\frac{\partial b_\lambda}{\partial t} = b_\theta\frac{\partial v_\lambda}{\partial\theta} + \frac{b_\lambda}{\sin\theta}\frac{\partial v_\lambda}{\partial\lambda} + b_z\frac{\partial v_\lambda}{\partial z} - v_\theta\frac{\partial b_\lambda}{\partial\theta} - \frac{v_\lambda}{\sin\theta}\frac{\partial b_\lambda}{\partial\lambda} - v_z\frac{\partial b_\lambda}{\partial z}.
\end{aligned}
$$

Note that the components of the magnetic force included in the equations of motion are of the order of the ratio of the Rossby number to the square of the Alfvén number, and hence these components are not included in the first three equations of Eq. (5) for the principal terms of the expansions. Their consideration is necessary when describing motions other than geostrophic motions, i.e., using the terms of the corresponding series of expansions of the desired functions by a small Rossby number of a higher order of smallness.

From the form of the equations of system Eq. (5) we can conclude that the velocity field is divergence-free, geostrophic and hydrostatic; and that the vertical density gradient is not given by a horizontally homogeneous density field, but is determined by the fluid motion. In the fifth equation of system Eq. (5), the parameter ν is given as $\nu = k_V r_0 U^{-1} D^{-2}$. If $k_V = 0,1\, sm^2/s$, $U = 1\ sm/s$, $D = 4 \cdot 10^6\, sm$ then $\nu = O(10^{-6})$. Note that the term proportional to ν, is rather small, but, nevertheless, it will be taken into account in system Eq. (5) in order to describe the thermal layer at the boundary between the Earth's liquid core and the mantle.

Let us note an important property of the dynamics of large-scale geostrophic motions of an electrically conducting fluid. It consists in the fact that, as in the case of ordinary hydrodynamics, the geostrophic approximation does not lead to a degenerate

character of the system of equations for the principal terms of the corresponding expansions, in contrast to geostrophic motions with a smaller horizontal scale L, such that Lr_0^{-1} it is much smaller than unity. It should be noted that at a large value of the horizontal scale of motion, the Maxwell equations of solenoidality and magnetic field induction for the principal terms of the corresponding expansions retain their form in the sense of the form of the initial named equations in the dimensional form. Note that the validity of the geostrophic approximation is violated in equatorial regions where the Coriolis force on horizontal currents is very weak. Thus, the geostrophic approximation by its very nature cannot be a global theory, so we assume that the considered motion occurs in a region located in the midlatitudes in the vicinity of latitude θ_0 and far from the equator.

Thus, the problem is to determine the density distribution and all magnetohydrodynamic quantities resulting from thermodynamic changes near the boundary of the region, assuming that such a problem is described by the large-scale dynamics equations derived above.

Let us consider the boundary conditions for the initial system. We will study the dynamics below the Eckmann layer adjacent to the boundary of the liquid layer. Since viscosity is negligible in the region under consideration, it is sufficient to set the normal velocity component at the upper boundary. Let the origin of coordinates be at the boundary of the liquid layer. Thus, $v_z = v_{ze}(\theta,\ \lambda,\ 0)$. At the upper boundary of the region under consideration, the density must be matched with the given density field at the surface of the layer, which varies insignificantly in the narrow Eckmann layer at the boundary of the liquid spherical region. Taking into account the State equation of $\rho_* = \rho_0(1 - \alpha T_*)$, we obtain

$$\rho(\theta,\ \lambda,\ 0) = -\frac{\alpha g D^2 F_0}{2\omega W r_0^2}\, T_s(\theta,\ \lambda), \tag{6}$$

where F_0—the characteristic value of surface temperature changes, α—the coefficient of thermal expansion. The function $T_s(\theta,\ \lambda)$ defines the horizontal structure of the surface temperature field and is of order $O(1)$. Further we choose the vertical scale of motion D such that

$$D = \sqrt{\frac{2\omega W r_0^2}{\alpha g F_0}}, \tag{7}$$

and, therefore, ρ is of order $O(1)$.

When the vertical scale of motion is chosen by the relation (7), the horizontal density changes in the layer will be of the same order as the horizontal changes in the surface density. Considering that $2\omega \approx 1,5 \cdot 10^{-5}\, s^{-1}, r_0 = 6 \cdot 10^8\, sm$, $\alpha F_0 \approx 3 \cdot 10^{-4}$, $g = 10^3\, sm \cdot s^{-2}$, $W = 10^{-2}\, sm \cdot s^{-1}$, we get an estimate for D : $D = 40\ km$.

This estimate agrees with known geophysical estimates. Since D is much smaller than the thickness of the liquid region volume, it is assumed z vary from $-\infty$ to 0.

At $z \to -\infty$ the density perturbation dampens and the vertical velocity component rushes to its asymptotic value. In addition to the considered boundary conditions, we require the fulfilment of the following conditions

$$b = b^{(e)}, \quad z = 0, \qquad v_\theta \to 0, \quad v_\lambda \to 0, \quad b_\theta \to 0, \quad b_\lambda \to 0, \qquad z \to -\infty. \tag{8}$$

We will construct spiral perturbations of the system Eq. (5) for which $\frac{\partial}{\partial \lambda} = 0, b_\lambda = 0$. Then the initial system takes the form

$$v_\theta = 0, \quad v_\lambda = \frac{1}{\cos\theta}\frac{\partial p}{\partial \theta}, \quad \frac{\partial v_z}{\partial z} = 0, \quad \rho = -\frac{\partial p}{\partial z}, \quad v_z \frac{\partial^2 p}{\partial z^2} = \nu \frac{\partial^3 p}{\partial z^3} - \frac{\partial^2 p}{\partial p \partial z},$$
$$\frac{\partial b_z}{\partial t} = b_\theta \frac{\partial v_z}{\partial \theta} - v_z \frac{\partial b_z}{\partial z}, \quad \frac{\partial b_\theta}{\partial t} = -v_z \frac{\partial b_\theta}{\partial z}, \quad b_\theta \frac{\partial v_\lambda}{\partial \theta} + b_z \frac{\partial v_\lambda}{\partial z} = 0, \quad \frac{\partial b_z}{\partial z} + \frac{\partial b_\theta}{\partial \theta} + b_\theta \, ctg\, \theta = 0. \tag{9}$$

The characteristics of the seventh Eq. (9) are the integral curves of the system of ordinary differential equations $dt = \frac{d\theta}{0} = -\frac{dz}{v_z} = \frac{b_\theta}{0}$, having functionally independent first integrals $\theta = C_1$, $z = -\int v_z(\theta, t)\, dt = C_2$, $b_\theta = C_3$.

Then the general solution of this equation is given by the formula $\Phi\big(\theta, z - \int v_z(\theta, t)\, dt, b_\theta\big) = 0$, where Φ is an arbitrary noncontinuously differentiable function. From the presented relation follows the required expression for the θ-component of the magnetic field $b_\theta = f\big(\theta, z - \int v_z(\theta, t)\, dt\big)$, where f is an arbitrary function determined from the corresponding boundary conditions. Thus, there exists a solution $b_\theta = \exp\big(\theta, z - \int v_z(\theta, t)\, dt\big)$. The ninth equation of the system (9) allows us to introduce the function $\psi(\theta, z)$ by the relations $b_z = \frac{1}{\sin\theta}\frac{\partial \psi}{\partial \theta}$, $b_\theta = -\frac{1}{\sin\theta}\frac{\partial \psi}{\partial z}$, hence

$$\psi(\theta, z, t) - \sin\theta \, \exp\left(z - \int v_z(\theta, t)\, dt\right) + C_0(\theta, t)$$

As a result of this study, the required magnetohydrodynamic characteristics can be represented in analytical form. In contrast to the previously considered stationary models, the value of the vertical velocity at infinity is determined not only by the parameter ν characterising the dissipation intensity, but also by the distribution of the surface temperature function.

The rotation frequency is clearly not included in the final expressions for the magnetohydro-dynamic fields presented in dimensionless form. This is due to the fact that the scale of motion is so large that the characteristic changes of the normal component of the angular velocity of the layer rotation on this scale are equal to $O(1)$. In addition, it should be noted that the angular velocity of the layer rotation is clearly included in the expressions describing the total changes of the density and pressure fields in space represented in the dimensionless form, which follows from the corresponding relations.

In conclusion, we note that the main result of the paper is the analytical solutions of the system of nonlinear partial derivative equations modelling the geostrophic motion in a layer of ideal electrically conductive inhomogeneous rotating fluid taking into account dissipation. The structure of the presented fields of magnetohydrodynamic quantities allows us to draw a qualitative conclusion about the existence of strong changes in the thin layer of the Earth's core adjacent to the boundary with the mantle. In the future, it is possible to carry out numerical analyses of the obtained analytical results in order to identify numerical estimates of the Earth's liquid core parameters and compare them with those known from seismic and gravity observations.

References

1. Aleshkov Y.Z. Mathematical modelling of physical processes. SPb.: Izd-vo SPbSU, 2001. 264 p.
2. Alven G., Felthammar K.-G. Cosmic Electrodynamics. M.: Mir, 1967. 260 p.
3. Gunko Yu.F., Norin A.V., Filippov B.V. Electromagnetic Gas Dynamics of Plasma. SPb.: Izd-vo SPbSU, 2003. 176 p.
4. Kauling T. Magnetic Hydrodynamics. Moscow: Atomizdat, 1978, 144 p.
5. Kirko I.M., Kirko G.E. Magnetic hydrodynamics. Modern vision of problems. M.-Izhevsk: SIC "Regular and Chaotic Dynamics", Izhevsk Institute of Computer Research. 2009. 632 p.
6. Kulikovskiy A.G., Lyubimov G.A. Magnetic hydrodynamics. Moscow: Logos, 2005. 328 с.
7. Landau L.D., Lifshits E.M. Electrodynamics of Continuous Media. Theoret-ical Physics. Т. VIII. M.: Nauka, 1992. 664 p.
8. Pedloski J. Geophysical hydrodynamics. In 2 vol. M.: Mir, 1984. Т. 1. 400 p., Vol. 2. 411 p.
9. Kholodova, S.E. Wave motions in a compressible stratified rotating liquid (in Russian) // Journal of Computational Mathematics and Mathematical Physics. 2008. Т. 47, № 12, P. 2107–2115.
10. Kholodova, S.E. Dynamics of a rotating layer of an ideal electrically conductive incompressible liquid (in Russian) // Journal of Computational Mathematics and Mathematical Physics. 2008. Т. 48, № 5, P. 151–167.
11. Kholodova, S.E. Quasigeostrophic motions in a rotating layer of an electrically conductive liquid (in Russian) // Applied mechanics and technical physics, 2009, No. 1, Vol. 50, P. 30–41.
12. Kholodova, S.E. Wave motions in a stratified electrically conductive rotating liquid (in Russian) // Journal of Computational Mathematics and Mathematical Physics. 2009. Т. 49, № 5, P. 916–922.
13. Peregudin, S.I.; Kholodova, S.E. Dynamics of a rotating layer of an ideal electrically conductive incompressible inhomogeneous liquid in the equatorial re-gion (in Russian) // Journal of Computational Mathematics and Mathematical Physics. 2010. Т. 50, № 11, P. 1–15.
14. Peregudin, S.I.; Kholodova, S.E. About the Peculiarities of Nonstationary Waves Propagation in a Rotating Spherical Layer of an Ideal Incompressible Stratified Electrically Conductive Liquid in the Equatorial Latitudinal Belt // Applied Mechanics and Technical Physics, 2011, No. 12, Vol. 52, P. 44–51.
15. Sedov L.I. Mechanics of Continuous Medium. In 2 vol. M., 1983. Т. 1. 528 p.; 1984. Т. 2. 560 p.
16. Shercliffe J. Course of Magnetic Hydrodynamics. M.: Mir, 1967. 320 p.
17. Kholodova S.E., Peregudin S.I. Waves in a Rotating Layer of an Ideal Electrically Conducting Incompressible Fluid with Allowance Effects of Diffusion of Magnetic Field // 20th International Workshop on BEAM Dynamics and Optimization, June 30–July 4, 2014, Russia, Saint-Petersburg, P. 133–134.

18. Kholodova S.E., Peregudin S.I. Mathematical and Numerical Analysis of the Waves Motion in Electrically Conducting Incompressible Fluid // International Conference on Numerical Analysis and Applied Mathematics (ICNAAM) Location:Rhodes, GREECE Date: SEP 22–28, 2014.
19. Needler G.T. A model for thermocline circulation in an ocean of finite depth // J. Marine Res., 1967, 25, P. 329-342.
20. Robinson A.R., Stommel H. The oceanic thermocline and the associated thermohaline circulation // Tellus, 1959, 11, P. 295-308.

Coastal Protection System on the Barrier Form of the Lagoon (North-East of Sakhalin)



V. V. Afanas'ev, I. O. Leont'ev, and A. V. Uba

Abstract Prediction of the vulnerability of sandy seashores to storm spills is very relevant, especially in connection with a possible increase in relative sea level caused by tectonics and climate change. The morpholithodynamic justification of the bank protection system makes it possible to transfer it to the category of nature-like ones and reduce the estimated cost by tens of times. For Holocene barrier-shaped bay-bars, when identifying vulnerable areas even on a "homogeneous" shore, the erosion index can be used, which, as the presented results show, has sufficient sensitivity. The experience of forming a beach in the area of erosion by restructuring the system of megafestoon distribution of beach sediments seems valuable and interesting.

Keywords Sakhalin Island · Coast dynamics · Mathematical modeling · Megacusps

1 Introduction

The study area is a complex coastal barrier form separating Piltun Bay from the Sea of Okhotsk. Areas with high coastal ledges, composed of Neogene-Pleistocene sediments (mainly unconsolidated, sandy-pelite fractions) alternate here with Holocene barbars proper. The exposed thickness of the Holocene marine formations within the bay-bar is about 30 m. There are no areas with high levels in the zone of late Holocene migrations of the straits. They were destroyed here in the first phases of coastal-marine accumulation [1].

V. V. Afanas'ev (✉) · I. O. Leont'ev · A. V. Uba
Sakhalin State University, Yuzhno-Sakhalinsk, Russia
e-mail: vvasand@mail.ru

Shirshov Institute of Oceanology of the Russian Academy of Sciences, Moscow, Russia

A. V. Uba
e-mail: vvasand@mail.ru

© The Author(s), under exclusive license to Springer Nature Switzerland AG 2024

V. Karev (ed.), *Proceedings of the 9th International Conference on Physical and Mathematical Modelling of Earth and Environmental Processes*, Springer Proceedings in Earth and Environmental Sciences, https://doi.org/10.1007/978-3-031-54589-4_39

Data on the intensity and activity of erosion were obtained by analyzing aerial photo information (flights in 1952, 1974) and space photo information (2014 and 2020). To construct erosion intensity maps, the QGIS 2.8.2 Wien program was used. All calculations were carried out in the ESPG:3395 system. Processing of aerial photo information arrays occurred as follows. At the first stage, electronic versions of the AFS flight strips for the period 1952–1985 were created. Then a raster topographic map at a scale of 1:100,000 was coordinated in the free cross-platform geographic information system QGIS (Quantum GIS) and all APS strips were coordinated using characteristic points. After implementing the transformation procedures, the degree of contour coincidence of the geographical objects of the highest quality APS strip with the drawing on the topographic map was checked. The most adequate option was chosen. The remaining APS bands were tied to it using almost the same reference points. From 1999 to 2020, coastal dynamics were analyzed based on interpretation of the CS in the QGIS 2.8.2 Wien environment.

After the implementation of the transformation procedures, on two scales, at one-hundred-meter intervals and five-hundred-meter intervals, the areas of land loss and the volume of the destroyed ledge were determined (Fig. 1). Areas for which the coastal zone deformation values are less than the image resolution are classified as stable.

An analysis of the features of the morpholithodynamics of complexly constructed and "classical" sand bars separating lagoons from the open sea showed that complexly constructed barrier forms are characterized by a higher variability of deformations of the sea edge of Holocene areas than completely Holocene barbars [2]. Such barrier forms are also characterized by a greater variety of morphometric parameters of the upper part of the coastal profile. In addition, areas located between the eroded high terraces are steadily shifting towards the lagoon (Fig. 2).

The average long-term erosion rates nowhere exceed 2 m/year. However, even in relatively stable areas of Holocene bay bars, erosion rates in some periods can exceed several meters per year.

2 Methods and Results

It is well known that a relatively narrow beach dissipates only part of the wave energy, the rest of which is spent on erosion of the dune belt or adjacent land. At the same time, a wide beach, as a rule, indicates a stable position of the coast. Storm erosion in Holocene barrier-shaped areas does not have irreversible consequences, i.e. the coast maintains dynamic balance and is able to recover from storm attacks.

The entire range of field studies of the beach was used—the main wave-damping form of relief of the coastal zone on the upper elements of the coastal profile.

The composition, morphometry, thickness and structure of beach deposits were determined. It was established that the features of erosion of the coastal ledge, fore-dunes, and low terraces in the rear edge of the beach, where zones of stable and eroded coast alternate, are tied to the rhythmic forms of the beach relief. Depending

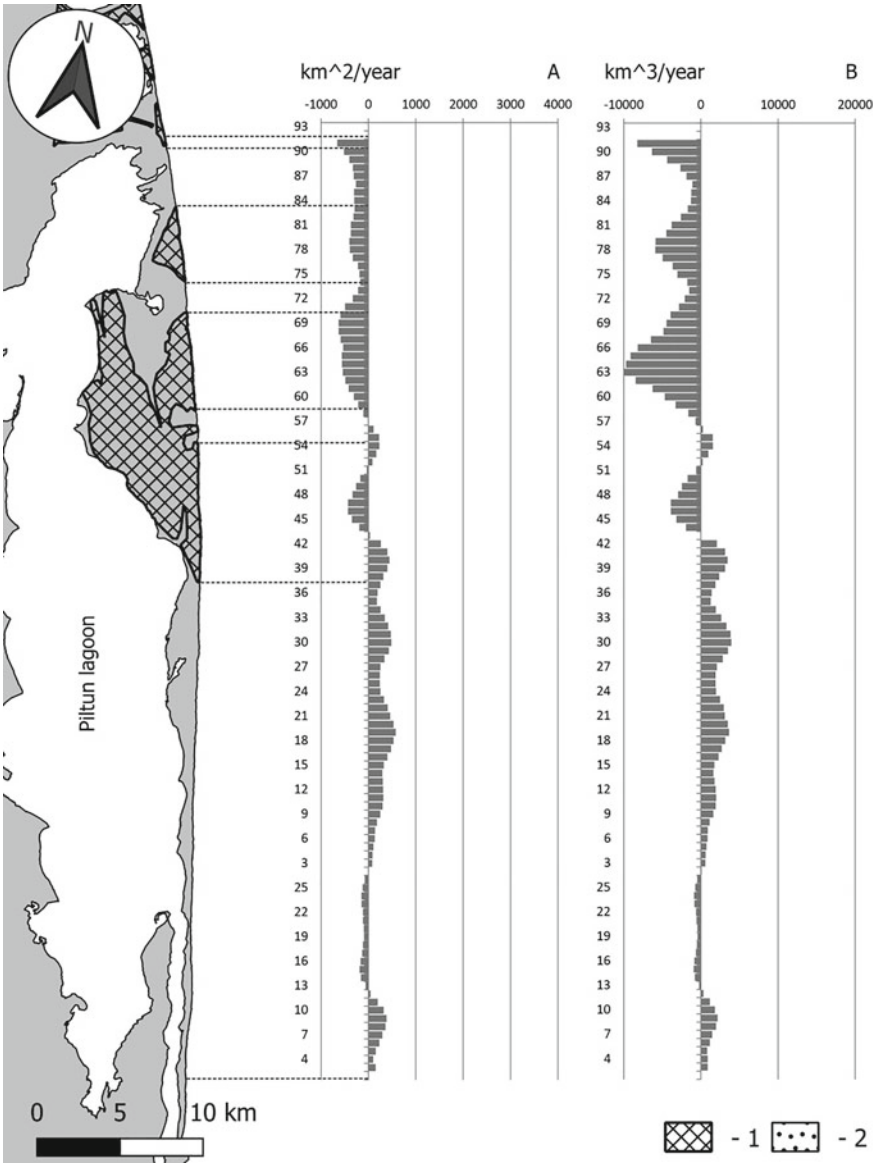


Fig. 1 Average long-term erosion rates of the complexly constructed barrier form of the Piltun Lagoon (averaging over 500-m sections): 1—high sea terraces, 2—low sea terraces



Fig. 2 Remains of reinforcement from wells drilled on the surface of the Holocene bay bar in the sea

on the type of forms, the position of the zones in space can either change, if we are talking about moving sand waves, or remain more or less stable, if we mean a sedentary system of megafestons.

When modeling the optimal parameters of a sandy beach, as well as calculating the index for assessing the danger of storm erosion, morphometric parameters of the above-water part of the beach were used as indicators of the state of the coast. Comparing the actual beach volume with the reference value V_{b*} can provide insight into the current state of the beach and its future changes.

The maximum elevation of the beach consists of the heights of wave run-up R, storm surge η, as well as tidal and seasonal level fluctuations $\tilde{\eta}$. The corresponding width of the beach depends on its slope $\beta_* = \tan\alpha$, where α is the average slope angle, and the volume per unit length of the coast is determined by the product of the linear dimensions of the beach

$$z_{b*} = R + \eta + \tilde{\eta}, l_{b*} = \frac{z_{b*}}{\beta_*}, V_{b*} = l_{b*} z_{b*}/2, \quad (1)$$

Высота заплеска на пологих песчаных берегах, подверженных воздействию штормовых волн, может быть оценена по зависимости [3]:

The splash height on flat sandy shores exposed to storm waves can be estimated from the relationship [3]:

$$R = 0.043\sqrt{H_{s0}L_0}, L_0 = \frac{g}{2\pi}T_p^2, \quad (2)$$

where H_{s0}, L_0, и T_p—significant height, length and period of the spectral peak in deep water. The heights of storm surges η and tides $\tilde{\eta}$ can be estimated based on available reference data.

The slope of the beach in equilibrium, according to [4], is determined by the relationship

$$\beta_* = 0.12\left(\frac{T_p\sqrt{gd_g}}{H_{sB}}\right)^{0.5}, \quad (3)$$

where d_g—average sand particle size (in meters), H_{sB}—significant wave height at the breaking point. For relatively steep storm waves, the value of H_{sB} in formula (3) can be replaced to H_{s0} without large errors [5], which simplifies the calculations.

Formula (3) predicts a relatively weak dependence of the slope on the sand size ($\sim d_g^{1/4}$). However, according to the observations of Bascom [6], the size of solid particles appears to be the main factor influencing the slope of the beach. The dependence he obtained for the minimum slope can be approximated as.

$$\beta_* = 0.237d_g^{3/2} - 0.010, 0.2 < d_g < 0.8\text{MM}. \quad (4)$$

In the future, it is recommended to use both of these dependencies in accordance with the actual data.

Thus, the given formulas determine the optimal parameters of the beach as a function of the characteristics of the tide, wind and waves, the morphology of the shore and the size of the material composing the beach.

Of greatest practical interest are the characteristics of the beach that correspond to fairly significant storm events, for example, storms with a return period of 1 year. If the actual volume of the beach V_b is less than the value V_{b*}, corresponding to such a storm, then at least once a year the foredune or adjacent land will be eroded to compensate for the deficiency of beach material. With noticeable differences in volumes, when $V_b < V_{b*}$, there is a high probability of progressive erosion and retreat of the coast. And vice versa, in the case $V_b > V_{b*}$, the supply of beach material turns out to be sufficient to maintain equilibrium. Thus, for example, the following ratio can be used as an index of coastal erosion:

$$I_e = \frac{V_b - V_{b*}}{V_{b*}}. \quad (5)$$

Taking into account possible errors in calculating both theoretical and actual beach volumes, it makes sense to highlight the range of index values $0.1 \leq I_e \leq 0.1$, for which an unambiguous assessment of the state of the coast is difficult due to small differences between V_b and V_{b*}. For shores falling within the specified range of I_e,

, the probability of erosion can be considered quite low. Positive values of the index I_e>0.1 characterize the state of the coast as stable (no erosion), and negative values $I_e < -0.1$ I—as vulnerable.

In the latter case, the value of I_e gives an idea of the relative volume of sediment deficit, which, in particular, makes it possible to predict the evolution of the retreating coast. Let us assume that the beach experiences a sediment deficiency in the volume $V_b - V_{b*} = \Delta V$, an abrasion cliff with a height of h_{cl} recedes at a speed of c_{cl}, and the proportion of beach-forming fractions in the cliff material is $n_b < 1$, of which only part k_b remains on the beach. The question arises: to what distance X_{cl} and for what time t_{cl} should the cliff retreat so that the deficit is replenished and the shore reaches dynamic equilibrium? Presenting the volume of beach material coming from the cliff as $V_{cl} = k_b n_b h_{cl} X_{cl}$, and equating it to the value ΔV, we find

$$X_{cl} = \frac{\Delta V}{k_b n_b h_{cl}}, \; t_{cl} = \frac{X_{cl}}{c_{cl}}. \tag{6}$$

Note that as the volume of the beach increases, the rate of cliff retreat should slow down. Therefore, the actual time t_{cl} will most likely be greater than the calculated one.

As an example, imagine that the sediment deficit on the beach is ΔV = -20 m^3/m. The cliff, characterized by a heigh t h_{cl} =5 m and a content of beach-forming material n_b=0.1, retreats at a rate of c_{cl}= 1 m/year, and half of the incoming sediment remains on the beach (k_b=0.5). According to (6), the retreat of the coast will stop when the cliff moves at a distance of X_{cl}= 80 m, which will require time t_{cl}=80 years. Such assessments can probably be useful when planning economic activities on abrasion banks.

As an object for testing the I_e index, we selected beaches that either end in a coastal bank or dune, or are adjacent to a cliff (Fig. 3.4). Based on available data, the average sand size on the beach is assumed to be d_g=0.5 mm.

The height of the wave splash, calculated by formula (2), is estimated as R=1.5 m. The values of the beach slope β_*, calculated by formulas (4) and (5), are equal to 0.043 and 0.074, respectively. Next we use the average value β_*=0.06. Thus, the optimal height, width and volume of the beach are determined by the following values: z_{b*}=2.7 m, l_{b*}=45.0 m, V_{b*}=60.8 m^3/m.

The actual parameters of the beaches were estimated based on the profiles shown in Figs. 3 and 4. The beach boundary corresponds to the point of increasing slope at the foot of the cliff or foredune.

The observed beach elevations vary in the range from 1.5 to 3.1 m and are generally less than the reference value z_{b*}=2.7 m. This can be interpreted as a sign of erosion conditions in the areas under consideration.

As for the width of the beaches and their volumes, they vary greatly from profile to profile. The fact is that the coastal area under consideration is characterized by the presence of developed rhythmic relief forms such as sand waves or megafestons, which determine the undulating pattern of the coastline. Beach profiles on accumulative shore ledges are characterized by significant width and a large supply of

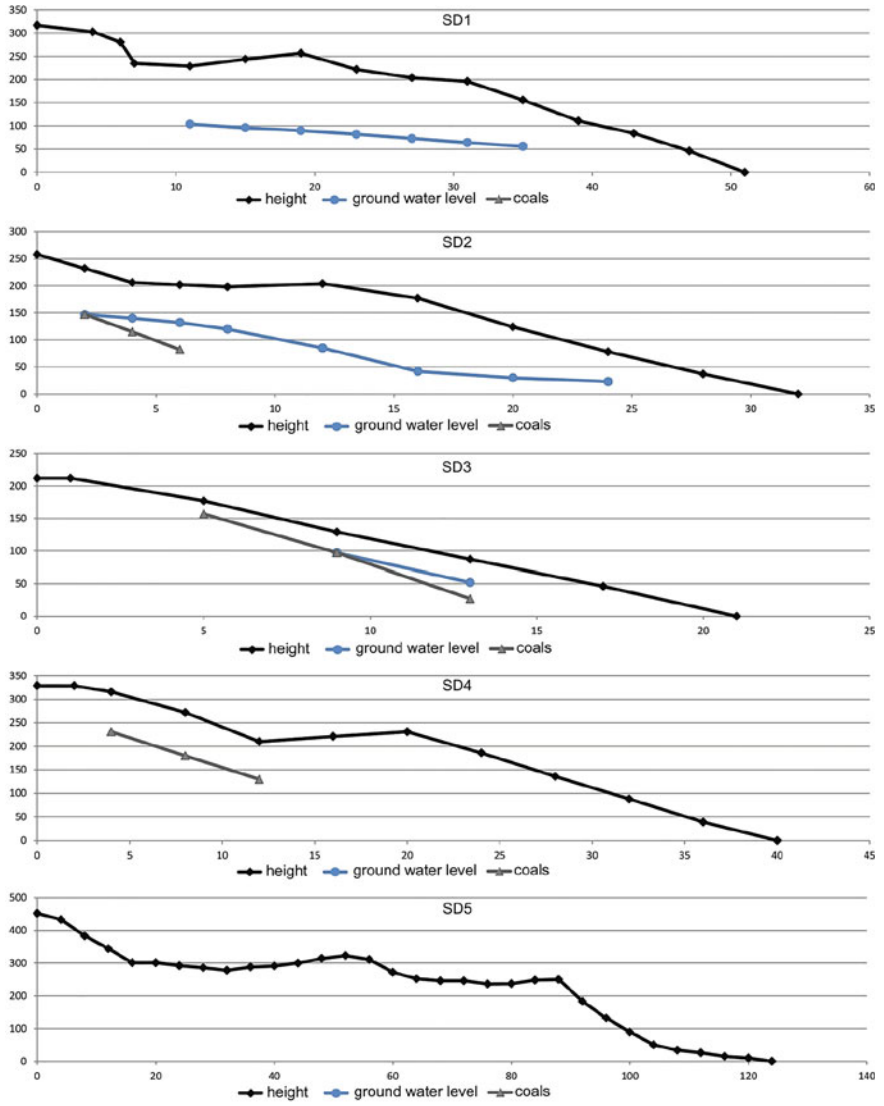


Fig. 3 Morphometric parameters, beach structure and position of the upper boundary of bedrock

material. This applies to profiles SD1, SD4, SD5. The erosion index here is positive everywhere, respectively—0.21; 0.08; 0.64 and characterizes the coast as stable.

On profiles falling on concave sections of the coast (SD3, SD1), the beaches are narrow and insufficiently voluminous. The situation is especially unfavorable on the SD3 profile (erosion index -0.84), where the thickness of the sand layer lying on a clayey substrate is less than 0.5 m. As the erosion index shows, the beach contains only 1/7 of the required volume of sand. A significant shortage of material is also

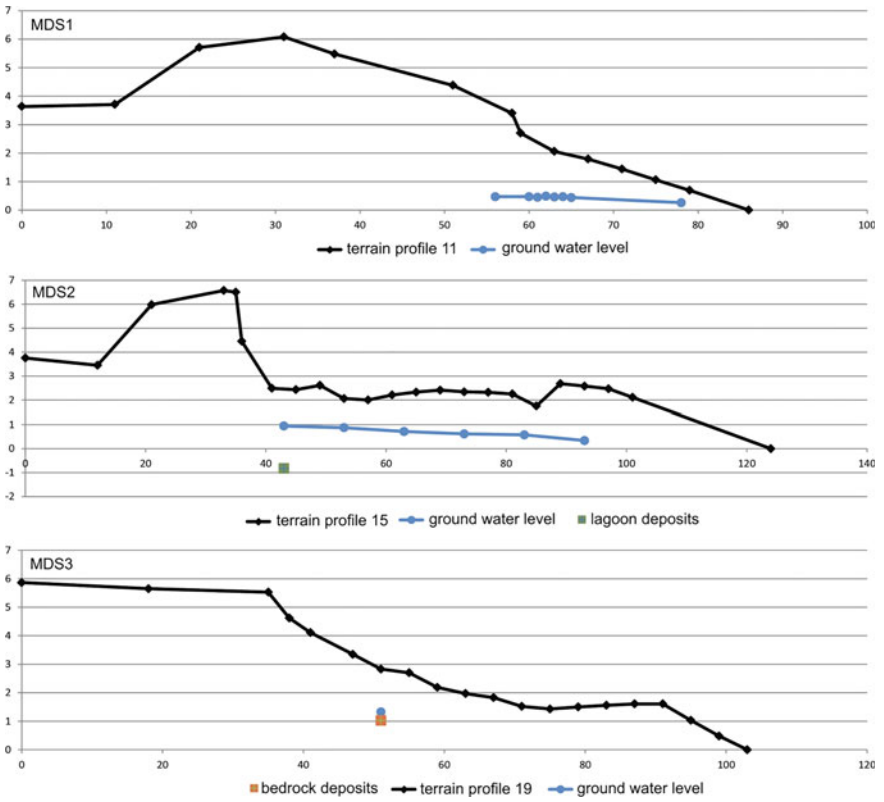


Fig. 4 Profiles of beach sections with a certain thickness of the active slope

observed on profile MDS1 (erosion index −0.77), where 3/4 of the required volume of sand is missing. Both profiles are characterized by maximum slopes (0.10 and 0.11). Obviously, progressive erosion should be expected in these areas.

Atypical properties are demonstrated by the MDS2 profile located on the accumulative protrusion. The width of the beach and the supply of sand here are quite large and, judging by the index value, the coast should be stable. However, the height of the beach does not exceed 1.8 m, and storm waves can probably reach the cliff and erode it. True, the recession rate should be low, since the wave splash weakens significantly when propagating over an almost horizontal bottom surface. The modeling results show that the erosion index is sufficiently sensitive and can be used to identify vulnerable areas even on a "homogeneous" section of the coast.

An additional factor contributing to coastal erosion is the rise in relative sea level, caused by both climate change and tectonic processes. An assessment based on the well-known Bruun rule [7] shows that a rise in level of 3 mm per year should cause an annual retreat of the coast by 0.2–0.3 m. In conditions of even a sufficient amount

of sediment, the coast actually recedes in areas between high terraces about twice as fast.

2.1 Basic Approaches to Solving the Problem of Engineering Protection

The main approaches were determined as a result of the analysis of the geological and geomorphological structure of the coastal zone, the features of morpholithodynamics and the morpholithodynamic regime in different areas of the complex barrier shape of the Piltun lagoon (Fig. 5).

Each site is characterized by its own morpholithodynamic position in a high-order morpholithosystem with a long (mid-late Holocene) history of development and features of modern morpholithodynamics associated with the conditions and possibilities for the mobilization of material from different elements of the coastal profile, transport and accumulation. This requires different approaches to assessing the magnitude of impacts and determining development scenarios and, accordingly, different approaches to solving the problem of protecting structures and communications.

Section No. 1. The high sea terrace is eroded at an average annual rate of more than 1.5 m/year, and in certain periods the rate of retreat of the coastal ledge exceeded 3 m/year. Sediment reserves in the coastal zone, when distributed evenly along the coast, make it possible to form a beach with parameters that ensure complete wave suppression during extreme storms. However, seasonal rearrangements of lithodynamic cells and trend changes in their plan position make the coastal zone vulnerable to erosion as a result of high-frequency storm events throughout the entire area.

Stabilization of the coastal ledge is possible with rigid fastening of the lower elements of the coastal ledge or can be ensured by measures that prevent the formation of a megafestoon distribution of beach material along the coast.

Section No. 2. Holocene bar with an average annual rate of displacement in the westerly direction of about 0.5 m. In some areas, peatlands with an apparent thickness of up to 1 m are exposed in the low coastal ledge. The relative stability of the coast is ensured by the erosion of adjacent sections of the coast and, as a result, the entry into the coastal zone of large volumes of beach-forming sediments. Erosion mainly results in seasonal rearrangements of lithodynamic cells and trend changes in their plan position. Protection by rigid wave-damping structures, according to the research conducted, is impossible, given the discontinuous occurrence of peat bogs at the base of the section, which could serve as a stop that distributes the load from the stone-concrete bank protection onto the underlying sands and silts. The most preferable option for protecting communications and structures would be to restore the dunes and secure them, primarily with vegetation.

Section No. 3. This section is characterized by a high coastal ledge and is destroyed very unevenly over time. Currently, throughout most of the site there is a narrow



Fig. 5 Location of bank protection areas

modern marine terrace covering the coastal ledge. Protection of this site is not required, due to the absence of the risk of destruction of structures and communications in the next 15–20 years. Moreover, washed away material entering the coastal zone from this area provides sediment for areas No. 2 and No. 4.

Section No. 4. Holocene bay bar with average long-term rates of displacement in a westerly direction from 2.0 m/year on the southern fragment to 0.5 m/year. In this area in November, as a result of the formation of a megafestoon structure, the bay-bar was washed out and a threat to the oil pipeline arose (Fig. 6). At the base



Fig. 6 Emergency work on the washout area on November 25, 2016

of the beach deposits at a level of about minus 2 m (BS 77) lie weak, fine-grained sands of lagoonal facies. The maximum thickness of the active layer at the foot of the coastal ledge exceeds 5 m, and taking into account changes in the elevations of the rear edge of the beach along the coast, it can reach 7 m.

Rigid structures are practically excluded in this situation. It should be noted that sediment reserves in the coastal zone along the 1800 m stretch between the North and South domes are about 250,000 m^3, which, with a uniform distribution, makes it possible to create a beach along the entire coast, providing complete wave extinction under the observed parameters of the coastal profile. Stabilization of the coastal ledge can be ensured by measures that prevent the formation of a megafestoon distribution of beach material along the coast, or by slope fastening with sandbags, which will need to be maintained in working condition at all times (sandbags).

It was in this area that an experiment was conducted to change the structure of the distribution of beach parameters along the coast. As a result of bypassing beach material from the megafestoon ledge on the southern flank of the site into the erosion zone dangerous for the oil pipeline, a beach up to 70 m wide was formed literally 2 weeks in front of temporary protective structures (Fig. 7).

Section No. 5. The average long-term erosion rate in area No. 5 in the area of the Southern Dome is about 1.5 m. This area is characterized by the largest volumes of debris entering the coastal zone during erosion of the coastal ledge. The beach lies on lithified soaking clays. The site, as well as the entire region, is characterized by an uneven distribution of beach sediments along the coast in the form of megafestoons. The maximum width reaches 120 m, the minimum 15–20 m. Section No. 5 is the only section where the use of heavy bank protection structures is possible with virtually no restrictions. The preferred option for protecting the South Dome production site is a slope-type fastening with a slope of 1:2–1:3 in the form of a multi-layer structure made of natural stone.



Fig. 7 The beach formed in September 2016 as a result of an experiment (status as of May 2017)

Section No. 6. As for the completely Holocene site No. 6, on a 60-year time scale the coastline shifted westward (erosion) only in the 8-km section in the middle part; in the remaining areas the formation of a modern terrace was observed (accumulation). Nevertheless, as the route survey showed, almost everywhere at present there is a ledge of erosion.

3 Conclusion

By analyzing the dynamics of the barrier accumulative Holocene-Pleistocene formation with a length of more than 60 km over a period of more than 50 years, the structure and quantitative characteristics of erosion and accumulation were established.

The average annual erosion rates do not exceed 2 m/year anywhere. The rate of erosion of high terraces approximately corresponds to the intensity of destruction of similar formations of the coastal plains. A characteristic feature of the coast is the presence of sand waves and megafestons with a period from 200–300 m to 500–800 m. In areas where beach "capes" are observed, the width of the beach zone is 65–80 m. No erosion of terraces and foredunes is observed in these areas. The erosion zones are confined to the "concavity" areas of megafestons, where the width of the beach at high tide is 3–8 m. It was with the formation of the megafestoon structure of the distribution of beach sediments that the erosion of the coastal ledge at site No. 4 in the fall of 2015 and the displacement of beach material in a volume of

approximately 120–150 thousand m^3 in a southerly direction, 1.0–1.5 km south of the erosion zone, were associated. Storm erosion in Holocene barrier-shaped areas does not have irreversible consequences, i.e. the coast maintains dynamic balance and is able to recover from storm attacks. However, in areas located between high terraces, there is a steady tendency for the embankment to shift towards the lagoon. It is for Holocene barrier-shaped bay-bars that the erosion index can be used to identify vulnerable areas even on a "homogeneous" shore, which, as the presented results show, has sufficient sensitivity.

The morpholithodynamic justification of the bank protection system makes it possible to transfer it to the category of nature-like ones and reduce the estimated cost by tens of times.

The experience of forming a beach in the area of erosion by restructuring the system of megafestoon distribution of beach sediments seems valuable and interesting.

References

1. Afanasyev V.V. Morpholithodynamics of lagoon straits of northeastern Sakhalin // Geomorphology. 2019.№ 2.№ 2. P.79–94.
2. Afanasyev V.V. Morpholithodynamic processes and development of the coasts of the contact zone of the subarctic and temperate seas of the Northern Pacific //Yuzhno-Sakhalinsk: IMGiG FEB RAS. – 2020. 234 p.
3. Stockdon, H. F., Holman, R. A., Howd, P. A., & Sallenger Jr, A. H. .Empirical parameterization of setup, swash, and runup // Coastal Engineering. 2006. V. 53. P. 573–588.
4. Sunamura T. Sandy beach geomorphology elucidated by laboratory modeling // Applications in coastal modeling. Eds. Lakhan V.C., Trenhail A.S. Elsevier, Amsterdam, 1989. P. 159–213.
5. Larson M., Kraus N.C. SBEACH: numerical model for simulating storm-induced beach change. Tech. Rep. CERC-89–9. 1989. US Army Eng. Waterw. Exp. Station. Coastal Eng. Res. Center.
6. Bascom V. Waves and beaches. L.: Gidrometeoizdat, 1966. 280 p.
7. Bruun P. The Bruun rule of erosion by sea-level rise: a discussion on large-scale two- and three-dimensional usages // J. of Coastal Res. 1988. V. 4. № 4. P. 627–648.

Hydrocarbon Composition of Kazantip Cape Coastal Sediments (Azov Sea, Crimea)



O. V. Soloveva and E. A. Tikhonova

Abstract The study of the hydrocarbon composition of coastal sediments at Kazantip Cape (Crimea) in the Azov Sea was conducted. On the one hand, this water area is suffered with a high level of anthropogenic load: recreation areas are located along the shores, hydrocarbon production is carried out on the cape, on the other hand, a part of the territory is a protected natural reserve. The final depot for the accumulation of any kind of pollutants and, accordingly, an indicator of the level of pollution, are bottom and coastal sediments. Determination of the qualitative and quantitative composition of hydrocarbons in coastal sediments was carried out using gas chromatography on a Kristall 5000.2 chromatograph. As a result, new data on the distribution of hydrocarbons in the bottom sediments of the coastal waters of Kazantip Cape with different levels of anthropogenic load were obtained. The places of their concentration were detected. The assessment of the level of hydrocarbon pollution and the probable sources of their entry into the marine environment was made. It was shown that the bottom sediments of the coastal zone of Kazantip Cape were not polluted and the concentrations of the main groups of hydrocarbons were within the average values for the Azov Sea. However, the presence of fresh influx of oil hydrocarbons, which can be of both anthropogenic and natural origin, was noted.

Keywords Hydrocarbons · Coastal sediments · Diagnostic indices · Kazantip Cape · Azov Sea

A lot of attention is paid to the study of coastal waters and their pollution. Heavy metals are mainly considered as pollutants of bottom sediments and water in coastal waters under anthropogenic influence [1, 2]. At the same time, pollution of water areas with organic substances is no less important, and often on a large scale [3, 4]. Currently, both domestic specialists [5] and foreign ones [6, 7] are working on issues

O. V. Soloveva · E. A. Tikhonova (✉)
A.O. Kovalevsky Institute of Biology, Southern Seas of RAS, 2, Nakhimov Avenue, Sevastopol 299011, Russia
e-mail: tihonoval@mail.ru

© The Author(s), under exclusive license to Springer Nature Switzerland AG 2024

V. Karev (ed.), *Proceedings of the 9th International Conference on Physical and Mathematical Modelling of Earth and Environmental Processes*, Springer Proceedings in Earth and Environmental Sciences, https://doi.org/10.1007/978-3-031-54589-4_40

of identifying hydrocarbons in components of the environment, including the marine environment. Despite a significant number of publications on this issue, problems associated with organic pollution, in particular with the origin of hydrocarbons, are not sufficiently covered. The objects of study are often water areas with high anthropogenic load, and obviously elevated levels of hydrocarbons (in particular, oil). The features of the content, distribution and migration of these compounds and substances within relatively favorable environmental waters have practically not been studied.

Kazantip Cape is a natural reserve area, on the one hand, and anthropogenically loaded place, on the other. The Kazantip Nature Reserve is located on the cape. Its shores are washed on one side by the waters of the Arabat Bay, on the other by the Kazantip Bay of the Azov Sea. The total area of the reserve is 450.1 hectares. The coastal aquatic complex of the cape is a wetland of international importance, which is protected under the Ramsar Convention. The inner part of Kazantip Cape is not part of the reserve; oil production is currently taking place here. The coast of Kazantip Cape is extremely rugged. The surface of many outer slopes is an alternation of karst sinkholes, cracks, and piles of rocks. Small bays are bordered by limestone cliffs that turn into steppe. In addition, on the shores of two bays (Russkaya Bay and Tatarskaya Bay) there are recreation areas from which organic substances can enter the sea [8].

It should be noted that a significant difficulty in interpreting data on hydrocarbon pollution is associated with the natural biogenic origin of many hydrocarbons (HCs). It is also necessary to distinguish between the natural background and pollutants and their sources of entry. At the present stage of development of science, the genesis of organic substances, including hydrocarbons, makes it possible to determine their molecular composition and biomarkers, which are calculated on its basis [9, 10], which to one degree or another indicate the origin of this class of substances.

Thus, the purpose of this study is to determine the levels and origin of hydrocarbons in bottom sediments of the coastal waters of a protected area (using the example of the Kazantip Nature Reserve) in order to assess the ecological quality of the environment according to the studied indicators.

1 Material and Methods

The material for the study was samples of the upper layer of sea bottom sediments, which were taken in the summer of 2021 in the coastal waters of Kazantip Cape (Azov Sea) with a manual sampler from depths of up to 1.5 m according to the schematic map (Fig. 1). Selection and preparation of samples of bottom sediments for the determination of hydrocarbons in them were carried out in accordance with regulatory documents [GOST 17.1.5.01-80; ISO 5667-12:1995; ISO 5667-19:2001]. The studied area is an aquatic complex of a natural rreserve. At the same time, oil production is carried out in the central part of the Kazantip Cape. Stations 1, 2 and 8 were located outside the protected area, St. 7—on its south-eastern border, the remaining stations (st. 3–6)—in water areas adjacent to the lands of the reserve.

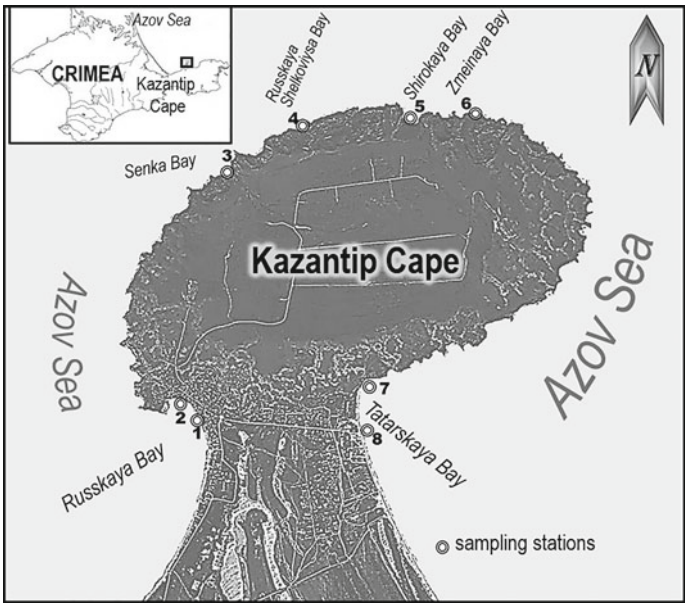


Fig. 1 Scheme of bottom sediment sampling in the coastal waters of the Kazantip Cape (Azov Sea), summer 2021

Determination of the concentrations of aliphatic hydrocarbons (AHC) and normal alkanes (n-alkanes) was carried out on the basis of the Spectrometry and Chromatography Shared Use Center of the Federal Research Center IBSS. A dried and sieved sample of 1–2 g was extracted into 150 ml of n-hexane in a Soxhlet apparatus for one hour. The resulting extract was purified using a glass column filled with alumina to remove polar compounds. The resulting extract was concentrated to 1 ml.

An aliquot of the concentrated extract was injected with a microsyringe into the evaporator of a Kristall 5000.2 gas chromatograph with a flame ionization detector heated to 250 °C. HC separation was carried out on an HT8 capillary column with dimensions of 30 m × 0.32 mm with a stationary phase thickness of 0.25 μm (Thermo Scientific). The column temperature was programmed from 40 °C to 300 °C (temperature rise rate 10 °C/min). The carrier gas flow (nitrogen) in the column is 2.5 ml/min. without splitting the flow. Detector temperature 320 °C.

Quantitative determination of n-alkane content was performed by absolute FID calibration with a mixture of n-alkanes. The latter was the standard sample ASTMD2887 Reference Gas Oil (SUPELCO, USA). To process the results, we used the Chromatek Analyst 3.0 software, the method of absolute calibration and percentage normalization.

The chromatographically unresolved mixture (UCM) was calculated by subtracting the peaks of chromatographically separated compounds from the total n-hexane-extracted hydrocarbon mixture. The total amount of AHC and UCM was quantified by taking the response factor as 1.0 based on n-alkanes.

In order to understand how hydrocarbons released into the environment were formed, there are markers - the ratio of certain normal and isoprenoid alkanes or their sum to each other. In this work, attention was paid to the following indices and ratios: CPI_2, Pr/Ph, C_{17}/Pr, C_{18}/Ph, LWH/HWH, C_{31}/C_{19}.

2 Results and Discussion

The AHC content in bottom sediments of the coastal waters Kazantip Cape ranged from 0.38 to 2.4, averaging 1.24 ± 0.25 mg/100 g (Fig. 2). The concentration of n-alkanes ranged from 0.17 to 0.96 mg/100 g. The concentrations characteristic for bottom sediments of the Azov Sea (40–100 mg/100 g) [12] were 1–2 orders of magnitude higher than the indicators we determined. These levels are safe from the point of view of their impact on biota [13].

At 7 out of 8 sampling stations there was no UCM (Table 1), which usually arises as a result of chronic hydrocarbon pollution [14].

Figure 3 shows an example of chromatograms with the absence of an UCM (St. 8) and with its presence of the last one (St. 6). It can be seen that the "hump" is formed in the region of low molecular weight compounds. The presence of a "hump" in the low-temperature region is more associated with the products of bacterial degradation of natural organic compounds [15] than with the accumulation of anthropogenic compounds [14].

In the sea bottom sediments of the Kazantip Cape, n-alkanes in the range C_{17}–C_{33} were identified (Fig. 4). At the same time, at St. 1, 2 (Russkaya Bay) and 7 (Tatarskaya Bay) peak was shifted towards high molecular weight compounds. In other areas, the distribution of n-alkanes was quite uniform with a slight predominance (up to 16% of the total) of relatively light compounds (C_{18}–C_{23}). At the station 6 (Zmeinaya Bay), where it was possible to record the presence of a methane-naphthene "hump",

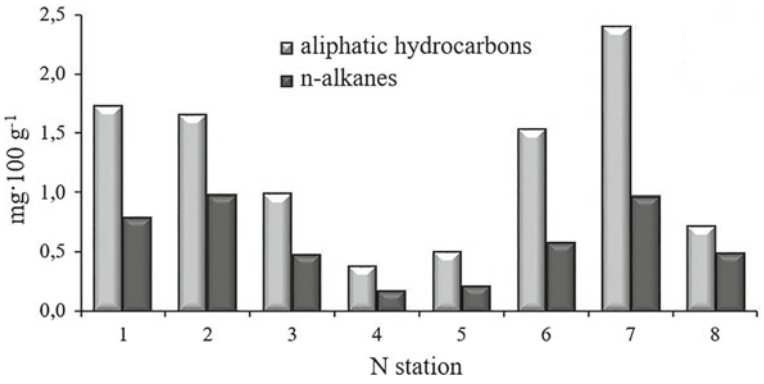


Fig. 2 Concentrations of aliphatic hydrocarbons and n-alkanes (mg/100 g) in bottom sediments in the coastal waters of the Kazantip Cape (Azov Sea), 2021

Table 1 Hydrocarbon composition (mg/100 g) of sea bottom sediments in the coastal area of the Kazantip Cape

Station №	AHC, mg/100 g	n-alkanes, mg/100 g	UCM, mg/100 g	Range of n-alkanes	Prevalent (>10%) n-alkanes
1	1.73	0.79	n/d*	C_{19}–C_{32}	C_{28}, C_{29}, C_{30}
2	1.65	0.97	n/d	C_{17}–C_{33}	C_{28}, C_{29}, C_{30}
3	0.99	0.47	n/d	C_{18}–C_{33}	C_{20}, C_{22}
4	0.38	0.17	n/d	C_{17}–C_{31}	C_{18}, C_{19}, C_{20}
5	0.50	0.21	n/d	C_{17}–C_{32}	C_{18}, C_{19}, C_{20}, C_{21}, C_{22}
6	1.53	0.57	6,63	C_{17}–C_{33}	C_{18}, C_{19}, C_{21}
7	2.4	0.96	n/d	C_{17}–C_{33}	C_{28}, C_{29}
8	0.72	0.48	n/d	C_{17}–C_{32}	C_{20}, C_{21}, C_{22}, C_{23}

*not detected (n/d)

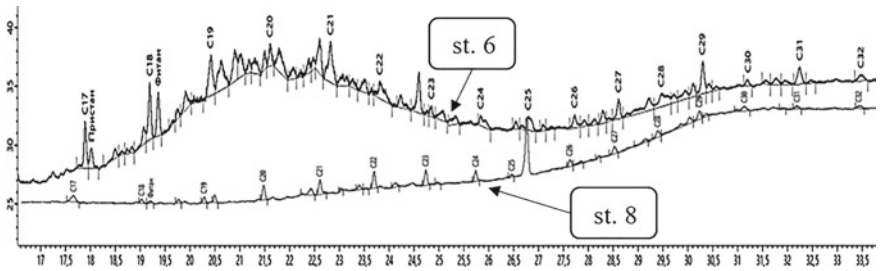


Fig. 3 Characteristic chromatograms of n-alkanes with a UCM (station 6) and without UCM (station 8) of bottom sediments of the coastal water area of the Kazantip Cape, 2021

the predominant compounds by mass were C_{18}, C_{19}, C_{21}—which are predominantly products of the vital activity of phyto- and bacterioplankton.

As a solution to the problem of identifying the pollution origin, an approach based on the use of geochemical markers has been proposed in domestic and foreign literature [15]. The classical method of differentiating hydrocarbons between biogenic or petroleum is based on a number of criteria, including ratios of aliphatic hydrocarbons—the oddity index CPI (carbon petroleum index)—or marker isoprenoids [15].

Analysis of diagnostic indices (Table 2) showed that the CPI_2 ratio [16, 17], which is often used to identify oil pollution, in this case allows us to diagnose the probable presence of oil hydrocarbons at the St. 7 in water area Tatarskaya Bay.

High concentrations of n-alkanes relative to iso-homologs (Pr, Ph), expressed by the ratios C_{17}/Pr and C_{18}/Ph in most cases exceed 1, which indicates an insignificant degree of transformation of n-alkanes in bottom sediments [18]. At the same time, the ratio of pristane and phytane content was below unity, which is a sign of the presence of petrogenic compounds [19].

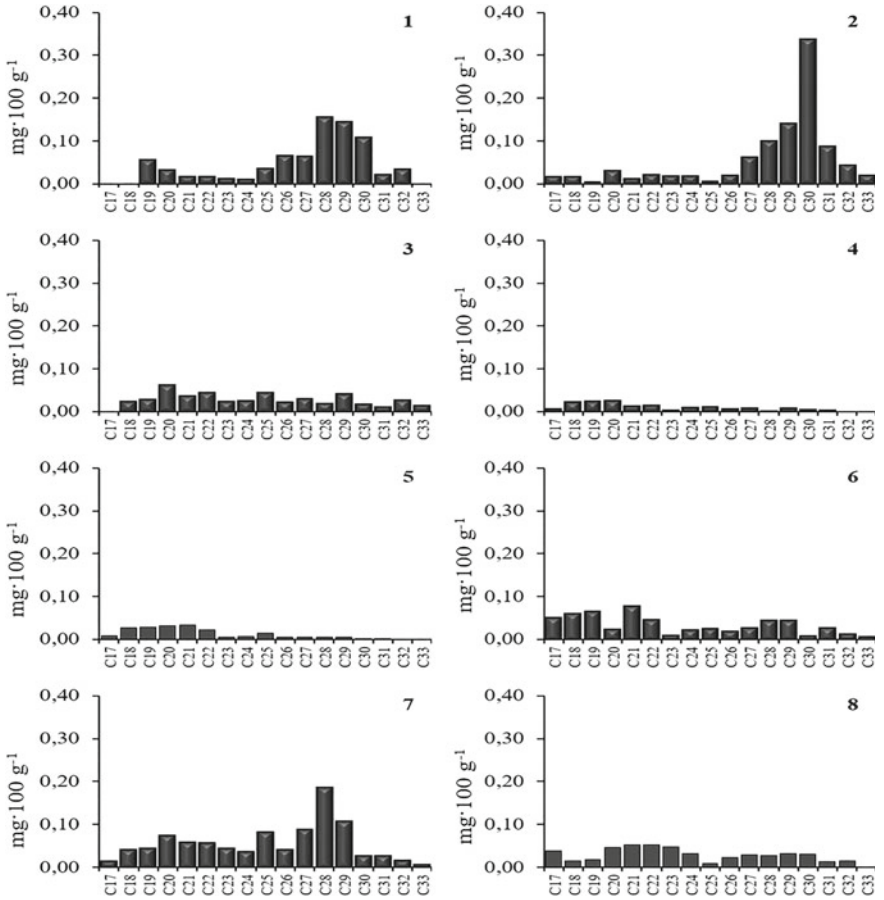


Fig. 4 Identified n-alkanes from bottom sediments of the coastal area of the Kazantip Cape, 2021

Table 2 Diagnostic indicators of bottom sediments in the coastal waters of the Kazantip Cape, 2021

Index	St. 1	St. 2	St. 3	St. 4	St. 5	St. 6	St. 7	St. 8
CPI_1	1.82	0.62	0.63	0.80	1.04	1.88	0.86	1.39
CPI_2	0.72	0.63	1.43	1.79	1.62	1.39	1.08	0.76
Pr/Ph	n/d*	0.34	0.00	0.08	0.27	0.57	0.04	0.00
C_{17}/Pr	n/d	4.71	n/d	5.55	2.21	1.91	7.00	n/d
C_{18}/Ph	n/d	1.51	0.96	1.56	1.76	1.28	0.82	1.41
LWH/HWH	0.19	0.13	0.71	1.72	2.81	1.29	0.44	0.87
C_{31}/C_{19}	0.39	15.37	0.38	0.16	0.08	0.43	0.62	0.72

*not detected (n/d)

The ratio of the content of n-alkanes with low and high molecular weight is also an indicator of the origin of hydrocarbons [20]. In our case, this ratio had values characteristic of the presence of fresh petroleum products at St. 4 (Russian Shelkovitsa Bay), 5 (Shirokaya Bay) and 6 (Zmeinaya Bay).

The ratio of n-alkanes C_{19} and C_{31} allows us to judge that the biogenic hydrocarbons of bottom sediments of the Kazantip Cape contain n-alkanes predominantly of allochthonous and mixed origin. In some cases (water areas of Russkaya Shelkovitsa Bay and Shirokaya Bay (st. 4, 5)), a predominance of autochthonous compounds was noted [21].

When interpreting data on the individual composition of n-alkanes and individual isoprenoids of sea bottom sediments and markers of the Kazantip Cape coast, it is necessary to take into account the high degree of development of the heterotrophic bacterial community, including hydrocarbon-oxidizing bacteria, in the waters of the Russian Bay and Tatarskaya Bay (st. 1, 2, 7), which confined to settlements and recreational areas and located outside the protected area [22] and having, as this study showed, high levels of AHC content in bottom sediments (Fig. 2). In other areas, with the exception of Zmeinaya Bay (St. 6) with increased concentrations of hydrocarbons located in the water area adjacent to the protected lands, the development indicators of hydrocarbon-oxidizing microflora [23] and hydrocarbon concentrations were low. It indicates an insignificant potential for self-purification from hydrocarbon pollution of bottom sediments.

The Azov Sea is inland sea, its coast and water area are intensively exploited, including for the purpose of transshipment and transportation of hydrocarbon raw materials, therefore it is characterized as polluted with oil and oil products [24]. The entry of these compounds with sea waters may be one of the reasons for their accumulation in coastal bottom sediments. The second probable reason for the accumulation of petroleum hydrocarbons in the bottom sediments of this water area may be oil production carried out in the central part of the basin of the Kazantip Cape. In the northern part of the cape, there are wells with brackish water that collects on the cape and accumulates in the area. Perhaps this fact is associated with the removal of oil from the areas of its production by these waters. At the same time, it should be noted that there is no information about the composition and reserves of groundwater at the study site, which complicates a detailed interpretation of the data.

3 Conclusion

In the coastal waters of the Kazantip Cape relatively low levels of AHC content were recorded (on average 1.24 ± 0.25 mg/100 g). They did not exceed typical values for the Azov Sea and not entailing negative biological effects. At the same time, markers of oil pollution were found in the composition of n-alkanes in coastal sediments, which are a sign of the presence of a negative anthropogenic impact on the aquatic complex, taking into account the protected status of most of the coast and the presence of nesting sites for a variety of avifauna in coastal waters.

Regarding the source of oil and oil products entering the bottom sediments of the coastal waters of the cape, their cause may be either the supply with sea water from other areas of the sea, which is generally subject to oil pollution, or local factors. As already indicated, there is an oil field in the central part of the cape and oil production is currently underway. Perhaps this fact is associated with the removal of petroleum products from their production sites by groundwater.

Acknowledgements The work was carried out within the framework of IBSS state theme "Molismological and biogeochemical foundations of marine ecosystems homeostasis" (no. 12103100515-8).

References

1. Sun C., Zhang Z., Cao H., Xu M., Xu L. 2019. Concentrations, speciation, and ecological risk of heavy metals in the sediment of the Songhua River in an urban area with petrochemical industries // Chemosphere. 219, 538–545.
2. Liu C., Yin J., Hu L., Zhang B. 2020. Spatial distribution of heavy metals and associated risks in sediment of the urban river flowing into the Pearl River Estuary, China // Archives of Environmental Contamination and Toxicology. 78, 622–630.
3. Nemirovskaya I.A., Onegina V.D., Konovalov B.V. 2017. Hydrocarbons in the Suspended Matter and the Bottom Sediments in Different Regions of the Black Sea Russian Sector // Physical Oceanography. 4, 46–58.
4. Nemirovskaya I.A., Khramtsova A.V. 2021. Features of the Hydrocarbon Distribution in the Bottom Sediments of the Norwegian and Barents Seas // Fluids. 6, 456.
5. Nemirovskaya I.A., Zavialov P., Khramtsova A.V. 2022. Hydrocarbon pollution in the waters and sediments of the Kerch Strait // Marine Pollution Bulletin. 180(1), 113760.
6. Zhang Z., Volkman J.K. 2020. Isotopicallly enriched n-alkan-2-ones with even chain predominance in a torbanite from Sydney Basin, Australia // Organic Geochemistry. 144, 104018.
7. Rushdi A.I., El-Mubarak A.H., Simoneit B.R.T. et al. 2021. Natural and anthropogenic sources of extractable organic matter in sediments from the coastal zone of the Arabian Gulf in Saudi Arabia, PREPRINT (Version 1) available at Research Square. https://doi.org/10.21203/rs.3.rs-1153446/v1.
8. Boltachev A.R., Alemov S.V., Zagorodnyaya Yu.A., Karpova E.L., Manzhos L.A., Gubanov V.V., Litvinyuk N.A. The underwater world of the Kazantip Nature Reserve: to the 15th anniversary of the Kazantip Nature Reserve. – Simferopol: Business-Inform, 2016. – 112 p.
9. Ekpo B.O., Fubara E.P., Ekpa O.D., Marynowski L. 2012. Distributions of fossil fuel biomarkers in sediments as proxies for petroleum contamination of coastal environment of the Niger Delta, Southeastern Nigeria // Journal of Applied Sciences in Environmental Sanitation. 7, 75–86.
10. Zhang S., Li S., Dong H. et al. 2014. An analysis of organic matter sources for surface sediments in the central South Yellow Sea, China: evidence based on microelement sand n-alkanes // Marine Pollution Bulletin. 88 (1–2), 389–397.
11. Orlov D.S., Sadovnikova L.K., Lozanovskaya I.N. Ecology and protection of the biosphere under the chemical pollution. Moscow: Higher School, 2002. 334 p.
12. Pavlenko L.F., Skrypnik G.V., Klimenko T.L., Anokhina N.S., Ekilik V.S., Sevostyanova V.S., Barabashin T.O. 2018. Long-term dynamics of oil pollution of the habitat of hydrobionts of the Azov Sea // Questions of fishing. 19(4), 534–544.
13. Mironov O.G., Milovidova N.Yu., Kiryukhina L.N. 1986. On the maximum permissible concentrations of petroleum products in bottom sediments of the coastal zone of the Black Sea // Hydrobiological gournal. 22(6), 76–78.

14. Nemirovskaya I.A. Oil in the ocean (pollution and natural sources). M.: Scientific world, 2013. 432 p. https://www.rfbr.ru/rffi/ru/books/o_1917147
15. Bouloibassi I., Saliot A. Investigation of anthropogenic and natural organic inputs in estuarine sediments using hydrocarbon markers (NAN, LAB, PAH) // Oceanologica Acta. 1993. Vol. 16, iss. 2. P. 145– 161. https://archimer.ifremer.fr/doc/00099/21043/18669.pdf
16. Petersen H.I., Nytoft H.P., Ratanasthien B., Foopatthanakamol A. 2007. Oils from Cenozoic rift-basins in central and northern Thailand: source and thermal maturity. Journal of petroleum geology. 30:59–78.
17. Commendatore M.G., Esteves J.L. 2004. Natural and anthropogenic hydrocarbons in sediments from the Chubut River (Patagonia, Argentina). Mar. Pollut. Bull. 48:910–918.
18. Tarozo R., Frena M., Madureira L.A.S. 2010. Geochemical markers as a tool to assess sedimentary organic matter sources of the Laguna estuarine system, South Brazil: aliphatic and polycyclic aromatic hydrocarbons. J. Braz. Chem. Soc. 21(12):2308–2318.
19. Volkman J.K., Holdsworth D.G., Neil G.P., Bavor H.J.J.R. 1992. Identification of natural, anthropogenic and petroleum hydrocarbons in aquatic sediments. Sci. Total Environ. 112:203–219.
20. Wang X.C., Sun S., Ma H.Q., Liu Y. 2006. Sources and distribution of aliphatic and polyaromatic hydrocarbons in sediments of Jiaozhou Bay, Qingdao (China). Mar. Pollut. Bull. 52:129–138.
21. Fagbote O.E., Olanipekun E.O. 2013. Characterization and sources of aliphatic hydrocarbons of the sediments of River Oluwa at Agbabu Bitumen deposit area, Western Nigeria. J. Sci. Res. Rep. 2(1):228–248.
22. Tikhonova E. A., Burdiyan N. V. 2020. Chemical and microbiological characteristics of bottom sediments of the coastal waters of the Kazantip Nature Reserve (Azov Sea) // Proceedings of the Karadag Research Station named after. T.I. Vyazemsky - nature reserve of the Russian Academy of Sciences. 5(2 (14)): 40–47.
23. Tikhonova E. A., Soloveva O. V., Burdiyan N. V. 2022. Bottom Sediments of the Kazantip Nature Reserve Coastal Water Area (Azov Sea) as an Indicator of the Water Area Well-being // Processes in GeoMedia – Volume 5 / Ed. T. Chaplina. Cham, Switzerland: Springer Nature Switzerland AG. 253–262. (Ser.: Springer Geology). https://doi.org/10.1007/978-3-030-85851-3_28
24. Matishov G.G., Stepanyan O.V., Kharkovsky V.M., Sawyer V.G. 2014. Modern data on pollution of the Azov and Black Seas by oil hydrocarbons // Bulletin of the Southern Research Center. 10 (4): 49–52.

Experimental Studies of Submerged Jets of Various Liquids



T. O. Chaplina and V. P. Pakhnenko

Abstract The article is devoted to the study of the characteristics of a submerged jet under various conditions. An extensive review is provided on the classification of jets, on methods for studying the characteristics of jets, general approaches to the experimental and numerical study of jets of positive buoyancy are described, and examples of experimental studies of various jet flows and methods for their visualization are given.

Keywords Submerged jets · Experimental and analytical model · Visualization · Shadow method · Moire effect

1 Introduction

At present, much research is devoted to the topic of submerged jet. The increased interest in the topic is related to the rapid development of a number of scientific branches, including geophysical hydrodynamics, chemical technology, nuclear power engineering, ecology.

The interest in the study of the submerged jet has a history of almost a century. The pioneering work was published in 1937 [1]. The suspended particle method was used to determine the velocity field at a distance much larger than the nozzle diameter. Assuming that the jet flows from a point fictitious source located inside the tip, the measured velocity profiles agree with the Schlichting's automodel solution [10]. The authors of the paper proposed a method for calculating the position of the fictitious source based on the condition of equality between the measured kinetic energy of the flow in the initial cross section of the jet and the energy calculated from the analytical formula from the definition.

T. O. Chaplina (✉) · V. P. Pakhnenko
A.Yu. Ishlinsky Institute for Problems in Mechanics, Prospect Vernadskogo 101-1, Moscow 119526, Russia
e-mail: tanya75.06@mail.ru

© The Author(s), under exclusive license to Springer Nature Switzerland AG 2024

V. Karev (ed.), *Proceedings of the 9th International Conference on Physical and Mathematical Modelling of Earth and Environmental Processes*, Springer Proceedings in Earth and Environmental Sciences, https://doi.org/10.1007/978-3-031-54589-4_41

In 1944, the paper [2] with an exact solution of the problem of a submerged jet in an infinite liquid medium in the absence of a gravity field was published. The problem was solved in spherical coordinates r, θ, φ. From the continuity and Navier–Stokes equations, taking into account axial symmetry around the polar axis ($v_\varphi = 0$), and conservation of the total momentum flow of the jet through a closed surface, the solution is obtained as a result of transformations:

1. Spatial distribution of jet velocity

$$v_r = \frac{1}{r}F(\theta),\ v_\theta = \frac{1}{r}f(\theta) \tag{1.1}$$

where $f(\theta) = -\frac{2\nu\sin\theta}{A-\cos\theta}$, $F(\theta) = 2\nu\left\{\frac{A^2-1}{(A-\cos\theta)^2} - 1\right\}$—some functions only from θ, A—is a constant.

2. Pressure distribution

$$p - p_0 = -\frac{4\rho\nu^2}{r^2}\frac{A\cos\theta - 1}{(A-\cos\theta)^2} \tag{1.2}$$

where the constant A is related to the total momentum flow in the jet P by the relation

$$P = 16\pi\nu^2\rho A\left\{1 + \frac{4}{3(A^2-1)} - \frac{A}{2}\ln\frac{A+1}{A-1}\right\} \tag{1.3}$$

3. Equation of the current line

$$\frac{r\sin^2\theta}{A-\cos\theta} = const \tag{1.4}$$

A characteristic view of the current lines is shown in Fig. 1:
Two special cases were also considered in [2]:

1. 1. Weak Jet (Small P, Large A)
   In this case from (1.2.3) we have

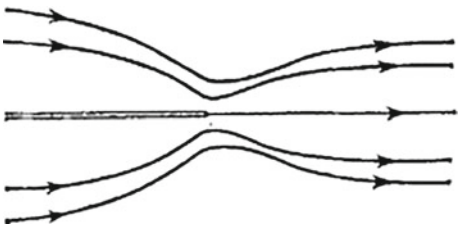


Fig. 1 Lines of current [2]

$$P = \frac{16\pi\nu^2\rho}{A} \tag{1.5}$$

For velocity we have

$$v_\theta = -\frac{P}{8\pi\nu\rho}\frac{\sin\theta}{r}, v_r = \frac{P}{4\pi\nu\rho}\frac{\cos\theta}{r} \tag{1.6}$$

2. Strong Jet (Large p, $A \to 1$)

$$A = 1 + \frac{\theta_0^2}{2}, \theta_0^2 = \frac{64\pi\nu^2\rho}{3P} \tag{1.7}$$

2.1 For Large Angles ($\theta \approx 1$) the Velocity Distribution is Expressed as

$$v_\theta = -\frac{2\nu}{r}ctg\frac{\theta}{2}, v_r = -\frac{2\nu}{r} \tag{1.8}$$

2.2 For Small Angles ($\theta \approx \theta_0$)

$$v_\theta = -\frac{4\nu\theta}{(\theta_0^2 + \theta^2)r}, v_r = 8\nu\frac{\theta_0^2}{(\theta_0^2 + \theta^2)^2 r} \tag{1.9}$$

The studies were continued and expanded. In [3], the influence of the Coandé effect - the jet deflection toward the wall—on the flow of a submerged rising jet near the bottom was studied.

2 Experimental Studies of a Submerged Jet

Particle Image Velocimetry (PIV) is often used in experimental studies of a submerged jet. The interaction of the jet with the free surface is investigated. In [4] it is shown that the dynamic characteristics of a submerged jet depend significantly on the depth of its axis. The laser fluorescence technique was used for qualitative visualization of the flow, while the time-resolved particle image velocity (PIV) technique was used for quantitative measurements. Three different depths were considered (Fig. 2). The Reynolds number in all experiments is 3500.

In the case of $H/D = 2$ (a), the spatial structures reflected backward flow induced by surface vibration along the boundary, and its subsequent deflection modified the flow structures in the horizontal center plane. The strong vibration of the free surface induced unsteady flow motion and resulted in a "compression effect" along the flow structures.

In the case of $H/D = 4$ (b), the upwelling motion of some vortices in the jet and their subsequent descent significantly changed the main spatial structures in both the vertical and horizontal central planes. When the jet was fully attached to the free

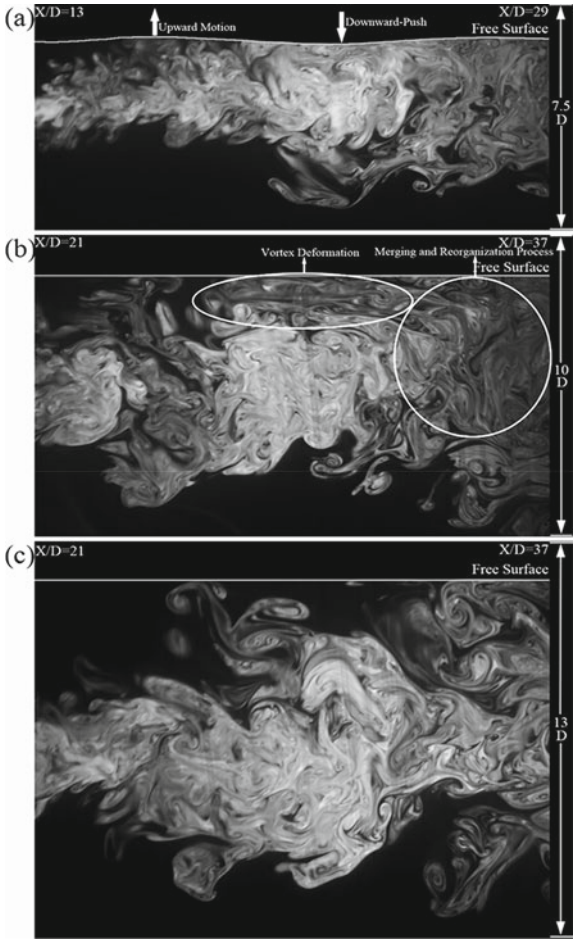


Fig. 2 Interaction of a jet with a free surface [4]

surface, the vortex structures underwent a process of merging and restructuring due to the vertical confinement of the free surface.

In the case of $H/D = 6$ (c), the main spatial structures in both the vertical and horizontal center planes showed an approximately symmetric pattern, indicating that the structures were not modified by the free surface. Once attached to the free surface, the jet did not undergo the process of merging and restructuring as shown in the case of $H/D = 4$.

In [6], the flow pattern and stability, i.e., tendency to bifurcate of horizontal buoyant jets with different Froude number (Fr) extending from low to moderate Reynolds numbers ($500 < \mathrm{Re} < 2000$) were investigated. Non-intrusive planar laser-induced fluorescence (PLIF) laser imaging technology was used for imaging and flow measurements. Three different flows characterized by unstable small-scale structures were identified in the Re-Fr parameter space, namely: “primary jet with vertical

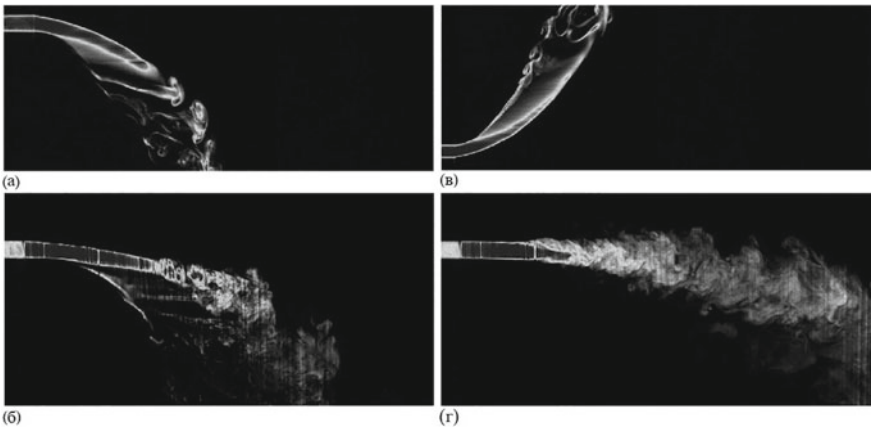


Fig. 3 Longitudinal images showing three different flow patterns in a horizontal flooded jet: (a)—primary jet with vertical secondary plume (Re = 221, Fr = 1.9), (b)—primary jet with pseudo-secondary jet (negative buoyancy, Re = 862, Fr = 4.3), (c)—primary jet with pseudo-secondary jet (positive buoyancy, Re = 359, Fr = 3.0), (d)—quasi-turbulent horizontal buoyant jet (Re = 2141, Fr = 10.7) [5]

secondary plume", "primary jet with pseudo-secondary jet" and "quasi-turbulent horizontal buoyant jet" identified from the imaging results (Fig. 3).

In [12], a three-dimensional numerical model of inclined turbulent jets with a density greater than that of the surrounding fluid is presented to study some jet parameters with turbulence schemes not previously used in this context, such as the standard diffusion hypothesis of the Boussinesq gradient and the common gradient, to explain the occurrence of buoyancy-induced turbulence. For this study, two jet displacement angles were chosen: 30° and 45° from horizontal. These two angles are chosen in this study because of the lower limiting heights of lift at 30° and 45°, which is critical for wastewater discharges into shallow waters compared to higher angles than these values. The temporal evolutions of jets for these cases were simulated using the open source CFD code OpenFOAM, which is based on the finite volume method. The results presented in this paper concern the geometric and flow properties of inclined dense jets. The densitometric Froude number of the effluent at the nozzle ranges from 10 to 34. Two Reynholds-averaged Navier–Stokes models with turbulence are applied to evaluate the accuracy of the numerical predictions: the realized k-ε (two-equation model) and the Launder Reece Rodi (Reynolds Stress Model—RSM).

In 2015, an article by Xiaofeng Yang from Shenzhen Institute of Wuhan University [13] was published to study the effect of hydrostatic pressure on the structure of the flow field of a submerged water jet. As a result of numerical simulation, it was shown that the maximum jet velocity decreases with increasing hydrostatic pressure. In addition, it was concluded that the change in hydrostatic pressure does not affect the size and configuration of the main part of the submerged jet.

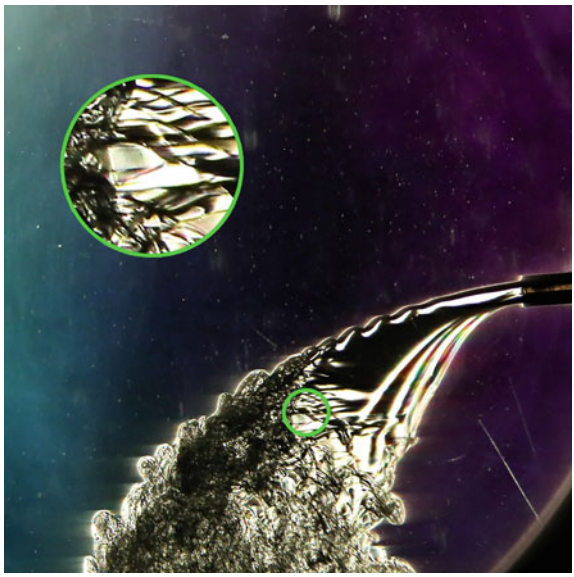


Fig. 4 Salt water (t = 20 °C, $\rho = 1010$ kg/m^3) is slowly poured into salt water ($\rho = 1015$ kg/m^3) of the same temperature

In the present work, the behavior of submerged water jets of different densities obtained by changing the salinity as well as gasoline jets were investigated.

In the present work 2 methods of jet visualization were used:

1. shadow method;
2. moiré effect method.

Below are images of jets obtained using the shadow method (Fig. 4).

As the temperature increases, the density of water decreases and the jet floats.

Figure 6 shows the schematic and photo of the experimental setup used for measurements with a visualization method based on the moiré effect.

The fluid supply system consists of a reservoir (1), a path and a nozzle (3). The fluid reservoir is mounted on a stand with adjustable height, which allows you to change the flow rate of the fluid. Using the divisions on the tank, you can control the volumetric flow of liquid. The experiment starts when the valve (2) is opened and a submerged jet is created. To fix the boundaries of areas with variable density, a moiré pattern is placed behind the volume with the base liquid. To record experiments, a photo/video camera (6) is installed in front of the vessel (4), the optical axis of which is perpendicular to the wall of the vessel with the base liquid and passes through the jet. The scale of the image is determined by means of a ruler (5). A diode lamp (7) is installed to illuminate the system. The ambient temperature is measured by a thermometer.

Measurements were carried out at different positions of the tank corresponding to different velocities of the flowing liquid. The liquid density was measured using an areometer.

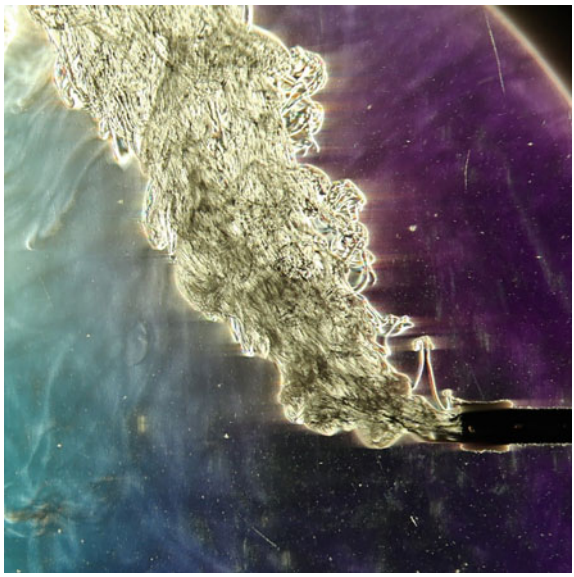


Fig. 5 In salt water (t = 20 °C, ρ = 1010 kg/m^3) is slowly poured water of the same salinity, heated in a kettle to 30 °C

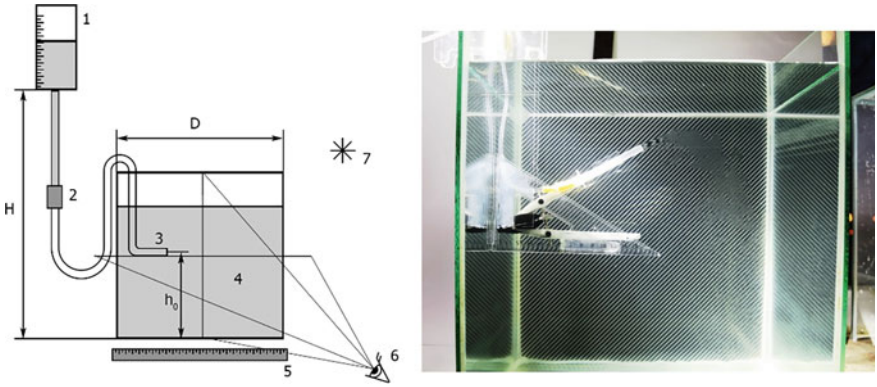


Fig. 6 Scheme of the experimental setup. 1—reservoir with liquid, 2—valve, 3—tube (nozzle) of small radius (2.1 mm), 4—vessel with base liquid (density S0, kg/m3), 5—ruler, 6—photo/video camera, 7—light source. The main dimensions of the installation: D = 30 cm—longitudinal dimension of the vessel; H = 55-100 cm—height of the tank above the bottom of the vessel; h_0—height of the nozzle center above the bottom

The scheme of the jet taking into account gravity was used for processing. Auxiliary lines intersecting in one point with the same angle between neighboring lines were selected in each image (Fig. 7). The coordinate axes were counted from the nozzle edge.

The following notations are introduced:

r_0 - nozzle radius (2.1 mm);

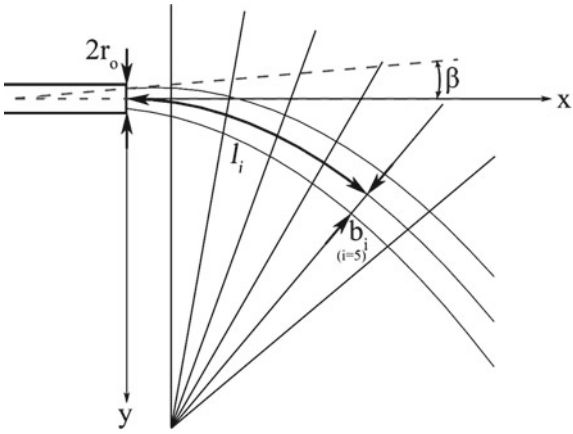


Fig. 7 Jet scheme taking into account the action of gravity

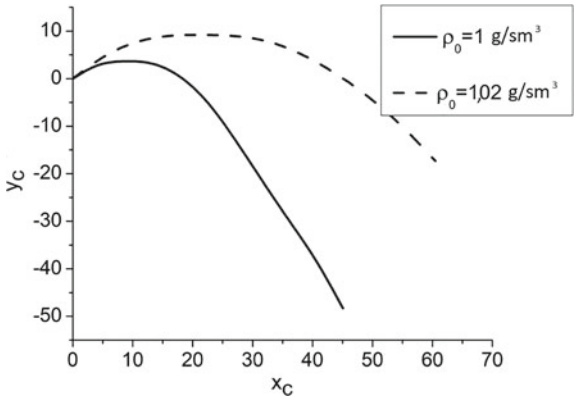


Fig. 8 Positions of the jet centerline at different base fluid densities ($\rho = 1.02$ g/cm^3, $\rho_0 = 1$ g/cm^3; $\rho = 1.05$ g/cm^3, $\rho_0 = 1.02$ g/cm^3)

l—distance from the nozzle along the jet centerline;

b_i—jet half-width at the i-th division;

β—jet angle;

v_0—initial speed;

C—degree of steepness of the jet centerline, or the coefficient at the highest degree in the parabola equation.

Experiments were performed for the same density difference between the base and inflow fluids, with the density of the base fluid varying (Fig. 8).

For comparison, consider experiments with petroleum products. The photo (Fig. 9) shows an experiment with a jet of gasoline flowing under pressure.

The graph (Fig. 10) shows the center lines of the jet for the initial velocity directions at angles 0° and 45° to the horizon. The steepness of the line increases with increasing angle of inclination.



Fig. 9 Submerged jets

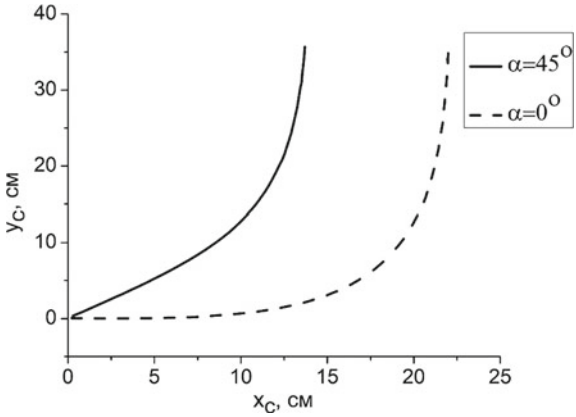


Fig. 10 Jet centerline as a function of the angle between the direction of the initial velocity and the horizon ($\rho = 0.72$ g/cm^3, $\rho_0 = 1$ g/cm^3)

Acknowledgements The work was carried out under the State Assignment 124012500441-6 (FFGN-2024-0007).

References

1. da C Andrade E.N., Tsien L.C. The velocity-distribution in a liquid-into-liquid jet //Proceedings of the Physical Society. – 1937. – T. 49. – №. 4. – C. 381–391.
2. Landau L.D. On a new exact solution of the Navier-Stokes equations // Dokl. Academy of Sciences of the USSR. – 1944. – V. 43. – No. 7. – P. 299–301.
3. Sobey R.J., Johnston A.J., Keane R.D. Horizontal round buoyant jet in shallow water //Journal of Hydraulic Engineering. – 1988. – V. 114. – №. 8. – pp. 910–929.
4. Wen Q. et al. Structure Analysis of a Low Reynolds Number Turbulent Submerged Jet Interacting With a Free Surface //Journal of Fluids Engineering. – 2014. – V. 136. – №. 10. – pp. 101104.

5. Sodjavi K. et al. PIV and electrodiffusion diagnostics of flow field, wall shear stress and mass transfer beneath three round submerged impinging jets //Experimental Thermal and Fluid Science. – 2016. – V. 70. – pp. 417–436.
6. Shao D. et al. Flow patterns and mixing characteristics of horizontal buoyant jets at low and moderate Reynolds numbers //International Journal of Heat and Mass Transfer. – 2017. – V. 105. – pp. 831–846.
7. Pokazeev K.V., Chaplina T.O., Chashechkin Yu.D. Ocean optics: Textbook. M.: MAX Press, 216 p. – 2010.
8. Prokhorov A.M. and others (eds.). Physical encyclopedic dictionary. – M.: Soviet Encyclopedia, 1984.
9. Matveev S. G. et al. Calculation of characteristics of jet flows of gaseous media in combustion chambers of gas turbine engines // textbook – Samara: Samar. state Aerospace. Univ. – 2011.
10. Kirchhoff G. Mechanics. - M.: Izd. Academy of Sciences of the USSR, 1962. - 404 p.
11. Wen Q. et al. Dynamic structures of a submerged jet interacting with a free surface // Experimental Thermal and Fluid Science. – 2014. – V. 57. – pp. 396–406.
12. Gildeh H.K. et al. CFD modeling and analysis of the behavior of 30 and 45 inclined dense jets—New numerical insights //Journal of Applied Water Engineering and Research. – 2015. – V. 4. – №. 2. – pp. 1–16.
13. Yang X. The Influence Of Confining Pressure On The Flow Field Structure Of Submerged Water Jet // Proceedings of the 5th International Conference on Civil Engineering and Transportation (ICCET 2015). – Atlantis Press, 2015. – V. 30. – pp. 1400–1404.
14. Kildibaeva S.R. Modeling the flow of hydrocarbons in a flooded jet //Modern problems of science and education. – 2014. – No. 6.
15. Shterenlikht D.V. Hydraulics. – 1984.
16. Zhang B. et al. New reconstruction algorithm for moiré tomography in flow field measurements //Optical Engineering. – 2006. – V. 45. – №. 11. – pp. 117002.

Origin of Solar System Comets in the Light of Galactocentric Paradigm



Azariy Barenbaum

Abstract The author's "cometoasteroid" concept of Solar System comets origin, based on Galactocentric paradigm ideas, is discussed. It is argued that long- and short-period comets we observe are daughter formations, products of collisions of galactic comets of Orion-Cygnus jet stream with asteroid belt bodies, captured by Sun attraction into orbits more diverse and distant than at asteroid belt bodies. These daughter objects are composed of substance of galactic origin comets frozen together with debris and vaporized material of asteroids. Long-period and short-period comets were formed in time interval from 5 to 0.7 Ma, and differ from each other in that the former have aphelion of its orbits is ~10^4–10^5 AU. Therefore, today they are returning back to the Sun for the first time. While, the second have never left Solar System limits, they gravitate towards the ecliptic plane and today have survived only in outer space between giant planets. At random convergences with these planets, they are thrown towards the Sun, and then we are observed them as members of the comets family of corresponding giant planet. It is shown that the stated concept explains well all main properties of observed comets in Solar System.

Keywords Galactic comets · Origin of long- and short-period comets · Galactocentric paradigm

1 Introduction

In connection with discovery of phenomenon of jet outflow of matter in spiral galaxies [5] and creation of Galactocentric paradigm [6], the author has no doubt that in the very near future this paradigm will become a unified worldview basis for all space sciences. In recent works [10–15], the author substantiated this conclusion using the example of solving a number of problematic issues in cosmology, astronomy and

A. Barenbaum (✉)
Oil and Gas Research Institute Russian Academy of Sciences (OGRI RAS), Gubkina Street, 3, Moscow, 119333, Russia
e-mail: azary@mail.ru

© The Author(s), under exclusive license to Springer Nature Switzerland AG 2024

V. Karev (ed.), *Proceedings of the 9th International Conference on Physical and Mathematical Modelling of Earth and Environmental Processes*, Springer Proceedings in Earth and Environmental Sciences, https://doi.org/10.1007/978-3-031-54589-4_42

geology. This article discusses the solution to another important problem—the origin of Solar System comets, posed to modern science at the turn of the 18th and 19th centuries.

In 1990 at the "2-th Vsekhsvyatskikh Readings on Physics and Dynamics of Comets" the author for the first time put forward a new hypothesis of Solar System comets origin [3], based on Galactocentric paradigm representations. Later, this hypothesis in the form of a more general physical concept was substantiated in books [5, 6].

The new concept states that Solar System comets are collision products of comets galactic origin with bodies of asteroid belt, captured by Sun's gravitational pull into elliptical orbits that are more diverse and distant than ones of the belt bodies. These "daughter" comets were born in asteroid belt of 5.0–0.7 Ma during period of Sun's stay in the Orion-Cygnus jet stream. They consist of icy substance of galactic comets (primordial comets) frozen together with solid (debris) and diffuse (evaporated) material of asteroids.

Thus, the comets we observe cannot be considered objects of only galactic or only circumsolar origin and they should be considered as a category of bodies of dual genesis specific to Solar System—"cometoasteroids". Below we offer a rationale for this "cometoasteroidic concept" that explains the origin and formation mechanism of observed comets. The focus is on the following issues:

- General information about observed comets,
- Review of origin hypotheses of observed comets,
- Brief description of Galactocentric paradigm representations,
- Information about galactic comets and their properties,
- Issues of galactic comets collision with asteroid belt bodies,
- Mechanism of long-period and short-period comets formation,
- Estimate of the number of both group comets in Solar System.

2 Observed Comets and Their Properties

People have been observing comets since ancient times. According to modern concepts, comets are cosmic bodies up to several tens of kilometers in size and weighing up to 10^{18} g, consisting of water ice, dust and gas particles mixed with solid stone material, which move around the Sun in elliptical orbits that are more distant and diverse, than for planets and asteroids.

Conditionally two main groups of such comets are distinguished: long-period—with periods of motion around Sun $T >> 200$ years, and short-period—with periods $T < 200$ years. The matter composition of both groups of comets is almost identical, but they differ sharply from each other in the nature of their trajectories. Comets of the first group have highly elongated orbits with eccentricity $e \cong 1$, chaotically oriented relative to Sun, whereas comets of the second group have orbits with significantly smaller sizes and eccentricities, strongly gravitate towards the ecliptic plane and rotate around Sun in same direction as planets and asteroids.

For most of their trajectory, all comets are inaccessible to observation from Earth. However, when they approaching the Sun at distances of less than 3–5 AU under the influence of solar radiation, comet ices evaporate, comet nucleus is surrounded by a luminous shell (coma), and intense outflow of gas and dust begins from nucleus. From that moment, comet's brightness increases sharply, and it becomes discoverable.

As a result of multiple spans near Sun, comets lose their mass, and their glow decreases. After complete disappearance of glow in place of "dead" comet, meteor streams and small asteroids often detected which differ little from ordinary bodies of asteroid belt. There are known cases of crushing and disintegration of cometary nuclei, as well as the falls of comets on planets and Sun. Astronomers observe about 5 comet appearances annually, about half of which were previously unknown.

Today, many properties of observed comets have been explained and understood [25, 35, 81, 23, 43, 44, 68, 72, 75], etc. And only fundamental question on the origin of comets themselves remains open, replete with a wide range of contradictory, often mutually exclusive judgments.

3 The Problem of Comets Origin

In accordance with two varieties of comets, hypotheses of their origin are usually divided into two groups: "capture", suggesting the capture of galactic comets by Sun, and "eruptive", that imply comets birth within Solar System.

The founder of the first idea is P. Laplace [41], who believed that comets are interstellar objects that may be gravitationally captured when approaching Sun. The facts confirming this point of view were first presented by Svedstrup [71], who discovered the connection between the perihelion of cometary orbits and Galaxy plane. Later, this connection was confirmed and detailed by [42, 54, 61, 67, 80] and others. The ideas about the galactic nature of comets in different years were developed by [20, 47, 85, 35], etc.

The eruptive idea of the comets origin belongs to P. Lagrange [40], who was the first to suggest that comets could arise as a result of ejection of matter by planets. Subsequently, this point of view was supported by Proctor [58], who explained the comets origin by strong volcanic activity on Jupiter, which took place 10 Ma. The eruption hypothesis of comets was shared by Drobyshevski [27] and Guliyev [30, 31]. There are for many years, a consistent advocate of the idea of comets ejection during volcanic eruptions, not only on large planets, but also jn their satellites, was Vsekhsvyatsky [81].

A number of supporters of eruptive hypothesis associate comets formation with asteroid belt. In particular, Koval [37] admits that comets could have arisen as a result of bombardment by asteroids of icy surfaces of satellites giant planets. Unlike him, Orlov [55, 56] believed that comets arise in asteroid belt itself during collisions of its bodies. This point of view was shared by Fesenkov [28], and supported by Davydov [24] and Radzievsky [60].

In the middle of the last century, Oort [51] proposed a hypothesis according to which the comets origin is associated with the explosion of the planet Phaeton, which existed earlier, according to Olbers' assumption, at the site of the modern asteroid belt. The explosion of Phaethon, according to Oort, led to the ejection of many comets, which created a huge "comet cloud" on Solar System outskirts. From this cometary reservoir, under the influence of various perturbations, comets come to the Sun today.

A year later, Oort [52] abandoned this version of comets formation and, following Sciparelli [64] and Schmidt [66], proposed that this comets cloud be considered a remnant of a protosolar nebula, preserved after formation of Solar System. Kuiper [39], and later Safronov [63], Öpike [53], Tsitsin [76] and many others agreed with this idea.

However, this opinion is contradicted by the results of Van Flandern [77, 78], who, based on a detailed analysis of the orbital elements of 60 long-period comets, whose perihelion are in the asteroid belt, came to the conclusion about reality of the planet explosion between Mars and Jupiter, moreover only 3 Ma.

The listed hypotheses, like other ideas not mentioned [23, 44, 72, 81] more or less fortunately explaining comets of one type, invariably experience difficulties in explaining comets origin another type. For capture hypotheses, these difficulties are associated with the complete absence of comets moving relative to Sun along strongly hyperbolic trajectories, as well as with a very low probability of capture by Sun of galactic comets and with their subsequent transformation into short-period comets. For eruptive hypotheses, on the contrary, difficulties arise in explaining origin of long-period comets and their connection with Galaxy plane.

The Oort comet cloud hypothesis is also not without its shortcomings. In the event of Sun passing through dense gas and dust clouds and as a result of flight near it of other stars, the Solar System would certainly have lost a significant part of its comets [2, 22, 26, 79]. Attempts to move the cometary reservoir closer to Sun [33, 74, 84], etc.) do not save the day.

4 Galactic Model

We begin the substantiation of the comet-asteroid hypothesis with brief information about the galactic model that describes the jet outflow phenomenon [5, 6, 11, 21].

According to Galactocentric paradigm, in the core of our Galaxy there is a continuous destruction of stars with dust and gas formation. This dust-gas matter first accumulates in the rapidly rotating gas-dust nuclear disk of Galaxy, from where they then flows out in the form of two jet streams that fan-like spread in galactic plane. Moving at a speed of $\approx$300 km/s from Galaxy center to its periphery, the substance of jet streams condenses into dense gas and dust clouds, comets and stars. These processes are sharply intensified at the places intersection of two jet streams with four spiral galactic arms of electromagnetic nature, rotating around Galaxy center at a constant angular velocity and accumulating gas-dusty matter.

However, objects emerging from galactic arms and jet streams behave differently. Those of them that were formed from gas-dust matter of jet streams inherit their high radial velocity and leave visible limits of Galaxy forever. Others, formed from gas and dust of galactic arms, remain in the arms and with time move into independent orbits around Galaxy center.

Our Sun (Solar System) belongs to the second type stars. Having arisen earlier in one of spiral arms, at now Sun is currently moving in galactic plane around Galaxy center in a slowly rotating elliptical orbit, quasiperiodically crossing the jet streams and galactic arms. During periods of such crossings, all objects in Solar System are exposed to intense bombardments by galactic comets. In Earth's geological history, the times of such bombardments are marked as epochs of global geological events (tectonic, climatic and biotic), which act as boundaries of different ranks of the Phanerozoic and Precambrian stratigraphic scale.

In Fig. 1 in projection onto galactic plane shows Sun's position of the relative to 4 arms and 2 jet streams of Galaxy. Here, we also showed the Sun orbit and its current position on it [12].

Due to uneven Sun's motion in orbit, rotation of the line apsides of orbit itself, as well as rotation of nuclear disk and Galaxy arms with their angular velocities, the picture (Fig. 1) changes rapidly over time. The model tracks this changing picture

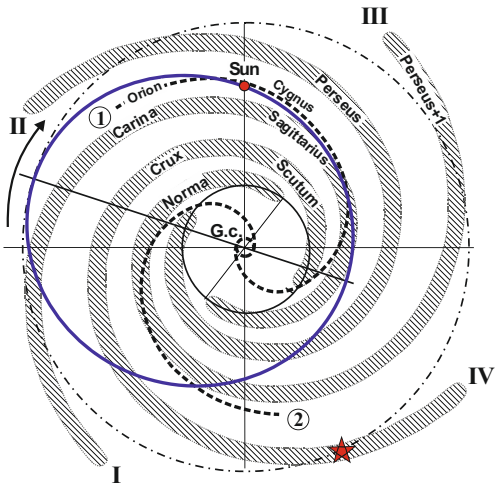


Fig. 1 The current position of the Sun in orbit (ellipse) relative to four galactic arms (Roman numerals) and two jet streams (Arabic numerals in circles) in projection onto Galaxy plane. The solar orbit is shown for the last revolution of Sun around Galaxy center (G.c.). The small circle in the center, where the jet streams flow out, is Galaxy nuclear disk. The larger circle where galactic arms begin determines the size of Galaxy isothermal core. The outer dotted ring corresponds to Galaxy corotation radius R*. The arrow indicates the direction of Sun moving on orbit, which coincides with rotation of Galaxy and rotation of the apses line (straight line) of solar orbit. The asterisk shows the place in arm Crux-Scutum (IV) where Solar System was formed earlier

and also makes it possible to calculate with high accuracy the times of Sun crossing jet streams and spiral arms of Galaxy [6, 18].

Figure 1 shows that Sun is currently on the inner side of Orion-Cygnus branch, which is the jet stream closest to Sun. Geological evidence suggests that Sun may have entered this jet stream about 5.0 Ma and left it about 0.7 Ma, so that for about 4 million years Solar System was bombarded by galactic comets [5, 6].

According to our comet concept, it was the bombardment of Solar System by comets of Orion-Cygnus jet stream that played a major role in formation of comets observed today. Note that the connection of Solar System comets with the Orion-Cygnus branch has been repeatedly suggested by specialists [50, 72].

In our comet concept this cometary bombardment also explains other "extraordinary" phenomena in Solar System [5]: the "peculiar" state of Sun [29], increased Earth's geological activity [1], strong turbulence of giant planets atmosphere [45], excited state of bodies in asteroid belt [62]; significant dustiness of interplanetary space [21]; as well as the presence in it of a large number of comets, meteorites and asteroids with a dynamically short lifetime [70].

5 Galactic Comets

It was previously noted that galactic comets, like young stars, arise in places where galactic arms interact with jet streams. Therefore, one should distinguish between comets of jet streams and galactic arms. The former move relative to Sun at a very high speed, the latter with speed is one or two orders of magnitude less. Both groups of galactic comets are currently inaccessible to detection from Earth, since they can be observed when Sun is respectively in jet streams and galactic arms. Today this is not the case. Therefore, everything that we know about galactic comets was obtained on the basis of an analysis of consequences of their falls on Earth and other planets [6].

The most studied comets of Orion-Cygnus jet stream, in which Sun was in period from 5.0 to 0.7 Ma. These comets moved relative to Sun at a speed of 450 km/s, had a core diameter of $0.1 \div 3.5$ km, a mass of $10^{12} \div 10^{17}$ g, and an energy of $10^{20} \div 10^{25}$ J. They consisted mainly of water ice with an admixture of carbon-containing components and had density $\approx$1.0 g/cm^3. The flow density of comets in Orion-Cygnus jet stream was 10^{-9} comets per year per km^2 [17].

In addition to their icy composition and very high rate falls onto planets, galactic comets differ from comets observed today in Solar System in other ways. Let's list them briefly:

1. The nuclei of galactic comets are exponentially distributed in diameter and not according to the inverse square law as in asteroids and comets of the Solar System. Accordingly the geological structures created by their falls, namely: seamounts (Earth); craters, seas and mascons (Moon, Mars and Mercury); montes, coronas,

diatremes, and shield volcanoes (Venus) are also characterized an exponential size distributions [8, 16].

2. Falls of galactic comets have character of comet "showers" lasting 2–5 mln years, which are repeated in 20–37 mln years. During one shower ~ 10^4–10^7 galactic comets can fall to planets. As a result, most of craters with diameter D > 10 km on terrestrial planets (except for Earth) are created by galactic comets. Due to the high frequency of comets falling, the surfaces of Moon, Mars and Mercury bombarded by them are 100% saturated with craters with D > 10 km. This saturation limit by craters is the same for Moon, Mars and Mercury and amounts to 150 craters per mln km^2 [17].
3. Unlike asteroids and comets of Solar System, which move in ecliptic plane, galactic comets move in Galaxy plane inclined to the ecliptic at an angle of 62°. As a result, at Sun's orbital movement, galactic comets alternately bombard the southern and northern hemispheres of planets [14]. The last time they bombarding southern hemisphere of all planets.
4. The specificity of galactic comets also lies in the different physical mechanisms of their interaction with planets with and without an atmosphere. If for asteroids with D ≈ 100 m or more, Earth's atmosphere has little effect on results of their fall [48], then galactic comets of the same size in Earth's atmosphere are completely destroyed, and their enormous kinetic energy causes heating asthenosphere rocks. On continents, this leads to rise of their surface, and in oceans, to the outpouring of lava to bottom and formation of seamounts [6, 7] and [9].

6 Collisions of Comets and Asteroids

The issue of interaction of galactic comets with bodies of asteroid belt deserves special attention. It is known that 98% of all asteroids discovered today in Solar System are concentrated between orbits of Mars and Jupiter in form of a wide toroidal ring (Fig. 2).

In this region of interplanetary space, they can exist for more than 4.6 billion years from moment of their origin, only slightly changing their orbital parameters over time. The distribution of asteroids by diameter in this ring is power law and with exception of largest of them is well obeys the inverse quadratic relationship [32]: $N(D_\alpha) = 10^5\ D_\alpha{}^{-2}$, where: $N(D_\alpha)$ is number of asteroids with diameters more than D_α (in km). This expression gives distribution of spectral density of asteroids over sizes $n(D_\alpha)$ in following form:

$$n(D_\alpha) = \frac{dN}{dD_\alpha} = -2 \times 10^5\, D_\alpha^{-3}. \tag{1}$$

Obviously, collisions of galactic comets with asteroids are in the nature of an explosion, in which energy is released, which is close in magnitude to kinetic energy

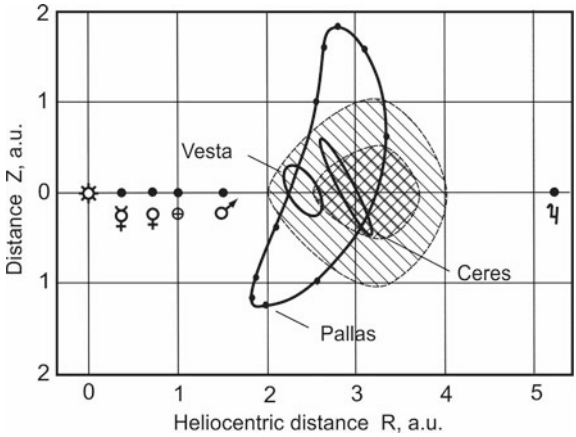


Fig. 2 The cross-section of asteroid belt by a plane perpendicular to the ecliptic plane and passing through Sun. The regions with different spatial density of asteroids are shaded. Shown the loops that asteroids Pallas, Ceres and West are making in this plane (according to L. Kresak)

of colliding bodies. Depending on size ratio of comet and asteroid, the processes initiated by their collision should be different.

When hit by a comet in large asteroid with mass ma significantly exceeding comet mass m_k, energy of explosion mainly goes on formation of crater with accompanying crushing and evaporation of asteroid substance and removal of ejection products from crater as well as on formation of a powerful shock wave. The comet body completely collapses and its substance evaporates and dissipates, mechanically and chemically mixing with asteroid material. The total mass of matter ejected at formation of the funnel can exceed 10–1000 times mass of comet itself. The rate of output of the main mass of rocks lies in limits from meters to several kilometers per second, and of evaporated matter can reach ~10 km/s [19]. At this for planets and very large asteroids most of ejected material falls back to their surface, while for small ones—is lost [69].

For smaller asteroid bodies ($m_\alpha \sim m_k$) the impact energy may be enough to cause, together with cumulative effect, the disintegration of asteroid and also break it into parts. In the case comet collision with very small stones ($m_\alpha << m_k$), both bodies go fully to ruin. This process is inevitably accompanied by release into interplanetary space of huge quantities of cometary and meteoritic dust.

Of great interest is a question about minimal size of asteroids D_α*, collisions with which are disastrous for galactic comets and about total number of such bodies in asteroid belt.

We find the value of critical diameter of asteroids D_α* from considerations of equality of binding energy E_k of cometary nucleus to kinetic energy of asteroid E_α in the comet rest frame. Assuming that comet nucleus is held by gravitational forces, we write its binding energy as $E_k = 6{m_k}^2 G/5D_k = \pi^2 {\rho_k}^2 {D_k}^5 G/30$, where G is gravitational constant, D_k is diameter of comet nucleus. The expression for the kinetic energy of asteroid has the form $E_a = m_a V^2/2 = \pi \rho_a {D_a}^3 V^2/12$, where V is mutual velocity of galactic comet and asteroid. Taking densities of cometary nuclei and asteroid equal, respectively, $\rho_k = 1$ g/cm^3 and $\rho_\alpha = 4$ g/cm^3 and assuming velocity

$V = 450$ km/s, dependence of value D^* km on diameter of cometary nucleus, we obtain in form $D_\alpha^* = 4.7 \times 10^{-7}\ {D_k}^{5/3}$. It follows that for comet with core diameter of $D_k \approx 3.5$ km, the cause of destruction is its collision with a half-meter asteroid, and at diameter $D_k \sim 200$ m, a comet can be destroyed by centimeter stone.

The total number of asteroids in belt $N(D_\alpha^*)$ collisions with which are disastrous for galactic comets can be estimated with formula (1) under assumption that given law is satisfied not only for great asteroids but also for more small unobserved objects. In this case, we have $N^* = N(D_\alpha^*) = 4.5 \times 10^{25}\ {D_k}^{-10/3}$. Whence we find that for galactic comets with a core diameter $D_k = 3.5$ km the number of "dangerous" asteroids in belt will be $\sim 7 \times 10^{13}$, and for comets with $D_k \sim 100$ m it will increase to $\sim 10^{19}$.

Since asteroid belt occupies space volume of $\sim 1.6 \times 10^{26}$ km^3 [69], in the first case, their concentration in belt will be $\sim 4 \times 10^{-13}$ km^{-3}, and in the second $\sim 6 \times 10^{-8}$ km^{-3}. For comparison, let us indicate volume of Earth $\sim 10^{12}$ km^3.

Thus, the concentration of "dangerous" asteroids in belt is negligible. At the same time, probability of colliding with such bodies for galactic comets is not small. As a measure of this probability, we introduce cross section comet destruction in collisions with asteroids S^*. Assuming that destruction causes any passage of comet at distance from asteroid less than the half-sum of diameters of both bodies, we have

$$\begin{aligned} S*(D_k) &= \frac{\pi}{4}\int_{D*}^{D_{\alpha m}} (D_\alpha + D_k)^2 n(D_\alpha)\cdot dD_\alpha \\ &= N*\left[D_k^2 + 2D_k D_\alpha^* + D_\alpha^{*2}\mathrm{In}\left(D_{\alpha m}/D_\alpha^*\right)\right], \end{aligned} \tag{2}$$

where: $D_{\alpha m} = 1000$ km is maximum diameter of asteroids.

The graph of cross section $S^*(D_k)$ is shown in Fig. 3 [5].

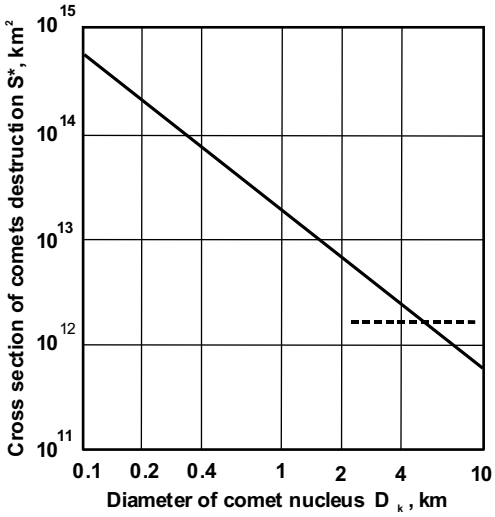


Fig. 3 Cross sections of galactic comet destruction in asteroid belt, depending on diameter of cometary nucleus. Dotted line is Sun's crsoss sectional area

It follows from our calculation that for galactic comets with core diameter D_k = 0.1–3.5 km, their destruction cross section in asteroid belt is $S^* \sim 10^{12}$–10^{15} km^2. This value is more than Sun cross-sectional area $S_\odot = 1.6 \times 10^{12}$ km^2 and even more so of all planets. In particular, for Jupiter $S_j = 1.6 \times 10^9$ km^2, and for Earth is 1.3×10^8 km^2.

Thus, the probability of galactic comets destruction in asteroid belt is two orders of magnitude greater than probability of their fall on all objects of Solar System. Hence, it is clear that asteroid belt is the main place where interaction of galactic comets with Solar System takes place.

From structure of formula (2) also follows that for $D_k \approx 0.1$ km a decisive contribution to the S^* value is due to collisions of comets with small-sized asteroids, while on share of large asteroids accounts for only ~10^{-4} part of all collisions. Therefore in asteroid belt, processes of evaporation and crushing of galactic comets must be significantly dominated, accompanied by ejection in interplanetary space of large amount of cometary gas and dust. But this conclusion does not mean that collisions of comets with large asteroids do not play a significant role, and they can be ignored. Because of significant cumulative effects, such collisions lead to intense disintegration of asteroids and ejection of their fragments from belt [6].

Thus, in collisions with galactic comets in asteroid belt, albeit with various probability, appear all known types of small bodies of Solar System: (1) large blocks of rocks—asteroids; (2) their small debris—meteorites; (3) destroyed nuclei of galactic comets; and also (4) finely dispersed substance, represented by cometary and meteoritic dust.

Let us be interested about the further fate of these neoplasms.

6.1 Interplanetary Dust

According to existing ideas [49], the suppliers of dust particles to interplanetary space can be: Sun's crown, asteroid belt, Kuiper belt, Oort cloud comets, giant planets, and Galaxy.

About interplanetary dust we, first of all, judge by micrometeorites falling to Earth, a smallest particles of a cosmic substance with dimensions from a micron to several millimeters. In its basic bulk, they are very porous brittle aggregates of dark color, similar in chemical composition to carbonaceous chondrites or, less frequently, consisting of associations of crystalline grains of minerals characteristic of other known types of meteorites [21].

In our concept, dust particles appear in asteroid belt, the evaporation of its bodies in collisions with galactic comets. At low temperatures, vapors and gases, as well as the smallest droplets of the substance melted by the impact, quickly cool and condense into dust aggregates. At the same time, a part of dust grains easily freezes with the debris of asteroids, settling on their surface, or are captured and included in nuclei of secondary comets being formed. Most of dust grains remain in a free state.

The behavior of such free dust particles in Solar System, in the main, is determined by their mass and sizes. Dust grains of very small diameters ($d < 10^{-5}$ cm) and masses ($10^{-15} \div 10^{-13}$ g) are quickly swept out of interplanetary space under influence of Sun's light pressure. Larger particles by action of Pointing-Robertson effect [57], on the contrary, move in spiral orbits towards Sun. The time of their fall on Sun (in years) is: $\tau = 3.5 \times 10^6 d\rho\, R^2$, where: ρ is density of dust particles mater, R is radius (AU) of initial orbits of dust particles, from which they begin move towards Sun.

For dust particles with a diameter of d ~ 10^{-4} cm and density of $\rho = 2.5$ g/cm^3, which begin to move from asteroid belt, the value $\tau = 5 \times 10^5$ years, and for the same dust particles thrown behind orbit Saturn $\tau = 50$ mln years. All other things being equal, larger and/or denser particles fall on Sun later.

When moving towards Sun, some of dust particles are intercepted by planets, their satellites and asteroids. So, for example, in Iapetus—satellite of planet Saturn, which rotates being constantly turned to Saturn by one side, the albedo of surface of its front hemisphere in direction of motion is an order of magnitude darker than the back hemisphere.

However, the most intense deposition of dust particles occurs in asteroid belt (Fig. 4), which is reflected in the peculiar arrangement of its bodies, covered with dust particles "heavily" (C-asteroids) and "weakly" (S-asteroids).

Figure 4-a, borrowed from [69], shows the dependence of the spatial density of C- and S-asteroids in belt on the Sun distance. And in Fig. 4-b, the same dependences are presented in semi logarithmic coordinate system [4]. We see that the distributions in belt of C- and S-asteroids are well approximated by formulas:

$$N_c(R) = 1.75 \exp[(R - R_0)/L], \tag{3}$$

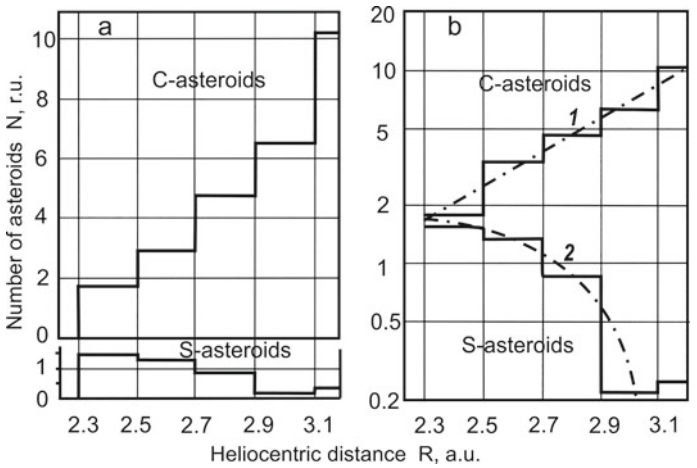


Fig. 4 Spatial density in asteroid belt of "dark" (C) and "light" (S) asteroids with diameter of more than 50 km as function of heliocentric distance in ordinary (a) and semi-logarithmic (b) coordinate system. The dotted dashed lines (1) and (2) correspond to formulas (3) and (4)

$$N_s(R) = 1.75\,[1 - \exp(-(R - R_0)/L)], \quad (4)$$

where: $R_0 = 2.3$ AU and $L = 0.42 \pm 0.02$ AU are constants.

Formulas (3) and (4) indicate the diffusive mechanism of dust penetration into asteroids belt. In this case, constant L has physical meaning of diffusion length $L = (n\sigma)^{-1}$, where n is spatial density of asteroids in belt, and σ is cross section for capture by asteroids of dust particles.

Analysis shows [5] that value of constant $L = 0.42$ AU can be explained by absorption of dust by asteroids with $D > 10$ cm. Other things being equal, dust deposition rate on asteroids surface grows as $\sim D^{8/5}$. Therefore, it is no accident that among bodies with diameter $D > 80$ km about 83% is of type C, that is they are covered with rather "crust" of dust and only 17% relate to type S [69].

There is greatest probability of dust deposition on biggest asteroids: Ceres, Pallas and Vesta. These asteroids often experience of collisions with galactic comets and capture fragments of rocks and dust that are formed at collisions. All three asteroids have close satellites and rich asteroid families, and their surface is characterized by a sharp heterogeneity of reflective properties. The latter circumstance does not allow us to classify these asteroids as S and C type, and forces them to pick out into separate class U [70].

Asteroids of smaller sizes are destroyed in collisions with galactic comets and may lose dust crust. Some of their fragments are lost and go beyond asteroids belt, while others remain (Eos, Koronis, Nyca, etc.). Some asteroids acquire satellites (Hebe, Herculina, etc.). Satellite systems are extremely unstable. All these asteroids as well as their family members have S-type, i.e. are "young". They had not yet covered themselves by dark dusty crust and, in contrast to "old" C-asteroids they do not avoid forbidden hatches [70].

Smaller asteroids, when colliding with galactic comets, are crushed and can lose their dust crust. Part of their debris is lost and leaves asteroid belt (for example, the groups of Apollo and Cupid), others remain and form families (Eos, Koronis, Nyca, etc.). Some asteroids acquire satellites (Hebe, Herculina, etc.). Satellite systems are extremely fragile.

All the named asteroids and members of their families are S-type, i.e. "young". They have not yet managed to become covered with a dark dusty crust and, unlike "old" C-asteroids, do not avoid forbidden hatches [70]. Over time, dust layer on asteroids surface increases and their color changes from light to dark.

A vivid example of C → S asteroids transformation are families Eos ($R = 3.02$ AU) and Koronis (2.87 AU). Time destruction of parental bodies these systems is ~ 1 Ma [70]. We believe that destruction parent asteroids in families Eos and Koronis occurred during last cometary bombardment. Therefore now their fragments of S-type sharply differ from all other bodies of outer zone belt.

Thus, the main reason for differences between C- and S-asteroids is varying degree of dustiness their surface. Character of distribution C- and S-asteroids in belt can be explained [4] as a result of simultaneous existence two competing processes: on

the one hand, deposition of dust particles on asteroids surface, and on the other, destruction of asteroids during their collisions with galactic comets.

6.2 Meteoric and Larger Bodies

For all small bodies of Solar System with masses greater than those of dust grains, the main factor determining their further fate is value of the initial velocity V, which they receive at birth. If the parent asteroid is great and does not fully destroying by the impact of galactic comet and velocity of secondary products is small and does not exceed $V_1 = D_\alpha \sqrt{\pi \rho_\alpha G} \approx 10^{-3}\ D_\alpha$ km/s, then material ejected by explosion is not able to overcome attraction of parent asteroid and falls back onto its surface.

If the velocity V of the ejected debris is in the range from V_1 to $V' = \sqrt{2}\ V_1$, then under certain conditions they can begin to rotate around parent body with mass m_α at a distance from its center $r < R\ (m_\alpha/M_\odot)^{2/5}$. The presence of one or even several close satellites has been found in many large asteroids. The lifetime of such "satellite" systems is short. Under the influence of disturbances from Jupiter and Sun, as well as other asteroids, the satellites must quickly fall on the central body, or leave it. Consequently, the very fact of existence of such systems testifies to their very recent formation.

The situation $V > V'$ is of the greatest interest to us. In this case, as in the case of complete destruction of asteroid, the newly formed bodies lose their connection with the parent asteroid. At the same time, a sufficiently large impulse can be transferred to some of them, which will allow them to leave not only asteroids belt, but also Solar System. The condition of "knocking out" asteroids from belt in the first approximation can be written in form: $\Delta V > V_x$, where ΔV is increment in velocity of asteroid (or its breakaway part) after collision with comet, V_x is the average chaotic velocity of asteroids in belt. In accordance with the momentum conservation law, the maximum ΔV obtained by asteroid in elastic collision with comet will be $\Delta V = Vm_\alpha/(m_\alpha + m_k)$, where V is comet velocity relative to asteroid. Hence, the condition for knocking bodies out of asteroid belt is reduced to the restriction $m_a \leq m_k/(V/V_x - 1)$.

Assuming $V = 450$ km/s, $V_x = 5$ km/s, and taking mass of large galactic comets $m_k \sim 10^{16}$ g, we obtain $m_\alpha \leq 10^{18}$ g. At a density of asteroid matter $\rho_\alpha = 4$ g/cm^3, specified mass corresponds to bodies with diameter $D_\alpha \leq 8$ km. Thus, a chance to go beyond belt limits have mainly bodies of small and medium-sized, and larger ones remain in belt. By this circumstance we explain the fact [70] that almost all asteroids outside belt, in particular, of the Apollo, Amur and Aton families, are mainly represented by bodies with a diameter of less than ten kilometers. This conclusion is fully valid also for daughter comets leaving belt.

Having become "free", daughter bodies begin to move along independent Keplerian orbits, determined by magnitude and direction of velocity V, which they acquire relative to Sun at birth moment. The influence of this speed on their further fate can be taken into account by representing V in center of mass system of colliding parent

bodies:

$$\mathrm{V} = |\mathrm{W} + \mathrm{U}| = \sqrt{\mathrm{W}^2 + \mathrm{U}^2 + 2\mathrm{WU} \times \cos(\vartheta)}, \tag{5}$$

where: W is bodies velocity in the center mass system of "parents", U is speed of the mass center relative to Sun, ϑ is angle between vectors W and U.

For secondary bodies captured by Sun, their velocity V at heliocentric distance R equal to the aphelion distance is related to eccentricity e and magnitude of orbit semi-major axis α by the expressions:

$$V = \sqrt{GM_{\odot}(2/R - 1/\alpha)} = V * \sqrt{1 - R/2\alpha} = V * \sqrt{\frac{R}{2\alpha}\left(\frac{1-e}{1+e}\right)} \tag{6}$$

where $V* = \sqrt{2GM_{\odot}/R}$ is critical speed of the secondary bodies ejection from belt, at which Sun is still able to hold them by its attraction. Assuming $R = 2.8$ a.e. that is equal to average radius of asteroid ring, for critical speed we will have $V^* = 25$ km/s.

Formula (6) indicates that only bodies remain in Solar System, whose initial velocity relative to Sun's lies within $V^*/\sqrt{2} \leq V < V^*$. If body is ejected from belt with speed V> V *, it leaves Solar System. If body speed is less than $V^*/\sqrt{2}$, then it will quickly fall on Sun. Therefore, for all newly formed bodies captured by the Sun gravity, orbital radii must satisfy the inequality $0 < R/\alpha \leq 1$, where upper limit corresponds to bodies remaining in belt, and lower ones to cometoasteroids whose orbits go far of belt.

Combining expressions (5) and (6), for capture of daughter bodies by Sun, we obtain the following condition

$$W^2 + U^2 + 2WU\cos(\vartheta) + \left(\frac{R}{2} - 1\right)V* < 0 \tag{7}$$

Formula (7) indicates that probability of secondary bodies to be captured by Sun is anisotropic and strongly depends on ratio of the masses of colliding comets and asteroids. To take into account the effects of anisotropy, we introduce velocity distribution function of daughter bodies *F (W, U)*, defining it as follows:

$$F(W, U) \cdot dW \cdot d\Omega = \frac{F_0}{4\pi}\left(\frac{W}{V*}\right)^{-\gamma} \sin(\vartheta) \cdot dW \cdot d\vartheta \tag{8}$$

where: γ is constant, F_0 is constant corresponding to the normalization condition

$$4\pi \int_{V'}^{\infty} dW \int_0^{\pi} F(W, \vartheta) \sin(\vartheta) \cdot d\vartheta = 1 \tag{9}$$

where V' is velocity of «running away» for daughter bodies.

In formulas (8) and (9), it is assumed that the distribution function *F (W, U)* is power-law in the velocities of daughter objects W, and isotropic in the angles ϑ of their ejection from belt in system of center mass of the parental bodies.

Let us analyze the consequences of formulas (7)–(9) for two limiting, but important cases. In the first case, galactic comets collide with very large asteroids ($m_\alpha >> m_k$), and in the second, with very small ones ($m_\alpha << m_k$).

6.2.1 Collisions of Galactic Comets with Large Asteroids

When comet collides with a very large asteroid, the speed of mass center U of colliding bodies practically coincides with speed of asteroid motion around the Sun $U = \sqrt{GM_\odot/R} = V^*/\sqrt{2}$, and ejection of daughter bodies occurs symmetrically to ecliptic plane. Substituting the value of velocity U in units of V^* into formula (7) and solving quadratic equation, the capture condition is obtained in the form:

$$W(\vartheta, R/\alpha) \le W* = \frac{V*}{\sqrt{2}}\left[\sqrt{1+\cos^2(\vartheta) - \frac{R}{\alpha}} - \cos(\vartheta)\right] \tag{10}$$

The probability of capture by Sun of daughter bodies $P(\vartheta, R/\alpha)$, leaving belt at different azimuthally angles, but characterized by the same values of semi-major axis of orbit, for the case $m_\alpha >> m_k$ is shown on Fig. 5.

The calculation was carried out according to formula

$$P(\vartheta, R/\alpha) = \int_{V'}^{W*} W\,dW \Big/ \int_{V'}^{\infty} W\,dW \tag{11}$$

for isotropic distribution of daughter bodies on angle ϑ and power-law mass distribution in formula (8) with constant $\gamma = 2$.

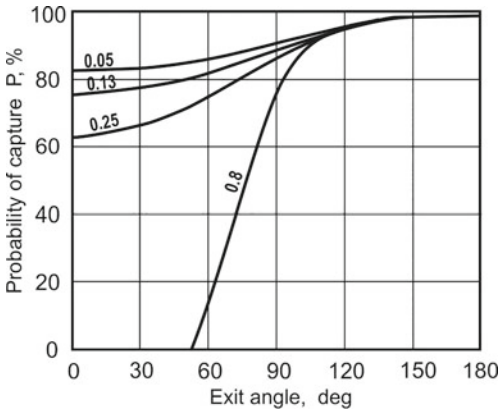


Fig. 5 Probability of capture by Sun of daughter bodies had arisen owing to collisions of galactic comets with "large" asteroids as a function of angle their ejection from belt and orbit radius. Curves are correspond parameter R/α of daughter bodies which reach orbits of Uranus (0.05), Saturn (0.13), Jupiter (0.25) and outward border of asteroid belt (0.8)

Figure 5 shows that bodies ejected in the opposite direction to motion parent asteroid have the greatest chance to remain in Solar System. Moreover, for bodies in asteroid belt, this case is the only possible one. With an increase in radius of orbit, the capture probability of daughter bodies by Sun $P(\vartheta, R/\alpha)$ begins to depend weakly on angle ϑ of their exit from belt.

Let us also pay attention to the fact that rotation periods of daughter bodies around Sun turn out to be more than those of parent asteroids, therefore, as a result of many acts of crushing, asteroids are displaced to outer edge of belt. Whereas very large asteroids, having experienced a small number of crushing, remain in the belt to their former places (see Fig. 2).

6.2.2 Collisions of Galactic Comets with Small Asteroids

In the case of $m_\alpha << m_k$, the situation changes radically. If previously, the predominant type of daughter bodies were debris of asteroids, which freezing with more or less amount of icy cometary material, but now secondary bodies, mainly are represented by substance of destroyed galactic comets.

In addition, the center mass of colliding bodies, it is no longer connected with asteroid, but with galactic comet. In this case, the speed is $U \approx 18$ V*, and the solution to Eq. (6) takes the form:

$$W* = 18V* \left[\sqrt{3.1 \cdot 10^{-3} \left(1 - \frac{R}{2\alpha}\right) - \sin^2(\vartheta)} - \cos(\vartheta) \right] \tag{12}$$

Function (12) has a physical meaning under more stringent restrictions on speed and direction of ejection bodies from asteroid belt. Now only bodies can remain in Solar System, which leave the belt with velocity $U - V* < W < U + V*$ and in a cone of angles $\Delta\vartheta \leq \pm 3°$, and in direction opposite to motion of galactic comet (Fig. 6).

Lets we note that angles ϑ in Fig. 6-a, and Fig. 6-b are postponed of sundry directions. The dependence (Fig. 6-a) is plotted for ecliptic plane, and angle ϑ is measured from direction of Sun motion in Galaxy. While the calculation (Fig. 6-b) refers to galactic plane making an angle of 62° with the ecliptic, and angle ϑ is measured from direction to Galaxy anticenter.

The probability of Sun capture of bodies formed in collisions with small asteroids is of the order of magnitude $(V*\Delta\vartheta/U)^2 \sim 3 \times 10^{-5}$, which is much lower than in the case when galactic comets are scattered by large asteroids.

With an increase in the asteroid mass, which comet collided with, the vector of preferred orientation of line apsid of daughter bodies orbits captured by Sun changes direction. In the case $m_\alpha >> m_k$, it lies in the ecliptic plane and coincides with direction of Sun's motion in Galaxy.

The connection of comets with galactic plane, first established by [71], was later confirmed by increasingly representative statistical observational data. Therefore,

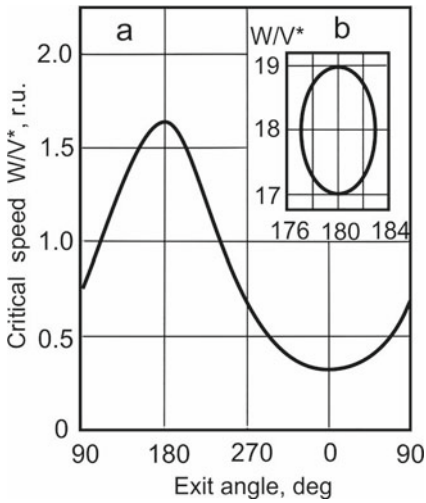


Fig. 6 Dependence of critical velocity of bodies on their ejection angle from belt in collisions of galactic comets with large (a) and small (b) asteroids: calculation using formulas (10) and (12) for $R/\alpha = 0$

supporters of galactic origin of comets in Solar System [68, 73], in a dispute with adherents of the eruptive idea, usually put forward this connection, as well as the obvious similarity in chemical composition of comets and interstellar gas, as very important, if not decisive argument.

7 Mechanism of Daughter Comets Formation

It has been noticed that young craters on planets are often bordered by radiation ejections of matter. These emissions have form "rays" of light color tapering towards the end. The rays are usually on order of several kilometers wide and ~100 km long. In very large craters, the emissions reach of ~1000 km in length and hundreds of kilometers in width. Often along the rays there are located clusters of small secondary craters [19, 48].

It is believed that the rays are formed as a result of cumulative ejection from crater of evaporated material of the impactor mixed with crushed material of surface rocks. The light color of the rays is given by presence of frozen water vapor and ice of other gases in their substance. Assuming that most of rays consist of water ice layer ~1 cm thick, the total matter mass of individual emissions will be at least $m = 10^{12}$–10^{15} g.

We believe that cumulative emissions of this kind occur when galactic comets collide not only with planets, but also with asteroids. In the latter case, the substance is thrown into outer space, where, under the action of self-gravity, it can form a secondary cometary body. The characteristic time of body formation can be estimated by formula

$$t \approx \left(\frac{2r^3}{Gm}\right)^{\frac{1}{2}} \tag{13}$$

where: m is the mass of ejected substance, r is the ejection length.

Since Sun gravity also acts on ejected matter, the initial size of ejection cannot exceed value

$$r \leq R\left(\frac{m}{M_\odot}\right)^{\frac{2}{5}} \tag{14}$$

where R is heliocentric distance of nucleus "assembly" of daughter cometary.

From formulas (13) and (14) it follows that if the length of ejection is ~5–500 km, and velocity dispersion in it does not exceed the first meters per second, then daughter comets with mass of ~10^{12}–10^{19} g can be formed already in asteroid belt itself.

Thus, ideas of supporters of eruptive formation of comets receive, at least on a qualitative level, quite acceptable theoretical justification. This mechanism in principle explains the composition and structure nucleus of cometary bodies in the model of [82, 83] as well as allows one to understand dimensions of observed comets themselves.

At $m \leq 10^{10}$ g, agglomeration of daughter comets becomes ineffective due to decrease in volume of space for matter collection, and at $m \geq 10^{20}$ g, the requirements for dispersion of ejection velocities are sharply tightened due to the short time (13). Of course, this mechanism does not exclude the possibility of daughter comets growth also due to additional addition to them of scattered gas and dust matter enveloping Solar System during period of bombardment by galactic comets [6].

Thus, our consideration shows that all secondary bodies, whether they remain in the belt or are thrown out of its limits and even outside the Solar System, are objects associated with their birth with asteroid belt. In this case, with the exception of the smallest dust grains, the rest bodies, be they fragments of asteroids, meteorites or daughter comets, move in the Solar System, obeying to formula (6).

Therefore, comets of Solar System and asteroids should be considered as extreme members of single series of secondary bodies "cometoasteroids" [65], which, according to our concept, are formed during collisions of galactic comets with asteroid belt bodies. Depending on radius of orbits, that cometoasteroids have acquired, ratio in their substance of "rocky" and "ice" components can vary: from the complete absence of ice in asteroid belt, where ice sublimes under the action of solar radiation, to its significant presence in comets, which spend most of their life far from Sun.

Let us now turn to a discussion of range of questions relating directly to observed comets, and also explain the reasons leading to appearance of long-period and short-period cometoasteroids.

8 Long-Period Comets

It has already been noted that comets with orbital period $T > 200$ years and semi-major axis of orbit $\alpha = T^{2/3} > 34$ AU are referred to as long-period comets. However, historically, long-period comets are often understood [43] more homogeneous group of bodies with periods of ~10^6 years, which is more than half of all comets of this type. The aphelion of such comets are at distance of more than 10^4 AU from the Sun, which causes the appearance of narrow maximum in their distribution in the $1/\alpha$ parameter at coordinates origin of (Fig. 7).

The frequent occurrence of such cometary orbits led [51, 52]) to assumption of the presence at distance of ~$10^4 \div 10^5$ AU from Sun of quasi-spherical relict cometary cloud, numbering 10^{12}–10^{13} comets, from where they penetrate into the inner region of Solar System. In view of the need to explain origin of other groups of long-period comets, the Oort hypothesis was subsequently transformed into ideas of existence of a whole system of "cometary reservoirs" located closer to Sun: of Whipple, Kuiper, Hills et al. [75].

The Galactocentric paradigm in a different way solves the problem of observed comets origin. In Solar System there are no "external" or "internal" reservoirs of relict comets preserved from the time of its formation, but there are daughter cometoasteroids. These objects formed and were ejected from asteroid belt in the time between 5.0 and 0.7 Ma during Sun's stay in Orion-Cygnus jet stream, and now rotation around Sun in orbits of greater radius than asteroids.

Therefore, long-period comets with periods of ~ 10^6 years are nothing more than the highest-speed group of cometoasteroids that left the belt with velocities close to V^*. They have an orbital semi-major axis $\alpha = t^{2/3} \sim 10^4$ AU and now are returning back to Sun. Since Sun is currently moving in Galaxy with an acceleration of +1.8 km/s per 1 million years [15], for cometoasteroids with periods of ~10^6 years, the reference frame associated with the Sun is not strictly inertial. As a result, their initially elliptical orbits are transformed into weakly hyperbolic and weakly parabolic.

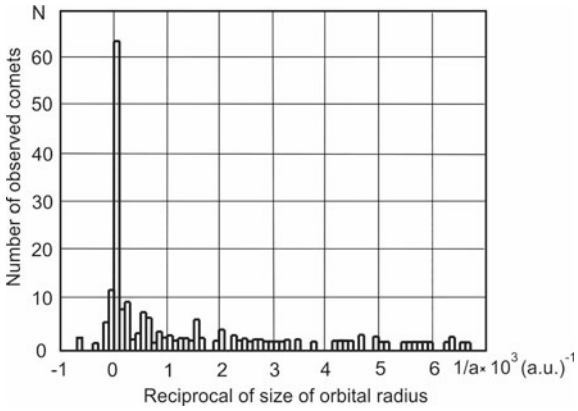


Fig. 7 Distribution of long-period comets by reverse large semi-axis of their orbit [43]

Let's discuss this issue in more detail. For this purpose, among entire multitude of cometoasteroids captured by Sun with orbital parameters $\alpha/R >> 1$, we will single out three of their main groups. In the first group of "New" we included those that return to Sun for first time after their ejection from asteroid belt, and to the other two groups of "Repeated" and "Tertiary" we include cometoasteroids completing their not first revolution around Sun.

Let's consider the features each of these cometoasteroids groups.

8.1 "New" Long-Period Cometoasteroids

According to given earlier definition, orbital period T of New cometoasteroids must be identically equal to the time t, that has elapsed since time of their formation in asteroid belt. Therefore, in accordance with formula (6), between initial velocity V, aphelia distance $R_{\alpha f} = (1 + e)\alpha \approx 2\alpha$, and time of formation such comets t, there exists a rigid functional connection:

$$V = V * \sqrt{1 - \frac{T_0^{2/3}}{2} t^{-2/3}} \approx V * \sqrt{1 - t^{-2/3}} \tag{15}$$

where T_0–period of orbital motion bodies in asteroid belt.

Believing that the formation of New cometoasteroids occurred during the last bombardment of Solar System by galactic comets, i.e. in the time interval $0.7 \leq t \leq 5.0$ Ma, it should be concluded:

(1) New cometoasteroids observed today should be ejected from the belt in a narrow range of initial velocities in vicinity of $V*$.
(2) Aphelion of orbits New cometoasteroids should be in interval distances from Sun $1.4 \times 10^4 \leq R_{\alpha f} \leq 5 \times 10^4$ AU.
(3) Ejection of New cometoasteroids from asteroid belt should be almost isotropic in all directions;
(4) Eccentricity of New orbits cometoasteroids should be practically equal to 1.

These parameters of New cometoasteroids orbits almost exactly determine the shape and dimensions of "cometary cloud", which according to the Oort hypothesis surrounds Solar System since its formation. However, as noted earlier, the long existence of such a cometary cloud near the Sun is physically impossible.

Therefore, it should be recognized that there is no excess of comets on the periphery of Solar System, and the so-called "Oort cloud" represents the geometric position of aphelion of cometoasteroids orbits that first time are returning back to Sun after their ejection from asteroid belt.

In other words, "Oort cloud" is not a place of real comets concentration, but only a spatial area of concentration of aphelion points of the most high-speed cometoasteroids that are returning to Solar System today. Since such objects return to Sun only

for the first time after their ejection from the belt and have not yet lost high concentrations of gas and dust, they are perceived as "young", i.e. large and bright comets, which, in accordance with ideology of the Oort hypothesis, are called "New".

Let $n(V, t)$ is cometoasteroids number flying from the belt in unit velocity interval per unit time. Suppose also that all these bodies were formed during the last Sun stay in Orion-Cygnus jet stream, at that with equal probability throughout this time range.

$$\mathrm{n(V,\,t)} = \begin{cases} 0 & t_1 > t > t_2 \\ n_0(v) & t_1 \le t \le t_2 \end{cases} \tag{16}$$

Then, the number of New comets returning to Sun every year we will found as.

$$n = \int_{V_1}^{V_2} n(V) \cdot dV \tag{17}$$

where: velocities V_1 and V_2 are calculated by formula (15) for Sun's entry time (t_1 = 5.0 Ma) and exit time (t_2 = 0.7 Ma) from jet stream Orion-Cygnus.

Bearing in mind that velocities V_1 and V_2 differ little from the value of V^*, at integrate (18) we obtain $n = n_0(V^*)(V_2 - V_1)$. Assuming that unknown cometary objects are detected annually in an amount of $n \approx 5$, of which New long-period comets are about half [23], we find the value of $n_0(V^*) \sim 10^4$ comets per year in interval of velocities 1 km/s. As a first approximation, we can also estimate number N of New long-period cometoasteroids currently existing in the Solar System. Taking into account also those of them that have never appeared near Sun, their number in order of magnitude is $N \sim 10^6 - 10^7$ [5].

8.2 "Repeated" Long-Period Cometoasteroids

This group of bodies is represented by cometoasteroids, which were ejected from the belt with lower initial velocities and, accordingly, have smaller periods and radiuses of orbits. On the histogram of Fig. 5 they form a long "tail" of distribution.

Each of observed "Repeated" cometoasteroids can in principle to finish its not first turnover around the Sun. Therefore, one would expect that number cometoasteroids of this type in Solar System should significantly exceed the number of "New" and grow linearly with a decrease in their period.

In reality however it does not happen that way. Due to motion Sun on galactic orbit with acceleration the reference system associated with Sun for the long-period cometoasteroids is not inertial. Therefore, when they return to Sun their originally elliptical trajectories are transformed becoming weakly hyperbolic or weakly parabolic.

But even small deformations of orbits long-period cometoasteroids usually lead to their loss by Solar System. The systematization of cometary trajectories performed by [46] shows that of 545 observed long-period comets, 162 comets had an elliptical

orbit, and 285 and 98 comets, respectively, were weakly parabolic and hyperbolic. This means that of all cometoasteroids returning to Sun, only $p = 162/545 \approx 30\%$ has a chance to complete its subsequent turnover around Sun, and 70% will be irretrievably lost.

Hence it is clear that the region of orbits with distances of aphelion $R_{\alpha f} \leq 1.4 \times 10^4$ AU should not only must be deprived of New cometoasteroids, but also will very much depleted by Repeated.

Let's consider this issue in more detail. Let $n_1(T) = n_0$ is number of cometoasteroids with a period (T) are fly out from asteroid belt per unit time, and p—probability of their "survival" for each return to Sun. Then after k turnovers around Sun, number of such bodies in Solar System will be equal to $n_k(T) = n_1(\mathrm{T})p^{k-1}$.

Since we only observe cometoasteroids whose orbital period is $T = t/k$, where t is the time elapsed since their fly out from asteroid belt, we can write

$$n(T) = n(T/k) \cdot p^{\frac{t}{T}-1} \tag{19}$$

where, as before, we will count

$$\mathrm{n(t/k)} = \begin{cases} \mathrm{n}_0 & \mathrm{t}_2 \leq \mathrm{t} \leq \mathrm{t}_1, \\ 0 & \mathrm{t}_2 > \mathrm{t} > \mathrm{t}_1. \end{cases} \tag{20}$$

Passing from the intensity cometoasteroids ejection $n(T)$ to the frequency of their detection, total number of cometoasteroids with periods within $t_1 \leq T \leq t_2$, returning annually to Solar System, we find by summation.

$$N(t_1 \leq T \leq t_2) = n_0(t_2 - t_1)\left\{1 + \sum_{2}^{5}\left(\frac{1}{k} - \frac{1}{k+1}\right) \cdot p^{k-1}\right\} \tag{21}$$

Formula (21) characterizes the frequency of cometoasteroids arrival in the main maximum in Fig. 7 and includes both New, as also part of Repeated cometoasteroids with period $t_1 \leq T \leq \mathrm{t}_2/2$. If we set $p = 0.3$ [5], then according to (21) we get $N = 1.0794\, n_0$. Since generation rate of New cometoasteroids is assumed equal to n_0, the proportion of repeated cometoasteroids in maximum (Fig. 7) is 7.94%. And at this 84.6% of repeated cometoasteroids have committed two, 12.7% − three, 2.3% − four and 0.4% − five complete turnovers around Sun.

8.3 "Tertiary" Long-Period Cometoasteroids

The character of function $N(1/\alpha)$ at the tail of distribution (see Fig. 7) gives we the suggests that some of these cometoasteroids could have formed after Sun left Orion-Cygnus jet stream. The reason for their appearance could be interactions in Solar System of cometoasteroids themselves. And, consequently, such objects in relation to New and Repeated cometoasteroids are, as it were, "Tertiary".

Tertiary cometoasteroids are characterized by a more complex and late originate. Due to this circumstance, in Fig. 7 they form a statistically extremely nonregular long "tail". It is not excluded, of course, that some cometoasteroids of tail are also a repeated cometoasteroids that lost mass in results of close spans near Sun or changed initial trajectory due to perturbations from planets.

Distinctive feature of this objects group is that as their periods decrease, they are less dependent on orbital Sun acceleration, and therefore their trajectories remain predominantly elliptical, and probability of returning to Sun approaches $p = 1$. The time formation of such cometoasteroids is $t << t_1$.

It follows that at least some "Tertiary" cometoasteroids made many revolutions around Sun. Therefore, the number of such cometoasteroids in Solar System should be small, of the same order as Repeat ones.

9 Short-Period Cometoasteroids

Short-period cometoasteroids are objects ejected from asteroid belt at a speed that prevents them flying out far from Sun. This group includes cometoasteroids with periods of $T < 200$ years around Sun. Such periods correspond to semi-major axis of orbits less than 36 AU, which determines localization of these objects in Solar System within the area of existence of known planets.

Short-period cometoasteroids are characterized by direct direction of motion around Sun, gravitate towards the ecliptic plane and, on average, have not very elongated orbits. Compared to long-period ones, they, on average, have lower masses and contain in their composition a larger percentage of solid clastic material of asteroids. Due to the short period T, these cometoasteroids practically "do not feel" the Sun orbital acceleration, therefore, from the moment of Sun exit from Orion-Cygnus jet stream, they were able to complete many, many thousands of revolutions around Sun.

It is obvious that in the epoch of Sun stay in jet stream there were much more such cometoasteroids than now. Therefore, today we see as short-period ones, only those of them that (1) escaped evaporation by solar radiation, (2) did not die in collisions in asteroid belt, (3) did not fall on surface of Sun and planets, and, finally, (4) were not captured by planet-giants and thrown out of Solar System by them.

The first two conditions for the "survival" of short-period cometoasteroids actually come down to the same requirement—perihelion of their orbits exceeding the outer radius of asteroid belt. We justify this conclusion by following simple considerations. Assuming that cometoasteroids reemit the incident solar radiation as absolutely black bodies, then their surface temperature T, depending on heliocentric distance R, in the first approximation must obey the law [57]: $T = 216/R^{1/2}$, where R is determined in AU, and T in degrees Kelvin.

Taking into account that significant part of cometoasteroids matter represented by water ice and frozen gas hydrates [23, 68] the temperature $T \approx 135°$K is critical. At this temperature, water ice under low pressure conditions turns into vapor, bypassing the liquid phase. Therefore, at higher temperatures, ice either does not form or quickly

sublimates. In the process of sublimation, a refractory layer of dust particles is formed on an open surface, which has high thermal insulation properties, which prevents further sublimation [34]. As a result of the formation of such a layer, cometoasteroid ceases to be observed as comet and in its manifestations qualifies as an asteroid.

The critical temperature $T \approx 135°\text{K}$ is reached at distance of $R' = 2.6\text{AU}$ from Sun, that actually coincides with inner boundary of the asteroid belt. From this it is clear that long-term existence of cometoasteroids, which are either directly in the belt, or often cross it, is physically impossible. During long-term orbital motion with perihelion $R_p = \alpha(1 - e) \leq R'$, cometoasteroids turn into swarms of meteoric bodies, which differ little from the same bodies of asteroid belt. Long-term orbital motion of cometoasteroids with perihelion $R_p \leq R'$ is also impossible for another reason. As a result of multiple passages through asteroid belt area, sooner or later they must experience a collision with its bodies and cease to exist as comets.

Thus, the place of survival of short-period cometoasteroids in Solar System, where they can persist as comets for relatively long time, is interplanetary space behind asteroid belt. However, this area cannot be considered completely safe for them, because it is here that cometoasteroids experience random encounters with giant planets.

Calculations by Kazimirchak-Polonskaya [35, 36] show that the behavior of short-period cometoasteroids in interplanetary space can be characterized as their rather long motion along fairly stable elliptical orbits, sometimes disrupted by their approach to planets. As a result of rapprochement, the transition of cometoasteroids from one quasi-stable orbit to another most often occurs. However, with a very close rapprochement, the comet ejection from Solar System and its "capture" by a giant planet are also possible. In the latter case, there is a high probability that cometoasteroid will be thrown away towards Sun at a distance of $R \leq 3 - 4$ AU, and then we will be able to detect it as object belonging to the cometary family of this giant planet.

The indicated character of cometoasteroids motion in interplanetary space is confirmed by the statistics of observations of short-period comets in inner region of Solar System (Fig. 8).

It can be seen from the figure that the distribution function N (k) of short-period cometoasteroids by the number of their appearances at small values of k is universal for all giant planets. In comet families of different giant planets the number of cometoasteroids that have completed $k = 2-3$ revolutions around Sun is related to number objects that have made only one revolution, by the ratio

$$N(k) = N(1) \cdot p^{k-1} \tag{22}$$

where constant p = 0.606.

Formula (22) indicates that transition of cometoasteroids from one quasi-stable orbit to another is a random short-term process, which is probabilistic in nature and clearly differs from cometoasteroids transition mechanism to orbits in the region k > 3.

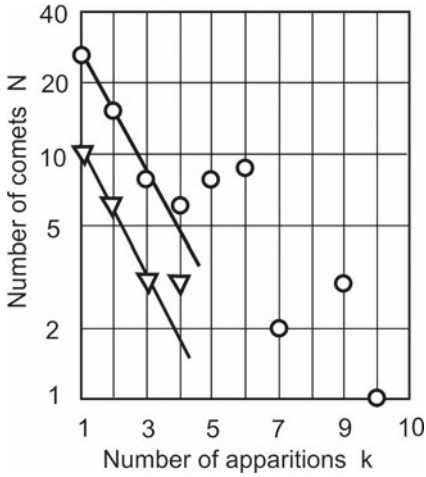


Fig. 8 Distribution of short-period cometoasteroids by the number of detections (k < 10) for Jupiter family (circles) and for families of Saturn, Uranus and Neptune combined (triangles)

The probability that cometoasteroids acquire "transitional" orbits is much higher than translating them on long-term "sustainable" ones. So, for example, the total number of random captures obeying rule (22) in Jupiter family is $N = \sum N(k) = 55$, and in combined Saturn-Uranus-Neptune family $N = 22$. Consequently, in Jupiter only for 37% of cases, the capture carried more or less prolonged character, and in 63% cases it was reduced only to the transfer of cometoasteroids from one unobservable state to another with a short-term entry into the glow zone. For planets farther from Sun, the proportion of such captures is higher and reaches 80%.

To explain the formation mechanism of cometary families and the distribution over them of the number of short-period cometoasteroids, let us turn to the following simplest model. Suppose that at heliocentric distance $R > 3$–4 AU in Solar System to the present time, a certain number of cometoasteroids have survived, whose orbits lie in ecliptic plane, and they revolve around Sun in forward direction.

Consider a cometoasteroid that accidentally flew distance (d) from some planet with mass M_i. Let, due to planet attraction, trajectory of this cometoasteroid deviates by angle χ. Then, in the center-of-mass system coinciding with planet, the value of angle χ will be determined by the relation [59]:

$$\sin\left(\frac{\chi}{2}\right) = \left[\sqrt{1 + \left(\frac{V^2 d}{GM_i}\right)^2}\right]^{-1} \tag{23}$$

where $V = |V_C - V_i|$is cometoasteroid speed relative to the i-planet.

We use expression (23) to estimate magnitude of cometoasteroid capture radius by planets. In this case, under "capture" we will understand such cometoasteroid interaction with planets, when it is thrown in direction of Sun and becomes accessible to detection as a comet. In the first approximation, such capture is accompanied by change in initial direction of cometoasteroid motion through an angle $\chi = \pi/2$. In

accordance with formula (23), this is equivalent to its flew at distance from planet $d_i \approx GM_i/V$. The probability w_i of such flew will be $W_i \approx d_i/(2\pi R_i)$, where R_i is the heliocentric distance of the i-planet. Substituting the expression for d_i into this formula, we obtain

$$W_i \approx \frac{1}{2\pi}\frac{M_i}{M_\odot}\left[\frac{V_i}{V_x}\right]^2 \tag{24}$$

where V_x denotes chaotic component of cometoasteroid speed relative to the average speed $V_i = \sqrt{GM_\odot/R_i}$.

The ratio V_i/V_x in formula (24) is a weak function of heliocentric distance. Therefore, to within a factor of order of unity, probability W_i of cometoasteroid ejection toward Sun is proportional to value of $M_i/M_\odot$. The calculation by formula (24) and actually observed number k_i of short-period comets in families of giant planet are shown in Fig. 9 [5]. The calculated values were found as $k_i = KM_i/\sum M_i$, where $K = 114$ is total number of comets in Jupiter, Saturn, Uranus and Neptune families [23].

Despite the simplified nature of our model, agreement between the results of calculations and observations is quite satisfactory. So, according to our calculations, the ratio of cometoasteroids number in Jupiter and Saturn-Uranus-Neptune families $W_U/(W_S + W_U + W_N) = 2.47$, whereas according to actual data it is 3.22. However, if this ratio is determined not for all comets, but only for the "transitional" group comets, for which, strictly speaking, the formula (24) is applicable, then the indicated ratio will be equal to $55/22 = 2.5$ and practically coincide with our calculation.

The explanation for this fact, of course, should be sought not so much in the theoretical model itself, as in the correctness of initial assumptions laid down in it. There are two of them: (1) the presence of many unobservable cometoasteroids

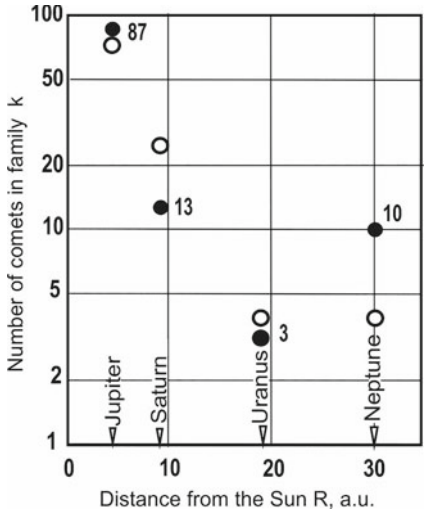


Fig. 9 Distribution of comets number by families of giant planets: black circles—observations [23], open circles—theoretical calculations [5], Numbers—number of observed comets in families of individual giant planets

behind asteroid belt, quite evenly distributed in interplanetary space and strongly gravitating towards the ecliptic plane, and (2) the random nature of cometoasteroids interaction with giant planets.

It also follows from structure of formula (24) that most probable interaction of cometoasteroids with planets occurs at aphelion portion of their trajectories, where cometoasteroids speed in magnitude and direction is as close as possible to planet orbital speed V_i. Therefore, for cometoasteroids of one family, aphelion distances turn out to be approximately equal to orbit radius of planet that captured them. This circumstance leads to grouping of known short-period comets into families of individual giant planets.

Taking the average speed of chaotic motion of cometoasteroids $V_x = 5$ km/s, we get that as a result of capture by giant planets, approximately one of ~10^3–10^4 cometoasteroids that accidentally find themselves near the planet can be thrown towards Sun and discovered as a short-period comet by astronomers. It is clear that such formation mechanism of cometary families is much more effective than transferring long-period cometoasteroids with orbital speed of ≈25 km/s to short-period orbit and even more so capture by giant planets of galactic comets, which moving relative to Sun at a speed of ≈450 km/s.

Interactions with giant planets throw low-velocity cometoasteroids both toward Sun and in other directions. With repeated bombardments of Solar System by galactic comets, this led to movement of such cometoasteroids beyond the outer boundary of Sun's planetary system [6]. As a result, they acquired trajectories that lay outside the orbits of Neptune and Pluto, which provided them with a significantly longer lifetime than at short-period cometoasteroids. Today they are very large objects with diameter of 200–800 km or more, moving in ecliptic plane and showing signs of cometary activity. Their number beyond Neptune orbit is ≈3000.

The average concentration of cometoasteroids (n) in interplanetary space in the ecliptic plane outside asteroid belt can be determined from the relation:

$$\nu = \pi n V_x \sum_{1}^{4} w_i d_i^2 \tag{25}$$

where ν is frequency arrival of short-period cometoasteroids into inner region of Solar System.

Assuming that astronomers detect previously unknown short-period cometoasteroids on average twice a year, using formula (25), we find $n \sim 3 \times 10^{-22}$ км$^{-3}$. For comparison, note that this value is ~10^5–10^8 times less than bodies concentration in asteroid belt, which are "dangerous" for galactic comets.

The total amount of cometoasteroids N in outer region of planetary system we determine by multiplying their concentration n in space volume occupied by these bodies $V = \pi h\ (R_N{}^2 - R_0{}^2)$, where R_N is Neptune orbit radius, h is "thickness" of localization zone of cometoasteroids. Assuming $h \sim 1$ AU, we arrive at value $N \sim 2.4 \times 10^7$. Knowing N we get estimate of lifetime τ short-period cometoasteroids

in interplanetary space. Normalizing N by quantity $\nu \sim 2$ year $^{-1}$, we find $\tau = N/\nu \sim 10^7$ years.

This result means that unlike long-period cometoasteroids, which almost all originated during the last Sun's stay in Orion-Cygnus jet stream some part of short-period cometoasteroids observed today could have been preserved since previous bombardment of Solar System by galactic comets.

10 Main Results and Conclusions

The author's concept of the formation of comets in Solar System, based on ideas of Galactocentric paradigm, is presented [6].

The creation of this concept became possible, firstly, as a result of discovery the phenomenon of jet outflow of gas and dust matter from the core of our and other spiral galaxies. And, secondly, due to the rejection of Kant-Laplace cosmogony hypothesis, which allows for the one-moment formation of Solar System and its planets, as well as their further evolution without taking into account physical processes in Galaxy.

It is shown that the short-period and long-period comets observed today are the collision products of galactic comets of Orion-Cygnus jet stream with bodies of the asteroid belt, captured by Sun attraction into orbits more diverse and distant than at asteroids. Such objects—"cometoasteroids" consist of comets matter of Galaxy origin, which is frozen together with debris and evaporated material of asteroids.

Short-period and long-period cometoasteroids were formed from 5 to 0.7 Ma, and are distinguished differ from each other in the fact that the first, never left limits system of Sun's planets, gravitate towards the ecliptic plane and today are preserved in outer space between giant planets. In the event of an accidental approach to these planets, they are thrown towards Sun. At a heliocentric distance of less than $3 - 5$ AU such cometoasteroids become detectable, and astronomers interpret them as short-period comets of the family of corresponding planet.

In contrast, long-period cometoasteroids have spent almost their entire life far beyond planetary system of Sun. They have very elongated orbits, and therefore many of them today return to Sun only for the first time after birth in asteroid belt. A high concentration of aphelion points of their orbits at a distance of $10^4 - 10^5$ AU from Sun is a direct consequence of these bodies ejection from belt in the time interval $5 - 0.7$ Ma, when Sun was in Orion-Cygnus jet stream.

The new concept not contradictory explains all the main properties of long-period and short-period comets in Solar System, combining the best aspects of known hypotheses of comets origin and at the same time eliminating their shortcomings. It favorably differs from "interstellar" hypotheses in that it does not encounter difficulties in explaining the formation of families of short-period comets, and from "eruptive" hypotheses in that it easily explains the peculiarities of orbits of various groups of long-period comets.

The author's concept also preserves the idea of existence near Sun of cometary bodies cloud. However, unlike the hypotheses of Oort, Kuiper, Hills, Whipple, Tsitsin

and others, this cloud consists not only of comets, but also of gas and dust and is an extremely non-stationary formation. This comet-gas-dust cloud arises during periods of Solar System bombardments by galactic comets and exists after that for ~10^7 years. It currently such cloud contains ~10^7 cometoasteroids of all types.

Thus, the new concept postulates a close connection between cometoasteroids and other small bodies in Solar System, primarily with asteroids and cosmic dust. There is no fundamental difference between cometoaste-roids and bodies in asteroid belt. The differences between these two groups of bodies are determined by parameters of their orbits. Most asteroids move in belt zone, where ice is evaporated by solar radiation, while cometoasteroids located outside this zone retain ice for a longer time.

And, finally, no less important dignity of cometoasteroidic concept is that it is a necessary component part of a more general system of representations—Galactocentric paradigm, which connects phenomena in Solar System and on its planets with physical processes in Galaxy [5, 6]. This paradigm is the worldviewgical basis of the Kuhnian scientific revolution [38] currently taking place in cosmic natural science.

References

1. Artyushkov E.V. (1994) Proc. Academy of Sciences, Vol. 336, No.5, pp. 680–683.
2. Bailey M.E. (1986) Month. Not. Roy. Astron. Soc. Vol. 218, No. 1, P.1–30.
3. Barenbaum A.A. (1990) Kometnyy Tsirkulyar. No. 418, Kiev State University, pp. 11-12.
4. Barenbaum A.A. (1990a) Kometnyy Tsirkulyar. No. 419, pp. 9–10.
5. Barenbaum A.A. (2002) Galaxy, Solar System, Earth. Subordinate processes and evolution (Moscow, PH: GEOS), 393 p.
6. Barenbaum A.A. (2010) Galaxycentric Paradigm in Geology and Astronomy (Moscow, PH: LIBROKOM), 544 p.
7. Barenbaum A.A. (2013) Physical-chemical and petrophysical studies in Earth Sciences: Proc. XIV Intern. Conf. (Moscow: IGEM RAN). pp. 31–42.
8. Barenbaum A.A. (2015) J. Physics: Conf. Ser., Vol. 653, 012073.
9. Barenbaum A.A. (2016) Tectonophysics and Topical Issues of Earth sciences: Conf. Proc. Vol. 2(5) (Moscow: Institute for Earth Physics RAN) pp. 430–438.
10. Barenbaum A.A. (2017) Actual Problems of Aviation and Aerospace Systems: Processes, Models, Experiment. №2(45), Vol. 22, pp. 89–96.
11. Barenbaum A.A. (2018) Engineering Physics, No. 9, pp. 30–47.
12. Barenbaum A.A. (2018a) Proceedings of All-Russian Annual Seminar on Experimental Mineralogy, Petrology and Geochemistry (VESEMPG-2018), Moscow: GEOKHI RAN, pp. 294–298.
13. Barenbaum A.A. (2021) Hubble's Law and the Cosmic Microwave Background in the Absence of the Big Bang. DOI:https://doi.org/10.9734/bpi/rtcps/v4/13528D
14. Barenbaum A.A. (2022) Solution of Problem Questions of Astronomy and Geology Using the Optimized Galactic Model. DOI:https://doi.org/10.1007/978-3-031-25962-3
15. Barenbaum A.A. (2023) On the issue of "True polar wander" Phenomenon and Its Alternative Physical Interpretation Based on Galactic Model. DOI: https://doi.org/10.1007/978-981-99-6575-5
16. Barenbaum A.A., Shpekin M.I. (2019) J. of Physics: Conf. Ser. Vol. 1147, 012057.
17. Barenbaum A.A., Shpekin M.I. (2021) J. of Physics: Conf. Ser. Vol. 1787, 012021.

18. Barenbaum A.A., Titorenko A.S. (2020) Proceedings of All-Russian Annual Seminar on Experimental Mineralogy, Petrology and Geochemistry (VESEMPG-2020). Moscow: GEOKHI RAN, pp. 210–215.
19. Bazilevsky A.T., Ivanov B.A., Florensky K.P. et al. (1983) Impact Craters on the Moon and Planets (Moscow, PH: Nauka), 200 p.
20. Bobrovnikoff N.T. (1929) Lick. Obs. Bull. No. 408, pp.28-38.
21. Brownlee D.E. (1984) Comets and Origin of Life (Moscow, PH: Mir), pp. 69–77.
22. Chepurova V.M., Shershkina S.L. (1989) Kinematika i fizika nebesnykh tel. Vol. 5, No. 4, pp. 82–87.
23. Churyumov K.I. (1980) Comets and their observation (Moscow, PH: Nauka),160 p.
24. Davydov V.D. (1981) Kosmicheskiye issledovaniya, Vol. 19, No. 5, pp. 749–762.
25. Dobrovolskiy O.V. (1966) Comets (Moscow, PH: Nauka), 288 p.
26. Dolgopolova E.N., Marochnik L.S. (1987) Astronomicheskii vestnik. Vol.21, No. 4, pp. 331–334.
27. Drobyshevski E.M. (1978) The Moon and the Planets. Holland. No.18. pp. 145–194.
28. Fesenkov V.G. (1951) Soviet Astronomy A.J. Vol. 28, No. 2, pp. 98–111.
29. Glushneva I.N. (1994) Astronomy reports, Vol. 71, No. 4, pp. 652–656.
30. Guliev A.S., Vsekhsvyatsky S.K. (1981) Soviet Astronomy. Vol. 59, No. 3, pp. 630–635.
31. Guliev A.S. (1992) Kinematics and Physics of Celestial Bodies, Vol. 8, No. 4, pp. 51–60.
32. Hartman W.K. (1978) Solar System, (Moscow, PH: Mir), pp. 167–186.
33. Hills J.G. (1982) Astron. J. Vol. 87, No. 6, pp. 906–910.
34. Ibadinov Kh.I. (1999) Astronomicheskii Vestnik. Vol. 33, No. 4, pp. 363–368.
35. Kazimirchak-Polonskaya E.I. (1978) Astrometriya i nebesnaya mekhanika. Moscow-Leningrad, Is. 7, pp. 340–383.
36. Kazimirchak-Polonskaya E.I. (1978) Astrometriya i nebesnaya mekhanika. Moscow-Leningrad, Is. 7, pp. 384–418.
37. Koval V.I. (1976) Astronomicheskii Tsirkulyar. No. 927, pp. 4–6.
38. Kuhn T.S. (1962) Structure of Scientific Revolutions. University of Chicago Press. (US) John Wiley & Sons. 264 p.
39. Kuiper G.P. (1951) Astrophysics / ed. J.A. Hynek, McCraw-Hill. Co. Inc., pp. 357–424.
40. Lagrange J.L. (1812) Sur l' origine oles cometes. Mem. VII. Paris, pp. 381–395.
41. Laplace P.S. (1796) Exposition du systeme du Monde. Paris. Ed 1–5.
42. Lyttleton R.A. (1948) Month. Not. Roy. Astron. Soc., Vol. 108, No.1, pp. 465–475.
43. Marochnik L.S. (1985) Svidaniye s kometoy (Moscow. PH: Nauka), 208 p.
44. Marov M.Ya. (1994) Astronomicheskii vestnik. Vol. 28, No. 4, pp. 5–85.
45. Marov M.Ya. (1981) Planets of Solar System, (Moscow, PH: Nauka), 256 p.
46. Marsden B.G. (1986) Catalogue of cometary orbits. Smithsonian Astrophys. Obs. Cambridge. MA.
47. McCrea W.N. (1953) La Physique des cometes. Liege. pp. 337–350.
48. Melosh H.J. (1989) Impact Cratering. A Geological Process (New York: Oxford University Press Inc.) 336 p.
49. Mironova E.N. (2015) Dust in the Solar System: Preprint FIAN, No. 10.
50. Napier W.M. (1985) Dynamics Comets. Origin and Evolution: Pros. 83-rd Collog. Rome. 1984. Dordrecht., pp. 31–41.
51. Oort J.H. (1950) Bull. Astron. Inst. Netherlands, Vol. 11, pp. 91–110.
52. Oort J.H. (1951) The observatory. Vol. 71, pp.120-147.
53. Öpike E.J. (1975) Irish Astron. J., Vol. 12, No. 31, pp. 1–48.
54. Oppenheim S. (1924) Probleme der Astronomie. Festschrift fur H. Seeliger. Berlin. pp. 131–143.
55. Orlov S.V. (1936) Soviet Astronomy A.J. Vol. 13, No. 3, pp. 232–238.
56. Orlov S.V. (1960) On the nature of comets, (Moscow, PH: AN SSSR), 191 p.
57. Physics of Space: Little encyclopedia, (1986) (Moscow, PH: Sov. Entsiklopediya), 783 p.
58. Proctor R.A. (1881) The Poetry of Astronomy. London. 156 p.
59. Putilin I.I. (1953) Minor planets, (Moscow, PH: Gostekhteoretizdat), 412 p.

60. Radzievsky V.V. (1995) Astronomicheskii vestnik. Vol. 29, No. 2, pp. 185–190.
61. Radzievsky V.V., Tomanov V.P. (1973) Astronomicheskii Vestnik. Vol. 7, No. 2, pp. 73–82.
62. Ruskol E.L. (1986) Results of Science and Technology. Astronomy, (Moscow, PH: VINITI), Vol. 28, pp. 3–116.
63. Safronov V.S. (1969) Evolution of preplanetary cloud and formation of Earth and planets (Moscow, PH: Nauka), 244 p.
64. Schiaparelli G.V. Siebente Note. 1871. Verlag von Th. von der Nahmer, Stettin, pp. *261*–267.
65. Shestaka I.S. (1995) Astronomicheskii Vestnik. Vol. 29, No. 5, S. 468–471.
66. Schmidt O.Yu. (1945) Doklady AN SSSR. Vol.49, No. 6, P.413–416.
67. Shorma S.D., Khonna M. (1988) Month. Not. Roy. Astron. Soc. Vol. 235, № No.4, pp. 1467–1471.
68. Shulman L.M. (1987) Comet nuclei (Moscow, PH: Nauka), 230 p.
69. Simonenko A.N. (1979) Meteorites – asteroid fragments (Moscow, PH: Nauka), 224 p.
70. Simonenko A.N. (1985) Asteroids, (Moscow, PH: Nauka), 208 p.
71. Svedstrup A. (1884) Astron. Nachr. Vol. 107, pp. 113–126.
72. Tomanov V.P. (1989) Comet cosmogony (Vologda: PH: VGPI), 96 p.
73. Tomanov V.P., Rodin D.A., Shilyaev A.S. Origin and evolution of comets. Vologda State Pedagogic Univer., Vologda, 166 p.
74. Tsitsin F.A. (1999) Zemlya i Vselennaya, No. 1, pp. 60–69.
75. Tsitsin F.A. (2009) Essays on the modern cosmogony of the solar system: Origins. Problems. Horizons. (Dubna: PH: Feniks+), 356 p.
76. Tsitsin F.A., Rastorguev A.S., Chepurova V.M. (1985) Astronomicheskii Tsirkulyar. No. 1408, pp. 5–8.
77. Van Flandern T.C. (1976) Proceedings of the 41st Colloquium of the International Astronomical Union Held in Cambridge, England, 17–19 August pp. 89–90.
78. Van Flandern T.C. (1992) Bul. Amer. Aston. Soc., Vol. 24, No. 3, p. 1062.
79. Van den Bergh S. (1982) J. Roy. Astron. Soc. Can., Vol. 76, No. 5, pp. 303–308.
80. Vitkovsky I.I. (1971) Astronomicheskii vestnik. Vol. 5, No. 2, pp. 82–88.
81. Vsekhsvyatsky S.K. (1967) The nature and origin of comets and meteoric matter (Moscow, PH: Prosveshcheniye), 184 p.
82. Whipple F.L. (1950) Astrophys. J. Vol. 111, No. 2, pp. 375–394.
83. Whipple F.L. (1951) Astrophys. J. Vol. 113, No. 3, pp. 464–474.
84. Whipple F.L. (1964) Astron. J. Vol. 69, p. 563.
85. Yabusbita S., Hasegawa I. (1978) Month. Not. Roy. Astron. Soc. Vol. 185, No. 2, pp. 549–553.

Studies of Mass Transfer of Gas Salt Clathrates. Determination of Mass Transfer Coefficient Value During Construction of Underground Excavation-Capacity in Rock Salt at Agcm

V. P. Malyukov

Abstract The research on peculiarities of mass transfer of rock salt with gas inclusions in crystals under hydrodynamic solution action (HSA)—peculiarities of mass transfer of gas salt clathrates under HSA is considered. Determination of the value of the mass transfer coefficient of rock salt for real conditions of construction of underground excavation-capacity at the Astrakhan gas condensate field by the proposed calculation method was carried out.

Keywords Gas salt clathrates · Real mass transfer coefficient · Gas release from the crystal

Natural gas hydrates (aqueous clathrates) are crystalline compounds formed under certain thermobaric conditions from water and gas. The name clathrates, from the Latin "clathratus", meaning "to cage", was given by Powell in 1948.

The first assumptions about the possibility of the existence of natural gas hydrates were made in 1943 by D. Katz, professor at the University of Michigan, and in 1946 by I.N. Strizhov, professor at the Gubkin Russian State University of Oil and Gas. B.A. Nikitn formulated the position that gas hydrates are solid clathrate solutions of gas molecules in water. In 1961, the discovery of V.G. Vasiliev, Y.F. Makogon, F.A. Trebin, A.A. Trofimuk, N.V. Chersky "The property of natural gases to be in a solid state in the earth's crust" [1] was registered, which announced a new natural source of hydrocarbons—gas hydrates. At the end of 1969, the world's first commercial development of a gas hydrate deposit (GHD) at the Messoyahskoye field was launched in Western Siberia [2].

V. P. Malyukov (✉)
Peoples' Friendship University of Russia, Moscow, Russia
e-mail: v.malyukov@mail.ru

© The Author(s), under exclusive license to Springer Nature Switzerland AG 2024

V. Karev (ed.), *Proceedings of the 9th International Conference on Physical and Mathematical Modelling of Earth and Environmental Processes*, Springer Proceedings in Earth and Environmental Sciences, https://doi.org/10.1007/978-3-031-54589-4_43

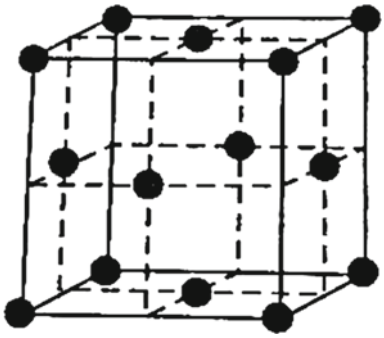


Fig. 1 Face-centered cubic lattice

According to the publications of foreign scientists and specialists the article [3, 4] on the development for the first time in the world of the Nankai gas hydrate field on the shelf off the coast of Japan was published.

Formal provisions of crystallography—the science of external forms of crystals were introduced in the XVIII th century by the French scientist R. Gayoui, O. Brave substantiated the position that only 14 different variants of particles arrangement in space are possible, provided that each of them has absolutely identical surroundings. These variants form 14 types of spatial lattices, which are united in 7 crystal forms called syngonies [5].

The nature of ionic bonding in NaCl crystal was first explained by M. Born. A NaCl crystal has a face-centered cubic lattice (FCC) structure (Fig. 1) in which each cation is surrounded by six anions, and vice versa. M. Born believes that for this reason it would be necessary to consider an ionic crystal as a giant molecule.

When determining the mass transfer coefficient from rock salt core samples [6] at HIOS for the Tuz-Gelu field (Turkey) and Leikovskoye salt stem (Ukraine), gas inclusions in rock salt crystals (gas salt clathrates—GSC) were detected. Following the definition of clathrates gas in rock salt crystals is "caged". During the construction of underground excavations-tanks in rock salt with gas inclusions in crystals there is a detachment of salt plates and gas release when the salt thickness decreases before the inclusion of gas in the crystal in the process of mass transfer, thus increasing the value of the mass transfer coefficient by 30% and accelerating the construction of the underground tank.

For the first time clathrate gas formation in rock salt crystals was detected [7] and the peculiarities of rock salt mass transfer at hydrodynamic impact of solution on GSC were considered.

The paper analyzes a set of geophysical methods for the investigation of the well and underground workings-capacity (UWC) in rock salt under the hydrodynamic impact of the solution (HIOS) at the Astrakhan gas condensate field (AGCF), including sonar of the underground workings-capacity, density gamma-gamma logging (GGL), thermal logging and cavernometry.

Hydrolocation allows obtaining data on the configuration, geometric dimensions and spatial orientation of underground reservoirs (UWC) and determining the bottom

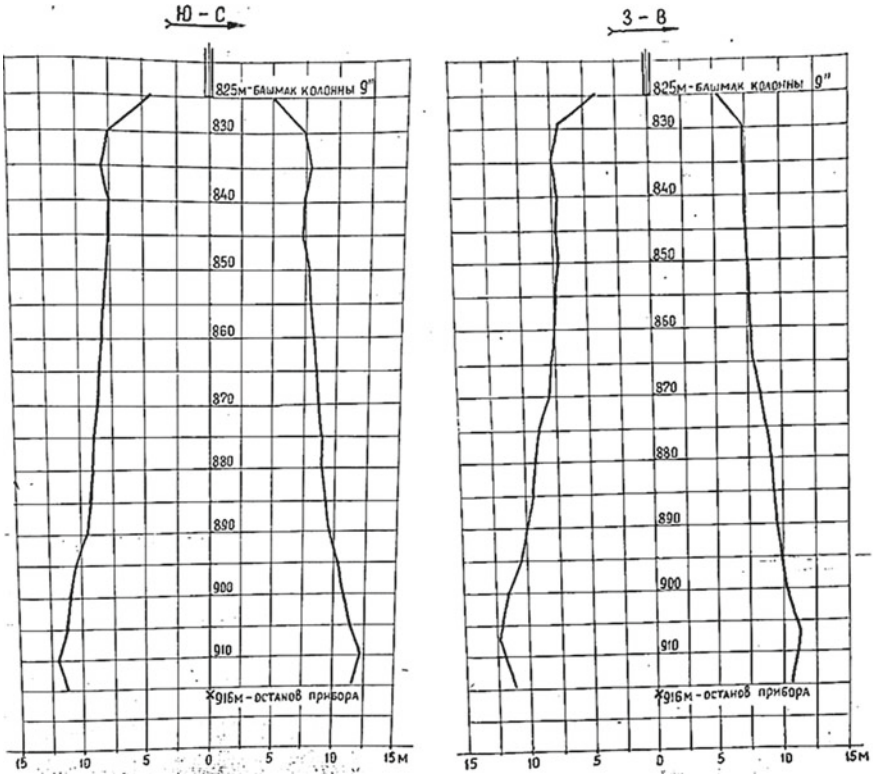


Fig. 2 Vertical section of excavation-capacity 9UP (South–North, West–East)

and vault elevations. Hydrolocation allows to draw horizontal and vertical sections and calculate the actual volume of the excavation.

The insoluble inclusions content in the salt sediments at the reservoir construction site according to the project is 5%. The actual insoluble content ratio was 8.7%.

According to the sonar data, the bottom of the excavation had elevations of 925 m, 922 m and 916 m from the ground surface, respectively, due to the deposition of insoluble inclusions on the bottom of the excavation. Horizontal sections of the excavation after the third stage of mining of the underground excavation-tank have a diameter in the interval 825–916 m from 9.5 m to 24.5 m. The volume of the reservoir by stages was: stage I—6200 m^3, stage II—13,500 m^3 and stage III—27,700 m^3 (Fig. 2).

According to the thermal logging data, the temperature in the developed reservoir averaged 39 $^{\circ}C$, while the reservoir temperature at the depth of excavation was 53 $^{\circ}C$.

The mass transfer coefficient of rock salt at HIOS is the main indicator that predetermines the technological parameters in the process of construction of UWC [8].

Mass transfer coefficients of rock salt equal to 0,917–1,194·10^{-5} m/s at dissolution duration of 45–120 min were obtained as a result of analytical and experimental determination of mass transfer coefficient of rock salt samples with height of 0.14–0.2 m.

Work [9] presents experimental results of mass transfer of rock salt samples measuring 1 × 0.3 × 0.15 m under natural turbulent convection. The mass transfer time of the sample was assumed to be equal to the time at which the mass transfer rate approaching a constant value occurred. These experiments yielded a mass transfer coefficient value of 1,878 m•10^{-5}/s for mass transfer of vertically placed 1 m high samples in aqueous solution at 24 °C.

Taking into account the studies carried out by domestic and foreign experts [10–14], this paper presents a practical calculation of the value of the mass transfer coefficient of rock salt under the hydrodynamic effect of the solution at a real object.

The mass transfer coefficient of rock salt on core samples (K_k) from the UWC interval is determined by the formula.

$$K_\kappa = \frac{\Delta G}{S_{\text{cp}} \bullet t \bullet \left(C_\pi - \overline{C}\right)} \tag{1}$$

where: K_κ—mass transfer coefficient of rock salt determined on core samples in the laboratory unit, m/s; ΔG—weight loss of the sample, g; S_{cp}—average dissolution surface, cm^2;

t—dissolution duration, s; $C_п$—limiting concentration of NaCl in aqueous solution; $\overline{C}$—average solvent concentration, g/cm^3.

It is proposed to determine the value of the mass transfer coefficient of rock salt of the underground excavation contour (K_B) under the hydrodynamic effect of the solution to be carried out according to the dependence:

$$K_B = \frac{\Delta G}{S_p \bullet t \bullet \left(C_\pi - \overline{C}\right)} \tag{2}$$

where: K_B—mass transfer coefficients of rock salt of the excavation contour, determined using actual data, m/s; ΔG—mass loss of rock salt of the excavation contour massif at the corresponding stage of underground reservoir mining, including precipitation of insoluble inclusions, kg; S_p—value of real mass transfer surface, m^2 t—duration of mining of the corresponding stage, s; $C_п$—limiting concentration of NaCl in aqueous solution, kg/m^3; $\overline{C}$—average concentration of solution during mining of the corresponding stage, kg/m^3.

The real mass transfer coefficient of rock salt at the first stage of development of underground reservoir 9UP at AGCF was $K_B = 1,0187 \bullet 10^{-5}$ m/s. Underground reservoir 9UP is located at an insignificant distance (hundreds of meters) from the reservoirs created by a special method (using nuclear charges) and is intended for blowing out the production wells of the AGCF.

References:

1. Vasiliev V.G., Makagon Y.F., Trebin F.A., Trofimuk A.A., Chersky N.V. Property of natural gases to be in a solid state in the Earth's crust // Discoveries of Soviet scientists. Moscow State University, 1988, vol.1. Discovery No. 75 of 25.07.1961, pp. 144–145.
2. Makogon Y.F. Natural gas hydrates: discovery and prospects // Gas Industry.—2001. —№ 5.
3. Malyukov V.P., Tokarev I.S. Studies of the Nankai gas hydrate field development // Bulletin of Peoples' Friendship University of Russia. Series: Engineering Research. 2018. V. 19. № 1. pp. 127—136.
4. Malyukov, V.P. Innovative technologies of gas hydrate fields development: monograph / V.P. Malyukov, K.A.Vorobyev.—Moscow: RUDN 2021 pp. 290.
5. Chang C., Vliet G.C., Sabrian A. "Mass transfer by natural convection at the interface of a salt bed and brine" Journal of Heat Transfer, Proceedings of the American Society of Mechanical Engineers. V 99, № 4, 1977, pp. 105–111.
6. Structure of crystals. M.: Nauka, 1962. - 181 c.
7. Malyukov V.P. Peculiarities of construction of underground excavations-capacities for storage of gas and oil products in rock salt with high gas content Publishing house: Vestnik RUDN. Engineering researches №3,2012. pp. 36 – 48.
8. Malyukov, V.P. Physical processes and technologies of construction of underground excavations-capacities at hydrodynamic impact of solution on rock salt: a monograph / V.P. Malyukov - Moscow: RUDN, 2021. pp. 299.
9. Durie R.W., Jessen F.W. The influence of surface factures in the salt dissolution process - Society of Petroleum Engineers J., 1964, 4, №3, pp 275-281.
10. Malyukov V.P. Experimental studies of mass transfer parameters during dissolution of rock salt from the interval of UGS embedment. Reports of the international conference on underground gas storage. Moscow, 1995. pp. 142–145.
11. Mazurov V.A. Underground gas reservoirs in rock salt deposits. M.: Недра, 1982. 212 с.
12. Smirnov V.I. Construction of underground gas and oil storages. -M.: Gazoil press., 2000. pp. 250.
13. Kazaryan V.A. Underground storage of gases and liquids V.1. Design. Construction. -M. - Izhevsk: Institute of Computer Studies, 2019. pp. 844.
14. Malyukov V.P., Ghazaryan V.A. Investigation of mass transfer during construction of underground storages in rock salt. Science and technology in the gas industry. № 1 (29), 2007. pp. 64–71.

On the Parameterization of Aerodynamic Roughness in Numerical Modeling of the Land Water Bodies

D. Gladskikh, E. Mortikov, and R. Ahtamyanov

Abstract This paper studies the influence of various parameterizations of aerodynamic roughness on the description of the thermal regime and heat flux into the atmosphere from the surface of the lake. Three parameterizations were used: modified Charnock formula, the one based on field measurements at the Gorky Reservoir and the one proposed for the Bolshoy Vilyui lake, Mozhaisk and Gorky reservoirs. The formulas were implemented into the three-dimensional model of thermohydrodynamics of an inland reservoir. The numerical experiments with setup corresponding to the Finnish lake Kuivajärvi in an open water period (May to October 2013) were conducted. The parameterization of roughness significantly affects the description of the temperature regime and heat fluxes, especially at the beginning and end of the open water period.

Keywords Inland water · Aerodynamic roughness · Numerical modeling · Wind–wave interaction

D. Gladskikh (✉)
Division of Geophysical Research, Institute of Applied Physics, Russian Academy of Sciences, Nizhny Novgorod, Russian Federation
e-mail: daria.gladskikh@gmail.com

D. Gladskikh · E. Mortikov · R. Ahtamyanov
Research Computing Center, M.V. Lomonosov Moscow State University, Moscow, Russian Federation

D. Gladskikh · E. Mortikov
Moscow Center for Fundamental and Applied Mathematics, Moscow, Russian Federation

E. Mortikov
Institute of Numerical Mathematics, Russian Academy of Sciences, Moscow, Russian Federation

R. Ahtamyanov
Faculty of Geography, M.V. Lomonosov Moscow State University, Moscow, Russian Federation

Hydrometcenter, Moscow, Russian Federation

© The Author(s), under exclusive license to Springer Nature Switzerland AG 2024

V. Karev (ed.), *Proceedings of the 9th International Conference on Physical and Mathematical Modelling of Earth and Environmental Processes*, Springer Proceedings in Earth and Environmental Sciences, https://doi.org/10.1007/978-3-031-54589-4_44

1 Introduction

Land water bodies are natural systems that are sensitive to climate change and at the same time play a direct role in these changes. Due to this, these water objects require consideration both when developing global climate models and when modeling and forecasting regional climate [1–4]. The most important characteristics of inland water bodies from the point of view of their role in climate formation are the fluxes of momentum, heat, moisture and greenhouse gases. Surface fluxes are typically dependent on turbulent mixing, which is parameterized on the basis on Monin–Obukhov similarity theory (MOST) [5], relating the vertical profile of horizontal wind speed and the physical structure of the ground surface to turbulent mixing (expressed as frictional velocity). The ground-surface structure is largely described through roughness length parameters: z_{0m} (aerodynamic roughness) and z_{0t} (roughness parameter for temperature). In MOST, the roughness parameters determine the interaction between the viscous sublayer and the rough surface [6]. The parameter of aerodynamic roughness z_{0m} can be evaluated based on the structure of the surface, and z_{0t} depend on a larger number of factors, including molecular viscosity and heat conductance [7, 8].

The wind profile law for the neutral stratification is:

$$U(z) = \frac{u_*}{\kappa} \ln \frac{z}{z_{0m}}, \tag{1}$$

where $u_* = \sqrt{\tau/\rho}$ is the friction velocity, τ is the wind stress, ρ is density, and $\kappa = 0.4$ is von Karman constant. Determination of z_{0m} is the subject of active research: in the recent decades, various schemes were developed for its evaluation [9–13]. Using a small dataset and dimensional reasoning, Charnock [14] proposed a parameterization of the roughness length which is still in use today. He argued that the short gravity waves are mainly responsible for the momentum transfer from air to ocean, and therefore the scaling parameters are acceleration of gravity g and the friction velocity $u*$. As a result, the expression for the roughness length over ocean waves becomes

$$z_{0m} = \frac{\alpha u_*^2}{g}. \tag{2}$$

Here α is the so-called Charnock coefficient—dimensionless parameter determined from wind speed data at 10 m. Experimental data [15] show that the values of Charnock coefficient can vary within more than an order of magnitude, depending on the conditions, and depend significantly on the characteristics of surface waves and water body depth [16].

Work [17] presents a modification of expression (2) with an additional term that takes into account the fact that the water surface may not be completely rough:

$$z_{0m} = \frac{\alpha u_*^2}{g} + \frac{\beta \nu}{u_*}. \tag{3}$$

Here β is dimensionless constant dependent on surface charateristics, and ν is kinematic viscosity. The parameter β is related to the Reynolds number Re and in oceanic conditions is taken equal to 0.11, and for lakes it can increase to 0.54 [18]. In weak winds, the water surface can be represented as a smooth solid wall, which is separated from the near-wall flow by a viscous sublayer. The predominance of the viscous mechanism of formation of the roughness parameter is observed at low wind speeds. The given expression (3) is used in the climate model of the Institute of Computational Mathematics of the Russian Academy of Sciences [18] to calculate the aerodynamic roughness parameter of the ocean surface.

Also, in a number of studies [19–21] on the parameterization of z_{0m}, the fact is noted that the roughness is due mainly to surface waves. For example, in [22] it is proposed to consider α in expression (2) as a function of the wave age $\frac{c_p}{u_{10}}$, where c_p is phase velocity of a surface wave at the spectral maximum, and u_{10} is wind speed at a height of 10 m. The wave age is also taken into account in the parameterization z_{0m} in [23] for Donuzlav lake: $z_{0m} = ah_r\left(\frac{c_p}{u_{10}}\right)^{-m}\mu^n$, where h_r is root mean square of wave height, μ is the wave steepness, and the constants *a, m, n* are chosen empirically. In [24], a "wind" parameterization of roughness for the lake surface was proposed, obtained on the basis of field measurements at the Gorky Reservoir:

$$z_{0m} = \exp\left(\ln z - \frac{\kappa}{\sqrt{C_D}}\right), C_D = \frac{0.00124}{u_{10}} + 0.00034 + 0.000049 * u_{10}. \quad (4)$$

Finally, using field data of the characteristics of atmospheric turbulence on the lake. Parameterization was proposed for the Bolshoy Vilyui lake, Mozhaisk and Gorky reservoirs [16]:

$$z_{0m} = \max\left(\alpha\frac{u_*^2}{g}, \beta\frac{\nu}{u_*}\right). \quad (5)$$

It should be noted that lakes represent a special type of surface in terms of interaction with the atmosphere, precisely because of the characteristics of surface roughness. Wave mechanisms differ in inland waters and the ocean, which is associated with differences in wave spread and depth, and it has also been established that the surface of a lake can be aerodynamically rougher than the open ocean [26]. It is also necessary to note the fact that weak wind conditions are more typical for inland water bodies than for the open ocean [25], and in this case, the roughness parameters are influenced by surface tension inhomogeneities and small-scale capillary waves [16, 26, 27].

This paper studies the influence of various parameterizations of aerodynamic roughness on the description of the thermal regime and heat flux into the atmosphere from the surface of the lake. For comparison, parameterizations given by formulas (3, 4, 5) were used. The comparison was made within a 3D lake model for a configuration corresponding to the open water period (May–October) for Lake Kuivajärvi (Southern Finland).

2 Methods and Approaches

To study the influence of various aerodynamic roughness parameterizations on the description of climatically significant characteristics of inland reservoirs, we used a three-dimensional model of thermohydrodynamics and biogeochemistry of an inland reservoir developed by the authors of this work based on a single hydrodynamic code that combines DNS, LES, and RANS approaches for calculating geophysical turbulent currents at high spatial and temporal resolution [28–31]. The numerical model includes equations of hydrodynamics in a stratified turbulent rotating layer of liquid in the shallow water approximation, as well as equations for heat and salinity transfer taking into account horizontal and vertical diffusion [32]. The equations of the model are as follows:

$$\frac{\partial u}{\partial t} = -A(u) + D_H(u, \chi_m) + D_z(u, K_m + \nu) - \mathbf{g}\frac{\partial \eta}{\partial x} - \frac{\mathbf{g}}{\rho_0}\frac{\partial}{\partial x}\int_z^\eta \rho dz' + f_{Cor} v,$$

$$\frac{\partial v}{\partial t} = -A(v) + D_H(v, \chi_m) + D_z(v, K_m + \nu) - \mathbf{g}\frac{\partial \eta}{\partial y} - \frac{\mathbf{g}}{\rho_0}\frac{\partial}{\partial y}\int_z^\eta \rho dz' - f_{Cor} u,$$

$$\nabla \bullet \mathbf{u} = \frac{\partial u}{\partial x} + \frac{\partial v}{\partial y} + \frac{\partial w}{\partial z} = 0,$$

$$\frac{\partial T}{\partial t} = -A(T) + D_H(v, \chi_h) + D_z(T, K_h + \lambda),$$

$$\frac{\partial S}{\partial t} = -A(S) + D_H(S, \chi_h) + D_z(S, K_h + \lambda),$$

$$\rho = \rho(T, s),$$

$$\frac{\partial \eta}{\partial t} = w. \tag{6}$$

Here $\mathbf{u} = (u, v, w)$ is the velocity vector, η is the free surface deviation from the equilibrium state, f_{Cor} is the Coriolis parameter, T is the temperature, S is the salinity, ρ is the density, $K_m(\chi_m)$ and $K_h(\chi_h)$ are coefficients of vertical (horizontal) turbulent viscosity and temperature conductivity, respectively, ν and λ are coefficients of molecular viscosity and temperature conductivity, respectively, and z is the vertical coordinate going from the water bottom $z = -H(x, y)$ to the surface. In addition, $A(q)$ is the advection operator, and $D_H(q, \lambda)$ and $D_z(q, K)$ are the operators defining horizontal and vertical diffusion with the coefficients λ and K, respectively.

Regarding the roughness parameterization, the default model configuration uses the Charnock parameterization modified by Kazakov and Lykosov [17], given above in the formula (3). The constants are assumed to be equal to the values $\alpha = 0.0144$, $\beta = 0.111$. The value of z_{0m} is calculated iteratively, i.e. recalculated at each step as the values of the incoming parameters are updated.

Additionally, configurations based on parameterizations, developed taking into account the characteristics of lakes as a specific type of underlying surface, were i into the model. One of the parameterizations was built on the basis of measurement data at the Gorky Reservoir [24] and is given in formula (4). Another one has been introduced in the form of formula (5), where the values of the constants (in accordance with the original work [16]) are as follows: $\alpha = 0.03$, $\beta = 0.135$.

To estimate the effect of aerodynamic roughness parameterization on the description of temperature and heat flux, the numerical experiments with setup corresponding to the Finnish lake Kuivajärvi were conducted. This small body of water is located in Southern Finland. The results of measurements made in 2013 [33–374] were used as atmospheric forcing data during the entire calculation time (components of wind speed, fluxes of short-wave radiation, sensible and latent heat), as well as a set of the initial conditions (for example, initial density vertical distribution). In the measurement area, the water depth was 11 m. A period from May to October of 2013 was chosen.

3 Results of Numerical Experiments

Using the formulation described in the previous section, a series of numerical experiments were carried out with various parameterizations of aerodynamic roughness. First, time series of vertical temperature distribution were compared. The results are shown in Figs. 1, 2, 3.

The figures show that the results obtained using formula (4) differ significantly from those obtained using (3) and (5). Next, the ratio of heat fluxes obtained using (3) and (4) was analyzed. The results are shown in Fig. 4.

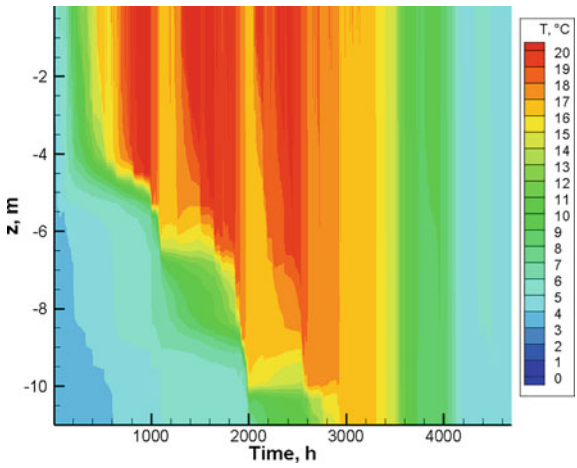


Fig. 1 Time–depth distribution of temperature in Kuivajärvi Lake, obtained with modified Charnock formula (3)

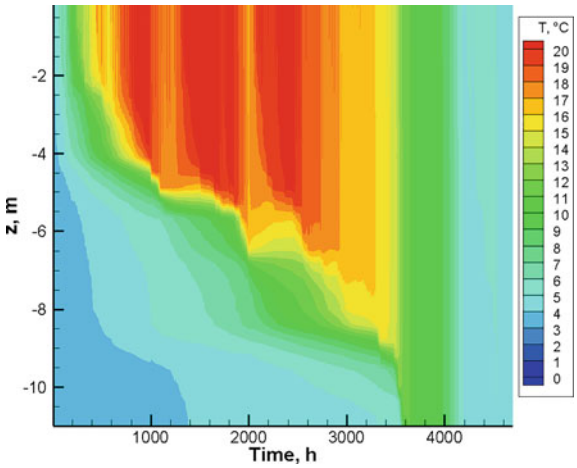


Fig. 2 Time–depth distribution of temperature in Kuivajärvi Lake, obtained with «wind» parameterizarion based on the field data from Gorky Reservoir (4)

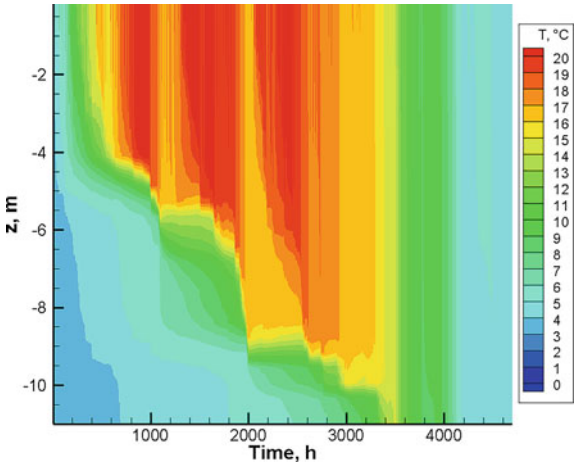


Fig. 3 Time–depth distribution of temperature in Kuivajärvi Lake, obtained with parameterizarion based on the field data from the Bolshoy Vilyui lake, Mozhaisk and Gorky reservoirs (5)

The figure shows that the greatest differences in fluxes are observed at the beginning of the open water season, when intense heating of the surface of the water body occurs, advancing the heating of the air, and at the end of the season, when convective circulations arise near the surface of the reservoir due to the fact that the surface of lake cool down more slowly than surface air.

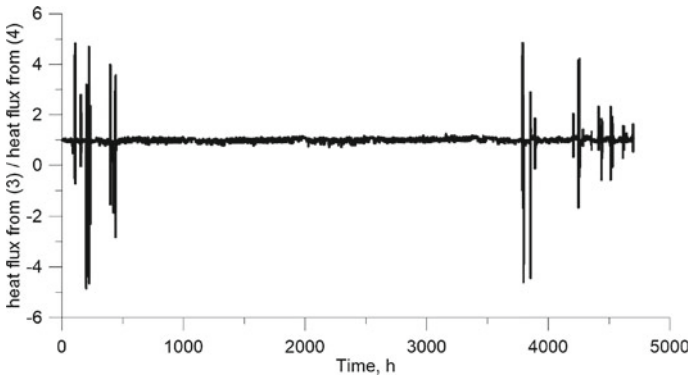


Fig. 4 The ratio of heat fluxes obtained using (3) and (4) for Kuivajärvi Lake

4 Conclusions

This paper studies the influence of various parameterizations of aerodynamic roughness on the description of the thermal regime and heat flux into the atmosphere from the surface of the lake. Inland water objects represent a special type of surface in terms of interaction with the atmosphere, precisely because of the characteristics of surface roughness. Three parameterizations of aerodynamic roughness were used: modified Charnock formula (3), the one based on field measurements at the Gorky Reservoir (4) and the one proposed for the Bolshoy Vilyui lake, Mozhaisk and Gorky reservoirs (5). The formulas were implemented into the three-dimensional model of thermohydrodynamics of an inland reservoir. The numerical experiments with setup corresponding to the Finnish lake Kuivajärvi in an open water period (May to October 2013) were conducted.

The figures show that the results obtained using formula (4) differ significantly from those obtained using (3) and (5). Also, this result is in better agreement with the data of field measurements of lake temperature given in [35]. However, due to the fact that the parameterization is based on empirical considerations, it may not give the same agreement for water bodies under significantly different conditions (surrounding terrain, wind speeds, width of the reservoir, etc.). "Charnock-based" parameterizations connect two asymptotics characteristic of wind regimes. At the same time, as we see, the differences between the results according to formula (3) and according to formula (5) differ slightly, since in formula (5) a separate option is highlighted for regimes of weak winds $z_{0m} = \beta \frac{\nu}{u_*}$, which, apparently, were practically not observed in the period under study.

In general, the parameterization of roughness significantly affects the description of the temperature regime and heat fluxes, especially at the beginning and end of the open water period.

Acknowledgements The work was supported by FSTP project "Study of processes in the boundary layers of the atmosphere, ocean and terrestrial waters and their parameterization in Earth system

models" within the project "Improvement of the global world-level Earth system model for research purposes and scenarios forecasting of climate change"

References

1. Krinner G. Impact of lakes and wetlands on boreal climate // J. Geophys. Res.: Atmospheres. 2003. V. 108. №. D16.
2. Thiery W. et al. The impact of the African Great Lakes on the regional climate //Journal of Climate. 2015. V. 28, N 10. P. 4061–4085.
3. Tranvik L.J., Downing J.A., Cotner J.B., Loiselle S.A., Striegl R.G., Ballatore T.J., Dillon P., Knoll L.B., Kutser T. et al. Lakes and reservoirs as regulators of carbon cycling and climate // Limnology and Oceanography. 2009. V. 54. P. 2298–2314.
4. Wang J. et al. Impacts of Lake Surface Temperature on the Summer Climate Over the Great Lakes Region // J. Geophys. Res.: Atmospheres. 2022. V. 127, N 11. e2021JD036231.
5. Monin, A.S.; Yaglom, A.M., Statisticheskaya gidromekhanika. Chast' 1; (Statistical Hydromechanics. Part 1), Golitsyn, G.S., Ed.; Nauka: Moscow, Russia,1965.
6. Garrat, t J.R., The Atmospheric Boundary Layer, Cambridge UK: Cambridge Univ. Press, 1997.
7. Stepanenko, V.M., Repina, I.A., Fedosov, V.E., Zilitinkevich, S.S., and Lykosov, V.N., An overview of parameterezations of heat transfer over moss-covered surfaces in the Earth system models, Izv., Atmos. Ocean. Phys., 2020, vol. 56, no. 2, pp. 101–111.
8. Varentsov, A.I., Zilitinkevich, S.S., Stepanenko, V.M., Tyuryakov, S.A., and Alekseychik, P.K., Thermal roughness of the fen surface, Boundary-Layer Meteorol., 2022, pp. 1−15.
9. Taylor, P. K., and M. J. Yelland, 2001: The Dependence of Sea Surface Roughness on the Height and Steepness of the Waves. J. Phys. Oceanogr., 31, 572–590.
10. Fairall, C.W., Bradley, E.F., Rogers, D.P., Edson, J.B., and Young, G.S., Bulk parameterization of air-sea fluxes for tropical ocean-global atmosphere coupledocean atmosphere response experiment, J. Geophys. Res.: Oceans, 1996, vol. 101 (C2), pp. 3747–3764.
11. Liu, W.T., Katsaros, K.B., and Businger, J.A., Bulk parameterization of air-sea exchange of heat and water vapor including the molecular constraints at the interface, J. Atmos. Sci., 1979, vol. 36, pp. 1722–1735.
12. Smith, S., Coefficients for sea surface wind stress, heat flux, and wind profiles as a function of wind speed and temperature, J. Geophys. Res-Oceans, 1988, vol. 93 (C12), pp. 15467–15472.
13. Vickers, D. and Mahrt, L., Sea-surface roughness lengths in the midlatitude coastal zone, Quarterly J. Royal Meteorol. Soc., 2010, vol. 136, no. 649, pp. 1089– 1093.
14. Charnock, H. Wind stress on water surface, Quarterly J. Royal Meteorol. Soc., 1955, vol. 81, pp. 639−640.
15. Artamonov, A.Yu., Buchnev, I.A., Repina, I.A., Skirta, A.Yu., Smirniov, A.S., and Tolpygin, L.I., Turbulent fluxes of heat and momentum and statistical characteristics of turbulence in the near-surface air in nearshore and deep-water zones of the Black Sea, Oceanology, 2005, vol. 45. Suppl. 1, pp. S27–S38.
16. Repina, I.A., Artamonov, A.Y., Kapustin, I.A. et al. Roughness Parameter of Shallow Water Bodies. Water Resour 50, 748–758 (2023).
17. Kazakov A.L., Lykosov V.N. On the parameterization of the interaction of the atmosphere with the underlying surface in the numerical modeling of atmospheric processes. Proceedings of ZapSibNII, 1982, p. 3–20.
18. Mathematical modeling of the Earth system / Volodin E.M.,. Galin V.Ya., Gritsun A.S. and others. Ed. Yakovlev N.G. — M.: MAX. Press, 2016. - 328 p.
19. Donelan, M. A., The dependence of the aerodynamic drag coefficient on wave parameters, paper presented at 1st International Conference on Meteorology and Air-Sea Interaction of the Coastal Zone, Am. Meteorol. Soc., Boston, Mass., 1982.

20. Donelan, M. A., F. W. Dobson, S. D. Smith, and R. J. Anderson, On the dependence of sea surface roughness on wave development, J. Phys. Oceanogr., 23, 2143–2149, 1993.
21. Kitaigorodskii, S. A., The Physics of Air-Sea Interaction (in Russian), Gidrometeorologich-eskoe Izdatel'stvo, Leningrad, 1970. (Isr. Program for Sci. Transl., Jerusalem, 1973).
22. Kitaigorodskii, S. A., and Y. A. Volkov, On the roughness parameter of the sea surface and the calculation of momentum flux in the near-water layer of the atmosphere, Izv. Acad. Sci. USSR Atmos. Oceanic Phys., Engl. Transl., 1, 973–988, 1965.
23. V.V. Fomin, V.A. Ivanov Unified numerical model of currents, waves and sediment transport of Lake Donuzlav // Marine Hydrophysical Journal. 2006. No. 2.
24. Kuznetsova A. M., Baydakov G. A., Papko V. V., Kandaurov A. A., Vdovin M. I., Sergeev D. A., Troitskaya Yu. I. Adjusting of wind input source term in WAVEWATCH III model for the middle-sized water body on the basis of the field experiment // Hindawi Publishing Corporation, Advances in Meteorology, vol. 2016, article ID 574602, 13 pp., doi:https://doi.org/10.1155/2016/8539127
25. Wüest, A. and Lorke, A., Small scale hydrodynamics in lakes, Annu. Rev. Fluid. Mech., 2003, vol. 35, pp. 373– 412.
26. Wu, J., The sea surface is aerodynamically rough even under light winds, Bound.-Layer Meteorol., 1994, vol. 69, nos. 1–2, pp. 149–158.
27. Mahrt, L., Vickers, D., Sun, J., Jensen, N.O., Jørgensen, H., Pardyjak, E., and Fernando, H., Determination of the surface drag coefficient, Bound. Layer Meteorol., 2000, vol. 99, no. 2, pp. 249–276.
28. Mortikov E. V., Glazunov A. V., Lykosov V. N. Numerical study of plane Couette flow: turbulence statistics and the structure of pressure–strain correlations // Russian Journal of Numerical Analysis and Mathematical Modelling. 2019. V. 34, N 2. P. 119–132.
29. Mortikov E.V. Numerical simulation of the motion of an ice keel in stratified flow // Izv. Atmos. Ocean. Phys. 2016. V. 52. P. 108–115.
30. Kadantsev E., Mortikov E., Zilitinkevich S. The resistance law for stably stratified atmospheric planetary boundary layers // Q.J.R. Met. Soc. 2021. V. 147, N 737. P. 2233–2243**
31. Gladskikh, D.S.; Stepanenko, V.M.; Mortikov, E.V. The effect of the horizontal dimensions of inland water bodies on the thickness of the upper mixed layer. Water Resour. 2021, 48, 226–234.
32. Gladskikh D., Ostrovsky L., Troitskaya Y, Soustova I, Mortikov E. Turbulent Transport in a Stratified Shear Flow // J. Mar. Sci. Eng. 2023. V. 11(1). P. 136.
33. Heiskanen, J.J.; Mammarella, I.; Ojala, A.; Stepanenko, V.; Erkkilä, K.M.; Miettinen, H.; Sandström, H.; Eugster, W.; Leppäranta, M.; Järvinen, H.; et al. Effects of water clarity on lake stratification and lake-atmosphere heat exchange. J. Geophys. Res. Atmos. 2015, 120, 7412–7428.
34. Mammarella, I.; Nordbo, A.; Rannik, Ü.; Haapanala, S.; Levula, J.; Laakso, H.; Ojala, A.; Peltola, O.; Heiskanen, J.; Pumpanen, J.; Vesala, T. Carbon dioxide and energy fluxes over a small boreal lake in Southern Finland. J. Geophys. Res. Biogeosciences 2015, 120, 1296–1314.
35. Stepanenko, V.; Mammarella, I.; Ojala, A.; Miettinen, H.; Lykosov, V.; Vesala, T. LAKE 2.0: A model for temperature, methane, carbon dioxide and oxygen dynamics in lakes. Geosci. Model Dev. 2016, 9, 1977–2006.

Waves at the Ice-Liquid Border from Localized Sources

V. V. Bulatov

Abstract In this paper we consider an infinite flow of homogeneous fluid that satisfies Euler's equations. A thin ice cover is modeled geometrically by a linear elastic plate, under which at a certain depth there is a localized wave disturbances source. In this paper, we apply an analysis that uses explicit asymptotic and analytical expressions for the Fourier integral forms of solutions describing wave structures at the interface between ice and infinitely deep liquid. Using a modification of the asymptotic saddle-point method, we study the far wave fields phase structures depending on various parameters of wave generation.

Keywords Ice · Deep liquid · Interface elevation · Dispersion relations · Far wave fields · Amplitude-phase structure · Asymptotic · Localized source

Numerous laboratory experiments, as well as field observations in the World Ocean, show that ice cover under natural conditions behaves like a thin elastic plate that floats on the surface of a liquid. In this regard, in this work we will consider the problem within the framework of an elastic plate model, regarding which, without limiting any physical generality, the following assumptions can be made: (i) there is a certain surface whose tensile or compression strains are given and do not change during bending; (ii) each elementary volume of the elastic layer of ice, which is orthogonal to the neutral surface in an undeformed state, remains straight and orthogonal to this surface after deformation; (iii) the deformation satisfies physical Hooke's law. A detailed overview of theoretical and experimental works on this topic is contained in [1–22].

Then the mathematical description of the problem is formulated as follows [3, 17, 20, 23, 24].

V. V. Bulatov (✉)
Ishlinsky Institute for Problems in Mechanics RAS, Vernadskogo Ave. 101-1, 119526 Moscow, Russia
e-mail: internalwave@mail.ru

© The Author(s), under exclusive license to Springer Nature Switzerland AG 2024

V. Karev (ed.), *Proceedings of the 9th International Conference on Physical and Mathematical Modelling of Earth and Environmental Processes*, Springer Proceedings in Earth and Environmental Sciences, https://doi.org/10.1007/978-3-031-54589-4_45

$$(\frac{\partial^2}{\partial\xi^2}+\frac{\partial^2}{\partial y^2}+\frac{\partial^2}{z^2})\Phi = q\delta(\xi)\delta(y)\delta(z-z_0)$$

$$\frac{D\Phi}{Dt}+g\lambda-C\left(\frac{\partial^2}{\partial\xi^2}+\frac{\partial^2}{\partial y^2}\right)\lambda+B\left(\frac{\partial^2}{\partial\xi^2}+\frac{\partial^2}{\partial y^2}\right)^2\lambda$$
$$+A\frac{D^2\lambda}{Dt^2}=0, z=0; \frac{D\lambda}{Dt}=\frac{\partial\Phi}{\partial z}, z=0; \Phi\to 0, z\to-\infty$$

$$\nabla\Phi=(u,v,w), \frac{D}{Dt}=V\frac{\partial}{\partial\xi}, A=\frac{l\rho_1}{\rho_0}, B=\frac{El^3}{12\rho_0(1-\nu_0^2)}, C=\frac{\sigma l}{\rho_0},$$

where flow velocity V is directed along the ξ axis, l—thickness ice cover, $q(q=const)$—mass power source, ρ_0—water density, ρ_1—ice density, Φ—velocity potential, $\lambda(\xi, y)$—elevation, $(V+u, v, w)$—velocity vector of an arbitrary fluid particle, z_0—source depth, g—gravity acceleration, E—ice Young's modulus, ν_0—Poisson's ratio, σ—initial voltage, $\rho_0=1025\frac{\text{kg}}{m^3}$, $\rho_1=0.9\rho_0$, $\text{E}=3\cdot10^5\ \frac{\text{H}}{\text{m}^2}$, $\nu_0=0.3$, $\sigma=10^5\ \frac{\text{H}}{\text{m}^2}$. Using the Fourier method, the solution to this problem can be obtained in the form

$$\lambda(\xi,y)=\frac{-iqV}{4\pi^2}\int_{-\infty}^{\infty}\int_{-\infty}^{\infty}\frac{\mu\exp(kz_0)}{(Ak+1)B(\mu,\nu)}\exp(-i\mu\xi-i\nu y)d\nu d\mu \qquad (1)$$

$$B(\mu,\nu)=\omega^2(k)-\mu^2V^2, k^2=\mu^2+\nu^2, \omega^2(k)=(k\left(g+Ck^2+Bk^4\right))(Ak+1)^{-1}$$

Integral (1) can be calculated both numerically and asymptotically [25–28]. In Figs. 1 and 2 we demonstrate the results of calculations of dispersion relations. Numerical analysis shows, that the dispersion curves can be convex everywhere (Fig. 1), $\mu''(\nu)>0$ for any values of the argument ν, then the wave structure excited by the source is a system of only longitudinal waves, and have two inflection points $\nu_{1,2}^*$ $(\mu''\left(\nu_{1,2}^*\right)=0)$ symmetrical with respect to the axis $\nu=0$ (Fig. 2). The presence of inflection points leads to the appearance of additional wave fronts and the generation of a transverse waves system.

Figures 3 and 4 show the results of calculations of dispersion surfaces at fixed values of ice thickness l (Fig. 3) and flow velocities V (Fig. 4). Horizontal cuts at fixed values of V (Fig. 3) and l (Fig. 4) make it possible to study the nature of the variability of dispersion dependencies by varying these parameters.

Figures 5, 6 and 7 show the results of calculations of phase structure for $q=5\frac{\text{m}^3}{\text{s}}$, $z_0=-2\text{m}$.

It's obvious that in the general case, the formulation of the problem of a nonlocal source also includes specifying certain boundary conditions on its surface. Even under the assumption that the fluid is ideal and the flow around the body is potential, finding its velocity field is a very complex mathematical task. It is obvious that the problem of flow around a system of point hydrodynamic features (sources,

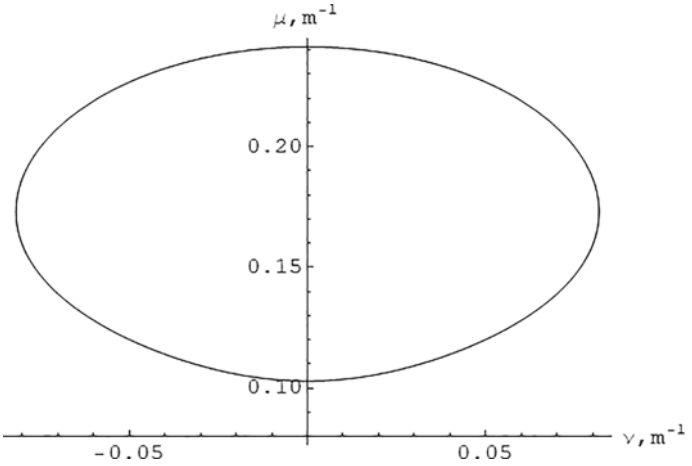


Fig. 1 Dispersion curve $\mu(\nu)$ at $l = 0.25\text{m}$, $V = 10\frac{\text{m}}{\text{s}}$

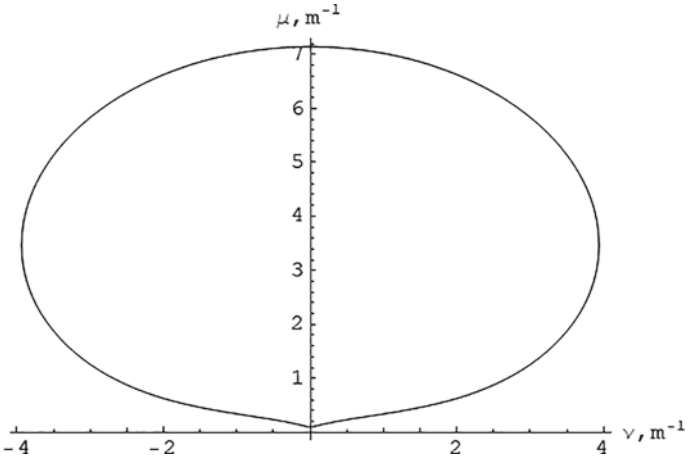


Fig. 2 Dispersion curve $\mu(\nu)$ at $l = 0.01\text{m}$, $V = 10\frac{\text{m}}{\text{s}}$

sinks, dipoles, etc.) is much easier to solve, since in this case there is no need to satisfy predetermined boundary conditions. On the current lines (surfaces) that arise when flowing around such a model system, the conditions of non-flow are satisfied automatically. This circumstance is used when solving problems of flow around bodies or impermeable boundaries modeled by specially selected systems of hydrodynamic features. With this approach to problems of flow around bodies, current lines (surfaces) are identified with impenetrable boundaries.

For example, when a stationary flow around a point source with a uniform boundless flow, a current line (surface) appears, representing the boundary of a blunted

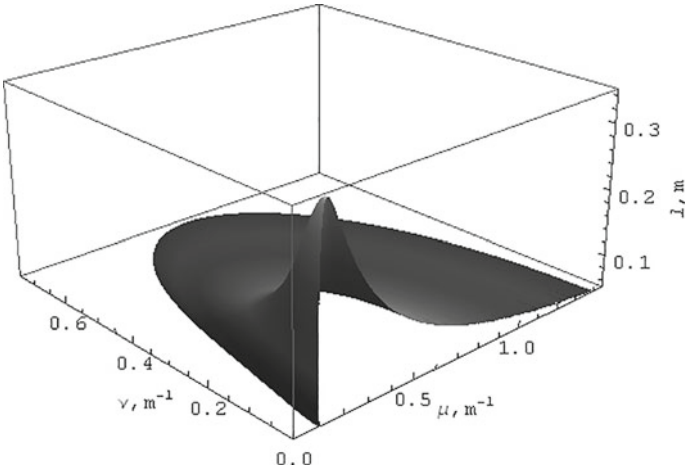


Fig. 3 Dependences $l = l(\mu, \nu)$ at $V = 10\frac{\text{m}}{\text{s}}$

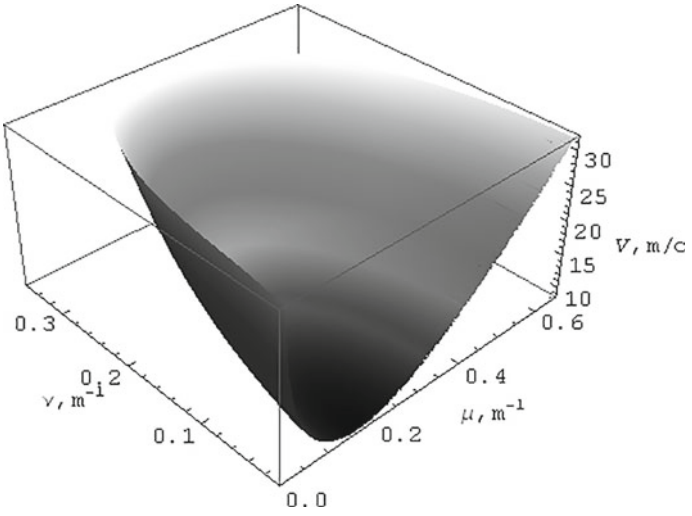


Fig. 4 Dependences $V = V(\mu, \nu)$ at $l = 0.25\text{m}$

body of infinite length, therefore, the flow around a point source is hydrodynamically equivalent to the flow around such a body. In another case, the source and sink, located one behind the other along the flow, model an ovoid-shaped body. A dipole in an unbounded plane flow generates a streamline enclosing it in the shape of a circle, so it models the transverse flow around a cylinder. In the three-dimensional case, a boundless spatial flow flowing around a dipole is equivalent to flowing around a ball.

The listed hydrodynamic features are often used when solving model problems in which accurate reproduction of the shape of a body placed in a flow is not of decisive

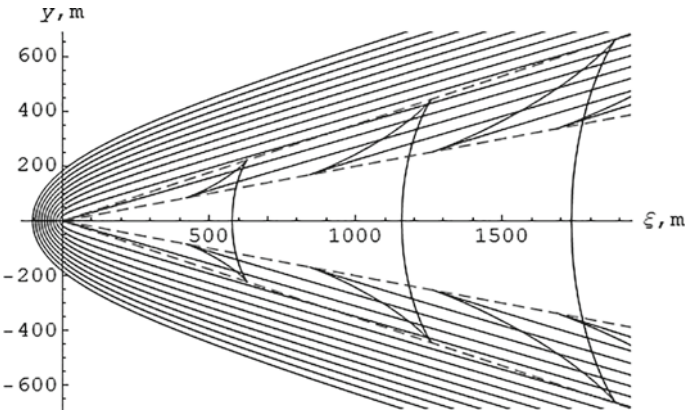


Fig. 5 Phase structure: $l = 0.25\text{m}$, $V = 30\frac{\text{m}}{\text{s}}$

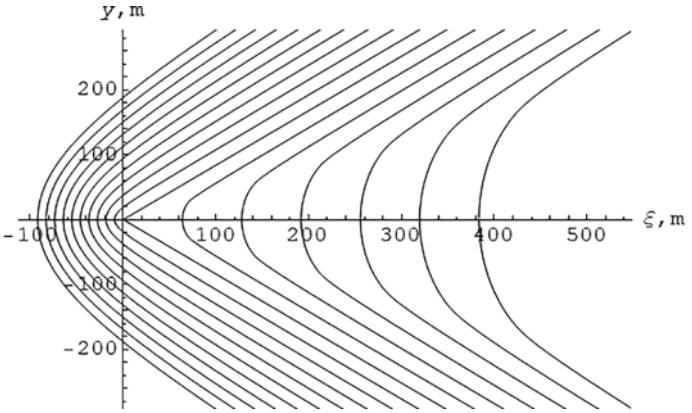


Fig. 6 Phase structure: $l = 0.1\text{m}$, $V = 10\frac{\text{m}}{\text{s}}$

importance. Such a method, to a large extent, can relate to the considered problem of generating wave disturbances at the boundary of ice and liquid, since replacing the body with a certain set of hydrodynamic features significantly simplifies the solution of this problem. Naturally, the question arises of how the presence of interfaces between ice and liquid affects the pattern of streamlines that arise when flowing around given hydrodynamic features. For example, can a dipole in a plane flow with a free boundary be considered a good model of a circular cylinder? From physical considerations, it is obvious that the deeper the dipole is, the more accurately it models the cylinder, and as the dipole approaches the ice-liquid interface, the streamline enclosing it will be distorted more and more and less accurately correspond to the contour of the cross section of the circular cylinder. Therefore, in particular, when

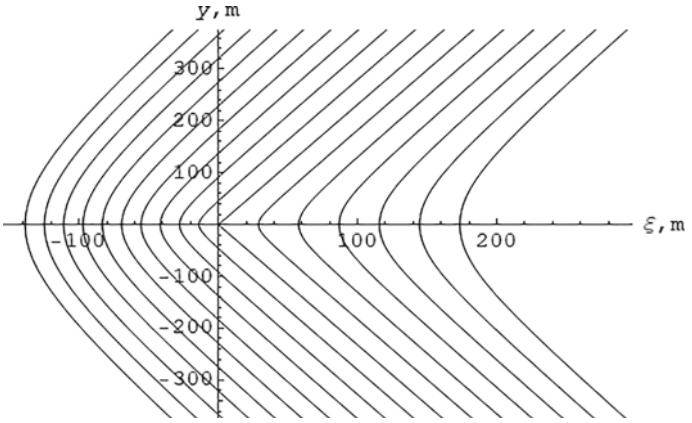


Fig. 7 Phase structure: $l = 0.1\text{m}$, $V = 7\frac{\text{m}}{\text{s}}$

considering flows of finite thickness under an ice cover, it is necessary to know which body can be modeled by the selected system of hydrodynamic features.

Acknowledgements The work is carried out with financial support from the RSF project 23-21-00194.

References

1. Lightill J (1978) Waves in fluids. Cambridge University Press, Cambridge
2. Whitham GB (1974) Linear and nonlinear waves. Willey-Interscience Publication, New York
3. Squire VA, Hosking RJ, Kerr AD, Langhorne PJ (2012) Moving loads on ice plates. Dordrecht: Springer Science & Business Media
4. Miropol'skii YuZ, Shishkina OV (2001) Dynamics of internal gravity waves in the ocean. Kluwer Academic Publishers, Boston
5. Vlasenko V, Stashchuk N, Hutter K (2005) Baroclinic tides. N.Y.: Cambridge University Press
6. Mei CC, Stiassnie M, Yue DK-P (2017) Theory and applications of ocean surface waves. Advanced series of ocean engineering. V. 42. World Scientific Publishing
7. Morozov TG (2018) Oceanic internal tides. Observations, analysis and modeling. Springer, Berlin
8. Velarde MG, Tarakanov RYu, Marchenko AV (Eds.) (2018) The ocean in motion. Springer Oceanography. Springer International Publishing AG, Berlin
9. Ozsoy E (2021) Geophysical fluid dynamics II. Stratified rotating fluid dynamics of the atmosphere-ocean. Springer Textbook in Earth Sciences. Geography and Environment. Springer Nature. Switzerland AG Cham
10. Bulatov VV, Vladimirov YuV (2012) Wave dynamics of stratified mediums. Nauka, Moscow
11. Bulatov VV, Vladimirov YuV (2019) A general approach to ocean wave dynamics research: modelling, asymptotics, measurements. OntoPrint Publishers, Moscow
12. Marchenko AV, Morozov EG, Muzylev SV, Shestov AS (2010) Interaction of short internal waves with the ice cover in an Arctic fjord // Oceanology 50(1): 18–27

13. Marchenko A, Morozov E, Muzylev S (2013) Measurements of sea ice flexural stiffness by pressure characteristics of flexural-gravity waves // Ann Glaciology 54: 51–60
14. Morozov EG, Zuev OA, Zamshin VV, Krechik VA, Ostroumova SA, Frey DI (2022) Observations of icebergs in Antarctic cruises of the R/V "Akademik Mstislav Keldysh" // Russian J Earth Sciences 2: 1–5.
15. Morozov EG, Marchenko AV, Filchuk KV, Kowalik Z, Marchenko NA, Ryzhov IV (2019). Sea ice evolution and internal wave generation due to a tidal jet in a frozen sea. // Appl. Ocean Research 87: 179–191
16. Il'ichev AT (2021) Effective wavelength of envelope waves on the water surface beneath an ice sheet: small amplitudes and moderate depths // Theor Math Physics 208 (3): 1182–1200
17. Savin AS, Savin AA (2015)Three-dimensional problem of disturbing an ice cover by a dipole moving in fluid // Fluid Dynamics 50 (5): 613–620.
18. Sturova IV (2021) Motion of a load over an ice sheet with nonuniform compression // Fluid Dynamics 56 (4): 503–512
19. Dinvay E, Kalisch H, Parau EI (2019) Fully dispersive models for moving loads on ice sheets // J. Fluid Mechanics 876:122–149
20. Sturova IV (2015) Radiation of waves by a cylinder submerged in water with ice floe or polynya // J. Fluid Mechanics 784 : 373–395
21. Pogorelova AV, Zemlyak VL, Kozin VM (2019) Moving of a submarine under an ice cover in fluid of finite depth // J Hydrodynamics 31(3): 562-569
22. Khabakhpasheva T, Shishmarev K, Korobkin A (2019) Large-time response of ice cover to a load moving along a frozen channel // Appl Ocean Research 86: 154–165
23. Bulatov VV, Vladimirov IYu, Morozov EG (2023) Far field of the perturbations in the interface between deep ocean and ice cover due to localized sources // Doklady Earth Sciences 512(2): 1050–1054
24. Bulatov VV, Vladimirovb IYu (2023) Far fields at the interface between an infinitely deep ocean and ice generated by a localized source // Izvestiya, Atmospheric and Oceanic Physics 59(3): 296–300
25. Bulatov VV, Vladimirov YuV, Vladimirov IYu (2019) Far fields of internal gravity waves from a source moving in the ocean with an arbitrary buoyancy frequency distribution // Russian J Earth Sci 19: ES5003
26. Svirkunov PN, Kalashnik MV (2014) Phase patterns of dispersive waves from moving localized sources // Phys.-Usp. 57 (1): 80–91
27. Gnevyshev V, Badulin S (2020) Wave patterns of gravity–capillary waves from moving localized sources // Fluids 5: 219
28. Borovikov VA (1994) Uniform stationary phase method. London: IEE electromagnetic waves. Series 40.

Persistent Organic Pollutants in Waterfowls of the Southern Primorye



Maksim A. Belanov, Maksim M. Donets, Mikhail Yu. Shchelkanov, Dmitry V. Pankratov, and Vasiliy Yu. Tsygankov

Abstract The work presents the levels of organochlorine pesticides (OCPs) and polychlorinated biphenyls (PCBs) in the organs of common teal, falcated duck and rhinoceros auklet from the Southern Primorye. Priority toxic chemicals for birds of different ecological groups have been identified. Birds making long migrations to south and southeast Asia are characterized by higher levels of OCP accumulation. Birds migrating to more urbanized areas are more exposed to PCBs. It is necessary to expand monitoring studies using non-invasive technologies to preserve bird populations and obtain more reliable information about current environmental pollution.

Keywords OCPs · PCBs · POPs · Waterfowls · Rhinoceros auklet · Common teal · Falcated duck

M. A. Belanov · M. M. Donets · V. Yu. Tsygankov (✉)
School of Advanced Engineering Studies, Institute of Biotechnology, Bioengineering and Food Systems, Far Eastern Federal University, Ajax 10, Russky Island, Vladivostok 690922, Russia
e-mail: tsig_90@mail.ru

Institute of the World Ocean (School), Far Eastern Federal University, Ajax 10, Russky Island, Vladivostok 690922, Russia

M. Yu. Shchelkanov
School of Medicine, Far Eastern Federal University, Ajax 10, Russky Island, Vladivostok 690922, Russia

M. Yu. Shchelkanov · D. V. Pankratov
Research Institute of Epidemiology and Microbiology Named After G.P. Somov Rospotrebnadzor, Vladivostok 690087, Russia

M. Yu. Shchelkanov
Federal Scientific Center of the East Asia Terrestrial Biodiversity Far Eastern Branch of the Russian Academy of Sciences, Vladivostok 690022, Russia

National Scientific Center of Marine Biology Far Eastern Branch, Russian Academy of Sciences, Vladivostok 690041, Russia

© The Author(s), under exclusive license to Springer Nature Switzerland AG 2024

V. Karev (ed.), *Proceedings of the 9th International Conference on Physical and Mathematical Modelling of Earth and Environmental Processes*, Springer Proceedings in Earth and Environmental Sciences, https://doi.org/10.1007/978-3-031-54589-4_47

1 Introduction

Persistent organic pollutants (POPs) are among the most dangerous toxicants in the world. Despite a more than twenty-year ban on the production and use of these compounds, POP residues are still found in a wide variety of environmental objects—fish, mollusks, birds, etc. [1, 2, 4–6].

The best-known representatives of POPs are organochlorine pesticides and polychlorinated biphenyls, the peak of whose use occurred in the second half of the 20th century, due to their insecticidal properties and widespread industrial use. Due to their chemical persistence and lipophilicity these compounds can accumulate in the food chains and to concentrate in their upper levels (biomagnification) due to their chemical persistence and lipophilicity. It is estimated that more than 90% of exposure to POPs is caused by consumption of contaminated food [14, 16].

Due to their physicochemical properties—lipophilicity and hydrophobicity—POPs are concentrated mainly in living organisms or bottom sediments rich with organic matter and are less likely to be detected in water [13]. Thus, to assess POPs contamination of the environment, it is possible to use indicator organisms. Moreover, the trophic level of the organism largely determines the scale of the reflected pollution (local or global levels).

Birds are among the most exposed groups of organisms to POPs and allow to monitor both local (non-migratory species) and global POPs pollution (migratory species) [15]. Due to good bioindication properties, some countries even form special monitoring programs using birds [8].

The aquatic ecosystems of Southern Primorye—are unique ecological complex in its biodiversity (especially in avifauna). The diversity of habitat conditions, as well as a wide range of different territories (wetlands, forests, coastal-island areas) allows many species to choose optimal conditions for nesting or use it as a "hub" on the route of seasonal migrations [9].

Birds generally occupy high trophic levels and are sensitive to environmental changes. Migratory birds, due to seasonal migrations and prolonged stay in the upper layers of the atmosphere, are subject to additional exposure to POPs and, thus, may reflect the air pollution of a particular area. The purpose of the work is to study the accumulation of OCPs and PCBs in the organs of the waterfowls of Southern Primorye and to determine the priority group of pollutants affecting birds in this region.

2 Materials and Methods

Three bird species were studied: common teal (*Anas crecca*, N = 4), falcated duck (*Mareca falcata*, N = 6) and rhinoceros auklet (*Cerorhinca monocerata*, N = 5). Samples were collected in 2021 in Southern Primorye (in April and May—common teal and falcated duck, in June—rhinoceros auklet). Licensed scientific shooting of

biological material of ducks was carried out in the Khankaisky district of Primorsky Krai. Rhinoceros auklet specimens were studied as part of the investigation of the mass mortality in July 2021 in Boisman Bay (Sea of Japan) [7]. Birds were dissected, liver, pectoral muscles and feathers were separated from the body. The samples were frozen (–20 °C) and delivered to the laboratory.

Before starting work, the feathers were washed with deionized water, dried and ground to 1 mm particles [3]. The muscles and liver were homogenized. POPs were extracted from homogenates and feather material with a hexane: acetone mixture, followed by destruction of coextractive components (lipids) with concentrated sulfuric acid and separated into polar (OCP) and nonpolar (PCB) phases on chromatographic columns using activated sorbent Florisil© 100–200 mesh. The main determination of the mass content of organochlorine xenobiotics in the biomaterial was carried out using a Shimadzu GCMS-QP2010 Ultra gas chromatography-mass spectrometer. In the studied samples, the following were determined among OCPs and PCBs: p,p′-DDT, o,p′-DDT, p,p′-DDD, o,p′-DDD, p,p′-DDE, o,p′-DDE, α-, β-, γ-, δ-HCH and PCB congeners 28, 52, 101, 118, 153, 138, 180 [5, 6].

Statistical analysis of the results was carried out using IBM SPSS Statistics software for Windows 10. The reliability of the data was assessed using a two-sided Kruskal–Wallis test with a significance level of $p \leq 0.05$.

3 Results and Discussion

POPs were found in all the samples analysed. OCP levels were significantly ($p \leq 0.05$) higher than PCBs in common teal feathers, muscles and liver, as well as falcated duck feathers (Fig. 1). In rhinoceros auklet organs, PCB concentrations were significantly ($p \leq 0.05$) higher than OCPs in all organs studied. The total content of OCPs in the feathers of the studied birds was found in the range from 87 to 1603, in the muscles—from 6 to 528, in the liver—from 3 to 1689 ng/g lipid weight (lw). PCB levels ranged from 11–4386, 9–15,044, to 12–18,103 ng/g lw.

In common teal feathers, OCPs were found in the range from 510 to 1603 ng/g lw. DDT and its metabolites were dominant among OCPs, varied within 8–1242 ng/g lw. At the same time, this group of compounds was detected fragmentarily—o,p'-DDE—1 sample (8 ng/g lw), p,p'-DDE—2 samples (410 and 436 ng/g lw), o,p '-DDD—1 sample (896 ng/g lw) and o,p'-DDT—1 sample (346 ng/g lw). HCH isomers were found in all studied feather samples in the range of 46–361 ng/g lw. The highest concentrations were detected for δ- and β-HCH—tracers of lindane (γ-HCH) breakdown in the environment. In muscles, OCPs were found fragmentarily (β-HCH—2.8, o,p'-DDD—240 ng/g lipids). In the liver, mainly tracers of HCH degradation were determined—δ- and β-HCH in the concentration range of 2.9–24.0 ng/g lw. Among DDTs, p,p'-DDE (20 ng/g lw) and o,p'-DDD (1035 ng/g lw) were detected.

PCBs in all organs were represented only by PCB 28 (with the exception of feathers, where PCB 118 and PCB 153 were recorded only once). PCB 28

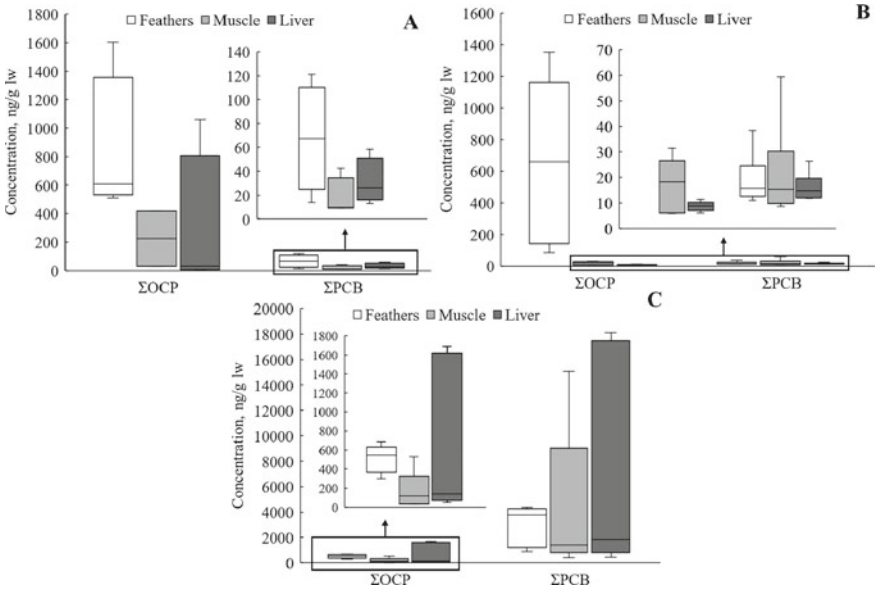


Fig. 1 Total concentrations of OCPs and PCBs in the studied organs of birds: **a** common teal, **b** falcated duck, **c** rhinoceros auklet

concentrations varied: in feathers—14–121, in muscles—9–42, in liver—13–58 ng/g lw.

In falcated duck, the range of OCPs in feathers varied from 40 to 1,098 ng/g lw. Among pesticides, the highest concentrations were found in DDT and its metabolites—from 131 to 969 ng/g lw. This group of compounds was represented exclusively by DDE. All studied isomers were found among HCH. The total concentrations of this group of compounds varied from 24 to 155 ng/g lw. As in the case of common teal, the δ- and β-isomers of HCH were dominant. In muscles and liver, only HCH isomers were found among OCPs with concentration ranges of 6–22 and 6–11, respectively. Tracers of long-term circulation of pollutants in the ecosystem also dominated here.

Among PCBs, in all studied samples of falcated duck, only PCB 28 was found with a concentration range: in feathers—11–38, in muscles—9–59, in liver—12–26 ng/g of lw.

Concentrations of OCPs in rhinoceros auklet feathers were the lowest among other birds and varied from 298 to 685 ng/g lw. Unlike common teal and falcated duck, most of pesticides here were HCH isomers with a concentration range from 85 to 417 ng/g lw. Among the studied isomers, only α-HCH was not detected, and among all forms of the compound, β-HCH was dominant. DDT and its metabolites in feathers were exclusively DDE, with concentrations ranging from 129 to 343 ng/g lw.

In rhinoceros auklet muscles, OCPs were found in the range of 30–528 ng/g lw. Unlike feathers, the majority of OCPs here were DDT and its metabolites with total

concentrations ranging from 15 to 384 ng/g lw. In addition to DDE isomers, o,p'-DDD, p,p'-DDD, and o,p'-DDT were found sporadically. Among the HCH isomers in muscles, γ- and β-isomers were found with a predominance of the more stable β-form. Total concentrations of HCH ranged from 11 to 144 ng/g lw.

In the liver, OCPs varied from 48 to 1,689 ng/g lw. The most of pesticides were DDT and its metabolites, ranging from 25 to 1,318 ng/g lw. This group of pollutants, along with tracers of long-term pollution (DDE and DDD), was also characterized by detection of the original DDT, indicating a recent input of this pesticide in the environment. Among HCH, as in the case of muscles, γ- and β-forms of the compound with a predominance of the more stable β-isomer were found in the liver. Total levels of HCH varied from 12 to 371 ng/g lw.

In contrast to common teal and falcated duck, PCBs in the organs of rhinoceros auklet were characterized by an extremely wide composition with a predominance of highly chlorinated congeners—118, 153, 138 and 180. The total levels of this group of pollutants varied in feathers—from 898 to 4,386, in muscles—from 419 to 15,044, in the liver—from 444 to 18,103 ng/g lw.

Bioaccumulation of POPs in birds is primarily associated with migratory behavior, feeding habits and life strategy of a particular bird species. The study identifies two groups of birds: those associated with wetlands ("freshwater" common teal, falcated duck) and coastal ("marine"—rhinoceros auklet). The first group of birds is similar in trophic status and ecological characteristics and feeds mainly on invertebrates, fish fry, some plant species and their seeds. Both species winter in southern or south-eastern Asia, and therefore cross a number of countries (Fig. 2) [9]. One such area is China, where widespread environmental contamination with POPs is known. This includes a seriously polluted atmosphere, where, for example, levels of DDT are considered to be among the highest in the world [11].

Passing through a contaminated area during migration, common teal and falcated duck are exposed to "atmospheric" POPs during flight, as well as biomagnification during feeding. As a result, a "fingerprint" of pollutants characterizing a specific area is formed on their feathers, as well as in their internal organs. In the case of common teal and falcated duck, we found higher levels of OCPs compared to PCBs, indicating a predominance of agricultural pollution compared to industrial one. Our data are also consistent with the results of [10], who identified DDT and HCH as the main pollutants for migratory birds in China.

Unlike common teal and falcated duck, rhinoceros auklet feeds mainly on anchovy, herring, Ammodytes and other hydrobionts, that is, organisms of a higher trophic level, due to which the levels of absorbed pollutants are higher [9]. When searching for food, rhinoceros auklet dives into the water column, which may increase the concentrations of POPs in its feathers. The concentrations of OCPs in the feathers of this species were the lowest compared to the other birds, the concentrations in the muscles were comparable, and in the liver they were maximum. At the same time, tens of times higher concentrations of PCBs were found here compared to the other birds (Fig. 1). Most likely, the maximum levels of PCBs in rhinoceros auklet are associated with the migratory characteristics of this species. Rhinoceros auklet winters in Japan, a highly urbanized country where there are higher concentrations

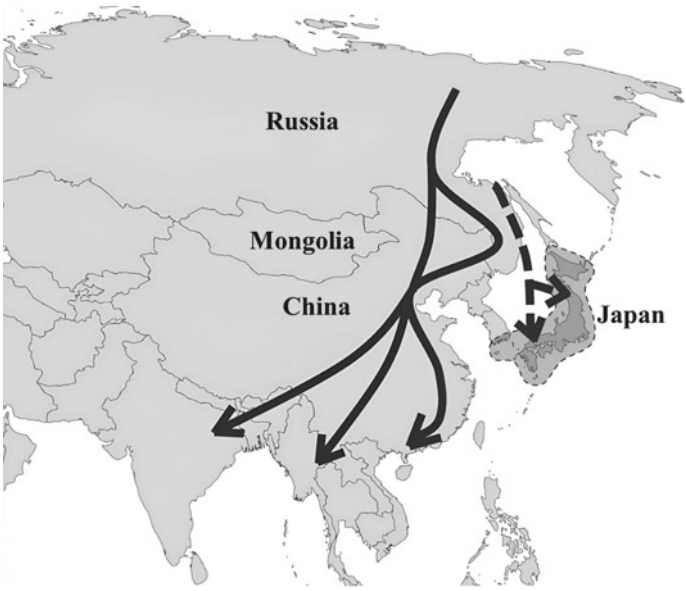


Fig. 2 Example of migration routes of the studied birds: solid line—common teal and falcated duck, broken line—rhinoceros auklet

of industrial chemicals compared to pesticides [12]. Kunisue et al. [10] also confirm the priority of PCBs as a toxicant of migratory birds in Japan and adjacent islands.

Unlike freshwater birds, where only PCB 28 was found, the widest congener composition of PCBs was recorded in the organs of rhinoceros auklet, with a predominance of highly chlorinated congeners—118, 153, 138 and 180 (Fig. 3). Such high levels and a wide composition may be associated with pollution of the rhinoceros auklet habitat (Sea of Japan), as well as with higher trophic food, because of which biomagnification processes are more intensive. In our previous work [5], we also noted a fold increase in PCB concentrations in flounder in the Sea of Japan compared to other regions and suggested the impact of active shipping on local ecosystems.

To estimate the time of OCPs circulation in the ecosystem, the ratio of the concentrations of DDT and its degradation product DDE and DDD and the ratio of the concentrations of the α- and β-forms to the γ-isomer of HCH are used. In the samples we studied, the predominance of β-HCCH and DDE was noted, which indicates a long-term presence of organic toxicants in the ecosystem and the absence of fresh entry in the areas where birds arrive.

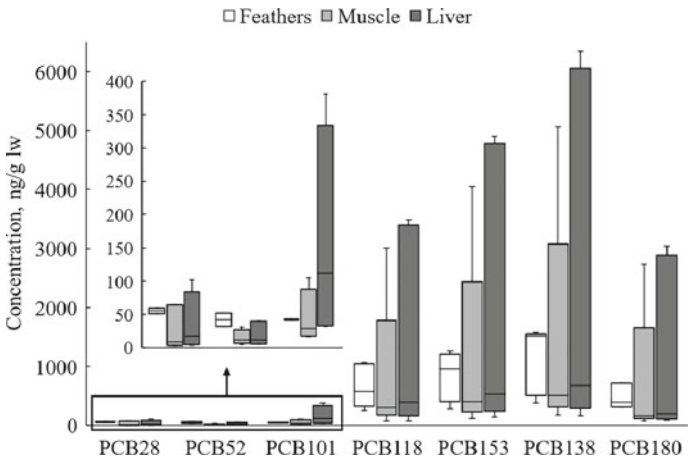


Fig. 3 Concentrations of individual PCB congeners in rhinoceros auklet organs

4 Conclusion

Thus, the ecological characteristics of different bird species determine the "fingerprints" of POPs in their organs. For birds migrating to areas of southern or south-eastern Asia, the priority group of pollutants are OCPs; for those migrating to more urbanized regions with active navigation—PCBs. The most indicative organs for monitoring of POPs are bird feathers, which accumulate pollutants from the atmosphere.

5 Financial Support.

This work was supported by the Ministry of Science and Higher Education of the Russian Federation (project number FZNS-2023-0011).

References

1. Belanov MA, Shchelkanov MYu, Pankratov DV, et al (2023) Persistent Organic Pollutants in Rhinoceros Auklet (Cerorhinca Monocerata) from the Sea of Japan. In: Chaplina T (ed) Complex Investigation of the World Ocean (CIWO-2023). Springer Nature Switzerland, Cham, pp 363–369. https://doi.org/10.1007/978-3-031-47851-2_43
2. Borovkova AD, Tsygankov VYu (2023) Chlorinated Organic Compounds in Mytilidae Mollusks from Nakhodka Bay (the Sea of Japan). In: Chaplina T (ed) Complex Investigation of the World Ocean (CIWO-2023). Springer Nature Switzerland, Cham, pp 381–386. https://doi.org/10.1007/978-3-031-47851-2_46

3. Dauwe T, Jaspers V, Covaci A, et al (2005) Feathers as a nondestructive biomonitor for persistent organic pollutants. Environ Toxicol Chem 24:442–449. https://doi.org/10.1897/03-596.1
4. Donets MM, Tsygankov VYu (2023) Organochlorine Compounds in the Amur (Heilong) River Basin (2000–2020): A Review. JoX 13:439–462. https://doi.org/10.3390/jox13030028
5. Donets MM, Tsygankov VYu, Boyarova MD, et al (2021) Flounders as indicators of environmental contamination by persistent organic pollutants and health risk. Marine Pollution Bulletin 164:111977. https://doi.org/10.1016/j.marpolbul.2021.111977
6. Donets MM, Tsygankov VYu, Gumovskiy AN, et al (2021) Organochlorine pesticides (OCPs) and polychlorinated biphenyls (PCBs) in Pacific salmon from the Kamchatka Peninsula and Sakhalin Island, Northwest Pacific. Marine Pollution Bulletin 169:112498. https://doi.org/10.1016/j.marpolbul.2021.112498
7. Dunaeva MN, Pankratov DV, Surovyi AL, et al (2022) Reconstruction of epizootic outbreak provoked the largescale death of Rhinoceros auklet on the coast of the Japan Sea in the Southern part of Primorsky Krai (July, 2021). Acta biomedica scientifica 7:90–97. https://doi.org/10.29413/ABS.2022-7.3.10
8. García-Fernández AJ (2014) Ecotoxicology, Avian. In: Encyclopedia of Toxicology. Elsevier, pp 289–294
9. Glushchenko YuN, Nechaev VA, Redkin YaA (2016) Birds of Primorsky Krai: a brief faunal overview. KMK Scientific Press Ltd., Moscow
10. Kunisue T, Watanabe M, Subramanian A, et al (2003) Accumulation features of persistent organochlorines in resident and migratory birds from Asia. Environmental Pollution 125:157–172. https://doi.org/10.1016/S0269-7491(03)00074-5
11. Lin T, Hu Z, Zhang G, et al (2009) Levels and Mass Burden of DDTs in Sediments from Fishing Harbors: The Importance of DDT-Containing Antifouling Paint to the Coastal Environment of China. Environ Sci Technol 43:8033–8038. https://doi.org/10.1021/es901827b
12. Monirith I, Ueno D, Takahashi S, et al (2003) Asia-Pacific mussel watch: monitoring contamination of persistent organochlorine compounds in coastal waters of Asian countries. Marine Pollution Bulletin 46:281–300. https://doi.org/10.1016/S0025-326X(02)00400-9
13. Mortimer M, Reichelt-Brushett A (2023) Persistent Organic Pollutants (POPs). In: Reichelt-Brushett A (ed) Marine Pollution – Monitoring, Management and Mitigation. Springer Nature Switzerland, Cham, pp 185–205
14. Polder A, Savinova TN, Tkachev A, et al (2010) Levels and patterns of Persistent Organic Pollutants (POPS) in selected food items from Northwest Russia (1998–2002) and implications for dietary exposure. Science of The Total Environment 408:5352–5361. https://doi.org/10.1016/j.scitotenv.2010.07.036
15. Tanabe S, Subramanian A (2006) Bioindicators of POPs: monitoring in developing countries. Kyoto University Press; Trans Pacific Press, Kyoto, Japan: Melbourne
16. Tsygankov VYu (2019) Organochlorine pesticides in marine ecosystems of the Far Eastern Seas of Russia (2000–2017). Water Research 161:43–53. https://doi.org/10.1016/j.watres.2019.05.103

Calculation of Multifrequency Impulse Effects on Inhomogeneous Media Using the Lebesgue Integral



I. Kh. Enikeev

Abstract In the work on the basis of the Lebesgue integral, a method for accounting for the averaged effect of a multifrequency pulse signal on the state of the medium with fixed initial data is proposed. A multiparameter analysis of the solution of the corresponding system of inhomogeneous differential equations has been carried out, and the asymptotics of the resulting solution with an unlimited increase in the parameters of the medium has been investigated. It is shown that at certain values of the determining parameters in the system, a resonance occurs, in which the amplitude and frequency of oscillations Systems depend on only one parameter and do not depend on the value of other parameters.

Keywords System of differential equations · Lebesgue integral · Multiparameter functionals · Impulse action

Many real physical processes (oscillations of a mathematical pendulum, wave propagation in elastic media, optimization of automatic control systems, etc.) lead to the need to consider nonlinear systems of differential equations. In practice, however, in a number of cases (small oscillations, small perturbations, etc.) nonlinearity can be neglected or the process under consideration or its part can be described by a linearized (reduced to a linear form) inhomogeneous system of differential equations. In this case, a linear system of differential equations is a simplified mathematical model for describing real physical processes in which internal characteristics are continuous and interconnected by linear functional dependencies.

So, let's consider an inhomogeneous system of linear differential equations with constant coefficients:

$$\frac{dy_i}{dx} = \sum_{k=1}^{n} a_{ik} y_k(x) + f_i(x), i = 1, 2, \ldots, n \tag{1}$$

I. Kh. Enikeev (✉)
Moscow Polytechnic University, Bolshaya Semyonovskaya Str., 38, 107023 Moscow, Russia
e-mail: enickeev.ix@yandex.ru

© The Author(s), under exclusive license to Springer Nature Switzerland AG 2024

V. Karev (ed.), *Proceedings of the 9th International Conference on Physical and Mathematical Modelling of Earth and Environmental Processes*, Springer Proceedings in Earth and Environmental Sciences, https://doi.org/10.1007/978-3-031-54589-4_48

where y_i are the desired functions, a_{ik} are the known constant coefficients, $f_i(x)$ are the functions describing the external influence on the system.

System (1) can be reduced to a single nth-order differential equation with constant coefficients:

$$y^n(x) + a_1 y^{(n-1)}(x) + \cdots + a_{n-1} y^1(x) + a_n y(x) = F(x) \tag{2}$$

In general, the right-hand side (2) may depend not only on the parameters that determine the nature of the external influence on the state of the environment, but also on the state of the system itself, for example: in a system at rest, the amplitude and frequency of the external influence are carried out with one intensity, in a system in an excited state, the intensity is different, and so on.In addition, many problems consider the impulse effect on a given system (laser and nanotechnology, etc.), as well as use spaces of random events and distribution functions that depend on random variables (probability theory, mathematical statistics, quantum mechanics, etc.), which leads to the need to consider on the right side of Eq. (2) functions that have an infinite number of break points. In this case, Obtaining integral characteristics that determine the external impact on the system under consideration is possible only with the use of the Lebesgue integral [1]. The construction of an algorithm for calculating the corresponding integrals is essential for solving this type of problem. This algorithm depends to a large extent on the properties of the set on which the functions in question are defined [2]. One of these algorithms is proposed in this paper. The essence of this algorithm is to use multiparameter functionals to compute the Lebesgue integral. Let the right side (2) look like this:

$$F(x) = f(x, \lambda, \alpha, \beta) = \begin{cases} 1, x \in E_1; \\ \frac{1-\cos\alpha x+\sin\alpha x}{x} e^{-\beta x}, \alpha \in R, \beta > 0, x \in I; \\ \frac{\sin\lambda x}{1+x^2}, \lambda \in R, x \in R/\{I\}. \end{cases} \tag{3}$$

In (3) E_1 is the set of values of the variable x, on which the solution of the homogeneous Eq. (2) turns to zero.

For some automatic control systems, the system of differential Eqs. (1) has the 9th order and, accordingly, Eq. (2) is a linear differential equation of the 9th order, the solution of which, under the appropriate initial conditions, is as follows:

$$y(x) = \cos 6x - 5\cos 5x + \cos 4x - 4\cos x + 7$$

Thus, E_1 is the set of solutions of the trigonometric equation:

$$\cos 6x - 5\cos 5x + \cos 4x - 4\cos x + 7 = 0 \tag{4}$$

I is a set of irrational numbers; R is the set of real numbers.

Let's find the set of E_1.

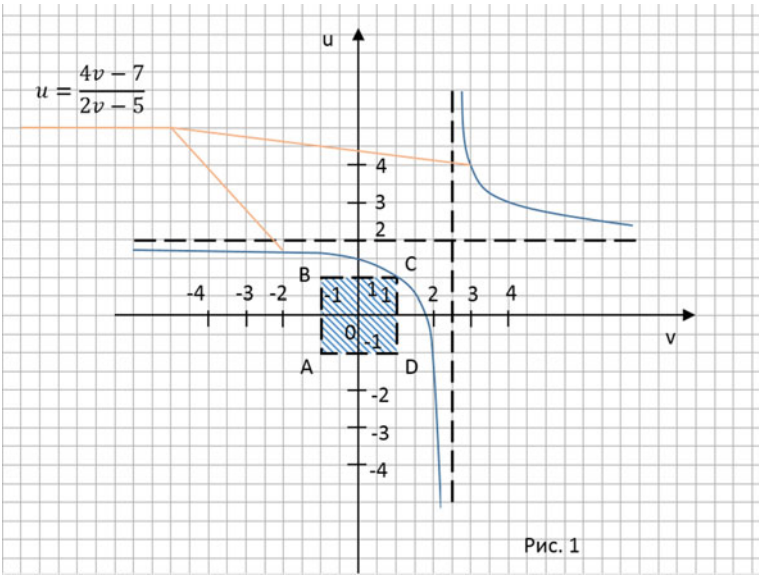


Fig. 1 Set of solutions of Eq. (4) in variables (v,u)

$$(4) \Leftrightarrow 2\cos 5x \cos x - 5\cos 5x - 4\cos x + 7 = 0 \Leftrightarrow$$

$$\left\{ \begin{array}{l} u = \cos 5x, |u| \le 1 \\ v = \cos x, |v| \le 1 \end{array} \right\} \Leftrightarrow 2uv - 5u - 4v + 7 = 0 \Leftrightarrow$$

$$u(2v-5) = 4v - 7 \Leftrightarrow u = \frac{4v-7}{2v-5} \tag{5}$$

Let's plot the function (5) in coordinates (v,u).Of (5) $\Rightarrow u'_v = \frac{4(2v-5)-2(4v-7)}{(2v-5)^2} = -\frac{6}{(2v-5)^2} < 0 \Rightarrow$ u = u(v) is a monotonically decreasing function.

$\lim\limits_{v\to\infty} \frac{4v-7}{2v-5} = 2 \Rightarrow u = 2$ – horizontal asymptote (3).

$\lim\limits_{v\to\frac{5}{2}} \frac{4v-7}{2v-5} = \infty \Rightarrow v = \frac{5}{2}$ – vertical asymptote.

Since $D(u) \in [-1; 1] HE(u) \in [-1; 1]$, of the sets defined by relation (3), we must take only those that fall within the shaded area in Fig. 1. As this figure suggests, this will be only one point C (1; (1) From which it follows that $u = 1, v = 1 \Leftrightarrow$ $\left\{ \begin{array}{l} \cos 5x = 1 \\ \cos x = 1 \end{array} \right. \Leftrightarrow$

$$\left\{ \begin{array}{l} x = \frac{2\pi k}{5},\ k \in Z \\ x = 2\pi n,\ n \in Z \end{array} \right. \Rightarrow k = 5n \Rightarrow x = 2\pi n,\ n \in Z \tag{6}$$

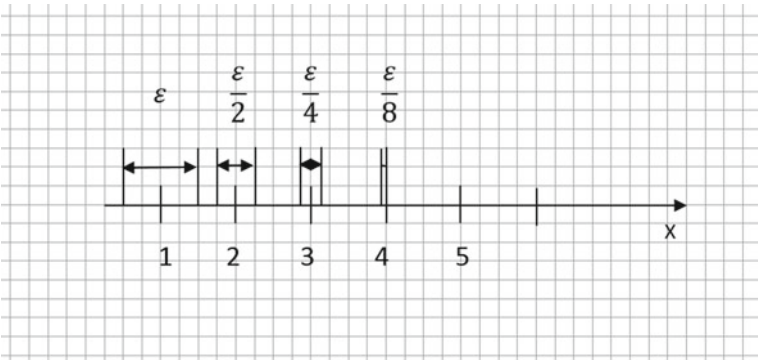


Fig. 2 Sequence of segments on the numerical axis

Thus the set E_1 is the set of transcendental numbers defined by the relation (6). Consider the set of N, which is the set of natural numbers. Each element $n \in N$ can be mapped to an element $x = 2\pi n \in E_1$. This means that it is possible to establish one-to-one correspondences between these sets, and therefore the set E_1 is countable.

Lemma 1 The measure of the set E_1 is 0.

Proof. Number all the points of the set E 1 with the numbers from 1, 2, 3,…, n,.. and draw these numbers on the numerical axis (Fig. 2).

Let a number, etc., where is $1 \in \left[1-\frac{\varepsilon}{2}; 1+\frac{\varepsilon}{2}\right], 2 \in \left[2-\frac{\varepsilon}{2^2}; 2+\frac{\varepsilon}{2^2}\right], 3 \in \left[3-\frac{\varepsilon}{2^3}; 3+\frac{\varepsilon}{2^3}\right]$ an arbitrarily small number. Then $\varepsilon > 0$ the number 1 is covered by the length segment ε, the number 2 is covered by the length segment $\frac{\varepsilon}{2}$, the $\frac{\varepsilon}{2^2}$ number 3 is covered by the length segment, and so on.

$$\varepsilon + \frac{\varepsilon}{2} + \frac{\varepsilon}{2^2} + \cdots - \frac{\varepsilon}{1-\frac{1}{2}} = 2\varepsilon$$

Since the set, $E_1 \sim N$ the measures of these sets coincide, that is, $\mu(E_1) = \mu(N)$, $Ho\mu(N) \le 2\varepsilon \Rightarrow \lim\limits_{\varepsilon\to 0} \mu(N) \le \lim\limits_{\varepsilon\to 0} 2\varepsilon = 0 \Rightarrow \mu(N) = 0 \Rightarrow \mu(E_1) = 0$.

Lemma 2 The set of all irrational numbers (I) has the cardinality of the continuum.

Proof. $I = R - Q$ where R is the set of real numbers and Q is the set of rational numbers. Since Q is a countable set, I is an uncountable set. $\Rightarrow \mu(I) = \mu(R - Q) = \mu(R) - \mu(Q) = \{\mu(Q) = 0\} = \mu(R)$ So I has the power of the continuum. A set of $R/\{I\} = Q$ rational numbers, which, by analogy with the one proved above, is also countable, and therefore has a measure of zero, i.e.$\mu(Q) = 0$.

Thus, the Lebesgue integral of from $f(x, \lambda, \alpha, \beta)$ is:

$$\int\limits_L f(x,\lambda,\alpha,\beta)\mathrm{d}\mu = \int\limits_{E_1} f(x,\lambda,\alpha,\beta)\mathrm{d}\mu + \int\limits_I f(x,\lambda,\alpha,\beta)\mathrm{d}\mu + + \int\limits_Q f(x,\lambda,\alpha,\beta)\mathrm{d}\mu \qquad (7)$$

Lemma 3 Lebesgue integral of a bounded function over the set of measure zero is equal to zero.

Proof. Let $f(x) \leq c npu\, x \in E, moz\partial a \int\limits_E f(x)d\mu \leq \int\limits_E cd\mu = c\int\limits_E d\mu = c\mu(E) = 0$.

On the basis of Lemmas 1, 2, 3 we have:

$$\int\limits_L f(x,\alpha,\beta) = \int\limits_I f(x,\alpha,\beta)d\mu = \int\limits_I \frac{1-\cos\alpha x+\sin\alpha x}{x}e^{-\beta x}d\mu = \int\limits_0^\infty \frac{1-\cos\alpha x+\sin\alpha x}{x}e^{-\beta x}dx$$

Let's take a look at the functionality:

$$F(f,\alpha,\beta) = \int\limits_0^\infty \frac{1-\cos\alpha x+\sin\alpha x}{x}e^{-\beta x}dx,$$

$$s\partial ef(x,\alpha,\beta) = \frac{1-\cos\alpha x+\sin\alpha x}{x}$$

Then

$$(f,\alpha,\beta) = \int\limits_0^\infty \frac{1+\sqrt{2}\sin(\alpha x-\frac{\pi}{4})}{x}e^{-\beta x}dx \tag{8}$$

Functional (8) has a special point x = 0 [3–5]. Let us define the integral function at this point:

$$f(x,\alpha,\beta) = \begin{cases} \frac{1+\sqrt{2}\sin(\alpha x-\frac{\pi}{4})}{x}e^{-\beta x}, x>0 \\ 0, x=0 \end{cases} \tag{9}$$

function $y = f(x,\alpha,\beta)$ НеПрерВИВНа $x \in [0;\infty)$ H $\alpha \in [0;\infty)$, so the functionality

$$I(\alpha,\beta) = \int\limits_0^\infty \frac{1+\sqrt{2}\sin(\alpha x-\frac{\pi}{4})}{x}e^{-\beta x}dx \tag{10}$$

Wehave:

$$f_{\alpha\prime}(x,\alpha,\beta) = \left(\frac{1+\sqrt{2}\sin(\alpha x-\frac{\pi}{4})}{x}\right)\prime e^{-\beta x} = \left(\frac{\sqrt{2}x\cos(\alpha x-\frac{\pi}{4})}{x}\right)e^{-\beta x} = \sqrt{2}\cos(\alpha x-\frac{\pi}{4})e^{-\beta x}$$

The functional $f_{\alpha}\prime(x,\alpha,\beta)=\sqrt{2}\cos(\alpha x-\frac{\pi}{4})e^{-\beta x}$ is continuous, which means that we can apply the theorem on the differentiation of the integral that depends on the parameter

$$I'_{\alpha}(\alpha,\beta)=\int\limits_0^{\infty}f'_{\alpha}(x,\alpha,\beta)dx=\int\limits_0^{\infty}\sqrt{2}\cos\Big(\alpha x-\frac{\pi}{4}\Big)e^{-\beta x}dx$$

$$=\left\{\begin{array}{c}u=\cos\big(\alpha x-\frac{\pi}{4}\big)\Rightarrow du=-\sin\big(\alpha x-\frac{\pi}{4}\big)\alpha dx\\ dv=e^{-\beta x}dx\Rightarrow\beta=-\frac{1}{\beta}e^{-\beta x}\end{array}\right\}$$

$$=\sqrt{2}\Big(-\frac{1}{\beta}e^{-\beta x}\cos\Big(\alpha x-\frac{\pi}{4}\Big)\Big)\Big|_0^{\infty}-\frac{\alpha}{\beta}\int\limits_0^{\infty}\sin(\alpha x-\frac{\pi}{4})e^{-\beta x}dx$$

$$=1-\frac{\alpha\sqrt{2}}{\beta}\int\limits_0^{\infty}\sin(\alpha x-\frac{\pi}{4})e^{-\beta x}dx$$

$$=\left\{\begin{array}{c}u^*=\sin\big(\alpha x-\frac{\pi}{4}\big)\Rightarrow du^*=\cos\big(\alpha x-\frac{\pi}{4}\big)\alpha dx\\ dv=e^{-\beta x}dx\Rightarrow v=-\frac{1}{\beta}e^{-\beta x}\end{array}\right\}$$

$$=1-\frac{\alpha\sqrt{2}}{\beta}\left(-\frac{1}{\beta}e^{-\beta x}\sin\Big(\alpha x-\frac{\pi}{4}\Big)\Big|_0^{\infty}+\frac{\alpha}{\beta}\int\limits_0^{\infty}\cos\Big(\alpha x-\frac{\pi}{4}\Big)e^{-\beta x}dx)\right)$$

$$=1+\frac{\alpha}{\beta^2}-\frac{\sqrt{2}\alpha^2}{\beta^2}\int\limits_0^{\infty}\cos\Big(\alpha x-\frac{\pi}{4}\Big)e^{-\beta x}dx)=1+\frac{\alpha}{\beta^2}-\frac{\sqrt{2}\alpha^2}{\beta^2}I_{\alpha}(\alpha,\beta)\Rightarrow$$

$$I_{\alpha}\prime(\alpha,\beta)\left(1+\frac{\alpha\sqrt{2}}{\beta^2}\right)=1+\frac{\alpha}{\beta^2}\Leftrightarrow I_{\alpha}^{\cdot}(\alpha,\beta)=\frac{\alpha+\beta^2}{\alpha^2\sqrt{2}+\beta^2}\Rightarrow$$

$$I(\alpha,\beta)=\int\frac{\alpha+\beta^2}{\alpha^2\sqrt{2}+\beta^2}d\alpha=\int\frac{\alpha d\alpha}{\alpha^2\sqrt{2}+\beta^2}+\beta^2\int\frac{d\alpha}{\alpha^2\sqrt{2}+\beta^2}$$

$$=\Big\{t=\sqrt{2}\alpha^2+\beta^2\Rightarrow dt=2\sqrt{2}\alpha d\alpha\Big\}=\frac{1}{2\sqrt{2}}\int\frac{dt}{t}+\frac{\beta^2}{\sqrt{2}}\int\frac{d\alpha}{\alpha^2+(\frac{\beta^2}{\sqrt[4]{2}})^2}$$

$$=\frac{1}{2\sqrt{2}}\ln|t|+\frac{\beta^2}{\sqrt{2}}\frac{\sqrt[4]{2}}{\beta}\operatorname{arctg}\frac{\alpha\sqrt[4]{2}}{\beta}+c=\frac{1}{2\sqrt{2}}\ln\Big|\sqrt{2}\alpha^2+\beta^2\Big|+\frac{\beta}{\sqrt[4]{2}}\operatorname{arctg}\frac{\sqrt{2}\alpha}{\beta}+c\Rightarrow$$

$$I(\alpha,\beta)=\frac{1}{2\sqrt{2}}\ln\Big|\sqrt{2}\alpha^2+\beta^2\Big|+\frac{\beta}{\sqrt[4]{2}}\operatorname{arctg}\frac{\sqrt{2}\alpha}{\beta}+c \tag{11}$$

Given that $I(0;\beta)=\int\limits_0^{\infty}\frac{1+\sqrt{2}\sin(-\frac{\pi}{4})}{x}e^{-\beta x}dx=0$ both the left and right sides (9) are continuous functions, $\forall\alpha\in[0;\infty)$ we find from (11) C at $\alpha=0$. We get:

$$0=\frac{1}{\sqrt{2}}\ln\beta+c\Leftrightarrow c=-\frac{1}{\sqrt{2}}\ln\beta,\beta>0\Rightarrow$$

$$I(\alpha,\beta)=\frac{1}{2\sqrt{2}}\ln\left(\frac{\sqrt{2}\alpha^2+\beta^2}{\beta^2}\right)+\frac{\beta}{\sqrt[4]{2}}\text{arctg}\frac{\sqrt{2}\alpha}{\beta},\beta\in(0;\infty) \tag{12}$$

Thus, the Lebesgue integral of the function $f(x,\alpha,\beta)$ is:

$$\int_L f(x,\alpha,\beta)d\mu=\int_I f(x,\alpha,\beta)d\mu=\int_0^\infty f(x,\alpha,\beta)dx=\frac{1}{2\sqrt{2}}\ln\left(\frac{\sqrt{2}\alpha^2+\beta^2}{\beta^2}\right)+\frac{\beta}{\sqrt[4]{2}}\text{arctg}\frac{\sqrt{2}\alpha}{\beta},\beta\in(0;\infty) \tag{13}$$

The second term on the right side (13) $\forall\beta\in(0;\infty)$ is a bounded function of the α variable, and the first one depends on the α according to the logarithmic law and $\alpha\Rightarrow 0$ when tends to zero. It can be concluded that this integral characteristic has a slight increase with an increase in the parameter α and increases significantly at. $\beta\Rightarrow 0$

As an example, let's look at a system whose functioning is determined by the equation:

$$y''+y\prime+\alpha-\alpha^2=f(\alpha,\beta)x, \tag{14}$$

where $f(\alpha,\beta)=\frac{1}{2\sqrt{2}}\ln\left(\frac{\sqrt{2}\alpha^2+\beta^2}{\beta^2}\right)+\frac{\beta}{\sqrt[4]{2}}\text{arctg}\frac{\sqrt{2}\alpha}{\beta},\beta\in(0;\infty),\alpha\in R.$

It is necessary to find the general solution of Eq. (14) and determine all the values of the parameter α at which Eq. (14) has a resonance in which the external perturbation $\beta\gg 1$ asymptotically approaches the linear function.

Decision:

$$y''+y\prime+\alpha-\alpha^2=0\Rightarrow K^2+K+\alpha-\alpha^2=0\Leftrightarrow \tag{15}$$

$$K_{1,2}=\frac{-1\pm\sqrt{1-4\alpha+4\alpha^2}}{2}=\frac{-1\pm\sqrt{(2\alpha-1)^2}}{2}=\frac{-1\pm(2\alpha-1)}{2}=\begin{bmatrix}\alpha-1\\-\alpha\end{bmatrix}\Rightarrow$$

$$y_0=\begin{cases}c_1e^{-\alpha x}+c_2e^{(\alpha-1)x},ec\pi u\alpha\neq\frac{1}{2}\\(c_1+c_2x)e^{\frac{x}{2}},ec\pi u\alpha=\frac{1}{2}\end{cases}$$

$$y_r=x^K(Ax+B), \tag{16}$$

where is $K=\begin{cases}0,if0-notaroof(15)\\1,if0-roof(15)\end{cases}$

and, accordingly, $y=y_0+y_r$

From (15) the ⇒ resonance will be when $\alpha\in\{0;1\}$. In the event of a resonance

$$y_r=Ax^2+Bx,y_r\prime=2Ax+B,y_r''=2A. \tag{16}$$

Substituting (16) into (15) we get:

$$2A + 2Ax + B + \alpha - \alpha^2 = f(\alpha, \beta)x \Rightarrow \begin{cases} 2A = f(\alpha, \beta) \\ 2A + B + \alpha - \alpha^2 = 0 \end{cases} \Leftrightarrow$$

$$A = \frac{f(\alpha, \beta)}{2}, B = \alpha^2 - \alpha - f(\alpha, \beta) \Rightarrow y_r = \frac{f(\alpha, \beta)x^2}{2} + \big(\alpha^2 - \alpha - f(\alpha, \beta)\big)x$$

$$y = y_0 + \frac{f(\alpha, \beta)x^2}{2} + \big(\alpha^2 - \alpha - f(\alpha, \beta)\big)x$$

If $\alpha = 0$, then $f(0, \beta) = 0$ there is no external perturbation.

If $\alpha = 1$, To $f(1, \beta) = \frac{1}{2\sqrt{2}} \ln\left(\frac{\sqrt{2}+\beta^2}{\beta^2}\right) + \frac{\beta}{4\sqrt{2}} arctg \frac{\sqrt{2}}{\beta}$ (1, 7).

From (1, 7) $\Rightarrow \lim\limits_{\beta \to \infty} f(1, \beta) = \sqrt[4]{2} \Rightarrow \lim\limits_{\substack{\beta \to \infty \\ \alpha = 1}} f(\alpha, \beta)x = \sqrt[4]{2}x \Rightarrow$

$y(x) = \sqrt[4]{2}x$ asymptote of the right side (12) at $\beta \ll 1$.

References

1. Biderman V. I. Elements of the Theory of Functions of the Actual Variable – Khabarovsk: Pacific State University Press, 2011. – 195 p.
2. Kuliev V. D., Lepyavin S. I. Tasks in functional analysis, Moscow: University of Mechanical Engineering, 2014. – 33 p.
3. Pogrebnoy, V. D. Theory of Functions of a Real Variable – Summa: Sumy State University, 2012. – 239 p.
4. Smirnov V. I. Higher mathematics course, v.2 – M.: Iz-vo "Nauka", 1974. – 479 p.
5. Shulikovskaya V. V. Elements of the Theory of Measure. Lebesgue integral. – Izhevsk, 2015. – 54 p.

Energy Spectra of Sea Level Fluctuations During Propagation Long Waves in Branched Bays



A. Yu. Belokon and D. I. Lazorenko

Abstract The present research represents a continuation of the study of the propagation of long waves in branched bays. The object of the investigation is a model bay, which has the characteristic dimensions, average depth and configuration of Dvoynaya Bay, located in the system of Sevastopol bays. Two types of bays were considered: a symmetrical bay, which consists of two identical bays, and an asymmetrical bay, which includes two bays of different lengths. Energy spectra of sea level fluctuations in the water area of bays were obtained during the propagation of long waves in them—such as a tsunami, as well as waves in the form of a soliton. It is shown that in symmetrical bays, tsunami waves can initiate level fluctuations with periods of 2.53, 6.12 and 3.62 min. The appearance of asymmetry influences the increase in the mode composition of level fluctuations in the bays and the appearance of peaks with periods of 7.79 and 15.39 min. When a wave propagates in the form of a soliton, in the case of symmetry, two peaks appear with periods of 2.53 and 1.99 min with a predominance of the first period. The difference in the length of adjacent bays leads to the emergence of other seiche oscillation modes with a predominant period of 7.79 min.

Keywords Long waves in bays · Branched bays · Seiches · Numerical modeling · SWASH

1 Introduction

Of great scientific and practical interest is the study of sea level fluctuations in systems from adjacent bays as a result of the penetration of long waves into them. For the Black Sea coast, one of the areas with complex geometry is the system of Sevastopol bays, which includes several bays with different configurations. One of them is Dvoynaya Bay. It is located 15 km from the center of Sevastopol, between Kamyshovaya Bay

A. Yu. Belokon (✉) · D. I. Lazorenko
Marine Hydrophysical Institute of the Russian Academy of Sciences, Kapitanskaya Street, 2, Sevastopol 299011, Russia
e-mail: a.bazykina@mhi-ras.ru

© The Author(s), under exclusive license to Springer Nature Switzerland AG 2024

V. Karev (ed.), *Proceedings of the 9th International Conference on Physical and Mathematical Modelling of Earth and Environmental Processes*, Springer Proceedings in Earth and Environmental Sciences, https://doi.org/10.1007/978-3-031-54589-4_49

and Cape Chersonesos, in the western part of the Heraclean Peninsula, and consists of Cossack and Solena bays.

The propagation of long waves in such bays can be accompanied by significant rises in sea level [1]. The Sevastopol region is a zone of seismic activity, which can lead to the occurrence of long waves, such as a tsunami. They are not catastrophic for this region, but their danger lies in the fact that they can lead to the formation of seiches in bays. The formation of the oscillation spectrum of each bay or bay can be influenced by the configuration of the coastline and bottom topography [2], as well as the presence of other bays nearby. Adjacent bays are connected, that is, periods of natural oscillations of both bays can appear in their spectra [3–5].

The propagation of waves from various hypothetical tsunami foci in a model bay, which has the characteristic dimensions, average depth and configuration of Dvoynaya Bay, has already been studied in [6]. It is shown that the length of adjacent bays affects the amplitude characteristics of sea level in the bays. This article presents results that are a continuation of research in branched bays. Using the Simulating WAves till SHore (SWASH) model [7], numerical simulation of the propagation of long waves in bays was performed. The sea level disturbance obtained for a tsunami from the most hypothetically dangerous source for a given region, as well as an elevation in the form of a soliton, were used as boundary conditions. Energy spectra of sea level fluctuations in branched bays were obtained when long waves penetrated their water area.

2 Mathematical Model

Numerical modeling was carried out using the nonlinear hydrodynamic model Simulating WAves till SHore (SWASH) [7]. The computational area was a basin having the configuration and average depth of Dvoynaya Bay. The studies were carried out for two types of branched bays. The first is a model symmetrical bay, which consists of two bays of equal length. The second is an asymmetric bay, which includes bays of various lengths. These computational domains are shown in Fig. 1 [6], where numbers 1–6 also indicate stations for which sea level fluctuations caused by long waves were analyzed. The depth of the bays was about 12 m.

Using a tsunami model for the entire Black Sea [8], which has a spatial resolution of 500 m and a time step of 1 s, sea level fluctuations near Dvoynaya Bay were obtained. On the left liquid boundary of the computational domain, the resulting mareograms were specified as boundary conditions for $x = 0$. The hypothetical focus of tsunami generation from an underwater earthquake with a magnitude of 7, which is the most dangerous for this area of Sevastopol, was modeled. The parameters of the tsunami foci were determined using empirical formulas from [9]. Initial displacements of the free sea surface in the form of an ellipse caused by earthquakes of magnitude 7 have a height of 1 m, the major and minor axes of the elliptical region are 50 and 29 km, respectively. The longitudinal axis of the ellipses is oriented along the 1500 m isobath. As a result of the lowering of the initial elevation of the sea level, a ring wave is formed, which spreads over time throughout the entire Black

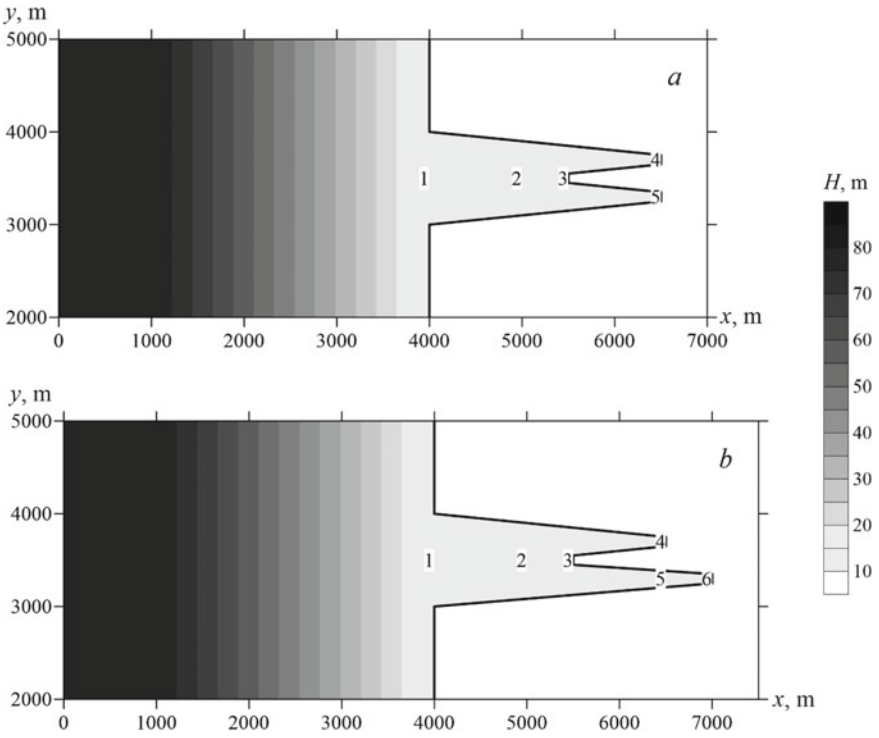


Fig. 1 Bottom topography of the computational area with symmetrical (**a**) and asymmetrical (**b**) bays and the position of stations 1–6 [6]

Sea; when it reaches the shelf, the tsunami front becomes almost flat. Thus, setting boundary conditions in the form of the resulting mareogram on the left boundary of the computational domain (Fig. 1) is completely justified. The calculations in SWASH model were performed for a period of 6 h with a step of 10 m in space and a step in time of 0.5 s.

3 Results of Numerical Experiments

Fluctuations in sea level in the coastal zone of Dvoynaya Bay when waves from the tsunami generation foci penetrate into it are shown in Fig. 2. It is shown that the maximum increase in sea level on the approach to the bay is 0.44 m, the maximum decrease is 0.24 m. The maximum energy occurs in the head wave, followed by oscillations of smaller amplitude. The travel time for tsunami waves from the focus of generation to the entrance to Dvoynaya Bay was 13 min.

The evolution of tsunami waves in Dvoynaya Bay was studied in [6]. It has been established that sea level fluctuations in asymmetric bays are in antiphase throughout the entire duration of the tsunami.

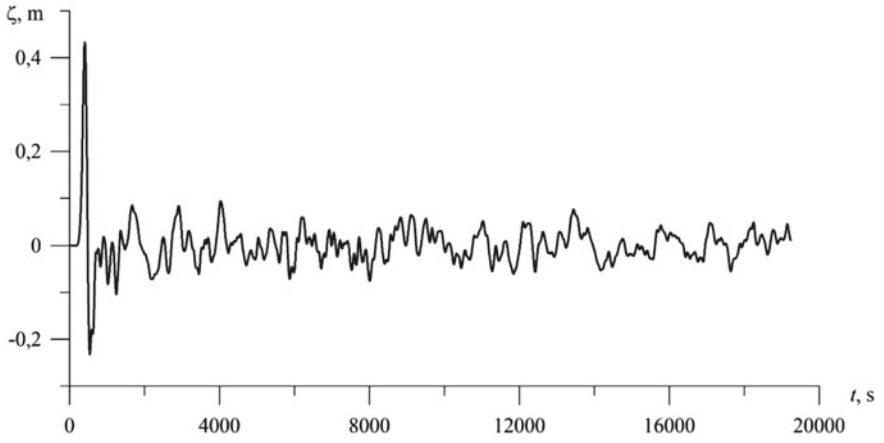


Fig. 2 Sea level fluctuations near Dvoynaya Bay caused by a tsunami

In Fig. 3 shows sea level fluctuations at stations 1–6 during the penetration of tsunami waves into symmetrical and asymmetrical bays. From Fig. 3 shows that at the entrance to the bays the amplitude of the waves increases by 2 times compared to the amplitude at the left boundary of the computational area and reaches 0.8 m (station 1). Tsunamis penetrate into the middle part of the bays, where the amplitude of level fluctuations increases to 1–1.5 m (stations 2, 3). At the tops of two symmetrical bays the level rises to 2.5 m (station 4 and 5). As for asymmetric bays, the presence of connected bays of different lengths leads to a decrease in sea level fluctuations in the shorter bay (station 4), and an increase in fluctuations in the longer bay (station 5). At the top of a long bay, the level rise can reach 2.8 m, and an amplitude of more than 1 m can be observed within 2 h (station 6).

Previous studies have already been carried out that showed that tsunami waves can excite seiche oscillations in bays [10]. To estimate the periods of seiche sea level fluctuations in the basin under consideration, time series at stations 1–6 with a length of 5 h and a resolution of 0.5 s were used. Calculations of the spectra were performed using the scripts given in [11]. In Fig. 4 shows the energy spectra for stations 1–6 when a tsunami penetrates the bays. In Table 1 for each of the bays shows the values of the resonant periods, ordered in descending order of the energy contribution of the corresponding modes. From Fig. 4 shows that for a symmetrical bay, three characteristic peaks with periods of 2.53, 6.12 and 3.62 min are distinguished in the spectra. Then, a peak with a period of 14.29 min appears in the middle part of the bay and in the branches. A study of energy spectra in asymmetric bays showed that the presence of asymmetry leads to an expansion of the mode composition of seiches. In the middle part of the bay for stations 1–3, the values of the characteristic periods for symmetrical bays are maintained or close to them. In addition, a number of periods are added that are not typical for symmetrical bays, with a predominance of the period of 7.79 min. As for the branches of asymmetric bays, characteristic periods do not appear in a relatively small bay, but two peaks appear with periods of 7.79

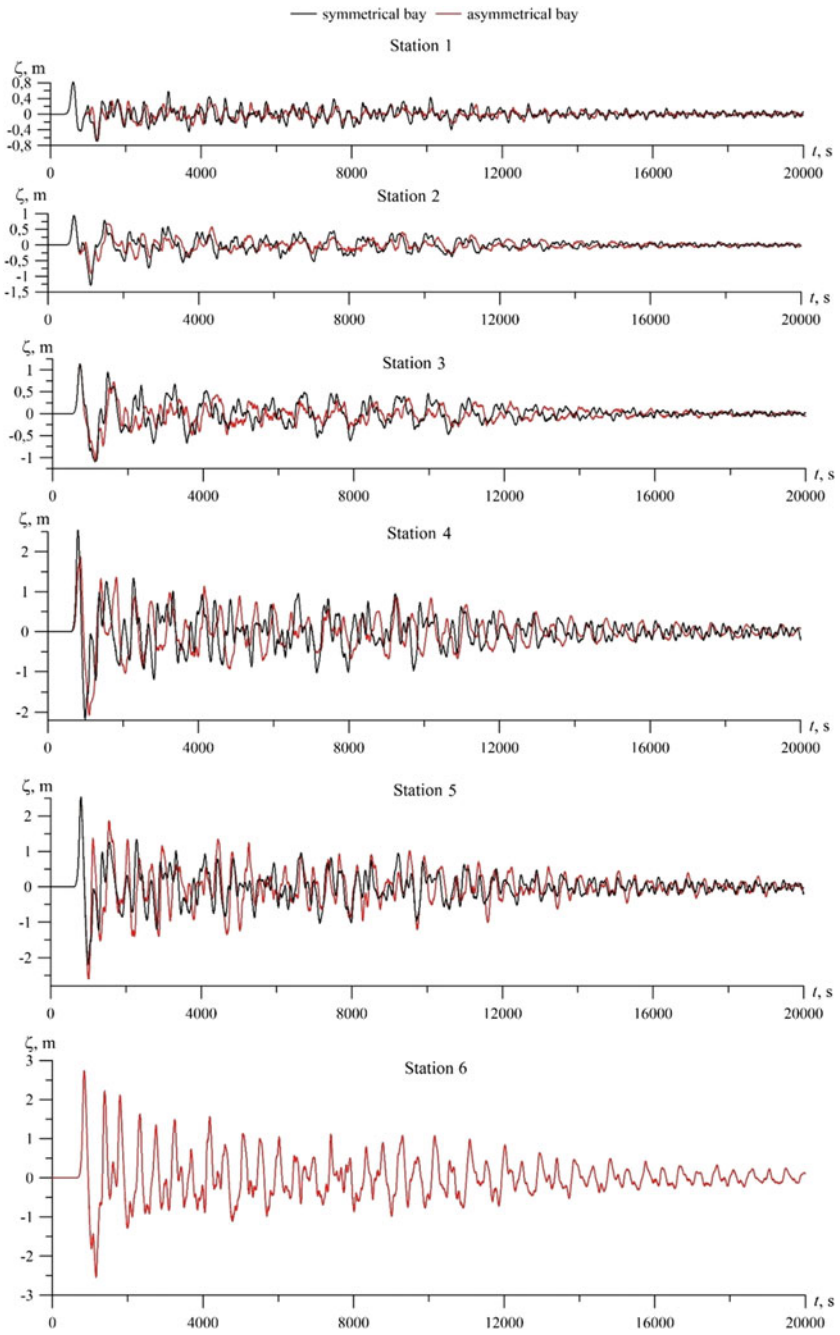


Fig. 3 Sea level fluctuations at stations 1–6 in bays caused by a tsunami

and 15.39 min (station 4). At the same time, in a relatively long bay, both periods characteristic of symmetrical bays and periods arising as a result of the influence of asymmetry appear (station 5). At the top of the long bay, similar periods appear, but with a significant predominance of the period of 7.79 min (station 6). Thus, the bays under study are connected, and the periods of natural oscillations of both bays appear in the spectra.

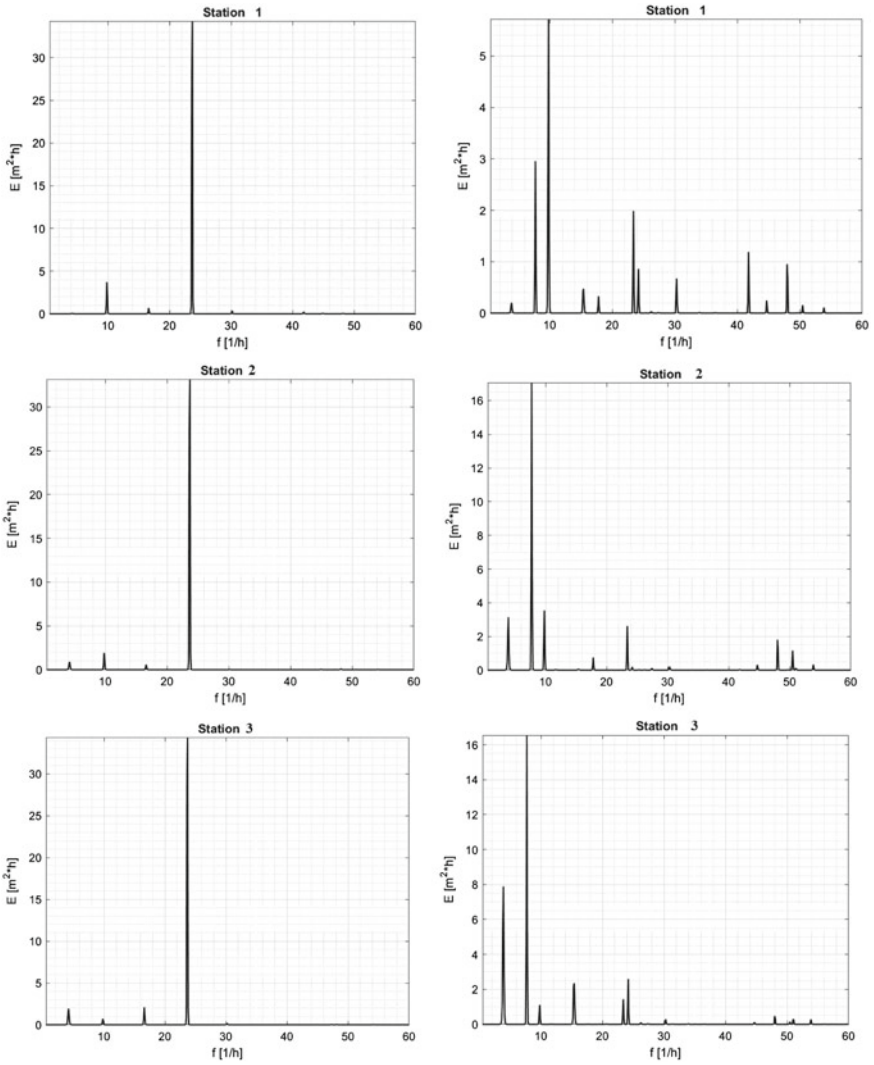


Fig. 4 Spectra of sea level fluctuations at points 1–6 during tsunami penetration into bays: first column—for a symmetrical bay; second column—for asymmetric bay

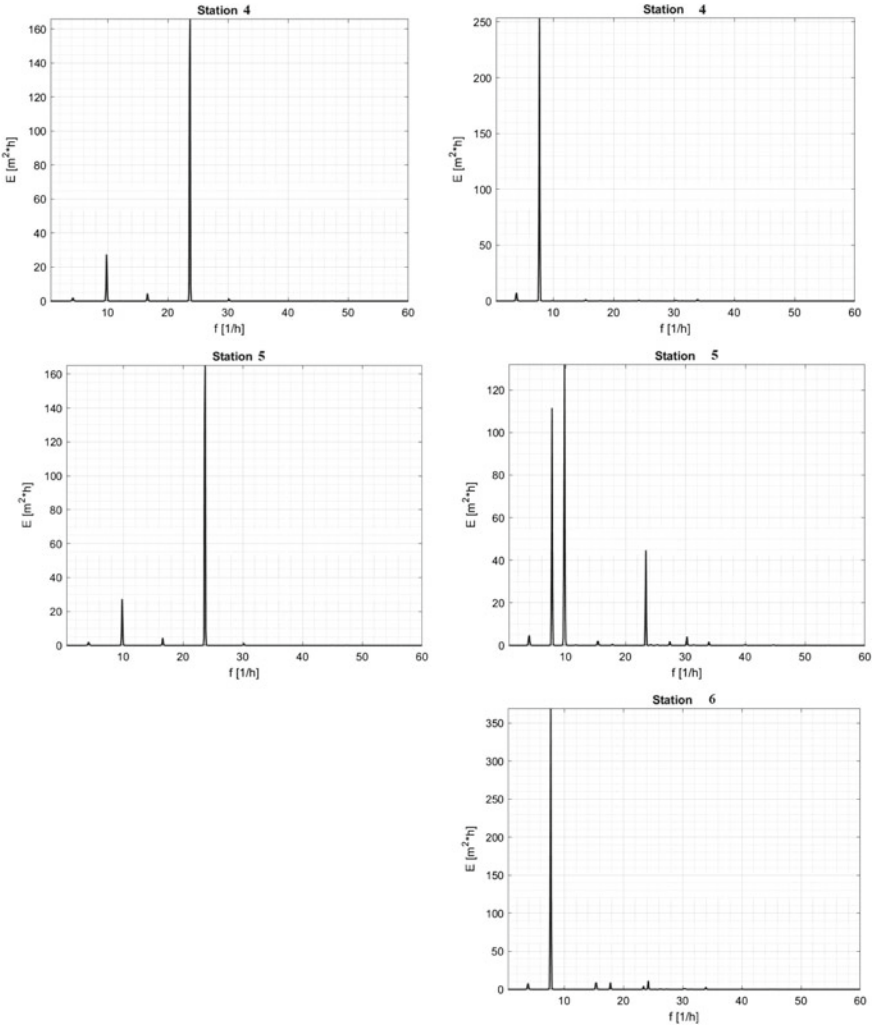


Fig. 4 (continued)

Another stage of the work was the mathematical modeling of level fluctuations in the bay under short-term external influence. In Fig. 5 shows sea level fluctuations at the boundary of the computational domain ($x = 0$) as the soliton passes towards the bay.

Table 1 Resonance periods (min) in symmetric and asymmetric bays at stations 1–6 in descending order of oscillation energy when tsunami waves penetrate the bays

Station	Symmetric bay		Asymmetric bay	
	Period of natural oscillations, min	Peak magnitude, m^2/Hz	Period of natural oscillations, min	Peak magnitude, m^2/Hz
1	2.53 6.12 3.62 1.99	34.2201 3.7178 0.6769 0.3463	6.12 7.79 2.56 1.44 1.25 2.48 1.98	5.7090 2.9575 1.9860 1.1904 0.9519 0.8597 0.6728
2	2.53 6.12 14.29 3.62	33.1207 1.9273 0.9019 0.56771	7.79 6.12 15.39 2.56 1.25 1.19	17.0327 3.5413 3.1513 2.6238 1.8134 1.1673
3	2.53 3.62 14.29 6.12	34.3208 2.0923 1.9386 0.7166	7.79 15.39 2.48 3.90 2.56 6.12	16.5462 7.8915 2.5959 2.3583 1.4393 1.1113
4	2.53 6.12 3.62 14.29	165.7737 27.4647 4.4725 1.9878	7.79 15.39	253.2755 7.3781
5	2.53 6.12 3.62 14.29	165.7737 27.4647 4.4725 1.9878	6.12 7.79 2.56 15.39 1.98 3.90	131.8699 111.5936 44.7113 4.7289 4.1649 2.0208
6	–	–	7.79 2.48 3.37 3.90 15.39 2.56	368.9512 11.2733 9.0208 8.9918 7.9604 4.4191

Sea level fluctuations at stations 1–6 during soliton penetration into symmetric and asymmetric bays are shown in Fig. 6. Here, just as in the case of a tsunami, sea level fluctuations in asymmetric bays are in antiphase. The influence of bay asymmetry is reflected in a decrease in the amplitude of sea level fluctuations in a relatively short bay and an increase in the amplitude in a relatively long bay. Maximum level rises in the bay can reach 3 m.

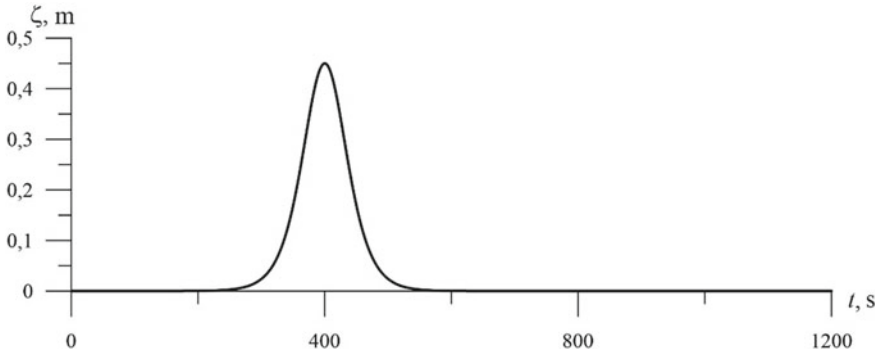


Fig. 5 Sea level fluctuations near Dvoynaya Bay (x = 0) during the passage of a wave in the form of a soliton

The energy spectra were calculated for stations 1–6 when the soliton penetrates into the bays. They are shown in Fig. 7. For each of the bays, the values of the resonant periods were obtained; they are given in Table 2. From Fig. 7 shows that in the case of symmetrical bays, two peaks with periods of 2.53 and 1.99 min appear at all stations with a predominance of the first period. The appearance of asymmetry leads to the appearance of a peak with a period of 7.79 min. O appears at all stations except station 1, predominating at the tops of asymmetric bays (stations 4 and 6).

4 Conclusions

This work continues the study of the propagation of long waves in branched bays. A model bay with the characteristic dimensions, average depth and configuration of Dvoynaya Bay, which is located in the Sevastopol bay system, was considered. Two types of bays were considered: symmetrical, which consists of two identical bays, and asymmetrical, which includes two bays of different lengths. Numerical experiments were performed using the SWASH model. At the entrance to the computational domain, the sea level disturbance obtained for a tsunami from the most hypothetically dangerous focus for the Sevastopol region was used, as well as a level rise in the form of a soliton. Energy spectra of sea level fluctuations in bays were obtained when long waves penetrated their water area. It is shown that in the case of tsunami waves propagating in symmetrical bays, three characteristic peaks with periods of 2.53, 6.12 and 3.62 min are distinguished in the spectra. It has been established that the presence of asymmetry leads to an expansion of the mode composition of seiche oscillation in bays. In this case, two peaks with periods of 7.79 and 15.39 min appear in the spectra for a relatively small bay, while the periods characteristic of this bay do not appear. At the same time, in a relatively long bay, both periods obtained for symmetrical bays and periods resulting from the influence of asymmetry appear. When a wave in the form of a soliton penetrates into symmetrical bays, two peaks

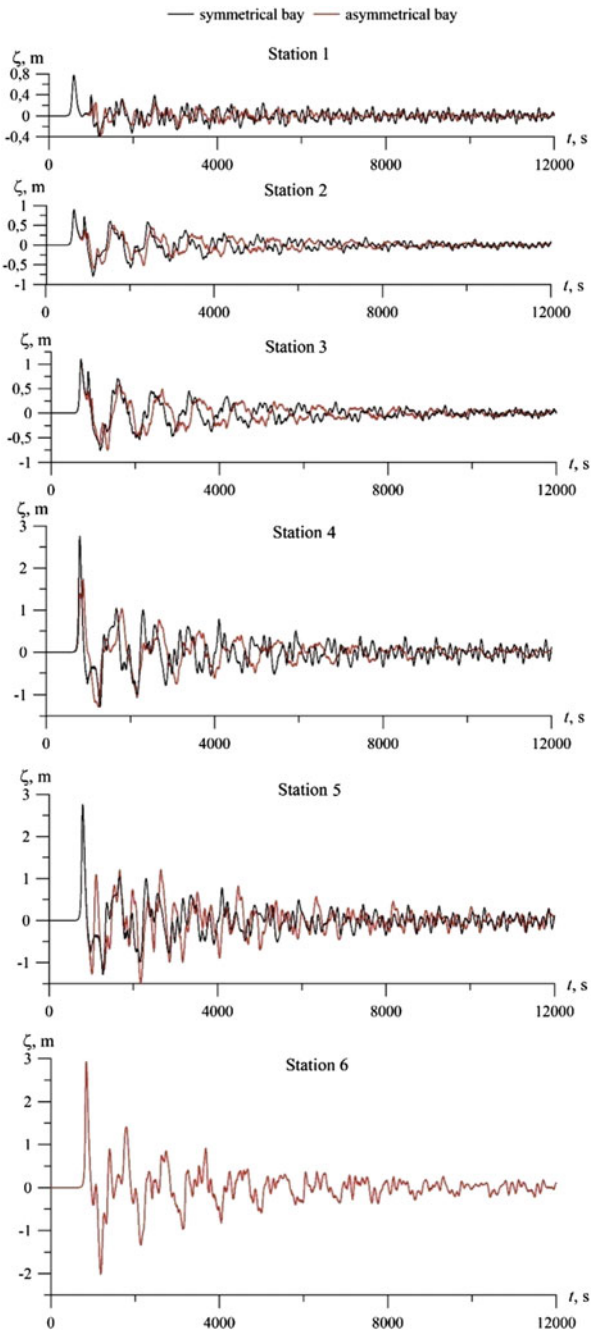


Fig. 6 Fluctuations in sea level at points 1–6 in bays caused by soliton penetration into the bays

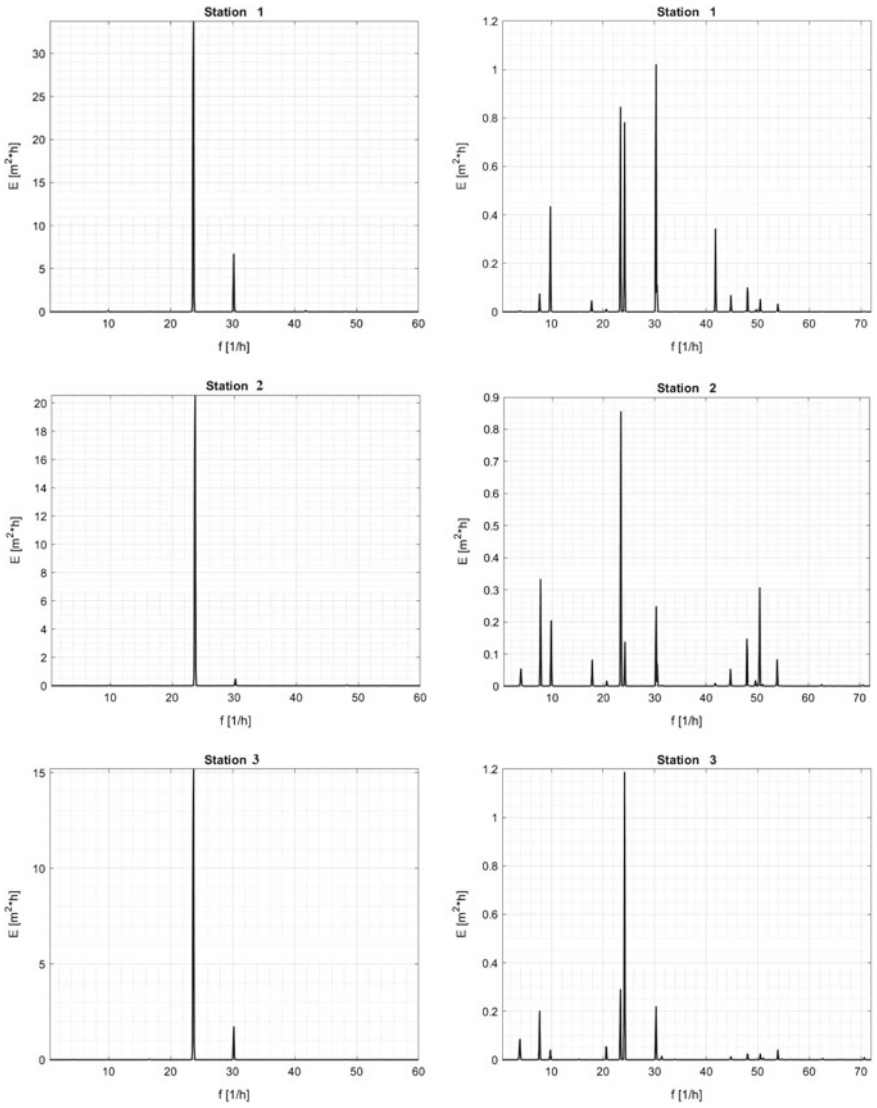


Fig. 7 Spectra of sea level fluctuations at stations 1–6 during soliton propagation into bays: first column—for a symmetrical bay; second column—for asymmetric bay

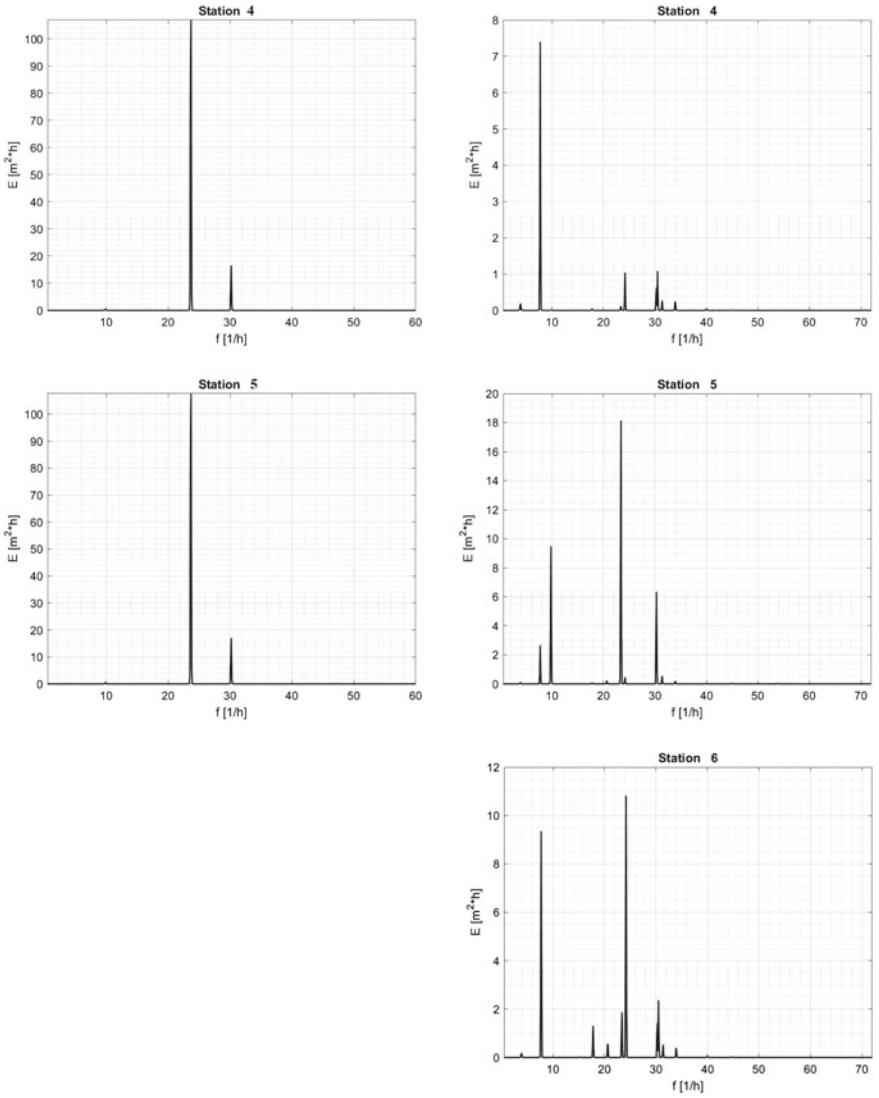


Fig. 7 (continued)

appear at all stations with periods of 2.53 and 1.99 min with a predominance of the first period. The appearance of asymmetry leads to the emergence of other modes of seiche oscillations with a predominant period of 7.79 min.

Table 2 Resonance periods (min) in symmetric and asymmetric bays at stations 1–6 in descending order of oscillation energy when soliton penetrates the bays

Station	Symmetric bay		Asymmetric bay	
	Period of natural oscillations, min	Peak magnitude, m^2/Hz	Period of natural oscillations, min	Peak magnitude, m^2/Hz
1	2.53 1.99	33.7727 6.7543	1.98 2.56 2.48 6.12 1.44 1.97 1.25	1.0220 0.8466 0.7827 0.4359 0.3438 0.1122 0.1005
2	2.53 1.99	20.5691 0.5135	2.56 7.79 1.19 1.98 6.12 1.25 2.48	0.8564 0.3337 0.3081 0.2488 0.2052 0.1481 0.1385
3	2.53 1.99	15.1925 1.7436	2.48 2.56 1.98 7.79 15.39	1.1883 0.2919 0.2209 0.2026 0.0864
4	2.53 1.99	106.9267 16.5597	7.79 1.97 2.48 1.98	7.3998 1.0883 1.0428 0.6329
5	2.53 1.99	107.6453 17.0628	2.56 6.12 1.98 7.79	18.1465 9.4869 6.3499 2.6656
6	–	–	2.48 7.79 1.97 2.56 1.98 3.37	10.8270 9.3537 2.3710 1.8730 1.4213 1.3107

Acknowledgements The work was carried out within the framework of the scientific theme of MHI No. FNNN-2021-0005. Mathematical modeling was performed on the MHI computing cluster (www.hpc-mhi.org).

References

1. Didenkulova, I. Tsunami runup in narrow bays: the case of Samoa 2009 tsunami // Nat. Hazards. 2013. V. 65, Iss. 3. P. 1629–1636
2. Goryachkin, Yu.N., Ivanov, V.A., Repetin, L.N. and Khmara, T.V., 2002. [Seiches in Sevastopol Bay]. In: UHMI, 2002. Trudy UkrNIGMI [Proceedings of UHMI]. Kiev: UHMI. Vol. 250, pp. 342–353. Available at: https://uhmi.org.ua/pub/np/250/29_Repetin.pdf
3. Manilyuk, Yu.V., Lazorenko, D.I. and Fomin, V.V., 2019. Resonance Oscillations on the System of Adjacent Bays. Physical Oceanography, 26(5), pp. 374-386. doi:https://doi.org/10.22449/1573-160X-2019-5-374-386
4. Manilyuk, Yu.V, Lazorenko, D.I. and Fomin, V.V., 2020. Investigation of Seiche Oscillations in the Adjacent Bays by the Example of the Sevastopol and the Quarantine Bays. Physical Oceanography, 27(3), pp. 242-256. doi:https://doi.org/10.22449/1573-160X-2020-3-242-256
5. Manilyuk, Y.V., Lazorenko, D.I. & Fomin, V.V. Seiche Oscillations in the System of Sevastopol Bays. Water Resour 48, 726–736 (2021). https://doi.org/https://doi.org/10.1134/S0097807821050122
6. Belokon, A.Yu., Lazorenko, D.I., Fomin, V.V., 2023. Propagation of Tsunami Waves in the Forked Bays. Processes in GeoMedia – Volume VII, Springer Geology. pp. 197–209. https://doi.org/10.1007/978-981-99-6575-5_20
7. SWASH User Manual. SWASH version 7.01 / The SWASH team. Delft: Delft University of Technology, 2012. 144 p
8. Bazykina, A.Yu., Mikhailichenko, S.Yu. and Fomin, V.V., 2018. Numerical Simulation of Tsunami in the Black Sea Caused by the Earthquake on September 12, 1927. Physical Oceanography, 25(4), pp. 295–304. doi:https://doi.org/10.22449/1573-160X-2018-4-295-304
9. Ulomov, V.I., Polyakova, T.P., Shumilina, L.S., Chernysheva, G.V., Medvedeva, N.S., Savarenskaya, O.E. and Stepanova, M.B., 1993. Experience in Earthquake Foci Mapping. *Seismichnost i Seismicheskoe Rayonirovanie Severnoy Evrazii.* Moscow: Institut Fiziki Zemli RAN, (1), pp. 99–108 (in Russian)
10. Fomin, V.V., Belokon, A.Yu, Kharitonova, L.V. and Alekseev, D.V., 2022. Numerical Simulation of Tsunami Wave Propagation to the Balaklava Bay. Physical Oceanography, 29(4), pp. 379–394. doi:https://doi.org/10.22449/1573-160X-2022-4-379-394
11. Winde, H.P., 2012. Wave Height from Pressure Measurements. Delft University of Technology, 49 p. Available at: https://repository.tudelft.nl/islandora/object/uuid%3Ae3b07efd-1ce9-4fd1-b051-c794c72959ca

Vegetation of Marshes of Coastal-Marine Wetlands (Carbon Landfill in Salmon Bay, Southern Sakhalin)



I. O. Rozhkova-Timina

Abstract The article considers the vegetation of the marsh meadows of the coast of the Sea of Okhotsk (Salmon Bay, the upper reaches of Aniva Bay). Relevés were made, then the taxonomic structure was calculated, an indicator value analysis was carried out according to D. N. Tsyganov's climatic scales (thermal and ombroclimatic regime) and hierarchical cluster analysis was conducted. 2 types of meadow vegetation, 5 formations and 6 associations were identified. In total, on the marsh meadows in the southern part of the island Sakhalin has identified 30 species of herbaceous plants belonging to 28 genera from 16 families. The most widely represented are Poaceae, Cyperaceae, Asteraceae, Rosaceae, Caryophylloideae, Fabaceae. Sakhalin salt marshes have many common types of vegetation with the marsh meadows of the seas of the Russian Arctic.

Keywords Coastal marsh · Halophytic vegetation · Sakhalin · Taxonomic structure

1 Introduction

In the coastal zone of the coasts of tidal seas—on muddy coastal drainages and in the estuaries of rivers—special habitats are formed. These are salty, carbon-rich marshes populated by specific plant communities [1]. The peculiarity of marsh meadows is that they are regularly exposed to salty or brackish waters, while restraining their wave activity [2]. The influence of marine waters on vegetation and soils is carried out not only directly by flooding by tides, storms and surges, but also through groundwater, which is connected to the sea by temporary watercourses [3].

I. O. Rozhkova-Timina (✉)
Federal State Budgetary Scientific Institution "Federal Research Center All-Russian Institute of Plant Genetic Resources Named After N.I. Vavilov", Sakhalin Scientific Research Institute of Agriculture—VIR Branch, Yuzhno-Sakhalinsk, Russia
e-mail: inna.timina@mail.ru

Sakhalin State University, Yuzhno-Sakhalinsk, Russia

© The Author(s), under exclusive license to Springer Nature Switzerland AG 2024

V. Karev (ed.), *Proceedings of the 9th International Conference on Physical and Mathematical Modelling of Earth and Environmental Processes*, Springer Proceedings in Earth and Environmental Sciences, https://doi.org/10.1007/978-3-031-54589-4_50

In the Russian Federation, the vegetation of coastal marshes has been studied in sufficient detail on the coasts of the Arctic seas: the White Sea [3, 4], the Barents Sea [5–8], the Bering Sea [9]; there is data concerning marsh meadows of the Kara, East Siberian, Chukchi Seas and the Laptev Sea [10]. At the same time, marsh meadows have not been studied on the coast of the Sea of Okhotsk, which, although it belongs to the Pacific Ocean basin, is geographically close to the Arctic. The scientific novelty of our work is that for the first time the vegetation of the coastal marshes on the coast of the Sea of Okhotsk (south of the island) was studied. Sakhalin!

2 Materials and Methods

Field work was carried out in the southern part of Sakhalin Island, in the upper reaches of Aniva Bay (Salmon Bay). In this area, the influence of the cold Sea of Okhotsk and the Soy branch of the warm Tsushima current collide, which is why meadow vegetation is formed in very specific conditions.

Geobotanical studies were conducted by the route method in July 2023. Figure 1 shows a schematic map of the points of relevés. The collection of field materials was based on general methodological guidelines [11]. Studies of the floral composition, cover, and height of the herbage were carried out on sample plots of 100 m2 in size, the selection of which required covering typical meadow communities; evaluating communities located on different terrain elements, in different microclimate conditions; observing the uniformity of the composition within the plots. During the work, an eye-measuring determination of the grass height, the cover and the percentage of plant species on the selected site was used. The system of Latin names of vascular plant species and synonyms is based on the check-list of S. K. Cherepanov [12].

The database of relevés was created in the IBIS 7.2 software [13], taxonomic and indicator value analyses were performed there either, and a resemblance matrix of relevés using Euclidean distance was calculated (Statsoft Statistica, WPGMA binding method). The results of hierarchical cluster analysis were the basis for the classification of meadow vegetation and the identification of plant associations and formations.

Using the scales of D. N. Tsyganov [14], it is possible to track the differences in climatic and soil conditions of phytocoenoses, reflected in the range of scores for each geographical point. We have chosen two climatic factors: the general thermal regime and the aridity-humidity climate regime. The calculation of average environmental statuses was carried out using double weighted average [13]. By using of D. N. Tsyganov's climatic scales, the types of meadow vegetation were identified.

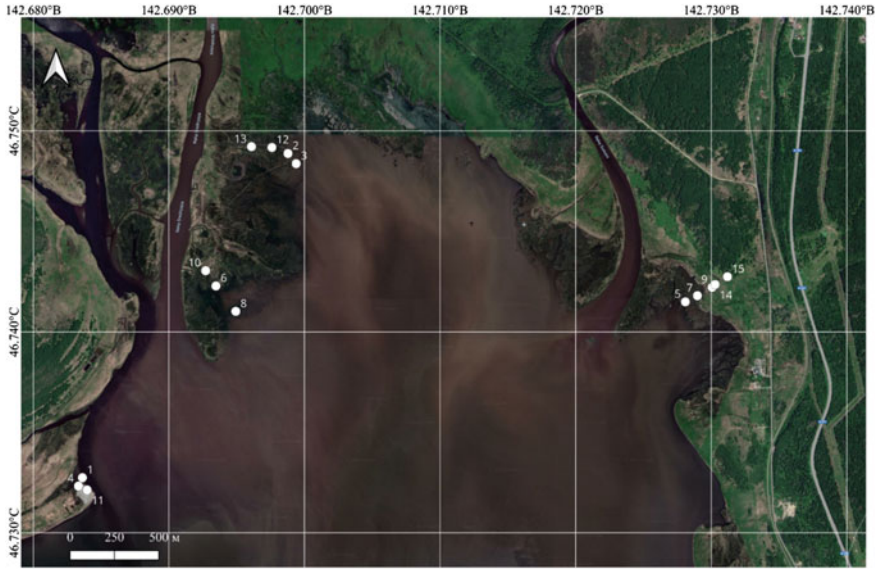


Fig. 1 A map of research points

3 Results and Discussion

In total, on the marsh meadows in the southern part of the island Sakhalin were identified 30 species of herbaceous plants (28 genera and 16 families). The species most widely represented are Poaceae (6 species), Cyperaceae, Asteraceae, Rosaceae, Caryophylloideae (3 species each), Fabaceae (2 species). At the same time, we see (Fig. 2) that the picture is quite different in terms of the frequency of occurrence of species: 6 Poaceae species are more common, but the second place is occupied by the only representative of the Juncaginaceae family: *Triglochin maritimum* L. This is followed by the families Cyperaceae, Rosaceae, Caryophylloideae and only after them Asteraceae. So Juncagináceae, yielding to a number of families in the number of species, benefit due to the prevalence.

When calculating the scales of D. N. Tsyganov, the following modes of climatic factors were determined: for the thermoclimatic scale, the boreal and subboreal regime, for the ombroclimatic scale, the subhumid climate. Thus, two types of vegetation were distinguished: boreal subhumid regime and subboreal subhumid regime. The subhumid range is characterized by the amount of precipitation (minus evaporation) of 0–400 mm per year [14]. Using cluster analysis (Fig. 3), 6 associations from 5 formations were identified.

Below is a brief description of the selected syntaxons.

VEGETATION OF THE BOREAL SUBHUMID CLIMATIC REGIME

Formation *Triglochineta maritima*

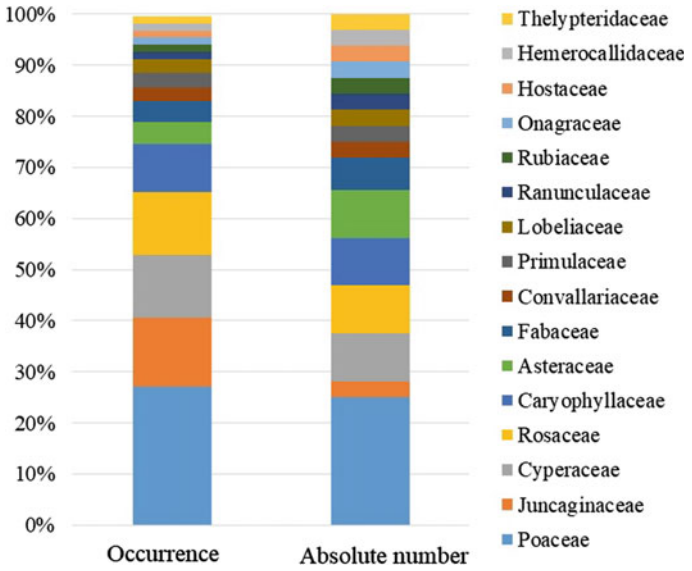


Fig. 2 Taxonomic structure of salt marsh vegetation of Salmon Bay

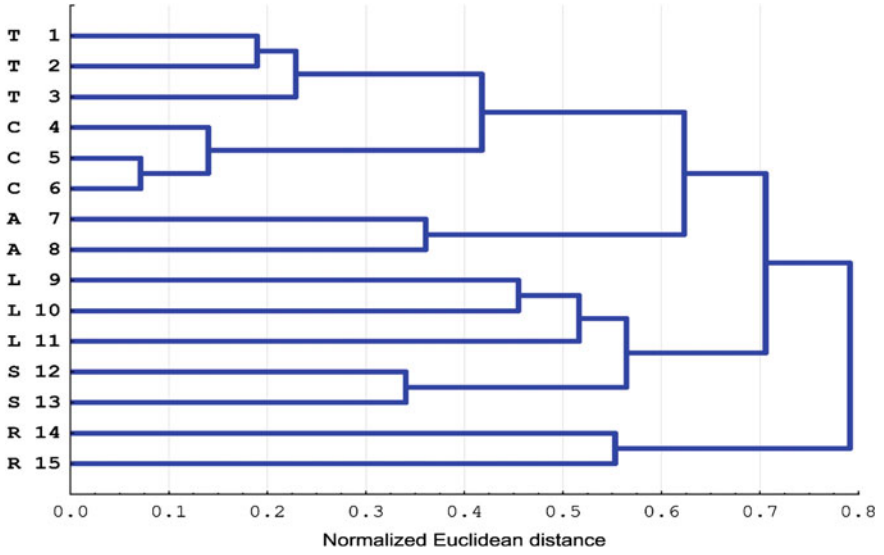


Fig. 3 Dendrogram of similarity of coastal marsh communities based on the results of hierarchical cluster analysis: linking method—WPGMA, resemblance index—Euclidean distance for cover of taxa. Associations **T**—Triglochinetum maritima caricosum subspathaceae, **C**—Caricosum subspathaceae triglochinetum maritime, **A**—Arctopoetum eminentis purum, **L**—Leymetum mollis purum, **S**—Stellarietum longifolia leymetum mollis, **R**—Rubetum arcticus phragmitetum australis

Triglochin maritimum L.—hemicryptophyte with leafless stem and ovoid fruits on spaced legs. The height of the plant is 10–30 cm [15]. It is distributed in the marsh meadows of the seas of the Arctic Ocean and the northern seas (Baltic, Northern) of the Atlantic Ocean [5, 16–18].

Association *Triglochinetum maritima caricosum subspathaceae*

The Association was previously registered at marshes in the estuary of the Chizha River (White Sea) [5, 17].

Community structure. These are two-species communities consisting of *Triglochin maritimum* (50–80% share in the herbage) and *Carex subspathacea* Wormsk. ex Hornem (share in herbage 20–50%). The total cover of the herbage is high (50–100%), the average height of the herbage is 30 cm.

Ecology and distribution. The association communities occupy small areas on the clay-silty drainages of the marshes in the immediate vicinity of the sea and are subject to daily flooding by tidal waters.

Formation *Cariceta subspathaceae*

Carex subspathacea Wormsk. ex Hornem.—the sedge is up to 20 cm tall, the stems are smooth. The pistillate spikelets are 5–10 mm long, the lower ones on short legs, surrounded by an expanded base of the bract leaf. It is an autochthonous element of the coastal flora and is distributed on the damp and salty sea coasts of Sakhalin, the Kuriles, the seas of the Arctic Ocean, as well as the island of Hokkaido, Eurasia and North America [5, 8–10, 15, 17, 19].

Associations *Caricetum subspathaceae triglochinetum maritima*

Community structure. The community structure is an evergreen small-species community with a cover of 50–90% and a height of 20–30 cm. The dominant species are *Carex subspathacea* (70–90% share in the herbage) and *Triglochin maritima* (15–30%). *Leymus mollis* (Trin.) Pilg., *Stellaria calycantha* (Ledeb.) Bong., *Glaux maritima* L. occur less frequently (1–10% in the herbage).

Ecology and distribution. These communities are located a little further (about 800 m) from the sea than the previous described association. Due to this, they have a higher content of sedge and a lower content of arrow-grass. However, these communities are also developed on silty-clay deposits and are affected by daily tides.

VEGETATION TYPE OF THE SUBBOREAL SUBHUMID CLIMATIC REGIME

Formation *Arctopoeta eminentis*

Arctopoa eminens (J. S. Presl.) Probat. (syn.: *Poa eminence* J. S. Presl.; *Poa alexeji* Sofeikova et Worosch.; *Poa eminens* var. *alexeji* (Sofeikova et Worosch.) Worosch; *Poa kurilensis* Hack.) is a large halophilic cereal with thick rhizomes and stems, with large bluish leaves and thick erect panicles. It is distributed on wet coastal meadows and sea sands of the Pacific Ocean coasts [15, 19]. A similar formation was identified in 2014 at the maritime marshes in the Korf Bay (Kamchatka Peninsula) [9].

Association *Arctopoetum eminentis purum*

Community structure. This association includes communities with a cover of 50–95% and an average grass height of 120–150 cm. The dominant species is *Arctopoa eminens* (the share in the herbage is 30–80%). Other species presented in a separate

publication: *Leymus mollis* (trin.) Pilg. (10%), *Potentilla anserina* L. (10–30%), *Schoenoplectus tabernaemontani* (C.C.Gmel.) Pala (10%), *Stellaria longifolia* Muhl. ex Willd. (10%), *Carex subspathacea* (7%). *Phragmites australis* (Cav.) Trin. ex Steud., *Fimbripetalum radians* (L.) Ikonn., *Triglochin maritimum* are represented in single and small numbers.

Ecology. These communities are developed on sandy substrates affected by syzygy tides and storms.

Formation *Leymeta mollis*

Leymus mollis (L.) Ikonn. (syn.: *Elymus arenarius* ssp. *mollis* (Trin.) Hulten; *Elymus cladostachys* Turcz.; *Elymus mollis* Trin.; *Leymus arenarius* ssp. *mollis* (Trin.) Tzvelev)—halophilic cereal, height from 50 to 130 cm (in our study—at least 120 cm), with a developed rhizome and long ears [15]. It is distributed on the seashores of the Russian Far East, China, Japan, and North America [9, 20]. Taking into account the synonymy of this species, we can talk about its distribution in the coastal territories of the seas of the Arctic Ocean [3, 17].

Association *Leymetum mollis purum*

Community structure. In the phytocoenoses of this association, the dominant species is *Leymus mollis* (the share in the herbage is 50–90%). Also common are *Carex cryptocarpa* C. A. Mey, *Ranunculus acris* L., *Phragmites australis, Rubia jezoensis* (Miq.) Miyabe & Kudo, *Sonchus arvensis* L., *Potentilla anserina*—their share in the herbage is 30–40%, *Calamagrostis epigeios* (L.) Roth., *Artemisia vulgaris* L., *Stellaria longifolia, Lathyrus pilosus* (Cham.) Hulten, *Agrostis scabra* Willd., *Rubus arcticus* L., *Poa palustris* L.—5–15%. The cover of the herbage is high (60–100%), the average height of the herbage is 100–150 cm.

Association *Stellarietum longifolia leymetum mollis*

Community structure. The cover of the herbage is high (90–100%), the average height of the herbage is 80–150 cm. The association is formed by phytocoenoses with dominant species *Leymus mollis* (50–80% share in herbage) and *Stellaria longifolia* (60–70% share in herbage). *Triglochin maritima* (10–20%), *Lobelia sessilifolia* Lamb., *Artemisia littoricola* Kitam are also present. (30%).

Ecology and distribution. Communities of this formation are close to intra-island psammophyte meadows. The territory is affected by syzygy tides.

Formation *Rubeta arcticus*

Rubus arcticus L. (syn.: *Rubus acaulis* auct.) is a low (up to 30 cm) herbaceous plant with pink flowers and triple leaves. It is distributed in North America, Northern Europe, in the north and northeast of the European part of Russia, in the Urals, Siberia, Sakhalin and the Kuril Islands, in northern Mongolia, in northern Japan ([15, 20].

Association *Rubetum arcticus phragmitetum australis*

Community structure. The cover of the herbage is high (80–100%), the average height of the herbage is 150–160 cm. The dominant species in this association are *Rubus arcticus* (50% share in the herbage) and *Phragmites australis* (40–50% share in the herbage). *Sanguisorba stipulata* Raf. (20–50%), *Thelypteris thelypteroides* (Michx.) Holub (60%), *Calamagrostis epigeios, Sanguisorba stipulata, Lathyrus pilosus* (20% each), *Thermopsis lupinoides* (L.) Link, *Lobelia sessilifolia* (10%

each), *Maianthemum bifolium* (L.) F.W. Schmidt (5–50%). *Hemerocallis middendorffii* Trautv is represented in small abundance. & C.A. Mey. (5%) and *Chamaenerion angustifolium* (L.) Scop. (1%). *Hosta rectifolia* Nakai and *Stellaria calycantha* have been found singly.

Ecology and distribution. The species represented in this association are not halophytes, however, they are located in the zone of syzygy tides.

4 Conclusion

Meadow communities of coastal marshes in the Salmon Bay of Aniva Bay are formed under the specific conditions of the influence of the cold Sea of Okhotsk and the Soy branch of the warm Tsushima current. Habitats are regularly flooded with salt water during tides and storms.

In total, on the marsh meadows in the southern part of the island Sakhalin were identified 30 species of herbaceous plants belonging to 28 genera from 16 families. The most widely represented are Poaceae (6 species), Cyperaceae, Asteraceae, Rosaceae, Caryophylloideae (3 species each), Fabaceae (2 species).

According to the results of the ecological and cenotic analysis of the community of maritime marshes in the southern part of the island Sakhalin is attributed to 5 plant formations and 6 associations. Sakhalin salt marshes have many common types of vegetation with the marsh meadows of the seas of the Russian Arctic: *Triglochin maritimum*, *Carex subspathacea*, *Arctopoa eminens*, *Leymus mollis*, *Phragmites australis*.

The work was carried out within the framework of the Project "Carbon landfill" of the Ministry of Education and Science of Russia, the code of the topic FEFF-2022–0027.

References

1. Campbell A., Fatoyinbo L., Goldberg L., Lagomasino D. Global hotspots of salt marsh change and carbon emissions // Nature. 2022. 612(7941):1–6. DOI: https://doi.org/10.1038/s41586-022-05355-z.
2. Zhang W., Ge Z., Li S, Tan L., Zhou K., Li Y., Xie L., Dai Z. The role of seasonal vegetation properties in determining the wave attenuation capacity of coastal marshes: Implications for building natural defenses // Ecological Engineering. 2022. Volume 175, P. 106494, doi.org/https://doi.org/10.1016/j.ecoleng.2021.106494.
3. Sergienko L. A., Dyachkova T. Y., Androsova V. I. Floristic richness and density of saltmarsh communities dominated by *Triglochin maritima* L. (Juncaginaceae) on the northern seas coasts // National Association of Scientists. 2020. N 53–1(53). P. 17–20.
4. Moseev D. S., Sergienko L. A., Leshchev A. V., Bragin A. V., Romanov R. E., Churakova E. Yu. Rare plant communities of lakes and river estuaries of the Arkhangelsk Region // Turczaninowia 24, 3: 138–162 (2021).

5. Lavrinenko O. V., Lavrinenko I. A. Classification of salt and brackish marshes vegetation of the Bolschezemel'skaya tundra (Barents sea coastal) // Phytodiversity of eastern Europe. 2018. Vol. 12, Is. 3. P. 82–143. doi: https://doi.org/10.24411/2072-8816-2018-10028.
6. Lavrinenko I. A. Typology and syntaxonomic composition of vegetation territorial units: novel approach suggested with the case study of arctic marshes // Vegetation of Russia. 2020. Vol. 39. P. 100–148. doi: https://doi.org/10.31111/vegrus/2020.39.100.
7. Moseev D. S., Sergiyenko L. A., Parinova T. A., Volkov A. G. Halophytic vegetation of the southern coast of the Pechora bay // Botanicheskii zhurnal. 2021. Vol. 106, Is. 11. P. 1050–1065. doi: https://doi.org/10.31857/S0006813621110053.
8. Lapina A. M., Ivanova K. V. Syntaxonomic composition and spatial structure of territorial units of vegetation of coastal marshes of the Malozemel'skaya tundra // Phytodiversity of eastern Europe. 2021. Vol. 15, Is. 3. P. 52–66. doi: https://doi.org/10.24412/2072-8816-2021-15-3-52-66.
9. Neshataeva V. Yu., Neshataev V. Yu., Korablev A. P., Kuzmina E. Yu. Vegetation of coastal salt marshes of the gulf of Korf (Olutorsky district, Kamchatka territory) // Botanicheskii zhurnal. 2014. Vol. 99, Is. 8. P. 868–894.
10. Sergienko L. A., Moseev D. S. Taxonomic structure and ecological-geographical characteristics of florocoenotic complex of the Russian Arctic coast // Proceedings of Petrozavodsk State University. 2015. Vol. 6(151). P. 28–33.
11. Field geobotany. Moscow; Leningrad, 1959–1972. Vol. 1–4.
12. Cherepanov S. K. Vascular plants of Russia and neighboring states (within the former USSR). St. Petersburg: Mir i sem'ya, 1995. 992 pp.
13. Zverev A. A. Methodological aspects of using indicator values in biodiversity analysis // Contemporary problems of ecology. 2020. Vol. 13, N 4. P. 321–332. doi: https://doi.org/10.1134/S1995425520040125.
14. Tsyganov D. N. 1983. Phytoindication of ecological regimes in the subzone of coniferous-deciduous forests. Moscow: Nauka, 1983. 195 p.
15. Tolmachev A. I. 1947. Key to higher plants of Sakhalin and the Kuril Islands. Leningrad: Nauka. 372 pp.
16. Sergienko L. A., Dyachkova T. Y., Androsova V. I. Habitats' characteristics and population structure of *Triglochin maritima* L. (Juncaginaceae) found in the intertidal zone of the White sea littoral // Proceedings of Petrozavodsk State University. 2017. № 2(163). P. 57–63.
17. Moseev D. S., Sergiyenko L. A. Coastal vegetation of the river estuaries on the Kanin peninsula // Vegetation of Russia. 2020. Vol. 39. P. 47–74. doi: https://doi.org/10.31111/vegrus/2020.39.47.
18. Lubińska-Mielińska S., Kącki Z., Kamiński D., Pétillon J., Evers C., Piernik A. Vegetation of temperate inland salt-marshes reflects local environmental conditions // Science of The Total Environment. 2023. Vol. 856, Part 2, P. 159015. doi: https://doi.org/10.1016/j.scitotenv.2022.159015.
19. Yurtsev B. A., Koroleva T. M., Petrovsky V. V., Polozova T. G., Zhukova P. G., Katenin A. E. Abstract of the flora of the Chukotka tundra. St. Petersburg, 2010. 628 p.
20. Afonin A. N., Green S. L., Dzyubenko N. I., Frolov A. N. (ed.) Agroecological atlas of Russia and neighboring countries: economically significant plants, their pests, diseases and weeds. 2008. http://www.agroatlas.ru.

Experimental Study of the Influence of Impermeable Inclusions on the Stress–Strain State of Cement in Sedimentary Rock Under the Influence of Filtration Flow

Iudochkin Nikita, Tairova Aliya, and Belyakov George

Abstract In the presented work, using the method of physical modeling, the interaction of the filtration flow with porous "cement" containing inclusions of "clastic material" is considered. For this purpose, an installation was created that made it possible to simultaneously visualize the filtration flow and deformations of the porous medium with registration of processes in real time, followed by decomposition of the video sequence into frames. For a medium simulating sandstone cement, elastic parameters were obtained experimentally. A technique for obtaining deformations for a poroelastic skeleton in experiments and converting deformations of a porous medium into stresses is proposed. The work considers several possible options for the geometry of the inclusion location. Based on photographic materials obtained during the study, the stresses created by the filtration flow along its direction and perpendicular to it were calculated. Thus, the stresses arising behind inclusions aligned with the flow have a positive sign, and behind those located across the flow or completely absent, the stresses have a negative value. Experiments have shown that inclusions located along the flow direction are characterized by tensile stresses. In the case of inclusions located perpendicular to the flow direction, compressive stresses arise. The obtained analytical estimates are in good agreement with the experimental results.

Keywords The fluid filtration · Porous medium · Stress–strain state · Filtration front

I. Nikita (✉) · T. Aliya · B. George
Institute of Geosphere Dynamics, Russian Academy of Science, 119334 Leninsky Prospekt, 38k1, Moscow, Russia
e-mail: rood818181@gmail.com

© The Author(s), under exclusive license to Springer Nature Switzerland AG 2024

V. Karev (ed.), *Proceedings of the 9th International Conference on Physical and Mathematical Modelling of Earth and Environmental Processes*, Springer Proceedings in Earth and Environmental Sciences, https://doi.org/10.1007/978-3-031-54589-4_51

1 Introduction

The movement of filtration flows in rocks is considered in various areas of geophysics, one of which is the oil and gas industry. Filtration of fluids, their evaluation, distribution in the formation and the pressure they create on the skeleton is of great importance for the effective recovery of hydrocarbons.

Assessing the elastic properties of reservoir cores in laboratory conditions allows us to build models and select the most effective field development strategy. However, it is difficult to determine the modulus of elasticity under complex compression using Hooke's law [1]. The desire to experimentally obtain the average Young modulus for cores consisting of different rocks led to a series of curves of changes in the Young modulus as a function of the applied stress [2]. The elastic modulus of a rock can be affected by the size of inclusions with a large Young modulus [3], as well as the size of the grains that make up the rock [4].

Using the example of West Siberian fields [5, 6], a sandstone reservoir can consist of clastic material (60–90%), cementing material (7–40%), voids (7–10%) and in rare cases detritus, which can be mineralized. The clastic material is represented by quartz (30–50%) and feldspar (30–55%). The cementing material is represented by fine-crystalline calcite (20–40%) and clay minerals (up to 5%). The values of elastic moduli and grain sizes of mineral that make up the sandstone layer are presented in Table 1.

The presented composition of sandstone can be divided into 2 groups: impermeable clastic material and cement with voids. Thus, the movement of filtration flow is possible inside the cement with voids, which is the skeleton of the reservoir, connecting grains of clastic material into a single rock. To evaluate the stresses arising when fluid is injected into the reservoir, an experimental setup was created and experiments were carried out with various locations of impermeable debris in the body of permeable cement.

Table 1 Characteristics of sandstone composition

Mineral	Young modulus (MPa)	Grains range (mm)
Quartz	$7 * 10^4$	0.06–0.1
Feldspar	$6.5 * 10^4$	
Calcite	$8.2 * 10^4$	–
Clay	95	

2 Experiment and Methodology for Its Implementation.

2.1 Experimental Setup

The experimental setup [7] is presented in Fig. 1. The core of the experimental setup is a Hele-Shaw cell, consisting of two optically transparent plates (S1, S2) measuring 125 × 500 mm and 15 mm thick. Between the plates there is a porous material (M1) with an initial thickness of 5 mm. A 10 × 10 mm mesh is pre-applied to the porous sheet. The space between the plates is separated from the environment by a rubber band (R1). The distance between the plates is 3.5 mm, so the sheet of porous material is subject to unilateral compression. A liquid with a viscosity of 0.3 Pa*s is pumped into the cell (S1, S2) through the pipe (t1). Under the influence of tangential stresses of the filtration flow, the stress–strain state of the poroelastic material (M1) changes, and a change in the mesh applied to the porous sheet is observed. The picture of deformations and propagation of the filtration front is recorded by a video camera (D6). The pressure of the injected liquid is recorded on the ADC by a pressure transducer (P) installed at the inlet to the cell.

Using a camera allow us to simultaneously record changes in the position of the mesh under the influence of liquid and the movement of liquid inside the porous medium. Both parameters are recorded simultaneously: the liquid front by photodiodes with a light filter $\lambda > 650$ nm (λ is the wavelength); poroelastic medium and a grid on it with a photodiode with light filter characteristics $\lambda < 500$ nM.

All experiments were carried out at a constant initial pressure of the injected liquid, equal to 300 kPa. The flow rate at this pressure ranged from 5 to 20 $m^3/s \bullet 10^{-6}$

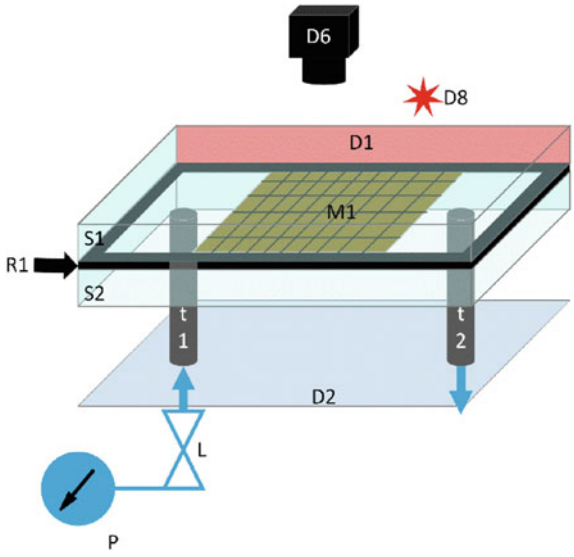


Fig. 1 Experimental setup

depending on the switching position. The flow rate was chosen in such a way as to ensure destruction of the material at the lowest value of liquid pressure. At lower fluid pressures, the poroelastic frame repacks [8]. At the initial moment, the poroelastic medium is filled with air with a dynamic viscosity of $18 \bullet 10^{-6}$ Pa•s.

According to the above data on the elastic modulus of sandstone composition in Table 1, the elastic modulus of clastic material is on average 67 GPa, the average elastic modulus of cement with voids is E≈51 GPa (with composition: 10% voids, 25% calcite, 5% clay). Thus, the elastic moduli for clastic material with the elastic modulus of cement and voids have similar values.

Taking into account the similar values of the elastic moduli of the clastic material and cement, as well as the dimensions of the Hele-Shaw cell, materials with similar values of the elastic modulus and Poisson's ratio were used. The clastic material imitated rubber and was represented by an inclusion in cement, elastic modulus 10 MPa, Poisson's ratio 0.5. Cement with voids was modeled with foamed polyurethane, the elastic modulus of the polyurethane from which the skeleton of foamed polyurethane consists is 10 MPa and Poisson's ratio 0.5 (at $t = 20^{\circ}$) [9]. Materials with higher Poisson's ratios were selected to improve the visibility of deformations that occur under the influence of filtration flow before failure.

The presented experiments examine the movement of the filtration flow and the stresses it creates inside the "cement" with inclusions. At the edges the "cement" is limited by impenetrable clastic materials. In the central part of the "cement" there is an impenetrable, stationary inclusion, which imitates the location of fragmentary material in the cement and is stationary relative to the layers above and below. Fragmentary materials oriented along or across the injected fluid flow. The direction of the axes is shown in Fig. 2.

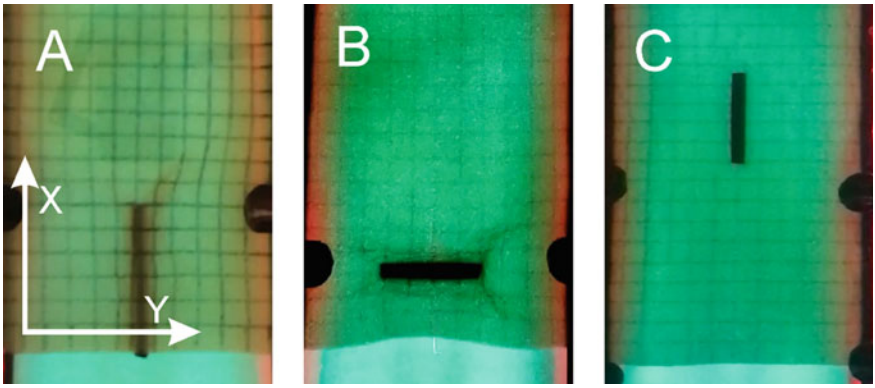


Fig. 2 Location of fragmentary materials in cement and direction of axes

2.2 Determination of Elastic Parameters of the Skeleton

The previously mentioned polyurethane foam used as cement, with a porosity of 0.98, inherits the characteristics of polyurethane only at the level of particles that make up the structural frame, therefore, to represent this material as a solid body, using the law (1) [10], Young modulus and Poisson's ratio for tension along the X axis and compression along the Y, Z axes using Hooke's law. Next, we will consider the skeleton as a solid body.

$$u_{ik} = \frac{1}{E}[(1+\mu)\sigma_{ik} - \mu\sigma_{ll}\delta_{ik}] \tag{1}$$

u_{ik}—is the deformation tensor; E—Young modulus (Pa); μ—Poisson's ratio; σ_{ik}—stress tensor (Pa); σ_{ll}—stresses in the orthogonal direction (Pa); δ_{ik}—Kronecker symbol. To describe stresses and strains, we use (1) and present it in a three-dimensional projection:

$$\begin{cases} \frac{\Delta x}{x}E = \sigma_{xx} - \mu(\sigma_{yy} + \sigma_{zz}) \\ \frac{\Delta y}{y}E = \sigma_{yy} - \mu(\sigma_{xx} + \sigma_{zz}) \\ \frac{\Delta z}{z}E = \sigma_{zz} - \mu(\sigma_{xx} + \sigma_{yy}) \end{cases} \tag{2}$$

$\frac{\Delta x}{x}$, $\frac{\Delta y}{y}$, $\frac{\Delta z}{z}$—is the relative elongation or compression along one of the axes; σ_{xx}, σ_{yy}, σ_{zz}—stresses along the X, Y and Z axes (Pa). In the described experiment, the dimensions of the porous medium are $x = 200\,\text{mm}$ $y = 100\,\text{mm}$ $z = 5\,\text{mm}$.

As the load σ_{xx} increases along the X axis, the compressive stress increases along the transverse axes and compression of the porous material occurs. Values Δx, Δy with increasing load were recorded after 1 min. Registration Δz was not possible due to the impossibility of direct measurement. Thus, from the system of Eq. (2) the unknowns are: Δz, E, μ, σ_{yy}, σ_{zz}. When considering a system of equations, the smallest range of values is taken by Poisson's ratio:

$$0 < \mu < 0.5$$

Let us express the Young modulus from the system of Eq. (2) for the first two equations, and then equal them:

$$\frac{x}{\Delta x}(\sigma_{xx} - \mu(\sigma_{yy} + \sigma_{zz}) = \frac{y}{\Delta y}(\sigma_{yy} - \mu(\sigma_{xx} + \sigma_{zz}) \tag{3}$$

and express from (3) Poisson's ratio:

$$\mu = \frac{\sigma_{xx} - \frac{\Delta xy}{x\Delta y}\sigma_{yy}}{\sigma_{zz} + \sigma_{yy} - \frac{\Delta xy}{x\Delta y}(\sigma_{xx} + \sigma_{zz})} \tag{4}$$

In the system of Eq. (2), when stretched along the X axis, Δy and Δz take negative values, Young modulus E takes only positive values, and therefore satisfies the condition: $E > 0$, then the stress values satisfy the following conditions:

$$\begin{cases} \sigma_{xx} \in \mathbb{R} | \sigma_{xx} > 0 \\ \sigma_{yy} \in \mathbb{R} | -\sigma_{xx} < 0 \\ \sigma_{zz} \in \mathbb{R} | -\sigma_{xx} < 0 \end{cases}$$

To calculate Young modulus and Poisson's ratio, we introduce an additional variable characterizing the load number and sign it "j". Then the Young modulus and Poisson's ratio will be constant regardless of the applied stress to the sample along the X axis. The transverse stress modulus, as well as the load, increases, then the condition for the values of $E, \sigma_{xx}, \sigma_{yy}, \sigma_{zz}$ and μ will take the following form:

$$\begin{cases} E_1 = ... = E_j = const \\ \mu_1 = ... = \mu_j = const \\ \sigma_{xx1} < ... < \sigma_{xxj} \\ \sigma_{yy1} > ... > \sigma_{yyj} \\ \sigma_{zz1} > ... > \sigma_{zzj} \end{cases} \tag{5}$$

The result of the conditions satisfying (5) is: $E = 4.5$ kPa and $\mu = 0.454$.

2.3 Methodology for Assessing Experimental Stresses

From the values of the elastic constants presented above, it is clear that the skeleton (Fig. 3), made of polyurethane with a porosity of 0.98, has a Young modulus 3 orders of magnitude less than a solid body made of the same material and has a lower ratio of lateral to axial deformation.

To study the stress–strain state of cement, a pre-applied mesh was used. The X axis is directed along the cell, the Y axis is perpendicular to it. The video sequence

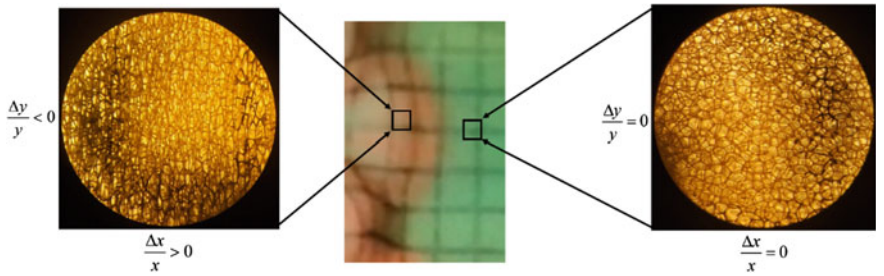


Fig. 3 Skeletal deformation (left) and its initial state (right) under a microscope

obtained during the experiment was divided into frames by using OpenCV library [11]. The first frame was selected, before the injection of the viscous liquid, and the frame preceding the destruction. For the area where the destruction of the skeleton occurred from the first and preceding frames, data on the coordinates of a 7×7 grid of cells was selected. The resulting matrices with coordinates were differentiated for X values along the X axis, for Y values along Y. The result for the matrices from the first frame is the lengths of the sides of the squares in the initial position along the X and Y axes—x_0, y_0. For the second matrix—deformations caused by filtration flow—x_i, y_i.

In the presented experiments, only the deformations along the X and Y axes and elastic constants are known from the system of Eq. (1). Considering that during the study the fluid flow acts along the X and Y axes, the stress created in the plane of the X and Y axes according to formula (1) will be equal to:

$$\sigma_{xy} = \frac{E}{1+\mu} u_{xy} \tag{6}$$

σ_{xy}—is the in-plane stress along the X and Y axes, u_{xy}—is the in-plane strain tensor along the X and Y axes, which, taking into account the obtained experimental data, will be equal to:

$$u_{xy} = \frac{1}{2}\left(\frac{x_i - x_0}{y_0} + \frac{y_i - y_0}{x_0}\right) \tag{7}$$

Substituting (7) into (6) it is clear that the stress in the plane of the X and Y axes depends only on the strain vectors along these axes, then the stresses along the X axis and along the Y axis will be projections of the stress modulus in the plane of the X and Y axes (6) and are equal:

$$\begin{aligned} \sigma_{xx} &= \left|\sigma_{xy}\right| \cos\alpha \\ \sigma_{yy} &= \left|\sigma_{xy}\right| \sin\alpha \end{aligned} \tag{8}$$

α is the angle between the X axis and the stress in the plane of the X and Y axes and is equal to:

$$\alpha = arctg \frac{u_{yy}}{u_{xx}} \tag{9}$$

u_{xx} and u_{yy} are the strain tensors along the X and Y axis and equal to:

$$u_{xx} = \frac{x_i - x_0}{x_0};\ u_{yy} = \frac{y_i - y_0}{y_0} \tag{10}$$

Considering that the numerical values of the strain tensors can have negative values, the angle will have the form:

$$\begin{array}{ll} \alpha & u_{xx} > 0 \\ \alpha + \pi & u_{xx} < 0 \text{ и } u_{yy} > 0 \\ \alpha - \pi & u_{xx} < 0 \text{ и } u_{yy} < 0 \\ \alpha - 2\pi & u_{xx} < 0 \text{ и } u_{yy} = 0 \end{array} \tag{11}$$

Let us substitute Eqs. (6), (7), (9) and (10) into (8). Then the stresses along the X and Y axes, taking into account conditions (11), will be found as:

$$\begin{aligned} \sigma_{xx} &= \left| \frac{E}{1+\mu} \frac{1}{2} \left(\frac{x_i - x_0}{y_0} + \frac{y_i - y_0}{x_0} \right) \right| \cos\left(arctg\left(\frac{(y_i - y_0)x_0}{y_0(x_i - x_0)} \right) \right) \\ \sigma_{yy} &= \left| \frac{E}{1+\mu} \frac{1}{2} \left(\frac{x_i - x_0}{y_0} + \frac{y_i - y_0}{x_0} \right) \right| \sin\left(arctg\left(\frac{(y_i - y_0)x_0}{y_0(x_i - x_0)} \right) \right) \end{aligned} \tag{12}$$

3 Experimental Results and Discussion

3.1 Experiment 1

An inclusion located at the edge of the "cement" (Fig. 4A) divides the filtration front in half. The cement begins to move, arching in its central parts between the inclusion and the "clastic material" along the edges of the cell along the X axis, and a compressed region of a parabolic profile is formed in front of the filtration front. Having passed along the inclusion, the filtration flow rushes into the pore space behind it, trying to bypass the compressed areas (Fig. 4B). Under the action of viscous stresses, the porous medium behind the inclusion is stretched along the X axis (Fig. 4C). At the boundary of the inclusion and cement, under the action of tensile stresses, the destruction of the porous skeleton occurs (Fig. 4D).

3.2 Experiment 2

The injected flow of viscous liquid, having reached the porous medium, penetrates into a depth of 0.2 cm and begins to move it (Fig. 5A). A compressed region is formed in front of the filtration front, which, having encountered the inclusion, begins to flow around it (Fig. 5B). A fixed and impenetrable inclusion, covering 50% of the channel width, divides the filtration front in half. Before the inclusion, an area is formed with a relative compression of up to 0.8 along the X-axis. The flow of a viscous liquid stretches the porous medium and forms a parabolic profile between the inclusion and impermeable debris along the edges of the cell. The filtration flow bypasses the

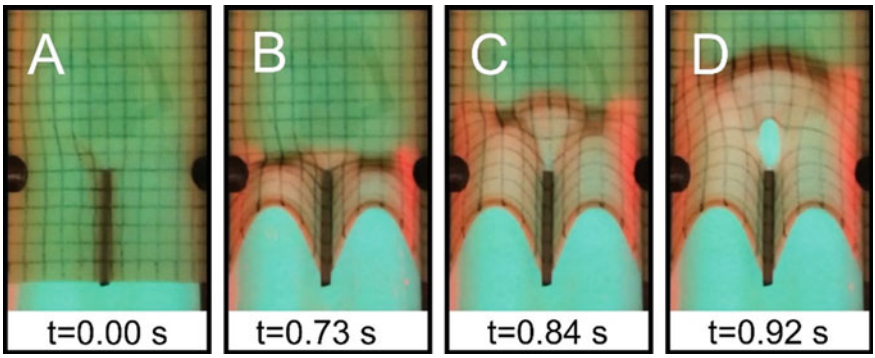


Fig. 4 Progress of experiment "A" (red light—filtration flow)

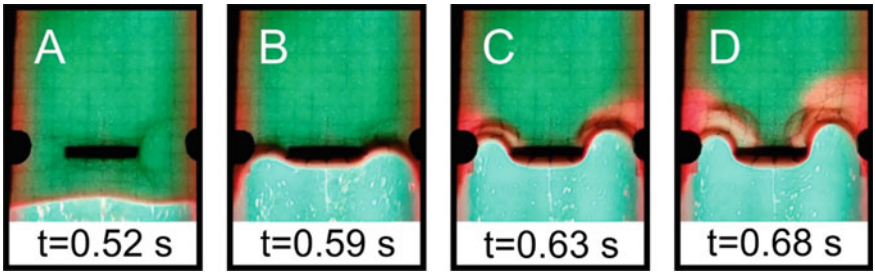


Fig. 5 Flow around the inclusion (red light—filtration flow)

compressed area along the clastic material and begins to fill the pore space of the cement along it (Fig. 5C). Having penetrated to a depth of 3 cm along the edge, the viscous liquid begins to fill the pore space of the cement behind the inclusion (Fig. 5D).

The divided filtration front behind the inclusion begins to move along the Y axis, trying to unite, it compresses the poroelastic material along the Y axis towards the center of the cell (Fig. 6A). By the time the filtration flows unite behind the inclusion, the liquid front moves another 3 cm deep into the cement along the X axis. Behind the inclusion, the filtration front, stretching the skeleton, rushes along the X axis and compresses along the Y axis (Fig. 6B). A new compressed area is formed in front of the filtration flow. At the interface between permeable cement and impermeable debris, failure occurs and the flow compresses the cement, creating a free space along the impermeable debris at the edge of the cell (Fig. 6C). The cement located behind the inclusion is stretched and destroyed under the stress of the filtration flow. The filtration flow continues to destroy the material along the edge of the cell (Fig. 6D).

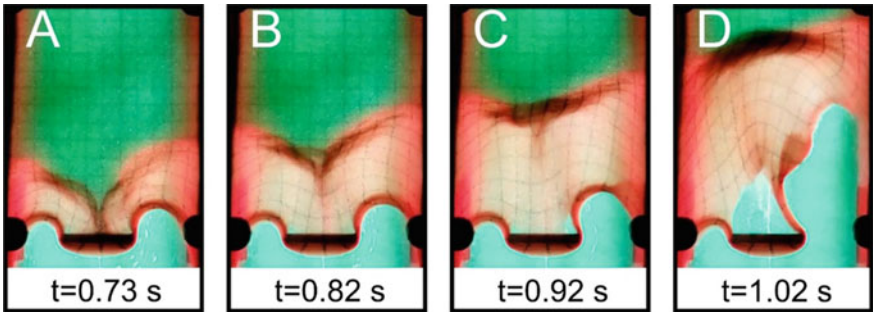


Fig. 6 Destruction of the porous skeleton (red light filtration flow)

3.3 Experiment 3

The course of the experiment with the inclusion of cement in the depths at the beginning of the filtration front moving deeper into the porous medium has a similar picture to experiment No. 1, the difference is: the absence of flow separation and a compressed area in front of the filtration front (Fig. 7A). The liquid penetrates deep into the porous medium and begins to move its edge along the X axis, which takes a parabolic shape with the apex in the center of the cell. Under the influence of filtration flow, the central part of the skeleton moves up to 6 cm along the X axis; on the left edge, at the boundary of permeable cement and impermeable clastic material, the cement begins to collapse (Fig. 7B) and the convex profile of the skeleton rotates clockwise by several degrees. After 0.03 s, destruction begins on the right edge. The compressed region in front of the filtration front, having reached the inclusion, tends to bypass it. The movement of the compressed region before switching on resembles the movement of a viscous fluid flowing around an inclusion. The stationary edge of the skeleton is tightened and the rate of destruction on the right-side increases, which leads to the rotation of the skeleton counterclockwise (Fig. 7C) and the rate of destruction is leveled off (Fig. 7D).

Compressed “cement” fills the space between the inclusion and the impervious debris at the edges (Fig. 8A). The destruction on the right side stops and the filtration flow accelerates along the left boundary (Fig. 8B), the destruction rate on the left side increases. The filtration flow advances the crack and, maintaining the filtration depth, destroys the porous material to the end (Fig. 8C).

3.4 Results

For each experiment, using the method presented above, the stress fields of the cement around the inclusion along the Y and X axes were calculated using formula (12). In the presented figures, in the central part there is a frame from which the stresses

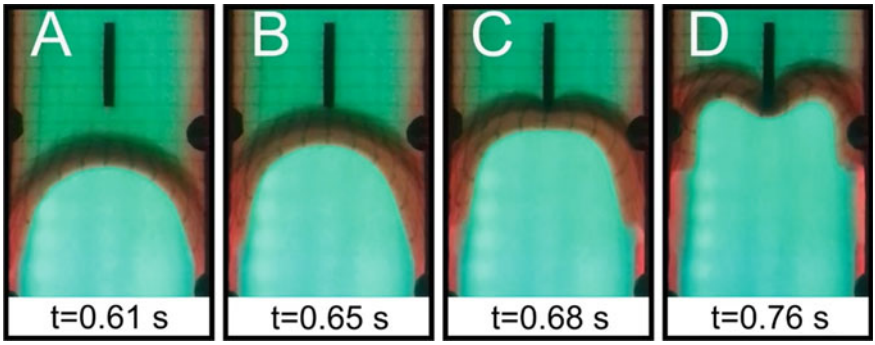


Fig. 7 Deformation of the free edge of the "cement"

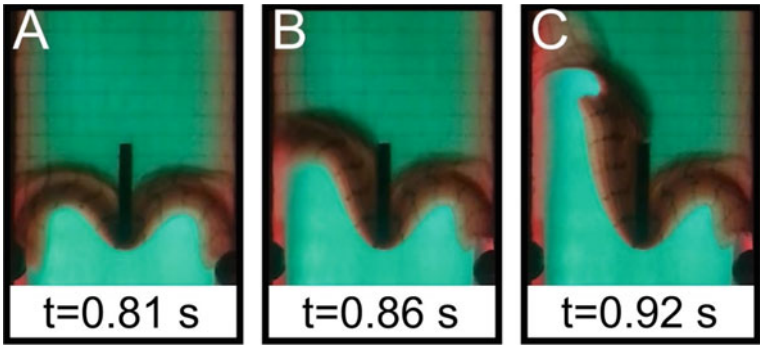


Fig. 8 Destruction of poroelastic material

were calculated, on the left side there is a stress field along the X axis, on the right side there is a stress field along the Y axis. For the experiment with an inclusion located along the injected flow, the stress was calculated behind the inclusion, before destruction cement (Fig. 9).

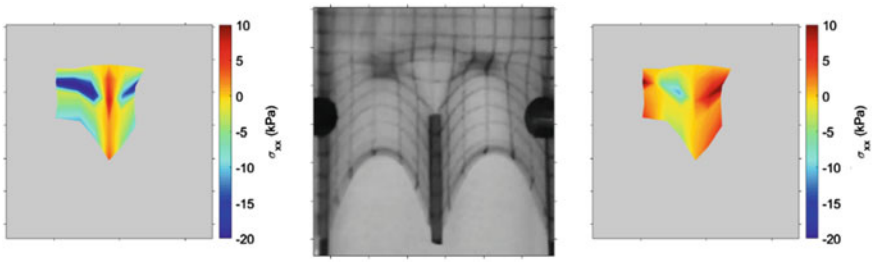


Fig. 9 Stresses with inclusion along the stream

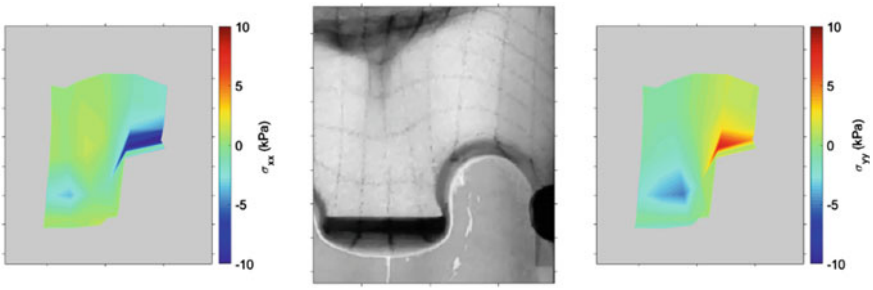


Fig. 10 Inclusion across the flow

For the experiment with an inclusion located across the injected flow, the stresses were calculated in the area of the right edge of the inclusion (Fig. 10). For a given inclusion location, the stress field has a negative sign.

For the experiment with an inclusion deep in the cement, the stresses were calculated before failure along the impermeable boundary (Fig. 11) and behind the inclusion, after completion of cement failure along the right side (Fig. 12). Before destruction along the impermeable boundary the stress has a negative sign, and behind the inclusion it has a positive sign.

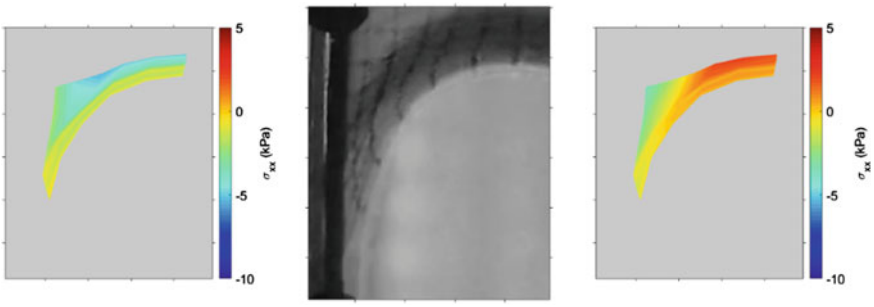


Fig. 11 Stresses at the edge of cement

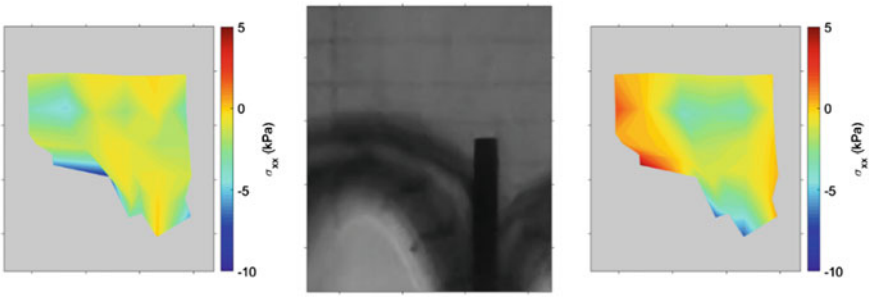


Fig. 12 Stresses behind inclusions deep in cement

4 Conclusion

In the presented model, when the fluid moves, deformations of the porous skeleton occur, leading to the appearance of a compressed region in front of the filtration front. Based on the patterns of changes in the position of the porous "cement," stress estimates around the inclusions were made.

Experiments have shown that inclusion location and absence can be divided into two groups. In the first group, the stresses along the flow are tensile; this group includes inclusions located along the direction of the flow. In the second group, the stresses along the flow are compressive and include inclusion across the injected flow or absence of inclusion. The results of this work may be useful for optimizing the method of hydraulic fracturing.

The work was carried out within the framework of the state assignment of the Ministry of Science and Higher Education of the Russian Federation (subject no. 122032900167-1)

References

1. B. A. Rychkov, I. V. Goncharova, N. M. Komartsov, M. A. Kulagina. Determination of the modulus of elasticity of rocks under complex loading // Bulletin of the Kyrgyz-Russian Slavic University. – 2020. – T. 20, No. 12. – P. 199–204.
2. Junqian Li. Quantitative evaluation on the elastic property of oil-bearing mudstone/shale from a Chinese continental basin / Li Junqian, Lu Shuangfang, Xue Haitao, Xie Liujuan and Zhang Pengfei // Energy exploration & exploitation. 2015. Vol. 33. N. 6. P. 851–868.
3. Kamenskikh, A. I. Calculation of effective moduli of elasticity of a quasi-isotropic medium with continuous spherical inclusions / A. I. Kamenskikh, G. B. Pigasov, A. I. Bychkov // Master's Journal. – 2016. – No. 2. – P. 104–108.
4. V. M. Samoilov, B. G. Ostronov The influence of grain sizes on the elastic modulus and strength of artificial graphites // Inorganic materials. – 2004. – T. 40, No. 4. – P. 425–429.
5. Koryukov, A. Yu. Petrographic study of rocks of the BT14 formation of the Russko-Rechenskoye field / A. Yu. Koryukov // Bulletin of Science. – 2022. – T. 1, No. 2(47). – pp. 163–165.

6. Koryukov, A. Yu. Petrographic study of rocks of the BT13 formation of the Russko-Rechenskoye field / A. Yu. Koryukov // Bulletin of Science. – 2022. – T. 1, No. 2(47). – pp. 159–162.
7. Torres T.M., Yudochkin N.A., Tairova A.A., Belyakov G.V. FILTRATION OF LIQUID IN AN ENVIRONMENT WITH VARIABLE PERMEABILITY. Dynamic processes in geospheres. 2022;14(2):52–61. https://doi.org/10.26006/29490995_2022_14_2_52.
8. D. G. Petrakov, G. M. Penkov, A. B. Zolotukhin Experimental study of the influence of rock pressure on the permeability of sandstone // Notes of the Mining Institute. – 2022. – T. 254. – P. 244–251. – DOI https://doi.org/10.31897/PMI.2022.24.
9. V. P. Grachev, A. S. Dzhalmukhanova, M. L. Bubnova / The influence of the rigidity of the polymer matrix on the photochemical transformations of photochromic compounds // High-molecular compounds. Series B. – 2020. – T. 62, No. 4. – P. 276–288. – DOI https://doi.org/10.31857/S230811392004004X.
10. Landau L. D., Lifshits E. M. Theoretical physics: Textbook. manual: For universities. In 10 volumes. T. VII. Theory of elasticity. - 5th ed., stereot. - M.: FISMAT LIT, 2003.-264 p.-ISB N 5-9221–0122-6 (T. VII).
11. Bradski, G. (2000) The OpenCV Library. Dr. Dobb's Journal of Software Tools. – 2000. – T. 120. – P. 122–125.

On the Possibility of Using the Lithosphere Relief to Estimate the Velocity at the Horizontal Upper Boundary of an Intensive Vortex in the Mantle Under the Eastern Part of the Mediterranean Sea



S. Yu. Kasyanov

Abstract The model problem of finding a stationary axisymmetric flow of an ideal fluid on the horizontal upper boundary of a cylindrical region at a known pressure set by the model relief of the lithosphere is considered. A smoothed axisymmetric model relief is used, reflecting the main features of the lithosphere relief of the eastern Mediterranean Sea. At a given pressure the radial distributions of velocity components describing stationary cyclonic circulation in an intra-mantle vortex which are determined by the model relief of the lithosphere are found from the solution of stationary equations of motion. The intramantium vortex is divided into an inner core and an outer part. The radial velocity in the vortex is continuous. The azimuthal velocity of the vortex undergoes discontinuities in areas of rapid elevation of the lithosphere relief with increasing radius. The azimuthal velocity discontinuities correspond to the position of the "wall" at the boundary of the outer part of the vortex with the inner core of the vortex and the presence of a "wall" inside the inner core of the vortex at the boundary of a narrow ring in which matter rotates even faster than in the "wall" at the boundary of the outer part of the vortex and the inner core of the vortex. The azimuthal velocity of the vortex increases sharply as it approaches from the periphery of the vortex to the "wall" of the outer part of the vortex and slowly increases as it approaches from the periphery of the vortex to the "wall" of a rapidly rotating narrow ring located inside the inner core of the vortex. In nature, at the "walls" inside and at the boundary of the inner core, an intense vortex formation with the dissipation of kinetic energy into heat should occur in an intra-mantle vortex. The latter leads to the appearance of zones of intense release of endogenous heat from the seabed into the water (mainly in the form of hot springs), which can affect the climate and the circulation of marine waters and be the cause of the observed abnormally rapid heating of the Mediterranean Sea.

S. Yu. Kasyanov (✉)
N.N.Zubov's State Oceanographic Institute, Roshydromet, Moscow, Russia
e-mail: skas53@yandex.ru

© The Author(s), under exclusive license to Springer Nature Switzerland AG 2024

V. Karev (ed.), *Proceedings of the 9th International Conference on Physical and Mathematical Modelling of Earth and Environmental Processes*, Springer Proceedings in Earth and Environmental Sciences, https://doi.org/10.1007/978-3-031-54589-4_52

Keywords Stationary axisymmetric flow · Ideal fluid · Lithospheric relief · Azimuthal velocity discontinuities · Intramantle vortex · Vortex core · Vortex formation · Dissipation of kinetic energy into heat · Endogenous heat release from the sea bottom into water · Hot springs · Anomalously fast heating of the Mediterranean Sea · Mediterranean Sea

1 Introduction. Formation of a System of Three Intense Large-Scale Vortices When the Satellite is Completely Buried in the Mantle

Earlier we proposed a hypothesis about the Earth's capture of a temporary satellite of the Earth and considered the geophysical consequences of orbital motion, deceleration and the satellite's sinking into the Earth's mantle [1–3]. At the final orbit turn when a partially submerged satellite was planning along the surface of the lithosphere and mantle before its final sinking a chain of "vortex half-rings" formed in the Earth's mantle similar to the vortices around the jet invading the liquid studied in experiments [4]. A chain of exits of "vortex half-rings" to the daytime surface is visible in the relief of the western Pacific Ocean [5]. When the satellite was completely submerged a vortex ring formed in the mantle [5, 6]. After the collapse of the vortex ring a quasi-stationary system of hot two-phase liquid–gas vortices formed in the mantle [6]. The main part of the energy of this system of hot vortices is contained in three large-scale vortices that make up the modern system of three energy-carrying vortices in the Earth's mantle. These are the vortices: (1) Himalayas + Tien Shan–Kolyma, (2) Kolyma–Yellowstone, (3) Yellowstone–Hudson Bay—the eastern part of the Mediterranean Sea [6] schematically presented in Fig. 1.

The modern system of three energy-carrying vortices in the Earth's mantle through the exit of the vortex (1) under the Himalayan-Tien Shan mountain ring is connected with a chain of exits of "vortex half-rings" to the daytime surface in the western Pacific Ocean [7].

The outlet of the intra-mantle vortex (3) to the daytime surface is located under the eastern part of the Mediterranean Sea. The motion of matter in this outlet of the intra-mantle vortex is cyclonic [6].

Previously, a one-dimensional diagnostic model was built that allows us to qualitatively assess the density, velocity and dependence of pressure on density in a vortex along a pre-selected circular current line [8]. In this paper, we will consider the qualitative and quantitative possibility of estimating the velocities of the motion of matter at the upper boundary of the intra-mantle vortex under the eastern part of the Mediterranean Sea. The simplest way to obtain such estimates is to solve the model problem of stationary axisymmetric motion of a homogeneous incompressible ideal fluid on a flat upper boundary of the vortex. In this case, the pressure distribution at the vortex boundary is assumed to be known and is determined by the hydrostatic pressure of the lithosphere and sea waters.

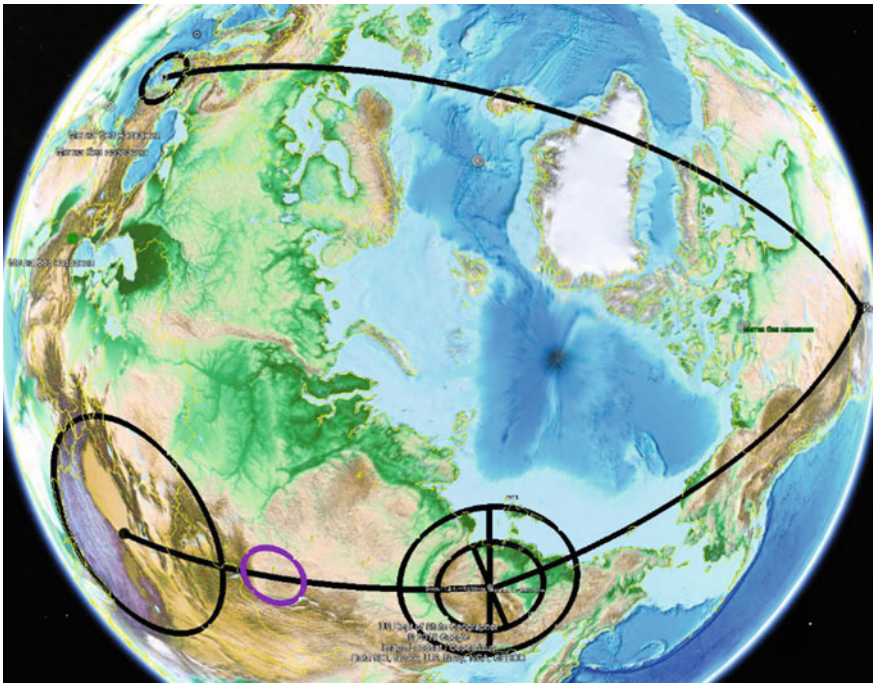


Fig. 1 A modern system of three energy-carrying vortices in the Earth's mantle Vortices: (1) Himalayas + Tien Shan–Kolyma, (2) Kolyma–Yellowstone, (3) Yellowstone–Hudson Bay–the eastern part of the Mediterranean Sea [6]

2 Construction of a Model Axisymmetric Relief for Solving a Model Axisymmetric Problem

To solve the axisymmetric model problem we will form some axisymmetric model relief reflecting the most important features of the lithosphere relief of the eastern Mediterranean Sea shown in Fig. 2.

Let us turn to Fig. 2. For the position of the epicenter of the intra-mantic vortex under the Mediterranean Sea in Fig. 2 point C is selected. As a basis for the formation of a model axisymmetric relief, we choose the relief of the lithosphere surface along the CE beam.

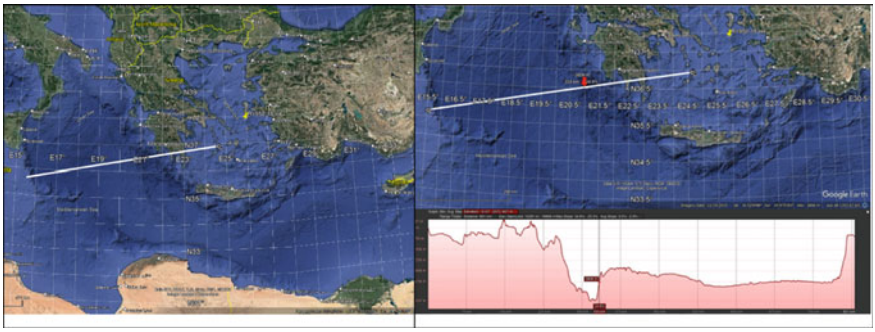


Fig. 2 Relief of the Mediterranean Sea. The choice of a beam as the basis for constructing a model relief for an axisymmetric problem. The CE beam is shown by a white line. Coordinates of point C—the epicenter of the intra-mantic vortex under the Mediterranean Sea: 36.950°N, 24.664°E. Coordinates of the end of the beam—point E: 35.685°N, 15.553°E. The right half of the figure shows the relief of the lithosphere of the Mediterranean Sea along the CE ray from the center to the periphery, that is, on the left the center of the vortex is point C, on the right the periphery is point E. The cartographic basis of Google Earth [9]

3 Algorithm for Constructing a Smoothed Model Relief of the Lithosphere

At the points of the CE beam with a step of 3257 m the averaged values of the GEBCO lithosphere relief array are calculated [10]. Averaging is carried out with a radius of 15/240 degrees of meridian (15 cells of the GEBCO array). Based on the calculated averaged values the spline interpolation is performed and the interpolated values are calculated in increments of 1 m. The smoothed model relief of the lithosphere of the Mediterranean Sea along the selected CE beam is shown in Fig. 3.

4 Formulation of a Model Axisymmetric Problem

The axisymmetric stationary motion of an ideal continuous medium is considered. The area of motion of a continuous medium is a round cylinder with a vertical axis and flat upper and lower boundaries. The area of motion of the continuous medium and its surrounding space rotates around the axis of the cylinder with a constant angular velocity Ω. At the upper boundary of the area of motion of the medium, the pressure distribution $p = p(r)$ is set unchanged in time.

Consider the equations of motion of a continuous medium on a flat horizontal upper boundary of a cylindrical region. The equations of unsteady axisymmetric motion of a homogeneous ideal incompressible fluid on a flat upper boundary of a cylindrical region have the form

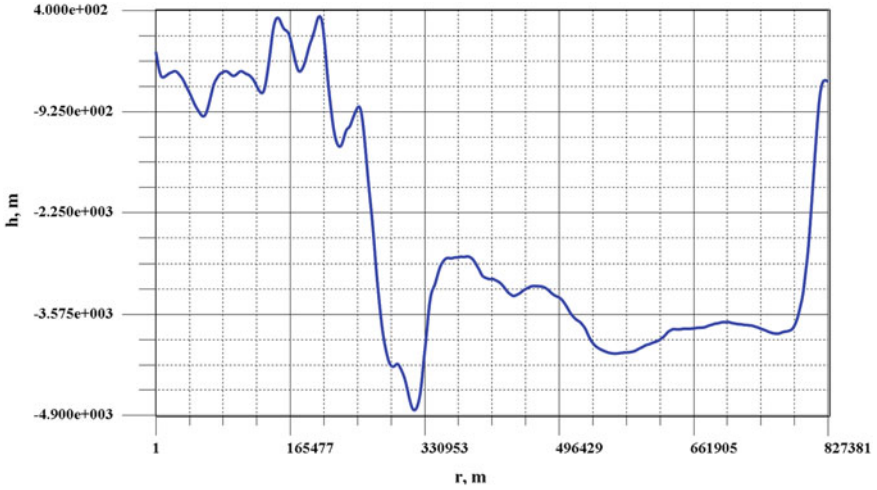


Fig. 3 Smoothed model relief of the lithosphere of the Mediterranean Sea along the selected CE beam

$$\frac{\partial V_r}{\partial t} + V_r \frac{\partial V_r}{\partial r} - \frac{V_\phi^2}{r} = -\frac{1}{\rho}\frac{\partial p}{\partial r} + 2\Omega V_\phi + \Omega^2 r \tag{1}$$

$$\frac{\partial V_\phi}{\partial t} + V_r \frac{\partial V_\phi}{\partial r} + \frac{V_r V_\phi}{r} = -2\Omega V_r \tag{2}$$

The system of two Eqs. (1) and (2) of the first order. Natural boundary conditions for $r = 0$ are $V_\phi = 0, V_r = 0$. Let's find the stationary states of this system of equations.

5 Equations of Stationary Axisymmetric Motion

$$V_r \frac{\partial V_r}{\partial r} - \frac{V_\phi^2}{r} = -\frac{1}{\rho}\frac{\partial p}{\partial r} + 2\Omega V_\phi + \Omega^2 r \tag{3}$$

$$V_r \frac{\partial V_\phi}{\partial r} + \frac{V_r V_\phi}{r} = -2\Omega V_r \tag{4}$$

From where it follows

$$\frac{1}{2}\frac{\partial V_r^2}{\partial r} = -\frac{1}{\rho}\frac{\partial p}{\partial r} + \frac{V_\phi^2}{r} + 2\Omega V_\phi + \Omega^2 r \tag{5}$$

$$V_r\left(\frac{\partial V_\phi}{\partial r}+\frac{V_\phi}{r}+2\Omega\right)=0 \tag{6}$$

The velocities V_r and V_ϕ can be found by integrating the system of Eqs. (3) and (6) at $V_r \neq 0$ and known pressure p.

The pressure is known in advance and is determined by the hydrostatic pressure of the lithosphere taking into account the pressure of the water column, so the continuity equation is not used to find the velocities V_r and V_ϕ. We will use the continuity equation only to estimate the direction of ascending and descending flows in the immediate vicinity of the upper boundary at which the velocities V_r and V_ϕ are estimated.

6 Special Cases

Note that for $V_r = 0$ Eq. (6) is satisfied for any V_ϕ.

If at $V_r = 0$ is the case $\frac{\partial p(r)}{\partial r} \geq 0$ then from Eq. (3) follows

$$V_\phi^2+2\Omega r V_\phi-\frac{r}{\rho}\frac{\partial p}{\partial r}+\Omega^2 r^2=0 \tag{7}$$

from where the two solutions for V_ϕ are finding

$$V_\phi=-\Omega r\pm\sqrt{\Omega^2 r^2+\frac{r}{\rho}\frac{\partial p}{\partial r}-\Omega^2 r^2}=-\Omega r\pm\sqrt{\frac{r}{\rho}\frac{\partial p}{\partial r}}. \tag{8}$$

Since the motion in the vortex is cyclonic, then in expression (8) we choose the plus sign. Thus, the azimuthal velocity V_ϕ undergoes a discontinuity in this case.

If at $V_r = 0$ is the case $\frac{\partial p(r)}{\partial r} < 0$ then Eq. (7) has no roots and it is impossible to find a stationary value of the azimuthal velocity V_ϕ from it. In this case

$$\frac{1}{2}\frac{\partial V_r^2}{\partial r}=-\frac{1}{\rho}\frac{\partial p}{\partial r}+\frac{V_\phi^2}{r}+2\Omega V_\phi+\Omega^2 r=-\frac{1}{\rho}\frac{\partial p}{\partial r}+\frac{1}{r}(V_\phi+\Omega r)^2>0.$$

Therefore when integrating along the radius of Eq. (5) the value $V_r^2(r)$ becomes positive. During integration a value $V_r^2(r)$ is calculated and the sign of the value $V_r(r)$ is chosen positive in accordance with the positive sign $\frac{\partial V_r}{\partial t}$ in Eq. (1).

Since, when integrating along the radius of Eq. (5) the value $V_r^2(r)$ becomes positive the condition $V_r \neq 0$ begins to be fulfilled. This allows us to find V_ϕ from (6) by means of integrating the equation

$$\frac{\partial V_\phi}{\partial r}+\frac{V_\phi}{r}+2\Omega=0. \tag{9}$$

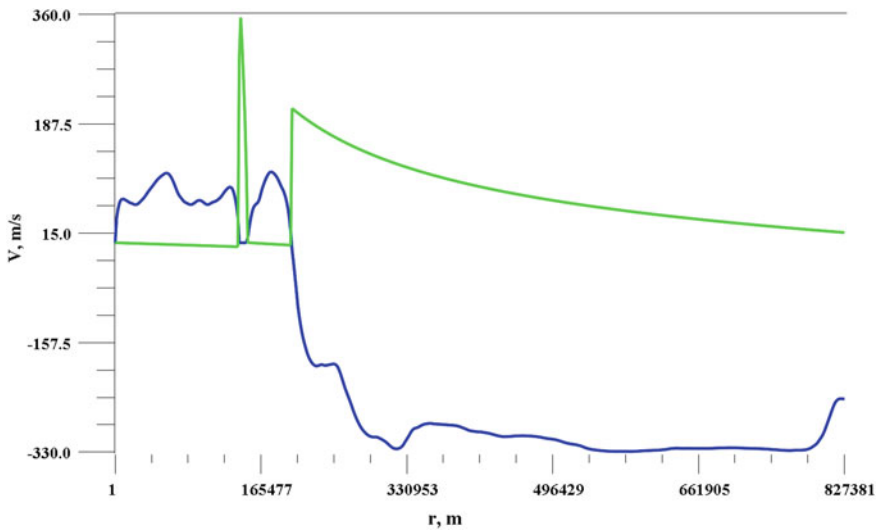


Fig. 4 Radial and azimuthal velocities of stationary axisymmetric motion. The blue curve is the radial velocity V_r, the green curve is the azimuthal velocity V_ϕ

7 The Result of Integrating the Equations of Motion

Taking into account the above special cases and natural boundary conditions $V_r = 0$, $V_\phi = 0$ for $r = 0$ the stationary equations of motion can be numerically integrated along the radius and the velocities V_r and V_ϕ on the radius dependences shown in Fig. 4 can be obtained.

In order to qualitatively imagine the spatial structure of the flow in a vortex we additionally involve the equation of continuity of an incompressible fluid in the axisymmetric case which was not used when finding velocities. From this equation according to the value of the derivative of the horizontal velocity presented in Fig. 5 at the upper boundary of the vortex motion region it is possible to qualitatively estimate the direction and relative intensity of vertical movements near the upper horizontal boundary of the vortex.

8 Conclusions

The model problem of finding a stationary axisymmetric flow of an ideal fluid on the horizontal upper boundary of a cylindrical region at a pressure constant in time, the distribution of which is given by the model relief of the lithosphere, is considered. A model axisymmetric relief is used, which reflects the main features of the lithosphere relief of the eastern Mediterranean Sea. The smoothed model axisymmetric relief

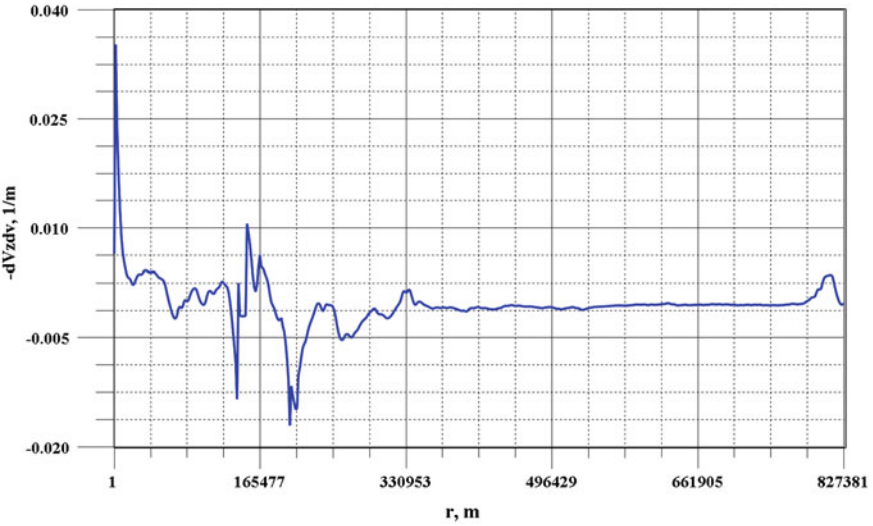


Fig. 5 The derivative of the horizontal velocity at the upper boundary of the vortex motion region (by virtue of the continuity equation it is equal to—dVz/dz, where Vz is the vertical velocity), reflecting the direction and relative intensity of vertical movements in the vicinity of the horizontal boundary

is constructed on the basis of data on the relief of the lithosphere of the eastern Mediterranean Sea.

With a pre-known pressure distribution, which is determined by a model axisymmetric smoothed relief of the lithosphere, a solution of the equations of motion describing a stationary cyclonic circulation in an intra-mantle vortex is found. The solution is determined by the smoothed model axisymmetric relief of the lithosphere and depends on smoothing. According to this decision, the intra-mantic vortex is divided into an inner core and an outer part.

The radial velocity of the vortex is continuous. The azimuthal velocity of the vortex undergoes discontinuities in areas of rapid elevation of the lithosphere relief with increasing radius. The azimuthal velocity discontinuities correspond to the position of the "wall" at the boundary of the outer part of the vortex with the inner core of the vortex and the presence of a "wall" inside the inner core of the vortex at the boundary of a narrow ring in which matter rotates even faster than in the "wall" at the boundary of the outer part of the vortex and the inner core of the vortex. The azimuthal velocity of the vortex increases sharply as it approaches from the periphery of the vortex to the "wall" of the outer part of the vortex and slowly increases as it approaches from the side of the vortex periphery to the "wall" of a rapidly rotating narrow ring located inside the inner core of the vortex.

The azimuthal velocity discontinuities inside the inner core of the vortex and at the "wall" of the inner core of the vortex are tangential discontinuities and may be unstable. At the "walls" inside and at the boundary of the inner core of the vortex,

intense vortex formation should occur with the dissipation of kinetic energy into heat. The latter leads to the appearance of local zones of intensive release of endogenous heat from the bottom into the water (mainly in the form of hot springs), which can affect the climate and the circulation of marine waters and be the cause of the observed abnormally rapid heating of the Mediterranean Sea.

References

1. Kasyanov S.Yu. Modeling of the orbital motion of a large asteroid during a descent with a deepening into the lithosphere and mantle of the Earth // Physical problems of ecology (ecological physics). 2012. No. 18. pp. 151–164. http://ocean.phys.msu.ru/pubs/ecophys/ecophys-18_pp150-246.pdf
2. Kasyanov S.Yu., Samsonov V.A. Estimation of tidal wave heights during planing of a large satellite on the surface of a liquid attracting spherical layer with a solid core // Proceedings of MIPT. 2017. Vol. 9, No. 3. pp. 14–20. (In Russian). https://mipt.ru/upload/medialibrary/d1a/2_kas_yanov_14_20.pdf
3. Kasyanov S, Samsonov V (2018) Effect of a tidal wave caused by large gliding satellite on formation of 220 km seismic boundary and split of the mantle into blocks. In: Karev V, Klimov D, Pokazeev K (eds) Physical and mathematical modeling of earth and environment processes. PMMEEP 2017. Springer Geology. Springer, Cham, pp 360–370. First Online 25 March 2018.https://doi.org/10.1007/978-3-319-77788-7_37. Print ISBN 978-3-319-77787-0, Online ISBN 978-3-319-77788-7
4. Gharib M, Rambod E, Shariff K (1998) A universal time scale for vortex ring formation. J Fluid Mech 360:121–140
5. Kasyanov, S.Y. (2021). Formation of System of Intense Vortices in the Mantle When a Large Temporary Earth Satellite is Immersed. In: Chaplina, T. (eds) Processes in GeoMedia—Volume III. Springer Geology. Springer, Cham. pp 217–232. https://doi.org/10.1007/978-3-030-69040-3_21
6. Kasyanov, S.Y., Samsonov, V.A. (2021). About the Modern System of Three Energy-Carrying Intensive Vortices in the Earth's Mantle. In: Chaplina, T. (eds) Processes in GeoMedia - Volume II. Springer Geology. Springer, Cham. pp 273–291. https://doi.org/10.1007/978-3-030-53521-6_31
7. Kasyanov S.Yu. (2023) Hydrodynamic interaction between two systems of intense intra-mantle vortices as a possible cause of the connection between distant earthquakes. In: Chaplina, T. Chaplina (eds) Processes in GeoMedia — Volume VII, pp 159–169, Springer Geology, https://doi.org/10.1007/978-981-99-6575-5_15
8. Kasyanov, S.Yu. (2022). On the Possibility of Use the Himalayan-Tien Shan Mountain Ring Relief to Assess the State of the Substance at the Boundary of Intense Vortex in the Underlying Mantle. In: Chaplina, T. (eds) Processes in GeoMedia—Volume IV. Springer Geology. Springer, Cham, pp 99–107. https://doi.org/10.1007/978-3-030-76328-2_11
9. Google Earth Pro. https://www.google.com/earth/about/versions/#download-pro
10. https://download.gebco.net/

Effect of Bottom Geometry on Surface Waves in a Vertical Circular Cylinder



S. V. Nesterov and V. A. Kalinichenko

Abstract In the approximation of long waves, the problem of standing waves in a circular cylindrical vessel with a rise at the bottom is formulated and numerically solved using the algorithm of accelerated convergence. As a result of the calculations, the natural frequency of the main wave mode was determined with high accuracy. To compare theoretical results, new experimental data on the excitation of standing surface gravity waves in a circular cylindrical vessel with parabolic and conical elevations at the bottom are presented. The coincidence of the calculated and measured values of the natural frequency of the fundamental wave mode in vessels with a profiled bottom is shown.

Keywords Standing surface waves · Circular cylindrical vessel · Natural frequency · Long wave approximation · Accelerated convergence method

1 Introduction

When considering the wave motions of a liquid with a free surface in vessels of arbitrary shape, one of the hydrodynamic problems is to determine the natural frequencies of oscillations. In classical works [1, 2], the case of fluid oscillations in a circular cylindrical vessel with a horizontal bottom was considered. In the middle of the last century, a large number of works were published in which the natural frequencies and modes of vibration of a liquid in a circular cylinder with a conical, parabolic and spherical bottom were determined—see, for example, [3–6]. This area of research, carried out mainly by variational methods, is related to the needs of space technology—calculation of fuel oscillations in tanks. Note that the authors of [3–6] attached special importance to the main wave mode, which has one diametrical nodal line.

S. V. Nesterov · V. A. Kalinichenko (✉)
Ishlinsky Institute for Problems in Mechanics, Russian Academy of Sciences, Moscow 119526, Russian Federation
e-mail: vakalin@mail.ru

© The Author(s), under exclusive license to Springer Nature Switzerland AG 2024

V. Karev (ed.), *Proceedings of the 9th International Conference on Physical and Mathematical Modelling of Earth and Environmental Processes*, Springer Proceedings in Earth and Environmental Sciences, https://doi.org/10.1007/978-3-031-54589-4_53

In the approximation of the theory of long waves, in [2] the problem of standing waves (seiches) in a circular cylinder is considered when the depth of the liquid decreases from the axis of the vessel to the walls according to a parabolic law. The specified geometry of the bottom of the vessel was used in [7, 8] to obtain isochronous oscillations of the liquid, in which the frequency of the waves (similar to the Huygens pendulum) does not depend on the amplitude.

This paper examines the influence of an elevation at the bottom of a circular cylinder on the natural frequencies of lower wave modes on the free surface of a liquid. All quantitative estimates were obtained by the accelerated convergence method in the shallow water approximation. The results of the theoretical model and laboratory experiment are compared. Note that the accelerated convergence method [9] was successfully tested by the authors in [10–12] for seiches in rectangular vessels with variable depth and width.

2 Waves in a Circular Cylindrical Vessel

The solution to the problem of gravitational waves on the free surface of an ideal incompressible fluid in a rigid circular cylinder of radius R_0 with a horizontal bottom is given in many publications, for example, [4–6]. The velocity potential $\phi(r, \varphi, \mathrm{z,t})$ and free surface displacement $\eta(r, \varphi, \mathrm{t})$ are determined by the following expressions

$$\phi(r, \varphi, \mathrm{z,t}) = [\alpha_{nm} \cos n\varphi + \beta_{nm} \sin n\varphi] J_n(k_{nm} r) \frac{\mathrm{ch}(k_{nm}(z+h))}{\mathrm{ch}(k_{nm}h)}$$

$$\eta(r, \varphi, \mathrm{t}) = [A_{nm} \cos n\varphi + B_{nm} \sin n\varphi] J_n(k_{nm} r) cos\omega_{nm} t \quad (n = 0,\ 1, ...,\ m = 1, 2...) \tag{1}$$

where (r, φ, z) are the cylindrical coordinates, z measured vertically upward from the undisturbed surface of the liquid; h—liquid depth; $J_n(k_{nm} r)$—Bessel function; α_{nm}, β_{nm}—time-dependent coefficients that can be expressed through harmonic functions $\sin \omega_{nm} t$.

The expression for the natural frequency is

$$\omega_{nm} = \sqrt{g k_{nm} \mathrm{th}(k_{nm} h)} \tag{2}$$

Using the boundary condition on the walls of the vessel $\partial\phi / \partial r|_{r=R_0} = J_n'(k_{nm} R_0) = 0$, for the first two axisymmetric modes we obtain $k_{01} R_0 = 3.832$ and $k_{02} R_0 = 7.015$, and for asymmetric modes—$k_{11} R_0 = 1.841$ and $k_{12} R_0 = 5.335$.

The wave profiles of maximum development calculated using (1) for axisymmetric (0, 1), (0, 2) and asymmetric modes (1, 1) and (1, 2) are shown in Fig. 1. The calculation was carried out for a vessel with a radius of $R_0 = 9.8$ cm with a liquid depth of $h = 4$ cm and $A_{nm} = 3$ cm, $B_{nm} = 0$.

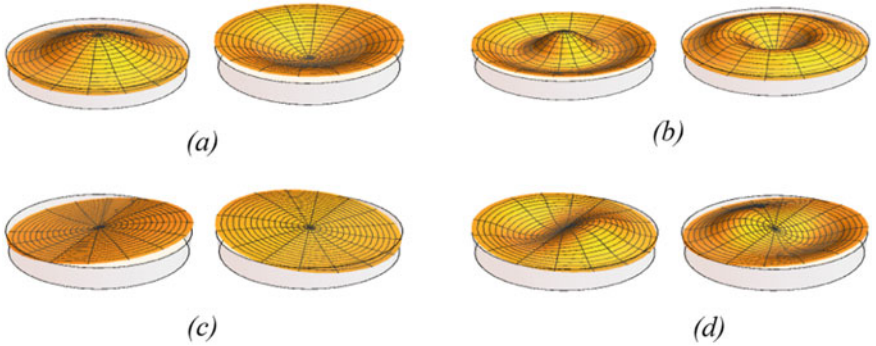


Fig. 1 Profiles of waves of maximum development for axisymmetric and asymmetric modes at $t = 0$, π/ω ($A_{nm} = 3$ cm, $B_{nm} = 0$; $R_0 = 9.8$ cm; $h = 4$ cm): (*a–d*)—(01), (0, 2), (1, 1) и (1, 2)

Consider the case where the depth of the pool $H = H_0\, f(r/R_0)$ depends on the distance measured from the center of the pool. Let us denote by $\eta = \eta(x, y, t)$ the elevation of the free surface above the level of the fluid at rest.

According to [2], the displacement of the free surface satisfies the differential equation

$$\frac{\partial^2 \eta}{\partial t^2} = g\left[\frac{\partial}{\partial x}\left(H\frac{\partial \eta}{\partial x}\right) + \frac{\partial}{\partial y}\left(H\frac{\partial \eta}{\partial y}\right)\right] \tag{3}$$

where g is the gravity acceleration.

Since waves represent time-periodic movements of the free surface, we will look for a solution to Eq. (3) in the form

$$\eta = u(x, y)e^{i\omega t} \tag{4}$$

After substituting (4) into Eq. (3) we obtain

$$\frac{\partial}{\partial x}\left(H\frac{\partial u}{\partial x}\right) + \frac{\partial}{\partial y}\left(H\frac{\partial u}{\partial y}\right) + \frac{\omega^2}{g}u = 0 \tag{5}$$

Using polar coordinates (r, φ), we get

$$\frac{1}{r}\frac{\partial}{\partial r}\left(Hr\frac{\partial u}{\partial r}\right) + \frac{1}{r^2}H\frac{\partial^2 u}{\partial \varphi^2} + \frac{\omega^2}{g}u = 0$$

We assume that $u = U_m(r)\begin{Bmatrix}\cos n\varphi \\ \sin n\varphi\end{Bmatrix}$, where n is an integer. The function $U(r)$ is subject to the following boundary conditions

$$|U_m(0)| \le M; \quad \left.\frac{dU_m}{dr}\right|_{r=R_0} = 0$$

Using the dimensionless variable $z = r/R_0$, we obtain the following Sturm–Liouville problem

$$\frac{d}{dz}\left(z\, f(z)\frac{dU_m}{dz}\right) + (\lambda\, z - \frac{n^2}{z} f(z))U_m = 0 \tag{6}$$

where $n = 0, 1, 2, ...,\ \lambda_{n,m} = \omega^2 R_0^2/(g H_0)$.

It is required to find eigenvalues $\lambda_{n,m}$ for which there are nontrivial solutions to Eq. (6) that satisfy the boundary conditions

$$|U_m(0)| \le M; \quad U_m'(1) = 0 \tag{7}$$

To solve the boundary value problem (6), (7), we introduce a regularizing parameter a

$$\left.\begin{array}{l} \dfrac{d}{dz}\left[(z+a)\, f(z)\dfrac{dU_m}{dz}\right] + (\lambda\, z - \dfrac{n^2}{z+a} f(z))U_m = 0 \\ |U_m(0)| \le M; \quad U_m' = 0 \end{array}\right\} \tag{8}$$

To find $\lambda_{n,m}$, the accelerated convergence method [9] is used. If the eigenvalues are found, then the dimensional natural frequencies of oscillations are determined by the formula

$$\omega_{n,m} = \frac{\sqrt{\lambda_{n,m}}}{R_0}\sqrt{g H_0}$$

All calculations are carried out under the assumption that the depth of the pool is given by expressions

$$f(z) = \begin{cases} 1 + b\, z^2 \\ 1 + b\, z \end{cases}$$

These bottom forms of the pool (paraboloid or cone) are quite simple to implement under experimental conditions.

Figure 2 shows the dependence of the dimensionless natural frequency $\sqrt{\lambda_{0,1}}$, $\sqrt{\lambda_{0,2}}$, $\sqrt{\lambda_{1,1}}$ and $\sqrt{\lambda_{1,2}}$ on the parameter b. The corresponding wave profiles for $b = 0$ see in Fig. 1. One can see from Fig. 2 that the dimensionless natural frequencies $\sqrt{\lambda_{n,m}}$ of symmetric and asymmetric wave modes increase monotonically with increasing parameter b, which characterizes the elevation at the bottom of the vessel,.

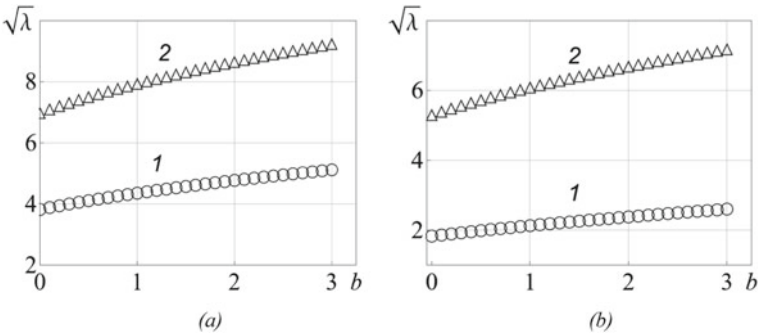


Fig. 2 Dependences of dimensionless natural frequencies on the parameter b: **a** axisymmetric wave modes $\sqrt{\lambda_{0,1}}$ (1) and $\sqrt{\lambda_{0,2}}$ (2); **b** asymmetric wave modes $\sqrt{\lambda_{1,1}}$ (1) and $\sqrt{\lambda_{1,2}}$ (2)

3 Experimental Verification of the Numerical–Analytical Model

In experiments, wave motions were studied under conditions of main and harmonic Faraday resonances [13, 14]. In the first case, for mode (1, 1), the frequency of vertical oscillations of the vessel was twice the frequency of the excited waves ($\Omega \sim 2\omega$); at harmonic resonance for mode (0, 1), these frequencies coincided ($\Omega \sim \omega$). At a fixed amplitude of the vessel $s = 0.7$ cm, variations Ω ensured the excitation of the corresponding wave mode (n, m). Water was used as the working fluid.

The wave pattern was recorded by a Canon PowerShot SX50HS digital camera (video recording speed 30 and 120 fps). The video image resolution was 0.15 mm/pixel. Subsequent processing of video frames was carried out using the ImageJ program. All experiments were carried out at room temperature 21–22 °C.

In the experiments, the natural frequency of gravitational waves was determined as follows. At one of the resonant frequencies Ω of the vessel oscillations, a wave mode (n, m) was excited. Then the vibration stand was turned off, and after the vessel had completely stopped (a time on the order of the wave period), video recording of the process of attenuation of the wave movements of water was carried out. Since the frequency of the waves significantly exceeds the attenuation coefficient, it was assumed that the process of wave attenuation occurs with its own frequency. This made it possible to estimate the natural frequency based on video recordings of damped waves.

The experiments used two vessels with radii $R_0 = 7$ and 9.8 cm at a water depth of $h = 3.7$ and 4 cm, respectively. The natural frequency of wave modes (0.1) and (1.1) in vessels with horizontal and profiled bottoms was estimated.

The profiled bottom was an elevation symmetrical relative to the axis of the vessel, made of technical plasticine. The bottom profiles were digitized by the ImageJ program, the data of which made it possible to obtain the following approximating dependencies

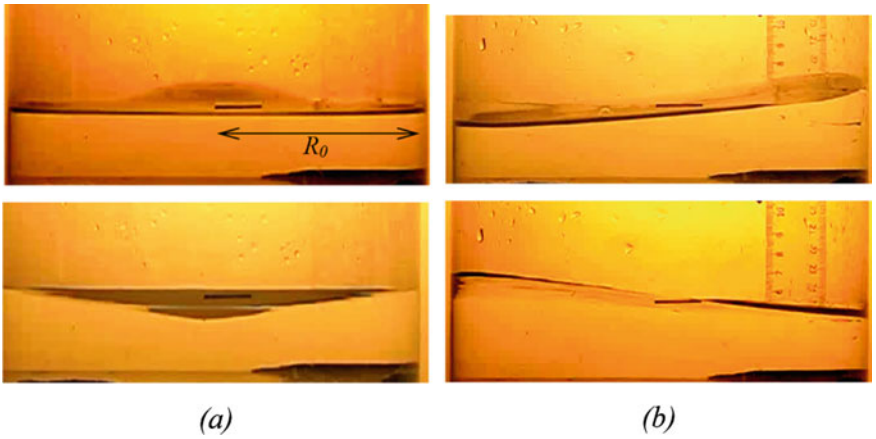


Fig. 3 Profiles of waves of maximum development in a circular cylinder of radius $R_0 = 9.8$ cm with a horizontal bottom at a liquid depth of $h = 4$ cm: **a**, **b** axisymmetric (0, 1) and asymmetric (1, 1) wave modes

$y = 2.66 - 0.05\,r^2$ at $R_0 = 7$ cm and $y = 1.45 - 0.15\,r$ at $R_0 = 9.8$ cm.

The natural frequencies of the (0, 1) and (1, 1) wave modes in vessels with a horizontal bottom were experimentally estimated. Photos of wave profiles in the case of a vessel with radius $R_0 = 9.8$ cm are presented in Fig. 3. One can see their complete correspondence with the shapes in Fig. 1 a and c. The natural frequencies of waves in vessels with a horizontal bottom, measured using the method described above, are given in Table. 1.

Table 1 Natural frequencies of wave modes in vessels with horizontal and profiled bottoms

$R_0 = 7$ cm, $h = 3.7$ cm						
Horizontal bottom				Profiled bottom		
Mode (n, m)	$\omega_{nm}(\mathrm{s}^{-1})$ experiment	$\omega_{nm}(\mathrm{s}^{-1})$ calculation		Mode (n, m)	$\omega_{nm}(\mathrm{s}^{-1})$ experiment	$\omega_{nm}(\mathrm{s}^{-1})$ calculation BVP (1.8)
		Equation (2)	BVP (1.8)			
(0, 1)	22.60 ± 0.99	22.72	22.76	(0, 1)	20.92 ± 1.85	22.75
(1, 1)	13.84 ± 0.23	13.96	13.90	(1, 1)	11.73 ± 0.72	11.43
$R_0 = 9.8$ cm, $h = 4$ cm						
Horizontal bottom				Profiled bottom		
Mode (n, m)	**$\omega_{nm}(\mathrm{s}^{-1})$ experiment**	**$\omega_{nm}(\mathrm{s}^{-1})$ calculation**		**Mode (n, m)**	**$\omega_{nm}(\mathrm{s}^{-1})$ experiment**	**$\omega_{nm}(\mathrm{s}^{-1})$ calculation BVP (1.8)**
		Equation (2)	BVP (1.8)			
(0, 1)	19.22 ± 0.65	18.82	18.74	(0,1)	18.20 ± 0.35	22.21
(1, 1)	11.03 ± 0.54	10.82	10.82	(1,1)	10.20 ± 0.50	10.75

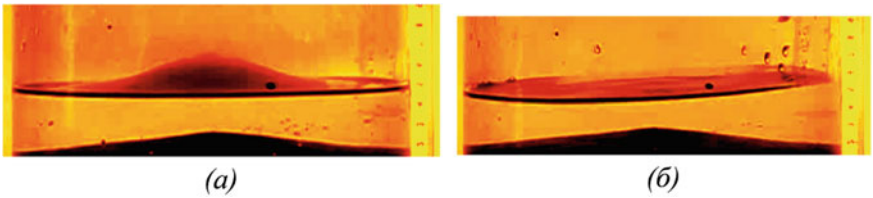


Fig. 4 Profiles of waves of maximum development in a circular cylinder of radius $R_0 = 9.8$ cm with a conical elevation at the bottom at a maximum liquid depth of 4 cm: **a**, **b** axisymmetric (0, 1) and asymmetric (1, 1) wave modes

Let us consider the wave motions of liquid in circular cylinders with a profiled bottom. Photographs of the wave modes (0, 1) and (1, 1) in the case of a vessel with radius $R_0 = 9.8$ cm are presented in Fig. 4. Visually, these profiles do not differ from those shown in Fig. 3. However, natural frequencies, as follows from Table 1, significantly lower than the values corresponding to a vessel with a horizontal bottom—a decrease in frequency of the order of 10–15%.

Below we interpret the experimental results on the decrease in natural frequencies of the wave mode (1, 1) in vessels with a bottom elevation within the framework of the shallow water model—BVP (8).

A vessel of radius $R_0 = 7$ cm had a bottom profile $y = 2.66 - 0.05\,r^2$ that corresponded to the liquid depth $H = 1.0122(1 + 2.6553z^2)$. The calculated dimensionless frequency of the (1, 1) wave mode is $\sqrt{\lambda_{1,1}} = 2.54037$. The corresponding dimensional frequency is $\omega_{1,1} = = 11.43\ \mathrm{s}^{-1}$. The natural frequency of the wave mode (1,1) measured in experiment (Table 1) is equal to $\omega_{1,1} = 11.73\ \mathrm{s}^{-1}$. Thus, the difference between the experimental data and numerical estimates is 2.6%.

The vessel of radius $R_0 = 9.8$ cm had a bottom profile $y = 1.45 - 0.15\,r$, which corresponded to a liquid depth of $H = 2.5488(1 + 0.4694z)$, $H_0 = 2.5488$. The calculated dimensionless frequency of the (1, 1) wave mode is $\sqrt{\lambda_{1,1}} = 2.1078$. The corresponding dimensional frequency is $\omega_{1,1} = 10.75\ \mathrm{s}^{-1}$. The natural frequency of the wave mode (1, 1) measured in the experiment (see Table 1) is $\omega_{1,1} = 10.20\ \mathrm{s}^{-1}$. Thus, the difference between the experimental data and numerical estimates is 5.3%.

Thus, presented in Sect. 1 numerical-analytical model describes well the experimental results of measuring the natural frequencies of standing surface gravitational waves in the case of a wave with one nodal line passing through the center of the vessel—wave mode (1, 1), Figs. 1c and 4b. This wave corresponds to a dimensionless natural frequency $\sqrt{\lambda_{1,1}}$. In addition, for the wave mode (1, 1), the requirement of the long-wave theory is satisfied quite well. Note that in the experiments carried out, waves with frequencies $\sqrt{\lambda_{0,1}}$, $\sqrt{\lambda_{0,2}}$, $\sqrt{\lambda_{1,2}}$ etc. no longer satisfy the long-wave approximation ($k_{nm}h < 1$). Therefore, the measured and calculated natural frequencies of the (0, 1) modes coincide much worse compared to the case of the (1, 1) mode—see Table 1.

4 Concluding Remarks

In the long-wave approximation, the problem of standing waves in a circular cylindrical vessel of variable depth is formulated and numerically solved using an accelerated convergence algorithm. As a result of the calculations, the natural frequency of the main wave mode was determined with high accuracy.

To compare theoretical results, new experimental data on the excitation of standing surface gravity waves in a circular cylindrical vessel with parabolic and conical elevations at the bottom are presented. The coincidence of the calculated and measured values of the natural frequency of the fundamental wave mode in vessels with a profiled bottom is shown.

Experimental confirmation of the effect of the bottom elevation on the frequency of the fundamental mode in a circular cylinder was obtained.

Acknowledgements This study was partially supported by the Government programs ## 123021700050-1 and 123021700044-1.

References

1. *Rayleigh L* (1876) On waves: Lond. Edinb. Dublin Philos. Mag. J. Sci. 1(4): 257–279. doi: https://doi.org/10.1080/14786447608639037.
2. *Lamb H* (1932) Hydrodynamics: Cambridge: Univ. Press.
3. *H R, Wang C J, Reddy RB* (1958) Variational solution of fuel sloshing modes: J Jet Propuls. 28(11): 729–736. doi:https://doi.org/10.2514/8.7443.
4. *Moiseev NN., Petrov AA.* (1966) The calculation of free oscillations of a liquid in a motionless container: Adv. Appl. Mech. 9: 91–154. doi:https://doi.org/10.1016/s0065-2156(08)70007-3.
5. *Abramson HN* (1966) The Dynamic behavior of liquids in moving containers: NASA SP-106.
6. *Ibrahim RA* (2005) Liquid sloshing dynamics: theory and applications: Cambridge Univ. Press 948 p.
7. *Kalashnik MV, Kakhiani VO, Lominadze DG, Patarashvili KI, Svirkunov PN, Tsakadze SD* (2004) Nonlinear isochronous oscillations of a fluid in a paraboloid: theory and experiment: Fluid Dyn 39: 790–800. doi:https://doi.org/10.1007/s10697-005-0013-8.
8. *Weidman P* (2016) New axisymmetric containers for isochronous sloshing: a tribute to B. Andreas Troesch: Inverse Probl. Sci. 24(7): 1240–1248 doi: https://doi.org/10.1080/17415977.2016.1160394.
9. *Akulenko LD, Nesterov SV* (2005) High-precision methods in eigenvalue problems and their applications: Boca Raton: CRC Press 255 p.
10. *Akulenko LD, Kalinichenko VA, Nesterov SV* (2012) Seiches in a channel with a sharp variation in the bottom relief: Fluid Dyn 47(3): 387–394. doi: https://doi.org/10.1134/S00154628120 3012X.
11. *Kalinichenko VA, Nesterov SV, Soe AN* (2017) Standing surface waves in a rectangular tank with local wall and bottom irregularities: Fluid Dyn 52(2): 230–238. doi:https://doi.org/10.1134/S0015462817020077.
12. *Nesterov SV* (2022) Natural frequencies and seiche forms in a channel with varying depth: Fluid Dyn 57: 887–890 doi: https://doi.org/10.1134/S0015462822070084.
13. *Kalinichenko VA, Nesterov SV, Sekerzh-Zen'kovich SYa, Chaykovskii AA* (1995) Experimental study of surface waves with Faraday resonance excitation: Fluid Dyn 30(1): 101–106.

14. *Kalinichenko VA, Kravtsov AV, Rodriguez-Mijangos R, Sekerzh-Zen'kovich SY, Flores-Espinoza R* (2000) Harmonic instability of the free surface of a low-viscosity liquid in a vertically oscillating vessel: J. Appl. Maths. Mechs. 64(2): 275–282. doi: https://doi.org/10.1016/S0021-8928(00)00049-6.

Wind Wave Regime in the Alupka Area



V. V. Fomin, A. A. Polozok, and I. N. Fomina

Abstract In this work, on the basis of mathematical modeling, the regime characteristics of wind waves in the area of the city of Alupka (Black Sea, southern coast of Crimea) are studied. To assess the statistical characteristics of waves in the coastal zone of the study area, we used data from retrospective calculations of wind waves in the Black Sea over a long period, obtained using the SWAN spectral model. The initial wind fields are presented by data from global atmospheric re-analyses ERA-Interim and ERA5 for 1979–2019 with a spatial resolution of 0.25°. Based on statistical processing of modeling results for the study area, information was obtained on the frequency of wave elements, the duration of storm and calm situations, and extreme wave characteristics. Waves with height of 0.25 and 0.5 m have the maximum frequency. This interval accounts for 43% of all cases. Waves with a height of 1 m occur in 12% of cases, and the frequency of waves with a height of 2.5 m is 1.3%. In most cases, waves in the study area come from the southwest–south–southwest sector (total frequency of 28%) and from the southeast–east-southeast sector (total frequency of 32%). The longest storm situations occur in December–January. The minimum duration of storms is observed in June.

Keywords Black Sea · Coastal zone of Alupka · Wind waves · Mathematical modeling · SWAN · Statistical characteristics

1 Introduction

The study of the wave regime of coastal waters is of great practical importance for the safety of navigation, design and operation of coastal infrastructure. Currently, in the coastal zone of southern Crimea, including in the area of the resort town of Alupka

V. V. Fomin · A. A. Polozok (✉)
Marine Hydrophysical Institute of the Russian Academy of Sciences, Sevastopol, Russia
e-mail: polozok.umi@gmail.com

I. N. Fomina
N.N.Zubov's State Oceanographic Institute, Moscow, Russia

© The Author(s), under exclusive license to Springer Nature Switzerland AG 2024

V. Karev (ed.), *Proceedings of the 9th International Conference on Physical and Mathematical Modelling of Earth and Environmental Processes*, Springer Proceedings in Earth and Environmental Sciences, https://doi.org/10.1007/978-3-031-54589-4_54

(Fig. 1), the reconstruction of bank protection structures is being actively carried out, and work is also underway on the design and construction of new infrastructure for the development of recreational activities. To carry out these activities, information about the regime characteristics of wind waves is required.

The purpose of this work is to perform a statistical analysis of wind-wave conditions in the Black Sea area adjacent to the Alupka region based on mathematical modeling data of waves over a long-term period.

There are several publications on the study of the wave regime of the Black Sea [1–5]. In this work, to assess the regime characteristics of waves in the coastal zone of the study area, we used reanalysis data from works [6, 7]. These data were obtained using the SWAN spectral wave model [8]. The choice of this reanalysis is due to the fact that the computational grid used is condensed in the region of the Crimean Peninsula and describes the wave fields in more detail compared to other reanalyses.

Below we analyze the operational and extreme characteristics of waves in the Alupka region. The operational characteristics of waves determine the background conditions for the operation of infrastructure facilities, the extreme characteristics of waves determine the regime of maximum loads on these facilities.



Fig. 1 Scheme of the coastal zone of the Alupka region. The rhombus shows the position of the computational mesh node at which the wind wave reanalysis data were taken

2 Initial Data

Data from global atmospheric reanalyses ERA-Interim and ERA5 for 1979–2019 with a spatial resolution of 0.25° were taken as the initial wind fields. These fields are freely available on the European Center for Medium-Range Forecasts website (http://apps.ecmwf.int). The results of validating the SWAN model using wave measurements on an offshore platform are presented in [1].

Reanalysis of wind waves using the SWAN model was carried out for the entire Black Sea on an unstructured mesh of 10,900 finite elements [6]. The angular resolution of the SWAN model was 10º. According to the frequency coordinate, varying in the range of 0.055–0.625 Hz, an uneven grid with 40 nodes was used. When integrating over time, an implicit difference scheme was used with a step of 30 min. As a result of retrospective calculations, an array of wave parameters in the Black Sea with a length of 41 years with a time discreteness of 1 h was obtained for each node of the computational grid. Further, the abbreviation SWAN-ERA is used to refer to this array. The computational grid node closest to Alupka was selected from the SWAN-ERA array. The sea depth at this point is 33 m (Fig. 1).

3 Operational Characteristics of Waves

Let's move on to consider the operational characteristics of waves for the Alupka region. In Figs. 2 and 3 show histograms of the frequency of significant wave height h_s and mean wave periods $\overline{\tau}$ according to SWAN-ERAI data.

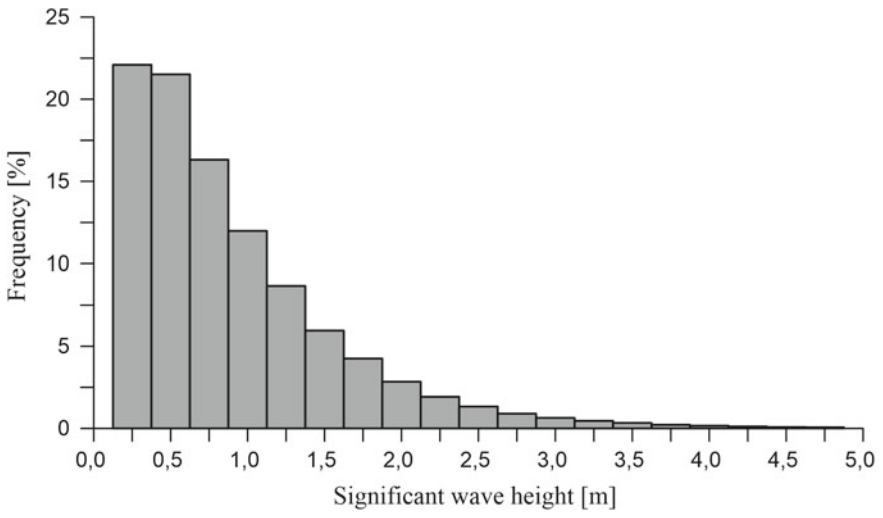


Fig. 2 Frequency of significant wave height (%) in the Alupka area according to SWAN-ERA data

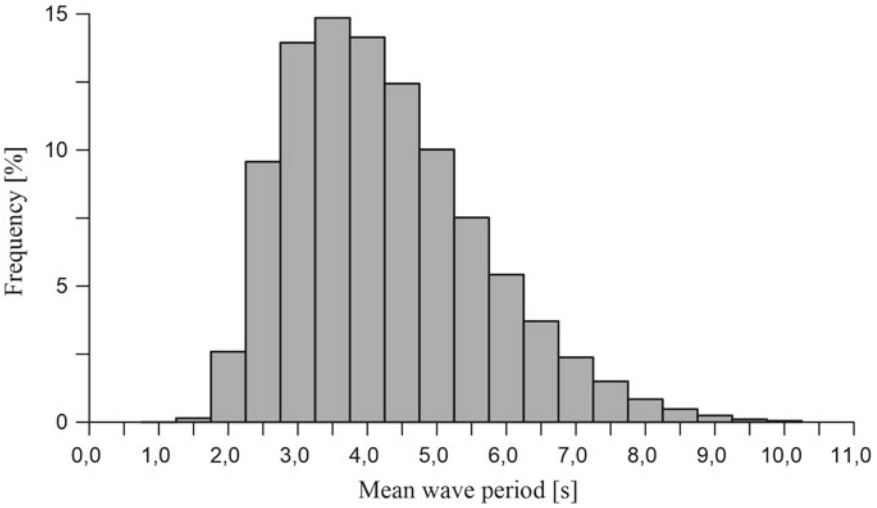


Fig. 3 Frequency of the mean wave period (%) in the Alupka region according to SWAN-ERA data

As you can see, waves with height of 0.25 and 0.5 m have the maximum frequency. This interval accounts for 43% of all cases. Waves with a height of 1 m occur in 12% of cases, and the frequency of waves with a height of 2.5 m is 1.3%.

The histogram of the frequency of mean periods of waves (Fig. 3) has a characteristic feature: the interval of 3–4 s is clearly visible on it, where the frequency of periods exceeds 13%, and 43% of all cases fall within the specified interval of periods.

The results of calculations of the frequency of the mean direction of waves in the Alupka area are shown in Fig. 4a. It follows that in most cases, waves in the study area come from the southwest–south-southwest sector (total frequency of 28%) and from the sector southeast–east–southeast (total frequency of 32%).

The distribution of the mean long-term significant wave height along the directions is shown in Fig. 4b. As can be seen, the highest wind waves approach the study area from the south-southwest. The long-term mean value for this direction is 1.5 m.

For the study area, the durations of stormy and calm situations were obtained. To estimate these characteristics, wave height of the 3% probability in the storm system ($h_{3\%}$) were used. For a given storm, equality $h_{3\%} = a$ means that 3 percent of all cases will have wave height greater than a. The calculation of $h_{3\%}$, as well as wave height of other probabilities, was carried out using the integral probability function of wave height distribution for a sea of finite depth [9].

Table 1 shows data on the mean long-term duration (day) by month of storm situations in the Alupka region. The duration of storm situations was determined for the following gradations of wave height: $h_{3\%} \geq 1.25$ m; $h_{3\%} \geq 2$ m; $h_{3\%} \geq 3$ m; $h_{3\%} \geq 4$ m; $h_{3\%} \geq 5$ m. The bottom line of the table for each gradation gives

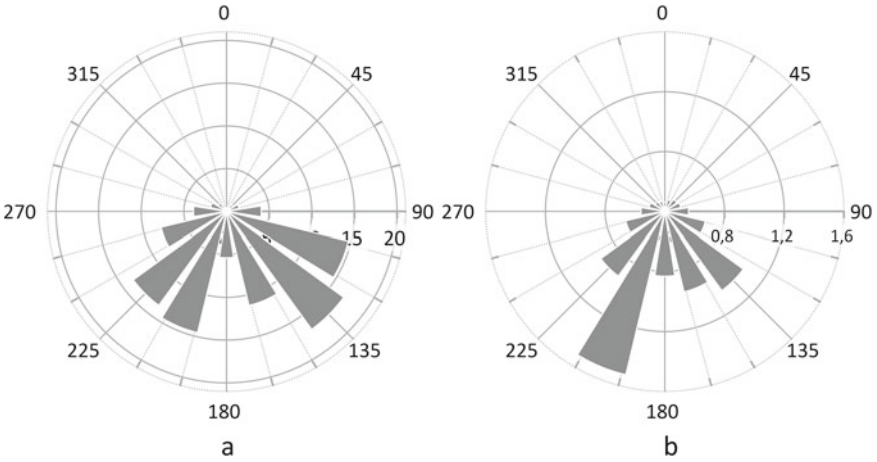


Fig. 4 Frequency of mean wave direction (%) (**a**) and distribution by direction of mean long-term values of significant wave height (m) (**b**) in the Alupka area according to SWAN-ERA data

its mean duration per year. As you can see, the longest storm situations occur in December–January. The minimum duration of storms is observed in June.

In Figs. 5, 6 show the distribution by year of the duration (day) of storms near the coast of Alupka according to SWAN-ERA data for four gradations of storm intensity: $h_{3\%} \geq 1.25$ m; $h_{3\%} \geq 2$ m; $h_{3\%} \geq 3$ m; $h_{3\%} \geq 4$ m. For these gradations, the mean long-term values of storm duration are respectively: 16.4 days; 9.7 days; 4.5 days; 2.0 days.

Table 1 Mean long-term duration (day) of storm situations by month in the Alupka region according to SWAN-ERA data

Months	$h_{3\%} \geq 1.25$ m	$h_{3\%} \geq 2$ m	$h_{3\%} \geq 3$ m	$h_{3\%} \geq 4$ m	$h_{3\%} \geq 5$ m
1	22.9	16.0	9.0	4.6	2.3
2	21.0	14.5	7.8	3.7	1.7
3	21.4	13.8	6.8	3.0	1.3
4	17.2	9.5	3.9	1.4	0.5
5	11.9	5.3	1.7	0.5	0.2
6	8.5	3.4	1.1	0.4	0.2
7	9.1	3.0	0.9	0.2	0.1
8	10.5	4.4	0.9	0.2	0.0
9	13.2	6.8	2.5	0.9	0.4
10	17.7	9.9	4.1	1.6	0.6
11	20.8	13.1	6.6	3.2	1.5
12	23.2	16.2	9.1	4.7	2.4
	16.4	9.7	4.5	2.0	0.9

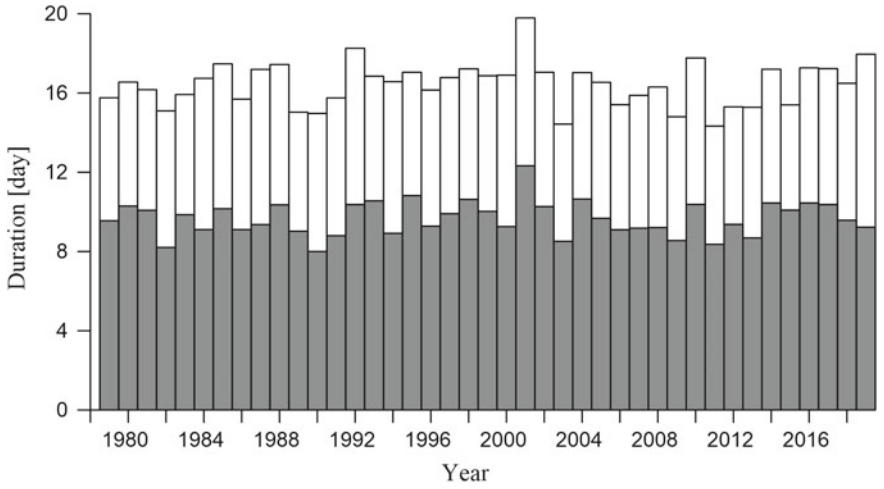


Fig. 5 Distribution by year of the duration of storm situations in the Alupka region for $h_{3\%} \geq 1.25$ m and $h_{3\%} \geq 2$ m (gray) according to SWAN-ERA data

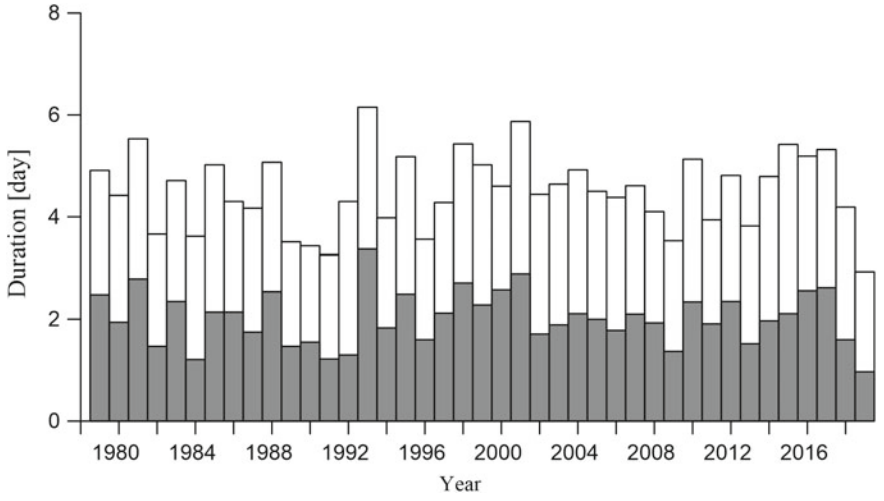


Fig. 6 Distribution by year of the duration of storm situations in the Alupka region for $h_{3\%} \geq 3$ m and $h_{3\%} \geq 4$ m (gray) according to SWAN-ERA data

In Fig. 7 shows the distribution by year of duration (day) of calm situations ($h_{3\%} \leq 0.25$ m) off the coast of Alupka according to SWAN-ERA data. The duration of calm situations varies from 0.3 to 2.1 days, and their mean value is 1.1 days.

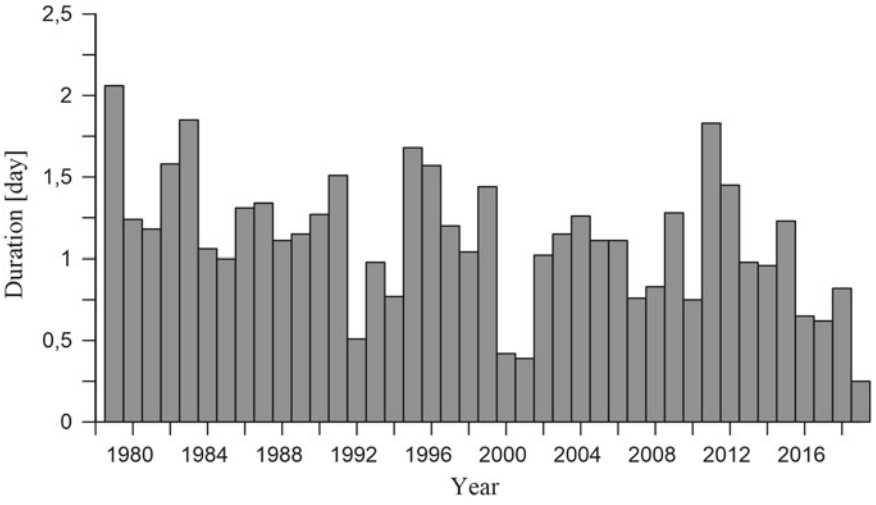


Fig. 7 Distribution by year of duration (days) of calm situations ($h_{3\%} \leq 0.25$ m) in the Alupka region according to SWAN-ERA data

4 Extreme Wave Characteristics

In Fig. 8 shows the distribution of annual maximum of significant wave height h_s in the Alupka region according to SWAN-ERA data for the period 1979–2019. As can be seen, the values of annual maximums h_s vary from 3.6 to 7.5 m. Their mean value is 5.2 m.

To estimate the maxima of mean wave height $\overline{h} = 0,63 \cdot h_s$ and mean wave periods $\overline{\tau}$, possible once every n years, we used the extreme Gumbel distribution [10], built on the basis of a sequence of annual maxima $\overline{h}$ and $\overline{\tau}$. Then, using the distribution functions of wave elements for a sea of finite height [9], which includes maxima $\overline{h}$ and $\overline{\tau}$, the height and periods of waves of different probability in a system of storms, possible once every n years, were determined.

The calculation results are given in Table 2. The values of the following quantities are given here: T—storm return period; $\overline{\lambda}$—mean wavelength; $h_{50\%}$—the height of the waves of supply is 50%; $h_{13\%}$—the height of the supply waves is 13%; $h_{3\%}$—the height of the supply waves is 3%; $h_{1\%}$—the height of the supply waves is 1%. In particular, it follows that for a storm that is possible once every 25 years, the value $h_{1\%}$ is 10 m. This value is usually used in the design of class 3 coastal protection structures [6].

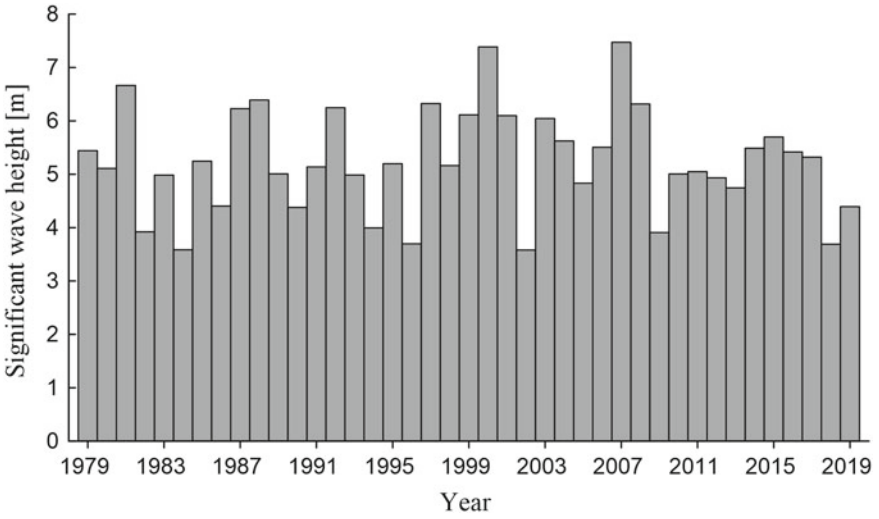


Fig. 8 Distribution of annual maximum significant wave height h_s in the Alupka region according to SWAN-ERA data

Table 2 Significant wave height h_s, mean wave height $\overline{h}$, mean wave period $\overline{\tau}$, mean wave length $\overline{\lambda}$, wave height 50% $h_{50\%}$, 13% $h_{13\%}$, 3% $h_{3\%}$ and 1% $h_{1\%}$ probability in a storm system possible in the Alupka area once a year, 5, 10, 25, 50 and 100 years

T (years)	h_s (m)	$\overline{h}$ (m)	$\overline{\tau}$ (s)	$\overline{\lambda}$ (m)	$h_{50\%}$ (m)	$h_{13\%}$ (m)	$h_{3\%}$ (m)	$h_{1\%}$ (m)
1	5.6	3.0	9.3	124	2.9	4.7	6	6.8
5	7.0	3.7	10.2	144	3.6	5.8	7.4	8.3
10	7.7	4.1	10.7	154	4.0	6.3	8.0	9.1
25	8.6	4.5	11.3	167	4.4	7.0	8.9	10.0
50	9.3	4.9	11.7	176	4.7	7.5	9.5	10.6
100	9.9	5.2	12.2	185	5.1	8.0	10.1	11.3

5 Conclusions

Mathematical modeling of wind-wave conditions in the area of the Black Sea adjacent to the coastal zone of Alupka was carried out, based on the tested spectral wave model SWAN. The main results of the research work are as follows.

Waves with height of 0.25 and 0.5 m have the maximum frequency. This interval accounts for 43% of all cases. Waves with a height of 1 m occur in 12% of cases, and the frequency of waves with a height of 2.5 m is 1.3%.

In most cases, waves in the study area come from the southwest-south-southwest sector (total frequency of 28%) and from the southeast–east–southeast sector (total frequency of 32%).

The highest wind waves approach the study area from the south-southwest. The long-term mean value for this direction is 1.5 m.

The duration of calm situations varies from 0.3 to 2.1 days, and their mean value is 1.1 days.

Acknowledgements The study was carried out within the theme of the Marine Hydrophysical Institute no. FNNN-2021-0005 «Coastal studies». Model calculations were carried out on the MHI computing cluster (hpc-mhi.org)

References

1. Polonsky A., Fomin V., Garmashov A. Characteristics of the Black Sea wind waves // Reports of the National Academy of Sciences of Ukraine, 2011. – No. 8. – P. 108–112. (In Russian)
2. Arkhipkin, V. S., Gippius, F. N., Koltermann, K. P., and Surkova, G. V.: Wind waves in the Black Sea: results of a hindcast study, Nat. Hazards Earth Syst. Sci., 14, 2883–2897, https://doi.org/10.5194/nhess-14-2883-2014, 2014.
3. Akpinar A., Ponce de León S. 2016. An assessment of the wind re-analyses in the modelling of an extreme sea state in the Black Sea. Dynamics of Atmospheres and Oceans 73, 61–75. https://doi.org/10.1016/j.dynatmoce.2015.12.002.
4. Akpinar A., Bingölbali B., Van Vledder G. 2017. Long-term analysis of wave power potential in the Black Sea, based on 31-year SWAN simulations. Ocean Engineering 130, 482–497. https://doi.org/10.1016/j.oceaneng.2016.12.023.
5. Onea F., Rusu L. A Long-Term Assessment of the Black Sea Wave Climate, Sustainability 2017, 9(10), 1875; https://doi.org/10.3390/su9101875.
6. Divinskii B., Fomin V., Kosyan R., Lazorenko D. Maximum Waves in the Black Sea // Proceedings of the Fourteenth International MEDCOAST Congress on Coastal and Marine Sciences, Engineering, Management and Conservation MEDCOAST 2019 (Marmaris, Turkey, 22–26 October 2019). – Mugla, Turkey: Mediterranean Coastal Foundation (MEDCOAST Foundation), 2019. – Vol. 2. – P. 799–810.
7. Divinsky B.V., Fomin V. V., Kosyan R. D. and Ratner Y. B. (2019), Extreme wind waves in the Black Sea, Oceanologia, V. 62, Issue 1, 2020, p. 23–30.
8. Booij. N., Ris. R.C., Holthuijsen L.H., A third-generation wave model for coastal regions. Model description and validation. // J. Geophys. Res., 1999, 104(C4), p. 7649–7666.
9. Krylov Yu. Spectral methods for the study and calculation of wind waves, Leningrad: Gidrometeoizdat, 1966. – 255 p. (In Russian)
10. Lopatoukhin L.J., Rozhkov V.A., Ryabinin V.E., Swail V.R, Boukhanovsky A.V., Degtyarev A.B. Estimation of extreme wind wave height // World Meteorological Organisation. JCOMM Technical Report WMO/TD-No. 1041. 2000.

Zoning and Modeling of the Underground Hydrosphere of the Orenburg Region



I. V. Kudelina, T. V. Leontyeva, and M. V. Fatyunina

Abstract The Orenburg region is located in the south of the Russian Federation, on the border with Kazakhstan, within the Southern Urals and the southeastern part of the Russian Platform. The sedimentary cover contains groundwater of varying chemical composition. Vertical zoning allows for hydrogeological zoning of the territory under consideration. The purpose of the study is to construct a model of the hydrosphere and hydrogeological zoning of the Orenburg region and adjacent territories. Research methods include mapping and zoning of the territory based on routine observations of the quality of natural waters and sources of pollution. As a result of the study, it was established that surface and groundwater in the field area have a varied chemical composition, depending on both natural and anthropogenic factors. Eight vertical hydrogeological zones are identified on the platform. The model of the hydrosphere with its hydrodynamic levels is presented as follows: (1) the upper level with local and regional underground flow; (2) the lower floor of the sedimentary cover and water-pressure system with regional aquifers and good conditions for the preservation of hydrocarbon deposits; (3) a floor of gravitational fractured waters up to the Conrad boundary, the movement of fluids, blocks and plates is geodynamic in nature; (4) the level of waters in a supercritical state from the Konrad border to 900 km.

Keywords Groundwater · Hydrosphere model · Underground flow · Fluids · Hydrodynamic levels

1 Introduction

The vertical zonation of groundwater is the basis of the hydrogeological zoning of the region. On regional maps of Russia the eastern part of the Russian Platform is classified as regions and belts in the sedimentary cover of which sulfate-halogen rocks play a significant role, replaced in the west by gypsum and anhydrites (maps of

I. V. Kudelina (✉) · T. V. Leontyeva · M. V. Fatyunina
Orenburg State University, Orenburg, Russia
e-mail: kudelina.inna@mail.ru

© The Author(s), under exclusive license to Springer Nature Switzerland AG 2024

V. Karev (ed.), *Proceedings of the 9th International Conference on Physical and Mathematical Modelling of Earth and Environmental Processes*, Springer Proceedings in Earth and Environmental Sciences, https://doi.org/10.1007/978-3-031-54589-4_55

All-Russian Research Institute of Hydrogeology and Engineering Geology (VSEGINGEO) and Geological Research Institute (VSEGEI)). The southern part of the platform is bordered by structures of the North Caspian basin. Ultra-strong brines with mineralization up to 350 g/l are common within its boundaries. A normal type of vertical zoning has formed here.

2 Results and Discussion

In the mountain-folded part of the study area, mainly fresh waters are distributed. Each district differs in vertical zoning, which is used when zoning the territory (Fig. 1). A hydrogeological region is distinguished [1, 2] by the sequence in the location and thickness of the comparable hydrogeochemical zones, by the chemical types of water or geochemical fields, taking into account the sequence of their location in the section. In the Cis-Ural region, we have identified eight hydrogeochemical zones in a vertical section [1]: hydrogenogenesis (4 zones), hydrohalogenesis (3 zones) and hydrometagenesis (1 zone). These terms were introduced into science by Fersman [3]. The hydrohalogenesis zone was characterized by Maksimovich [4], and the hydrometagenesis zone—A. Ya. Gaev within the boundaries of the geochemical zone of metagenesis.

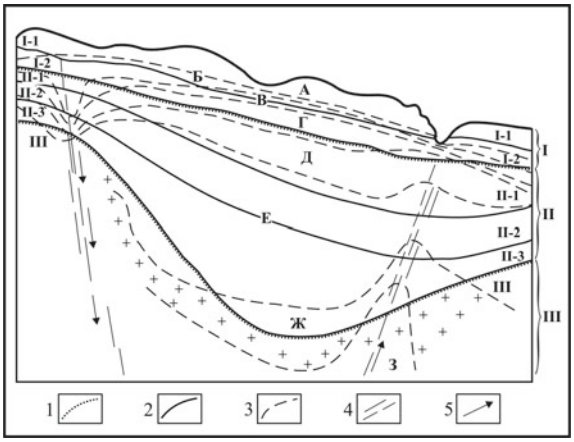


Fig. 1 Zoning of the Orenburg region: 1—hydrodynamic, 2—hydrogeological and 3—hydrogeochemical; 4—tectonic disturbances, 5—fluid movement. Level of water exchange: I—from active to slow; II—very difficult at the bottom of the cover; III—in the foundation. Floors in rock complexes: I-1—Meso-Cenozoic; I-2—Upper Permian; II-1—Moscow-Kungur; II-2—Frasnian-Verean; II-3—Proterozoic-Kynovsky; III—foundation. Hydrogen zones: A—carbonate, Б—sulfate, C—sulfate–chloride and chloride-sulfate, D—chloride. Hydrohalogen zones: Д—maximum, Е—equilibrium, Ж—inherited, З– hydrometagenic

A. Ya. Gaev identified hydrogeochemical zones in the hydrogenation zone: (1) hydrocarbonate; (2) sulfate; (3) sulfate–chloride and chloride-sulfate; (4) chloride [1, 5]. In the zone of hydrohalogenesis, we have identified 3 zones that differ in the degree of metamorphization of brines from weak at the top ($r_{Na}/r_{Cl} > 0.7$), but with high mineralization due to leaching of rock salt. At the bottom of the cover, the metamorphization of brines increases ($r_{Na}/r_{Cl} < 0.5$) under the influence of deep basement fluids. Due to the hydrogeological closure of the subsoil and the presence of petroleum products and organic substances in the zone of equilibrium hydrohalogenesis, a sharply reducing environment has formed, which favors the formation of hydrocarbon deposits.

Thermal brines are formed in the foundation under conditions of hydrometagenesis. They were uncovered by ultra-deep drilling and traced to the zone of inherited hydrohalogenesis and the Kynovsky water barrier. Associated with them is the gas saturation of the lower sedimentary cover with helium, hydrogen, etc. The waters of the zones of chloride hydrogenation and maximum hydrohalogenesis interact in the process of tectogenesis and orogenesis, forming signs of cryptohypergenesis, in which hydrocarbons are destroyed already during inherited and maximum hydrohalogenesis. Hydrocarbon deposits are well preserved during equilibrium hydrohalogenesis. The very presence of a zone of equilibrium hydrohalogenesis in the section and the significant thickness of the rocks in this zone indicate the presence and good preservation of hydrocarbon deposits.

In the mountain-folded mountainous Urals, zones of hydrohalogenesis have been identified only in depressions and troughs, but in general the structures of the Urals are hydrogeologically open. On the arches and ledges of the crystalline basement (Tokmovsky, Kotelnichsky, etc.), the zone of equilibrium hydrohalogenesis has not been identified due to the semi-open hydrogeological regime. On the Nemsky, Kukmorsky arches and in the Kazan-Kazhimsky trough, this zone corresponds to a small part of the section and is developed locally with a semi-closed regime. In a closed type of section, where the thickness of the sedimentary cover increases, this zone reaches several kilometers in thickness. The highest level of subsoil closure is characteristic of areas where salt-bearing and sulfate-halogen rock strata occur in the Permian deposits. They are capable of accumulating gas and gas-condensate deposits of hydrocarbons and forming gas caps of oil fields.

In the Cis-Ural region, the thickness of the sedimentary cover grows in the south-eastern direction, varying from 1–2 km above the projections of the basement, for example, the Tokmovsky and Kotelnichsky arches, and increasing to 12 km or more in the near-wall zones of troughs and syneclises (Caspian, Cis-Ural, etc.). New materials on the geology of the territory have made it possible to clarify the previously identified patterns [4, 6]: (1) in different hydrogeological conditions, the correspondence of hydrogeological levels and hydrogeochemical zones changes; (2) the thickness of the hydrogenation zones reaches a maximum in the north-west of the Cis-Urals above the basement arches, where no hydrohalogenesis zones have been identified; (3) in river valleys in areas of subsidence of the foundation and central parts of artesian basins, local uplifts with domes of salt water and brines have been identified; (4) the

depths of the same hydrogeochemical zones increase significantly where tectonic disturbances of the foundation take place.

Ultra-deep drilling and geological and geophysical studies in different areas, including the study region, have discovered increased hydrogeological activity in the deep zones of the earth's crust, rocks with increased permeability and porosity [4, 6, 7]. These petrophysical features of rocks and hydrogeological activity cannot be explained only gravitational properties of water. This is probably due to the geodynamic features of the mantle and crust. The geodynamic mechanism of development and closure of tectonic cracks between blocks of the mantle and the earth's crust manifests itself in the form of pushing fluids into the sedimentary cover and sucking them back through the fracturing of the mantle and basement.

This mechanism of fluid movement along cracks in the mantle and basement is confirmed by: (1) the discovery of demineralized water among brines in the deep horizons of the earth's crust; (2) identification of brines in the form of domes within the upper horizons in depressions and deflections of the foundation; (3) the formation of geodynamic, hydrogeochemical and geothermal anomalies in areas of tectonic foundation disturbances. They were also established using helium photography data. As a rule, the concentration of helium dissolved in water does not rise above $n \bullet 10^{-5}$ ml/l, and in areas of tectonic disturbances it reaches $n \bullet 10^{-2} \div n$ ml/l. (with $n = 1 \div 10$). Oxygen in amounts up to 0.2 g/l was also detected in tectonic disturbances in brines. According to L. K. Gutsalo, this is due to the processes of radiolysis.

V. G. Gerasimov and A. R. Kinzikeev wrote about the hydrogeological activity of deep faults on the territory of Tatarstan and Bashkortostan. L. A. Anisimov, S. M. Kiselgof, A. V. Tsygankov described these features of the deep horizons of the earth's crust for the territory of the Lower Volga region [8–10]. Similar deep reservoirs were identified by hydrogeologists in different regions of the country: Terek-Sunzha region (A. M. Nikanorov and O. E. Bartsev), South Caspian depression (A. G. Durmishyan and M.3. Rachinsky), etc. [11–13]. AND I. Gaev and I. V. Kudelina in the earth's crust and mantle to depths of 700–900 km identified two hydrogeological levels with fissure-vein gravitational waters up to the Conrad boundary and a floor with waters in a supercritical state below the Conrad boundary [5, 11].

From these positions we consider the model of the hydrosphere of the region under study:

1. The hydrodynamic floor is the upper one in the volume of hydrogeological floors of local and regional underground runoff.
2. The lower level of the sedimentary cover is a single water-pressure system with powerful regional aquifers and good conditions for the formation of hydrocarbon deposits. This has been noted in the literature by dozens of researchers, starting with V. F. Raabena (1970); L. N. Rozanova (1979) and others [14–16].
3. Hydrodynamic floor of predominantly gravitational waters of the crystalline basement and upper mantle to the Conrad boundary. Fluids here move along tectonic fracturing, which is formed and renewed during constant deformations of the earth's crust and mantle. They are geodynamic or tectono-hydraulic in

nature. The conclusion about the hydrogeological activity of the lower horizons of artesian basins belongs to Tolstikhin [8, 11].

3 On the Nature of the Relationship Between Hydrodynamic Levels

The nature of the relationship between hydrodynamic levels still remains unclear, since there are no reliable methods for assessing it and the relationship itself is very variable in time and space. In order to assess these relationships over a certain period of time and characterize the elements of the hydrogeological structure of the region, we carried out a stratigraphic linkage of the hydrodynamic, hydrogeological and geochemical division of the region's section on one diagram. This made it possible to stratigraphically compare geodynamic and hydrogeological levels with vertical geochemical zones. The Volga-Kama and Caspian artesian basins and the folded region of the Urals are well distinguished by these elements. Each of the regions is characterized by its own type of vertical zoning and the degree of hydrogeological closure of the subsoil. Areas with high rock thickness within the zone with equilibrium hydrohalogenesis, as a rule, have a good degree of closure of the subsoil.

If this zone wedges out of the section, which occurs in the folded mountainous Urals, the hydrogeological regime becomes open (Fig. 2, type I). In the Cis-Ural region, the degree of hydrogeological closure of the subsoil due to the inconsistency of aquifer complexes changes so significantly that it has become possible to distinguish four more types of areas, each of which is characterized by its own type of zonation. There are four types of hydrogeological regions identified in the Cis-Urals. Each of them has its own type of zonation, level of closure and a number of hydrogeological features (Fig. 2, types II–V). There are areas that are well closed, closed and semi-closed. The latter are located above the projections of the foundation of the Tokmovsky Kotelnichsky and other vaults.

Territories with a zone of equilibrium hydrohalogenesis in the section are well closed. For example, in the Belskaya Depression, zones of hydrohalogenesis were established from a depth of 200 m. In the geological section of the sedimentary cover, the zone of equilibrium hydrohalogenesis has significant thickness. A good level of subsoil closure ensures the formation and preservation of hydrocarbon deposits, gas caps of oil fields and a high percentage of hydrogen and helium in them.

The zone of equilibrium hydrohalogenesis is formed when the thickness of the hydrohalogenesis zones is more than 3 km. The mineralization of brines in the zone of equilibrium hydrohalogenesis is 240–280 g/l with a sulfate coefficient of 0.1–0.2. The reaction of the medium changes from neutral to slightly acidic. In the zone of maximum hydrohalogenesis, brine mineralization reaches 350–400 g/l, which is due to the good solubility of the sulfate-halogen layer containing potassium and magnesium chlorides. This is typical for areas where the foundation is submerged and the maximum thickness of the sedimentary cover (Fig. 2V). Examples are the Belskaya depression and the northern side of the Caspian syneclise (Fig. 3).

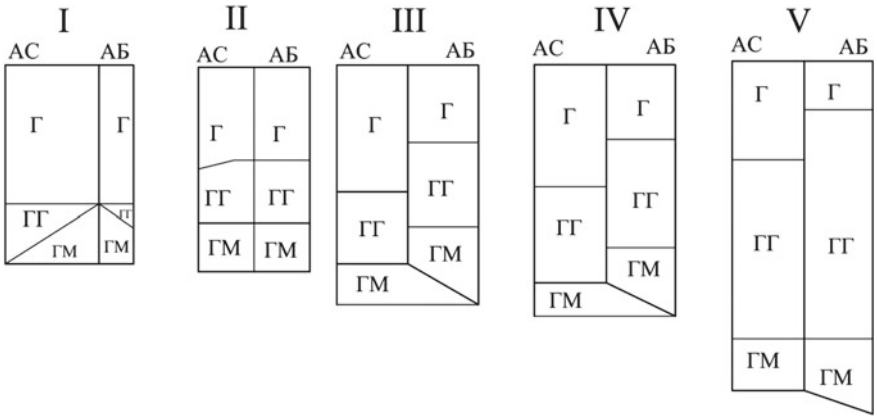


Fig. 2 Vertical zoning of the Orenburg region in areas with different hydrogeological closedness or openness: I—completely open; II—half open; III—half closed; IV—closed; V—exclusively closed. Structures: AC—vaulted; AB—pool. Geochemical zones: hydrogenogenesis: А, Б, В, Г hydrohalogenesis D, E, G and hydrometagenesis 3 (Fig. 1)

The hydrogeologically well-closed province is distinguished by an exceptionally wide distribution in the geological section of zones of hydrohalogenesis due to zones of hydrogenation. This is typical for the artesian basins of the Solikamsk, Belsk and other depressions. The zone with the maximum level of hydrohalogenesis processes was found here already at depths of up to 200 m and occupies a significant part of the section in the sedimentary cover. Exceptionally good subsoil closure with hydrocarbon deposits is ensured by Permian sulfate-halogen rocks present in the section. Thanks to them, deposits of gaseous hydrocarbons, gas caps of oil fields and the presence of high helium content in the composition of gases were formed. The most favorable conditions for the accumulation and preservation of oil deposits and their gas caps were formed precisely under conditions of equilibrium hydrohalogenesis. Large hydrocarbon deposits are confined to areas with the maximum thickness of the rocks of this geochemical zone (3 km or more).

The mineralization of chloride-sodium-calcium brines in the zone of equilibrium hydrohalogenesis does not exceed 240–280 g/l. They are characterized by low sulfate values (0.1–0.2), average metamorphization, neutral or slightly acidic reaction of the medium and calcium concentrations in the brine of 15–19 g/l (17–22% equivalent) with a magnesium content of 6.0 -7.5%-eq. An increase in the thickness of the zones of chloride hydrogenogenesis and maximum hydrohalogenesis above the arched inherited neotectonic uplifts of the basement has been established. Maximum hydrohalogenesis is characterized by brines with mineralization up to 350–400 g/l due to potassium and magnesium salts. In these areas, the foundation experiences significant subsidence, and the sedimentary cover acquires maximum thickness. This has been established for the structures of the Cis-Ural region and the Caspian syneclise.

The closed province is located west and north-west of the previous one. The thickness of the cover sediments decreases somewhat and the halogen deposits

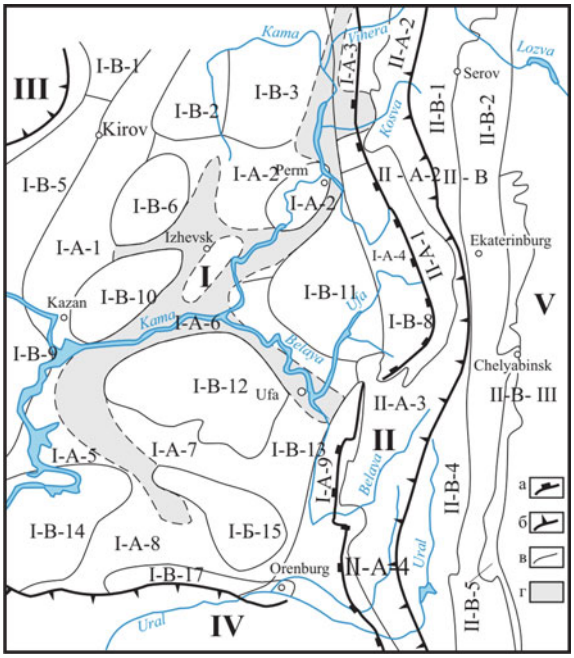


Fig. 3 Scheme of zoning of groundwater in the region according to A. Ya. Gaev and I. V. Kudelina: Borders: regions (**a**), districts (**b**), Kama-Kinel system of troughs (**c**). Specific regions: I—Volga-Kama; II—mountain-folded; III—Moscow; IV—Caspian; V—West Siberian; areas with different closedness: II1—absent; II2, I2—very weak, I3—weakened; I4—good and I5—well closed. Basins of troughs and depressions: I-A-1—Kazan-Kazhimsky; I-A-2—Verkhnekamsk; I-A-Z—West Solikamsk, I-A-4—West Yuryuzano-Sylvensky; I-A-5—Melekessky; I-A-6—Blagoveshchensky; I-A-7—Sernovodsko-Abdulinsky; I-A-8—Buzuluksky; I-A-9—Zapadno-Belsky; I-A1—Kama-Kinelsky. Basins of domes and monoclines: I-B-1—Sysolsky; I-B-2—Komi-Permyatsky, I-B-Z—Kama; I-B-4—East Solikamsk, I-B-5—Kotelnichsky; I-B-6—German; I-B-7—Perm, I-B-8—East Yuryuzano-Sylvensky; I-B-9—Tokmovsky; I-B-10—Kukmorsky; I-B-11—Bashkir; I-B-12—Almetyevsko-Belebeevsky; I-B-13—South-East platform; I-B-14—Zhigulevsko-Pugachevsky; I-B-15—Orenburg, I-B-16—East Belsky; I-B-17—Onboard Prikaspiysky. Basins of the post-miogeosynclinal Urals: II-A-1—Verkhnevishersky; II-A-2—Kizelovsko-Teplogorsk; II-A-Z—Beloretsko-Chusovskaya; II-A-4—Zilair-Verkhnesakmarsky; II-A-5—Sarinsko-Guberlinsky. Basins of the post-eugeosynclinal Urals: II-B-1—Verkhnelozvinsko-Karpinsky; II-B-2—Tagilo-Turinsky; II-B-3—Yekaterinburg; II-B-4—Alapaevsko-Sibaysky; II-B-5—Magnitogorsk-Orsky

become even more significant, which are partially replaced by sulfate-carbonate rocks. Accordingly, the degree of subsoil closure, the gas factor, and the gas saturation of waters decrease, gas deposits and basin caps in oil fields disappear. At the same time, the thickness of the zone of chloride hydrogenogenesis increases, especially due to a significant reduction in the zone with equilibrium hydrohalogenesis. However, the number of hydrogeochemical zones and the order of their placement in the section do not change. To the west and northwest, the closedness of the subsoil and the mineralization of water, as well as the thickness of the sedimentary cover,

decreases. Sulfate-carbonate rocks partially replace halogen deposits. The power of hydrohalogenesis zones, including equilibrium, is reduced. The picture of vertical zoning changes due to an increase in the thickness of hydrogenation zones while maintaining their number and sequence of occurrence in the section. But the mineralization of brines does not exceed 300 g/l, since magnesium and potassium chlorides disappear from the composition of sulfate-halogen rocks.

The province with semi-closed subsoil is located to the west and north-west of the characterized ones. It is located in the Kazan-Kazhimsky trough and in those parts of the Melekess depression and the Kama monocline that are adjacent to the arched uplifts of the basement (Nemsky, Komi-Permyatsky, etc.). Near the basement, the zones of hydrogenation increase in thickness due to the reduction of zones of hydrohalogenesis, which in some places wedge out completely from the section. The existence of oil deposits in the past is indicated by the products of their destruction, established in the geological section, including the Kynovsky horizon. The waters of this part of the section are characterized by an unstable chemical composition, since they represent a mixture of waters from different zones. Already in zones of maximum hydrohalogenesis and chloride hydrogenogenesis, their mineralization decreases, but in deep subsurface horizons demineralized brines are found less frequently.

On the basement ledges, the sedimentary cover reduces its thickness to 1 km. Examples are the Tokmovsky and Kotelnichsky vaults. Above them, the vertical zoning also changes, and the hydrogeological regime becomes semi-open. Here, the zones of hydrogenation dominate the section, and hydrohalogenesis manifests itself only in the lower layers of the sedimentary cover in the form of demineralized brines with an unstable composition.

At the basement ledges, the sedimentary cover thins to 1–1.5 km. The zonation and water regime are changing. It becomes semi-open with a predominance of hydrogenation zones in the section. Demineralized brines were identified in the lower part of the cover. Their chemical composition is extremely unstable, which is explained by the different closedness, drainage, washing and flow of the sedimentary cover.

We also used the zoning of the Orenburg region to assess the prospects for industrial oil and gas potential. Areas with a strong zone of equilibrium hydrohalogenesis are very promising. They are confined to subsidence zones in the sedimentary cover, which takes place in the Kazan-Kazhim trough system, in the near-wall areas of the Caspian syneclise with a thickness of Proterozoic-Devonian rocks, in fractured basement rocks, in particular, in the Kama monocline.

In the hydrogeologically open regions of the Urals, fresh waters are common to depths of hundreds and even several thousand meters. With depth they become salty. Their formation is influenced by landscape-climatic and structural-geological conditions. Landscape and climatic conditions manifest themselves zonally from forest-steppe and steppe zones to dry steppes. The structures of the Urals are represented in the west by post-miogeosynclinal formations, and in the east by post-eugeosynclinal submeridional formations. When the submeridional structures of the Urals intersect with sublatitudinal landscape-climatic zones, areas differing in hydrogeological sections are formed. Latitudinal landscape-climatic zones differ in the composition and concentrations of water-dissolved organic substances.

If in taiga regions up to the southern taiga, water-dissolved organic substances are represented mainly by fulvic compounds, then in forest-steppe and steppe regions—by humic compounds. Fulvic compounds in waters of classes T_6 and T_7 are characterized by dispersion in the vertical section of the aeration zone with conversion to organic carbon from 10–25 to 2–5 mg/l in the horizontal runoff zone. That is, there is a scattering of fulvic compounds down the section. In forest-steppes and steppes, organic carbon, being dissolved, is represented by humic compounds. Unlike fulvic acids, the content of humic compounds increases with depth, but does not exceed 6–8 mg/l under conditions of the horizontal runoff zone [1].

The regions of eastern Orenburg are confined mainly to the steppe zone of the post-eugeosynclinal Urals. In structural and geological terms, they are represented by the structures of the Tagil-Magnitogorsk and East Ural troughs and the East Ural uplift. In addition, more detailed structures are identified—the Ashchebutak and Irendyk anticlinoria. The relief in the eastern Orenburg region changes from mountainous with the Irendyk-Krykty ridges, then a strip of hilly-ridged and ridge-small hilly forms transitional before the flat Trans-Urals with flat-ridged forms and with individual hills. On watersheds their elevations do not exceed 400 m, and their relative elevations are 50 ÷ 160 m.

Water flow is confined to the Tobol and Ural macro-basins with a gully-beam network with rare flat-bottomed hollows. The amount of precipitation decreases significantly from 450 in the northwest to 250 mm in the southeast. The average air temperature in the region is +2 °C, with the amount of precipitation compared to the evaporation value being 2–3 times less. Chernozems and dark chestnut soils are widespread, and salt marshes and solonetzes appear in the extreme southeast.

The geological structure in the Eastern Orenburg region is dominated by volcanic-sedimentary Devonian and Carboniferous rocks. They are overlain by Meso-Cenozoic sediments. The structure of the Irendyk anticlinorium is dominated by Devonian diabase and andesitic porphyrites, albitophyres, dacites and their tuffs and tuff-sandstones. Synclinal folds are composed of rocks: (1) Berezovsky formation, that is, Upper Tournaisian and Lower Visean under stages; (2) the Kizil Formation from the Middle, Upper Visean and Namurian complexes and (3) the Urtazym Formation or Moscovian Stage. The Berezovskaya Formation contains limestone conglomerates containing interlayers and lenses of cherts and dolomites, while carbonates predominate in the Kizil Formation. Meso-Cenozoic sediments are unconformably overlain by Paleozoic rocks, which are found within karst sinkholes, depressions and erosion-tectonic depressions (Orskaya, Tanalykskaya, etc.). Mesozoic-Cenozoic sediments consist of different-aged weathering crust formations and marine sediments of Upper Cretaceous and Paleogene age.

Martin [17] well described karst in the region, developed to depths of 200–300 m and well regulating water flow when there is a lack of moisture. He established the linear nature of its development and a close connection with tectonic movements and disturbances, thanks to which in river valleys and, in particular, the river. Dogwood springs are unloaded, the flow rate of which reaches 180 m^3/h, and the flow rate of wells is 500–2500 m^3/h [18]. Surface runoff is in some places absorbed by karst

forms, for example, along the river. M. Kizil, stream. Yakai et al. Waters in Meso-Cenozoic deposits occur sporadically in lenses and interlayers in sand-gravel-pebble deposits. Fresh waters are concentrated in alluvium. They provide water to large cities. In general, in the Eastern Orenburg region there is a sharp shortage of drinking water.

Water flow is characterized by exceptional unevenness and high technogenic load. Demands for water are growing, requiring the development of new efficient technologies, and, above all, replenishment of water intakes by accumulating part of the flood runoff. Water accumulation is carried out through the construction of dams that create backwater of river waters. Such an object could be the Kumak reservoir, the waters of which supply water to the Svetlinsky district and the city of Yasny. According to the Company Votemiro T. V. Leontyeva under the guidance of prof. A. Ya. Gaev made a forecast of the consumption of water intake wells necessary to replenish water reserves and the planned water intake. Calculations were performed at NSL = 291 m (normal retaining level) and at ULV = 283 m (maximum water discharge level). Based on the results of routine observations, the dependences of the productivity of wells and the chemical composition of water on the amount of water pressure on the river were determined.

Groundwater reserves are planned to be replenished at the expense of the Verkhne-Kumak reservoir, which accumulates melt water with an annual share of 90–95%. The reservoir's catchment area of 1,400 km^2 provides an annual water flow of 88.06 million m^3 and an annual flow of 1.91 m^3/s with asymmetry coefficients of 3.8 and variations of 1.5. The maximum water flow in 1994 was 6.42, and the minimum in 1951 was 0.05 m^3/s. The flood in March–April lasts 30 days with a peak level rise in mid-April with an average flow of 237 m^3/s and a discharge volume of 67.9 million m^3, and in 1994—1139 m^3/s and 317 million m^3. The minimum flood in 1951 was 7.491 m^3/s and 0.12 million m^3. Water flow is extremely uneven, and rain floods are unstable. Water is used to supply water to the population and enterprises of Yasny and the village Svetly. The normal retaining level of the FSL is 291.50 m, and with the ULV it is 283.00 m. On May 15, 2006, a level of 294.45 m was reached, and on April 1, 2008—287.05 m. The amplitude of level changes reaches 5.04 m, not usually exceeding 2.60 m. The long-term reservoir level is 290.54 m.

Due to unsatisfactory water pipelines, water losses are very significant. Water from the reservoir is used to supply water to the Kiembaevsky Mining and Processing Plant (Yasny) and the nickel silicate plant (Svetly village). To maintain the quality of water in the downstream, sanitary releases in the amount of 0.5 million m^3/year are used.

The reservoir is not used for other purposes except for water supply. On the right bank of the reservoir, near the pumping station, there is a water-measuring post for a special service that carries out routine monitoring of the operation of the reservoir and the water level in it.

4 Conclusion

Thus, using the example of the southeast of the Russian Platform and the mountain-folded mountainous regions of the Urals, a model of the hydrosphere with gravitational waters and waters in a supercritical state is proposed. The latter occupy a significant volume of the hydrosphere below the Conrad boundary. In the platform part of the study area, hydrodynamic levels are identified in the sedimentary cover, representing a water-pressure system with regional aquifers and hydrocarbon deposits. Below them are identified: (1) a layer with the geodynamic nature of the movement of gravitational fluids and blocks of the earth's crust and upper mantle to the Conrad boundary; (2) a layer of water in a supercritical state from the Conrad boundary to 900 km, where earthquake hypocenters appear.

Based on these data, we can conclude that within the zone of equilibrium hydrohalogenesis, conditions are most favorable for the accumulation and preservation of hydrocarbon deposits. The presence of this zone in the section, its great thickness, lithological and stratigraphic conditions at its upper and lower boundaries characterize the degree of hydrogeological closure of the subsoil. It is in areas with such conditions that large and unique hydrocarbon deposits are formed. In the region under study, the processes of hydrocarbon accumulation took place and continue to function where the Permian sediments contain salt-bearing strata of significant thickness, and the closure of the subsoil increases sharply. Gaseous hydrocarbons also accumulate here, forming deposits and gas caps in oil fields. Therefore, the study and mapping of hydrohalogenesis zones is of great exploratory importance.

References

1. Gaev A.Ya. Hydrogeochemistry of the Urals and issues of groundwater protection. Sverdlovsk: Ural Publishing House. Univ., 1989. 368 p.
2. Silin-Bekchurin A.I. Zonal and azonal processes of groundwater formation // Proceedings of the Laboratory of Hydrogeological Problems of the USSR Academy of Sciences. M., 1958. T. 16. pp. 181–186.
3. Fersman A.E. Selected works. M.: Publishing House of the USSR Academy of Sciences, 1955. T. 3. 798 p.; T. 4. 588 p.
4. Maksimovich G.A. Hydrogeochemical zones of the platform//Chemical geography and hydrogeochemistry. Perm, 1964. Issue. 3(4). pp. 101–120.
5. Gaev A.Ya. Fundamental and applied problems of the hydrosphere. Part II. Environmental problems: textbook. allowance / A.Ya. Gaev, M.A. Tikhonenko, Yu.A. Killin; under general ed. AND I. Gaeva. – M.: University Book, Editorial and Publishing House of the Russian New University, 2018. – 200 p., ill.
6. Gaev A.Ya., Khomentovsky A.S. On deep hydrodynamics (using the example of the eastern Russian Platform) // Dokl. Academy of Sciences of the USSR. 1982. T. 263, No. 4. P. 967–970.
7. Well drilling results. 20,000 for a crystalline foundation in Tat. ASSR / R.T. Muslimov, T.A. Lapinskaya, I.X. Kaveev, V.I. Filippovsky, // Sov. geol. 1977. No. 6. pp. 110–116.
8. Problems of regional dynamics of artesian waters. L.: Subsoil. Leningr. department, 1972. 61 p.

9. Kopylov I.S. Hydrogeological role of geodynamic active zones // International Journal of Applied and Fundamental Research. – 2014. – No. 9–3. – pp. 86–90.
10. Lagutin E.I., Mambetalieva Sh.M. Hydrogeochemical zones of the hydrosphere of Kyrgyzstan. Science, new technologies and innovations of Kyrgyzstan. 2018. No. 3. pp. 192–196
11. Kudelina I.V. On the zonality of fluid systems of the Southern Urals and Cis-Urals / I. V. Kudelina // International scientific research journal, 2020. - No. 11 (101), part 2, November. - pp. 71–75.
12. Pyankov S.V. Geoinformation support for modeling hydrological processes and phenomena: monograph / S.V. Pyankov, A.N. Shikhov; Perm. state national research univ. – Perm, 2017. – 148 p., ill.
13. Proceedings of the National Academy of Sciences, 2013; DOI:https://doi.org/10.1073/pnas.1220301110.chemport.ru.
14. Abdelali, A., Nezli, I.E., Kechiched, R., Attalah, S., Benhamida, S.A., Pang, Z., 2020. Geothermometry and geochemistry of groundwater in the Continental Intercalaire aquifer, southeastern Algeria: insights from cations, silica and SO4–H_2O isotope geothermometers. Appl. Geochem. 113, 104492 https://doi.org/10.1016/j.apgeochem.2019.104492.
15. Hadj Ammar, F., Deschamps, P., Chkir, N., Zouari, K., Agoune, A., Hamelin, B., 2020. Uranium isotopes as tracers of groundwater evolution in the Complexe Terminal aquifer of southern Tunisia. Quat. Int. https://doi.org/10.1016/j.quaint.2020.01.024.
16. Hakimi-Dedjell, Y., Orban, P., Chettih, M., Brouy‘ ere, S., 2019. Towards a rational exploitation of the groundwater resources of the Algerian Sahara, Ghardaia region: actual situation and recommendations. Special issue. Geo-Eco-Trop 43 (3), 375–384. http://www.geoecotrop.be/uploads/publications/pub_433_07.pdf.
17. Martin V.I. Hydrogeology and types of karst in Bashkiria: Author’s abstract. dis. ...cand. geol.-mineral. Sci. Perm, 1975. 31 p.
18. Hydrogeology of the USSR. M.: Nedra, 1972. T. 14. 648 p.; 1972. T. 43. 272 p.

On the Possibility of Using Lithospheric Topography to Estimate the Velocity at the Horizontal Upper Boundary of an Intense Vortex in the Mantle Beneath the Sea of Japan Region



S. Yu. Kasyanov

Abstract The model problem of finding a stationary axisymmetric flow of a homogeneous incompressible ideal fluid on the horizontal upper boundary of a cylindrical region at constant pressure, which is given by a model axisymmetric lithospheric relief constructed on the basis of the lithospheric relief of the Sea of Japan region, is considered. The radial distribution of the azimuthal and radial velocity components describing the anticyclonic circulation in the intramantle vortex under the Sea of Japan region is found from the solution of the equations of motion. The vortex is divided into an inner core and an outer part. The radial velocity of the vortex is continuous. The azimuthal velocity of the vortex undergoes discontinuities in the areas of rapid elevation of the lithosphere relief with increasing radius, corresponding to the positions of the "wall" of the inner core of the vortex and the "wall" of the outer part of the vortex. The azimuthal velocity of the vortex sharply increases as it approaches the "wall" of the outer vortex in the direction from the periphery to the vortex center. Similarly, the azimuthal velocity increases as it approaches the "wall" of the inner vortex core. The azimuthal velocity discontinuities at the "wall" of the inner vortex core and at the "wall" of the outer vortex are tangential discontinuities and may be unstable. In reality, intensive vortex formation with dissipation of kinetic energy into heat and intensive release of endogenous heat from the sea bottom into the water (mainly in the form of hot springs), which can influence the sea water circulation, should occur in the vicinity of azimuthal velocity discontinuities at the "wall" of the inner vortex core and at the "wall" of the outer part of the vortex.

Keywords Stationary axisymmetric flow · Ideal fluid · Lithospheric relief · Azimuthal velocity discontinuities · Intramantle vortex · Vortex core · Vortex formation · Dissipation of kinetic energy into heat · Endogenous heat release from the sea bottom into water · Hot springs · Sea of Japan

S. Yu. Kasyanov (✉)
N.N. Zubov State Oceanographic Institute, Roshydromet, Moscow, Russia
e-mail: skas53@yandex.ru

© The Author(s), under exclusive license to Springer Nature Switzerland AG 2024

V. Karev (ed.), *Proceedings of the 9th International Conference on Physical and Mathematical Modelling of Earth and Environmental Processes*, Springer Proceedings in Earth and Environmental Sciences, https://doi.org/10.1007/978-3-031-54589-4_56

1 Introduction

As part of the development of the hypothesis of the Earth's capture of a temporary Earth satellite, we considered the geophysical consequences of the satellite's orbital motion, deceleration, and sinking into the Earth's mantle [1–3]. The gradual decrease of the satellite orbit led to the fact that in the perigee of the orbit the satellite glided along the surface of the Earth's lithosphere and mantle. Tides in the mantle caused by the satellite's orbital motion led to the melting of the asthenosphere layer in the mantle, which subsequently partially solidified [1–3]. The satellite's full immersion into the mantle occurred in the vicinity of the Philippine Islands.

Trajectory of the satellite's plunge into the Earth's mantle during the final orbit. In the relief of the Pacific Ocean, shown in Fig. 1, the trace of the satellite's plunge trajectory during the final orbit, running from the U.S. coast through the Hawaiian Islands and the Mariana Basin to the Philippine Islands, stands out. During the final revolution of the orbit, the partially immersed satellite made oscillatory motions in the vertical direction while gliding along the surface of the lithosphere and mantle. The quasi-periodic motions in the vertical direction left traces in the vertical structure of the mantle temperature and density fields preserved up to the present time, which can be seen on the seismic section [4]. These vertical oscillations of the satellite led to the formation of a sinusoidal trace in the relief of the ocean floor—the Mid-Pacific Mountains [5].

During the final orbit, before the satellite's full penetration into the mantle, the depth of partial immersion of the satellite while gliding along the surface of the lithosphere and mantle increased. Before the satellite's final sinking into the mantle, a chain of "vortex semi-rings" was formed around its trajectory in the Earth's mantle, similar to the vortices around a jet invading a liquid studied in the experiments [6]. The chain of outlets of these "vortex semi-rings" on the day surface can be seen in the relief of the western part of the Pacific Ocean in Fig. 1 [5]. Then, at the full immersion of the satellite, a vortex ring was formed in the mantle [5, 7]. After the vortex ring disintegration, a quasi-stationary system of hot two-phase liquid–gas vortices was formed in the mantle [7], which is based on the present-day system of three energy-carrying vortices in the Earth's mantle. These vortices are: (1) Himalayas + Tian Shan-Kolyma, (2) Kolyma-Yellowstone, (3) Yellowstone-Hudson Bay-Eastern Mediterranean Sea [7].

By analogy with the jet invading a liquid in the laboratory experiment [6], the jet of hot (molten and partially vaporized) matter formed in the mantle behind the invading body created a chain of hot vortex semi-rings in the mantle around the trajectory of the body, which have been preserved up to the present time. The exit of one of the vortex semi-rings to the day surface formed the relief of the lithosphere under the Sea of Japan (see Fig. 1). Due to the mechanism of vortex formation in the mantle beneath the Sea of Japan region, the matter motion in it is anticyclonic. The chain of vortex semi-rings is hydrodynamically connected with the system of three energy-carrying vortices in the Earth's mantle [8], which is controlled by astronomical factors [7].

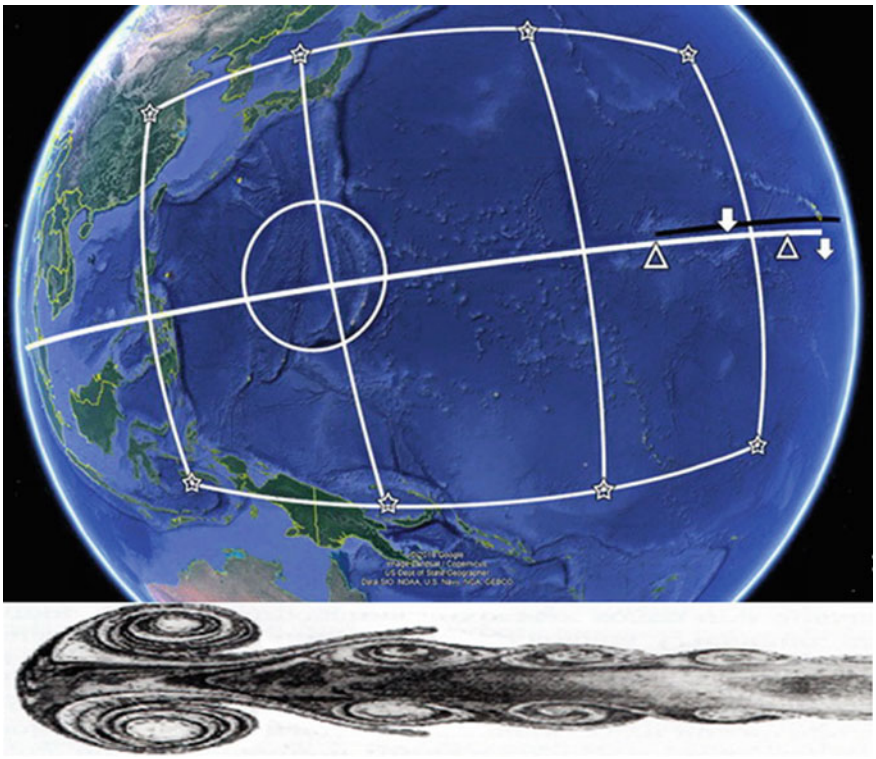


Fig. 1 Relief of the western Pacific Ocean and the trajectory of the temporary Earth satellite sinking into the mantle from Hawaii to the Philippine Islands [5]. The triangles are the areas of ascent and the arrows are the areas of trajectory lowering. The black line is a seismic section [4]. Stars—preserved southern outcrops of the "vortex semi-rings" and positions of the non-preserved northern outcrops symmetric to them relative to the trajectory. The Mariana Basin region is marked with a circle. Below is a similar chain of vortices around the jet invading the liquid in the laboratory experiment [6]

Consequently, the vortex state in the mantle under the Sea of Japan region is also controlled by astronomical factors.

Previously, we have shown that it is possible to estimate the density, velocity, and pressure-density dependence along a circular current line selected in advance at the upper boundary of the intramantle vortex [9]. The purpose of the present work is an approximate estimation of the velocities of the vortex substance at the upper boundary using the known topography of the lithosphere of the Sea of Japan region. Such an estimation is constructed within the framework of solving the model problem of stationary axisymmetric motion of a homogeneous incompressible ideal fluid at the flat upper boundary of the vortex. It is assumed that the pressure at the vortex boundary is known and equal to the hydrostatic pressure of the lithosphere and sea water.

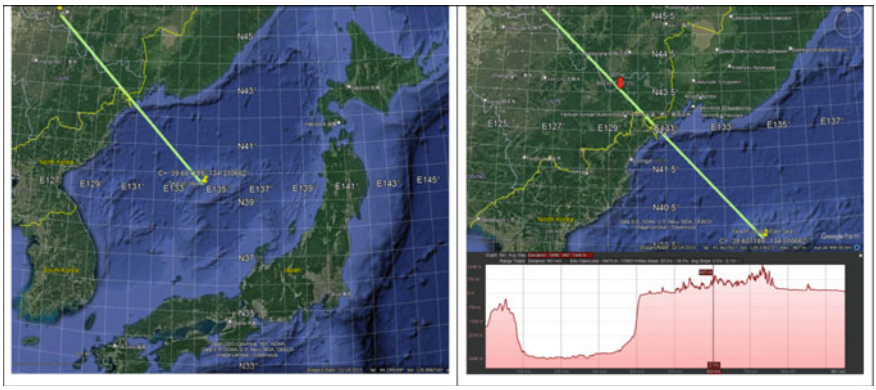


Fig. 2 Relief of the Sea of Japan. Selection of a ray as a basis for model relief construction for axisymmetric problem. The CE ray is shown as a white line. Coordinates of point C—the epicenter of the intramantle vortex under the Sea of Japan: 39.607°N, 134.311°E. Coordinates of the end of the beam—point E: 45.741°N, 126.233°E. The right half of the figure shows the relief of the lithosphere along the CE ray in the direction from the center to the periphery, i.e., the vortex center on the left is point C, and the vortex periphery on the right is point E. Cartographic basis Google Earth [10]

2 Relief Construction for Solving the Model Axisymmetric Problem

To solve the axisymmetric model problem, let us form some axisymmetric model relief reflecting the most important features of the lithospheric relief of the Sea of Japan region shown in Fig. 2.

Point C is chosen as the position of the epicenter of the intramantle vortex beneath the Sea of Japan in Fig. 2. As a basis for forming the axisymmetric model relief, we choose the relief of the lithospheric surface along the CE ray.

3 Algorithm for Constructing the Smoothed Model Relief of the Lithosphere.

The averaged values of the GEBCO lithospheric relief array [11] are calculated at the points of the CE beam with a step of 3731 m. The averaging is performed with a radius of 15/240 degrees meridian (15 cells of the GEBCO array). Spline interpolation is performed on the calculated averaged values and interpolated values of the smoothed model lithospheric relief are calculated in 1 m increments. The smoothed model relief of the lithosphere of the Sea of Japan region along the selected CE ray is shown in Fig. 3.

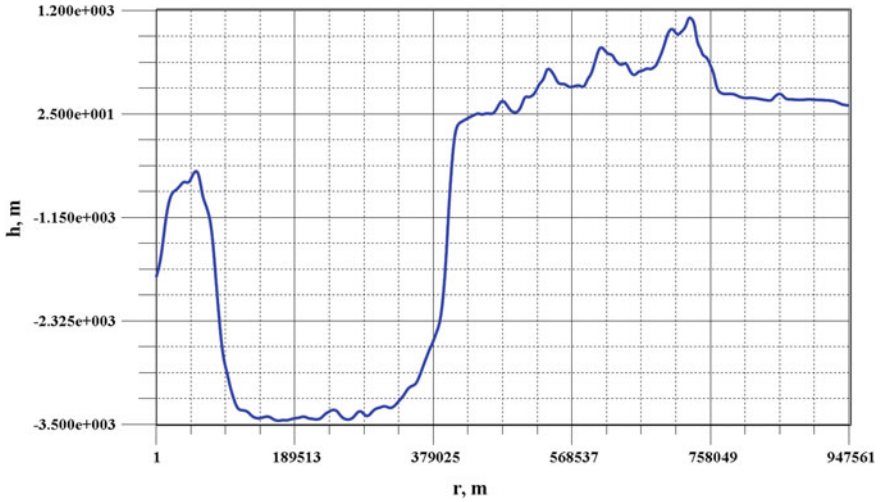


Fig. 3 Smoothed model topography of the lithosphere of the Sea of Japan region along the selected CE ray

4 Formulation of the Model Axisymmetric Problem

The axisymmetric stationary motion of an ideal incompressible fluid in a circular cylinder with a vertical axis and flat upper and lower boundaries is considered. The region of motion of the medium and the surrounding space rotates around the cylinder axis with constant angular velocity Ω. On the upper boundary of the medium motion region a time invariant pressure distribution is set $p = p(r)$.

The equations of unsteady axisymmetric motion of a homogeneous ideal incompressible fluid on the flat upper boundary of the cylindrical region have the form:

$$\frac{\partial V_r}{\partial t} + V_r \frac{\partial V_r}{\partial r} - \frac{V_\phi^2}{r} = -\frac{1}{\rho}\frac{\partial p}{\partial r} + 2\Omega V_\phi + \Omega^2 r \tag{1}$$

$$\frac{\partial V_\phi}{\partial t} + V_r \frac{\partial V_\phi}{\partial r} + \frac{V_r V_\phi}{r} = -2\Omega V_r \tag{2}$$

A system of two Eqs. (1) and (2) of first order. The natural boundary conditions at $r = 0$: $V_\phi = 0$, $V_r = 0$. Let us find the stationary states of this system of equations.

5 Equations of Stationary Axisymmetric Motion

$$V_r \frac{\partial V_r}{\partial r} - \frac{V_\phi^2}{r} = -\frac{1}{\rho}\frac{\partial p}{\partial r} + 2\Omega V_\phi + \Omega^2 r \tag{3}$$

$$V_r \frac{\partial V_\phi}{\partial r} + \frac{V_r V_\phi}{r} = -2\Omega V_r \tag{4}$$

From where

$$\frac{1}{2}\frac{\partial V_r^2}{\partial r} = -\frac{1}{\rho}\frac{\partial p}{\partial r} + \frac{V_\phi^2}{r} + 2\Omega V_\phi + \Omega^2 r \tag{5}$$

$$V_r\left(\frac{\partial V_\phi}{\partial r} + \frac{V_\phi}{r} + 2\Omega\right) = 0 \tag{6}$$

The velocities V_r and V_ϕ can be found by integrating the system of Eqs. (3) and (6) at known pressure p and $V_r \neq 0$.

The pressure is known in advance and is determined by the hydrostatic pressure of the lithosphere, taking into account the water column, so the continuity equation is not used to find the velocities V_r and V_ϕ. Let us use the continuity equation only to estimate the direction of upward and downward flows in the vicinity of the upper boundary where the velocities V_r and V_ϕ are estimated.

6 Special Cases

Note that when $V_r = 0$ Eq. (6) is satisfied at any V_ϕ.

If $V_r = 0$ takes place at $\frac{\partial p(r)}{\partial r} \geq 0$, then it follows from Eq. (3):

$$V_\phi^2 + 2\Omega r V_\phi - \frac{r}{\rho}\frac{\partial p}{\partial r} + \Omega^2 r^2 = 0, \tag{7}$$

whence we find two solutions for V_ϕ:

$$V_\phi = -\Omega r \pm \sqrt{\Omega^2 r^2 + \frac{r}{\rho}\frac{\partial p}{\partial r} - \Omega^2 r^2} = -\Omega r \pm \sqrt{\frac{r}{\rho}\frac{\partial p}{\partial r}} \tag{8}$$

Since the motion in the vortex is anticyclonic, we choose the minus sign in expression (8).

Thus, the azimuthal velocity V_ϕ in this case undergoes a discontinuity.

If at $V_r = 0$, $\frac{\partial p(r)}{\partial r} < 0$, then Eq. (7) has no roots and we cannot find a stationary value of the azimuthal velocity V_ϕ from it.

In this case

$$\frac{1}{2}\frac{\partial V_r^2}{\partial r} = -\frac{1}{\rho}\frac{\partial p}{\partial r} + \frac{V_\phi^2}{r} + 2\Omega V_\phi + \Omega^2 r = -\frac{1}{\rho}\frac{\partial p}{\partial r} + \frac{1}{r}(V_\phi + \Omega r)^2 > 0.$$

Therefore, when integrating over the radius of Eq. (5), the value $V_r^2(r)$ becomes positive. When integrating $V_r^2(r)$, the value of $V_r(r)$, is calculated, and the sign of the value is chosen positive in accordance with the positive sign $\frac{\partial V_r}{\partial t}$ in Eq. (1).

Since the value $V_r^2(r)$ becomes positive when integrating over the radius of Eq. (5), then the condition $V_r \neq 0$ begins to be fulfilled. This allows us to find V_ϕ from Eq. (6) by integrating equation

$$\frac{\partial V_\phi}{\partial r} + \frac{V_\phi}{r} + 2\Omega = 0 \tag{9}$$

7 Result of Integration of the Equations of Motion

Taking into account the above special cases and natural boundary conditions $V_\phi = 0$, $V_r = 0$ at $r = 0$, the stationary equations of motion can be numerically integrated over the radius and the dependences of velocities V_r and V_ϕ on the radius, shown in Fig. 4, can be obtained.

The continuity equation, which did not need to be used to find the velocities when the pressure distribution is known in advance from the lithospheric topography,

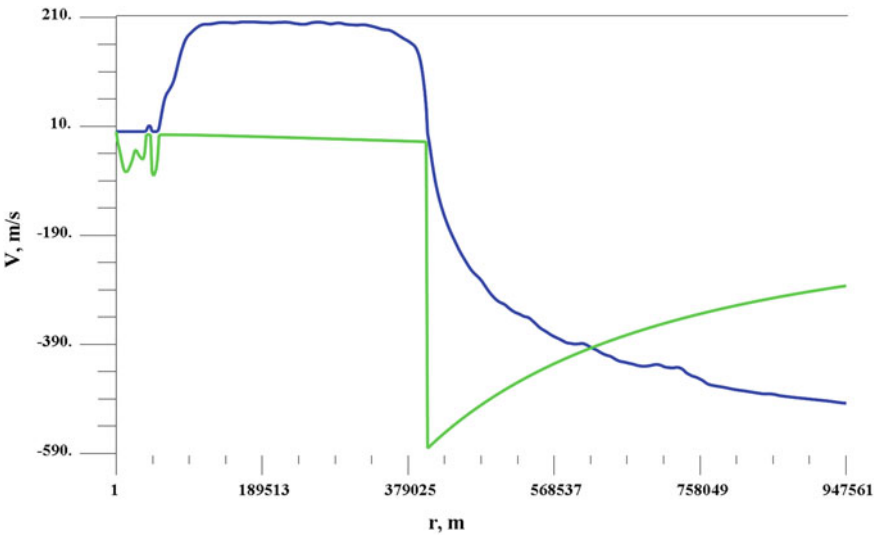


Fig. 4 Radial and azimuthal velocities of stationary axisymmetric motion. Blue curve—radial velocity V_r, green curve—azimuthal velocity V_ϕ

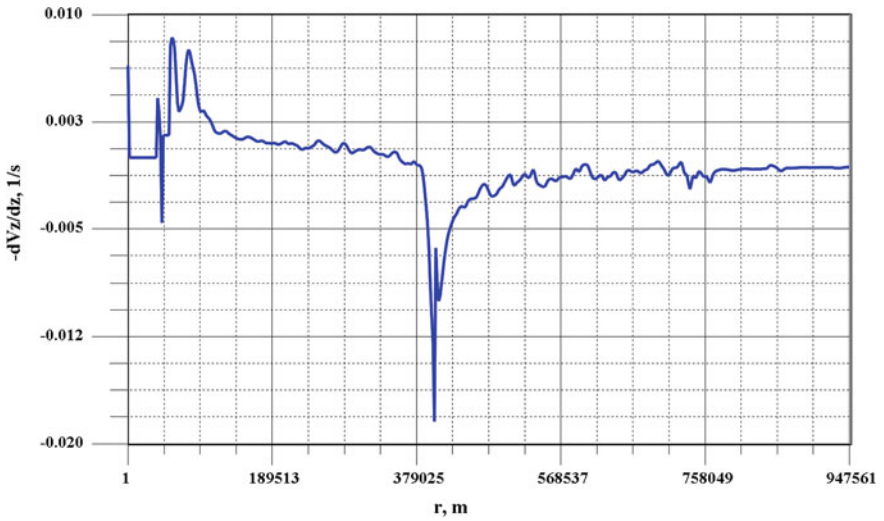


Fig. 5 Divergence of the horizontal velocity at the upper boundary of the vortex motion region (equal to −dVz/dz, where Vz is the vertical velocity), reflecting the direction and relative intensity of vertical motions in the vicinity of the horizontal boundary

allows us to better visualize the spatial structure of the flow in the vortex. Therefore, for a qualitative assessment of the structure of vertical motions at the horizontal vortex boundary, we additionally use the equation of continuity of a homogeneous incompressible fluid in the axisymmetric case. From this equation according to the value of the horizontal divergence presented in Fig. 5, we can qualitatively estimate the direction and relative intensity of vertical motions in the nearest vicinity of the upper horizontal boundary of the vortex.

8 Conclusions

The model problem of finding a stationary axisymmetric flow of an ideal fluid on the horizontal upper boundary of a cylindrical region under time-constant pressure, the distribution of which is given by the model relief of the lithosphere, is considered. The smoothed model axisymmetric relief is constructed on the basis of data on the real relief of the lithosphere of the Sea of Japan region.

The solution of the equations of motion describing the anticyclonic circulation in the intramantle vortex is found. The solution is determined by the smoothed model axisymmetric lithospheric topography and depends on the smoothing.

The vortex is divided into an inner core and an outer part. The radial velocity of the vortex is continuous. The azimuthal velocity of the vortex undergoes discontinuities in areas of rapid uplift of the lithospheric topography with increasing radius. The azimuthal velocity discontinuities correspond to the positions of the “wall” of the

vortex inner core and the "wall" of the vortex outer part. The azimuthal velocity of the vortex sharply increases when approaching the "wall" of the outer part of the vortex in the direction from the periphery to the center of the vortex and similarly increases as it approaches the wall of the inner core of the vortex.

The azimuthal velocity discontinuities at the "wall" of the inner vortex core and at the "wall" of the outer part of the vortex are tangential discontinuities and may be unstable.

Taking into account non-ideality of matter in the intramantle vortex in nature, intensive vortex formation with dissipation of kinetic energy into heat should occur at the "wall" of the inner core of the intramantle vortex and at the "wall" of the outer part of the vortex. The latter leads to the appearance of local zones of intensive endogenous heat release from the sea bottom into the water (mainly in the form of hot springs), which can influence the sea water circulation.

References:

1. Kasyanov S.Yu. Modeling of orbital motion of a large asteroid during descent with deepening into the Earth's lithosphere and mantle // Physical Problems of Ecology (Environmental Physics). 2012. № 18. С. 151–164. http://ocean.phys.msu.ru/pubs/ecophys/ecophys-18_pp150-246.pdf
2. Kasyanov S.Yu., Samsonov V.A. Estimation of tidal wave heights during gliding of a large satellite on the surface of a liquid attracting spherical layer with a solid core // Proceedings of MIPT. 2017. Т. 9, № 3. С. 14–20. https://mipt.ru/upload/medialibrary/d1a/2_kas_yanov_14_20.pdf
3. Kasyanov S, Samsonov V (2018) Effect of a tidal wave caused by large gliding satellite on formation of 220 km seismic boundary and split of the mantle into blocks. In: Karev V, Klimov D, Pokazeev K (eds) Physical and mathematical modeling of earth and environment processes. PMMEEP 2017. Springer Geology. Springer, Cham, pp 360–370. First Online 25 March 2018. https://doi.org/10.1007/978-3-319-77788-7_37, Print ISBN 978-3-319-77787-0, Online ISBN 978-3-319-77788-7
4. Cao Q, Van der Hilst RD, de Hoop MV, Shim S-H (2011) Seismic imaging of transition zone discontinuities suggests hot mantle west of Hawaii. Science 332(6033):1068–1071. https://doi.org/10.1126/science.1202731
5. Kasyanov, S.Y. (2021). Formation of System of Intense Vortices in the Mantle When a Large Temporary Earth Satellite is Immersed. In: Chaplina, T. (eds) Processes in GeoMedia—Volume III. Springer Geology. Springer, Cham. pp 217–232. https://doi.org/10.1007/978-3-030-69040-3_21
6. Gharib M, Rambod E, Shariff K (1998) A universal time scale for vortex ring formation. J Fluid Mech 360:121–140
7. Kasyanov, S.Y., Samsonov, V.A. (2021). About the Modern System of Three Energy-Carrying Intensive Vortices in the Earth's Mantle. In: Chaplina, T. (eds) Processes in GeoMedia - Volume II. Springer Geology. Springer, Cham. pp 273–291. https://doi.org/10.1007/978-3-030-53521-6_31
8. Kasyanov S.Yu. (2023) Hydrodynamic interaction between two systems of intense intra-mantle vortices as a possible cause of the connection between distant earthquakes. In: Chaplina, T. Chaplina (eds) Processes in GeoMedia — Volume VII, pp 159–169, Springer Geology, https://doi.org/10.1007/978-981-99-6575-5_15
9. Kasyanov, S.Yu. (2022). On the Possibility of Use the Himalayan-Tien Shan Mountain Ring Relief to Assess the State of the Substance at the Boundary of Intense Vortex in the Underlying

Mantle. In: Chaplina, T. (eds) Processes in GeoMedia—Volume IV. Springer Geology. Springer, Cham, pp 99–107. https://doi.org/10.1007/978-3-030-76328-2_11
10. Google Earth Pro. https://www.google.com/earth/about/versions/#download-pro
11. https://download.gebco.net/

Development of the Concept of a Modern Approach to Well Construction



R. R. Galliamov and R. A. Ismakov

Abstract The primary objectives of this research involve examining the principles and techniques of employing both retrospective and real-time analyses in the construction of oil and gas wells. Furthermore, considerable time invested by engineering teams in formulating a drilling plan for the drilling crew could be optimized through partial or complete automation. A data-centric approach to automated drilling scheduling for wells sharing similar design and geological characteristics is proposed, aiming to enhance the categorization of operations based on the IADC drilling classification.

Keywords Analysis of processes · Non-productive time · Cross-well correlation analysis · Bottom hole assembly · Drilling fluid · Surface data logging · Kick-off · Accident · Failure

1 Introduction

Well construction represents the most expensive phase in the life cycle of an oil field. Oil and gas companies meticulously calculate all potential costs to ensure that the funds invested in well construction not only recover over time but also generate profits during operation. The time allocated for each well construction operation is strictly regulated. However, the time spent on specific activities, such as casing cementing or the lowering of the casing, may vary significantly among different oil and gas companies.

Meanwhile, some oil and gas companies face challenges in accurately calculating their well construction expenses, incurring significant costs and losses that could potentially be reduced. Additionally, engineering teams invest a considerable amount of time in developing a drilling plan for the drilling crew, which could be fully or

R. R. Galliamov (✉) · R. A. Ismakov
Federal State Budgetary Educational Institution of Higher Education, Ufa State Petroleum Technical University, Ufa, Russia
e-mail: gallyamovrustam96@gmail.com

© The Author(s), under exclusive license to Springer Nature Switzerland AG 2024

V. Karev (ed.), *Proceedings of the 9th International Conference on Physical and Mathematical Modelling of Earth and Environmental Processes*, Springer Proceedings in Earth and Environmental Sciences, https://doi.org/10.1007/978-3-031-54589-4_57

partially automated. In the development of automated drilling scheduling for wells, an approach based on utilizing various data obtained during the construction of wells with similar project and geological characteristics is proposed. Furthermore, some enhancements to the classification of drilling operations based on IADC codes are suggested.

Currently, leading global oilfield service companies are developing similar digital products to address the described challenges. However, the utilization of these products in the Russian well construction market is heavily restricted due to sanctions and the cost of ready-made solutions.

Throughout the study, algorithms and standards for determining planned durations of operations have been examined. Additionally, a proposed approach to conducting the workflow for well construction planning allows for an analytical review of best practices and technologies used at all stages of the work cycle. This is based on retrospective macro-data from well construction, micro-data from sensors on drilling rigs, obtained through the WITS/WISML data transmission protocol.

2 Analysis of the Current State and Future Development Prospects of the Oil and Gas Industry

Worldwide, the oil and gas industry is experiencing a reduction in low-cost hydrocarbon reserves, leading to a decline in the profitability of field development. Decreased economic indicators necessitate increased efficiency in the operations of oil and gas enterprises through the optimization of technological processes. One solution in this realm is the utilization of new digital technologies based on big data [1].

In accordance with Russia's energy strategy for the period up to 2035, the development of the domestic market for high-tech service and engineering services is identified as a key task for the domestic oil industry. Maintaining and increasing hydrocarbon production in Russia determines the stability not only of the oil and gas sector but also of the country's economy as a whole. This is impossible without the use of new technologies and big data.

According to KPMG (KPMG International Limited), currently, only 5% of the data received from operating rigsite is processed. The potential for increasing operational efficiency through process optimization in the planning, design, construction, and analysis of well construction results based on more data can reach 30% [2].

Currently, leading global oilfield service companies are developing digital products to address these challenges. However, the use of these products in the Russian drilling market is severely restricted due to sanctions and the cost of ready-made solutions. Additionally, in many cases globally, either several separate applications from one company or services provided by different companies create inconvenience for customers [2].

The idea of creating a software suite operating on a single platform and through a web browser will allow customers to use a unified application for their activities. Digital transformation in leading Russian extraction companies is accompanied by the implementation of elements of a digital oilfield, including those related to well construction processes [1].

Key Problems:

1. Low Quality of Manual Documentation

The manual preparation of reporting documentation results in low-quality outputs, posing challenges in terms of accuracy and reliability [3].

2. Lack of Transparent Key Performance Indicator (KPI) Tracking [4]

There is a deficiency in transparently tracking key performance indicators during well construction, hindering the ability to assess project effectiveness.

3. Insufficient Real-Time Control Over Well Construction Processes

Inadequate real-time monitoring and control over well construction processes lead to potential inefficiencies and difficulties in responding promptly to issues.

4. Underutilization of Production Data:

The data received from oilfield assets is not adequately utilized for making informed production decisions, limiting the potential for optimizing operations.

5. Relevance to Stakeholders:

The identified problems are pertinent to a range of stakeholders, including oil and gas companies, drilling firms, service providers, and remote support centers involved in well construction.

Innovation:

1. Analysis Based on Mathematical Algorithms [5]

The scientific and technical novelty lies in the application of mathematical algorithms developed during experimental and industrial work on Russian projects. These algorithms are employed for the analysis of key performance indicators in well construction processes.

2. Adaptation of IADC Codes

The use of the International Association of Drilling Contractors (IADC) classification codes, adapted to the specific conditions of the Russian drilling and well development market, contributes to a standardized and globally recognized approach.

The combination of these original approaches aims to address the identified problems and enhance the efficiency and effectiveness of well construction processes in the oil and gas industry.

Solution

Objective and Scope of the Methodology:

1. The methodology is designed for the automation of the analysis of techno-economic indicators throughout the lifecycle of well construction. Its primary objectives include:
2. Enhancing Process Efficiency:

Achieving increased efficiency in work processes through the automation of operational tasks and the reduction of working hours spent on preparing reporting documentation.

3. Remote Monitoring of Well Construction [7]

Facilitating remote monitoring of the well construction process, allowing for real-time oversight without the need for physical presence at the site.

4. Data-Driven Decision Making:

Enabling decision-making based on statistical analysis, utilizing gathered data to inform and guide the decision-making process.

5. Mitigating Technological Risks:

Reducing technological risks during well construction through systematic analysis and proactive measures.

6. Reducing Well Construction Time [8]

Minimizing the overall time required for well construction operations through streamlined processes and informed decision-making.

The data requirements and their transmission are presented in Fig. 1 [5].

Principles

Figure 2 illustrates the principle of a modern approach to well construction time analysis. The conservative principle involves considering visible non-productive time, including the following classes of non-productive time (Fig. 2).

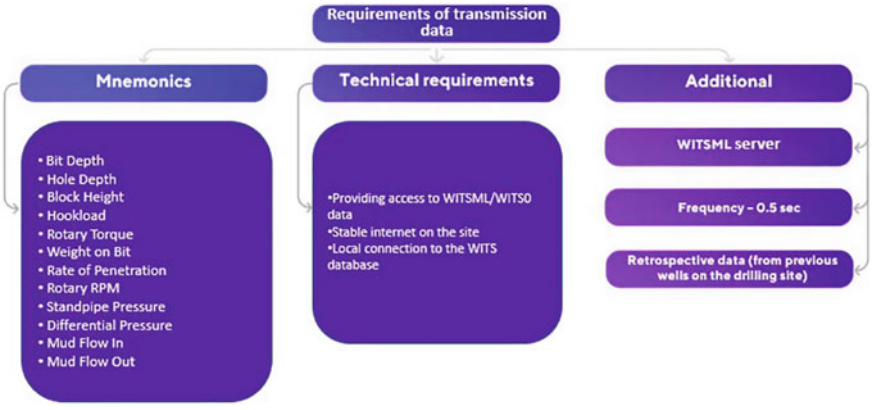


Fig. 1 Data requirements

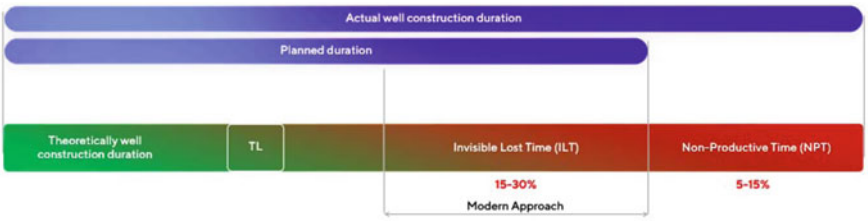


Fig. 2 Modern approach to well construction time analysis [6]

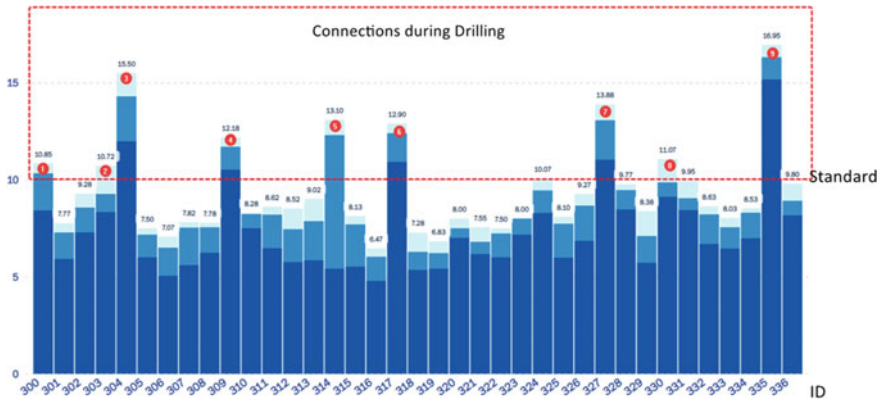


Fig. 3 Real-time calculation of invisible lost time

Time spent by the drilling crew addressing production, technical, or technological errors leading to accidents (blowouts, foreign objects falling into the well, surface equipment accidents, etc.).

Complications (absorption, sticking of the drilling or casing string, wellbore instability, etc.) and defects (unforeseen equipment failures, deviation from the wellbore trajectory, defects during casing, etc.).

Downtime due to equipment breakdowns and waiting for the drilling crew due to equipment failure, lack of material and technical resources and/or contractor personnel, adverse weather conditions, power outages, etc.

Time spent on repairing drilling equipment [6].

In the second stage, "preparation for the drilling process," based on the analysis of composite well drilling time, Invisible Lost Time (ILT) is identified. A set of the best methods to reduce NPT is determined, and available technologies for reducing time spent on well construction are selected.

Invisible Lost Time is defined as the difference between the established norm and the actual time spent on all types of work. Identifying and preventing the occurrence of Invisible Lost Time becomes possible with efficient resource allocation and auxiliary work planning.

An example of Invisible Lost Time is presented in Fig. 3. Thus, ILT exceeded 30 min in less than a full day of drilling, indicating a loss of effective time by more than 2%.

Summing up all the above, the definition of both effective and non-effective time, as well as its thorough analysis, will help approach the technical limit of well construction.

3 Operation Codes

In order to standardize to bring into a uniform system or reporting form, an enhanced classification of operation codes has been established. This classification is based on the International Association of Drilling Contractors (IADC) classification of drilling operations, enabling us to compare similar operations with each other.

The classification codes are based on 9 main codes that determine the type of operation (drilling, installation works, disconnection, well casing, etc.).

The second part of the well construction operation code consists of sub-codes that provide a more detailed characterization of the operations. For example, according to Table 1, rotary drilling with a drill string and a PDM has the code 201 (200—main drilling code, 001—detailed description).

Table 1 Classification of operations

Operation type	Code
Productive time	
Derreck building	101–199
Drilling	201–299
RIH/POOH	301–399
Circulation	401–399
Logging	501–599
Casing	601–699
Cementing	701–799
RU/LD surface equipment	801–899
Completion	901–999
Sub-operations	1001–1099
Non-productive time	
Accident	2001–2099
Incidents	2101–2199
Failure	2201–2299
Down time	2301–2399
Repair	2401–2499
Geological	2501–2599

4 Best Composite Well

A composite well is assembled from sections with minimal time—it is not merely the best well, but a well that combines the best practices of individual operations (Fig. 4).

An ideal well can be considered one that has no non-productive time and achieves maximum efficiency in all operations through the application of modern innovative technologies.

However, such an ideal well may not always be optimal in terms of current profitability. Modern technologies are expensive, although they promise superior results in the future. Nevertheless, composite wells are positioned to be the driving force behind progress.

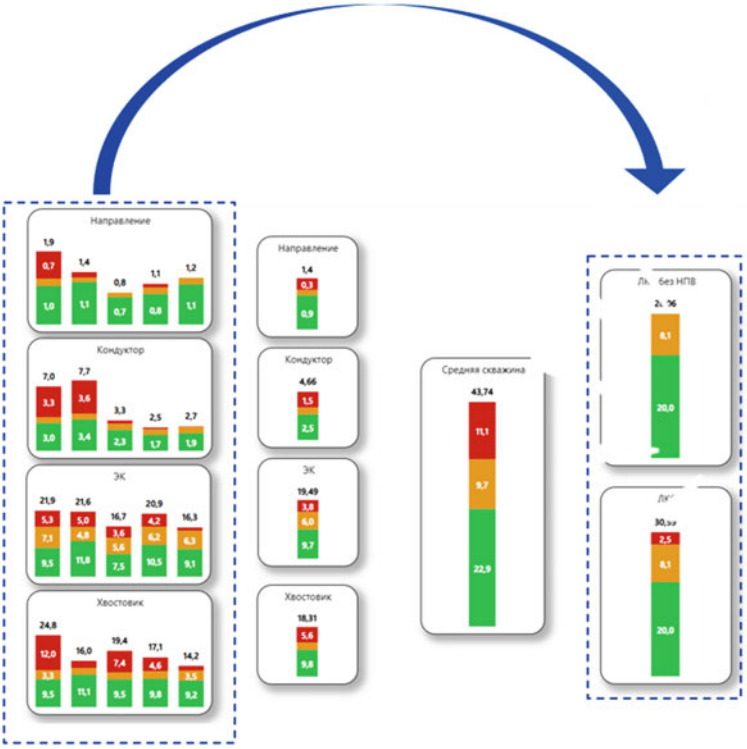


Fig. 4 The process of constructing the best composite well

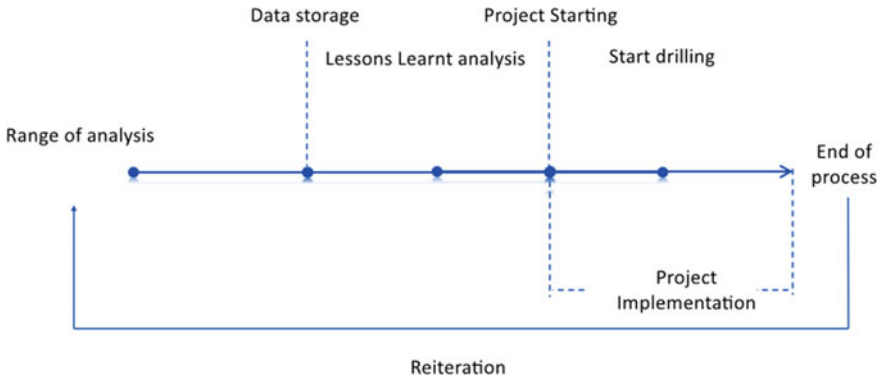


Fig. 5 Roadmap of well construction

5 Conclusion

Based on the findings of this study, a principle for the workflow of planning and implementing a project, such as the construction of oil and gas wells, is proposed.

According to Fig. 5, early planning will provide greater flexibility during the implementation phase, allowing for the refinement of technological measures and the development of a group working project considering statistical information from previously drilled wells.

Analytical monitoring during construction drilling will enable the achievement of optimal composite well construction time.

References

1. "Russian Oil Well Drilling Market: Current State and Development Scenarios Until 2030" – 2022. – URL: http://www.rpi-consult.ru/reports/dobycha-nefti-i-gaza/rossiyskiy-rynok-bureniya-2022/. (Accessed: October 2, 2023).
2. "Oilfield Services Market in Russia: Focus on Diversification" – 2022. – URL: https://vygon.consulting/products/issue-1952/ - (Accessed: October 2, 2023).
3. Tavallali, Bakhtazma, Meymandpour, Sadeghi, and Hamed. 2015. "A Drilling Scheduling Toolbox For Oil and Gas Reservoirs. " 12th International Symposium on Process Systems Engineering and 25th European Symposium on Computer Aided Process Engineering.
4. Ashok, P., Ambrus, A., Ramos, D., Lutteringer, J., Behounek, M., Yang, Y. L., Thetford, T., and Weaver, T., 2016, "A Step by Step Approach to Improving Data Quality in Drilling Operations: Field Trials in North America," SPE Intelligent Energy International Conference and Exhibition, Aberdeen, Scotland, UK, Society of Petroleum Engineers.
5. Tsivinskiy, D.K. "Application of Statistical Analysis Method in the Oil and Gas Industry: Educational Manual." - 2nd ed., revised and expanded. - Samara: Samara State Technical University, 2014. - 377 p., with illustrations.
6. John P de Wardt; Peter H Rushmore; Phillip W Scott: True Lies: Measuring Drilling and Completion Efficiency, URL: https://doi.org/10.2118/178850-MS.

7. Sugiatmo Kasmungin Universitas Trisakti The Effect of Invisible Lost Time on Drilling Performance of Geothermal Wells Journal of Earth Energy Science Engineering and Technology 3(1) DOI:https://doi.org/10.25105/jeeset.v3i1.6662.
8. Invisible Lost Time Measurement and Reduction Contributes to Optimizing Total Well Time by Improving ROP and Reducing Flat Time Published: 04/23/2018 URL: https://www.slb.com/resource-library/technical-paper/so/spe-192319.

The Black Sea Northern Part Spatial Zoning in Terms of the Mixing Processes Intensity Based on the Data Processing Results of 87, 92, 102 and 110 Voyages of the R/V "Professor Vodyanitsky"

D. A. Kazakov, A. S. Samodurov, and O. I. Pavlenko

Abstract The paper examines the results of expeditionary work carried out by the Turbulence department of the Marine Hydrophysical Institute of RAS in the Black Sea on the R/V Professor Vodyanitsky in various seasons of 2016–2019 in order to clarify the local and seasonal parts of the models of vertical turbulent exchange in the thermocline region. Graphs of seasonal variability in buoyancy frequency N and vertical turbulent exchange coefficient K were plotted. The study area was also divided into regions according to hydrological features and bottom topography, followed by a correlation analysis of the vertical turbulent diffusion coefficient variability with depth in each region. The dependencies profiles obtained, averaged over the selected regions, were compared with the 1.5D model and showed good convergence in the region of the seasonal and main thermoclines. The data covers the summer-autumn period and was collected using the Sigma-1 sounding complex. They include the shelf, slope and deep-water part of the economic zone of the Black Sea near the Crimean coast. The dependences $K(N)$, $K(z)$, $N(z)$ were obtained based on existing semi-empirical models of vertical turbulent exchange. The estimates were based on an analysis of the spectra of vertical gradients of horizontal velocity pulsations. The spectra were calculated at three-meter depth intervals for each station, which at a signal sampling frequency of 100 Hz made it possible to obtain a reliable estimate. The main result of the work carried out is taking into account the characteristics of the selected regions in order to obtain in the future more accurate models of vertical turbulent exchange.

Keywords Black sea · Energy dissipation · Stratified layer · Vertical turbulent exchange · Buoyancy frequency · Measuring complex · Field measurements · Turbulence models · 1.5D model

D. A. Kazakov (✉) · A. S. Samodurov · O. I. Pavlenko
Marine Hydrophysical Institute of RAS, 29800 Sevastopol, Russian Federation
e-mail: dk@mhi-ras.ru

© The Author(s), under exclusive license to Springer Nature Switzerland AG 2024

V. Karev (ed.), *Proceedings of the 9th International Conference on Physical and Mathematical Modelling of Earth and Environmental Processes*, Springer Proceedings in Earth and Environmental Sciences, https://doi.org/10.1007/978-3-031-54589-4_58

1 Introduction

Over the past decades, there has been a growing trend in scientific and practical problems solving in the seas and oceans ecosystems state forecasting. One of the key methods to patterns determination of the marine systems state changes is the turbulent exchange models development for their further application in predictive models of various scales and areas of application. Therefore, the purpose of this paper is an attemption to identify the patterns that determine the vertical structure of mixing in the Black Sea, based on well-known semi-empirical approaches to determining the turbulent regime in stratified layers of the sea using data on the hydrological and topographical features of the region under study. This would make it possible to provide a clearer picture of the dependence of turbulent exchange intensity on environmental conditions and physical processes affecting vertical mixing in the stratified layers of the studied region. Such dependencies could provide us better model results on a spatial grid in future.

To solve this problem, hydrological data and data on the fine and microstructure of hydrophysical fields from 87, 94, 102 to 110 voyages of the R/V Professor Vodyanitsky for 2016–2019 were used. Information collection was carried out in the northern part of the Black Sea within the economic zone of Russia in order to obtain the characteristics of vertical turbulent mixing and background characteristics of the environment in the study region. The data covers the spring–summer-autumn period, which allows us to draw certain statistical conclusions. The study was carried out by the departments of turbulence and oceanography of the MHI RAS. Research in this region included obtaining the vertical turbulent diffusion coefficient K dependences on the buoyancy frequency N and on the depth z based on the flow fluctuation characteristics in the upper hundred-meter layer of the sea. Dependences were compared with hydrological data at the corresponding stations, as well as a general analysis of the study areas hydrophysical features and their surroundings was carried out.

2 Methods and Data Processing

The background hydrological characteristics were recorded using a CTD SBE 911plus complex, and the zonal and meridional components of current velocity in the upper layer from 5–10 to 300 m were recorded using an Acoustic Doppler Current Profiler (ADCP).

The Sigma-1 (see Fig. 1) complex was used as a microstructural measuring probing device, the operating principle of which is to record fluctuating hydrophysical quantities during the free fall of the probe at a speed of 0.7 $m \cdot s^{-1}$ to a given depth.

The peculiarity of the Sigma-1 complex is that it directly measures velocity fluctuations. The horizontal component is selected from them, and the smoothed values of the pulsation gradient $\Delta u/\Delta z$ in a certain layer are calculated, from which the rate



Fig. 1 Microstructural probe "Sigma-1" with a standard combination of sensors: fluctuation of temperature, electrical conductivity and flow speed

of dissipation of turbulent energy ε is determined with iterative method. First, the boundary wave numbers k_l (defining the inertial subrange of the turbulence spectrum from low frequencies) and k_{max} are determined, then the spectrum of du/dz is calculated by the Welch's method [1]: records are divided into overlapping segments, which are multiplied by the Hann time window, then a Fourier transform is performed, followed by averaging of the spectral functions over all segments. The quality of the obtained pulsation spectra was estimated from the average absolute deviation from the Nasmyth model spectrum [2]. Then the dispersion $\left[\overline{(du/dz)^2}\right]$ is determined by integrating of spectrum values in a selected range of wave numbers. The dissipation rate of turbulent energy is determined by relation

$$\varepsilon = \frac{15}{2}\nu\left[\overline{(du/dz)^2}\right]. \tag{1}$$

This value of ε is used to calculate the Kolmogorov (non-dimensional) wave number:

$$k_c = (1/2\pi)(\varepsilon/\nu^3)^{1/4}, \tag{2}$$

where ν—kinematic viscosity. If the stop conditions are not met, the cycle is repeated, starting with the calculation of the spectrum. The stopping criteria are a small change in the value of k_c (less than the step in the spectrum Δk) and the excess of k_c over k_{max}. Due to the relatively high probe sinking speed, the vertical speed component is not taken into account, and a vertical gradient of horizontal fluctuations is used: first, noise contamination caused by vibration of the device is removed, then a bandpass filter is used to limit the frequencies of the measured fluctuations.

The coefficient of vertical turbulent diffusion is calculated according to the formula proposed by Osborne [3]:

$$K \cong \frac{R_f}{1 - R_f}\frac{\varepsilon}{N^2}, \tag{3}$$

where R_f is the dynamic Richardson number (the ratio of the potential energy increase rate in the system to the rate of energy input there, spent on mixing). In papers

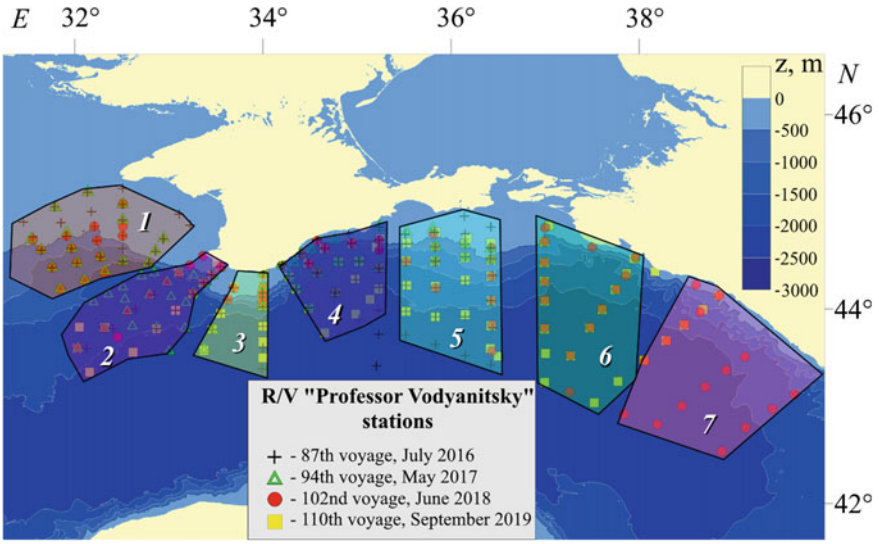


Fig. 2 Sounding stations layout from the R/V "Professor Vodyanitsky" and the regions identified in it according to the distribution of K values and their characteristic hydrological features

[4–6] its constancy was established for the considered phenomena using various approaches. $N = \sqrt{\frac{g}{\rho}\frac{\partial \rho}{\partial z}}$ is the buoyancy frequency, or Brent-Väisälä, calculated through the potential density and its gradient, and accordingly implicitly including the temperature and salinity components. The R_f value in this study was taken equal to ¼, in accordance with the approximate result from [5].

The completed stations layout and the timing of the expeditions are presented in Figs. 1 and 2.

3 Results and Discussion

Spatial distributions of K and N were obtained for the upper hundred-meter layer with a depth interval of 3 m. Averaged dependencies were analyzed for stations in which the depth of the site is in four ranges: from 0 to 100 m; from 100 to 500 m; from 500 to 1300 m; more than 1300 m (in accordance with the presence of possible effects described in [7]). Figure 3 shows profiles for the corresponding depth ranges.

Tracing the profiles transformation as the depth of the station location increases, one can notice that the calculated distributions repeat the model distribution of K and N with their characteristic inflection points, but with larger coefficient values. This is especially clearly seen in the example of the 94th cruise: the data were collected mainly in the northwestern part of the study region and in the area of a sloping bottom near the Prikerchensky region. With an increase in the number of stations carried out

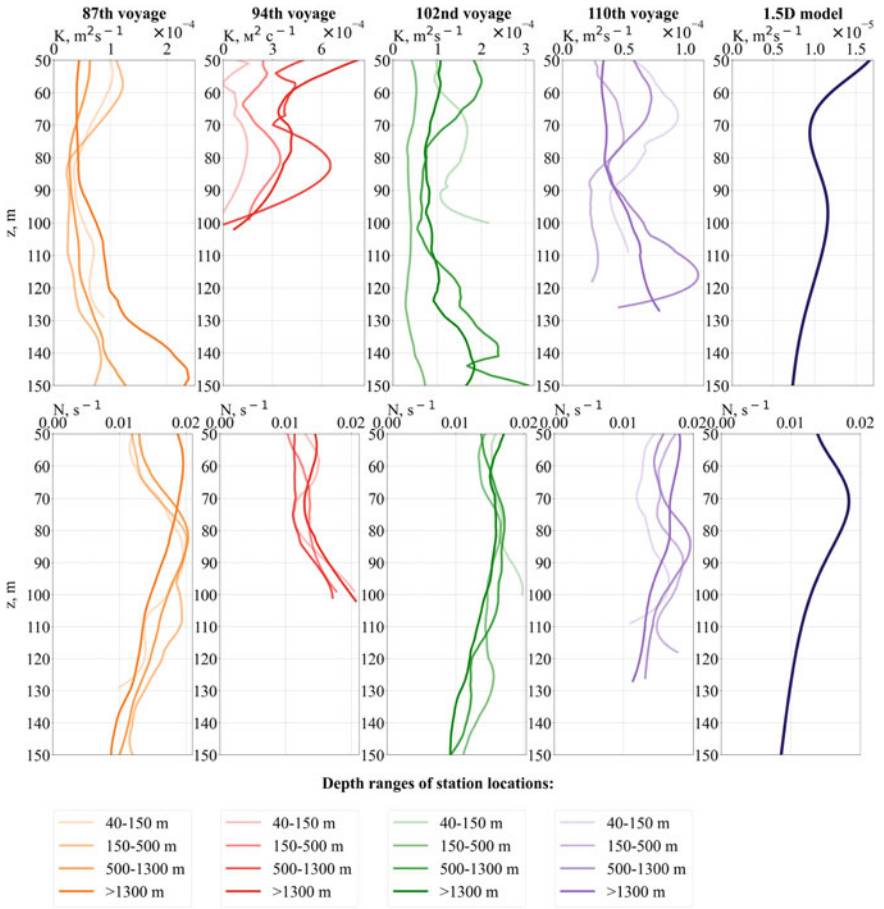


Fig. 3 $K(z)$ and $N(z)$ profiles based on measurement results (8 graphs on the left) and 1.5D model (far right). The degree of color saturation in the graphs corresponds to a certain depth range of the stations locations

mainly over the deep-water part of the Black Sea (87th, 102nd, 110th cruises), the change in K with depth approaches the model range of values—about 10^{-5} m^2s^{-1}. This indicates a decrease in the coastal hydrophysical phenomena influence on the overall picture of turbulent mixing in depth ranges of 500 m and more, which confirms the significant effect on exchange processes in the upper stratified layers of the Black Sea of the effects described in [8].

Figure 4 gives an idea of the power law approximation $K \cong A \cdot N^{\alpha}$ in the study area. The values of the dependence degrees vary from $\alpha = -1.5$ to $\alpha = -2.3$, which, however, on average for voyages gave a result close to $\alpha \approx -1.8$. The coefficients A differ significantly by several orders of magnitude. Such differences are due to special hydrological regimes in the depth ranges under consideration and the fact

that several conventional depth areas are covered in which mixing occurs due to various physical mechanisms as stated earlier in [9].

In the 94th voyage, which occurred at the end of spring—beginning of summer, the degrees of dependence varied depending on the depth of the place from $\alpha = -1.9$ to $\alpha = -2.6$, on average $\alpha \approx -2.2$. In the summer 102nd voyage $\alpha = -1.6 \div -2.7$, on average also $\alpha \approx -2.2$. However, for the autumn 110th voyage, the order of values for coefficient A and the degrees of dependence has changed: $\alpha = -0.7 \div -2.3$ with

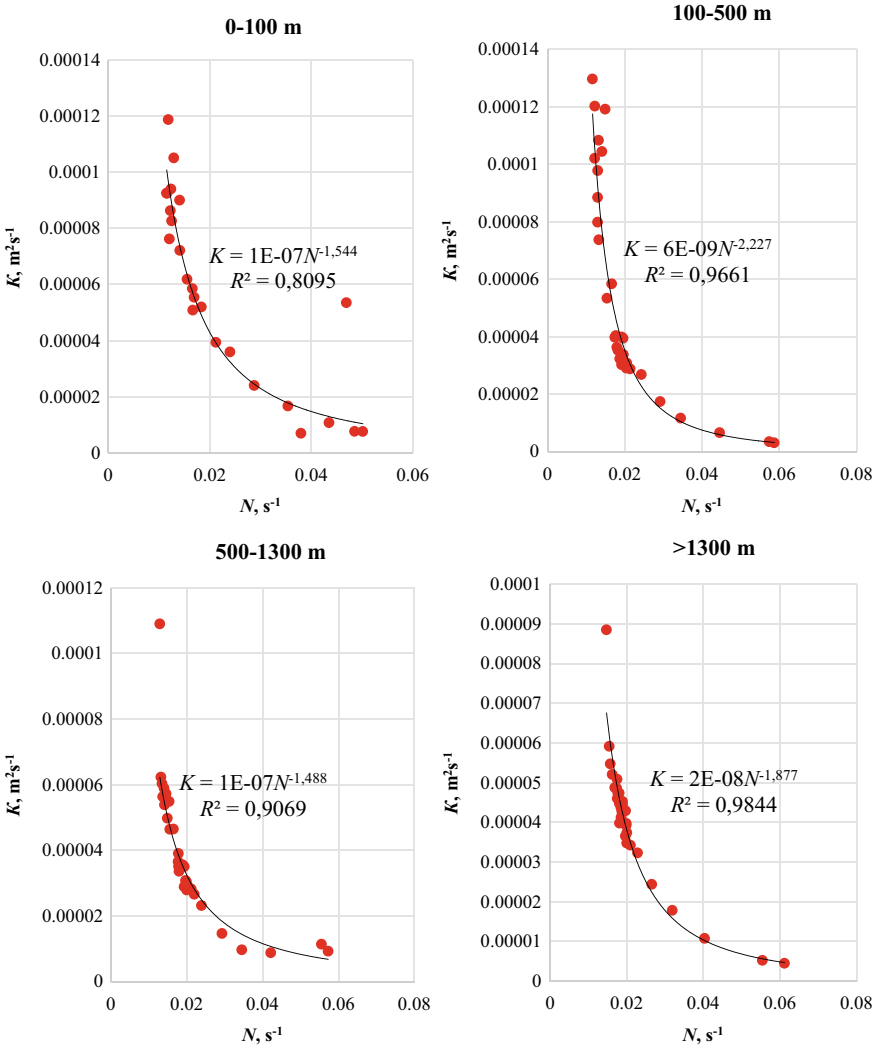


Fig. 4 Approximation power dependences of $K(N)$ based on the results of processing data from cruise 87 of the R/V "Professor Vodyanitsky" for July 2016 in the previously described depth intervals

an average value $\alpha \approx -1.5$. It shows a change in the general hydrological regime in the study region.

For a number of stations, the calculation of K gave ambiguous results due to the uneven distribution of the coefficient with depth and having a strong scatter in values. This could be explained by the peculiarity of horizontal flows [10–13]. However, for a more confident answer, more statistical data is needed, which was partially obtained through auxiliary equipment: CTD and ADCP probes. An example of calculation results comparison with actual current velocities at one of the stations is shown in Fig. 5. The coefficient values on the station increase to maximum in the layer from 40 to 70 m and from 140 to 160 m. In the same depth ranges, a current is observed, which can give rise to shear instability. For a more thorough analysis of the dependence of changes in the intensity of turbulent exchange with depth on the speed and direction of the flow, correlation matrices were constructed for all the main characteristics of turbulence, measurements of auxiliary probes and additional parameters of the environment, such as: direction of the flow, gradients of the flow velocity vector and the angle of its direction. Thermohaline characteristics of the environment were also considered for correlation. A total of matrices were built for each voyage, each station separately, as well as for the average values indicated in Fig. 2 regions, in accordance with the circulation features in them from works [10–13]. An example of a matrix with the main part of the parameters under consideration can be seen in Table 1. The Pearson correlation coefficient between K and current speed was for regions 1–7 in the range from −0.863044 (4th region, voyage 87) to −0.435623 (7th region, voyage 110); correlation between other parameters and K were lower, but showed good convergence in depth ranges where K increased. This tells us about the relationship of the coefficient with hydrological conditions at stations in a particular selected region (Figs. 6 and 7).

The results of the analysis of expeditions data collected with correlation matrices involved showed that the most likely reason for the increase in K values is the combined effect of several factors intensifying turbulent mixing: the stations with higher coefficients were located in the zone of action of anticyclonic branches, or in the zones of intermittency of cyclonic and anticyclonic eddies of the Main Black Sea Current (MBSC) and at sharp drops in depths [14]. Also, when comparing the results with currently known hydrological data [12, 13, 15–17], a relationship was established between the depth of maximum K and the penetration depth of the upper quasi-homogeneous layer (UQL), the depth of the cold intermediate layer (CIL) and the maximum vertical temperature gradient (VTG): the higher the CIL and the VTG maximum rise, the closer to it the K maximum will be. At the same time, the lower the boundary of the UQL is located, the higher the maximum values of K will lie. This also explains the anomalous values of K, since stations with them combine these factors: a large depth of the UQL (up to 50 m near the Kerch Peninsula) with a relatively small CIL depth (~70 m above the sea shelf).

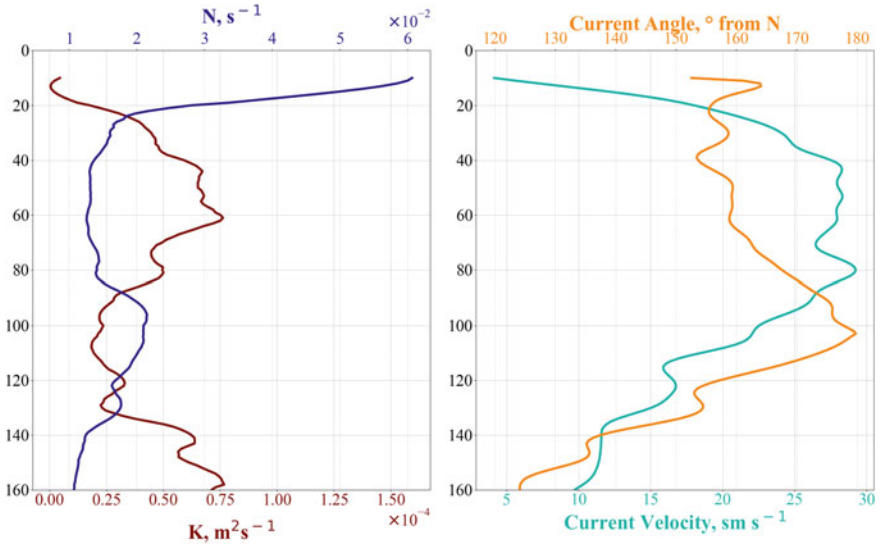


Fig. 5 Turbulent diffusion coefficient distribution and buoyancy frequency distribution (left) and current speed and direction (right) with depth according to the calculation results and ADCP measurement data at station No. 10 87 of the R/V "Professor Vodyanitsky" voyage

4 Conclusion

The main result of the study is the identification of seven regions with their own characteristics of K distribution, determined by certain hydrological and dynamic conditions in them during the period under study (Fig. 1):

1. Characterized by the presence of the Sevastopol anticyclone with a relatively gentle bottom slope, as well as the MBSC core passing nearby.
2. Characterized by the presence of two relatively large vortices on both sides of the MBSC: anticyclonic in direction near the coast and cyclonic in the offshore part.
3. Characterized by the presence of an anticyclone near the coast at higher MBSC velocities and a sharp drop in depths.
4. It is located in the Crimean anticyclone zone of action and the presence of two strong countercurrents nearby on the shelf and on its slope. Also a zone of sloping bottom with rapid depth increase.
5. It is located on the edge of the summer anticyclonic gyre with a large number of K anomalies on the sea shelf. A low-lying boundary of the UQL and a high-lying CIL core with VGT maxima.
6. Zone of action of the anticyclonic meander alternating with the MBSC.
7. Characterized by the presence of intermittent coastal countercurrents along the coast formed due to submesoscale shelf eddies and the MBSC [18].

Table 1 Correlation Matrix for 1st region of 87th voyage R/V "Professor Vodyanitsky". T_CTD, S_CTD, σ_CTD—temperature, salinity and density recorded by CTD SBE 911plus; T_grad, S_grad, σ_grad are gradients of previous values by *z*; Current, Cur_ang—current speed and its direction according to north recorded by ADCP and Cur_grad, Cur_ang_grad are their gradients

	K	T_CTD	S_CTD	σ_CTD	T_grad	S_grad	σ_grad	Current	Cur_grad	Cur_ang	Cur_ang_grad
K	1	−0.21	0.758	0.712	0.27	−0.66	−0.391	−0.738	0.26549	0.116	0.101944
T_CTD	−0.21	1	−0.45	−0.63	−0.985	−0.02	0.9413	0.5221	−0.5275	−0.2751	0.082345
S_CTD	0.758	−0.45	1	0.976	0.504	−0.61	−0.581	−0.968	0.38603	0.352	−0.05471
σ_CTD	0.712	−0.63	0.976	1	0.675	−0.54	−0.736	−0.968	0.45825	0.3693	−0.06732
T_grad	0.27	−0.98	0.504	0.675	1	−0.03	−0.963	−0.575	0.5316	0.2787	−0.08285
S_grad	−0.66	−0.02	−0.61	−0.54	−0.028	1	0.2703	0.6614	−0.1323	−0.1366	−0.01226
σ_grad	−0.39	0.941	−0.58	−0.74	−0.963	0.27	1	0.6695	−0.5149	−0.2755	0.075402
Current	−0.74	0.522	−0.97	−0.97	−0.575	0.661	0.6695	1	−0.4441	−0.3387	0.040723
Cur_grad	0.265	−0.53	0.386	0.458	0.532	−0.13	−0.515	−0.444	1	0.2144	0.080079
Cur_ang	0.116	−0.28	0.352	0.369	0.279	−0.14	−0.276	−0.339	0.21435	1	0.014237
Cur_ang_g	0.102	0.082	−0.05	−0.07	−0.083	−0.01	0.0754	0.0407	0.08008	0.0142	1

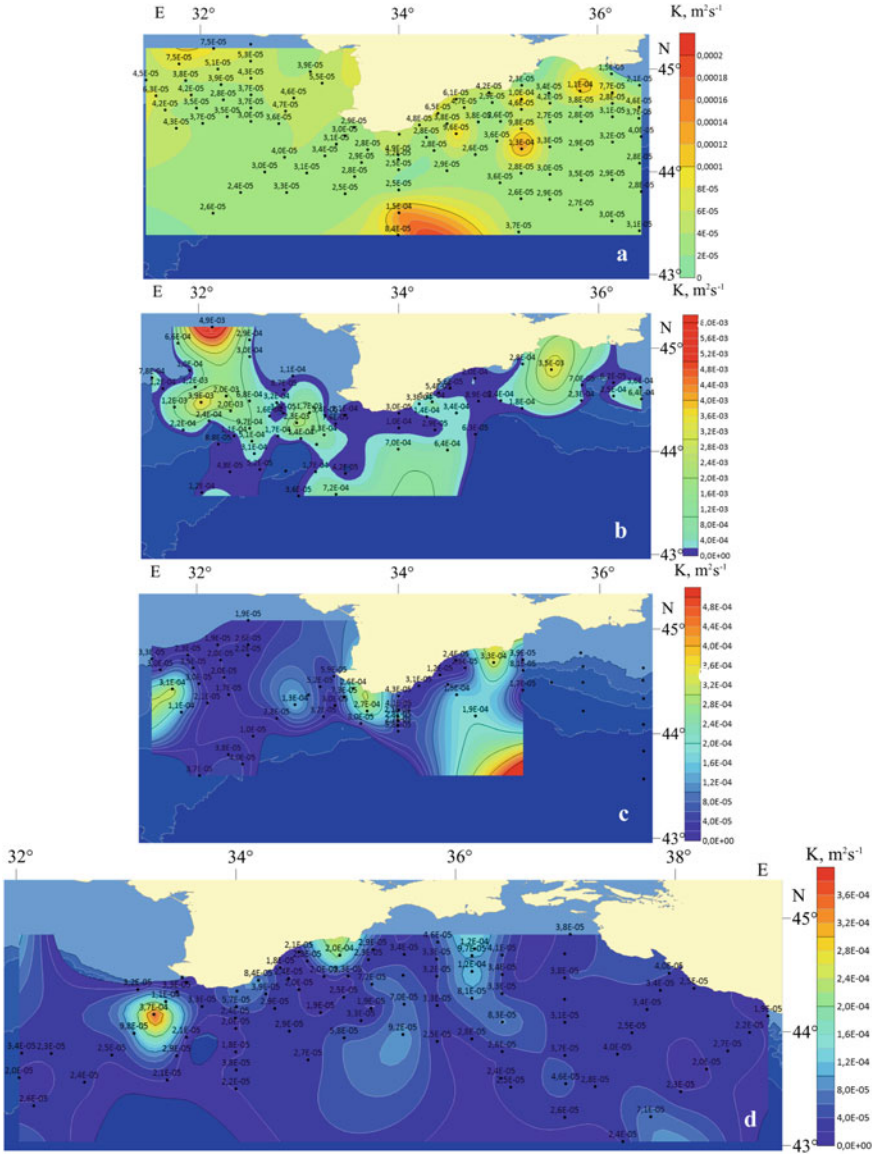


Fig. 6 Average values of K at stations 87 (**a**), 94 (**b**), 102 (**c**) and 110 (**d**) voyages of the R/V "Professor Vodyanitsky"

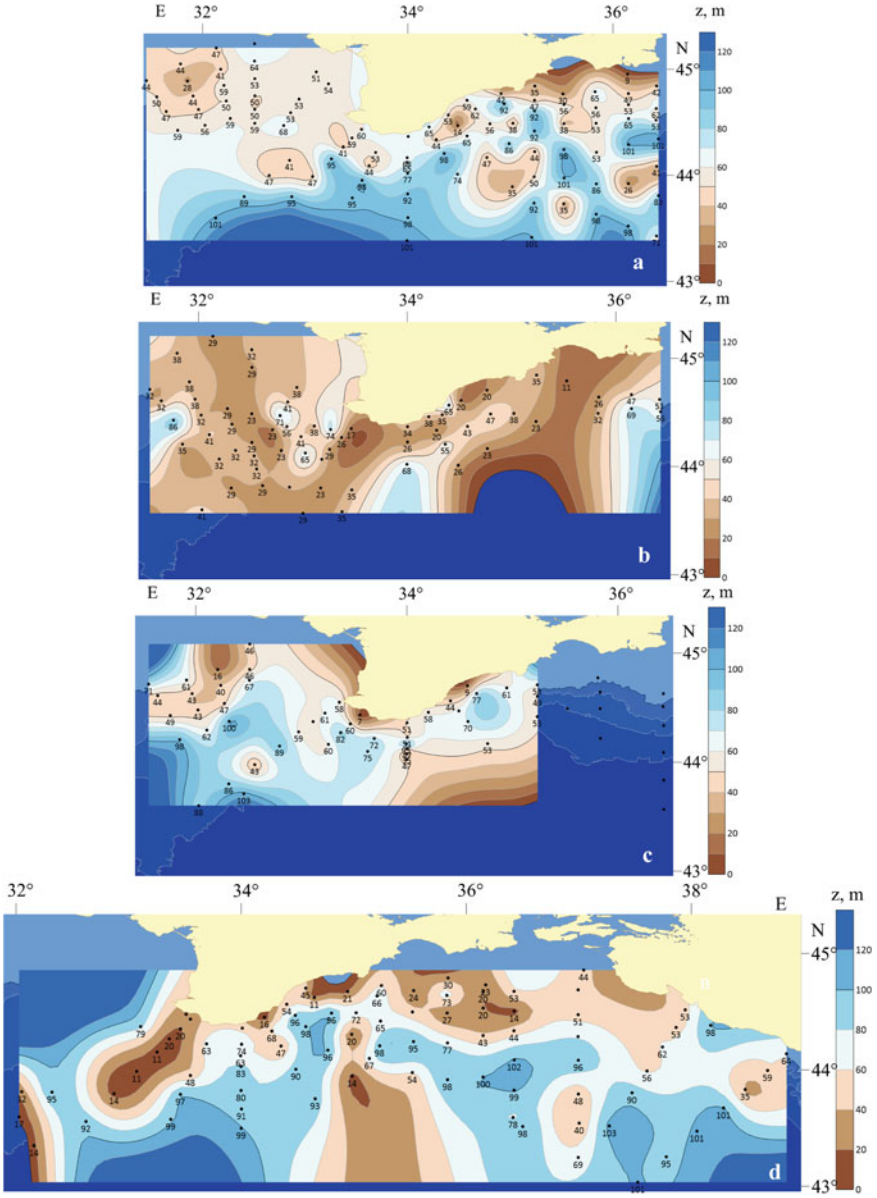


Fig. 7 Depth of the maximum value of K at stations 87 (**a**), 94 (**b**), 102 (**c**) and 110 (**d**) cruises of the R/V "Professor Vodyanitsky"

The results obtained will be used in further studies with each area separately in order to identify additional features for the corresponding values of K and create a refined vertical turbulent exchange spatial model using statistical and machine learning methods.

Acknowledgements The study was carried out within the framework of the state task FNNN-2021-0004 (code "Oceanological processes") and with the grant support of the Russian Science Foundation project No. 22-17-00150 (code "Turbulent structure"). I would also like to thank the staff of oceanography department of the MHI RAS for kindly provided data and to express my very great appreciation to Dr. Belokopytov Vladimir Nikolaevich for his valuable and constructive suggestions during the planning and development of this research work.

References

1. Welch, P. D. (1967). The use of Fast Fourier Transform for the estimation of power spectra: A method based on time averaging over short, modified periodograms (PDF), *IEEE Transactions on Audio and Electroacoustics*, AU-15 (2): 70–73, doi: https://doi.org/10.1109/TAU.1967.1161901
2. Oakey, N.S. (1982). Determination of the Rate of Dissipation of Turbulent Energy from Simultaneous Temperature and Velocity Shear Microstructure Measurements. *Journal of Physical Oceanography*, 12, 256–271
3. Osborn, T.R. (1980) Estimations of local rate of vertical diffusion from dissipation measurements. *J. Phys. Oceanogr*. – Vol. 10, – P. 83–89 https://doi.org/10.1175/1520-0485(1980)010<0083:EOTLRO>2.0.CO;2
4. Thorpe, S.A. (1973). Experiments of Instability and Turbulence in a Stratified Shear Flow. *Journal of Fluid Mechanics*, 61(4), pp. 731–751. doi: https://doi.org/10.1017/S0022112073000911
5. Mcewan, A.D. (1983). The Kinematics of Stratified Mixing through Internal Wavebreaking. Journal of Fluid Mechanics, 128, pp. 47–57. doi: https://doi.org/10.1017/S0022112083000373
6. Mcewan, A.D. (1983). Internal Mixing in Stratified Fluids. *Journal of Fluid Mechanics*, 128, pp. 59–80. doi:https://doi.org/10.1017/S0022112083000385
7. Samodurov, A. S., Chukharev, A.M., Kazakov, D.A. (2021) Basic Regularities of Vertical Turbulent Exchange in the Mixed and Stratified Layers of the Black Sea. *Physical Oceanography*. – Vol. 28, No. 4. – P. 376–391. – DOI https://doi.org/10.22449/1573-160X-2021-4-376-391. – EDN FFEAVY.
8. Sutherland, P., Melville, W. K. (2015) Field measurements of surface and near-surface turbulence in the presence of breaking waves. *Journal of Physical Oceanography*. Vol. 45, no. 4. P. 943–965. doi: https://doi.org/10.1175/JPO-D-14-0133.1
9. Kazakov, D.A., Samodurov, A.S. (2021) Estimation of the Vertical Turbulent Exchange Intensity in the Main Pycnocline Layer in the Prikerchensky Area of the Black Sea Shelf. *Ecological Safety of Coastal and Shelf Zones of Sea*. – Vol. 2. – P. 94–105. – DOI https://doi.org/10.22449/2413-5577-2021-2-94-105. – EDN RFDEWU.
10. Artamonov, Yu.V., Shutov, S.A., Skripaleva, E.A., et al. (2018). Water Circulation in the Northern Black Sea in Summer 2016 (Based on the Data Obtained in the 87th Cruise of the R/V Professor Vodyanitsky). *Physical Oceanography*, 25(1), pp. 52–66. doi:https://doi.org/10.22449/1573-160X-2018-1-52-66
11. Artamonov, Yu.V., Skripaleva, E.A., Fedirko, A.V., et al. (2020). Waters Circulation in the Northern Part of the Black Sea in Summer – Winter of 2018. *Ecological Safety of Coastal and Shelf Zones of Sea*, (1), P. 69–90. doi: https://doi.org/10.22449/2413-5577-2020-1-69-90 (In Russian)

12. Artamonov, Yu.V., Fedirko, A.V., Skripaleva, E.A., et al. (2019). Water Structure in the Area of the Rim Black Sea Current in Spring And Summer 2017 (94th, 95th Cruises of the R/V "Professor Vodyanitsky"). *Ecological Safety of Coastal and Shelf Zones of Sea.* № 1. – P. 16–28. – DOI https://doi.org/10.22449/2413-5577-2019-1-16-28. – EDN ABVXOP. (In Russian)
13. Fedirko, A.V., Artamonov, Yu.V., Deryushkin, D.V., Nikolsky, N.V., Ozerov, S.A., Skripaleva, E.A., Shutov, S.A., Shapovalov, R.O., Shapovalov, Yu.I., Shcherbachenko, S.V. (2020). Circulation and thermohaline structure of the northern part waters of the Black Sea according to hydrological measurements in 2019 (106, 108, 110, 111th cruises of the R/V "Professor Vodyaniyky"). *Itogi ekspeditsionnykh issledovaniy v 2019 godu v Mirovom okeane, vnutrennikh vodakh i na arkhipelage Shpitsbergen. Materialy konferentsii. Moskva, 26–27 fevralya 2020* [Results of expeditionary research in 2019 in the World Ocean, inland waters and the Spitsbergen archipelago. Conference materials. Moscow, 26–27 February 2020]. Sevastopol, 2020, P. 206–212
14. Samodurov A.S., Chukharev A.M., Nosova A.V., Globina L.V. (2013). Internal Waves Intensification in the Shelf Break Region as a Factor of the Vertical Exchange Intensification. *Fundamental and Applied Hydrophysics.* 6(2):12–24. (In Russian)
15. Artamonov, Yu.V., Alekseev D.V., Skripaleva, E.A., et al. (2017). Thermohaline Structure of Water near the Crimea Coast and Adjacent Open Water Area of the Black Sea at Summer 2016. *Ecological Safety of Coastal and Shelf Zones of Sea.*– № 3. – P. 20–31. – EDN ZMZFVL. (In Russian)
16. V.N. Belokopytov. (2019). Seasonal Variability of Vertical Thermohaline Stratification on the Black Sea Shelf of Crimea. *Ecological Safety of Coastal and Shelf Zones of Sea.* № 3. P. 19–24. – DOI https://doi.org/10.22449/2413-5577-2019-3-19-24. – EDN ASAMOV. (In Russian)
17. Kubryakov, A.A., Belokopytov, V.N., Zatsepin, A.G., et al. (2019). The Black Sea Mixed Layer Depth Variability and Its Relation to the Basin Dynamics and Atmospheric Forcing. *Physical Oceanography*, 26(5), P. 397–413. doi:https://doi.org/10.22449/1573-160X-2019-5-397-413
18. Zatsepin, A.G., Piotouh, V.B., Korzh, A.O. et al. (2012). Variability of currents in the coastal zone of the Black Sea from long-term measurements with a bottom mounted ADCP. Oceanology 52, 579–592 https://doi.org/10.1134/S0001437012050177

New Image Particle Method for Kinetic Simulation of Wakes in Plasma with Weak and Strong Coupling



Maxim Glebovich Ponomarev

Abstract New Image Particle Method is introduced to simulate charged particle fluxes that allows to include effects of generated electric and magnetic fields in addition to all previous results for charged particle flows simulations in external electromagnetic fields. These electric and magnetic fields can be unlimited and non stationary. The general expression for this "image particle" collision integral $C^{image}\left(\overrightarrow{r}, \overrightarrow{v}, t\right)$ is obtained here as well. According to this new "Image Particle Method", the collision integral $C^{image}\left(\overrightarrow{r}, \overrightarrow{v}, t\right)$ with this "image particle" describes the effects from these induced electric $\overrightarrow{E_{ind}}$ and magnetic $\overrightarrow{B_{ind}}$ fields.

Keywords Weak coupling · Intermediate coupling · Strong coupling · Weak magnetization · Strong magnetization · Extreme magnetization · Geomagnetic fields · Magnetic fields · Charged particle flows · Magnetic field effect on ionized flows · Plasma · Geomagnetism · Charged particle sources · Explosive charged particle sources · Charged particle fluxes · Electric and magnetic field effects · Effect of induced electric and magnetic fields · Electromagnetic fields

1 Introduction

This article introduces yet another example from extensive number of innovative physical models with applications to real world problems published in [1–48].

Specifically, this paper describes novel "Image Particle Method" that reduces the problem of arbitrary generated (induced) electric and magnetic fields to consideration of interaction with image particles through the corresponding collision integral. The general expression for this "image particle" collision integral is obtained here as well.

M. G. Ponomarev (✉)
Cambridge Research and Consultancy, Cambridge, UK
e-mail: maxim.pv@gmail.com

Adyghe State University, Maykop, Russia

© The Author(s), under exclusive license to Springer Nature Switzerland AG 2024

V. Karev (ed.), *Proceedings of the 9th International Conference on Physical and Mathematical Modelling of Earth and Environmental Processes*, Springer Proceedings in Earth and Environmental Sciences, https://doi.org/10.1007/978-3-031-54589-4_59

These kinetic simulations extend directly previous results by Ponomarev MG, published in [1–5, 7, 8, 21–48].

It is worth to note that this method is another new one in addition to previous "Imaginary Emission Method". In real problems these two methods can be used in the same models. Especially, the "Imaginary Emission Method" reduced the problem of wakes in plasma to consideration of charged particle flows from the "Imaginary Emission" sources [22–24, 26].

Any possible magnetization regimes and all possible cases of coupling are described in short in Sects. 2 and 3. The new Image Particle Method is introduced and the corresponding new collision integral is derived in Sect. 4.

2 Different Cases of Coupling

The medium, plasma can be in different regimes of coupling [49]. We start from the one component plasma (OCP) model to introduce the subject. The OCP is useful because its equilibrium and near-equilibrium properties depend on a single parameter, the Coulomb coupling parameter $\Gamma = q^2/(ak_BT)$. It is defined as the ratio of the mean potential energy per particle $\frac{q^2}{a}$, where $a = (3/4\pi n)^{1/3}$ is the Wigner–Seitz radius, divided by the mean kinetic energy per particle k_BT, T is the temperature, and k_B is the Boltzmann constant. The degree of non-ideality of the system (the degree to which many-body interactions affect the properties of the ensemble of ions) is described by this Coulomb coupling parameter.

Namely, when Γ increases, the OCP dynamics transforms from a nearly collisionless, gaseous regime for $\Gamma \ll 1$ continuously through a more correlated, liquid-like regime that corresponds to $\Gamma > 50$. At $\Gamma = 175$, the OCP shows a first-order fluid–solid phase transition.

The OCP shows these different types of strong coupling effects on the transport properties corresponding to different variations of Γ.

This description of the one component plasma (OCP) model is added just to show different coupling regimes with reference to different values of the Coulomb coupling parameter $\Gamma = q^2/(ak_BT)$.

The new Image Particle Method is applicable for all 3 coupling regimes below. And this new Image Particle Method can be applied not only for the one component plasma (OCP) model.

2.1 Weak Coupling Cases

Weak coupling cases are the most investigated in physics. The charged particle interaction potential is long range. Large angles of scattering impacts are extremely less frequent in weakly coupled or rarefied plasmas. The charged particles are moving on

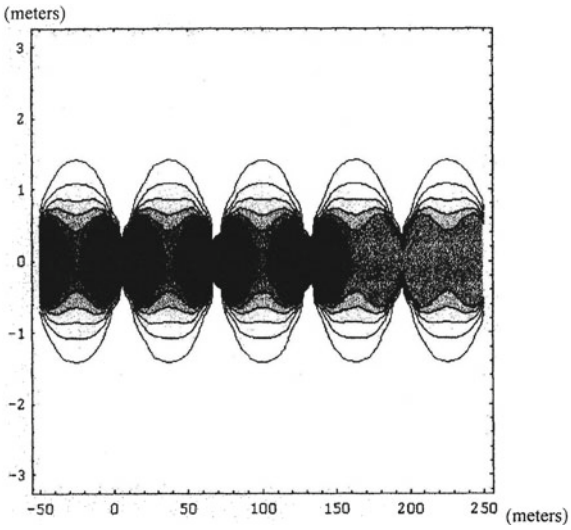


Fig. 1 Cross-sections of isodensity contours (at the plane of magnetic field) for the disturbances of ion concentration by the circular disk. The absorbing disk moves in parallel to the magnetic field. The center of the disk is located at the point 0 at the left side of this Figure. The brighter contours show the higher ion concentrations. The darker contours correspond to the lower ion concentrations

infinitesimal chain of infinitesimal deviations (infinitesimal perturbations). It is due to the Coulomb potential screening by the polarisation of background particles. The usual approximation of the Boltzmann equation here is the Landau equation, which derived by taking into account only the small angle, grazing collisions.

The result for the simulation of magnetic field effect on the wake for the circular disk is presented at the Fig. 1. The boundary condition on the disk surface corresponds to the case of absorbing disk surface.

2.2 Strong Coupling Cases

The strong coupling cases correspond to coupling strengths higher than 50. This regime shows strong interparticle interactions which give rise to the cage-effect [50].

All particles became trapped for some period of time in the cage formed by its immediate neighbors, rebounding until it overcomes the energy barrier and diffuses to a neighboring cage.

2.3 Intermediate Coupling Cases

Less is known about the transition region between the weakly-coupled gas-like regime and the strongly-coupled liquid-like regime. In this region, both kinetic and interaction effects influence momentum and energy transport. Table 1 summarises different coupling regimes [49].

Table 1 Different regimes spanning from weak to strong coupling

Weekly coupled regime	Gas-like
Intermediate regime	Liquid-like, fluid
Strongly coupled regime	Solid, crystal

Table 2 Different regimes of plasma magnetisation

Zero magnetization	$r_c > \lambda_{col}$
Weak magnetization	$\lambda_D < r_c < \lambda_{col}$
Strong magnetization	$r_L < r_c < \lambda_D$
Extreme magnetization	$r_c < r_L < \lambda_D$

3 Different Magnetization Regimes

The medium, plasma can be in different regimes of magnetization. The effect of magnetization on plasma flows can be defined by comparing the Debye distance λ_D, Larmor radiusr_c, Landau length r_L, and Coulomb collision mean free path λ_{col}. [51].

Table 2 summarises physical conditions for different cases, regimes of plasma magnetisation [52].

4 Image Particle Method

The problems of charged particle fluxes are described via the following Boltzmann equation in the centimetre-gram-seconds (CGS) unit system:

$$\frac{\partial f_i(\vec{r},\vec{v},t)}{\partial t} + \vec{v}\cdot\frac{\partial f_i(\vec{r},\vec{v},t)}{\partial \vec{r}} + \frac{e}{m}\left(\frac{1}{c}\left[\vec{v},\vec{B}\right]+\vec{E}\right)\cdot\frac{\partial f_i(\vec{r},\vec{v},t)}{\partial \vec{v}} = Q_i(\vec{r},\vec{v},t) + \sum\nolimits_{j=1}^{N} C_{ij}\left(f_i(\vec{r},\vec{v},t), f_j(\vec{r},\vec{v},t)\right) \quad (1)$$

In this paper we will use equivalent equation in the metre-kilogram-seconds (SI, System International):

$$\frac{\partial f_i(\vec{r},\vec{v},t)}{\partial t} + \vec{v}\cdot\frac{\partial f_i(\vec{r},\vec{v},t)}{\partial \vec{r}} + \frac{e}{m}\left(\left[\vec{v},\vec{B}\right]+\vec{E}\right)\cdot\frac{\partial f_i(\vec{r},\vec{v},t)}{\partial \vec{v}} = Q_i(\vec{r},\vec{v},t) + \sum\nolimits_{j=1}^{N} C_{ij}\left(f_i(\vec{r},\vec{v},t), f_j(\vec{r},\vec{v},t)\right) \quad (2)$$

where:

(i) we take into account collisions of "i" type particles with N types of "j" particles, so that the collision integral of "i" particle with the "j" particle has the following form:

$$C_{ij}\left(f_i\left(\overrightarrow{r}, \overrightarrow{v}, t\right), f_j\left(\overrightarrow{r}, \overrightarrow{v}, t\right)\right);$$

(ii) $Q_i\left(\overrightarrow{r}, \overrightarrow{v}, t\right)$ simulates the source of "i" type particles.

Let's consider induced electric $\overrightarrow{E_{ind}}$ and magnetic $\overrightarrow{B_{ind}}$ fields of arbitrary, unlimited values so that

$$\overrightarrow{E} = \overrightarrow{E_0} + \overrightarrow{E_{ind}} \tag{3}$$

$$\overrightarrow{B} = \overrightarrow{B_0} + \overrightarrow{B_{ind}} \tag{4}$$

Then we have the Boltzmann equation in the following form:

$$\frac{\partial f_i(\vec{r}, \vec{v}, t)}{\partial t} + \vec{v} \cdot \frac{\partial f_i(\vec{r}, \vec{v}, t)}{\partial \vec{r}} + \frac{e}{m}\left(\left[\vec{v}, \left(\overrightarrow{B_0} + \overrightarrow{B_{ind}}\right)\right] + \left(\overrightarrow{E_0} + \overrightarrow{E_{ind}}\right)\right) \cdot \frac{\partial f_i(\vec{r}, \vec{v}, t)}{\partial \vec{v}}$$
$$= Q_i(\vec{r}, \vec{v}, t) + \sum\nolimits_{j=1}^{N} C_{ij}\left(f_i(\vec{r}, \vec{v}, t), f_j(\vec{r}, \vec{v}, t)\right) \tag{5}$$

Hence, after substitution into the Boltzmann equation, Eq. 2, we have $\overrightarrow{E_{ind}}$, $\overrightarrow{B_{ind}}$ as field like collision integrals in the right part of this equation:

$$\frac{\partial f_i\left(\overrightarrow{r}, \overrightarrow{v}, t\right)}{\partial t} + \overrightarrow{v} \cdot \frac{\partial f_i\left(\overrightarrow{r}, \overrightarrow{v}, t\right)}{\partial \overrightarrow{r}} + \frac{e}{m}\left(\left[\overrightarrow{v}, \overrightarrow{B_0}\right] + \overrightarrow{E_0}\right) \cdot \frac{\partial f_i\left(\overrightarrow{r}, \overrightarrow{v}, t\right)}{\partial \overrightarrow{v}} = Q_i\left(\overrightarrow{r}, \overrightarrow{v}, t\right)$$
$$-\frac{e}{m}\left(\left[\overrightarrow{v}, \overrightarrow{B_{ind}}\right] + \overrightarrow{E_{ind}}\right) \cdot \frac{\partial f_i\left(\overrightarrow{r}, \overrightarrow{v}, t\right)}{\partial \overrightarrow{v}} + \sum\nolimits_{j=1}^{N} C_{ij}\left(f_i\left(\overrightarrow{r}, \overrightarrow{v}, t\right), f_j\left(\overrightarrow{r}, \overrightarrow{v}, t\right)\right) \tag{6}$$

Therefore, we introduced the solution with taking into account unlimited induced electric and magnetic fields $\overrightarrow{E_{ind}}$, and$\overrightarrow{B_{ind}}$. We introduce new way to represent these induced fields as fields generated by the imaginary charged particles. And introduce the corresponding collision integrals in the following equation:

$$C^{image}\left(\overrightarrow{r}, \overrightarrow{v}, t\right) = -\frac{e}{m}\left(\left[\overrightarrow{v}, \overrightarrow{B_{ind}}\right] + \overrightarrow{E_{ind}}\right) \cdot \frac{\partial f_i\left(\overrightarrow{r}, \overrightarrow{v}, t\right)}{\partial \overrightarrow{v}} \tag{7}$$

So, we have represented the problem of taking into account induced electric and magnetic fields in the new way by considering these induced fields as generated by the imaginary particles. Namely the effect of the induced field is the same as the collision integral Eq. 7. The equation with this new term has the following form:

$$\frac{\partial f_i\left(\overrightarrow{r}, \overrightarrow{v}, t\right)}{\partial t} + \overrightarrow{v} \cdot \frac{\partial f_i\left(\overrightarrow{r}, \overrightarrow{v}, t\right)}{\partial \overrightarrow{r}} + \frac{e}{m}\left(\left[\overrightarrow{v}, \overrightarrow{B_0}\right] + \overrightarrow{E_0}\right) \cdot \frac{\partial f_i\left(\overrightarrow{r}, \overrightarrow{v}, t\right)}{\partial \overrightarrow{v}} = Q_i\left(\overrightarrow{r}, \overrightarrow{v}, t\right)$$
$$+C^{image}\left(\overrightarrow{r}, \overrightarrow{v}, t\right) + \sum\nolimits_{j=1}^{N} C_{ij}\left(f_i\left(\overrightarrow{r}, \overrightarrow{v}, t\right), f_j\left(\overrightarrow{r}, \overrightarrow{v}, t\right)\right) \tag{8}$$

5 Conclusions

This paper introduces new method to simulate charged particle fluxes that allows to include effects of generated electric and magnetic fields in addition to all previous results for charged particle flows simulations in external electric and magnetic fields. These electric and magnetic fields can be unlimited and non stationary. The general expression for this "image particle" collision integral is obtained here as well. Of course, both this "image particle", and the other "image particles" are always imaginary.

According to this new "Image Particle Method", the collision integral $C^{image}\left(\overrightarrow{r}, \overrightarrow{v}, t\right)$ with this image particle describes the effect from these induced electric $\overrightarrow{E_{ind}}$ and magnetic $\overrightarrow{B_{ind}}$ fields.

References

1. Maxim Glebovich Ponomarev Exact Analytical Expression for Maximum Heat Flux from Impulsive Sources of Charged Particles in Magnetic Field // Processes in GeoMedia—Volume VII, October 2023, DOI: https://doi.org/10.1007/978-981-99-6575-5_31.
2. Carati D., Ponomarjov M. G. Statistical description of currents induced by two electron cyclotron counter-propagating waves // ELECTRON CYCLOTRON EMISSION AND ELECTRON CYCLOTRON HEATING. Proceedings of the 12th Joint Workshop. Held 13–16 May 2002 in Aix-en-Provence, France. Edited by Gerardo Giruzzi (Association Euratom-CEA sur la Fusion, France). Published by World Scientific Publishing Co. Pte. Ltd., 2003. ISBN #9789812705082, pp. 77–82.
3. Gun'ko, Yu.F., Ponomarev, M.G. The charged particles emission in a magnetic field // Vestnik Sankt-Peterburgskogo Universiteta. Ser 1. Matematika Mekhanika Astronomiya. 1993. n2. 89–94.
4. Gun'ko, Yu.F., Ponomarev, M.G. The charged particle layer expansion in a magnetic field // Vestnik Sankt-Peterburgskogo Universiteta. Ser 1. Matematika Mekhanika Astronomiya. 1995. n4. 105–108.
5. Gun'ko, Yu.F., Ponomarev, M.G. The charged particle distribution due to emission in a magnetic field // Astronomische Nachrichten. 1995. 316. 1. 17–21.
6. A case for new statistical software testing models/May, J.; Ponomarev, M.; Kuball, S.; Gallardo, J. // 2006 Annual Reliability and Maintainability Symposium, RAMS'06; Newport Beach, CA; United States; 23 January 2006 through 26 January 2006; Category number CH3744; Code 69734, Proceedings - Annual Reliability and Maintainability Symposium, Article number 1677399, 349–353. DOI: https://doi.org/10.1109/RAMS.2006.1677399.
7. Ponomarev M. Physical Foundations of Mechanics. Part 1. Newtonian Mechanics // World of Science LLC. 2023. 1–83 p.
8. Ponomarev M. Physical Foundations of Mechanics. Part 2. Relativistic Mechanics // World of Science LLC. 2023. 1–78 p.
9. Ponomarev M., Johanning L., Parish D., Enhancing precision and reliability of tri-axial load cells for mooring load measurements // Proc. of the 3rd International Conference on Ocean Energy. 6 October. 2010. (ICOE2010). ISBN 978-84-693-5467-4.
10. Ponomarev M. A novel physical model to enhance precision and performance of 3-dimensional force sensors // Processes in Geomedia 2022. No2(32). p.1589–1600.

11. Ponomarev M. Experimental validation of novel physical model for improvement of sensing 3-dimensional fluid flow loads and responses in real sea conditions with South Western Mooring Test Facility (SWMTF) // Processes in Geomedia 2022. No2(32). 1579–1589.
12. Ponomarev M. A Novel Physical Model to Enhance Precision and Performance of Multidimensional Force Sensors // Physical and Mathematical Modeling of Earth and Environment Processes – 2022, Proceedings of 8th International Scientific Conference-School, Springer, 347–364, ISBN 978-3-031-25961-6.
13. Ponomarev M., Johanning L., Parish D., Experimental validation of novel physical model for improvement of sensing multidimensional fluid flow loads and responses in real sea conditions with South Western Mooring Test Facility // Physical and Mathematical Modeling of Earth and Environment Processes – 2022, Proceedings of 8th International Scientific Conference-School, Springer, 365–376, ISBN 978-3-031-25961-6.
14. Digital radiographic inspection technique for production friendly quality assessment of PM parts/Ponomarev M.G., Kappatos V., Selcuk C., Gan T.-H., Amos M., Halai H., Gierl C., Iovea M. // Powder Metallurgy. 2013. 56. 2. 92–95.
15. PM Dimensional Control: Development of a Digital Radiographic Inspection Technique for Production Friendly Quality Assessment of Powder Metallurgy Parts/M. G. Ponomarev, V. Kappatos, C. Selcuk, T.-H. Gan, M. Amos, H. Halai, C. Gierl, M. Iovea // Proceedings of the International Euro Powder Metallurgy Congress and Exhibition. Euro PM 2012. 2012. Volume 1. Basel. Switzerland. 16 September 2012 through 19 September 2012. Code 105676.
16. Ponomarev M.G., Selcuk C., Gan T.-H. Construction of pattern recognition system optimized for X-ray inspection of plastic electronics and OLED displays // 51st Annual Conference of the British Institute of Non-Destructive Testing 2012. NDT 2012. BINDT 2012. Northamptonshire. United Kingdom. 11 September 2012 through 13 September 2012. Code 107048. pp. 354–360.
17. Defect detection and classification system for automatic analysis of digital radiography images of PM parts/M. G. Ponomarev, C. Selcuk, T.-H. Gan, M. Amos, I. Nicholson, M. Iovea, M. Neagu, B. Stefanescu, G. Mateiasi // Powder Metallurgy. 2014. 57. 1. 17–20.
18. Non Destructive Testing: A Defect Detection and Classification System for Automatic Analysis of Digital Radiography Images of Powder Metallurgy Parts/M. G. Ponomarev, C. Selcuk, T.-H. Gan, M. Amos, I. Nicholson, M. Iovea, M. Neagu, B. Stefanescu, G. Mateiasi // International Powder Metallurgy Congress and Exhibition. Euro PM 2013. Gothenburg. Sweden. 15 September 2013 through 18 September 2013. Code 110976.
19. Preliminary NDT investigation of sintered powder metallurgy parts by high-resolution TDI based X-ray digital radiography/M. Iovea, M. Neagu, B. Stefanescu, G. Mateiasi, H. Halai, M. Amos, M. Ponomarev, V. Kappatos, C. Selcuk, T.-H. Gan, C. Gierl // 2012. Volume 1. European International Powder Metallurgy Congress and Exhibition. Euro PM 2012. Basel. Switzerland. 16 September 2012 through 19 September 2012. Code 105676.
20. PM parts fast in-line X-ray digital radiography/M. Iovea, M. Neagu, B. Stefanescu, G. Mateiasi, A. Clarke, I. Nicholson, M. Ponomarev, V. Kappatos, C. Selcuk, T.-H. Gan // International Powder Metallurgy Congress and Exhibition. Euro PM 2013. European PM Conference Proceedings.1. 2013. European Powder Metallurgy Association (EPMA).
21. A molecular dynamics study of a 5 keV C60 fullerene impact on a two-component organic molecular sample/Ponomarev M.G., Garrison B.J., Vickerman J.C., Webb R.P. // Surface and Interface Analysis. Wiley Online Library. 2011. 43. 1-2. 107–111.
22. Ponomarjov M. G. Imaginary-emission method for modeling disturbances of all magnetoplasma species: Reflecting and absorbing objects in motion through a rarefied plasma at different angles to the ambient magnetic field // Physical Review E. 1996. 54. 5. 5591–5598.
23. Ponomarjov M. G. Disturbances of the ambient magnetoplasma due to its interactions with object surfaces. Imaginary emission method. Far-wake of objects moving through a rarefied plasma at different angles to the ambient magnetic field // Planetary and Space Science. 1995. 43. 10–11. 1419–1427.
24. Ponomarjov M. G. Space flows and disturbances due to bodies in motion through the magnetoplasma // Astrophysics and Space Science. 2000. 274. 1. 423–429.

25. Ponomarjov M. G. Pressure of charged particle flows in ambient magnetic fields // Astronomische Nachrichten. 1997. 318. 3. 187–192.
26. Ponomarjov M. G. 3D time-dependent kinetic simulation of space plasma disturbances due to moving bodies with the ambient magnetic field effect // Advances in Space Research. 2002. 29. 9. 1397–1402.
27. Ponomarjov M. G., Gunko Y. F. Kinetic modeling of charged particle cloud expansion and emission in magnetic and electric fields // Planetary and Space Science. 1995. 43. 10–11. 1409–1418.
28. Ponomarjov M. G. Acceleration and transport of particles in collisionless plasmas: Wakes due to the interaction with moving bodies // Astrophysics and Space Science. 2001. 277. 1. 39–44.
29. Ponomarjov M. G. Outer atmosphere and wake of space objects, kinetic simulation. Disturbances of ambient magnetoplasma due to diffuse reflecting bodies in motion // APS Division of Plasma Physics Meeting Abstracts. 1998. abstract id. U9Q.09.
30. Ponomarjov M. G. Simulation of oscillations in charged particle systems under the ambient magnetic field control // 2nd International Conference. Control of Oscillations and Chaos (COC 2000). St. Petersburg, Russia. 5 July 2000 through 7 July 2000. Code 57512. Proceedings (Cat. No.00TH8521), 2000, vol.1. pp. 167–170. doi: https://doi.org/10.1109/COC.2000.873548.
31. Ponomarjov M. G. 3D Collisional Kinetic Simulation of Stratifications and Flute Structures of Plasma Flows and Wakes in External Magnetic Fields // AAS, DPS Meeting. No 32. id.15.10. 2000. Bulletin of the American Astronomical Society. Vol. 32, p.1022.
32. Ponomarjov M. G., Carati D. Enhanced acceleration of electrons populations by crossing electron cyclotron waves in an ambient magnetic field, Resonant Moments method // Advances in Space Research. 2006. Volume 38. Issue 8. 1576–1581.
33. Ponomarjov M. G. Outer atmosphere and wake of space objects, kinetic simulation. Disturbances of ambient magnetoplasma due to diffuse reflecting bodies in motion // American Physical Society, Division of Plasma Physics Meeting, November 16–20, 1998 New Orleans, LA. abstract id. U9Q.09.
34. Ponomarjov M. G. 3D Kinetic Dynamical models of Ionized HII Clouds in External Magnetic Field // Ionized Gaseous Nebulae. 2000. Mexico City. November 21–24. meeting abstract id. 44.
35. Ponomarjov M. G. Kinetic simulation of stratifications and flute structures of charged particle jets and wakes in the ambient magnetic field // Bulletin of the Astronomical Society. 1999. Vol. 31. No. 4. p. 1157. id.53.12.
36. Ponomarjov M. G. 3D Collisional Kinetic Simulation of Stratifications and Flute Structures of Plasma Flows and Wakes in External Magnetic Fields // 32nd Annual Meeting of the Division for Planetary Sciences. 23–27 October 2000. Pasadena. California. USA. Session 15. Outer Planets IV-Aurorae and Magnetospheres. 2000/10/24. Abstract 15.10. 1022.
37. Ponomarjov M. G. Kinetic Simulation of Magnetic Field Effects on Stratifications and Flute Structures of Space Plasma Flows and Wakes of Bodies // 2001 Joint Assembly American Geophysical Union Spring Meeting. Boston. Massachusetts. USA. Abstracts. 2001. SM52B-04.
38. Ponomarjov M. G., Carati D. Search for optimal 3D wave launching configurations for the acceleration of charged particles in a magnetized plasma: Resonant Moments Method // American Physical Society. 46th Annual Meeting of the Division of Plasma Physics. 15–19 November. 2004. Savannah. GA. MEETING ID: DPP04. abstract id. RP1.042.
39. Ponomarjov M. G. New Ways of Protecting Astronomical Equipment and Solar Batteries of Spacecrafts // American Astronomical Society, DPS meeting No 29, id.27.02. Bulletin of the American Astronomical Society. 1997. Vol. 29. p.1023.
40. Ponomarjov M. G., Carati D. Acceleration of charged particles by crossed cyclotron waves, Resonant Moments Method // 35th COSPAR Scientific Assembly. 18–25 July 2004. Paris. France. p. 2851.
41. Ponomarjov M. G., Carati D. Kinetic Simulations of Relativistic Electron Flows in Time-Dependent Electromagnetic Fields // Electron Cyclotron Emission and Electron Cyclotron Heating. Conference Proc. World Scientific Publishing Co Pte Ltd. 2003. 137–142.

42. Ponomarjov M. G. Kinetic simulation of magnetic field effects on wakes of meteoroids imaginary emission method // European Space Agency, (Special Publication) ESA SP. 2001. 495. 295–300.
43. Ponomarjov M. G., Carati D. Search for optimal 2D and 3D wave launching configurations for the largest acceleration of charged particles in a magnetized plasma, Resonant Moments Method // arXiv 2004. https://arxiv.org/format/physics/0411075 arXiv:physics/0411075 [physics.plasm-ph].
44. Ponomarjov M. G. 3D time-dependent kinetic simulation of turbulent plasma flows under the effect of external magnetic field // American Physical Society. 42nd Annual Meeting of the APS Division of Plasma Physics combined with the 10th International Congress on Plasma Physics October 23–27. 2000 Québec City. Canada Meeting ID: DPP00. abstract id. NO1.007. https://ui.adsabs.harvard.edu/abs/2000APS..DPPNO1007P/abstract.
45. Ponomarjov M. G. Kinetic modeling magnetic field effect on ion flows, disturbances and wakes in space plasma // Space plasma simulation: proceedings of the Sixth International School/ Symposium. ISSS-6. Garching. Germany. 3–7 September. 2001. Edited by J. Büchner, C.T. Dum, and M. Scholer. Berlin: Schaltungsdienst Lange o.H.G. 2001. p.328.
46. Ponomarjov M. G., Carati D. Acceleration of electron populations by crossing EC waves in an external magnetic field // 13th Joint Workshop on Electron Cyclotron Emission and Electron Cyclotron Resonance Heating. Nizhny Novgorod. Russia. 2004. Conference paper https://ec13.iapras.ru/papers/Ponomarjov.pdf.
47. Ponomarjov M. G., Carati D. Enhanced acceleration of charged particles by crossing electromagnetic waves in a magnetized plasma, resonant moments method // 2004. ffhal-00001926v1f. https://hal.archives-ouvertes.fr/hal-00001926v1.
48. Webb R. P., Ponomarev M. Molecular dynamics simulation of low energy cluster impacts on carbon nanotubes // Nuclear Instruments and Methods in Physics Research Section B: Beam Interactions with Materials and Atoms. 2007. 255. 1. 229–232.
49. Jérôme Daligault, Scott D. Baalrud Plasma transport theory spanning weak to strong coupling. AIP Conf. Proc., 2015, 1668, 040002.
50. Z. Donko, G. J. Kalman, and K. I. Golden Caging of Particles in One-Component Plasmas. Phys. Rev. Lett., 2002, 88, 225001.
51. S. D. Baalrud and J. Daligault Transport regimes spanning magnetization-coupling phase space // Phys. Rev. E, 2017, 96, 043202.
52. Louis Jose, Scott D. Baalrud A Generalized Boltzmann Kinetic Theory for Strongly Magnetized Plasmas with Application to Friction // Phys. Plasmas, 2020, 27, 112101.

On the Possible Influence of an Intense Vortex in the Mantle Beneath the Sea of Japan Region on the Formation of Lithospheric Relief and Sea of Japan Water Circulation



S. Yu. Kasyanov

Abstract The paper considers the possibility of the formation of the relief of the Sea of Japan region under the influence of the hot intramantle vortex located beneath it. The presence of the intramantle vortex explains the origin of the shape of the Sea of Japan, the structure and features of the relief of the bottom and coast of the Sea of Japan, and the location of volcanoes and hot springs in Japan. On the basis of a model axisymmetric problem of ideal fluid motion at known pressure, the structure of a vortex containing an inner core and an outer part with azimuthal velocity discontinuities at the boundary of the inner core of the vortex and at the boundary of the outer part of the vortex is revealed. The large-scale intramantle vortex under the Sea of Japan region excites smaller mesoscale intramantle vortices. The intramantle vortices supply heat (in the form of hot fluids) to endogenous heat sources from the sea bottom to the water and create anticyclonic vortices in the inner part of the Sea of Japan waters, which is confirmed by drifter data and satellite observations.

Keywords Relief of the sea of Japan region · Intramantle vortex · Volcanoes · Hot springs · Mud volcanoes · Ideal incompressible fluid · Velocity discontinuities · Vortex core · Endogenous heat sources · Convection · Instability · Secondary vortices · Vortex formation · Dissipation of kinetic energy · Anticyclonic vortices · Water circulation · Drifters · Drifting buoys

1 Introduction

In previous works, the process of lowering the orbit and tangential penetration into the Earth's mantle of a temporary satellite captured by the Earth was considered [1–3].

S. Yu. Kasyanov (✉)
N.N. Zubov State Oceanographic Institute, Roshydromet, Moscow, Russia
e-mail: skas53@yandex.ru

© The Author(s), under exclusive license to Springer Nature Switzerland AG 2024

V. Karev (ed.), *Proceedings of the 9th International Conference on Physical and Mathematical Modelling of Earth and Environmental Processes*, Springer Proceedings in Earth and Environmental Sciences, https://doi.org/10.1007/978-3-031-54589-4_60

The displacement of the upper mantle layers relative to the lower ones due to tides in the mantle caused by the satellite's circulation led to the melting of the asthenosphere layer in the mantle (partially solidified by the present time) and the formation of the present-day 220 km seismic boundary [1–3].

In the trajectory sections near the perigee of the orbit, the satellite glided along the surface of the Earth's lithosphere and mantle. Traces of the satellite's gliding during the last few revolutions of the orbit are preserved in the relief of the Pacific Ocean shown in Fig. 1. During the last orbital revolution before full immersion into the mantle, the satellite travelled from Hawaii through the Mariana Basin to the Philippine Islands. In this case, the satellite was partially immersed in the mantle and under the action of the mantle flow running over it made oscillatory movements in the vertical direction, which led to the formation of a sinusoidal trace in the relief of the ocean floor—the Mid-Pacific Mountains [4]. The trace of the satellite's vertical motions is preserved in the vertical structure of the mantle temperature and density fields and is visible on the seismic section [5]. The satellite's full immersion into the mantle occurred in the vicinity of the Philippine Islands.

During the final orbit, before the satellite's full penetration into the mantle, the depth of partial immersion of the satellite while gliding along the surface of the lithosphere and mantle increased. Gliding of the satellite caused melting and partial evaporation of the lithosphere and mantle and formation of a region of hot molten matter in the mantle with a jet in the centre.

Around this jet, a chain of "vortex semi-rings" was formed, similar to the vortices around an invading liquid jet studied in the experiments [6]. The chain of outlets of these "vortex semi-rings" on the day surface, preserved up to the present time, can be seen in the relief of the western part of the Pacific Ocean in Fig. 1 [4].

At full immersion of the satellite into the mantle, a vortex ring was formed [4, 7]. After the vortex ring disintegration, a quasi-stationary system of hot two-phase liquid–gas vortices was formed in the mantle [7], which is based on the present-day system of three energy-carrying vortices in the Earth's mantle. These vortices are: (1) Himalaya + Tian Shan—Kolyma, (2) Kolyma—Yellowstone, (3) Yellowstone—Hudson Bay—Eastern Mediterranean Sea [7].

Of particular interest is the vortex semi-ring formed in the mantle around the satellite's trajectory during its approximately half-dive in the Mariana Basin. The northern exit to the day surface of this vortex semi-ring formed the relief of the lithosphere under the Sea of Japan (see Fig. 1). The mechanism of vortex formation around the downward directed trajectory of the body at partial immersion in the mantle explains the characteristic shape of the lithosphere relief of the Sea of Japan. Due to the mechanism of vortex formation in the mantle under the area of the Sea of Japan, the motion of matter in it is anticyclonic.

In addition, it should be noted that during the satellite's sinking by about half in the area of the Mariana Basin, a shock wave with Mach number $M = 1$ was formed in the mantle [4, 9], the trace of which goes from the Mariana Basin to the Japanese Islands (see Fig. 1). Recently it was noticed that the chain of vortex semi-rings is hydrodynamically connected with the system of three energy-carrying vortices in the Earth's mantle [9], which is controlled by astronomical factors [7]. Consequently,

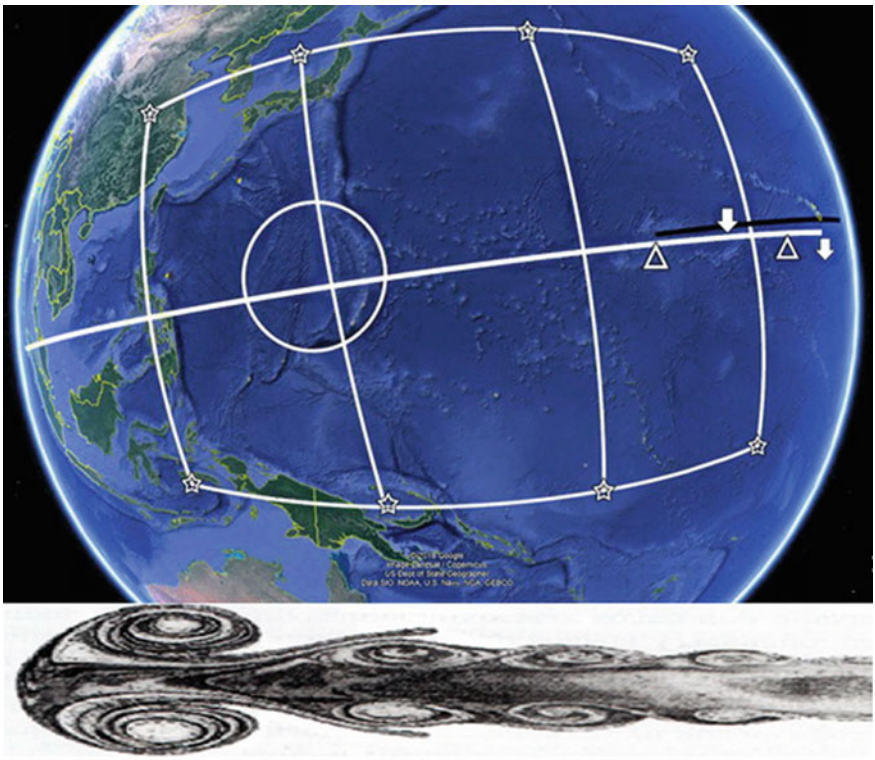


Fig. 1 Relief of the western part of the Pacific Ocean and penetration trajectory of a temporary Earth satellite into the mantle in the area from Hawaii to the Philippine Islands [4]. The triangles are the areas of ascent and the arrows are the areas of trajectory lowering. Black line—seismic section [5]. Stars—preserved southern outcrops of the "vortex semi-rings" and positions of the non-preserved northern outcrops symmetrical to them relative to the trajectory. The Mariana Basin region is marked with a circle. At the bottom is a similar chain of vortices around the jet invading the liquid in the laboratory experiment [6]. Cartographic basis Google Earth [8]

the state of the vortex in the mantle under the Sea of Japan region and the heat flow from the sea bottom into the water associated with the vortex are also controlled by astronomical factors.

2 Relief of the Sea of Japan and Distribution of Endogenous Heat Sources

Figure 2 shows the three-dimensional relief structure of the Sea of Japan.

Due to the mechanism of the intramantle vortex formation, the southeastern branch of the exit of the intramantle vortex to the day surface under the Sea of Japan region

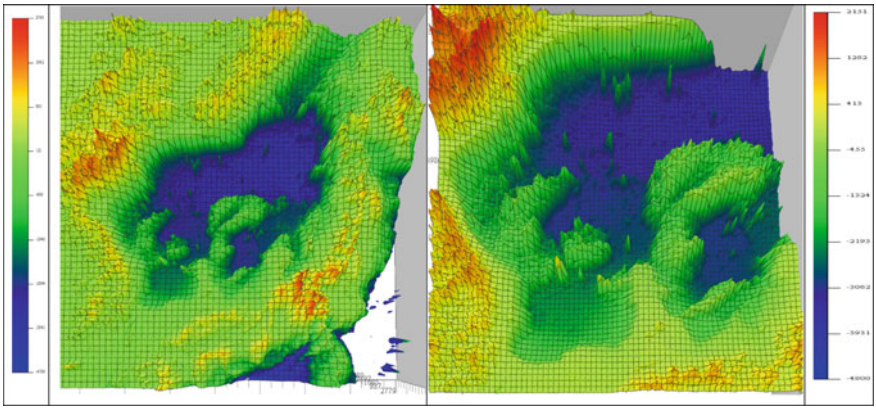


Fig. 2 3D relief of the Sea of Japan according to the GEBCO array data [10]. In the central part of the sea, the Yamato submarine elevation is sharply distinguished

is elevated and the upward movement of the vortex substance occurs on it. The Japanese Islands are located at the southeastern boundary of the anticyclonic intramantle vortex. Therefore, the lithosphere of the Japanese Islands is elevated due to the fact that they are located above the ascending branch of the vortex and due to the gyroscopic forces.

At the boundary of the intramantle vortex there is dissipation of kinetic energy accompanied by active heat release. The vortex boundary passes near the coast of the Sea of Japan. The heat coming from the zone of dissipation of kinetic energy of the vortex leads to the formation of a ring of magmatic volcanoes around the Sea of Japan, shown in Fig. 3.

In addition to magmatic volcanism, Japan has mud volcanism and a large number of hot springs. Mud volcanoes in Japan are located in nine distinct areas shown in Fig. 4. Of these, two areas of mud volcanism are located on land. These are a group of 9 mud volcanoes in the coastal part of Hokkaido Island described as "Niikappu" and three small mud volcanic hotspots (Gamo, Murono, Shosenji) in the Tokamati-Matsudai area in central Japan. The remaining seven areas of mud volcanism are located in the surrounding waters surrounding Japan from the east, mainly along deep-sea troughs [12].

The map of hot springs in Japan is shown in Fig. 5.

Analyses of the three-dimensional relief structure and the location of magmatic volcanoes, mud volcanoes, and hot water springs in the Sea of Japan region suggest the existence of two main areas of hot matter in the underlying mantle. One such area is a ring around the periphery of the Sea of Japan, while the other is located in the central part of the sea. This conclusion is confirmed when considering the map of seismic Pn wave velocity anomalies in the mantle shown in Fig. 6.

The formation of the lithospheric relief structure shown in Fig. 2, the location of volcanoes (see Figs. 3 and 4) and hot water springs (see Fig. 5), and the structure of the seismic wave velocity field (see Fig. 6) is fully explained by the presence of hot

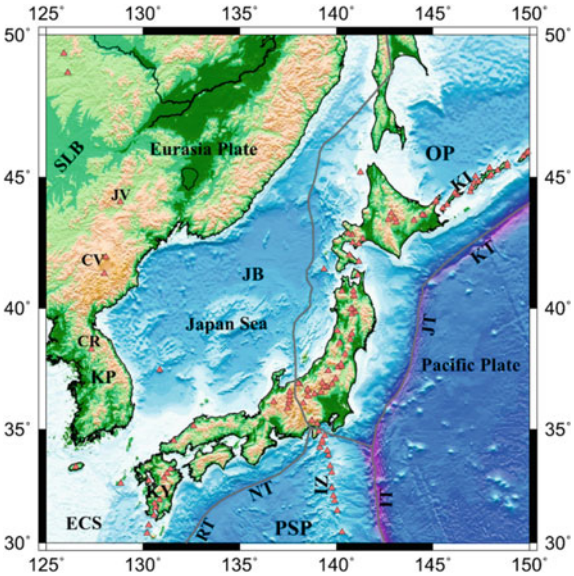


Fig. 3 Simplified tectonic map of the Sea of Japan region with the location of magmatic volcanoes. CR = Chuga-Ryong volcano; CV = Changbaishan volcano; ECS = East China Sea; IT = Izu-Bonin Trench; IZ = Izu Islands; JB = Japan Basin; JT = Japan Trench; JV = Jingpohu volcano; KI = Kuril Islands; KP = Korea Peninsula; KT = Kuril Trench; KY = Kyushu Island; NT = Nankai Trough; OP = Okhotsk Plate; PSP = Philippines Sea Plate; RT = Ryukyu Trench; SLB = Songliao Basin. Triangles denote Quaternary volcanoes, and grey lines denote plate boundaries. Background colours represent topography [11]



Fig. 4 Overview diagram of mud volcano areas in Japan. 1-Niikappu Prefecture; 2-Tokamati-Matsudai; 3-the outer escarpment of the Japan Trough; 4-island slope; 5, 6-Nankai Trough; 7-Kumano Trough; 8-shelf zone of Shikoku Island; 9-shelf zone of Kyushu Island; 10-area of Tanegashima Island [12]

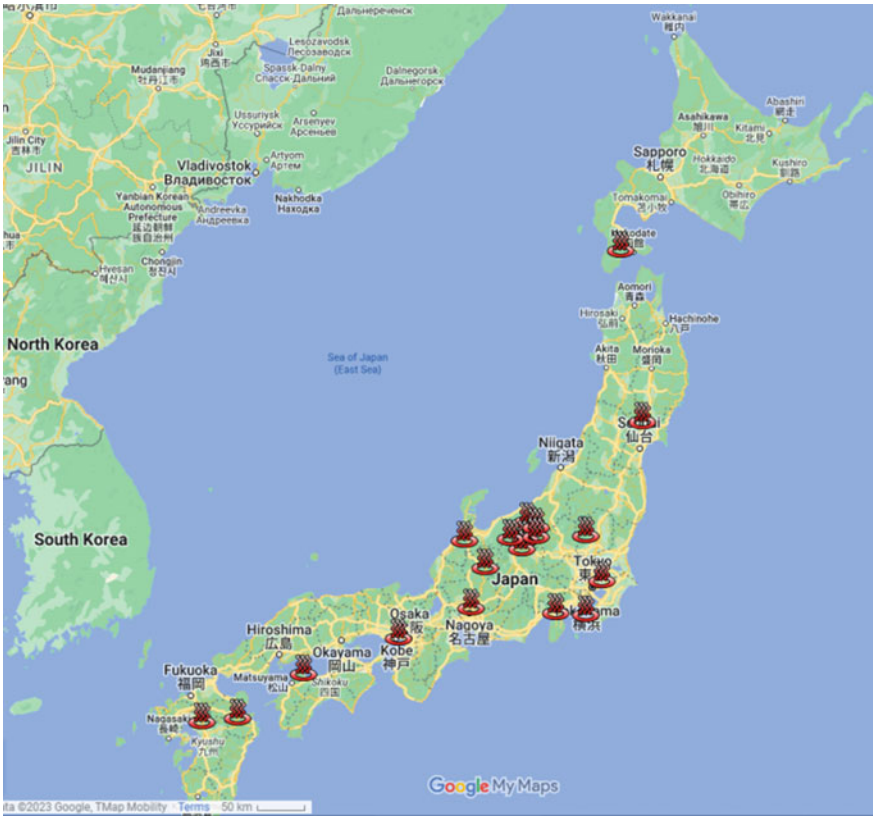


Fig. 5 Location of hot springs in Japan [13]

anticyclonic rotating liquid matter in the mantle beneath the Sea of Japan region. This confirms the validity of the hypothesis stated in the introduction about the formation of the lithospheric relief of the Sea of Japan region under the influence of a hot vortex in the mantle beneath this region. It is of interest to estimate the structure of currents in the vortex as far as possible. Approximately, the velocities of the vortex substance near the upper boundary can be estimated from the known relief of the lithosphere of the Sea of Japan region. Previously, we have shown that it is possible to estimate the density, velocity, and pressure-density dependence along a circular current line selected in advance at the upper boundary of the intramantle vortex [14]. In the present work, the estimation of flow velocities in the vortex is constructed within the framework of solving the model problem of stationary axisymmetric motion of a homogeneous incompressible ideal fluid at the flat upper boundary of a cylindrical vortex. It is assumed that the pressure at the vortex boundary is known and equal to the hydrostatic pressure of the lithosphere and sea water.

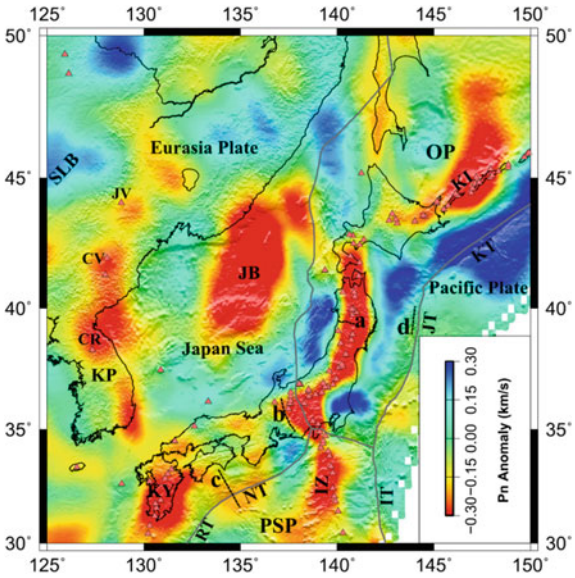


Fig. 6 Pn lateral velocity variations in the study area. Red areas correspond to low velocity, and blue areas correspond to high velocity. Triangles denote Quaternary volcanoes, and grey lines denote plate boundaries. Dashed black lines marked a, b, c, and d denote four profile lines, respectively [11]. Other notations are as in Fig. 3

3 Construction of the Lithospheric Topography for Solving the Modelled Axisymmetric Problem

In order to solve the axisymmetric model problem, let us form some axisymmetric model relief, which qualitatively reflects the most important features of the lithosphere relief of the Sea of Japan region, shown in Fig. 7.

In Fig. 7, point C is chosen as the position of the epicentre of the intramantle vortex under the Sea of Japan.

As a basis for forming a model axisymmetric relief, we choose the relief of the lithospheric surface along the CE ray.

At the points of the CE beam, the averaged values of the GEBCO lithospheric relief array [10] are calculated at 3731 m increments. The averaging is performed with a radius of 15/240 degrees of meridian (15 cells of the GEBCO array). Spline interpolation is performed on the calculated averaged values and interpolated values of the smoothed modelled lithospheric relief are calculated in 1 m steps. The obtained smoothed model relief of the lithosphere of the Sea of Japan along the selected CE ray is shown in Fig. 8.

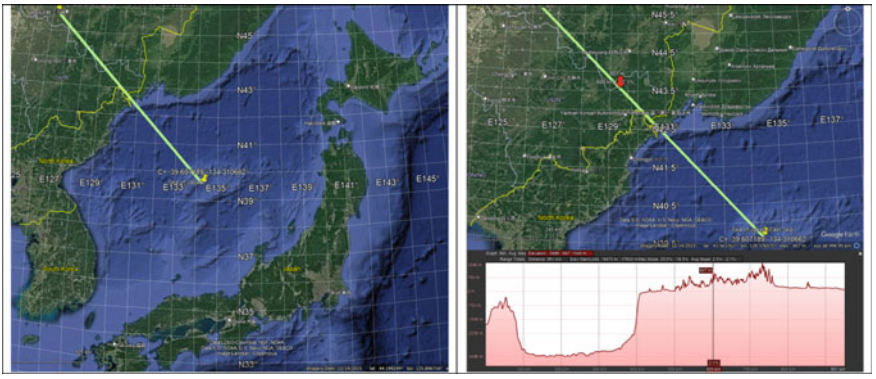


Fig. 7 Relief of the Sea of Japan. Selection of the ray as a basis for building the model relief for axisymmetric problem. The CE ray is shown as a white line. Coordinates of point C—the epicentre of the intramantle vortex under the Sea of Japan: 39.607°N, 134.311°E. Coordinates of the end of the beam—point E: 45.741°N, 126.233°E. The right half of the figure shows the relief of the lithosphere along the CE ray in the direction from the centre to the periphery, i.e. on the left the centre of the vortex—point C, on the right the periphery of the vortex—point E. Cartographic basis Google Earth [8]

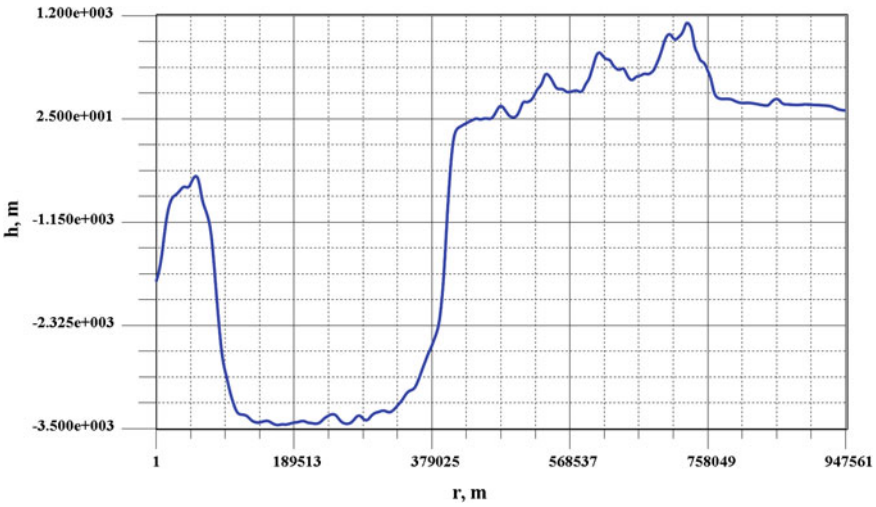


Fig. 8 Smoothed model relief of the lithosphere of the Sea of Japan along the selected CE ray

4 Formulation of a Model Axisymmetric Problem

The axisymmetric stationary motion of an ideal incompressible fluid in a circular cylinder with a vertical axis and flat upper and lower boundaries is considered. It is considered in a coordinate system rotating around the cylinder axis with constant

angular velocity Ω. At the upper boundary of the medium motion region, a time-invariant pressure distribution is set $p = p(r)$.

The equations of unsteady axisymmetric motion of a homogeneous ideal incompressible fluid on the flat upper boundary of the cylindrical region have the form:

$$\frac{\partial V_r}{\partial t} + V_r \frac{\partial V_r}{\partial r} - \frac{V_\phi^2}{r} = -\frac{1}{\rho}\frac{\partial p}{\partial r} + 2\Omega V_\phi + \Omega^2 r \tag{1}$$

$$\frac{\partial V_\phi}{\partial t} + V_r \frac{\partial V_\phi}{\partial r} + \frac{V_r V_\phi}{r} = -2\Omega V_r \tag{2}$$

The system of Eqs. (1) and (2) is a system of two ordinary differential equations of the first order. Natural boundary (initial) conditions are given on the symmetry axis (at $r = 0$): $V_\phi = 0, \quad V_r = 0$. Let us find the stationary states of this system of equations.

The equations of stationary axisymmetric motion have the form:

$$V_r \frac{\partial V_r}{\partial r} - \frac{V_\phi^2}{r} = -\frac{1}{\rho}\frac{\partial p}{\partial r} + 2\Omega V_\phi + \Omega^2 r \tag{3}$$

$$V_r \frac{\partial V_\phi}{\partial r} + \frac{V_r V_\phi}{r} = -2\Omega V_r \tag{4}$$

From where

$$\frac{1}{2}\frac{\partial V_r^2}{\partial r} = -\frac{1}{\rho}\frac{\partial p}{\partial r} + \frac{V_\phi^2}{r} + 2\Omega V_\phi + \Omega^2 r \tag{5}$$

$$V_r\left(\frac{\partial V_\phi}{\partial r} + \frac{V_\phi}{r} + 2\Omega\right) = 0 \tag{6}$$

The velocities V_r and V_ϕ can be found by integrating the system of Eqs. (3) and (6) at known pressure p.

The pressure is known and is determined by the hydrostatic pressure of the lithosphere, taking into account the water column. Therefore, the continuity equation is not needed to find velocities V_r and V_ϕ, but it can be used to estimate the direction of upward and downward flows in the vicinity of the upper boundary at which velocities V_r and V_ϕ are estimated.

5 Special Cases

Note that Eq. (6) is satisfied at $V_r = 0$ any V_ϕ.

If at $V_r = 0$ occurs $\frac{\partial p(r)}{\partial r} \geq 0$, then from equation (3) it follows:

$$V_\phi^2 + 2\Omega r V_\phi - \frac{r}{\rho}\frac{\partial p}{\partial r} + \Omega^2 r^2 = 0, \tag{7}$$

whence there are two solutions for V_ϕ:

$$V_\phi = -\Omega r \pm \sqrt{\Omega^2 r^2 + \frac{r}{\rho}\frac{\partial p}{\partial r} - \Omega^2 r^2} = -\Omega r \pm \sqrt{\frac{r}{\rho}\frac{\partial p}{\partial r}} \tag{8}$$

Since the motion in the vortex is anticyclonic, we choose the minus sign in expression (8).

Thus, the azimuthal velocity V_ϕ in this case undergoes a discontinuity.

If at $V_r = 0$ occurs $\frac{\partial p(r)}{\partial r} < 0$, then Eq. (7) has no roots and it is impossible to find a stationary value of the azimuthal velocity.

In this case

$$\frac{1}{2}\frac{\partial V_r^2}{\partial r} = -\frac{1}{\rho}\frac{\partial p}{\partial r} + \frac{V_\phi^2}{r} + 2\Omega V_\phi + \Omega^2 r = -\frac{1}{\rho}\frac{\partial p}{\partial r} + \frac{1}{r}(V_\phi + \Omega r)^2 > 0.$$

Therefore, when integrating over the radius of Eq. (5), the value becomes positive. When integrating, the value $V_r^2(r)$ is calculated and the sign of the value $V_r(r)$ is chosen positive in accordance with the positive sign of the value $\frac{\partial V_r}{\partial t}$ in Eq. (1).

Since the value $V_r^2(r)$ becomes positive when integrating over the radius of Eq. (5), than the condition $V_r \neq 0$ starts to be satisfied. This allows us to find V_ϕ from Eq. (6) by integrating Eq. (9):

$$\frac{\partial V_\phi}{\partial r} + \frac{V_\phi}{r} + 2\Omega = 0. \tag{9}$$

6 Integration Result of the Equations of Motion

Taking into account the above special cases and natural boundary conditions $V_\phi = 0, \quad V_r = 0$, at $r = 0$ the stationary equations of motion can be numerically integrated over the radius and the dependences of velocities V_r and V_ϕ on the radius, shown in Fig. 9, can be obtained.

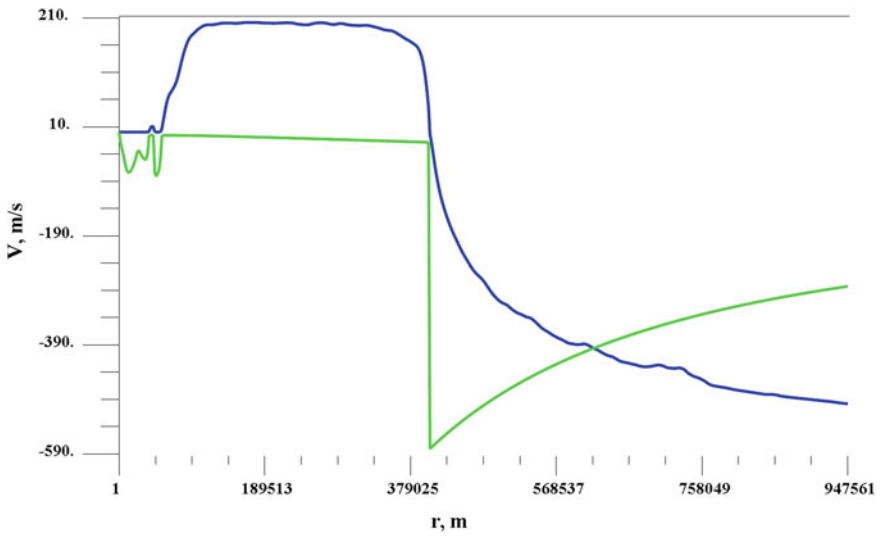


Fig. 9 Radial and azimuthal velocities of stationary axisymmetric motion. Blue curve—V_r (radial velocity), green curve—V_ϕ (azimuthal velocity)

7 Conclusions from the Analysis of the Axisymmetric Vortex Model

Thus, consideration of the model problem allowed us to find a solution to the equations of motion describing the stationary axisymmetric anticyclonic circulation at the boundary of the intramantle vortex. The solution is determined by the smoothed model axisymmetric lithospheric topography and depends on the smoothing. The vortex is separated into an inner core and an outer part. The radial velocity of the vortex is continuous. The azimuthal velocity of the vortex undergoes discontinuities in areas of rapid uplift of the lithospheric topography with increasing radius. The azimuthal velocity discontinuities correspond to the positions of the "wall" of the vortex inner core and the "wall" of the vortex outer part. The azimuthal velocity of the vortex increases as it approaches the wall of the outer part of the vortex from the vortex periphery and increases more sharply as it approaches the wall of the inner core of the vortex.

The discontinuities of the vortex azimuthal velocity at the "wall" of the vortex inner core and at the "wall" of the vortex outer part are tangential discontinuities and can be unstable. Taking into account non-ideality of the substance of a real intramantle vortex in the nature, at the "wall" of the inner core of the intramantle vortex and at the "wall" of the outer part of the vortex there should occur vortex formation and intensive dissipation of kinetic energy into heat. The latter eventually leads to the appearance of local zones of intensive release of endogenous heat from

the sea bottom into the water (mainly in the form of hot springs), which can influence the sea water circulation.

8 Formation of Mesoscale Secondary Vortices in the Mantle Under the Sea of Japan Region Due to Instability of Azimuthal Velocity Discontinuities

Due to the instability of azimuthal velocity discontinuities in the mantle, mesoscale secondary vortices appear near the "wall" of the inner core of the vortex and near the "wall" of the outer part of the vortex surrounding the Sea of Japan. Some of them, as can be seen from Fig. 2, manifest themselves in the form of abrupt changes in the sea bottom relief. The ocean floor relief structures with large relief height gradient create large spatial pressure gradients, which determine the structure of stationary motion in the intramantle vortex.

Figure 10 shows the field of Pn wave velocity anisotropy and the field of Pn wave velocity anomalies in the mantle [11]. Due to the presence of radial stratification by matter density in the rotating vortex, the propagation velocity of Pn waves in the azimuthal direction should be higher than in the radial direction. Due to this, by the orientation of the strokes corresponding to the directions of the fastest propagation of Pn waves, we can identify intensive motions directed along the "wall" of the outer part of the large-scale vortex under the area of the Sea of Japan and several mesoscale vortices near this "wall" of the vortex. (The "wall" of the outer part of the large-scale vortex under the Sea of Japan region covers the Sea of Japan from the outside.) The locations of these eddies are consistent with the directions of the most rapidly propagating Pn waves obtained from earlier studies in 2005 and 2006 [15, 16].

The chains of mesoscale secondary vortices near the "wall" of the outer part of the large-scale vortex beneath the Sea of Japan region can also be identified by the alternating areas of maxima and minima of the Pn wave velocity anomalies in the mantle along this "wall" in Figs. 6 and 10.

In the field of gravity anomalies in free air presented in Fig. 11 [17], traces of some mesoscale secondary vortices are clearly visible. Traces of other mesoscale secondary vortices are revealed by a more detailed analysis using the field of isostatic gravity anomalies presented in Fig. 12. The mesoscale secondary vortex system of the Japan Sea sub-area has slowly evolved through time. Thermal traces of vortex positions at various previous time points are preserved in the gravity anomaly fields, which creates ambiguity and makes it difficult to determine the locations of secondary vortices in the mantle on the gravity anomaly maps.

In Fig. 13, circles schematically mark some of the candidates for possible locations of secondary mesoscale vortices in the Earth's mantle that have arisen along the vortex "walls". This scheme is preliminary and requires refinement during subsequent detailed analyses.

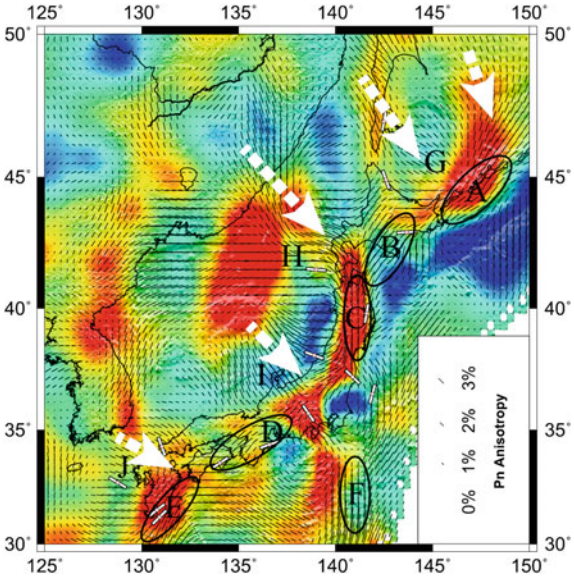
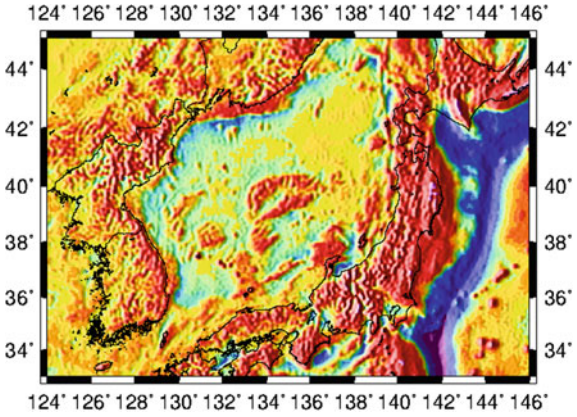


Fig. 10 Tomographic image of the Pn velocity and anisotropy in the study area. The velocity color bar is the same as in Fig. 6. Short black bars represent the fast direction of the anisotropy with their lengths proportional to the magnitude of anisotropy. Regions exhibiting large anisotropy and having dense ray coverage are outlined with black ovals. Thick dashed white arrow lines mark inferred regional mantle flow direction above the slab [11]. The white bars with a pink core indicate the fast direction measured from previous shear-wave splitting studies [11, 15, 16]

Fig. 11 Field of gravity anomalies in free air [17]



A small black circle around the epicentre of the intramantle vortex under the Sea of Japan (point C in Fig. 7, which has coordinates 39.607°N, 134.311°E) schematically marks the position of the "wall" of the inner core of the vortex. Black circles mark the chain of secondary mesoscale vortices in the Earth's mantle that originated on

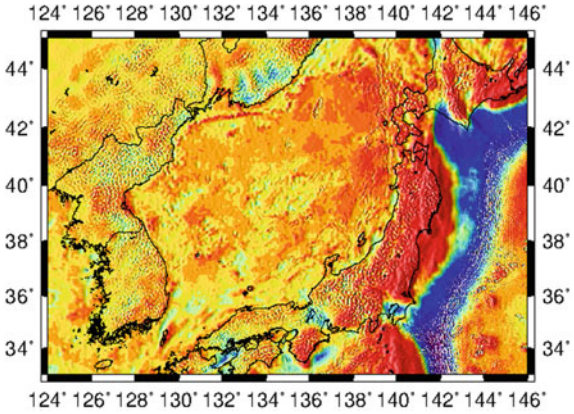


Fig. 12 Field of isostatic gravity anomalies [17]

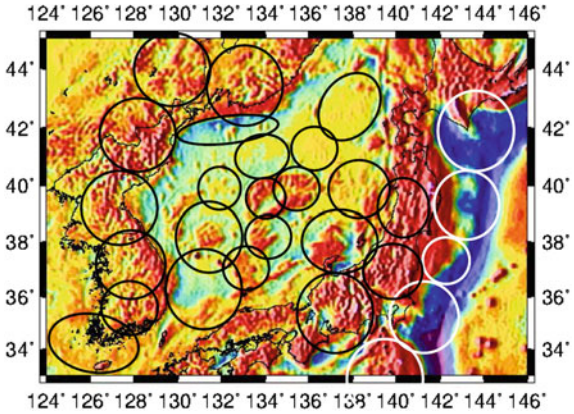


Fig. 13 The field of gravity anomalies in free air [17] and a preliminary scheme of the possible location of secondary mesoscale vortices in the Earth's mantle under the Sea of Japan region

the outer side of the "wall" of the inner core of the intramantle vortex. Also, black circles indicate a chain of secondary mesoscale vortices in the Earth's mantle formed along the "wall" of the outer part of the vortex surrounding the Sea of Japan. White circles indicate a chain of secondary mesoscale vortices in the Earth's mantle located along the deep-water troughs off the eastern coast of Japan.

9 Influence of Endogenous Heat from Intramantle Vortices on the Surface Circulation of the Waters of the Sea of Japan

Topologically, the Sea of Japan is similar to a cylindrical vessel with heated side walls and bottom heated in the centre. On a rotating Earth in such a vessel, cyclonic motion along the side walls of the vessel and anticyclonic motion over the heated

area in the centre occur at the fluid surface. The hot fluid flows propagating from the southeastern boundary of the intramantle vortex passing under the Japanese Islands lead to heating and uplift of the deep waters of the Sea of Japan along the coast of Japan and compensatory outflow of surface waters from the coast. Thus, intense endogenous heat fluxes into the water near the shores of the Sea of Japan cause cyclonic coastal circulation in the sea. As a result, the Tsushima Current is intensified.

Flows of hot fluids in the mantle and lithosphere propagate from hot intramantle vortices in the form of vortex cords rising to the sea bottom [18]. In the inner part of the sea, they rise from the core of the large-scale intramantle vortex and from secondary mesoscale vortices. Rising to the sea bottom, the hot fluid flows create submarine elevations of the sea bottom relief and form sources of endogenous heat on the sea bottom, mainly in the form of hot liquid jets [18]. In this way, endogenous heat from the sea bottom creates upward convective flows of seawater. Convective flows of seawater ascending to the sea surface and the topographic effect of bottom elevation acting unidirectionally with them form mesoscale anticyclonic eddies in the surface water layer of the Sea of Japan.

Figure 14 shows a map of the surface currents of the Sea of Japan based on satellite image analysis data from 1988–1996, which revealed seven major anticyclonic eddies [19]. Figure 15 shows a map of the surface currents of the Sea of Japan constructed by us using a computer information and reference system [20–22] based on an array of drifter observations from 1990 to 2022.

The locations of anticyclonic eddies in the current maps shown in Figs. 14 and 15 correlate with the positions of the maximums of gravity anomalies and with the possible locations of mesoscale eddies in the mantle in Fig. 13.

10 Examples of Individual Trajectories of Buoys Drifting in the Sea of Japan Captured by Anticyclonic Vortices

Here are some examples of individual trajectories of buoys drifting in the Sea of Japan captured by anticyclonic eddies, constructed in this work with the help of the computer information and reference system [20–22].

Buoy № 9,628,885 (Fig. 16) has been making anticyclonic motion over the southern spur of the Yamato High for a long time. The southern spur of the Yamato Seamount is formed by the outflow of a hot secondary mesoscale intramantle vortex located south of the inner core of the large-scale intramantle vortex. The endogenous heat from this vortex creates upward convective jets and forms an anticyclonic motion in the surface water layer above the southern spur of the Yamato High. Leaving this anticyclonic water vortex near the Japanese coast, the buoy began to make a complex cyclonic motion along the coast and then found itself in another anticyclonic water vortex formed under the influence of endogenous heat sources located on the seafloor above another mesoscale intramantle vortex.

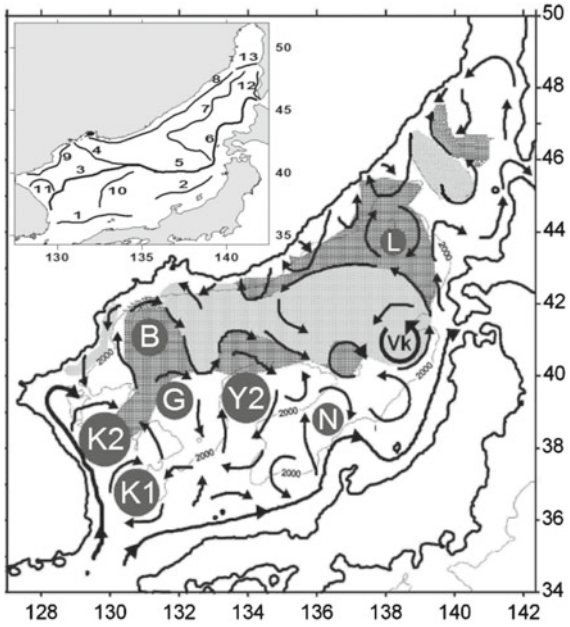


Fig. 14 Map of surface currents of the Sea of Japan based on the data of satellite image analysis 1988–1996. The seven main anticyclonic eddies are labelled K1, K2, G, B, Y2, N, L. The cyclonic vortex is designated by the letters Vk [19]

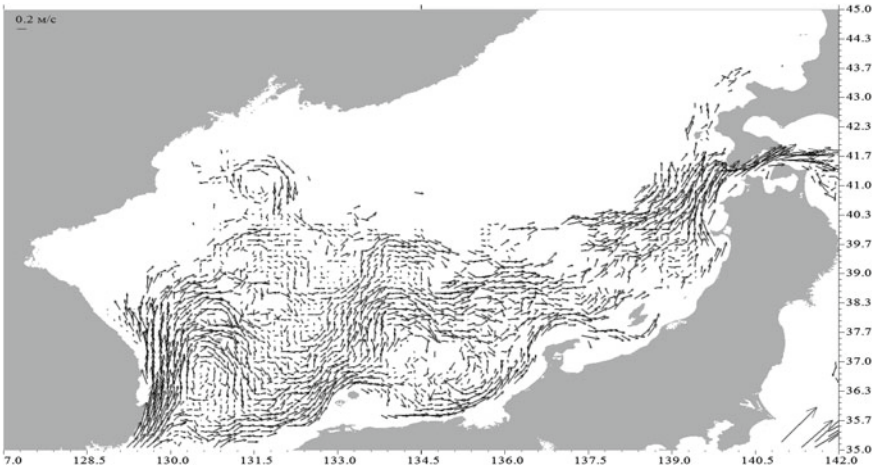


Fig. 15 Map of surface currents of the Sea of Japan based on the drifter observations of 1990–2022 [20–22]

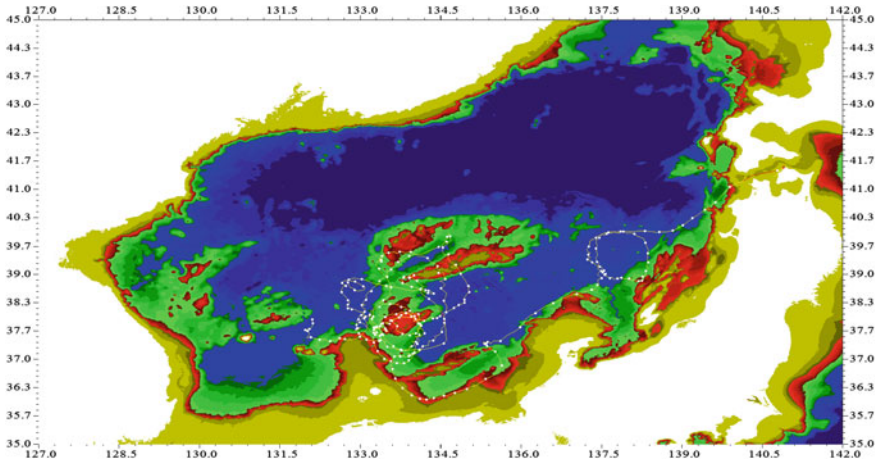


Fig. 16 Trajectory of drifting buoy № 9,628,885

Buoy № 9,619,795 (Fig. 17) made an anticyclonic motion over the location of the inner core of the intramantle vortex.

Buoy № 9,820,192 (Fig. 18) rotated in the anticyclonic motion over the elevation of the relief of the southern spur of the Yamato Hills and then made a bicyclonic motion near the heated coast of Japan.

Buoy № 9,916,043 made an anticyclonic motion over the secondary intramantle vortex located to the north of the inner core of the intramantle vortex (Fig. 19).

Thus, the individual drifter trajectories show the presence of anticyclonic motion of the waters of the Sea of Japan over the secondary mesoscale intramantle vortices

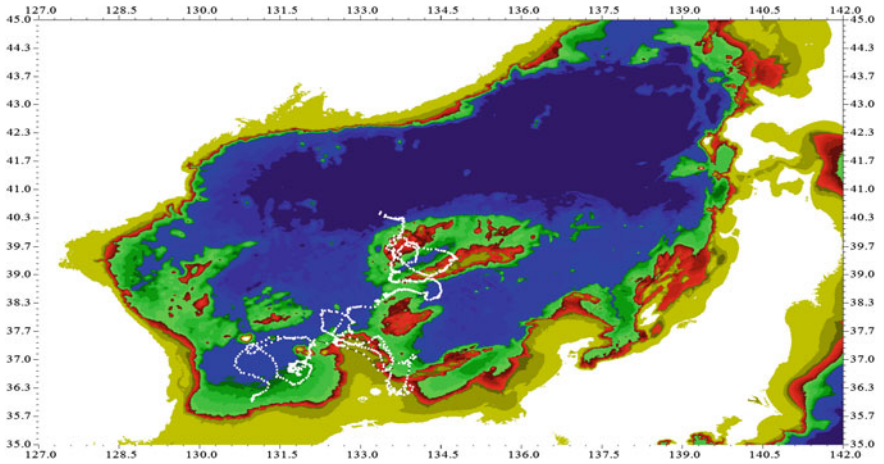


Fig. 17 Trajectory of drifting buoy № 9,619,795

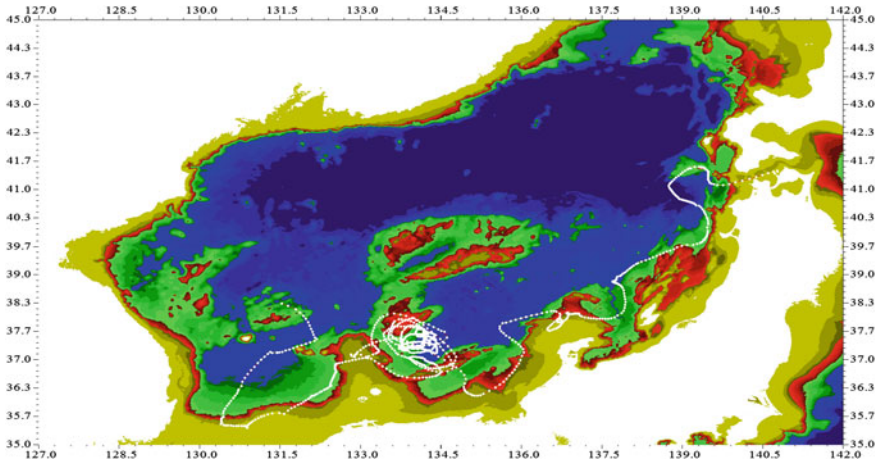


Fig. 18 Trajectory of buoy № 9,820,192

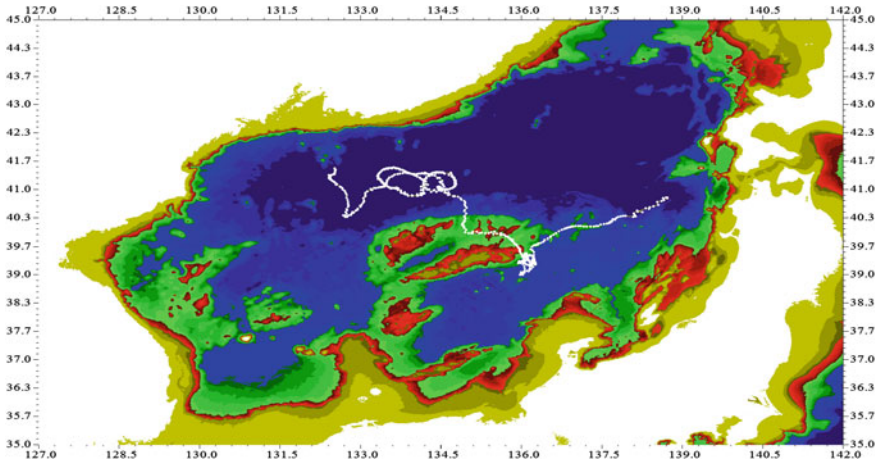


Fig. 19 Trajectory of buoy № 9,916,043

and over the inner core of the large-scale intramantle vortex, as well as the presence of cyclonic motion near the heated Japan Sea coast. The cause of these motions is the endogenous heat supplied by the intramantle vortices.

11 Conclusion

The relief of the Sea of Japan region could have been formed under the influence of the hot intramantle vortex located under it. The presence of the intramantle vortex explains the origin of the shape of the Sea of Japan, the structure and features of the relief of the bottom and coast of the Sea of Japan, and the location of volcanoes and hot springs of Japan. Based on the solution of a model axisymmetric problem about the motion of an ideal incompressible fluid at the upper boundary of the vortex at a known pressure, the structure of an idealised intramantle vortex is revealed. The vortex is divided into an inner core and an outer part. The radial velocity of the vortex is continuous, and the azimuthal velocity undergoes discontinuities at the boundary of the inner core of the vortex and at the boundary of the outer part of the vortex.

In a real intramantle vortex in nature in the vicinity of azimuthal velocity discontinuities at the two "walls" of the idealised vortex there is an intensive dissipation of kinetic energy with the release of a large amount of heat and vortex formation.

A large-scale intramantle vortex under the Sea of Japan region excites smaller mesoscale intramantle vortices. The intramantle eddies are a supplier of heat energy to endogenous heat sources from the sea bottom to the water, which in turn create anticyclonic eddies in the inner part of the Sea of Japan. The heat from the intramantle eddies is transported upward in vortex cords of hot fluids rising through the mantle and lithosphere to the seafloor. Endogenous heat from the inner core of the large-scale vortex in the mantle and from the secondary vortices excited by it creates convective water flows rising from the sea bottom, which lead to the appearance of anticyclonic vortices in the surface layer of the Sea of Japan waters.

At the same time in the coastal waters of the Sea of Japan, the heat released at dissipation of kinetic energy at the boundary of the outer part of the large-scale intramantle vortex creates a cyclonic circulation, which is confirmed by observations of drifting buoys.

The anticyclonic eddies in the Sea of Japan are traced from drifter observations and satellite images. The location of anticyclonic eddies in the Sea of Japan is consistent with their convective origin from the endogenous heat of intramantle eddies.

The circulation of the Sea of Japan waters is controlled by astronomical factors because the state of the vortex in the mantle beneath the Sea of Japan region and the vortex-related heat flux from the sea bottom to the water are controlled by astronomical factors.

References

1. Kasyanov S.Yu. Modelling of orbital motion of a large asteroid during descent with deepening into the Earth's lithosphere and mantle // Physical Problems of Ecology (Environmental Physics). 2012. № 18. P. 151–164. http://ocean.phys.msu.ru/pubs/ecophys/ecophys-18_pp150-246.pdf

2. Kasyanov, S.Yu.; Samsonov, V.A. Estimation of tidal wave heights during gliding of a large satellite on the surface of a liquid attracting spherical layer with a solid core // Proceedings of MIPT. 2017. T. 9, № 3. P. 14–20. https://mipt.ru/upload/medialibrary/d1a/2_kas_yanov_14_20.pdf
3. Kasyanov S, Samsonov V (2018) Effect of a tidal wave caused by large gliding satellite on formation of 220 km seismic boundary and split of the mantle into blocks. // Physical and mathematical modeling of earth and environment processes. PMMEEP 2018. Springer Geology. Springer, Cham, P. 360–370. https://doi.org/10.1007/978-3-319-77788-7_37,
4. Kasyanov, S.Y. (2021). Formation of System of Intense Vortices in the Mantle When a Large Temporary Earth Satellite is Immersed // Processes in GeoMedia—Volume III. Springer Geology. Springer, Cham. P. 217–232. https://doi.org/10.1007/978-3-030-69040-3_21
5. Cao Q, Van der Hilst RD, de Hoop MV, Shim S-H (2011) Seismic imaging of transition zone discontinuities suggests hot mantle west of Hawaii. Science 332(6033):1068–1071. https://doi.org/10.1126/science.1202731
6. Gharib M, Rambod E, Shariff K (1998) A universal time scale for vortex ring formation. J Fluid Mech 360: P. 121–140
7. Kasyanov, S.Y., Samsonov, V.A. (2021). About the Modern System of Three Energy-Carrying Intensive Vortices in the Earth's Mantle. // Processes in GeoMedia - Volume II. Springer Geology. Springer, Cham. P. 273–291. https://doi.org/10.1007/978-3-030-53521-6_31
8. Google Earth Pro. https://www.google.com/earth/about/versions/#download-pro
9. Kasyanov S.Yu. (2023) Hydrodynamic interaction between two systems of intense intra-mantle vortices as a possible cause of the connection between distant earthquakes // Processes in GeoMedia — Volume VII, P. 159–169, Springer Geology, https://doi.org/10.1007/978-981-99-6575-5_15
10. https://download.gebco.net/
11. Lü, Y., Li, J., Liu, L., & Zhao, L.-F. (2019). Complex uppermost mantle structure and deformation beneath the Northwest Pacific region. Journal of Geophysical Research: Solid Earth, 124, P. 6866–6879. https://doi.org/10.1029/2019JB017356
12. https://mudvolcanoazblog.wordpress.com/%d1%8f%d0%bf%d0%be%d0%bd%d0%b8%d1%8f/.
13. https://www.google.com/maps/d/viewer?mid=10u4g4LJ5y-uln9iSRNOspG1glF4&hl=en&ll=37.67512528461306%2C135.7910155&z=6
14. Kasyanov, S.Yu. (2022). On the Possibility of Use the Himalayan-Tien Shan Mountain Ring Relief to Assess the State of the Substance at the Boundary of Intense Vortex in the Underlying Mantle // Processes in GeoMedia—Volume IV. Springer Geology. Springer, Cham, P. 99–107. https://doi.org/10.1007/978-3-030-76328-2_11
15. Long, M. D., & van der Hilst, R. D. (2005). Upper mantle anisotropy beneath Japan from shear wave splitting. Physics of the Earth and Planetary Interiors, 151(3-4), P. 206–222. https://doi.org/10.1016/j.pepi.2005.03.003
16. Nakajima, J., Shimizu, J., Hori, S., & Hasegawa, A. (2006). Shear-wave splitting beneath the southwestern Kurile arc and northeastern Japan arc: A new insight into mantle return flow. Geophysical Research Letters, 33, L05305. https://doi.org/10.1029/2005GL025053
17. https://bgi.obs-mip.fr/data-products/outils/wgm2012-visualizationextraction/#/form-wgm2012-model
18. Kasyanov, S.Y. (2022). Hypothesis of a Possible Cause of Warming in the Arctic Due to Energy Dissipation of Intensive Two-Phase Vortices in Earth's Mantle // Processes in GeoMedia—Volume IV, pp 253–269. Springer Geology. Springer, Cham. https://doi.org/10.1007/978-3-030-76328-2_26
19. Nikitin A.A., Danchenkov M.A., Lobanov V.B., Yurasov G.I. Izvestiya TINRO 2009, vol. 157, P. 158–167
20. Nikitin O.P., Kasyanov S.Yu., Muzyka G.V. Computer information and reference system "Surface currents of the World Ocean" // Proceedings of GOIN. 2005. Issue 209. P. 75–89.
21. Kasyanov S.Yu., Nikitin O.P. Computer atlas of Lagrangian currents in the surface layer of the World Ocean// Researched in Russia. 2001. № 154. P. 1768–1776

22. Nikitin O.P., Kasyanov S.Y., Muzyka G.V. World ocean surface currents visualization software // Proceedings of the 3rd International workshop on computer science and information technologies CSIT'2001. V. 2 (Regular papers). Ufa. Russia. 2001. P. 32–41

Development of a Thermometric Well on a Site Without Natural Cover of the Moscow State University Meteorological Observatory



V. E. Gagarin, A. V. Koshurnikov, G. A. Rzhanitsyn, and D. M. Frolov

Abstract The paper presents the first results of drilling and constructing a thermometric well on the site without natural cover at the Moscow State University meteorological observatory by extracting and studying core from the well. Information is given on soil moisture, thermal conductivity and heat capacity of the soil, as well as freezing temperature.

Keywords Climate change · Frozen ground · Thermometric well · Ground core · Soil moisture · Thermal conductivity · Heat capacity

According to climate websites [1–3], the past six months have become the warmest on Earth in the entire history of observations. From May to September 2023, the average air temperature on Earth was +16.465 °C. This is the highest value in the entire history of observations, which is 0.658 °C higher than the average value for May–September 1991–2020. In June, the average air temperature in the Northern Hemisphere was +20.715 °C, which is the highest indicator in the entire history of observations. This value is 0.572 °C higher than the climatic norm for the period 1991–2020. According to the Japanese reanalysis JRA-55 [4] in July the average air temperature on the planet was +17.11 °C. This is the highest value since 1836. The temperature has never exceeded +17° before. In July 2023, the temperature was above normal (1991–2020) by 0.72 °C. In the Northern Hemisphere, the anomaly is +0.81 °C. The most significant anomalies were recorded around Antarctica. There the anomaly was +1.53 °C. According to the Japanese reanalysis JRA-55, in August 2023, the average air temperature on the planet was +16.91 °C. This is the highest value since at least 1836. In the Northern Hemisphere, the anomaly is +0.93 °C. Previously, August 2016 was the warmest. Then the average temperature was + 16.62 °C. September 2023 was also the warmest on record, following the warmest August, July and June 2023. In September 2023, the average temperature on Earth

V. E. Gagarin · A. V. Koshurnikov · G. A. Rzhanitsyn · D. M. Frolov (✉)
Geographical Faculty of Lomonosov Moscow State University, Moscow, Russia
e-mail: denisfrolovm@mail.ru

© The Author(s), under exclusive license to Springer Nature Switzerland AG 2024

V. Karev (ed.), *Proceedings of the 9th International Conference on Physical and Mathematical Modelling of Earth and Environmental Processes*, Springer Proceedings in Earth and Environmental Sciences, https://doi.org/10.1007/978-3-031-54589-4_61

was +16.58 °C. This is 0.87 °C higher than normal according to the Japanese reanalysis JRA-55. In the Northern Hemisphere, the anomaly is 0.99 °C. Never before in September has the temperature exceeded +16°. Previously, September 2020 was the warmest—the temperature turned out to be +15.98 °C, which is much lower than now. October 2023 also became the warmest on record. The global temperature was +15.47 °C, which is 0.79 °C higher than the climatic norm for the period 1991–2020. In the Northern Hemisphere the anomaly was +1.15 °C.

The impact of climate change on the state of permafrost soils is considered in works [5–7]. For example in Norilsk this summer-autumn was unusual as a large amount of precipitation in summer and a long autumn led to saturation of the seasonally thawed layer of frozen soils in the city with moisture and water. This will lead to strong ice formation and the formation of ice in the lowlands and places of local lowering of the relief and may harm buildings and constructions. A particularly active process is expected when the temperature drops below minus 20°. In addition, abnormal conditions in autumn and summer can lead to serious damage to the asphalt pavement and significant subsidence on highways.

In general permafrost engineering plays an important role in risk assessment and ensuring the reliability of facilities, especially on permafrost soils. Permafrost undergoes cyclic freezing and thawing, leading to changes in its physical and mechanical properties. The scientific field of permafrost engineering studies the laws and processes associated with such soils and their impact on engineering structures. The assessment of risks associated with engineering projects on permafrost soils requires a special approach that takes into account the characteristics of these soils.

In the frame of the mentioned above issues and according to a publication in the media [8], Russian government decree was issued in November 2023, according to which a system of state background monitoring of the state of permafrost will appear in Russia. The decree on its creation and operation was signed by Prime Minister Mikhail Mishustin. Such monitoring will help to gain a more complete understanding of how permafrost is changing due to global climate change, as well as to understand how much greenhouse gases will be released into the atmosphere when permafrost thaws.

Information from the background monitoring system will be used for modeling and scenario forecasting of climate change, will help prevent the negative impact of such changes on economic sectors and the quality of life of citizens, and will contribute to the creation and trouble-free operation of infrastructure in permafrost areas, affecting up to 65% of the country's territory.

In addition, the system for background monitoring of the state of permafrost will become part of the unified system of state environmental monitoring. Roshydromet will be responsible for the creation and operation of this new subsystem. Russian President Vladimir Putin instructed the government to make changes to Russian legislation aimed at creating a state system for monitoring the state of permafrost based on the observation network of Roshydromet.

Temperature monitoring at the MSU meteorological observatory site has been carried out for a long time [9], however, in the light of the described rapid climate changes and considered circumstances in the fall of 2023 through the efforts of



Fig. 1 Drilling of an experimental well on the site without natural cover at the Moscow State University meteorological observatory

staff and students of the Department of Cryolithology and Glaciology and the Laboratory of Snow Avalanches and Mudflows of the Faculty of Geography of MSU, drilling of an experimental well began on the site without natural cover at the MSU meteorological observatory (Fig. 1).

When drilling an experimental well on the site without natural cover, a soil core was taken at the Moscow State University meteorological observatory (Fig. 2).

The soil core extracted during drilling was studied in laboratory conditions. The mass soil moisture was determined (by weighing the original and dried samples), as well as the thermal conductivity and heat capacity of the constituent soil rocks using the KD2 and KD2Pro devices [10, 11]. The results are presented in the graphs in Fig. 3.

The graph shows that the mass moisture content of the core soil samples was about 17–20%. The thermal conductivity of the core soil samples was 1.2–1.5 W/m K and the heat capacity of the core samples of the constituent soil was about 2 MJ/m^3 K and, in general, varied quite moderately with depth. Also, for the selected soil samples from the drilled well, the freezing point was determined, which turned out to be about −2 °C (Fig. 4).

Also, on the site without natural cover at the Moscow State University meteorological observatory, soil temperature was monitored using thermometers. The results of its long-term averaging are shown in Fig. 5.



Fig. 2 Soil core from an experimental well on the site without natural cover at the Moscow State University meteorological observatory

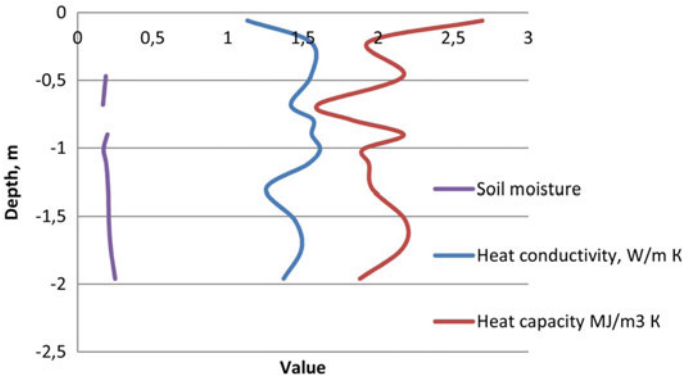


Fig. 3 Soil moisture, thermal conductivity and heat capacity of the constituent soil samples of a core from an experimental well on the site without natural cover at the Moscow State University meteorological observatory

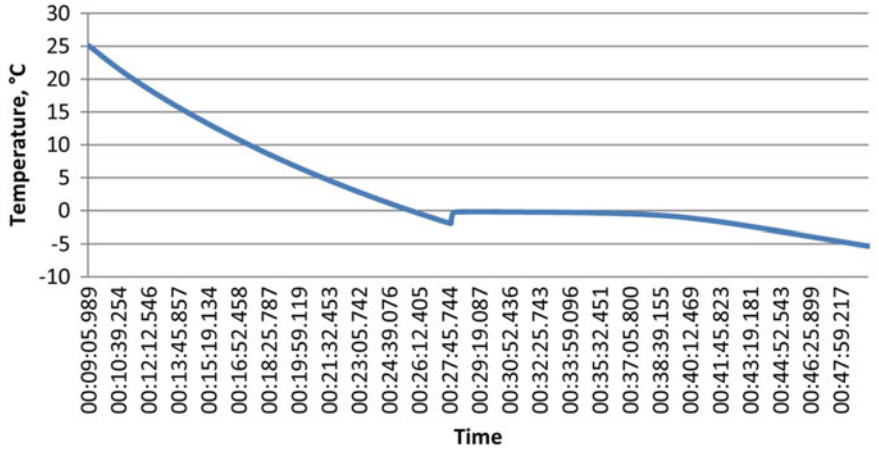


Fig. 4 Freezing temperature of soil core samples from an experimental well on the site without natural cover at the Moscow State University meteorological observatory

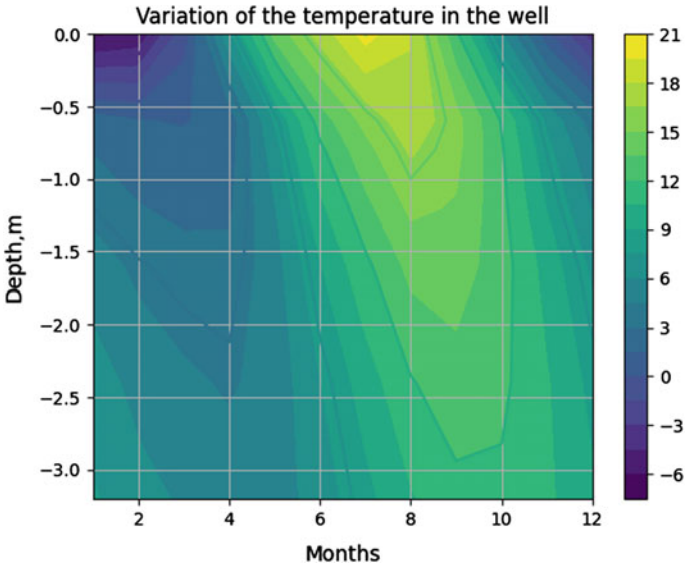


Fig. 5 Annual change in ground temperature on the site without natural cover at the Moscow State University meteorological observatory (long-term averaging)

The diagram on Fig. 5 indicates in particular that the depth of seasonal freezing on the site without natural cover at the Moscow State University meteorological observatory is about 30 cm.

The work was carried out in accordance with the state budget theme “Evolution of the cryosphere under climate change and anthropogenic impact” (121051100164-0), “Danger and risk of natural processes and phenomena” (121051300175-4).

References

1. https://climate.copernicus.eu/
2. https://public.wmo.int/en/media/news/
3. https://www.nasa.gov/
4. https://jra.kishou.go.jp/JRA-55/index_en.html
5. M. Kanevskiy, Y. Shur, D. A. Walker, T. Jorgenson, M. K. Raynolds, et al., The shifting mosaic of ice-wedge degradation and stabilization in response to infrastructure and climate change, Prudhoe Bay Oilfield, Alaska, USA. Arctic Science 8(2), 498–530 (2021). https://doi.org/10.1139/as-2021-0024
6. A. Jan, SL Painter, Permafrost thermal conditions are sensitive to shifts in snow timing, Environ. Res. Lett. 15, 084026 (2020) DOI https://doi.org/10.1088/1748-9326/ab8ec4
7. B. Cao, S. Gruber, D. Zheng, The ERA5-Land soil temperature bias in permafrost regions, The Cryosphere 14, 2581–2595 (2020). Doi: https://doi.org/10.5194/tc-14-2581-2020
8. https://ria.ru/20231102/monitoring-1906859842.html
9. DM Frolov, GA Rzhanitsyn, SA Sokratov, et al., Monitoring of seasonal variations in ground temperature at the observation site of Lomonosov MSU, E3S Web of Conferences 371, 03004 (2023). DOI: https://doi.org/10.1051/e3sconf/202337103004
10. https://manualzz.com/doc/6951299/kd2-manual?ysclid=ln336htxkb730280231
11. https://decagon.ru/environment/kd2pro/

The Potential of Sustainability, Evolution and Adaptation of Coastal Geosystems in the Conditions of Climatic and Man-Made Changes (The Example of Sakhalin)

V. V. Afanas'ev

Abstract Morpholithodynamic features and trends of coastal zone development, technogenic load, location and geospatial parameters of dangerous, vulnerable coasts of Sakhalin Island are considered, which should become the basis for increasing both socio-economic and natural sustainability of the coasts in conditions of rapid and man-made changes. The peculiarities of the response of coasts composed of easily erodible rocks and rocky shores to these changes are shown. Attention is paid to the emission of climatically active gases during the destruction of biomorpholithosystems of the coast. Quantitative data on the most representative in this respect coast of the Amur Estuary are presented.

Keywords Adaptation · Coastal impact of climate change · Technogenic load on the coast · Nature-based solutions

1 Introduction

Trends in modern coastal morpholithogenesis at the regional and global level are mainly associated with changes in climate and sea level. The most common view is that the main result of sea level rise is the erosion of accumulative sandy coasts and land retreat. However, it is far from clear-cut.

As complex adaptive systems, coastal zones, depending on evolutionary trends and in accordance with morpholithodynamic laws, respond differently to rapidly changing natural and climatic conditions and external socio-economic pressure, either completely reorganizing or retaining actual or potential functions. In the second case, we are talking about the ability of the coast to self-organization and sustainable response to external factors [1]. Sustainability, as practice shows, cannot be

V. V. Afanas'ev (✉)
Sakhalin State University, Yuzhno-Sakhalinsk, Russia
e-mail: vvasand@mail.ru

© The Author(s), under exclusive license to Springer Nature Switzerland AG 2024

V. Karev (ed.), *Proceedings of the 9th International Conference on Physical and Mathematical Modelling of Earth and Environmental Processes*, Springer Proceedings in Earth and Environmental Sciences, https://doi.org/10.1007/978-3-031-54589-4_62

ensured by rigid resistance to natural-technogenic changes and high-cost preservation of existing coastal systems. The basis for sustainable response to probable future changes are solutions in line with evolutionary-adaptive properties of natural-economic coastal systems. A scientifically based approach to coastal zoning and planning on an appropriate spatial and temporal scale, taking into account the evolutionary and adaptive properties of coastal zones, is the basis for increasing both socio-economic and natural-natural sustainability.

At present, the problem of coastal protection is not identified in the Sakhalin Oblast regulations. However, it is present and tends to worsen. In order to mitigate risks and reduce the impact of natural hazards, these risks need to be assessed and managed. The absence of a general scheme of coastal protection, zoning schemes and planning restrictions of the coast make the problem of protection of residential areas and transportation communications practically unsolvable. This is despite the fact that scientific assessments have been carried out for Sakhalin coasts, forecasts of seashore dynamics have been made and associated impacts on coasts vulnerable to morpholithodynamic alterations have been identified.

The technogenic load on the shores of Sakhalin Island in the form of concrete, sheet piling, ripple walls, slope-type structures, concrete-stone embankments, coal galleries, breakwaters and berths is very significant. Their total length is more than 130 km [2]. Approximately 120 km of coastline requires coastal protection solutions in the near term (Fig. 1). Of these, 51.5 are road sections, 31.3 are railroad sections, 8.0 are settlement lands, 17.3 are sections operated by oil and gas enterprises, and 9.6 km are urgent protection areas with different types of coastal use.

2 Methods and Results

Data on scour intensity and scour activity were obtained by analyzing aerial photoinformation (1952, 1974 flights) and space photo information (2014 and 2020). QGIS 2.8.2 Wien program was used to construct scour intensity maps. All calculations were performed in the ESPG:3395 system. The processing of aerial photo information arrays was carried out as follows. At the first stage, electronic versions of the APS swaths of aerial photographs for the period 1952–1985 were created. Then coordinate georeferencing of the raster topo map of 1:100 000 scale in the free cross-platform geoinformation system QGIS (Quantum GIS) and coordinate georeferencing of all APS strips by characteristic points was carried out. After realization of transformation procedures, the degree of contour matching of geographical objects of the best quality APS strip with the figure on the topo map was checked. The most adequate variant was selected. The other APS strips were tied to it practically by the same reference points. From 1999 to 2020 the coastal dynamics was analyzed on the basis of CS interpretation in QGIS 2.8.2 Wien environment.

After realization of transformation procedures, the areas of land loss and the volume of destroyed scarp were determined at different scales. The areas for which the values of coastal zone deformations are less than the image resolution are classified

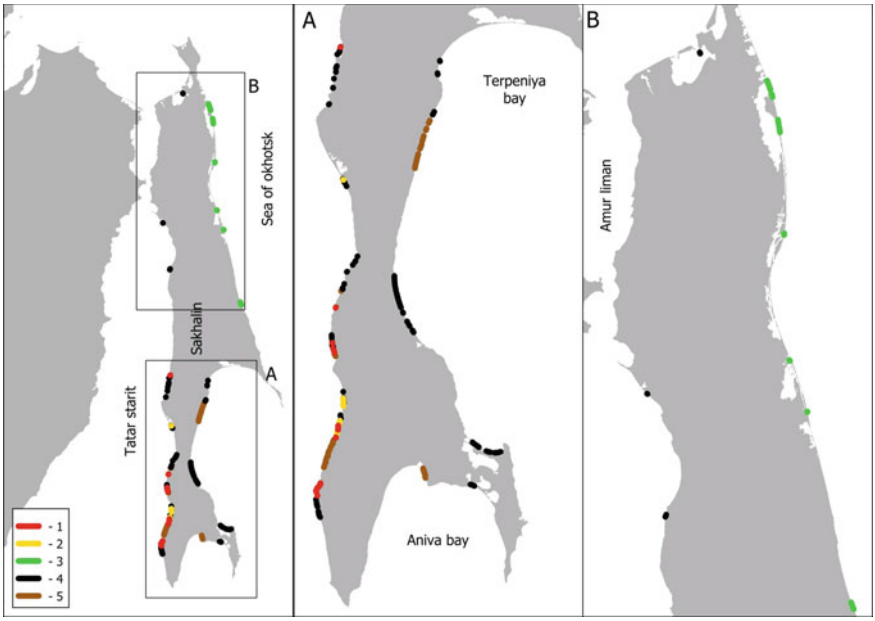


Fig. 1 Scheme of hazardous shoreline areas on Sakhalin Island. Sakhalin coastline hazardous areas requiring shore protection solutions. 1—areas of immediate protection with different types of coastal use; 2—residential areas; 3—areas operated by the oil and gas complex; 4—highways in the risk zone; 5—railroad infrastructure in the risk zone

as stable. Detailed field observations of coastal zone dynamics were carried out on practically all types of coasts on Sakhalin Island. Calculation and analysis of the long-term course of changes in wind-wave activity allowed the coast to be zoned according to the peculiarities of the morpholithodynamic regime.

On the basis of maps of morphogenetic types of coasts and morpholithodynamic settings, the geological-geomorphological and morphodynamic differences of the coasts of Sakhalin Island, whose eastern shores are subarctic and western shores are washed by the temperate sea, were digitized and considered [3].

As a result, for some regions, specific features of scouring activity changes have been established. For example, the correspondence of actual trends in coastal zone development, established as a result of observations and analysis of different years' APS arrays, to long-term changes in the intensity of wind-wave impact on the shore (calculated wind-energy characteristics) allowed the construction of statistical models for predicting scour of the northern shores and shores of Terpeniya Bay on Sakhalin Island [4, 5]. For example, the shores of Terpeniya Bay began to erode intensively. For example, the shores of Terpeniya Bay began to erode intensively in the early 1960s, but areas with mean annual velocities of 1.8–2.2 m/year were eroding as early as the early 1950s. The spatial structure of coastal erosion in the coastal section from Vzmorie to Starodubskoye is determined by the erosion rhythm

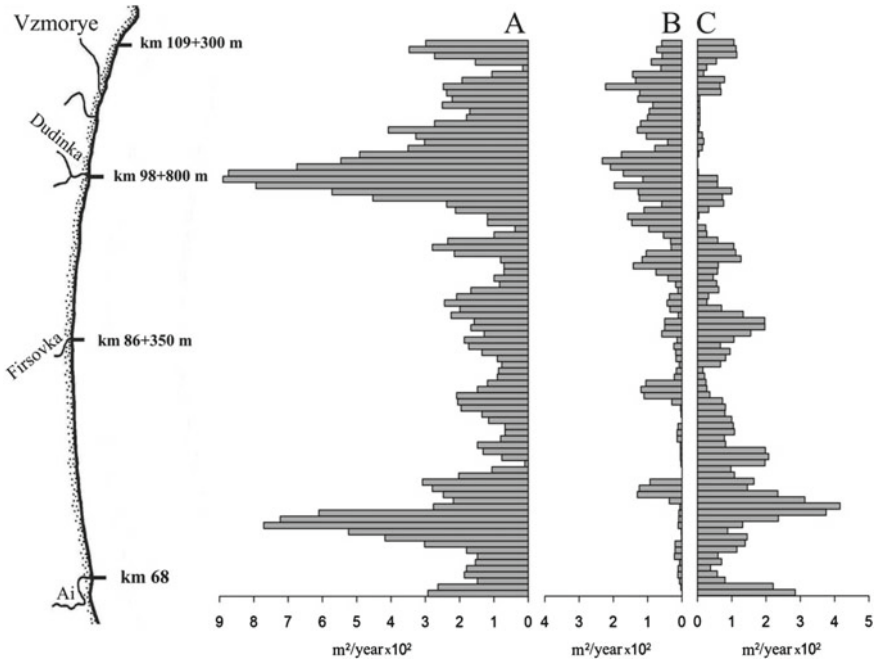


Fig. 2 Coastal scour of Terpeniya Bay in the Vzmorie-Starodubskoye section (mean annual values averaged over 500-m intervals): **A**—1952–1991, **B**—1991–2013, **C**—formation of low marine terraces at the stage of coastal morpholithosystem restoration after closure of sand pits in the beach zone

with a wavelength of about 30 km (Fig. 2). The coastal scarp 3–6 km to the north of Sovetskoye settlement and in the area of Dudino station is most actively eroded.

The average annual rates of coastal retreat here are 2 m/year, with an average value of 0.5 m/year for the entire area. Interestingly, when analyzing the intensity of abrasion on the U.S. open coast, the value of the wavelength of the scour rhythm equal to the value established by us was obtained [6]. But if on the U.S. coast there is no clear explanation for this, in our case one "peak" is confined to the location of the quarry (where more than 4 million m^3 of sand has been extracted from the beach for several decades), and the other—to the zone of divergence of wave energy fluxes calculated according to the methodology developed by the Problem Research Laboratory for the Development of the North [7]. After the closure of sand pits located in the beach zone in 2008, the morpholithodynamic system began to recover rapidly, which was reflected in the formation of low marine terraces. However, in the last five years, the coastal morpholithosystem has been reverting to its previous scour pattern. It is likely that the coast's ability to self-organize is largely related to the configuration of the shoreline that was formed during the last rhythm of coastal-marine accumulation, which determines the distribution of wave energy, sediment load, and beach parameters.

When it comes to barrier forms and free-type accumulative forms, the main planned reorganizations (reduction, increase in area and volume of sediment load) are to a large extent related precisely to the mechanisms of development of these forms, which are determined by the parameters of longshore sediment transport, the tendencies of displacement of lagoonal straits and seasonal features of the structure of the coastal profile [8, 9]. Accumulative forms whose appearance was formed during the last rhythm of coastal-marine accumulation associated with the rise in ocean level, if they do not lose their connection with feeding areas, do not degrade, but only reorganize. And even increase their area, both in subarctic and Arctic coastal conditions. Only recently it has become clear that minimal displacements are noted for obliques and bars, while maximum erosion rates are observed on the shores of plains formed by the descent of lakes. The Beaufort Sea lagoon shore erosion rates are significantly higher than the bar displacement rates, besides, the area of lagoons increases also due to the joining of thermokarst lakes [10].

The area of barrier islands on the coast of the Beaufort Sea, for example, increased by 10% in the period 1940–2000 [11]. During the erosion of the high-land shores of the Lyakhovsky Islands, new accumulative forms are formed, the area of which is approximately 10% of the washed-out lowland area, and their volume approximately corresponds to the volume of the beach-forming fraction in the section of the coastal scarp [12]. Barrier islands on the Arctic deltaic coasts of Russia are also stable or increasing [13].

The well-established opinion that shores composed of rocks of stability class 5–7 will practically not respond to a sea level rise of 2–4 m is shared by us on the main points. However, the sensitivity of rocky shores to climatic changes is mainly determined by the peculiarities of subaerial weathering. The observed intensive destruction of shores of moderately cold seas, characterized by a long period of "open sea" at negative air temperatures and, accordingly, by multiple cycles of freezing and thawing, is likely to decrease with climate warming. Conversely, the currently more stable rocky shores of the subarctic seas will begin to erode faster under warming [5]. Taking into account that the rate of destruction of rocky shores even of high stability class in structurally and tectonically weakened zones can reach up to one meter and more per year, changes in the rate of subaerial weathering processes must be taken into account in the zoning of coasts and the proposed construction of facilities and infrastructure with a long service life.

Recently, coastal retrospective and predictive morpholithodynamic models have become very relevant in the development of methods for assessing the emission of climatically active gases into the ocean–atmosphere system during coastal erosion and, consequently, the resulting restructuring of emission-stock properties of coastal geosystems (drying and change in the thermal regime of peatlands on the coast, degradation of marshes and drying beds, etc.). For example, the thickness of peat deposits in modern coastal bluffs eroded, as shown in Fig. 3, at rates of up to 2 m/year reaches 6 m [14]. And average annual values of the volume of peat deposit, which during erosion enters the Amur estuary and Nevelsky Strait is about 100 thousand m^3/year [15].

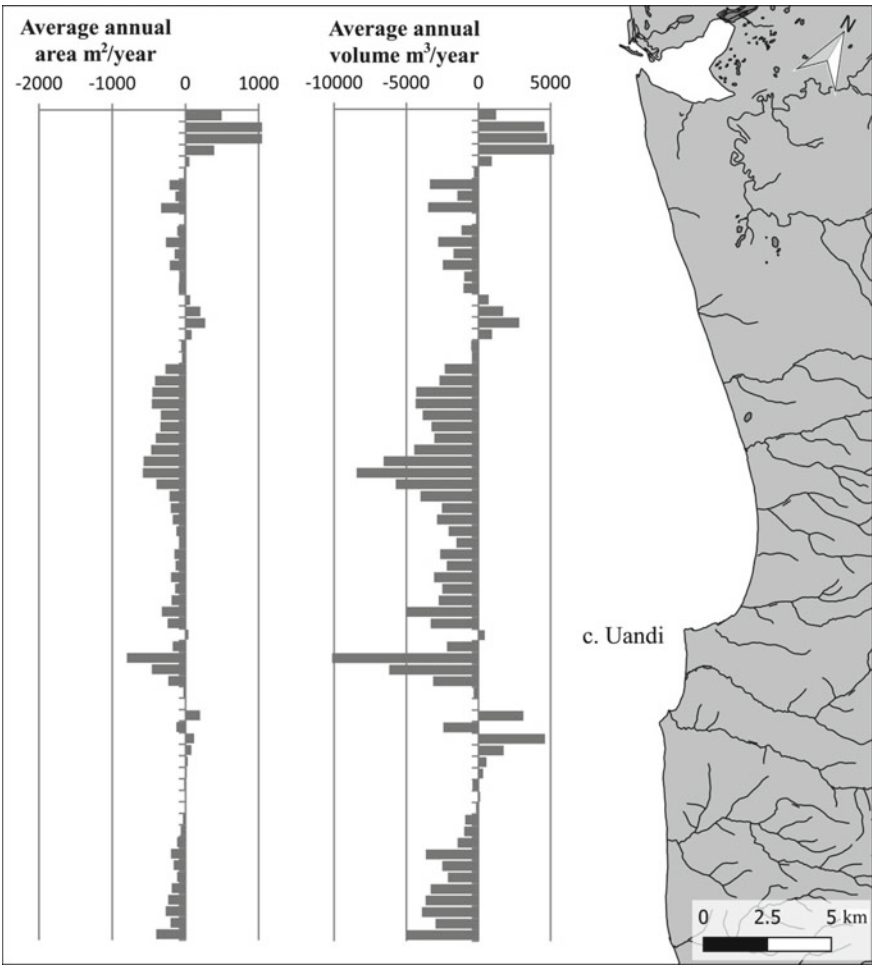


Fig. 3 Spatial plan of erosion of the northern shores of the Tatar Strait (averaged over 500 m sections, period of 40 years)

3 Conclusion

Rigid resistance to natural-technogenic changes and high-cost preservation of existing natural-economic coastal systems cannot ensure the sustainability of complex adaptive systems, such as coastal zones. The basis for sustainable response to probable future changes should be decisions in accordance with morpholithodynamic laws in line with evolutionary-adaptive trends of natural-economic coastal systems.

Thus, a science-based approach to coastal zoning and planning at an appropriate spatial and temporal scale, taking into account the evolutionary and adaptive properties of coastal zones, is the basis for increasing both socio-economic and natural-natural sustainability.

For Sakhalin, the main spatial and temporal parameters of morpholithodynamic changes were determined. The theory of morpholithodynamics of "cold" shores has been developed. Specific features of coastal destruction were determined in case of beach material reserves in the coastal zone, which are sufficient to form a fully wave-absorbing beach at extremely strong waves and high tidal surge levels. The first nature-like full-scale experiments on coastal protection using the mechanisms of formation of megafeston structure of beach parameters distribution were carried out.

The main morpholithodynamic trends can be defined as follows. As coastal erosion intensifies, sediment continues to accumulate and the area in areas of inherited accumulation increases. Bars and spits, which do not lose their connection with feeding areas, do not degrade, but only reorganize and even increase their area, both in subarctic and arctic coastal conditions. The rates of abrasion-denudation destruction of rocky shores of subarctic seas should increase with climate warming and vice versa in cold temperate regions should decrease. Since in the first case the average annual number of freezing and thawing cycles at negative air temperatures during the open sea period will increase, and in the second case it will decrease.

The above and the created schemes of anthropogenic load and dangerous, vulnerable coasts of Sakhalin Island should become the basis for increasing both socio-economic and natural coastal resilience.

References

1. Klein R. J., T. Smit, M. J., Goosen, H., & Hulsbergen, C. H. Resilience and vulnerability: coastal dynamics or Dutch dikes? // Geographical Journal. 1998. pp. 259–268.
2. Afanasyev, V.V. Geomorphological aspects of the problem of protecting the shores of Sakhalin Island / V.V. Afanasyev // Geomorphology. 2015. № 2(182). pp. 28–37.
3. Ignatov E. I., Afanas'ev V. V., Uba V. The Shores of the Northern Pacific Contact Zones // Processes in GeoMedia—Volume V. Springer, Cham, 2022. pp. 157–168.
4. Afanasyev V.V. Erosion of the coast of northwestern Sakhalin // Coastal zone of the Far Eastern seas. L.: Publishing House of the USSR State Defense, 1991. pp. 98–104.
5. Afanasyev V.V. Morpholithodynamic processes and development of the coasts of the contact zone of the subarctic and temperate seas of the Northern Pacific // Yuzhno-Sakhalinsk: IMGiG FEB RAS. 2020. pp. 234.
6. Dolan R., Hayden B. Storms and shoreline configuretion // J. Sediment. Petrol. 1981, 51, No 3. pp. 737–744.
7. Popov B.A., Sovershaev V.A. Some features of the dynamics of the Arctic coasts of Asia // Sea Coasts. Questions of geography. M.: Mysl, 1982. pp. 105–116.
8. Afanasyev V.V. Morpholithodynamics of lagoon straits of northeastern Sakhalin // Geomorphology. 2019. № 2. pp. 79–94.
9. Leontiev, I. O. Dynamics of the lagoon coast of north-eastern Sakhalin using the example of the Nyisky Bay system and the Plastun spit / I. O. Leontiev, V. V. Afanasyev // Oceanology. 2016. T. 56, № 4. pp. 618–626.

10. Brown J. et al. Long-term rates of coastal erosion and carbon input, Elson Lagoon, Barrow, Alaska //Eighth International Conference on Permafrost. 2003. pp. 21–25.
11. Gibbs A. E., Richmond B. M. National assessment of shoreline change—Summary statistics for updated vector shorelines and associated shoreline change data for the north coast of Alaska, US-Canadian Border to Icy Cape. US Geological Survey, 2017. №. 2017–1107.
12. Pizhankova E. I., Dobrynina M. S. Dynamics of the coast of the Lyakhov Islands (results of interpretation of aerospace images) // Cryosphere of the Earth. 2010. T. 14. №. 4. pp. 66–79.
13. Grigoriev M. N. et al. Shore dynamics on the northwest coast of the Lena Delta, Laptev Sea, Siberia//Arctic Coastal Dynamics. 2001. pp. 17.
14. Khotinsky N.A. Holocene of Northern Eurasia: Experience of transcontinental correlation of stages of development of vegetation and climate: To the 10th INQUA Congress, (Great Britain, 1977). M.: Science. p. 200.
15. Afanas' ev V. V. Biogenic Morpholitogenesis on Sea Coasts Sakhalin Island //Processes in GeoMedia—Volume VII. Singapore: Springer Nature Singapore, 2023. pp. 221–229.

Assessment of Investment Scenarios for Russia's Energy Transition to Carbon Neutrality Using the Monte Carlo Method



K. V. Pokazeev, K. S. Degtyarev, D. A. Solovyev, and M. Y. Berezkin

Abstract Research on developing strategies for achieving carbon neutrality becomes increasingly relevant in the context of global energy transformation and the pursuit of reducing carbon footprint. This article presents a quantitative analysis of the investment costs required to transform the Russian Federation's electric power sector. The study assesses the range of possible investments using the Monte Carlo method to model various scenarios of energy consumption and electricity production from non-carbon sources. During the research, scenarios with total electricity consumption ranging from 6,800 to 12,800 TWh were considered, corresponding to the additional need for energy production from non-carbon sources, excluding the existing level of generation (1,200 TWh). The modelling included the distribution of energy consumption among atomic, hydro, wind, solar, geothermal, and biofuel stations, considering their shares in total generation and capacity factors (CF). For each scenario, the required capacity and corresponding investment costs were calculated. The modelling results revealed a significant range of potential investments, emphasizing the importance of considering uncertainties in energy policy planning. The most economically advantageous scenario was the one with a total electricity consumption of 6,800 TWh, which implied minimal investment costs due to the optimal combination of different types of generating capacity. This scenario showcases the potential of nuclear energy as a dominant source in achieving carbon neutrality with relatively low investments. The study underscores the complexities of transitioning to non-carbon energy sources and the importance of an integrated approach considering economic, technological, and environmental factors.

K. V. Pokazeev
Faculty of Physics, Lomonosov Moscow State University, Moscow, Russia
e-mail: sea@phys.msu.ru

D. A. Solovyev (✉)
P.P. Shirshov Institute of Oceanology, Russian Academy of Sciences, Moscow, Russia
e-mail: solovev@ocean.ru

K. S. Degtyarev · M. Y. Berezkin
Faculty of Geography, Lomonosov Moscow State University, Moscow, Russia
e-mail: mberezkin@inbox.ru

© The Author(s), under exclusive license to Springer Nature Switzerland AG 2024

V. Karev (ed.), *Proceedings of the 9th International Conference on Physical and Mathematical Modelling of Earth and Environmental Processes*, Springer Proceedings in Earth and Environmental Sciences, https://doi.org/10.1007/978-3-031-54589-4_63

The obtained data can serve as a basis for developing strategies in the energy sector and formulating government policies towards carbon neutrality.

Keywords Carbon neutrality · Investment scenarios · Monte Carlo method · Energy transformation · Renewable energy sources

1 Introduction

The transition to carbon–neutral energy sources aimed at minimization of the impact of human activities on climate change is one of the most critical challenges of our time [1]. In the context of the Russian Federation, a country with vast energy resources and significant electricity needs, this issue becomes particularly relevant and complex. Strategic planning for the transition to carbon neutrality requires a deep and multi-faceted analysis, including assessing technical capabilities, economic costs, and potential development pathways of the electric power sector [2].

This article addresses the issue of calculating investment costs for achieving carbon neutrality in the Russian electric power sector. The primary focus is on analyzing various scenarios of energy consumption and production and assessing specific investment costs for constructing power stations of different types. The methodological basis of this research is the Monte Carlo method, which allows for considering uncertainties and iterative modelling to identify the most economically viable scenarios.

Developing methodologies for assessing investment costs for achieving carbon neutrality is crucial in implementing a global energy transition scenario. Calculating investment costs enables a more efficient allocation of resources among different projects and initiatives to reduce greenhouse gas emissions. This helps avoid unnecessary expenses and ensures maximum efficiency in achieving carbon neutrality goals.

Calculating investment costs for the transition to carbon neutrality is particularly important for the Russian economy. Russia is one of the world's largest economies and a significant producer and consumer of energy based on fossil fuels [3]. According to the International Energy Agency, in 2020, Russia ranked fourth globally in terms of greenhouse gas emissions (GHG), totalling 1.6 billion tons of CO_2 equivalent [4]. Achieving carbon neutrality will require significant changes in the structure of the energy sector and other industries linked to GHG emissions. Assessing investments can aid in developing strategies for adapting to these changes.

Russia has substantial potential in renewable energy sources, primarily solar and wind energy [5]. Calculating investments can help determine the resources and financing needed to develop the utilization of these sources effectively.

We have previously validated the methodology for calculating the investment in achieving carbon neutrality in Berezkin et al. [6] and Degtyarev et al. [7], and it relies on the following initial assumptions:

- The carbon sequestration capacity of ecosystems is not taken into account, given the high uncertainty in this matter and prevailing global approaches that focus on accounting for anthropogenic emissions and their direct reduction. It is assumed that carbon neutrality is achieved solely by reducing anthropogenic greenhouse gas (GHG) emissions to zero [8].
- Zero GHG emissions will be achieved by 2060.
- The country's energy consumption must be entirely met by electricity from non-carbon sources, including nuclear power stations and renewable energy sources (hydro, wind, and solar).

As of 2021, energy consumption in Russia is estimated at 1,180 million tons of conditional fuel [9], corresponding to 9,600 TWh or 9,600 billion kWh. According to Ref. [10], it was 8,700 billion kWh. There is a gradual trend of increasing energy consumption in Russia, according to Ref. [9]: 948 million tons of conditional fuel in 2005, 1,043 million in 2010, 1,071 million in 2015, and 1,180 million in 2021. Data from Ref. [10] shows a similar trend—an increase from less than 26 EJ (7,222 TWh) in 2000 to over 31 EJ in 2021.

We systematically consider scenarios where the average annual energy consumption in the country ranges from 8,000 to 14,000 TWh.

The first scenario, where energy consumption in 2060 falls below the current level, is also plausible, considering the potential for technological advancements in energy-saving industries and at the household level. Additionally, since the beginning of the twenty-first century, per capita energy consumption has been decreasing by 0.5–1% annually in the United States, Western Europe, and Japan (according to Ref. [10]); in Japan, with a declining population, energy consumption is decreasing in absolute terms.

Currently, in Russia, approximately 1,140 TWh [10], or 13% of total energy consumption, roughly rounded to 1,200 TWh, is provided by non-carbon sources.

Thus, as an assumption, we presume that, depending on the scenario, there is a need to provide the following through electricity generated from non-carbon sources:

- 8,000–1,200 = 6,800 TWh (6,800 billion kWh).
- 10,000–1,200 = 8,800 TWh (8,800 billion kWh).
- 12,000–1,200 = 10,800 TWh (10,800 billion kWh).
- 14,000–1,200 = 12,800 TWh (12,800 billion kWh).

Based on the electricity generation capacity of these sources, we calculated the need for generating capacity using data on the average capacity factor (CF) for power stations of these types. The calculation formula in this case is:

$$C = \frac{P}{8760h.} \cdot CF,$$

where: C is the required capacity in TWh, P is the electricity production in TWh-hours, 8760 is the time corresponding to the 1st year in hours, CF is the Capacity

Factor, which is the ratio of the actual electricity production to the electricity production that would be generated if the power station operated at its installed capacity, expressed as a percentage (%).

2 Initial Data

Comprehensive initial data for modelling the energy scenario of assessing investment costs for Russia's transition to carbon neutrality are presented in Table 1. These data include the range of energy consumption in Russia, the shares of various types of power stations in energy generation, the capacity factor (CF) for different types of stations, and specific investment costs for the construction of stations of each type.

Table 1 Comprehensive initial data for modelling the energy scenario of assessing investment costs for Russia's transition to carbon neutrality. *Source* Refs. [10–12]

Parameters	Unit	Minimum	Maximum
Energy consumption in Russia	TWh	8 000	14 000
Shares of different types of stations in the generation of this amount of energy (%):			
Nuclear	%	5%	50%
Hydro	%	5%	50%
Wind	%	5%	25%
Solar	%	5%	25%
Geothermal	%	2%	25%
Biofuel	%	2%	25%
Total	%	100%	100%
Average CUF of stations of each type (%):			
Nuclear	%	70%	90%
Hydro	%	30%	50%
Wind	%	20%	35%
Solar	%	10%	20%
Geothermal	%	50%	80%
Biofuel	%	50%	80%
Specific investment costs (*per* 1 kW *of installed capacity of the station*) *for different types of power stations*:			
Nuclear	million RUB./kW	N/A	180000
Hydro	million RUB./kW	N/A	140000
Wind	million RUB./kW	N/A	85000
Solar	million RUB./kW	N/A	65000
Geothermal	million RUB./kW	N/A	200000
Biofuel	million RUB./kW	N/A	180000

3 Problem Statement

The problem statement for estimating investment costs for achieving carbon neutrality in Russia involves analysing a series of scenarios, each considering a combination of different parameters in the Russian energy sector. These parameters include:

1. Initially, it is necessary to determine the volume of energy consumption in Russia based on the proposed range from 8,000 to 14,000 TWh. Considering the current level of energy consumption provided by non-carbon sources (1,200 TWh), it is necessary to calculate the additional volume of energy required to achieve the specified energy consumption goals. The analysis should consider discrete values of additional electricity consumption obtained from non-carbon sources: 6,800, 8,800, 10,800, and 12,800 TWh.
2. Subsequently, each volume of energy consumption must be allocated among different energy sources: nuclear energy, hydroelectric power, wind power, solar power, geothermal energy, and biofuels. Minimum and maximum shares in total energy generation have been established for each source, with the total share of all sources equaling 100%. These shares can change discretely, with a 5% step (or 2% for geothermal and biofuel energy).
3. In the next step, knowing the shares of each energy source, the specific volume of energy generated for each type of source should be calculated by the total energy consumption. Based on the Coefficient of Utilization of Installed Capacity (CUIC) for each type of power station, it is necessary to determine the installed capacity needed to produce the calculated volume of energy.
4. With known specific investment costs for constructing power stations of different types per kW of installed capacity, it is necessary to calculate the total amount of investments required to meet the specified energy consumption conditions, considering the installed capacity of each type of power station. Maximum investment values are used as a basis for calculations.
5. A sensitivity analysis method using Monte Carlo modelling is applied to determine possible costs and identify the most economically efficient scenario. This method allows for thousands of iterations in which input data are randomly varied within their possible ranges, taking into account risks and uncertainties in the estimates.

As a result of the analysis, a range of potential investment costs will be obtained, and the most economically advantageous scenario for achieving carbon neutrality in the Russian energy sector will be identified. This will enable informed decision-making regarding investment directions and the development of a strategy for transitioning to cleaner energy sources.

4 Methods and Approaches to Problem Solving

The Monte Carlo method is a statistical technique used to approximate complex probabilistic processes. It allows for estimating the distribution of possible outcomes in situations with uncertainty or randomness. In assessing investment costs for achieving carbon neutrality, the Monte Carlo method can be applied to model different scenarios and assess the range of possible costs, considering uncertainties in input data.

To implement the Monte Carlo method in the context of the given task, we can use the following steps:

1. Choose an energy consumption scenario E:
   Scenario E is selected from a discrete set of values {6800, 8800, 10800, 12800} TWh.
2. Generate shares of energy sources D_i:
   For each energy source (i), generate a random share D_i from a uniform distribution within the specified range and step. For example, this would be a uniform distribution for nuclear power stations ranging from 5 to 50%, with a 5% step.
3. Calculate the energy generation for each source P_i:
   Calculate the volume of energy generation for each source P_i using the formula:

$$P_i = E \times \frac{D_i}{100}$$

4. Determine the required installed capacity C_i:
   Use a random value of the capacity factor K_i for each type of power station from the corresponding uniform distribution. Calculate the capacity C_i using the formula:

$$C_i = \frac{P_i}{8760 \times \frac{K_i}{100}}$$

5. Calculate the total investment costs I:
   Calculate the total construction cost I for each source by using the maximum specific investment costs Z_i:

$$I = \sum_i (C_i \times Z_i)$$

6. Iterations and statistical analysis:
   Repeat steps 2–5 for 1500 iterations to generate a sample of total costs.
   Perform statistical analysis on the obtained sample (mean, median, standard deviation, confidence intervals, etc.).
7. Determine the least costly scenario:

Identify the scenario with the lowest average cost I or the lowest cost within a specified confidence interval.

It is important to note that during modelling, ensuring that the sum of all shares D_i for each iteration equals 100% is essential. This means that after generating random shares for each source, values may be normalized to make them sum up to 100%.

Programming the Monte Carlo model involves using a random number generator to create distributions and applying the above mathematical calculations at each iteration step.

This approach allows for considering uncertainties in input data and assessing risks associated with investments in carbon–neutral technologies.

5 Results and Discussion

Monte Carlo calculations for estimating investment costs for the transition to carbon neutrality in the Russian electricity sector were performed for 1500 iterations for each energy consumption scenario. As a result, 4500 scenarios of total costs were generated. The calculations were carried out using the PyCharm Community Edition 2023.2.3 software environment.

The results of Monte Carlo modelling for assessing investment costs for achieving carbon neutrality in different energy consumption scenarios in Russia are presented below in Table 2 (all values in trillion Russian rubles (RUB)).

These results demonstrate the range of possible investment costs for each energy consumption scenario. The cost increases with the increase in energy demand, which is logical, considering the need to build additional capacity to achieve carbon neutrality.

The graph (Fig. 1) presents investment costs for the transition to carbon neutrality for various energy consumption scenarios in Russia (6800, 8800, 10800, and 12800 TWh). The blue line represents average calculated costs, the green dashed line represents minimum cost estimates, and the red dashed line represents maximum cost estimates. As energy consumption increases, investment costs also rise.

Table 2 Investment costs for achieving carbon neutrality in different energy consumption scenarios in Russia. *Source* Author's Calculations

Energy consumption scenario	Average cost (trillion RUB)	Minimum cost (trillion RUB)	Maximum cost (trillion RUB)
6800 TWh	249.120	184.298	334.674
8800 TWh	323.372	250.009	441.628
10800 TWh	397.471	306.465	521.722
12800 TWh	470.484	366.631	641.708

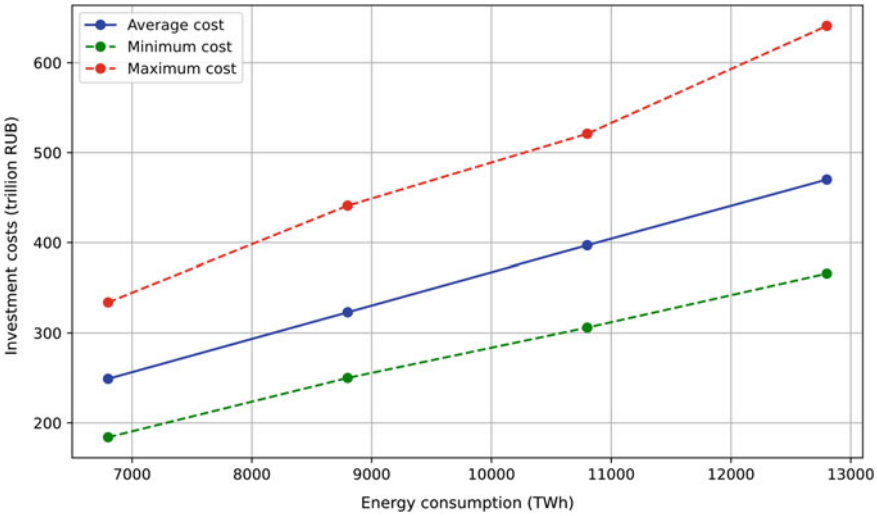


Fig. 1 Investment costs for Russia's transition to carbon neutrality. *Source* Author's Calculations

With the increase in energy consumption volume, total investment costs for achieving carbon neutrality increase. This indicates a direct correlation between the planned level of energy consumption and the need for capital investments.

The highest investment costs are required for the scenario with a consumption of 12800 TWh, implying a significant economic burden for the country, requiring well-thought-out financing strategies and possibly government support.

The lowest costs are observed for the scenario with a consumption of 6800 TWh, which may suggest higher investment efficiency at a lower level of energy consumption increase and opportunities for optimizing the structure of generating capacity.

The cost variation between scenarios underscores the importance of selecting an optimal energy balance structure and investing in the most efficient technologies to reduce overall costs.

The graph also reflects the importance of considering risks and uncertainties associated with changes in technology prices, economic fluctuations, and the political environment, which can impact final costs.

Final costs should be compared not only with economic indicators but also with the social and environmental benefits that investments in carbon neutrality can bring, including reducing carbon emissions and improving the quality of the environment.

It is essential to view investment costs not as a one-time expense but as investments in the long-term development and reorientation of the energy sector towards sustainable and renewable energy sources.

The most cost-effective scenario among all modelled scenarios was the one with an energy consumption of 6,800 TWh. The total investment cost for this scenario

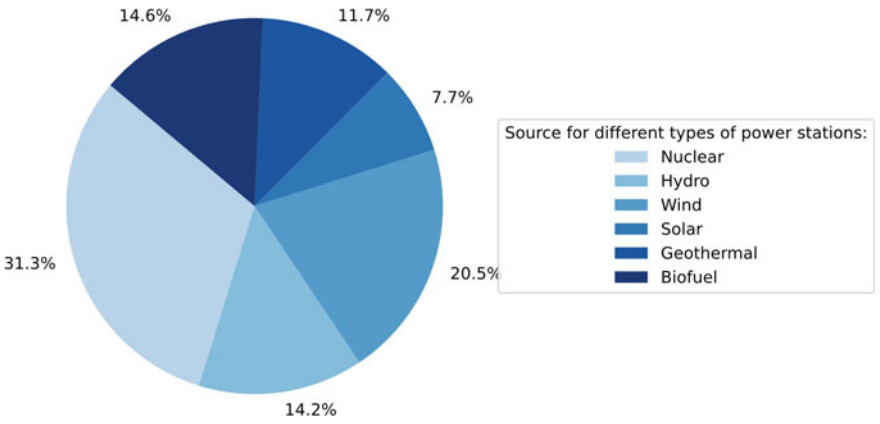


Fig. 2 Cost Structure for the scenario with 6800 TWh of Energy Consumption, %. *Source* Author's Calculations

was approximately 198.58 trillion rubles, and its cost structure is shown in the pie chart (Fig. 2).

Let us examine the cost structure for this scenario in detail (all values are provided in trillion rubles):

- Nuclear Power Stations (NPS): approximately 62.21
- Hydroelectric Power Stations (HPS): approximately 28.16
- Wind Power Stations (WPS): approximately 40.62
- Solar Power Stations (SPS): approximately 15.29
- Geothermal Power Stations: approximately 23.32
- Biomass Power Stations: approximately 28.97

These results reflect the lowest total cost considering variations in the shares of energy sources, Capacity Utilisation Factors (CUF), and investment costs for the scenario with an additional 6800 TWh of energy supply.

Next, based on the available data on specific investment costs (per installed capacity unit): NPS—180,000 rubles/kW, HPS—140,000 rubles/kW, WPS—85,000 rubles/kW, SPS—65,000 rubles/kW [11, 13] (respectively, and multiplying these values by the total required capacities (Table 2)), we calculate the overall investment cost.

The data (Table 3) reflect the required capacities for each type of power station needed to meet Russia's energy needs within the transition to a carbon neutrality framework.

Based on the results presented in the table for the scenario of total energy consumption of 6800 TWh, a significant amount of new generating capacity is required to meet the energy demand of 6800 TWh through non-carbon sources. This is especially true for nuclear power stations, which must provide half of the total volume, requiring the installation of many new capacities due to their high Capacity Utilisation Factor (CUF). Nuclear power stations (NPS) are leading in providing non-carbon energy.

Table 3 Example calculation of energy capacity requirements for the most cost-effective scenario with 6800 TWh of energy consumption. *Source* Author's Calculations

Source for different types of power stations:	Total electricity production, TWh	Share of sources in electricity production, %	Production by each source, TWh	Capacity factor, %	Required capacities, GW
Nuclear	6800	50.0	3400.0	90.0	431.2
Hydro		15.0	1020.0	50.0	232.8
Wind		16.0	1088.0	35.0	354.8
Solar		5.0	340.0	20.0	194.0
Geothermal		8.0	544.0	80.0	77.6
Biofuel		6.0	408.0	80.0	58.2

In contrast, the contribution of hydroelectric power stations (HPS) and other renewable energy sources (wind, solar, geothermal, and bioenergy installations) is also significant but to a lesser extent. The high CUF of nuclear stations (90%) allows them to generate a large amount of electricity with relatively lower installed capacity than other sources with lower CUF. The required capacities are directly related to the investment costs of building new capacities. Given the significant required capacities for nuclear energy, this will likely require substantial investments despite the high efficiency of these stations. The indicators in the table reflect a strategy of diversifying energy sources. The distribution of shares among different types of power stations can reduce risks associated with dependence on one type of generation and improve the reliability of the energy supply.

6 Conclusions

According to estimates provided by VTB Capital, Russia's investment costs for achieving carbon neutrality may exceed 400 trillion rubles (approximately $5 billion) [14].

Our estimates of investment costs for the transition to carbon neutrality in the Russian electric power sector for various scenarios of energy consumption growth (Fig. 1) are near the estimates by VTB Capital and our previous assessments [7, 15]. However, they are approximately 3–5 times higher than the figures mentioned in the Strategy for the socio-economic development of the Russian Federation with low greenhouse gas emissions by 2050 (from now on referred to as the Strategy). At the same time, according to the Strategy, the reduction of anthropogenic GHG emissions should account for only 30% of their total reduction [16]. The investments required for transitioning to carbon neutrality pose a significant challenge to the Russian economy. However, the high Capacity Utilisation Factor (CUF) of nuclear and hydroelectric power stations may partially offset the high investment costs.

The calculations allow us to choose the optimal path for the energy transition to carbon neutrality in Russia because they consider various factors affecting the efficiency and cost-effectiveness of different energy sources. Among these factors for each energy source, we can highlight the existing level of development and infrastructure, potential and prospects, technological and economic conditions, and environmental and social consequences.

Thus, the results of the calculations presented enable us to compare different energy transition scenarios and select the one that provides maximum efficiency in achieving carbon neutrality goals with minimal costs and risks.

The obtained results are of great importance for choosing the optimal path to carbon neutrality in Russia's energy sector. They allow for a more efficient distribution of resources among various projects and initiatives aimed at reducing greenhouse gas emissions. They also help avoid unnecessary expenses and ensure maximum efficiency in achieving carbon neutrality goals. Additionally, they contribute to the development of new technologies and innovations in the energy field, which can enhance the competitiveness of the Russian economy in the global market.

To achieve the energy transition goals, active support from the government, the development of effective energy policies, and the mobilisation of financial resources for research and the development of new technologies will be required. It is also essential to ensure public awareness and support regarding carbon neutrality and its economic and environmental benefits.

Our calculations demonstrate an attempt to create a sustainable energy system that could reduce carbon emissions and provide long-term environmental sustainability. While the data provide a general idea of the required capacities, it is essential to consider construction time, financing possibilities, and social and environmental factors that may affect the implementation of such projects.

The presented modelling results represent one of the possible scenarios for the transition to carbon neutrality in the Russian electric power sector, emphasising the need for significant investments in developing non-carbon energy generation.

Acknowledgements The work was carried out within the framework of State Assignment No. 121051400082-4 (data processing) and with the support of the Ministry of Education and Science of the Russian Federation State Assignment No. FMWE-2023-0002 (construction of a neural model).

References

1. Pokazeev K.V., Solovyev D.A. Report "Overcoming the Limits" and New Solutions to Global Problems // Springer Proceedings in Earth and Environmental Sciences. Springer, 2023. Pp. 527–536.
2. Berezkin M.Y., Butuzov V.A., Bushuev V.V., Degtyarev K.S., Zaichenko V.M., Zalikhanov A.M., Kalinina O.Y., Karpachevskiy A.M., Nefedova L.V., Nechayev A.M., Nigmatulin R.I., Popova E.N., Sapozhnikov F.V., Sinyugin O.A., Solovyev A.A., Solovyev D.A., Shilyakina M.N. Energy Study, geography and environmental Earth. Moscow, Russia: Publishing House "Energia," 2020.

3. Bushuev V.V. POWER ENGINEERING OF RUSSIA (selected articles, reports, presentations 2019–2021). Volume 5 "Russian Energy-Information Cosmoplanetary Civilization." Moscow: "Energia," 2021.
4. Russia will achieve carbon neutrality by 2060 [Online resource]. 2021. https://news.un.org/ru/story/2021/10/1411842 (accessed: August 31, 2023).
5. Andreenko T.I., Gabderakhmanova T.S., Danilova O.V. Atlas of Renewable Energy Resources in Russia: Scientific Edition. Moscow: D.I. Mendeleev University of Chemical Technology of Russia, 2015.
6. Berezkin M.Y., Degtyarev K.S., Sinyugin O.A. Approaches to Assessing Investment Costs for Global Energy Transition // Environment and Energy Studies. 2022. No. 1. Pp. 4–17.
7. Degtyarev K.S., Solovyev D.A., Berezkin M.Y. Approaches to Assessing Costs for Transition to Low-Carbon Development in Russia // Energy Policy. 2023. No. 6(184). Pp. 100–110. https://doi.org/10.46920/2409-5516_2023_6184_100.
8. Zamolodchikov D.G. Carbon Cycle and Climate Change // Environment and Energy Studies. 2021. No. 2. Pp. 53–69.
9. Energy Resource Balance 2005–2021 [Online resource]. 2023. https://rosstat.gov.ru/storage/mediabank/elbalans_2022.xlsx (accessed: August 14, 2023).
10. Statistical Review of World Energy [Online resource]. 2023. https://www.bp.com/en/global/corporate/energy-economics/statistical-review-of-world-energy.html (accessed: August 14, 2023).
11. State Stimulus System for Energy Storage in Russia [Online resource]. https://minenergo.gov.ru/node/489 (accessed: August 14, 2023).
12. Report on the Operation of the Unified Energy System of Russia in 2021 [Online resource]. 2022. https://www.so-ups.ru/fileadmin/files/company/reports/disclosure/2022/ups_rep2021.pdf (accessed: August 14, 2023).
13. Rosatom Preliminarily Defines the Maximum Cost of Capital Construction for One Nuclear kWt at 183 Thousand Rubles [Online resource]. 2022. https://www.atomic-energy.ru/news/2022/01/25/121255 (accessed: August 14, 2023).
14. VTB Capital Presents Assessment of Decarbonization Costs for the Russian Economy and Its Industries [Online resource]. 2021. https://bankinform.ru/news/117904 (accessed: August 14, 2023).
15. Degtyarev K.S., Berezkin M.Y., Pokazeev K.V., Solovyev D.A. Prospects for Carbon Neutrality in Russia: Calculation of Investment Costs // Physical and Mathematical Modeling of Processes in Geoenvironments: Ninth International Scientific Conference for Young Scientists. 2023. Pp. 145–152.
16. Porfiriev B.N., Shirov A.A. Strategies for Socio-Economic Development with Low Greenhouse Gas Emissions: Scenarios and Realities for Russia // Bulletin of the Russian Academy of Sciences. 2022. No. 5(92). Pp. 415–423.

Distribution of Spatial Long Waves to the Channel with the Deformable Basis



S. I. Peregudin and S. E. Kholodova

Abstract The problem of construction of the mathematical model describing distribution of three-dimensional waves in the channel which bottom can move, be deformed and change is considered. The mathematical model describing distribution of long waves without taking into account and in view of dispersion and amplitude parameters, and also in K-d V approximations is presented.

Keywords Waves of finite amplitude · Nonlinear flows and waves · Long waves · Waves in the channel · Bulk medium · Mathematical modeling · Computational experiment

The issues of internal wave propagation have been studied by fluid mechanics since the beginning of the last century [6]. Internal waves can occur both in a liquid with a free surface and in a channel. In natural conditions, it is rare enough when the surface of the channel bottom retains its original shape and remains solid, impermeable and non-deformable. As a result of fluid movement, organic and inorganic suspended solids settle on the bottom. Over time, a mobile deformable layer is formed on the initially solid horizontal bottom of the channel, which is a mixture of sand, silt, clay or gravel. As a result of fluid flow, the interface between the liquid and bottom layers takes on a wave-like shape.

The issue of sand wave generation and motion has been studied by hydrodynamicists since the beginning of the 20-th century. Initially, this problem was considered experimentally [3, 4, 7, 8, 10], as a result of which an experimental dependence between the velocity of liquid motion and the velocity of sand waves was established. The first theoretical substantiation of the issue in question belongs to F. Exner, who derived an equation linking the solid flow rate to the shape of the bottom surface

S. I. Peregudin (✉)
St. Petersburg State University, Saint Petersburg, Russia
e-mail: s.peregudin@spbu.ru

S. E. Kholodova
ITMO University, Saint Petersburg, Russia

© The Author(s), under exclusive license to Springer Nature Switzerland AG 2024

V. Karev (ed.), *Proceedings of the 9th International Conference on Physical and Mathematical Modelling of Earth and Environmental Processes*, Springer Proceedings in Earth and Environmental Sciences, https://doi.org/10.1007/978-3-031-54589-4_64

and formulated a hypothesis of a linear dependence of the solid flow rate on the bottom velocity. In the works of M. A. Velikanov this hypothesis was generalised to the case of pro- arbitrary dependence of bottom matter on bottom velocity. F. I. Frankl [10] considered a plane problem of sand wave motion taking into account the hydrodynamics of the water layer, assuming the motion of the undisturbed flow to be potential with constant velocity, and considering the disturbances themselves to be small.

In the works by Y. Z. Aleshkov [3, 4] a more general case—the nonpotential motion of a layer of inhomogeneous fluid over a bulk medium—is considered. In article [8] the case of potential motion of one and two layers of an ideal incompressible fluid over a bottom consisting of bulk material is considered, in monograph [7] the process of propagation of internal waves in a channel of variable depth with a non-deformable base is studied, in article [9] internal and surface waves over a deformable bottom are studied in the long-wave approximation. Next, a mathematical model describing the propagation of long waves on the surface of a density jump in a variable-depth channel with a deformable bed will be presented.

Consider the problem of motion of two layers of an ideal heavy incompressible fluid in a channel above a deformable bottom. Let us model the considered medium as a three-layer medium—two layers of homogeneous fluid, ground. The lower liquid has density ρ_1, the upper liquid has density ρ_2. Let us arrange the Cartesian rectangular coordinate system in such a way that the plane $z_1 = 0$ coincides with the undisturbed surface of the water layers interface, the axis z_1 is directed vertically upwards. The average thickness of the upper layer is—H_2^*, the lower layer has a height H_0^*. The inner surface of the undeformed solid cover has the form $z_1 = H_2^* + \eta_2^*(x_1,\ y_1)$, the water-layer interface surface—$z_1 = \eta_1^*(x_1,\ y_1)$, the liquid-soil interface surface—$z_1 = -H^*(x_1,\ y_1,\ t_1) = -H_0^* + \eta^*(x_1,\ y_1,\ t_1)$. Waves are formed on the interface surface of water layers, at movement of the bottom layer there is interaction of liquid with ground, particles of the bottom layer also come in motion.

Then the velocity potential $\phi_j^* = \phi_j^*(x_1,\ y_1,\ z_1,\ t_1),\ j = 1,\ 2$ by virtue of the non-degeneracy equation [2] satisfies the Laplace equation

$$\Delta\phi_j^*(x_1,\ y_1,\ z_1,\ t_1) + \frac{\partial^2}{\partial z_1^2}\phi_j^*(x_1,\ y_1,\ z_1,\ t_1) = 0, \qquad \Delta = \frac{\partial^2}{\partial x_1^2} + \frac{\partial^2}{\partial y_1^2}.$$

The pressure in the fluid is determined from the Lagrange-Cauchy integral

$$\frac{p_j}{\rho_j} + \phi_{jt_1}^* + \frac{1}{2}\left[\left|\nabla\phi_j^*\right|^2 + \left(\phi_{jz_1}^*\right)^2\right] + gz_1 = f_j^*(t_1), \qquad \nabla = \left(\frac{\partial}{\partial x_1}, \frac{\partial}{\partial y_1}\right),$$

where g—acceleration of gravity, $f_j^*(t_1)$—arbitrary function of time. On the surface of the solid cover the conditions of non-flow are fulfilled [2]

$$\nabla\eta_2^*\,\nabla\phi_2^* = \phi_{2z_1}^*, \qquad z_1 = H_2^* + \eta_2^*(x_1,\ y_1).$$

At the interface of liquid medium, kinematic $\eta^*_{1t_1} + \nabla\eta^*_1 \nabla\phi^*_1 = \phi^*_{1z_1}, \qquad z_1 = \eta^*_1(x_1,\ y_1,\ t_1)$

and dynamic

$$\rho_1\left[\phi^*_{1t_1} + \frac{1}{2}\left[\left|\nabla\phi^*_1\right|^2 + \left(\phi^*_{1z_1}\right)^2\right]\right] - \rho_2\left[\phi^*_{2t_1} + \frac{1}{2}\left[\left|\nabla\phi^*_2\right|^2 + \left(\phi^*_{2z_1}\right)^2\right]\right] +$$
$$+g(\rho_1 - \rho_2)\eta^*_1 = \rho_1 f^*_1 - \rho_2 f^*_2, \qquad z_1 = \eta^*_1(x_1,\ y_1,\ t_1)$$

conditions.

On the surface of the liquid-soil interface the boundary conditions will take the form:

$$\eta^*_{t_1} + \nabla\eta^*\nabla\phi^*_1 = \phi^*_{1z_1}, \qquad \eta^*_{t_1} + div\,\mathbf{Q}^* = 0, \qquad z_1 = -H^*_0 + \eta^*(x_1,\ y_1,\ t_1),$$

where $\mathbf{Q}^* = \left(Q^*_x,\ Q^*_y\right)$—function characterising the solid flow rate [3, 4, 7–9].

Let us simplify the original problem using the long-wave representation [1, 2, 4, 5, 7–9]. Let us introduce dimensionless coordinates and time

$$x_1 = Lx, \qquad y_1 = Ly, \qquad t_1 = \frac{L}{\sqrt{gH_*}}, \qquad H^*_0 = H_* H_0, , \qquad H^*_2 = H_* H_2,$$

and the dimensionless desired functions

$$\phi^*_j = L\sqrt{gH_*}\phi_j, \quad \eta^* = H_*\eta, \quad \eta^*_j = H_*\eta_j, \quad f^*_j = gH_* f_j, \quad \mathbf{Q}^* = H_*\sqrt{gH_*}\mathbf{Q},$$

where L и H_*—are characteristic horizontal and vertical scales, respectively. The initial problem in dimensionless form will take the following form

$$\mu\Delta\phi_j + \frac{\partial^2}{\partial z_1^2}\phi_j = 0, \qquad \mu = \left(\frac{H_*}{L}\right)^2,$$

$$\mu\nabla\eta_2\nabla\phi_2 = \phi_{2z}, \qquad z = H_2 + \eta_2(x,\ y),$$

$$\mu\left(\eta_{1t} + \nabla\eta_1\nabla\phi_1\right) = \phi_{1z}, \qquad \rho_1\left[\phi_{1t} + \frac{1}{2}|\nabla\phi_1|^2 + \frac{1}{2\mu}(\phi_{1z})^2\right] -$$
$$-\rho_2\left[\phi_{2t} + \frac{1}{2}|\nabla\phi_2|^2 + \frac{1}{2\mu}(\phi_{2z})^2\right] + g(\rho_1 - \rho_2)\eta_1 = \rho_1 f_1 - \rho_2 f_2, \quad z_1 = \eta_1(x,\ y,\ t),$$

$$\mu\left(\eta_t + \nabla\eta^*\nabla\phi_1\right) = \phi_{1z}, \qquad \eta_t + div\,\mathbf{Q} = 0, \qquad z_1 = -H_0 + \eta(x_1,\ y_1,\ t_1).$$

Let us assume, according to F. Exner, that the dependence of the solid flow rate components on the bottom velocity of the liquid is linearly dependent [3, 4, 8, 9]

$$Q_x(x,\ y,\ t) = \kappa_1 u_{1b}(x,\ y,\ t), \qquad Q_y(x,\ y,\ t) = \kappa_2 u_{2b}(x,\ y,\ t),$$
$$u_{1b}(x,\ y,\ t) = \phi_{1x}\big|_{z=-H_0+\eta(x,\ y,\ t)}, \qquad u_{2b}(x,\ y,\ t) = \phi_{1y}\big|_{z=-H_0+\eta(x,\ y,\ t)},$$

where values $\kappa_1,\ \kappa_2$ are characterised by soil rheology and should be determined experimentally for each water area. Taking into account this assumption, the last boundary condition will take the following form

$$\eta_t + \kappa_1 (u_{1b})_x + \kappa_2 (u_{2b})_y = 0, \qquad z_1 = -H_0 + \eta(x_1,\ y_1,\ t_1).$$

Considering the equations of fluid motion and boundary conditions on the deformable bottom and solid cover, representing the velocity potentials in the form of degree series on the dispersion parameter μ [1]

$$\phi_j(x,\ y,\ z,\ t) = \sum_{i=0}^{+\infty} \phi_{ji}(x,\ y,\ z,\ t)\, \mu^i,$$

we conclude that the dependence $\phi_j = \phi_j(x,\ y,\ z,\ t)$ on the vertical coordinate has the following form

$$\phi_1(x,\ y,\ z,\ t) = \sum_{k=0}^{+\infty} \alpha_k(x,\ y,\ z,\ t;\ \mu)\, (z + H_0 - \eta(x,\ y,\ t))^k,$$
$$\phi_2(x,\ y,\ z,\ t) = \sum_{k=0}^{+\infty} \beta_k(x,\ y,\ z,\ t;\ \mu)\, (z - H_2 - \eta_2(x,\ y,\ t))^k.$$

Having performed the necessary differentiation, we conclude that the Laplace equation in the long-wave approximation is equivalent to the recurrence relation for the coefficients of the corresponding degree series

$$\alpha_{k+2} = \mu \frac{(k+1)\left[2\nabla\eta\, \nabla\alpha_{k+1} + \Delta\eta\, \alpha_{k+1}\right] - \Delta\alpha_k}{(k+1)\,(k+2)\left(1 + \mu|\nabla\eta|^2\right)},$$
$$\beta_{k+2} = \mu \frac{(k+1)\left[2\nabla\eta_2\, \nabla\beta_{k+1} + \Delta\eta_2\, \beta_{k+1}\right] - \Delta\beta_k}{(k+1)\,(k+2)\left(1 + \mu|\nabla\eta_2|^2\right)}, \qquad k \geq 0.$$

Kinematic conditions on the surface of the deformable bottom and non-deformable cover mean

$$\alpha_1 = \mu \frac{\eta_t + \nabla\eta\, \nabla\alpha}{1 + \mu|\nabla\eta|^2}, \qquad \beta_1 = \mu \frac{\nabla\eta_2\, \nabla\beta}{1 + \mu|\nabla\eta_2|^2}, \qquad \alpha = \alpha_0, \qquad \beta = \beta_0,$$

the boundary condition relating the ordinate of the bottom surface to the solid flow will take the form

$$\eta_t + \kappa_1[\alpha_{xx} - \eta_{xx}\, \alpha_1 - \eta_x\, \alpha_{1x}] + \kappa_2\left[\alpha_{yy} - \eta_{yy}\, \alpha_1 - \eta_y\, \alpha_{1y}\right] = 0.$$

From the recurrence relations for $\alpha_k,\ \beta_k$ it is easy to see that the coefficients $\alpha_1,\ \alpha_2,\ \beta_1,\ \beta_2$ have order $\mu, \alpha_3,\ \alpha_4,\ \beta_3,\ \beta_4 -$ have order μ^2, and $\alpha_k,\ \beta_k,\ k \geq 5$, will have order not lower than μ^2. To be precise μ^2 let us give approximate expressions for $\alpha_k,\ \beta_k,\ k \leq 4$:

$$\alpha_1 = \mu(\eta_t + \nabla\eta\nabla\alpha) - \mu^2|\nabla\eta|^2(\eta_t + \nabla\eta\nabla\alpha), \quad \beta_1 = \mu\nabla\eta_2\,\nabla\beta - \mu^2|\nabla\eta_2|^2\,\nabla\beta,$$

$$\alpha_2 = -\frac{1}{2}\mu\Delta\alpha + \frac{1}{2}\mu^2\big[\nabla(\nabla\eta(\eta_t + \nabla\eta\nabla\alpha)) + \nabla\eta\,\nabla(\eta_t + \nabla\eta\nabla\alpha) + |\nabla\eta|^2\,\Delta\alpha\big],$$

$$\beta_2 = -\frac{1}{2}\mu\Delta\beta + \frac{1}{2}\mu^2\big[\nabla(\nabla\eta_2\,\nabla\beta) + \nabla\eta_2\,\nabla(\nabla\eta_2\,\nabla\beta) + |\nabla\eta_2|^2\,\Delta\beta\big],$$

$$\alpha_3 = -\frac{\mu^2}{6}[(\Delta(\eta_t + \nabla\eta\nabla\alpha)) + \nabla(\nabla\eta\nabla\alpha) + \nabla\eta\,\nabla\,(\Delta\alpha)], \qquad \alpha_4 = \frac{1}{24}\mu^2\Delta^2\alpha,$$

$$\beta_3 = -\frac{\mu^2}{6}[(\Delta(\nabla\eta_2\nabla\beta)) + \nabla(\nabla\eta_2\nabla\beta) + \nabla\eta_2\,\nabla\,(\Delta\beta)], \qquad \beta_4 = \frac{1}{24}\mu^2\Delta^2\beta.$$

Since the $\alpha_k,\ \beta_k,\ k \in \mathbf{N}$ Laplace equations are expressed through $\alpha,\ \beta$, the dynamic condition on the interface and the boundary condition on the deformed bottom form a closed system with respect to the unknown functions $\alpha(x, y, t),\ \beta(x, y, t),\ \eta(x, y, t),\ \eta_1(x, y, t)$.

Using the asymptotic representation by the dispersion parameter of the coefficients of the power series and the smallness of the amplitude parameter $\varepsilon = \alpha H_*^{-1}$ (α— amplitude of the wave on the surface of the density jump), assuming $\alpha \sim \varepsilon\alpha,\ \beta \sim \varepsilon\beta\ ,\ \eta \sim \varepsilon\eta,\ \eta_1 \sim \varepsilon\eta_1$ we conclude that the above system of equations with partial derivatives includes the following partial problems linear models without dispersion and with dispersion, as well as a nonlinear model without dispersion $\mu = 0$. The asymptotic methods used in [1–5, 7–9] can be used to solve the obtained boundary value problem. In the numerical implementation of this problem, a modern integrated software development environment should be used.

References

1. Aleshkov Y.Z. Theory of interaction of waves with obstacles. L.: Izd-wo LSU, 1990. 372 p.
2. Aleshkov Yu.Z. Currents and Waves in the Ocean. S-Pb.: Izd-vo S-Peterb. un-ta, 1996. 226 p.
3. Aleshkov, Yu.Z. Waves on the surface of bulk media caused by a liquid flow (in Russian) // Vestn. of S.-Peterb. S.-Peterb. un-ta. Ser. 1. 2001. Vyp. 4 (№ 25). P. 35–43.
4. Aleshkov Y.Z. Remarkable works on applied mathematics. SPb.: Izd-vo S-Petersburg. un-ta, 2006. 311 p.
5. Ilyichev A.T. Solitary Waves in Models of Hydromechanics. Moscow: Fizmatlit, 2003. 256 p.
6. Krauss W. Internal waves. L.: Gidromet, 1968. 270 p.
7. Peregudin S.I. Wave Motions in Liquid and Bulk Media. St. Petersburg: Izd-vo St. Petersburg University, 2004. 288 p.
8. Peregudin S.I. Fluid flow over a bulk medium // Mathematical Modelling, Vol. 16, No. 8/2004, P. 70–76.

9. Peregudin, S.I. Propagation of long waves in an inhomogeneous liquid over a deformable bottom (in Russian) // Mathematical Modelling, V. 17, No. 4/2005, P. 3–9.
10. Frankl, F.I. About the motion of sand waves (in Russian) // Dokl. of the USSR Academy of Sciences, 1953. T. 89, № 1. P. 29–32.

Marine Carbonate System Parameters Variability in the Kara Sea in 2019 and 2021

N. K. Alekseeva, I. V. Shved, A. D. Tarasenko, T. N. Eremeiko, A. E. Novikhin, I. A. Gangnus, A. V. Vesman, N. A. Lis, E. A. Chernyavskaya, and M. S. Makhotin

Abstract Our study addresses the variability of marine carbonate system parameters, including the buffer capacity of the Kara Sea ecosystem. We use in situ data obtained in 2019 and 2021 (shipboard chemistry and biology measurements) to calculate marine carbonate system parameters. The results reveal that the aragonite saturation state Ω_{Ar} was greater than 1 in the Kara Sea throughout the studied period, with a decrease of this parameter in 2021 compared to 2019. Organic matter mineralization processes were more intense in 2021. The buffer capacity remained in a state of equilibrium, but displayed a tendency toward a decrease.

Keywords Marine carbonate system · CO_2 · Kara Sea · Chlorophyll–a

1 Introduction

According to NOAA's Global Monitoring Laboratory [1], globally averaged atmospheric carbon dioxide (CO_2) level is increasing every year. The Arctic region is the most sensitive to global climate change which occurs about three times faster and encompasses a wide range of natural processes here. Polar regions are particularly vulnerable to ocean acidification due to low temperatures and reduced buffering capacity are expected to experience extensive low pH conditions and reduced carbonate mineral saturation (Ω) in the near future; however, the effects of anthropogenic CO_2 input on pH and Ω will vary by ocean region [2]. Small changes in the marine carbon amount, and dissolved inorganic carbon (DIC) in particularly, can have a significant impact on the dynamics of the marine carbonate system and the

N. K. Alekseeva (✉) · I. V. Shved · A. D. Tarasenko · T. N. Eremeiko · A. E. Novikhin · I. A. Gangnus · A. V. Vesman · N. A. Lis · E. A. Chernyavskaya · M. S. Makhotin
Arctic and Antarctic Research Institute, 199397 Saint Petersburg, Russia
e-mail: nkalekseeva@aari.ru

Moscow State University, 119991 Moscow, Russia

© The Author(s), under exclusive license to Springer Nature Switzerland AG 2024

V. Karev (ed.), *Proceedings of the 9th International Conference on Physical and Mathematical Modelling of Earth and Environmental Processes*, Springer Proceedings in Earth and Environmental Sciences, https://doi.org/10.1007/978-3-031-54589-4_65

ocean–atmosphere fluxes of carbon dioxide, which in turn can accelerate climate change [3].

Marine ecosystems possess significant buffering capacity, maintaining system equilibrium against external forces. The primary buffering reaction in the ocean is the equilibrium dissociation of carbonic acid formed when the atmospheric CO_2 dissolves in seawater, which can be described in terms of marine carbonate system. Marine carbonate system parameters aid to evaluate the photosynthesis and mineralization of organic matter processes, the buffering capacity of marine ecosystem and changes in the CO_2 concentration in seawater and its transfer to the atmosphere [4]. These parameters include partial pressure of carbon dioxide (pCO_2), pH, total alkalinity (TA) and dissolved inorganic carbon, chlorophyll concentration, aragonite saturation state (Ω_{Ar}), and the Revelle factor, which determines the resilience or buffer capacity of the marine ecosystem in response to various environmental factors.

The Revelle factor [5] is used to quantify ocean sensitivity to an increase in atmospheric carbon dioxide. It is expressed as the ratio between the change in pCO_2 and the change in DIC concentration at constant temperature, salinity, and total alkalinity. A higher Revelle factor signifies lower ocean buffer capacity and a faster change in ocean pCO_2. In general, the partial pressure of carbon dioxide is unstable in the surface layer and depends on production or mineralization of organic matter.

Aragonite (Ar) being a form of calcium carbonate is an essential mineral for various kinds of marine organisms, as it is used to build skeletons and shells like those in corals and molluscs [6]. The study of aragonite saturation state (Ω_{Ar}), current trends of Ω_{Ar} changes and factors affecting it, is extremely important because Ω_{Ar} is predicted to decrease in the world ocean, which may negatively affect marine ecosystems [7]. As pH decreases, carbonate ion concentration and hence Ω_{Ar} also decrease. When $\Omega_{Ar} < 1$, a water mass is considered unsaturated, and dissolution is favoured thermodynamically [8]. However, such water mass has a destructive effect on marine calcifiers skeletons or shells [9]. This makes monitoring Ω_{Ar} crucial for the conservation of marine ecosystems.

The aim of our work was to estimate the change in marine carbonate parameters in the surface and deep-water layers in the Kara Sea in 2019 and 2021.

2 Material and Methods

Marine physical, chemical and biogeochemical regimes are closely related: temperature and salinity of water masses and their dynamics impact oxygen and carbon dioxide saturation in seawater, and redistribution of nutrients in a water column. In the Kara Sea, marine chemical system state is formed under the influence of Atlantic and Barents Sea waters and freshwater river discharge [10]. This makes the Kara Sea a region with potentially complex water mass interactions, each exhibiting distinct characteristics.

In this work, we use the in situ measurements obtained in 2019 on board the R/V Prof. Multanovskiy and measurements obtained in 2021 on board the R/V Akademik

Tryoshnikov in the Kara Sea. Seawater samples were processed in the ship laboratory to assess the main parameters of the carbonate system (pH and total alkalinity). To determine chlorophyll–a concentration, one litre of water was sampled from the Niskin bathometer into a plastic bottle. The chlorophyll–a was then extracted onto a GF/F glass fiber filter via vacuum filtration [11]. Pigments deposited on the filter were extracted with 90% acetone and analyzed using the fluorescence method using Turner Designs Trilogy fluorimeter. The following components of the marine carbonate system were calculated in the "Program Developed for CO_2 System calculations" [12]: equilibrium partial pressure of carbon dioxide, hydrocarbonate ion, carbonate ion, dissolved carbon dioxide, aragonite saturation state, and the Revelle factor.

3 Results and Discussion

Partial pressure of carbon dioxide in the water productive layer (0–30 m) was higher in 2021, presumably as a result of a more intense photosynthetic activity: 379 mcatm in 2021 versus 262 mcatm in 2019 (Figs. 1 and 2). The partial pressure of carbon dioxide in the surface layer is much lower compared to the bottom waters, while the pH distribution displays the opposite pattern. Dissolved inorganic carbon concentration in the surface productive layer (0–5 m) measured in 2019 was 1600 μmol/l, and DIC and TA concentrations demonstrated similar distribution (Fig. 1). In 2021, there is an increase in all parameters in the productive layer except for the aragonite saturation state (Fig. 2). In the entire productive layer, the aragonite saturation state was higher than 1, thus the conditions for the development of planktonic forms of calcifiers can be considered favourable. There is a slight decrease in this parameter over the studied period: Ω_{Ar} was 1.82 in 2019, and Ω_{Ar} was 1.56 in 2021. Compared to 2019, the amount of carbonate ion CO_3^{2-} has also decreased. The buffer capacity of the marine ecosystem in the productive layer was laying within the range of 8–20 typical for seawater [13]. However, the Revelle factor increased from 13 in 2019 to 15 in 2021, which may indicate a rapid change in the partial pressure of carbon dioxide and, consequently, a potential decrease in the buffering capacity of the marine ecosystem (Figs. 1 and 2). In the surface 0–5 m layer, the concentrations of total alkalinity were 1400–1800 μmol/l, and dissolved organic carbon was 1400–1700 μmol/l in 2019; in 2021, these parameters increased to 1920–1980 μmol/l and 1850–1950 μmol/l, respectively. The evaluation of the whole productive layer suggests a decrease in total alkalinity and an increase in dissolved inorganic carbon concentrations (Fig. 3).

The near-bottom layer was enriched with carbon dioxide compared to the surface layer, which can be explained by mineralization of autochthonous and allochthonous organic matter. In 2019 in the layer under the productive layer, pCO_2 was 304 mcatm, and in 2021, the pCO_2 was 459 mcatm. It seems reasonable that with the increase of dissolved carbon dioxide concentrations there is an inverse relationship with the pH value, which significantly decreased from 8.17 in 2019 to 7.99 in 2021. We assume that in 2021, the process of organic matter mineralization was more intense due to the larger input of organic matter in the productive layer with river runoff.

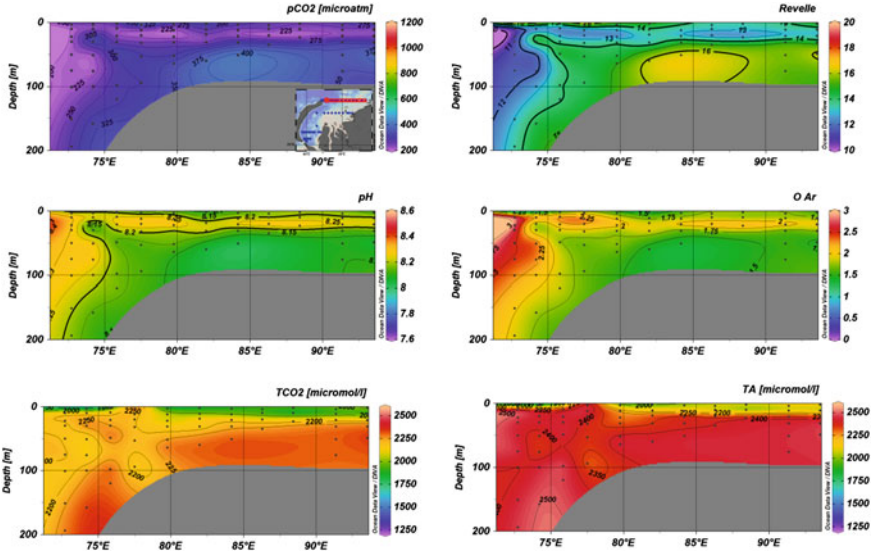


Fig. 1 Distribution of marine carbonate system parameters in the Kara Sea in 2019, where pCO_2 is partial pressure of CO_2; TCO_2 is dissolved inorganic carbon, Revelle is Revelle factor; Ω_{Ar} is aragonite saturation state; TA is total alkalinity

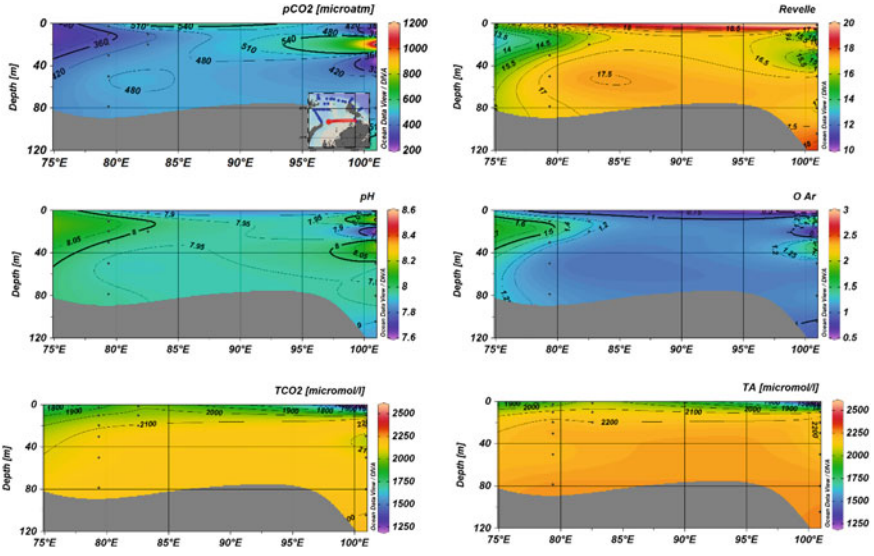


Fig. 2 Distribution of marine carbonate system parameters in the Kara Sea in 2021, where pCO_2 is partial pressure of CO_2; TCO_2 is dissolved inorganic carbon, Revelle is Revelle factor; Ω_{Ar} is aragonite saturation state; TA is total alkalinity

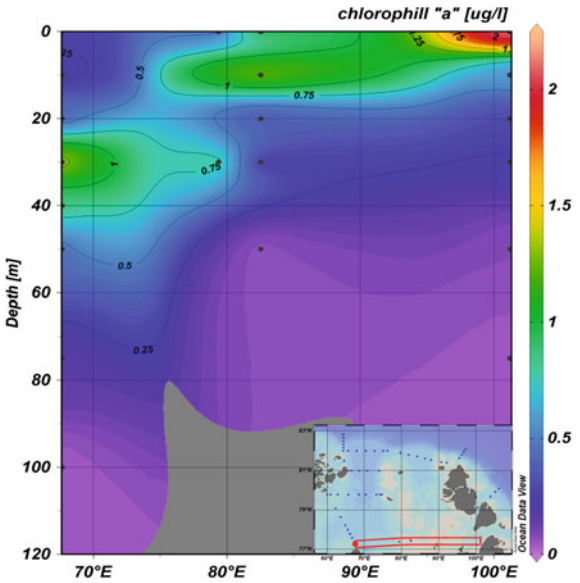


Fig. 3 Chlorophyll–a distribution in the Kara Sea in 2021

The deep layer is favorable for the existence of calcifiers and is characterized by a sufficient aragonite saturation ($\Omega_{Ar} > 1$). However, Ω_{Ar} decreased from 1.76 in 2019 to 1.31 in 2021 (Fig. 3). In the mid–layer under productive layer, there is a shift in the carbonate equilibrium imbalance, thus a potential decrease in the buffer capacity of the marine ecosystem, as the Revelle factor increased from 14 in 2019 up to 16.2 in 2021. Total alkalinity and dissolved inorganic carbon distributions were uniform in the deep layer over the studied period: total alkalinity concentration decreased from 2452 μmol/l in 2019 to 2350 μmol/l in 2021, and dissolved inorganic carbon content increased slightly from 2232 μmol/l in 2019 to 2244 μmol/l in 2021.

Phytoplankton contains green pigment, chlorophyll, which absorbs sunlight, photosynthesize, and utilize carbon dioxide to release oxygen into the atmosphere. As the concentration of chlorophyll–a in water increases, the process of active vegetation starts [8]. Phytoplankton absorbs carbon dioxide, thereby increasing the seawater pH and alkalizing it. In this context, we evaluate the carbonate system state together with the chlorophyll–a (chl–a) concentration. As the microalgae develop actively in the photic zone, we investigated the upper 0–100 m layer in 2021 and the surface 0–30 m layer in 2019.

In 2019, pH increased up to 8.25 in the surface layer, with a decrease of pCO_2 to 225 μatm along with the high value of chlorophyll–a concentration of 1.59 μg/l (Figs. 1 and 3). With the pH higher than 6.5, the alkalinity has a favourable effect on the increase of phytoplankton productivity.

In 2021, high values of chlorophyll–a were observed in the surface 0–30 m layer, where the phytoplankton bloom occurred. Oceanographic stations selected for this study were done in the shallow water area where the clear ice–melted water could remain presumably, which facilitates active photosynthesis. The maximum of chl–a,

2.11 μg/l, was measured southward the Severnaya Zemlya Archipelago, which is consistent with low partial pressure in this area and increased pH values.

4 Conclusion

Based on in situ measurements in the Kara Sea in 2019 and 2021, both photosynthesis and organic matter mineralization predominantly occur in the upper productive layer. Plankton organisms utilize CO_2 to synthesize the organic matter, which subsequently sinks to deeper layers, undergoing mineralization by bacteria and other organisms. Consequently, deeper water layers become enriched with CO_2, leading to a decrease in pH. These conditions are favourable for carbonate formation, indicated by Ω_{Ar} exceeding the equilibrium value of 1, although there is a decline in Ω_{Ar} from 2019 to 2021. Enhanced organic matter mineralization in 2021, likely attributed to the important river runoff, is supported by elevated carbon dioxide partial pressure and decreased pH values. The buffer capacity remains in equilibrium, but a tendency toward decrease is observed.

It should be noted that the direction of carbon dioxide flux through the air–water interface is not constant in time and space. While on a relatively short time scale (several years), the average annual flux of CO_2 into the ocean is assumed to be constant, the need for ongoing monitoring of the marine ecosystem for accurate assessments is clear.

Acknowledgements This work was supported by the Federal scientific and technological program for ecological development of the Russian Federation for 2021–2030 (169-03-2023-081 in 2023).

References

1. Lan X., Tans P., Thoning K.W. Trends in globally averaged CO_2 determined from NOAA Global Monitoring Laboratory measurements. Version 2023-11.
2. Tynan E., Clarke J.S., Humphreys M.P., Ribas-Ribas M., Esposito M., Rérolle V.M., Schlosser C., Thorpe S.E., Tyrrell T., Achterberg E.P. Physical and biogeochemical controls on the variability in surface pH and calcium carbonate saturation states in the Atlantic sectors of the Arctic and Southern Oceans // Deep–sea Research Part II: topical Studies in Oceanography. 2016. 127, p. 7–27.
3. Pipko I., Pugach S., Savelieva N., Luchin V., Dudarev O., Sergienko N., Semiletov I. Carbonate Characteristics of the Gulf of Anadyr Waters // Doklady Nauk o Zemle, 2019. 487, p. 867–871.
4. Tishchenko P.Ya., Tishchenko P.P., Zvalinsky V.I., Shkirnikova E.M., Chichkin R.V., Lobanov V. B. Carbonate system of the Amur Bay (Sea of Japan) in the summer of 2005 // Izvestiya TINRO. 2006. (In Russian).
5. Egleston E.S., Sabine C.L., Morel F.M. Revelle revisited: Buffer factors that quantify the response of ocean chemistry to changes in DIC and alkalinity // Global Biogeochemical Cycles, 2010. V. 24 (1), GB1002.
6. Romankevich E.A., Vetrov A.A. Cycle of Carbon in the Russian Arctic Seas. M.: Nauka, 2001. 302 p. (In Russian).

7. Orr J., Fabry V., Aumont O. et al. Anthropogenic ocean acidification over the twenty-first century and its impact on calcifying organisms // Nature, 2005. 437. p. 681–686.
8. Harris K.E., DeGrandpre M.D., Hales B. Aragonite saturation state dynamics in a coastal upwelling zone // Geophysical Research Letters, 2013. 40 (11), p. 2720–2725.
9. Doney S.C., Fabry V.J., Feely R., Kleypas J. Ocean acidification: the other CO2 problem // Annual Review of Marine Science, 2009. V. 1, p. 169–192.
10. Feely R.A., Sabine C.L., Lee K., Berelson W., Kleypas J., Fabry V.J., Millero F.J. Impact of anthropogenic CO_2 on the $CaCO_3$ system in the oceans // Science, 2004. 305, 5682. p. 362–366.
11. Arar E.J., Collins G.B. Method 445.0 In Vitro Determination of Chlorophyll-a and Pheophytin in Marine and Freshwater Algae by Fluorescence. // U.S. Environmental Protection Agency, Washington, DC, 1997.
12. Robbins L.L., Hansen M.E., Kleypas J.A., Meylan, S.C. CO2calc: A user-friendly seawater carbon calculator for Windows, Max OS X, and iOS (iPhone) // U.S. Geological Survey Open–File Report 2010. 2010. 17 p. л.
13. Jiang LQ., Carter B.R., Feely R.A., Lauvset S.K., Olsen A. Surface ocean pH and buffer capacity: past, present and future // Scientific Reports 2019. 9 (18624).

Chlorinated Organic Compounds in Mollusks Soft Tissue from Vostok Bay (The Sea of Japan)

Aleksandra D. Borovkova, Maksim M. Donets, and Vasiliy Y. Tsygankov

Abstract This study presents current data on the levels of persistent organic pollutants (POPs) in Mytilidae mollusks' soft tissues from Vostok Bay (the Sea of Japan). The highest concentrations of OCPs are typical for Litovka Bay, where the Litovka River flows in, carrying runoff from the continental part of Primorsky Krai. The maximum levels of PCBs were found in mussels from Sredniaya Cove, where Ship Repair Plant enterprise was previously operated. It is necessary to expand and consolidate existing monitoring using mussels.

Keywords POPs · OCPs · PCBs · Mollusks · Bivalvia · Marine ecosystems

1 Introduction

The World Ocean creates habitat for plenty of living organisms. Due to the high level of urbanization of coastal regions, anthropogenic pressure on the ocean shelf zones is constantly growing. For that very reason ocean waters pollution has become one of the most pressing environmental issues over past decades.

Persistent organic pollutants (POPs) are regarded as one of the most underinvestigated and baleful substances. It negatively influences natural ecosystems functioning and human health. The main difference between POPs and pollutants that are constantly present in the natural environment and exhibit their toxicity when natural concentrations are exceeded is their origin—these substances are xenobiotics. As a result, in such a short period of time (since the 60 s of the last century), living organisms did not have the opportunity to develop adaptations to them [2, 11].

A. D. Borovkova · M. M. Donets · V. Y. Tsygankov (✉)
School of Advanced Engineering Studies, Institute of Biotechnology, Bioengineering and Food Systems, Far Eastern Federal University, Ajax 10, Russky Island, Vladivostok 690922, Russia
e-mail: tsig_90@mail.ru

Institute of the World Ocean (School), Far Eastern Federal University, Ajax 10, Russky Island, Vladivostok 690922, Russia

© The Author(s), under exclusive license to Springer Nature Switzerland AG 2024

V. Karev (ed.), *Proceedings of the 9th International Conference on Physical and Mathematical Modelling of Earth and Environmental Processes*, Springer Proceedings in Earth and Environmental Sciences, https://doi.org/10.1007/978-3-031-54589-4_66

POPs include intentionally produced compounds for the purpose of sanitary and epidemiological control and agriculture (DDT and its metabolites, HCH isomers), and unintentionally released chemical agents in the elaboration of some manufacturing processes and during combustion (PCBs, dioxins, furans) [6].

POPs are characterized by high resistance to chemical, physical and biological factors. Furthermore, toxicants feature the ability to store in adipose tissues of living organisms. Due to transboundary transport with the aid of water and air masses, persistent organic pollutants are able to roam and precipitate accumulating in aquatic and terrestrial ecosystems outermost the source of the pollution [1, 11].

Even low concentrations of POPs exhibit genotoxic, immunotoxic and carcinogenic effects. Both of the most commonly used insecticides, chlorinated bicarbonates and organic phosphates, are known to directly affect the human nervous system. Persistent organic pollutants can cause various skin diseases, dysfunction of the immune, reproductive, hormonal, nervous systems, contribute to the development of diabetes and congenital malformations [2].

Organochlorine pesticides (OCPs) are one of the largest POPs groups and used as pesticides in agriculture, forestry and manufacturing industry. OCPs belong to the unit of pollutants hazardous to biota. The majority of these substances are both extremely toxic and exhibit pronounced cumulative properties. Organochlorine pesticides are able to accumulate in ample quantities in the organism and, in addition, be transmitted through food chains. Due to their physicochemical properties, OCPs are exceptionally slowly disintegrate in the natural environment, actively accumulate in various components of ecosystems and are able to be transported over long distances by virtue of volatility. Reintegration and condensation of OCPs lead to the fact that they, entering the ecosystem in warmer regions, are transferred to cold temperate and polar latitudes—places remote from anthropogenic activities [7, 11]. In areas where pesticides are actively used in agriculture, the population experiences an increased incidence of cancer [9], endocrine and reproductive disorders, and various neurotoxic effects [8].

At the present time, the majority of countries have forbidden production and utilization of these pesticides. However, some states, such as China and India, still retain the right to produce and use DDT, which leads to contamination of the territories not only of the users themselves, but also of their neighbors.

Bivalves are one of the most widely used groups of organisms in indicating pollution of coastal marine areas. This class includes representative species of benthic fauna, closely associated with the substrate and widespread throughout the world. These species are characterized by a long life cycle, high tolerance to various environmental conditions and limited movement, unlike fish. Having a close intercommunication with the substrate and, thus, reflecting the level of contamination of a particular area bivalves are capable of accumulating in their bodies a wide range of different pollutants present in the environment [3]. One of the programs for monitoring POPs pollution in aquatic ecosystems is Mussel Watch, which aims to evaluate environmental contamination levels using shellfish as bioindicators [10].

Currently, coastal waters of the Sea of Japan, such as Peter the Great Bay, contamination issue with persistent organic pollutants is not studied enough and relevant for

this region. Therefor the aim of the study is to determine the levels of content and grade of transformation of organochlorine compounds (isomers of HCH, DDT and its metabolites, PCBs) in mollusks of the Mytilidae family from Vostok Bay (the Sea of Japan).

2 Materials and Methods

Two species of Bivalvia mollusks of Mytidae family (*Crenomytilus grayanus*, *Modiolus modiolus*) were used in order to indicate pollution. The samples were collected from different parts of Vostok Bay (the Sea of Japan) in the summer of 2017 (Fig. 1).

Mollusks' soft tissues were analyzed for levels of OCPs and PCBs. Lipids were extracted from homogenate (10–20 g) using a n-hexane: acetone mixture, with subsequent disintegration of fat components with concentrated sulphuric acid. The obtained POPs extract was separated with non-polar (for PCB) and polar (for OCP) solvents on a chromatographic column with Florisil®. Concentrations of organochlorine pesticides (OCPs) (α-HCH, β-HCH, γ-HCH, δ-HCH, o,p′-DDT, p,p′-DDT, o,p′-DDD, p,p′-DDD, o,p′-DDE, and p,p′-DDE) and polychlorinated biphenyls (PCBs) (congeners 28, 52, 155, 101, 118, 143, 153, 138, 180, 207) in samples were measured

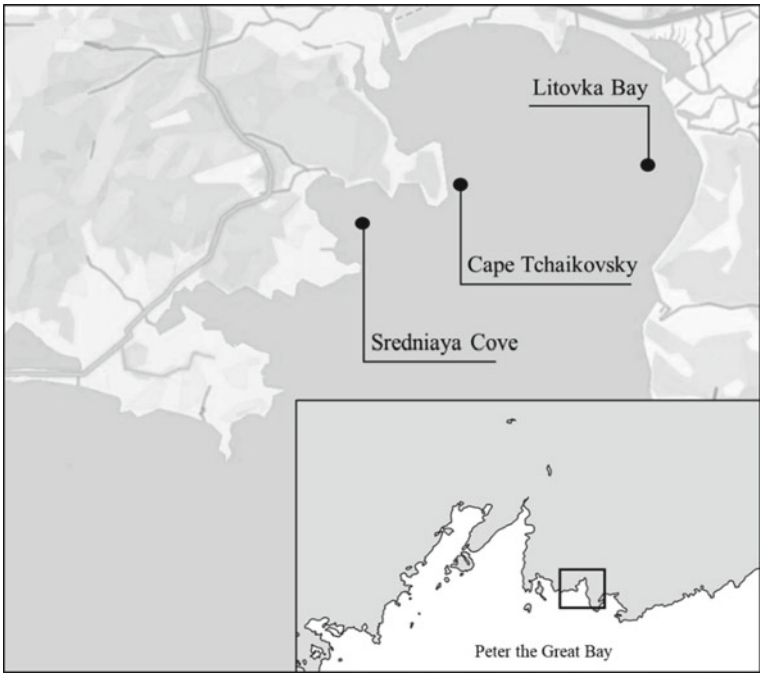


Fig. 1 Map of sampling location

by gas chromatography–mass spectrometry (GC–MS), and gas-chromatography with electron capture detector (GC–ECD) for validation of results [4, 5].

3 Results and Discussion

The results of the study showed the presence of persistent organic pollutants in all shellfish specimens ranging from 2.8 to 453.4 ng/g lipid weight (lw). OCP concentrations prevailed over PCB levels at all stations. Among the pesticides, the DDT group predominated, with the preponderate metabolite DDE, which characterizes the decomposition of the original compound and indicates a long-standing entry of the toxicant into the water area.

Among HCHs, the β-isomer predominated, also indicating chronic toxicant residence in the environment. However, the ratio of α- and γ-isomers showed a predominance of the γ-form, which might indicate a recent intake of pollutants. The presence of forms characterizing fresh pollution of the water area might be associated with the phenomenon of transboundary transfer of xenobiotics by air masses from areas where they are still used in agriculture.

Polychlorinated biphenyls were present in all samples ranging from 4.8 to 230.2 ng/g lw. Low-chlorinated 28 and 52 PCBs predominated. Highly chlorinated PCBs were found in the mollusks soft tissue from the territory of the Sredniaya Cave and Cape Tchaikovsky, the predominant congeners were 138 and 153 PCBs. Qualitative composition of detected POPs is shown in Fig. 2.

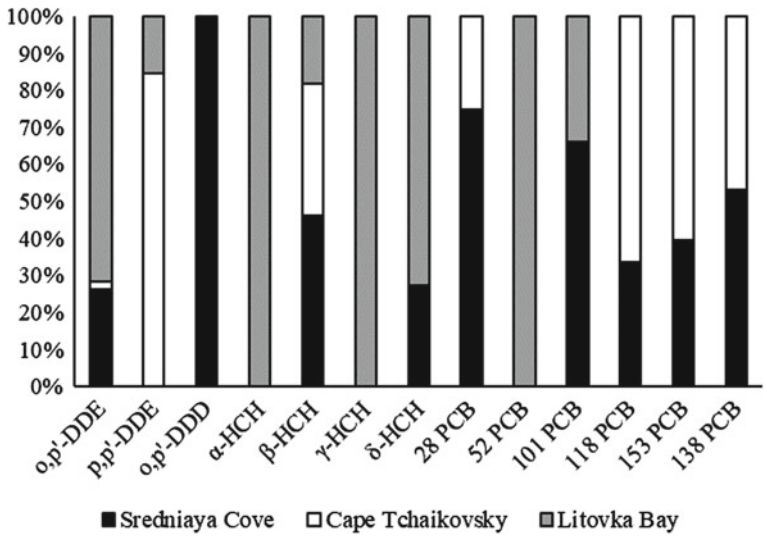


Fig. 2 Qualitative composition of detected POPs

Table 1 ∑POPs content in mollusk soft tissue from Vostok Bay (the Sea of Japan)

Sampling location	N	Fat, %	Species	∑DDT[4]	∑HCH[5]	∑PCB[6]
Litovka Bay	6	*Modiolus modiolus*	0,20–1,33 0,66 ± 0,38	<LOD–161,9 66,43 ± 51,13	<LOD–30,0 18,40 ± 10,62	<LOD-230,2 39,86 ± 52,42
Cape Tchaikovsky	5	*Crenomytilus grayanus*	0,44–0,65 0,52 ± 0,09	<LOD–665,0 225,83 ± 380,33	<LOD–12,5	<LOD–54,9 29,01 ± 12,73
Sredniaya Cove	10	*Modiolus modiolus*	0,003–0,009 0,005 ± 0,002	<ПО–453,4 169,33 ± 123,93	<ПО–179,3 29,59 ± 45,27	<ПО–43,1 19,10 ± 13,92

[1]Range, min–max; Mean ± standard deviation; [3]Below detection limit; [4]Total content of p,p′-DDT, o,p′-DDT, p,p′-DDE, o,p′-DDE, p,p′-DDD and o,p′-DDD; [5]Total content of α-HCH, β-HCH, γ-HCH and δ-HCH; [6]Total content of PCB 28, PCB 52, PCB 101, PCB 118, PCB 153, PCB 138 and PCB 180

Mean levels of ∑POPs in mollusks' soft tissues from studied areas are presented in Table 1. The highest concentrations of OCPs were recorded on the territory of the Litovka Bay. Among the xenobiotics o,p′-DDE dominated. Detected concentrations varied from 10.4 to 453.4 ng/g lw. Metabolites indicating fresh contamination (o,p′-DDT, p,p′-DDT) were below detection limits. Such results might be implicated by the high anthropogenic load exerted on the water area—the bay is a popular vacation spot for the local population in the summer. In addition, the Litovka River flows into the Litovka Bay, carrying runoff from the continental part of the Primorsky Territory, where pesticides were actively used for agricultural crops treatment in the latter half of the twentieth century. This circumstances might have led to basin contamination with forms that characterize the long-standing influx of pollutants into the water body.

The highest PCBs concentrations were detected in the mollusks' soft tissue from the Sredniaya Cove (from 5.6 to 230.2 ng/g of lw). Back in the late 40 s of the twentieth century, the Gaydamak Ship Repair Plant enterprise operated in Gaydamak Bay. Today, due to a number of reasons that led to the closure of the enterprise, the Livadia Repair and Shipbuilding Plant operates on the site of the State Repair Plant, specializing in the repair of steam boilers, cleaning the sides and bottoms of ships, repairing main engines, gearboxes and shaft lines. In this regard, the detection of increased PCB concentrations in the samples from Sredniaya Cove compared to other stations might be associated with the removal of pollutants by water masses from the southern part of the bay, both in the past and at the present time.

4 Conclusion

Thus, the data obtained in current study demonstrate the proceeding pollution of marine offshore zones of the Sea of Japan by persistent organic pollutants. Decomposition products of the original compounds predominated in all soft tissue samples, indicating a long-term presence of toxicants in the environment. The entry of forms

in small concentrations, indicating recent basil contamination, might be associated with the phenomenon of transboundary transport of pollutants within water and air masses from areas where pesticides continue to be used for agricultural and medical purposes. The results of the study confirm the relevance and importance of continuing monitoring examination of the levels of chlorinated hydrocarbons in the Far Eastern seas of Russia.

Financial Support This work was supported by the Ministry of Science and Higher Education of the Russian Federation (project number FZNS-2023-0011).

References

1. Boyarova MD (2008) Current Levels of Organochlorine Pesticides in Aquatic Organisms of Peter the Great Bay (Sea of Japan) and Lake Khanka. Thesis for the degree of Candidate of Biological Sciences (Ph.D. Biol. Sci.), Far Eastern Federal University.
2. Carson R (2002) Silent spring, 40th anniversary ed., 1st Mariner Books ed. Houghton Mifflin, Boston.
3. Chahouri A, Yacoubi B, Moukrim A, Banaoui A (2023) Bivalve molluscs as bioindicators of multiple stressors in the marine environment: Recent advances. Continental Shelf Research 264:105056. https://doi.org/10.1016/j.csr.2023.105056.
4. Donets MM, Tsygankov VYu, Boyarova MD, et al (2021a) Flounders as indicators of environmental contamination by persistent organic pollutants and health risk. Marine Pollution Bulletin 164:111977. https://doi.org/10.1016/j.marpolbul.2021.111977.
5. Donets MM, Tsygankov VYu, Gumovskiy AN, et al (2021b) Organochlorine pesticides (OCPs) and polychlorinated biphenyls (PCBs) in Pacific salmon from the Kamchatka Peninsula and Sakhalin Island, Northwest Pacific. Marine Pollution Bulletin 169:112498. https://doi.org/10.1016/j.marpolbul.2021.112498.
6. El-Shahawi MS, Hamza A, Bashammakh AS, Al-Saggaf WT (2010) An overview on the accumulation, distribution, transformations, toxicity and analytical methods for the monitoring of persistent organic pollutants. Talanta 80:1587–1597. https://doi.org/10.1016/j.talanta.2009.09.055.
7. Fuoco R, Giannarelli S (2019) Integrity of aquatic ecosystems: An overview of a message from the South Pole on the level of persistent organic pollutants (POPs). Microchemical Journal 148:230–239. https://doi.org/10.1016/j.microc.2019.04.076.
8. Kaiser J, Enserink M (2000) Treaty Takes a POP at the Dirty Dozen. Science 290:2053–2053. https://doi.org/10.1126/science.290.5499.2053.
9. Oxengendler GI (1991) Poisons and organisms. St. P. Science.
10. Tanabe S (2000) Asia-Pacific Mussel Watch Progress Report. Marine Pollution Bulletin 40:651–651. https://doi.org/10.1016/S0025-326X(00)00019-9.
11. Tsygankov V Yu (ed) (2020) Persistent organic pollutants (POPs) in the Far East region: seas, organisms, people: monograph. Far East Federal University, Vladivostok. https://doi.org/10.24866/7444-4891-2.

Hydrography Tapering and Stream Order Computing for GIS-Based Mapping

D. A. Ignatenko, N. A. Razvalov, O. P. Yakimova, I. E. Sidorina, and A. V. Kochetova

Abstract Existing tools in geographic information systems (GIS) do not allow to automatically map hydrography, taking into account both the stream's order (so that streams vary in widths) and the flow direction (so that streams taper). The article focuses on developing a QGIS plugin for displaying hydrographic networks according to automatically determined lengths, orders and parts of the course. Rivers are divided into segments, line features are transformed into polygons (by setting a buffer with a varying width), and then the resulting objects are merged back into single streams. In this paper, automated and modified by the authors Hack's algorithm is used to determine stream orders from vector data. To correctly visualize hydrography, the user has to select the main river and run the plugin: it will automatically determine the necessary parameters, transform the geometry and apply the style. The article discusses previous studies and the capabilities of modern GIS in the field of tapered visualization, which helps to highlight the advantages (including the reduction of time needed or accounting for the stream hierarchy and flow direction) and disadvantages (mainly scale limitations) of the developed plugin. As a result, proposed solution can be recommended to correctly display hydrography for small-scale mapping.

Keywords Hydrographic modeling · Hydrological mapping · QGIS plugin · Python · Tapered lines · Stream order for vector data · River networks visualization

1 Introduction

Modern visualization tools in geographical information systems (GIS) have limited graphical capabilities [1]. Several techniques are typically employed when automating the mapping of river systems in GIS:

D. A. Ignatenko (✉) · I. E. Sidorina · A. V. Kochetova
Saint Petersburg State University, Saint Petersburg 199034, Russia
e-mail: st110672@student.spbu.ru

N. A. Razvalov · O. P. Yakimova
P. G. Demidov Yaroslavl State University, Yaroslavl 150003, Russia

© The Author(s), under exclusive license to Springer Nature Switzerland AG 2024

V. Karev (ed.), *Proceedings of the 9th International Conference on Physical and Mathematical Modelling of Earth and Environmental Processes*, Springer Proceedings in Earth and Environmental Sciences, https://doi.org/10.1007/978-3-031-54589-4_67

all linear hydrographic objects have the same symbolization, the thickness is constant, and the user only sets the color (Fig. 1a);
streams of different order are represented by lines of different thickness (Fig. 1b);
different colors and thicknesses are assigned to the streams depending on their order (Fig. 1c).

This, at best, only takes into consideration the hierarchy of tributaries, but does not sufficiently illustrate their flow direction making it challenging to understand the hydrographic network and the entire map.

In reality, rivers have a more complex geometry: most often, the width of the riverbeds gradually increases from source to mouth, so the river system looks like

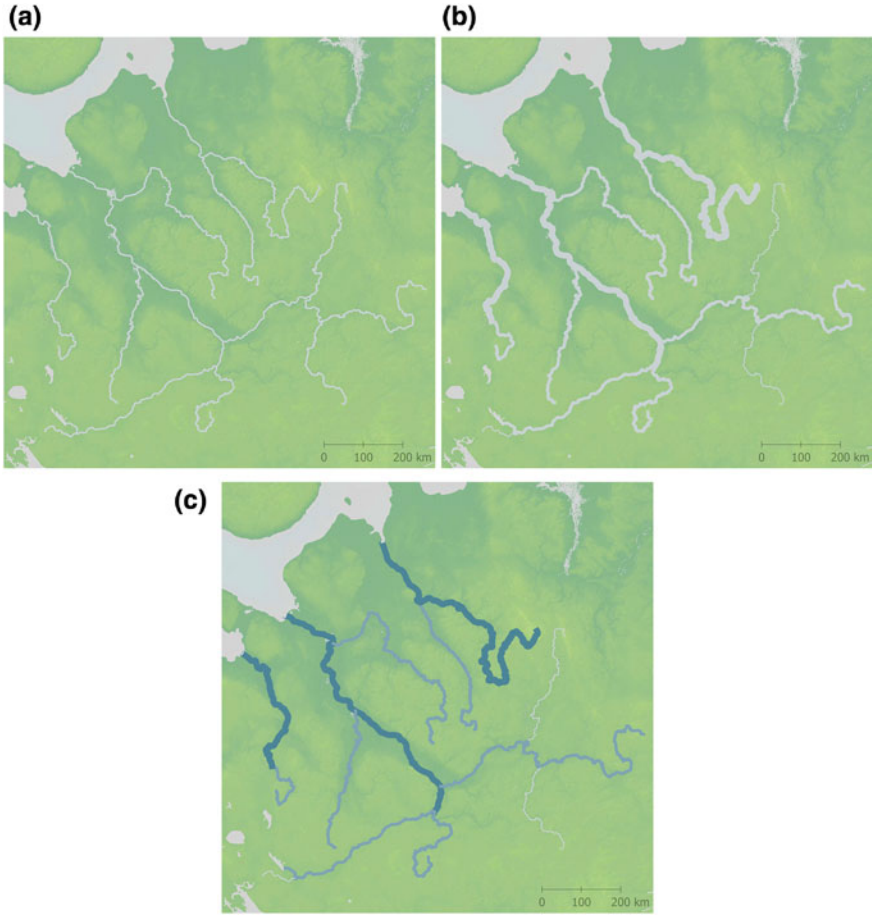


Fig. 1 Incorrect automated hydrography visualization in GIS on the example of the Onega, Northern Dvina and Mezen watersheds: **a**—a basic linear object; **b**—lines of different thickness; **c**—lines of different color and thickness

one seamless network of streams flowing smoothly into each other. Currently, one can achieve such an effect on maps by manually editing each river's width [2] or setting each width value at the source and at the mouth. The development of a software algorithm that allows automated implementation of such visualization of hydrographic information has become the goal of this study.

Streams can be displayed on analogue maps in a linear or polygonal manner, depending on their width and map scale. Rivers are typically shown as a single line with a gradual thickening from the source to the mouth from 0.1 to 0.5 mm. When depicting rivers as polygons, 0.1 mm is allocated for each coastline and at least 0.3 mm for the gap between them.[1] As an example, for a map with a scale of 1:100,000, the transition to a polygonal visualization usually starts when a riverbed's width is 10–60 m (for an off-scale symbol, so the total thickness will be at least 0.5 mm) and over 60 m (for maintaining the actual width, which will be at least 0.6 mm on a map).

If we look at rivers as vector object in GIS, it is evident that the aforementioned option is not suitable for working when the scale changes may occur. Hence there is a need to determine other criteria and display parameters, taking into account cartographic recommendations given above.

Noteworthy is the fact that the hydrographic modeling within the context of this study was carried out on the example of some northwestern rivers of Russia, namely the Onega, the Northern Dvina and the Mezen. These rivers have sufficient lengths for small-scale mapping, which made it possible to choose their watersheds as a visual illustration for demonstrating the capabilities of the developed plugin.

2 Materials and Methods

On the technical side, the implementation of hydrographic mapping in a tapered way involves changing the geometry of linear features, which can be done in several ways. The ability to use these algorithms by experts in other fields without programming skills was a key consideration in the process of development. In this regard, the task of creating a QGIS (version 3.28.0) plugin with a user-friendly interface arose. For these purposes, the Python programming language (version 3.9.5) was chosen, which, due to its integration into GIS, allows to implement a number of geometry modification operations.

There are various parameters on which the width of the riverbed may depend, both physically (terrain, rocks composition, climate, etc.) and when displayed on the map (scale, extent, purpose of the map, degree of generalization, etc.). However, in this study we will focus on the following characteristics that determine the size linear object buffers:

part of a river's course;
river's length;

[1] Recommendations P 52.08.874–2018. Determination of hydrographic characteristics using cartographic method. Saint-Petersburg: Roshydromet; 2018. 178 p.

stream order.

Most often, the river in the lower course has a much wider riverbed than at the upper course. We can try to reflect this on the map. In this paper, we will consider the part of a river's course as the ratio of a specific segment's number (each segment is the line between two nearest vertices, starting from the source) to the total number of segments that make up the river. For instance, with the total number of segments equal to 100, the parameter of the river's course will vary throughout the river from 0.01 at the source to 1 at the mouth. This will help to taper the river by multiplying the initial constant line width by these values for each segment.

Regarding the second parameter, it should be mentioned that in our case measuring the lengths of rivers does not require the accuracy of the cartometric operations: it is important that the measurements are accurate in relation to one another, i.e., the method described in this article only requires that the lengths for all objects are calculated in one projection with meters as the unit of measurement. Additionally, the stream's length often correlates with the width of the riverbed, since large rivers generally have more tributaries, a larger catchment area, etc. This pattern in combination with the river's course parameter will allow to set up an even smoother and more intuitively understandable visualization of the network.

Stream order also has an indirect relation to the width. Normally there is a pattern: the main rivers and tributaries of the first orders accumulate the flow of tributaries of higher orders, which makes them wider. Although such an assumption does not always turn out to be true in reality, it can be utilized to make river's system structure easier to perceive when mapping hydrography.

It is not difficult to automatically determine river's length: these cartometric operations are implemented in many GIS and programming libraries. But two of the remaining characteristics in the context of automating their calculation should be considered in more detail.

2.1 Stream Order Calculation

There are various ways to obtain spatial data on hydrography: from interpreting topographic and hydrographic survey data or vectorizing topographic maps to using remote sensing technologies with much more advanced data processing techniques [3]. Depending on the data source, the quality can vary in a significant range. However, in general, obtaining data with predetermined stream orders in the public domain is very unlikely. It is also impractical for a large amount of data to define the orders manually. Hence the need to develop an automated algorithm for these purposes and integrate it into a plugin.

Prior to choosing the right method for determining stream orders in the context of this article, the most widely used existing algorithms should be considered (Fig. 2).

The Strahler method [4] is among the first to be mentioned: it is frequently used in scientific research and implemented as a tool in many geographic information

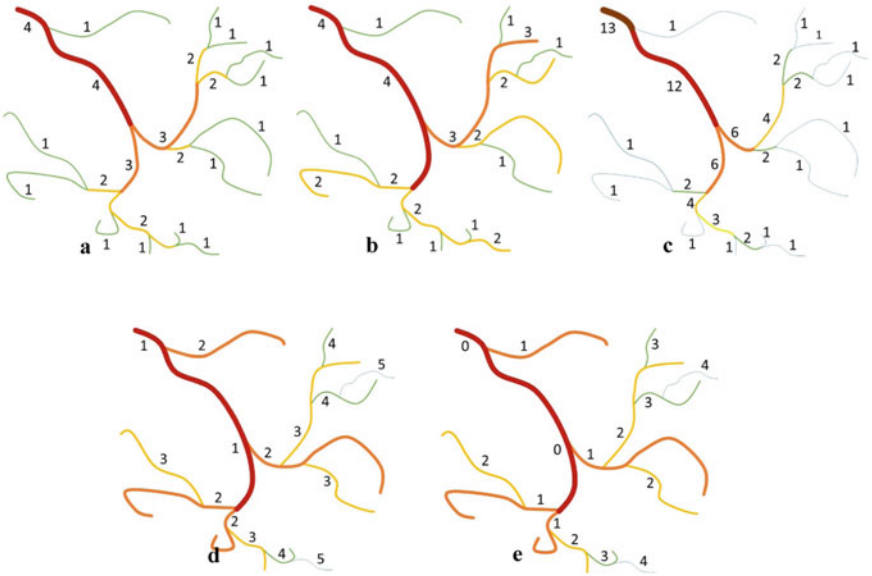


Fig. 2 Algorithms for the stream order delineation by: **a**—Strahler; **b**—Horton; **c**—Shreve; **d**—Hack; **e**—Hack, modified by the authors for the purpose of the study

systems (especially when working with raster images). In the context of vector data, its automated implementation makes it possible to organize the hydrographic network in a relatively short period of time, but it can be quite complex [5]. Ordering is performed from the source to the mouth (from top to bottom); rivers of the first order are the most remote tributaries. When two streams with the same order combine, the new stream is assigned a number that is greater by one. And if there is an intersection of two rivers with different orders, the larger one is assigned to the resulting stream.

Though less frequently employed, the Horton algorithm is also widely recognized [6]. Here, rivers of the first order have no tributaries, of the second order—accept first-order streams as tributaries, etc. The most important difference is that the main river throughout its entire length has the same (maximum possible) ordinal number. Therefore, gradually moving back from the mouth to the sources, some tributaries receive a new higher order than they would have according to Strahler's classification.

Another commonly employed system, which likewise assigns the number 1 to the farthest-reaching tributaries (from top to bottom), was proposed by Shreve [7]. But, unlike the Strahler method, when streams merge, two numbers denoting their order are summed up. A similar method was proposed by Scheidegger, but numbering is performed only in even digits [8]: i.e., the order of the river is determined by the sum of the orders of the rivers merging upstream.

Fundamentally different systems were proposed by Gravelius and Hack.[2] They are based on determining the orders in the direction from the mouth to the source (from bottom to top). According to it, the main river has the order of 1, each of its tributaries has 2, etc. This algorithm is more intuitive. It is often used not only when mapping a hydrographic network, but also when performing more complex operations with river systems in GIS. For example, conflating a digital elevation model with reference hydrographic lines [9] in order to improve the correctness of mapping of hydrography. However, there are drawbacks as well: the difficulty of comparing tributaries of the same order flowing into the river in its upper and lower courses; the need to choose the main stream when merging occurs (or to decide that a new river was formed at the confluence of other two), etc.

The choice of stream order classification depends on the goals pursued. Each of them has its advantages and disadvantages, however, in this study one of the key factors is a clear perception of the river networks on the map. It is desirable that the river system is not just tapered and tree-like, but that the thickness of the streams allows the map user to visually separate them from their tributaries to simplify obtaining thematic information from the map, even if in reality these rivers are similar in riverbed's width.

These criteria are most satisfied by the Hack algorithm. However, in author's opinion, it also has another significant disadvantage in addition to the aforementioned: tributaries, for example, of the first order are assigned the value "2", the second order—"3", etc. In the attribute table, after plugin's execution, in the order field, the user would see these numbers and could interpret them incorrectly. In this regard, Hack's classification has been modified: the main river of the basin is assigned the value 0, and the tributaries are numbered according to their actual names, for instance, first order is given "1".

2.2 Automated Tapered Mapping of Hydrography

Once the rivers' length and order have been established, the course needs to be automatically calculated. It was defined above as the ratio of the segment number to their total amount. Every river is segmented into a set of new features (lines between two nearest vertices); all attributes of the river are preserved. Next, the total number of segments for each river is calculated, and they are numbered for each stream, starting from 1 at its source.

After determining all the necessary characteristics, we can start setting the buffer zone for each of the segments. Additionally, we introduce a coefficient that performs the function of a scale factor (a number that determines the degree of exaggeration of the riverbed's width, depending on the needs of the user and the scale of the product). And the following equation is obtained:

[2] Hack J. Studies of longitudinal stream profiles in Virginia and Maryland, 1957.

$$B_1 = \mathrm{k} \bullet \frac{1}{(Or+1)} \bullet \log_{10} L \bullet \frac{N}{C} \tag{1}$$

where B_1 is the width of the buffer for a specific line segment; k is a custom (scale) coefficient; Or is the stream order; L is the river's length; N is the ordinal number of a specific segment; C is the total number of the river segments.

It is necessary to give some explanations to the equation:

the scale factor is chosen empirically, while a value close to 2000 is recommended for small-scale maps;
since the order of the main river of the catchment area in this study is assumed to be 0, it is necessary to add one to the value in the denominator to avoid algorithm failures;
the logarithmic function of the length allows for a more active increase in width at the sources, and then a smooth one in the middle and lower courses.

However, there are streams whose source is located at the confluence of the other two. In such cases, the algorithm would still start displaying the river from the minimum value, which would violate the smoothness and integrity of the network visualization. In order to avoid such incorrect mapping, Eq. (1) is applied only to some of the more remote tributaries whose order value does not exceed 80% of the maximum order. For example, if the network is represented by the main river and tributaries up to the 6th order, then the algorithm is applied only for 5 and 6.

When the tributary is larger, a rule is set: all segments lying in the first 40% of the total count (regardless of the N/C parameter) are displayed with a buffer of the same width calculated as:

$$B_2 = 0.4 \bullet k \bullet \frac{1}{(Or+1)} \bullet \log_{10} L \tag{2}$$

where B_2 is the width of the buffer set for the upper courses of larger rivers.

And the rest 60% of the larger streams' segments are calculate by Eq. (1). This approach makes it possible not only to solve the problem of visualizing rivers whose source is located at the confluence of two tributaries, but also to highlight a more important riverbed out of two in cases where the merging scheme is standard.

The resulting polygonal segments of each stream must then be converted back into a single object. To accomplish this, we will dissolve them by attribute. When selecting the field in the attribute table for which the dissolving will be performed, we will focus on the length of the stream. The length in meters, calculated to the nearest thousandths, is a much more unique value for each river than its name.

When every stream is now a single feature, one more problem still remains: the default symbology for polygons in QGIS is not suitable for the mapping purposes (and not only because of the randomly generated color scheme). The issue is that the boundaries of features do not disappear when they intersect, which creates an overlay effect instead of merging. To solve these problems, the module automatically connects a style file (.qml), which was prepared in advance and registered as a

resource. It applies a light blue fill and a dark blue stroke and visually unites rivers at the confluence points, which allows us to get a single and continuous visualization of the river network.

3 Results

The study's findings led to the development of two algorithms: determining stream orders according to the modified Hack's classification and displaying hydrographic networks taking into account the hierarchy of tributaries and the flow direction.

The implementation of the first of them assumes that before launching the module, the user must select the main river of the watershed in the active layer. The value "0" is automatically assigned to it. At the first iteration, all linear objects intersecting with the main river are assigned the value "1". Then tributaries of the first order are automatically selected as well, and iterations continue until the last stream that does not have intersections with not yet selected features is found. As a result, a new field with these orders appears in the attribute table of the file, which in itself carries useful information, and can also be used for further visualization.

The second algorithm, using Eqs. (1) and (2), as well as other methods described above, allows us to transform linear geometry into a tapered polygonal one and display it with the correct stylization. So, within a few seconds, the user receives a ready-to-use hydrography layer, which can be utilized both for applying thematic information on top of it, and as a component of a base map.

Figure 3 illustrates the benefits of processing hydrography data using the algorithms suggested in this article as opposed to the commonly used techniques for automated mapping in GIS (Fig. 1).

4 Discussion

Other implementations of automated tapered rivers' visualization have their own advantages and disadvantages.

One of the leaders among GIS software at the moment is ArcGIS Pro. In this GIS, to visualize river network accounting for its flow direction, it is proposed to work with the symbology, namely, to apply the "tapped polygon" visualization effect[3] to the linear layer. The user sets the width of the line at the source and at the mouth for the entire layer, and then rivers are drawn automatically in a tapered manner. In this case, automatic calculation of additional information about the stream (length, order, numbers and counts of segments) is not required, which is both a benefit and

[3] Nelson J. How to make tapered rivers in ArcGIS Pro. URL: https://www.esri.com/arcgis-blog/products/arcgis-pro/mapping/how-to-make-tapered-rivers-in-arcgis-pro/.

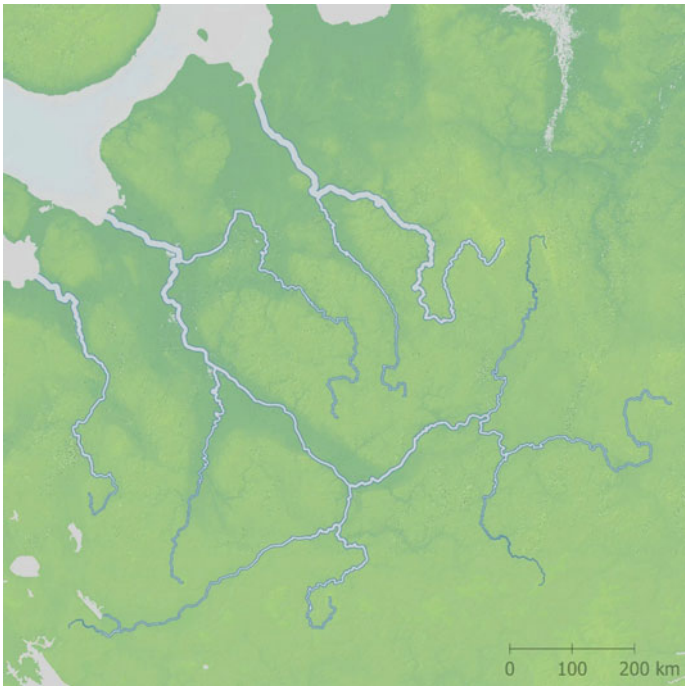


Fig. 3 Automated hydrography mapping on the example of the Onega, Northern Dvina and Mezen river basins using the developed plugin

a drawback. The width here accounts only for flow direction, but the hierarchical element is either lost or can be done manually.

There are various options available for displaying tapered hydrography in the open-source QGIS. It was proposed to use a geometry generator that allows to transform geometry using the syntax of QGIS expressions in the process of rendering.[4] The advantage of this option is that there is no need to create a new file, i.e., as in ArcGIS Pro, work is done only with the style of displaying linear objects. However, with any change of the extent (scaling, moving, etc.), the rendering starts over. Even with relatively small amounts of data, this can take a long time.

Another open-source TAS and GRASS GIS allow us to solve a different problem—determine stream orders according to greater number of classifications (including Hack's algorithm [10]) than the rest of the more well-known software. However, they will still need a raster digital elevation model as an auxiliary material, which is a significant drawback.

Another approach makes use of meteorological data to achieve a similar goal. The overlay of linear river features on the interpolated by weather stations layer allows to extract precipitation data and use it to set the width of the riverbed [11]. Such

[4] Graser A. Better river styles with tapered lines. URL: https://anitagraser.com/2017/04/17/better-river-styles-with-tapered-lines/.

hydrography visualization may be more correct in hydrological terms, although, depending on the type of river feeding and other factors, precipitation may not play the main role in the total runoff. However, one of the major disadvantages is the need to involve third-party data, along with concerns of its relevance, the quality of the interpolation and other aspects.

Among the disadvantages of the research presented in this article, is the suitability of this method only for small-scale and, in some cases, medium-scale (provided that the scale factor is changed and selected empirically) GIS-based mapping. This is due, firstly, to the exaggeration of the river's width on a map (in comparison to the real one), and, secondly, to the fact that the boundaries of the buffer zones do not reflect the actual shorelines. It is possible only at smaller scales. That way, if we zoom in too much, we will need ground truth data for an accurate map.

In addition, this method requires digitizing direction to be the same for all of the lines (upstream or downstream). Nevertheless, if this rule was initially broken, and after running the plugin, one or more streams look like they flow in the opposite direction, it is enough to simply deploy the "revers line direction" tool[5] on these rivers and run the plugin again.

5 Conclusion

The conducted research clearly demonstrates the possibility of automated visualization of hydrographic networks, taking into account the hierarchy of tributaries and the direction of their flow. The developed algorithms for determining stream orders and displaying river systems can significantly reduce the time spent on preparing the hydrography layer: instead of manually processing or symbolizing each river, this task is solved in a few clicks by launching the developed QGIS plugin. In addition to saving time, the advantages include: simple and user-friendly interface; no need for constant rendering; the ability to take into account both the hierarchy and flow direction; a combination of all the necessary functions in one module (from splitting geometry and stream ordering depending on intersections to automatic application of symbology used for hydrographic data).

Despite the disadvantages described in the previous chapter, this plugin can be recommended for small-scale mapping to professionals who need a correctly visualized hydrography layer for thematic or general-purpose maps.

In future research, it makes sense to consider the possibility of creating an algorithm that automates not only stream ordering or their polygonal visualization, but also the process of initial preparation of linear hydrographic data. For instance, facilitating the creation of "one river—one feature" system from the available fragmentary data or assisting with faster stream naming and other hydrographic tasks automation.

[5] Vector geometry. Reverse line direction. URL: https://docs.qgis.org/3.16/en/docs/user_manual/processing_algs/qgis/vectorgeometry.html#reverse-line-direction.

Acknowledgements Part of the research concerning stream order determination was funded by the Demidov Yaroslavl State University (project No.GM-2023-03)

References

1. Sidorina I.E., Pozdnyakova N.A., Panidi E.A., Andreeva T.A., Litvinova M.V. Integration of traditional and modern methods in GIS-based mapping // InterCarto, InterGIS. 2019. Vol.25. №1. P.35–46. DOI: https://doi.org/10.35595/2414-9179-2019-1-25-35-46.
2. Mei Y., Li L. A cartographic data model for better geographical visualization based on knowledge // The International Archives of the Photogrammetry, Remote Sensing and Spatial Information Sciences. 2008. Vol.XXXVII-B2. P.611–616.
3. Kolesnikov A.A., Kikin P.M., Panidi E.A., Rusina A.G. Using systems of parallel and distributed data processing to build hydrological models based on remote sensing data // The International Archives of the Photogrammetry, Remote Sensing and Spatial Information Sciences. 2021. Vol.XLIII-B4–2021. P.111–116. DOI: https://doi.org/10.5194/isprs-archives-XLIII-B4-2021-111-2021.
4. Strahler A.N. Quantitative analysis of watershed geomorphology // Transactions, American Geophysical Union. 1957. Vol.38. №6. P.913–920. DOI: https://doi.org/10.1029/tr038i006p00913.
5. Gleyzer A., Denisyuk M., Rimmer A., Salingar Y. A fast recursive GIS algorithm for computing Strahler stream order in braided and nonbraided networks // JAWRA Journal of the American Water Resources Association. 2004. Vol.40. №4. P.937–946. DOI: https://doi.org/10.1111/j.1752-1688.2004.tb01057.x.
6. Horton R.E. Erosional development of streams and their drainage basins; hydrophysical approach to quantitative morphology // Geological Society of America Bulletin. 1945. Vol.56. №3. P.275–370. DOI: https://doi.org/10.1130/0016-7606(1945)56[275:EDOSAT]2.0.CO;2.
7. Shreve R.L. Statistical Law of Stream Numbers // The Journal of Geology. 1966. Vol.74. №1. P.17–37. DOI: https://doi.org/10.1086/627137.
8. Cedeno A.F., Sinichenko E.K., Gritsuk I.I. Structural approach to the assessment of morphometric characteristics of river basins of Manabi Province (Ecuador) // Vestnik RUDN: Engineering research. 2015. №1. P.52–61.
9. Samsonov T.E. Automated Conflation of Digital Elevation Model with Reference Hydrographic Lines // ISPRS International Journal of Geo-Information. 2020. Vol.9. №5. P.1–40. DOI: https://doi.org/10.3390/ijgi9050334.
10. Jasiewicz J. Towards the topologically correct drainage network: integration between TAS GIS and GRASS GIS software // GIS Ostrava. 2009. P.1–6.
11. Magyari-Sáska Z. Precipitation used as key factor in tapered line based river representation // Geographia Technica. 2020. Vol.15. №2. P.212–221. DOI: https://doi.org/10.21163/GT_2020.152.20.

Modelling of Stress–Strain State of Artificially Improved Foundation During Construction of a Residential Complex in a Megacity



Dmitriy Neguritsa, German Alekseev, Evgeny Medvedev, Konstantin Slobodin, and Ivan Tereshin

Abstract At scientific and technical support of construction, it is necessary to model geomechanical processes at different stages of construction of a multifunctional residential complex with underground car park with the use of artificially improved base—structural geotechnical array, performed in order to improve strength and deformation characteristics and to ensure regulatory requirements for limiting absolute and relative deformations of foundations. The impact of construction on the surrounding soil-rock massif and structures falling within the zone of influence was assessed.

Keywords Modelling · Stress–strain state · Artificially improved base · Structural geotechnical array · Soil–cement elements

1 Introduction

Ensuring the specified quality parameters of construction objects under construction, operation and reconstruction, provided that the safety of surrounding buildings and structures is ensured during the renovation of metropolitan areas for the construction of residential complexes, when projects are implemented in areas surrounded by dense urban development on the site of pre-existing facilities, does not meet modern requirements for the rational use of urban areas [1, 2]. The complexity of the implementation of residential construction projects consists in the complexity of construction conditions with unique layout and the need to take into account the

D. Neguritsa (✉) · G. Alekseev · E. Medvedev · K. Slobodin
National Research Moscow State University of Civil Engineering, Moscow, Russia
e-mail: neguritsadl@mgri.ru

D. Neguritsa · I. Tereshin
Sergo Ordzhonikidze Russian State University for Geological Prospecting, Moscow, Russia

© The Author(s), under exclusive license to Springer Nature Switzerland AG 2024

V. Karev (ed.), *Proceedings of the 9th International Conference on Physical and Mathematical Modelling of Earth and Environmental Processes*, Springer Proceedings in Earth and Environmental Sciences, https://doi.org/10.1007/978-3-031-54589-4_68

impact on the surrounding development and communications that fall within the zone of influence of construction [3–5].

During the implementation of scientific and technical support of the construction of unique buildings and structures, geotechnical calculations of the impact of the construction object on the surrounding development by the finite element method are performed, the zone of influence is determined and the forecast of incremental deformation of structures of existing buildings and underground utilities located in the zone of influence is performed [6, 7].

The object is an 11-section residential complex of different storeys with an underground car park located in Moscow.

The underground car park is 2-level, includes a part under the residential building and a remote part. Dimensions in plan of the underground part in axes are: 250 × 106 m.

The multifunctional residential complex consists of the following sections:

Section 1—(25–27) storey, "anchoring" the sharp northern corner of the site.

Section 2—(20–21) storey.

Section 3—(26–28) storey.

Section 4—(26–28) storey.

Section 5—(20–21) storey.

Section 6—(24–26) storey, "fixes" the southern corner of the site.

Sections 7…9—low-rise stylobate.

Sections 10 and 11—low-rise stylobate.

The scheme of division of the multifunctional residential complex into sections is presented in Fig. 1: Category of complexity of engineering and geological conditions of the construction site—III (complex), geotechnical category of the object—3.

The residential building and low-loaded parts of the underground car park have separate foundation slabs separated by expansion joints. The underground part of the complex is divided by expansion joints into separate sections due to a significant difference in the height of the buildings and the load acting on the foundation.

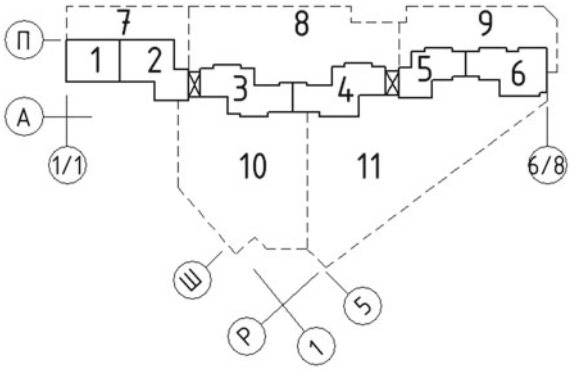


Fig. 1 Diagram of building division into sections

The level of responsibility of the structure is increased. The level of responsibility of buildings is increased, construction class. According to the totality of factors, the complexity category of engineering and geological conditions of the site is complex.

The building frame is spatial, monolithic, reinforced concrete, consisting of pylons and horizontal slabs, with cores and diaphragms of rigidity, which are the walls of stairwells, lift shafts, internal walls.

As the main type of foundations for high-rise buildings, monolithic foundation slabs are used on a natural base reinforced with soil–cement elements, while structural solutions are required to reinforce the base under the foundations of high-rise parts of the building.

Under the foundation slabs of Sections №1—№ 6 an artificially improved base—a structural geotechnical array—is provided in order to improve strength and deformation characteristics and to meet the regulatory requirements for limiting absolute and relative deformations of foundations. The principle of the geotechnical array consists in the vertical reinforcement of the soil base with rigid elements using the technology of soil jet grouting and the creation of a surface flexible spreading layer (Fig. 2).

The flexible spreading layer with a height of 600 mm is made of igneous crushed stone. The spreading layer is compacted until the modulus reaches 30 MPa. Reinforcement of the natural soil is performed by individual vertical rigid soil–cement elements (SCE) of 1300 mm diameter, which are arranged in a regular grid in plan. Placement of the soil–cement elements in plan: on a grid with a spacing of 2.6 × 2.6 m.

The soil–cement elements are made by two-component technology of jet grouting of soils, based on the use of energy of the cement mortar jet for destruction and simultaneous mixing of natural soil with its partial replacement by the cement mortar.

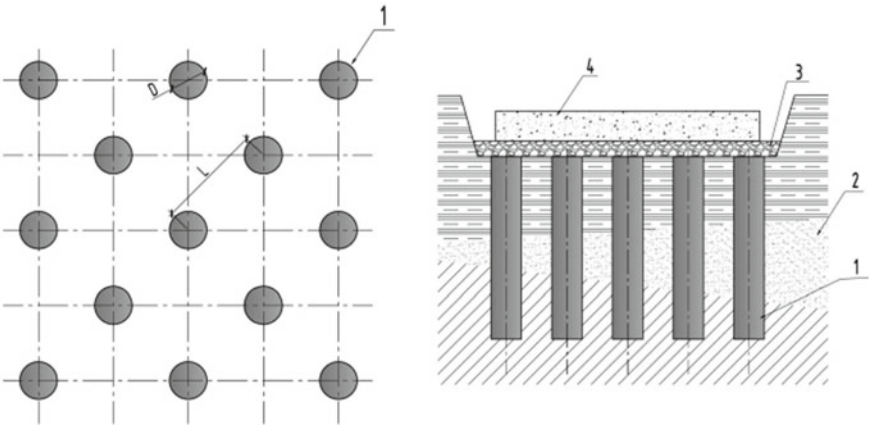


Fig. 2 Structural solution of the structural geotechnical array: plan and vertical section: 1—vertical reinforcing elements; 2—soil base; 3—distribution layer; 4—foundation structure

After hardening, a new material is formed—soil cement, which has increased strength and deformation characteristics compared to natural soil.

At the maximum pressure acting on the surface of the geomassif, equal to 550 kPa, the design resistance to compression of the material of reinforcing elements should be not less than 3.7 MPa, the designated design resistance of soil cement to compression Rsb.n = 4.0 MPa.

Overall dimensions of the structural geotechnical massif: horizontal dimensions in plan—within the foundations' spot with a minimum of 0.3 m beyond the contour, upper boundary—0.2 m below the foundation sole; consolidation zone thickness: from 7.0 to 12.0 m.

1.1 Structural Solutions of the Excavation Enclosure

The underground part of the building has a complex shape with total dimensions of 259 × 118 m. The bottom of the excavation is arranged for the hull and stylobate parts. Locally there are depressions for the pits of lift structures. The depth of the excavation from the actual relief marks is variable 11–14 m.

The excavation is developed with the "wall-in-soil" (hereinafter referred to as WIG) fencing, with deepening into the water-retaining layer of Jurassic clays along the entire perimeter. During the construction period, the WIG acts as an impervious blanket and prevents water from entering the excavation. Construction dewatering is carried out to pump out the water contained in the water-logged soils within the WIG contour.

The WIG is designed as a trench trench, 800 mm thick, made of monolithic reinforced concrete with reinforcement, the stability of which is ensured by a 2-tier spacer system of pipes and sub-braces, as well as the depth of the WIG below the bottom of the excavation at least 14 m. The spacing of spacers and struts is variable, up to 7 m.

2 Modelling of VAT of the System "Foundation-Foundation-Underground Part-Surrounding Development"

The object and its foundation are considered in unity, i.e. taking into account the interaction between the structure and the foundation. The numerical finite element method [8–10] is used for joint calculation of the system "Foundation-foundation-underground part-surrounding development". Modelling is carried out in spatial formulation using the software package "PLAXIS".

The considered complex occupies an area with a complex geological structure to a depth of 50 m. To build a finite element model of the array were used the

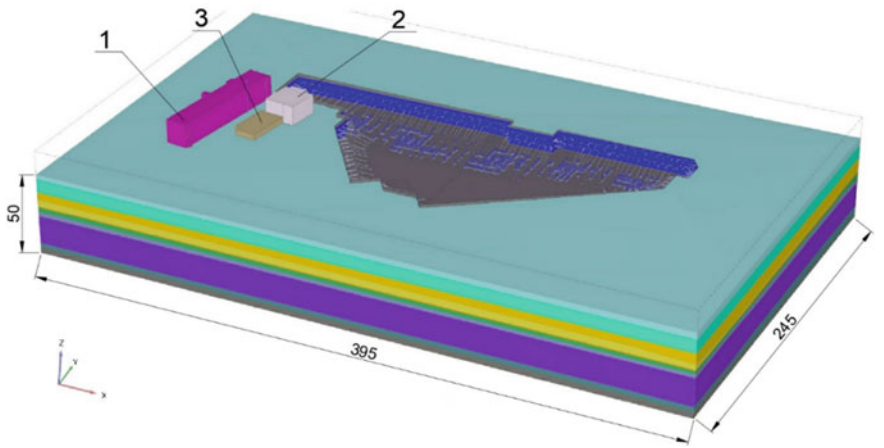
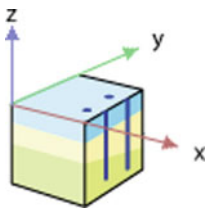


Fig. 3 Calculation scheme (at the last stage of modelling): (1) Five-storey cultural and educational building with a basement; (2) Two-storey building; (3) One-storey building

results of engineering-geological surveys in the spot of the construction site. As a computational model was chosen a soil massif with the dimensions in plan 245 × 395 m of heterogeneous composition with varying thickness of layers, according to the data of geological surveys (Fig. 3).

The following boundary conditions were assigned for the model by fixings:

- on the surface of the design area—free movement of nodes in all directions;
- on the lateral boundaries of the computational domain—free movement in the vertical direction (along the Z axis) and sliding along the boundary;
- at the bottom of the design area—prohibition of movement in all directions



Based on the analysis of the results of engineering-geological surveys, the following geomechanical models describing the stress–strain state of the foundation soils comprising the considered array were selected:

elastic–plastic model with hardening (Hardening soil or HS);
elastic–plastic model with hardening soil and stiffness at small deformations (HS small);
isotropic continuum model for modelling weathered Hoek–Brown rock (Hoek–Brown model or HB).

The models allow describing elastic and plastic components of ground medium deformations based on elastic–plastic Drucker-Prager theory (associated variant) for FEM complexes.

The main feature of the HS model is the dependence of soil stiffness on stresses, and the possibility to distinguish between soil stiffness under loading and stiffness under unloading.

Main characteristics of the model:

Fracture parameters as in the Coulomb-Mohr model:

c—sseffective adhesion;

φ—effective angle of internal friction;

ψ—angle of dilatancy.

Basic parameters of soil compressibility.

E_{50}^{ref}—secant modulus in standard drained triaxial tests;

E_{oed}^{ref}—tangent modulus in primary compressive compression;

m—index for the dependence of stress level on strain modulus.

Additional parameters.

E_{ur}^{ref}—modulus at unloading/re-loading;

p^{ref}—initial stress for moduli, kPa;

K_0^{nc}—lateral pressure coefficient at normal compaction (by default $K_0^{nc} = 1 - sin\varphi$).

The HS small model is a modification of the elastoplastic model with soil strengthening discussed above, observing an increase in soil stiffness at small deformations.

At low strain levels, most soils exhibit stiffnesses greater than the stiffness at the notional ("engineering") strain, and this stiffness varies nonlinearly with strain. This behaviour is described in the HS small model using two parameters in addition to HS:

G_0—initial shear modulus or shear modulus at ultra-small strains.

$\gamma_{0.7}$—is the level of shear strain at which the secant shear modulus G_S decreases to about 70% of the value of G_0.

In cases of service loads, the HS small model gives more accurate displacement values than the HS model. In addition, the model can be used in cases where small ground motions need to be taken into account, such as soil interaction problems with retaining walls.

The HB model is an isotropic elastic-ideal-plastic model for weathered rock based on the Hoek–Brown fracture criterion. This criterion, which is nonlinearly stress-dependent, describes shear and tensile failure using a continuous function and is well known to most geologists and mining engineers. In addition to the elastic parameters (E and v), the model also contains the parameters used in practice: unbroken rock uniaxial compressive strength (aci), geological strength index (GSI) and disturbance factor (D). The Hoek Brown fracture criterion is the best nonlinear approximation of rock strength.

3 Modelling of the Object's Structures. Application of Loads

A Linear Elastic (LE) model was used to describe the mechanical behaviour of the structural materials (concrete, metal) of the designed Object.

The LE model is based on Hooke's law for isotropic elasticity. It contains only two main parameters: Young's modulus E and Poisson's ratio υ.

The calculation of reinforced soil–cement structures is performed according to limit states. Direct determination of forces in the reinforcing elements is allowed if the reinforcing elements and soil–cement are entered separately in the calculation domain.

Since the degree of reinforcement of natural soil with GCE is 20%, it was decided to model vertical columns reinforcing the soil mass as separate special elements "Embedded beam".

3.1 Modelling of Soil Consolidation by Vertical Reinforcing Elements of GCE

The interaction between vertical elements and the surrounding soil (soil cluster element) is modelled using special interface elements. An elastic–plastic model is used to describe the interface behaviour.

Regarding plastic behaviour, the material dataset distinguishes between Skin resistance (Resistance on the side surface) (in units of force per unit length of the submerged beam) and Base resistance (under the end of the beam) (in units of force). For the resistance at the lateral surface as well as for the resistance under the end, a failure criterion is used to distinguish between elastic and plastic behaviour of the interface. With elastic behaviour, relatively small displacement differences occur at the interface (i.e. displacement between the pile/anchor bolt and the soil/rock), whereas with plastic behaviour, permanent sliding can occur.

In order for the interface to remain elastic, the shear force t_s at a point is given by the condition:

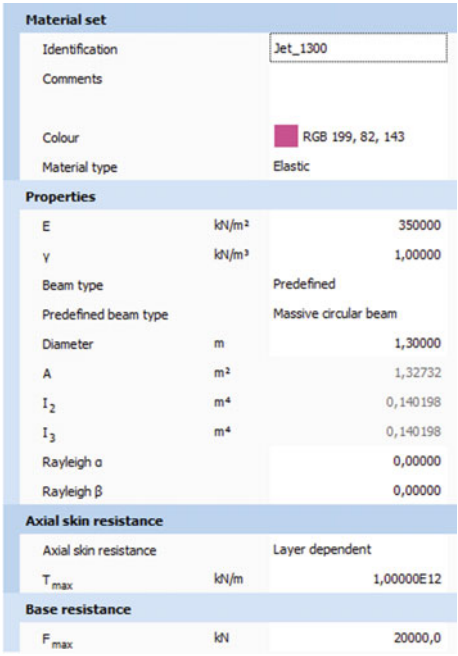
$|t_s| < T_{max}$, where T_{max} is the equivalent private resistance on the lateral surface at that point.

For plastic behaviour, the shear force t_s is given by the condition:

$$|t_s| = T_{max}$$

The barrel resistance is specified by specifying the axial resistance at the lateral surface F_{skin} and the resistance under the heel F_{max}. Using this approach, the total bearing capacity of the vertical element is given by the condition (Fig. 4):

$$N_{pile} = F_{max} + F_{skin}$$



Material set		
Identification		Jet_1300
Comments		
Colour		RGB 199, 82, 143
Material type		Elastic
Properties		
E	kN/m²	350000
γ	kN/m³	1,00000
Beam type		Predefined
Predefined beam type		Massive circular beam
Diameter	m	1,30000
A	m²	1,32732
I_2	m⁴	0,140198
I_3	m⁴	0,140198
Rayleigh α		0,00000
Rayleigh β		0,00000
Axial skin resistance		
Axial skin resistance		Layer dependent
T_{max}	kN/m	1,00000E12
Base resistance		
F_{max}	kN	20000,0

Fig. 4 Adopted characteristics for pile modelling

The calculation was performed for the main combination of loads, and the values of forces transferred from the upper structures to the foundations of the Facility were taken iteratively, 3 iterations were performed.

4 Stages of Mathematical Modelling of the Object Construction

Stage 1: Loading of the design area with own weight of the soil and determination of the initial stress–strain state of the soil mass.

Stage 2: Modelling of the surrounding development. Displacement zeroing Fig. 5.

Stage 3. Modeling the construction of a wall in the ground, soil–cement elements, excavation of a pit with preservation of the soil berm Fig. 6.

Stage 4: Modelling of the crushed stone cushion (spreading layer), stage 1 of the foundation slabs (building elevation), the first spreading belt, the upper level of the underpinnings and struts (Fig. 7).

Step 5: Modelling of excavation of the excavation with preservation of the soil berm with the second spreading belt, lower level of underpinning and struts (Fig. 8).

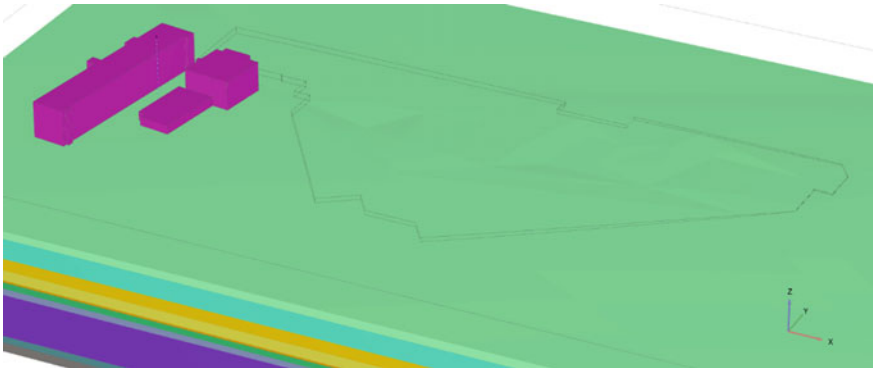


Fig. 5 Modelling of the surrounding development. Zeroisation of displacements

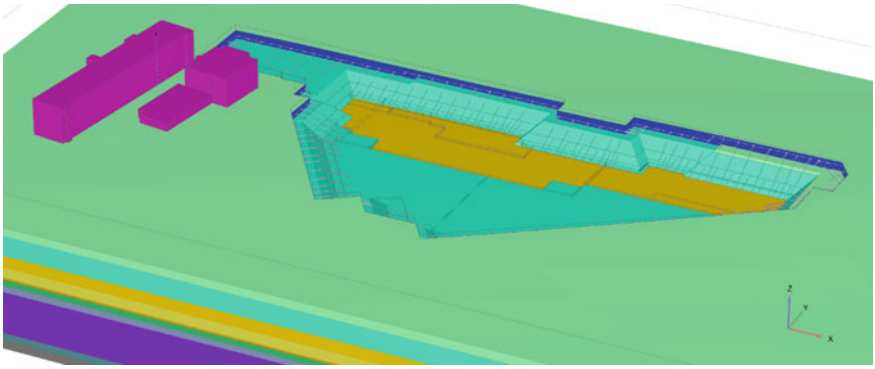


Fig. 6 Modeling the construction of a wall in the ground, soil–cement elements, excavation of a pit while preserving the soil berm

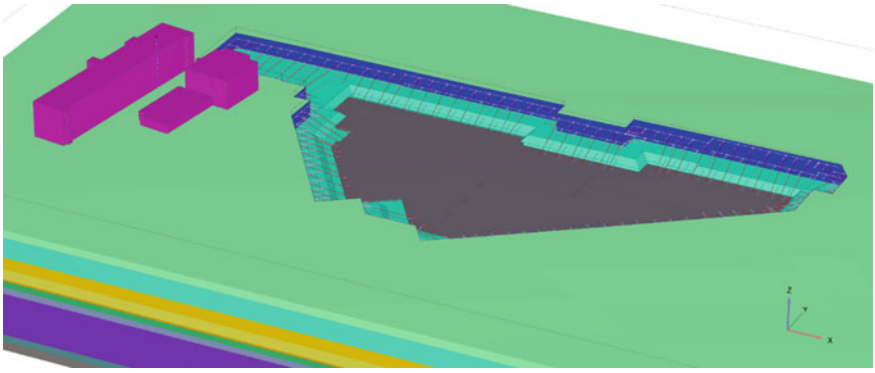


Fig. 7 Modelling of the crushed stone cushion (spreader layer), stage 1 of the foundation slabs (building elevation), the first distribution belt, the top level of struts and braces

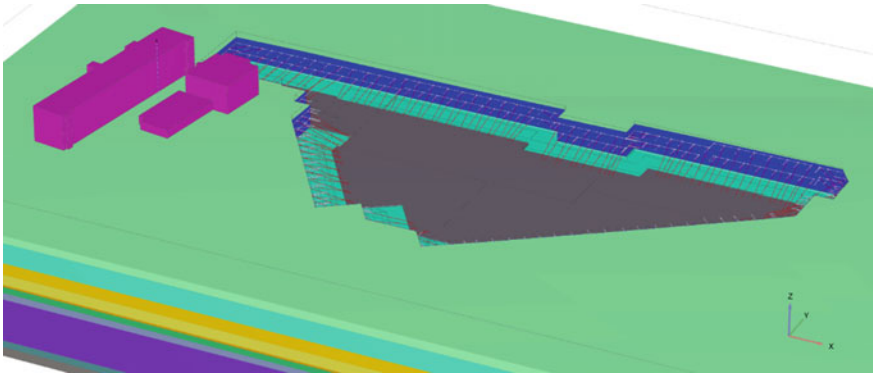


Fig. 8 Modelling of excavation of the excavation with preservation of the soil berm with the second spreading belt, lower level of underpinning and struts

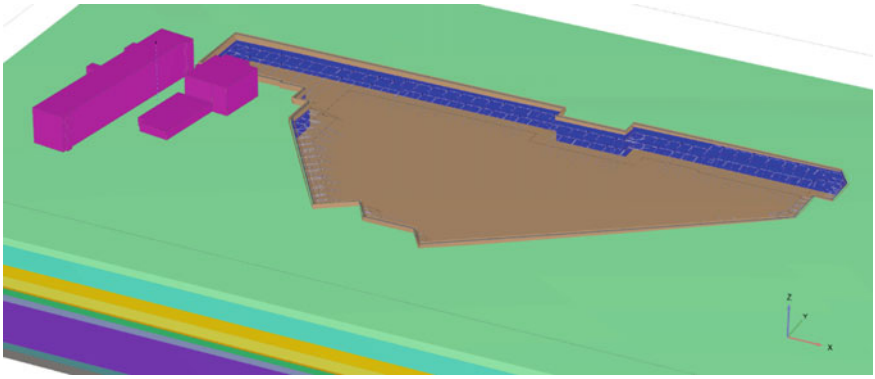


Fig. 9 Modelling of excavation completion up to design levels, foundation slab arrangement (low-rise stylobate), application of loads from the upper structures of the building

Stage 6: Modelling of the excavation completion to the design levels, foundation slab arrangement (low-rise stylobate), application of loads from the upper structures of the building (Fig. 9).

5 Results of the Calculation of VAT of the System "Foundation-Foundation-Earth Part- Surrounding Development"

Geomechanical calculation of VAT of the system under consideration was successfully completed, therefore, after application of all loads from the structures on the foundation, the soil massif is in the pre-limit state, i.e. the zones of plastic flow of the

Table 1 The results of the system VAT calculation

Section Object	Length of GCE, m	Maximum projected values		Limit base deformations of foundations of new construction projects,	
		Subsidence s, cm	Relative difference in subsidence, Δs/L	Maximum s_u^{max} or average $\bar{s}_u$ subsidence, cm	Relative difference in subsidence, Δs/L
1	6.0	11.0	0.0010	18	0.003
2	6.0	11.4	0.0015		
3	8.0	12.3	0.0015		
4	12.0	11.2	0.0010		
5	7.0	8.6	0.0006		
6	7.0	7.7	0.0006		

soil under the building foundation are closed and there is no loss of bearing capacity in the soil. The stability of the complex under consideration is ensured.

The results of the system VAT calculation were analysed for each stage (see Table 1) in three iterations. Comparison of the calculation results of the II-th and III-th iterations showed satisfactory convergence in the nature and values of the distribution of isopoles of settlements and stresses under the footings of the foundations of the Object (Fig. 10).

The area of spreading influence of the excavation does not exceed 20 m and, as shown in Fig. 10, is rapidly attenuated (Figs. 11 and 12).

The results of calculations are presented in graphical form (isopoles, epuples) and summarised in a summary table (see Table 1) for the third iteration at the final stage of modelling.

The maximum settlement of the Facility was 12.3 cm (Sect. 3), relative difference $\Delta s/L = 0.0015$. According to SP 22.13330, the calculated predicted deformations of the Object do not exceed the maximum permissible values ($s_u^{max} = 18.0$ cm, $\Delta s/L = 0.003$, $\Delta s/L = 0.003$). The maximum predicted deformations of the Object, detailed by sections, are presented in Table 1. Settlement values at key points of the Object sections are presented in Fig. 13.

The modelling carried out in the process of scientific and technical support of construction showed the development of deformation processes during the construction of a residential complex in a megacity on artificially improved base at all stages of construction within the established safe limits. The obtained results will be used in the organisation of surveying and geodesic monitoring during construction.

«This work was financially supported by the Ministry of Science and Higher Education of Russian Federation (grant # 075–15-2021–686). Tests were carried out using research equipment of The Head Regional Shared Research Facilities of the Moscow State University of Civil Engineering»

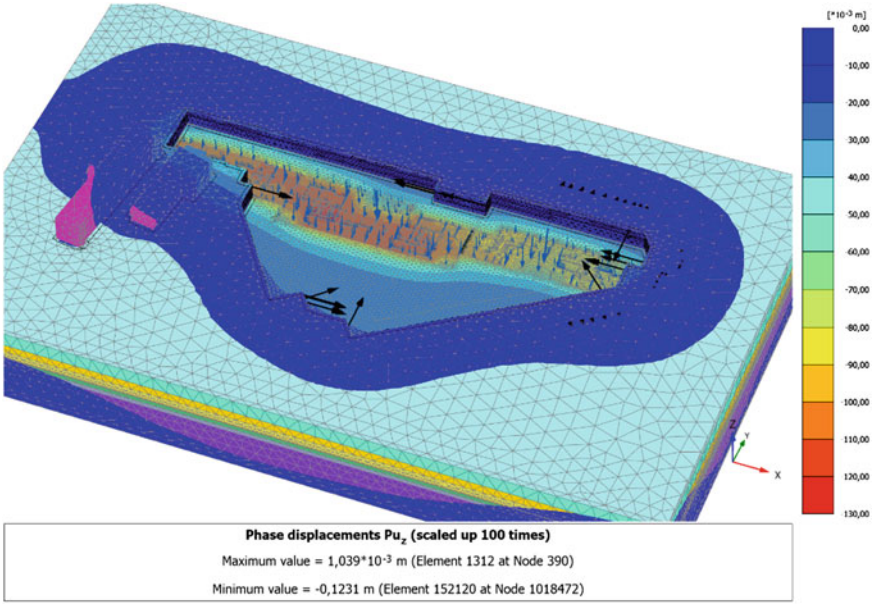


Fig. 10 Isopoles of vertical deformations (settlements) of the soil massif at the final stage of modelling

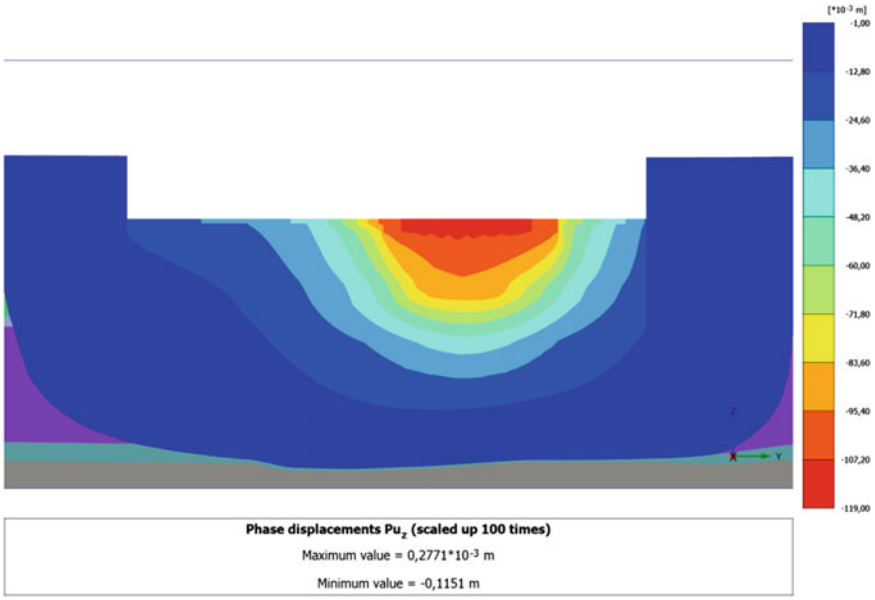


Fig. 11 Isopoles of vertical deformations (settlements) of the soil massif along section A-A* at the final stage of modelling

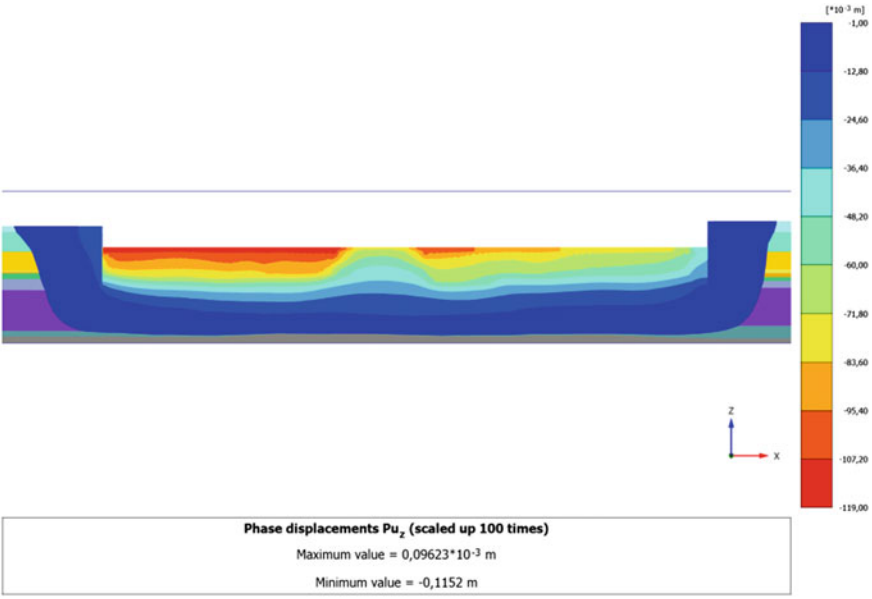


Fig. 12 Isopoles of vertical deformations (settlements) of the soil massif along section B-B* at the final stage of modeling

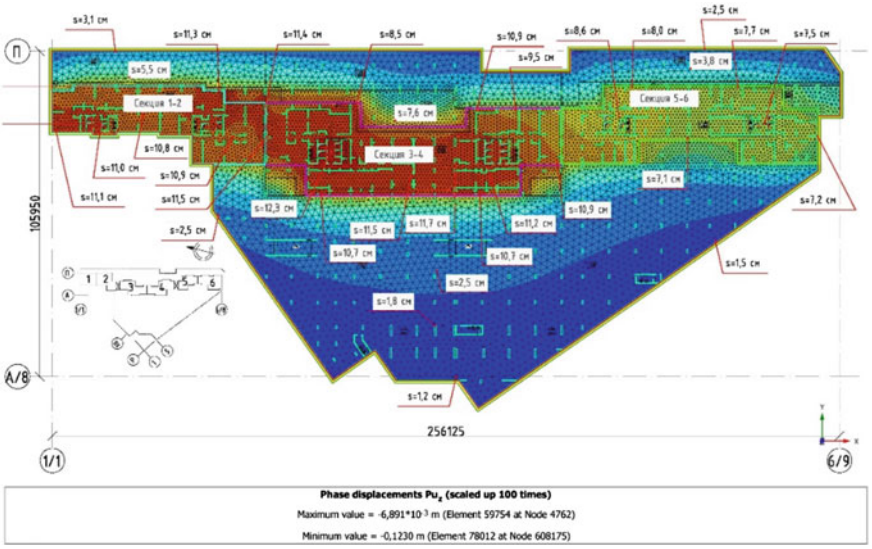


Fig. 13 Precipitation values at key points in the sections

References

1. Broere W. Urban problems - Underground solutions // Proc. 13th World Conf. of ACUUS: Advances in Underground Space Development. 2012 (2013). P. 1528–1539.
2. Magsin, Sammantha L., Gilbert Paul H., Ariaratnam Samuel T, etc. Underground Engineering for Sustainable Urban Development // Geo-Congress 2014 Technical Papers : Geo-Characterization and Modeling for Sustainability ; 2014. Pp. 3861–3870. https://doi.org/10.1061/9780784413272.374
3. Kartozia B.A., Korchak A.V., Levchenko A.N. Problems of methodology and practice of underground space development in megacities // Mining Journal. 2014. no. 9. C. 60–64.
4. Kulikova, E.Yu.; Potapova, E.V. Synthesis of management decisions to ensure the safety of underground construction // Mining information and analytical bulletin (scientific and technical journal). 2022. no. 2. p. 62–69
5. Hongjun W. Earth human settlement ecosystem and underground space research // Procedia Engineering. 2016, Vl. 165, P. 765-781. DOI: https://doi.org/10.1016/j.proeng.2016.11.774.
6. Neguritsa D.L., Alekseev G.V., Tereshin A.A., Medvedev E.A., Slobodin K.M. Deformation Processes Modelling throughout Underground Construction Within Megapolis Limits / / Springer Geology. Processes in GeoMedia—Volume IV. 2022. P. 215–227. DOI: https://doi.org/10.1007/978-3-030-76328-2_23.
7. Neguritsa D. The problems of monitoring the deformation processes in the integrated development of the underground space of metropolitan cities // E3S Web of Conf. 56, 02027 (2018). DOI: https://doi.org/10.1051/e3sconf/20185602027 EDN: BPLCIV
8. Dmitriev S. V. Solution of elastic problem by finite element method. Visualisation of the stress tensor // Mining information and analytical bulletin (scientific and technical journal). 2017. no. 7. P. 222-227.
9. Leslie Banks-Sills Update—Application of the Finite Element Method to Linear Elastic Fracture Mechanics // Applied Mechanics Reviews. 2010. 63(2):020803-1–020803-17. DOI: https://doi.org/10.1115/1.4000798.
10. Pierpaolo Oreste Back-analysis techniques for the improvement of the understanding of rock in underground constructions // Tunnelling and Underground Space Technology, Volume 20, Issue 1, 2005. P. 7–21. https://doi.org/10.1016/j.tust.2004.04.002.

Theoretical Calculations of Plasmon Spectra for a Rectangle with a Two-Dimensional Electron Gas

Denis V. Fateev, Olga V. Polischuk, and Konstantin V. Mashinsky

Abstract In this work, a method is developed and the excitation spectra of plasmon resonances in a rectangle with a two-dimensional electron gas are calculated. The normal incidence of an arbitrarily polarized electromagnetic wave on a rectangle with a two-dimensional gas is studied. The absorption, extinction, and forward and backward scattering spectra of the incident wave are calculated. The instantaneous distributions of the spatial charge distribution in a plasmon are constructed along a rectangle with a two-dimensional gas. It is found that almost the entire extinction of the incident wave is spent on the absorption of the wave by charges in a two-dimensional electron gas.

Keywords Plasmon · Two-dimensional electron gas · Terahertz

1 Introduction

Many works are devoted to the use of terahertz (THz) plasmons in a two-dimensional electron gas to create THz detecting devices [2, 3]. Theoretical work is usually limited to quasi-electrostatic models because THz plasmons are slow waves. However, the use of such electrostatic approaches loses information about such electrodynamic effects as plasmon-plasmon scattering [4] or an increase in the effective wavelength in plasmon resonators [5], as well as radiative plasmon damping. Another limitation of the existing theoretical approaches is the use of two-dimensional problems, in which the solutions are assumed to be homogeneous and isotropic in the direction in the plane of the two-dimensional electron transverse to the plasmon wave vector. Such approaches are justified for plasmonic structures, the sizes of which in this

D. V. Fateev (✉) · O. V. Polischuk · K. V. Mashinsky (✉)
Kotelnikov Institute of Radio Engineering and Electronics, Russian Academy of Sciences (Saratov Branch), Saratov, Russia
e-mail: fateevdv@yandex.ru

K. V. Mashinsky
e-mail: fateevdv@yandex.ru

© The Author(s), under exclusive license to Springer Nature Switzerland AG 2024

V. Karev (ed.), *Proceedings of the 9th International Conference on Physical and Mathematical Modelling of Earth and Environmental Processes*, Springer Proceedings in Earth and Environmental Sciences, https://doi.org/10.1007/978-3-031-54589-4_69

direction considerably exceed the plasmon wavelength. However, experimentally created samples of single plasmonic THz devices (Knap & Lusakowski, 2004), as a rule, have transverse dimensions not exceeding 20–30 microns, which does not exceed 10 plasmon wavelengths.

In this paper, we developed an algorithm for calculating the resonance spectra of plasmon excitation in a three-dimensional structure—rectangle with a two-dimensional electron gas by the integral equation method.

2 Materials and Methods

A rectangle with a two-dimensional (2D) electron gas is located in a plane separating two dielectric half-spaces with different permittivities. The rectangle has dimensions w, the width in the OY direction is l. An electromagnetic wave of arbitrary polarization in the THz range falls normally on the interface between the media and scatters on a rectangle. The scattered field has evanescent components that excite plasmons in the 2D electron gas. The developed method consists of the following steps. At the first stage, the electric and magnetic fields of the scattered waves were expanded into a dual space Fourier integral in the directions OX and OY, and the dependence of the Fourier components on the z coordinate was assumed to be exponential. Maxwell's equations are solved in semi-infinite dielectric media surrounding a rectangle with a two-dimensional electron gas. Solutions in dielectric media were matched using boundary conditions for the in-plane components of the electric and magnetic fields. It was possible to form integral equations using Ohm's law for currents j_x and j_y in 2D gas, which was described by conductivity in the Drude form σ [4]: The system of integral equations is solved by Galerkin procedure via expanding the unknown currents j_x and j_y in serieses on Legandre polinomials along x and y directions. This allows for transforming the system of integral equations into infinite system of algebraic equations with respect to the expansion coefficients of currents. The system of integral equations is solved by Galerkin procedure via expanding the unknown currents j_x and j_y in serieses on Legandre polinomials along x and y directions. This allows for transforming the system of integral equations into infinite system of algebraic equations with respect to the expansion coefficients of currents. Using calculated currents make it possible to calculate the induced electric and magnetic fields at any point of the structure under consideration.

3 Results

Knowing the induced fields and currents in the structure, the forward and backward scattering cross sections were calculated by integrating the Poynting fluxes in the far fields in the upper and lower half-space (Fig. 1). The absorption cross section of the

structure was calculated by integrating the Joule-Lenz expression over the area of the rectangle (Fig. 1).

The absorption and scattering cross sections together constitute the extinction cross section of the structure. The calculated absorption cross sections have a resonant character, which corresponds to the excitation of various plasmon modes in the structure. It is found that the excited plasmon resonances have a double quantization of the wave vector $q = \sqrt{q_x^2 + q_y^2}$: along x-direction $q_x \approx \frac{\pi}{w} p$, and along y-direction $q_y \approx \frac{\pi}{l} p_1$, p и p_1 are integers. The quantized wave vector therefore has two indices $q_{p,p_1} = \pi \sqrt{\frac{p^2}{w^2} + \frac{p_1^2}{l^2}}$, and therefore the plasmon resonances are characterized by two quantum numbers (p,p_1).

Using the continuity equation, the distribution of the linear charge density

$$\rho = -\frac{i}{\omega}\left(\frac{\partial j_x}{\partial x} + \frac{\partial j_y}{\partial y}\right) \tag{1}$$

is calculated in plasmon resonance along a rectangle with a two-dimensional gas. Instantaneous distributions of charge density at plasmon resonance frequencies 0.4009 THz, 0.7342 THz, 0.9675 THz, and 1.551 THz (Fig. 1) are constructed, which allow drawing conclusions about quantum numbers (Fig. 2). A plasmon at a frequency of 0.4009 THz corresponds to quantization (0,1), at a frequency of 0.7342 THz—(1,0), at a frequency of 0.9675 THz—(2,1), and at a frequency of

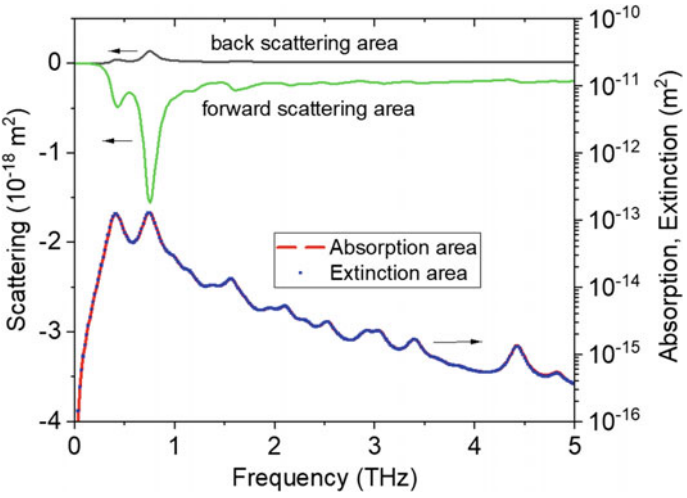


Fig. 1 Spectra of the absorption cross section (red curve), extinction cross section (blue dots), back scattering cross section (black curve), and forward scattering cross section (green curve) for the structure parameters $w = 1$ μm, l $w = 2$ μm. Two dimensional gas was accounted using Drude conductivity with parameters relaxation time 1 ps, electron density $2 \cdot 10^{11} cm^{-2}$, and effective mass 0.067. The electric field vector of the incident wave is directed at an angle of 45 degrees relative to the OX axis

1.551 THz—(1,2). The logarithmic plot of extinction and absorption spectra show that the fundamental plasmon modes with quantization (0,1) and (1,0) are most efficiently excited in the rectangle, while the extinction cross section drops by an order of magnitude or more for higher plasmon resonances. Figures 2 demonstrate a strong accumulation of charge at the edges of the rectangle, which significantly modifies the plasmon modes, which had been calculated using a two-dimensional approach with uniformity along the OY axis. Such charge accumulation is associated with an increase in the electric field at the boundaries of a rectangle with a two-dimensional electron gas, due to the emerging boundary condition, leading to a jump in the normal component of the electric field at the charged interface between the media.

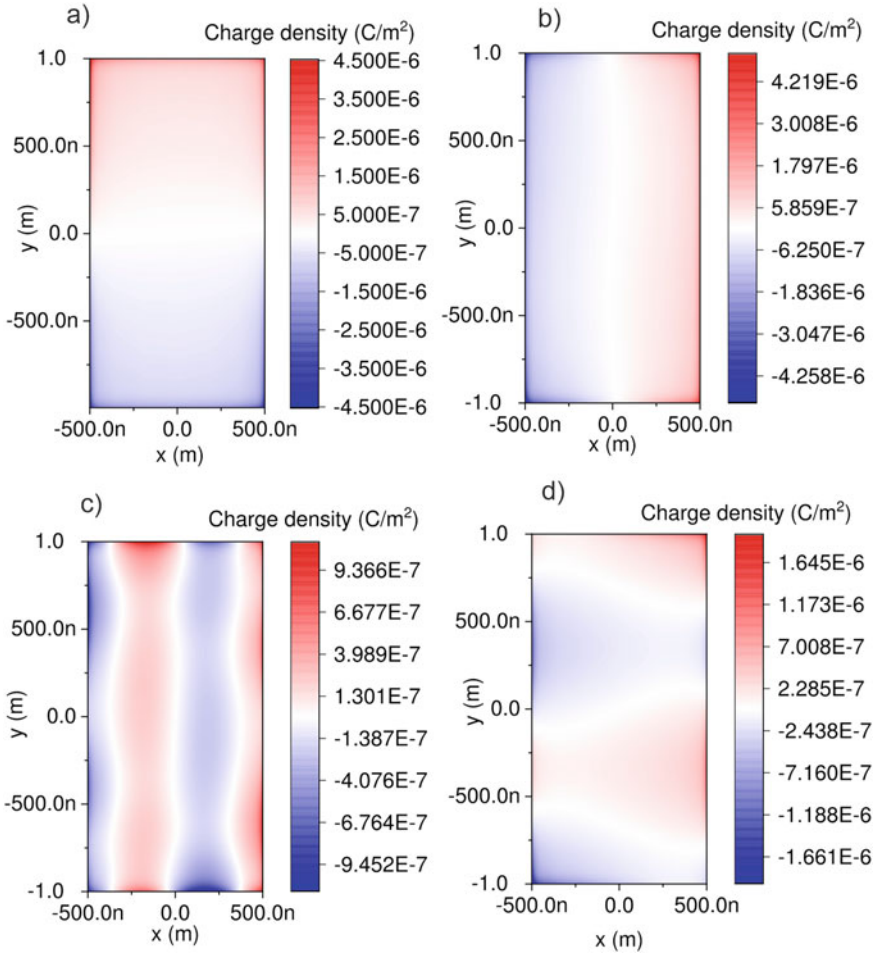


Fig. 2 Instantaneous charge density distributions over the plane of a rectangle with a two-dimensional electron gas in plasmon resonances from Fig. 1 at frequencies: **a** 0.4009 THz, **b** 0.7342 THz, **c** 0.9675 THz, and **d** 1.551 THz

4 Discussion

Note that the incident wave most effectively excites fundamental plasmon resonances, since they have the largest dipole moment. Moreover, the wave extinction cross section consists almost entirely of wave absorption in a rectangle with a two-dimensional electron gas. Therefore, such plasmonic resonators can be used to efficiently convert the energy of an incident wave into plasmons, which can be used, for example, to create THz detectors. However, despite the fact that the forward and backward scattering cross sections are incomparably smaller than the absorption cross sections, they can be used to identify the polarization of the incident wave. Since the scattering cross sections of fundamental resonances with charge oscillations along the short and along the long side differ significantly in magnitude.

5 Conclusion

Thus, in this work, using the developed three-dimensional algorithm for calculating the resonant excitation spectra of plasmons using the integral equation method, we obtained plasmon spectra for a rectangle with a two-dimensional electron gas. The instantaneous spatial distributions of the charge density in plasmon resonances are calculated. It is found that the incident wave most effectively excites the fundamental plasmon modes with quantization (0,1) and (1,0). Plasmon modes show a strong accumulation of charge at the edges of the rectangle, which significantly modifies the plasmon modes and, therefore, requires the use of three-dimensional algorithms instead of the widely used two-dimensional ones.

Acknowledgements This work was supported by the Russian Science Foundation, project № 22-19-00611.

References

1. Knap, W., Lusakowski, J., Parenty, T., Bollaert, S., Cappy, A., Popov, V. V. & Shur. M. S (2004). Terahertz emission by plasma waves in 60 nm gate high electron mobility transistors. *Applied Physics Letters. 84(13)*, 2331.
2. Meziani, Y. M., Handa, H., Knap, W., Otsuji, T., Sano, E., Popov, V. V., Tsymbalov, G. M., Coquillat, D. & Teppe., F. (2008). Room temperature terahertz emission from grating coupled two-dimensional plasmons. *Applied Physics Letters*, *92*, 201108.
3. Popov, V. V. (2011). Plasmon excitation and plasmonic detection of terahertz radiation in the grating-gate field-effect-transistor structures. *J Infrared Milli Terahz Waves*, *32*, 1178–1191.
4. Popov, V. V., Polischuk, O. V. &. Shur, M. S. (2005). Resonant excitation of plasma oscillations in a partially gated two-dimensional electron layer. *Journal of Applied Physics*, *98*, 033510.
5. Popov, V. V., Tsymbalov, G. M., Shur, M. S. & Knap, W., (2005). The resonant terahertz response of a slot diode with a two-dimensional electron channel. *Semiconductors. 39(1)*, 142–146.

Features of the Algorithm for Calculating Induced Currents by an Electromagnetic Wave in a Rectangle with a Two-Dimensional Electron Gas



Denis V. Fateev, Olga V. Polischuk, and Konstantin V. Mashinsky

Abstract In this theoretical work, the developed algorithm for calculating induced currents in a three-dimensional structure with a two-dimensional electron gas is presented using the example of a rectangle. The steps of the method and the basic equations are shown, which make it possible to create a computer program for calculations. The main studies of the convergence of the method, the calculation time are carried out, and the conditions for the convergence of the calculation of higher plasmon resonances in the structure of a rectangle with a two-dimensional electron gas are clarified.

Keywords Integral equation method · Plasmon · Two-dimensional electron gas · Terahertz

1 Introduction

Recently, a wide interest has been shown in the creation of terahertz (THz) devices using two-dimensional plasmons both for the localization and for amplification of electromagnetic fields, and with the application of the nonlinear properties of plasmons [4]. Traditionally, a two-dimensional electron gas is formed during the formation of a quantum well in the conduction band in a semiconductor heterostructures. It is known that, in field-effect transistors with a two-dimensional electronic channel and planar dimensions of micron and submicron range, it is possible to excite THz two-dimensional plasmons [3]. Based on the properties of two-dimensional plasma waves, theoretical studies of THz plasmon effects are solved in a two-dimensional formulation of the problem, considering the direction perpendicular to the propagation of a plasmon to be infinite and homogeneous [1, 5]. Such a statement of the

D. V. Fateev (✉) · O. V. Polischuk · K. V. Mashinsky
Kotelnikov Institute of Radio Engineering and Electronics, Russian Academy of Sciences (Saratov Branch), Saratov, Russia
e-mail: fateevdv@yandex.ru

© The Author(s), under exclusive license to Springer Nature Switzerland AG 2024

V. Karev (ed.), *Proceedings of the 9th International Conference on Physical and Mathematical Modelling of Earth and Environmental Processes*, Springer Proceedings in Earth and Environmental Sciences, https://doi.org/10.1007/978-3-031-54589-4_70

problem greatly simplifies the solutions both in dispersion problems and in problems of excitation of plasmons by an external electromagnetic wave. Such a two-dimensional theoretical approach can be quite applicable to plasmonic structures, in which the lateral size in the direction transverse to the direction of plasmon propagation exceeds the THz plasmon wavelength by an order of magnitude or more, which is quite experimentally achievable in plasmonic structures created on the basis of semiconductor heterostructures. At a typical micron wavelength of a THz plasmon, the size of semiconductor heterostructures can reach several millimeters [2]. However, the dimensions of the created plasmonic structures are often comparable to those of a short wavelength of plasmons, and communication with a long electromagnetic wave is carried out using additional antennas. In structures of such sizes, the influence of edge effects of induced fields on the response of such structures becomes significant and sometimes dominant.

In this paper, the features of the algorithm for calculating the induced currents by an electromagnetic wave in a rectangle with a two-dimensional electron gas, which is a development of the two-dimensional integral equation method, are developed and studied.

2 Materials and Methods

The excitation of a two-dimensional current in a rectangle with a two-dimensional electron gas, on the plane of which an electromagnetic wave of arbitrary polarization is normally incident, is studied. The length of the rectangle in the OX direction is denoted as w, the width in the OY direction is l, and the wave falls on the rectangle in the OZ direction. The OXY plane separates two half-spaces with different dielectric permittivities. The developed method consists of the following steps. At the first stage, the electric and magnetic fields of the scattered waves were expanded into a dual space Fourier integral in the directions OX and OY, and the dependence of the Fourier components on the z coordinate was assumed to be exponential. Maxwell's equations are solved in semi-infinite dielectric media surrounding a rectangle with a two-dimensional electron gas. Solutions in dielectric media were matched using boundary conditions for the in-plane components of the electric and magnetic fields. It was possible to form integral equations using Ohm's law for currents j_x and j_y in 2D gas, which was described by conductivity in the Drude form σ [5]:

$$\begin{cases} j_x(x,y) = \sigma \int_{-l/2}^{l/2} \int_{-w/2}^{w/2} dx'dy' j_x(x',y') G^{xx}_{q_x,q_y}(x,x',y,y') \\ \qquad + \sigma \int_{-l/2}^{l/2} \int_{-w/2}^{w/2} dx'dy' j_y(x',y') G^{xy}_{q_x,q_y}(x,x',y,y') + \sigma Z_{0x} E_{in,x}, \\ j_y(x,y) = \sigma \int_{-l/2}^{l/2} \int_{-w/2}^{w/2} dx'dy' j_x(x',y') G^{yx}_{q_x,q_y}(x,x',y,y') \\ \qquad + \sigma \int_{-l/2}^{l/2} \int_{-w/2}^{w/2} dx'dy' j_y(x',y') G^{yy}_{q_x,q_y}(x,x',y,y') + \sigma Z_{0y} E_{in,y}, \end{cases} \tag{1}$$

where $G^{mn}_{q_x,q_y}(x, x', y, y')$—kernels of integral equations, with $n, m = x, y$, Z_{0x} and Z_{0y} are the Fresnel transmission coefficients. The system of integral equations is solved by Galerkin procedure via expanding the unknown currents j_x and j_y in serieses on Legandre polinomials along x and y directions. This allows for transforming the system of integral equations into infinite system of algebraic equations with respect to the expansion coefficients of currents. The expansion of the unknown currents in a double series in terms of Legendre polynomials was cut off to the order of the polynomial N, taking into account the convergence of the solution

$$\begin{aligned} j_x(\chi'_x, \xi'_y) &= \sum_{n,n1=0}^{N} \beta^{(x)}_{n,n1} P_{n1}(\xi'_y) P_n(\chi'_x) \\ j_y(\chi'_x, \xi'_y) &= \sum_{n,n1=0}^{N} \beta^{(y)}_{n,n1} P_{n1}(\xi'_y) P_n(\chi'_x) \end{aligned} \tag{2}$$

where $P_n(\chi'_{Mx})$ are the Legandre polinomials, $\beta^{(x,y)}_{n,n1}$ are the expansion coefficients of currents, (χ'_{Mx}, ξ'_{My}) are the spatial coordinates (x, y) reduced to the segment $[-1,1]$. Each term on the right side of the equation with the unknown current thus created N^2 equations, and, accordingly, unknown expansion coefficients. The matrix of an algebraic system consists of elements of the form:

$$M_{n1,r1,n,r} = \sigma \frac{lw}{4\pi^2} i^{r_1+r} i^{n+n1} (-1)^{n+n1} W_{n1,r1,n,r} - \frac{\delta_{nr}}{2r+1} \frac{\delta_{n_1 r_1}}{2r_1+1}, \tag{3}$$

where

$$W_{n1,r1,n,r} = \int_{-\infty}^{+\infty} J^{(s)}_{n1}\left(q_y \frac{a}{2}\right) J^{(s)}_{r1}\left(q_y \frac{a}{2}\right) \int_{-\infty}^{+\infty} Z(q_x, q_y) J^{(s)}_{n}\left(q_x \frac{w}{2}\right) J^{(s)}_{r}\left(q_x \frac{w}{2}\right) dq_x dq_y \tag{4}$$

and $Z(q_x, q_y)$ are the admittances of the system, calculated using Maxwell equations, $J_n^{(s)}\left(q_x \frac{w}{2}\right)$ are the spherical Bessel functions, (q_x, q_y) are the wave vectors in Fourier representation, n, $n1$ are the string matrix element indexes, and $и r$, $r1$ are the column matrix element indexes.

3 Results

The total size of the square matrix of the system of equations was $2N^2$. The convergence of the results was determined by comparing the calculated induced currents obtained with a successive increase in the size of the system matrix $2N^2$. A separate necessary condition for the calculations was the convergence of the calculation of the matrix elements, each of which was a dual integration in the space of wave vectors in the directions q_x and q_y. The numerical integration of each such coefficient was calculated taking into account the convergence and under the condition that the integrals in the wave space are split into integration inside the light cone $q_x, q_y \leq \frac{\omega}{c}\sqrt{\varepsilon}$ and outside the light cone $q_x, q_y > \frac{\omega}{c}\sqrt{\varepsilon}$ with ε—the highest dielectric permittivity of the environments. Such a partition was necessary to speed up calculations, since for subwave structures the outgoing and evanescent induced fields have a spatial scale that differs by an order of magnitude or more. The main difference between the developed method and that used in two-dimensional problems is a significant slowdown in calculations in this method due to an increase in the size of the matrix with an increase in the number of Legendre polynomials in the expansion as $2N^2$, compared with two-dimensional problems, where the size of the matrix grows linearly with N. . Double integration in the momentum space when calculating matrix elements also leads to a significant slowdown in calculations, which reduces to one-dimensional integration when solving two-dimensional problems. In this regard, the calculation time for each matrix element of a three-dimensional problem also grows quadratic as compared to two-dimensional solutions. The resulting system of algebraic equations is solved using the Gauss elimination method, by reducing the system matrix to a triangular form. The calculated induced currents made it possible to determine the resonant electrodynamic properties of a rectangle with a two-dimensional electron gas. For this purpose, the extinction area of rectangle with a two-dimensional gas was calculated (Fig. 1). Finding the convergence of the solution showed the need to take into account 12 Legendre polynomials in the expansion of currents to study the first four plasmon resonances. To perform calculations, a program was created in the Fortran programming language. The calculations were performed on a personal computer based on a 10-core processor, which made it possible to calculate the properties of the system at a given frequency in 15 s.

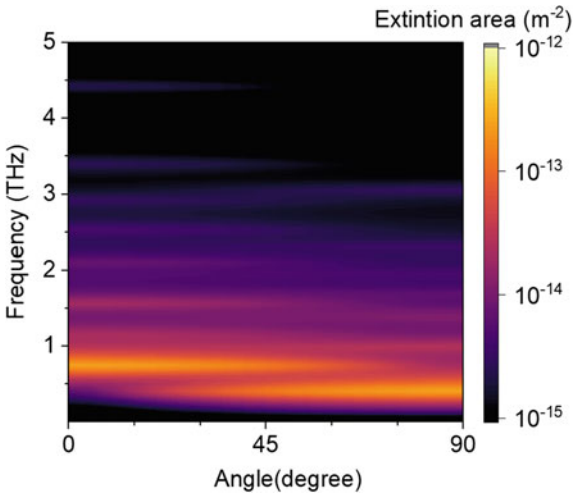


Fig. 1 Dependence of extinction area spectra on the electric field polarization angle of normally incident wave. Parameters of the rectangle are $w = 1\,\mu m$, $l = 2\,\mu m$. Two dimensional gas was accounted using Drude conductivity with parameters: momentum relaxation time 1 ps, electron density $2 \cdot 10^{11} cm^{-2}$, and electron effective mass 0.067

4 Discussion

The calculation results showed the possibility of studying three-dimensional terahertz plasmonic structures containing elements with a two-dimensional electron gas using the developed integral equation method. For calculations, a personal computer with a large number of cores and a programming language with the possibility of full-fledged parallelization of calculations are required. The results of calculations using the developed method, in comparison with the finite element methods, do not carry information about the modes of the solution region. Therefore, the use of this method is expedient in cases where it is necessary to calculate the true resonant conditions for the excitation of plasmons in three-dimensional structures.

5 Conclusion

Thus, in this work, an algorithm for calculating the induced currents by an electromagnetic wave in a rectangle with a two-dimensional electron gas is developed, and programs for calculating these currents are created. Conditions for the convergence of the developed algorithm are found and comparisons are made of the speed of this algorithm with similar algorithms for calculating properties in two-dimensional problems. The developed algorithm makes it possible to more accurately predict the electromagnetic properties of a rectangle with a two-dimensional electron gas compared to commercial programs based on the finite element method, since it does not require the system under study to be placed in the solution domain. And, therefore, the modes of the solution region are not mixed into the true solutions for the system under consideration. The development of the proposed algorithm will allow

us to study multilayer three-dimensional structures, and also, a separate class of problems can be problems with spatial dispersion in a two-dimensional electron gas, which cannot be solved by finite element methods.

Acknowledgements This work was supported by the Russian Science Foundation, project № 22-19-00611.

References

1. Fateev, D. V., Mashinsky, K. V., Polischuk, O. V. & Popov, V. V. (2019). Excitation of propagating plasmons in a periodic graphene structure by incident terahertz waves. *Physical Review Applied*, *11*, 064002.
2. Marem'yanin, K. V., Ermolaev, D. M., Fateev, D. V., Morozov, S. V., Maleev, N. A., Zemlyakov, V. E., Gavrilenko, V. I., Popov V. V. & Shapoval, S. Yu. (2010). Wide-aperture detector of terahertz radiation based on GaAs/InGaAs transistor structure with large-area slit grating gate. *Tech. Phys. Lett.*, *36*, 365–368.
3. Meziani, Y. M., Handa, H., Knap, W., Otsuji, T., Sano, E., Popov, V. V., Tsymbalov, G. M., Coquillat, D. & Teppe., F. (2008). Room temperature terahertz emission from grating coupled two-dimensional plasmons. *Applied Physics Letters*, *92*, 201108.
4. Popov, V. V. (2011). Plasmon excitation and plasmonic detection of terahertz radiation in the grating-gate field-effect-transistor structures. *J Infrared Milli Terahz Waves*, *32*, 1178–1191.
5. Popov, V. V., Polischuk, O. V. &. Shur, M. S. (2005). Resonant excitation of plasma oscillations in a partially gated two-dimensional electron layer. *Journal of Applied Physics*, *98*, 033510.